Transactions of the ASME®

Transactions of the ASME, Journal of Heat Transfer (ISSN 0022-1481) is published quarterly (Feb., May, Aug., Nov.) for $210.00 per year by The American Society of Mechanical Engineers, 345 East 47th Street, New York, NY 10017. Second class postage paid at New York, NY and additional mailing offices. POSTMASTER: Send address changes to Transactions of the ASME, Journal of Heat Transfer, c/o THE AMERICAN SOCIETY OF MECHANICAL ENGINEERS, 22 Law Drive, Box 2300, Fairfield, NJ 07007-2300.
CHANGES OF ADDRESS must be received at Society headquarters seven weeks before they are to be effective. Please send old label and new address. **PRICES:** To members, $40.00, annually: to nonmembers, $210.00. Add $30.00 for postage to countries outside the United States and Canada.
 INDEXED by Applied Mechanics Reviews and Engineering Information, Inc. Canadian Goods & Services Tax Registration #126148048.

Journal of Heat Transfer

Published Quarterly by The American Society of Mechanical Engineers

VOLUME 117 • NUMBER 3 • AUGUST 1995

TECHNICAL PAPERS

Perspective Paper

558 Perspective: Issues in CHF Modeling—The Need for New Experiments
P. Sadasivan, C. Unal, and R. Nelson

Heat Conduction

568 Experimental Evidence of Hyperbolic Heat Conduction in Processed Meat
K. Mitra, S. Kumar, A. Vedavarz, and M. K. Moallemi

574 Prediction and Measurement of Temperature Fields in Silicon-on-Insulator Electronic Circuits
K. E. Goodson, M. I. Flik, L. T. Su, and D. A. Antoniadis

582 Heat Transfer Within a Steel-Reinforced Porous Concrete Slab Subjected to Microwave Heating
W. Li, M. A. Ebadian, T. L. White, and D. Foster

Forced Convection

590 Heat Transfer Enhancement in Narrow Channels Using Two and Three-Dimensional Mixing Devices
S. V. Garimella and D. J. Schlitz

597 Influence of Turbulence Parameters, Reynolds Number, and Body Shape on Stagnation-Region Heat Transfer
G. J. Van Fossen, R. J. Simoneau, and C. Y. Ching

Natural and Mixed Convection

604 Introduction to the Method of Average Magnitude Analysis and Application to Natural Convection in Cavities
P. S. Lykoudis

611 A Thermocapillary Convection Experiment in Microgravity
Y. Kamotani, S. Ostrach, and A. Pline

619 Three-Dimensional Natural Convection in an Enclosure With an Internal Isolated Vertical Plate
M. Yang and W. Q. Tao

626 The First Instability Mechanism in Differentially Heated Cavities With Conducting Horizontal Walls
R. J. A. Janssen and R. A. W. M. Henkes

634 Unsteady Three-Dimensional Natural Convection in an Inclined Air Slot With a Hexagonal Honeycomb Core
Y. Asako, Y. Yamaguchi, T. Yamanaka, and M. Faghri

641 Buoyant Pulsating Exchange Flow Through a Vent
T. A. Conover, R. Kumar, and J. S. Kapat

649 Computation of Turbulent Flow in Mixed Convection in a Cavity With a Localized Heat Source
E. Papanicolaou and Y. Jaluria

659 Combined Buoyancy and Pressure-Driven Flow Through a Shallow, Horizontal, Circular Vent
L. Y. Cooper

668 Natural Convection Heat Transfer in a Rectangular Enclosure With a Transverse Magnetic Field
S. Alchaar, P. Vasseur, and E. Bilgen

Radiative Transfer

674 Thermal Analysis of In-Situ Curing for Thermoset, Hoop-Wound Structures Using Infrared Heating: Part I—Predictions Assuming Independent Scattering
B.-C. Chern, T. J. Moon, and J. R. Howell

681 Thermal Analysis of In-Situ Curing for Thermoset, Hoop-Wound Structures Using Infrared Heating: Part II—Dependent Scattering Effect
B.-C. Chern, T. J. Moon, and J. R. Howell

Boiling Heat Transfer

687 Effects of Dissolved Gas Content on Pool Boiling of a Highly Wetting Fluid
S. M. You, T. W. Simon, A. Bar-Cohen, and Y. S. Hong

693 Heat Transfer During Liquid Contact on Superheated Surfaces
J. C. Chen and K. K. Hsu

698 A Theoretical Model for Flow Boiling CHF From Short Concave Heaters
J. E. Galloway and I. Mudawar

Melting and Solidification

708 Heat Transfer in Excimer Laser Melting of Thin Polysilicon Layers
X. Xu, C. P. Grigoropoulos, and R. E. Russo

716 The Effect of Turbulence on Solidification of a Binary Metal Alloy With Electromagnetic Stirring
P. J. Prescott and F. P. Incropera

Heat Transfer in Porous Media

725 Investigation of Non-Darcian Forced Convection in an Asymmetrically Heated Sintered Porous Channel
G. J. Hwang, C. C. Wu, and C. H. Chao

733 Early Initiation of Natural Convection in an Open Porous Layer Due to the Presence of Solid Conductive Inclusions
A. Delmas and E. Arquis

Heat Pipes

740 Heat Transfer During Evaporation on Capillary-Grooved Structures of Heat Pipes
D. Khrustalev and A. Faghri

TECHNICAL NOTES

748 Transient Thermal Constriction Resistance in a Finite Heat Flux Tube
H. R. B. Orlande and M. N. Özişik

751 Derivation of the Casimir Limit Phonon Distribution Using the Boltzmann Transport Equation
Y. Polsky and Y. Bayazitoglu

755 Heat Conduction Through a Barrier Made of a Suspension of Disklike Particles
P. Furmanski and J. M. Floryan

758 Mean Free Path and Apparent Thermal Conductivity of a Gas in a Porous Medium
S. Q. Zeng, A. Hunt, and R. Greif

762 Analytical Solution for Transient Laminar Fully Developed Free Convection in Open-Ended Vertical Concentric Porous Annuli
M. A. Al-Nimr and T. T. Darabseh

765 An Equation for Laminar Flow Heat Transfer for Constant Heat Flux Boundary Condition in Ducts of Arbitrary Cross-Sectional Area
T. Yilmaz and E. Cihan

767 The Optimal Spacing for Cylinders in Crossflow Forced Convection
A. Bejan

770 Exact Solution of Nonsteady Thermal Boundary Layer Equation
A. S. Dorfman

772 Heat Transfer From a Flat Plate to a Fully Developed Axisymmetric Impinging Jet
D. Lee, R. Greif, S. J. Lee, and J. H. Lee

776 Onset of Flow Reversal and Penetration Length of Natural Convective Flow Between Isothermal Vertical Walls
K. D. Kihm, J. H. Kim, and L. S. Fletcher

779 An Adsorption Model for the Superheat at the Critical Heat Flux
R. Reyes and P. C. Wayner, Jr.

782 Condensation Heat Transfer on Vertical Axis, Axisymmetric, Rotating Surfaces
L. W. Byrd and M. A. Haney

785 Pulsed Laser Heating of Highly Absorbing Particles
J. P. Longtin, T. Q. Qiu, and C. L. Tien

788 The Spectral-Line Weighted-Sum-of-Gray-Gases Model for H_2O/CO_2 Mixtures
M. K. Denison and B. W. Webb

792 Monte Carlo Solutions for Radiative Heat Transfer in Irregular Two-Dimensional Geometries
G. Parthasarathy, H. S. Lee, J. C. Chai, and S. V. Patankar

795 Radiometric Measurements of Wall Temperatures in the 800 K to 1150 K Range for a Quartz Radiant Heating Tube
L. G. Blevins, Y. R. Sivathanu, J. P. Gore, and M. A. Shahien

797 Approximate Formulation for Coupled Conduction and Radiation Through a Medium With Arbitrary Optical Thickness
S. Q. Zeng, A. J. Hunt, R. Greif, and W. Cao

799 Predictions of Void Fraction in Convective Subcooled Boiling Channels Using a One-Dimensional Two-Fluid Model
Lin-Wen Hu and Chin Pan

(Contents continued on page 567)

(Contents continued)

803 Phase Transformation in Materials With Nonuniform Phase Transition Temperatures
Jen Shin Hong and B. Rubinsky

ANNOUNCEMENTS

581 Change of address form for subscribers

596 Announcement: Heat Transfer Memorial Award

806 Information for Authors

Perspective Paper

Perspective: Issues in CHF Modeling—The Need for New Experiments

P. Sadasivan

C. Unal

Engineering and Safety Analysis Group.

R. Nelson

Advanced Reactor Safety Group.

Technology and Safety Assessment Division,
Los Alamos National Laboratory,
Los Alamos, NM 87545

Nucleate boiling and critical-heat-flux (CHF) phenomena have been studied extensively for several decades. However, a satisfactory mechanistic description remains elusive. Although the influences of some system parameters such as heater geometry, body forces, etc., have been elucidated, the influences of several others remain in dispute. In this paper, we present our perspective on the current state of CHF modeling. We list possible parameters that are relevant in the process and discuss the interactions among these parameters. The consequences of such interactions are also discussed. We focus on the simplest configuration—saturated pool boiling on flat heaters. Additional complexities such as orientation effects, flow effects, enhanced surfaces, etc., are not addressed. We highlight specific areas on which we believe experimental efforts should focus to obtain improved mechanistic models of CHF. Experimental techniques used in previous studies are evaluated, and recommendations for new or modified techniques are discussed. We believe CHF must be looked at in the boiling plane (q and ΔT) rather than merely as a single heat-flux point. Mechanistically, this leads us to view CHF as the limiting point of the nucleate boiling region rather than as an independent entity. Experimentally, this means that issues related to the high-heat-flux region must be studied and their effects on CHF investigated.

I Introduction

Over the last several decades, there has been a continued interest in the study of critical heat flux (CHF). The principal reason for this is that accurate prediction of CHF has a number of useful practical applications, mainly in improving the operating efficiencies of heat transfer equipment involving phase change. A plethora of empirical correlations for CHF is now available in the literature, with each applicable to somewhat narrow ranges of experimental conditions. From a mechanistic viewpoint, although the influences of some parameters such as heater geometry, body forces, etc., have been clarified at least to a limited extent, an overall mechanistic description is still unavailable.

We should emphasize that this paper is not intended to be a detailed review of previous work in this field. A number of excellent traditional review articles appear periodically in the literature, the most recent one being that by Katto (1994), and a repetition of such work would serve little purpose. Instead, our objective is to look at the problem on a fundamental level—the various parameters involved in the process and the potential interactions among them.

As just pointed out, the influences of parameters such as gravity, heater material, and heater size have been clarified to varying extents. This was facilitated by the availability of suitable experimental techniques to investigate these aspects. At the same time, those parameters that were not amenable to experimental control and/or measurement were often neglected. Wetting effects and surface temperature effects fall under this category. With rapid advances in instrumentation, many of these parameters are more amenable to control and measurement; indeed, wetting effects recently emerged into consideration. With this in mind, it is useful to take a fresh look at the process uncluttered by equations and specifics of models. Rather we should look at the whole picture, in other words, the forest rather than the trees. If we can identify the various possible parameters involved and their interactions, it would help to focus future experimental efforts toward clarifying specific effects. It is hoped that this exercise would help to initiate a discussion on a basic level. With this in mind, we do not attempt to rank the parameters in any order of importance.

II Current Models

The two major schools of thought that have emerged on the controlling mechanism of CHF are both based on hydrodynamic instability. The main difference between the two approaches is in the location of the instability with respect to the heater. We will use the term "far-field model" to refer to models that focus on the instability in the far-field vapor passages. Similarly, we will use the term "near-surface model" to refer to models that focus on the instabilities in the tiny vapor passages that are postulated to intersperse the liquid-rich macrolayer immediately adjacent to the heater surface.

The far-field model for CHF, originally proposed by Zuber (1958), was the first theoretical formulation of CHF. The fundamental notion of this approach is that CHF is dictated by an instability in the vapor–liquid interface of the vapor jets emanating from the heater surface during nucleate boiling. The onset of instability leads to a breakdown in the process of vapor removal from the heater surface, leading eventually to complete vapor blanketing of the surface. In a power-controlled system, this causes the surface temperature to increase dramatically, whereas in a temperature-controlled system, this causes a slight reduction in the heat flux.

Over the years since the far-field theory was first proposed, the basic idea, together with appropriate configuration-specific

Contributed by the Heat Transfer Division for publication in the JOURNAL OF HEAT TRANSFER. Manuscript received by the Heat Transfer Division December 1994; revision received April 1995. Keywords: Boiling, Measurement Techniques. Associate Technical Editor: R. Viskanta.

modifications, has been used to predict CHF in a variety of situations with fairly remarkable success. Reviews, such as those by Lienhard (1988), Dhir (1990), and Katto (1992), provide detailed accounts of many of these results. It is important to realize that, because of the very nature of this model, the heater surface temperature does not enter into consideration; CHF is solely a function of the hydrodynamics of the vapor flow in the large vapor columns above the heater. The vapor flow from the heater is influenced by two principal factors: the vapor generation at the heater as a result of the heat flux, and the vapor escape path or pattern from the heater surface. Thus, the heater geometry influences CHF through its heat transfer area and the hydrodynamic flow pattern, which the given geometric configuration produces.

One natural consequence of the wide acceptance of the hydrodynamic description of CHF is that many CHF studies concentrate on the measurement of CHF alone, without considering the heater surface temperatures. We believe two somewhat unrelated factors have driven this approach. First, in many practical applications where knowledge of CHF is required, the objective really is to maximize the heat that can be dissipated from a heater to a surrounding cooling fluid. In this respect, the perceived importance of the surface temperature was diminished. The objective was to avoid the transition to film boiling, with the accompanying orders-of-magnitude increases in surface temperature. The actual value of the surface temperature was less important. Second, from an experimental viewpoint, it is far less complicated to develop apparatus to determine CHF alone through measurement of the power input, rather than having to monitor the surface temperatures as well.

Kirby and Westwater (1965) and Yu and Mesler (1977) reported the existence of a thin liquid-rich layer beneath the large vapor mushrooms and on the heater surface itself. The possible role of this so-called macrolayer in nucleate boiling and CHF was not explored for several more years. In 1983, Haramura and Katto (1983) proposed an alternate CHF theory based on the role of the macrolayer. Their model still retained the basic element of the Zuber model—that hydrodynamic instabilities dictate the occurrence of CHF. However, they proposed that the controlling instabilities occur not at the walls of the large vapor columns as envisioned by Zuber but rather at the walls of the tiny vapor stems around active nucleation cavities that intersperse the liquid macrolayer on the heater surface itself. This instability controls the thickness of the macrolayer. If the surface void fraction is known, one can determine how much liquid is present on the heater surface using this value of the macrolayer thickness. Haramura and Katto (1983) proposed that CHF occurs when the heat flux is sufficient to evaporate the macrolayer completely before liquid resupply of the evaporating macrolayer. For simple geometries such as a horizontal flat plate, the resupply time corresponds to the mushroom bubble's lifetime.

Questions have been raised by several investigators over the validity of applying Helmholtz instability considerations to vapor stems with heights on the order of 100 μm as proposed by Haramura and Katto (1983). Further, the role of the heater wall itself in causing or suppressing the instability also is not clear. Haramura and Katto postulate that CHF occurs at the instant the macrolayer dries out during a hovering period. This is inconsistent with the experimental results of, among others, Kirby and Westwater (1965), which show that CHF occurs at one of the dry spots before evaporation of the macrolayer. Despite these and other reservations about the near-surface instability approach, the notion that CHF is controlled by near-surface phenomena reawakened interest in the region close to the heater surface.

One feature of Zuber's model (1958) is that it treats nucleate boiling and CHF as two independent entities—the occurrence of CHF was unrelated to the nucleate boiling region immediately preceding it. This model relates mainly to the liquid side of the picture. Also, although Haramura and Katto's (1983) model focuses our attention on a region nearer the wall, their model also relates only to the liquid side. Although not included by Haramura and Katto, surface characteristics might enter the liquid portion of this picture through surface tension, contact angle, or active nucleation site density.

To any extent, both theories are based on the idea that some adverse event occurs on the liquid side to eliminate the cooling liquid, resulting in the heater surface experiencing a runaway thermal transient. Interestingly enough, neither theory investigates this runaway thermal transient or the phenomena that might be involved with it. If we take the near-surface instability theory as an example, drying of the macrolayer on a thick highly conductive heater, such as copper, some small "epsilon" time just before bubble departure does not result in a thermal runaway (see Unal et al., 1992). Ultimately, the surface does not care because the dry time is small compared with the wet time, and significant heating of the surface cannot occur. A similar argument can be made regarding the far-field instability models; however, the delay in liquid resupply argued within the model is more than that "epsilon" implied by the near-surface instability model. Fundamentally, we do not understand why, if the surface is going to have a thermal runaway, the thermal stability of the surface might not enter into the problem.

It has been shown fairly conclusively by several studies, beginning with Berenson (1962), that all variables affecting nucleate boiling influence the transition boiling region as well. Thus, we have a situation in which some variables essentially are viewed as being relevant in the entire portion of the boiling curve from low-heat-flux nucleate boiling through the transition boiling region, *except at one point in between (i.e., at CHF)*. This seems physically unrealistic. Because CHF occurs as the upper limit of the nucleate boiling region, it is reasonable to expect that the different physical phenomena involved in the nucleate boiling region should interact such that CHF results. A realistic CHF model would be one that is a natural outcome of the description of the high-heat-flux nucleate boiling region. One possible hypothesis would be that basic information currently accepted as being pertinent to the nucleate boiling process, and not to the CHF, rightfully should be important in CHF as well. Even if CHF were purely the consequence of an instability, this does not necessarily mean that it cannot account for possible nonhydrodynamic effects. The conditions that lead to instability could be determined in part by nonhydrodynamic factors relevant to the high-heat-flux regime.

The relevant elements (features and phenomena) of the overall problem can be classified under three broad categories: those that characterize the heater side, those that characterize the fluid side, and those that characterize the heater-fluid interface. There also could be interactions among various elements, both within a category and across categories. As a result of such interactions, modeling CHF in reality is a conjugate problem, unlike the more simplistic scenario envisioned by either the original far-field instability model or the more recent near-surface instability model. To focus our effort better, we will concentrate on the simplest configuration—saturated pool boiling on horizontal flat heaters (see Fig. 1). If the full scope and nature of the CHF mechanism are to be understood, we must first identify the individual effects and then examine the interactions. We will explore our perspective of these issues further in this paper.

We first will look at the individual features and then discuss the consequences of the interactions among them. Experimental techniques that have been and could be used to clarify various effects are discussed. In the end, development of better mechanistic models can be achieved only by obtaining further experimental data to clarify the issues we discussed above. Improved analytical or numerical models will eventually help the practicing engineer to design boiling systems with better efficiencies and eliminate the need to use unduly high factors of safety in the design.

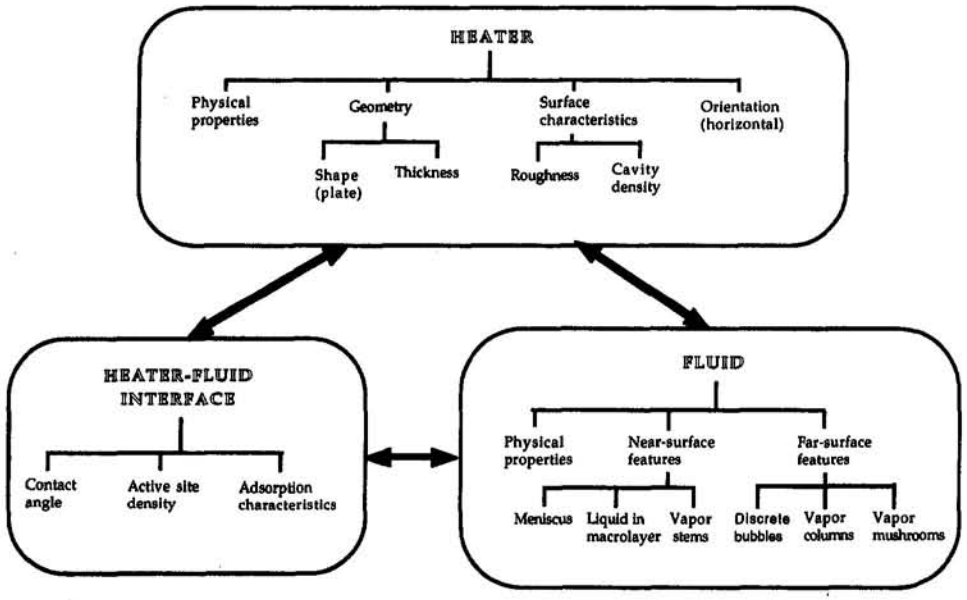

Fig. 1 The conjugate problem in saturated pool boiling CHF on flat heaters

III Heater Side Influences

Figure 1 shows the heater characteristics that we will discuss here. We will divide those further into two rather broad subcategories: one associated with the boiling surface and the other characterizing the heater in general.

(A) Microgeometry of the Heater Surface. The main surface characteristics are: (1) the density and distribution of available cavities, (2) the shape of the cavities, and (3) the roughness of the surface. These factors may not be independent of each other because they are all affected by the method of surface preparation. In boiling experiments, the heater surface is typically prepared to varying surface roughnesses using different grades of emery paper or sand blasting. One open question is whether heater surfaces with sufficiently reproducible site densities can be made. Identical surface preparation methods (such as using the same grade of emery paper in the same mechanical motion) are commonly used as a way to maintain uniformity of surface characteristics from one experiment to another. However, it is not clear if this is sufficient to maintain uniformity in the site density characteristics. The structure of the surface is also influenced by the method used to fabricate the material—the structure could be very different depending on whether the material was fabricated by forging, extrusion, or other methods.

Determining the density and distribution of available cavities on a heater surface is relatively straightforward. Scanning electron microscopy is one commonly used approach. It is also important to address the issue of changes in the cavity distribution as a result of aging of the surface. Formation of oxide layers and other such modifying influences must be tracked.

The interrelationship, if any, between the two characteristics remains unclear. Ramilison et al. (1992) were able to show that proper consideration of the surface roughness as an independent variable could help in part to reconcile differences in the CHF values obtained by several investigators. However, it is not clear if the surface roughness is indeed an independent variable. Further experiments are needed to verify this conclusion. Indeed, the definition of surface roughness is itself debatable. Surface roughness measurements obtained using profilometers may not be an adequate description of the surface because different surface microgeometries could yield similar profilometer results. This is an area where a multidisciplinary approach with material science could prove useful.

A map of all cavities present on the surface is only part of the picture. As is well known, not all of these cavities can become active and nucleate. The heat transfer characteristics in the macrolayer at any heat flux depend directly on the cavities that are active; thus, the dependence on the original cavity distribution is indirect. Although active site density is recognized to play an important role in nucleate boiling, neither the far-field nor the near-surface instability model considers this parameter in their descriptions of CHF. Yet if CHF is to be the natural upper bound of the nucleate boiling regime, we should expect the nucleation site density to be relevant in CHF as well. The density of active cavities at any heat flux is determined by the interaction of several phenomena. This will be discussed further in Sec. V.B.

(B) Geometry and Material Properties. The important characteristics under this category are: (*a*) heater size (length scale), (*b*) heater thickness, and (*c*) heater thermal properties. Heater size effects have been studied extensively and appear to be an issue that is understood well. However, the same is not true of thickness and thermal properties. Many studies assume isothermality of the heater, thus neglecting these effects. Although several studies have shown clearly that CHF on low-thermal-mass heaters such as thin ribbons is dramatically different from that on thicker heaters, a common tendency has been to treat thin ribbons as special cases—cases for which conventional CHF models fail to describe the process adequately (Bergles, 1992).

Heater thermal properties and thickness affect the process of heat conduction through the heater. Although individual studies have shown the effect of heater thickness diminishing as thickness increases or as conductivity increases, it is not clear how these are related to other parameters such as the site density. These parameters also play a role in the interactions between the heater and fluid sides, which in turn could cause transient activation and deactivation of nucleation sites. Such thermal interactions among cavities have been examined for low heat fluxes by Pasamehmetoglu and Nelson (1991) using numerical simulations and by Kenning (1990, 1992) experimentally. Recent numerical studies by Sadasivan et al. (1994) indicate that similar interactions occur in the macrolayer region; however, this has not been validated experimentally.

IV Fluid Side Influences

Figure 1 indicates the fluid characteristics that we will discuss. We will divide these further into three subcategories: one

associated with the fluid properties, the other near-surface (macrolayer) characteristics, and the third characterizing the far-field or flow pattern.

(A) Properties. Conventional hydrodynamic models of CHF recognize the role of fluid thermodynamic properties. These models concentrate solely on such properties and their role in causing hydrodynamic instabilities in large vapor columns over the heater. Fluids commonly used in boiling experiments include water, lower alcohols, and freons. These cover a wide range of physical properties—density ratios, latent heats, and surface tension. The influence of these properties is well recognized. However, their interaction with other parameters such as wetting and site density is an area that needs to be explored further.

Another property generally neglected is fluid viscosity. However, in experimental setups where induced convection in the pool must be considered, fluid viscosity could become important. Differences in data among studies using the same heater–fluid combination could result from differences in the relative size of the heater as compared with the overall cross-sectional dimensions of the liquid pool. Induced convective effects on CHF have been studied by Lienhard and Keeling (1970).

Fluid properties also play a role through their interaction with the heater side. Features of the heater-fluid interface, such as the contact angle, active site density, and adsorption at the periphery of the vapor stem bases, are determined by the interaction of the fluid properties with other features on the heater and fluid sides. This will be discussed further in Sec. V.B, and the effect of contact angle or wetting will be included at various locations within the paper.

(B) Macrolayer. The macrolayer is present in a number of models for pool nucleate boiling [see Pasamehmetoglu et al. (1993) and Fujita (1995) for reviews of present nucleate boiling models]. Also as noted earlier, the near-surface instability model proposed by Haramura and Katto (1983) is based on the role of the macrolayer. Thus, the macrolayer is believed to be important to the process of boiling and possibly CHF. However, the underlying physics associated with its formation is unclear. Currently, it appears that the formation of the macrolayer for moderately wetting fluids may be a result of the lateral coalescence of bubbles before their escape from the boiling surface. This concept has been investigated in modeling efforts by Bhat et al. (1983), Sadasivan et al. (1992), and Shoji and Kuroki (1994). It has been supported by experimental observations by El-Genk and Guo (1992) and Shoji and Kuroki (1994). Although this idea is certainly in its initial stages, it does suggest one way in which active site density might play a role in high-heat-flux nucleate boiling and CHF.

Improved characterization of the macrolayer is one area where advances in instrumentation potentially could be used to great advantage. Gaertner (1965) measured macrolayer characteristics, such as vapor stem diameter and stem spacing, using photography; such an approach clearly would have considerable uncertainty associated with the results. It also would not provide sufficient information on the transient nature of the phenomenon. Dhir and Liaw (1987) deduced vapor stem and related data from their time and area-averaged measurements of void fraction close to the heater surface. The use of area averaging provides only average void fraction values and precludes the identification of local stem characteristics. Also, measurements must be made as close to the heater surface as possible. In their experiments, Dhir and Liaw were unable to approach closer than 400 μm from the heater surface because of increasing uncertainties associated with the densitometric techniques. It currently is not clear how the densitometric measurements could be adapted to make similar measurements closer to the heater surface.

Theoretical analyses commonly assume a simple configuration of vapor stems, such as a square grid. The actual distribution of the stems could be widely different. The main reason is that stems are generally associated with individual nucleation sites, and these sites typically are not distributed over the heater surface in a regular manner. Also, the question of whether the stem configuration in the macrolayer is a steady one or whether it changes over time from transient thermal or hydrodynamic interactions is an open issue.

If we are to obtain a clearer picture of the vapor stem structure in the macrolayer, we must concentrate on making local measurements. One possible way of shedding more light on the macrolayer structure would be to use the conductivity probe approach used by Iida and Kobayasi (1970). However, instead of focusing on the spatial variations in the void fraction and attempting to map the void fraction profile over the entire surface, it is necessary to obtain localized transient data on the output signal of the probe at selected points very close to the heater surface. When such data are obtained at a sufficient number of points, the transient variation of the signal at a given point would provide information about temporal variations in the vapor stem configuration. Obviously, the efficacy of such an approach would depend on the ability to make the probe tips as small as possible. Iida and Kobayasi used a probe tip that was 40 μm in diameter, which imposed a limit on how close to the heater surface they could approach; reducing the size further would enable data to be obtained even closer to the heater surface. Indeed, Inada et al. (1987) used the same technique to obtain void fraction measurements within 2 to 3 μm from the surface. Their results show that the surface void fraction cannot be estimated accurately by extrapolating void fraction data obtained at distances greater than 50 μm from the heater surface. This further underscores the need for making measurements within a few microns of the surface.

The resistance probe technique described by Ragheb and Cheng (1979) and thermocouple probes, such as those used by Yu and Mesler (1977) and Lee et al. (1982), also could be adapted to detect transient variations in the void fraction close to the heater surface. However, these microthermocouple probes suffer from a lack of durability and tend to break frequently. Another possibility is to adapt the fiber-optic probe method developed by Neti et al. (1986) for use above the heater surface. Here the limitations would be the fiber core diameter and the coated diameter. These would have to be as small as current technology would permit.

The role of the vapor stems on the heat dissipation process is another issue that remains unresolved. Several analytical studies of macrolayer heat transfer (Bhat et al., 1983; Prasad et al., 1985, etc.) neglect the vapor stems entirely. On the other hand, the analysis of Dhir and Liaw (1987) assumes that all heat dissipation occurs on the walls of the vapor stems. The model of Pasamehmetoglu et al. (1993) found that the dominant mode of heat dissipation is phenomena associated with the triple phase contact line[1] at the periphery of the base of the vapor stems. Several studies (e.g., Wayner and Coccio, 1971, and Wayner et al., 1976) have shown that the triple contact line, such as is found at the base of the stems, can act as a highly efficient localized heat sink. This is the area where the influences of contact angle become evident as well. Therefore, this area needs more attention. Obviously, experimental resolution of the fine details of the vapor stem bases would be difficult in an actual boiling situation because of the extremely small scales involved. However, it would be possible to gain more information on the triple contact lines and their influence on heat dissipation characteristics by carrying out independent experiments that focus on the meniscus region alone. Because it is known from boiling studies that changes in heater surface material alter the

[1] The reader should realize that the term "line" is used from a macro perspective. If the scale is reduced enough, the "line" is actually a contact region.

contact angle and change the boiling curve, it would be illuminating to investigate these effects in isolated meniscus experiments. Such studies would help to identify the route through which vapor stems do or do not influence the heat transfer process.

For wetting fluids, the presence of a macrolayer or at least a macrolayer with many stems as we tend to envision for the moderately wetting fluids, is less clear. With a highly wetting fluid, the discrete bubble regime of nucleate boiling extends very close to CHF. This will be discussed briefly below as it relates to the far field. Lateral coalescence of these discrete bubbles is just beginning to occur at heat fluxes just below CHF so that some coalesced bubbles as well as discrete bubbles appear on the heater [see Tong et al., (1991) and Carvalho and Bergles (1994)]. The importance of the macrolayer as it relates to nucleate boiling and CHF is currently unclear for these fluids.

(C) Far-Field Flow Pattern. The far-field flow pattern constitutes the kernel of the hydrodynamic instability model of CHF. Zuber and others envisioned vapor flow in the far field in the form of vapor jets or columns and postulated that CHF occurred when these passages broke down as a result of instabilities. The near-surface instability model focused on the macrolayer, but the point to be kept in mind is that the far field does enter into this model as well, through consideration of the hovering period of the mushroom bubbles that cover the macrolayer. The far-field flow patterns can affect the hovering period, which in turn affects the periodicity of replenishment of the macrolayer. In this sense, the far field is relevant in one form or another to both the models.

The presence and role of jets and columns in the far field on CHF need to be revisited. Are they as important as the Zuber model postulates? Or are they as unimportant as the near-surface instability model postulates? Also, what is the connection, if any, between the far-field flow pattern and the behavior of the mushroom bubbles closer to the surface?

It also must be pointed out that wettability, which may be construed as being relevant only to near-surface models, also may affect the far-field patterns. For highly wetting fluids, the discrete bubble region has been observed to extend to higher heat fluxes. Under these conditions, the far field is likely to be still in the form of discrete bubbles with fewer coalesced bubbles or mushrooms. The existence of jets and columns is also unlikely. The change in the flow pattern would appear to occur from at least two sources. First, the highly wetting fluid has an even more effective microlayer at the bottom of each discrete bubble, thus requiring fewer bubbles to remove the heat when compared with a moderately wetting fluid. Second, the bubbles depart at a smaller size because of the decrease in surface tension associated with a highly wetting fluid. These two factors combine to extend the discrete bubble region to higher heat fluxes. These characteristics require further study to define the effects of slightly decreasing wettability, or vice-versa, and the behavior as lateral coalescence begins.

Basic experiments, such as those of Gaertner (1965), must be repeated with modern visualization equipment and clearly defined surfaces and boiling fluids. The fluids and heater surfaces should be chosen to cover a broad range of wetting conditions from highly wetting to nonwetting conditions. The issue of wettability is discussed further in the next section.

V Heater–Fluid Interface

Figure 1 shows the heater–fluid interface characteristics that will be discussed. We will divide these into three subcategories: one associated with the contact angle, another the active site density, and the third characterizing the adsorption characteristics.

(A) Contact Angle. A commonly used parameter to characterize the heater–liquid interface is surface wettability. The static liquid–solid contact angle is the popular measure of this parameter; more fundamental quantities, such as the specific surface energies, also could be used as a measure of the surface wettability. The wettability of a liquid on a given heater material depends on the properties of the heater and the liquid.

Although numerous studies have pointed out the importance of wettability in nucleate boiling, its influence on CHF is less clear. When studying nucleate boiling, the boiling curve usually is observed—both the heat flux and the corresponding heater wall superheat simultaneously—but studies of parametric influences on CHF typically focus on the heat flux alone. Thus, the actual parametric effects on the burnout point—the heat flux and the corresponding wall superheat—could be masked. As an example, consider the pool boiling data of Gaertner (1965) obtained with water and water–salt solutions. Water has a considerably larger contact angle on the copper heater surface used than does the water–salt solution. There is only a small difference in the CHF values for the two cases; however, the wall superheats at CHF differ by almost 80°C. If the site density remains unchanged, the difference in wettability has caused a significant change in the wall superheat at CHF but not in the CHF value itself. This effect clearly could be masked if the heater surface temperature were not monitored in the experiments. This underscores the importance of also monitoring the wall superheat in CHF studies.

From a practical viewpoint, another issue indicates that greater attention should be given to the heater surface temperatures. As mentioned earlier, the old notion was that all we are interested in is how to maximize the heat dissipation capability. However, this could change as newer applications of boiling as a heat removal mechanism emerge. For example, in the application area of electronic cooling, we are interested in dissipating the heat generated while at the same time maintaining component temperatures below acceptable levels.

There are a number of unresolved issues regarding contact angle. It currently is not clear whether the equilibrium contact angle is appropriate for use in typical boiling situations. Some studies have used oxidized surfaces as a means of altering the contact angle. Oxide films have substantially lower thermal conductivity than their parent material, which could alter the thermal behavior of the heater. For small oxide layer thicknesses (on the order of a micron or so), we can expect little effect, but if oxidation is allowed to continue for several hours (as is the case in some studies), the thickness of the oxide layer could be considerably higher. This could alter the thermal behavior, especially for cavity interactions, and allow the possibility of losing some cavities entirely. Also, if meniscus evaporation is the dominant component of heat transfer, a static contact angle would be the more accurate choice if the meniscus generally is stable. If there are oscillations in the meniscus, as has been observed in some cases by Mirzamoghadam and Catton (1988), the contact line moves frequently and the dynamic contact angle may be more appropriate. If dynamic contact angles are appropriate, the issue of advancing and receding contact angles must also be considered.

(B) Active Site Density. The density of active sites on the heater surface is affected by the interaction of several parameters on the heater and liquid sides, as well as the liquid–solid contact angle. The distribution of available cavities on the heater surface and the liquid–solid contact angle determine which cavities potentially could activate. At the same time, the transport properties of the heater affect the extent of the thermal interaction among the cavities, causing activation and deactivation of individual cavities.

As noted in Sec. IV.B, the lateral coalescence of bubbles from neighboring active sites appears to play a role in high-heat-flux nucleate boiling and CHF for moderately wetting fluids. For highly wetting fluids, the generation of discrete bubbles with some lateral coalescence of a limited number of bubbles appears to reflect the active sites. A sufficiently accurate predictive capa-

bility has not yet been developed regarding the active site density. Indeed, Rohsenow (1988) identified this to be one critical area where further work must be done.

Only a few attempts to characterize the site density quantitatively have been reported so far. Gaertner (1965) used his own measurements of site density data to propose that the site density distribution fits a Poisson distribution. Yang and Kim (1988) proposed that the active site density can be expressed in terms of the cavity mouth radius and cone angle. They used a Poisson distribution for the cavity radius and a normal distribution for the cone angle. These approaches still require knowledge of the average cavity density, which must be measured experimentally.

Experimental measurements of active sites in the high-heat-flux nucleate boiling regime are extremely difficult. In the low-flux region, the sites can be counted visually because the vapor escape pattern is still in the form of discrete bubbles. Gaertner (1965) used photographs of the heater surface at low fluxes to obtain active site data. This method should remain useful for highly wetting fluids. However, in the high-heat-flux region for moderately wetting fluids, these bubbles merge to form large vapor mushrooms that obscure the view of the heater surface. Gaertner and Westwater (1960) used nickel salts dissolved in water to detect the presence of nucleation sites. During boiling, nickel was deposited on the heater surface in areas where no active nucleation site was present.

Wang and Dhir (1991) used still pictures of a portion of the heater surface to determine the active site density. At high heat fluxes, they injected small quantities of subcooled water near the surface to condense the vapor mushrooms, thus obtaining a better view of the heater surface. However, they point out that unless extreme care is taken, this method could lead to an underestimation of the number of cavities. This approach still could give reasonable estimates of the site density. Thus, although the numbers may not be exact, such experiments could give valuable information on the trends in the influence of site density on the heat transfer.

Brown (1967) suggested that site density data could be obtained indirectly by studying bubble nucleation from supersaturated solutions. The advantage of this method is that gas bubbles grow much more slowly than vapor bubbles, thus permitting easier and more accurate counting of the sites. This approach later was used with some improvements by Eddington et al. (1978). However, this method has not been proved for high heat fluxes.

Another possibility to consider is the use of artificial cavities generated on a high-quality heater surface where the cavity distribution would be known a priori. This would enable easier identification of the active cavity distribution and sizes.

(C) Adsorption Characteristics. As we pointed out earlier, the triple interface contact line at the base of the vapor stems could act as localized heat sinks because of meniscus evaporation effects. Part of the enhancement in heat transfer in the meniscus region is ascribed to the presence of an extremely thin adsorbed film of liquid on the heater surface. Thus, the adsorption characteristics at the heater–liquid interface become important. Long-range intermolecular forces significantly affect the properties and behavior of thin films. Flow in thin films is primarily driven by a gradient in the "disjoining pressure" (Adamson, 1968). The disjoining pressure is primarily a function of the film thickness, and the nature of the liquid and solid substrate.

The disjoining pressure is related to the film thickness through the Hamaker constant, which is a representation of the various intermolecular forces in the liquid–vapor–solid system. Thus, the proper consideration of meniscus heat transfer requires quantification of the Hamaker constant. Currently, little quantitative information is available on the Hamaker constant for liquid–solid systems commonly used in boiling experiments. This is exacerbated further by the fact that the evaluation of the constant for polar liquids such as water is considerably more complicated than for nonpolar liquids. Lay and Dhir (1994) had to assume a value of the Hamaker constant in their semi-analytical model of heat transfer in the meniscus region. Their paper did not discuss what effect this assumption has on the results. This appears to be an area where multidisciplinary efforts with surface chemists might prove beneficial. The need for experiments on meniscus heat transfer already has been discussed in Sec. IV.B.

VI Interactions

In the preceding section, we discussed the parameters that characterize the heater–liquid interface (see Fig. 1). These effects are determined largely by the interaction of the properties on the liquid and solid side. Such interactions among the various features of the liquid and the heater suggest the possibility that CHF really is a conjugate problem requiring that both heater and liquid side phenomena be considered concurrently. In this section, we will examine other manifestations of the conjugate nature of the problem.

(A) Liquid Resupply. A fundamental difference between the various possible approaches to modeling CHF is in how each approach views the process of supply of liquid to the near-surface region. See Sec. IV.C on fluid far-field flow patterns.

The far-field hydrodynamic model of Zuber (1958) focuses on a structure of large vapor columns above the heater. These columns are assumed to feed into large vapor bubbles above them. The implication is that although a macrolayer may exist on the heater surface, there is sufficient space between the large vapor columns above it that fresh liquid is able to reach the macrolayer continuously. This continuous replenishment is an invariant feature during the boiling process, rendering it irrelevant to the mechanism of CHF.

On the other hand, the near-surface instability theory of Haramura and Katto (1983) assumes that the large vapor bubbles are fed directly from the macrolayer, and because the vapor mushrooms are packed very closely at high heat fluxes, liquid replenishes the macrolayer only intermittently—when one or more vapor bubbles depart the heater region above the macrolayer.

Liquid resupply to the near-surface region is dictated by the process of vapor removal from the surface. This process is determined by the orientation and geometry effects on the heater side, as well as the fluid properties. This aspect also potentially is a connecting link between the near-surface CHF models and the conventional far-surface instability model of Zuber (1958). Although the continuous resupply process implicit in the Zuber model is not supported by experimental data, the vapor columns and possible instabilities on their walls could alter the resupply process.

As outlined earlier, several experimental studies have confirmed that localized dryout of the macrolayer can occur. This is particularly true for moderately wetting fluids and suggests that the scenario of continuous replenishment of the macrolayer is unlikely. If liquid resupply indeed is intermittent, we must consider the effect of intermittent resupply of liquid to the macrolayer next. The nucleate boiling model of Dhir and Liaw (1987) ignores the effect of a periodic resupply of liquid by assuming that the thermal layer is in a steady state. But the experimental measurements of Yu and Mesler (1977), showing periodic drops in the heater surface temperature, suggest that the resupply of liquid to the heater surface disturbs the entire liquid layer. This led Pasamehmetoglu et al. (1993) to assume that the entire macrolayer was replaced. Whether the intermittent resupply of liquid causes the entire superheated liquid from the previous period to be washed away or whether some mixing occurs is an issue that must be resolved. One key area on which

experimental efforts need to be focused is the issue of the dynamics of liquid resupply to the heater surface and the effect of the resupply on the heater and macrolayer liquid temperatures.

The frequency of liquid resupply is related to the hovering period of the mushroom bubbles. Experiments using heaters with dimensions on the order of the Taylor wavelength usually result in a single mushroom bubble over the heater at any time. Similar experiments with larger heaters will result in multiple mushroom bubbles over the surface and will help to identify their effect on the liquid resupply process.

The small scales involved make it difficult to monitor the temperatures in the entire macrolayer. However, rapid-response temperature sensors could be used very close to the heater surface to monitor the transient variation in the macrolayer temperature at selected locations. The efficacy of this method would depend largely on minimizing the size and time constant of the temperature sensors. Fast-response thermocouples with bead sizes on the order of 0.1 μm have been developed by Williams and Wickramasinghe (1986) using sequential deposition techniques. More conventional microthermocouples have somewhat larger bead sizes and consequently poorer response characteristics. As already mentioned, these sensors have relatively poor durability. Also, unless adequate care is taken, measurement errors could result from convective losses from the lead wires. In the event of macrolayer dryout at the location of the sensor, radiation from the heater surface to the thermocouple also could become significant.

(B) Conduction Within the Heater. The fact that heater thermal characteristics and the physical geometry of the heater come into play under some experimental conditions suggests strongly that we give full consideration to the conduction problem within the heater together with the vapor flow characteristics on the liquid side of the heater. This notion of a conjugate problem flies in the face of conventional CHF models outlined earlier. However, this is not an altogether novel idea by any means. Over the years since Zuber's formulation (1958) of his CHF model, there have been limited experimental data to support this notion. For example, in his 1965 paper, Gaertner found a decrease in the slope of the boiling curve in the upper portion of the nucleate boiling region immediately preceding CHF. He attributed this to the formation of dry areas on the heater surface. If dry spots play a role in CHF, then it is natural to expect that the mechanism of CHF must involve the conjugate heat transfer problem.

Kirby and Westwater (1965), van Ouwerkerk (1972), Tong et al. (1991), Carvalho and Bergles (1994), and Gaertner (1965) all observed dry areas on the heater surface. Many of these observations, but not all, are related to highly wetting fluids. The occurrence of dry areas has been attributed to the localized dryout of the macrolayer. It is possible that CHF is the consequence of the rapid growth of these dry areas as suggested by several of the researchers. Unal et al. (1992, 1993) presented numerical results to support this idea. In the absence of adequate experimental validation, it must be considered merely as a hypothesis at this time. However, the arguments are physically sound; therefore, this is an area where further experimental efforts are warranted.

If dry patches form, spatial temperature variations on the heater surface will occur. This issue will be discussed in Sec. VII.C. If CHF is indeed connected with the formation of dry spots or patches on the heater surface, this is a strong argument for the idea that CHF is a natural outcome of the nucleate boiling process. That is, dry regions form on the heater surface in high-flux nucleate boiling, and depending on the overall conduction process within the heater (determined in part by the far-field flow dynamics above the heater surface), the dry regions interact to cause the occurrence of CHF. This suggests that studies purportedly dealing with CHF alone actually should include the high-heat-flux nucleate boiling region as well in their considerations because one is tied closely with the other.

VII Other Issues

This section will discuss issues that do not fit neatly into the previous discussions.

(A) The Second Transition Region. As has been mentioned previously, Gaertner's (1965) experiments with water on copper heaters show a dramatic reduction in the slope of the boiling curve in the high-heat-flux nucleate boiling region before CHF. Gaertner attributed this to the formation of dry patches on the heater surface. This region of reduced slope of the boiling curve, the so-called second transition region, has not been observed consistently in all studies. For this reason, the second transition region often has been suspected of being merely an experimental artifact in Gaertner's experiments (see Dhir, 1990).

It should be noted that Gaertner's data are not the only ones to show a second transition region. Iida and Kobayasi's (1970) pool boiling experiments conducted with water on a thick copper 30-mm-dia heater indicated a boiling curve slope change at high heat fluxes. The data of Katto and Yokoya (1968) and Carvalho and Bergles (1994) also show a similar behavior. Simon and Wu (1993) report observing similar behavior in their flow boiling experiments; they note that the second transition region is more prominent as the heater thickness is increased.

The numerical studies of Unal et al. (1992, 1993) suggested different conditions that must be satisfied simultaneously for the second transition region to be observed. These might serve as useful guidelines for experimenters seeking to prove or disprove the hypothesis.

The analyses of Unal et al. (1992, 1993) used experimental data from several sources—Gaertner (1965), Gaertner and Westwater (1960), and Wang and Dhir (1991). Not all of these studies measured all the relevant parameters involved in their calculations. For example, although Wang and Dhir measured the contact angles, they did not report measurements of vapor stem diameters. Gaertner (1965) reported stem diameters and included contact angles on Teflon-coated surfaces in the discussion section of his paper, but he did not report contact angle values for his copper surfaces. Unal et al. (1992, 1993) assumed that data for the same liquid–heater combination but from different sources could be adjusted heuristically to be used in their study. This obviously increases the uncertainty in their results, but their primary contribution is that they have shown that it is possible to see the second transition region in some cases, yet not see it in other situations.

These considerations suggest that it would not be prudent to conclude that the second transition region is an artifact simply based on the fact that it is not observed in every experiment. A renewed experimental effort in this area with a view toward making all necessary measurements—site density, contact angle, and macrolayer characteristics such as vapor stem distribution and sizes—under the same experimental conditions would be useful. A final conclusion on the existence of, and the possible role of, the second transition region necessarily would have to be deferred until such experimental data became available. It may be worthwhile to undertake relatively simple experiments designed to provide qualitative information on the role of possible dry spots on the heater surface in causing the second transition region. The simplicity or apparent lack of sophistication in these experiments should not detract from their usefulness.

For a moderately wetting fluid (water), Katto and Yokoya (1968) used an interference plate at various distances above the heater surface and postulated that the macrolayer thickness is equal to the separation distance below which the heat transfer

characteristics are affected by the presence of the interference plate. This approach could be easily modified to create localized variations in the macrolayer thickness. Instead of using a large interference plate over the entire heater surface, as Katto and Yokoya did, smaller plates could be positioned extremely close to localized areas over the surface; this would, in effect, limit liquid resupply locally and would cause the formation of dry spots. Comparing the resulting boiling curve data with reference curves obtained without the use of interference plates would shed light on the role of dry spots in causing the second transition region.

As mentioned by Gaertner (1965) and supported by the recent studies of Unal et al. (1992, 1993), the formation of dry patches is related to localized dryout of the macrolayer. Intuitively it would seem that the formation of dry patches will increase the spatial variations in temperature on the heater surface. The macrolayer thickness ultimately is related to the local site-density values. The issues of dry patch formation and its role in the second transition region could be investigated using "synthetic" surfaces prepared such that they have localized high nucleation site densities. Comparing the boiling curve data with reference curves again would provide information on the role of localized high site density areas in the second transition region.

For highly wetting fluids as studied by Carvalho and Bergles (1994), for example, the study of the second transition region may be somewhat easier because of the presence of many discrete bubbles as opposed to the large mushroom bubbles in moderately wetting fluids. Thus, visual means of seeing the dry regions may be possible for small boiling surface.

For larger boiling surfaces using any fluid, the best way to indicate the presence of dry regions may be through the determination of a significant spatial variation of the surface temperature distribution as discussed below.

(B) Importance of Temporal Variations in Surface Temperature. Although it is intuitively clear that the heat flux on the heater surface is of a transient nature because of the periodic nature of the bubble formation and removal processes, the temporal variation in the surface temperature commonly is overlooked. Instead, the common approach is to measure a surface and time-averaged temperature by some means. It currently is clear that the controlling phenomena in nucleate boiling occur over time scales that are on the order of tens of milliseconds. For example, the periodic replenishment of the macrolayer, if any, occurs at a fairly high frequency. Thus, an experiment making only time-averaged measurements of surface temperature would not detect this, whereas a setup rigged appropriately for high-frequency transient temperature measurements would capture this information. Basically, we are leaving out something if we continue to look only at surface and time-averaged values. We must begin looking at temporal variations of temperature if we are to develop complete mechanistic models for CHF and high-heat-flux nucleate boiling.

The small time scales involved in boiling phenomena necessitate the use of sensors with extremely small response times. Gatowski et al. (1989) evaluated several types of surface-temperature sensor. Their results show that embedded sensors, such as the eroding-type thermocouple, platinum thin-film resistance sensor, and vacuum-deposited Bendersky-type thermocouples, could be developed to have response times as low as 0.1 ms. Such low response times make them attractive candidates for use in heater surface thermometry in boiling experiments. Udell et al. (1990) discuss several microsensors for thermometry that appear to be good candidates for use in boiling studies, but such technology appears to be in the developmental stage.

(C) Spatial Temperature Variations on the Heater Surface. Associated with the issue of temporal variations in the temperature are spatial variations in temperature. The common tendency has been to use heaters made of highly conducting materials such as copper and to assume that the high conductivity will cause the heater surface temperatures to be uniform. However, limited experimental data are available to indicate that the instantaneous heater surface temperature could vary over a fairly wide range in the regions close to CHF.

In Sec. VII.A, we discussed possible ways to create localized dry areas on the heater surface. If the heater in these experiments is instrumented with fast-response thermocouples or vapor-deposited film-resistance thermometers at several locations on the surface, a comparison of the transient temperature data at points within and outside the potential dry areas will provide information on the extent of spatial variations in temperature and provide information on whether dry patches form on the heater surface.

Raad and Myers (1971) used liquid crystals coated on the back of a steel heater plate and observed that there are significant temperature variations across the heater. If dry areas are formed, as observed by Gaertner (1965) and others in experiments with thick copper plates, it is quite likely that there could be fairly significant spatial temperature variations on the surface. Also, as suggested by several studies (Judd and Lavdas, 1980; Shoukri and Judd, 1978; Sultan and Judd, 1978), the continuous activation and deactivation of individual nucleation sites could lead to spatial surface temperature variations on the length scale of the spacing between nucleation sites.

Kenning (1990, 1992) analytically showed that spatial variations in the temperature as a result of interactions between individual nucleation sites could be on the same order as the surface superheat. Pasamehmetoglu and Nelson (1991) investigated the interaction between individual sites by looking at the conduction problem within the heater numerically. They found that even in the case of copper, there can be fairly significant nonlinear interaction effects, depending on the spatial distribution of the cavities.

The detection of such small-scale temperature variations is a rather formidable task, especially in the case of heaters of large thicknesses. This is another area where experimental efforts need to focus. Although a transient surface-temperature map of the entire heater surface is most desirable from the point of view of detecting both spatial and temporal variations, obtaining such a map by experimental means is a formidable task. Liquid crystal thermography has been used by Kenning (1990, 1992) and Watwe and Hollingsworth (1994) to map surface temperature. However, this method can be used only with sufficiently thin heaters. Even for thin heaters, current technology in liquid crystals does not permit measurements much above surface temperatures of 100°C, although this upper limit of operating temperatures can be expected to increase over time. The response time of the liquid crystal coating is another limiting factor in such experiments.

For obtaining an overall picture of the surface temperature variations, an alternate approach would be to instrument several sensors on the surface and monitor their output. Yu and Mesler (1977), for example, obtained local surface temperature data, but their experiments focused on a single point on the heater surface and did not include monitoring of the variations in temperature over the heater surface. Using similar sensors at multiple points on the surface would be helpful. However, such an approach should be coupled with visual information to identify liquid-side behavior or with a very large number of point measurements to provide a sufficient ensemble.

Traditionally, temperature measurements are made in a time-averaged sense (as in the case of thermocouples located at points) or in a volume-averaged sense (as in cases where known resistance-versus-temperature relationships of the heater material are used to determine the temperature of electrically heated wires). One approach when using thermocouples is to locate them at various depths from the heater surface and then obtain the surface temperature by solving an inverse conduction problem. However, such an approach clearly would fail to identify

small-scale temporal and spatial variations on the surface. Thus, such averaged measurements may mask the real dynamics of the boiling phenomena on the heater surface. Resolution of the issues relating to the formation and growth of dry patches hinges solely on the availability of detailed experimental observations of the heater surface temperature distribution on a fine scale. Such a detailed microscopic transient set of temperature data also would help to establish more definitively the nature of the second transition region.

VIII Conclusions

In this paper, we attempted to review the current state of CHF modeling efforts by highlighting specific areas on which we believe experimental efforts should focus to obtain an improved mechanistic explanation for CHF. Traditionally, CHF has been viewed as an independent entity and has been treated as a purely hydrodynamic phenomenon distinct from the nucleate boiling region. We make the case for recognizing that CHF is the limiting point of the nucleate boiling region and must be viewed as linked to the high-heat-flux end of the nucleate boiling region. Therefore, experiments dealing with CHF actually will be complete only if they also make measurements of the high-heat-flux nucleate boiling region leading up to CHF. This would, for example, help to resolve the issue of the role of dry area formation and the second transition region on CHF. We must begin looking at CHF in the boiling plane (q and ΔT) rather than merely as a single heat-flux point. Simultaneous measurements of heater surface temperatures are necessary.

Further, we suggest that measurements of heater surface temperatures in an averaged manner (volume and/or time-averaged) actually mask the dynamics of the phenomena. An improved mechanistic explanation of CHF also requires that experimental efforts be directed toward making high-resolution and high-frequency measurements of the heater surface temperatures. Microsensor technology appears to be one area that shows promise in this respect. Experiments also should look at elucidating the role of liquid supply to the heater surface and how this affects the transient variation of heater surface temperatures. Experiments designed to make transient local point measurements of surface temperature and near-surface vapor content will help in developing a clearer picture of the characteristics of the macrolayer.

From our perspective, the areas on which future experimental efforts should focus are as follows:

- **Heater Surface Physical Characteristics:** Identifying the available cavity distribution before the experiments.
- **Active Site Distribution:** With knowledge of the available sites, developing noninvasive site counting methods.
- **Macrolayer Characteristics:** Measuring both the temporal and spatial characteristics of macrolayer at distances of less than 10 μm from the surface; understanding its relationship to CHF.
- **Contact Angle Effects:** Identifying the appropriate measure of wettability to be used—static versus dynamic angles, advancing vs receding angles.
- **Liquid Resupply Effects:** Measuring transient variations in temperature on the heater surface and in the macrolayer region to clarify resupply characteristics. Identifying the effect of multiple mushroom bubbles on resupply by means of experiments with larger heaters.
- **Heater Conduction Effects:** Measuring temporal and spatial variations in the heater surface temperature; clarifying the formation and behavior of surface dry areas in the second transition region and immediately before CHF.
- **Heater Surface Rewetting Characteristics:** Investigating the relation between rewetting temperature and contact angle for different heater–liquid combinations covering a wide range of contact angles.

In closing, we would add two final notes. First, this paper has been limited to the case of saturated pool boiling on a horizontal flat surface. However, we believe this discussion provides the basic structure (see Fig. 1) for extension into other situations. For example, flow affects the vapor removal mechanism and therefore liquid resupplied to the heater surface. Crossflow over a tube geometry produces one characteristic whereas flow along a tube produces another. Second, in the past we have looked for a single model, either the far-field instability model or the near-surface model, to apply in all situations. However, in this search for a "unified" model, have we failed to recognize the possibility that different phenomena might control in different situations? The conjugate problem has a number of phenomena within it.

References

Adamson, A. W., 1968, "An Adsorption Model for Contact Angle and Spreading," *Journal of Colloid and Interface Science,* Vol. 27, pp. 180–187.

Berenson, P. J., 1962, "Experiments on Pool-Boiling Heat Transfer," *Int. J. Heat Mass Transfer,* Vol. 5, pp. 985–999.

Bergles, A. E., 1992, "What Is the Real Mechanism of CHF in Pool Boiling?" *Proceedings of the Engineering Foundation Conference on Pool and External Flow Boiling,* Santa Barbara, CA. pp. 165–170.

Bhat, A. M., Saini, J. S., and Prakash, R., 1983, "Heat Transfer in Nucleate Boiling at High Heat Fluxes," *Int. J. Heat Mass Transfer,* Vol. 26, pp. 833–840.

Brown, W. T., Jr., 1967, "Study of Flow Surface Boiling," Ph.D. Thesis, Department of Mechanical Engineering, MIT, Cambridge, MA.

Carvalho, R. D. M., and Bergles, A. E., 1994, "The Pool Nucleate Boiling Flow Patterns of Vertically Oriented, Small Heaters Boiling on One Side," *10th International Heat Transfer Conference Proceedings,* Heat Transfer 1994, Vol. 5, pp. 25–30.

Dhir, V. K., and Liaw, S. P., 1987, "Framework for a Unified Model for Nucleate and Transition Pool Boiling," ASME JOURNAL OF HEAT TRANSFER, Vol. 111, pp. 739–746.

Dhir, V. K., 1990, "Nucleate and Transition Boiling Heat Transfer Under Pool and External Flow Boiling," *Proc. 9th International Heat Conference,* Vol. 1, pp. 129–155.

Eddington, R. I., Kenning, D. B. R., and Korneichev, A. I., 1978, "Comparison of Gas and Vapor Bubble Nucleation on a Brass Surface in Water," *Int. J. Heat Mass Transfer,* Vol. 21, pp. 855–862.

El-Genk, M. S., and Guo, Z., 1992, "Transient Critical Heat Flux for Inclined and Downward-Facing Flat Surfaces," presented at the 28th National Heat Transfer Conference, San Diego, CA.

Fujita, Y., 1995, "Frontiers in Boiling Heat Transfer," *Proceedings of the ASME/JSME Thermal Engineering Conference,* Maui, HI, Vol. 2, pp. 13–26.

Gaertner, R. F., and Westwater, J. W., 1960, "Population of Active Sites in Nucleate Boiling Heat Transfer," *Chem. Engr. Prog. Symp.,* Ser. 56, pp. 39–48.

Gaertner, R. F., 1965, "Photographic Study of Nucleate Boiling on a Horizontal Surface," ASME JOURNAL OF HEAT TRANSFER, Vol. 87, pp. 17–29.

Gatowski, J. A., Smith, M. K., and Alkidas, A. C., 1989, "An Experimental Investigation of Surface Thermometry and Heat Flux," *Experimental Thermal and Fluid Science,* Vol. 2, pp. 280–292.

Haramura, Y., and Katto, Y., 1983, "A New Hydrodynamic Model of Critical Heat Flux, Applicable Widely to Both Pool and Forced Convection Boiling on Submerged Bodies in Saturated Liquids," *Int. J. Heat Mass Transfer,* Vol. 26, pp. 389–399.

Iida, Y., and Kobayasi, K., 1970, "An Experimental Investigation on the Mechanism of Pool Boiling by a Probe Method," *Proc. Int. Heat Transfer Conf.,* Vol. 5, Paper No. B1.3.

Inada, S., Miyasaka, Y., and Sakumoto, M., 1987, "Heat Transfer of a Liquid–Solid Contact in a Subcooled Pool Boiling Regime (Transition-Type Boiling Regime and Minute Bubble Emission Boiling Regime)," *JSME International Journal,* Vol. 30, pp. 1957–1964.

Judd, R. L., and Lavdas, C. H., 1980, "The Nature of Nucleation Site Interaction," ASME JOURNAL OF HEAT TRANSFER, Vol. 102, pp. 461–464.

Katto, Y., and Yokoya, S., 1968, "Principal Mechanism of Boiling Crisis in Pool Boiling," *Int. J. Heat Mass Transfer,* Vol. 11, pp. 993–1002.

Katto, Y., 1992, "Critical Heat Flux in Pool Boiling," *Proceedings of the Engineering Foundation Conference on Pool and External Flow Boiling,* Santa Barbara, CA, pp. 151–164.

Katto, Y., 1994, "Critical Heat Flux," *Int. J. Multiphase Flow,* Vol. 20, Suppl., pp. 53–90.

Kenning, D. B. R., 1990, "Wall Temperatures in Nucleate Boiling: Spatial and Temporal Variations," *Proceedings of the 1990 International Heat Transfer Conference,* Jerusalem, Vol. 6, pp. 33–38.

Kenning, D. B. R., 1992, "Wall Temperature Patterns in Nucleate Boiling," *Int. J. Heat Mass Transfer,* Vol. 35, pp. 73–86.

Kirby, D. B., and Westwater, J. W., 1965, "Bubble and Vapor Behavior on a Heated Horizontal Plate During Pool Boiling Near Burnout," *Chem. Engr. Prog. Symp.,* Ser. 61, No. 57.

Lay, J. H., and Dhir, V. K., 1994, "A Nearly Theoretical Model for Fully Developed Nucleate Boiling of Saturated Liquids," *Proceedings of 10th International Heat Transfer Conference,* Vol. 5, pp. 105–110.

Lee, L., Chen, J. C., and Nelson, R. A., 1982, "Surface Probe for Measurement of Liquid Contact in Film and Transition Boiling on High-Temperature Surfaces," *Rev. Sci. Instrum.*, Vol. 53, pp. 2053–2059.

Lienhard, J. H., and Keeling, K. B., 1970, "An Induced Convection Effect Upon the Peak Boiling Heat Flux," ASME JOURNAL OF HEAT TRANSFER, Vol. 92, pp. 1–5.

Lienhard, J. H., 1988, "Burnout on Cylinders," ASME JOURNAL OF HEAT TRANSFER, Vol. 110, pp. 1271–1286.

Mirzamoghadam, A. V., and Catton, I., 1988, "Holographic Interferometry Investigation of Enhanced Tube Meniscus Behavior," ASME JOURNAL OF HEAT TRANSFER, Vol. 110, pp. 208–213.

Neti, S., Butrie, T. J., and Chen, J. C., 1986, "Fiber-Optic Liquid Contact Measurement in Pool Boiling," *Rev. Sci. Instrum.*, Vol. 57, pp. 3043–3047.

Pasamehmetoglu, K. O., and Nelson, R. A., 1991, "Cavity to Cavity Interaction in Low Heat Flux Nucleate Boiling," *AIChE J.*, Vol. 87, pp. 342–351.

Pasamehmetoglu, K. O., Chappidi, P. R., Unal, C., and Nelson, R. A., 1993, "Saturated Pool Nucleate Boiling Mechanisms at High Heat Fluxes," *Int. J. Heat Mass Transfer*, Vol. 36(15), pp. 3859–3868.

Prasad, N. R., Saini, J. S., and Prakash, R., 1985, "The Effect of Heater Wall Thickness on Heat Transfer in Nucleate Pool Boiling at High Heat Flux," *Int. J. Heat Mass Transfer*, Vol. 28, pp. 1367–1375.

Raad, T., and Myers, J. E., 1971, "Nucleation Studies in Pool Boiling on Thin Plates Using Liquid Crystals," *AIChE J.* Vol. 17, pp. 1260–1261.

Ragheb, H. S., and Cheng, S. C., 1979, "Surface Wetted Area During Transition Boiling in Forced Convective Flow," ASME JOURNAL OF HEAT TRANSFER, Vol. 101, pp. 381–383.

Ramilison, J. M., Sadasivan, P., and Lienhard, J. H., 1992, "Factors Influencing Burnout on Flat Heaters," ASME JOURNAL OF HEAT TRANSFER, Vol. 114, pp. 287–290.

Rohsenow, W. M., 1988, "What We Don't Know and Do Know About Nucleate Pool Boiling Heat Transfer," *Proceedings of the ASME Winter Annual Meeting*, pp. 169–172.

Sadasivan, P., Chappidi, P. R., Unal, C., and Nelson, R. A., 1992, "Possible Mechanisms of Macrolayer Formation," *Int. Comm. Heat Mass Transfer*, Vol. 19, pp. 801–815.

Sadasivan, P., Unal, C., and Nelson, R. A., 1994, "Non-linear Aspects of High Heat Flux Nucleate Boiling Heat Transfer—Formulation & Results," *Proc. 1994 IMECE*, ASME HTD-Vol. 298, pp. 91–114.

Shoji, M., and Kuroki, H., 1994, "A Model of Macrolayer Formation in Pool Boiling," *10th International Heat Transfer Conference Proceedings*, Heat Transfer 1994, Vol. 5, pp. 147–152.

Shoukri, M. S. M., and Judd, R. L., 1978, "A Theoretical Model for Bubble Frequency in Nucleate Boiling Including Surface Effects," *6th Int. Heat Transfer Conference Proceedings*, Toronto, Canada, PB-6, pp. 145–150.

Simon, T., and Wu, P.-S., 1993, "Flow Boiling Critical Heat Flux on Small Heated Regions," *High Heat Flux Engineering II*, Proceedings of the High Heat Flux Engineering Symposium, Int. Symp. Opt. Appl. Sci. and Engr.

Sultan, M., and Judd, R. L., 1978, "Spatial Distribution of Active Sites and Bubble Flux Density," ASME JOURNAL OF HEAT TRANSFER, Vol. 100, pp. 56–62.

Tong, W., Bar-Cohen, A., and Simon, T. W., 1991, "Investigation of Bubble Flow Regimes in Nucleate Boiling of Highly-Wetting Liquids," *ASME/JSME Thermal Engineering Proceedings*, Vol. 2, pp. 433–439.

Udell, K. S., Pisano, A. P., Howe, R. T., Muller, R. S., and White, R. M., 1990, "Microsensors for Heat Transfer and Fluid Flow Measurements," *Experimental Thermal and Fluid Science*, Vol. 3, pp. 52–59.

Unal, C., Daw, V., and Nelson, R. A., 1992, "Unifying the Controlling Mechanisms for the Critical Heat Flux and Quenching: The Ability of Liquid to Contact the Hot Surface," ASME JOURNAL OF HEAT TRANSFER, Vol. 114(4), pp. 972–982.

Unal, C., Sadasivan, P., and Nelson, R. A., 1993, "On the Hot-Spot-Controlled Critical Heat Flux Mechanism in Saturated Pool Boiling, Part II: The Influence of Contact Angle and Nucleation Site Density," ASME JOURNAL OF HEAT TRANSFER, Vol. 115(3), pp. 813–816.

van Ouwerkerk, H. J., 1972, "Burnout in Pool Boiling: The Stability of Boiling Mechanism," *Int. J. Heat Mass Transfer*, Vol. 15, pp. 25–34.

Wang, C. H., and Dhir, V. K., 1991, "Effect of Surface Wettability on Active Nucleation Site Density During Pool Boiling of Water on a Vertical Surface," *Proc. ASME/AIChE National Heat Transfer Conference*, Minneapolis, MN, ASME HTD-159, pp. 89–96.

Watwe, A. A., and Hollingsworth, D. K., 1994, "Liquid Crystal Thermal Images of Surface Temperature During Incipient Pool Boiling," *J. Exp. Thermal Fluids Science*, Vol. 9, pp. 22–33.

Wayner, P. C., and Coccio, C. L., 1971, "Heat and Mass Transfer in the Vicinity of the Triple Interline of a Meniscus," *AIChE J.* Vol. 17, pp. 569–574.

Wayner, P. C., Kao, Y. K., and LaCroix, L. V., 1976, "The Interline Heat-Transfer Coefficient of an Evaporating Vapor Film," *Int. J. Heat Mass Transfer*, Vol. 19, pp. 487–492.

Williams, C. C., and Wickramasinghe, H. K., 1986, "High Resolution Thermal Microscopy," *Proc. IEEE Ultrasonics Symposium*, Williamsburg, VA, 393–397.

Yang, S. R., and Kim, R. H., 1988, "A Mathematical Model of the Pool Boiling Nucleation Site Density in Terms of the Surface Characteristics," *Int. J. Heat Mass Transfer*, Vol. 31, pp. 1127–1135.

Yu, C. L., and Mesler, R. B., 1977, "Study of Nucleate Boiling Near the Peak Heat Flux Through Measurements of Transient Surface Temperature," *Int. J. Heat Mass Transfer*, Vol. 20, pp. 827–840.

Zuber, N., 1958, "Stability of Boiling Heat Transfer," ASME JOURNAL OF HEAT TRANSFER, Vol. 80, pp. 711–720.

Experimental Evidence of Hyperbolic Heat Conduction in Processed Meat

K. Mitra

S. Kumar

A. Vedavarz

M. K. Moallemi

Department of Mechanical Engineering,
Polytechnic University,
6 Metrotech Center,
Brooklyn, NY 11201

The objective of this paper is to present experimental evidence of the wave nature of heat propagation in processed meat and to demonstrate that the hyperbolic heat conduction model is an accurate representation, on a macroscopic level, of the heat conduction process in such biological material. The value of the characteristic thermal time of a specific material, processed bologna meat, is determined experimentally. As a part of the work different thermophysical properties are also measured. The measured temperature distributions in the samples are compared with the Fourier results and significant deviation between the two is observed, especially during the initial stages of the transient conduction process. The measured values are found to match the theoretical non-Fourier hyperbolic predictions very well. The superposition of waves occurring inside the meat sample due to the hyperbolic nature of heat conduction is also proved experimentally.

Introduction

The traditional Fourier heat conduction equation implies an infinite speed of propagation of the thermal wave, indicating that a local change in temperature causes an instantaneous perturbation in the temperature at each point in the medium, even if the intervening distances are large. To consider the finite speed of wave propagation, a damped wave model is proposed in the literature by using a variety of reasonings and derivations. Its development is presented in detail in the review articles by Joseph and Preziosi (1989, 1990). According to this formulation, the heat flux equilibrates to the imposed temperature gradient via a relaxation phenomenon characterized by a thermal relaxation or thermal characteristic time. From the point of view of heat transfer in materials with nonhomogeneous inner structures such as biological materials, the thermal characteristic time can be defined as the time necessary for accumulating thermal energy required for propagative heat transfer to a particular point in the medium (Kaminski, 1990). The value of this characteristic time is of importance since conduction processes that occur for time periods of the order of the thermal characteristic time may exhibit significant non-Fourier behavior.

Many studies in the literature have considered mathematical solutions to a variety of problems via hyperbolic conduction models (Joseph and Preziosi, 1989, 1990; Wiggert, 1977; Kim et al., 1990; Rastegar, 1989; Kar et al., 1992). Thermodynamic validity of the hyperbolic equations and the range of parameters where non-Fourier considerations are important have also been recently considered (Lavine and Bai, 1994; Vedavarz et al., 1994a, b). The thermal characteristic time for meat products was estimated to be on the order of 20–30 seconds (Kaminski, 1990) but its value has not been measured. In addition, no work is reported that directly validates the hyperbolic nature of heat conduction in biological materials by comparing experimentally observed temperature or flux distributions with the non-Fourier predictions. Recently Tzou (1992) compared the wave solution for the temperature rise induced by a propagating crack tip in steel with the experimental results obtained by Zehnder and Rosakis (1991) to conclude the wave nature of heat conduction.

Four different experiments are reported here for different kinds of boundary conditions. The temperature histories of thermocouples embedded in the samples are recorded and the experimental results show instantaneous jumps in temperatures when the heat waves reach the thermocouples. The phenomenon of superposition of waves occurring due to two heat waves approaching each other from two sides is verified. Both addition and subtraction of waves is observed. By comparing the experimental temperatures with theoretical predictions, the hyperbolic model is shown to be a valid macroscopic representation of the heat transfer in biological materials. The corresponding thermal characteristic time is found to be approximately 16 seconds. This large value of the characteristic time has significant implications in the modeling of many bio-heat transfer processes, especially in those that occur for short durations such as laser surgery.

Experiments Conducted

The value of the thermal characteristic time τ can be calculated theoretically for solids such as metals and dielectrics when the dominant heat carriers are either electrons or phonons (Ashcroft and Mermin, 1976; Vedavarz et al., 1994a). While there is no experimental method to measure the thermal characteristic time directly, the value for processed meat and other bio-materials can be found by measuring the thermal diffusivity and the penetration time. The penetration time, t_p, is the time required for the thermal wave to reach the specified location x_p within the medium. This implies that the velocity of the propagating wave can be determined as follows:

$$v = \frac{x_p}{t_p}. \tag{1}$$

By knowing the wave velocity, the value of τ can be determined from the following relation (Kaminski, 1990):

$$\tau = \frac{\alpha}{v^2}. \tag{2}$$

Here $\alpha = \kappa/\rho C$, where α is the thermal diffusivity, κ the thermal conductivity, ρ the density, and C the specific heat. To calculate the thermal characteristic time for the processed meat, κ, ρ, C, and v are to be measured.

The values of the different thermophysical parameters ascertained experimentally, including their uncertainties, are shown in Table 1. Thermal conductivity is determined by measuring the steady-state axial temperature gradients across cylindrical metallic bars of known thermal conductivities between which the sample is inserted. The temperature distribution is kept one dimen-

Contributed by the Heat Transfer Division for publication in the JOURNAL OF HEAT TRANSFER. Manuscript received by the Heat Transfer Division October 1992; revision received March 1994. Keywords: Conduction, Thermophysical Properties. Associate Technical Editor: R. Viskanta.

sional by insulating the outer cylindrical surfaces of the bar and the sample. The specific heat of the sample is measured by a Differential Scanning Calorimeter (Du Pont Instruments, Module 910 attached with 9900 computer model) over the temperature range of 5 to 30°C. The density is measured by measuring the mass of the sample by a sensitive mass balance and the volume of the sample.

The data acquisition (Model, HP 3497A) used is set on 0–0.1 V range with $5\frac{1}{2}$ digits resolution, implying least count of 1 μV, which corresponds to 0.025°C when a T-type thermocouple is used. The data acquisition is calibrated against a function generator to study its response compared to the various applied pulses. Different pulses such as square wave and sinusoidal are applied and the output of the data acquisition is found to match well with the input signal of the function generator, which is also observed with an oscilloscope. All experiments use copper-constantan (T-type) thermocouples having wire diameter of 0.127 mm (0.05 in.) and a bead diameter of approximately three times the wire diameter. The thermocouples are individually calibrated against an alcohol-in-glass thermometer (having ±0.05°C uncertainty), which ensures an accuracy of ±0.15°C.

The four different experimental configurations and their boundary conditions are schematically depicted in Fig. 1. The processed meat (bologna) samples are in the shape of finite cylinders of approximately 10 cm (4 in.) diameter. The samples are well insulated on all sides (except on the planar sides, which are in contact with each other) to prevent any radial heat flow. Adequate pressure is applied to ensure that perfect contact is established between the thermocouples and the samples and between the different contacting samples. High thermal conductivity grease is applied at the interfaces of contacting samples to eliminate the effect of thermal contact resistance. The thermocouple beads are also coated with thermal grease to enhance contact. The thermocouples are inserted radially so that the leads follow an isothermal path to minimize conduction losses. All the thermocouples are connected to a computerized data acquisition system. The samples that need to be cooled for establishing different initial temperature conditions are refrigerated along with the insulation and the embedded thermocouples to prevent any thermal inertia effects at the initial stages of the experiment. Each experiment is conducted a minimum of three times and the data are reported for one since the deviation between different runs is not phenomenologically significant and the experiments are repeatable. It is ensured that sufficient time elapsed between each experiment so that no temperature gradients are present in the sample.

As a validation of the experimental setup and data collection and processing, two identical aluminum samples (whose dimensions are the same as those of the meat samples) at different temperatures are brought in contact with each other. The measured temperature profiles match the Fourier predictions within the experimental uncertainty of the thermocouples (±0.2°C).

Experiment I. This experiment is conducted to show that heat waves take a finite time to reach a particular point inside the meat sample contrary to the instantaneous heat propagation as predicted by the Fourier model. Two identical meat samples at different initial temperatures are brought into contact with each other. One sample is refrigerated to 8.2°C and the other is at room temperature of 23.1°C. Thermocouples are embedded in the cold sample and in the room temperature sample at distances of 6.6 and 6.3 mm, respectively, from the interface of contact. Thermocouples are also placed at the interface of the two samples.

Table 1 Experimentally measured properties of processed meat

Table 1. Experimentally measured properties of processed meat.		
Variable	Value	Units
Thermal conductivity κ	0.80 ± 0.04	W/m·K
Density ρ	1230 ± 10	kg/m^3
Specific heat C	4.66 ± 0.20	kJ/kg·K
Thermal diffusivity α	$1.40\times10^{-7} \pm 0.12\times10^{-7}$	m^2/s

Experiment II. This experiment is performed to demonstrate the wave superposition phenomenon (addition) occurring when two waves traveling toward each other meet within the sample. Three samples are brought into contact, two large refrigerated ones at 8.5°C and one thin room temperature sample of 17.4°C, so that the thin room temperature sample is sandwiched between the two large refrigerated ones. The room temperature sample, which is between the two cold samples, is much less in thickness than the cold samples to ensure that the heat wave has sufficient amplitude even after traversing the entire thickness of the thin sample. Thermocouples are placed at the interface of the cold and room temperature samples, as well as inside the samples. The thermocouple inside the room temperature sample is at a distance of 3.8 and 5.7 mm from the top and bottom cold samples, respectively.

Experiment III. This experiment is also performed to show wave superposition (subtraction) by using a setup similar to that in the previous experiment, but with initial temperatures selected to cause wave subtraction in the middle sample as opposed to wave addition in the previous experiment. The three samples arranged in the large-thin-large sequence are initially at 24.1°C, 14.3°C, and 6.2°C, respectively. The thermocouple inside the middle sample is at a distance of 3.2 and 7.2 mm from the top and bottom interfaces, respectively.

Experiment IV. This experiment also shows that heat waves have finite propagation speed (cf. Experiment I). A cold meat sample is brought into contact with a warm constant temperature aluminum plate as depicted in Fig. 1(b). The sample along with the insulation is first refrigerated to 8.1°C, which is lower than the temperature of the constant temperature plate maintained at 28.2°C. The temperature of the plate is controlled by circulating a coolant through a pipe network attached to the back of the plate. The coolant temperature is maintained by a constant temperature bath. Thermocouples are placed within the sample at distances of 6.6 and 14.0 mm from the contacting surface, and at the con-

Nomenclature

C = specific heat
d = nondimensional thickness
D = dimensional thickness
h_{cont} = dimensional thermal contact conductance
q = heat flux
Q = nondimensional heat flux
R = nondimensional contact resistance
t = time
t_p = penetration time
T = temperature
v = propagation wave velocity
x = space coordinate
x_p = specified location
α = thermal diffusivity
ζ = nondimensional time
θ = nondimensional temperature
κ = thermal conductivity
ρ = density
τ = thermal characteristic time
χ = nondimensional space coordinates
∇ = gradient

Subscripts

c = cold temperature sample
f = Fourier
i = initial
m = medium temperature sample
r = room temperature sample
ref = reference temperature

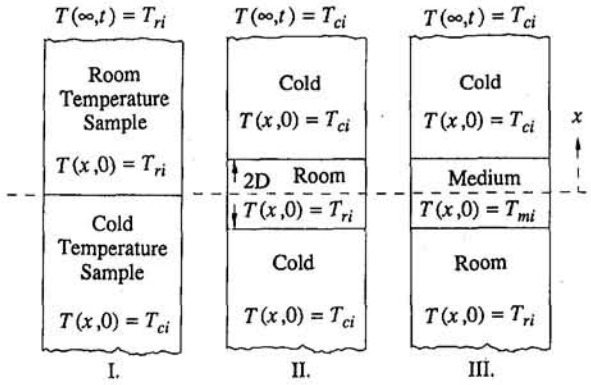

Fig. 1(*a*) Schematic of the experimental conditions for Experiments I, II, and III

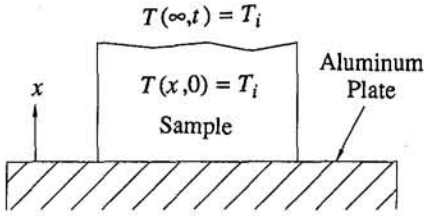

Fig. 1(*b*) Schematic of the experimental conditions for Experiment IV

tact interface. The constant temperature plate also has many thermocouples embedded in it to monitor the plate temperature. The penetration time and propagation wave velocity is measured in the same manner as the experiments above.

Theoretical Profiles

Defining nondimensional variables as

$$\theta = \frac{T - T_i}{T_{\text{ref}} - T_i}, \quad Q = \frac{q\sqrt{\alpha\tau}}{\kappa(T_{\text{ref}} - T_i)}, \quad \chi = \frac{x}{\sqrt{\alpha\tau}}, \quad \zeta = \frac{t}{\tau}, \quad (3)$$

the hyperbolic conduction equation and the energy equation in a one-dimensional coordinate system are written as (Cattaneo, 1958; Joseph and Preziosi, 1989)

$$Q + \frac{\partial Q}{\partial \zeta} + \frac{\partial \theta}{\partial \chi} = 0, \quad \frac{\partial Q}{\partial \chi} + \frac{\partial \theta}{\partial \zeta} = 0. \quad (4)$$

Here θ is the nondimensional temperature, Q the nondimensional heat flux, ζ the nondimensional time, χ the nondimensional space coordinate, t the time, x the space coordinate, T the temperature, q the heat flux, T_{ref} the reference temperature, T_i the initial temperature, κ the thermal conductivity, C the specific heat, ρ the density, α the thermal diffusivity, and τ the thermal characteristic time of the processed meat.

The boundary and initial conditions used for obtaining the theoretical temperature profiles corresponding to the different experiments are shown in Figs. 1(*a*) and 1(*b*). In all the cases considered, the temperatures at large distances from the interface ($|x| \to \infty$) are taken equal to the corresponding initial temperatures. The temperature at the interface of contact between different samples is initially the mean of the adjacent samples, and for Experiment IV the interface temperature is taken as the temperature of the plate T_{plate}. The theoretical hyperbolic temperature profiles corresponding to the boundary and initial conditions of the different experiments conducted are obtained by the method of characteristics using Eq. (4). Details of the method are not presented here for brevity and can be found elsewhere (Wiggert, 1977). The theoretical nondimensional Fourier temperature profiles for the specified experiments are given as (Carslaw and Jaeger, 1959)

$$\theta_f = \text{erfc}\left[\frac{\chi}{2\sqrt{\zeta}}\right], \quad T_{\text{ref}} = \frac{T_{ci} + T_{ri}}{2} \text{ (I)}, \quad T_{\text{ref}} = T_{\text{plate}} \text{ (IV)}, \quad (5)$$

$$\theta_f = \text{erfc}\left[\frac{d + \chi}{2\sqrt{\zeta}}\right] + \text{erfc}\left[\frac{d - \chi}{2\sqrt{\zeta}}\right], \quad T_{\text{ref}} = \frac{T_{ci} + T_{ri}}{2} \text{ (II)}, \quad (6)$$

$$\theta_f = \text{erfc}\left[\frac{d + \chi}{2\sqrt{\zeta}}\right] + \frac{T_{ci} - T_{mi}}{T_{ri} - T_{mi}} \text{erfc}\left[\frac{d - \chi}{2\sqrt{\zeta}}\right], \quad T_{\text{ref}} = \frac{T_{ri} + T_{mi}}{2} \text{ (III)}, \quad (7)$$

where $d = D/\sqrt{\alpha\tau}$ represents the nondimensional thickness of the sample sandwiched between the other two semi-infinite samples.

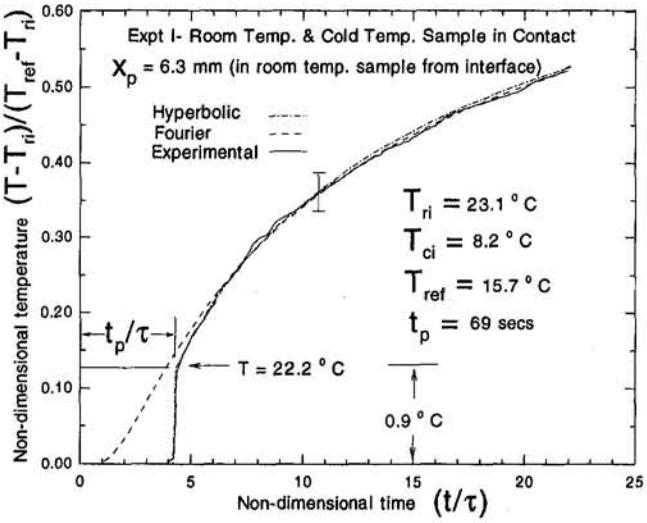

Fig. 2(*a*) Experimental results of nondimensional temperature versus time for Experiment I, for thermocouple at x = 6.3 mm

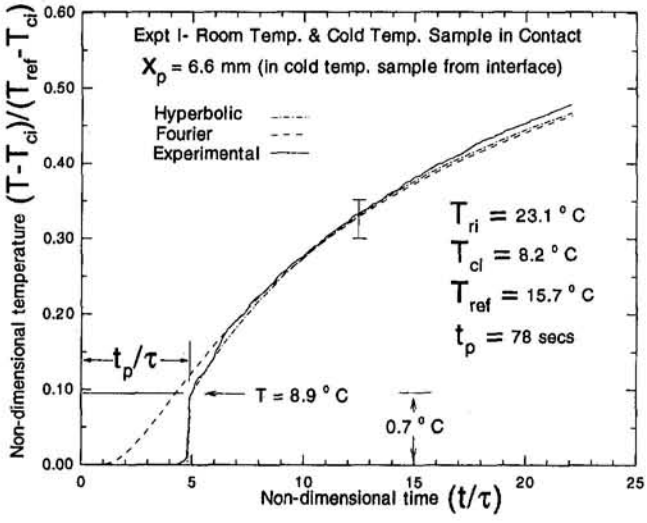

Fig. 2(*b*) Experimental results of nondimensional temperature versus time for Experiment I, for thermocouple at x = 6.6 mm

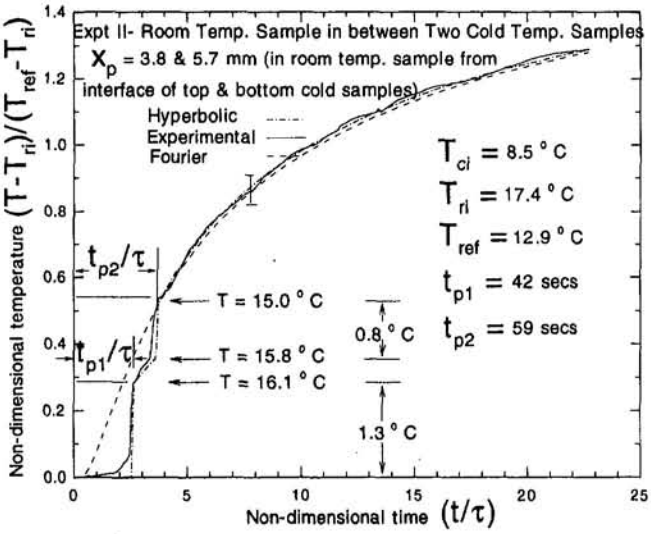

Fig. 3(*a*) Experimental results of nondimensional temperature versus time for Experiment II, for thermocouple at x = 3.8 and 5.7 mm from interface of top and bottom cold samples, respectively

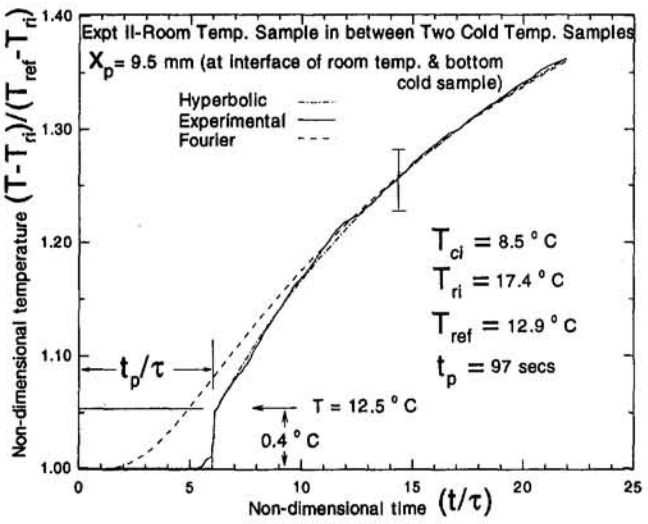

Fig. 3(*b*) Experimental results of nondimensional temperature versus time for Experiment II, for thermocouple at the interface of cold and room temperature samples

Results and Discussion

The results of the experiments described above offer compelling evidence of the wave nature of heat conduction in processed meat (bologna). The fact that a finite time occurs before the thermocouples embedded within the media register any temperature deviations, and that the temperature changes abruptly, indicate a wave behavior of the conduction mechanism in such material. These phenomena are clearly evident from the experimental data of Figs. 2–5. The superposition phenomenon of waves, which occurs due to two heat waves approaching from each other, is also experimentally verified as shown in Figs. 3(*a*) (addition of wave amplitudes) and 4 (subtraction of wave amplitudes).

The value of thermal characteristic time τ has been evaluated experimentally by noting the instant t_p at which the imposed temperature boundary condition causes the thermocouples located at x_p to display a significant deviation (i.e., greater than its uncertainty) from the initial temperature. Equation (1) then determines the propagation velocity v and, along with the values of thermophysical parameters of the sample, the thermal characteristic time is obtained via Eq. (2). The uncertainty in the thermocouple reading is ±0.2°C, and the corresponding uncertainty in the thermocouple position and time readings are 0.3 mm and 0.5 second, respectively. The thermal time constant of the thermocouple is on the order of 0.05 second (Figliola and Beasley, 1991). Using Eqs. (1)–(2) and applying the uncertainty analysis, the value of τ obtained is in the range of 15–17 with an uncertainty of ±2.1 seconds (13.6 percent). The results of the various experiments are tabulated in Table 2. However, it is worth mentioning that out of 38 experimental plots, 28 showed consistent penetration time t_p, 4 showed temperature jumps less than 0.2°C but consistent t_p, 2 showed large irregular jumps but consistent t_p, and 4 showed no jump in temperature.

The theoretical hyperbolic curves in Figs. 2–5 have been generated by the method of characteristics using the mean value of the experimentally determined values of τ, along with the other measured properties presented in Table 1 and 2. The theoretical Fourier curves are obtained via Eqs. (5)–(7).

The results for Experiment I are shown in Figs. 2(*a*) and 2(*b*). The experimental temperature profiles from thermocouples embedded in both the cold and room temperature samples exhibit strong non-Fourier behavior. In case of Experiment II, the results of the thermocouples inside the room temperature sample and at the interface of the cold and room temperature samples are reported in Figs. 3(*a*) and 3(*b*). The experimental data for the thermocouple in the middle sample, Fig. 3(*a*), clearly show two temperature jumps associated with the two wave fronts that originated from the two interfaces. The presence of the two jumps cannot be explained by classical Fourier theory and is only possible if the heat propagation is via heat waves and the jumps are a manifestation of the addition of the two positive amplitude waves via superposition. After the heat wave from one side reaches the point where the thermocouple is placed, it causes a jump in temperature, but the heat wave from the other end has not reached the point. The temperature then continues to increase until a second jump in temperature takes place when the heat wave from the other end of the sample reaches the point where the thermocouple is placed inside the room temperature sample. After that, the temperature continues to rise due to the combined effect of two waves. The result of the thermocouple placed at the interface of the cold and room temperature samples is shown in Fig. 3(*b*). The interface temperature attains the intermediate temperature $(T_{ci} + T_{ri})/2$ at the instant of contact and stays constant at this value until the wave generated by the other interface reaches it. At that instant the temperature exhibits a sharp jump and subsequently varies in accordance with hyperbolic wave pre-

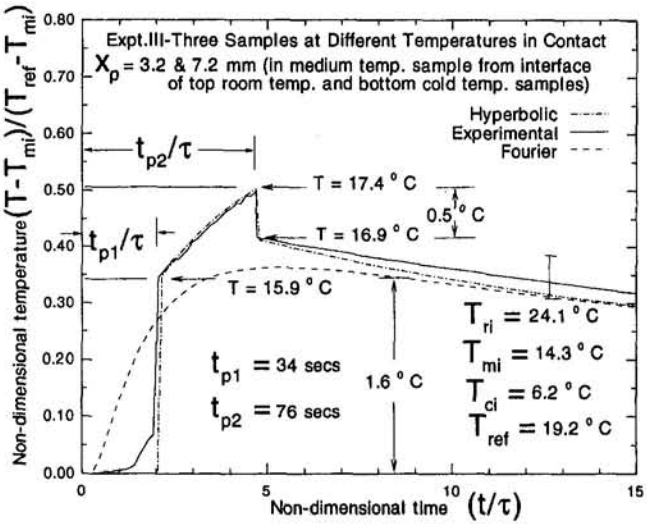

Fig. 4 Experimental results of nondimensional temperature versus time for Experiment III, for thermocouple at x = 3.2 and 7.2 mm from interface of room temperature and cold temperature samples, respectively

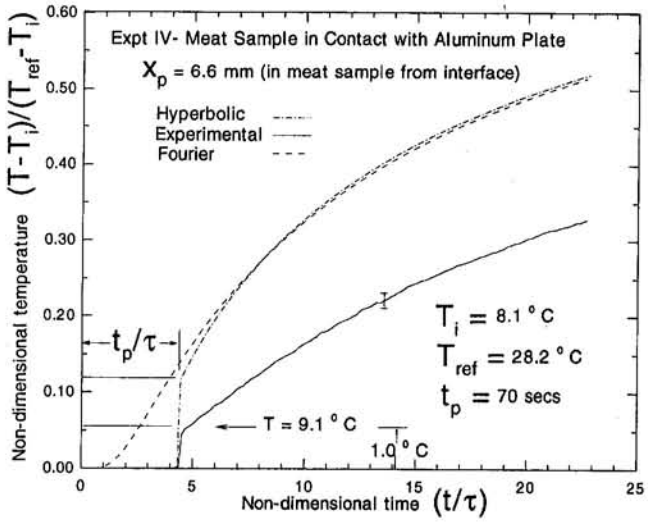

Fig. 5(*a*) Experimental results of nondimensional temperature versus time for Experiment IV, for thermocouple at x = 6.6 mm

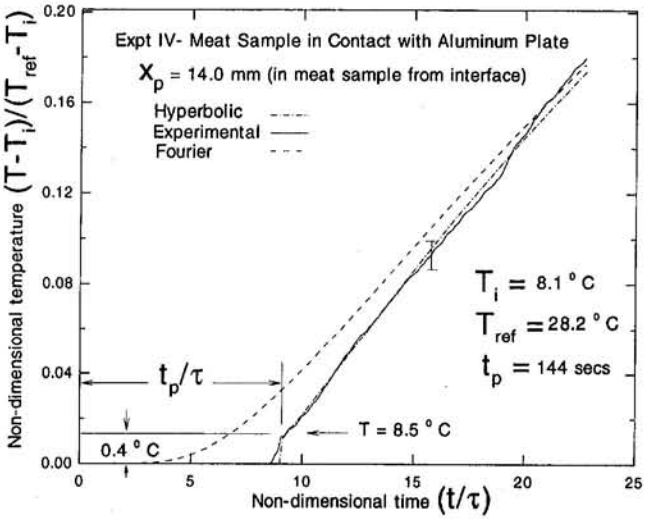

Fig. 5(*b*) Experimental results of nondimensional temperature versus time for Experiment IV, for thermocouple at x = 14.0 mm

dictions. Results similar to Fig. 3(*a*) for the thermocouple embedded in the middle sample are obtained by Experiment III, the difference being the subtraction of waves due to the superposition of a positive and a negative amplitude wave. These experimental results, presented in Fig. 4, cannot be explained via Fourier theory and are matched only by the hyperbolic non-Fourier model.

Experiment IV, which is different from the previous ones by virtue of the different technique for introducing the jump boundary condition, is examined in Figs. 5(*a*) and 5(*b*). The previous experiments relied on the contact between different temperature meat samples to establish the required boundary condition, while Experiment IV uses an aluminum plate that is maintained at a constant temperature via a flow circuit. In Fig. 5(*a*) for Experiment IV, there is a difference between the experimental data and the theoretical hyperbolic heat conduction curves for the thermocouple at x = 6.6 mm. The main problem with this experiment is the inability of the cooling mechanism to instantaneously attain a constant interface temperature between the meat sample and the aluminum plate. During the initial phase of the experiment it is found to be 4–5°C less than the set constant plate temperature. But as time increases, the interface temperature attains that of the specified constant temperature aluminum plate. The experimental data and the theoretical hyperbolic curve match for the thermocouple at x = 14.0 mm as shown in Fig. 5(*b*). This is because

Table 2 Experimentally measured values

Table 2. Experimentally measured values.				
Expt.	TC #	x_p (mm)	t_p (secs)	τ (secs)
I	1	6.3 in room temperature sample	67	15.8
	2	6.6 in cold temperature sample	72	16.6
II	1	3.8 from top cold sample, 1st jump	40	15.5
		5.7 from bottom cold sample, 2nd jump	59	15.1
	2	9.5 from top cold sample at interface	99	15.2
III	1	3.2 from room temperature sample, 1st jump	33	14.9
		7.2 from cold temperature sample, 2nd jump	76	15.6
IV	1	6.6 from aluminum plate	70	15.8
	2	14.0 from aluminum plate	145	15.1
Mean Value of τ = 15.5 ± 2.1 seconds (uncertainty = ± 13.6%).				

the initial deviations of the surface temperature from constant temperature conditions have a lesser influence on the thermocouple further away from the interface due to larger elapsed time as compared to the thermocouple closer to the surface. This is in contrast to Experiments I, II, and III where the theoretical and experimental curves are better matched due to the fact that the interface temperature attains a constant value virtually instantaneously at contact since both cold and warm samples have the same thermal properties. However, the results of the two thermocouples in Experiment IV also show abrupt jumps in temperature and the value of τ obtained from these jumps matches that of the previous experiments. The results of Experiment IV are being presented to show that different techniques yield similar results.

Some possible mechanisms affecting the interpretation of the results within the context of traditional Fourier analysis are examined next. The first is the consideration of thermocouple error. The conservative estimate of uncertainty in the temperature measurement is ±0.2°C (indicated by the error bars of 0.4°C in the corresponding graphs) and that in the time is 0.5 second. Since the measured temperature jumps are consistently much higher than the uncertainty (except for thermocouples placed at large distances from the boundaries where the jump is approximately twice the uncertainty), thermocouple error can be ruled out as a source of the observed trend. In addition, the thermal time constant for the thermocouple is approximately 0.05 second. A second consideration is the effect of thermal contact resistances within a Fourier framework. The jump in temperature that takes place inside the sample may appear to occur due to thermal con-

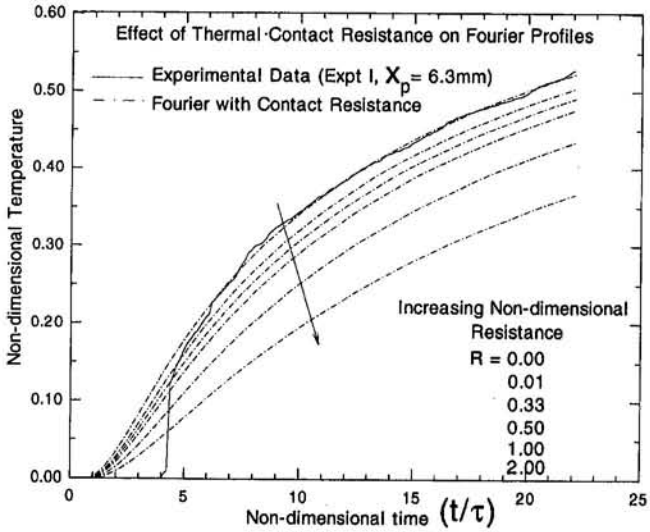

Fig. 6 Effects of thermal contact resistance on Fourier profiles for thermocouple at x = 6.3 mm, for Experiment I

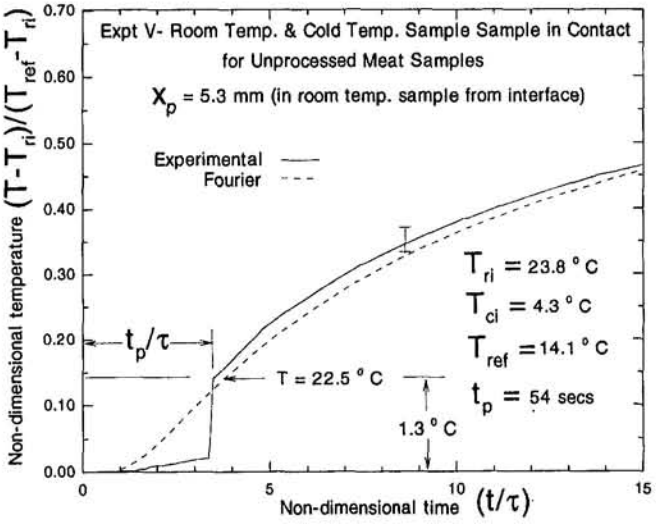

Fig. 7 Results for Experiment V for a thermocouple at x = 5.3 mm in room temperature sample for two raw pork meat samples in contact (similar to Experiment I)

tact resistance at the interface. Figure 6 shows the effects of thermal contact resistances on Fourier profiles for one such thermocouple position at x = 6.3 mm for Experiment I. The theoretical Fourier profiles for the case of two semi-infinite medium in contact with each other having a thermal contact resistance at the interface are generated using the solution given as (Carslaw and Jaeger, 1959)

$$\theta_f = \text{erfc}\left[\frac{\chi}{2\sqrt{\zeta}}\right] - \exp\left(\frac{\chi}{R} + \frac{\zeta}{R^2}\right)\text{erfc}\left[\frac{\chi}{2\sqrt{\zeta}} + \frac{\sqrt{\zeta}}{R}\right], \quad (8)$$

where

$$R = \frac{\kappa}{\sqrt{\alpha\tau}h_{\text{cont}}}. \quad (9)$$

Here R is the nondimensional contact resistance and h_{cont} the dimensional contact conductance (inverse of thermal contact resistance). The results for a given thermocouple location of this solution for various nondimensional contact resistances and the experimental results shown in Fig. 6 depict the fact that the jump in temperature that occurs inside the sample cannot be explained by a thermal contact resistance at the interface.

Conclusions

This paper demonstrates experimentally that the *macroscopic* description of the transient heat conduction processes in biological materials is accurately described by a non-Fourier damped wave model rather than a Fourier model. While the actual *microscopic* description of the conduction processes may be represented by more complicated models, the present hyperbolic non-Fourier description is appropriate for describing *macroscopically* the transient conduction processes in processed meat.

The definitions of the measured thermophysical properties required by the model, such as density, specific heat, and thermal conductivity, remain unchanged from their classical definitions and their magnitudes are obtained by the standard techniques. The values of the thermal characteristic time required by the model are obtained by using these thermophysical properties.

The results and findings presented in the paper have a tremendous impact on the modeling and prediction of bio-heat transfer and lay the foundation for further analyses that will yield better predictive tools for heat and mass transfer processes in complex biological systems. The use of the hyperbolic model of heat conduction, along with the measured values of the thermal characteristic time, for analyzing heat transfer in processed meat (bologna) shows significant difference from traditional Fourier-based results. This indicates that the use of traditional analyses may not be accurate for modeling and predicting heat transfer phenomena in bio-systems. Further research is needed to analyze different kinds of materials, such as the results presented in Fig. 7 for raw pork meat (Experiment V), to establish the effects of hyperbolic conduction in practical applications.

References

Ashcroft, N. W., and Mermin, N. D., 1976, *Solid State Physics*, Saunders Publishing, Philadelphia, PA.

Carslaw, H. S., and Jaeger, J. C., 1959, *Conduction of Heat in Solids*, Oxford Science Publications, pp. 60–90.

Cattaneo, C., 1958, "A Form of Heat Conduction Equation Which Eliminates the Paradox of Instantaneous Propagation," *Comptes Rendus*, Vol. 247, pp. 431–433.

Figliola, R. S., and Beasley, D. E., 1991, *Theory and Design for Mechanical Measurements*, Wiley, pp. 141–178.

Joseph, D. D., and Preziosi, L., 1989, "Heat Waves," *Reviews of Modern Physics*, Vol. 61, pp. 41–73.

Joseph, D. D., and Preziosi, L., 1990, "Addendum to the Paper Heat Waves," *Reviews of Modern Physics*, Vol. 62, pp. 375–391.

Kaminski, W., 1990, "Hyperbolic Heat Conduction Equation for Materials With a Nonhomogeneous Inner Structure," ASME JOURNAL OF HEAT TRANSFER, Vol. 112, pp. 555–560.

Kar, A., Chan, C. L., and Mazumder, J., 1992, "Comparative Studies on Nonlinear Hyperbolic and Parabolic Heat Conduction for Various Boundary Conditions: Analytic and Numerical Solutions," ASME JOURNAL OF HEAT TRANSFER, Vol. 114, pp. 14–20.

Kim, W. S., Hector, L. G., and Özişik, M. N., 1990, "Hyperbolic Heat Conduction Due to Axisymmetric Continuous or Pulse Surface Heat Sources," *Journal of Applied Physics*, Vol. 68, pp. 5478–5485.

Lavine, A. S., and Bai, C., 1994, "Hyperbolic Heat Conduction in Thin Domains," *Thermal Science and Engineering*, Vol. 2, pp. 185–190.

Rastegar, S., 1989, "Hyperbolic Heat Conduction in Pulsed Laser Irradiation of Tissue," *Society of Photo-Optical Instrumentation Engineers, Thermal and Optical Interactions With Biological and Related Composite Materials*, Vol. 1064, pp. 114–117.

Tzou, D. Y., 1992, "Experimental Evidence for the Temperature Waves Around a Rapidly Propagating Crack Tip," ASME JOURNAL OF HEAT TRANSFER, Vol. 114, pp. 1042–1045.

Vedavarz, A., Kumar, S., and Moallemi, M. K., 1994a, "Significance on Non-Fourier Heat Waves in Conduction," ASME JOURNAL OF HEAT TRANSFER, Vol. 116, pp. 221–224.

Vedavarz, A., Mitra, K., and Kumar, S., 1994b, "Hyperbolic Temperature Profiles for Laser Surface Interactions," *Journal of Applied Physics*, to appear.

Wiggert, D. C., 1977, "Analysis of Early-Time Transient Heat Conduction by Method of Characteristics," ASME JOURNAL OF HEAT TRANSFER, Vol. 99, pp. 35–40.

Zehnder, A. T., and Rosakis, A. J., 1991, "On the Temperature Distribution at the Vicinity of Dynamically Propagating Cracks," *Journal of the Mechanics and Physics of Solids*, Vol. 39, pp. 385–415.

K. E. Goodson[1]
Assoc. Mem. ASME

M. I. Flik[2]

Department of Mechanical Engineering.

L. T. Su[3]

D. A. Antoniadis

Department of Electrical Engineering and Computer Science.

Massachusetts Institute of Technology, Cambridge, MA 02139

Prediction and Measurement of Temperature Fields in Silicon-on-Insulator Electronic Circuits

Field-effect transistors (FETs) *in conventional electronic circuits are in contact with the high-thermal-conductivity substrate. In contrast, FETs in novel silicon-on-insulator* (SOI) *circuits are separated from the substrate by a thermally resistive silicon-dioxide layer. The layer improves the electrical performance of SOI circuits. But it impedes conduction cooling of transistors and interconnects, degrading circuit reliability. This work develops a technique for measuring the channel temperature of SOI FETs. Data agree well with the predictions of an analytical thermal model. The channel and interconnect temperatures depend strongly on the device and silicon-dioxide layer thicknesses and the channel–interconnect separation. This research facilitates the thermal design of SOI FETs to improve circuit figures of merit, e.g., the median time to failure* (MTF) *of FET–interconnect contacts.*

1 Introduction

The performance and reliability of electronic circuits are affected by temperature fields in transistors and interconnects. As transistor dimensions decrease, thermal conduction within a few micrometers of these heat sources governs an increasing fraction of the transistor-to-coolant temperature difference in an electronic system. This is very important in novel silicon-on-insulator (SOI) electronic circuits, where transistors are separated from the substrate by a thermally resistive silicon-dioxide layer, often fabricated by implanting oxygen ions into a single-crystal silicon wafer. Figure 1 is a cross section of a SOI field-effect transistor (FET), whose common dimensions are given in Table 1. Almost all of the device power is dissipated in the channel. The electrically insulating implanted layer prevents latchup between devices and reduces the parasitic capacitance of the transistor due to the substrate, facilitating faster circuits (Colinge, 1991). But the implanted silicon-dioxide layer has a low thermal conductivity, and impedes conduction cooling of the channel through the substrate. The SOI circuit designer must know the resulting temperature rise in interconnects and devices.

McDaid et al. (1989) showed that the temperature rise decreased the drain current of a SOI FET for given gate and drain voltages by assuming one-dimensional heat conduction through the implanted layer from an isothermal FET. Goodson and Flik (1992) predicted the temperature field in a SOI FET by treating the source, drain, gate, and interconnects as cooling fins for the Joule-heated channel. They showed that the temperature varies significantly within the FET, and indicated that the temperature rise could reduce the electromigration-limited reliability of interconnects. For application of SOI circuits below 77 K, e.g., in hybrid superconductor-semiconductor circuits, phonon-boundary scattering was shown to influence the temperature field strongly in FETs.

Experimental confirmation of the analysis of Goodson and Flik (1992) requires a technique for measuring temperature locally in transistors with spatial resolution comparable to the channel length, $2L_g$, which can be smaller than 0.5 μm. Lifka and Woerlee (1990) estimated the transistor-to-substrate thermal resistance for SOI circuits through the local melting of a coating, an approach that lacks the needed spatial resolution. Bunyan et al. (1992) used noise thermometry to measure temperatures in SOI transistors. This approach requires experimental structures very different from those in a circuit, yielding an impact on the temperature field that needs to be assessed. For non-SOI semiconductor devices, Brugger (1991) and Ostermeier et al. (1992) performed temperature measurements with submicrometer spatial resolution using micro-Raman spectroscopy. But the impact of the incident radiation on the performance of transistors is not known. The promising method of Majumdar et al. (1993) and Lai et al. (1993) uses an atomic force microscope to determine local temperature fields in circuits. Future research will almost certainly make this method effective for transistors with channel lengths much less than 1 μm.

This work develops a technique to measure the channel temperature of SOI FETs with a resolution in the direction of current flow of 0.32 μm, the FET channel length. The gate serves as an electrical-resistance thermometer for the channel temperature. This approach was used by Mautry and Trager (1990) for bulk (non-SOI) circuits, in which the characteristic length scale of the temperature field is much larger than FET dimensions. The gate is not isothermal in SOI circuits, in which the high thermal resistance of the implanted layer causes a large fraction of the channel-to-coolant temperature difference to occur within transistors. In the present work, thermal analysis yields the average channel temperature from the electrical resistance measured along the nonisothermal gate. Room-temperature data are compared with predictions of the analysis of Goodson and Flik (1992). Analysis estimates the impact of the channel–interconnect separation and the implanted-silicon-dioxide layer thicknesses on the reliability of FET–interconnect contacts.

This work helps to determine the effect of the implanted-layer thermal resistance on the practical potential of SOI technology. The experimental method developed here investigates thermal conduction processes within and very near transistors and interconnects. These conduction processes must be understood before transistor design based on thermal analysis, i.e., *device-level thermal design,* can accompany traditional electrical design of devices to yield circuits of optimal performance and reliability.

2 Thermal Analysis

SOI circuits are made of materials with very different thermal conductivities, shown in Table 2. Goodson and Flik (1992) used the difference in the conductivities to develop a simple thermal

[1] Stanford University, Mechanical Engineering Department, Stanford, CA 94305.
[2] Behr GmbH & Co., Mauserstrasse 3, 70469 Stuttgart, Federal Republic of Germany.
[3] IBM Corporation, East Fishkill Facility, 1580 Route 52 (E40), Hopewell Junction, NY 12533.

Contributed by the Heat Transfer Division and presented at the ASME/AIChE National Heat Transfer Conference, Atlanta, Georgia, August 8–11, 1993. Manuscript received by the Heat Transfer Division September 1993; revision received May 1994. Keywords: Conduction, Electronic Equipment, Measurement Techniques. Associate Technical Editor: R. Viskanta.

model for thermal conduction in SOI circuits. Section 2.1 reviews the analysis and Section 2.2 applies it to the experimental structure.

2.1 Steady-State SOI FET Thermal Model. The model of Goodson and Flik (1992) is for steady-state FET operation, which is the case in most measurements of FET electrical properties. The time required for steady state to be achieved is near $(d_o)^2/(k_o/C_o)$, where k_o/C_o is the thermal diffusivity of silicon dioxide, yielding about 200 ns at 300 K. The model is also useful for the case of steady-periodic power dissipation in clock-driven circuits at points separated from the channel heater by at least one thermal penetration depth. The thermal penetration depth in the silicon source and drain is approximately $(\tau k_d/C_d)^{1/2} = 0.4$ μm, where k_d/C_d is the thermal diffusivity of heavily doped silicon, and $\tau = 5$ ns is a typical clock period.

Heat flow from the tops of devices and interconnects is shown in Section 2.2 to be negligible. The channel was modeled as an isothermal heating source. This neglects the complex distribution of heating intensity in the channel, yielding a small error in the average channel temperature that is estimated at the end of Section 2.1. Variations in the temperature of the substrate–silicon dioxide interface are small compared to the channel-temperature rise. This interface was assumed to have the uniform temperature T_0.

The source, drain, gate, and interconnects were modeled by Goodson and Flik (1992) as one-dimensional cooling fins for the channel, arranged as shown in Fig. 2. The heat loss per unit fin length was assumed to be $h_f w_f (T_f - T_0)$, where T_f is the local fin temperature and w_f is the fin width in the direction normal to heat flow. The heat transfer coefficient is $h_f = \Psi k_o/d_{fo}$, where d_{fo} is the thickness and k_o/d_{fo} is the inverse volume resistance of the silicon-dioxide layer beneath. The dimensionless function Ψ was derived by Goodson and Flik (1992) to account for two-dimensional conduction in the silicon dioxide. The function depends

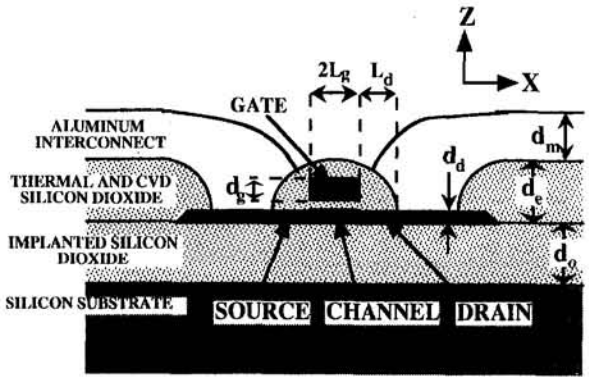

Fig. 1 Cross section of a silicon-on-insulator (SOI) field-effect transistor (FET)

Nomenclature

A = area, m^2
A_f = fin cross-sectional area, m^2
a = characteristic length of test structure, m
C = specific heat at constant volume per unit volume, $J\ m^{-3}\ K^{-1}$
c_p = specific heat at constant pressure per unit mass, $J\ kg^{-1}\ K^{-1}$
d = layer thickness, m
d_e = total thickness of thermally grown and CVD silicon dioxide, m
d_{go} = thickness of silicon-dioxide layer between gate and channel, m
d_o = thickness of implanted-silicon-dioxide layer, m
d_{fo} = thickness of silicon dioxide between fin and substrate, m
E_e = electromigration activation energy, J
$F_G(Y)$ = shape function for temperature distribution in gate
G = channel-to-air thermal conductance, $W\ K^{-1}$
g = acceleration due to gravity, $m\ s^{-2}$
h = heat transfer coefficient, $W\ m^{-2}\ K^{-1}$
I_D = drain current, A
I_G = gate current, A
J = current density, $A\ m^{-2}$
K_e = electromigration constant, s
k = thermal conductivity, $W\ m^{-1}\ K^{-1}$
k_B = Boltzmann constant = $1.38 \times 10^{-23}\ J\ K^{-1}$
k_c = channel thermal conductivity, $W\ m^{-1}\ K^{-1}$
k_o = thermal conductivity of silicon dioxide, $W\ m^{-1}\ K^{-1}$
k_s = thermal conductivity of lightly doped silicon, $W\ m^{-1}\ K^{-1}$
L_d = separation between gate and metal interconnect, m
L_g = half-length of gate in X direction, m
L_m = half-length of interconnect between devices in X direction, m
MTF = median time to failure, s
m = $(h/kd)^{1/2}$ = inverse thermal healing length of fin, m^{-1}
P = device power, W
P_{avg} = time-averaged device power, W
R_c = channel-to-substrate thermal resistance = $1/G$, $K\ W^{-1}$
R_G = electrical resistance of gate in Y direction, Ω
$R_G(T)$ = gate-electrical-resistance calibration function, Ω
T = temperature, K
T_c = average channel temperature, K
$T_G(Y)$ = gate temperature distribution, K
ΔT_G = average temperature rise in gate, K
$T_{m,max}$ = maximum interconnect temperature, K
T_0 = substrate temperature, K
V_G = voltage drop along gate, V
V_{GS} = gate-source voltage drop, V
V_{DS} = drain-source voltage drop, V
v = air velocity, $m\ s^{-1}$
w_f = fin width in X–Y plane, m
w_d = channel width in Y direction, m
w_c = separation between channel and gate contacts in Y direction, m
w_m = width of metal interconnect in Y direction, m
X = coordinate in plane of substrate, m
Y = coordinate in plane of substrate, m
Z = coordinate normal to plane of substrate, m
Z_1, Z_2, Z_3, Z_4 = constants, Eqs. (1)–(4)
β = coefficient of thermal expansion, K^{-1}
ϵ = emissivity
μ = viscosity, $kg\ m^{-1}\ s^{-1}$
ρ = mass density, $kg\ m^{-3}$
σ = Stefan–Boltzmann constant = 5.67×10^{-8} $W\ m^{-2}\ K^{-4}$
τ = clock period, s
Ψ = two-dimensional conduction function

Subscripts

d = property or dimension of source and drain
f = property or dimension of fin
g = property or dimension of gate
m = property or dimension of metal interconnect
o = property or dimension of silicon dioxide layer

Table 1 Common dimensions of SOI FET devices and those of the test structures used here

Dimensions	In FET (μm)	In Test Structure (μm)
implanted-SiO_2 thickness, d_o	0.4	0.293 - 0.503
additional-SiO_2 thickness, d_e	0.60	0.60
interconnect thickness, d_m	0.5	1
device thickness, d_d	0.08	0.041 - 0.177
gate thickness, d_g	0.30	0.29
gate-channel separation, d_{go}	0.0055	0.0055
channel-interconnect separation, L_d	0.5	0.8 - 3.8
gate half-width, L_g	0.25	0.16
device width, w_d	0.8	10
channel-gate contact separation, w_e	2	2

Table 2 Thermal conductivities of SOI circuit materials. These values are discussed in Section 2.2. The channel thermal conductivity was not used by Goodson and Flik (1992), but is needed in Section 3.2 for the analysis of the experimental data.

Region or Component	Material	Thermal conductivity at T_0 = 303 K (W m^{-1} K^{-1})
substrate	single-crystal silicon, 3 x 10^{15} boron atoms cm^{-3}	$k_s = 148^*$
channel	single-crystal silicon 6 x 10^{17} boron atoms cm^{-3}	$k_c = 148^*$
source and drain	single-crystal silicon, 1 x 10^{20} arsenic atoms cm^{-3}	$k_d = 63^*$
gate	polysilicon, 1 x 10^{20} arsenic atoms cm^{-3}	$k_g = 30^{**}$
interconnect	aluminum, 1 mass-percent silicon	$k_m = 239^*$
SOI implanted layer	silicon dioxide, implanted	$k_o = 1.40^{***}$
other insulating layers	silicon dioxide, thermally grown and CVD	$k_o = 1.40^{***}$

*Touloukian et al. (1970) **Tai et al. (1988) ***Sugawara (1969)

only on the ratio of the width of the fin and the thickness of the thermally resistive layer below the fin. The values of Ψ used here range between 1.016 and 1.028 for conduction from the source and drain, between 1.051 and 1.064 for conduction from the interconnects, and between 2.349 and 2.925 for conduction from the gate. The largest Biot numbers for the test structures in the present manuscript, $d_f h_f / k_f$, where k_f and d_f are the fin conductivity and thickness, are 0.028 for the source and drain fins, 0.029 for the gate fin, and 0.00782 for the interconnect fins. The fin thermal healing length is $1/m = (kA_f/hw_f)^{1/2}$, where k and A_f are the thermal conductivity and cross-sectional area of the fin. The distance from a heating source over which the fin temperature recovers to the substrate temperature is of the order of the healing length. The healing lengths are $1/m_m = (k_m d_m/h_m)^{1/2} \sim 7$ μm for the interconnects, $1/m_d = (k_d d_d/h_d)^{1/2} \sim 1$ μm for the source and drain, and $1/m_g = (k_g d_g/h_g)^{1/2} \sim 1.5$ μm for the gate.

The length in the X direction of the contact between the interconnect and the drain is approximately 3 μm. Because this length is substantially smaller than the healing length of the interconnect fins, Goodson and Flik (1992) neglected the different heat transfer coefficient between the interconnect and the substrate over this length. A single fin is used for the interconnect and the contact region with the heat transfer coefficient that prevails when the interconnect is above the thermal and CVD silicon-dioxide layers. This slightly overestimates the thermal resistance between the channel and substrate, but substantially simplifies the analysis.

The width of the interconnect, source, and drain fins in the Y direction, 10 μm, is larger than the healing length in these fins. This makes possible significant temperature variation in this direction, which is not considered by the present fin analysis. Temperature variation due to conduction from the sides of these fins is small because the thermal resistance for conduction by a unit area through one healing length in the fin, approximately $(d_o d_f)^{1/2}/(k_o k_f)^{1/2}$, is much smaller for each fin than the thermal resistance for conduction from a unit area of the fin side to the substrate, approximately d_o/k_o. But temperature variation in the Y direction due to conduction through the gate fin is significant. The error is estimated using an analytical solution to the three-dimensional thermal-conduction equation in the implanted silicon-dioxide layer and the channel, source, and drain. The difference between the conductivity of the channel and that of the source and drain is neglected and the source and drain fins are assumed to be very long in the X direction. Heat generation in the channel is modeled using a uniform heat-flux boundary condition at the top surface of the channel. Heat loss to the gate is modeled using a heat flux condition from the top of the channel near the edge, $w_d - d_d \le |Y| \le w_d$. The average channel temperature rise is slightly larger than those calculated by neglecting temperature variation in the Y direction in the channel, which is the approximation of the simple multifin analysis used in this manuscript. The relative error in the predictions given here is less than 3 percent for a channel width $w_d = 0.3$ μm and less than 7 percent for $w_d = 10$ μm.

The devices were assumed to be in an infinite linear array, each connected by an interconnect of length $2L_m$, and each dissipating the same power P. This idealization resulted in an estimate of the worst-case temperature distribution in a real circuit for a given value of the device separation, $2L_m$. It yielded the two planes of symmetry shown, which were adiabatic boundaries. The temperature and location in the interconnect are given by T_m and the parameter x_m, in the drain by T_d and x_d, and in the gate by T_g and x_g. The parameters x_m, x_d, and x_g are not related to the coordinates X, Y, and Z. The channel temperature is T_c. The gate is separated from the channel by a silicon-dioxide layer of thickness $d_{go} = 5.5$ nm, whose thermal resistance is negligible, yielding $T_g(x_g = 0) = T_c$. The fin equations were solved by requiring temperature continuity and energy conservation at the fin interfaces, yielding

$$T_m - T_0 = Z_1 \cosh [m_m(L_m - x_m)] \quad (1)$$

$$T_d - T_0 = Z_2 \exp[m_d x_d] + Z_3 \exp[-m_d x_d] \quad (2)$$

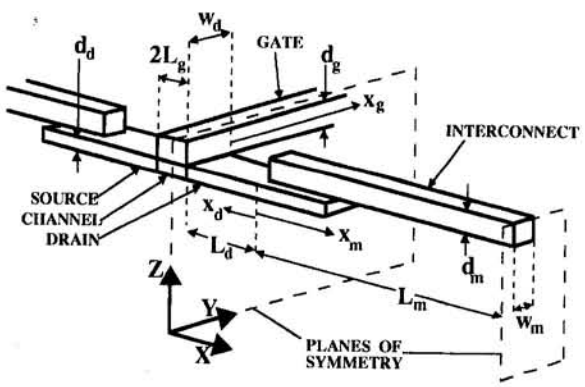

Fig. 2 Geometry of the thermal model of a SOI FET (Goodson and Flik, 1992)

$$T_g - T_0 = Z_4 \exp[-m_g x_g] \quad (3)$$

The variables Z_1, Z_2, Z_3, and Z_4 were determined by solving a set of four simultaneous algebraic equations, given in matrix form by Goodson and Flik (1992). The channel temperature is $T_c = T_g(x_g = 0) = Z_4 + T_0$. The maximum temperature in the interconnect, at the interconnect–device contact, is $T_{m,\max} = T_m(x_m = 0) = Z_2 + Z_3 + T_0$. The channel-to-substrate thermal resistance is $R_c = Z_4/P$.

The isothermal-channel approximation does not account for the strong spatial dependence of the rate of heat generation in the channel (e.g., Ostermeier et al., 1992; Fushinobu and Majumdar, 1993). The greatest error occurs when the transistor is saturated, which results in heat generation predominantly near the channel–drain interface. An upper bound for the error is estimated using the fin method of Goodson and Flik (1992) and the assumption that all of the heat generation occurs within a region at the channel–drain interface of length in the X direction two orders of magnitude less than the channel length, $L_g/50$. Conduction to the gate and the difference between the channel thermal conductivity and that of the source and drain are neglected. This approximate analysis of the error yields a highly nonuniform channel temperature rise. But the *average* channel-temperature rise differs by less than 0.5 percent from that predicted by assuming an isothermal channel. The analysis of Goodson and Flik (1992) is therefore appropriate for predicting the average channel temperature rise, which is measured by the experimental technique developed here. In contrast, this analysis of the error shows that the isothermal-channel approximation results in a significant underprediction of the temperature rise of the drain–interconnect contact. For $L_d = 0.5$ and 1.5 μm, the relative errors are 13 and 11 percent, respectively.

The analysis neglects thermal boundary resistances. Goodson et al. (1994) measured the effective thermal conductivities for conduction normal to the implanted silicon-dioxide layers in the present study bounded below by silicon and above by aluminum. The data agree closely with the conductivity of bulk silicon dioxide, making a significant thermal boundary resistance between the implanted layer and the silicon dioxide unlikely. Data are needed for the boundary resistance between the buried silicon dioxide and the silicon device, as well as the resistances at the boundaries of the thermally grown silicon dioxide. Goodson et al. (1993) measured the effective conductivities for conduction normal to chemical-vapor-deposited layers fabricated using the same method as those in the present study. They obtained upper bounds for the thermal boundary resistance between the aluminum and the silicon dioxide that would not significantly change the values of h_f for the interconnects in the present work. The thermal resistances that impede conduction from the channel to the gate and from the source and drain to the interconnects are unknown. If significant, these resistances will cause the analysis here to underpredict the channel-to-substrate thermal resistance.

2.2 Application to the Experimental Test Structure

Thermal Conductivities. Table 2 gives the thermal conductivities used in the model. Goodson et al. (1994) measured the thermal conductivity of implanted-silicon-dioxide layers in SOI wafers near room temperature. The data agreed within the experimental error with the value recommended for bulk amorphous silicon dioxide (Sugawara, 1969), so the bulk value is used here. The bulk value is also used for thermally grown silicon dioxide, supported by the data of Goodson et al. (1993). The thermal conductivities reported for chemical-vapor-deposited (CVD) silicon-dioxide layers do not agree, but are in general less than the bulk value (Schafft et al., 1989; Brotzen et al., 1992; Goodson et al., 1993). Due to the lack of a consensus among the data for CVD silicon-dioxide layers, the bulk value is used in this case as well. The resulting error is very small because the thermal resistance of the implanted silicon-dioxide layer is much more important than that of the CVD layers.

The source and drain are single-crystal silicon doped with approximately 1×10^{20} arsenic atoms cm^{-3}. The most appropriate existing data are for bulk single-crystal silicon doped with 1.7×10^{20} phosphorus atoms cm^{-3} (Touloukian et al., 1970). There are no thermal conductivity data available for the gates in the present research, which were polysilicon heavily doped with arsenic atoms. Tai et al. (1988) and Völklein and Baltes (1992) measured thermal conductivities near 30 W m^{-1} K^{-1} in polysilicon layers heavily doped with phosphorus. The data are consistent with the thermal diffusivity data of Mastrangelo and Muller (1988), also for phosphorus-doped polysilicon layers. The conductivity $k_g = 30$ W m^{-1} K^{-1} is used here. The conductivity above 300 K of silicon with less than 10^{18} dopant-atoms cm^{-3} differs little from that of intrinsic silicon (Touloukian et al., 1970), which is used for k_c and k_s here. The thermal conductivity of aluminum layers containing 1 mass percent of silicon has not been measured directly. The thermal conductivity calculated using the Wiedemann-Franz law (Kittel, 1986) and the electrical resistivity measured here of these layers is within 4 percent of the thermal conductivity recommended for bulk aluminum (Touloukian et al., 1970), so the bulk value is used here.

The substrate temperature during the measurements was $T_0 = 303$ K, and the largest channel temperature was $T_c = 403$ K. The thermal model in Section 2.1 neglects the temperature dependence of the thermal conductivities of the SOI FET materials. This is a good approximation between 303 and 433 K for silicon dioxide and aluminum, whose bulk thermal conductivities vary by less than 13 and 2 percent in this range, respectively. But the thermal conductivity of the heavily doped silicon source and drain varies more significantly in this temperature range. To help overcome this difficulty, the temperature $(T_0 + T_c)/2$, averaged for all of the data, is used when interpolating k_d.

Dimensions. Figure 3 compares the experimental test structure with a FET device. The measured dimensions of the test structures are given in Table 1. The interconnect lengths are very long compared to $1/m_m$, so that $L_m = \infty$ is used. The gate of the FET in the test structure extends out from both sides of the channel to interconnect contacts in the Y direction. This results in a plane of symmetry normal to the Y axis, i.e., an X–Z plane, at $Y = 0$. The temperature field in each half of the test structure is predicted by the thermal model. The thermal analysis is applied using $w_d = (w_d)_{\text{test structure}}/2$, $w_m = (w_m)_{\text{test structure}}/2$, and $P = (P)_{\text{test structure}}/2$.

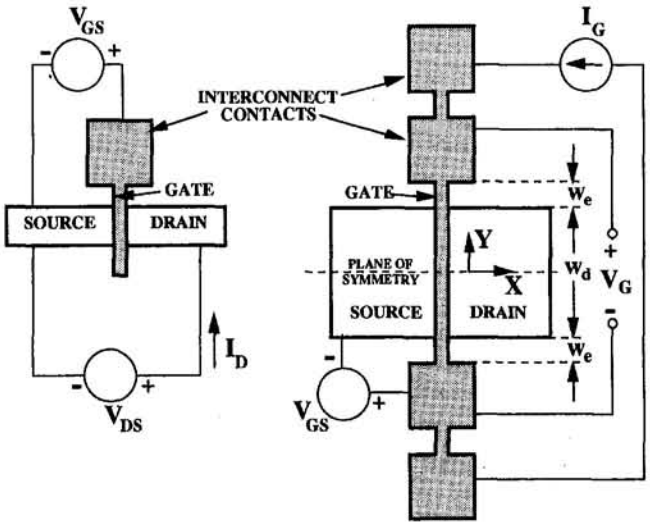

a) FET DEVICE. b) TEST STRUCTURE.

Fig. 3 Top views of: (a) FET device; (b) test structure

Parameter Uncertainties. An uncertainty in the predictions of the thermal analysis results from the use of parameters, e.g., thermal conductivities and dimensions, which may differ from those in the test structure. This uncertainty is estimated using the sum-of-squares technique (e.g., Holman, 1984) and the analytical model. The largest expected error is ±10 percent. The uncertainties in k_d and d_d are the largest contributors.

Heat Transfer to Ambient Air. The test structure is exposed to ambient air, but heat transfer to the air is neglected. This is justified by the small value of the channel-to-air thermal conductance compared to the channel-to-substrate thermal conductance, which is predicted in this work to be $1/R_c \sim 0.5 - 2 \times 10^{-4}$ W K^{-1}. The channel-to-air thermal conductance is of the order of that from an isothermal disk of radius a on the boundary of a semi-infinite medium of conductivity k, $G = 4ak$ (Carslaw and Jaeger, 1959). Using $a = w_d/2$ and the room-temperature conductivity of air yields $G = 5.2 \times 10^{-7}$ W K^{-1}. An order-of-magnitude analysis of the momentum equation estimates the air velocity near the device due to buoyancy forces (Rohsenow and Choi, 1961), $v = \rho g a^2 \beta (T_c - T_0)/\mu$, where g is the acceleration due to gravity, and ρ is the density, μ is the viscosity, and $\beta \sim 1/T_0$ is the approximate coefficient of thermal expansion of the air. Using room-temperature properties and $T_c - T_0 = 130$ K yields $v = 6.6$ μm s^{-1}. The thermal conductance contributed by the air motion is of the order of $G = v\pi a^2 \rho c_p = 6.2 \times 10^{-13}$ W K^{-1}, where c_p is the specific heat per unit mass at constant pressure of air. The thermal conductance due to radiation is of the order of $G = 4\epsilon\sigma T_0^3 A$, where ϵ is the emissivity of the surface, σ is the Stefan–Boltzmann constant, and A is the area of the emitting surface. Using $\epsilon = 1$ and $A = \pi a^2$ yields $G = 5.0 \times 10^{-10}$ W K^{-1} at room temperature.

3 Channel-Temperature Measurement Technique

This section describes the technique for measuring the channel temperature of SOI FETs. Section 3.1 describes the apparatus and the general procedure, and Section 3.2 calculates the channel temperature from the measured gate resistance. Section 3.3 determines the experimental uncertainty.

3.1 Apparatus and Procedure. Figure 3 shows the experimental structure. The electrical resistance of the gate depends strongly on temperature. It serves as an electrical-resistance thermometer. The calibration measures the gate electrical resistance, R_G, as a function of temperature when there is no drain current, i.e., when the gate is isothermal, yielding $[R_G(T)]_{\text{calibration}}$. The substrate temperature is controlled using a Temptronic Model TP38B chuck, a copper disk with a diameter of 88.9 mm and a thickness of 19.1 mm, to which the wafer is secured by suction. A thermocouple with one junction soldered to the chuck surface measures the chuck temperature. The chuck is maintained at the temperature T_0 and the gate resistance is measured for varying values of the drain-source voltage drop, V_{DS}, and the gate-source voltage drop, V_{GS}, i.e., for several different device powers, $P = I_D V_{DS}$.

The *average gate temperature* is defined as that of the gate segment whose resistance is measured, i.e., the segment between the voltage contacts. The average channel temperature is T_c, which is shown in Section 3.2 to be very well approximated by the average temperature of the gate segment over the channel. The average gate temperature considers the gate segments not over the channel heater, and is less than T_c. The FET gate-temperature variation is more important in a SOI wafer, where most of the temperature drop occurs within a few micrometers of the channel due to the implanted layer, than in a normal substrate, where the temperature-drop length scale is the thickness of the substrate, i.e., a few hundred micrometers. This temperature variation must be considered when calculating T_c from R_G.

3.2 Temperature Distribution in the Gate. The gate temperature variation in the Y direction is

$$T_G(Y) = T_0 + \Delta T_G F_G(Y) \tag{4}$$

where ΔT_G is the average gate-temperature rise from T_0 and $F_G(Y)$ is a shape function of average value unity that is defined for $|Y| < w_c + w_d/2$. For each measured R_G, ΔT_G is determined iteratively using

$$R_G = \int_{-w_c - w_d/2}^{w_c + w_d/2} [R_G(T_0 + \Delta T_G F_G(Y))]_{\text{calibration}} \frac{dY}{2w_c + w_d} \tag{5}$$

The thermal resistance of the silicon-dioxide layer between the channel and gate, $d_{go}/(2L_g w_d k_o) = 1.2 \times 10^3$ K W^{-1}, is small compared to the thermal resistance for conduction along the gate to the contact in the Y direction, $w_c/(2L_g d_g k_g) = 7.31 \times 10^5$ K W^{-1}. This means that the channel- and gate-temperature distributions are almost identical for $|Y| < w_d/2$. The average channel temperature is

$$T_c = T_0 + \int_{-w_d/2}^{w_d/2} \Delta T_G F_G(Y) \frac{dY}{w_d} \tag{6}$$

The channel-to-substrate thermal resistance is $R_c = (T_c - T_0)/P = (T_c - T_0)/(I_D V_{DS})$.

Two shape functions are now developed, from which Eqs. (5) and (6) yield upper and lower bounds for T_c for a given R_G. Each shape function must be even, due to the test-structure symmetry about $Y = 0$, and continuous. Because of the large width in the X direction of the gate-interconnect contacts, 4 μm, compared to the gate width, $2L_g = 0.32$ μm, the contacts are very nearly isothermal at the substrate temperature, T_0. This yields the boundary conditions $F_G(Y) = 0$ at $Y = \pm(w_c + w_d/2)$. For a given R_G, T_c calculated using Eqs. (5) and (6) increases with the difference between unity and the average of $F_G(Y)$ over $-w_d/2 < Y < w_d/2$, i.e., with the assumed difference between the average gate and channel temperatures. Shape LB assumes a linear temperature profile in the gate segments not over the channel, which neglects conduction down through the buried silicon-dioxide layer, and an isothermal channel. Both assumptions underestimate the difference between the average channel and average gate temperatures, yielding a lower bound for T_c. Shape LB is

$$F_G(Y) = \frac{w_d + 2w_c}{w_d + w_c}, \quad |Y| < \frac{w_d}{2} \tag{7}$$

$$F_G(Y) = \left[\frac{w_d + 2w_c}{w_d + w_c}\right] \frac{[(w_c + w_d/2) - |Y|]}{w_c}, \quad \frac{w_d}{2} < |Y| < w_c + \frac{w_d}{2} \tag{8}$$

An overestimate of the difference between the average gate and channel temperatures requires an overestimate of the temperature drop between the center and the edge of the channel in the Y direction. This is calculated by isolating the channel and gate from the source and drain, in which thermal conduction reduces the channel-temperature variation in the Y direction. The gate and channel are grouped together as a composite fin, which meets a fin of different internal properties and heat transfer coefficient at $Y = w_d/2$. Solving the heat equation in the two fins yields shape UB, which has a larger average in the channel region than shape LB. Values of $T_c - T_0$ calculated using shapes UB and LB differ by less than 8 percent, and the simpler shape LB is used here, Eqs. (7) and (8). This function does not describe the temperature distribution in the channel. Rather, it is a shape function which, when used in Eqs. (5) and (6), yields a value for T_c close to the *average* channel temperature. The difference between the upper and lower bounds is used in the experimental-uncertainty analysis.

3.3 Experimental Uncertainty. The uncertainty in $R_c = (T_c - T_0)/P$ has three significant, independent components: (*a*) There is a relative uncertainty of 4 percent in

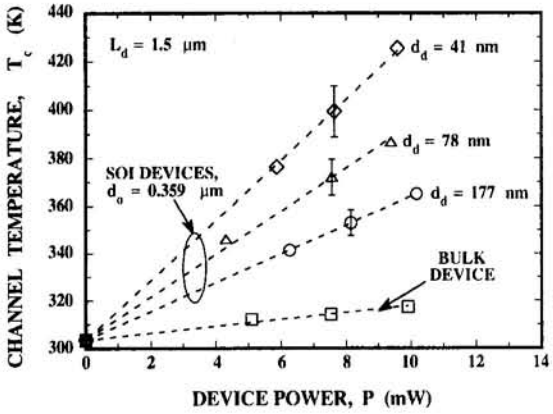

Fig. 4 Channel-temperature data for SOI FETs with varying device thicknesses, compared with data for a bulk (non-SOI) FET

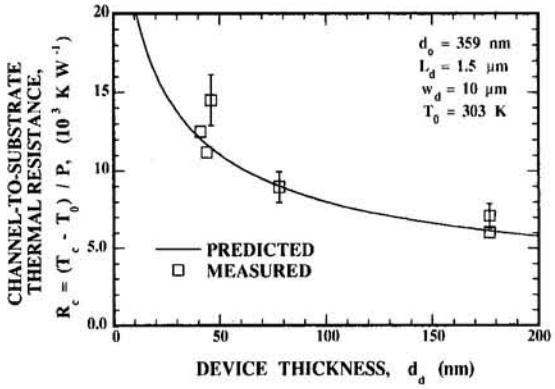

Fig. 5 The channel-to-substrate thermal resistance, R_c, as a function of the device thickness

$T_c - T_0$ due to the error in the substrate-temperature change measured by the chuck thermocouple (Goodson et al., 1994). (*b*) A relative uncertainty of 6.6 percent in $T_c - T_0$ is due to the measurement of R_G. (*c*) A relative uncertainty of 8 percent in $T_c - T_0$ is due to the approximate shape function for the temperature profile in the gate, as shown in Section 3.2. The total relative uncertainty in R_c is ±11 percent, determined using the sum-of-squares technique (Holman, 1984).

4 Results and Discussion

Section 4.1 compares data for the channel-to-substrate thermal resistance of SOI FETs with predictions of the thermal analysis of Section 2. The thermal analysis is used in Section 4.2 to estimate the influence of the implanted silicon-dioxide layer on the reliability of highly integrated SOI circuits.

4.1 Channel-to-Substrate Thermal Resistance. Channel-temperature measurements are performed on SOI test structures with varying values of L_d, d_d, and d_o. Test structures fabricated from bulk (non-SOI) wafers are measured for comparison. The device voltages satisfy $0\text{ V} < V_{DS} < 3\text{ V}$ and $V_{GS} = 2$ V and 2.5 V, which are typical operating conditions. The device powers vary between 3 and 14 mW, and the values of $T_c - T_0$ vary between 5 and 130 K. The power dissipated in the gate electrical-resistance thermometer is at least two orders of magnitude smaller than the device power.

The channel-to-substrate thermal resistance, R_c, varies by less than the experimental uncertainty for varying powers from a single device, as shown in Fig. 4 for three SOI devices and one bulk device, i.e., a device fabricated in a conventional wafer, which lacks the implanted silicon-dioxide layer in SOI wafers. The data for each device for varying powers fall near a line originating at $P = 0$ and $T_0 = 303$ K, whose slope is R_c. Values of R_c for the SOI devices are as much as 10 times larger than R_c for the bulk device, due to the thermal resistance of the implanted silicon-dioxide layer. The value of R_c decreases with increasing SOI device thickness, d_d. In Figs. 5 and 6, each data point is the average of the values of R_c measured in a single test structure. Uncertainty bars are only given for selected data to avoid cluttering of the figures. Each data point is the average of the values of R_c measured in a single test structure. Uncertainty bars are only given for selected data to avoid cluttering of the figures.

Figure 5 shows that the sensitivity of R_c to the device thickness is predicted by the thermal model of Section 2. Increasing d_d reduces the channel temperature for a given power. The parameters k_d and d_d are not independent, but always appear as a product in the solution for the temperature distribution (Goodson and Flik, 1992). Thus, the channel temperature is also sensitive to k_d, which depends on the doping level in the source and drain. The agreement is excellent considering the uncertainties of the thermal conductivities and dimensions used in the analysis. Section 2.2 estimated that the potential relative error in the predictions due to these uncertainties is ±10 percent. The differences in the experimental data at device thicknesses near 45 μm in Fig. 5 do not indicate a poor repeatability of the experimental method. Each data point is for a different experimental structure. Because R_c depends sensitively on the structure dimensions, the uncertainty in the measurement of structure dimensions can yield data on a single graph that are apparently inconsistent when only the uncertainty in the measurement of R_c is considered.

Figure 6 shows the dependence of R_c on the implanted-silicon-dioxide layer thickness. The data support the predictions of the model, and indicate that R_c is as sensitive to d_d as it is to d_o. This is in contrast to the predictions of McDaid et al. (1989), whose model assumed that R_c is independent of d_d. By modeling one-dimensional conduction in the implanted-silicon-dioxide layer, these researchers predicted that $R_c = d_o/(Ak_o)$, where A is the device area in the X-Y plane. This neglects the spreading of the temperature profile into the source and drain fins with increasing d_o, and is not consistent with the data. This can be remedied by a simple scaling analysis. The area in the source and drain with significant temperature rise is of the order of $A = 2w_d/m_d$, where the thermal healing length $1/m_d$ is approximately $(k_d d_d d_o/k_o)^{1/2}$. Using $R_c = d_o/(Ak_o)$ with this expression for A yields

$$R_c \approx \frac{1}{2w_d}\left(\frac{d_o}{k_o k_d d_d}\right)^{1/2} \tag{9}$$

which is in qualitative agreement with the data in Fig. 6. This shows that R_c is roughly proportional to $d_o^{1/2}$, and that the sensitivity of R_c to d_o and d_d is similar, i.e., halving d_o and doubling

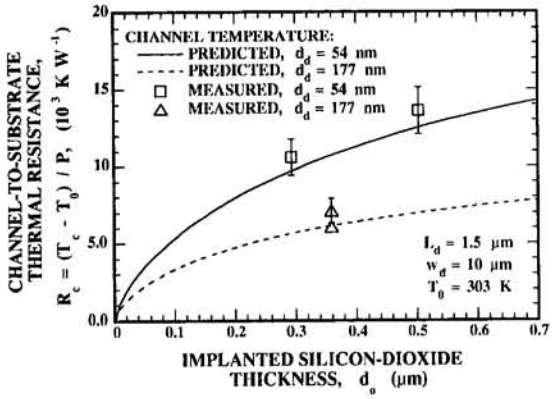

Fig. 6 The channel-to-substrate thermal resistance as a function of the implanted silicon-dioxide layer thickness

d_d have the same impact, if all other parameters are held constant. Equation (9) is valid only when the thermal healing length in the source and drain is smaller than the channel–interconnect separation, i.e., $1/m_d < L_d$. Otherwise, there is significant heat conduction into the interconnects, which are more effective fins than the source and drain because of their large thickness and high thermal conductivities.

4.2 Electromigration-Limited Reliability of FET-Interconnect Contacts. The FET-interconnect contact temperature *increases* as L_d is reduced, because this brings the contact nearer to the channel heat source. This reduces the reliability of the contact, whose electromigration-limited mean time to failure (MTF) decreases with increasing temperature. This section estimates the reduction of the MTF of FET–interconnect contacts due to the implanted layer in SOI circuits and demonstrates the potential for overcoming this problem through transistor-level thermal design. Electromigration is the motion of metal atoms in the interconnect in the direction of electron flow due to electron-lattice momentum transfer. This causes interconnect failure due to void formation, particularly near FET–interconnect contacts, where the flux of metal atoms diverges. The temperature dependence of the MTF limited by electromigration is (e.g., Black, 1967)

$$\mathrm{MTF} = K_e \exp\left(\frac{E_e}{k_B T}\right) \tag{10}$$

where E_e is the activation energy for atomic diffusion, $k_B = 1.38 \times 10^{-23}$ J K^{-1} is the Boltzmann constant, T is the temperature, and K_e is a function of the electrical current density, the geometry, and the microstructure and purity of the metal. Equation (10) agrees well with data for FET-interconnect contacts if $E_e = 0.5$ eV $= 8 \times 10^{-20}$ J is used (Chern et al., 1986).

The FET device dimensions in Table 1 are used with an interconnect length between devices of $2L_m = 4$ μm. The FETs experience steady-periodic heating with pulses of 1.61 W for one tenth of each clock cycle, where 1.61 W is the steady-state power of a SOI device with these dimensions (Woerlee et al., 1989). The analysis in Section 2 provides a good estimate of the nearly steady-state FET-interconnect contact temperature if the time-averaged power is used, $P_{\mathrm{avg}} = 0.161$ W. The resulting contact temperature rise is less than 8 K, and depends strongly on d_v and L_d. Figure 7 uses Eq. (10) to show the ratio of the MTF for FET–interconnect contacts in a SOI circuit to that for contacts in a bulk circuit. These predictions assume that the substrate temperature in the SOI case is equal to that in the bulk case. The difference between the two contact temperatures is due to the thermal resistance of the implanted silicon-dioxide layer. The MTF increases as L_d is increased, because the interconnect moves away from the channel heater. It may be possible to improve circuit reliability by increasing L_d, but this must be weighed against the need for compact devices. Reducing d_v also increases the MTF, because this reduces the contact temperature.

Figure 7 provides the type of information needed to make decisions effectively during the design of SOI circuits, but the predictions are very approximate. Because Eq. (10) has only been experimentally verified using accelerated testing, i.e., the use of electrical current densities and temperatures which are higher than those found in an operating circuit, Fig. 7 can at best show the expected trends. In a real device, the rate of heat generation will be greatest near the drain contact, causing this contact to have the lowest MTF. But the isothermal-channel approximation of Goodson and Flik (1992) yields identical temperatures in the source and drain contacts. As discussed in Section 2.1, this underpredicts the temperature rise of the drain contact by as much as 13 percent. The resulting error in the normalized MTF in Fig. 7 is less than 10 percent.

5 Conclusions

The analysis of Goodson and Flik (1992) tends to underpredict the data presented here. This is due in part to the assumption of an isothermal channel, which results in about a 7 percent underprediction of the channel-to-substrate thermal resistance, as discussed in Section 2.1. The underprediction may be due in part to thermal boundary resistances in the structure, which, as discussed in Section 2.1, are not considered by the analysis. Another important possibility is that the thermal conductivities of the interconnects and source and drain, which have not been measured, may be less than the bulk values used here. Better agreement will require more research on thermal conductivities and boundary resistances in circuits.

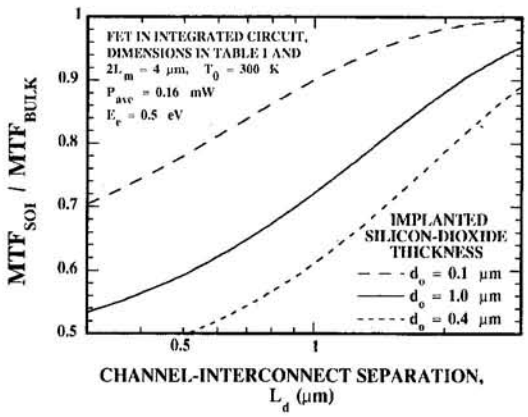

Fig. 7 Predicted dependence of the median time to failure (MTF) of FET–interconnect contacts on the channel–interconnect separation

The mean time to failure of a circuit and the channel mobility are important to the design of circuits. They are affected by the channel and interconnect temperatures, which are shown here to depend strongly on design parameters, e.g., k_d, d_d, d_v, and L_d. Some of these parameters also affect the electrical performance of the device directly. In order to achieve circuits of optimal performance and reliability, design for electrical performance should be accompanied by device thermal design, i.e., the choice of dimensions, materials, and processing techniques that enhance heat conduction within a few micrometers of the device. This work provides a basis for the thermal design of SOI FETs.

This work shows that the steady-state channel-temperature rise in SOI FETs due to Joule heating is significant. Electrical-property measurements performed on devices in the steady state are affected by this temperature rise due to the strong dependence of the channel mobility on temperature. The steady-state data may not be applicable to devices in an integrated circuit, where the channel-heating is time dependent. More work is needed to determine time-dependent temperature fields in integrated SOI circuits.

Acknowledgments

Professors Carl V. Thompson and Borivoje B. Mikic of M.I.T. provided valuable comments. K.E.G. and L.T.S. were supported by academic fellowships from the Office of Naval Research and AT&T Bell Labs, respectively. The SOI wafers used in this study were provided by IBIS Corp., Danvers, Massachusetts. D.A.A. and L.T.S. acknowledge the support of the Semiconductor Research Corporation (SRC) under contract No. 92-SP-309.

References

Black, J. R., 1967, "Mass Transport of Aluminum by Momentum Exchange With Conducting Electrons," *Proceedings of the IEEE Reliability Physics Symposium*, pp. 148–159.

Brotzen, F. R., Loos, P. J., and Brady, D. P., 1992, "Thermal Conductivity of Thin SiO_2 Films," *Thin Solid Films*, Vol. 207, pp. 19–7201.

Brugger, H., 1991, "Raman Spectroscopy for Characterization of Lasered Semiconductor Materials and Devices," in: *Light Scattering in Semiconductor Structures and Superlattices*, K. J. Lockwood and J. F. Young, eds., Plenum, New York, pp. 259–274.

Bunyan, R. J. T., Uren, M. J., Alderman, J. C., and Eccleston, W., 1992, "Use of Noise Thermometry to Study the Effects of Self-Heating in Submicrometer SOI MOSFET's," *IEEE Electron Device Letters*, Vol. 13, pp. 279–281.

Carslaw, H. S., and Jaeger, J. C., 1959, *Conduction of Heat in Solids*, Oxford University Press, New York, pp. 214–216.

Chern, J. G. J., Oldham, W. G., and Cheung, N., 1986, "Electromigration in Al/Si Contacts—Induced Open-Circuit Failure," *IEEE Transactions on Electron Devices*, Vol. ED-33, pp. 1256–1262.

Colinge, J. P., 1991, *Silicon-on-Insulator Technology: Materials to VLSI*, Kluwer Academic Publishers, Boston, pp. 1–5.

Fushinobu, K., and Majumdar, A., 1993, "Heat Generation and Transport in Submicron Semiconductor Devices," in: *Heat Transfer on the Microscale*, ASME HTD-Vol. 253, F. M. Gerner and K. S. Udell, eds., pp. 21–28.

Goodson, K. E., and Flik, M. I., 1992, "Effect of Microscale Heat Conduction on the Packing Limit of Silicon-on-Insulator Electronic Devices," *IEEE Trans. on Components, Hybrids, and Manufacturing Technology*, Vol. 15, pp. 715–722.

Goodson, K. E., Flik, M. I., Su, L. T., and Antoniadis, D. A., 1993, "Annealing-Temperature Dependence of the Thermal Conductivity of CVD Silicon-Dioxide Layers," *IEEE Electron Device Letters*, Vol. 14, pp. 490–492.

Goodson, K. E., Flik, M. I., Su, L. T., and Antoniadis, D. A., 1994, "Prediction and Measurement of the Thermal Conductivity of Amorphous Dielectric Layers," ASME JOURNAL OF HEAT TRANSFER, Vol. 116, pp. 317–323.

Holman, J. P., 1984, *Experimental Methods for Engineers*, McGraw-Hill, New York, pp. 50–57.

Kittel, C., 1986, *Introduction to Solid State Physics*, Wiley, New York.

Lai, J., Carrejo, J. P., and Majumdar, A., 1993, "Thermal Imaging and Analysis at Sub-micrometer Scales using the Atomic Force Microscope," in: *Heat Transfer on the Microscale*, ASME HTD-Vol. 253, F. M. Gerner and K. S. Udell, eds., pp. 13–20.

Lifka, H., and Woerlee, P. H., 1990, "Thin Simox SOI Material for Half-Micron CMOS," *Proceedings of the European Solid State Device Research Conference*, pp. 453–456.

Majumdar, A., Carrejo, P., and Lai, J., 1993, "Thermal Imaging Using the Atomic Force Microscope," *Appl. Phys. Lett.*, Vol. 62, pp. 2501–2503.

Marcus, R. B., and Sheng, T. T., 1983, *Transmission Electron Microscopy of Silicon VLSI Circuits and Structures*, Wiley, New York, pp. 80–82.

Mastrangelo, C. H., and Muller, R. S., 1988, "Thermal Diffusivity of Heavily Doped Low Pressure Chemical Vapor Deposited Polycrystalline Silicon Films," *Sensors and Materials*, Vol. 3, pp. 133–142.

Mautry, P. G., and Trager, J., 1990, "Self-Heating and Temperature Measurement in Sub-μm-MOSFETs," *Proceedings of the IEEE International Conference on Microelectronic Test Structures*, Vol. 3, pp. 221–226.

McDaid, L. J., Hall, S., Mellor, P. H., Eccleston, W., and Alderman, J. C., 1989, "Physical Origin of the Negative Differential Resistance in SOI Transistors," *Electronics Lett.*, Vol. 25, pp. 827–828.

Ostermeier, R., Brunner, K., Abstreiter, G., and Weber, W., 1992, "Temperature Distribution in Si-MOSFET's Studied by Micro Raman Spectroscopy," *IEEE Trans. Electron Devices*, Vol. 39, pp. 858–863.

Rohsenow, W. M., and Choi, H. Y., 1961, *Heat, Mass, and Momentum Transfer*, Prentice-Hall, Englewood Cliffs, NJ, p. 155.

Rowe, D. M., and Bhandari, C. M., 1986, "Preparation and Thermal Conductivity of Doped Semiconductors," *Progress in Crystal Growth and Characterization*, Vol. 13, pp. 233–289.

Schafft, H. A., Suehle, J. S., and Mirel, P. G. A., 1989, "Thermal Conductivity Measurements of Thin-Film Silicon Dioxide," *Proceedings of the IEEE International Conference on Microelectronic Test Structures*, Vol. 2, pp. 121–124.

Sugawara, A., 1969, "Precise Determination of Thermal Conductivity of High Purity Fused Quartz from 0° to 650°C," *Physica*, Vol. 41, pp. 515–520.

Tai, Y. C., Mastrangelo, C. H., and Muller, R. S., 1988, "Thermal Conductivity of Heavily-Doped Low-Pressure Chemical Vapor Deposited Polycrystalline Silicon Films," *J. Appl. Phys.*, Vol. 63, pp. 1442–1447.

Touloukian, Y. S., Powell, R. W., Ho, C. Y., and Klemens, P. G., 1970, "Thermal Conductivity: Metallic Elements and Alloys," in: *Thermophysical Properties of Matter*, Vol. 1, IFI/Plenum, New York, pp. 9, 326, 330, and 335.

Völklein, F., and Baltes, X. X., 1992, "A Microstructure for Measurement of Thermal Conductivity of Polysilicon Thin Films," *J. Microelectromechanical Systems*, Vol. 1, pp. 193–196.

Woerlee, P. H., van Ommen, A. H., Lifka, H., Juffermans, C. A. H., Plaja, L., and Klaassen, F. M., 1989, "Half-Micron CMOS on Ultra-Thin Silicon on Insulator," *Proceedings of the IEEE International Electron Devices Meeting*, pp. 821–824.

W. Li

M. A. Ebadian
Fellow ASME

Department of Mechanical Engineering,
Florida International University,
Miami, FL 33199

T. L. White
Fusion Energy Division.

D. Foster
Chemical Technology Division.

Oak Ridge National Laboratory,
Oak Ridge, TN 37831

Heat Transfer Within a Steel-Reinforced Porous Concrete Slab Subjected to Microwave Heating

The concrete decontamination and decommissioning (D&D) process using microwave technology is investigated theoretically in this paper. A one-dimensional uniform plane wave is assumed for the microwave propagation and the microwave field and the power dissipation within the concrete. Also, by considering the effects of the microwave frequencies, a one-dimensional model of unsteady heat and mass transport in the concrete is developed to evaluate variations of the temperature and pressure distributions with the heating time. The effects of the microwave frequency (f), microwave power intensity ($Q_{0,avg}$), the thermal boundary conditions on the front wall, and the concrete porosity (ϕ) on the microwave power dissipation ($Q_{d,avg}$), temperature (T), pressure (P), and evaporation rate (Δm) distributions are all investigated in the present model. Finally, the effects of the presence of a steel reinforcement and its location on the microwave power dissipation, and the temperature and inner steam pressure distributions are discussed accordingly.

1 Introduction

Massive amounts of concrete are used for shielding in many nuclear facilities such as reactors, canyon buildings, hot cells, waste processing plants, etc. Many of these installations have concrete floors that are contaminated. In most cases, only the outer surface of the concrete, to a depth of several centimeters, is highly radioactively contaminated. At some stage, this contaminated concrete layer must be removed and will require disposal as radioactive waste. The bulk of the concrete, however, can be disposed of as nonradioactive material. To a varying extent, all currently used mechanical techniques generate secondary wastes, such as dust or waste water in the process of decontaminating the radioactively contaminated concrete surface. Storage and recycling of these secondary radioactive wastes also cause many other problems.

Since the first experiment performed by Watson (1968) on concrete breaking by microwaves, a new and innovative application for microwave technology has been extended for spalling the radioactively contaminated concrete layer. Several groups, Yasunaka et al. (1987) in Japan, Hills (1989) in Europe, and White et al. (1992) and Li et al. (1993, 1994) in the United States, have begun investigations and technology development for this new process. Based on experiments reported by Hills (1989) and White et al. (1992), it is generally agreed that when subjected to microwave heating, concrete spalling is due mainly to internal tensile stress or pressure created by the generation of steam from the water present in the relatively impermeable porous concrete. Therefore, the concrete spalling time (t_s) is defined as the time it takes to heat the concrete until the maximum inner steam pressure equals the concrete tensile strength.

As stated, steam pressure plays an important role in concrete decontamination. Steam generation, and therefore pressure distribution, are directly related to heat transfer and water evaporation within the porous concrete materials. Harmathy (1969) derived a set of governing equations for heat transfer with moisture in porous media during the pendular state. Huang et al. (1979) extended the Harmathy (1969) work to include the funicular state, and predicted temperature, moisture concentration, and pressure distribution profiles by different theoretical approaches. To describe the dynamic phenomena occurring in heated materials, Wei et al. (1985a) modified Whitaker's (1977) derivations and applied his equations to the material with a simple model of microwave heating (Wei et al., 1985b).

Recently, Li et al. (1993) discussed heat transfer within a concrete slab subjected to microwave assault, limiting the heat transfer mechanism to pure conduction. Since the temperature-induced inner pressure and stress distributions are key factors for spalling a concrete layer, a new theoretical model of unsteady heat and mass transfer for solids, liquids, vapor, and air within the porous concrete was developed by Li et al. (1994). The results were limited in the modeling with the temperature independent dielectric properties. In comparison to that previous work, the temperature-dependent concrete dielectric properties are coupled in the present analysis. Also, temperature variations will result in changes in the dielectric properties; these changes will, in turn, affect the microwave energy dissipation. The temperature and pressure distributions obtained from the current porous concrete model are also investigated by considering the variations of the microwave frequency (f), concrete porosity (ϕ), and the microwave power intensity ($Q_{0,avg}$). When steel reinforcement is present in the concrete, the microwave energy will be blocked and additional energy will be reflected directly from the steel reinforcement. In the present paper, the effects of the steel reinforcement mesh within the porous concrete on the temperature and steam pressure distributions and the corresponding concrete spalling time are also analyzed.

2 Basic Assumptions and Concrete Properties

2.1 A Homogeneous and Isotropic Porous Medium. Concrete is basically a mixture of cement and aggregate, both of which are porous. The voids may occupy from a fraction up to 20 percent of the whole volume of the concrete. The pores within the cement can be classified as gel pores and capillary pores. The average diameters of the gel pores and the capillary pores, respectively, are 18 Å and 200 Å. In a macroscopic sense, it is quite reasonable to assume that the actual pore structure within porous concrete is uniformly distributed. Therefore, a heat and mass transfer model for a *homogeneous and isotropic* porous medium can be used in the theoretical modeling and analysis. In this study, the solid matrix is further assumed to be rigid and nondeformable.

Contributed by the Heat Transfer Division for publication in the JOURNAL OF HEAT TRANSFER. Manuscript received by the Heat Transfer Division January 1994; revision received November 1994. Keywords: Augmentation and Enhancement, Condensation, Porous Media. Associate Technical Editor: R. A. Nelson, Jr.

2.2 Local Thermal Equilibrium. According to studies on concrete properties as summarized by Neville (1981), the hydropermeability of concrete is of the order 7×10^{-16} m/s, and the total surface area per unit of concrete is of the order 4×10^{8} m^{-1}. As indicated by White et al. (1992), in the concrete D&D process, the concrete usually takes less than a minute to break. Therefore, movement of the liquid, vapor, and air through the concrete is very slow. In the meantime, all phases within the concrete have a sufficiently large area to achieve equilibrium. Thus, it is reasonable to assume that the local thermal equilibrium between all phases (liquid, vapor, air, and the solid concrete matrix) is achieved instantaneously. This infers that all thermal properties for all phases can be employed in the calculation, and the energy equations for the solid concrete, the liquid, the vapor, and the air can be combined in one temperature.

2.3 Dielectric and Thermal Properties. It is a well-known fact that the concentration of ferromagnetic material in concrete is negligible. Hence, the difference between the magnetic permeability of the concrete (μ) and the air (μ_{air}) can also be neglected. The concrete dielectric permittivity is strongly dependent on the temperature and the microwave frequency. The dielectric constant and effective dielectric loss, ϵ' and ϵ''_{eff}, respectively, of the concrete complex dielectric permittivity ($\epsilon = \epsilon' - j\epsilon''_{eff}$) for a frequency range of 0.896 to 18.0 GHz and temperatures ranging from 20 to 250°C are reported by Ebadian and Li (1992).

Since only a small amount of liquid and vapor escapes from the concrete during the microwave heating process, the variations of ρ, C_p, and k in the concrete are negligible, and these values are treated as constants. Except for the dielectric properties, the same concrete properties used by Li et al. (1993), such as concrete density (ρ), specific heat (C_p), thermal conductivity (k) and tensile strength (σ_t), are employed in this paper. The liquid and the vapor within the concrete are considered as pure water and water steam, respectively. Air is treated as the ideal gas in the whole process. The properties of pure water and steam documented by Reid et al. (1987) and Haar et al. (1984) are applied in the computation. The related formulations were summarized and listed by Li et al. (1994). It is further assumed that there is no chemical reaction during the process, i.e., there is no generation of air and other chemical components.

2.4 The Steel Reinforcement. In the current paper, the steel reinforcement within the concrete is treated as a thin layer having uniform reflection and transmission. It is assumed that the presence of the steel reinforcement within the concrete will not affect the previous assumptions of a homogeneous and isotropic porous medium and a local thermal equilibrium. The layer thickness is very thin and might be totally neglected in the heat and mass transfer, but it has certain dielectric properties that cause part of the microwave energy to be reflected. A fraction of the reflection (β) caused by the steel reinforcement is further assumed to be equal to a fraction of the cross-sectional area of the concrete taken up by the steel mesh. For example, the steel reinforcement mesh consists of steel bars or wire of a certain diameter (d) with horizontal and vertical spaces (L_h and L_v), respectively, as shown in Fig. 1. The steel reinforcement reflection (β) equals $[(L_h + L_v)d - d^2]/(L_h L_v)$, where d = 2.5 cm and $L_h = L_v = 25$ cm, and $\beta = 0.19$.

3 The Microwave Field and Power Dissipation

The problem of concrete decontamination is related to electromagnetic fields. An accurate evaluation of the microwave field will determine the amount of heat dissipation within the porous concrete.

3.1 The Microwave Field. Generally, microwaves are electromagnetic waves having frequencies ranging from 300 MHz to 300 GHz. Therefore, microwaves satisfy Maxwell's equation. During the decontamination process, the front surface of a concrete slab ($z = 0$) is directly exposed to the microwave

Nomenclature

C_p = specific heat of the concrete, $J\ kg^{-1}K^{-1}$
d = diameter of the steel reinforcement bar, m
E_x = electric potential, $V\ m^{-1}$
E_0 = wave amplitude of the initial electric potential, $V\ m^{-1}$
E^+, E^- = complex constants, Eqs. (3) and (4)
f = microwave frequency, s^{-1} Hz
H_y = magnetic potential, $A\ m^{-1}$
h = heat transfer coefficient, $W\ m^{-2}K^{-1}$
Im = imaginary part of the complex number
j = imaginary number = $\sqrt{-1}$
k = thermal conductivity, $W\ K^{-1}\ m^{-1}$
k_{eff} = effective thermal conductivity, $W\ K^{-1}\ m^{-1}$
L = thickness of the concrete, m
L_h = distance between the horizontal steel reinforcement bars, m
L_s = location of the steel reinforcement mesh, m
L_v = distance between the vertical steel reinforcement bars, m
N = number of divisions in the numerical calculation
P = pressure, $Pa\ Nm^{-2}$
Q_d = microwave power dissipation, $W\ m^{-3}$
Q_0 = microwave power intensity, $W\ m^{-2}$
Re = real part of the complex number
r = complex constant determined by the dielectric properties, Eq. (5)
S = volume saturation
s = node number where steel reinforcement mesh is located
T = temperature, K, °C
T_∞ = ambient temperature, K, °C
t = time, s
V = migration velocity vector, $m\ s^{-1}$
Z = field independence, Eq. (9)
z = coordinates, m
β = microwave energy reflection due to the steel reinforcement
β_t = total reflection due to the steel reinforcement
Γ = reflection coefficient, Eq. (9)
Δh_v = specific enthalpy of evaporation, $J\ kg^{-1}$
Δm = evaporation rate, $kg\ s^{-1}$
ϵ = complex dielectric permittivity = $\epsilon' - j\epsilon''_{eff}$, Fm^{-1}
ϵ_{air} = dielectric permittivity of air, 8.86×10^{-12}, Fm^{-1}
ϵ' = real part of the complex dielectric permittivity, or dielectric constant, $F\ m^{-1}$
ϵ'' = imaginary part of the complex dielectric permittivity, or dielectric loss, $F\ m^{-1}$
ϵ''_{eff} = effective dielectric loss = $\epsilon'' + \sigma/\omega$, $F\ m^{-1}$
η = complex constant, Eq. (5)
η' = imaginary complex constant for the steel reinforcement layer
λ = wave length of the microwave, m
μ = magnetic permeability, Henries m^{-1}, or viscosity, $N\ s\ m^{-2}$
μ_{air} = magnetic permeability of air = $4\pi \times 10^{-7}$, Henries m^{-1}
ρ = density, $kg\ m^{-3}$
σ = electric conductivity, Ohm^{-1}
σ_t = concrete tensile strength, $Pa\ Nm^{-2}$
ϕ = concrete porosity
ω = relative humidity of the microwave or angle frequency = $2\pi f$, $rad\ s^{-1}$

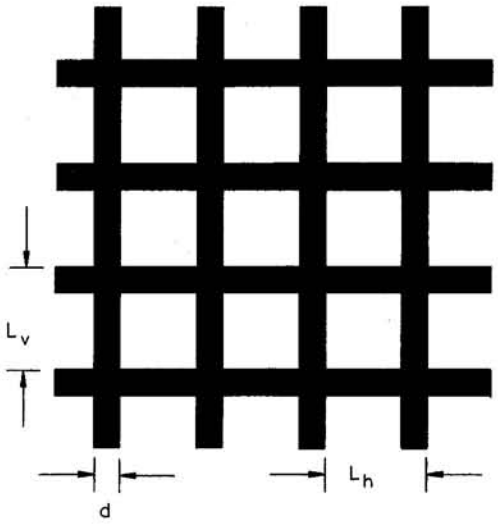

Fig. 1 Geometry of the steel reinforcement mesh

source. The steel reinforcement mesh is located at a distance (L_s) from the front surface of the concrete slab with a total thickness (L). The steel reinforcement within the concrete is treated as an infinite thin layer, and has no dielectric loss ($\epsilon''_{\text{eff},s} = 0$), and $\mu_s = \mu_{\text{air}}$. The steel reinforcement layer has a certain dielectric constant, ϵ'_s, which has a uniform reflection and transmission. The concrete slab is further divided into N subdivisions, and the complex dielectric permittivity, ϵ, is assumed to be uniform in each small subdivision, and is a function of the local temperature, as well as the microwave frequency.

The general governing equation for the harmonic electromagnetic fields in the ith ($i = 0, \ldots, N + 1$) subdivision can be simplified as follows for the plane microwave traveling in the z direction (Johnk, 1988; Iskander, 1992):

$$\frac{dE_x^i}{dz} = -j\mu\omega H_y^i \tag{1}$$

$$\frac{dH_y^i}{dz} = -j\omega E_{\epsilon_i}^i. \tag{2}$$

A general solution for these equations can be specified as:

$$E_x^i = E_0 \left(E_i^+ e^{-r_i z} + E_i^- e^{r_i z}\right) \tag{3}$$

$$H_y^i = \frac{E_0}{\eta_i} \left(E_i^+ e^{-r_i z} - E_i^- e^{r_i z}\right), \tag{4}$$

in which

$$r_i = \sqrt{j\omega\epsilon_i} \quad \text{and} \quad \eta_i = j\mu_i\omega/r_i, \tag{5}$$

where E_x and H_y are the electric and magnetic field potential, μ_i is the magnetic permeability ($\mu_i = \mu_{\text{air}}$), and ϵ_i is the complex dielectric permittivity at the ith division of the concrete. E_i^+ and E_i^- are the constants to be determined by the boundary conditions. For the plane wave, electric and magnetic potentials, E_x and H_y, must be continuous across the entire concrete slab. Mathematically, this statement can be expressed as:

$$E_x^i(z_i) = E_x^{i+1}(z_i) \quad \text{and} \quad H_y^i(z_i) = H_y^{i+1}(z_i), \tag{6}$$

where $i = 0, 1, 2, \ldots, N$.

3.2 Treatment of the Steel Reinforcement. When the ($s + 1$)th subdivision is concerned, the infinite thin steel reinforcement layer is met on the left side of the division. In the sth division, the energy reflection ratio due to the steel reinforcement, $\|\Gamma_s(z_s)\|^2$, has the following relation:

$$\|\Gamma_s(z_s)\|^2 \equiv \left\| \frac{Z_s - \eta'}{Z_s + \eta'} \right\|^2$$

$$= \beta + (1 - \beta) \left\| \frac{Z_s - \eta_s}{Z_s + \eta_s} \right\|^2 \equiv \beta_t, \tag{7}$$

in which η' is an imagined constant for the steel reinforcement. Thus, η' can be expressed as:

$$\eta' = \frac{(1 + \beta_t)\,\text{Re}\,(Z_s) \pm \sqrt{4\,\text{Re}^2(Z_s)\beta_t - (1 - \beta_t)^2\,\text{Im}^2(Z_s)}}{1 - \beta_t}, \tag{8}$$

where

$$\Gamma_i = \frac{E_i^-}{E_i^+} e^{2r_i z} \quad \text{and} \quad Z_i(z) = \frac{E_x^i}{H_y^i} = \eta_i \frac{1 + \Gamma_i(z)}{1 - \Gamma_i(z)}. \tag{9}$$

Starting from the subdivision of $N + 1$ backward, all E_i^+ and E_i^- can be calculated as $E_0^+ = 1$ and $E_{N+1}^- = 0$.

3.3 Incident Power and Power Dissipation. Since the frequencies of microwaves are very high (from 300 MHz to 300 GHz), the time scale of the variation of the microwave field is much smaller than that of the temperature variation in the concrete. One can then separate the sinusoidal variation of the microwave with the unsteady heat transport phenomena and use the time average of the incident power intensity ($Q_{0,\text{avg}}$) and power dissipation ($Q^i_{0,\text{avg}}$), which has the following relation, as indicated by Metaxas and Meredith (1983):

$$Q_{0,\text{avg}} = E_0^2/(240\pi), \tag{10}$$

and

$$Q^i_{d,\text{avg}} = 120\pi(\omega\epsilon''_{\text{eff},i})\, Q_{0,\text{avg}} \left[\text{Re}^2(E_x^i/E_0) + \text{Im}^2(E_x^i/E_0)\right]. \tag{11}$$

It should be noted that the time-averaged microwave power dissipation ($Q^i_{d,\text{avg}}$) is proportional to the product of the dielectric loss, $\epsilon''_{\text{eff},i}$, and the square of the norm of the complex electric potential (E_x^i), while both are strongly dependent on the temperature.

Nomenclature (cont.)

Subscripts

air = air
avg = time average
b = back surface of the concrete slab
f = front surface of the concrete slab
i = value at the ith node
max = maximum value
p = phase, 0 = solid phase; 1 = liquid phase; 2 = vapor phase; 3 = air phase
s = steel reinforcement
sat = saturation
0 = initial condition at $t = 0$

Superscript

i = value at the ith node

Other

$\|E\|^2$ = norm of the complex value = $E \cdot E^*$

4 Heat and Mass Transfer

4.1 The Governing Equations. By conservation of mass, momentum, and energy in a porous medium, the governing equations of mass, momentum, and energy for the solid (0), liquid (1), vapor (2), and air (3) phases can be derived by using a volume (local) average technique. As indicated, the concrete spalling time using microwave heating technology is less than one minute. The time for water and vapor or air moving between two consecutive wave peaks under a unit pressure gradient within the concrete slab is about 8.6×10^7 s (2.4×10^4 h). Thus, the liquid, vapor, and air movement can be neglected as an approximation, and only the evaporation is considered. Therefore, the governing equations for a one-dimensional problem can be further simplified to the following equations as:

Mass Conservation:

$$\phi \frac{\partial}{\partial t}(S_1\rho_1) + \Delta m = 0 \tag{12}$$

$$\phi \frac{\partial}{\partial t}[(1 - S_1)\rho_2] - \Delta m = 0 \tag{13}$$

$$\frac{\partial}{\partial t}[(1 - S_1)\rho_3] = 0 \tag{14}$$

Momentum Conservation:

$$V_p = 0, \quad p = 1, 2, 3, \tag{15}$$

while the pressures of all the fluid phases can be determined by the state equation as the functions of temperature (T) and densities (ρ_i) only. Thus,

$$P_p = f_p(T, \rho_p), \quad p = 1, 2, 3. \tag{16}$$

Energy Conservation:

$$(\rho C_p)_0 \frac{\partial T}{\partial t} = \frac{\partial}{\partial z}\left(k_{\text{eff}} \frac{\partial T}{\partial z}\right) + Q_{d,\text{avg}}(T, z) - \Delta m \Delta h_v + \frac{\partial P_1}{\partial t}, \tag{17}$$

where

$$S_2 = S_3 = 1 - S_1, \tag{18}$$

$$(\rho C_p)_0 = (1 - \phi)\rho_0 C_{p,0} + \phi \sum_{p=1}^{3} S_p \rho_p C_{p,p} \tag{19}$$

$$k_{\text{eff}} = (1 - \phi)k_0 + \phi \sum_{p=1}^{3} S_p k_p, \tag{20}$$

in which Δm is the evaporation rate during the heating process; ϕ is the porosity of the concrete system; and S, ρ, and V are the volume saturation ratio, density, and migration velocity of the different phases, respectively. Volume saturation ratio, S, is defined as the fraction volume of each phase (liquid, 1, vapor, 2, and air, 3) in the void space. T is the equilibrium temperature, $C_{p,0}$ is the specific heat of the solid concrete, and k and C_p are the thermal conductivity and specific heat for each phase, respectively. $Q_{d,\text{avg}}$ is the time-averaged microwave power dissipation for all phases in the concrete, and Δh_v is the water evaporation enthalpy. Since $(1 - \phi)\rho_0 C_{p,0}$ is dominant in $(\rho C_p)_0$, the variations resulting from the changes of S_i and ρ_i are insignificant. Therefore, the initial value of $(\rho C_p)_0$ is used in the calculation. Similar to $(\rho C_p)_0$, the initial value of k_{eff} is also used during the calculation.

4.2 The Constitutive State Equations. Totally, there are four equations for heat and mass transfer in the concrete (three for continuity and one for energy) with six unknown parameters (one volume saturation, three densities, one evaporation rate, and one temperature), while the vapor, air, and liquid pressures are considered as dependent variables. Therefore, two more equations are needed to determine all the parameters. In the porous concrete, liquid pressure is assumed to be the same as tensile stress within the solid concrete without considering capillary pressure. This pressure equals the summation of the vapor and air pressures as:

$$P = P_1 = P_2 + P_3. \tag{21}$$

The concrete to be decontaminated is usually more than ten years old, and it might initially be assumed that the vapor pressures (P_2) within the concrete is a function of the relative humidity around the concrete, which has the following relationship:

$$P_2 = \omega P_{\text{sat}}, \tag{22}$$

where ω is the relative humidity around the concrete. For simplicity, saturated vapor ($\omega = 1$) is used in the analysis. In the heating process, the fraction of the vapor phase practically dominates the air–vapor mixture. Therefore, it is assumed that the vapor pressure equals the saturation pressure of the vapor, i.e., $P_2 = P_{\text{sat}}(T)$ throughout the entire process.

4.3 The Initial and Boundary Conditions. The initial conditions of all densities (ρ_i), liquid volume saturation (S_1), and the boundary condition of the temperature (T), can be specified as:

$$\rho_1 = \rho_{1,0}, \quad \rho_2 = \rho_{2,0}, \quad \rho_3 = \rho_{3,0}, \quad S_1 = S_{1,0}, \quad T = T_0 \quad \text{and} \quad P_1 = P_{1,0} \quad \text{at} \quad t = 0, \tag{23}$$

where $P_{1,0}$ is the atmospheric pressure (101.3 kPa). All initial conditions should also satisfy the state equations at the initial temperature (T_0) and pressure ($P_{1,0}$).

In actual practice, a strong vacuum cleaner is always used with the concrete decontamination process to minimize dust generation. The entire area of the microwave applicator is totally covered by vacuum cleaner. Therefore, strong convection is involved near the surface around the microwave applicator. Based on the structure of the applicator and the vacuum system, it is estimated that the heat transfer coefficient around the vacuum cleaner (h_f) is about 35 W/m^{2}K. The heat transfer coefficient on the back surface is approximately 15 W/m^{2}K. The boundary conditions on both sides of the concrete wall may be approximated as:

$$-\rho_1 V_1 \Delta h_v + h_f(T - T_\infty) - k_{\text{eff}} \frac{\partial T}{\partial z} = 0, \quad \text{at} \quad z = 0, \tag{24}$$

$$-\rho_1 V_1 \Delta h_v + h_b(T - T_\infty) + k_{\text{eff}} \frac{\partial T}{\partial z} = 0, \quad \text{at} \quad z = L, \tag{25}$$

where the first term is induced by the phase change on the boundary. h_f and h_b are the convective heat transfer coefficients on the front and back surfaces, respectively, and T_∞ is the ambient temperature ($T_\infty = 20$°C).

4.4 Solution Procedure. The governing equation is rewritten in dimensionless form after introducing several dimensionless parameters, as performed by Li et al. (1994). The finite difference method is then used to solve Eq. (25). To ensure that each wavelength of the microwaves in the concrete, $\lambda \approx 1/f\sqrt{\mu_{\text{air}}\epsilon'}] \approx 6.3 \times 10^{-3}$ m for $f = 18$ GHz, has more than 60 subdivisions in the numerical calculation, the total subdivision number of $N = 6{,}000$ is used in the analysis.

5 Results and Discussion

From our previous investigations, it is known that the maximum temperature and pressure are located in the region near

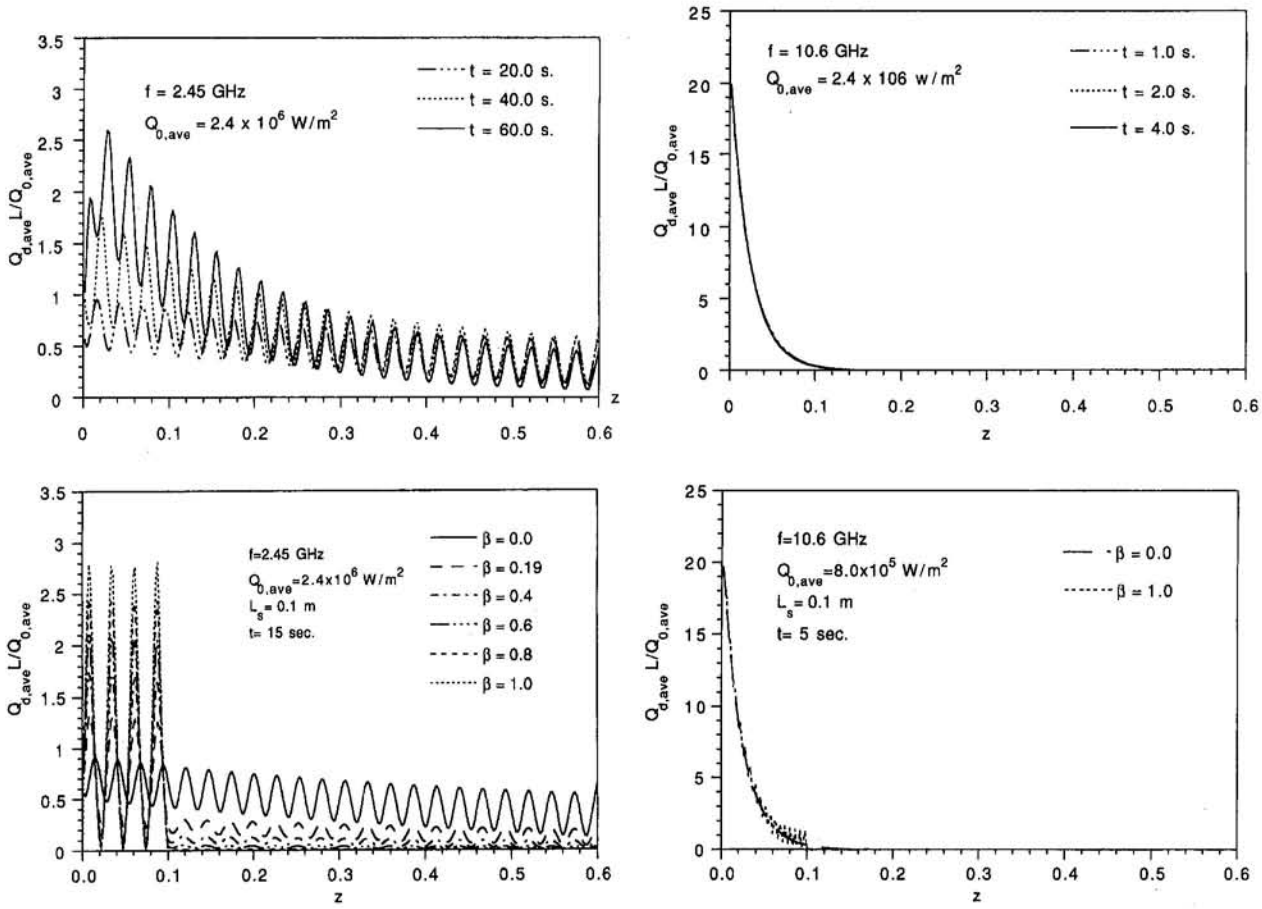

Fig. 2 Dimensionless power dissipation ($Q_{d,ave}L/Q_{0,avg}$) within a 0.6-m-thick concrete slab with and without steel reinforcement for different microwave frequencies: (*a*) f = 2.45 GHz with no steel reinforcement; (*b*) f = 10.6 GHz with no steel reinforcement; (*c*) f = 2.45 GHz with steel reinforcement; and (*d*) f = 10.6 GHz with steel reinforcement

the front surface of the concrete slab. Therefore, the thermal boundary conditions on the back surface of the concrete slab will not significantly affect the temperature and pressure distributions. In order to predict the effects of the estimated boundary conditions, two more extreme cases ($h_f = \infty$ and $h_f = 0.0$) on the front wall were studied in addition to the case of $h_f = 35$ W/(m^2K). It is anticipated that any convective thermal boundary condition will be between these two extreme cases. From the precalculation, it is seen that the temperature and pressure distributions for the two extreme cases of $h_f = 0.0$ and $h_f = \infty$ are almost identical except near the front wall. It is concluded that the effect of the thermal boundary conditions on the temperature and pressure distributions is negligible in actual practice. Therefore, $h_f = 35$ W/(m^2K) was used in all calculations.

5.1 Microwave Power Dissipation. In Figs. 2(*a*) and 2(*b*), the time-averaged dimensionless microwave power dissipations ($Q_{d,avg}L/Q_{0,avg}$), at different heating times within the concrete with no steel reinforcement, for frequencies of 2.45 GHz and 10.6 GHz, respectively, are presented. For the low frequency ($f \leq 2.45$ GHz), the microwave has a very strong capability to penetrate the concrete. Therefore, in combination with the propagating wave, the strong reflection from the back wall interface (concrete–air) results in a standing wave within the slab. As a result of the dielectric loss, this standing wave decays along the propagating wave direction. For a higher frequency ($f \geq 10.6$ GHz), the wave penetration drops significantly. When the wave reaches the back wall of the concrete, its amplitude approaches almost zero. Thus, no standing wave is formed within the concrete and the corresponding power dissipation decreases monotonically. Therefore, the microwave energy almost dissipates at a distance of less than 10 cm from the front surface for the higher frequency of $f = 10.6$ GHz.

It is also seen from Fig. 2 that the maximum value of the dimensionless microwave power dissipation ($Q_{d,avg}L/Q_{0,avg}$) increases with the heating time (t). As the concrete temperature elevates with time, the dielectric constant (ϵ') increases, which results in a decrease of the electric field (E_x). Simultaneously, the effective dielectric loss (ϵ''_{eff}) increases with the temperature. The final product of the declining electric field potential (E_x) and the increase of the effective dielectric loss (ϵ''_{eff}) augments the microwave power dissipation as the temperature rises. For example, the maximum microwave energy dissipation for $Q_{0,avg} = 2.4 \times 10^6$ W/m^2 and for $f = 2.45$ GHz increases 230 percent in a 60 second period during heating. For the higher microwave frequencies, the microwave penetration becomes smaller, regardless of how the dielectric permittivity changes. In Fig. 2(*b*), the variation of the maximum power dissipation due to the variation of dielectric properties for 10.6 GHz or higher cannot be identified.

With the presence of the steel reinforcement, the electric field (E_x) will be altered significantly, depending on the reflection and the location of the reinforcement (β and L_s). In Fig. 2(*c*), the distributions of the dimensionless microwave power dissipation ($Q_{d,avg}L/Q_{0,avg}$) within the concrete slab for $L_s = 0.1$ m and different values of β at the same specified time ($t = 15$ s) are presented, in which the cases of $\beta = 0$ and $\beta = 1$ correspondingly represent no steel reinforcement and a perfect reflector. When the reflection from the reinforcement increases, more microwave energy will be dissipated between the concrete front surface and the location of the reinforcement. In the meantime,

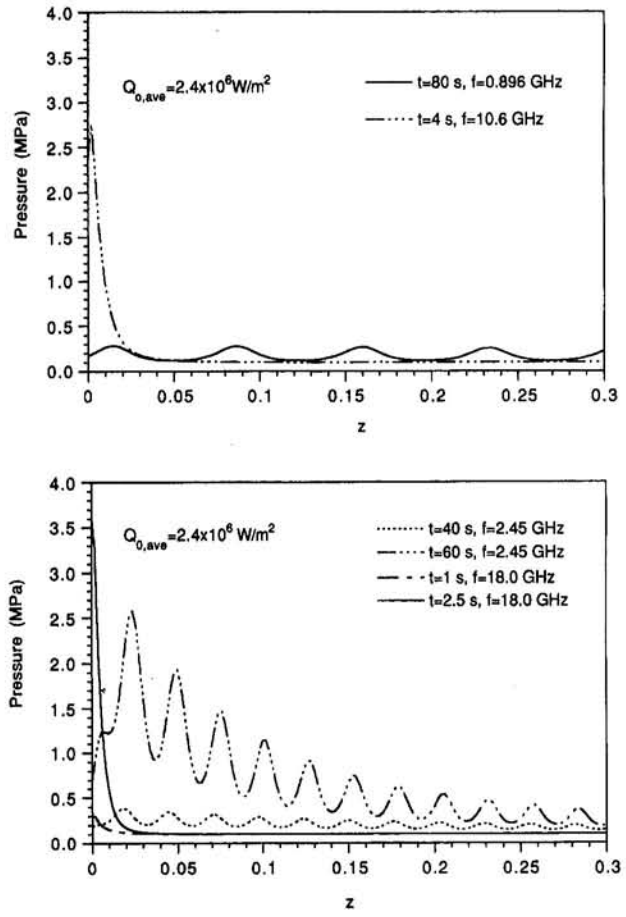

Fig. 3 Variations of the pressure distribution within a 0.6-m-thick concrete slab for h_f = 35 W/m²K and h_b = 15 W/m²K, when ϕ = 0.1 and $Q_{0,avg}$ = 2.4 × 10⁶ W/m²: (*a*) f = 0.896 GHz and f = 10.6 GHz; (*b*) f = 2.45 GHz and f = 18.0 GHz

the power dissipation beyond the reinforcement decreases as β increases. The maximum value of power dissipation $(Q_{d,avg})_{max}$ increases dramatically in the presence of the reinforcement. Compared to the case with no reinforcement (β = 0.0), the maximum power dissipation increases 57, 126, 178, 211, and 227 percent for β = 0.19, 0.4, 0.6, 0.8, and 1.0, respectively, for f = 2.45 GHz.

Figure 2(*d*) represents the dimensionless microwave power distributions for f = 10.6 GHz and L_s = 0.1 m at t = 5 s with two extreme values of β (0 and 1). It is illustrated that the presence of an extremely strong steel reinforcement, (β = 1.0) at L_s = 0.1 m, slightly affects the distribution of the power dissipation near the location of the reinforcement, since the electric field (E_x) has already decayed to a very low level. Thus, with no changes, or only slight changes in power dissipation, the effect of the steel reinforcement on the temperature and pressure distributions will definitely be insignificant.

5.2 Effect of the Frequency (f) on the Pressure (P) Distributions. In Figs. 3(*a*) and 3(*b*), the typical patterns of the pressure distribution and their variation for different frequency (f) are present. In the figures, only the distribution within part of the concrete with a significant variation ($0 < z < 0.3$ m) is plotted, while in the calculation, the concrete thickness of 0.6 m (L = 0.6 m) is used. For microwave frequencies of 0.896 GHz and 2.45 GHz, the peaks of the pressure distribution decay slowly along the microwave propagation direction (z). As time elapses, the temperature anywhere within the concrete rises almost proportionally and retains the same shape. It is also seen from Figs. 3(*a*) and 3(*b*) that as the microwave frequency increases to a higher value (to 10.6 GHz and 18.0 GHz), only one pressure peak shifts toward the front surface, similar to the microwave power dissipation. Therefore, the pressure near the front surface rises more quickly than that of the low microwave frequencies, such as 0.896 and 2.45 GHz.

Figure 3 illustrates that for a microwave frequency higher than 2.45 GHz, the pressure at a position located deeper than 0.15 m (z/L = 0.2) does not change significantly as compared to the initial pressure (0.1013 MPa). It also shows that for the 0.896 GHz frequency and $Q_{0,avg} = 2.4 \times 10^6$ W/m², the maximum pressure is still lower after 60 seconds than the minimum tensile strength of concrete (σ_t = 4.0 MPa). For the 2.45 GHz frequency, the maximum pressure takes about 65 seconds to reach concrete tensile strength. For the 10.6 GHz frequency and $Q_{0,avg} = 2.4 \times 10^6$ W/m², it takes less than 5 seconds to exceed this value, while for the 18.0 GHz frequency, the heating time is reduced to less than 3 seconds to break the concrete.

5.3 Effect of Porosity (ϕ). The patterns of the evaporation rate ($\Delta m/\phi$) are similar to the corresponding microwave power dissipations. Based on the calculation, for different values of ϕ(ϕ = 0.1, 0.2, and 0.3), $\Delta m/\phi$ is almost identical at the same specified time for both frequencies of 2.45 and 10.6 GHz. From this we infer that the evaporation rate (Δm) is linearly proportional to the concrete porosity (ϕ).

The effects of concrete porosity (ϕ) on the maximum temperature, the maximum pressure, and the evaporation rate ($\Delta m/\phi$) with different heating times are listed in Table 1. In this table, ϕ = 0.0 refers to the results of the solid concrete conduction model calculated by Li et al. (1993). Only the maximum temperature is given in this column since the pressure of the steam and air mixture is not defined within the solid concrete. It is seen from this table that as porosity increases, the maximum temperature and pressure decrease slightly with the same heating time for a specific value of the microwave frequency. For higher concrete porosity, there is more void space and more liquid phase within the concrete. Thus, more liquid needs to be evaporated during the heating process for a specific microwave power intensity. Therefore, more energy will be used to evaporate the liquid. Table 1 shows that as the concrete porosity varies from 0.0 to 0.3, the maximum temperature and pressure barely change for the same heating time. In practice, the microwave power intensity used for the concrete D&D process is very high, which induces a very large energy dissipation within the concrete. Thus, only a small extra amount of energy is needed to evaporate the liquid as the concrete porosity varies

Table 1 Effect of porosity (ϕ) on the maximum temperature, pressure, and evaporation rate (Δm) at a power intensity of $Q_{0,avg}$ = 2.4 × 10⁶ W/m²

	ϕ=0.0*	ϕ=0.1			ϕ=0.2			ϕ=0.3		
Time sec.	T_{max} °C	T_{max} °C	P_{max} MPa	$\Delta m/\phi\times10^3$ kg/m³ s	T_{max} °C	P_{max} MPa	$\Delta m/\phi\times10^3$ kg/m³ s	T_{max} °C	P_{max} MPa	$\Delta m/\phi\times10^3$ kg/m³ s
f=2.45 GHz										
5.0	34.5	34.5	0.11	0.273	34.5	0.11	0.266	34.5	0.11	0.266
10.0	46.7	46.7	0.12	0.389	46.6	0.12	0.389	46.6	0.12	0.389
15.0	57.8	57.7	0.13	0.566	57.7	0.13	0.566	57.7	0.13	0.566
20.0	68.7	68.7	0.15	0.848	68.6	0.15	0.847	68.6	0.15	0.846
25.0	80.1	80.1	0.17	1.322	80.1	0.17	1.321	80.0	0.17	1.318
30.0	92.7	92.7	0.21	2.174	92.6	0.21	2.168	92.6	0.21	2.163
35.0	107.3	107.3	0.27	3.783	107.2	0.27	3.768	107.2	0.27	3.754
40.0	124.8	124.7	0.38	6.883	124.6	0.38	6.843	124.5	0.38	6.802
45.0	146.0	145.7	0.59	12.833	145.6	0.59	12.720	145.4	0.59	12.607
50.0	170.4	170.1	0.98	23.265	169.8	0.97	22.970	169.4	0.97	22.682
55.0	196.7	196.2	1.64	38.614	195.7	1.63	37.943	195.1	1.61	37.297
60.0	222.3	221.6	2.62	58.029	220.8	2.59	56.710	220.1	2.55	55.450
f=10.6 GHz										
1.0	70.0	70.0	0.15	18.94	70.0	0.15	18.92	70.0	0.15	18.91
2.0	118.5	118.4	0.34	71.18	118.3	0.34	70.94	118.3	0.34	70.69
3.0	165.1	164.8	0.88	178.92	164.6	0.87	177.37	164.4	0.87	175.85
4.0	210.2	209.6	2.11	389.13	209.1	2.09	381.94	208.6	2.07	375.03
5.0	253.1	252.0	4.39	842.90	250.1	4.31	808.85	250.0	4.24	777.70

*Li et al. (1993).

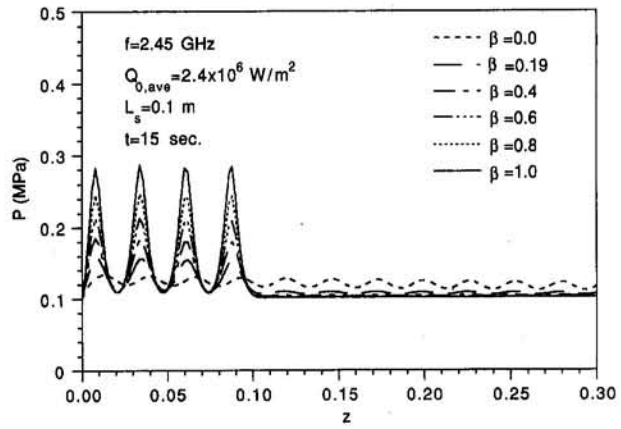

Fig. 4 Variation of the pressure distributions (P) within a 0.6-m-thick concrete slab with the steel reinforcement located at L_s = 0.1 m at t = 15 s, f = 2.45 GHz, and $Q_{0,avg}$ = 2.4 × 10^6 W/m^2

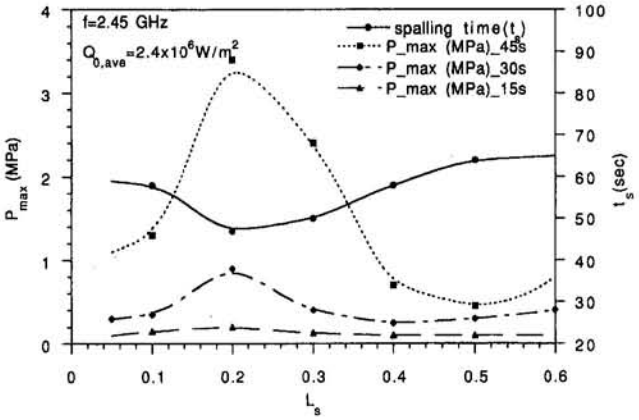

Fig. 5 Variations of the maximum pressure (P_{max}) and the concrete spalling time (t_s) with different reinforcement locations when β = 0.19, f = 2.45 GHz, and $Q_{0,avg}$ = 2.4 × 10^6 W/m^2

from 0.1 to 0.3. Thus, one may conclude that the effect of concrete porosity on the temperature and pressure distributions and their variations can be neglected during the microwave heating process.

5.4 Effect of the Steel Reinforcement. As discussed before, for the higher microwave frequency ($f \geq$ 10.6 GHz), presence of the steel reinforcement does not affect the distribution and the variation of the microwave power dissipation within the concrete. Therefore, for the higher microwave frequency ($f \geq$ 10.6 GHz), no further effects of the steel reinforcement on the temperature, and thus, pressure distributions are expected.

The typical pressure distributions for f = 2.45 GHz, Q_{avg} = 2.4 × 10^6 W/m^2 with a steel reinforcement having different values of β within a 0.6 m thick concrete slab are plotted in Fig. 4. Similar to Fig. 3, only the portion with significant variation is plotted in Fig. 4. When different reinforcements are present, the pressure distributions are totally different. As the value of β increases, the maximum pressure increases, too. For example, at t = 15 s, the values of P_{max} are 0.1585, 0.1848, 0.2130, 0.2470, and 0.2879 (MPa) for β = 0.19, 0.4, 0.6, 0.8, and 1, respectively, while at t = 45 s, the values of P_{max} are 1.3361 and 3.0026 (MPa) for β = 0.19 and 0.4. As the value of β further increases, the maximum pressure already exceeds the concrete tensile strength at t = 45 s. In addition to a rise in the maximum pressure, the locations of this maximum pressure also shift deeper into the concrete. This deeper location will cause more concrete to be removed.

The concrete spalling time, with and without different steel reinforcements (different values of β), for f = 2.45 GHz with $Q_{0,avg}$ = 2.4 × 10^6, and for f = 10.6 GHz with $Q_{0,avg}$ = 8.0 × 10^5 W/m^2, is tabulated in Table 2. The experimental findings reported by White et al. (1992) are also listed for comparison. It is shown that with a fixed location of the reinforcement (L_s = 0.1), the concrete spalling time (t_s) decreases as the value of β increases. At a 2.45 GHz frequency, more microwave energy is reflected from the steel reinforcement for a larger value of β, thus more energy is dissipated in front of the reinforcement instead of passing through the location of the reinforcement. With a higher maximum power dissipation, the maximum temperature and pressure are initiated, hence, a short time is required to spall the concrete. At a 10.6 GHz frequency, nearly all the microwave energy is dissipated ahead of the reinforcement (L_s = 0.1 m). Therefore, the presence of different reinforcements does not change the corresponding spalling time (t_s). As an overall evaluation, the calculated concrete spalling time (t_s) agrees very well with the experimental findings.

Table 2 Comparison of the concrete spalling time

β	Exp**	0.0	0.1	0.19	0.3	0.4	.06	0.8	1.0
t_s, sec. for f=2.45 GHz $Q_{0,ave}$=2.4×10^4 W/m^2	~59 (β=0)	65.39	63.98	58.21	53.20	48.98	42.89	38.67	35.86
t_s, sec. for f=10.6 GHz $Q_{0,ave}$=8.0×10^3 W/m^2	~15 (β<0.2, L_s>.05m)	16.48	16.40	16.38	16.35	16.33	16.30	16.27	16.25

**White et al. (1992).

For different locations of the reinforcement (L_s), the maximum pressure (P_{max}) for f = 2.45 GHz, $Q_{0,avg}$ = 2.4 × 10^6 W/m^2, and β = 0.19 with different heating times (t) is plotted in Fig. 5. The corresponding concrete spalling time (t_s) for f = 2.45 GHz, $Q_{0,avg}$ = 2.4 × 10^6 W/m^2, and β = 0.19 is also presented in Fig. 5.

It is also seen from Fig. 5 that when the reinforcement is located very close to the front surface, a large amount of reflected microwave energy is transferred through the layer between the concrete front surface and the reinforcement. When the reinforcement is located deeper, the energy reflected through the front surface is lessened. Thus, more microwave energy is dissipated within the concrete and a higher maximum temperature and pressure (T_{max} and P_{max}) are achieved at a specific heating time. When the reinforcement is located at a depth further than 0.25 m, the maximum temperature and pressure (T_{max} and P_{max}) begin to decrease, since the maximum energy dissipation composed by the incident and reflected microwaves starts to decrease. It is shown in Fig. 5 that the concrete spalling time (t_s) decreases and then increases as the location of the reinforcement varies from the front wall to the back wall. This implies that for different locations (L_s) of the same reinforcement, different heating times are needed to spall the same concrete with the same microwave frequency (f) and power intensity ($Q_{0,avg}$). A minimum spalling time occurs when $L_s \approx$ 0.25 m because of the behaviors of T_{max} and P_{max}.

6 Concluding Remarks

The microwave power dissipation and pressure distributions and their variations within a 0.6-m-thick concrete slab subjected to microwave attack have been analyzed in the present paper. The effects of different parameters in the current analysis on temperature, pressure, and evaporation rate (Δm) distributions and their variations have been discussed. Based on these discussions, the following facts may be concluded:

1 For different microwave frequencies (f), the patterns of power dissipation, temperature, and pressure distributions are totally different. As frequency (f) increases, the microwave penetration decreases sharply, and then the power dissipation decays significantly. For a low microwave frequency ($f <$ 2.45 GHz), as the heating time elapses, the total power dissipation

and its maximum dissipation value within the concrete change dramatically. For a high microwave frequency ($f > 10.6$ GHz), the power dissipation and its maximum value barely change, since the penetration of the high microwave frequencies is low. At the same microwave power intensity ($Q_{0,\text{avg}}$), a higher maximum temperature and steam pressure within the concrete are achieved for the higher microwave frequencies, which means less time is required to spall the concrete.

2 In this application of using a microwave heating technique, the effect of the thermal boundary conditions on the temperature and pressure distributions is limited to a small region near the front wall, and is negligible in actual practice. In the meantime, under a high microwave power intensity during the microwave D&D process, only a small amount of energy is used to evaporate the residual water within the concrete. Thus, the effect of the concrete porosity (ϕ) on the temperature and pressure distributions and their variations can also be safely neglected.

3 With the presence of the steel reinforcement, part of the microwave energy is reflected from the reinforcement. As a portion of the microwave reflected from the steel reinforcement (β) increases, more energy is dissipated between the concrete front surface and the location of the reinforcement. For a low microwave frequency ($f \leq 2.45$ GHz), the maximum value of the power dissipation $(Q_{d,\text{avg}})_{\max}$ becomes much higher as compared to the case without the steel reinforcement. For a microwave frequency of 10.6 GHz or higher, the microwave power dissipation ($Q_{d,\text{avg}}$), and the temperature (T) and pressure (P) distributions are slightly affected by the presence of the steel reinforcement.

4 For a microwave frequency of 2.45 GHz, when the reinforcement is present, the maximum temperature and pressure ($T_{\max}$ and $P_{\max}$) rise significantly as the value of β increases. The concrete spalling time (t_s) steadily decreases as the value of β increases when the reinforcement is located at a fixed position (L_s). The maximum temperature and pressure ($T_{\max}$ and $P_{\max}$) and the concrete spalling time (t_s) also vary with the location of the reinforcement. Both the maximum temperature and pressure distributions reach the highest value when $L_s = 0.25$ m for a microwave frequency of 2.45 GHz.

Acknowledgments

The results presented in this paper were obtained in the course of research sponsored by the Department of Energy.

References

Ebadian, M. A., and Li, W., 1992, "Concrete Decontamination and Decommissioning by Using Microwave Technology," Final Report, DOE research grant #DE-AC05-840R21400.

Haar, L., Gallagher, J. S., and Kell, G. S., 1984, *NBS/NRC Steam Tables,* Hemisphere Publishing, New York.

Harmathy, T. Z., 1969, "Simulation Moisture and Heat Transfer in Porous Systems With Particular Reference to Drying," *I & EC Fund.,* Vol. 8, p. 92.

Hills, D. L., 1989, "The Removal of Concrete Layers From Biological Shields by Microwave," *EUR 12185,* Nuclear Science and Technology, Commission of the European Communities.

Huang, C. D. L., Siang, H. H., and Best, C. H., 1979, "Heat and Moisture Transfer in a Concrete Slab," *Int. J. Heat Mass Transfer,* Vol. 22, pp. 257–266.

Iskander, M. F., 1992, *Electromagnetic Fields and Waves,* Prentice-Hall, New Jersey.

Johnk, C. T. A., 1988, *Engineering Electromagnetic Fields and Waves,* 2nd ed., Wiley, New York.

Li, W., Ebadian, M. A., White, T. L., and Grubb, R. G., 1993, "Heat Transfer Within a Radioactively Contaminated Concrete Slab Applying a Microwave Heating Technique." ASME JOURNAL OF HEAT TRANSFER, Vol. 115, pp. 42–50.

Li, W., Ebadian, M. A., White, T. L., Grubb, R. G., and Foster, D., 1994, "Heat and Mass Transfer in a Contaminated Porous Concrete Slab With Variable Dielectric Properties," *Int. J. Heat Mass Transfer,* Vol. 37, pp. 1013–1027.

Metaxas, A. C., and Meredith, R. J., 1983, *Industrial Microwave Heating,* Peter Peregrinus, London, United Kingdom.

Neville, A. M., 1981, *Properties of Concrete,* 3rd ed., Pitman, MA.

Reid, R. C., Prausnitz, J. M., and Poling R. E., 1987, *The Properties of Gases and Liquids,* 4th ed., McGraw-Hill, New York.

Watson, A., 1968, *Microwave Power Engineering,* Vol. 2, Academic Press, New York.

Wei, C. K., Davis, H. T., Davis, E. A., and Gordon, J., 1985a, "Heat and Mass Transfer in Water-Laden Sandstone: Convective Heating," *AIChE J.,* Vol. 31, No. 8, pp. 1338–1348.

Wei, C. K., Davis, H. T., Davis, E. A., and Gordon, J., 1985b, "Heat and Mass Transfer in Water-Laden Sandstone: Microwave Heating," *AIChE J.,* Vol. 31, No. 5, pp. 842–848.

Whitaker, S., 1977, "A Theory of Drying in Porous Media," *Advances in Heat Transfer,* Vol. 13.

White, T. L., Grubb, R. G., Pugh, L. P., Foster, D., Jr., and Box, W. D., 1992, "Removal of Contaminated Concrete Surfaces by Microwave Heating—Phase I Results," *Proceedings of 18th American Nuclear Society on Waste Management,* Waste Management 92, Tucson, AZ.

Yasunaka, H., Shibamoto, M., and Sukagawa, T., 1987, "Microwave Decontaminator for Concrete Surface Decontamination in JPDR," *Proceedings of the Int. Decommissioning Symposium,* pp. 109–115.

Heat Transfer Enhancement in Narrow Channels Using Two and Three-Dimensional Mixing Devices

S. V. Garimella
Cray-Research Associate Professor.
Mem. ASME

D. J. Schlitz[1]
Graduate Research Assistant.

Department of Mechanical Engineering,
University of Wisconsin—Milwaukee,
P.O. Box 784,
Milwaukee, WI 53201

The localized enhancement of forced convection heat transfer in a rectangular duct with very small ratio of height to width (0.017) was experimentally explored. The heat transfer from a discrete square section of the wall was enhanced by raising the heat source off the wall in the form of a protrusion. Further enhancement was effected through the use of large-scale, three-dimensional roughness elements installed in the duct upstream of the discrete heat source. Transverse ribs installed on the wall opposite the heat source provided even greater heat transfer enhancement. Heat transfer and pressure drop measurements were obtained for heat source length-based Reynolds numbers of 2600 to 40,000 with a perfluorinated organic liquid coolant, FC-77, of Prandtl number 25.3. Selected experiments were also performed in water (Prandtl number 6.97) for Reynolds numbers between 1300 and 83,000, primarily to determine the role of Prandtl number on the heat transfer process. Experimental uncertainties were carefully minimized and rigorously estimated. The greatest enhancement in heat transfer relative to the flush heat source was obtained when the roughness elements were used in combination with a single rib on the opposite wall. A peak enhancement of 100 percent was obtained at a Reynolds number of 11,000, which corresponds to a transitional flow regime. Predictive correlations valid over a range of Prandtl numbers are proposed.

Introduction

The primary motivation for this study was to find localized enhancement techniques for the heat transfer from discrete heat sources for a variety of practical applications requiring effective cooling over small zones, as in electronics cooling, turbine blades, nuclear reactors, and, to some extent, compact heat exchangers. In the area of electronics cooling, the widely different dissipation rates from different chips on a single circuit board in a computer result in large temperature differences between these chips, when exposed to identical heat transfer coefficients. Thus, even when the maximum temperature attained by the hottest chip is held within acceptable limits, both electronic and mechanical failures could occur due to large *interchip* temperature differences. Local enhancement techniques are thus necessary to equalize temperatures across the circuit board, by selectively cooling the hotter chips. Enhanced internal cooling of turbine blades would similarly allow the designer to increase the turbine inlet temperature while maintaining a constant blade temperature, and thus increase the thrust and power output of gas turbines.

The heat transfer in these narrow passages can be enhanced by using surface modifications to increase the available surface area as well as the turbulence and mixing levels in the flow. The basic principles of convective heat transfer enhancement are common to a host of engineering applications as identified above, and these areas have each spawned a considerable amount of research directed at understanding the complex flow patterns and heat transfer in these situations.

Early analytical studies attempted to predict heat transfer rates due to discrete-heating boundary conditions imposed on a surface in laminar and turbulent flows. Spalding (1961) provided a general method for determining local heat transfer rates through a turbulent boundary layer on a wall downstream of a sudden temperature discontinuity. Cess and Shaffer (1959) presented solutions for laminar flow between parallel plates with a symmetric wall heat flux. The corresponding solution for turbulent flow was presented by Hatton and Quarmby (1963). Sogin (1960) calculated heat transfer rates from several isothermal strips in tandem in laminar and turbulent flow, which were verified with mass transfer experiments.

Heat transfer in duct flows with two and three-dimensional roughness elements has been studied extensively. Han et al. (1978) studied the effect of rib geometry on friction factor and Stanton number for fully developed turbulent air flow. Kukreja et al. (1991) reported the effect of varying the length and configuration of transverse discrete ribs mounted on both walls of a square channel on heat transfer and friction factor, with applications to turbine blade cooling. Much of the attention devoted to investigating random or repeated-rib type roughness has focused on very small elements—at least an order of magnitude less than the boundary layer thickness, and for tubes, one or two orders of magnitude less than the tube diameter (Dipprey and Sabersky, 1963; Webb et al., 1971). The behavior of different kinds of roughness has been described in studies by Baumann and Rehme (1975), Dalle Donne and Meyer (1977), and Meyer (1980) among others, based on whether the flow in the cavities between roughness elements is confined or interacting. Transformations have been suggested that can be used to apply results from one duct geometry to others. Kader and Yaglom (1977) made the first clear distinction between two and three-dimensional roughness. The heat transfer dependence on roughness Reynolds number derived in their model was different for the two kinds of roughness; such a difference was also

[1]Current address: Engineer, Rockwell Automation, Milwaukee, WI 53024.

Contributed by the Heat Transfer Division and presented at the ASME Winter Annual Meeting, Anaheim, California, November 8–13, 1992. Manuscript received by the Heat Transfer Division January 1994; revision received February 1995. Keywords: Augmentation and Enhancement, Electronic Equipment, Forced Convection. Associate Technical Editor: T. W. Simon.

reported by Garratt and Hicks (1973). This would suggest that on a larger scale, two-dimensional ribs would behave differently from three-dimensional elements.

Forced convection from larger three-dimensional elements in rectangular ducts has been studied among others by Sparrow et al. (1982), Moffat et al. (1985), and Roeller et al. (1991) in air, and by Incropera et al. (1986) and Garimella and Eibeck (1990, 1991) using liquid coolants. The effect of element and duct dimensions as well as the element spacing density on the heat transfer were investigated. Other configurations such as pin fins for heat transfer enhancement have been studied by Steuber and Metzger (1986) and Kelecy et al. (1987). Several of these studies presented correlations for heat transfer from protrusions to air. Kelecy et al. (1987) also attempted to correlate data for different liquid coolants, but could not satisfactorily account for the wide variations in Prandtl number between liquids.

Recent efforts by Garimella and Schlitz (1993) have focused on locally enhancing heat transfer from particular protruding elements in an array by using vortex generators on the wall opposite from the elements. The vortex generators were found to yield enhancements as high as 17 percent, and significantly, this enhancement was found to be localized on one element.

Although a large body of literature exists that deals with heat transfer enhancement due to two-dimensional ribs and three-dimensional roughness elements, the enhancement of heat transfer using a combination of two and three-dimensional devices on opposite walls has not been investigated. This combined effect is especially significant for heat transfer enhancement in localized regions. Since ribs can locally enhance heat transfer from three-dimensional roughness elements, they can be selectively placed above the elements in those areas where particularly large heat transfer rates are required, such as at hot chips on a computer board or near the leading edge of turbine blades.

This paper describes an experimental investigation of the localized enhancement of heat transfer in ducts of small height-to-width ratio. The central objective is to extend the limits of the heat transfer coefficients that can be obtained in forced convection, without recourse to phase change or impingement configurations. In the experiments, heat transfer from a small heated area of the duct wall is enhanced in stages by allowing the heat source to protrude off the wall, by adding three-dimensional roughness elements upstream of the heat source, and further, by installing two-dimensional transverse ribs on the wall opposite the heat source. The enhancement in heat transfer is effected through increased mixing as well as locally increased velocities. Except for a small heated patch, the rest of the channel wall is unheated, since localized enhancement is sought. Moreover, since the flow in these narrow passages is usually well mixed, the local heat transfer behavior is largely independent of upstream conditions. Hence, results for the discrete heat source could be applied to other heating conditions, provided the bulk-mean temperature at a given location is known.

The strategy of the present experiments was to first obtain heat transfer coefficients for a flush heat source and then to determine the enhancement obtained by allowing the (single) element to protrude off the wall. An array of roughness elements was then added, in order to determine whether further enhancement was possible due to the modifications in the flow field and the increased mixing that results. The last set of experiments involved the installation of ribs on the opposite wall to enhance heat transfer locally from the flush as well as the protruding heat sources. The pressure drop in each case was measured to quantify the penalty in pumping power required for the heat transfer enhancement obtained by each technique. The experiments were performed over a range of Reynolds numbers and at different heat flux levels, and were carefully designed to minimize uncertainties. The tests were conducted with FC-77 and water to obtain results at significantly different Prandtl numbers.

Experimental Setup and Procedures

The experiments were carried out in a closed-loop liquid-flow facility. The horizontal, plexiglass test section has a cross section of 11 cm by 4 cm, and is 60 cm long. The temperature at the test-section inlet is maintained constant by means of an inline cooling-coil heat exchanger and a computer-controlled immersion heater in the flow loop. A converging section at the inlet to the test section has a series of screens and honeycomb to ensure uniform inlet flow. Liquid exits the test section through a rotameter, which was carefully calibrated using a volumetric technique with a graduated tank and stop watch. A perfluorinated organic liquid, FC-77, was used as the coolant for the bulk of the experiments. Selected experiments were also performed in water to determine the effect of Prandtl number on the heat transfer results. Both liquids were degassed prior to each experiment.

The test section has a removable top wall. Different channel aspect ratios can be set by installing top walls of different thicknesses. The channel height (H) for the present study was set at 0.2 cm. The transition in channel height from 4 cm to 0.2 cm is accomplished through a smooth 30 deg angle machined in the top wall at the channel inlet and exit to minimize separation. The top wall also contains static pressure taps to measure pressure drop over a test-section length of 6.5 cm, as shown in Fig. 1. The pressure taps in the top wall were connected to a pressure transducer, which was calibrated using U-tube and inclined-tube manometers for the different ranges of pressure drop.

The bottom wall of the test section contains a hatch into which is fitted a removable module that holds the heat source and roughness elements. The square heat source is 1 cm on the side (L). The enhancement due to roughness elements over the flush heat source was tested in two configurations: (i) a single heated protrusion with a height B of 0.06 cm ($H/B = 3$), and (ii) an array of unheated roughness elements mounted on the

Nomenclature

A = exposed surface area of heat source, cm^2
B = protrusion height, cm
C_D = drag coefficient = $\Delta P / {}^1/_2\, \rho U^2$
C_p = specific heat, J/kg K
D = channel hydraulic diameter, cm
h = heat transfer coefficient, W/m^2 K
H = channel height, cm
k = thermal conductivity, W/m K
L = length and width of heat source, cm
Nu_L = Nusselt number based on length of heat source = hL/k
ΔP = pressure drop, N/m^2
Q_{out} = heat transfer rate from heat source to coolant, W
Q_{supply} = power supplied to cartridge heater, W
Re_D = Reynolds number based on channel hydraulic diameter = UD/ν
Re_L = Reynolds number based on length of heat source = UL/ν
S = interprotrusion spacing, cm
T = temperature, °C
U = mean inlet velocity, m/s
ρ = density, kg/m^3
ν = kinematic viscosity, m^2/s

Subscripts

h = element surface
i = fluid inlet conditions

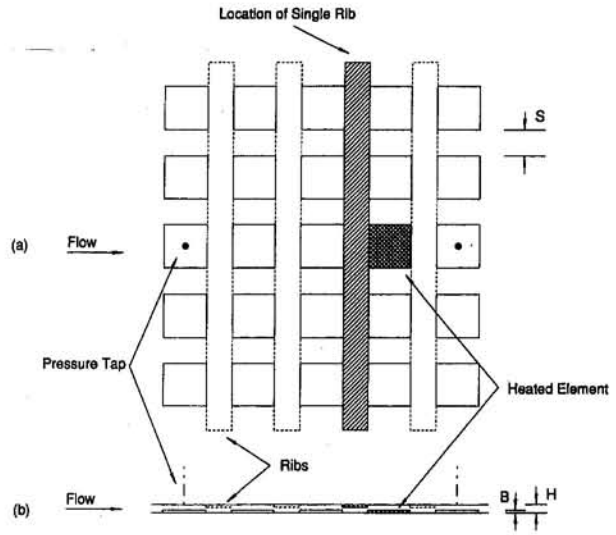

Fig. 1 Geometric details of the test section including the location of heat source, protrusions and ribs: (*a*) plan view, (*b*) side view; the pressure taps shown are located 6.5 cm apart

bottom wall in 15 spanwise rows of 5 elements each. The elements in the array have a spacing, S, in both directions of 0.6 cm (S/L = 0.6). In the case of the element array, the single heated protrusion is located in the center of the tenth row. As established by Garimella and Eibeck (1990), the flow reaches a fully developed state after the fourth row of the array. Hence, the heat source in the tenth row can be considered to be in a fully developed region. The situation tested most closely resembles stacked computer boards carrying unpackaged chips. Transverse ribs used for enhancing the heat transfer from the bottom wall were installed on the opposite wall at the locations identified in Fig. 1. The streamwise dimension of the ribs was equal to the spacing S between roughness elements; the rib height was the same as that of the roughness elements (B).

A single, discrete heat source is used in the experiments in preference to heating the entire bottom wall to facilitate local heat transfer measurements. Garimella and Eibeck (1990) showed that when a liquid is used as coolant, the flow even immediately downstream of a heated element is well mixed, with the temperature everywhere equal to the bulk-mean temperature. This behavior of liquids is in contrast to the thermally stratified nature of the flow downstream of discrete heat sources in air, as discussed by Anderson and Moffat (1991). This is attributable primarily to the heat capacity (ρC_p) of liquids (both FC-77 and water) being over three orders of magnitude greater than for air; thus the temperature rise in liquids is much smaller, resulting in an absence of thermal stratification. The upstream heating in liquids is thus satisfactorily accounted for by using the bulk-mean temperature as the reference in the definition of the heat transfer coefficient. In addition, since the flow in these narrow passages is usually turbulent, the local heat transfer behavior is largely independent of upstream conditions.

Details of construction of the heat source are shown in Fig. 2. A cartridge heater was installed in a copper stem, which was heavily insulated on all sides except the top. The copper stem is cylindrical over most of its length, with a 0.6 mm-high square "hat" on top. Heat losses from the sides of the stem are minimized by imbedding the copper stem (k = 397 W/m K) in polypropylene insulation (k = 0.12 W/m K); a detailed conduction analysis used to calculate the heat loss is described in the next section. Two heat sources were fabricated—one with the copper stem flush with the bottom wall, and the other with the tip protruding into the flow to a height (B) of 0.6 mm. The element temperature was obtained from a thermocouple (T-type, 36 gage) installed with silver print (a solution that leaves pure silver upon drying) into a 0.5-cm-long, 0.1-cm-dia hole at a depth of 0.075 cm from the tip of the copper stem. Experiments were conducted at a nominal power output (Q_{out}) of 11 W. Selected results obtained at a power output of 23 W demonstrated a negligible effect of heat flux on the heat transfer coefficient for Reynolds numbers (UL/ν) greater than 5000, indicating a pure forced convection regime.

Thermocouples were also installed in the flow, both upstream and downstream of the test section. The inlet flow was maintained at 20 ± 0.1°C for all the experiments, with a corresponding Prandtl number of 25.3 for FC-77 and 6.97 for water. The experiments with FC-77 were conducted at heat source length-based Reynolds numbers (UL/ν) ranging from 2600 to 40,000, while a wider range from 1300 to 83,000 was studied for water; this corresponds to channel height-based Reynolds numbers (UH/ν) of 500 to 7500 for FC-77 and 250 to 15,500 for water. The mean inlet velocity, U, is measured in the narrow channel of height H. The volumetric flow rates corresponding to the Reynolds number ranges are 46.9 to 720 cm^3/s for FC-77 and 27.4 to 1800 cm^3/s for water. Since the heat source length (L) was held constant in the experiments, the Reynolds numbers used in the presentation of the results should be viewed merely as nondimensional approach velocities.

The voltage supplied to the cartridge heater using a dc power supply was measured using a digital multimeter, and was maintained constant to within 1 mV (±0.01 percent of heat source output). The thermocouples and pressure transducer were hooked up to a Fluke Helios Plus data acquisition system and read using a personal computer. The pressure drop measurement was averaged over 500 readings while the temperature data were averaged over 50 readings. After the power level and flow rate were set, the element temperature was allowed to reach steady state, typically in 10 min, before measurements were recorded. For Q_{out} = 11 W, the element temperature ranged from 94°C at the lowest flow rate to 34°C at the highest for FC-77; the corresponding temperatures in water were 44°C and 23°C.

The reported pressure drop measurements were estimated to be accurate to within ±0.5 percent at the larger Reynolds numbers, increasing to roughly ±7 percent at Re = 5300. The uncertainty in the Reynolds number calculation ranged from ±10 percent at Re = 2600 to ±6 percent at 40,000 (to less than ±2 percent at 83,000), and resulted primarily from inaccuracies in reading the flowmeter. A detailed error analysis revealed uncertainties in the calculation of the heat transfer coefficient to be always less than ±4 percent. All uncertainties cited here are at a confidence level of 95 percent.

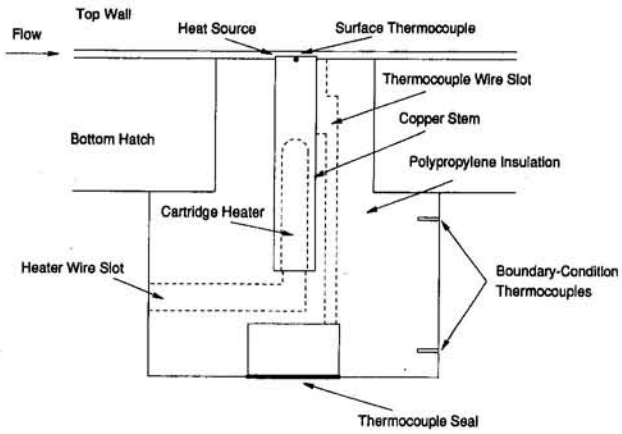

Fig. 2 Heated element construction details (side view)

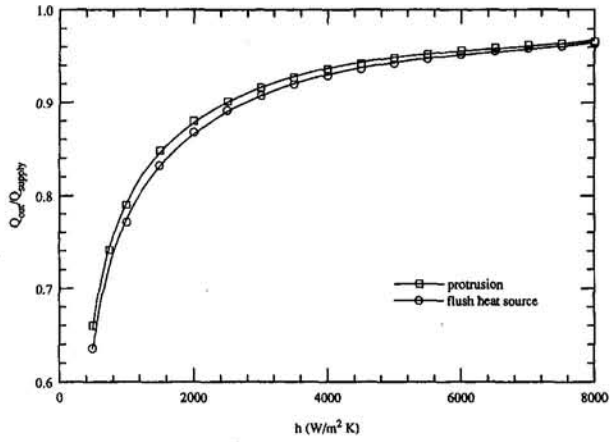

Fig. 3 Calculated ratio of power output to input as a function of heat transfer coefficient for FC-77 (similar calculations performed for water)

Conduction Analysis

A two-dimensional, axisymmetric conduction analysis of the copper stem-insulation combination was carried out. The heat transfer coefficient is calculated according to the equation:

$$h = \frac{Q_{out}}{A\,(T_h - T_i)} \tag{1}$$

where A is the exposed area of the heat source and Q_{out} is the heat leaving the source through the exposed area. The two-dimensional, steady-state heat conduction equation with heat generation was solved in cylindrical coordinates with boundary conditions specified as: insulated planes of symmetry; prescribed temperature on the outside of the insulation (obtained from thermocouples in the insulation, see Fig. 2); and specified heat transfer coefficient on the top boundary exposed to the flow, with a T_i for the fluid of 20°C. A control-volume approach was used for finite-differencing the governing equation, with a 35 by 35 mesh. This procedure involves breaking up the domain into small isothermal volumes and calculating the heat transferred through the surfaces of adjacent volumes. An effective thermal conductivity was used at the interfaces between materials. The calculation proceeded until the sum of the calculated heat sources/sinks in all the control volumes of the domain reached 0.1 percent of the heat supplied to the cartridge heater (Q_{supply}). A tighter convergence of 0.001 percent resulted in no significant changes in the temperature distribution; nor did the use of a 50 by 46 mesh, thus establishing the grid independence of the results.

A number of cases were analyzed with different heat transfer coefficients imposed on the top surface. Based on the results of these computational runs, a relationship between Q_{out}/Q_{supply} and the heat transfer coefficient, h, was obtained as shown in Fig. 3 for FC-77, for the flush and protruding heat sources with both coolants. The magnitude of heat input into the copper block (Q_{supply}) was found not to influence this ratio. Also, at the heat transfer coefficients obtained in this study, 90 percent or more of the power supplied is realized as the heat-source output (Q_{out}). A fourth-order least-squares curve fit with the functional form, $Q_{out}/Q_{supply} = \phi\,(h)$, was obtained for each heat source–coolant combination, as illustrated in Fig. 3. Along with Eq. (1), this expression was used to obtain the heat transfer coefficient from the measured Q_{supply} in each experimental run. By using this approach, the heat losses in the copper block assembly were accurately accounted for, resulting in reduced uncertainties in the calculation of the heat transfer coefficient.

Results and Discussion

Heat transfer and pressure drop results are presented in this section for the flush heat source, and then for the various stages of enhancement—the heated protrusion, the array of roughness elements, and the ribs on the opposite wall—along with the corresponding increases in pressure drop. The characteristic length used in the definition of the nondimensional parameters, the Reynolds and Nusselt numbers, is the length of the heat source, L. Except in the viscosity-correction term in the correlations proposed, all thermophysical properties are evaluated at the liquid temperature at the test-section inlet.

Heat transfer coefficients for the flush heat source with FC-77 and water are presented in Fig. 4, as curves of Nusselt number versus Reynolds number. Nusselt numbers for the protruding heat source, enhanced by an array of roughness elements, are also presented. Also included are results for a single heated protrusion in FC-77. The heat transfer coefficients for the two liquids fall in distinct groups, reflecting the influence of the different thermophysical properties; for instance, the heat transfer coefficient at $Re_L = 40{,}000$ is on the order of 6000 W/m^{2}K for FC-77 and 23,000 W/m^{2}K for water.

A number of interesting observations can be made from Fig. 4. First, the heat transfer coefficient for a single protrusion is greater than that for a flush heat source. This can be attributed to the perturbation to the flow field caused by the protrusion, since the increase in exposed area is incorporated in the definition of the convection coefficient. The resulting increase in mixing has an enhancing effect on the heat transfer. However, as the Reynolds number increases, and the flow approaches a fully turbulent state, the additional perturbation to the flow field by the single protrusion progressively diminishes, and the heat transfer coefficients for the two cases converge. The major effect due to the protrusion appears to be an earlier triggering of transition, as illustrated by the change from laminar to turbulent slopes occurring at lower Reynolds numbers for the protrusions. Away from transition, the difference between the flush and protruding heat sources is less significant.

The array of roughness elements yields a larger heat transfer coefficient than the single protruding element, especially for FC-77. Two competing effects influence the heat transfer coefficient in this case, as has been pointed out in previous studies (Moffat et al., 1985). On the one hand, a single protrusion is exposed to the entire approach flow, unlike interior elements in an array, which have a reduced exposure due to the blockage from upstream elements. This would tend to cause the heat transfer coefficient to be greater for the single element than for one in an array. On the other hand, the interior elements experience an enhancement in heat transfer due to the greater levels of mixing and turbulence in the interior flow relative to the approach flow. In the present study, the enhancement due to the greater mixing in the array interior is evidently a stronger effect than that due to full exposure to the approaching flow.

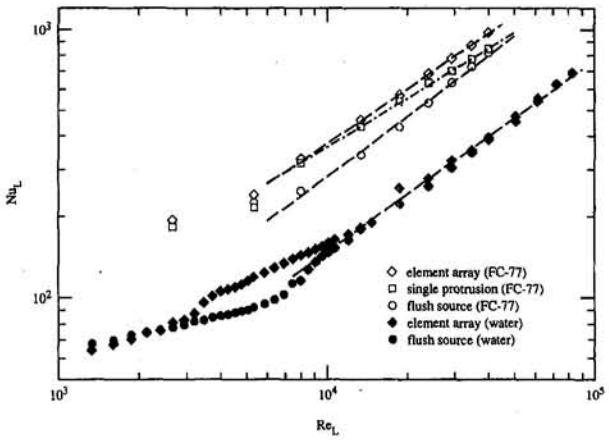

Fig. 4 Nusselt numbers for the flush and protruding heat sources with FC-77 and water as a function of Reynolds number

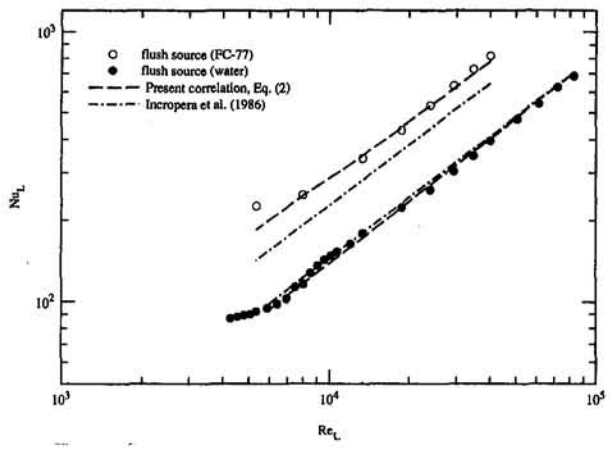

Fig. 5 Comparison of the experimental data for the flush source with predictions from the present study and the literature

This effect is more pronounced at the higher Reynolds numbers, and is manifested in the single protruding element behaving more like the array at the lower Reynolds numbers, and like the flush element as the Reynolds number increases.

The heat transfer coefficients in turbulent flow for the flush and protruding heat sources in FC-77 and water were correlated with least-squares curve fits. The Nusselt number was correlated against the Reynolds and Prandtl numbers. A viscosity-correction term was used in the correlations as suggested in the literature (Sieder and Tate, 1936) to account for the strong temperature dependence of the viscosity, especially for FC-77. The heat transfer from the flush heat source to both fluids in the range $10{,}000 < \mathrm{Re}_L < 80{,}000$ is correlated by the equation:

$$\mathrm{Nu}_L = 0.0370\ \mathrm{Re}_L^{0.784}\mathrm{Pr}^{0.5}\left(\frac{\mu_i}{\mu_h}\right)^{0.13} \qquad (2)$$

Predictions using this equation differ from the experimental data by a standard deviation of 3 percent, with an average error of ±2.7 percent. The heat transfer from the heated protrusion with the array of roughness elements for the same range of Reynolds numbers is correlated by:

$$\mathrm{Nu}_L = 0.1495\ \mathrm{Re}_L^{0.661}\mathrm{Pr}^{0.5}\left(\frac{\mu_i}{\mu_h}\right)^{0.13} \qquad (3)$$

which differs from the experimental data by an average error of ±10 percent with a standard deviation of 11 percent. The exponents for Prandtl number and viscosity ratio in Eq. (3) were adjusted to coincide with those in Eq. (2). Lower Prandtl number exponents were tried, but resulted in a significant deterioration in the predictions from the correlations. There is evidence in the literature (Webb, 1987) that the Prandtl number exponent in this equation is expected to be higher when roughened surfaces are used (as in the present study), compared to the exponent of 0.33 to 0.4 for smooth surfaces.

The experimental data and the correlation for the flush heat source with both liquids are compared in Fig. 5 with the predictions of Incropera et al. (1986, Eq. (12) in that paper). In this figure, the Nusselt numbers with the two liquids could not be normalized with Pr^n, since the exponent n takes a value of 0.5 in Eq. (2) above, while Incropera et al. suggest a value of 0.38. While the water data are predicted very well by both correlations, the agreement with the FC-77 data of the present correlation is better than that of Incropera et al. The underprediction with the latter correlation results from the lower Prandtl number exponent used.

Although the exponent of the Reynolds number in Eqs. (2) and (3) is different (due to the difference in the nature of the flow fields), a combined correlation for the flush and protruding heat sources is also proposed for convenient design predictions:

$$\mathrm{Nu}_L = 0.0973\ \mathrm{Re}_L^{0.698}\mathrm{Pr}^{0.5}\left(\frac{\mu_i}{\mu_h}\right)^{0.13} \qquad (4)$$

Predictions from this equation differ from the experimental data by an average error of ±10 percent, with a standard deviation of 12 percent. All the experimental Nusselt numbers are collected to within ±15 percent of this equation. The correlating equations proposed here are clearly geometry dependent and should be used only for discrete heat sources in narrow channels. Wider ranges of geometric and flow parameters are currently under investigation.

The enhancement in heat transfer from the flush heat source achieved by installing ribs on the opposite wall is depicted in Fig. 6 for FC-77. It is clear from the figure that enhancements on the order of 60 percent can be obtained by installing one rib just upstream of the flush source (see Fig. 1 for placement locations). Experiments were also conducted to measure the enhancement obtained due to the single rib placed at two other locations: directly above the flush source, and just downstream. However, the greatest enhancement was obtained for the case shown here, where the rib is installed just upstream of the element as shown in Fig. 1 (shaded rib). If enhancement is desired over a longer streamwise length, a series of ribs would be used. The presence of such additional ribs appears to decrease the enhancement obtained using a single rib; however, significant levels of enhancement still persist.

The combined enhancement of heat transfer by raising the flush heat source into a protrusion and by installing additional roughness elements as well as ribs on the opposite wall is shown in Fig. 7. Just as in the case of the flush source, the installation of a rib just upstream of the heated protrusion in the array causes a significant increase in the heat transfer coefficient. The extent of enhancement is also slightly reduced when four ribs are used instead of one. Data for the single heated protrusion (with no additional roughness elements) are included for reference in this figure.

The percentage enhancements for the configurations tested in this study are plotted in Fig. 8, where enhancement is defined with respect to the flush heat source, as $(h - h_{\mathrm{flush}})/h_{\mathrm{flush}}$ expressed as a percentage. The Reynolds number Re_D based on channel hydraulic diameter is included as a scale on the top axis. The best performance is obtained from the element array with a single rib, with peak enhancements of almost 100 percent; the performance is not degraded significantly when multiple ribs are used. The single rib on the opposite wall also causes considerable enhancement in heat transfer for the case of the flush heat source.

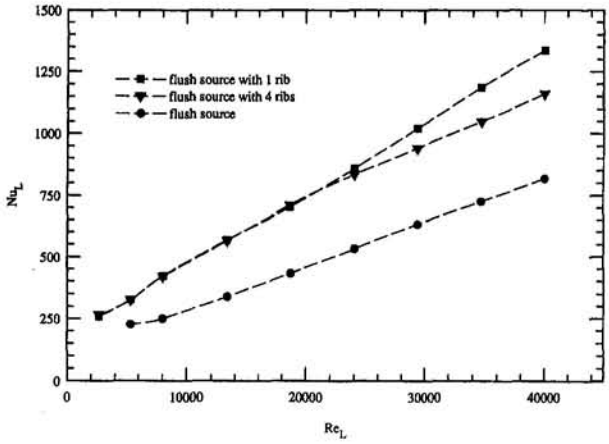

Fig. 6 Influence of the ribs on the opposite wall on the heat transfer from the flush heat source to FC-77

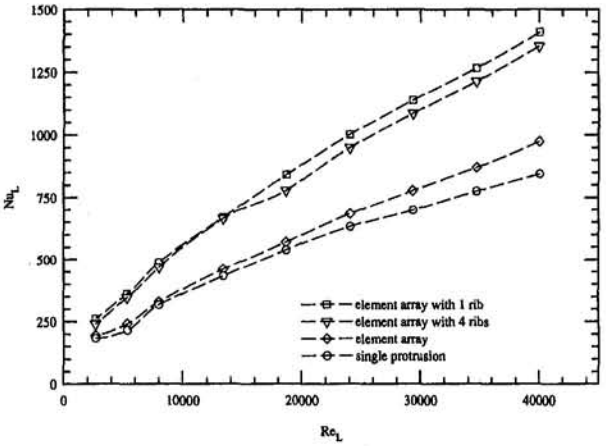

Fig. 7 Combined influence of protrusions and ribs on the heat transfer from the flush heat source to FC-77

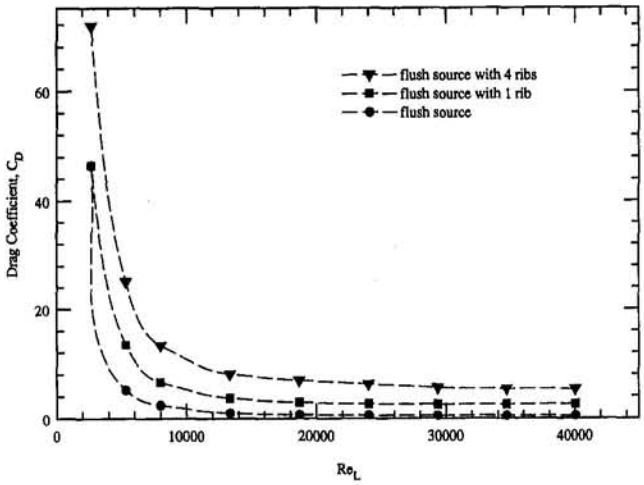

Fig. 9 Drag coefficient in FC-77 for the flush heat source with and without ribs on the opposite wall

For every configuration considered in this study, Fig. 8 shows that the peak enhancements occur at Reynolds numbers (UL/ν) between 8000 and 12,000. These Reynolds numbers are also those at which a change in slope can be discerned in Figs. 4, 6, and 7 in the Nusselt number variations with Reynolds number, indicating the onset of transition in the flow regime. Thus, the peak enhancement in heat transfer, whether due to the addition of roughness elements to the heated protrusion or due to ribs on the opposite wall, occurs in the transitional flow regime. This is a common feature that has been observed in previous studies of enhancement devices (Garimella and Schlitz, 1993), and appears to be caused by an earlier triggering of transition by the enhancement devices.

The pressure drop, nondimensionalized as drag coefficient C_D, for the flush heat source (parallel-plates channel) is presented as a function of Reynolds number in Fig. 9, and the increases due to the introduction of ribs are also shown. As expected, the pressure drop is greatest for the four ribs and least for the parallel-plates channel with the flush heat source. The drag coefficients for the single protrusion and the array of roughness elements over a length of 6.5 cm (four rows) are shown in Fig. 10. It is interesting that the single protrusion causes a larger drag coefficient than the array at low (laminar) Reynolds numbers.

The results obtained in this study point to several additional areas that need investigation. For instance, the enhancement in heat transfer obtained from installing ribs on the opposite wall is likely to be dependent on the channel height used. Parametric analyses should be undertaken to study the influence of channel height on this enhancement. However, the enhancement in heat transfer obtained by installing an array of roughness elements on the heated wall has been clearly established, and is likely to be realized over a wide range of channel heights. Additional work is required to understand the effect of the aspect ratio of the roughness elements, as well as to clarify the role of the coolant Prandtl number.

Conclusions

Heat transfer from a square, discrete flush heat source was enhanced progressively by using a protruding heat source, an array of roughness elements, and ribs on the opposite wall in a narrow rectangular channel. The protruding heat source with additional roughness elements was found to yield significant enhancements due to the mixing and turbulence induced into the flow by the upstream elements. The heat transfer coefficient for a single heated protrusion was comparable to that in an array at the lower Reynolds numbers, and to the flush heat source as the Reynolds number increases. Selected experiments performed in water illustrated the Prandtl number dependence of the heat transfer results. Predictive correlations are proposed for flush and protruding heat sources, valid over a wide range of Prandtl number.

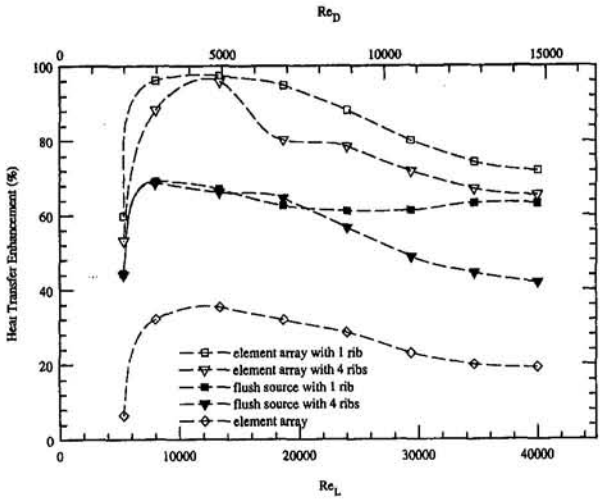

Fig. 8 Percent enhancement in heat transfer to FC-77 for all cases relative to the flush heat source

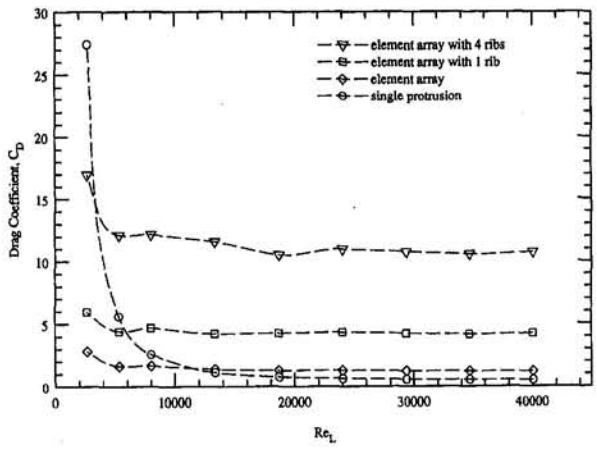

Fig. 10 Drag coefficient in FC-77 for the protrusions with and without ribs on the opposite wall

Ribs installed on the opposite wall were found to enhance significantly heat transfer from the flush and protruding heat sources in all cases. Of all the configurations tested, the highest heat transfer coefficients were obtained with the array of roughness elements in combination with a single rib just upstream of the heated protrusion; a peak enhancement of 100 percent was obtained in this case relative to the flush source. Introduction of additional ribs decreased the heat transfer slightly, but still yielded significant levels of enhancement over the cases with no ribs. The enhancement was greatest in the transitional flow regime for all cases.

References

Anderson, A. M., and Moffat, R. J., 1991, "Direct Air Cooling of Electronic Components: Reducing Component Temperatures by Controlled Thermal Mixing," ASME JOURNAL OF HEAT TRANSFER, Vol. 113, pp. 56–62.

Baumann, W., and Rehme, K., 1975, "Friction Correlations for Rectangular Roughness," *Int. J. Heat Mass Transfer,* Vol. 18, pp. 1189–1197.

Cess, R. D., and Shaffer, E. C., 1959, "Heat Transfer to Laminar Flow Between Parallel Plates With a Prescribed Wall Heat Flux," *Appl. Scientific Research,* Vol. 8, Section A, pp. 339–344.

Dalle Donne, M., and Meyer, L., 1977, "Turbulent Convective Heat Transfer From Rough Surfaces With Two-Dimensional Rectangular Ribs," *Int. J. Heat Mass Transfer,* Vol. 20, pp. 583–620.

Dipprey, D. F., and Sabersky, R. H., 1963, "Heat and Momentum Transfer in Smooth and Rough Tubes at Various Prandtl Numbers," *Int. J. Heat Mass Transfer,* Vol. 6, pp. 329–353.

Garimella, S. V., and Eibeck, P. A., 1990, "Heat Transfer Characteristics of an Array of Protruding Elements in Single Phase Forced Convection," *Int. J. Heat Mass Transfer,* Vol. 33, pp. 2659–2669.

Garimella, S. V., and Eibeck, P. A., 1991, "Fluid Dynamic Characteristics of the Flow Over an Array of Large Roughness Elements," ASME *Journal of Electronic Packaging,* Vol. 115, pp. 367–373.

Garimella, S. V., and Schlitz, D. J., 1993, "Reducing Inter-chip Temperature Differences in Computers Using Vortex Generators in Forced Convection," *ASME Journal of Electronic Packaging,* Vol. 115, pp. 410–415.

Garratt, J. R., and Hicks, B. B., 1973, "Momentum, Heat, and Water Vapor Transfer to and From Natural and Artificial Surfaces," *Quart. J. Roy. Met. Soc.,* Vol. 99, pp. 680–687.

Han, J. C., Glicksman, L. R., and Rohsenow, W. M., 1978, "An Investigation of Heat Transfer and Friction Characteristics for Rib-Roughened Surfaces," *Int. J. Heat Mass Transfer,* Vol. 21, pp. 1143–1156.

Hatton, A. P., and Quarmby, A., 1963, "The Effect of Axially Varying and Unsymmetrical Boundary Conditions on Heat Transfer With Turbulent Flow Between Parallel Plates," *Int. J. Heat Mass Transfer,* Vol. 6, pp. 903–914.

Incropera, F. P., Kerby, J., Moffatt, D. F., and Ramadhyani, S., 1986, "Convection Heat Transfer From Discrete Sources in a Rectangular Channel," *Int. J. Heat Mass Transfer,* Vol. 29, pp. 1051–1058.

Kader, B. A., and Yaglom, A. M., 1977, "Turbulent Heat and Mass Transfer From a Wall With Parallel Roughness Ridges," *Int. J. Heat Mass Transfer,* Vol. 20, pp. 345–357.

Kelecy, F. J., Ramadhyani, S., and Incropera, F. P., 1987, "Effect of Shrouded Pin Fins on Forced Convection Cooling of Discrete Heat Sources by Direct Liquid Immersion," *Proc. ASME/JSME Heat Transfer Conference,* Hawaii, pp. 387–394.

Kukreja, R. T., Lau, S. C., McMillin, R. D., and Chandra, P. R., 1991, "Effect of Length and Configuration of Transverse Discrete Ribs on Heat Transfer and Friction for Turbulent Flow in a Square Channel," *ASME/JSME Thermal Engineering Procs.,* Vol. 3, pp. 213–218.

Meyer, L., 1980, "Turbulent Flow in a Plane Channel Having One or Two Rough Walls," *Int. J. Heat Mass Transfer,* Vol. 23, pp. 591–608.

Moffat, R. J., Arvizu, D. E., and Ortega, A., 1985, "Cooling Electronic Components: Forced Convection Experiments With an Air-Cooled Array," ASME HTD-Vol. 48, pp. 17–27.

Roeller, P. T., Stevens, J., and Webb, B. W., 1991, "Heat Transfer and Turbulent Flow Characteristics of Isolated Three-Dimensional Protrusions in Channels," ASME JOURNAL OF HEAT TRANSFER, Vol. 113, pp. 597–603.

Sieder, E. N., and Tate, C. E., 1936, "Heat Transfer and Pressure Drop of Liquids in Tubes," *Ind. Eng. Chem.,* Vol. 28, p. 1429.

Sogin, H. H., 1960, "Laminar Transfer From Isothermal Spanwise Strips on a Flat Plate," ASME JOURNAL OF HEAT TRANSFER, Vol. 82, pp. 53–63.

Spalding, D. B., 1961, "Heat Transfer to a Turbulent Stream From a Surface With a Step-wise Discontinuity in Wall Temperature," *Int. Developments in Heat Transfer,* Part II, pp. 439–446.

Sparrow, E. M., Niethammer, J. E., and Chaboki, A., 1982, "Heat Transfer and Pressure Drop Characteristics of Arrays of Rectangular Modules Encountered in Electronic Equipment," *Int. J. Heat Mass Transfer,* Vol. 25, pp. 961–973.

Steuber, G. D., and Metzger, D. E., 1986, "Heat Transfer and Pressure Loss Performance for Families of Partial Length Pin Fin Arrays in High Aspect Ratio Rectangular Ducts," *Proc. 8th International Heat Transfer Conference,* C. L. Tien et al., eds., Vol. 6, pp. 2915–2920.

Webb, R. L., Eckert, E. R. G., and Goldstein, R. J., 1971, "Heat Transfer and Friction in Tubes With Repeated-Rib Roughness," *Int. J. Heat Mass Transfer,* Vol. 14, pp. 601–617.

Webb, R. L., 1987, "Enhancement of Single-Phase Heat Transfer," *Handbook of Single-Phase Convective Heat Transfer,* S. Kakac et al., eds., Wiley New York, Chap. 17, p. 17.51.

Influence of Turbulence Parameters, Reynolds Number, and Body Shape on Stagnation-Region Heat Transfer

G. J. Van Fossen

R. J. Simoneau

NASA Lewis Research Center,
Cleveland, OH 44135

C. Y. Ching
Syracuse University,
Syracuse, NY

This experiment investigated the effects of free-stream turbulence intensity, length scale, Reynolds number, and leading-edge velocity gradient on stagnation-region heat transfer. Heat transfer was measured in the stagnation region of four models with elliptical leading edges downstream of five turbulence-generating grids. Stagnation-region heat transfer augmentation increased with decreasing length scale but an optimum scale was not found. A correlation was developed that fit heat transfer data for isotropic turbulence to within ±4 percent but did not predict data for anisotropic turbulence. Stagnation heat transfer augmentation caused by turbulence was unaffected by the velocity gradient. The data of other researchers compared well with the correlation. A method of predicting heat transfer downstream of the stagnation point was developed.

Introduction

Heat transfer to a stagnation region is important in many engineering applications; none, however, is more critical than in the gas turbine where combustor exit temperatures often exceed the melting point of superalloy turbine airfoil materials. The highest heat transfer rate on a turbine airfoil usually occurs at the stagnation point, which makes it essential to obtain an accurate prediction of heat transfer in this region.

For a laminar free stream, stagnation-region heat transfer can be found if the pressure distribution is known using Frossling's solution (1958). Free-stream turbulence can augment stagnation-region heat transfer; enhancement of 190 percent over laminar values has been measured (Yeh et al., 1993). Turbulence intensities of 11 and 15 percent were measured at the exit of combustors in Zimmerman (1979) and Goebel et al. (1993), respectively. The length scale of combustor turbulence was not measured in either of these studies.

Stagnation-region heat transfer augmentation in the presence of free-stream turbulence is believed to be caused by vortical filaments that are convected into the stagnation region where they are stretched by the divergence of streamlines. Stretching causes the vorticity to be amplified through conservation of angular momentum (see Morkovin, 1979, for a review). It has been shown both experimentally and numerically (Hanarp and Suden, 1982; Van Fossen and Simoneau, 1987; Rigby and Van Fossen, 1991) that vorticity in the stagnation region causes heat transfer to be increased while the boundary layer remains laminar.

Turbulent eddies that are very large relative to the size of the bluff body are not stretched and, therefore, act only as mean flow variations. Eddies that are very small are destroyed by viscous dissipation before they can interact with the boundary layer. This leads to the hypothesis that somewhere between these two extremes there must be an optimum eddy size that causes the highest heat transfer augmentation.

It also seems reasonable that higher leading-edge velocity gradients would cause more rapid stretching of the vortical filaments as they are convected past the leading edge, thus causing higher heat transfer augmentation.

Three specific goals of the present research were: (1) to determine if an optimum eddy size exists, (2) to study the effect of leading-edge velocity gradient on stagnation-region heat transfer augmentation, and (3) to develop a more accurate prediction tool that could be used by designers to evaluate stagnation-region heat transfer.

Results of past experiments that attempted to correlate heat transfer augmentation as a function of turbulence intensity and Reynolds number, while ignoring the length scale (Zapp, 1950; Giedt, 1951; Seban, 1960; Schnautz, 1958; Smith and Kuethe, 1966; Kestin and Wood, 1971; Lowery and Vachon, 1975; Mehendale et al., 1991), were not entirely successful. Any resulting correlations usually predict the author's data but not data from other researchers.

There have been several attempts to isolate the effect of turbulence length scale in addition to intensity on stagnation-region heat transfer; Dyban et al. (1975) used perforated plates and a fully developed turbulent pipe flow, while Yardi and Sukhatme (1978) used four different grids. Both of their results showed increasing augmentation with decreasing scale, but they did not correlate the data based on this finding.

More recently, Ames (1990) used simulated combustor segments to generate turbulence with the length-scale-to-cylinder-diameter ratio greater than 1.0 and measure its effect on heat transfer to the stagnation point of three different diameter cylinders. Ames developed a new correlating parameter involving Reynolds number, turbulence intensity, and what he called an energy scale, which correlated his data as well as the data of several other researchers.

For the present work, stagnation-region heat transfer was measured on four elliptical leading-edge models with major to minor axis ratios of 1:1, 1.5:1, 2.25:1, and 3:1. Stagnation-region heat transfer was measured with each of five different grids at various distances upstream of each model. Data were taken at Reynolds numbers based on leading-edge diameter ranging from 37,000 to 228,000. Turbulence intensities were in the range of 1.1 to 15.9 percent while the ratio of integral length scale to cylinder diameter ranged from 0.05 to 0.30. Dimensionless stagnation point velocity gradient ranged from 1.2 to 1.8.

Contributed by the Heat Transfer Division for publication in the JOURNAL OF HEAT TRANSFER. Manuscript received by the Heat Transfer Division April 1994; revision received November 1994. Keywords: Forced Convection, Modeling and Scaling, Turbulence. Associate Technical Editor: T. W. Simon.

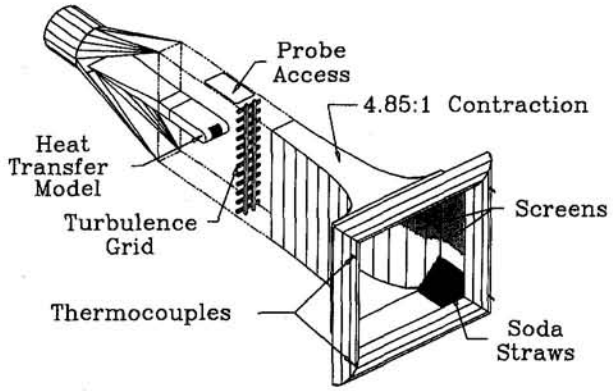

Fig. 1 Wind tunnel

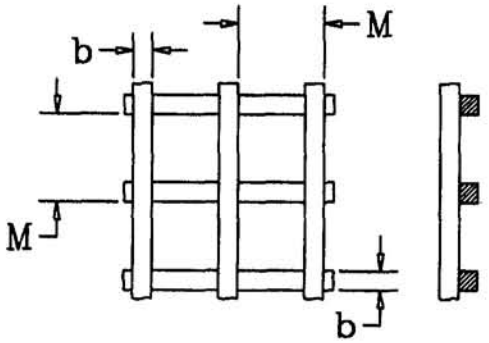

Fig. 2 Biplane grid configuration

The effect of turbulence intensity, length scale, Reynolds number, and leading-edge velocity gradient on stagnation-region heat transfer will be presented as a correlation that fit the heat transfer data for the square bar grids to within ±4 percent. The data of other researchers will also be compared with the correlation. A method for determining the heat transfer distribution downstream of the stagnation point will also be presented.

Test Facility, Instrumentation, and Data Acquisition

Wind Tunnel. The experiments were carried out in the wind tunnel shown in Fig. 1. Air drawn from the test cell passed through a flow-conditioning section and a 4.85:1 contraction before entering the 15.2-cm-wide by 68.6-cm-high test section. The maximum velocity attainable was about 46 m/s. Clear tunnel turbulence levels were less than 0.5 percent. After leaving the test section, air passed through a transition section into a 10-in. pipe in which a flow-measuring orifice and a butterfly valve were located. Four chromel-constantan thermocouples around the perimeter of the inlet measured the stagnation temperature. A hot-wire probe could be positioned anywhere in the test section within the confines of the window shown in Fig. 1.

Turbulence Grids. Five turbulence-generating grids were used; four were square bar, square mesh, biplane grids. The fifth grid consisted of an array of parallel wires oriented perpendicular to the streamwise and spanwise directions. Grid parameters are defined in Fig. 2 and dimensions are given in Table 1. Henceforth grids will be referred to by the symbols given in this table. Turbulence-generating grids could be installed from 2.41 to 52.3 cm upstream of the model stagnation point.

Heat Transfer Models. Figure 3 is a photograph of the four heat transfer models, which had elliptical leading edges with ratios of major to minor axes of 1:1, 1.5:1, 2.25:1, and 3:1. All models had the same radius of curvature, R, of 3.30 cm at the stagnation point, and wedge-shaped afterbodies that extended about 61 cm downstream to eliminate vortex shedding. Figure 4 shows a comparison of the model profiles and the tunnel walls as well as a typical cross section showing the heat flux gage arrangement. The 1:1 model had 19 heat flux gages and the other models all had 29 gages embedded symmetrically about the stagnation line. Each heat flux gage consisted of an aluminum strip 6.60 cm long by 0.476 cm wide and 0.32 cm deep with an electric heater glued to the back and a chromel-alumel thermocouple embedded in a groove. The farthest downstream gages on either side of the stagnation point were used as guard heaters to minimize heat losses in the streamwise direction. A guard heater behind the gages prevented conduction to the interior of the model. The average gap between the aluminum strips was 0.25 mm and was filled with epoxy. The aluminum strips were maintained at a constant temperature (±0.2°C) by a specially designed control circuit (see Van Fossen et al., 1984).

Leading-edge velocity gradients for each of the four models were calculated using an invicid two-dimensional panel code (McFarland, 1985); the calculation included the tunnel side-

Nomenclature

A = surface area of gage, m^2
B = blockage, ratio of model thickness to tunnel height
b = bar width of turbulence-generating grid, cm
d = diameter of model leading edge = $2R$, cm
Fr(s/R) = Frossling number
k = thermal conductivity of air, W/m-K
M = mesh spacing of bars in turbulence grid, cm
Pr = Prandtl number
q = heat flow, W
R = leading-edge radius, cm
Re = Reynolds number
$R(\tau)$ = autocorrelation of velocity signal
r = regression coefficient
$r(s)$ = local recovery factor
s = surface distance from stagnation, cm
T = temperature, K
Tu = turbulence intensity
U = mean velocity, m/s
u' = rms of fluctuating streamwise velocity, m/s
v' = rms of fluctuating spanwise velocity, m/s
x = streamwise distance, cm
Λ = integral length scale of turbulence, cm
ρ = air density, kg/m^3
τ = time shift, s
Φ = heat transfer augmentation factor, Eq. (9)

Subscripts

avg = average
b = bar width
d = leading-edge diameter
EI = electrical heating
gap = epoxy-filled gap between gages
r = recovery
lam = laminar
rad = radiation
st = static
t = total
turb = turbulent
w = wall
x = streamwise
∞ = free stream

Table 1 Turbulence grid dimensions

Grid	b, cm (in.)	M/b	% Open Area
G1	1.270(.500)	4.5	60.5
G2	0.635(.250)	4.5	60.5
G3	0.318(.125)	4.5	60.5
G4	0.159(.063)	4.5	60.5
G5*	0.051(.020)	12.5	92.0

*Grid G5 - array of parallel wires

walls. Velocity gradients made dimensionless by the free-stream velocity and the leading-edge radius of curvature were 1.80, 1.52, 1.32, 1.20 for the 1:1, 1.5:1, 2.25:1, and 3:1 models, respectively.

Hot-Wire Instrumentation. Turbulence measurements were obtained using a two-channel, constant-temperature, linearized, hot-wire anemometer system. Turbulence intensities and autocorrelations were measured using a standard, 5 μm, single hot wire; a crossflow type X-wire probe was used for two component measurements.

Data Acquisition. A Fast Fourier Transform spectrum analyzer was used to obtain the autocorrelation data. The analyzer was programmed to average 400 sequential autocorrelations to obtain a single autocorrelation for analysis. A personal computer was interfaced to the spectrum analyzer for data storage and processing.

Steady-state operating conditions (temperatures, pressures, gage voltages and currents, etc.) were recorded on the Laboratory data acquisition system called ESCORT (Miller, 1978).

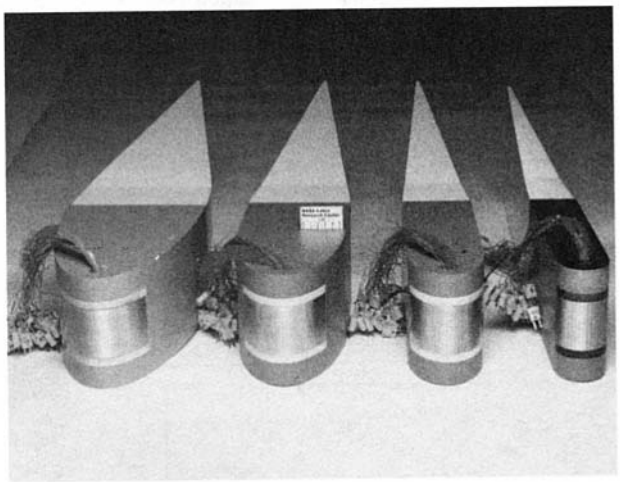

Fig. 3 Stagnation heat transfer models

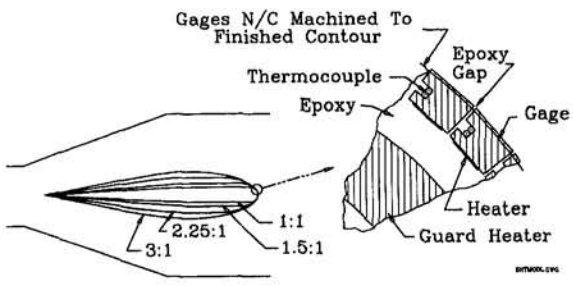

Fig. 4 Model profile comparison and heat flux gage arrangement

Data Reduction and Uncertainty Analysis

Turbulence

Intensity. The hot wires were calibrated in an air jet using a two-point, iteration method (DISA Information Department, 1999). The frequency response of the hot-wire anemometer system was estimated to be 30 kHz using the standard square-wave test. The local turbulence intensity for the linearized single wire was calculated as the ratio of the rms to mean linearized bridge voltage. Two component turbulence intensities were calculated from the linearized signals of the X-wire using the method of Champagne et al. (1967).

Integral Length Scale. Measurement of integral length scale is described fully in Van Fossen et al. (1994); briefly, the availability of a spectrum analyzer that could compute the autocorrelation made this method the natural choice. To eliminate the problem of low-frequency noise that keeps the autocorrelation from approaching zero in a consistent manner, autocorrelation data between $0.33 \le R(\tau) \le 1.0$ were fit with the exponential function using least squares:

$$R(\tau) = e^{-c_r \tau} \tag{1}$$

Length scale was obtained by integrating Eq. (1) between 0 and ∞ and multiplying by the mean velocity. Correction for the hot-wire length was not made; the smallest integral scale measured was 2.6 times the active length of the hot wire.

Heat Transfer. An energy balance was solved to determine the Frossling number for each gage:

$$\mathrm{Fr}(s/R) = \frac{(q_{EI} - q_{\mathrm{rad}} - q_{\mathrm{gap}})d}{A[T_w - T_r(s)]k\sqrt{\mathrm{Re}_d}} \tag{2}$$

where q_{EI} is the heat added to the gage by the heater, q_{rad} is the heat lost by radiation, q_{gap} is the heat conducted away from the gage to the epoxy gap and the unguarded ends of the heaters, A is the exposed gage surface area, T_w is the gage temperature, $T_r(s)$ is the local recovery temperature, k is the thermal conductivity of air, and Re_d is the Reynolds number.

An estimate of the gap loss, q_{gap}, can be obtained from an exact solution for two-dimensional heat conduction in a rectangle. See Van Fossen et al. (1984) for details.

Corrections for radiation heat loss, q_{rad}, were made assuming gray body radiation to black surroundings and an emissivity of 0.05 for the aluminum gage. The gap loss was about 10 percent of the total heat flow, while the radiation heat loss was on the order of 0.2 percent.

The recovery temperature was calculated as

$$T_r(s) = T_{st,\infty} + r(s)\,(T_t - T_{st,\infty}) \tag{3}$$

where $T_{st,\infty}$ is the static temperature upstream of the model. The local recovery factor, $r(s)$, was calculated as

$$r(s) = 1 - \left(\frac{\rho U(s)}{(\rho U)_\infty}\right)^2 (1 - \sqrt{\mathrm{Pr}}) \tag{4}$$

The local mass flow ratio, $\rho U(s)/(\rho U)_\infty$, was found from a numerical solution of flow over the model that included the tunnel walls (Rigby and Van Fossen, 1992).

Following the results of Rigby and Van Fossen (1992), the thermal conductivity and viscosity of air were evaluated at the free-stream total temperature from equations given in Hillsenrath et al. (1955).

Table 2 Uncertainty in Frossling number

Error Component At 20:1 Odds %	Bias		Precision	
	Experimental Velocity Range			
	Max	Min	Max	Min
$\delta(q_{BI})/q_{BI}$	0.21	0.25	3.04	2.97
$\delta(q_{rad})/q_{rad}$	20.47	20.47	0.76	0.64
$\delta(q_{gap})/q_{gap}$	13.80	13.40	0.76	0.67
$\delta(q_{total})/q_{total}$	1.24	1.70	3.31	3.35
$\delta(d)/d$	0.12	0.12	0.00	0.00
$\delta(A)/A$	1.08	1.08	0.00	0.00
$\delta(\Delta T)/\Delta T$	4.68	4.68	0.77	0.68
$\delta(k)/k$	0.00	0.00	0.00	0.00
$\delta(Re_d)/Re_d$	5.76	11.91	0.10	2.15
$\delta(Fr)/Fr$	5.74	7.84	3.40	3.58
Combined Uncertainty in Fr(s/R), %	6.67	8.62		

The Reynolds number, Re_d, was based on the diameter of the leading edge, d, and the mass-velocity averaged between the flow area with maximum model blockage and the unblocked flow area, that is,

$$(\rho U)_{avg} = (\rho U)_\infty \frac{(2 - B)}{2(1 - B)} \tag{5}$$

where the blockage, B, is the ratio of maximum model thickness to tunnel height. Blockage ranged from 0.096 for the circular leading edge to 0.293 for the 3:1 ellipse.

Uncertainty Analysis. Estimates of the bias error of each measuring instrument were made and combined by the method of Kline and McClintock (1953). Estimates of the precision of each measurement were calculated from 20 samples of each steady-state measurement and combined by the same method. Results of the uncertainty analysis for the Frossling number are presented in Table 2.

The uncertainty in turbulence intensity and length scale was estimated using the method suggested by Yavuzkurt (1984) and is presented in Table 3.

Results and Discussion

Turbulence

Intensity. Turbulence intensity was measured as a function of distance downstream of each grid, without the heat transfer model in place, at three different velocities. Each grid and velocity gave slightly different characteristics, so intensity data for each case were fit with a power law curve of the form

Table 3 Hot-wire data uncertainty

Error Component at 20:1 Odds %	Bias		Precision	
	Experimental Velocity Range			
	Max	Min	Max	Min
$\delta(U_{cal\ jet})$	3.41	15.34	0.10	0.32
δ(linearizer fit)	0.77	0.77	0.77	0.77
$\delta(Tu, \Lambda_x/d)$	3.50	15.36		

Table 4 Curve fits of turbulence intensity and length scale data: $Tu = a(x/b)^m$; $\Lambda_x = I(x/b)^p$

Grid	Velocity symbol	Re_b	a	m	r_{Tu}	I	p	$r_{\Lambda/b}$
G1	R1	38650	206.1	-0.875	0.9950	0.240	0.500	0.6668
	R2	18000						
	R3	7934						
G2	R1	17190	146.3	-0.780	0.9987	0.272	0.500	0.8564
	R2	9514	135.3	-0.758	0.9989			
	R3	4452	138.9	-0.778	0.9986			
G3	R1	8935	132.2	-0.765	0.9997	0.264	0.500	0.9799
	R2	4780	156.3	-0.824	0.9995			
	R3	2470	149.4	-0.830	0.9992			
G4	R1	4571	80.15	-0.665	0.9998	0.303	0.500	0.8838
	R2	2297	89.46	-0.693	0.9995			
	R3	1174	75.05	-0.677	0.9997			
G5	R1	1634	23.68	-0.470	0.9852	4.658	0.116	0.8560
	R2	792	23.38	-0.453	0.9848	3.255	0.199	0.9572
	R3	340	52.73	-0.568	0.9975	10.01	0.051	0.4359

$$Tu = a\left(\frac{x}{b}\right)^m \tag{6}$$

Coefficients for each of the curve fits appear in Table 4 along with the regression coefficient, r_{Tu}, for each curve fit. Turbulence intensity was found to vary by less than 5 percent in the spanwise direction.

Isotropy. Figure 5 shows the ratio u'/v', which is a measure of isotropy for the turbulence, versus distance from the grid. Turbulence for grids G3 and G4 is nearly isotropic while that for the parallel wires, G5, shows highly nonisotropic behavior with u'/v' values ranging from a high of 1.42 down to 0.95 depending on Reynolds number and distance from the grid.

Length Scale. Roach (1987) developed a correlation for the integral length scale of grid-generated turbulence of the form

$$\frac{\Lambda_x}{b} = I\sqrt{\left(\frac{x}{b}\right)} \tag{7}$$

Length scale data from the square bar grids were found to have the same square root of distance dependence but the coefficient, I, varied from grid to grid and was an average of 35 percent larger than the value found by Roach. The coefficients for the length scale correlation and regression coefficient, $r_{\Lambda/b}$, are also found in Table 4.

Turbulence intensity and length scale used in the following correlations were evaluated from the curve fits in Table 4 using

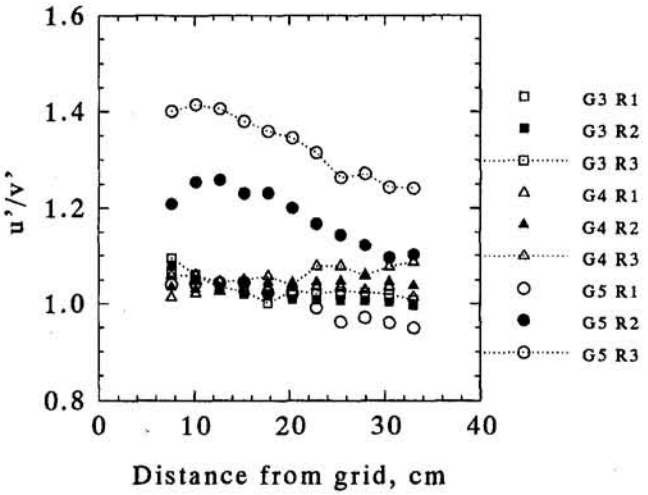

Fig. 5 Isotropy of turbulence from grids G3, G4, and G5

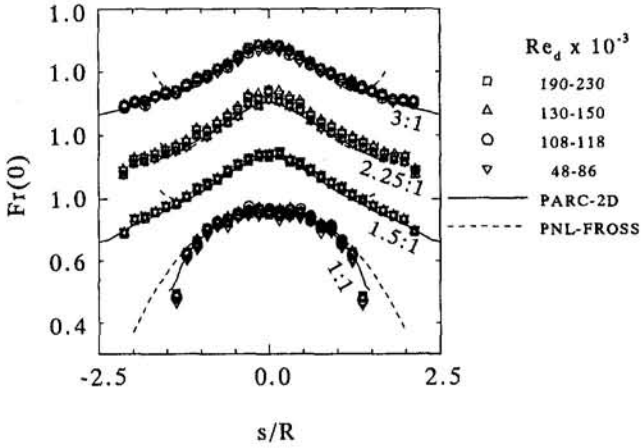

Fig. 6 Frossling number distribution compared to PARC-2D and Frossling solutions

the distance from the grid to the stagnation point of the model. Turbulence intensity varied from 1.1 to 15.9 percent. The ratio of length scale to leading-edge diameter ranged from 0.05 to 0.30.

Heat Transfer

Verification of Experimental Method. Frossling number data in the leading-edge region with no turbulence grid in the tunnel are presented as a function of surface distance from stagnation made dimensionless by the leading-edge radius, R, in Fig. 6. In all but one case the data agree to within the estimated experimental error with the two-dimensional numerical solution from the PARC code (Rigby and Van Fossen, 1992) and the Frossling solution, which was obtained using the velocities calculated from the panel code (McFarland, 1985), thus confirming the accuracy of the experimental technique. The worst agreement is for the 2.25:1 model; experimental results are from 1.4 to 9.2 percent above the numerical at the stagnation point. This model exhibited erratic behavior; on some days, the model gave results that agreed quite well with the numerical results, and on other days, large errors were observed. No obvious cause could be found; therefore, the data for this model are presented as is.

It is interesting to note past design practice to estimate leading-edge heat transfer to a turbine airfoil. Heat transfer at the stagnation point for laminar flow was calculated from a circular cylinder in crossflow correlation using the radius of curvature of the stagnation point. Various multipliers were then applied to this result to account for turbulence. Since all four models have the same radius of curvature at the leading edge, it is obvious from Fig. 6 that this method only works for a circular leading edge. An accurate prediction of the laminar, leading-edge heat transfer can be obtained from the Frossling solution, given the surface velocity distribution, or from a numerical solution for laminar flow over the airfoil.

Stagnation Region Augmentation—Circular Leading Edge. Figure 7 shows the Frossling number at stagnation plotted against the correlating parameter, $Tu\mathrm{Re}_d^{1/2}$, developed by Smith and Kuethe (1966). The heat transfer augmentation continues to increase as scale decreases; therefore, for the present data, no optimum length scale was found. The correlation developed by Lowery and Vachon (1975), also shown in the figure, predicts the heat transfer data only in a narrow range of scales. As the parameter $Tu\mathrm{Re}_d^{1/2}$ increases beyond about 40, the correlation turns downward instead of continuing up as the data indicate.

The stagnation heat transfer data from the model with the circular leading edge behind the square bar grids was fit with the function

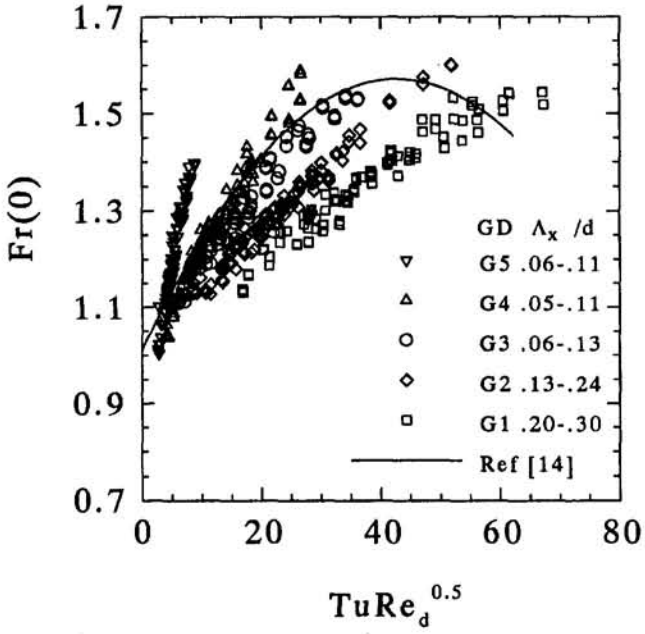

Fig. 7 Stagnation point Frossling number versus $Tu\,\mathrm{Re}^{1/2}$ showing effect of length scale

$$\mathrm{Fr}(0) = 0.00799\sqrt{Tu\mathrm{Re}_d^{0.8}\left(\frac{\Lambda_x}{d}\right)^{-0.574}} + C \qquad (8)$$

The constant, C, was set to the zero-turbulence Frossling number of 0.939, which was calculated from the PARC-2D code. The other constants were determined from a least-squares fit of the data. The curve fit and the data are compared in Fig. 8; Eq. (8) correlates the data to within ±4 percent as shown by the bands drawn on either side of the correlation.

Turbulence for grids G1 through G4 was isotropic; turbulence for the array of parallel wires, G5, was not. The stagnation heat transfer data for grid G5 are compared to Eq. (8), developed for grids G1 through G4, in Fig. 9. As seen in Fig. 5, anisotropy is greatest closest to the wires. The data at high values of the abscissa in Fig. 9 were taken closest to the wires, which is

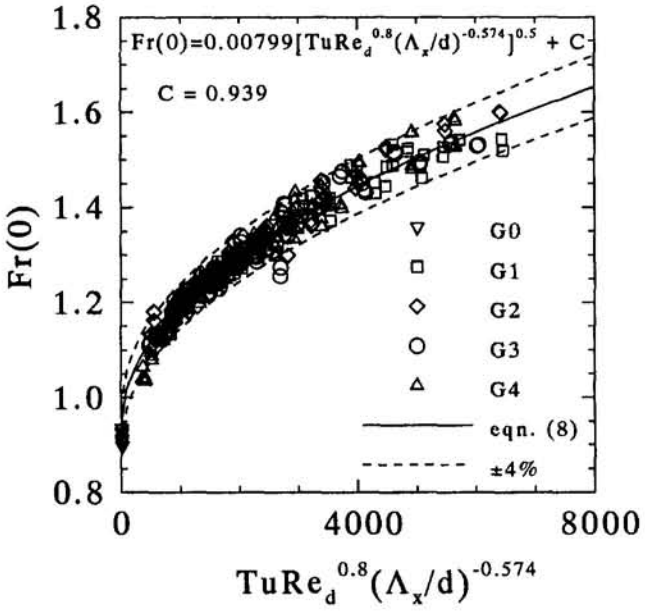

Fig. 8 Stagnation point Frossling number for grids G1–G4 versus correlating parameter

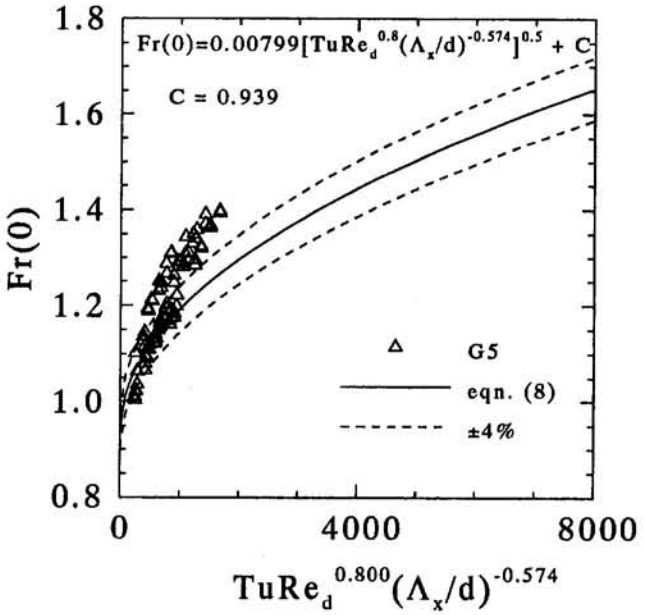

Fig. 9 Comparison of stagnation point correlation with grid G5 data (parallel wires)

where agreement with the correlation is the poorest. A possible explanation is that the parallel wires produced vorticity that was predominantly normal to the spanwise and streamwise directions; this vorticity was stretched, and thus amplified, by acceleration around the leading edge. As distance from the wires increases, isotropy increases and the heat transfer data agree more closely with the correlation.

Figure 10 is a comparison of the stagnation heat transfer data of other authors who used similar turbulence generators (Yeh et al., 1993; Smith and Kuethe, 1966; Mehendale et al., 1991; Lowery and Vachon, 1975) with the present correlation. For cases where the authors did not measure length scale, it was estimated using the correlations given in Table 4. The data of the other authors are in good agreement with the present correlation, falling mostly within the ±10 percent bands drawn about the correlation of Eq. (8).

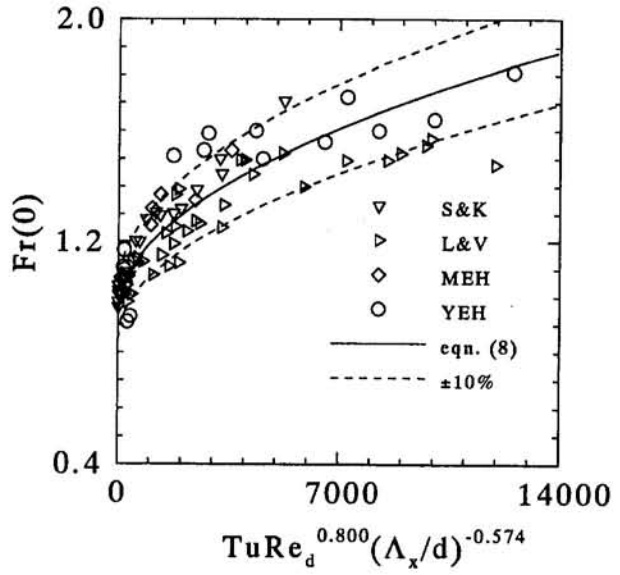

Fig. 10 Circular leading edge stagnation Frossling number data of other authors compared to correlation

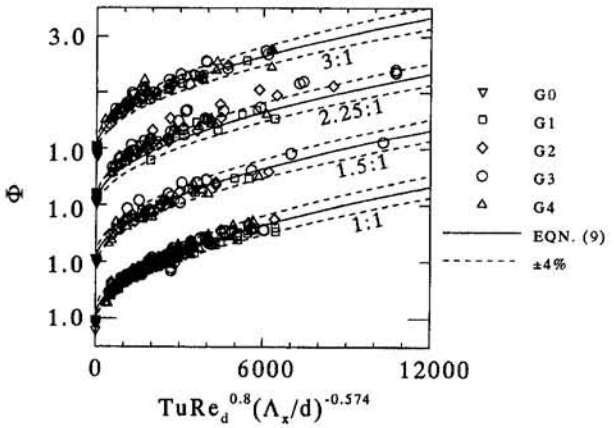

Fig. 11 Comparison of stagnation point heat transfer augmentation data and correlation for elliptical leading edges

Stagnation Region Augmentation—Elliptical Leading Edges. Following numerical results in Rigby and Van Fossen (1992), the correlation for the circular leading edge, Eq. (8), was modified by dividing by the laminar stagnation Frossling number. The modified correlation then gives the stagnation point heat transfer augmentation factor, Φ, due to free-stream turbulence:

$$\Phi = \frac{\mathrm{Fr}(0)_{\mathrm{turb}}}{\mathrm{Fr}(0)_{\mathrm{lam}}} = 0.00851\sqrt{Tu\ \mathrm{Re}_d^{0.8}\left(\frac{\Lambda_x}{d}\right)^{-0.574}} + 1 \quad (9)$$

Values for the terms $\mathrm{Fr}(0)_{\mathrm{lam}}$ for the four models are 0.939, 0.870, 0.811, and 0.775 in order from the circular leading edge to the 3:1 ellipse; these values were also taken from the PARC-2D numerical solution with inlet mass flow defined by Eq. (5).

Comparison of the correlation for stagnation heat transfer augmentation by free-stream turbulence and the experimental data is shown in Fig. 11. In general, the fit is excellent, falling mostly within the ±4 percent bands drawn about the correlation. The 2.25:1 model has the most scatter; as mentioned earlier, this model had problems. If the Frossling number for the 2.25:1 model had been normalized using the average of the experimental data instead of the numerical solution, agreement with Eq. (9) would have been much better. The excellent agreement for the other three models confirms the validity of this correlation method.

As shown by Frossling's solution, the level of heat transfer at the stagnation point for zero-turbulence flow depends on the velocity gradient. Equation (9) predicts the heat transfer augmentation above laminar levels and yet contains no term that involves the velocity gradient at the stagnation point. Thus, the hypothesis that heat transfer augmentation above laminar levels should increase in the presence of higher velocity gradients seems to be disproven by the present data.

Distribution of Heat Transfer Around Leading Edge. Figure 12 is a plot of the Frossling number normalized by the stagnation value versus dimensionless surface distance from the stagnation point for each of the models. The symbols represent the average of the Frossling number data for the turbulent free stream for all grids, Reynolds numbers, and grid positions. The dotted lines represent the standard deviation of the normalized data and the solid line is the PARC solution for a laminar free stream, which has been similarly normalized. Agreement between the normalized turbulent heat transfer distribution and the normalized laminar distribution is good; thus, a good prediction of the heat transfer at a given distance from the stagnation point can be obtained by using Eq. (9) to predict the stagnation heat transfer, then multiplying by the ratio of local to stagnation heat transfer from a solution for the laminar free stream, that is,

$$\mathrm{Fr}(s/R)_{\mathrm{turb}} = \left(\frac{\mathrm{Fr}(s/R)}{\mathrm{Fr}(0)}\right)_{\mathrm{lam}} \mathrm{Fr}(0)_{\mathrm{turb}} \qquad (10)$$

Conclusions

Spanwise-averaged stagnation-region heat transfer measurements have been made on four models with elliptical leading edges downstream of five turbulence generators. The ratio of major to minor axes for the elliptical leading edges ranged from 1:1 to 3:1; all models had the same leading-edge radius of curvature. Velocity gradients at the stagnation point made dimensionless by the leading-edge radius and free-stream velocity ranged from 1.20 to 1.80. Four of the turbulence generators were square mesh, square bar, biplane grids with identical mesh spacing to bar width ratios and bar widths ranging from 0.16 to 1.27 cm. The fifth turbulence generator was an array of parallel wires oriented normal to the model spanwise direction. Reynolds numbers based on leading-edge diameter ranged from 37,000 to 228,000, turbulence intensities ranged from 1.1 to 15.9 percent, and the ratio of integral length scale to leading-edge diameter ranged from 0.05 to 0.30. Conclusions are summarized as follows:

1 Low-turbulence heat transfer results agree with both the Frossling solution and a numerical solution to within estimated experimental accuracy validating the experimental method.

2 The calculation of laminar leading-edge heat transfer by cylinder in crossflow correlations can lead to large errors for noncircular profiles.

3 Augmentation of stagnation-region heat transfer by turbulence increases as integral length scale decreases, but no optimum length scale was found for $\Lambda_x/d \geq 0.05$.

4 A correlation for stagnation heat transfer augmentation above laminar levels for the four square bar grids was developed that reduced data scatter to ±4 percent for three of the four models and predicted the data of other authors to ±10 percent.

5 Dimensionless heat transfer augmentation is independent of body shape and therefore velocity gradient at the stagnation point.

6 The correlation did not predict the heat transfer for the array of parallel wires, indicating that augmentation must also be a function of isotropy of the turbulent flow field.

7 Frossling number downstream of stagnation normalized by the stagnation value can be represented by a universal curve for both laminar and turbulent flow.

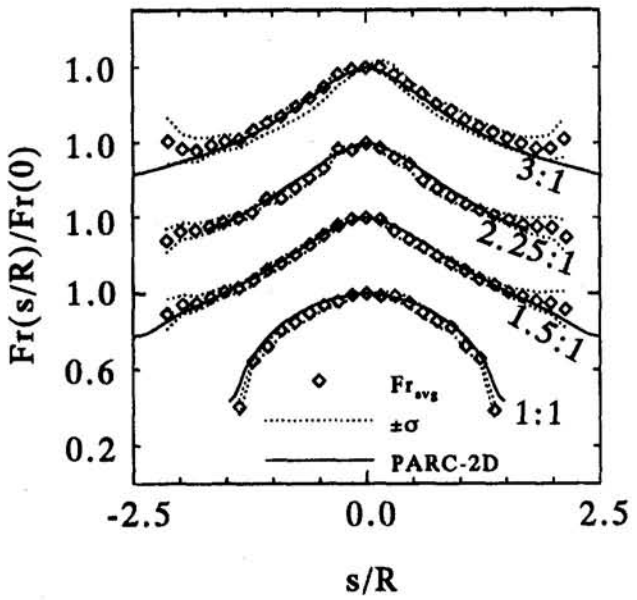

Fig. 12 Distribution of averaged, normalized Frossling number downstream of stagnation point

References

Ames, F. E., 1990, "Heat Transfer With High Intensity, Large Scale Turbulence: The Flat Plate Turbulent Boundary Layer and the Cylindrical Stagnation Point," PhD Thesis, Stanford Univ., CA.

DISA Information Department, 1999, *DISA Type 55M25 Linearizer Instruction Manual,* p. 7, example 1.

Champagne, F. H., Sleicher, C. A., and Wehrmann, O. H., 1967, "Turbulence Measurements With Inclined Hot Wires," *J. Fluid Mech.,* Vol. 28, pp. 153–182.

Dyban, Y. P., Epic, E. Y., and Kozlova L. G., 1975, "Heat Transfer in the Vicinity of the Front Stagnation Point of a Cylinder in Transverse Flow," *Heat Transfer—Soviet Research,* Vol. 7, No. 2, pp. 70–73.

Frossling, N., 1958, "Evaporation, Heat Transfer, and Velocity Distribution in Two-Dimensional and Rotationally Symmetrical Laminar Boundary-Layer Flow," NACA TM-1432.

Giedt, W. H., 1951, "Effect of Turbulence Level of Incident Air Stream on Local Heat Transfer From Cylinders," *J. Aeronautical Sciences,* Vol. 18, No. 11, pp. 725–730.

Goebel, S. G., Abuaf, N., Lovett, J. A., and Lee, C.-P., 1993, "Measurements of Combustor Velocity and Turbulence Profiles," ASME Paper No. 93-GT-228.

Hanarp, L. R., and Suden, B. A., 1982, "Structure of the Boundary Layers on a Circular Cylinder in the Presence of Free Stream Turbulence," *Letters in Heat and Mass Transfer,* Vol. 9, pp. 169–177.

Hillsenrath, J., Beckett, C. W., Benedict, W. S., Fano, L., and Hobe, H. J., 1955, "Tables of Thermal Properties of Gases," NBS Circular 564.

Kestin, J., and Wood, R. T., 1971, "The Influence of Turbulence on Mass Transfer From Cylinders," ASME JOURNAL OF HEAT TRANSFER, Vol. 93, pp. 321–327.

Kline, S. J., and McClintock, F. A., 1953, "Describing Uncertainties in Single-Sample Experiments," *Mechanical Engineering,* Vol. 75, Jan., pp. 3–8.

Lowery, G. W., and Vachon, R. I., 1975, "Effect of Turbulence on Heat Transfer From Heated Cylinders," *Int. J. Heat Mass Transfer,* Vol. 18, No. 11, pp. 1229–1242.

McFarland, E. R., 1985, "A FORTRAN Computer Code for Calculating Flows in Multiple-Blade-Element Cascades," NASA TM 87104.

Mehendale, A. B., Han, J. C., and Ou, S., 1991, "Influence of High Mainstream Turbulence on Leading Edge Heat Transfer," ASME JOURNAL OF HEAT TRANSFER, Vol. 113, pp. 843–850.

Miller, R. L., 1978, "ESCORT: A Data Acquisition and Display System to Support Research Testing," NASA TM-78909.

Morkovin, M. V., 1979, "On the Question of Instabilities Upstream of Cylindrical Bodies," NASA CR-3231.

Rigby, D. L., and Van Fossen, G. J., 1991, "Increased Heat Transfer to a Cylindrical Leading Edge Due to Spanwise Variations in the Free-Stream Velocity," presented at the AIAA 22nd Fluid Dynamics, Plasma Dynamics & Lasers Conf., Honolulu, HI, June 24–26.

Rigby, D. L., and Van Fossen, G. J., 1992, "Increased Heat Transfer to Elliptical Leading Edges Due to Spanwise Variations in the Freestream Momentum: Numerical and Experimental Results," AIAA Paper No. 92-3070.

Roach, P. E., 1987, "The Generation of Nearly Isotropic Turbulence by Means of Grids," *Int. J. Heat Fluid Flow,* Vol. 8, No. 2, pp. 89–92.

Schnautz, J. A., 1958, "Effect of Turbulence Intensity on Mass Transfer From Plates, Cylinders, and Spheres in Air Streams," PhD Thesis, Oregon State College.

Seban, R. A., 1960, "The Influence of Free Stream Turbulence on the Local Heat Transfer From Cylinders," ASME JOURNAL OF HEAT TRANSFER, Vol. 82, pp. 101–107.

Smith, M. C., and Kuethe, A. M., 1966, "Effects of Turbulence on Laminar Skin Friction and Heat Transfer," *The Physics of Fluids,* Vol. 9, No. 12, pp. 2337–2344.

Van Fossen, G. J., Simoneau, R. J., Olsen, W. A., Jr., and Shaw, R. J., 1984, "Heat Transfer Distributions Around Nominal Ice Accretion Shapes Formed on a Cylinder in the NASA Lewis Icing Research Tunnel," Paper No. AIAA-84-0017; also NASA TM-83557.

Van Fossen, G. J., and Simoneau, R. J., 1987, "A Study of the Relationship Between Free-Stream Turbulence and Stagnation Region Heat Transfer," ASME JOURNAL OF HEAT TRANSFER, Vol. 109, pp. 10–15.

Van Fossen, G. J., Simoneau, R. J., and Ching, C. Y., 1994, "Influence of Turbulence Parameters, Reynolds Number, and Body Shape on Stagnation-Region Heat Transfer," NASA TP-3487.

Yardi, N. R., and Sukhatme, S. P., 1978, "Effects of Turbulence Intensity and Integral Length Scale of a Turbulent Free Stream on Forced Convection Heat Transfer From a Circular Cylinder in Cross Flow," *Proc. of the 6th Int. Heat Transfer Conf.,* Paper No. FC(b)-29, pp. 347–352.

Yavuzkurt, S., 1984, "A Guide to Uncertainty Analysis of Hot-Wire Data," ASME *Journal of Fluids Engineering,* Vol. 106, pp. 181–186.

Yeh, F. C., Hippensteele, S. A., Van Fossen, G. J., Poinsatte, P. E., and Ameri, A., 1993, "High Reynolds Number and Turbulence Effects on Aerodynamics and Heat Transfer in a Turbine Cascade," Paper No. AIAA-93-2252.

Zapp, G. M., 1950, "The Effect of Turbulence on Local Heat Transfer Coefficient Around a Cylinder Normal to an Air Stream," M.S. Thesis, Oregon State College.

Zimmerman, D. R., 1979, "Laser Anemometer Measurements at the Exit of a T63-C20 Combustor," NASA CR-159623.

Introduction to the Method of Average Magnitude Analysis and Application to Natural Convection in Cavities

P. S. Lykoudis
School of Nuclear Engineering,
Purdue University,
West Lafayette, IN 47907

The method of Average Magnitude Analysis is a mixture of the Integral Method and the Order of Magnitude Analysis. The paper shows how the differential equations of conservation for steady-state, laminar, boundary layer flows are converted to a system of algebraic equations, where the result is a sum of the order of magnitude of each term, multiplied by a weight coefficient. These coefficients are determined from integrals containing the assumed velocity and temperature profiles. The method is illustrated by applying it to the case of drag and heat transfer over an infinite flat plate. It is then applied to the case of natural convection over an infinite flat plate with and without the presence of a horizontal magnetic field, and subsequently to enclosures of aspect ratios of one or higher. The final correlation in this instance yields the Nusselt number as a function of the aspect ratio and the Rayleigh and Prandtl numbers. This correlation is tested against a wide range of small and large values of these parameters.

1 Introduction

The Average Magnitude Analysis (AMA) is a simple method by which the differential equations of conservation for incompressible, steady-state, laminar flow are converted to an equivalent system of algebraic equations. This is done by taking the average of each term of the equations between the wall and the edge of the boundary layer rather than taking the average of the sum of all the terms on the basis of given velocity and temperature profiles in the fashion of the Integral Methods (IM). The result is a sum of the Order of Magnitude (OM) of each term, multiplied by a nondimensional weight coefficient emerging from the averaging process.

Many years ago Lykoudis and Yu (1963), and Lykoudis and Dunn (1973) used the AMA technique in the solution of two problems involving electrostrictive and ponderomotive forces, without, however, a formal presentation of the method. One may think of the AMA technique as a generalization of the Order of Magnitude Analysis (OMA) where all terms of the conservation equations stand side by side with their weight coefficients, rather than the two terms that the ordinary OMA argument can handle.

The AMA technique will be illustrated in Sections 2 and 3 by solving the drag and heat transfer problem over an infinite flat plate. The case of natural convection over a vertical flat plate will be considered in Section 4. In section 5 the AMA method is applied to the case of natural convection in the presence of a horizontal magnetic field. The case of natural convection in low aspect ratio enclosures will be dealt with in Section 5.

2 The Drag Over an Infinite Flat Plate

The conservation equations are:

$$\frac{\partial u}{\partial x} + \frac{\partial v}{\partial y} = 0 \tag{1}$$

$$\frac{\partial (u^2)}{\partial x} + \frac{\partial (uv)}{\partial y} = \nu \frac{\partial^2 u}{\partial y^2} \tag{2}$$

Using the following definitions:

$$\bar{u} = \frac{u}{U}, \quad \bar{v} = \frac{v}{V}, \quad u_a = \int_0^\delta u dy,$$

$$\bar{y} = \frac{y}{\delta}, \quad D_u = \left.\frac{\partial \bar{u}}{\partial \bar{y}}\right|_{\bar{y}=0} \tag{3}$$

we set:

$$\left[\frac{\partial u}{\partial x}\right]_a \cong -\left[\frac{U_\infty - U_a}{x}\right], \quad \left[\frac{\partial v}{\partial y}\right]_a \cong -\left[\frac{V_a - 0}{\delta_M}\right] \tag{4a}$$

$$\left[\frac{\partial (u^2)}{\partial x}\right]_a \approx \frac{U_\infty^2 - U_a^2}{x},$$

$$\left[\frac{\partial (uv)}{\partial y}\right]_a \cong -\left[\frac{U_\infty V_a - 0}{\delta_M}\right] \cong \frac{U_\infty (U_\infty - U_a)}{x} \tag{4b}$$

$$\left[\nu \frac{\partial^2 u}{\partial y^2}\right]_a \cong \frac{\text{Shear Force}}{\rho \cdot (\text{Volume})} \cong \frac{\tau_w \cdot (x \cdot 1)}{\rho (x \cdot 1 \cdot \delta)} \cong \nu D_u \left(\frac{U_\infty}{\delta_M^2}\right) \tag{4c}$$

Equations (1) and (2), after using Eqs. (3) and (4), become:

$$-\left(\frac{U_\infty - U_a}{x}\right) + \frac{V_a}{\delta_M} = 0, \quad \text{or} \tag{5a}$$

$$-\langle 1 - \bar{u}_a \rangle \left(\frac{U_\infty}{x}\right) + \langle 1 \rangle \frac{V_a}{\delta_M} = 0, \quad \text{or} \tag{5b}$$

$$-(U_\infty - U_a)\delta_M + V_a x = 0 \tag{5c}$$

Contributed by the Heat Transfer Division for publication in the JOURNAL OF HEAT TRANSFER. Manuscript received by the Heat Transfer Division October 1993; revision received October 1994. Keywords: Enclosure Flows, Forced Convection, Natural Convection. Associate Technical Editor: J. R. Lloyd.

$$-\frac{(U_\infty^2 - U_a^2)}{x} - \left[\frac{U_\infty V_a}{\delta_M}\right]$$

$$\cong -\frac{(U_\infty^2 - U_a^2)}{x} + \frac{U_\infty(U_\infty - U_a)}{x} \cong \nu D_u\left(\frac{U_\infty}{\delta_M^2}\right) \quad (6a)$$

$$-\langle 1 - \bar{u}_a^{\,2}\rangle\left(\frac{U_\infty^2}{x}\right) + \langle 1 - \bar{u}_a\rangle\left(\frac{U_\infty^2}{x}\right)$$

$$\cong -\langle \bar{u}_a(1 - \bar{u}_a)\rangle\left(\frac{U_\infty^2}{x}\right) \cong \langle D_u\rangle\left(\nu\,\frac{U_\infty}{\delta_M^2}\right) \quad (6b)$$

$$\bar{u}_a(1 - \bar{u}_a)U_\infty^2\delta_M = \nu D_u\left(\frac{U_\infty}{\delta_M}\right)(x\cdot 1) \quad (6c)$$

In Eq. (6*b*) we have used the continuity Eq. (5*b*) for the calculation of $[\partial(uv)/\partial y]_a$ as shown in Eq. (4*b*). We call the nondimensional quantities in the angular brackets in Eqs. (5*b*) and (6*b*) that multiply the OM of each term of the equations of conservation "weight coefficients." Observing Eqs. (5*c*) and (6*c*), note that the AMA technique is equivalent to the application of mass and momentum conservation in a control volume of length x, unit depth, and height δ_M using average velocity values.

In presenting Prandtl's idea of the boundary layer concept for the first time, most of the textbooks argue the case by comparing the OM of each term of the conservation equations without the capability of forming their sum. In the present development, where the OM of each term is accompanied by its weight coefficients, the proof that $(\partial p/\partial x) \cong (\partial p/\partial y)(\delta/x)$ comes out smoothly without ambiguity. To obtain this result it is necessary to add to the system the equation of motion in the y direction, and perform the averaging process.

Before we solve these equations for the unknown δ_M in order to derive an expression for C_f, we need to bring forth two corrections to obtain a better approximation. The first has to do with the calculation of the drag at the wall. Clearly, it was calculated in Eq. (4) at the end of the plate at x. But since analysis shows that $\delta \propto x^{1/2}$ with local stress $\propto x^{-1/2}$, the overall drag for the whole x is twice as much with the one calculated at x. This means that the right-hand side of Eq. (6*c*) needs to be multiplied by a coefficient $\lambda_M = 2$. The second correction has to do with the averaging of momenta fluxes, essentially equating $\int u(1-u)dy$ with $\gamma\bar{u}_a(1-\bar{u}_a)$. Taking into account these two corrections, Eq. (6*b*) becomes:

$$\gamma\bar{u}_a(1 - \bar{u}_a)U_\infty^2\delta_M = \lambda\left(\nu\,\frac{U_\infty}{\delta_M}\right)x \quad (7)$$

Solving for δ_M/x we find:

$$\delta/x \cong \frac{K_\delta}{\sqrt{\mathrm{Re}_x}}, \quad \text{where} \quad K_\delta \equiv \sqrt{\frac{\lambda_M D_u}{\gamma\bar{u}_a(1 - \bar{u}_a)}} \quad (8)$$

One can easily show that the skin friction coefficient C_f is given by:

$$C_f \equiv \frac{K_f}{(\mathrm{Re})^{1/2}}, \quad \text{with} \quad K_f = \frac{2D_u}{K_\delta} \quad (9)$$

Equations (8) and (9) are identical with the Integral Method (IM) results. For a cubic velocity profile with $\bar{u}_a = \frac{5}{8}$, $D_u = 1.5$, and $\gamma = \frac{104}{17}$ we obtain: $K_\delta = 4.64$ and $K_f = 0.646$. Note that the exact Blasius results are $K_\delta = 5.00$ and $K_f = 0.664$.

3 Heat Transfer Over an Infinite Flat Plate

We shall assume a constant wall temperature. The energy equation is:

$$\frac{\partial(uT)}{\partial x} + \frac{\partial(vT)}{\partial y} = \alpha\,\frac{\partial^2 T}{\partial y^2} \quad (10)$$

We set $\Theta \equiv T/T_w$, and for algebraic convenience $T_\infty = 0$. We note:

$$\left[\frac{\partial(uT)}{\partial x}\right]_a \cong \frac{(u_a T_a - 0)}{x}, \quad \left[\frac{\partial(vT)}{\partial y}\right]_a \cong \frac{(0 - 0)}{\delta_T} \quad \text{and}$$

$$\left[\alpha\,\frac{\partial^2 T}{\partial y^2}\right]_a \cong \alpha\,\frac{D_T(T_w - 0)}{\delta_T^2}, \quad \text{where} \quad D_T = \left.\frac{\partial\Theta}{\partial\bar{y}}\right|_{\bar{y}=0} \quad (11)$$

Nomenclature

A = cell aspect ratio = H/L
Bo = Boussinesq number = $(\mathrm{Gr})\cdot(\mathrm{Pr})^2$
Bo* = modified Boussinesq number = Bo·Nu
C_f = skin friction coefficient
c_p = specific heat at constant pressure
D_u = defined in Eq. (3)
D_T = defined in Eq. (11)
f = function defined in Eq. (25)
Gr = Grashof number = $g\beta(\Delta T)L^3/\nu^2$
g = gravity constant
H = height of the cell defined in Fig. 1
h = film coefficient
k = coefficient of thermal conduction
K_{HT} = defined in Eq. (15)
K_{Pr} = defined in Eq. (24)
K_f = defined in Eq. (9)
K_δ = defined in Eq. (8)
L = horizontal length of the cell defined in Fig. 1
Ly = Lykoudis number = $(\sigma_e B^2/\rho)/[g\beta(\Delta T)/L]^{1/2}$
m = numerical constant defined in Eq. (40)
Nu = Nusselt number = hL/k
n = numerical constant defined in Eq. (25)
p = pressure
Pr = Prandtl number = ν/α
Q_X, Q_H, Q_L = heat transfer rates defined in Fig. 1
Ra = Rayleigh number = $(\mathrm{Gr})\cdot(\mathrm{Pr})$
$\mathrm{Ra}_{\mathrm{Pr}}$ = defined in equation (38)
Re = Reynolds number = UL/ν
T = temperature
u, v, w = velocity component in the x, y, and z directions
x, y, z = Cartesian coordinates
α = thermal diffusivity
β = volumetric coefficient of expansion
γ = coefficient of momentum correction in Eq. (8)
δ = boundary layer thickness
Θ = nondimensional temperature = T/T_W
μ = coefficient of viscosity
ν = kinematic viscosity
ρ = mass density
σ_e = electric conductivity
$\Delta T = T_{\mathrm{Hot}} - T_{\mathrm{Cold}}$

Subscripts and Superscripts

a = average value defined in Eq. (4)
M = pertains to the momentum boundary layer
T = pertains to the thermal boundary layer
x = in the x direction
y = in the y direction
∞ = pertains to the free stream

Using Eq. (11) in Eq. (10) we obtain the following:

$$\frac{u_a T_a}{x} \cong \alpha D_T \left(\frac{T_w}{\delta_T^2} \right) \tag{12a}$$

$$\langle \bar{u}_a \rangle \left(\frac{U_\infty T_a}{x} \right) \cong \langle D_T \rangle \left(\alpha \frac{T_w}{\delta_T^2} \right) \tag{12b}$$

$$\rho c_p T_a U_a (\delta \cdot 1) \cong \left[\frac{k(T_w - 0)}{\delta_T} \right] \cdot (x \cdot 1) \tag{12c}$$

In Eq. (12b) the quantities in the angular brackets are the weight coefficients multiplying the OM terms. Equation (12c) is the energy conservation equation derived in a control volume using average values. If we introduce the thermal energy flux corrections factor ζ along with the averaging coefficient for overall heat transfer λ_T, the final AMA energy equation is:

$$\frac{\zeta U_a \Theta}{x} \cong \lambda_T \frac{\alpha D_T}{\delta_T^2} \tag{13}$$

In this equation we should add the subscript e to U_a, to note that this is the value of the average velocity taken at the edge of the thermal boundary layer. When Pr is high with $\delta_M \gg \delta_T$ as a first approximation we can assume a linear velocity profile, for the purpose of calculating U_{ae}; that is, we take:

$$\frac{U_{ae}}{U_\infty} \cong \frac{\delta_T}{\delta_M} \tag{14}$$

Using Eq. (14) in Eq. (15),[1] solving for x/δ_T, and using the approximation $\mathrm{Nu} \cong D_T x/\delta_T$ we find:

$$\mathrm{Nu} \cong K_{HT}\, \mathrm{Re}^{1/2} \cdot \mathrm{Pr}^{1/3}$$

with

$$K_{HT} \equiv \left(\frac{\zeta D_T^2 \Theta_a \bar{u}_a}{\lambda_T K_\delta} \right)^{1/3} \tag{15}$$

Using cubic profiles for velocity and temperature, $K_{HT} \cong 0.358$. The exact value from IM is $K_{HT} \cong 0.339$. If we solve Eq. (13) for δ_T/x and divide with the value of δ_M from Eq. (8) we find:

$$\frac{\delta_T}{\delta_M} \cong \left(\frac{\lambda_T D_T}{\zeta \Theta_a \bar{u}_a K_\delta^2} \right)^{1/3} \mathrm{Pr}^{-1/3} \tag{16}$$

For the present work the value of this constant is equal to 0.903 compared to the exact 1.025.

For liquid metals we set $u_{ae} = U_\infty$ and $\zeta = 1$ and solve for Nu as before to obtain:

$$\mathrm{Nu} \cong \left(\frac{D_T \Theta_a}{\lambda_T} \right)^{1/2} \mathrm{Pe}^{1/2} \tag{17}$$

For the present work the constant in parentheses is equal to 0.530 versus 0.565 for the exact.

4 Natural Convection Over an Infinite Vertical Flat Plate

Using the Boussinesq approximation, the equations of conservation for mass, momentum, and energy are:

$$\frac{\partial u}{\partial x} + \frac{\partial v}{\partial y} = 0 \tag{18}$$

$$\frac{\partial (u^2)}{\partial x} + \frac{\partial (uv)}{\partial y} = \nu \frac{\partial^2 u}{\partial y^2} + g\beta(T - T_e) \tag{19}$$

$$\frac{\partial (uT)}{\partial x} + \frac{\partial (vT)}{\partial y} = \alpha \frac{\partial^2 T}{\partial y^2} \tag{20}$$

We set the constant wall temperature as T_W. Let U be the characteristic yet unknown thermal velocity driven by buoyancy. Using the AMA procedure as described above, the following equations are equivalent to Eqs. (19) and (20):

$$\langle \bar{u}_a^2 \rangle \left(\frac{U^2}{x} \right) \cong \langle D_u \rangle \left(\frac{\nu U}{\delta_M^2} \right) + \langle 1 \rangle g\beta(T_\nu - T_e) \tag{21}$$

$$\langle \bar{u}_a \Theta_a \rangle \frac{U}{x} \cong \langle D_T \rangle \frac{\alpha}{\delta_T^2} \tag{22}$$

This is an algebraic system of two equations with three unknowns, namely U, δ_M, and δ_T, and is equivalent to the differential Eqs. (18), (19), and (20). Solving Eq. (22) for U, and introducing it into Eq. (21) we find:

$$\frac{x^4}{\delta_T^2 \delta_M^2} \left[1 + \left(\frac{\alpha}{\nu} \right) \left(\frac{\bar{u}_a}{\Theta_a} \right) \left(\frac{D_T}{D_u} \right) \left(\frac{\delta_M}{\delta_T} \right)^2 \right] \left(\frac{D_T D_u}{u_a \Theta_a} \right)$$

$$\cong \frac{g\beta(T_w - T_e)x^3}{\nu\alpha} \tag{23}$$

Observe that the inverse of second term in the left-hand side of Eq. (23) denotes the ratio of the viscous over the inertia forces calculated on the basis of the thermal velocity U. Since this ratio is proportional to the Prandtl number $\mathrm{Pr} = \nu/\alpha$, it is legitimate to attach this physical meaning to the Prandtl number in the case of natural convection. For liquid metals $\mathrm{Pr} \ll 1$ implying that the viscous term is very small compared to the inertia. It follows that the buoyancy term drives the inertia force, and viscosity does not enter into the picture for a heat transfer calculation. On the other hand if Pr is large, the opposite is true. The inertia term is small, and the buoyancy force not only overcomes the frictional force inside the thermal boundary layer, but is also capable of driving the fluid outside by the mechanism of viscosity. In other words the edge of the thermal boundary layer acts as a moving plate, as it faces the bulk of the fluid where there are no temperature gradients.

To get out of the dilemma of one missing equation for the case of moderate or large Prandtl numbers, we note that the locus of the maximum velocity will certainly be in the neighborhood of $y \cong \delta_T$, the region where the driving thermal force is present. This means that it is appropriate (mandatory) to use the thickness δ_T, in the place of δ_M for the heat transfer calculation. Going back to the case of liquid metals, we note once again that δ_M is absent, and therefore there is no harm in setting $\delta_M = \delta_T$. Since in the two asymptotic cases for $\mathrm{Pr} \to 0$ and $\mathrm{Pr} \to \infty$, by setting $\delta_M = \delta_T$ we obtain correct results, we use this equality throughout.

We can now proceed to the calculation of the Nusselt number from $\mathrm{Nu} \cong D_T(x/\delta_T)$. After some algebra we obtain:

$$\mathrm{Nu} \cong K_{HT} \cdot \mathrm{Ra}^{1/4} \frac{1}{\left(1 + \frac{K_{\mathrm{Pr}}}{\mathrm{Pr}} \right)^{1/4}}$$

where:

$$K_{HT} = \left(\frac{\Theta_a \bar{u}_a D_T^3}{D_u} \right)^{1/4}, \quad K_{\mathrm{Pr}} \cong \left[\left(\frac{\bar{u}_a}{\Theta_a} \right) \left(\frac{D_T}{D_u} \right) \right] \tag{24}$$

[1] This step is instructive. We have: $(\Theta_a/L)[U_\infty \cdot (\delta_T/\delta_M)] \cong \alpha D_T/\delta_T^2$. By visual observation this is the beginning of where the $\frac{1}{3}$ power of the Prandtl number enters into the calculation of the Nusselt number. See also Eq. (42) of p. 38 in Bejan (1984).

Note that this equation yields the asymptotic results,

$$f_1 = \mathrm{Nu}_{\mathrm{Pr}\to\infty} \propto \mathrm{Ra}^{1/4} \quad \text{and} \quad f_2 = \mathrm{Nu}_{\mathrm{Pr}\to 0} \propto \mathrm{Bo}^{1/4} \tag{25}$$

For a cubic velocity profile, and a parabolic one for the temperature, we have the values: $\theta_a = \frac{1}{3}$, $\bar{u}_a = \frac{1}{12}$, $D_T = 2$, $D_u = 1$, from which: $K_{HT} = 0.687$ compared to the exact 0.508, and $K_{\mathrm{Pr}} = 0.50$ compared to the exact 0.952 from IM theory.

We now use the technique of the well-known approximation of a continuous function $f(x)$ in terms of its asymptotic values for small and high x given by f_1 and f_2 by setting:

$$f = f_1 \Big/ \left[1 + \left(\frac{f_1}{f_2} \right)^n \right]^{1/n}$$

Note that this equation is functionally identical to Eq. (25) for $n = 1$. With an exponent $n = \frac{9}{16}$, Eq. (24) becomes:

$$\mathrm{Nu} \cong \frac{0.687\ \mathrm{Ra}^{1/4}}{\left\{ 1 + \left(\dfrac{0.500}{\mathrm{Pr}} \right)^{9/16} \right\}^{4/9}} \tag{26}$$

Churchill and Chu (1975) suggest for best fit of all data:

$$\mathrm{Nu} \cong 0.68 + \frac{0.67\ \mathrm{Ra}^{1/4}}{\left\{ 1 + \left(\dfrac{0.492}{\mathrm{Pr}} \right)^{9/16} \right\}^{4/9}} \tag{27}$$

A few final observations: If one traces the origin of the quantity in the right-hand side of Eq. (23), that is the Rayleigh number Ra, he will discover that it is the ratio of the buoyancy force over the viscous force, calculated on the basis of the thermal velocity $U$when Pr is very high. If we go to the other extreme of liquid metals where the relevant number in Eq. (27) is the ratio $\mathrm{Ra}/(1/\mathrm{Pr}) = \mathrm{Ra}\cdot\mathrm{Pr}$, that is the Boussinesq number Bo, independent of viscosity, and again follow its appearance from the fundamental equations, it will be seen that it corresponds to the ratio of the buoyancy forces over the inertia, again on the basis of the thermal velocity U. *These physical interpretations, however, are asymptotic meanings for* Ra *and* Bo *for the cases of large and small Prandtl numbers, and they lose these meanings for the in-between cases.* Investigators who attach to the Grashof number, $\mathrm{Gr} = \mathrm{Ra}/\mathrm{Pr}$, the meaning just given to Ra are wrong. The Grashof number as such plays no role in the heat transfer of natural convection problems. On the other hand it is the nondimensional number that determines transition to turbulence, as established recently in Bejan and Lage (1990) and in experiments by Vitharana and Lykoudis (1994).

This picture is essentially the one presented by Bejan (1984), who correctly brings forth previous misunderstandings on the nature of the layers δ_T and δ_M. Bejan uses OM arguments to establish the relevant scales for small and large viscosity. The development here is equivalent, but as has been seen, the argument for the heat transfer calculation and the meaning of the numbers Pr, Ra, and Bo has progressed differently.

5 Natural Convection Over an Infinite Flat Plate in the Presence of a Horizontal Magnetic Field

This is the problem that Lykoudis (1962) solved using three methods: integral, collocation, and an analog computer. The AMA technique, the details of which are not presented here, yields the following result for the Nusselt number:

$$\mathrm{Nu} \cong \left\{ \frac{2\Theta_a^2 D_T\ \mathrm{Bo}^{1/2}}{\mathrm{Ly} + \left\{ \mathrm{Ly}^2 + 4\left(\dfrac{D_a\Theta_a^2}{\bar{u}_a D_T} \right)\left[\dfrac{\bar{u}_a D_T}{\Theta_a D_u} + \mathrm{Pr} \right] \right\}^{1/2}} \right\}^{1/2} \tag{28}$$

In a nondimensional form, as defined in Lykoudis and Dunn (1973):

$$\overline{\mathrm{Nu}} = \frac{\mathrm{Nu} - 1}{\mathrm{Nu}_0 - 1} \cong \left\{ \frac{(\frac{4}{3})^{1/4}}{\mathrm{Ly} + \{\mathrm{Ly}^2 + \frac{4}{3}\}^{1/2}} \right\}^{1/2} \tag{29}$$

The numerical constant $\frac{4}{3} = 1.333$ was found by Lykoudis (1962) by the collocation method to be $\frac{4}{7} = 0.571$, and by the Integral Method, $\frac{16}{7} = 2.286$. The analog computer solution, more reliable, is in excellent agreement with the AMA solution. Of course one cannot emphasize enough times that the results of all integral methods, including AMA, are checked against experimental values, and an adjustment of the numerical constants is always necessary. For this reason the value of the Integral Methods rests mainly in their capability to yield good functional relations for drag and heat and mass transfer rates in terms of the correct nondimensional numbers.

6 Natural Convection in Enclosures

Here we shall examine the case of a natural convection cavity of height H, thickness L, and depth equal to 1. We shall assume that the two vertical walls are heated and cooled, respectively, whereas the top and bottom sides are insulated. This is one of many possible cases. This problem is of recent importance and reviews on the subject by Catton (1978) and Ostrach (1972, 1982) can be consulted. An extensive review of experimental and numerical work along with empirical correlations can be found in Churchill (1983). There is also an abundance of theoretical and numerical work that can be found in Batchelor (1954), Bejan (1979), Berkovsky and Polevicov (1976), Gill (1962), Okada and Ozoe (1992), Ozoe and Okada (1989), and Viskanta et al. (1986). These references are only few, and are selected because this paper will make specific use of some of their results.

For the problem at hand there does not seem to exist a single correlation capable of yielding the Nusselt number for all ranges of Raleigh, Prandtl, and Aspect Ratio A. However there are extensive experimental data for all fluids including the difficult liquid metals, and also a plethora of numerical solutions.

The aim of the paper is to use the AMA method without attempting to calculate the weight coefficients that multiply the OM terms as already explained. In order to simplify the algebra, we shall assume that these coefficients are equal to 1. When we arrive at the end result for the Nusselt number, we shall enter numerical constants, which we shall then determine from numerical and theoretical asymptotic solutions with the added help of experimental data.

In order to convert the essentially three-dimensional problem to a two-dimensional one, we use the following scheme as depicted in Fig. 1. Following the explanation of the caption in Fig. 1, and using AMA throughout, we have:

$$Q_X = Q_H + Q_L \tag{30}$$

$$Q_X \approx k\frac{(\Delta T)_x}{\delta}\cdot X, \quad Q_H \approx k\frac{(\Delta T)_y}{\delta}H,$$

$$Q_L \approx k\frac{(\Delta T)_x}{X}L \tag{31}$$

Setting $(\Delta T)_x \cong (\Delta T)_y$ and substituting Eq. (31) into Eq. (30), we obtain:

$$\frac{X}{\delta} \approx \frac{H}{\delta} + \frac{L}{X} \tag{32}$$

We now write the two equations of conservation for momentum and energy:

$$\bar{g} \equiv g\left(\frac{\Delta\rho}{\rho} \right) \cong \frac{vU}{\delta^2} + \frac{U^2}{X} \tag{33}$$

$$\frac{U}{X} \cong \frac{\alpha}{\delta^2} \tag{34}$$

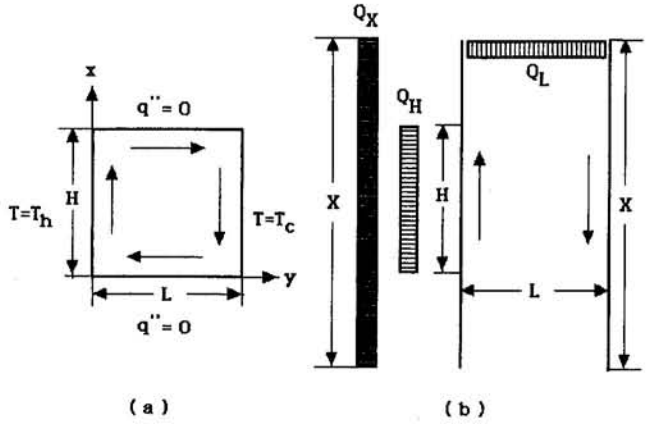

Fig. 1 Geometric and thermal definitions of an enclosure with constant heat flux at the two vertical walls with insulated upper and lower boundaries. The third dimension is perpendicular to the paper, and is assumed to be large compared to the other dimensions, so that there are no velocity and temperature gradients acting in the *z* direction. Figure 1(*b*) converts Fig. 1(*a*) to an equivalent thermal circuit by deploying the height *H* to an unknown height *X* such that the heat flux Q_X conducted normal to *X* is equal to the heat Q_H conducted normal to *H* and Q_L normal to *L*.

We now eliminate U from Eqs. (33) and (34), solve for X, and substitute this value of X in Eq. (32) to find:

$$\mathrm{Nu}_L^7 + \beta_1 \frac{\mathrm{Ra}_L}{\left(1 + \frac{\beta_2}{\mathrm{Pr}}\right)} (A)\cdot\mathrm{Nu}_L^4 \cong \beta_3 \left[\frac{\mathrm{Ra}_L}{\left(1 + \frac{\beta_2}{\mathrm{Pr}}\right)}\right]^2 \quad (35)$$

Here, we have inserted three numerical constants, β_1, β_2, and β_3, to account for the combination of the weight coefficients that we have assumed to be equal to 1.

Equation (35) is a quadratic in terms of Ra and yields the final result. It can be solved explicitly for Ra_L in terms of Nu, Pr, and $A = H/L$. But we shall first determine the two asymptotic solutions for very small and very high $A\cdot\mathrm{Ra}$. These solutions are:

$$A\cdot\mathrm{Ra} \gg 1 \quad \mathrm{Nu}_L \cong \left[\left(\frac{\beta_3}{\beta_1}\right)^{1/4} \frac{\mathrm{Ra}_L}{A\cdot\left(1 + \frac{\beta_2}{\mathrm{Pr}}\right)}\right]^{1/4} \quad (36)$$

$$A\cdot\mathrm{Ra} \ll 1 \quad \mathrm{Nu}_L \cong \beta_3^{1/7}\left[\frac{\mathrm{Ra}_L}{\left(1 + \frac{\beta_2}{\mathrm{Pr}}\right)}\right]^{2/7} \quad (37)$$

These two equations are already established in the literature.

We can now proceed to fix the β constants. The purpose of this note is not to make a critical appraisal of all available theories, numerical and experimental work. The point here is that one can use the general solution given by Eq. (35) and bring it into an agreement with the data that one can show are more reliable than others. Nevertheless, in order to test the validity of the suggested correlation, we shall fix the constants β by looking at the collection of data as presented in Churchill (1983), Berkovsky and Polevicov (1976), and Okada and Ozoe (1992). The values we have chosen are as follows: To satisfy high $(A\cdot\mathrm{Ra})$ data we use the familiar asymptotic solution given by Bejan (1979) in his note on the work of Gill (1962), which in turn was a followup of the early work of Batchelor (1954). Bearing in mind Eq. (36) we set: $(\beta_3/\beta_1)^{1/4} = 0.363$. To satisfy low A data such as those cited in Fig. 15 of Churchill (1983) and the extensive numerical data of Berkovsky and Polevicov (1976), we choose $\beta_3^{1/7} = 0.18$. For $\mathrm{Ra}_{\mathrm{Pr}}$ we choose a correlation of the type:

$$\mathrm{Ra}_{\mathrm{Pr}} \equiv \frac{\mathrm{Ra}}{\left[1 + \left(\frac{\beta_2}{\mathrm{Pr}}\right)^{1/m}\right]^m} \quad (38)$$

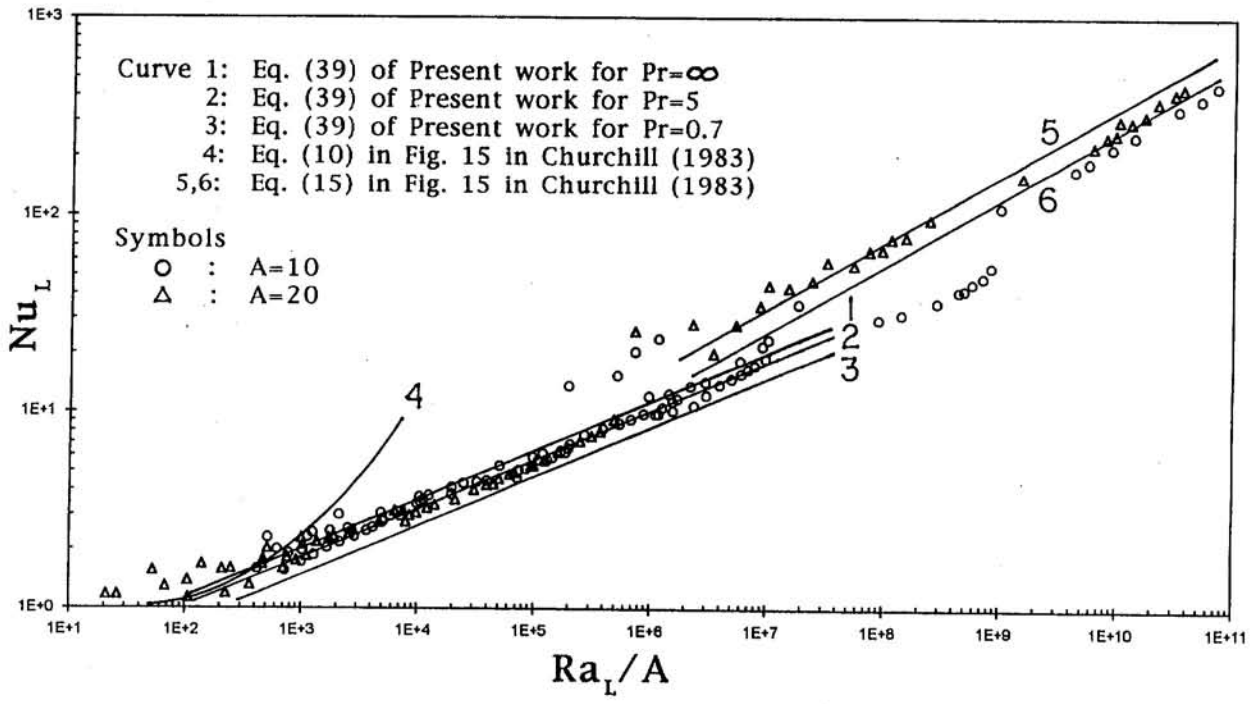

Fig. 2 Comparison of Eq. (39) of present work with the data and correlations cited in Fig. (15) of Churchill (1983), for channels of high aspect ratio *A*, heated and cooled on the vertical sides

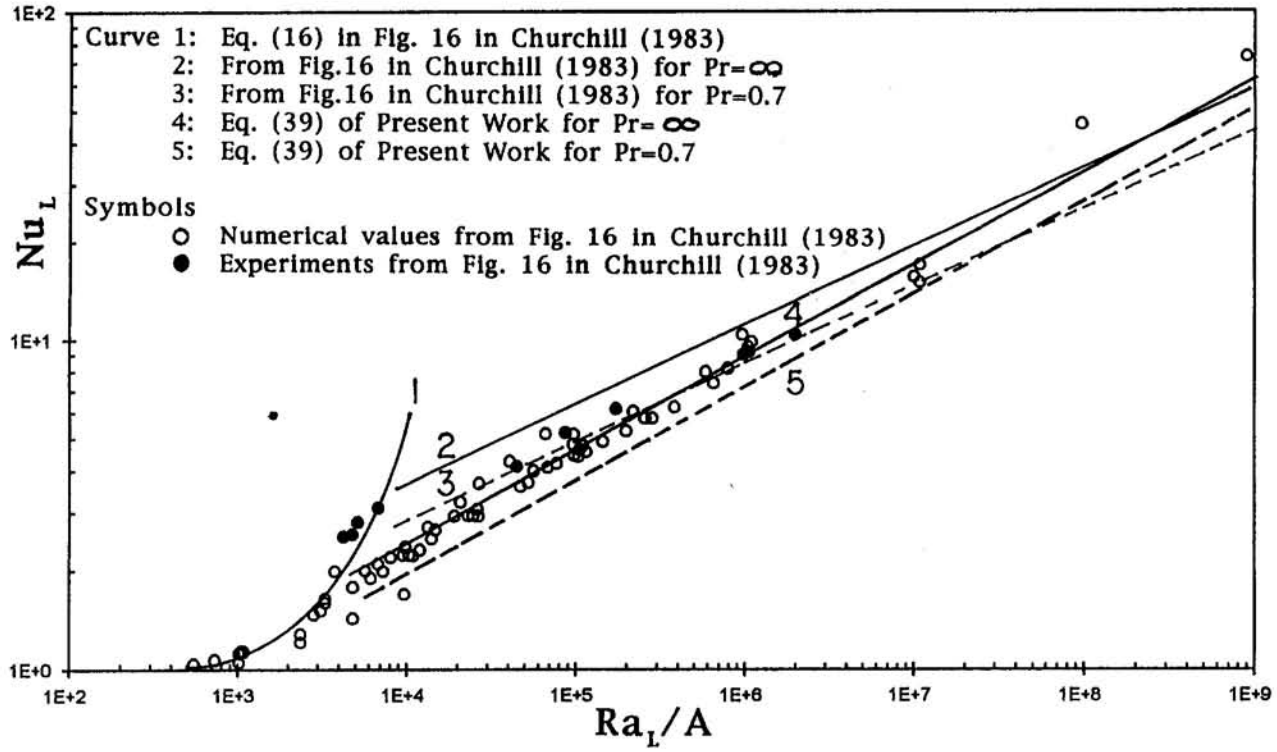

Fig. 3 Comparison of Eq. (39) of present work for channels of aspect ratio near unity, heated and cooled on the vertical sides as per data in Fig. (16) of Churchill (1983)

In contrast to the three β constants, which emerge from the weight coefficients, the exponent m is introduced artificially. In order to satisfy liquid metal data we set: $\beta_2 = 0.001$ and $m = 4$.

At this point we present for convenience an approximation of the fundamental (Eq. (35)). This approximation is based on the method of the interpolating function as presented in Eq. (25). *In this case the power n is not a free parameter, neither is it determined from experimental data.* It is adjusted for best fit of the interpolating function f, which is made to agree with the value of f at the point where $f_1 = f_2$ (that is, by equating the two Eqs. (36) and (37)). This is an easy calculation that leads to a transcendental equation for n, which is satisfied for $n = 5.5$. The end result, which has incorporated the values of the constants β, already adopted, is:

$$\mathrm{Nu} \cong \frac{0.18(\mathrm{Ra_{Pr}})^{2/7}}{\{1 + [0.5(\mathrm{Ra_{Pr}^{1/7}} \cdot A)^{1/4}]^{5.5}\}^{1/5.5}} \qquad (39)$$

Comparison of this equation with Eq. (35) shows that the error is less than 3 percent for the region of interest of $\mathrm{Ra} > 10^3$.

In Figs. 2–4 we compare Eq. (39) with experimental data and theories as stated before. Figure 2 is taken from Churchill (1983) and contains large aspect ratio data. His three correlations, which are a mixture of Bejan's analysis and empirical adjustments, yield values for Nu that coincide with those of Eq. (39). The agreement of Eq. (39) with the data is good for the range $\mathrm{Ra}/A = 10^3$ to 10^6 and perhaps 10^7 where transition to turbulence begins. The correlation fails for $\mathrm{Ra}/A < 5 \times 10^3$ where Bachelor's correlation is applicable.

Figure 3 is also taken from Churchill (1983) and contains data for channels of aspect ratio near unity. Here, Churchill's correlations follow a $\frac{1}{4}$ slope, the same slope valid for large A. However it seems that the theoretical slope of $\frac{2}{7}$ of Eq. (37) for small A is favored by the data. Of course the slope of $\frac{2}{7}$ is supported by the numerical data of Berkovsky and Polevicov (1976) who suggest empirically a slope corresponding to a power of 0.290, which is very close to $\frac{2}{7} = 0.286$.

Finally, Fig. 4 is Fig. 5 from Okada and Ozoe (1992) and is a collection of numerical and experimental data for liquid metals at constnat heat flux. In this case Boussinesq is the appropriate nondimensional number. We calculate Nu in terms of the modified Boussinesq number Bo* so that the asymptotic Eq. (37) becomes:

$$\mathrm{Nu} \cong \frac{0.260\mathrm{Bo}^{*2/9}}{[\mathrm{Pr}^{1/m} + \beta_2^{1/m}]^{2m/9}} \qquad (40)$$

For the above we still take the values $\beta_2 = 0.001$ and $m = 4$. In Fig. 4 note that the experimental data of Okada and Ozoe (1992) for gallium favor the $\frac{2}{7}$ slope, and also that the present correlation gives a good spread for the cases of Prandtl numbers between the values of 0.01, 0.025, and 0.05. All in all the present

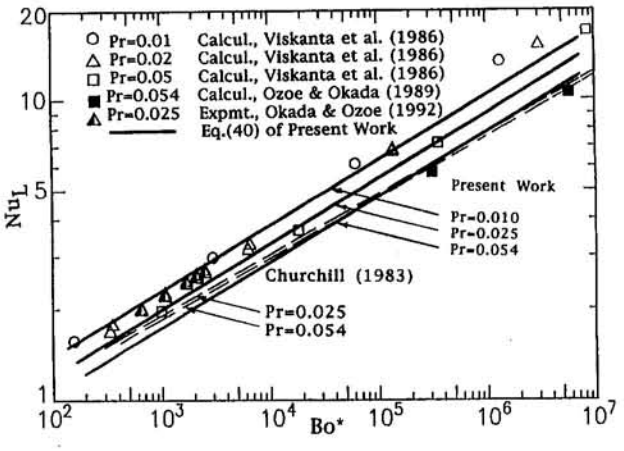

Fig. 4 Comparison of Eq. (40) of present work with the numerical and experimental data quoted in Okada and Ozoe (1992)

correlation seems to do well with the numerical calculations of Viskanta et al. (1986) and Ozoe and Okada (1989).

We summarize the results of this work by noting that the present correlation has made use of the numerical constant $(\beta_3/\beta_1)^{1/4} = 0.363$ from Bejan's theoretical solution, the value $\beta_3^{1/7} = 0.18$ from numerical calculations cited in Churchill compatible with Berkovsky and Polevikov's numerical work, and the two values for β_2 and m necessary to fix the relationship of Eq. (40). These two values are different from the ones suggested in Churchill (1983), $\beta_2 = 0.5$ and $m = \frac{9}{16}$, or those of Berkovsky and Polevicov (1976), $\beta_2 = 0.2$ and $m = 1$. Had we chosen these values for β_2 and m the present correlation would not have been as successful.

7 Conclusions

The Average Magnitude Method (AMA) was first introduced by solving the problem of drag and heat transfer over an infinitely long flat plate. It was shown that it is equivalent to the familiar integral method.

When the problem of natural convection over an infinitely long vertical flat plate was solved, it was shown that the AMA method had an advantage of clarity and simplicity over the integral method in terms of the role and meaning of the nondimensional numbers Ra, Bo, and Pr. The same problem was solved in the presence of a horizontal magnetic field.

Finally the AMA method was applied to the solution of the natural convection problem in enclosures where because of the complexity of the geometry and boundary conditions it was not possible to calculate the three weight coefficients. The problem was handled by carrying these coefficients as unknowns. They were subsequently determined from a mixture of theoretical, numerical, and experimental information. The final correlation yielded the Nusselt number as a unique function of Ra, Pr, and aspect ratio A, and was found to be adequate when tested against a wide range, of small and high values of these parameters.

Acknowledgements

The author is indebted to Mr. Cheng-Shiun Jan for his help in the preparation of Figs. 2 and 3.

References

Batchelor, G. K., 1954, "Heat Transfer by Free Convection Across a Closed Cavity Between Vertical Boundaries at Different Temperatures," *Q. Appl. Math.*, Vol. 12, pp. 209–233.

Bejan, A., 1979, "Note on Gill's Solution for Free Convection in a Vertical Enclosure," *J. Fluid Mech.*, Vol. 90, pp. 561–568.

Bejan, A., 1984, *Convective Heat Transfer*, Wiley, New York.

Bejan, A., and Lage, J. L., 1990, The Prandtl Number Effect on the Transition in Natural Convection Along a Vertical Surface," ASME JOURNAL OF HEAT TRANSFER, Vol. 112, pp. 787–790.

Berkovsky, B., and Polevicov, M. V. K., 1976, "Numerical Study of Problems of High Intensity Free Convection," *Heat Transfer and Turbulent Buoyant Convection*, D. B. Spalding and N. Afgan, eds., Hemisphere, New York.

Catton, I., 1978, "Natural Convection in Enclosures," *Proc. 6th Int. Heat Transfer Conf.*, Toronto, Vol. 6, pp. 13–31.

Churchill, S. W., and Ozoe, H., 1973, "Correlations for Laminar Forced Convection in Flow over an Isothermal Flat Plate and in Developing and Fully Developed Flow in an Isothermal Tube," ASME JOURNAL OF HEAT TRANSFER, Vol. 95, p. 78.

Churchill, S. W., and Chu, H. H. S., 1975, "Correlating Equations for Laminar and Turbulent Free Convection From a Vertical Plate," *Int. J. Heat Mass Transfer*, Vol. 18, pp. 1323–1329.

Churchill, S. W., 1983, "Heat Exchanger Design Handbook," X. X. Schlunder, ed., sec. 2.5.8, Hemisphere, New York.

Gill, A. E., 1962, "The Boundary Layer Regime for Convection in a Rectangular Cavity," *J. Fluid Mechanics*, Vol. 26, pp. 515–536.

Lykoudis, P. S., 1962, "Natural Convection of an Electrically Conducting Fluid in the Presence of a Magnetic Field," *Int. J. Heat Mass Transfer*, Vol. 5, pp. 23–34.

Lykoudis, P. S., and Yu, C. P., 1963, "The Influence of Electrostrictive Forces in Natural Thermal Convection," *Int. J. Heat Mass Transfer*, Vol. 6, pp. 853–862.

Lykoudis, P. S., and Dunn, P. F., 1973, "MagnetoFluid/Mechanic Heat Transfer From Hot Film Probes," *Int. J. Heat Mass Transfer*, Vol. 16, pp. 1493–1452.

Okada, K., and Ozoe, H., 1992, "Experimental Heat Transfer Rates of Natural Convection in Molten Gallium Suppressed Under an External Magnetic Field in Either the X, Y, or Z Direction," ASME JOURNAL OF HEAT TRANSFER, Vol. 114, pp. 107–114.

Ostrach, S., 1972, "Natural Convection in Enclosures," *Advances in Heat Transfer*, Vol. 8, pp. 161–227.

Ostrach, S., 1982, "Natural Convection Heat Transfer in Cavities and Cells," *Heat Transfer*, Vol. 1, pp. 365–379, Hemisphere.

Ozoe, H., and Okada, K., 1989, "The Effect of the Direction of the External Magnetic Field on the Three-Dimensional Natural Convection in a Cubical Enclosure," *Int. J. Heat Mass Transfer*, Vol. 32, No. 10, pp. 1939–1954.

Viskanta, R., Kim, D. M., and Gau, C., 1986, "Three-Dimensional Natural Convection Heat Transfer of Liquid Metals in a Cavity," *Int. J. Heat Mass Transfer*, Vol. 29, No. 3, pp. 475–485.

Vitharana, V. L., and Lykoudis, P. S., 1994, "Criteria for Predicting the Transition to Turbulence in Natural Convection Along a Vertical Surface," ASME JOURNAL OF HEAT TRANSFER, Vol. 116, No. 3, pp. 633–638.

A Thermocapillary Convection Experiment in Microgravity

Y. Kamotani

S. Ostrach

Department of Mechanical and Aerospace Engineering,
Case Western Reserve University,
Cleveland, OH 44106

A. Pline

NASA Lewis Research Center,
Cleveland, OH 44135

Results are reported of the Surface Tension Driven Convection Experiment (STDCE) aboard the USML-1 Spacelab, which was launched on June 25, 1992. In the experiment, 10 cSt silicone oil was placed in an open 10-cm-dia circular container, which was 5 cm deep. The fluid was heated either by a cylindrical heater (1.11 cm diameter) located along the container centerline or by a CO_2 laser beam to induce thermocapillary flow. Several thermistor probes were placed in the fluid to measure the temperature distribution. The temperature distribution along the liquid-free surface was measured by an infrared imager. Tests were conducted over a range of heating powers, laser-beam diameters, and free surface shapes. An extensive numerical modeling of the flow was conducted in conjunction with the experiments. Some results of the temperature measurements with flat free surfaces are presented in this paper and they are shown to agree well with the numerical predictions.

1 Introduction

Surface tension variations along a liquid-free surface caused by nonuniform temperature distributions induce so-called thermocapillary flows in the bulk liquid. In a terrestrial environment such flows are usually overshadowed by buoyancy-driven flows, except in configurations of small dimension (less than several mm). In the reduced-gravity environment of space, however, buoyancy is greatly reduced and thermocapillarity becomes an important driving force for fluid motion (Ostrach, 1982). In such applications as crystal growth from melts, two-phase flows with heat transfer, and thermocapillary migration of bubbles and droplets, thermocapillary flow is known to play an important role. For that reason much attention has been given in recent years to thermocapillary flow analysis. Much of past work was done numerically (e.g., Fu and Ostrach, 1983; Zebib et al., 1985; Carpenter and Homsy, 1990). Since thermocapillary flow experiments in one-g must be conducted in very small systems to minimize buoyancy effects, they can cover only limited ranges of parameters. Therefore, it is necessary to perform experiments in microgravity over a wide range of conditions to investigate and describe thermocapillary flows fully and to validate numerical analyses.

It is also known that thermocapillary flows in open containers become oscillatory under certain conditions (e.g., Preisser et al., 1983; Kamotani et al., 1984, 1992; Velten et al., 1991) but its cause is not yet completely understood. The least understood part is the role free surface deformability plays in the oscillation mechanism. Based on past ground-based experimental work the authors suggested a physical model that emphasized the importance of deformable free surface (Kamotani et al., 1984). On the other hand, some investigators consider the oscillation phenomenon to be the result of instability that could occur even with an undeformable free surface (Xu and Davis, 1984; Shen et al., 1990; Neitzel et al., 1991, 1993; Kuhlmann and Rath, 1993). According to the latter concept, only one dimensionless parameter, called the Marangoni number (Ma), specifies the critical condition for the onset of oscillations. Therefore, further evidence was sought to determine the importance of free surface deformation by conducting experiments in space over a wide range of conditions.

A series of experiments was conceived to study thermocapillary flows in microgravity. The first experiment, called the Surface Tension Driven Convection Experiment (STDCE), was conducted on the first U.S. Microgravity Laboratory Mission (USML-1) on the Space Shuttle Columbia (STS-50), launched on June 25, 1992. The main objectives of the STDCE were to study the velocity and temperature fields in detail in nonoscillatory thermocapillary flows and to determine whether Ma alone can specify the onset of oscillations. In a second series of experiments (STDCE-2), scheduled to be conducted aboard USML-2 in 1995, the focus will be on the oscillation phenomenon, including the measurement of free surface deformation.

In order to complement the space experiments, as well as assist in their design, an extensive numerical analysis of thermocapillary flow was conducted for both flat and curved free surfaces under both steady and transient (nonoscillatory) conditions. Some results of the temperature measurements with flat free surfaces are presented here and compared with the numerical results. It was also found that despite the fact that Ma in the STDCE was up to five times as large as the critical Ma determined in one-g tests, no oscillations occurred.

2 Description of STDCE

The specific objectives of the STDCE were to determine the extent and nature of thermocapillary flows, the effect of heating mode and level, the effect of the liquid free-surface shape, and the onset conditions for oscillatory flows. The detailed requirements of the experiment are given by Ostrach and Kamotani (1989). Its design and important considerations behind it are discussed by Kamotani and Ostrach (1987). The development of the STDCE flight hardware is described by Pline et al. (1990) and the performance of the hardware during the flight is reported by Pline et al. (1993).

Experimental System. The basic experimental configurations are illustrated in Fig. 1. 10 cSt silicone oil was used as the test fluid. The pertinent physical properties of the fluid are: $\rho = 935$ kg/m^3, $\alpha = 9.5 \times 10^{-8}$ m^2/s, $\mu = 9.4$ cp at 25°C, and $\sigma_T = -5.5 \times 10^{-5}$ N/m°C. The fluid was placed in a circular container, 10 cm in diameter and 5 cm in depth. The container side was made of 5-mm-thick copper with copper tubing coiled around the outside of the side wall for cooling water circulation. The top rim of the side wall had a sharp edge to pin the fluid. The bottom wall consisted of plexiglass of uneven thickness (average thickness 8 mm) because of a filling hole and the attachment of a lens assembly for flow visualization

Contributed by the Heat Transfer Division for publication in the JOURNAL OF HEAT TRANSFER. Manuscript received by the Heat Transfer Division October 1993; revision received October 1994. Keywords: Microgravity Heat Transfer, Thermocapillary Flows. Associate Technical Editor: J. R. Lloyd.

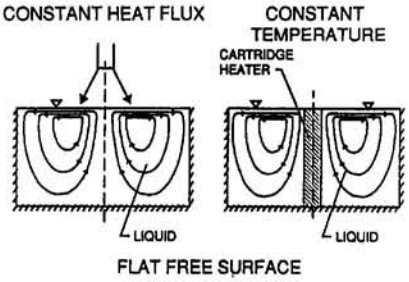

Fig. 1 Test configurations for STDCE with flat free surfaces

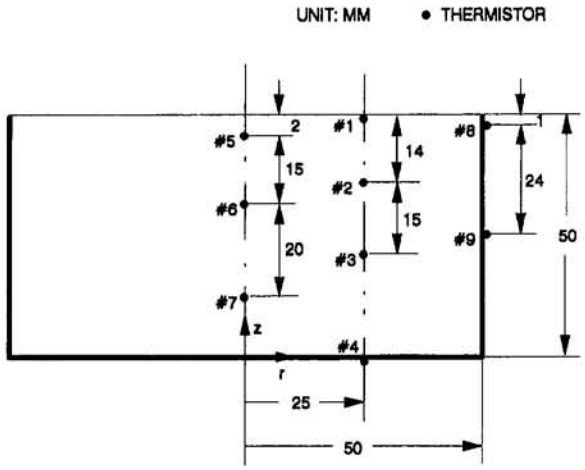

Fig. 2 Location and numbering of thermistors

through the bottom wall. To minimize contamination of the test fluid, the container inner surface was maintained clean and dry until the experiment, with the fluid and air both contained within a closed fluid loop. Two heating modes were employed: CO_2 laser heating (called the Constant Flux experiment (CF)) and heating by a cylindrical heater placed along the container centerline (called the Constant Temperature experiment (CT)). The diameter of the submerged heater was set at 1.11 cm, while the laser beam diameter was variable. The laser power was adjustable from 0.2 to 3 W and the submerged heater power from 1 to 20 W. The mean absorption length of the CO_2 laser (10.6 μm wavelength) by the test fluid was measured to be 0.060 mm (Pline et al., 1990), so the laser beam was absorbed within a relatively very short distance from the free surface. The emissivity of the fluid surface was determined to be 0.9 (Pline et al., 1990). The free surface shape was varied by adjusting the total volume of fluid in the container. Figure 1 shows both CF and CT configurations with flat free surfaces. The surface was set within ± 1 mm of the prescribed location.

The temperature field in the bulk fluid was measured by 9 thermistor probes at various locations in the fluid and in the container walls, the positions being shown in Fig. 2. The top of thermistor No. 1 touched the free surface; one probe measured the ambient temperature above the fluid free surface and six thermistors monitored the submerged heater shell temperature. The three probes along the container centerline were removed during the CT tests. The diameter of the thermistors in the fluid was 0.5 mm. The temperature data were taken once every 100 milliseconds during tests, digitized, stored, and downlinked to the ground station at appropriate intervals for monitoring purposes. The resolution of the digital data was 0.1°C and the accuracy of thermistor sensors was ± 0.1°C.

A thermographic technique was employed to obtain information on the temperature distribution along the free surface, of particular importance since it is directly related to the driving thermocapillary force. The infrared imaging system used in the STDCE is described by Pline and Butcher (1990b). The operating wavelength was 8–14 μm and the mean absorption length of the fluid in that range was measured to be 0.012 mm. As will be discussed later, the thermal boundary layer thickness along the free surface can become comparable to the absorption length noted above in certain relatively small areas, but along most of the free surface the boundary layer is much thicker than the absorption length, so the infrared data are considered to represent the surface temperature. The minimum detectable temperature difference was 0.1°C and the spatial resolution was 1 mm. Its feasibility and accuracy were checked in a ground-based experiment (Pline, 1988). This technique was found to be useful in studying the oscillation phenomenon (Kamotani et al., 1992).

The flow field was studied by flow visualization and the video record of the flow is being analyzed using a particle image velocimetory (PIV) technique. The flow field data is reported separately (Kamotani et al., 1994a).

Parametric Ranges. The important dimensionless parameters for the present experiment in the case of flat free surface are: Ma (Marangoni number) $= \sigma_T \Delta T H/\mu\alpha$, Pr (Prandtl number) $= \nu/\alpha$, Ar (aspect ratio) $= H/R$, Hr (relative heater size) $= D_H/D$. In the CT configuration ΔT in Ma is the temperature difference between the heater and the side wall. Since the total power input is specified in the CF tests, the ΔT is not known a priori. However, because the thermocapillary flow driving force is closely related to ΔT and to make comparison between the CT and CF tests convenient, Ma based on ΔT is used in both cases in the present paper, ΔT being determined from the numerical analysis for the CF tests.

Nomenclature

Ar = aspect ratio = H/R
a = radiation absorption coefficient
D = container diameter
D_H = heater diameter in CT configuration and CO_2 laser beam diameter in CF configuration
H = container height
Hr = relative heater size = D_H/D
k = thermal conductivity of fluid
Ma = Marangoni number = $\sigma_T \Delta T H/\mu\alpha$
Pr = Prandtl number = ν/α
Q = total heat input
(r, z) = coordinate system defined in Fig. 2
R = container radius
Ra = radiation parameter = $\epsilon\sigma^* T_a^3 H/k$
S = surface deformation parameter = $\sigma_T \Delta T/\sigma(1/\mathrm{Pr})$
t = time
T = temperature
T_a = ambient temperature
T_c = side wall temperature
(u, v) = velocity components
α = thermal diffusivity
ΔT = overall temperature difference along free surface
ϵ = emissivity of free surface
θ = dimensionless temperature = $(T - T_c)/\Delta T$
θ_a = dimensionless ambient temperature
μ = fluid dynamic viscosity
ν = fluid kinematic viscosity
ρ = fluid density
σ = surface tension
σ^* = Stefan–Boltzmann constant
σ_T = temperature coefficient of surface tension
ψ = stream function in cylindrical coordinates

In one-g, heat loss occurs at the free surface mainly through natural convection to the surrounding air, but in microgravity, radiation loss to the enclosure wall becomes important. Since the temperature difference between the free surface and the surroundings is relatively small compared to their absolute temperatures, the radiation loss can be represented by Ra (radiation parameter) $= \epsilon\sigma^* T_a^3 H/k$.

The range of each parameter covered in the STDCE was as follows: $3.6 \times 10^4 \leq \text{Ma} \leq 3.1 \times 10^5$, $78 \leq \text{Pr} \leq 97$, $Ar = 1.0$, $Hr = 0.111$ for CT and 0.05, 0.1, and 0.3 for CF, and Ra $= 0.5$. The physical properties are evaluated at the mean fluid temperature. The range of Pr reflects the fact that the fluid viscosity varies with temperature. In ground-based tests in the CT configuration using a small container (4 mm diameter), the critical Ma for the onset of oscillations was found to be 6.5×10^4 (Kamotani et al., 1992), so the maximum value of Ma in the STDCE was about five times that value.

3 Numerical Analysis

The program for the flat free surface is based on the SIMPLER algorithm by Patankar (1980). The flow is assumed to be laminar, incompressible, and axisymmetric. The fluid properties are considered to be constant, except for viscosity, which varies with temperature. The program provides both transient and steady solutions of the Navier–Stokes and energy equations. The coordinate system used in the analysis is defined in Fig. 2. The coordinates (r, z) are nondimensionalized by R and H, respectively. The velocity components (u, v) and stream function ψ (in cylindrical coordinates) are made dimensionless by $\sigma_T \Delta T/\mu$ and $\sigma_T \Delta T RH/\mu$, respectively. The temperature T is nondimensionalized as $\theta = (T - T_c)/\Delta T$.

The no-slip condition is used on the side and bottom walls, and on the heater surface in the CT configuration. The hydrodynamic boundary condition along the free surface is a shear stress balance, namely $\partial u/\partial z = -Ar\ \partial\theta/\partial r$ (dimensionless). The bottom wall is assumed to be thermally insulated. The side-wall temperature and, in the CT tests, the heater temperature are given by the experimental data. Both temperatures change with time during the tests. The dimensionless thermal boundary condition along the free surface is $\partial\theta/\partial z = -4Ra\ (\theta - \theta_a)$, where θ_a is given by the data. In the CF configuration, the laser beam is absorbed internally so that a heat source term is added to the energy equation. The dimensionless source term is given as $2Qa/(\pi k \Delta T Hr^2) \exp(-2/Hr^2 r^2) \exp[-aH(1 - z)]$. The viscosity–temperature relationship used in the present analysis is $\mu/\mu_r = 1.0 - 1.71 \times 10^{-2}(T - T_r) + 1.06 \times 10^{-4}(T - T_r)^2$, where T is in °C and $\mu_r = 9.4$ cp at $Tr = 25$°C. The relation is based on the information in the product manual (1983) and is valid in the temperature range of the STDCE.

A nonuniform grid system is adopted with meshes graded toward the hot and cold walls and toward the free surface. In the CT cases the free surface temperature varies very sharply near the heater due to the presence of a thin thermal boundary layer along the heater surface. As a result, the free-surface velocity increases very sharply in that region and an accurate resolution of the surface velocity distribution near the heater is the most important requirement for the numerical grid. The surface velocity distributions computed with three different grids are shown in Fig. 3(*a*). The computed case corresponds to the main CT test and is discussed in detail below. The 46 × 41 (radial × vertical) grid with the smallest radial mesh size of 0.001 next to the heater is not adequate. The 58 × 51 and 67 × 60 grids with the smallest mesh sizes of 0.0005 and 0.0003, respectively, give nearly the same distribution. With all three grids the maximum stream function and the total heat transfer rate are all within 1 percent of each other. Therefore the 58 × 51 grid is used both for the steady and transient CT computations. In the CF configuration there exists a very thin thermal boundary layer along the free surface in the region

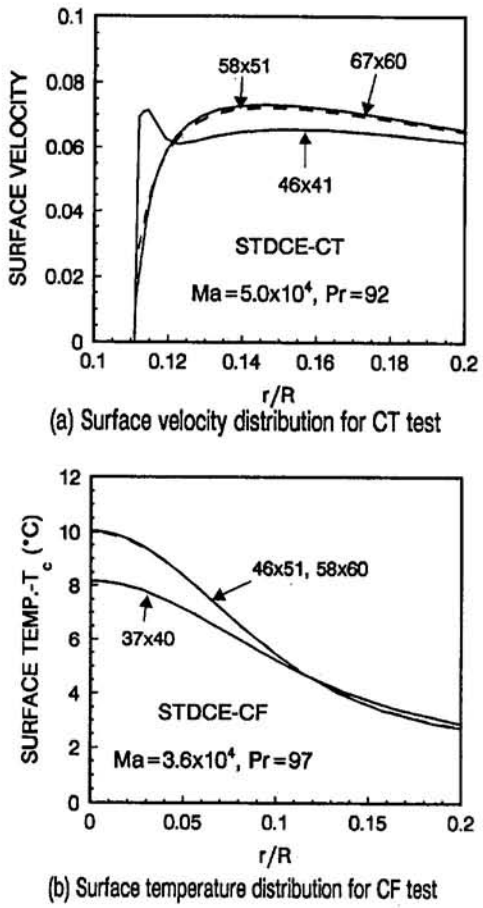

Fig. 3 Comparison of results obtained with various grid systems

heated by the laser beam, so an accurate prediction of the surface temperature distribution near the heated region becomes important. In Fig. 3(*b*) the surface temperature distributions computed with three different grids, 37 × 40, 46 × 51, and 58 × 60 with the smallest axial mesh sizes next to the free surface of 0.005, 0.001, and 0.0005, respectively, are shown for the main CF test. Based on Fig. 3(*b*) the 46 × 51 grid is used for the CF transient and steady analysis.

In the following discussion the numerical results are compared with the experimental data. One source of error must be considered in that comparison because the experimental data are used as the inputs to the numerical analysis. Since the value of Ma in the computation is based on the experimental data of T_h and T_c in the CT configuration, and on Q and T_c in the CF configuration, Ma is affected by the measurement errors of those quantities. For both configurations the value of Ma is estimated to contain ± 5 percent error, including the estimated errors in the physical property values. It can be shown (Chang, 1994) that in the range of Ma studied herein the dimensionless heat transfer coefficient (Nusselt number) varies as $\text{Ma}^{1/4}$ in the CT configuration and as $\text{Ma}^{1/3}$ in the CF configuration. The dimensionless temperature field depends similarly on the Ma, which means that the error in the computed dimensionless temperature due to the error in Ma is ±2 percent at most.

4 Results and Discussion

In the STDCE a total of 11 CF and 7 CT tests were conducted with flat free surfaces. It had been estimated that about one hour would be needed to obtain thermal equilibrium. Considering such relatively long transient period, it was decided that only one CF and one CT one-hour test would be conducted to study the complete transient flow and thermal development.

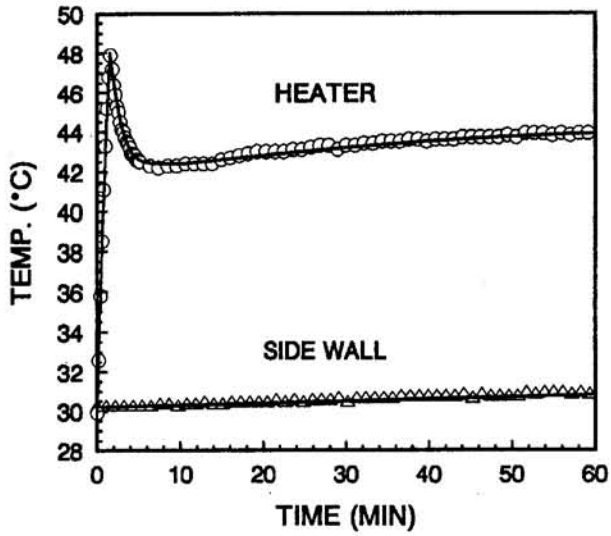

Fig. 4 Variation of heater and side wall temperatures with time for CT test (symbols denote experimental data and solid lines are inputs to numerical analysis)

These two tests are discussed below. The other tests were shorter duration tests to determine whether the flow would become oscillatory.

CT One-hour Test. Before the test the free surface was checked through video downlink to be flat and no appreciable motion existed in the fluid. Figure 4 shows how the heater and side wall temperature varied during the one-hour period after the heating started. The power to the heater was boosted for the first 90 seconds to shorten the warm-up time of the heater. Judging from the heater temperature overshoot in Fig. 4, the power boost was slightly too large. After the boost period the heater power was adjusted but the heater temperature increased gradually throughout the one-hour period. The side wall temperature variation was relatively small, about 0.6°C increase after one hour. The readings of the two thermistors in the side wall were the same within the resolution of the data acquisition system (±0.1°C). Of the six thermistors in the heater shell, four of them were positioned in the top $\frac{2}{3}$ of the heater length and read within ±0.2°C of each other (the data in Fig. 4 are the average of those). However, the two thermistors near the heater bottom read about 0.5°C below the above average, probably due to the end heat losses. The solid lines in Fig. 4 are used as inputs to the numerical analysis.

Figure 5 shows the computed streamlines and isotherms at t = 2 min. The streamline pattern shows that the entire fluid is in motion at this time. The overall flow structure changes little beyond this time, which agrees with the actual observation of the flow. In comparison, in one-g the flow in this large system

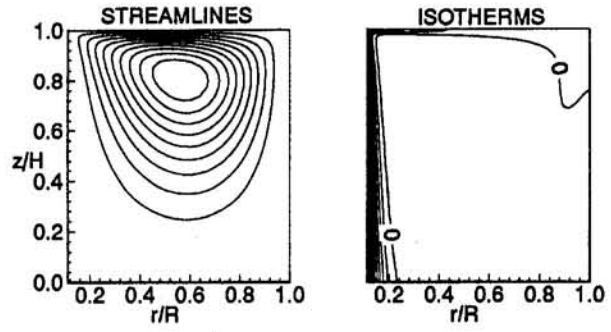

Fig. 5 Streamlines and isotherms at t = 2 min for CT test

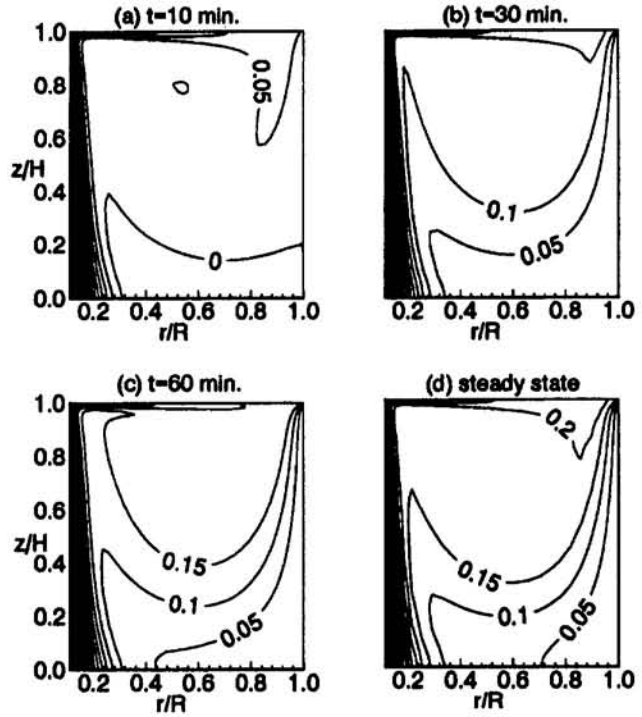

Fig. 6 Isotherms at various times for CT test

is confined to a thin region near the surface because of stratification. The isotherms in Fig. 5 suggest that the temperature is basically equal to the initial temperature over most of the flow field. The liquid initial temperature was about 0.5°C below the side wall temperature.

The transient development of the temperature field is shown in Fig. 6, based on the numerical analysis. Heat is transferred from the heater to the bulk liquid by convection first along the free surface and then into the interior region. The steady-state profile in Fig. 6 is computed based on the thermal boundary conditions at t = 60 min, which shows that the temperature field at t = 60 min (Fig. 6c) is not yet steady. The reason it did not become steady by t = 60 min (the transient starting period was established to be about 60 min) was that the heater temperature continued to increase, as seen in Fig. 4. Figure 6 also shows the presence of a thin thermal boundary layer along the heater.

In the CT tests thermistors No. 1–No. 3 (Fig. 2) measured the fluid temperature. The outputs from those probes are compared with the numerically predicted values in Fig. 7 and good agreement is shown. For some reason the No. 3 probe output seemed to be too high because, although it was below the No. 2 probe (Fig. 2), its reading was always above that of No. 2, which does not seem to be correct (see the isotherms in Fig. 6). In any case the difference between the No. 3 probe reading and the numerical prediction is at most 0.4°C, which is only 3 percent of ΔT. As shown in Fig. 7(b), relative to the overall temperature variation in the liquid, agreement between the analysis and data can be said to be excellent (for clarity only readings Nos. 1 and 2 are shown in Fig. 7b). As mentioned above, the fluid temperature was still increasing after the one-hour period.

The infrared imager did not require in situ calibration, but for a reason not yet fully understood its readings seemed to have shifted, judging from a comparison of its measurement of the fluid initial temperature with that measured by the thermistors. It was calibrated before and after the flight but no drifting was found. For that reason, instead of determining the absolute temperature of the free surface, the surface temperature change from the initial temperature was computed. Figure 8 shows the

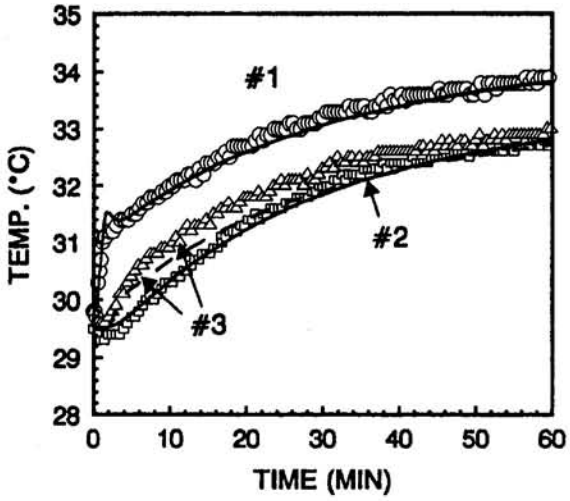

(a) Fluid temperature variation

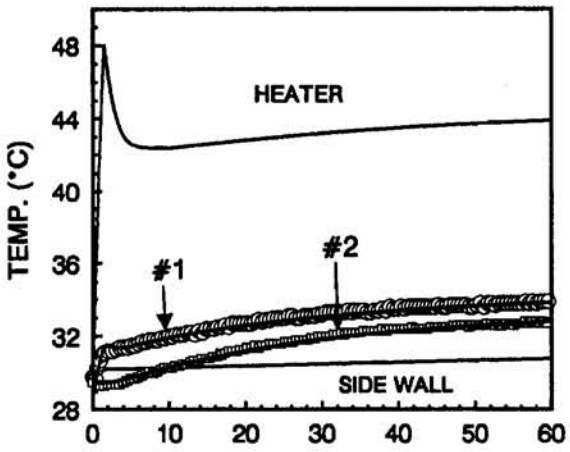

(b) Fluid and boundary temperatures

Fig. 7 Comparison of thermistor data with numerical results for CT test

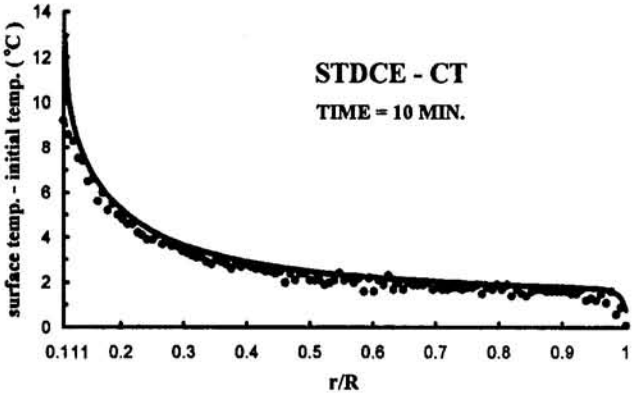

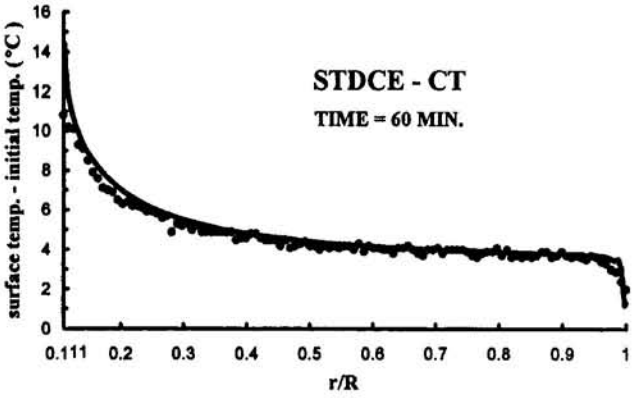

Fig. 8 Comparison of infrared imager data with numerical results for CT test (points are experimental data and lines are numerical results)

relative surface temperature distributions at $t = 10$ and 60 min. The data and numerical prediction agree very well. As seen in Fig. 8, the surface temperature drops sharply near the heater and, as a result, the surface velocity increases very sharply and attains its peak near the heater, as Fig. 3 shows. Comparison of the profiles at $t = 10$ and 60 min indicates that the overall profile does not change much with time, it only shifts as the fluid warms up. Since the driving force is dependent on the slope of the of the profile, the velocity field does not change much with time.

The total heat transfer at the heater is calculated to be 1.18 W, while the total power input to the heater was measured to be 1.2 W, so about 2 percent of the input is considered to be lost by conduction through the base of the heater. Of the 1.18 W of the net heat input to the fluid, 14 percent is lost by radiation from the free surface according to the numerical analysis. The ratio of the net heat input to the total heat lost from the fluid (radiation loss plus conduction at the cold wall) is computed to be 1.19 at $t = 60$ min, showing again that the temperature field was not in equilibrium at that time.

CF One-hour Test. The thermal conditions for the CF test are shown in Fig. 9. The laser beam power remained constant at 0.48 W throughout. The beam diameter was 1.0 cm. However, the side-wall temperature kept increasing and changed by 1.5°C (15 percent of ΔT) after one hour. Since in the CT test the side wall temperature did not change that much despite the fact that the heat input to the fluid was greater, the side wall temperature increase in the CF test was not because of the heat input from the laser beam. Considering the fact that the air temperature above the fluid also increased by the rate shown in Fig. 9, the increase is considered to be due to the ambient temperature increase, due probably to an increase in thermal loading of the Shuttle avionics air system. In all other tests the side wall temperature remained at about 25°C. The solid lines in Fig. 9 are the inputs to the numerical analysis. The air temperature is assumed to represent the surrounding wall temperature in the calculation of the radiation loss from the free surface.

The computed isotherm patterns at various times are pre-

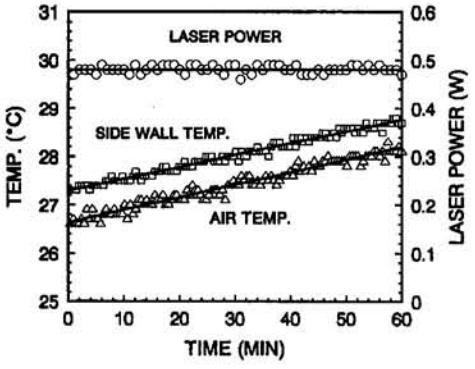

Fig. 9 Thermal boundary conditions for CF test (symbols denote experimental data and solid lines are inputs to numerical analysis)

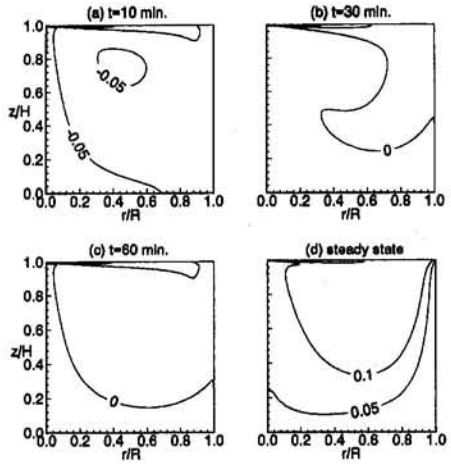

Fig. 10 Isotherms at various times for CF test

sented in Fig. 10. The steady-state pattern is based on the thermal conditions at $t = 60$ min. Although it is not shown, the streamline pattern is similar to that in the CT test (Fig. 5) and in about two minutes the pattern is set as in the CT case. The initial liquid temperature was about 0.6°C below the side wall temperature. At $t = 10$ min heat was spread only along the free surface and most of the fluid temperature remained unheated. Even at $t = 30$ min a large portion of the fluid had a temperature below the side-wall temperature but convection was beginning to heat up the interior. At $t = 60$ min most of the fluid had a temperature just above the side-wall temperature, but the temperature distribution was not yet close to the steady profile. The main reason the fluid temperature remained low compared to the side wall for such a long period was the continuous increase of the latter temperature, as discussed above. Also, compared to the CT case, the total heating area was smaller in the CF test, so that the bulk temperature remained relatively low in the latter case.

Figure 11(a) shows the computed maximum fluid temperature and comparison between the Nos. 1 and 2 thermistor readings and the numerical prediction. The maximum temperature kept increasing partly because of the side-wall temperature increase and partly because the temperature field was not in equilibrium. The figure shows good agreement between the data and the prediction. In Fig. 11(b) the temperature scale is expanded to show three thermistor readings. As discussed in the CT case, the reading of No. 3 thermistor seemed to be slightly too high (close to the reading of the probe at the free surface), but the difference between the data and the prediction is about 0.4°C, which is only 4.5 percent of the ΔT. In the CF test the three thermistors along the container centerline provided additional data and these readings are given in Fig. 11(c) along with the numerical prediction. These readings are all close, and the predicted temperature variations follow the data closely. According to the isotherms in Fig. 10, the thermal boundary layer thickness along the free surface is less than 1.5 mm near the center, so the No. 5 thermistor, which was located at 2 mm from the surface, was just outside the boundary layer. The infrared imager data are compared with the predicted relative surface temperature distributions at $t = 10$ and 60 min in Fig. 12. They agree well, but the imager data was lower than the prediction near the heated region because of the presence of a very thin thermal boundary layer there. Because of the thin boundary layer, practically there is no accurate way to measure the surface temperature near the center. The data at $r/R = 0.5$ agree with the No. 1 thermistor data.

As for the overall thermal balance based on the numerical analysis, 14 percent of the total heat input to the fluid is lost by radiation from the free surface at $t = 60$ min. The ratio of the total heat input to the total heat out from the fluid is 3.4 at $t = 60$ min so that the temperature field is still far from equilibrium, even after one hour. The overall ΔT is 10°C when steady state is reached, as seen in Fig. 3(b), but ΔT at $t = 60$ min is still about 9°C, according to Fig. 11(a).

By comparing the results of the CT and CF tests presented above one can say that although the flow structures are similar (simple unicellular structure), the temperature fields are different: In the CT case the overall fluid temperature is higher and there exists a very noticeable thermal boundary layer all along the heater surface, while in the CF case a thermal boundary

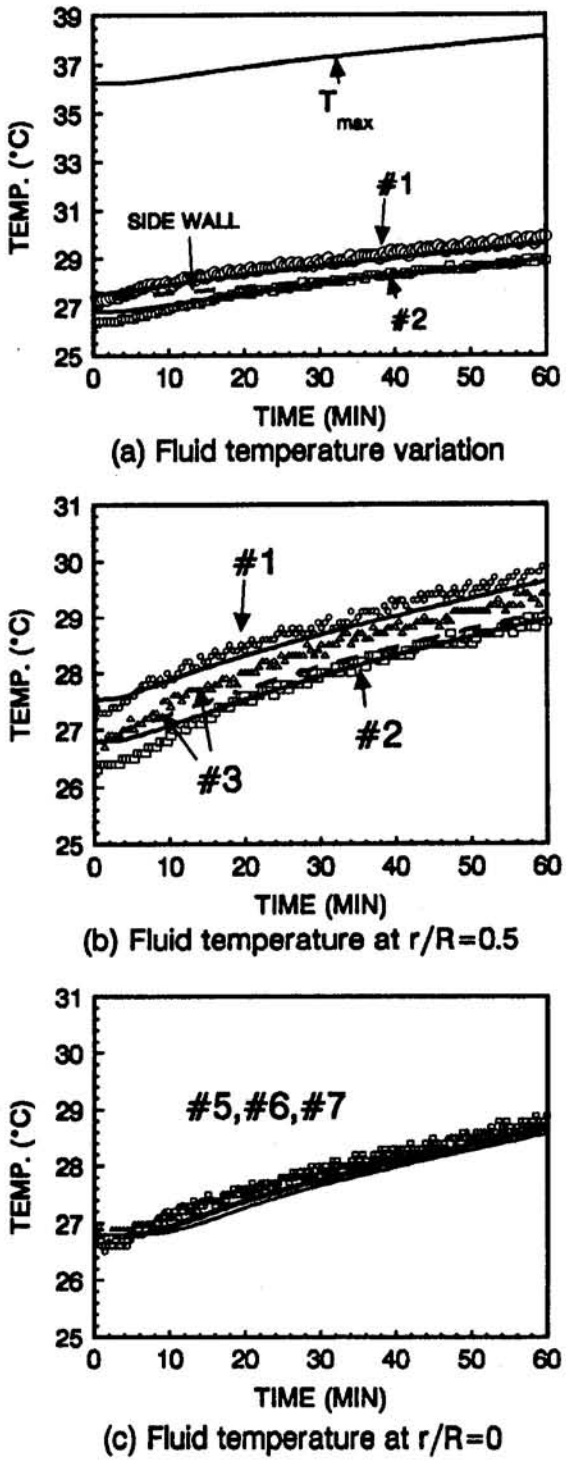

Fig. 11 Comparison of thermistor data with numerical results for CF test

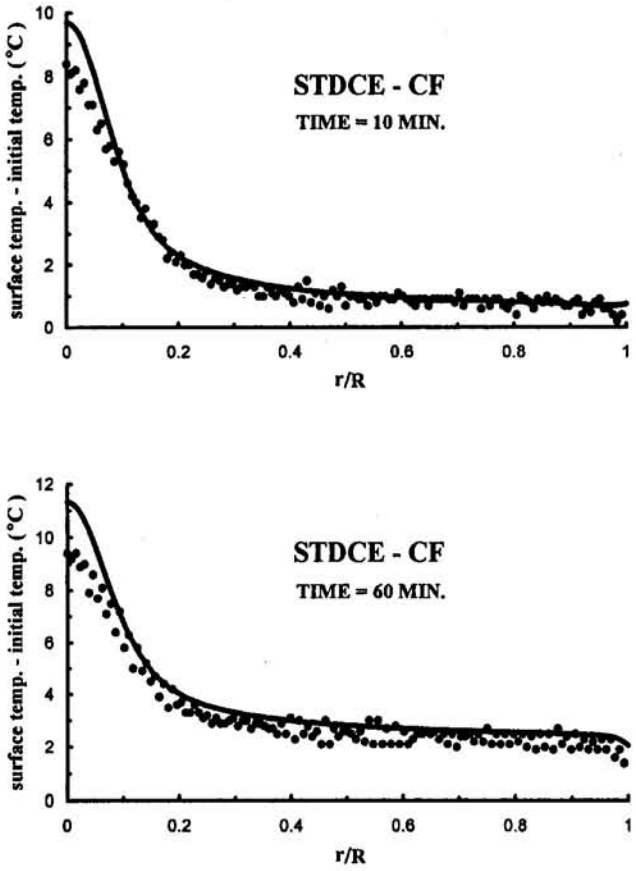

Fig. 12 Comparison of infrared imager data with numerical results for CF test

layer exists along the free surface, mainly in the heated region. In both cases the free surface temperature drops sharply in a relatively small region near the center (the so-called hot-corner region) and the flow is driven mainly in the hot-corner region. Although no oscillations were found in the present experiment, ground-based tests have shown that the oscillation phenomenon is very much influenced by the heating mode.

5 Concluding Remarks

Some of the temperature data taken in the STDCE experiment conducted aboard the USML-1 Spacelab in 1992 are presented. The results for a one-hour CT (Constant Temperature) test and for a one-hour CF (Constant Flux) test are given and compared with the results of the numerical analysis conducted in conjunction with the experiment. The tests covered a range of Ma up to 3.1×10^5. The temperature data were taken by thermistors and an infrared imager. Aside from some problems discussed above, the hardware performed well in general, and a large number of valuable data were collected. The temperature data presented in the present paper agree well with the numerical prediction. A validation of a numerical analysis for thermocapillary flow in such a high Marangoni range has not been done in the past. A total of 20 CF and 18 CT tests were conducted with flat and curved free surfaces under varieties of conditions. The thermal field did not become quite steady in any of the STDCE tests. However, the surface temperature profile (not the absolute level) and the thermal boundary layer in the heated region were established within ten minutes after the start of each test. Since the surface temperature gradient is the flow driving force, the flow field did not change appreciably after that time. G-jitter caused by thruster firings induced small but visible free surface disturbances, which quickly dumped and, therefore, did not change the steady flow field.

No oscillations were observed in any of the tests despite the fact that Ma was up to five times larger than the range of Ma where oscillations occurred in one-g tests. The unsteady conditions in the STDCE cannot explain that much discrepancy as the velocity field and the important region of the temperature were nearly steady in those tests. The range of Pr in our ground-based experiments were: Pr = 19–27 in the CT configuration (Kamotani et al., 1992) and Pr = 23–51 in the CF configuration (Lee et al., 1994), while in the STDCE the range was Pr = 78–97. Data (Lee et al., 1994) show that the critical Ma is not a strong function of Pr in one-g tests. Therefore, the difference in Pr cannot account for the nonexistence of oscillations in the STDCE. It is also noted that in conjunction with the STDCE some tests were performed in the Glovebox aboard the USML-1 to study oscillatory thermocapillary flows in the CT configuration using smaller containers (1 and 3 cm diameter) than in the STDCE and with the same test fluids (Pr = 20–51) as in our one-g tests (Kamotani et al., 1994b). The flow remained steady even at Ma about eight times larger than the critical Ma in one-g tests. It is thus obvious that the onset condition of oscillations is not determined by Ma itself.

Acknowledgments

The authors wish to express their appreciation to many people, especially the NASA Lewis Research Center engineering and operations teams, who contributed to make the STDCE a successful and important experiment. Special thanks to Dr. Eugene Trinh who, as a payload specialist aboard the USML-1, conducted the STDCE tests tirelessly and expertly for many hours. We also gratefully acknowledge the financial support of NASA for this experiment. The work done at Case Western Reserve University was supported by NASA under contract NAS 3-25973 with Mr. T. P. Jacobson of the NASA Lewis Research Center as the Project Manager and Dr. R. Thompson as the Project Scientist.

References

Carpenter, B. M., and Homsy, G. M., 1990, "High Marangoni Number Convection in a Square Cavity: Part II," *Physics of Fluids A*, Vol. 2, pp. 137–149.

Chang, A., 1994, "Scaling Analysis of Thermocapillary Flows in Cylindrical Containers," Ph.D. Thesis, Department of Mechanical and Aerospace Engineering, Case Western Reserve University, Cleveland, OH.

Fu, B., and Ostrach, S., 1983, "Numerical Simulation of Floating-Zone Thermocapillary Flows," *Proceedings, 4th European Symposium on Materials Sciences Under Microgravity (ESA SP-191)*, pp. 239–245.

Kamotani, Y., Ostrach, S., and Vargas, M., 1984, "Oscillatory Thermocapillary Convection in a Simulated Floating-Zone Configuration," *Journal of Crystal Growth*, Vol. 66, pp. 83–90.

Kamotani, Y., and Ostrach, S., 1987, "Design of a Thermocapillary Flow Experiment in Reduced Gravity," *Journal of Thermophysics and Heat Transfer*, Vol. 1, pp. 83–89.

Kamotani, Y., Lee, J. H., and Ostrach, S., 1992, "An Experimental Study of Oscillatory Thermocapillary Convection in Cylindrical Containers," *Physics of Fluids A*, Vol. 4, pp. 955–962.

Kamotani, Y., Ostrach, S., and Pline, A., 1994a, "Analysis of Velocity Data Taken in Surface Tension Driven Convection Experiment in Microgravity," accepted for publication in *Physics of Fluids*.

Kamotani, Y., Ostrach, S., and Pline, A., 1994b, "Oscillatory Thermocapillary Flow Experiment (OTFE)" *Proceedings, Joint Launch + One Year Science Review of USML-1 and USMP-1 With the Microgravity Measurement Group*, Ramachandran et al., eds., NASA Conference Publication No. 3272, Vol. 2, pp. 701–715.

Kuhlmann, H. C., and Rath, H. J., 1993, "Hydrodynamic Instabilities in Cylindrical Thermocapillary Liquid Bridges," *Journal of Fluid Mechanics*, Vol. 247, pp. 247–274.

Lee, H. J., Ostrach, S., and Kamotani, Y., 1994, "A Study of Oscillatory Thermocapillary Convection in Circular Containers With CO_2 Laser Heating," Report EMAE/TR-94-213, Department of Mechanical and Aerospace Engineering, Case Western Reserve University, Cleveland, OH.

Neitzel, G. P., Law, C. C., Jankowski, D. F., and Mittlemann, H. D., 1991, "Energy Stability of Thermocapillary Convection in a Model of the Float-Zone Crystal-Growth Process. II: Nonaxisymmetric Disturbances," *Physics of Fluids A*, Vol. 3, pp. 2841–2846.

Neitzel, G. P., Chang, K. T., Jankowski, D. F., and Mittlemann, H. D., 1993, "Linear Stability Theory of Thermocapillary Convection in a Model of the Float-Zone Crystal Growth Process," *Physics of Fluids A*, Vol. 5, pp. 108–114.

Ostrach, S., 1982, "Low-Gravity Fluid Flows," *Annual Review of Fluid Mechanics,* Vol. 14, pp. 313–345.

Ostrach, S., and Kamotani, Y., 1989, "Science Requirements Document for the Surface Tension Driven Convection Experiment in Reduced Gravity," Case Western Reserve University, Cleveland, OH.

Patankar, S. V., 1980, *Numerical Heat Transfer and Fluid Flow,* Hemisphere Pub., Washington, DC.

Pline, A., 1988, "Surface Temperature Measurements for the Surface Tension Driven Convection Experiment," NASA TM 101353.

Pline, A., Jacobson, T. P., Wanhainen, J. S., and Petrarca, D. A., 1990, "Hardware Development for the Surface Tension Driven Convection Experiment," *Journal of Spacecraft and Rockets,* Vol. 27, pp. 312–317.

Pline, A., and Butcher, R. L., 1990, "Spacelab Qualified Infrared Imager for Microgravity Science Applications," *Thermosense XII,* SPIE Vol. 1313, pp. 250–258.

Pline, A., Jacobson, T. P., Kamotani, Y., and Ostrach, S., 1993, "Surface Tension Driven Convection Experiment," AIAA Paper No. 93-4312.

Preisser, F., Schwabe, D., and Scharmann, A., 1983, "Steady and Oscillatory Thermocapillary Convection in Liquid Columns With Free Cylindrical Surface," *Journal of Fluid Mechanics,* Vol. 126, pp. 545–567.

Product Manual for Silicone Fluids, 1983, Report S-9G, Silicone Products Division, General Electric Company, New York.

Shen, Y., Neitzel, G. P., Jankowski, D. F., and Mittlemann, H. D., 1990, "Energy Stability of Thermocapillary Convection in a Model of the Float-Zone Crystal-Growth Process," *Journal of Fluid Mechanics,* Vol. 217, pp. 639–660.

Velten, R., Schwabe, D., and Scharmann, A., 1991, "The Periodic Instability of Thermocapillary Convection in Cylindrical Liquid Bridges," *Physics of Fluids A,* Vol. 3, pp. 267–279.

Xu, J.-J., and Davis, S. H., 1984, "Convective Thermocapillary Instabilities in Liquid Bridges," *Physics of Fluids A,* Vol. 27, pp. 1102–1107.

Zebib, A., Homsy, G. M., and Meiburg, E., 1985, "High Marangoni Number Convection in a Square Cavity," *Physics of Fluids,* Vol. 28, 3467–3476.

Three-Dimensional Natural Convection in an Enclosure With an Internal Isolated Vertical Plate

M. Yang[1]

W. Q. Tao

School of Energy and Power Engineering,
Xi'an Jiaotong University,
Xi'an, Shaanxi 710049
People's Republic of China

Natural convection in a cubic enclosure with an internal isolated heated vertical plate was investigated both experimentally and numerically. The internal plate was suspended under the lower surface of the enclosure top wall and electrically heated. The six enclosure walls were at a lower constant temperature. The plate average Nusselt number and the air temperature in the enclosure symmetry plane were experimentally determined in the range of $Ra = 8 \times 10^4$ to 5×10^7. Numerical simulations of laminar natural convection in the same configuration were performed. The agreement between the test data and the numerically predicted values is reasonably good, with a maximum deviation in plate average Nusselt number of 12.3 percent and that in air temperature of 9.4 percent. Detailed temperature and velocity distributions in four cross sections were presented for the case of $Ra = 6.57 \times 10^5$.

Introduction

For the past three decades, natural convection heat transfer in enclosures has been extensively studied because of its ever-increasing application in areas where basic data for buoyant enclosure flows are needed. Despite the intensity of the effort, knowledge in this field is still limited. It turns out that most of the studies in the existing literature are concerned with the enclosures within which there is no internal island(s) (Ozoe et al., 1976, 1986; Bohn et al., 1984; Yang, 1988; etc.) or with partitioned enclosures (Nansteel and Grief, 1981; Bajorek and Lloyd, 1982; Chang et al., 1982; Bilski et al., 1986; Jelti et al., 1986; Karki et al., 1992). As far as the natural convection in enclosures with internal isolated (i.e., not bounded by any part of the enclosure boundaries) is concerned, a search of the literature has shown that there is only a limited number of publications, most of which are related to the two-dimensional problem (Sparrow and Charmchi, 1981; Warrington and Crupper, 1981; Sparrow et al., 1984; Adlam, 1986; Zhang et al., 1991; Sathe and Jashi, 1992; Yang and Tao, 1992; Esteki et al., 1993; Wang et al., 1994).

Natural convection in three-dimensional enclosures with internal isolated island(s) is of interest in many engineering fields. These include energy transfer in rooms and buildings, heating of evaporators in a refrigerating compartment of a domestic refrigerator, cooling of an electronic board, etc. The existence of the internal isolated island provides new complexity in the numerical and experimental techniques.

With this short review as a background, attention is now turned to the purpose of this study. The problem to be studied in this paper is the natural convection in a cubic enclosure with an internal isolated vertical plate. This configuration is shown in Fig. 1(*a*). As seen there, the internal plate has a uniform temperature T_h, while the six surfaces of the enclosure have a uniform but different temperature T_c. The enclosure is filled with air. The steady-state, laminar natural convection in the enclosure is investigated by both experimental and numerical methods. It has been shown by the present authors (Yang et al., 1993) that as long as no bifurcation occurs, the results obtained from the present configuration may be applied to that shown in Fig. 1(*b*), which is a simplified model for a refrigerating compartment of a domestic refrigerator.

Experimental Apparatus and Data Reduction

The test cell is a cubic enclosure with interior dimensions of 100 mm. A pictorial view of it is shown in Fig. 2, where the top and bottom walls are removed. Before screwing the top plate to the four lateral walls, the internal plate is suspended under the lower surface of the top plate by two thin wires with desired length. The wires also serve as conducting wires for the power supply. The dimensions of the internal plate are $55 \times 80 \times 6$ mm. The position of the internal plate is shown in Fig. 1(*a*).

Each of the six enclosure walls consists of an aluminum plate 2 mm thick and a plastic plate 8 mm thick. At one side of the plastic plate a zigzag cooling channel with a square cross section of 5×5 mm^2 is milled. This side of the plastic plate is then glued to the aluminum plate to form a wall. The internal isolated plate has a sandwiched structure. Its center is a resin plate of 0.5 mm, around which 0.2 mm constantan wire is wound to serve as heating element. Mica sheets are glued on the two sides of the resin plate. Two aluminum plates of 2 mm thickness are then glued on the mica sheets to form a heating plate.

To measure the inner surface temperature of the enclosure, five thermocouples (copper-constantan) are installed into each of the six enclosure walls, located to within 1 mm of the enclosure inner surface. One of the five thermocouples is located at the center of each wall, and the other four are situated at the two diagonals. To measure the surface temperature of the internal plate, four thermocouples are placed on the surfaces of the plate, among which two thermocouples are located at one side on its center vertical line, and the other two are located at the opposite side on its center horizontal line. In the course of the experiment, cooling of the enclosure walls is accomplished by pumping water through the milled channel of the six walls. The temperature of the cold water at the inlet of the cooling channel is maintained constant by a thermostat (within ±0.1°C). The difference in water temperatures at the inlet and the outlet of the cooling channel is less than 0.4°C. The spatial variations of

[1] Present address: Department of Power Engineering, Northwest Institute of Electric Power Engineering, Jilin, Jilin 132012, People's Republic of China.

Contributed by the Heat Transfer Division for publication in the JOURNAL OF HEAT TRANSFER. Manuscript received by the Heat Transfer Division March 1994; revision received November 1994. Keywords: Enclosure Flows, Natural Convection, Numerical Methods. Associate Technical Editor: J. R. Lloyd.

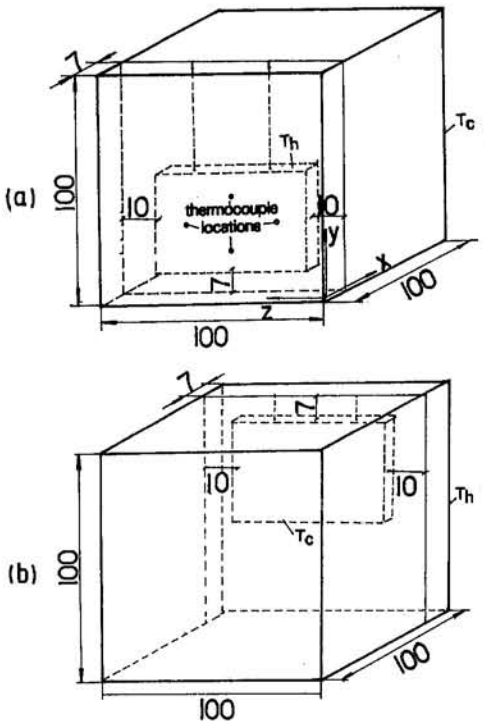

Fig. 1 The geometry considered: (*a*) inner plate heated, (*b*) inner plate cooled

the surface temperature for both the internal plate and the enclosure walls were less than 1–2 percent of the overall temperature difference. Therefore, the heated and the cooled surfaces may be considered isothermal.

The entire experimental system is shown in Fig. 3. The enclosure is set in a larger box made of steel. To extend the Rayleigh number variation range, the pressure in the steel box can be regulated by a vacuum pump or a compressor. A small metal tube with an outer diameter of 1.5 mm is used to connect the box and the enclosure. In the course of evacuation or compression, a valve in the small tube line is opened and the pressure in the enclosure is regulated. After a full balance between the pressures in the box and in the enclosure is reached, the valve is closed and the enclosure is then ready for experiment.

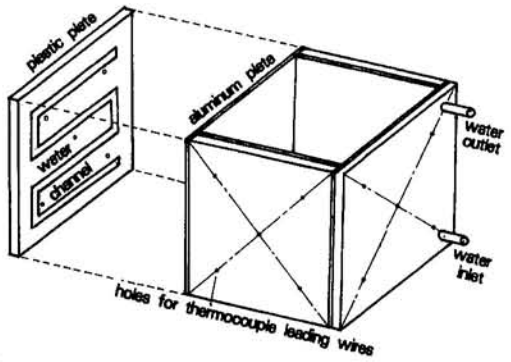

Fig. 2 Pictorial view of the test enclosure (top and bottom walls removed)

The heating power is measured by a dynamometer. To examine its readout an ampmeter and a voltmeter are also connected in the electrical circuit of the heating system. To reduce the radiative heat transfer, the surfaces of the heating plate are covered by very thin adhesive aluminum foil, whose normal surface emissivity is measured by the comparison method at room temperature (0.073). The measured emissivity of the enclosure inner surface is 0.17. Nine thermocouples are located in the middle plane of the enclosure to measure the air temperatures. All the thermocouple signals are detected and recorded by a HP 3054 data acquisition system.

Thermal properties of the air in the enclosure are calculated at a temperature determined by the following equation:

$$T_r = (6T_c + T_h)/7 \tag{1}$$

The characteristic length used in calculating the Nusselt number and Rayleigh number is $H = 55$ mm (the height of the internal plate).

The average heat transfer coefficient of the isolated vertical plate is calculated by

$$h = Q_c/(A_1(T_h - T_c)) \tag{2}$$

The average Nusselt number and the Rayleigh number are

Nomenclature

a = thermal diffusivity of fluid, m^2/s
A_1 = total heat transfer area of the heated plate, m^2
A_2 = total area of the enclosure inner surface, m^2
C_p = specific heat capacity of air, J/kg°C
F = dimensionless time = $\tau\, u_r/H$
g = gravitational acceleration, m/s^2
h = heat transfer coefficient, $W/m^2°C$
H = height of the internal isolated plate, m
I, J, K = indices of grid point in X, Y, and Z coordinates
k = thermal conductivity, W/m°C
K_r = ratio of thermal conductivity = k/k_f
Nu = Nusselt number
p = pressure, Pa
P = dimensionless pressure = $p/(\rho\, u_r^2)$
Pr = Prandtl number
Q = heat transfer rate, W
Ra = Rayleigh number
T = temperature, °C
T_r = reference temperature, °C
u_r = reference velocity = $(\mathrm{Ra\ Pr})^{1/2}a/H$, m/s
u, v, w = velocity components in x, y, and z directions, m/s
U, V, W = dimensionless velocities in three coordinates; $U = u/u_r$, etc.
x, y, z = coordinates, m
X, Y, Z = dimensionless coordinates; $X = x/H$, etc.
β = volume expansion coefficient, K^{-1}
δ = percentage deviation in temperature = $(T_e - T_p)/\Delta T$
$\Delta T = T_h - T_c$, °C
ϵ = surface emissivity
μ = dynamic viscosity, kg/m s
Θ = dimensionless temperature = $(T - T_c)/(T_h - T_c)$
σ_0 = Stefan–Boltzmann constant
τ = time, s

Subscripts

1, 2 = heated and cooled surface, respectively
c = convective
e = experimental
f = fluid
p = predicted
r = radiative

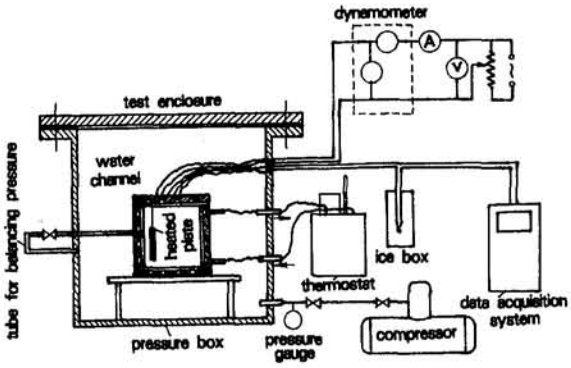

Fig. 3 Diagram of the measurement system

$$\mathrm{Nu} = hH/k, \quad \mathrm{Ra} = g\beta H^3(T_h - T_c)\rho 2C_p/(k\mu) \qquad (3)$$

In the pressure and temperature variation ranges of this study, air may be regarded as an ideal gas, hence, the density is proportional to the pressure. The Rayleigh number is then directly related to the square of the pressure

$$\mathrm{Ra} = Cg\beta H^3(T_h - T_c)C_pP^2/(k\mu) \qquad (4)$$

where C is a coefficient dependent upon the temperature. In this study the air pressure varied from 6 kPa to about 0.4 MPa, and a variation range of Ra from 8.4×10^4 to 5.0×10^7 was obtained, which not only covers the conventional variation range of Ra for the cooling of electronic boards, but also partly covers the Rayleigh number range for the natural convection in refrigerator compartment. The convective heat transfer rate, Q_c, is determined from the total power input by subtracting the radiative heat transfer rate Q_r. The radiative heat transfer problem considered is a two-surface system and Q_r may be determined by

$$Q_r = \frac{A_1\sigma_0[(T_h/100)^4 - (T_c/100)^4)]}{1/\epsilon_1 + A_2/A_1(1/\epsilon_2 - 1)} \qquad (5)$$

For most of the cases tested, the radiative heat transfer rate, Q_r, is less than 5 percent of the total power input. The percentage value is a bit larger (<8 percent) only for a few cases. It is worth noting that although this relative percentage is not large, its value is subjected to change after a period of operation of the heating plate. In the course of the experiments, we regularly repeated some case in order to ensure the reproducibility of the data. Once the reproducibility became bad, the aluminum foil at the heating surface was replaced by a new one.

An uncertainty analysis conducted along the line proposed by Kline and McClintock (1953) shows that the maximum uncertainty in the measured Nusselt number is 10.5 percent, and that in the Rayleigh number is 12.5 percent. It should be noted that of the total 34 data points, 30 points have much smaller uncertainties in Nu and Ra (less than 6 and 7 percent, respectively). Only for the four data in the lower Rayleigh number region, the uncertainties become larger. This is because in the lower Rayleigh number region the overall temperature difference, $T_h - T_c$, is quite small (~5°C), leading to a relatively large uncertainty. The method suggested in Eckert and Drake (1972) was adopted to estimate the errors in air temperature measurement. The following parameters were adopted: diameter of thermocouple junction = 1 mm, emissivity of junction surface = 0.2, convective heat transfer coefficient of the junction = 10–40 W/m²°C, enclosure wall temperature = 20°C. This leads to an air temperature measurement error of 0.3–1.2°C. This means that the actual air temperature may be higher than the value of the thermocouple's reading by this amount. The fact that our numerically predicted air temperatures are mostly higher than the measured values is qualitatively agreeable with this estimation.

Experimental Results and Discussion

Air Temperature. For the sake of brevity, the data of the measured air temperature will be presented later with the numerically predicted values. Only one thing is to be stated here. In order to locate the thermocouples in the enclosure, three metal wires were suspended in the enclosure. These wires and the leading wires of the thermocouples for measuring the air temperature might have some effect on the air flow in the enclosure. To make sure that this effect is small enough to be neglected, at least as far as the average Nusselt number was concerned, measurements were repeated after the entire experimental plan was completed and these additional wires were withdrawn from the enclosure (however, the leading wires of the four thermocouples for measuring the surface temperatures of the heating plate were left in position). It was found that the withdrawing of the wires did not have a measurable effect on the average Nusselt number.

Average Nusselt Number Correlation. For the 34 data points, a regression analysis gave the following correlation

$$\mathrm{Nu} = 0.662\ \mathrm{Ra}^{0.232}(8.4 \times 10^4 < \mathrm{Ra} < 5.0 \times 10^7) \qquad (6)$$

The maximum deviation between the predicted and test data is 5.5 percent.

Attention is now turned to the comparison between Eq. (6) and the correlation for a isothermal plate in infinite space. Churchill and Chu (1975) proposed the following equation:

$$\mathrm{Nu} = 0.68 + 0.670\ \mathrm{Ra}^{1/4}[1 + (0.492/\mathrm{Pr})^{7/16}]^{-4/9}$$
$$(0 < \mathrm{Ra} < 10^9) \qquad (7)$$

The test data and Eqs. (6) and (7) are presented in Fig. 4. It can be found that the heat transfer rate of the vertical plate in the confined space studied in this paper is less than that in infinite space. With the decrease in Rayleigh number, the difference between the Nusselt numbers predicted by Eqs. (6) and (7) decreases. This is an expected result. For the natural convection around a vertical plate, when the plate is situated in an extensive medium a plume will occur at its trailing edge and this plume can rise freely without any restriction. The higher the Rayleigh number, the stronger the flow of the plume. If the plate is positioned in an enclosure such as the one studied in the present work, the rising flow of the plume is restricted. It is mainly this restriction that affects the plate heat transfer. Obviously, with the decrease in the Rayleigh number, the effect caused by the confined space on the flow pattern around the heated plate will be less significant, and so is the difference between the plate Nusselt numbers of the two configurations.

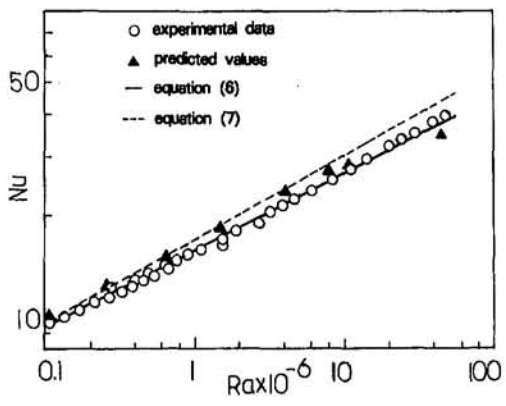

Fig. 4 Heat transfer data

Table 1 Predicted and measured air temperatures in symmetry plane

No	1	2	3	4	5	6	7	8	9
x, mm	$x = 21.8$	21.8	21.8	56.3	56.3	56.3	90.8	90.8	90.8
y, mm	$y = 10.0$	31.0	70.0	11.0	31.0	70.0	11.0	35.0	95.0
				Ra = 0.107×10^6, $\Delta T = 6.93$°C					
T_e	20.43	21.09	22.80	20.29	20.44	21.06	20.32	20.42	20.57
T_p	20.71	21.25	22.72	20.41	20.82	21.71	20.39	20.95	20.72
δ, percent	4.0	2.3	−1.2	1.7	5.5	9.4	1.0	7.6	2.2
				Ra = 0.269×10^6, $\Delta T = 17.93$°C					
T_e	20.75	22.22	26.59	20.57	21.12	22.96	20.62	21.36	21.99
T_p	21.48	22.71	26.08	20.97	21.91	24.60	21.07	22.79	22.51
δ, percent	4.1	2.7	2.9	2.2	4.4	9.1	2.5	8.0	2.9
				Ra = 0.657×10^6, $\Delta T = 49.28$°C					
T_e	21.90	24.66	37.01	21.17	22.94	28.11	21.70	24.38	25.07
T_p	23.42	26.53	34.44	22.32	24.75	32.36	23.30	28.07	27.88
δ, percent	3.1	3.8	−5.3	2.3	3.7	8.6	3.2	7.5	5.7
				Ra = 1.55×10^6, $\Delta T = 49.47$°C.					
T_e	21.83	24.11	32.46	21.43	23.67	28.22	22.04	25.03	28.06
T_p	23.29	26.23	32.96	22.48	24.81	32.23	24.50	28.81	27.74
δ, percent	3.0	4.3	1.0	2.1	2.3	8.3	5.0	7.6	−0.6
				Ra = 4.34×10^6, $\Delta T = 49.31$°C					
T_e	21.69	23.60	29.38	21.49	23.85	28.05	22.08	25.17	29.74
T_p	23.03	25.74	32.35	22.67	25.30	32.30	23.61	27.79	29.71
δ, percent	2.7	4.3	6.0	2.4	2.9	8.6	3.1	5.3	−0.1
				Ra = 8.6×10^6, $\Delta T = 48.85$°C					
T_e	21.58	23.37	28.66	21.48	23.66	28.09	21.93	24.63	30.64
T_p	22.74	25.45	32.26	22.55	25.26	32.11	22.90	26.52	32.79
°, percent	2.4	4.3	7.4	2.2	3.3	8.2	2.0	3.9	4.4
				Ra = 11.5×10^6, $\Delta t = 49.07$°C					
T_e	21.53	23.33	28.56	21.42	23.60	28.30	21.91	24.56	30.71
T_p	22.60	25.38	32.14	22.41	25.23	32.08	22.83	26.43	33.08
δ, percent	2.2	4.1	7.3	2.0	3.3	7.7	1.9	3.8	4.8
				Ra = 49.0×10^6, $\Delta T = 71.21$°C					
T_e	21.84	24.88	33.35	22.14	25.54	33.60	22.63	27.64	36.06
T_p	24.01	27.63	36.99	23.82	27.69	37.23	24.26	28.53	40.46
δ, percent	3.0	3.9	5.1	2.4	3.0	5.1	2.3	1.3	6.2

Numerical Modeling

The following assumptions are adopted in the numerical analysis:

1 The fluid in the enclosure is of Boussinesq type;
2 the fluid flow and heat transfer are laminar and at steady state;
3 the dissipation term in energy equation is neglected.

Using the definitions given in the nomenclature, we may obtain the following dimensionless governing equations:

$$\frac{\partial U}{\partial F} + U\frac{\partial U}{\partial X} + V\frac{\partial U}{\partial Y} + W\frac{\partial U}{\partial Z} = -\frac{\partial P}{\partial X} + \frac{\mathrm{Pr}}{(\mathrm{Ra\ Pr})^{1/2}}\left(\frac{\partial^2 U}{\partial X^2} + \frac{\partial^2 U}{\partial Y^2} + \frac{\partial^2 U}{\partial Z^2}\right) \quad (8)$$

$$\frac{\partial V}{\partial F} + U\frac{\partial V}{\partial X} + V\frac{\partial V}{\partial Y} + W\frac{\partial V}{\partial Z} = -\frac{\partial P}{\partial Y} + \frac{\mathrm{Pr}}{(\mathrm{Ra\ Pr})^{1/2}}\left(\frac{\partial^2 V}{\partial X^2} + \frac{\partial^2 V}{\partial Y^2} + \frac{\partial^2 V}{\partial Z^2}\right) + \Theta \quad (9)$$

$$\frac{\partial W}{\partial F} + U\frac{\partial W}{\partial X} + V\frac{\partial W}{\partial Y} + W\frac{\partial W}{\partial Z} = -\frac{\partial P}{\partial Z} + \frac{\mathrm{Pr}}{(\mathrm{Ra\ Pr})^{1/2}}\left(\frac{\partial^2 W}{\partial X^2} + \frac{\partial^2 W}{\partial Y^2} + \frac{\partial^2 W}{\partial Z^2}\right) \quad (10)$$

$$\frac{\partial \Theta}{\partial F} + U\frac{\partial \Theta}{\partial X} + V\frac{\partial \Theta}{\partial Y} + W\frac{\partial \Theta}{\partial Z} = \frac{K_r}{(\mathrm{Ra\ Pr})^{1/2}}\left(\frac{\partial^2 \Theta}{\partial X^2} + \frac{\partial^2 \Theta}{\partial Y^2} + \frac{\partial^2 \Theta}{\partial Z^2}\right) \quad (11)$$

$$\frac{\partial U}{\partial X} + \frac{\partial V}{\partial Y} + \frac{\partial W}{\partial Z} = 0 \quad (12)$$

The initial fields used in the computation are

$$F = 0, \quad U = V = W = P = \Theta = 0.0 \qquad (13)$$

The computation domain is half of the enclosure. The boundary conditions are as follows:

$$X = 0, \quad U = V = W = \Theta = 0.0$$

$$X = 1.8, \quad U = V = W = \Theta = 0.0$$

$$Y = 0, \quad U = V = W = \Theta = 0.0$$

$$Y = 1.8, \quad U = V = W = \Theta = 0.0$$

$$Z = 0, \quad U = V = W = \Theta = 0.0$$

$$Z = 0.909, \quad \partial U/\partial Z = \partial V/\partial Z = \partial \Theta/\partial Z = 0.0, \quad W = 0.0. \qquad (14)$$

In addition, the conditions of $U = V = W = 0.0$ and $\Theta = 1$ are required for the isolated plate.

The governing equations were discretized by the finite volume approach (Patankar, 1980). The power law was used to discretize the convection–diffusion term. The SIMPLE algorithm was adopted. The resulting algebraic equations were solved by the successive line underrelaxation method (SLUR). Special attention was paid to the treatment of the isolated region. The details of the numerical technique may be found in Yang (1991) and Yang and Tao (1992).

A nonuniform grid system was used. The grid point layout was carefully tailored to accommodate the relatively steep gradients adjacent to the surfaces of the vertical plate. Preliminary computations were performed in two grid systems for Ra = 6.57×10^5: $42 \times 42 \times 22$ and $26 \times 29 \times 15$ (in X–Y–Z). The plate average Nusselt number changes from 19.00 (with $26 \times 29 \times 15$) to 18.78 (with $42 \times 42 \times 22$). Since this difference is not large, the grid system of $26 \times 29 \times 15$ was adopted for all computations to save computation time. Two convergence criteria were used for terminating the iteration: The absolute maximum residual of mass flow rate of all the control volume was less than 10^{-7}, and the absolute maximum relative change of any dependent variable for all the grid points in two successive iterations was less than 10^{-5}. It usually took 600–800 iterations to reach convergence.

Numerical Results and Discussion

Overall Heat Transfer Results. The predicted average Nusselt number at different Rayleigh numbers are shown in Fig. 4 by solid triangles. It can be seen that the agreement between the predicted and tested data is reasonably good. The largest deviation is 12.3 percent. For most cases, the predicted Nusselt number is a bit higher than the test data. This may be partly attributed to the grid network system adopted in the computation. It is expected that if a finer grid system is used the agreement will be improved.

Air Temperature. The numerically predicted air temperatures in the symmetric plane ($Z = 0.909$) are listed in Table 1 for different Rayleigh number cases. Also included are the test data measured by the thermocouples, which are the averaged values of three successive readings within 6–8 minutes with a maximum deviation between different readings of 0.1°C. It can be seen that all 72 data points have a relative temperature deviation (δ) less than 9.4 percent, therefore, the agreement should be considered satisfactory.

Velocity Fields. The main features of the flow fields will be described via velocity vectors for Ra = 6.57×10^5. For the sake of brevity, only the velocity vectors in selected X–Y planes

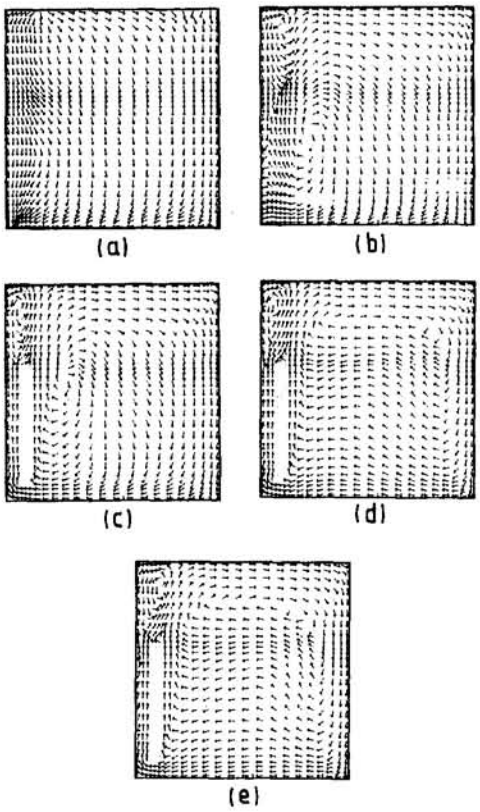

Fig. 5 *U–V* velocity vectors: (*a*) $K = 2$ ($Z = 0.0182$), (*b*) $K = 4$ ($Z = 0.118$), (*c*) $K = 6$ ($Z = 0.200$), (*d*) $K = 11$ ($Z = 0.554$), (*e*) $K = 15$ ($Z = 0.909$)

are presented. Figure 5 shows the U–V vectors in X–Y planes (Z = const). For the plane $K = 2$, which is close to the side wall of the enclosure, the fluid motion is mainly limited to the narrow region adjacent to the sidewall. In this X–Y plane, the air flows from the top surface to the bottom, and then moves to the left corner and leaves the plane via the three-dimensional effect (velocity W). The fluid flow gradually becomes strong as the X–Y plane approaches the heated plate. This can be seen from the velocity vectors in the plane $K = 4$ (Fig. 5*b*). This plane is just near the one end of the heated plate. It can be observed that there is a circulation in this plane whose center region is the projected area of the heated plate. When the selected plane crosses the heated plate, the flow pattern in the X–Y plane is significantly different from that discussed above. The velocity vectors in the plane $K = 6$ give a representative pattern (Fig. 5*c*). It may be observed that here two vortices are formed, one in the left upper corner, and the other at the right hand of the heated plate. The fluid flow at the right hand of the plate becomes stronger when the X–Y plane approaches the symmetry plane. This is characterized by the parallel running velocity vectors in the core region of the vortex (Fig. 5*d*). For the other X–Y planes ($K = 11$–15), the flow patterns are mainly the same with some minor changes in the core regions of the two vortices. Figure 5(*e*) shows the velocity vectors of the symmetry plane. It is interesting to note that for the planes $K = 11$ to $K = 15$, the flow pattern in each plane is quite similar to that of a two-dimensional result (Wang et al., 1994) whose dimensions are close to the symmetry plane of this study.

The three-dimensional nature of the flow becomes evident in the region around the ends of the heated plate. This can be seen clearly from the distributions of W component in Z direction. The W velocity distributions in four X–Y planes are shown in Fig. 6 for $K = 2$, 4, 6, and 11. The three-dimensional effect is quite strong in the planes $K = 4$ and 6, where the maximum

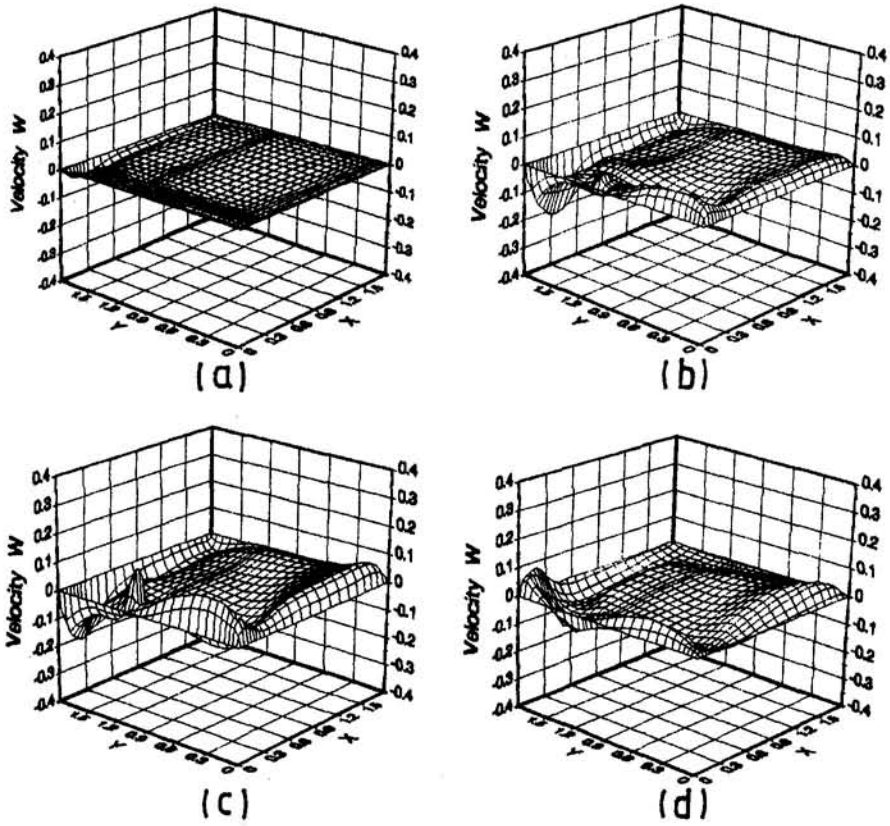

Fig. 6 *W* velocity distributions: (*a*) $K = 2$, (*b*) $K = 4$, (*c*) $K = 6$, (*d*) $K = 11$

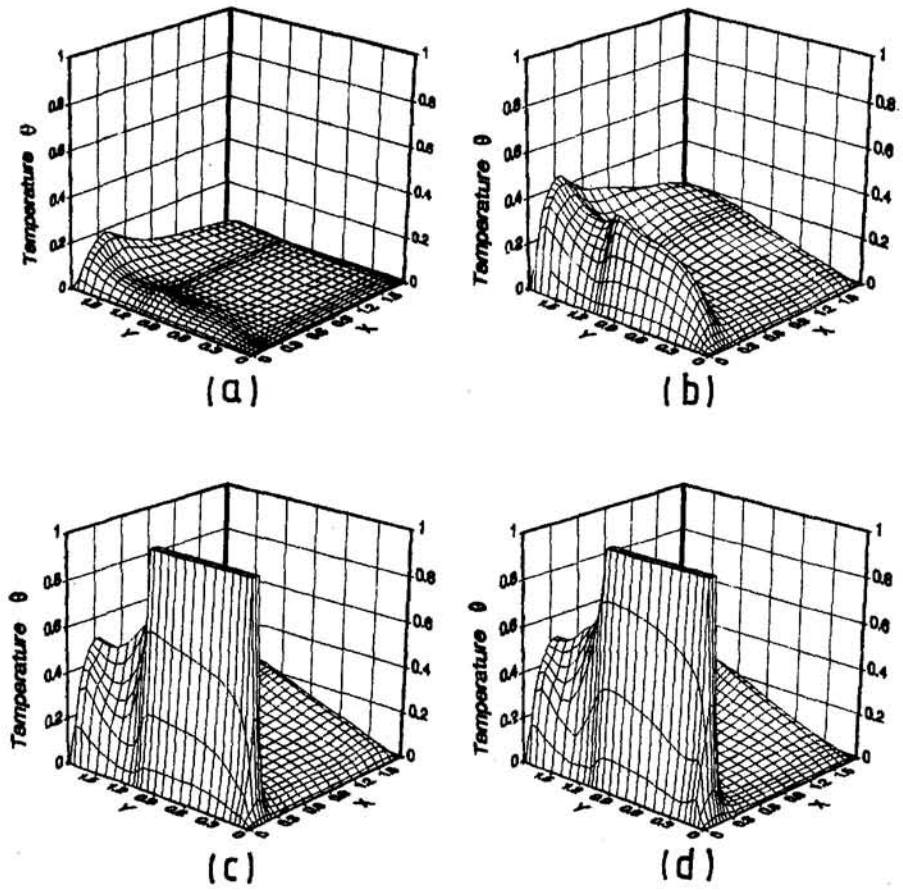

Fig. 7 Temperature distributions: (*a*) $K = 2$, (*b*) $K = 4$, (*c*) $K = 6$, (*d*) $K = 11$

dimensionless W velocity may be as large as 0.2. It can also be noticed that near the top of the enclosure the values of W are negative, while near the enclosure bottom the values are positive. This is an indication of the overall flow pattern in the enclosure: Air is heated near the vertical plate and moves up to the top surface. There it is cooled and flows to the side walls. Then it falls down along the side walls, being cooled further. When approaching the bottom it turns around and moves along the bottom cold surface towards the heating plate. Thus a complete circulation is formed.

Temperature Fields. The temperature distribution is presented via three-dimensional pictures in selected $X-Y$ planes for the case of $Ra = 6.57 \times 10^5$. Figure 7 shows the distributions in four $X-Y$ planes. The temperature distributions conform to the velocity fields discussed earlier. When the heating plate is approached, the air temperature in the same $X-Y$ plane becomes less uniform and the local temperature gradient becomes larger. Once the $X-Y$ plane crosses the vertical plate, the temperature distribution pattern basically remains the same, and this can be seen from Figs. 7(c) and 7(d). There is a very strong temperature gradient in the region around the heating plate.

Concluding Remarks

Natural convection in a cubic enclosure with an internal isolated vertical plate has been investigated both experimentally and numerically. In the low Rayleigh number region, the plate average Nusselt number is quite close to that of a vertical plate situated in infinite space. The difference between the average Nusselt numbers of a vertical plate in a confined space and in infinite space gradually becomes large with increasing Rayleigh number. Numerically predicted Nusselt number and air temperature agree with the test data quite well. It is revealed that the three-dimensional effect (i.e., the flow in the direction of the Z coordinate) is quite significant in the region around the ends of the vertical plate, while for the plane normal to the plate and near the symmetry plane, the flow pattern is quite similar to that of a two-dimensional result.

Acknowledgments

This work was initially supported by the Special Research Foundation for Doctorate Financed by the National Education Committee of China. Near the end of the work, it was also supported by the National Natural Science Foundation of China.

References

Adlam, J. H., 1986, "Computation of Two Dimensional Time Dependent Natural Convection in a Cavity Where There Are Internal Bodies," *Computers & Fluids,* Vol. 14, pp. 141–149.

Bajorek, S. M., and Lloyd, J. R., 1982, "Experimental Investigation of Natural Convection in Partitioned Enclosures," ASME JOURNAL OF HEAT TRANSFER, Vol. 104, pp. 527–532.

Bilski, S. M., Lloyd, J. R., and Yang, K. T., 1986, "An Experimental Investigation of the Laminar Natural Convection Velocity Field in Square and Partitioned Enclosures," *Proceedings, 8th International Heat Transfer Conference,* Hemisphere Publishing Corp., Washington, DC, pp. 1513–1518.

Bohn, M. S., Kirkpatrick, A. T., and Olson, D. A., 1984, "Experimental Study of Three-Dimensional Natural Convection of High-Rayleigh Numbers," ASME JOURNAL OF HEAT TRANSFER, Vol. 106, pp. 339–345.

Chang, L. C., Lloyd, J. R., and Yang, K. T., 1982, "A Finite Difference Study of Natural Convection in Complex Enclosures," *Proceedings, 7th International Heat Transfer Conference,* Hemisphere Publishing Corp., Washington, DC, pp. 183–188.

Churchill, S. W., and Chu, H. H. S., 1975, "Correlating Equations for Laminar and Turbulent Free Convection From a Vertical Plate," *International Journal of Heat and Mass Transfer,* Vol. 18, pp. 1323–1329.

Eckert, E. R. G., and Drake, R. M., Jr., 1972, *Analysis of Heat and Mass Transfer,* McGraw Hill, New York.

Esteki, M. H., Reizes, J. A., and Behnia, M., 1993, *Natural Convection Heat Transfer From Electronic Components Located in an Enclosure, Transport Phenomena in Thermal Engineering,* J. S. Lee et al., eds., Begell House, Inc., New York, Vol. 2, pp. 1157–1162.

Jelti, R., Acharya, S., and Zimmerman, E., 1986, "Influence of Baffle Location on Natural Convection in a Partially Divided Enclosure," *Numerical Heat Transfer,* Vol. 10, pp. 521–536.

Karki, K. C., Sathyamurthy, P. S., and Patankar, S. V., 1992, "Natural Convection in a Partitioned Cubic Enclosure," ASME JOURNAL OF HEAT TRANSFER, Vol. 114, pp. 410–417.

Kline, S. J., and McClintock, F. A., 1953, "Describing Uncertainties in Single Sample Experiments," *Mechanical Engineering,* Vol. 75, Jan., pp. 3–8.

Nansteel, M. W., and Grief, R., 1981, "Natural Convection in Undivided and Partially Divided Rectangular Enclosures," ASME JOURNAL OF HEAT TRANSFER, Vol. 103, pp. 623–629.

Ozoe, H., Yamamoto, K., Churchill, S. W., and Sayama, H., 1976, "Three Dimensional Numerical Analysis of Laminar Natural Convection in a Confined Fluid Heated From Below," ASME JOURNAL OF HEAT TRANSFER, Vol. 98, pp. 202–207.

Ozoe, H., Mouri, A., Hiramitus, M., Churchill, S. W., and Lior, N., 1986, "Numerical Calculation of Three Dimensional Turbulent Natural Convection in a Cubical Enclosure Using a Two-Equation Model for Turbulence," ASME JOURNAL OF HEAT TRANSFER, Vol. 108, pp. 806–813.

Patankar, S. V., 1980, *Numerical Heat Transfer and Fluid Flow,* Hemisphere, Washington, DC.

Sathe, S. B., and Joshi, Y., 1992, "Natural Convection Liquid Cooling of a Substrate-Mounted Protrusion in a Square Enclosure: A Parametric Study," ASME JOURNAL OF HEAT TRANSFER, Vol. 114, pp. 401–409.

Sparrow, E. M., and Charmchi, M., 1983, "Natural Convection Experiments in an Enclosure Between Eccentric and Concentric Vertical Cylinders of Different Height and Diameter," *International Journal of Heat and Mass Transfer,* Vol. 26, pp. 133–143.

Wang, Q. W., Yang, M., and Tao, W. Q., 1994, "Natural Convection in a Square Enclosure With an Internal Isolated Vertical Plate," *Wärme- und Stoffübertragung,* Vol. 29, pp. 161–169.

Warrington, R. O., Jr., and Crupper, G., Jr., 1981, "Natural Convection Heat Transfer Between Cylindrical Tube Bundles and a Cubical Enclosure," ASME JOURNAL OF HEAT TRANSFER, Vol. 103, pp. 103–107.

Yang, K. T., 1988, "Transitions and Bifurcations in Laminar Bouyant Flow in Confined Enclosure," ASME JOURNAL OF HEAT TRANSFER, Vol. 110, pp. 1191–1204.

Yang, M., 1991, "Natural Convection in Enclosure With Internal Isolated Bodies," Ph.D. Thesis, Department of Power Machinery Engineering, Xi'an Jiaotong University, People's Republic of China.

Yang, M., and Tao, W. Q., 1992, "A Numerical Study of Natural Convection Heat Transfer in a Cylindrical Envelope With Internal Concentric Slotted Hollow Cylinder," *Numerical Heat Transfer,* Vol. 22, Part A, pp. 289–306.

Yang, M., Tao, W. Q., Wang, Q. W., and Lue, S. S., 1993, "On Identical Problems of Natural Convection in Enclosures and Applications of the Identical Character," *Journal of Thermal Science,* Vol. 2, pp. 105–113.

Zhang, H. L., Wu, Q. J., and Tao, W. Q., 1991, "Experimental Study of Natural Convection Heat Transfer Between Cylindrical Envelope and Internal Concentric Heated Octagonal Cylinders With or Without Slots," ASME JOURNAL OF HEAT TRANSFER, Vol. 113, pp. 116–122.

The First Instability Mechanism in Differentially Heated Cavities With Conducting Horizontal Walls

R. J. A. Janssen
Department of Applied Physics,
Delft University of Technology,
P.O. Box 5046,
2600 GA Delft, The Netherlands

R. A. W. M. Henkes
Research Fellow,
Department of Aerospace Engineering,
Delft University of Technology,
P.O. Box 5058, 2600 GB,
Delft, The Netherlands

A classical configuration in thermal engineering is the rectangular cavity that is differentially heated over two opposing vertical walls. In this paper, the instability mechanism responsible for the transition from steady to time-periodic flow in both two and three-dimensional cavities with perfectly conducting horizontal walls is studied. For both air ($Pr = 0.71$) and water ($Pr = 7.0$), the instability is a thermal instability resulting from an unstable stratification in the boundary layers along the horizontal cavity walls. The frequency is in good agreement with the frequency predicted using Howard's model (1966). For air, the perturbations arise at fixed depths in the cavity whereas for water they travel along the hot and cold walls of the cavity.

1 Introduction

The study of natural-convection flows in rectangular enclosures that are differentially heated over two opposing vertical sides has received much attention in the past decades both experimentally and numerically. A considerable part of this effort has been directed toward the transition from laminar to turbulent in these flows. Often, the beginning of the transition to turbulence in these cavity flows is characterized by the occurrence of separate instabilities in the flow, each of which is identified by the appearance of a discrete frequency in the flow. For air-filled, differentially heated cavities with adiabatic horizontal walls, the results of Le Quéré and Alziary de Roquefort (1985) and Janssen and Henkes (1995) clearly show that the first instability occurred in the flow divergence arising in the flow after the vertical boundary layers have been turned horizontal and that it was a shear-driven Kelvin–Helmholtz instability.

For differentially heated cavities with *conducting* horizontal walls, the first instability has also been studied. Winters (1987), who performed a linear stability analysis of the steady flow of air in the square cavity, calculated the critical Rayleigh number to be 2.1092×10^6, which is in good agreement with the value of 2.10×10^6 calculated by Henkes (1990) and with the results of Le Quéré and Alziary de Roquefort (1985) and Jones and Briggs (1989). These results were all for a two-dimensional cavity filled with air. Janssen et al. (1993) calculated the transition to time-periodic flow inside an air-filled three-dimensional, rectangular cavity with conducting horizontal walls. Their results suggest that the instability mechanism is the same in the two and three-dimensional configuration. The three dimensionality of the configuration manifests itself in a wavelike modulation of the amplitude distribution of the oscillations.

Le Quéré and Alziary de Roquefort (1986) interpreted the first instability in the two-dimensional cavity with conducting horizontal walls as originating in the boundary layers along the horizontal walls of the cavity and assumed, rather speculatively, that it was a thermal instability. This is in marked contrast to the explanation proposed by Winters (1987), who suggested a resonance mechanism between Tollmien–Schlichting waves in the vertical boundary layers and internal gravity waves in the stratified core region of the cavity.

The present study investigates the physical nature of the instability mechanism responsible for the transition to unsteadiness in air-filled, differentially heated cavities with conducting horizontal walls. It is found that the oscillations are caused by a thermal instability occurring due to the unstable stratification in the boundary layers along the horizontal walls in agreement with the original suggestion of Le Quéré and Alziary de Roquefort (1986). Evidence for this conjecture is provided by (*i*) the results of flow visualization, (*ii*) the fact that the oscillations are directly buoyancy-driven, and (*iii*) the good agreement between the numerical results calculated for the cavity and predictions made by using a simple phenomenological model proposed by Howard (1966) to explain the generation of buoyant elements ("thermals") in the flow above a heated horizontal plate. Also results for water ($Pr = 7$) are presented. Similarities and discrepancies between the results for the two Prandtl numbers are discussed.

2 Mathematical Description

2.1 Flow Equations. Considered is a rectangular cavity with height H, width W, and depth D, as depicted in Fig. 1. The left and right vertical walls are both isothermal; the left wall is hot with temperature T_h, and the right wall is cold with temperature T_c. The remaining four walls are taken to be either adiabatic or conducting. The gravitation g acts in the negative x_2 direction. Air is the working fluid.

The flow in the cavity is described by the three-dimensional, unsteady Navier–Stokes equations. Under the Boussinesq approximation, these equations read:

$$\frac{\partial u_j}{\partial x_j} = 0 \tag{1}$$

$$\frac{\partial u_i}{\partial t} + \frac{\partial u_i u_j}{\partial x_j} = -\frac{1}{\rho}\frac{\partial p}{\partial x_i} + g\beta(T - T_0)\delta_{i2} + \nu\frac{\partial^2 u_i}{\partial x_j^2} \tag{2}$$

$$\frac{\partial T}{\partial t} + \frac{\partial u_j T}{\partial x_j} = a\frac{\partial^2 T}{\partial x_j^2}. \tag{3}$$

Here, the summation convention has been used, i.e., a summation (from 1 to 3) has to be performed over repeated indices

Contributed by the Heat Transfer Division for publication in the JOURNAL OF HEAT TRANSFER. Manuscript received by the Heat Transfer Division June 1994; revision received October 1994. Keywords: Enclosure Flows, Flow Instability, Natural Convection. Associate Technical Editor: J. R. Lloyd.

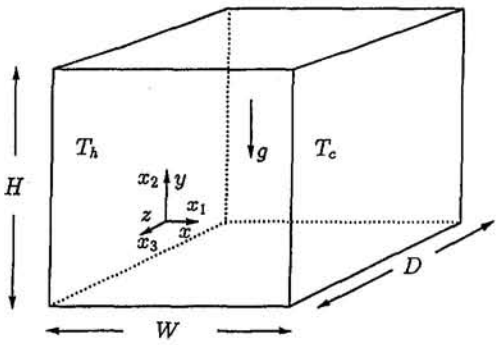

Fig. 1 Geometry under investigation

in every term. In Eqs. (1)–(3), u_i denotes the velocity component in the x_i direction, t denotes time, ρ is the (constant) density, p is the pressure, β is the coefficient of thermal expansion, T is the temperature, T_0 is a reference temperature, δ is the Kronecker delta, ν is the kinematic viscosity, and a the thermal diffusivity.

To fully specify the mathematical problem, boundary conditions have to be given. For the velocities, the no-slip condition at all walls is taken:

$$u_1 = u_2 = u_3 = 0 \text{ at } x_1 = 0, W; x_2 = 0, H; x_3 = 0, D. \quad (4)$$

For the temperature, different boundary conditions apply at the various walls. The left and right vertical walls are *always* isothermal:

$$T = T_h \quad \text{at} \quad x_1 = 0 \quad (5)$$

$$T = T_c \quad \text{at} \quad x_1 = W. \quad (6)$$

The top/bottom horizontal ($x_2 = 0, H$) walls are taken to be perfectly conducting:

$$T = T_h - (x_1/W)(T_h - T_c) \quad \text{at} \quad x_2 = 0, H. \quad (7)$$

The lateral, vertical walls ($x_3 = 0, D$) are taken to be adiabatic:

$$\frac{\partial T}{\partial x_3} = 0 \quad \text{at} \quad x_3 = 0, D. \quad (8)$$

The set of Eqs. (1)–(3) can be made dimensionless using the length scale H, the time scale $H/(g\beta\Delta TH)^{1/2}$, the temperature scale $T_0 = (T_h + T_c)/2$, and the temperature difference $\Delta T = T_h - T_c$. This leads to a set of nondimensionalized equations, which are governed by only two characteristic numbers: the Rayleigh number $\mathrm{Ra} \equiv g\beta\Delta TH^3/(\nu a)$ and the Prandtl number $\mathrm{Pr} \equiv \nu/a$. For air, $\mathrm{Pr} = 0.71$. Substituting these same scales in the boundary conditions, Eqs. (4)–(8), shows that there are two additional parameters, apart from the Rayleigh and Prandtl number, on which the flow depends. These are the aspect ratios of the cavity:

$$A_x \equiv H/W, \quad A_z \equiv D/H \quad (9)$$

and they are of a purely geometric nature. The transition is studied by performing calculations for increasing values of the Rayleigh number using a fixed set of values for the Prandtl number and aspect ratios. The influence of the latter parameters may then be studied by performing subsequent calculations (again for increasing Rayleigh numbers) with different values for the Prandtl numbers and/or aspect ratios.

The governing Eqs. (1)–(3) allow *two* spatial symmetries. First, the solution can be symmetric around the line ($W/2$, $H/2$, x_3):

$$\begin{aligned} u_1(x_1, x_2, x_3, t) &= -u_1(W - x_1, H - x_2, x_3, t) \\ u_2(x_1, x_2, x_3, t) &= -u_2(W - x_1, H - x_2, x_3, t) \\ u_3(x_1, x_2, x_3, t) &= u_3(W - x_1, H - x_2, x_3, t) \\ T(x_1, x_2, x_3, t) &= (T_h + T_c) - T(W - x_1, H - x_2, x_3, t) \\ p(x_1, x_2, x_3, t) &= p(W - x_1, H - x_2, x_3, t), \end{aligned} \quad (10)$$

(see also Fig. 1). Second, it can be symmetric in the plane $x_3 = D/2$:

$$\begin{aligned} u_1(x_1, x_2, x_3, t) &= u_1(x_1, x_2, D - x_3, t) \\ u_2(x_1, x_2, x_3, t) &= u_2(x_1, x_2, D - x_3, t) \\ u_3(x_1, x_2, x_3, t) &= -u_3(x_1, x_2, D - x_3, t) \\ T(x_1, x_2, x_3, t) &= T(x_1, x_2, D - x_3, t) \\ p(x_1, x_2, x_3, t) &= p(x_1, x_2, D - x_3, t). \end{aligned} \quad (11)$$

The boundary conditions, Eqs. (4)–(8), admit the same two symmetries. Janssen et al. (1993) found that these two symmetries were maintained in the flow after the bifurcation to unsteady flow. Consequently, in all calculations performed in this study, the symmetries given by Eqs. (10) and (11) were employed to reduce the computational effort required to solve the Navier–Stokes equations (1)–(3).

For ease of notation, in the following x_1, x_2, and x_3 will be denoted as x, y, and z, respectively, and u_1, u_2, and u_3 will be denoted as u, v, and w, respectively.

Nomenclature

a = thermal diffusivity
A_x = height over width aspect ratio = H/W
A_z = depth over height aspect ratio = D/H
D = depth of cavity
f = frequency
g = acceleration of gravity
H = height of cavity
$i_{\max}$ = number of grid points in x_1 direction
p = pressure
Pr = Prandtl number = ν/a
q_* = dimensionless height = $y/2(at_*)^{1/2}$ (Eq. (16))
Ra = Rayleigh number = $g\beta\Delta TH^3/(\nu a)$
t = time
t_* = averaging time in Eq. (16)
T = temperature
T_0 = reference temperature
u = velocity component
u_i = velocity component ($i = 1, 2, 3$)
v = vertical velocity component
x = coordinate direction between hot and cold walls
x_i = coordinate direction ($i = 1, 2, 3$)
w = velocity component in lateral direction
W = width of cavity
y = vertical coordinate direction
z = lateral coordinate direction
β = coefficient of thermal expansion
δ_{ij} = Kronecker delta
Δ = difference
λ_z = wavelength in x_3 ($= z$) direction
ν = kinematic viscosity
ρ = density
ϕ = generic variable

Subscripts

bl = related to horizontal boundary layers
c = quantity related to cold vertical wall
h = quantity related to hot vertical wall

2.2 Energy Balance. In principle, the Navier–Stokes equations, as presented in the previous section, completely describe the mathematical problem. It is, however, instructive to consider the kinetic energy for which the conservation equation can be derived from the Navier–Stokes equations. To derive the equation describing the conservation of *fluctuating* kinetic energy, first the Reynolds decomposition into a mean and a fluctuating quantity is performed. For a scalar variable $\phi(x_i, t)$, this means:

$$\phi(x_i, t) = \bar{\phi}(x_i) + \phi'(x_i, t) \quad \text{with}$$

$$\bar{\phi}(x_i) = \lim_{t_{av}\to\infty} \frac{1}{t_{av}} \int_{-t_{av}/2}^{t_{av}/2} \phi(x_i, t)dt. \quad (12)$$

The equation describing the conservation of fluctuating kinetic energy, $u_i' u_i'/2$, can be derived from the momentum equation (Eq. (2)) in the Navier–Stokes equations. First, the momentum equation is multiplied by u_i, after which the decomposition is introduced in the resulting equation. From this equation, the original momentum equation multiplied by $\bar{u}_i$ is subtracted. This results in an equation describing the conservation of fluctuating kinetic energy, which reads:

$$\frac{\partial u_i' u_i'/2}{\partial t} = \underbrace{-\frac{\partial}{\partial x_j}\left(u_i' \bar{u}_j \bar{u}_i + u_j u_i' u_i'/2 + u_j' p/\rho + \nu u_i' \frac{\partial u_i}{\partial x_j}\right)}_{\text{I}}$$

$$\underbrace{+ \bar{u}_i \bar{u}_j \frac{\partial u_i'}{\partial x_j} - \nu \frac{\partial \bar{u}_i}{\partial x_j}\frac{\partial u_i'}{\partial x_j} + g\beta u_i'(\bar{T} - T_0)\delta_{i2}}_{\text{II}}$$

$$\underbrace{- u_i' u_j' \frac{\partial \bar{u}_i}{\partial x_j} - \nu\left(\frac{\partial u_i'}{\partial x_j}\right)^2 + g\beta u_i' T' \delta_{i2}}_{\text{III}}. \quad (13)$$

Here, the first group of terms on the righthand side (denoted by I) is a divergence. Integrating Eq. (13) over the entire cavity, employing Gauss' divergence theorem and the fact that all fluctuating velocity components at all cavity walls are zero, shows that the terms in group I do not contribute to the total fluctuating kinetic energy. This group can be interpreted as representing transport of fluctuating kinetic energy. The second group, denoted by II, contains terms that are all *linear* in the fluctuating velocity components. Reynolds-averaging of Eq. (13) would make the terms in this group zero (for a periodic oscillation in the flow, taking an average over one period of the oscillation suffices to make the terms in group II equal to zero). Group III contains terms that neither by integration in space nor by integration in time can be made equal to zero. These terms describe production and dissipation of fluctuating kinetic energy. The term $-u_i' u_j' \partial \bar{u}_i/\partial x_j$ describes the production of fluctuating kinetic energy by the shear of the mean flow, $g\beta u_i' T' \delta_{i2}$ describes the production of fluctuating kinetic energy by buoyancy forces, and $-\nu(\partial u_i'/\partial x_j)^2$ describes the viscous dissipation of fluctuating kinetic energy.

3 Numerical Treatment

Equations (1)–(3) are discretized by the finite-volume method, employing a staggered grid. The integration in time is performed fully implicitly: All spatial derivatives are evaluated at the new time level. The unsteady term, the fluxes through the sides of the finite volumes, and the source are further discretized with finite differences. The unsteady term is discretized with three time levels, giving a second-order truncation error in time. Both the diffusion as well as the convection part of the fluxes are discretized using standard, second-order accurate, central differences.

The grid is constructed by first distributing the velocity grid lines according to a stretching function. This distribution is such that the boundaries of the physical domain coincide with velocity grid lines. Second, the scalar points are placed precisely in the center of the scalar volumes. For the u velocities, the stretching function is chosen as:

$$\frac{x_i}{W} = \frac{i}{i_{max}} - \frac{1}{2\pi}\sin\left(2\pi \frac{i}{i_{max}}\right) \quad i = 0, 1, \ldots, i_{max}. \quad (14)$$

A similar function is used in the y and z directions. This distribution concentrates grid points in the boundary layers along the walls.

The discretized equations are solved, using a line Gauss–Seidel method for all variables except for the pressure correction, which is solved using a preconditioned version of the conjugate-gradient method. Details about the solution procedure may be found in Janssen et al. (1993) and in Janssen and Henkes (1993).

Table 1 Grid dependence in the two-dimensional square and three-dimensional cubical cavity for Ra = 2.5×10^6 and Pr = 0.71

Two-dimensional square cavity		Three-dimensional cubical cavity	
Grid	$\frac{fH}{(g\beta\Delta TH)^{1/2}}$	Grid	$\frac{fH}{(g\beta\Delta TH)^{1/2}}$
30^2	0.272	30^3	0.296
60^2	0.247	60^3	0.263
120^2	0.256	120^3	0.266

4 Results

4.1 Accuracy. Winters (1987) and Henkes (1990) calculated the critical Rayleigh number for the transition to unsteady flow in the air-filled square cavity with conducting horizontal walls to be approximately 2.1×10^6. For the cubical cavity, Janssen et al. (1993) found the critical Rayleigh number to be between 2.25×10^6 and 2.35×10^6. To investigate the numerical accuracy of the present results, systematic grid refinement was employed for the flow in both the two-dimensional square and the three-dimensional cubical cavity at a Rayleigh number of 2.5×10^6, just above the critical value. Table 1 gives the grid dependence of the calculated frequency of the oscillation for both configurations. Obviously, approximately 60^3 grid points are necessary in the cubical cavity to calculate the frequency of the oscillation accurately (within ±1 percent). The difference between the present results for the two-dimensional square cavity and those of Le Quéré and Alziary de Roquefort (1986), Winters (1987), and Jones and Briggs (1989) is very small: the largest difference of 2.7 percent is found with the frequency calculated by Jones and Briggs (1989). The agreement between the various, calculated frequencies is thus very good, showing that all numerical studies capture the same physics accurately.

4.2 Instability Mechanism. As the results in Section 4.1 show, there is only a small difference between the values of the frequencies and critical Rayleigh numbers for the two and three-dimensional configurations. This, together with the close similarity between flow visualizations for the two-dimensional

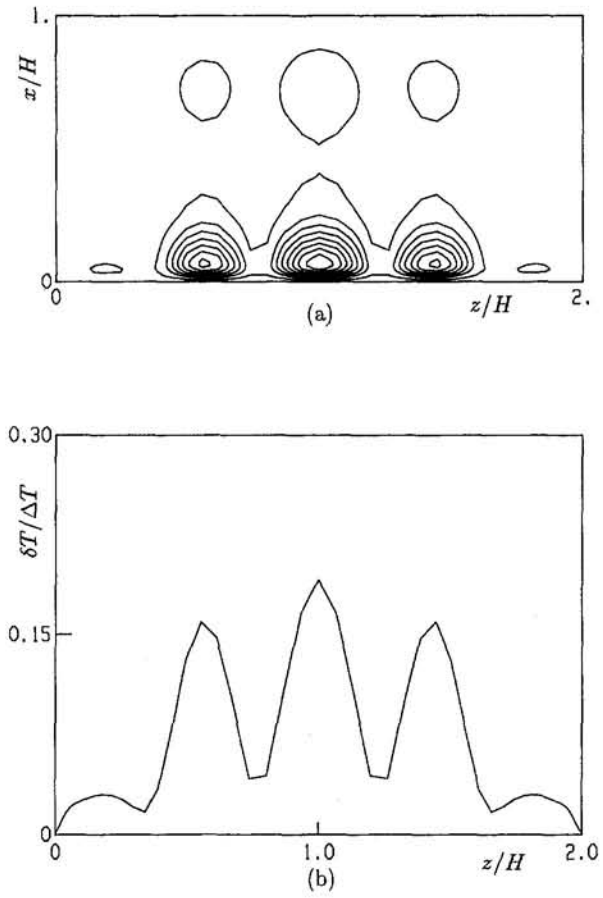

Fig. 2 Amplitudes of the temperature oscillations for $A_z = 2$ at $y/H = 0.1$ and along the line $(x/W, y/H) = (0.048, 0.1)$. Contour lines correspond to 0.2, 0.3, 0.4, 0.5, 0.6, 0.7, 0.8, and 0.9 times the maximum value.

square and the three-dimensional cubical cavity and the result that the flow near the lateral midplane $z = D/2$ of the cubical cavity is mainly two-dimensional, led Janssen et al. (1993) to conclude that the instabilities in both the two and the three-dimensional configurations are caused by the same physical mechanism.

The three dimensionality of the configuration, studied by Janssen et al. (1993), manifested itself in the amplitude distribution of the oscillations. The distribution of the temperature oscillations in the plane $y = H/10$ of the cavity with $A_z = 2$ at $\mathrm{Ra} = 2.5 \times 10^6$ is shown in Fig. 11(a) of Janssen et al. (1993) and reproduced here for convenience in Fig. 2(a). Figure 2(b) shows the distribution along the line $x = 0.048W$ in the plane $y = H/10$ (Fig. 11b of Janssen et al., 1993). These figures show the occurrence of various local maxima in the amplitude distribution at different z positions. The fact that these local maxima in the distribution are approximately equally large, except very near the lateral walls, supports the assumption that the observed modulation is a *wave*like modulation of the fluctuating quantities in the third dimension.

To investigate the instability mechanism responsible for the first instability in the cavities with conducting horizontal walls in more detail, Fig. 3 shows the instantaneous temperature fluctuations (contours) and the velocity fluctuations (vectors) in the lateral midplane $z = D/2$ of the cubical cavity. The fluctuations were calculated by subtracting the time-averaged temperature and velocity values in every grid point from the instantaneous values at four time instants distributed uniformly over one period of the oscillation. Looking at the temperature fluctuations, it is clear that the phenomenology of the oscillations in the flow is characterized by the presence of localized regions ("spots" or "blobs") of locally hot and cold fluid. Figure 3 shows that these hot and cold spots are amplified in the boundary layers along the horizontal walls of the cavity. The contour levels used in the figure (see caption) indicate that there is a considerable amplification; in fact, a close examination of the amplitudes of the temperature oscillations (not shown here) shows that there is an approximately fivefold increase in the amplitude of the oscillations, thus indicating a strong amplification, in the second half of the horizontal boundary layers. The hot and cold spots are subsequently convected with the vertical boundary layers and decrease in strength in the second half of these boundary layers. As can be seen from the time-averaged temperature distribution in the plane $z = D/2$ (shown in the center of Fig. 3), the regions where the hot and cold spots are amplified (i.e., the second half of the horizontal boundary layers) are unstably stratified. The same results were found in the two-dimensional square cavity.

In Fig. 4, the fluctuations in the plane $x = 0.048W$, near the hot cavity wall are shown at the same time instants as in Fig. 3. The combined temperature and velocity fields of the oscillations shown in Fig. 4 suggest that this instability is characterized by the formation of "thermals" in the flow. Thermals are discrete buoyant masses of fluid ascending or descending in an ambient medium due to a difference in density (Gebhart et al., 1988). The velocity fields associated with these thermals (as calculated for instance by Elder, 1968) show a striking similarity with the *fluctuating* velocity fields depicted in Fig. 4: the presence of two vortical structures centered next to the buoyant mass of fluid. As Fig. 3 shows, in the plane $z = D/2$, the velocity fluctuations have a different appearance: a single vortical structure that is not symmetric. This difference is probably caused by the close proximity of the hot and cold spots to the hot and cold walls of the cavity.

If the instability is indeed a thermal instability, it is expected that the fluctuating kinetic energy, $u_i' u_i'/2$, is produced mainly by buoyancy forces, i.e., the instability is directly buoyancy

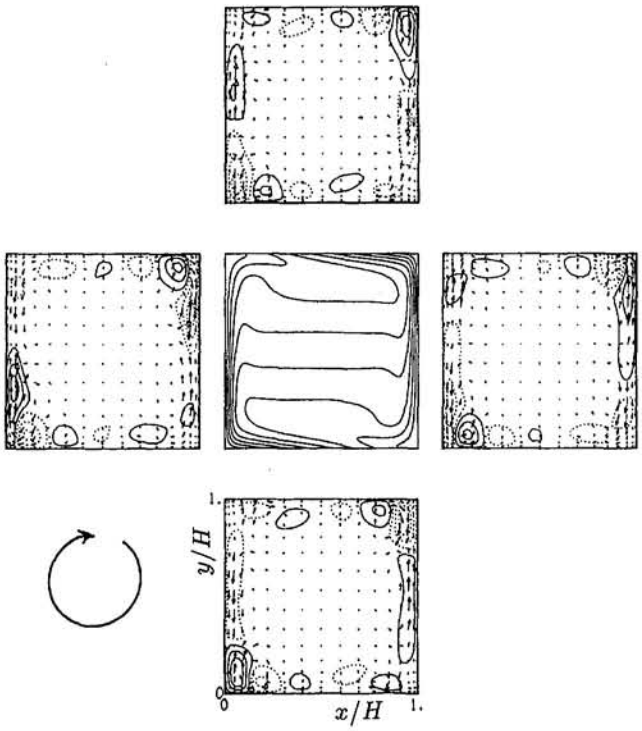

Fig. 3 Temperature and velocity perturbations at $z = D/2$ in the cubical cavity with conducting horizontal walls at four time instants distributed uniformly over one period of the oscillation. $\mathrm{Ra} = 2.5 \times 10^6$ and $\mathrm{Pr} = 0.71$. T' values: ± 0.01, ± 0.04, and $\pm 0.075\Delta T$; dotted contours correspond to negative values. In the center, the time-averaged temperature is shown.

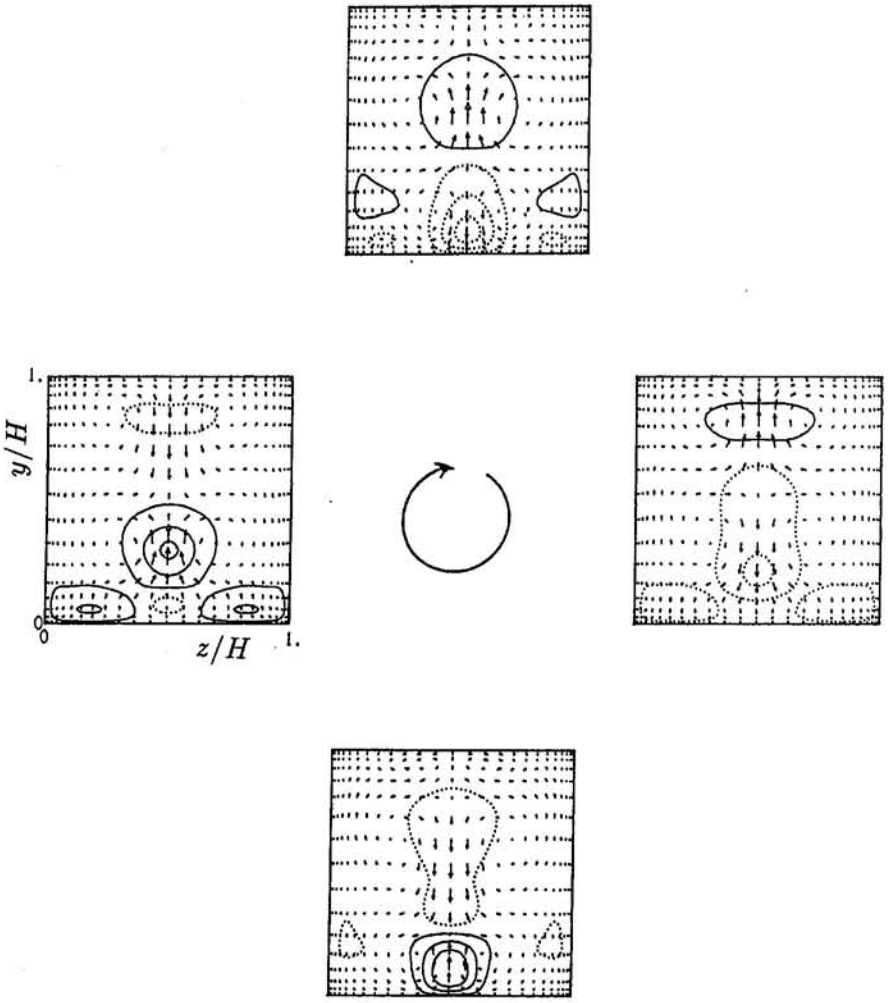

Fig. 4 Combined temperature and velocity perturbations at $x/W = 0.048$. Same time instants and contour levels as in Fig. 3.

driven. In Eq. (13), the buoyancy production term, $g\beta u_i' T' \delta_{i2}$, should be the dominant term. To investigate this point, Eq. (13) is integrated over one period of the oscillation of the two-dimensional flow in the square cavity at Ra = 2.5×10^6 for Pr = 0.71. This calculation showed that approximately 98 percent of the total fluctuating kinetic energy was produced by the buoyancy forces, in agreement with the assumed thermal instability.

Thermals generally arise in *deep* layers of fluid that are heated from below. In analogy to the classical analyses of Rayleigh (1916) and Pellew and Southwell (1940) of Bénard's experiments (1900) regarding the onset of convection in a thin layer of fluid heated from below, Howard (1966) proposed that the diffusive thermal boundary layer in a deep layer of fluid becomes unstable to small perturbations if a critical value of the Rayleigh number Ra_{bl}, based on the temperature difference over the boundary layer and on its height, is reached. In the situation envisaged by Howard (1966), convection occurs because of an instability occurring in the *time-dependent* boundary layer, which is formed through the diffusion of heat into the fluid. This boundary layer is described by the (one-dimensional) unsteady heat-diffusion equation, the solution of which in a semi-infinite domain is given by:

$$T(y, t) = \Delta T_{bl} \operatorname{erfc}\left(\frac{y}{2(at)^{1/2}}\right). \quad (15)$$

Here, ΔT_{bl} denotes the temperature difference across the thermal boundary layer. Because the thermals are convected into the fluid and thus separate from the surface, the boundary layer is disrupted and must be formed again. In this way, a cyclic process results and thus a transition to time-dependent flow, constituting the main phenomenological difference between the thermal instability in a *deep* (Howard, 1966) and in a *thin* (Rayleigh, 1916) layer of fluid.

If it is assumed that the time for the thermal to separate from the surface can be neglected compared to the time for the boundary layer to grow, Eq. (15) provides the possibility to estimate the time-averaged temperature distribution in the thermal boundary layer. Integrating and averaging Eq. (15) from $t = 0$ to $t = t_*$ gives:

$$\bar{T}(q_*) = \Delta T_{bl}\left[(1 + 2q_*^2)\operatorname{erfc}(q_*) - \frac{2}{(\pi)^{1/2}} q_* \exp(-q_*^2)\right], \quad (16)$$

where

$$q_* \equiv \frac{y}{2(at_*)^{1/2}}.$$

Figure 5 shows the time-averaged temperature distribution as a function of height at $x = W/4$ and $z = D/2$ in the unstably stratified boundary layer along the lower wall of the cavity for

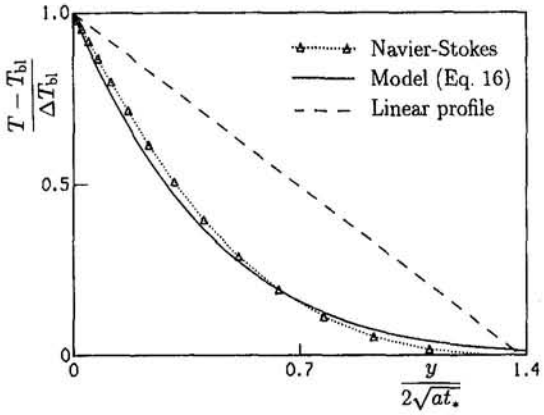

Fig. 5 Time-averaged temperature distribution in the lower boundary layer at (x/W, z/D) = (0.25, 0.5). Cubical cavity, Ra = 2.5×10^6 and Pr = 0.71.

Pr = 0.71. In calculating $q_* \equiv y/2(at_*)^{1/2}$, t_* has been taken equal to the period of the oscillation in the flow and ΔT_{bl} to the temperature difference between the lower wall and the top of the unstably stratified region, which is given by the position where $\partial \bar{T}/\partial y = 0$. Also shown is the distribution according to Eq. (16) and the linear conduction profile that applies in Rayleigh's theoretical analysis of Bénard's experiments (1900). The agreement between the calculated time-averaged temperature distribution in the cavity and Eq. (16) is remarkable in view of the total neglect of all convective transport in deriving Eq. (16). A similar good agreement is obtained at other horizontal locations in the boundary layer at least for $x/W \leq 0.4$.

The linear stability of one-dimensional diffusive thermal boundary layers, both in a finite and a semi-infinite region, has been investigated numerically by Foster (1965, 1968). Foster studied the stability of the temperature distribution given by Eq. (15) by superposing a two-dimensional disturbance on this distribution and by solving the two-dimensional form of the temperature Eq. (3) linearized in the disturbances assuming a single wavenumber horizontal variation of the disturbance. Because of the time dependence of the base temperature distribution (Eq. (15)), no eigenvalue relation could be used. Instead, the linearized disturbance equations had to be integrated in time. Foster's calculations (1965, 1968) show that a minimum critical time is necessary for the solution, described by Eq. (15), to become unstable. During this time, heat is conducted into the quiescent fluid. Sparrow et al. (1970) suggested, rather arbitrarily, that the height of the unstable boundary layer could be estimated as:

$$y_{bl}(t) = 2.77(at)^{1/2}. \tag{17}$$

At this height, $T(y(t))$ is $0.05\Delta T_{bl}$ according to Eq. (15), showing that 95 percent of the temperature difference takes place over the height y_{bl}. Substituting the minimum critical times calculated by Foster (1968) into Eq. (17) shows that these times correspond to critical Rayleigh numbers in the range 2×10^3–5×10^3. These values are of the same order of magnitude as the critical Rayleigh numbers for Rayleigh–Bénard convection in a thin layer of fluid calculated by Rayleigh (1916) and Pellew and Southwell (1940).

Figure 6 shows the local Rayleigh number, $\mathrm{Ra}_{bl}(x)$, of the unstably stratified boundary layer along the lower horizontal wall in the plane $z = D/2$ for Ra = 2.5×10^6 and Pr = 0.71. Here, $\mathrm{Ra}_{bl}(x)$ is given by:

$$\mathrm{Ra}_{bl}(x) = \frac{g\beta\Delta T_{bl}(x) y_{bl}^3(x)}{\nu a}. \tag{18}$$

The temperature difference $\Delta T_{bl}(x)$ is taken as the difference between the temperature of the lower wall and the temperature at $y = y_{bl}(x)$. The height $y_{bl}(x)$ is taken as the position at which $\partial \bar{T}/\partial y = 0$. Figure 6 shows that Ra_{bl} grows for decreasing x toward a maximum value at $x = x_{\mathrm{Ra,max}}$. For smaller values of x, the proximity of the hot cavity wall causes the flow to be turned vertical and Ra_{bl} to decrease to zero. Since it is difficult to determine a precise x location and corresponding critical $\mathrm{Ra}_{bl}(x)$ value at which the perturbations in the flow start to grow significantly, a representative value of Ra_{bl} was estimated by horizontally averaging $\mathrm{Ra}_{bl}(x)$ for $x > x_{\mathrm{Ra,max}}$. Furthermore, ΔT_{bl} was estimated in the same way. Substituting Eq. (17) for the height and ΔT_{bl} for the temperature difference over the thermal boundary layer as representative values in the definition of the Rayleigh number gives Ra_{bl} (Eq. (18)) and solving for $f = 1/t$ results in:

$$\frac{fH}{(g\beta\Delta TH)^{1/2}} = 2.77^2 \left(\frac{\Delta T_{bl}/\Delta T}{\mathrm{Ra}_{bl}}\right)^{2/3} \mathrm{Ra}^{1/6}\mathrm{Pr}^{-1/2}. \tag{19}$$

For air (Pr = 0.71) at Ra = 2.5×10^6, $\mathrm{Ra}_{bl} = 1.9 \times 10^3$ and $\Delta T_{bl} = 0.23\Delta T$, resulting in a dimensionless frequency $fH/(g\beta\Delta TH)^{1/2} = 0.26$, which is very close to the value $fH/(g\beta\Delta TH)^{1/2} = 0.266$ obtained from the numerical integration of the Navier–Stokes equations. Although this agreement is excellent, it is also somewhat fortuitous since it is based on a quite arbitrary estimate of the boundary layer thickness using a 95 percent drop of ΔT_{bl} (Eq. (17)).

Henkes and Le Quéré (1995) investigated the stability of the two-dimensional flow in a square, differentially heated cavity with conducting horizontal walls to three-dimensional disturbances. Periodic boundary conditions were imposed in the z direction. Henkes and Le Quéré (1995) found that the two-dimensional flow was unstable to a three-dimensional disturbance at Ra = 1.8×10^6 with amplified wavelengths λ_z in the range $0.6 < \lambda_z/H < 1.1$. However, they find that a symmetry-breaking bifurcation, in which the spatial line symmetry (Eq. (10)) is broken, has a larger growth rate than the bifurcation which preserves these symmetries (the same range of wavelengths is amplified, however). Furthermore, this symmetry-breaking bifurcation results in a steady flow, whereas the symmetry-preserving bifurcation results in a time-periodic flow with frequency $fH/(g\beta\Delta TH)^{1/2} = 0.27$. The agreement between the results of the present calculations and those concerning the symmetry-preserving bifurcation found by Henkes and Le Quéré (1995) is good, except for the critical Rayleigh number at which the bifurcation takes place. The larger growth rate calculated by Henkes and Le Quéré (1995) for the symmetry-breaking bifurcation may be caused by the periodic boundary conditions in the z direction used in their calculations. In Foster's (1968) linear stability analysis of the diffusive thermal

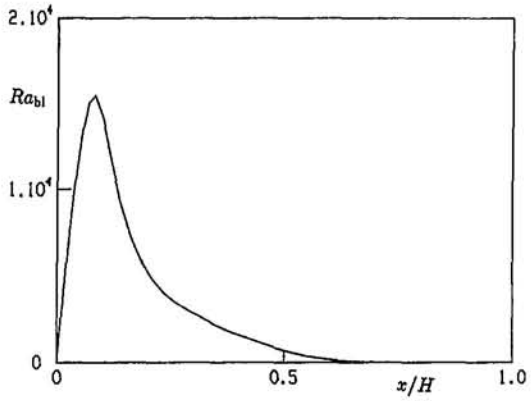

Fig. 6 $\mathrm{Ra}_{bl}(x)$ at $z = D/2$ in the cubical cavity with conducting horizontal walls

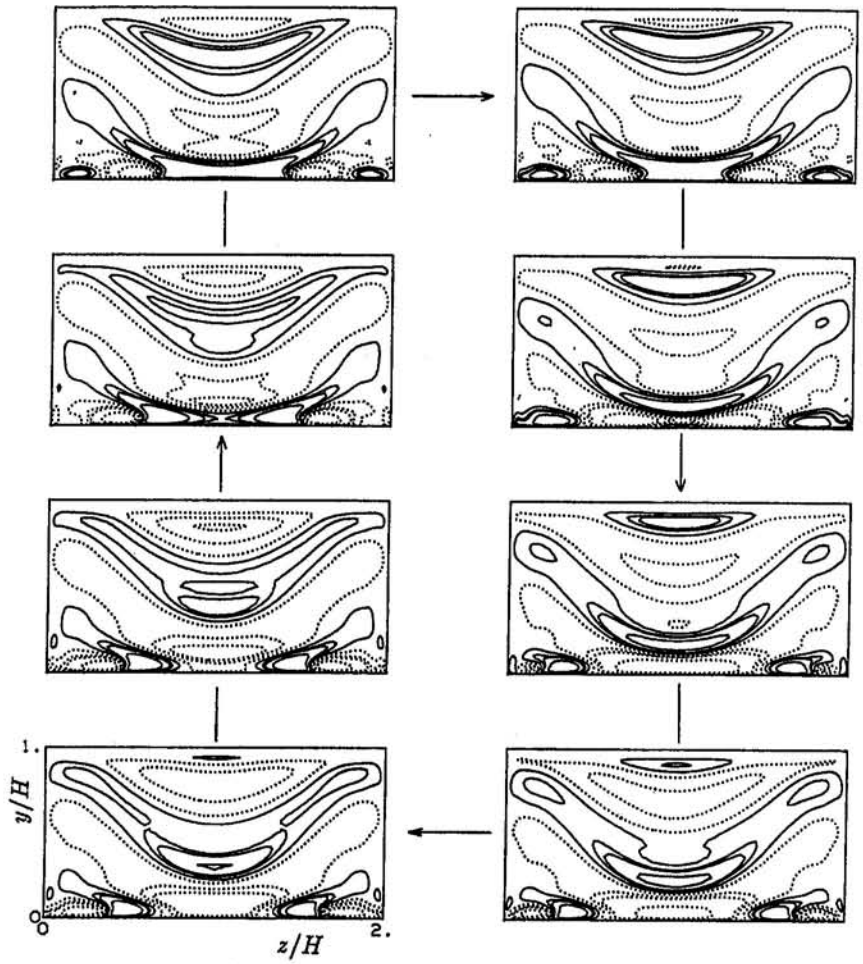

Fig. 7 Temperature perturbations at $x/W = 0.048$ for $A_z = 2$ and Pr = 7.0 T' values: ± 0.015, ± 0.03, ± 0.04, and $\pm 0.075\Delta T$. Dotted contour lines correspond to negative values. The time instants are distributed uniformly over one period of the oscillation.

boundary layer (Eq. (15)), also a rather broad range of wavelengths was amplified. Converting his most amplified dimensionless wavelength to the cavity configuration results in $\lambda_z/H = 0.4$, in reasonable agreement with the wavelengths observed in the present numerical calculations.

For water with Pr = 7.0, the oscillations in the flow show a remarkable difference with those found for Pr = 0.71. Figure 7 shows the hot and cold spots in the plane $x/W = 0.048$ for the cavity with $A_z = 2$ at Ra = 8×10^6. It shows that the perturbations for Pr = 7.0 move parallel to the hot wall in the z direction from the lateral walls toward the midplane $z = D/2$ of the cavity, before being convected upward into the vertical boundary layer. The same physics are found for $A_z = 4$ and $A_z = 8$. This is in marked contrast to the results calculated for Pr = 0.71 and shown in Fig. 4. The distance in the z direction between the hot and cold spots is not constant over the depth of the cavity. For $A_z = 2$, the distance between the hot and cold spot closest to the lateral walls of the cavity varies between $0.20H$ and $0.35H$, resulting in wavelengths of $0.4H$–$0.7H$. For $A_z = 4$ and $A_z = 8$, wavelengths of $0.6H$–$0.8H$ and $0.5H$–$0.6H$ were found, respectively. Foster (1968) also calculated the most-amplified wavelength for the thermal boundary layer given by Eq. (15) for Pr = 7.0. He obtained a most-amplified wavelength $\lambda_z/H = 0.25$.

The origin of this instability for Pr = 7.0 in the three-dimensional configuration, its relation with the instability in the two-dimensional square cavity for Pr = 7.0, and its relation with the instability occurring for Pr = 0.71 is not entirely clear. For the two-dimensional square cavity, $5 \times 10^6 < \mathrm{Ra}_{cr} < 6 \times 10^6$ and $fH/(g\beta\Delta TH)^{1/2} = 0.161$ at Ra = 8×10^6. In three-dimensional calculations using a 80^3 grid in the cubical cavity, $7 \times 10^6 < \mathrm{Ra}_{cr} < 8 \times 10^6$ and $fH/(g\beta\Delta TH)^{1/2} = 0.205$ at Ra = 8×10^6. For $A_z = 2$, 4, and 8, $fH/(g\beta\Delta TH)^{1/2} = 0.195$ at Ra = 8×10^6 and Pr = 7.0. Hence, the difference in the frequency between the two-dimensional and three-dimensional cases is 22–28 percent for Pr = 7.0, whereas it is only 4 percent for Pr = 0.71. Furthermore, the perturbations in the three-dimensional cavity for Pr = 7.0 are seen to originate near the lateral walls of the cavity, which is not the case for Pr = 0.71. For Pr = 7.0 the perturbations are therefore probably influenced by the presence of these lateral cavity walls.

On the other hand, the agreement between the observed wavelengths and the wavelength predicted by Foster (1968) is no worse for Pr = 7.0 than for Pr = 0.71. Furthermore, if the frequency of the oscillation is estimated employing the heat-conduction model and using the calculated time-averaged temperature distribution in the plane $z/D = 0.07$ for $A_z = 2$, where the perturbations are found to originate, a frequency of 0.19 $(g\beta\Delta TH)^{1/2}/H$ is obtained, in very good agreement with the frequency of 0.195 $(g\beta\Delta TH)^{1/2}/H$ derived from the numerical integration of the Navier–Stokes equations. Finally, in planes parallel to the lateral walls of the cavity, the phenomenology of the combined temperature and velocity fluctuations is the same for Pr = 0.71 and Pr = 7.0, as can be seen by comparing Fig. 8 for Pr = 7.0 in the plane $z/D = 0.07$ ($A_z = 2$) with Fig. 3 for Pr = 0.71 in the plane $z/D = 0.5$.

The instabilities found in the present calculations for Pr = 0.71 and 7.0 have characteristics that are similar to those found

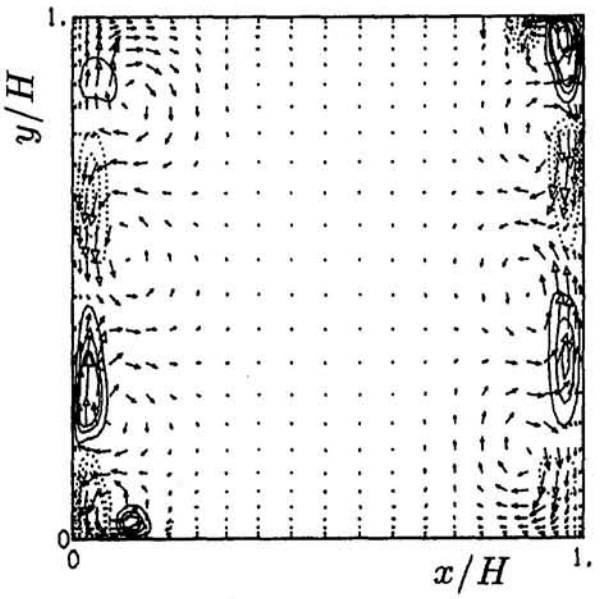

Fig. 8 Combined temperature and velocity perturbations at $z/D = 0.07$ in the cavity with $A_z = 2$ and Pr = 7. Same contour levels as in Fig. 3.

in direct numerical simulations of Rayleigh–Bénard convection in a finite box with $A_x = 0.5$ and $A_z = 4$, described by Kessler et al. (1984) and Kessler (1987), for Rayleigh numbers of up to 7×10^4. Kessler et al. (1984) and Kessler (1987) find, for both Pr = 0.71 and 7.0, that the Rayleigh–Bénard convection rolls develop instabilities. The resulting oscillations, however, are completely different for the two Prandtl numbers considered: For Pr = 0.71, the convection rolls are periodically contracted at fixed locations along their axes, whereas for Pr = 7.0, the perturbations move along the axes of the rolls. These findings are in qualitative agreement with the results obtained in the present study for the cavities that are differentially heated over opposing vertical walls and have conducting horizontal walls.

5 Conclusions

In the present study, instabilities that arise in the flow in differentially heated, rectangular cavities with conducting horizontal walls during the transition to turbulence have been investigated.

For air-filled (Pr = 0.71) cavities with conducting horizontal walls, the transition from steady to time-periodic flow is caused by a Rayleigh–Bénard instability occurring in the unstably stratified boundary layers along the conducting horizontal walls. This instability may be understood as an instability of a growing, time-dependent diffusive thermal boundary layer, using Howard's model (1966). This models predicts a frequency in good agreement with the actually calculated frequency and it predicts the formation of thermals that are indeed observed in the flow. The three dimensionality appears as a wavelike modulation with wavelength λ_z in the amplitude distribution of the flow. The wavelength varies slightly with the aspect ratio A_z. This wavelike modulation may be understood from Foster's calculations (1965, 1968) of the linear stability of a time-dependent diffusive thermal boundary layer, which predict amplification in a range of wavelengths. The most amplified of these wavelengths ($0.4H$) is in reasonable agreement with the wavelengths ($0.7H$–$0.9H$) observed in the present calculations. These wavelengths are also in good agreement with the wavelengths ($0.6H$–$1.1H$) obtained by Henkes and Le Quéré (1995), who investigated the three-dimensional stability of the two-dimensional flow in the square cavity. However, contrary to the present calculations, Henkes and Le Quéré (1995) found that the line symmetry (Eq. (10)) in the cavity was broken. This may be caused by the periodic boundary conditions they used in the z direction.

For water with Pr = 7, the instability is less well understood than for air. It originates near the lateral walls of the cavity (even for A_z as large as 8). The frequency of the oscillations is again in agreement with Howard's model but the perturbations, which are still convected in planes of constant z, also take the form of traveling waves in the z direction, similar to oscillations observed in Rayleigh–Bénard convection (Kessler et al., 1984; Kessler, 1987) for this Prandtl number.

References

Bénard, H., 1990, "Les tourbillons cellulaires dans une nappe liquide," *Revue Générale Sciences Pures Appliées,* Vol. 11, pp. 1261–1271, 1309–1328.

Elder, J. W., 1968, "The Unstable Thermal Interface," *Journal of Fluid Mechanics,* Vol. 32, pp. 69–96.

Foster, T. D., 1965, "Stability of a Homogeneous Fluid Cooled Uniformly From Above," *Physics of Fluids,* Vol. 8, pp. 1249–1257.

Foster, T. D., 1968, "Effect of Boundary Conditions on the Onset of Convection," *Physics of Fluids,* Vol. 11, pp. 1257–1262.

Gebhart, B., Jaluria, Y., Mahajan, R. L., and Sammakia, B., 1988, *Buoyancy-Induced Flows and Transport,* Hemisphere, New York.

Henkes, R. A. W. M., 1990, "Natural-Convection Boundary Layers," PhD thesis, Delft University of Technology, The Netherlands.

Henkes, R. A. W. M., and Le Quéré, P., 1995, "Three-Dimensional Transition of Natural-Convection Flows," submitted to *Journal of Fluid Mechanics.*

Howard, L. N., 1966, "Convection at High Rayleigh Number," *Proceedings, 11th International Congress Applied Mechanics,* Springer, pp. 1109–1115.

Janssen, R. J. A., and Henkes, R. A. W. M., 1993, "Accuracy of Finite-Volume Discretizations for the Bifurcating Natural-Convection Flow in a Square Cavity," *Numerical Heat Transfer B,* Vol. 24, pp. 191–207.

Janssen, R. J. A., Henkes, R. A. W. M., and Hoogendoorn, C. J., 1993, "Transition to Time-Periodicity of a Natural-Convection Flow in a 3D Differentially Heated Cavity," *International Journal of Heat and Mass Transfer,* Vol. 36, No. 11, pp. 2927–2940.

Janssen, R. J. A., and Henkes, R. A. W. M., 1995, "Influence of Prandtl Number on Instability Mechanisms and Transition in a Differentially Heated Square Cavity," *Journal of Fluid Mechanics,* Vol. 290, pp. 319–344.

Jones, D. N., and Briggs, D. G., 1989, "Periodic Two-Dimensional Cavity Flow: Effect of Linear Horizontal Thermal Boundary Condition," ASME JOURNAL OF HEAT TRANSFER, Vol. 111, pp. 86–91.

Kessler, R., Dallmann, U., and Oertel, H., 1984, "Nonlinear Transitions in Rayleigh–Bénard Convection," *Turbulence and Chaotic Phenomena in Fluids,* T. Tatsumi, ed., Elsevier, pp. 173–178.

Kessler, R., 1987, "Nonlinear Transition in Three-Dimensional Convection," *Journal of Fluid Mechanics,* Vol. 174, pp. 357–379.

Le Quéré, P., and Alziary de Roquefort, T., 1985, "Transition to Unsteady Natural Convection of Air in Differentially Heated Cavities," *Proceedings, 4th International Conference on Numerical Methods in Laminar and Turbulent Flow,* pp. 841–852.

Le Quéré, P., and Alziary de Roquefort, T., 1986, "Transition to Unsteady Natural Convection of Air in Vertical Differentially Heated Cavities: Influence of Thermal Boundary Conditions on the Horizontal Walls," *Proceedings, 8th International Heat Transfer Conference,* pp. 1533–1538.

Pellew, A., and Southwell, R. V., 1940, "On Maintained Convective Motion in a Fluid Heated From Below," *Proceedings of the Royal Society of London,* Vol. A176, pp. 312–343.

Rayleigh, Lord, 1916, "On Convection Currents in a Horizontal Layer of Fluid, When the Higher Temperature is on the Under Side," *Philosophical Magazine,* Vol. 32, pp. 529–546.

Sparrow, E. M., Husar, R. B., and Goldstein, R. J., 1970, "Observations and Other Characteristics of Thermals," *Journal of Fluid Mechanics,* Vol. 1, pp. 793–800.

Winters, K. H., 1987, "Hopf Bifurcation in the Double-Glazing Problem With Conducting Boundaries," ASME JOURNAL OF HEAT TRANSFER, Vol. 109, pp. 894–898.

Unsteady Three-Dimensional Natural Convection in an Inclined Air Slot With a Hexagonal Honeycomb Core

Y. Asako

Y. Yamaguchi

T. Yamanaka

Department of Mechanical Engineering,
Tokyo Metropolitan University,
Tokyo, 192-03, Japan

M. Faghri

Department of Mechanical Engineering and
Applied Mechanics,
University of Rhode Island,
Kingston, RI 02881-0805
Fellow ASME

Unsteady three-dimensional natural convection heat transfer in an inclined air slot with a hexagonal honeycomb enclosure is investigated numerically. The numerical methodology is based on an algebraic coordinate transformation technique that maps the hexagonal cross section onto a rectangle. The transformed governing equations are solved with a control volume discretization scheme using a fully implicit method with time. The computations are performed for inclination angles in the range of 60 to 80 deg for Ra = 10^4, and in the range of 45 to 80 deg for Ra = 10^5, for Prandtl number of 0.7, and for a fixed aspect ratio of H/L = 5. A conductive thermal boundary condition for the honeycomb side walls is considered. Both periodic and nonperiodic oscillating solutions are obtained depending on the inclination angle and Rayleigh number. The complex flow patterns are presented in form of particle trajectory maps and are compared with the flow visualization results using microcapsulated liquid crystals.

Introduction

An air slot with a hexagonal honeycomb core is often used as a thermal insulating wall. Inside such a slot the main mechanisms of heat transfer are by natural convection and radiation. A summary of the literature in buoyancy-induced flows was brought together by Gebhart et al. (1988). This included a chapter in natural convection in enclosures and partial enclosures. From a study of this information, it is evident that three-dimensional natural convection inside enclosures is limited to simple geometries such as a rectangular box or a horizontal cylinder, except for the experimental work by Cane et al. (1977) and Smart et al. (1980) on hexagonal honeycomb enclosures.

This motivated the numerical studies by Asako et al. (1989, 1990, 1991) for steady natural convection in a vertical and inclined air slot with a hexagonal honeycomb core. These studies were limited to small inclination angles depending on Ra and the aspect ratio. The computations were unstable for large inclination angles because of the oscillatory nature of the flow. This is evident from a series of experimental and numerical studies by Ozoe et al. (1974a, 1974b, 1975, 1977a, 1977b) for two and three-dimensional inclined rectangular enclosures with large inclination angles. Other related studies are by Yang et al. (1987) who carried out numerical analysis for tilted three-dimensional longitudinal rectangular enclosure, and by Hamady et al. (1989) who studied the effect of inclination on the steady natural convection in an air-filled enclosure. These studies motivated the present work on the unsteady three-dimensional natural convection in an inclined hexagonal honeycomb enclosure with large inclination angles. A related work by Krishnamurti (1973) investigated oscillatory flows in Bénard convection in a horizontal layer.

The numerical methodology uses an algebraic coordinate transformation developed previously by Faghri et al. (1984). The solutions are obtained for conductive thermal boundary condition, for the inclination angles of 60 and 80 deg for Ra = 10^4, and for the inclination angles of 45, 60, and 80 deg for Ra = 10^5, for Prandtl number of 0.7, and for a fixed aspect ratio of $H/L = 5$. The complex flow patterns are presented in the form of particle trajectory maps, and are compared with the flow visualization results using microcapsulated liquid crystals.

Formulation

Description of the Problem. The problem to be considered in this study is shown in Fig. 1. It involves the solution of unsteady three-dimensional heat transfer for laminar natural convection in an inclined hexagonal honeycomb enclosure with conductive side walls. As seen in this figure, the hexagonal end walls are kept at uniform temperature θ_H and θ_C, respectively. The inclination angle denoted by ϕ is zero when the end wall stands vertically and takes positive values when the hot end wall is lower than the cold end wall. The geometry of the problem is specified by the height (H) and length (L). If L is chosen as the reference length then H/L and the inclination angle are the only geometric parameters of the problem.

Conservation Equations. The governing equations to be considered are the continuity, momentum, and energy equations. Constant thermophysical properties are assumed, except for the density in the buoyancy force term. The following dimensionless variables are used:

$$X = x/L, \quad Y = y/L, \quad Z = z/L, \quad T = t/(L^2/\nu),$$
$$U = u/(\nu/L), \quad V = v/(\nu/L), \quad W = w/(\nu/L),$$
$$P = p/\rho(\nu/L)^2, \quad \Theta = (\theta - \theta_m)/(\theta_H - \theta_C) \qquad (1)$$

where θ_m is the average temperature of the end walls and is expressed by $\theta_m = (\theta_H + \theta_C)/2$. Upon introduction of the dimensionless variables and parameters, the governing equations take the following forms:

$$\partial U/\partial X + \partial V/\partial Y + \partial W/\partial Z = 0 \qquad (2)$$

$$\partial U/\partial T + U(\partial U/\partial X) + V(\partial U/\partial Y) + W(\partial U/\partial Z) = -\partial P/\partial X + \nabla^2 U \qquad (3)$$

Contributed by the Heat Transfer Division for publication in the JOURNAL OF HEAT TRANSFER. Manuscript received by the Heat Transfer Division May 1994; revision received February 1995. Keywords: Natural Convection, Numerical Methods. Associate Technical Editor: J. R. Lloyd.

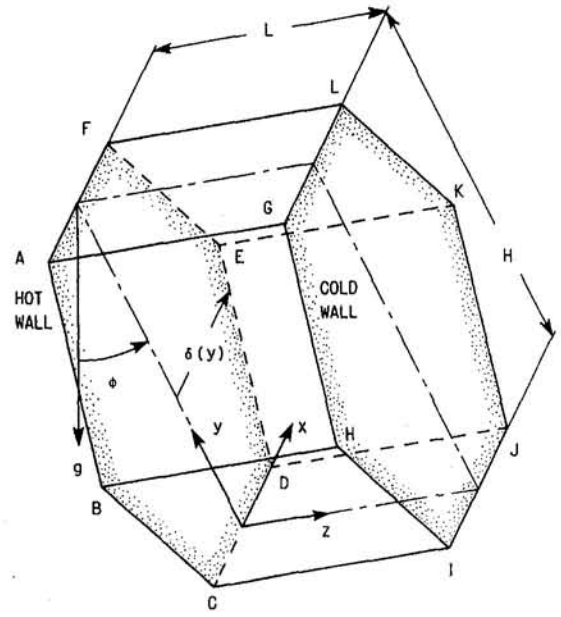

Fig. 1 Schematic diagram of an inclined honeycomb enclosure

$$\partial V/\partial T + U(\partial V/\partial X) + V(\partial V/\partial Y) + W(\partial V/\partial Z) = -\partial P/\partial Y + \nabla^2 V + (\mathrm{Ra/Pr})\Theta \cos\phi \quad (4)$$

$$\partial W/\partial T + U(\partial W/\partial X) + V(\partial W/\partial Y) + W(\partial W/\partial Z) = -\partial P/\partial Z + \nabla^2 W + (\mathrm{Ra/Pr})\Theta \sin\phi \quad (5)$$

$$\partial \Theta/\partial T + U(\partial \Theta/\partial X) + V(\partial \Theta/\partial Y) + W(\partial \Theta/\partial Z) = (1/\mathrm{Pr})\nabla^2\Theta \quad (6)$$

where

$$\nabla^2 = \partial^2/\partial X^2 + \partial^2/\partial Y^2 + \partial^2/\partial Z^2 \quad (7)$$

To complete the formulation of the problem, it remains to discuss the boundary and the initial conditions. These are at $T > 0$

$$\begin{aligned} \text{at all walls:} \quad & U = V = W = 0 \\ \text{on the hot wall:} \quad & \Theta = 0.5 \\ \text{on the cold wall:} \quad & \Theta = -0.5 \\ \text{on the side wall:} \quad & \Theta = 0.5 - Z \end{aligned} \quad (8)$$

and at $T = 0$

$$U = V = W = 0$$

$$\Theta = 0.5 - Z \quad (9)$$

Numerical Solutions. A simple algebraic coordinate transformation is used that maps the hexagonal cross section onto a rectangle. Specifically, the X, Y coordinates are transformed into η, ξ coordinates by the relations

$$\eta = X/[\delta(y)/L], \quad \xi = Y \quad (10)$$

where $\delta(y)$ is the half-width of the honeycomb enclosure. The solution domain is extended to the whole domain rather than the half-domain used by Asako et al. (1989) for the steady solution. Therefore, the transformed solution domain is bounded by $\eta = -1$ to 1 and $\xi = 0$ to H/L. The transformed equations and their discretization and solution methodology are documented in earlier papers by Asako et al. (1989, 1990, 1991). The discretization procedure for the equations is based on the control volume power-law scheme (1981), and the discretized equations are solved using a line-by-line method.

The computations are performed for Pr of 0.7, for inclination angles in the range of 60 to 80 deg for Ra = 10^4, and for inclination angles of 45, 60, and 80 deg for Ra = 10^5, and for a fixed aspect ratio of $H/L = 5$ where steady-state solutions were unstable. A summary of the parametric specifications for simulations 1 through 5 is presented in Table 1.

Table 1 Summary of parametric specifications

Run	Ra	ϕ	H/L
1	10^4	60 deg	5
2	10^4	80 deg	5
3	10^5	45 deg	5
4	10^5	60 deg	5
5	10^5	80 deg	5

All computations were performed with (32 × 32 × 22) grid points. These grids were distributed uniformly over the solution domain in the η, ξ, and Z coordinate directions. Supplementary runs were performed with the coarse grids (22 × 22 × 18) and the fine grids (42 × 42 × 32) to investigate the effect of the grid size for the time step of $\Delta T = 2 \times 10^{-3}$. The change in the Nusselt number at $T = 0.2$ between the fine and medium grids, and coarse and medium grids were 0.1 and 0.3 percent, respectively. Therefore, medium grids were chosen for all computations.

The effect of time step on the area-averaged Nusselt number was investigated using three different steps in Table 2. These Nusselt numbers are the time-averaged values during $T = 0$ to 0.1 or $T = 0$ to 0.2. As seen from this table, the differences between the Nusselt numbers are small. Therefore, the time steps $\Delta T = 2 \times 10^{-3}$ and 5×10^{-4} were chosen for Ra = 10^4

Nomenclature

H = height of a hexagonal honeycomb enclosure
h = local heat transfer coefficient
h_m = average heat transfer coefficient
L = axial length of a hexagonal honeycomb enclosure
Nu = local Nusselt number
Nu_m = average Nusselt number
Pr = Prandtl number
P = dimensionless pressure
p = pressure
Q = total heat transfer from a hot wall
q = heat flux from a hot wall
Ra = Rayleigh number
T = dimensionless time
t = time
U, V = dimensionless velocity components
u, v = velocity components
W = dimensionless axial velocity component
w = axial velocity component
X, Y = dimensionless coordinates
x, y = coordinates
Z = dimensionless axial coordinate
z = axial coordinate
$\delta(y)$ = half-width of a hexagonal enclosure
η = transformed coordinate = $X/\{\delta(y)/L\}$
Θ = dimensionless temperature
θ_m = averaged temperature = $(\theta_H + \theta_C)/2$
θ_H = hot wall temperature
θ_C = cold wall temperature
μ = viscosity
ν = kinematic viscosity
ξ = transformed coordinate = Y
ρ = density of the fluid
ϕ = inclination angle

Table 2 Effect of time step on time-averaged Nusselt number

Run	Ra	ϕ	ΔT	Nu	Period
1	10^4	60 deg	5×10^{-3}	1.569	0 to 0.2
			2×10^{-3}	1.568	
			1×10^{-3}	1.568	
2	10^4	80 deg	5×10^{-3}	1.580	0 to 0.2
			2×10^{-3}	1.541	
			1×10^{-3}	1.536	
3	10^5	45 deg	1×10^{-3}	3.362	0 to 0.2
			5×10^{-4}	3.361	
			2×10^{-4}	3.361	
4	10^5	60 deg	1×10^{-3}	3.341	0 to 0.2
			5×10^{-4}	3.345	
			2×10^{-4}	3.346	
5	10^5	80 deg	1×10^{-3}	2.961	0 to 0.1
			5×10^{-4}	2.964	
			2×10^{-4}	2.965	

and 10^5, respectively, to maintain relatively moderate computing time.

The convergence criterion in each time step was that the value of the mass flux residuals divided by the total mass flow in each control volume is under 10^{-8} at each time step. The underrelaxation factors for the velocities and pressure were 0.5 and 0.8, respectively.

Nusselt Numbers. The local and average heat transfer coefficients on the hot wall are defined as

$$h = q/(\theta_H - \theta_C) \tag{11}$$

$$h_m = Q/[A_H(\theta_H - \theta_C)] \tag{12}$$

where q is the local heat flux, A_H is the area of the hexagonal hot wall equal to $(3/2)H^2 \tan(\pi/6)$, Q is the total heat transfer rate from the hot wall. The Nusselt number expressions are as follows:

$$\mathrm{Nu} = hL/k = -(\partial\Theta/\partial Z)_H \tag{13}$$

$$\mathrm{Nu}_m = h_m L/k = -\int_0^{H/L}\int_{-1}^{1} (\partial\Theta/\partial Z)_H(\delta/L) \times d\eta d\xi/[(3/2)(H/L)^2 \tan(\pi/6)] \tag{14}$$

It is noteworthy that Nu_m is the area-averaged Nusselt number and is a function of time.

Results and Discussion

The results were obtained for five different runs as summarized in Table 1. They are presented in the form of flow patterns, local and averaged Nusselt number, and a comparison with flow visualization experiments as follows:

Flow Patterns. The particle trajectory method is used to show complex flow patterns in the hexagonal honeycomb enclosure. Results for simulation 2 (Ra = 10^4, ϕ = 80 deg, H/L = 5) are presented in Fig. 2. The particles are distributed at all the computational grid points on $Z = 0.1$ plane at dimensionless time $T = 0.9$. These particles move because of fluid motion and their locations at the dimensionless time $T = 0.92$ are presented in Fig. 2(*a*). Figures 2(*b*) and 2(*c*) show the particle locations at $T = 2.52$ and 4.02, respectively. These particles were distributed at the grid points on $Z = 0.1$ at $T = 2.5$ and 4.0, respectively. As seen from Fig. 2(*a*), an ascending flow from the horseshoe-shaped area is observed in the enclosure at $T = 0.92$. The area of the ascending flow changes with time in Figs. 2(*b*) and 2(*c*).

The results of the simulation 4 (Ra = 10^5, ϕ = 60 deg, H/L = 5) are presented in Fig. 3. Figures 3(*a*), 3(*b*), and 3(*c*) are the results at T = 0.108, 0.208, and 0.308, respectively. These particles were distributed at all computational grid points on $Z = 0.1$ plane at T = 0.1, 0.2, and 0.3, respectively. As seen from these figures, the main flow structure is unicellular. However, superimposed rolls that align their axis in the y direction can be observed [Figs. 3(*b*) and 3(*c*)].

The results of simulation 5 (Ra = 10^5, ϕ = 80 deg, H/L = 5) are presented in Fig. 4. Figures 4(*a*), 4(*b*), and 4(*c*) are the results at T = 0.104, 0.204, and 0.304, respectively. The particles were distributed at all grid points at T = 0.1, 0.2, and 0.3, respectively. The main flow structure is unicellular at T = 0.104. About five or six ascending flows can be observed in the enclosure at T = 0.204 and 0.304. In this case, the flow pattern transition from unicellular to multicellular occurs between T = 0.1 and 0.2. The results of simulation 1 (Ra = 10^4, ϕ = 60 deg, H/L = 5) are not shown here, but the main flow structure in the enclosure is unicellular.

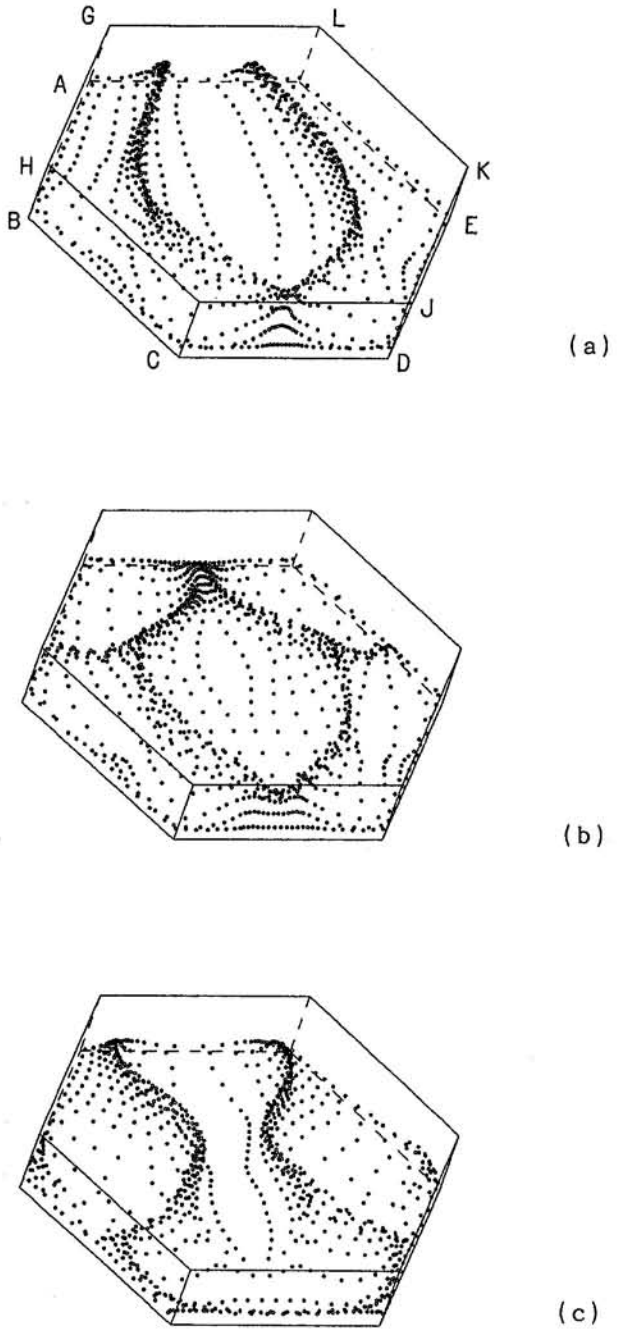

Fig. 2 Particle trajectories for simulation 2: (*a*) T = 0.92; (*b*) T = 2.52; (*c*) T = 4.02

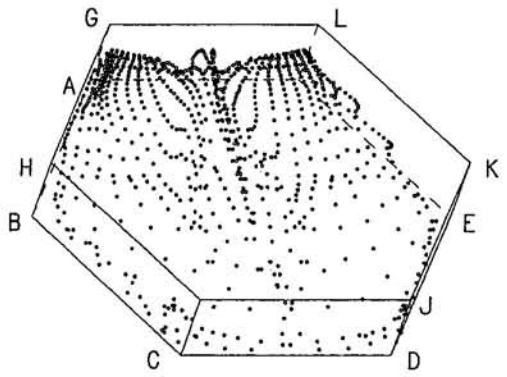

(a)

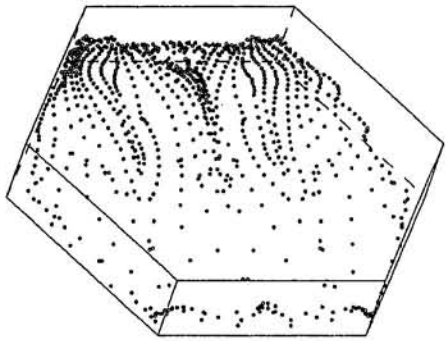

(b)

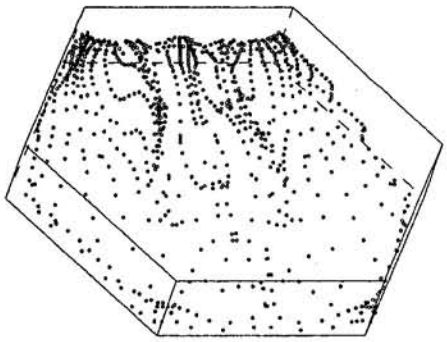

(c)

Fig. 3 Particle trajectories for simulation 4: (*a*) $T = 0.108$; (*b*) $T = 0.208$; (*c*) $T = 0.308$

Local Nusselt Number. The contour plots of local Nusselt number on the hot wall are presented in Fig. 5. These results correspond to flow patterns presented in Fig. 2. As seen from Fig. 5, the local Nusselt number is low in the areas where the flow is ascending and it is high in the areas where the flow is descending. The local Nusselt number changes with time corresponding to the changes in the flow patterns. It is noteworthy to observe that the Nusselt number is symmetric on the hot wall.

Area-Averaged Nusselt Number. The area-averaged Nusselt number on the hot wall for Ra = 10^4 and 10^5 is plotted as a function of the dimensionless time in Figs. 6 and 7, respectively. It increases rapidly during the starting period and oscillates with time. From the initial condition of Eq. (9), its value is unity at $T < 0$. The marks in the figures show the time correspondence with Figs. 2 to 4.

As seen from both figures, only the result for simulation 1 is periodic. Figure 7, in simulation 5, shows that the area-averaged Nusselt number increases with time in stepwise fashion at $T = 0.18$. This increase corresponds to flow pattern transition.

Time-Averaged Nusselt Number. The time and area-averaged Nusselt number on the hot wall for the simulation 1 during $T = 0.99$ to 4.89 is about 1.80. The area-averaged Nusselt number for simulation 2 fluctuates in the range from 1.85 to 2.15, except for the starting period. The time-averaged value during $T = 1$ to 5 is 1.98. The time-averaged values during $T = 0.1$ to 0.3 for simulations 3 and 4 are 3.43 and 3.43, respectively. The time-averaged Nusselt number for simulation 5 after the flow pattern transition ($T > 0.2$) is 3.87. Since only simula-

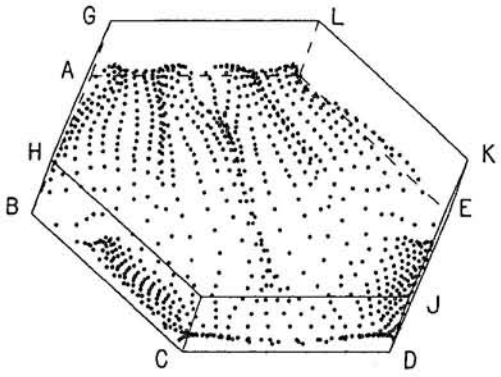

(a)

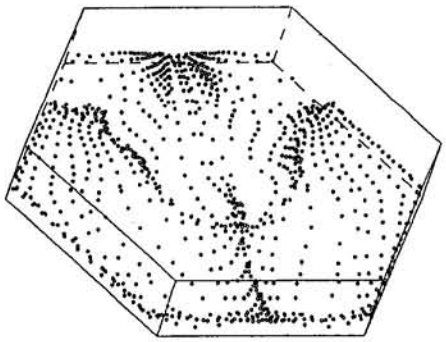

(b)

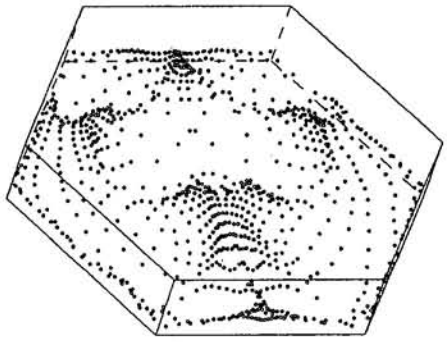

(c)

Fig. 4 Particle trajectories for simulation 5: (*a*) $T = 0.104$; (*b*) $T = 0.204$; (*c*) $T = 0.304$

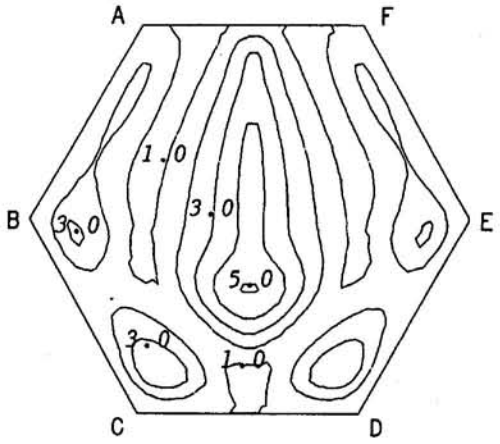

(a)

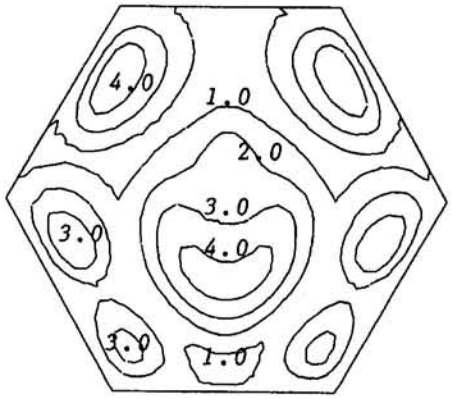

(b)

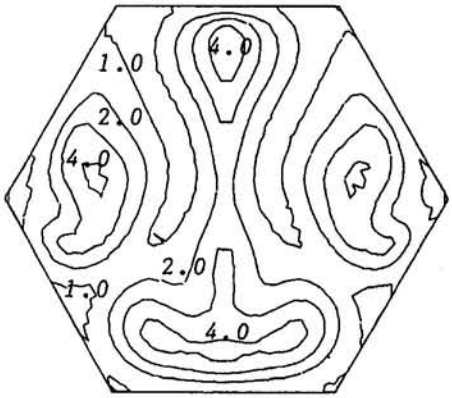

(c)

Fig. 5 Local Nusselt number on the hot wall for simulation 2: (*a*) T = 0.92; (*b*) T = 2.52; (*c*) T = 4.02

tion 1 is periodic, 13 cycles from T = 0.99 to 4.89 is chosen for the integration interval.

The time and area-averaged Nusselt numbers on the hot wall are plotted as a function of the inclination angle ϕ, with the Rayleigh number as the curve parameter in Fig. 8. The values in the range of the inclination angle from −90 to 45 deg for Ra = 10^4 and from −90 to 30 deg for Ra = 10^5 are the steady-state solution obtained in the earlier paper by Asako et al. (1991). The time and area-averaged Nusselt number increases from unity as the inclination angle increases for both Rayleigh numbers and it decreases after it reaches a maximum

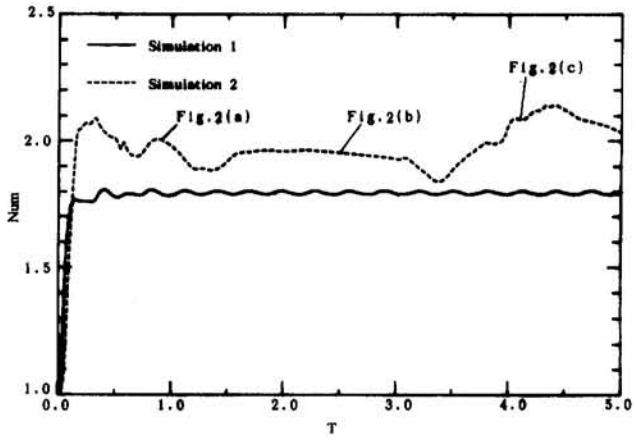

Fig. 6 Area-averaged Nusselt number on the hot wall as a function of time for Ra = 10^4

value, and it increases again after it reaches a minimum value near ϕ = 60 deg. This change corresponds to the flow pattern transition. Namely, the flow structure for ϕ = 80 deg is multicellular for both Ra = 10^4 and 10^5. However, the main flow structure for $\phi \leq$ 60 deg is unicellular. The same trends were observed experimentally in the paper by Ozoe et al. (1974a) for a square channel.

Flow Visualization. Flow visualization experiments were performed using microcapsulated liquid crystals in a temperature range of 25 to 30°C. The description of the experimental apparatus is facilitated by reference to Fig. 9, which shows the cross section of the test section. As seen in this figure, the height (H) and the thickness (L) of the honeycomb enclosure are 200 mm and 40 mm, respectively. The hot and the cold walls are made of a 5-mm-thick copper plate and 2-mm-thick plexiglass and the side walls are made of plexiglass to enable the motions of liquid crystals to be observed. For the same reason, a water jacket with dimensions (250 × 250 × 20 mm, length × width × height), made of plexiglass, is mounted on the cold wall. The temperature-controlled cooling water is used to maintain the cold wall to the desired temperature. Two electronic plate heaters are attached on the back side of the hot wall and surface temperatures of the hot and cold walls are sensed by thermocouples.

Silicon oils with kinematic viscosities of 500 and 6000 mm^2/s containing 5 mg of microcapsulated liquid crystals per 100 cc of oil were used as the working fluid. A change in the color of liquid crystals occurs because of the change in temperature.

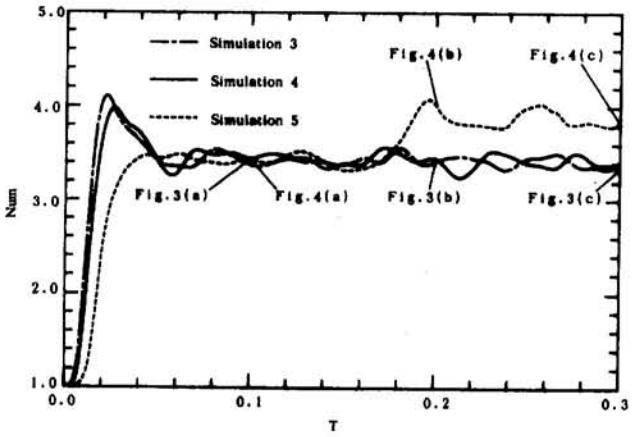

Fig. 7 Area-averaged Nusselt number on the hot wall as a function of time for Ra = 10^5

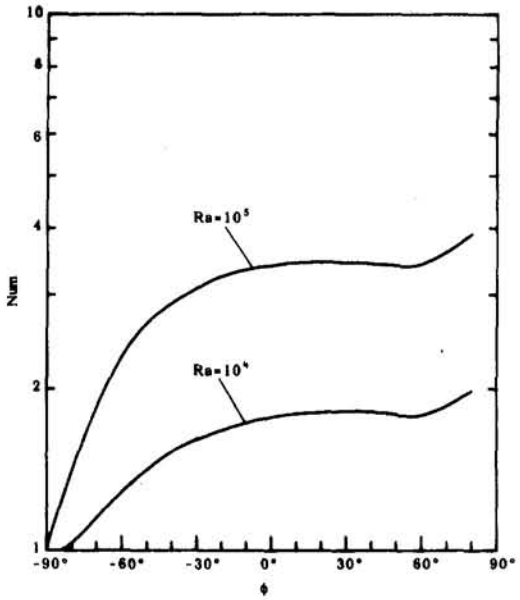

Fig. 8 Time and area-averaged Nusselt number on the hot wall as a function of the inclination angle

In this way, the temperature distribution in the midplane of hot and cold walls was observed.

Photographs of temperature distribution are presented in Figs. $10(a, b, \text{and } c)$, respectively, for Ra = 2.5×10^4 and $\phi = 80$ deg, for Ra = 2.8×10^5 and $\phi = 60$ deg, and for Ra = 2.0×10^5 and $\phi = 80$ deg. These conditions nearly correspond to those of the numerical simulations 2, 4, and 5, respectively. It is noteworthy that the Prandtl number of silicon oil is much higher than the value used for the numerical computation. The thermal boundary conditions of the experiment with plexiglass side walls do not exactly coincide with those for the numerical computation where conductive wall boundary conditions were assumed.

The color of liquid crystals changes from red to blue via green because of a change in temperature. In the photographs, blue represents areas of high temperature where flow is ascending. The multicellular flow can be seen in Fig. $10(a)$. Similar flow patterns were obtained by numerical simulation 2 [see Fig. $2(b)$]. As seen from Fig. $10(b)$, rolls that align their axis in the y direction are superimposed on the main unicellular flow. Similar flow patterns are obtained in simulation 4 [see Fig. $3(b)$]. In Fig. $3(b)$, this can be seen in the upper part of the hot wall where the flow near the hot wall is observed. Ascending flows can be seen in Fig. $10(c)$ where the flow patterns are multicellular, similar to those obtained by numerical simulations.

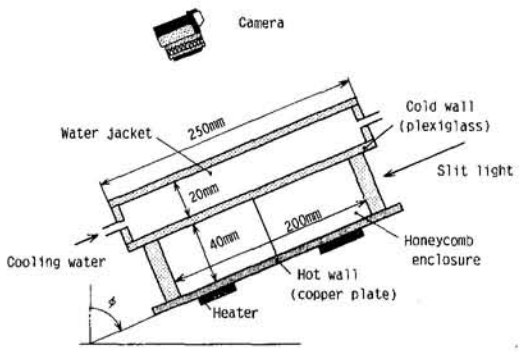

Fig. 9 A cross section of the test section for the flow visualization

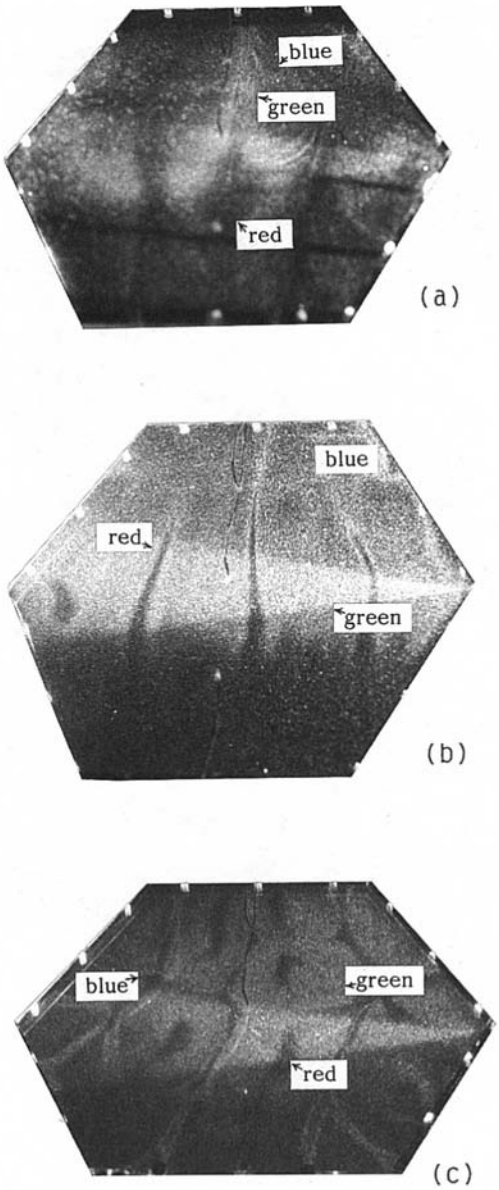

Fig. 10 Photographs of the flow visualizations for: (*a*) Ra = 2.5×10^4, $\phi = 80$ deg; (*b*) Ra = 2.8×10^5, $\phi = 60$ deg; (*c*) Ra = 2.0×10^5, $\phi = 80$ deg

Concluding Remarks

Three-dimensional unsteady natural convection heat transfer characteristics in an inclined hexagonal honeycomb enclosure were obtained numerically and were compared with flow visualization results using microcapsulated liquid crystals. The computations were performed for large inclination angles where steady solutions were unstable. The main conclusions are:

(a) Flow is unsteady but symmetric for high inclination angles.
(b) The main flow structure is unicellular for $\phi \leq 60$ deg, and is multicellular for $\phi = 80$ deg with transition occurring between $\phi = 60$ and 80 deg.
(c) The time and area-averaged Nusselt numbers increase from unity as the inclination angle increases and decreases after it reaches a maximum value, and increases again after it reaches a minimum value near $\phi = 60$ deg.
(d) Flow patterns similar to those obtained by numerical computations are observed by using a microcapsulated liquid crystal flow visualization technique.

References

Asako, Y., Nakamura, H., and Faghri, M., 1989, "Three-Dimensional Laminar Natural Convection in Horizontal Hexagonal Honeycomb Enclosure," *Numerical Heat Transfer,* Vol. 15, pp. 67–86.

Asako, Y., Nakamura, H., and Faghri, M., 1990, "Three-Dimensional Laminar Natural Convection in a Vertical Air Slot With Hexagonal Honeycomb Core," ASME JOURNAL OF HEAT TRANSFER, Vol. 112, pp. 130–136.

Asako, Y., Nakamura, H., Chen, Z., and Faghri, M., 1991, "Three-Dimensional Laminar Natural Convection in an Inclined Air Slot With Hexagonal Honeycomb Core," ASME JOURNAL OF HEAT TRANSFER, Vol. 113, pp. 906–911.

Bejan, A., and Tien, C. L., 1978, "Laminar Natural Convection Heat Transfer in a Horizontal Cavity With Different End Temperature," ASME JOURNAL OF HEAT TRANSFER, Vol. 100, pp. 641–647.

Cane, R. L. D., Hollands, K. G. T., Raithby, G. D., and Unny, T. E., 1977, "Free Convection Heat Transfer Across Inclined Honeycomb Panels," ASME JOURNAL OF HEAT TRANSFER, Vol. 99, pp. 86–91.

Faghri, M., Sparrow, E. M., and Prata, A. T., 1984, "Finite Difference Solutions of Convection-Diffusion Problems in Irregular Domains Using a Non-orthogonal Coordinate Transformation," *Numerical Heat Transfer,* Vol. 7, pp. 183–209.

Gebhart, B., Jaluria, Y., Mahajan, R. L., and Sammakia, B., 1988, *Buoyancy Induced Flows and Transport,* Hemisphere, Washington DC.

Hamady, F. J., Lloyd, J. R., Yang, H. Q., and Yang, K. T., 1989, "Study of Local Natural Convection Heat Transfer in an Inclined Enclosure," *Int. J. Heat Mass Transfer,* Vol. 32, No. 9, pp. 1697–1708.

Krishnamurti, R., 1973, "Some Further Studies on the Transition to Turbulent Convection," *Journal of Fluid Mechanics,* Vol. 60, part 2, pp. 285–303.

Ozoe, H., Sayama, H., and Churchill, S. W., 1974a, "Natural Convection in an Inclined Square Channel," *Int. J. Heat Mass Transfer,* Vol. 17, pp. 401–406.

Ozoe, H., Yamamoto, K., Sayama, H., and Churchill, S. W., 1974b, "Natural Convection in an Inclined Rectangular Channel Heated on One Side and Cooled on the Opposing Side," *Int. J. Heat Mass Transfer,* Vol. 17, pp. 1209–1217.

Ozoe, H., Sayama, H., and Churchill, S. W., 1975, "Natural Convection in an Inclined Rectangular Channel at Various Aspect Ratios and Angles—Experimental Measurements," *Int. J. Heat Mass Transfer,* Vol. 18, pp. 1425–1431.

Ozoe, H., Sayama, H., and Churchill, S. W., 1977a, "Natural Convection Patterns in a Long Inclined Rectangular Box Heated From Below, Part 1. Three-Directional Photography," *Int. J. Heat Mass Transfer,* Vol. 20, pp. 123–129.

Ozoe, H., Yamamoto, K., and Churchill, S. W., 1977b, "Natural Convection Patterns in a Long Rectangular Box Heated From Below, Part 2. Three-Dimensional Numerical Results," *Int. J. Heat Mass Transfer,* Vol. 20, pp. 131–139.

Patankar, S. V., 1981, "A Calculation Procedure for Two-Dimensional Elliptic Situations," *Numerical Heat Transfer,* Vol. 4, pp. 409–425.

Patankar, S. V., 1980, *Numerical Heat Transfer and Fluid,* Hemisphere, Washington, DC.

Smart, D. R., Hollands, K. G. T., and Raithby, G. D., 1980, "Free Convection Heat Transfer Across Rectangular-Celled Diathermanous Honeycombs," ASME JOURNAL OF HEAT TRANSFER, Vol. 102, pp. 75–80.

Yang, H. Q., Yang, K. T., and Lloyd, J. R., 1987, "Laminar Natural-Convection Flow Transitions in Tilted Three-Dimensional Longitudinal Rectangular Enclosures," *Int. J. Heat Mass Transfer,* Vol. 30, No. 8, pp. 1637–1644.

Buoyant Pulsating Exchange Flow Through a Vent

T. A. Conover

R. Kumar[1]

J. S. Kapat

Department of Mechanical Engineering,
Clemson University,
Clemson, SC 20634

Buoyancy-driven bidirectional pulsating exchange flow through a vent in a horizontal partition is studied experimentally using a brine/water system. The associated transient and pulsating exchange flows were studied by densimetric measurements, flow visualization, and laser Doppler velocimetry (LDV) measurements for three different vent length-to-diameter ratios: 0.106, 0.0376, and 0.008. A time scale, based on the rate of decay of the density difference between the two compartments, is developed that collapses all experimental data regarding the decay of density in the top compartment into one curve. Flow visualization was used to understand the flow features contributing to the pulsating flow and to provide a quantitative measure of the major pulsation frequency. Interfacial instability between brine and water at the vent was found to contribute to the pulsation. The pulsation frequencies and their decay were determined from the power spectrum of LDV measurements. For the small length-to-diameter ratios (0.008 and 0.0376) there are two different frequencies that decay at different rates, suggesting multiple flow processes that contribute to flow pulsations.

Introduction

A heavier fluid located on the top of a lighter fluid and separated by a horizontal plate or vent constitutes a gravitationally unstable system. In the absence of any externally forced pressure difference across the vent, such a system is characterized by a countercurrent (i.e., bidirectional) buoyancy-driven flow through the vent. This paper addresses such flows for vents with small aspect (i.e., length-to-diameter) ratio ($L/D < 1$).

Much research has been done in the general area of natural convection in enclosures (i.e., Gebhart et al., 1988; Jaluria and Cooper, 1989). Many of these studies did not include the role of interconnecting vents in natural convection between adjacent compartments. Brown and Solvason (1962) and Brown (1962) were among the first to study the natural convection through openings in vertical and horizontal partitions of enclosures. Air was used as the fluid medium. Their studies covered a range of 0.0825 to 0.75 for the vent or opening aspect ratio (defined as the ratio of length to the linear dimension of the cross section) and a range of 3×10^4 to 4×10^7 for Gr, the Grashof number. The corresponding range for (densimetric) Reynolds number was 1000 to 10,000. With the help of experimental data and analysis, Brown and Solvason formulated a correlation between heat transfer rate and the independent parameters, Gr, aspect ratio, and Pr. This study was confined to the global effect of the buoyant flow through the vents, yielding an overall heat transfer coefficient. The flow characteristics inside and around the vents were not explored.

Fire-induced flow through openings in vertical walls of an enclosure was first studied and documented by Prahl and Emmons (1975). Mathematical models of the flow have been proposed by Steckler et al. (1982, 1984) and Emmons (1988). Flow contraction and head losses at the vent were modeled through the use of a flow coefficient by invoking Bernoulli's equation. The effects of variable density, turbulence, viscosity, and thermal diffusion were neglected. Steckler et al. (1984) did not find any dependence of the measured flow coefficient on fire strength, opening geometry, and fire location.

Steckler et al. (1986) gave theoretical justifications for using brine/water analog for studying fire-induced flows in enclosures. In this configuration, hot and cold fluids were replaced by fresh water and brine solution, respectively. The density of the heavier fluid (i.e., the brine solution) can be controlled by the concentration of salt in the solution. Steckler et al. (1986) showed that analogy between the two flow configurations existed provided that Reynolds number (based on vent height and velocity of buoyant fluid) and the vent aspect ratio were the same, and that Prandtl number for air in the fire-induced flow was the same as Schmidt number for brine in water for the brine/water analog.

The brine/water analog to study buoyant flows through vents between enclosures has been used by several researchers. Epstein (1988) and Conover and Kumar (1993) have used the analog to study the special case where the externally applied pressure difference across the vent is zero. Tan and Jaluria (1992) and Jaluria et al. (1993) have studied cases where the vent flow is governed by both pressure and density differentials across the vent.

Epstein (1988) studied buoyancy-driven countercurrent exchange flow through openings in horizontal partitions between two enclosures using an arrangement similar to the one in this study, shown in Fig. 1. At the start of the experiment, the bottom enclosure contains fresh water and the top one contains brine. In contrast to the thermal analog, the brine/water system provides an inherently transient flow. As a result of the exchange flow, the density differential between the two enclosures continuously decreases, and hence the bidirectional exchange flow through the vent also decreases with time. This process continues until the density differential becomes so small that the exchange flow can hardly be observed.

Epstein found that for a fixed aspect ratio of the vent, the volumetric exchange flow rate ($Q(t)$) at any instant scales as

$$Q(t) \sim \sqrt{\frac{D^5 g \Delta\rho(t)}{\bar{\rho}(t)}} \equiv Q_\Delta(t) \quad \text{or}$$

$$Q(t) = Q^* Q_\Delta(t) \tag{1}$$

where D is the linear dimension of the cross section of the vent, $\Delta\rho(t)$ is the instantaneous difference between the densities of the two enclosures, and $\bar{\rho}(t)$ is the instantaneous average of those two densities, Q_Δ is the instantaneous scale for flow rate, and Q^* is called the flow coefficient, which, according to Epstein's observation, depends mainly on the vent aspect ratio. This result agrees with earlier results by Keulegan (1958).

[1] Current address: Knolls Atomic Power Laboratory, Schenectady, NY.

Contributed by the Heat Transfer Division for publication in the JOURNAL OF HEAT TRANSFER. Manuscript received by the Heat Transfer Division July 1994; revision received November 1994. Keywords: Building Heat Transfer, Flow Visualization, Natural Convection. Associate Technical Editor: Y. Jaluria.

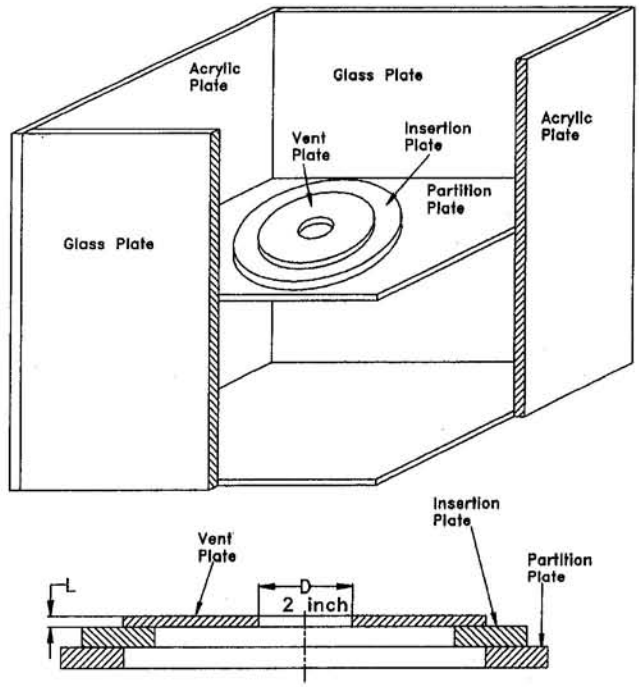

Fig. 1 Test section geometry

Here, the exchange flow was defined as the minimum flow from either enclosure to the other necessary to account for the observed transport of salt from the top enclosure to the bottom. This flow rate may not be exactly equal to the total upward flow rate or the total downward flow rate at any given horizontal cross section of the test apparatus because of local recirculation and entrainment.

Epstein identified four different flow regimes on the basis of the vent aspect ratio. Those four flow regimes are: (I) oscillatory exchange flow regime (for $L/D \leq 0.15$), (II) a countercurrent Bernoulli flow regime (for $0.15 \leq L/D \leq 0.4$), (III) a regime of combined turbulent binary diffusion and Bernoulli flow (for $0.4 \leq L/D \leq 2.75$), and (IV) a regime of pure binary turbulent diffusion (for $L/D \geq 2.75$).

Tan and Jaluria (1992) and Jaluria et al. (1993) further extended Epstein's work to include cases where there may be a nonzero pressure differential across the vent. They studied the vent flow for the aspect ratio range of 0.0144 to 6.0. The main focus was to find the critical pressure differential that distinguishes the unidirectional flow regime from the bidirectional flow regime. The study also included flow visualization with shadowgraphy for different pressure differential across the vent. The effect of pressure differential has also been reported by Heskestad and Spaulding (1991) and Cooper (1994).

The case of zero pressure differential across the vent has been studied by Conover and Kumar (1993), who used laser Doppler velocimetry (LDV) and densimetry to study the flow behavior for aspect ratio close to 1. Their experimental results are in agreement with those obtained by Epstein.

The current work, which is a continuation of the work of Conover and Kumar (1993), concentrates on the oscillatory regime of exchange flow. For aspect ratios of 0.008, 0.0376, and 0.106, the nature of oscillation is studied with shadowgraphy for flow visualization and with LDV, and the frequencies of oscillation are identified. Densimetric measurements are performed to study the decay of brine density in the top enclosure. The time-resolved flow-visualization photographs are analyzed to interpret the sequence of flow features around the vent.

Experimental Apparatus

Test Section. The experimental flow chamber for the salt-water flow analog was built entirely of transparent materials for flow visualization. Figure 1 is a drawing of the test section with one corner cut away to show the vent. Two opposing side panels were built of 0.5-in.-thick plate glass for LDV access with minimal scattering and distortion. The remaining parts were built of 0.5-in.-thick acrylic sheet. The chamber was left open at the top.

A horizontal acrylic partition plate was permanently sealed in place to divide the chamber into upper and lower compartments. An insertion plate with a 5-in.-dia hole at the center was sealed to the partition plate by an O-ring. Holes 2 in. in diameter (which served as vents) were bored in plates of varying thickness. During experiments with a specific aspect ratio, the plate with the desired vent aspect ratio was glued to the insertion plate.

The lower compartment was 15 in. square by approximately $12\frac{7}{16}$ in. high. Accounting for the volume of structural protrusions, the volume of the lower compartment (V_L) was 2802 in.^{3} (0.0459 m^3). The upper compartment was 15 in. square by about $10\frac{7}{16}$ in. high. The volume of the upper compartment (V_H), accounting for the insertion plate, was 2295 in.^{3} (0.0376 m^3). Slight variations of upper compartment volume due to changing insertion plates were accounted for in the analysis.

Nomenclature

A_{vent} = cross-sectional area of vent
D = vent diameter
$\Delta\rho$ = difference between top and bottom compartment densities
f = pulsation frequency
g = acceleration of gravity
Gr = Grashof number = $g(\Delta\rho/\bar{\rho})D^3/\nu_H^2$
i = index in curve fitting corresponding to different data points
L = vent length
N = number of data points used in curve fitting
ν = kinematic viscosity
Pr = Prandtl number
Q = exchange volumetric flow rate
Q^* = normalized flow rate $\equiv Q/Q_\Delta$
ρ = density
$\bar{\rho}$ = arithmatic average of the top and bottom compartment densities
ρ_f = asymptotic limit for the density in either compartment when the density difference would become zero as time $\to \infty$
Re = densimetric Reynolds number = $\sqrt{Dg\Delta\rho/\bar{\rho}D}/\nu_H$
S_{yx} = standard error of fit
t = time measured from the beginning of experiments
t^* = normalized time $\equiv t/t_\Delta$
τ = time measured from the beginning of a pulsation cycle
v, w = velocity components parallel to the y and z axes, respectively
V = volume of a compartment
V_Δ = velocity scale
W_n = vertical velocity at vent as given by Q and A_{vent}
x, y, z = coordinate axes, with z as the vertical axis

Subscripts

Δ = scale for normalization
f = final value
H = related to the top compartment
$H, 0$ = initial value, related to the top compartment
L = related to the bottom compartment
$L, 0$ = initial value, related to the bottom compartment

The velocity of the water plume in the upper compartment was low enough that there were no significant disturbances or gravity waves on the free surface. The absence of a solid barrier was assumed to have a negligible effect on the exchange flow.

Densimetric Experimental Procedure. The lower chamber was filled with filtered tap water and its density was measured in situ with an Ertco hydrometer (accuracy: ± 0.2 kg/m^3 at 95 percent CI) to establish the initial $\rho_{L,0}$. The vent was then closed with a rubber stopper and the upper chamber filled with a brine solution of the desired density. The brine density was measured to establish the initial $\rho_{H,0}$. After both liquids came to rest, the stopper was removed from the vent tube and drawn upward at the same speed as the developing water plume, so as not to impart any unnatural motion to the flow. The flow in the vent became independent of the stopper motion after a few seconds. The flow was allowed to proceed for a predetermined time before being stopped again with the stopper. After the vent was closed, the upper chamber was stirred to make the brine homogeneous and ρ_H was measured again. This was repeated several times until ρ_H had progressed at least half the way to the theoretical final value ρ_f:

$$\rho_f = \frac{\rho_{H,0} V_H + \rho_{L,0} V_L}{V_H + V_L}. \tag{2}$$

The measurement intervals were chosen with increasing length to cause approximately equal changes of the upper chamber average density ρ_H, since the rate of decay of ρ_H decreased substantially during the course of the experiment.

LDV Apparatus. Velocity measurements were made in the water plume in the upper compartment using a two-dimensional three-beam laser-Doppler velocimetry system. This system used a 35 mW He–Ne laser source with a three-way beam splitting and frequency shifting for velocity sign resolution. Liquids in both compartments were seeded with 10 μm polystyrene microspheres prior to each run. Light scattered forward from these microspheres was received by a photomultiplier tube, and the Doppler frequencies corresponding to two velocity components were measured by two counter-type signal processors. The digital outputs of the two counters were recorded by a computer. This system is described in more detail by Conover and Kumar (1993). Despite difficulties caused by the refractive index variations in the plume, it was usually possible to obtain a data rate of 200–300 samples per second with this system.

The coordinate system for velocities measured by LDV placed the origin on the axis of the vent at its upper edge, since measurements were made in the upper compartment. The x axis was horizontal and parallel to the optical axis of the LDV system, and normal to the glass wall. The y axis was horizontal and perpendicular to the x axis, and the z axis was vertical, forming a right-handed Cartesian system. The v and w components of velocity were measured parallel to the y and z axes.

Flow Visualization. Time-resolved flow visualization of the base of the plume was undertaken, guided by the quantitative understanding of flow rates and pulsation frequencies already acquired. The refractive index variations of the flow made the plume and some features of the flow within the vent readily visible in room light, but difficult to photograph. The pulsating flows were apparent in the small aspect ratio vents. LDV time series taken with the measuring volume on the vent axis, 1.5 cm above the vent, identified one or two dominant frequencies in each flow, decreasing monotonically as the density difference decayed, but velocity measurements at that single location did not reveal the overall flow features.

The features of the plume were given high contrast by shadowgraphy, in which parallel white light was directed from a projector through the test section and onto a screen, where the shadows of the refractive index fluctuations were readily recorded by a standard VHS video camera. No view of the flow within the vent was possible by this technique because of obstructions in the test section, but observations allowed some connection between features in the base of the plume and those in the vent itself. The video recorded 60 frames per second, giving complete resolution of the pulsations, which occurred at frequencies slower than 1 Hz in the plume. By reviewing the video, the average pulsation frequency over several cycles was determined by counting the number of video frames per pulsation. A VCR was used to advance the video frame by frame, and by adjusting the video monitor brightness and contrast, selected frames of the video were rephotographed using a standard 35 mm still camera.

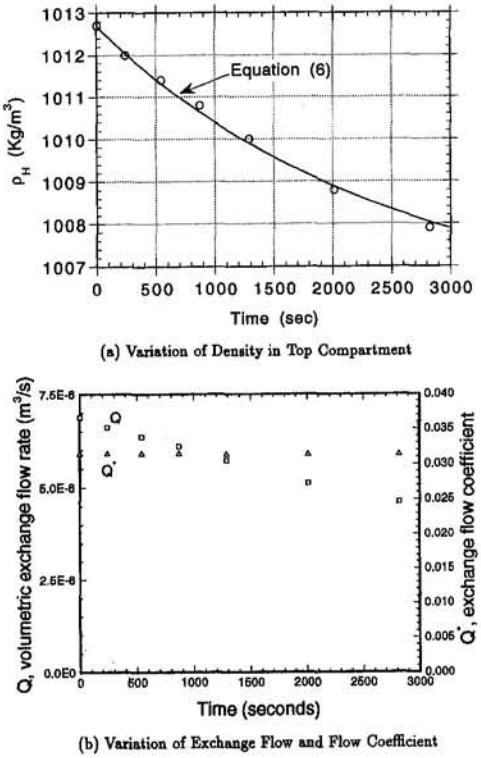

Fig. 2 Density and exchange flow variation for $L/D = 0.0376$ and initial $\Delta\rho/\bar{\rho} = 1.2$ percent

Results and Discussion

Volumetric Exchange Flow Rate, $Q(t)$. A typical decay of density in the upper compartment is shown in Fig. 2(a) for the aspect ratio of $L/D = 0.0376$. Associated with this decay, there is a corresponding increase of density in the lower compartment such that total mass in the two compartments is conserved. Starting with the mass balances in the individual compartments, Epstein (1988) derived an expression for the volumetric exchange flow rate:

$$Q = \frac{-V_H \dfrac{d\rho_H}{dt}}{(\rho_H - \rho_{L,0}) - \dfrac{V_H}{V_L}(\rho_{H,0} - \rho_H)}. \tag{3}$$

The term $d\rho_H/dt$ in the expression for Q is obtained from experimentally obtained $\rho_H(t)$ such as the one presented in Fig. 2(a). A curve-fitting of the experimental data facilitates the calculation of $d\rho_H/dt$.

Epstein's finding that the flow coefficient Q^* (defined in Eq. (1)) is a constant for a given L/D provides a rationale for a

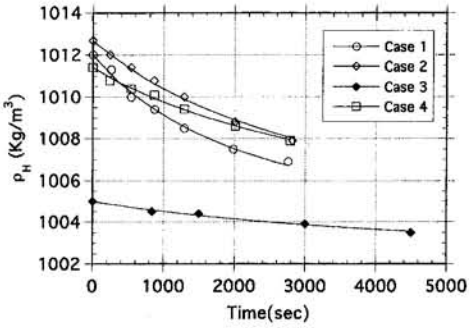

(a) Decay of Density

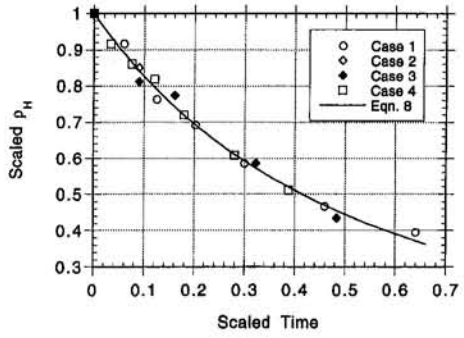

(b) Decay of Normalized Density

Fig. 3 Density variation in top compartment for all four cases

proper regression function for $\rho_H(t)$. From Eqs. (1) and (3), we write

$$-V_H \frac{d\rho_H}{dt} = Q^* \left(\frac{D^5 g}{\bar{\rho}}\right)^{1/2} \left(\frac{V_H + V_L}{V_L}(\rho_H - \bar{\rho})\right)^{3/2}. \quad (4)$$

If we integrate Eq. (4) and we replace[2] $\bar{\rho}$ by ρ_f, we obtain

$$\rho_H(t) = \rho_f + \left\{\frac{1}{\sqrt{\rho_{H,0} - \rho_f}} + \frac{Q^*}{2V_H}\left(\frac{D^5 g}{\rho_f}\right)^{1/2}\left(\frac{V_H + V_L}{V_L}\right)^{3/2} t\right\}^{-2}. \quad (5)$$

This expression suggests that a proper regression function to fit ρ_H versus time data would be

$$\frac{\rho_H(t) - \rho_f}{\rho_{H,0} - \rho_f} = \frac{1}{(1 + \lambda t)^2} \quad (6)$$

where λ is the regression parameter. This regression is calculated for each experimental run and $(d\rho_H/dt)(t)$ is determined. Then, using Eq. (3), Q is calculated.

The standard error of fit as calculated by

$$S_{\rho t} = \sqrt{\frac{1}{N-2}\sum_{i=1}^{N}(\rho_{H,i} - \rho_H(t_i))^2} \quad (7)$$

is 0.12 kg/m^3, which is of the order of the hydrometer resolution, and hence can be considered to be statistically insignificant. Since $S_{\rho t}$ reflects experimental uncertainty as well as appropriateness in the choice of the regression function, the small number for $S_{\rho t}$ indicates that Eq. (6) fits the data quite well, which is also suggested by that the correlation coefficient is within 0.5 percent of unity.

[2] $\bar{\rho}$ is different from ρ_f only when V_H and V_L are different. $\bar{\rho}$ approaches ρ_f asymptotically as $t \to \infty$. In the current set of experiments, the maximum difference between the two was 0.5 percent.

Table 1 Operating parameters for the four cases tested

Cases	L/D	Operating Ranges of $\frac{\Delta\rho}{\bar{\rho}}$	Operating Ranges of Re	Q^*
Case 1	0.106	1.2% – 0.4%	4650 – 2685	0.0425
Case 2	0.0376	1.2% – 0.4%	4650 – 2685	0.0301
Case 3	0.0376	0.5% – 0.2%	2998 – 1940	0.0353
Case 4	0.008	1.2% – 0.4%	4650 – 2685	0.0278

Recognizing that Eq. (6) is nondimensional, λ has the inverse units of time. Recasting Eq. (5) in a form similar to Eq. (6), we obtain

$$\frac{\rho_H - \rho_f}{\rho_{H,0} - \rho_f} = (1 + t^*)^{-2}, \quad (8)$$

where

$$t^* = t/t_\Delta,$$

and

$$t_\Delta = \sqrt{\frac{\rho_f}{\rho_{H,0} - \rho_f}}\frac{2V_H}{Q^*\sqrt{D^5 g}}\left(\frac{V_L}{V_H + V_L}\right)^{3/2}. \quad (9)$$

Substituting for Q^* from Eq. (1), we simplify Eq. (9) to

$$t_\Delta = \frac{V_H}{Q}\left(2\sqrt{\frac{\Delta\rho}{\rho_{H,0} - \rho_f}}\left(\frac{V_L}{V_H + V_L}\right)^{3/2}\right). \quad (10)$$

From Eq. (10), t_Δ appears to be a physically reasonable time scale for the decay of the driving potential, $(\rho_H - \rho_L)$. It can be seen from Eq. (8) that at $t = t_\Delta$ (i.e., at $t^* = 1$), $(\rho_H - \rho_L)$ decreases by a factor of 4.0 from the initial density difference. Figure 3(*b*) shows that the density data collapse into one curve for all the four cases when the time is normalized by the time scale given by Eq. (9). The regression parameter, λ, is found to be the inverse of this time scale calculated for each experimental condition. This is possible only because Q^* is a constant, which will be verified next. The plot of Q and Q^* versus time for $L/D = 0.0376$ is presented in Fig. 2(*b*). It must be noted that Q^* varies by only 0.33 percent over the course of the experiment, whereas Q decreases by 33 percent. Plots of Q^* versus time

Table 2 Epstein's (1988) results for oscillatory exchange flows

L/D	$\frac{\Delta\rho}{\bar{\rho}}$	Re (approx.)	Q^* (expt)	Q^* (eqn. 23)
0.015	9.1%	8790	0.0498	0.0550
0.015	3.8%	5680	0.0590	0.0550
0.028	9.9%	2360	0.0529	0.0551
0.028	3.4%	1380	0.0610	0.0551

(From Epstein's theory, $Q^* = 0.04$ for $L/D \leq 0.15$)

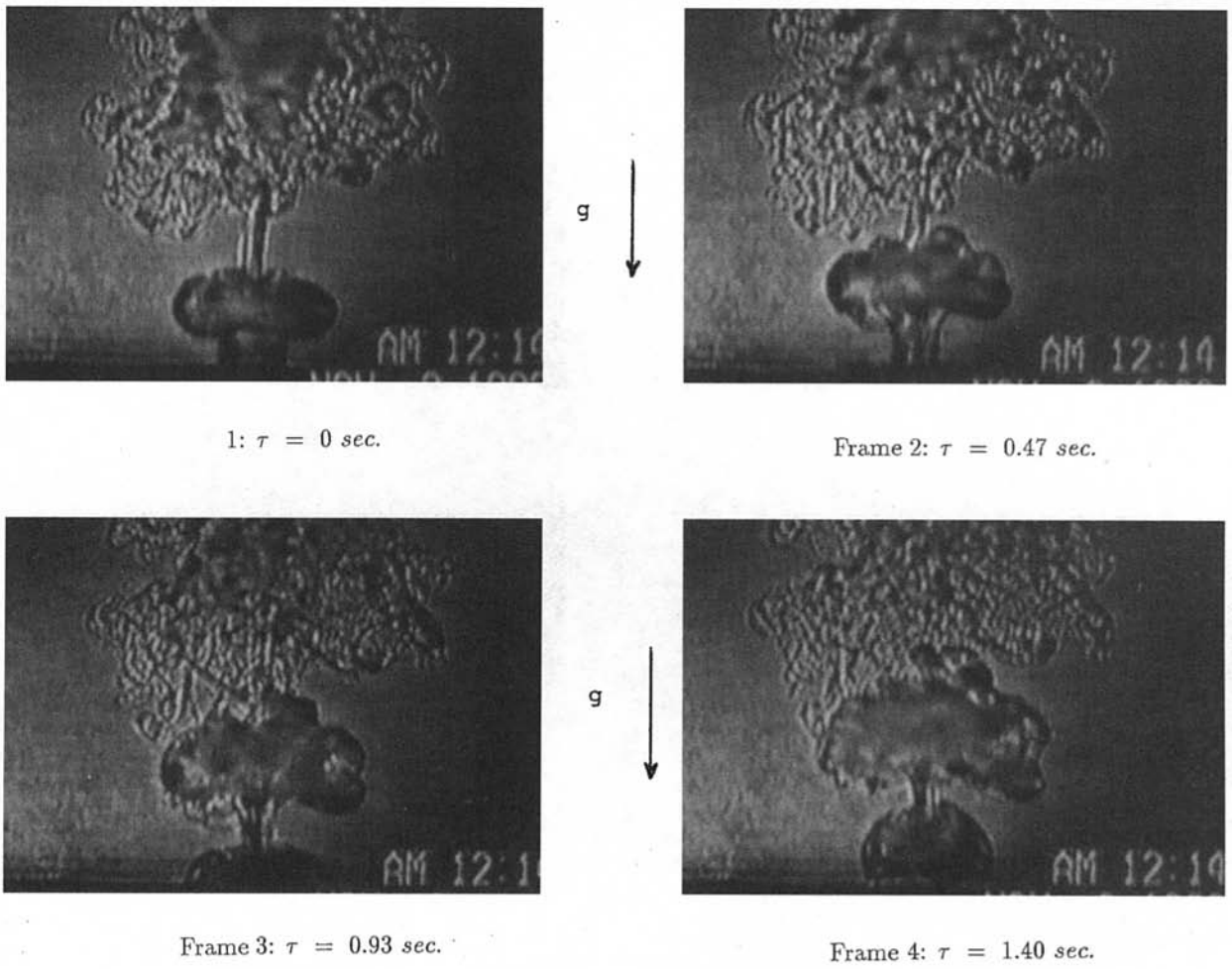

1: $\tau = 0$ *sec.*

Frame 2: $\tau = 0.47$ *sec.*

Frame 3: $\tau = 0.93$ *sec.*

Frame 4: $\tau = 1.40$ *sec.*

Fig. 4 Shadowgraphic flow visualization for $L/D = 0.0376$

for other cases also showed that Q^* remained constant throughout the experiment.

The values of Q^* for different cases as well as the operating parameters are given in Table 1.

For comparison, the results from Epstein's (1988) study for oscillatory flow regime are given in Table 2. Epstein's experimental values for Q^* are different from those obtained in this study. The differences may be attributed to higher values of $\Delta\rho/\overline{\rho}$ and Re. The Boussinesq assumption is not valid for large values of the parameter $\Delta\rho/\overline{\rho}$, causing the exchange flow to depend on that parameter. However, in Epstein's study as well as in the current study, it can be seen that increase in $\Delta\rho/\overline{\rho}$ reduces Q^* slightly (e.g., compare Case 2 and Case 3 of the current study). More studies are needed to clarify this apparent difference between the results of these two studies. It should be noted that Epstein's theoretically predicted value (0.04 for all $L/D < 0.15$) for Q^* is closer to the results of the current study compared to his experimental results.

Flow Visualization. The flow field for Case 2 is studied in detail with shadowgraphic flow visualization. Study of the shadowgraphic images captured in a video tape reveals the flow pulsation. As the density differential decreases with time because of the exchange flow, the pulsation frequency also decreases. This is consistent with the observation that the continuous decay in density differential causes the *driving force* behind the exchange, and hence also the flow rate, to decrease. A frame-by-frame study also reveals the time period and hence the frequency of pulsation.

The pulsation process occurs as follows. First, the brine in the top compartment and the water in the bottom compartment flow radially inward toward the vent at low velocities on either side of the vent. As the two flows reach the vent, an interface is formed between brine and water. The interface oscillates with concentric waves that begin at the vent edge and grow in amplitude as they progress inward. When the wave crest reaches almost half the radius inward it becomes unstable and breaks off as a water blob upward into the brine compartment. A quarter of a cycle later, the trough of the interfacial wave approaches half the vent radius, and breaks downward as a brine blob into the water compartment.

The photographs in Fig. 4 show the details of this process. The entire cycle of pulsation is pictured in 8 frames at an interval of $\frac{1}{8}$ of a period. The pictures are taken 1200 seconds after the start of an experiment with $L/D = 0.0376$ and initial $\Delta\rho/\overline{\rho} = 1.2$ percent. The cycle begins at $\tau = 0$ (where τ is the time from the start of this cycle) and ends at $\tau = 3.73$ seconds. The last photograph shown is taken at $\tau = 3.27$ seconds since flow patterns are identical at $\tau = 0$ and $\tau = 3.73$ seconds. It should be noted that the period of the cycle would increase as time progresses, i.e., as the driving potential decays.

The interfacial wave at the vent becomes unstable and develops into a plume. This can be seen in frame 1. Following the plume rises a toroidal blob of water enveloping the long stem left over by the plume. The toroidal blob rises toward the plume (frame 2) and moves closer to the plume (frame 3). At the same time, it can be seen in frame 3 that a new toroidal blob emerges upward from the vent. This blob is more visible in

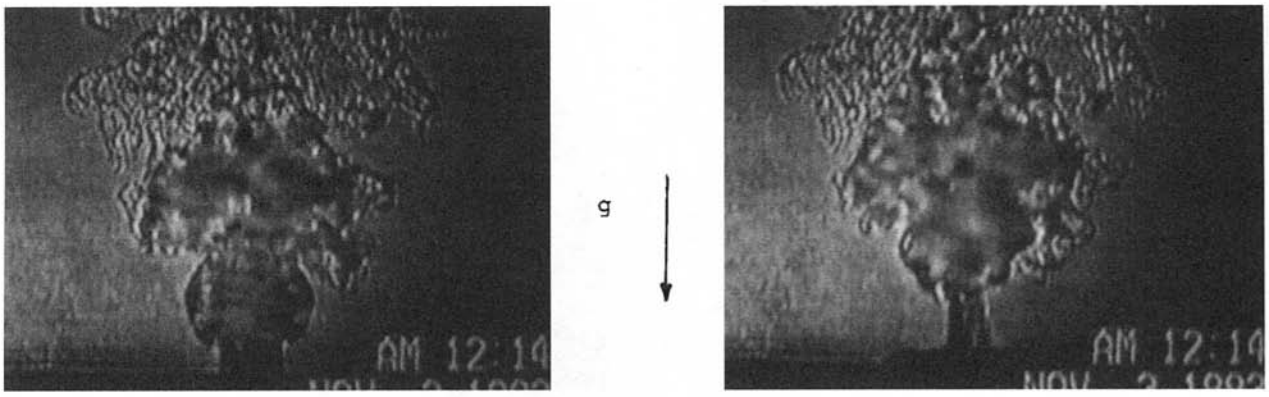

Frame 5: $\tau = 1.87$ *sec.*

Frame 6: $\tau = 2.33$ *sec.*

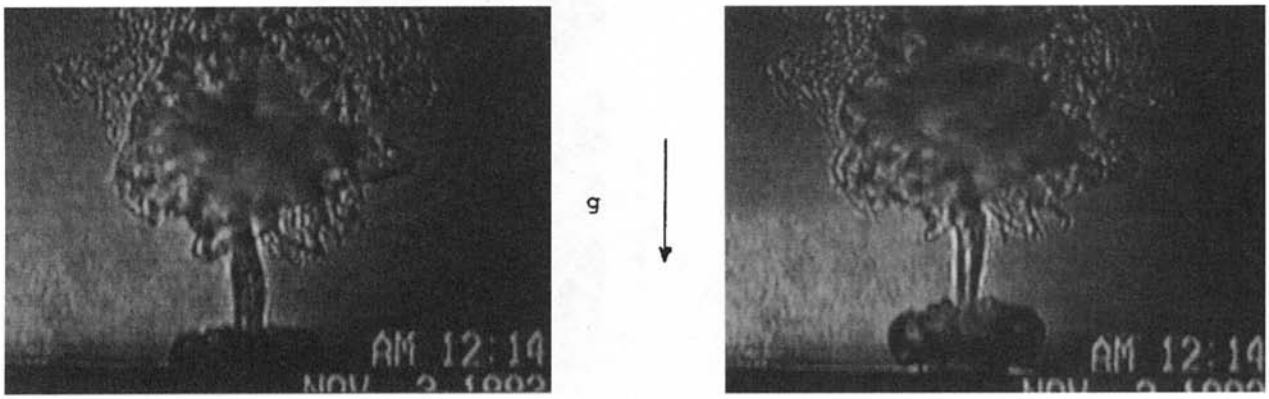

Frame 7: $\tau = 2.80$ *sec.*

Frame 8: $\tau = 3.27$ *sec.*

Fig. 4 (Continued)

frame 4 in which the previous blob has not yet completely merged with the plume. The new blob rises in the wake of the previous blob and hence merges with the plume much faster as shown in frames 5 and 6. In frame 6, the plume is in the shape of a bigger cloud and entrains less brine, and hence moves upward faster. Therefore, the third blob that originates at the vent (frame 7) is unable to catch up with the plume and a long stem is formed between the plume and this blob (frame 8), and the cycle repeats itself.

When the cycle is ongoing in the top compartment, a mirror image of the same process takes place in the lower compartment. The events in the two compartments are out-of-phase by a quarter of a period. When the long stem appears in the top compartment as shown in frame 2, a toroidal brine blob flows downward, and the cycle continues with alternating water and brine pulsations.

LDV Measurements. LDV measurements confirm the qualitative flow patterns suggested by flow visualization. The LDV measurements are performed not at the edge of the vent but half a vent diameter above it. As a result the vertical component of flow as measured by LDV also includes entrainment, with the upward motion in the center and the downward motion in the outer portion of the upper compartment. For this reason, in this study, LDV measurements are used for spectral analysis only, and not for quantitative analysis of flow. Representative velocity profiles obtained from LDV measurements can be found in Conover and Kumar (1993).

For the purpose of spectral analysis of the pulsating flow, the vertical component of velocity is monitored on the axis of the vent at about half a vent diameter above the upper edge of the vent. The frequency of pulsations is measured from the power spectrum of LDV data. Figure 5(a) shows the spectrum at a typical instant for Case 2, $L/D = 0.0376$. A single clearly defined frequency can be identified from the spectrum at 0.55 Hz. The frequency bin width is 0.01 Hz. For this case, LDV measurements are performed 11 times during the transient process; in each measurement the time series of data is taken for about 100 seconds. The pulsation frequency decreases by about 0.01 Hz over 100 seconds. Hence there is negligible spectral broadening at the frequency of pulsation. Thus the frequency of pulsation as calculated from the spectrum is not affected by the long sampling duration.

As the *driving force* for the buoyant flow decreases with time, so does the frequency of pulsation. Figure 5(b) shows the decay in the pulsation frequency for Case 2 ($L/D = 0.0376$). After the first point, the pulsation frequency decreases monotonically from 0.7 Hz to 0.45 Hz. The curve shown is a line proportional to $Q(t)$ with the constant of proportionality equal to 0.104 Hz/cm^3/s. If the first point is ignored, the frequency decays about 25 percent faster than the flow rate.

The corresponding spectrum for Case 1 is shown in Fig. 6(a). For this aspect ratio of $L/D = 0.106$, the interface between fluids from two compartments is usually disorganized, and the interface can be seen to be moving up and down the vent. Pulsations can often, but not always, be seen; periodicity is still readily apparent in spectral analysis. Experiments with still larger aspect ratio do not produce any pulsating flow. Thus the demarcation between regimes I and II is around $L/D = 0.106$ for this set of experiments.

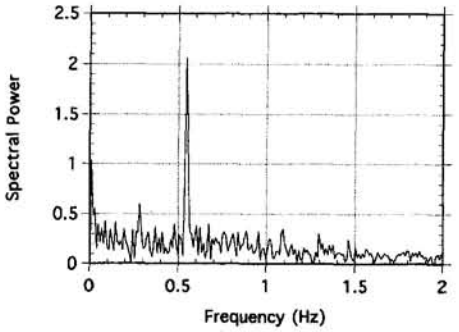

(a) Typical Power Spectrum for Pulsation

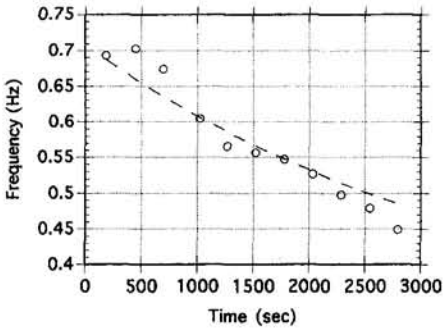

(b) Decay of Pulsation Frequency

Fig. 5 Pulsation frequency for $L/D = 0.0376$

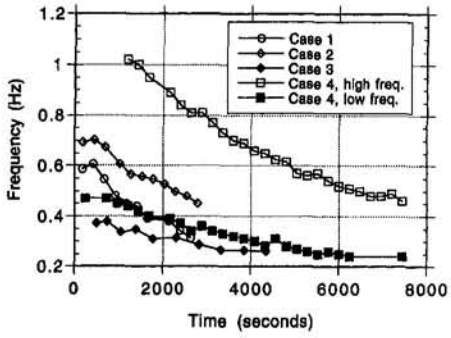

(a) Pulsation Frequency

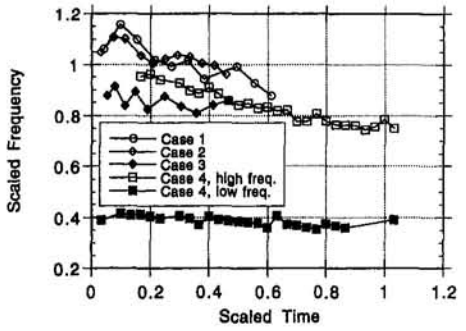

(b) Normalized Pulsation Frequency

Fig. 7 Decay of pulsation frequency

For the smallest aspect ratio that is studied (Case 4: $L/D = 0.008$), spectral analysis (Fig. 6(b)) suggests the presence of two frequencies. These two frequencies are found to decay at different rates, suggesting that the physical origins of these two frequencies are perhaps different. The lower frequency decays at the same rate as the exchange flow. The higher frequency decreases in the same way as in the other cases, i.e., at a rate faster than the rate of decay of the exchange flow. A second peak at a lower frequency ($\approx$ 0.3 Hz) can also be seen for $L/D = 0.0376$ (Fig. 5(a)) although this second peak is less dominating than the other. Figure 7(a) shows the decay of pulsation frequencies for all cases. For Case 1 ($L/D = 0.0376$), only the dominant frequency is shown in this figure.

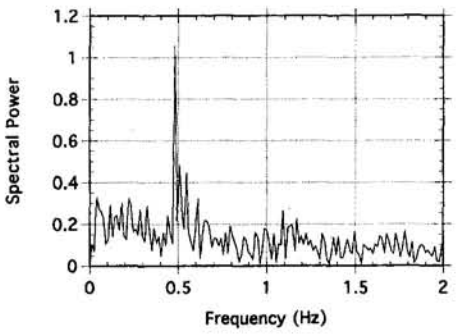

(a) $L/D = 0.106$

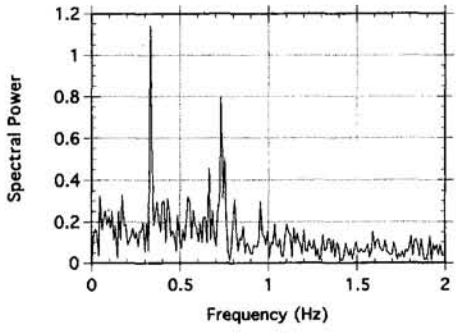

(b) $L/D = 0.008$

Fig. 6 Typical power spectra

This second peak may be attributed to a secondary phenomenon of the formation of secondary ripples in the circumferential direction in the brine-water interface. At the vent edge the ripples are about $\frac{1}{8}$ in. or $\frac{3}{16}$ in. from crest to crest with amplitude approximately equal to L in the two thinnest vents ($L/D = 0.0376, 0.008$; these ripples are not observed for $L/D = 0.106$). Proceeding inward radially, the ripples become closer together and increase in amplitude. The superimposed ripples become unstable and the ripples quickly disappear in the rolling motion of the ascending (or descending) blobs. The ripples make the flow three dimensional because there is a significant circumferential dependency of axial and radial velocities at the point where the ripples get unstable.

Figure 7(b) shows the decay of pulsation frequency for all cases where time has been scaled by t_Δ and the frequency has been scaled by $f_\Delta = W_n(t)/\sqrt{LD} = Q(t)/0.5A_{vent}\sqrt{LD}$. Here, $W_n(t) = Q(t)/0.5A_{vent}$ is the velocity at the vent as given by $Q(t)$. This frequency scale f_Δ has been found to work better than the more natural scales of frequency such as W_n/L or W_n/D. This indicates that the pulsation phenomenon is governed not by L or D alone, but by both L and D. This figure also shows that the higher frequency for Case 4 ($L/D = 0.008$) is the one that scales with the pulsation frequencies for the other cases. This indicates that the origin for the lower frequency for Case 4 is different from that for the other frequencies.

Summary and Conclusions

The pulsating flow phenomenon of a buoyant flow in vents with low aspect ratio ($L/D \leq 0.106$) has been observed with

flow visualization and LDV measurements. A phenomenological model has been given and conclusions made as follows:

1 The volumetric exchange flow rate Q scaled by $Q_\Delta = \sqrt{D^5 g \Delta\rho/\bar{\rho}}$ has been found to be a function of aspect ratio L/D only, for Reynolds number range of $1940 \leq \mathrm{Re}_\Delta \leq 4650$.
2 A time scale for this transient process, based on rate of decay of ρ_H, collapses all experimental data sets for decay of ρ_H into one curve.
3 Flow visualization shows large recirculation motions in the two compartments forcing brine in the top compartment and water in the bottom compartment to flow radially inward toward the vent, forming an interface at the vent. At a certain radial distance from the vent center, the interface becomes unstable, contributing to alternating water and brine pulsations in the two compartments. The frequency of this pulsation has been determined from spectral analysis of LDV data.
4 For vents with aspect ratios of 0.008 and 0.0376, a second frequency was found from the spectral analysis. The interfacial waves, found responsible for the primary pulsation frequency, grow in amplitudes as they move radially inward, forming secondary ripples in the circumferential direction. These ripples, which have been found only in very low aspect ratio vents, may be the cause of the second pulsation.
5 $f_s = W_n(t)/\sqrt{LD}$ has provided a frequency scale for the decaying frequencies for all cases studied. A plot of scaled frequencies as a function of scaled time clearly separates the pulsation frequencies caused by different flow phenomena.

Acknowledgments

The authors acknowledge the financial support provided by the US Department of Energy through a DOE/SCUREF grant.

References

Brown, W., 1962, "Natural Convection Through Rectangular Openings in Partitions—2: Horizontal Partitions," *Int. J. Heat Mass Transfer,* Vol. 5, pp. 869–878.

Brown, W., and Solvason, K., 1962, "Natural Convection Through Rectangular Openings in Partitions—1: Vertical Partitions," *Int. J. Heat Mass Transfer,* Vol. 5, pp. 859–868.

Conover, T. A., and Kumar, R., 1993, "LDV Study of Buoyant Exchange Flow Through a Vertical Tube," presented at the 5th International Conference on Laser Anemometry: Advances and Applications, Veldohoven, Netherlands.

Cooper, L. Y., 1994, "Combined Buoyancy- and Pressure-Driven Flow Through a Shallow Horizontal Circular Vent," Report NISTIR 5384, National Institute of Standards and Technology, Gaithersburg, MD.

Emmons, H., 1988, "Vent Flows," *SFPE Handbook of Fire Protection Eng.,* Soc. Fire Protection Eng., Boston, MA, Sec. 1, Chap. 8.

Epstein, M., 1988, "Buoyancy-Driven Exchange Flow Through Small Openings in Horizontal Partitions," ASME JOURNAL OF HEAT TRANSFER, Vol. 110, pp. 885–893.

Epstein, M., and Kenton, M., 1989, "Combined Natural Convection and Forced Flow Through Small Openings in a Horizontal Partition, With Special Reference to Flows in Multicomponent Enclosures," ASME JOURNAL OF HEAT TRANSFER, Vol. 111, pp. 980–987.

Gebhart, B., Jaluria, Y., Mahajan, R. L., and Sammakia, B., 1988, *Buoyancy Induced Flows and Transport,* Hemisphere, New York.

Heskestad, G., and Spaulding, R. D., 1991, "Inflow of Air Required at Wall and Ceiling Apertures to Prevent Escape of Fire Smoke," *Proc. 3rd Intl. Symp. Fire Safety Science,* Elsevier, New York, pp. 919–928.

Jaluria, Y., and Cooper, L. Y., 1989, "Negatively Buoyant Wall Flows Generated in Enclosure Fires," *Prog. Energy Combust. Sci.,* Vol. 15, pp. 159–182.

Jaluria, Y., Lee, S. H.-K., Mercier, G. P., and Tan, Q., 1993, "Visualization of Transport Across a Horizontal Vent Due to Density and Pressure Differences," *Visualization of Heat Transfer Processes,* ASME HTD-Vol. 252; pp. 65–81.

Keulegan, G., 1958, *Twelfth Progress Report on Model Laws for Density Currents: The Motion of Saline Fronts in Still Waters,* National Bureau of Standards, Report No. 5831.

Prahl, J., and Emmons, H. W., 1975, "Fire Induced Flow Through an Opening," *Combust. and Flame,* Vol. 25, pp. 369–385.

Steckler, K. D., Quintiere, J. G., and Rinkinen, W. J., 1982, "Growth of Fire in Building Compartments," *19th Symposium (Int.) on Combustion,* The Combustion Institute, Pittsburgh, PA, pp. 913–920.

Steckler, K. D., Baum, H., and Quintiere, J. G., 1984, "Fire Induced Flow Through Room Openings—Flow Coefficients," *20th Symposium (Int.) on Combustion,* The Combustion Institute, Pittsburgh, PA, pp. 1591–1600.

Steckler, K. D., Baum, H., and Quintiere, J. G., 1986, "Salt Water Modeling of Fire Induced Flows in Multicompartment Enclosures," *21st Symposium (Int.) on Combustion,* The Combustion Institute, Pittsburgh, PA, pp. 143–149.

Tan, Q., and Jaluria, Y., 1992, "Flow Through a Horizontal Vent in an Enclosure Fire," *Fire and Combustion Systems,* ASME HTD-Vol. 199; pp. 115–122.

Computation of Turbulent Flow in Mixed Convection in a Cavity With a Localized Heat Source

E. Papanicolaou
Institute of Hydromechanics,
University of Karlsruhe, 71628 Karlsruhe,
Federal Republic of Germany
Assoc. Mem. ASME

Y. Jaluria
Department of Mechanical &
Aerospace Engineering,
Rutgers, The State University
of New Jersey,
New Brunswick, NJ 08903
Fellow ASME

A numerical simulation of the turbulent transport from an isolated heat source in a square cavity with side openings is presented in this work. The openings allow an externally induced air stream at ambient temperature to flow through the cavity and, thus, mixed convection arises. Results for the turbulent regime are obtained, by employing a suitable, high-Reynolds-number form of the $K-E$ turbulence model. A stream function–vorticity mathematical formulation is used, along with the kinetic energy and dissipation rate equations and an expression for the eddy viscosity. A time-marching scheme is employed, using the ADI method. The values of the Reynolds number Re, associated with the external flow, and the Grashof number Gr, based on the heat flux from the source, for which turbulent flow sets in are sought. Two typical values of the Reynolds number are chosen, Re = 1000 and Re = 2000, and turbulent results are obtained in the range $Gr = 5 \times 10^7 - 5 \times 10^8$. For both values of Re, the average Nusselt number over the surface of the source is found to vary with Gr in a fashion consistent with previous numerical and experimental results for closed cavities, while the effect of Re in the chosen range of values was small.

Introduction

The interaction between a buoyancy-induced thermal plume from a heat source and an externally driven cold flow inside a cavity constitutes a physical configuration, which is often encountered in electronic cooling applications and ventilation of rooms, among others. Similar convective heat transfer problems involving turbulent flow have been studied numerically in recent years by various investigators. Among the existing computational models, the $K-E$ model has been the most widely used one, particularly in internal flows, i.e., flows in enclosures, cavities and channels.

The study by Nielsen (1975) appears to be the first to have used the $K-E$ model for a recirculating flow. Buoyancy effects were included in the vorticity equation but not in the k and ϵ equations. This was also the first study to deal with a mixed convection problem, using the Archimedes number, which is the same as the Richardson number Gr/Re^2, as the governing parameter. The ventilation of a room was also the motivation for the three-dimensional study by Hjertager and Magnussen (1977). Their $K-E$ model included buoyancy effects only in the momentum equations and not in the k and ϵ equations.

It was only in the work by Fraikin et al. (1982) that a recirculating flow was solved numerically using the $K-E$ model with the buoyancy effects included both in the equations of motion and in the k and ϵ equations. They considered natural convection in a cavity with two differentially heated side walls and perfectly conducting horizontal boundaries. In this configuration, it is now known from more recent studies (see Papanicolaou and Jaluria, 1992, for a review) that a Hopf bifurcation occurs at a Rayleigh number of approximately 2.2×10^5. Fraikin et al. obtained results in the transition range, for Grashof number $Gr = 6.6 \times 10^6 - 10^8$, corresponding to Rayleigh numbers $Ra = 4.32 \times 10^6 - 7.2 \times 10^7$. They derived a correlation for the average Nusselt number in terms of the Grashof number. Turbulent flow results for mixed convection in shallow enclosures of various aspect ratios were also obtained in the numerical work by Cha and Jaluria (1984) using an eddy-viscosity model.

Ozoe et al. (1984) used the $K-E$ model for three-dimensional natural convection computations in a cubical enclosure ($Ra = 10^6$), using a vector potential-vorticity formulation. The same configuration was studied in the presence of an external horizontal flow by Ozoe et al. (1986), at Re = 123 and 61.4, and Rayleigh number fixed at $Ra = 10^7$. Two-dimensional results for natural convection in water were also presented by Ozoe et al. (1985), for enclosures with aspect ratio (length/height) of 1 and 2 and heated from the sides, for $Ra \geq 10^{10}$.

A mixed convection problem was studied numerically and experimentally by Hoogendoorn (1985), who simulated the stratified flow of air in a corridor adjacent to a room with a fire. He obtained results using the $K-E$ model for a shallow enclosure of aspect ratio (length/height) equal to 7 and two air streams at different temperatures flowing through. Humphrey and To (1986) obtained results both for both natural and mixed convection flow in a partially opened cavity. They used a variation of the low-Reynolds-number $K-E$ model (Launder and Spalding, 1974), with variable density in their governing equations and the effect of the temperature fluctuations T' included. Mixed convection results were obtained for $Re^2/Gr = 0.4$, 0.85, 21.3, and 85.4 and heat transfer correlations were derived.

More recently, numerical results were presented by Abrous and Emery (1989), Hanjalic and Vasic (1990), and Nobile et al. (1990) for turbulent natural convection in a cavity. The studies by Abrous and Emery (1989) and Hanjalic and Vasic (1990) considered a variety of boundary conditions on the vertical and horizontal walls, along with internal partitions in the cavity. In addition, Abrous and Emery (1989) studied the effects of localized heating at the bottom surface and of a horizontal injection of cold air into the cavity, two aspects that are of relevance in the present investigation.

Here, the turbulent transport from an isolated, constant heat flux source is simulated, in a square cavity with two openings, allowing for a throughflow of air. The basic configuration is shown in Fig. 1. It is similar to the cavity studied by Papanicolaou and Jaluria (1990), except for a channel of length L_o, which is added at the outflow. The purpose of this channel will be explained later. All the walls of the cavity are taken as

Contributed by the Heat Transfer Division and presented at the ASME Winter Annual Meeting, Anaheim, California, November 8–13, 1992. Manuscript received by the Heat Transfer Division February 1994; revision received January 1995. Keywords: Enclosure Flows, Mixed Convection, Turbulence. Associate Technical Editor: R. Viskanta.

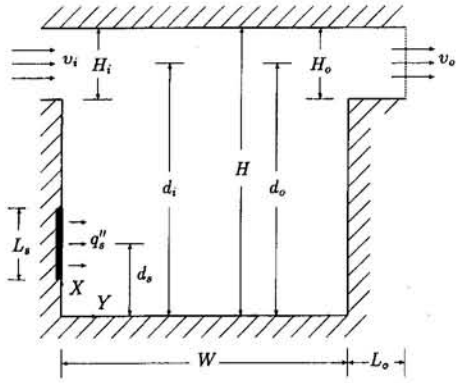

Fig. 1 Physical model of the cavity with adiabatic walls and a flush source on the left side wall, used to obtain solutions for turbulent flow

adiabatic, therefore all the heat generated by the source is carried away from the enclosure by the exiting airflow. As of this date, there are no available data, numerical or experimental, for turbulent flow in such a configuration, which involves: (*a*) a cavity heated from the side with *localized* rather than uniform *heating;* (*b*) a heat source subject to a *constant heat flux* as opposed to an isothermal *condition* and all other walls adiabatic; (*c*) interaction between a vertical buoyancy-driven flow and a horizontal forced flow, i.e., two flows in directions *perpendicular to each other.*

The laminar regime for the flow and heat transfer in such a configuration has been studied in a previous work by Papanicolaou and Jaluria (1990). Conjugate effects and multiple heat sources have also been considered (Papanicolaou, 1991). The governing parameters are the Reynolds number Re of the external flow, and the Grashof number Gr based on the constant heat flux from the source. For a fixed Re, it is known (Papanicolaou and Jaluria, 1990, 1992) that there is a critical Grashof number Gr_{cr} at which transition from a laminar to a periodic, oscillatory regime occurs. If Gr is further increased, it is expected that other transitions will take place, eventually leading to the turbulent regime. Here, only the initial stages of the turbulent flow regime are investigated, by specifying values of Gr at least an order of magnitude higher than Gr_{cr} and by using a suitable turbulence model. Results for the flow, temperature, and heat transfer are obtained, the average Nusselt number from the source is computed, and comparisons are made with previous studies, wherever applicable.

Mathematical Formulation

Model Equations. The governing equations are obtained in a stream function-vorticity formulation and the K–E model is used in its high-Re (or standard) form. The stream function equation is the same as that in the laminar case (Papanicolaou and Jaluria, 1990), while the vorticity equation is obtained by taking the *curl* of the momentum equation, and is written in the form given by Fraikin et al. (1982). The equations are nondimensionalized as shown in the nomenclature and, keeping in mind that they describe only variations in the mean quantities, the following system of dimensionless equations can be written:

Vorticity Transport Equation:

$$\frac{\partial \Omega}{\partial \tau} + \nabla\cdot(\vec{V}\,\Omega) = -\frac{\mathrm{Gr}}{\mathrm{Re}^2}\frac{\partial \theta}{\partial Y} + \frac{1}{\mathrm{Re}}\nabla^2\Omega + \frac{1}{\mathrm{Re}}\left(\frac{\partial^2}{\partial X^2} - \frac{\partial^2}{\partial Y^2}\right)\left[\nu_t^*\left(\frac{\partial U}{\partial Y} + \frac{\partial V}{\partial X}\right)\right] - \frac{1}{\mathrm{Re}}\frac{\partial^2}{\partial X \partial Y}\left[2\nu_t^*\left(\frac{\partial U}{\partial X} - \frac{\partial V}{\partial Y}\right)\right] \quad (1)$$

Stream Function Equation:

$$\nabla^2\Psi = -\Omega \quad (2)$$

Nomenclature

C_P = specific heat under constant pressure
d = vertical distance from the bottom of the cavity
E = dimensionless rate of dissipation of K; $E = \epsilon H_i^2/\nu v_i^2$
g = magnitude of the gravitational acceleration
Gr = Grashof number = $g\beta\Delta T H_i^3/\nu^2$
$\bar{h}$ = average heat transfer coefficient over the surface of the heat source
H = height of the cavity
H_i, H_o = height of the inlet and outlet openings, respectively
k = turbulent kinetic energy
K = dimensionless turbulent kinetic energy = k/v_i^2
L_s = length of the heat source
Nu_s = average Nusselt number over the surface of the heat source
P = dimensionless local pressure = $p/\rho v_i^2$
Pr = Prandtl number of air = ν/α
q_s'' = heat flux per unit surface area of the source
Re = Reynolds number = $v_i H_i/\nu$
T = local temperature
u, v = vertical and horizontal velocity components, respectively
$\vec{V}$ = dimensionless velocity vector = $(U, V) = (u/v_i, v/v_i)$
W = width of the cavity
x, y = vertical and horizontal coordinate distances, respectively
X, Y = dimensionless vertical and horizontal coordinate distances, respectively; $X = x/H_i$, $Y = y/H_i$
α = thermal diffusivity of air
α_t = eddy diffusivity of heat
β = coefficient of thermal expansion of air $\equiv -(1/\rho)(\partial\rho/\partial T)_p$
ΔT = temperature scale = $q_s'' H_i/\lambda$
ϵ = rate of dissipation of turbulent kinetic energy
θ = dimensionless temperature = $(T - T_i)/\Delta T$
λ = thermal conductivity of air
ν = kinematic viscosity of air
ν_t^* = turbulent/molecular viscosity ratio = ν_t/ν
ρ = density of air
σ_K, σ_E = Prandtl number for the turbulent kinetic energy and its rate of dissipation, respectively
σ_t = turbulent Prandtl number = ν_t/α_t
τ' = physical time
τ = dimensionless time = $\tau'(v_i/H_i)$
v_i = mean value of the horizontal velocity component at the inflow
Ψ = dimensionless stream function; $U = \partial\Psi/\partial Y$, $V = -\partial\Psi/\partial X$
Ω = dimensionless vorticity = $\partial V/\partial X - \partial U/\partial Y$

Subscripts

E, W, N, S = neighbor grid point to the right, left, top, and bottom of the control volume, respectively
P = grid point at the center of the control volume
w = value of a variable at the wall

Energy equation:

$$\frac{\partial \theta}{\partial \tau} + \nabla\cdot(\vec{V}\theta) = \frac{1}{\mathrm{Re}}\left(\frac{1}{\mathrm{Pr}} + \frac{\nu_t^*}{\sigma_t}\right)\nabla^2\theta \tag{3}$$

Turbulent Kinetic Energy Equation:

$$\frac{\partial K}{\partial \tau} + \nabla\cdot(\vec{V}K) = \frac{1}{\mathrm{Re}}\nabla\cdot\left[\left(1 + \frac{\nu_t^*}{\sigma_K}\right)\nabla K\right] - E - G + P \tag{4}$$

Dissipation Rate Equation:

$$\frac{\partial E}{\partial \tau} + \nabla\cdot(\vec{V}E) = \frac{1}{\mathrm{Re}}\nabla\cdot\left[\left(1 + \frac{\nu_t^*}{\sigma_E}\right)\nabla E\right] - C_2\frac{E^2}{K} - C_3 G\frac{E}{K} + C_1 P \tag{5}$$

where ∇ is the two-dimensional Laplacian operator and, in order to write Eqs. (4) and (5) in a compact form, two dimensionless quantities P and G are defined as follows:

$$P \equiv \frac{1}{\mathrm{Re}}\nu_t^*\left[2\left(\frac{\partial U}{\partial X}\right)^2 + 2\left(\frac{\partial V}{\partial Y}\right)^2 + \left(\frac{\partial U}{\partial Y} + \frac{\partial V}{\partial X}\right)^2\right],$$

$$G \equiv -\frac{\mathrm{Gr}}{\mathrm{Re}^3}\left(\frac{\nu_t^*}{\sigma_t}\right)\left(\frac{\partial \theta}{\partial Y}\right) \tag{6}$$

The quantity P represents the production of turbulent kinetic energy due to shear, while G, the production of turbulent kinetic energy due to buoyancy. The constants appearing in the equations of the model are set at the following values: $C_\mu = 0.09$, $C_1 = 1.44$, $C_2 = 1.92$, $C_3 = 0.7$, $\sigma_K = 1.0$, $\sigma_E = 1.3$, and $\sigma_t = 0.9$ (Launder and Spalding, 1974). The value of the constant C_3, which only appears in flows with buoyancy effects, is obtained as an average of the corresponding values for vertical and horizontal shear layers. C_3 is a function of the flux Richardson number R_f, which has different values for vertical and horizontal layers and, as discussed by Fraikin et al. (1982), the suggested, average value for C_3, obtained from the two limiting cases, is 0.7. Although derived for different types of flow, the values of these constants have been used successfully with no modifications in natural-convection problems as the ones already referenced. Sensitivity studies for the constants were conducted by Fraikin et al. (1982) and Abrous and Emery (1989). When each of the constants C_1, C_2, and σ_t was individually varied by ±20 percent, the velocities and Nusselt numbers varied within reasonable amounts (less than 10 percent), while the turbulent variables were found to be more sensitive.

In conclusion, the equations to be solved are Eqs. (1)–(5), along with the equation for the eddy viscosity, which is written in nondimensional form as:

$$\nu_t^* = \mathrm{Re}\, C_\mu \frac{K^2}{E} \tag{7}$$

Boundary Conditions. The boundary conditions for the cavity under consideration state that the velocity components are zero ($U = V = 0$) at the solid walls, while for the temperature the gradient normal to the wall is taken as zero (adiabatic condition, $\partial\theta/\partial X = 0$ or $\partial\theta/\partial Y = 0$). The inlet velocity $V_i(X)$ is taken as constant across the opening (uniform flow), at a dimensionless value equal to 1. Since the dimensionless height of the inlet opening is $H_i^* = 1$, the dimensionless stream function at all walls below the inlet and outlet openings is given the value $\Psi = 1$ (dimensionless flow rate of the oncoming flow), while at the top surface: $\Psi = 0$. At the inlet, the temperature condition is $\theta = 0$, while at the heat source, the corresponding boundary condition in dimensionless quantities turns out to be: $\partial\theta/\partial Y = -1$.

The inlet value for K was obtained by assuming 1 percent fluctuations for the inlet velocity V_i. By means of the equation defining K as the sum of velocity fluctuations (Launder and Spalding, 1974), this yields a value $K_i = 10^{-2}$. Initial values for one of the remaining two turbulent quantities ν_t^* or E must then be specified. Here the inlet eddy viscosity $\nu_{t,i}^*$ is arbitrarily assigned a small value, i.e., 10^{-2}, corresponding to an essentially laminar oncoming flow. E_i is then computed from Eq. (7). At the walls the values of K and ν_t^* are set equal to 0. The value of the vorticity at the wall Ω_w is computed from the value of the stream function, as for the laminar case (Papanicolaou and Jaluria, 1990). The corresponding formula is presented below.

At the outflow, the gradients of all variables have been taken equal to zero. In order for this condition to be accurate, it has to be imposed at a certain distance from the right vertical wall. Therefore, at the outflow opening, a channel of length $L_c^* = 0.5$, i.e., $\frac{1}{8}$ of the width of the cavity, is added and the zero-gradient outflow boundary condition is imposed at that location, where $Y = 4.5$. This distance was found to be adequate. The value of the dissipation rate E at the wall is undetermined, because, from the definition of the length scale of turbulence l in the K–E model (Launder and Spalding, 1974), $E \propto K^{3/2}/l$ and, as pointed out by Fraikin et al. (1982), at the wall both K and l are equal to zero. Therefore, the approach used by Fraikin et al. (1982) and Ozoe et al. (1984, 1985, 1986) is employed. All these studies used a stream function–vorticity formulation, but the same version of the K–E model was also used in a primitive variable formulation, by Nobile et al. (1990). According to this approach, E is not solved for at the wall in the numerical solution, but only up to the first grid point from the wall. At that point, denoted by a subscript p, the value of E is prescribed by the equation:

$$E_p = \frac{C_\mu^{3/4} K_p^{3/2}}{\kappa(\delta n)_p} \tag{8}$$

where C_μ is the constant appearing in Eq. (7), κ is von Karman's constant and is equal to 0.42, and $(\delta n)_p$ is the distance of the first grid point from the wall (Fraikin et al. 1982). For details on the derivation of Eq. (8), see Rodi (1980) and Arpaci and Larsen (1984). Equation (8) is used to compute the value of E_p after the value K_p has been computed.

Equation (8) is the only wall function that is still being used for natural convection boundary layers. As discussed by Henkes (1990), the logarithmic wall functions for the velocity and the temperature given by Launder and Spalding (1974) are not valid for natural convection boundary layers; this is true for Eq. (8) as well. However, this equation has been used successfully in the numerical studies mentioned above. It is also recommended that $x^+ < 11.5$ at the first grid point in natural convection boundary layers (Henkes, 1990). This was also checked in our computations as discussed later, since a natural convection boundary layer is expected to develop over the source, along the left vertical wall.

Numerical Scheme—K–E Model

Discretization of the Equations. The numerical procedure is similar to the one described by Papanicolaou and Jaluria (1990) for the equations that govern the laminar flow. However, there are two additional equations, Eqs. (4) and (5), and additional terms in the vorticity equation for turbulent flows. All these require special treatment, especially the source terms in the equations. Equations (1) and (3)–(5) can be written in the

following common form:

$$\frac{\partial \phi}{\partial \tau} + \nabla \cdot \bar{J} = S_\phi \tag{9}$$

where $\bar{J} = \bar{V}\phi - \Gamma_\phi \nabla \phi$ is the total (convective + diffusive) flux. It can now be recognized that the diffusion coefficient for the vorticity is the same as in the discretization of the laminar flow equations, i.e., $\Gamma_\Omega = 1/\mathrm{Re}$. The diffusion coefficients in the θ, K, and E equations are, respectively:

$$\Gamma_\theta = \frac{1}{\mathrm{Re}}\left(\frac{1}{\mathrm{Pr}} + \frac{\nu_t^*}{\sigma_t}\right), \quad \Gamma_K = \frac{1}{\mathrm{Re}}\left(1 + \frac{\nu_t^*}{\sigma_K}\right),$$

$$\Gamma_E = \frac{1}{\mathrm{Re}}\left(1 + \frac{\nu_t^*}{\sigma_E}\right) \tag{10}$$

The corresponding source terms are:

$$S_\Omega = -\frac{\mathrm{Gr}}{\mathrm{Re}^2}\frac{\partial \theta}{\partial Y} + \frac{1}{\mathrm{Re}}\left(\frac{\partial^2}{\partial X^2} - \frac{\partial^2}{\partial Y^2}\right)\left[\nu_t^*\left(\frac{\partial U}{\partial Y} + \frac{\partial V}{\partial X}\right)\right] - \frac{1}{\mathrm{Re}}\frac{\partial^2}{\partial X \partial Y}\left[2\nu_t^*\left(\frac{\partial U}{\partial X} - \frac{\partial V}{\partial Y}\right)\right],$$

$$S_\theta = 0, \quad S_K = P + G - E,$$

$$S_E = (C_1 P + C_3 G)\frac{E}{K} - C_2\frac{E^2}{K} \tag{11}$$

The next step is to integrate Eq. (9) over each control volume, as described by Patankar (1980), to obtain the following algebraic equation:

$$\frac{\partial \phi}{\partial \tau}\Delta V + \sum_i a_i(\phi_p - \phi_i) = \int_{\Delta V} S_\phi dV \tag{12}$$

where $i = N, S, E, W$, and the coefficients a_i are as defined by Papanicolaou and Jaluria (1990). The power-law approximation (Patankar, 1980) is used here for the convective terms, since it provides a fairly accurate representation for the flux $\bar{J}$ of the transported quantities between two adjacent nodes, while also being computationally more efficient than the exact, exponential expression. The integration of the source terms S_ϕ requires a series of algebraic manipulations, details of which can be found in Papanicolaou (1991). After the integrations are carried out and the algebraic form of the equations is obtained, the Alternating Direction Implicit (ADI) method is applied to the energy, vorticity, kinetic energy, and dissipation rate equations, exactly as described by Papanicolaou and Jaluria (1990). The application of the ADI method leads to tridiagonal systems for each of the variables θ, Ω, K, and E. The stream function equation is solved by the Successive Over-Relaxation (SOR) method (Roache, 1972) and the wall vorticity is computed from the formula:

$$\Omega_w = -\frac{2(\Psi_{w+1} - \Psi_w)}{(\Delta n)^2} \tag{13}$$

This is a first-order formula, which is valid for nonuniform grids as well. It is more stable than the second-order form (Roache, 1972), whose accuracy is reduced for nonuniform grids. Therefore, this first-order approximation was found to be adequate here.

Computational Grid. The cavity shown in Fig. 1 is discretized using a 31 × 39 nonuniform grid. The locations of the grid points in the Y direction are given by the functions suggested by Henkes (1990):

$$Y_j = \frac{1}{2}W^*\left[1 + \frac{\tanh\{a_1(j/n - \frac{1}{2})\}}{\tanh(a_1/2)}\right] \tag{14}$$

where $j = 1, 2, \ldots, n$ and n is the total number of grid points in the horizontal direction, inside the cavity. The parameter a_1 is given by $a_2 = a_1/\sinh(a_1)$, where the best choice for a_2 in the present case was found to be $a_2 = 0.15$. This value does not severely reduce the minimum grid spacing and therefore allows for a reasonably high value of the time step. In the X (vertical) direction there are more constraints, because the placement of the grid points must guarantee that $H_i^* = L_s^* = 1$. In order to have better control on these fixed dimensions, a locally nonuniform grid in the X direction was chosen. Near the bottom of the cavity a region of geometrically reducing grid spacings is considered, above which the grid is uniform up to the bottom of the inlet and outlet openings. Then, across the openings, the grid points X_j are placed according to Eq. (14), where W^* should be replaced by H_i^* and n by the total number of grid spacings across the openings.

Table 1 Comparison of selected results obtained with the present code and those obtained by Fraikin et al. (1982). The results refer to natural convection in a closed cavity with perfectly conducting horizontal walls, at Gr = 6 × 10⁶.

Results of	$\overline{Nu}_H$	V_{max}	U_{max}	$\nu_{t,max}^*$	K_{max}	E_{max}
Fraikin et al. (1982)	23.5	266.13	343.62	3.19	6.65×10^3	4.49×10^6
Present work (geometric grid)	21.37	265.78	350.92	2.85	7.22×10^3	3.63×10^6
Present work (hyperbolic grid)	21.94	265.79	351.32	2.84	7.17×10^3	3.60×10^6

Computational Procedure. The computations start from the laminar solution at the same Reynolds number and a smaller Grashof number. In order to obtain the turbulent flow solution, a small perturbation in the flow field has to be introduced. An initial turbulent kinetic energy field was obtained by assuming 1 percent fluctuations for the local velocity components U and V. The values of the remaining two turbulent variables ν_t^* and E are obtained in a fashion similar to what was previously described in deriving the corresponding inlet values. The initial values of K, ν_t^*, and E are not expected to affect the final steady state, provided that they are small enough and they are only needed to introduce turbulence in the numerical solution. If the flow is still in the laminar regime, the numerical procedure should converge to zero values for all the turbulent flow quantities. Once the first turbulent solution is obtained for certain Reynolds and Grashof numbers, it can be used as the initial condition for higher Reynolds or Grashof numbers.

To determine whether convergence to steady state has been attained, a relative error, defined as the difference between the values at two successive time levels (n) and $(n + 1)$ over the value at level (n) for each variable ϕ, is monitored with time. This continues until the error attains a value less than 10^{-4} while, in addition, the relative error in the overall energy balance becomes less than 10^{-2}. All the computations at the production level were run on a CRAY Y-MP supercomputer at the Pittsburgh Supercomputing Center (PSC) and required an average of 0.24 seconds of CPU time/time step. Most of the development runs were made on a 3100 VAX station and these required 3.55 seconds per time step. Based on the CRAY data, the total CPU time for the results presented here was about 38 hours.

Code Validation. The turbulence model was validated by checking the results against those of Fraikin et al. (1982), which were numerical and experimentally validated. They studied the natural convection flow in a closed cavity, differentially heated from the sides and with perfectly conducting horizontal walls. The comparison for a Grashof number of Gr = 6 × 10⁶ is shown in Table 1, in terms of the maximum values of selected quantities. The grid dimensions used here were of the same order, i.e., a 21 × 21 grid was used for the comparison while

Fraikin et al. used a 21 × 21 and a 25 × 25 grid. However, the distribution of the grid points was different. Fraikin et al. (1982) used trigonometric functions to obtain the nodal coordinates, while two different types of nonuniform grid were used here: one where there are two nonuniform zones of grid points next to the vertical walls, with the distances between the nodes being reduced geometrically and a uniform grid at the core of the cavity, and the other where the distances of the nodes are given by Eq. (14), i.e., using hyperbolic functions. The values compared in Table 1 show a fairly good agreement. A few other comparisons with the natural convection problem, in terms of heat transfer, are made later in the paper, again indicating good agreement.

Results and Discussion

Definition of Parameters. The geometric parameters of Fig. 1, in their dimensionless form denoted by an asterisk (*), are specified as follows: $H_i^* = 1.0$, $H^* = 4.0$, $L_s^* = 1.0$, $d_s^*/H^* = 0.25$, $d_i^*/H^* = 0.875$, $d_o^*/H^* = 0.875$, and $W^*/H^* = 1$. The fluid is air, with a Prandtl number equal to Pr = 0.71 at room temperature. The values for the Reynolds and Grashof numbers are chosen in the range where turbulent flow is expected and which is also representative of flows encountered in several practical applications. For instance, if the application of interest is a cavity inside an air-cooled electronic system, where air enters at an inlet velocity of 1 m/s through an opening of 2–4 cm at 32°C, the Reynolds number can be found to vary in the range Re = 1100–2200. Similarly, for heat fluxes of order $q_s'' = 0.5$–1 W/cm^2, which are typical of high-power, air-cooled electronic modules and for the same opening dimensions, the Grashof number varies in the range Gr = 0.5×10^7–10^8. However, one should not view this study as exclusively tied to electronic cooling, as it would relate equally well for instance to applications such as the ventilation of a room in the presence of heat sources (Mokhtarzadeh-Dehghan et al., 1990).

As mentioned earlier, an attempt is made here to determine the onset of the turbulent regime by specifying Grashof numbers that are at least an order of magnitude greater than Gr_{cr}, for two Reynolds numbers. The values of the Reynolds number chosen are 1000 and 2000, for which solutions for laminar flow have been previously obtained (Papanicolaou and Jaluria, 1990). Of particular interest here is the heat transfer from the source to the fluid. Since our first grid point is always located within the viscous sublayer, the heat transfer is computed as in the laminar case (Papanicolaou and Jaluria, 1990). Therefore, the mean Nusselt number is given by:

$$\overline{\mathrm{Nu}} = \frac{1}{\lambda}\int_0^1 \frac{q_s''}{T_s(X) - T_i} H_i\, dX = \int_0^1 \frac{1}{\theta_s(X)}\, dX \qquad (15)$$

where $\theta_s(X)$ is the local temperature at the surface of the heat source.

Flow and Thermal Fields. For Reynolds number Re = 1000, it was found by Papanicolaou and Jaluria (1990) that the flow is laminar and steady up to Gr = 10^6, where Gr/Re^2 = 1. At Gr = 10^7, the solution became oscillatory. Oscillatory results were also obtained at Gr = 5×10^7, with Gr/Re^2 = 50, using the K–E model and starting with the solution at Gr = 10^6 as the initial condition. The numerical procedure led to a solution characterized by nonzero values for the turbulent quantities ν_t^*, K, and E, but also by very regular, periodic oscillations for all variables, similar to those found by Papanicolaou and Jaluria (1990, 1992). The random fluctuations of turbulence start making their appearance, as verified by the maximum value of the eddy viscosity, which is $\nu_{t,\max}^* = 8.2$. Similar oscillations have also been reported by Ozoe et al. (1985), in their computations of turbulent natural convection in a closed cavity using the K–E model. The oscillatory behavior can be an indication that the flow is still in the transition regime for the specific values of the parameters. The exact extent of this regime was outside the scope of this study, as a suitable transition model was not employed.

Table 2 Comparison of selected results obtained at various Grashof and Reynolds numbers in turbulent flow

Results	Re=1000			Re=2000		
Gr	5×10^7	10^8	2×10^8	5×10^7	10^8	5×10^8
Gr/Re^2	50	100	200	12.5	25	125
Ψ_{max}	1.198	1.222	1.269	1.083	1.103	1.177
$\theta_{s,max} \times 10^2$	5.819	4.847	4.060	5.560	4.748	3.227
$\overline{Nu}_s$	20.54	25.05	30.26	21.81	25.66	38.47
$K_{max} \times 10^2$	6.19	21.2	33.1	2.27	3.58	18.8
E_{max}	1.23	3.42	4.71	0.55	0.66	3.14
$\nu_{t,max}^*$	8.2	33.9	53.6	5.2	8.9	57.6

The oscillations in our case were damped at large time when Gr was increased to 10^8. At this value, the results are characterized by steady mean values and the amount of turbulence is increased, as verified by the value of the turbulent viscosity, which is now 33.9 times the value of the molecular viscosity ($\nu_{t,\max}^* = 33.9$). The maximum value of the kinetic energy $K_{\max}$ is increased by approximately four times from its value at Gr = 5×10^7. The value 5×10^7 for the Grashof number, which is based on the height of the inlet opening H_i^*, at the same value of ΔT, corresponds to a value of $\mathrm{Gr}_H = 3.2 \times 10^9$ based on the height H^* of the enclosure, which is typically used to define the Grashof number in natural convection in enclosures. The value Gr = 10^8 corresponds to $\mathrm{Gr}_H = 6.4 \times 10^9$. Paolucci and Chenoweth (1989) found the flow to be already weakly turbulent at Ra = 4×10^8, or Gr = 5.63×10^8, for natural convection in a closed, differentially heated cavity of aspect ratio 1. Therefore, it is reasonable to expect a fair amount of turbulence at the value Gr = 10^8, of the Grashof number based on our definition. The Grashof number was then increased to Gr = 2×10^8 and, after a very long sequence of decaying oscillations in the mean flow variables, the numerical solution converged to steady state. The amount of turbulence increased further and the value of the eddy viscosity was $\nu_{t,\max}^* = 53.6$. For Re = 2000, the values of Gr were incremented as shown in Table 2 and the corresponding amount of turbulence was found to increase as shown on the same table.

The streamlines for Re = 1000 and 2000 and for two values of the Grashof number in each case, are shown in Figs. 2 and 3, respectively. One may observe in these figures that, at these high values of both Re and Gr there is a shift of the maximum stream function toward the right vertical wall, compared to the laminar results (Papanicolaou and Jaluria, 1990). Both the recirculation due to buoyancy and the forced flow now carry higher levels of momentum, which are transferred toward the outflow. Near the outflow, both flows impinge on the right vertical wall and this is where most of the turbulence is generated, as will be shown later. When buoyancy dominates, at large values of Gr/Re^2 the location of the maximum stream function appears to move higher and the external flow becomes almost horizontal, without being able to penetrate towards the bottom.

The isotherms, for the same values of Gr and Re as in Figs. 2 and 3, are shown in Figs. 4 and 5. The patterns are qualitatively

similar to those found for laminar flow (Papanicolaou and Jaluria, 1990). In the region of the interaction between the buoyancy-induced flow from the source and the external forced flow, a stratified layer at a relatively low temperature develops at about $X = 3$. Along the heat source, a thermal boundary layer is clearly observed, with a thickness that is smaller than in the laminar case, since the value of Gr is now larger. As Gr increases, both the thermal boundary layer over the source and the thermally stratified horizontal layer become thinner and the temperature gradients increase. In the closed cavity problem, such as that studied by Markatos and Pericleous (1984), Henkes (1990), and Nobile et al. (1990), this thinning of the boundary layers along the heated and the cooled walls with an increase in the Rayleigh number has been clearly demonstrated, accompanied by an almost stagnant, thermally stratified core. In the present case, the incoming forced flow does not allow for such an orderly stratification to develop, but a more distorted isotherm pattern is present instead. The isotherms tend to become almost horizontal near the bottom of the cavity, as Gr increases. The corresponding values of the dimensionless temperature θ decrease with Gr. However, the actual values increase, if one considers the product $\theta \times \mathrm{Gr}$, which is proportional to the physical temperature excess over the inlet (ambient) temperature $(T - T_i)$.

Transient Results. The evolution to steady state of all variables follows the pattern shown for the two typical quantities, $K_{\max}$ and $\nu^*_{t,\max}$ and for Re = 1000, Gr = 10^8 in Fig. 6. Steady state is always attained through a long sequence of gradually decaying, periodic oscillations. Unfortunately, there are limitations on the time step due to both numerical and physical constraints and the number of time steps required for steady state cannot be kept very small. A physical constraint has been suggested by Thompson et al. (1985), according to which the dimensional time step is constrained by:

$$\Delta\tau \leq \left(g\beta \frac{\partial T}{\partial y}\right)^{-1/2} \tag{16}$$

where $\partial T/\partial y$ in their study is the vertical temperature gradient. This criterion is due to the presence of internal gravity waves in the cavity during the transient state. These have to be damped out before steady state can be attained. Henkes (1990) suggested a different form of the same criterion, where the period τ_{BV} of the Brunt-Väisälä waves is taken as the upper bound for the time step. However, there are also additional limitations due to numerical stability considerations, which require a time step several times lower than the value of τ_{BV}. It was finally found that, at the chosen values of the Reynolds number Re = 1000 and 2000, the time step could not be higher than 2×10^{-2} and, sometimes, it had to be reduced to 5×10^{-3}. As either one of the Grashof or the Reynolds number increases, the time required for steady state also increases. Generally, steady state is attained in the range τ = 600–1800, for the Re and Gr values considered here.

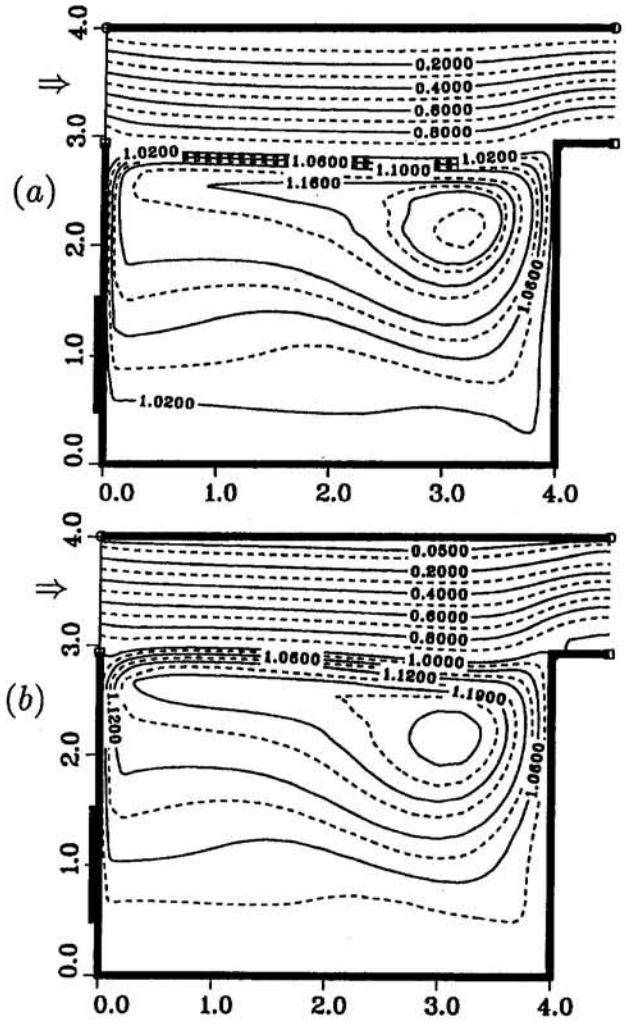

Fig. 2 Calculated streamlines for Re = 1000 and (*a*) $\mathrm{Gr/Re^2}$ = 100; (*b*) $\mathrm{Gr/Re^2}$ = 200

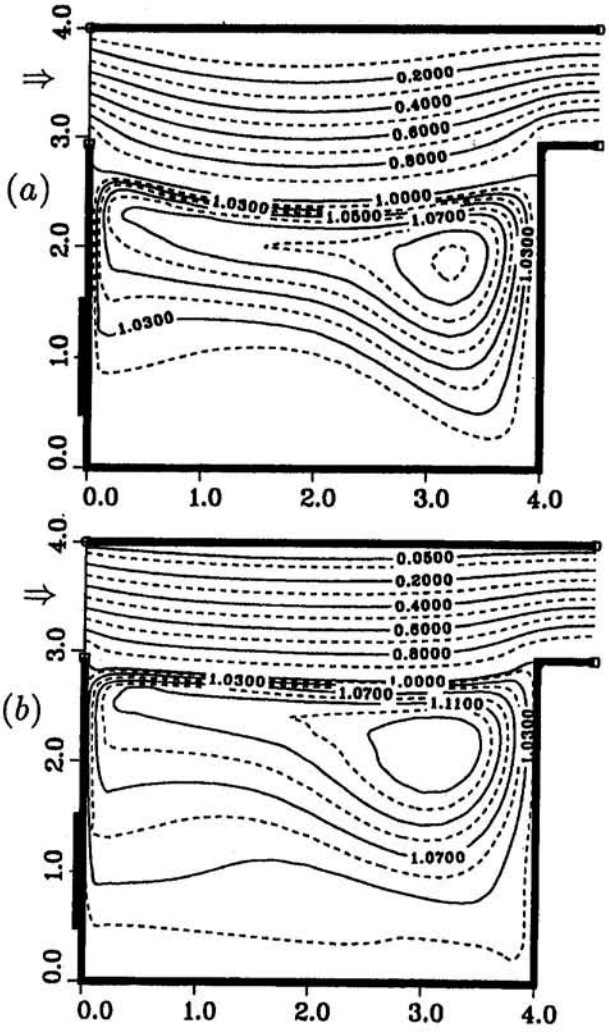

Fig. 3 Calculated streamlines for Re = 2000 and (*a*) $\mathrm{Gr/Re^2}$ = 25; (*b*) $\mathrm{Gr/Re^2}$ = 125

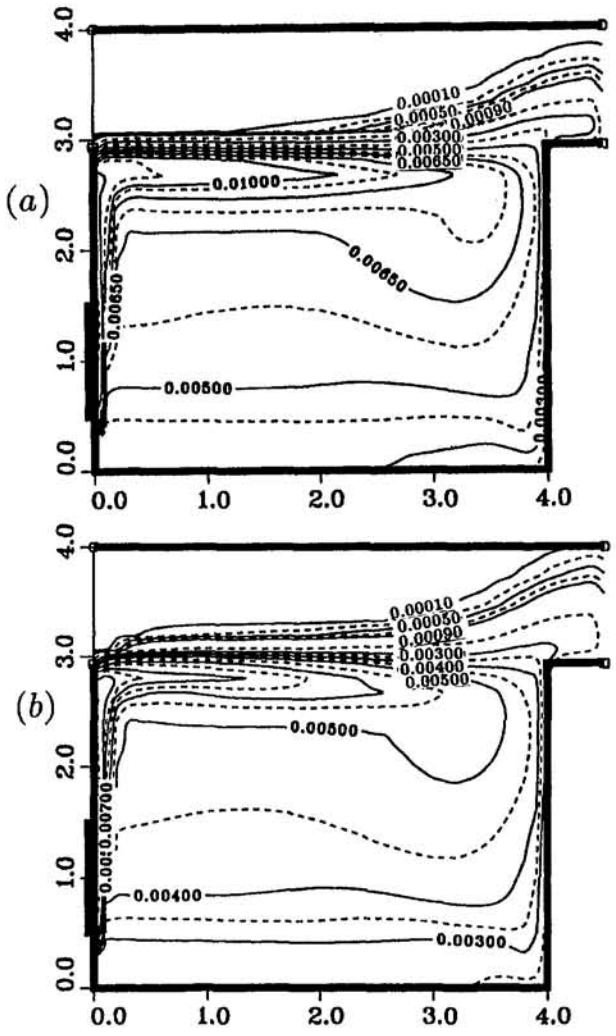

Fig. 4 Calculated isotherms for Re = 1000 and (*a*) $Gr/Re^2 = 100$; (*b*) $Gr/Re^2 = 200$

Turbulent Quantities—Selected Profiles. Typical contours of constant eddy viscosity $\nu^*_{t,\max}$ are shown in Fig. 7 for Re = 2000. This figure shows that much of the turbulence develops at the upper part of the right vertical wall. This is where the buoyancy-induced flow from the source, reinforced by the forced flow, impinges on the right side wall and tends to generate turbulence, whose level increases with an increase in Re and Gr, as the impingement becomes gradually more violent. The same trends were observed in the corresponding contour plots at Re = 1000.

Our values of K and E were compared to the corresponding values reported in studies dealing with the more familiar problem of natural convection in a closed cavity (Fraikin et al., 1982). Taking into account the differences in the nondimensionalization and with K_n, E_n as the dimensionless values in the natural convection problem and K_m, E_m the corresponding values in the mixed convection problem, it was found that: $K_n = 16\ \mathrm{Re}^2 K_m$, $E_n = 256\ \mathrm{Re}^3 E_m$. Therefore, at Re = 1000 and $Gr = 10^8$, for instance, where $K_{\max} = 0.212$, the same value in natural convection scales is equal to 3.392×10^6, which is one order of magnitude higher than the corresponding value of $K_{\max}$ found by Fraikin et al. (1982) at $Gr = 10^8$. Our values of $\nu^*_{t,\max}$ are also an order of magnitude higher. $Gr = 10^8$ was the highest Grashof number considered in their study, and since their results were claimed to be in the transition regime, one may conclude that our results extend beyond the transition regime and, at least for the highest values of Gr considered at each Re, our results lie in the fully turbulent regime. The main results of interest, for all the values of Gr and Re, are summarized in Table 2.

The computed velocity profiles for various values of Gr and Re are shown in Fig. 8, at $X = (\frac{2}{3})H^*$, downstream of the heat source. For two of the profiles shown, one at Re = 1000, $Gr = 10^8$ and the other at Re = 2000, $Gr = 5 \times 10^8$, corresponding to high values of Gr/Re^2, 100 and 125, respectively, the flow is seen to be upward along the left vertical wall, where buoyancy dominates, and downward near the right vertical wall. When the forced flow dominates (at low values of Gr/Re^2), the flow is upward over both walls at the same coordinate X. In Fig. 9, the temperature distribution along the vertical midplane is shown, for the same values of the parameters as in Fig. 8. For $Gr = 10^8$, the distribution for Re = 1000 and 2000 in dimensionless values θ can be directly compared. It is observed that higher temperatures develop for Re = 1000 than for Re = 2000 at the vertical midplane. A shift in the location of the maximum temperature to larger values of X with increasing Gr is also observed.

Heat Transfer Results. The results for the heat transfer from the source are expressed in terms of the mean Nusselt number $\overline{\mathrm{Nu}}_s$, as defined by Eq. (15). In order for this to be valid, it was always checked that the first grid point lay in the viscous sublayer, especially along the left vertical wall where the heat source is mounted. The viscous sublayer generally

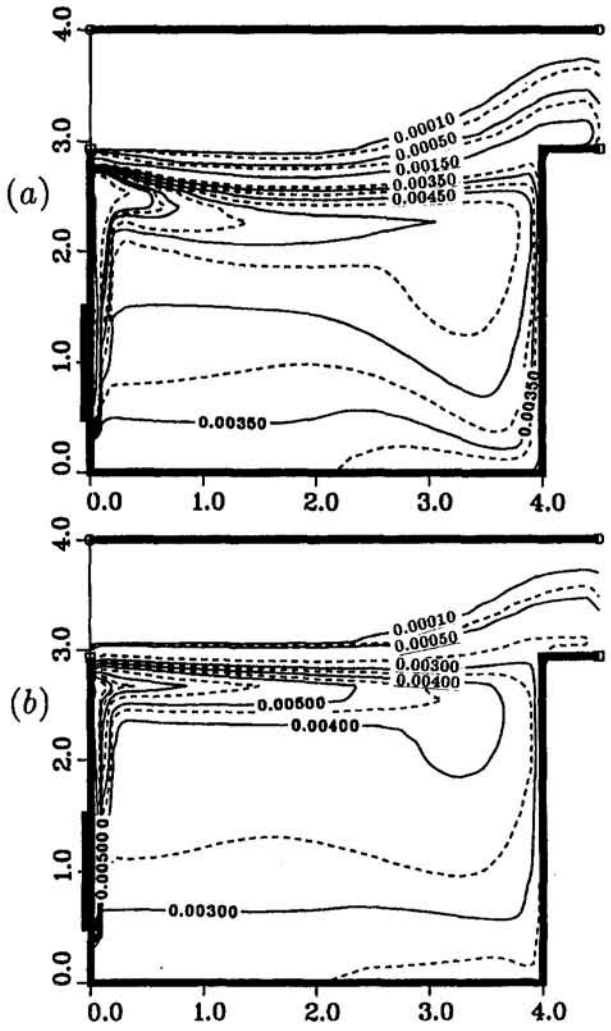

Fig. 5 Calculated isotherms for Re = 2000 and (*a*) $Gr/Re^2 = 25$; (*b*) $Gr/Re^2 = 125$

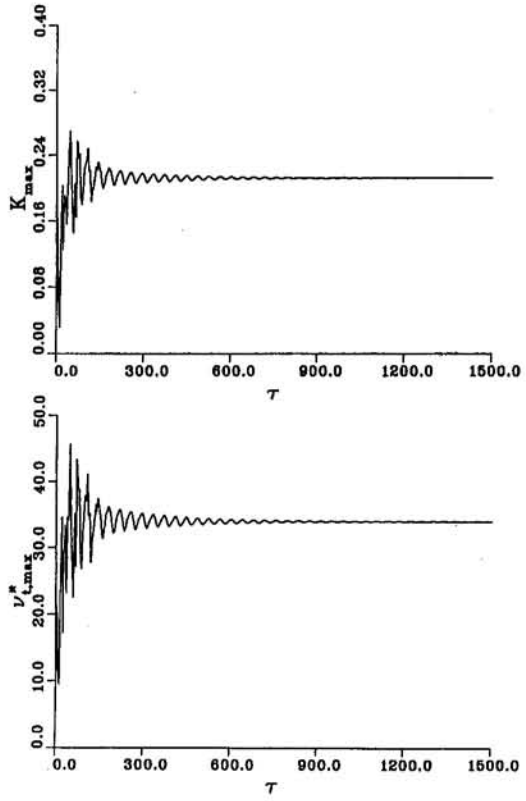

Fig. 6 Evolution to steady state of the maximum value of the turbulent kinetic energy K_{max} and the eddy viscosity $\nu^*_{t,max}$, for Re = 1000 and Gr = 10^8 (Gr/Re^2 = 100)

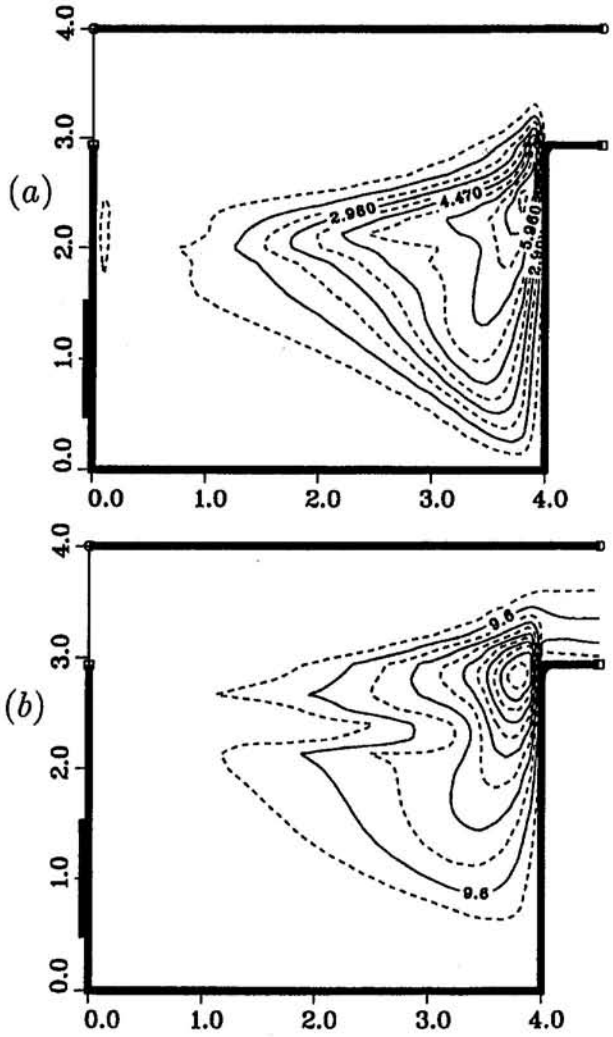

Fig. 7 Calculated values of the eddy viscosity for Re = 2000 and (*a*) Gr/Re^2 = 25 ($\nu^*_{t,max}$ = 8.9); (*b*) Gr/Re^2 = 125 ($\nu^*_{t,max}$ = 57.6)

extends up to $y^+ = 11.5$ (Henkes, 1990), but for natural convection this limit is as low as $y^+ \approx 4$, as shown by Humphrey and To (1986). Our first grid point from all horizontal and vertical walls did not have a value of y^+ greater than 6.5, while in most cases the condition $y^+ \leq 3$ was satisfied. The values of $\overline{Nu}_s$ are plotted against Gr/Re^2 in Fig. 10, both for laminar and turbulent flow, at Reynolds numbers 1000 and 2000. The transition from the laminar to the turbulent regime and the corresponding range of Gr/Re^2 is clearly seen in Fig. 10. For both Reynolds numbers, the variation in the laminar regime is almost linear for Gr/Re^2 > 0.1 and at the transition there is a departure from linearity to higher values of $\overline{Nu}_s$, before the turbulent regime is attained. In this regime, the variation of $\overline{Nu}_s$ is again linear. A correlation of the form:

$$\overline{Nu}_s = a\ Gr^b\ Re^c \tag{17}$$

was sought, based on the numerical results at Re = 1000 and 2000. The best fit was found at values: $a = 0.134$, $b = 0.26$, $c = 0.06$. In order to show the variation in terms of Gr/Re^2, $\overline{Nu}_s$ is divided by Re$^{0.58}$ and the following correlation is finally obtained:

$$\frac{\overline{Nu}_s}{Re^{0.58}} = 0.134\left(\frac{Gr}{Re^2}\right)^{0.26} \tag{18}$$

This has an overall correlation coefficient of 0.995, which shows that the fit is very good, at least in the parametric ranges considered (Table 2). This correlation is shown in graphic form in Fig. 11, where it can be seen that dividing by Re$^{0.58}$ makes the data collapse into the same straight line for both Reynolds numbers. For a more accurate estimate of the effect of the Reynolds number over a wider range, additional values of Re are needed.

Unfortunately, there are no available experimental or numerical data for the effect of Re in a configuration that closely resembles ours. Most of the available experimental data are for the limiting case of natural convection in closed cavities and mainly for aspect ratios height/width greater or equal to 5. However, the effect of Gr found in such studies is very similar to the present one. Fraikin et al. (1982) found a Gr$^{0.275}$ dependence of the mean Nusselt number over the hot wall of their cavity, in agreement with their experimental results. This was taken as valid in the range Gr = 6×10^6–10^8, which they

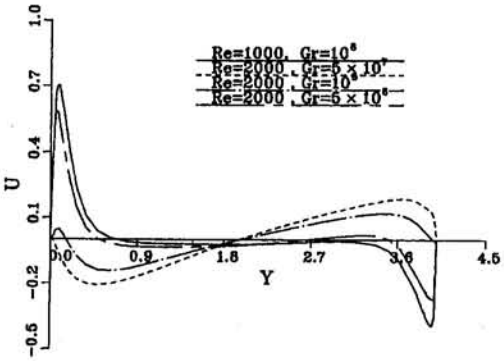

Fig. 8 Vertical velocity *U* profiles at $X = (\frac{2}{5})H^*$ for various Grashof and Reynolds numbers

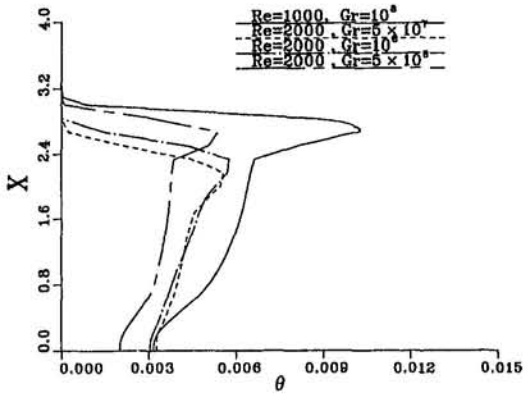

Fig. 9 Temperature distribution at the vertical midplane for various Grashof and Reynolds numbers

claimed was in the transition regime. Markatos and Pericleous (1984) studied natural convection in a closed cavity with adiabatic walls and found a $Gr^{0.329}$ dependence in the range $10^6 < Ra \leq 10^{12}$ and a $Gr^{0.245}$ dependence in the range $10^{12} < Ra \leq 10^{16}$. In the results of both Fraikin et al. (1982) and Markatos and Pericleous (1984), the cavity had an aspect ratio of 1 and the Grashof number was based on the total height of the cavity. The results of Hanjalic and Vasic (1990) also confirmed a $\frac{1}{3}$ power law for the variation of Nu with Ra at values $Ra > 10^{10}$ and isothermal heating, but reported previous experimental data that showed lower exponents, for different heating conditions.

In general, for isothermally heated, closed cavities the values reported for the exponent lie in the range 0.24–0.33. In this study, the corresponding value was found to be within the same range (Eq. (18)), which gives additional confidence in the numerical model used. The agreement can be attributed to the fact that the heat transfer from the source still takes place within a natural convection boundary layer, although discrepancies are expected due to the constant heat flux condition at the source and the different temperature distribution in the core of the cavity.

Grid Refinement. The number of grid points used in this study is in general comparable to what has been used in most of the previous studies on turbulent natural convection already referenced, especially for cavities of aspect ratio 1 and with the high-Re form of the K–E model employed. The effect of the grid dimensions was also checked on a finer grid, 51 × 64, with 51 × 51 nodes inside the cavity, for one of the cases considered, Re = 2000 and Gr = 10^8. The first grid point was maintained at the same position from the solid boundaries as before, since the viscous sublayer was not meant to be resolved in this version of the model. When the maximum values of the main mean-flow quantities were compared, the difference was 3.6 percent in Ψ_{max}, 4.8 percent in the maximum heat source temperature $\theta_{s,max}$, 4.1 percent in U_{max}, 6.2 percent in V_{max}, and 0.2 percent in the mean Nusselt number from the source. This was found quite satisfactory, when the difference in the computational effort required between the two grids was considered.

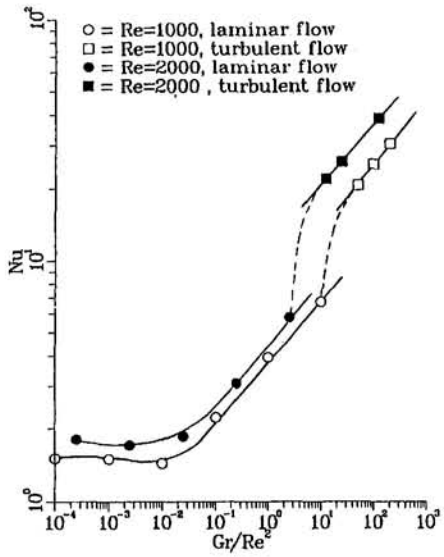

Fig. 10 Variation of the mean Nusselt number at the source with Gr/Re^2, for laminar and turbulent flow, at Re = 1000 and 2000

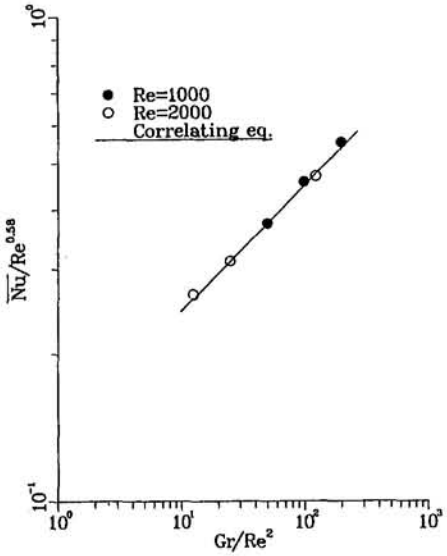

Fig. 11 Variation of the mean Nusselt number at the source with Gr/Re^2 for turbulent flow, along with the correlating equation based on the results for Re = 1000 and 2000

Conclusions

Turbulent convection in a two-dimensional, square cavity with a localized, constant-heat-flux source was simulated numerically. Mixed convection arises as the buoyancy-induced flow from the source interacts with an externally induced cold throughflow. The turbulent flow variables first attained values of significant magnitude for $Gr/Re^2 = 25$ at Re = 1000 and for $Gr/Re^2 = 12.5$ at Re = 2000. In the former case, however, the mean values exhibited oscillatory behavior, which suggests that the flow might still have been in the transition regime. Most of the turbulence developed near the right vertical wall of the cavity, opposite to the location of the heat source and near the outflow opening. The production of turbulence at that location was predominantly due to shear, while a small amount was generated due to buoyancy, along the left vertical wall, right above and in the thermal boundary layer of the heat source. Correlating equations for the heat transfer rate were derived. The average Nusselt number from the source was only slightly affected by the Reynolds number and was found to vary as $Gr^{0.26}$, which is close to the numerically and experimentally derived correlations for pure natural convection in closed cavities.

Acknowledgments

The authors would like to acknowledge the support from NSF, under grant No. CBT-88-03049, the Pittsburgh Supercomputing Center (PSC), under grant No. CBT900042P, and the

Dept. of Mechanical and Aerospace Engg., Rutgers University, for this work.

References

Abrous, A., and Emery, A. F., 1989, "Turbulent Free Convection in Square Cavities With Mixed Boundary Conditions," in: *Heat Transfer in Convective Flows,* R. K. Shah, ed., ASME HTD-Vol. 107, pp. 117–130.

Arpaci, V. S., and Larsen, P. S., 1984, *Convection Heat Transfer,* Prentice-Hall, Englewood Cliffs, NJ.

Cha, C. K., and Jaluria, Y., 1984, "Effect of Thermal Buoyancy on the Recirculating Flow in a Solar Pond for Energy Extraction and Heat Rejection," ASME *Journal of Solar Energy Engineering,* Vol. 106, pp. 428–437.

Fraikin, M.-P., Portier, J. J., and Fraikin, C. J., 1982, "Application of a $k-\epsilon$ Turbulence Model to an Enclosed Buoyancy Driven Recirculating Flow," *Chem. Eng. Commun.,* Vol. 13, pp. 289–314.

Hanjalic, K., and Vasic, S., 1990, "Numerical Simulation of Free Convection in Single- and Multiple-Zone Rectangular Cavities," *Proc. 9th Int. Heat Transfer Conf.,* Jerusalem, Israel, Vol. 2, pp. 579–584.

Henkes, R. A. W. M., 1990, "Natural Convection Boundary Layers," Ph.D. Thesis, Delft University, Delft, The Netherlands.

Hjertager, B. H., and Magnussen, B. F., 1977, "Numerical Prediction of Three-Dimensional Turbulent Buoyant Flow in a Ventilated Room," in: *Heat Transfer and Turbulent Buoyant Convection,* D. B. Spalding and N. Afgan, eds., Vol. II, pp. 429–442, Hemisphere, Washington DC.

Hoogendoorn, C. J., 1985, "The Flow of Stratified Air Layers in Horizontal Channels," in: *Natural Convection: Fundamentals and Applications,* S. Kakac, W. Aung, and R. Viskanta, eds., pp. 443–460, Hemisphere, Washington DC.

Humphrey, J. A. C., and To, W. M., 1986, "Numerical Simulation of Buoyant, Turbulent Flow—II. Free and Mixed Convection in a Heated Cavity," *Int. J. Heat Mass Transfer,* Vol. 29, pp. 593–610.

Launder, B. E., and Spalding, D. B., 1974, "The Numerical Computation of Turbulent Flows," *Comp. Meth. Appl. Mech. Eng.,* Vol. 3, pp. 269–289.

Markatos, N. C., and Pericleous, K. A., 1984, "Laminar and Turbulent Natural Convection in an Enclosed Cavity," *Int. J. Heat Mass Transfer,* Vol. 27, No. 5, pp. 755–772.

Mokhtarzadeh-Dehghan, M. R., El Telbany, M. M. M., and Reynolds, A. J., 1990, "Transfer Rates in Single-Sided Ventilation," *Building and Environment,* Vol. 25, No. 2, pp. 155–161.

Nielsen, P. V., 1975, "Prediction of Air Flow and Comfort in Air Conditioned Spaces," *ASHRAE Transactions,* Vol. 81, part II, pp. 247–259.

Nobile, E., Sousa, A. C. M., and Barozzi, G. S., 1990, "Turbulent Buoyant Flows in Enclosures," *Proc. 9th Int. Heat Transfer Conf.,* Jerusalem, Israel, Vol. 2, pp. 543–548.

Ozoe, H., Mouri, A., Hiramitsu, M., Churchill, S. W., and Lior, N., 1984, "Numerical Calculation of Three-Dimensional Turbulent Natural Convection in a Cubical Enclosure Using a Two-Equation Model," in: *Fundamentals of Natural Convection/Electronic Equipment Cooling,* L. C. Witte and L. S. Saxena, eds., ASME HTD-Vol. 32, pp. 25–32.

Ozoe, H., Mouri, A., Ohmuro, M., Churchill, S. W., and Lior, N., 1985, "Numerical Calculations of Laminar and Turbulent Natural Convection in Water in Rectangular Channels Heated and Cooled Isothermally on the Opposing Vertical Walls," *Int. J. Heat Mass Transfer,* Vol. 28, No. 1, pp. 125–138.

Ozoe, H., Miyachi, H., Hiramitsu, M., and Matsui, T., 1986, "Numerical Computation of Natural Convection in a Cubical Enclosure With Ventilation for Both a Laminar and a Two-Equation Turbulent Model," *Proc. 8th Int. Heat Transfer Conf.,* San Francisco, CA, Vol. 4, pp. 1489–1494.

Paolucci, S., and Chenoweth, D. R., 1989, "Transition to Chaos in a Differentially Heated Vertical Cavity," *J. Fluid Mech.,* Vol. 201, pp. 379–410.

Papanicolaou, E., and Jaluria, Y., 1990, "Mixed Convection From an Isolated Heat Source in a Rectangular Enclosure," *Num. Heat Transfer,* Part A, Vol. 18, pp. 427–461.

Papanicolaou, E., 1991, "Mixed Convection From Isolated Heat Sources in a Cavity: a Study of Various Regimes and Configurations," Ph.D. Thesis, Rutgers University, New Brunswick, NJ.

Papanicolaou, E., and Jaluria, Y., 1992, "Transition to a Periodic Regime in Mixed Convection in a Square Cavity," *J. Fluid Mech.,* Vol. 239, pp. 489–509.

Patankar, S. V., 1980, *Numerical Heat Transfer and Fluid Flow,* Hemisphere, Washington DC.

Roache, P. J., 1972, *Computational Fluid Dynamics,* Hermosa Publishers, Albuquerque, NM.

Rodi, W., 1980, "Turbulence Models and Their Application in Hydraulics—A State of the Art Review," International Association of Hydraulic Research, Delft, The Netherlands.

Thompson, C. P., Wilkes, N. S., and Jones, I. P., 1985, "Numerical Studies of Buoyancy Driven Turbulent Flow in a Rectangular Cavity," in: *Numerical Methods in Thermal Problems,* R. W. Lewis and K. Morgan, eds., *Proc. 4th Int. Conf.,* Swansea, United Kingdom, pp. 353–364.

Combined Buoyancy and Pressure-Driven Flow Through a Shallow, Horizontal, Circular Vent

L. Y. Cooper
Building and Fire Research Laboratory,
National Institute of Standards and Technology,
Gaithersburg, MD 20899

Combined buoyancy and pressure-driven (i.e., forced) flow through a horizontal vent is considered where the vent-connected spaces are filled with fluids of different density in an unstable configuration (density of the top is larger than that of the bottom). With zero-to-moderate cross-vent pressure difference, Δp, the instability leads to bidirectional exchange flow between the two spaces, e.g., as in the emptying from the bottom of a liquid-filled can with a single vent opening. For relatively large Δp, the flow through the vent is unidirectional, from the high to the low-pressure space, e.g., as is the case when the can has a large enough second vent at the top. Problems of a commonly used unidirectional orifice vent flow model, with Bernoulli's equation and a constant flow coefficient, C_D, are discussed. First, the orifice model does not predict bidirectional flows at zero-to-moderate Δp. Also, when Δp exceeds the critical value, Δp_{FL}, which defines the onset of unidirectional or "flooding" flow, there is a significant dependence of C_D on the relative buoyancy of the upper and lower fluids (i.e., C_D is not constant). Analysis of relevant boundary value problems and of available experimental data leads to a mathematical vent flow model, which removes the problems of the orifice flow model. The result is a general algorithm to calculate flow through shallow, horizontal, circular vents under high-Grashof-number conditions.

Introduction and Background

Consider the flow through a horizontal vent where the fluids in the vent-connected spaces near the elevation of the vent are of arbitrary density. Assume that in each space, away from the vent, the environment is relatively quiescent with pressure well approximated by the hydrostatic pressure. As in Fig. 1, designate the spaces as *T*op and *B*ottom and let the subscripts T and B, respectively, refer to conditions in these spaces near the vent elevation, but removed far enough laterally so that variations to the quiescent far-field environment, due to vent flows that may exist, are negligible. $\dot{V}_T$ and $\dot{V}_B$ are volume flow rates through the vent from top to bottom and bottom to top, respectively. The flow is determined by the vent design, i.e., shape and depth, L; densities, ρ_T and ρ_B; and cross-vent pressure difference

$$\Delta p = p_H - p_L \geq 0; \quad p_H = \max(p_T, p_B);$$
$$p_L = \min(p_T, p_B) \tag{1}$$

The subscripts H and L will always refer to the conditions on the *H*igh and *L*ow-pressure sides of the vent, respectively. When $\Delta p = 0$, the high/low-pressure designations are arbitrary. In cases where gas flows are involved, Δp is assumed to be small compared to p_B and p_T.

$$\Delta p/\bar{p} \ll 1; \quad \bar{p} = (p_H + p_L)/2 = (p_B + p_T)/2 \tag{2}$$

The objective of this work is to develop a mathematical model for predicting, for arbitrary specified p_T and p_B, the rates of flow through the vent under conditions involving unstable configurations, where

$$\Delta\rho = \rho_T - \rho_B > 0 \tag{3}$$

With zero-to-moderate Δp, the instability leads to bidirectional exchange flow between the two spaces (Taylor, 1950; Epstein, 1988; Brown, 1962; Epstein and Kenton, 1989; Tan and Jaluria, 1991). As flows enter the upper and lower spaces they are upward and downward-buoyant, respectively, and they rise and fall as plumes to the far field. For relatively large Δp, the vent flow is unidirectional, from high to low pressure. Sufficiently deep into the low-pressure space, the flow is dominated by buoyancy forces, continuing to the far field as a buoyant plume. Photographs of the far-field plume flows are presented by Tan and Jaluria (1991) for both the bidirectional and unidirectional flow regimes.

Only quasi-steady features of the flows being studied will be discussed and analyzed. Thus, even when the flows are fluctuating, it is assumed that time scales that characterize their fluctuations are small compared to characteristic times of a particular applications problem of interest, and that meaningful time-averaged flow characteristics can be established.

The Standard Vent Flow Model and its Shortcomings. There is a simple, effective model for estimating the flow through both horizontal and vertical vents, which is typically used in zone-type model simulations of compartment fire phenomena (see, e.g., Mitler and Emmons, 1981; Tanaka, 1983; Cooper and Forney, 1990; Cooper, 1990). The model, referred to here as the standard model, uses a unidirectional orifice-type flow assumption with Bernoulli's equation and a constant orifice flow coefficient, C_D, to compute the rate of flow through the vent (Emmons, 1988; Cooper, 1989). For a vertical vent, the cross-vent hydrostatic pressure difference (generated by stably stratified environments in the vent-joined spaces) and, therefore, the predicted cross-vent flow flux generally varies with eleva-

Contributed by the Heat Transfer Division and presented at the ASME International Mechanical Engineering Congress and Exhibition, Chicago, Illinois, November 6–11, 1994. Manuscript received by the Heat Transfer Division May 1994; revision received November 1994. Keywords: Fire/Flames, Mixed Convection, Natural Convection. Associate Technical Editor: Y. Jaluria.

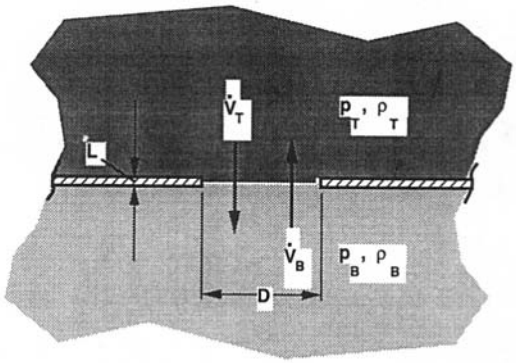

Fig. 1 The basic horizontal-vent configuration

tion, i.e., from the top to the bottom of the vent. However, for horizontal vents the situation is much simpler in that the cross-vent pressure difference, Δp, and, therefore, the cross-vent flow flux is predicted to be uniform along the entire vent opening.

There is a basic problem with the standard model in the case of horizontal vents since it always predicts unidirectional flow, i.e., for any Δp

$$\dot{V}_H = \dot{V}_{H,ST} = C_D A_V (2\Delta p/\rho_H)^{1/2}; \quad \dot{V}_L = \dot{V}_{L,ST} = 0 \quad (4)$$

where: $\dot{V}_H$ and $\dot{V}_L$ are net volume flow rates through the vent from the high to low pressure and from the low to high-pressure side of the vent, respectively; A_V is vent area; and the subscript *ST* refers to predictions of the *ST*andard model. This flow description seems reasonable, except for the incorrect prediction that there will always be unidirectional flow when $\Delta p \neq 0$, and that the flow is zero when $\Delta p = 0$.

To illustrate this, consider a condition of near-zero Δp, and assume that $\rho_T > \rho_B$, e.g., the vent joins a relatively small-density environment below from a relatively high-density environment above. Such a scenario involves a state of hydrodynamic instability, where a two-directional exchange flow develops and where a unidirectional description of the flow is always invalid. The situation is illustrated by a common experiment involving the emptying from the bottom of a liquid-filled can with a single vent opening or of a liquid-filled bottle. In both cases, a thin sheet of plastic across the opening will maintain the system in a static state ($\Delta p = 0$ across the interface). But the hydrostatic system is unstable, and removal of the plastic sheet leads immediately to emptying of the vessel by means of simultaneous, identical-flow-rate, cross-vent exchanges of liquid from above and air from below.

The Mixed Flow Regime. The relevant fluid-dynamic instability for unbounded horizontal interfaces has been studied theoretically by Taylor (1950). For the unstable configuration and for an experimental configuration that intrinsically leads to $\Delta p = 0$ (a tank divided by a horizontal partition with a vent, where the upper and lower spaces are filled with incompressible fluids of relatively high and low density, respectively), Epstein (1988) established a correlation of exchange-flow-rate data from salt-/fresh-water exchange-flow experiments. Also, Brown (1962) established heat transfer correlations from analogous hot-air/cold-air exchange-flow experiments.

For any unstable arrangement of densities, if Δp is small enough, there will be a bidirectional or exchange flow through the vent. However, if Δp is large enough the vent flow will be

Nomenclature

A_V = vent area
C_D = vent flow coefficient, Eq. (4)
$C_{D,\mathrm{HS}}$, $C_{D,\infty}$ = C_D of Heskestad and Spaulding (1989); at large Re = 0.6
$C_D^{(N)}$; $C_{D,FL}^{(N)}$ = C_D for Problem N; $C_D^{(N)}$ at onset of flooding
C_p = specific heat at constant pressure
D = characteristic span of vent opening, diameter
$\mathrm{Fr_{HS}}$ = Froude number of Heskestad and Spaulding (1989), Eq. (9)
$\overline{\mathrm{Fr}}_H^{(N)}$, $\overline{\mathrm{Fr}}_L^{(N)}$ = Froude numbers for Problem N, Eq. (18)
$\overline{\mathrm{Fr}}_{H,FL}^{(N)}$ = $\overline{\mathrm{Fr}}_H^{(N)}$ at onset of flooding
Gr; $\mathrm{Gr_{HS}}$; $\overline{\mathrm{Gr}}$ = Grashof number; Gr of Heskestad and Spaulding (1989); Eq. (15)
g = acceleration of gravity
k = thermal conductivity
L = depth of vent
M = Eq. (36)
m_N = for $N = 1$: Eqs. (38)–(40), for $N = 2$: Eq. (41)
p; $p^{(N)}$; $p^{*\prime(N)}$ = pressure; p for Problem N; dimensionless $p^{(N)}$, Eq. (14)
p_H, p_L; $\overline{p}$ = far-field p on high-, low-pressure side of vent, near the vent elevation; Eq. (2)
$\overline{\mathrm{Pr}}$ = Prandtl number, Eq. (15)
R = gas constant
T; $T^{(N)}$; $T^{*\prime(N)}$ = absolute temperature; T for Problem N; dimensionless $T^{(N)}$, Eq. (14)
T_T, T_B = far field T in top, bottom space
$\overline{\mathrm{T}}$ = Eq. (10)
$U_i^{(N)}$; $U_i^{*(N)}$ = velocity for Problem N; dimensionless $U_i^{(N)}$, Eq. (14)
$\dot{V}_{EX,MX}$ = maximum exchange flow rate
$\dot{V}_{H,FL}$ = $\dot{V}_H$ at onset of flooding
$\dot{V}_H$; $\dot{V}_{H,ST}$ = net volumetric flow rate from high to low-pressure side of vent; $\dot{V}_H$ for the standard model
$\dot{V}_L$; $\dot{V}_{L,ST}$ = net volumetric flow rate from low to high-pressure side of vent; $\dot{V}_L$ for standard model
$\dot{V}_H^{(N)}$; $\dot{V}_{H,FL}^{(N)}$ = $\dot{V}_H$, $\dot{V}_{H,FL}$ for Problem N
$\dot{V}_N$; $\dot{V}_N^{(N)}$ = Eq. (5); $\dot{V}_N$ for Problem N
$\dot{V}_L^{(N)}$ = $\dot{V}_L$ for Problem N
$X_i^{(N)}$; $X_i^{*(N)}$ = Cartesian coordinates for Problem N; dimensionless $X_i^{(N)}$, Eq. (15)
Δp = Eq. (1)
Δp_{FL}; $\Delta p_{FL}^{(N)}$ = Δp at onset of flooding; Δp_{FL} for Problem N
ΔT = Eq. (12)
$\Delta \rho$ = Eq. (3)
ϵ = dimensionless $\Delta\rho$, ΔT, Eq. (15)
μ; $\overline{\mu}$ = dynamic viscosity; Eq. (10)
ν = kinematic viscosity
Π; $\Pi_{FL}^{(N)}$ = dimensionless Δp, Eq. (15); dimensionless $\Delta p_{FL}^{(N)}$, Eq. (20)
ρ; $\rho^{(N)}$; $\rho^{*\prime(N)}$ = density; ρ for Problem N; dimensionless $\rho^{(N)}$, Eq. (14)
ρ_T, ρ_B; $\overline{\rho}$ = far-field ρ in top, bottom space; Eq. (15)
σ_1, σ_2 = Eqs. (26) and (29)

unidirectional. Indeed, there will always be a value $\Delta p = \Delta p_{FL}$, denoted as the critical or flooding value of Δp, which separates a unidirectional or *FL*ooding flow regime (for $\Delta p \geq \Delta p_{FL}$), where $\dot{V}_L = 0$, from a mixed flow regime ($0 \leq \Delta p < \Delta p_{FL}$), where $\dot{V}_L > 0$, $\dot{V}_L$ being the above-mentioned exchange flow. Also, associated with any Δp_{FL} value is a corresponding volumetric flooding flow rate, denoted by $\dot{V}_{H,FL}$.

Epstein and Kenton (1989) extended the work of Epstein (1988) to $\Delta p \neq 0$. They studied the mixed flow regime with salt/fresh-water experiments, measuring flow rates and $\dot{V}_{H,FL}$, but not Δp. Tan and Jaluria (1991) carried out similar experiments, measuring Δp directly. However, the major focus here will be on large-Gr-driven turbulent flows, and, as will be shown, it seems that the latter experiments, carried out with relatively small-D ($D \leq 0.0127$ m) vents, involved relatively small Gr and laminar or transition flows.

Let $\dot{V}_N$ denote the *N*et volume flow rate from the high to the low-pressure side of the vent.

$$\dot{V}_N = \dot{V}_H - \dot{V}_L \geq 0 \tag{5}$$

This is the forced or pressure-driven part of the flow. At one end point of the mixed flow regime, $\Delta p = \Delta p_{FL}$. There, $\dot{V}_L = 0$, i.e., the exchange flow phenomenon vanishes, and $\dot{V}_N = \dot{V}_H = \dot{V}_{H,FL}$. At the other end point, $\Delta p = 0$. There, the buoyancy-driven part of the flow, $\dot{V}_L$, reaches the *MaX*imum *EX*change flow rate, $\dot{V}_{EX,MX}$, where, in the case of incompressible nondiffusive flows, continuity considerations require that $\dot{V}_N = 0$, i.e., $\dot{V}_H = \dot{V}_L = \dot{V}_{EX,MX}$. It is assumed here that the latter $\Delta p = 0$ conditions even hold for cold-gas-over-hot-gas systems. This is consistent with the assumption that any effects of diffusive transport that may lead to significant variations in density are removed from the region of the vent and are mainly found in the plumelike flow regions above and/or below the vent.

In view of the above, the standard model vent flow description of Eq. (4) must be modified as follows: There is a mixed flow regime, defined by $0 \leq \Delta p \leq \Delta p_{FL}$, where $\dot{V}_L \geq 0$. In this regime

$$\dot{V}_H(\Delta p = 0) = \dot{V}_{EX,MX} \leq \dot{V}_H \leq \dot{V}_H(\Delta p = \Delta p_{FL}) = \dot{V}_{H,FL} \tag{6}$$

$$\dot{V}_L(\Delta p = \Delta p_{FL}) = 0 \leq \dot{V}_L \leq \dot{V}_L(\Delta p = 0) = \dot{V}_{EX,MX} \tag{7}$$

Plots of $\dot{V}_H$, $\dot{V}_L$, and $\dot{V}_N$ in the mixed-flow regime, consistent with Eqs. (5)–(7) and for the arbitrarily selected value, $\dot{V}_{EX,MX}/\dot{V}_{H,FL} = 0.3$, are sketched in Fig. 2.

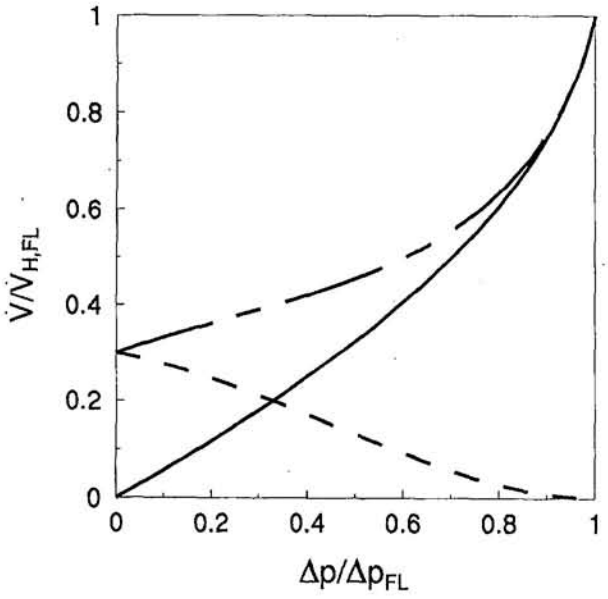

Fig. 2 Sketch of $\dot{V}_H/\dot{V}_{H,FL}$, – – –; $\dot{V}_L/\dot{V}_{H,FL}$, – · –; and $\dot{V}_N/\dot{V}_{H,FL}$ ——, as functions of $\Delta p/\Delta p_{FL}$ in the mixed flow regime for the arbitrarily selected value, $\dot{V}_{EX,MX}/\dot{V}_{H,FL} = 0.3$

The Unidirectional Flow Regime and the Significant Dependence of C_D on Relative Buoyancy. In addition to the difficulties of using the standard flow model in the mixed flow regime, there is also a problem in the unidirectional flow regime. In particular, use of a fixed value for C_D, denoted here as $C_{D,\infty} = 0.60$ (Perry, 1949) and associated with the orifice coefficient for high-Reynolds-number flows through an orifice joining two regions of like fluids, is generally invalid. (Note that 0.68 rather than 0.60 has been recommended by Emmons (1988) for general use in buoyancy-driven vent flows and that this has typically been used in zone fire model vent flow calculations.)

Using fire-generated hot/cold-air experiments and unstable horizontal vent configurations with high pressure at the top, it has been shown by Heskestad and Spaulding (1989) that, until $\Delta p \gg \Delta p_{FL}$, there is a significant dependence of C_D on the relative buoyancy of the cross-vent environments, e.g., compared to $C_{D,\infty} = 0.60$, they measured C_D at the flooding condition, $C_{D,FL}$, to be in the range 0.15–0.21.

The fact that there is a difference between C_D for stable and unstable configurations is not surprising. For example, consider expected differences in the entrance flow near the vent, and their effects on C_D, for the two cases: (1) a less-dense fluid, below, penetrating a more-dense fluid, above (unstable), and (2) a more-dense fluid, below, penetrating a less-dense fluid, above (stable). In the former case, the entering fluid will tend to rise from the vent to the upper space in a buoyant plume, whereas in the latter case the entering fluid will rise to a maximum elevation, move outward and downward to the bottom of the upper space, and continue its outward movement there, away from the vent opening, as a radial "floor jet."

For shallow (i.e., small L/D) circular vents of length L, $L/D = 0.011$ data of Heskestad and Spaulding (1989) indicate a smooth dependence of C_D on the relative buoyancy as expressed by Froude number (below, the subscript HS refers to the names Heskestad and Spaulding). From these data and from other considerations, Heskestad and Spaulding (1989) conclude that for unidirectional flow

$$C_{D,\mathrm{HS}} = C_{D,\mathrm{HS}}(\mathrm{Fr}_{\mathrm{HS}}, \mathrm{Gr}_{\mathrm{HS}}); \quad \lim_{\mathrm{Fr}_{\mathrm{HS}} \to \infty} C_{D,\mathrm{HS}} = C_{D,\infty} \tag{8}$$

$$\mathrm{Fr}_{\mathrm{HS}} = (\dot{V}_H/A_V)/[2gD(\rho_T - \rho_B)/\rho_T]^{1/2};$$

$$\mathrm{Gr}_{\mathrm{HS}} = g\rho_T(\rho_T - \rho_B)D^3/\bar{\mu}^2 \tag{9}$$

$$\mu = \mu(T); \quad \bar{\mu} = \mu(\bar{T}); \quad \bar{T} = (T_T + T_B)/2 \tag{10}$$

Equation (8) indicates a general dependence of $C_{D,\mathrm{HS}}$ on $\mathrm{Gr}_{\mathrm{HS}}$. However, for the shallow circular-vent data of Heskestad and Spaulding (1989) ($\mathrm{Gr}_{\mathrm{HS}}$ of the order of 10^7), $C_{D,\mathrm{HS}}$ was in fact insensitive to changes in $\mathrm{Gr}_{\mathrm{HS}}$ and no systematic variation of $C_{D,\mathrm{HS}}$ on $\mathrm{Gr}_{\mathrm{HS}}$ was observed. Included in the data of Heskestad and Spaulding (1989) are specifically determined values at the flooding condition. For shallow circular vents, these latter data will be seen below to augment the flooding data of Epstein and Kenton (1989).

Results of Heskestad and Spaulding (1989) include limited data on each of several vent designs other than shallow circular vents. These data indicate that orifice coefficient representations analogous to Eq. (8) can likely be established for vent designs other then shallow circular vents. In this regard, reliable results will require additional testing.

Representing Flow Rates as Explicit Functions of Δp. The objective of this work is a model for unidirectional and mixed flow regimes in unstable configurations, where the high pressure is either at the top or bottom and where flow rates are given as functions of Δp. As mentioned, the Heskestad and Spaulding (1989) study provided data for flow rate versus Δp, but only for unidirectional flow with high pressure at the top.

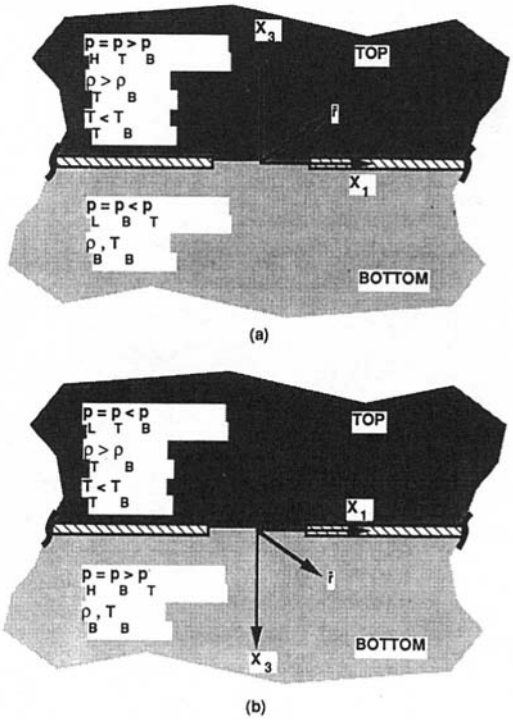

Fig. 3 (*a*) Configuration 1 and (*b*) Configuration 2 illustrating conditions associated with boundary value problems 1 and 2, respectively

Also, in the mixed flow regime, flow rates, but not Δp, were measured by Epstein and Kenton (1989). To establish the desired dependence of flow on Δp for the mixed flow regime, other considerations will be required in addition to the data.

The development of the flow model will be based on theoretical considerations of the relevant boundary value problems and on the above-mentioned data. Theoretical considerations will be presented in the next section. Following this, the sequence of model development will be: establish estimates for the onset of unidirectional flow, i.e., the flooding flow conditions; complete the model for the unidirectional flow regime; and develop the model for the mixed flow regime.

Flow Dynamics for Unstable Configurations: Theoretical Considerations

An unstable configuration with $p_T = p_H > p_B = p_L$, i.e., net flow from top to bottom, is designated as Configuration 1. Similarly, an unstable configuration, but with $p_B = p_H > p_T = p_L$, i.e., net flow from bottom to top, is designated as Configuration 2. The configurations are sketched in Figs. 3(a) and 3(b).

The Boundary Value Problems. Boundary value problems associated with Configurations 1 and 2, where the top and bottom spaces are filled with the same ideal gas, are discussed by Cooper (1993). These are identified as Problems 1 and 2, respectively. In the formulation of these problems, the Eq. (2) assumption leads to the approximation

$$\rho T = \text{const} = \rho_T T_T = \rho_B T_B = \bar{p}/R \tag{11}$$

where R is the gas constant and temperatures T_T and T_B correspond to specified ρ_T and ρ_B through Eq. (11). With the constraint of Eq. (3), Eq. (11) leads to the expected result

$$\Delta T = T_B - T_T > 0 \tag{12}$$

Note that Eq. (11) is a good approximation if (Cooper, 1993)

$$\Delta\rho g|X_3|/\bar{p} \ll 1 \quad \text{throughout the region of interest} \tag{13}$$

and that Eq. (13) is always satisfied in practical problems, e.g., ventilation of heated/cooled spaces and spread of smoke (i.e., fire-heated and -contaminated air) during fires in multiroom facilities.

Designate the dependent variables, velocity, pressure, density, and temperature, for Problem N, $N = 1$ or 2, as $U_i^{(N)}$, $p^{(N)}$, $\rho^{(N)}$, and $T^{(N)}$, respectively. Then, through the equations of conservation of mass, momentum, energy, and the modified equation of state, Eq. (11), all of these variables are found to be functions of the coordinates, $X_i^{(N)}$; the temperature-dependent material properties, $C_p(T)$, $k(T)$, and $\mu(T)$; and the specified parameters of a particular problem of interest.

Problems 1 and 2 are put in dimensionless form by introducing dimensionless dependent variables:

Problem 1:

$$U_i^{*(1)} = U_i^{(1)}/(2gD\epsilon)^{1/2};$$

$$p^{*\prime(1)} = (p + \bar{p} - g\bar{\rho}X_3)/(2g\Delta\rho D);$$

$$\rho^{*\prime(1)} = (\rho/\bar{p} - 1)/\epsilon; \quad T^{*\prime(1)} = (1 - T/\bar{T})/\epsilon$$

Problem 2:

$$U_i^{*(2)} = U_i^{(2)}/(2gD\epsilon)^{1/2};$$

$$p^{*\prime(2)} = (p - \bar{p} - g\bar{\rho}X_3)/(2g\Delta\rho D);$$

$$\rho^{*\prime(2)} = (1 - \rho/\bar{p})/\epsilon; \quad T^{*\prime(2)} = (T/\bar{T} - 1)/\epsilon \tag{14}$$

Neglecting pdV work and viscous dissipation in the energy equation, it has been shown by Cooper (1993) that the variables of Eq. (14) are functions only of $X_i^{*(N)}$ and the parameters ϵ, Π, $\bar{\text{Gr}}$, and $\bar{\text{Pr}}$, where[1]

$$X_i^{*(N)} = X_i^{(N)}/D; \quad \epsilon = \Delta\rho/\bar{\rho} = \Delta T/\bar{T} < 2;$$

$$\bar{\rho} = (\rho_T + \rho_B)/2 \tag{15}$$

$$\Pi = \Delta p/(4g\Delta\rho D); \quad \bar{\text{Gr}} = 2gD^3|\epsilon|/[\mu(\bar{T})/\bar{\rho}]^2;$$

$$\bar{\text{Pr}} = C_p(\bar{T})\mu(\bar{T})/k(\bar{T})$$

Thus, for example,

$$U_i^{*(N)} = U_i^{*(N)}(X_i^{*(N)}; \Pi, \epsilon, \bar{\text{Gr}}, \bar{\text{Pr}}) \tag{16}$$

In addition, it was shown that replacing ϵ by $-\epsilon$ in Problem 1 leads to Problem 2, and replacing ϵ by $-\epsilon$ in Problem 2 leads to Problem 1. This reflection-type relationship in the parameter ϵ between the two problems implies a corresponding relationship between their solutions, e.g.,

$$U_i^{*(1)}(X_i^{*(1)}; \Pi, \pm\epsilon, \bar{\text{Gr}}, \bar{\text{Pr}}) = U_i^{*(2)}(X_i^{*(2)}; \Pi, \mp\epsilon, \bar{\text{Gr}}, \bar{\text{Pr}}) \tag{17}$$

where similar equations can be written for the $p^{*\prime(N)}$, $\rho^{*\prime(N)}$, and $T^{*\prime(N)}$. Below, Eq. (17)-type relationships will be found to be very useful in combining analyses and correlations of previously published data from a mix of different Configuration 1 and 2-type experiments. Also, the reflection relationship is consistent with the necessary result that, for limiting small values of ϵ, when the Boussinesq approximation is valid, Problems 1 and 2 become identical, and the flow phenomena represented by the two Problems are mirror reflections of one another in the $X_3 = 0$ plane.

For $N = 1$ or 2, $\dot{V}_H^{(N)}$ and $\dot{V}_L^{(N)}$ can be calculated, in principle, from integrals of $U_3^{(N)}$ over the area of the vent, i.e., at $X_3^{(N)} =$

[1] Since $\epsilon > 0$, the absolute value designation for ϵ is unnecessary here. However, it will be useful in later applications of Eq. (15). A similar note is relevant below in the presentation of Eqs. (31) and (37).

Table 1 Results derived from the Configuration-1 experimental data of Heskestad and Spaulding (1989) for flow through a D = 0.153 m, L/D = 0.011 circular vent, and from Eqs. (22) and (24) for $\bar{\mathrm{Fr}}_{H,FL}^{(1)}$ and $\Pi_{FL}^{(1)}$, respectively

Test{1}	ϵ	$\mathrm{Fr}_H^{(1)}$	Π	$C_D^{(1)}$	$\bar{\mathrm{Gr}}$ {6}	$\mathrm{Fr}_H^{(1)}/\mathrm{Fr}_{H,FL}^{(1)}$ {6}	$C_D^{(1)}/C_{D,\infty}$ {5}	$\Pi/\Pi_{FL}^{(1)}$ {6}
54{2}	0.521	0.216	0.601	0.156	$2.99(10^7)$	0.924	0.261	1.10
55{2}	0.559	0.243	0.532	0.188	$3.49(10^7)$	1.02	0.314	0.923
56{2}	0.282	0.186	0.467	0.146	$4.64(10^7)$	0.910	0.243	1.24
59{2}	0.373	0.227	0.392	0.198	$4.74(10^7)$	1.05	0.329	0.901
60{2}	0.474	0.238	0.456	0.196	$4.06(10^7)$	1.04	0.326	0.900
61{2}	0.260	0.248	0.382	0.214	$4.66(10^7)$	1.23	0.356	1.04
53{3}	0.521	0.257	0.657	0.178	$2.99(10^7)$	1.10	0.296	1.21
53{3,4}	0.521	0.474	0.708	0.316	$2.99(10^7)$	2.03	0.527	1.30
53{3,4}	0.521	0.661	0.848	0.403	$2.99(10^7)$	2.83	0.671	1.56
53{3,4}	0.521	0.814	0.111	0.434	$2.99(10^7)$	3.48	0.723	2.04
54{4}	0.521	0.461	0.631	0.326	$2.99(10^7)$	1.97	0.543	1.16
55{4}	0.559	0.262	0.455	0.219	$3.49(10^7)$	1.10	0.366	0.790
56{4}	0.282	0.342	0.603	0.235	$4.64(10^7)$	1.57	0.392	1.59

{1} See TABLES III and VI of Heskestad and Spaulding (1989).

{2} Identified by Heskestad and Spaulding (1989) as the flooding condition, i.e., the $\mathrm{Fr}_H^{(1)}$, Π, and $C_D^{(1)}$ values for this datum point are $\mathrm{Fr}_{H,FL}^{(1)}$, $\Pi_{FL}^{(1)}$, and $C_{D,FL}^{(1)}$, respectively.

{3} Same fuel and fuel flow rate as Test Condition 54.

{4} T_∞ and T_0 are not presented by Heskestad and Spaulding (1989); it is assumed here that the values of these were the same as the values measured in the same test, i.e., the same fuel and fuel flow rate, but at flooding conditions.

{5} $C_{D,\infty}$ = 0.60 is from Perry (1949); $\mathrm{Fr}_{H,FL}^{(1)}$ and $\Pi_{FL}^{(1)}$ are from Eqs. (22) and (24), respectively.

{6} In calculating $\bar{\mathrm{Gr}}$ from Eq. (15), kinematic viscosity, $\nu(\bar{T}) = \mu(\bar{T})/\bar{\rho}$, is from Hilsenrath (1955)

$$\nu(\bar{T}) = [0.04128(\bar{T}/\mathrm{K})^{5/2}(10^{-7})/(\bar{T}/\mathrm{K} + 110.4)]\,\mathrm{m}^2/\mathrm{s}$$

0. Dimensionless flow rates are then defined in terms of the following Froude numbers, which also satisfy Eq. (17)-type relationships (Cooper, 1993)

$$\bar{\mathrm{Fr}}_H^{(N)}(\Pi, \epsilon, \bar{\mathrm{Gr}}, \bar{\mathrm{Pr}}) = (\dot{V}_H^{(N)}/A_V)/(2gD\epsilon)^{1/2};$$
$$\bar{\mathrm{Fr}}_L^{(N)}(\Pi, \epsilon, \bar{\mathrm{Gr}}, \bar{\mathrm{Pr}}) = (\dot{V}_L^{(N)}/A_V)/(2gD\epsilon)^{1/2} \qquad (18)$$

Unidirectional Flow

The Flow Coefficient and the Large-Gr Assumption. The C_D of Eq. (4) remains useful for unidirectional flow regime. Using Eqs. (15) and (18) in this leads to the following definition of $C_D^{(N)}$, which also satisfies an Eq. (17)-type relationship

$$C_D^{(N)} = C_D^{(N)}(\Pi, \epsilon, \bar{\mathrm{Gr}}, \bar{\mathrm{Pr}}) = [(\rho_H/\bar{\rho})/(4\Pi)]^{1/2}\bar{\mathrm{Fr}}_H^{(N)};$$
$$\lim_{\bar{\mathrm{Fr}}_H^{(N)} \to \infty} C_D^{(N)} = C_{D,\infty}; \quad \rho_H/\bar{\rho} = \begin{cases} 1 + \epsilon/2, & N = 1 \\ 1 - \epsilon/2, & N = 2 \end{cases} \qquad (19)$$

C_D is for a particular vent design and would generally vary from one design to another, e.g., shallow circular versus shallow square vents. *Unless noted otherwise, the remainder of this work focuses only on turbulent, large-$\bar{\mathrm{Gr}}$ flow through small-L/D circular vents,* where "small-L/D" means, approximately, $L/D < 0.10$, and where the "large-$\bar{\mathrm{Gr}}$" terminology will be clarified below.

The Flooding Condition

The Region of Turbulent, Large-$\bar{\mathrm{Gr}}$ Flow. For fixed ϵ, $\bar{\mathrm{Gr}}$, and $\bar{\mathrm{Pr}}$ there is a specific Π, associated with Δp_{FL} and depending on N, that leads to flooding. This is designated as $\Pi_{FL}^{(N)}$, where (Cooper, 1993)

$$\Pi_{FL}^{(N)} = \Pi_{FL}^{(N)}(\epsilon, \bar{\mathrm{Gr}}, \bar{\mathrm{Pr}}) \equiv \Delta p_{FL}^{(N)}/(4g\Delta\rho D) \qquad (20)$$

and corresponding values of $\bar{\mathrm{Fr}}_H^{(N)}$, $\dot{V}_H^{(N)}$, and $C_D^{(N)}$ are designated as $\bar{\mathrm{Fr}}_{H,FL}^{(N)}$, $\dot{V}_{H,FL}^{(N)}$, and $C_{D,FL}^{(N)}$ respectively.

Heskestad and Spaulding (1989) present data from Configuration-1 experiments with air ($\bar{\mathrm{Pr}}$ = 0.7) in the unidirectional flow regime. $\bar{\mathrm{Fr}}$, Π, ϵ, and $\bar{\mathrm{Gr}}$ corresponding to their data are presented in Table 1. Included are 13 sets of data, where 6 of these are associated with the flooding condition. [The theoretical analysis given above is for perfect gas media and is valid for the entire range $-2 < \epsilon < 2$. However, for $|\epsilon| \ll 1$, when the Boussinesq approximation is applicable, there is an analogy between Fig. 1-type problems involving perfect gases and incompressible or nearly incompressible liquids. In the case of small-ϵ problems involving liquids, buoyancy effects that drive the exchange flows can be the result of temperature differences or of concentration differences of a solvent. This is the justification for use of the salt/fresh-water data (where $|\epsilon| < 0.2$) of Epstein and Kenton (1989), Tan and Jaluria (1991), and Heskestad and Spaulding (1989) in the data analyses to follow.]

Flooding conditions were measured in the salt/fresh-water experiments ($\bar{\mathrm{Pr}} \approx 7$) of Epstein and Kenton (1989) and Tan and Jaluria (1991). All small-L/D flooding data from Epstein and Kenton (1989), Tan and Jaluria (1991), and Heskestad and Spaulding (1989) are presented in Table 2. The salt-water experiments involved both Configurations 1 and 2 (referred to by Epstein and Kenton (1989) as "draining" and "injection" experiments, respectively). Since Δp was not measured by Epstein and Kenton (1989), $\Pi_{FL}^{(N)}$ and $C_{D,FL}^{(N)}$ are not available for their data.

For these data, $\bar{\mathrm{Fr}}_{H,FL}^{(N)}$ versus $\bar{\mathrm{Gr}}$, is plotted in Fig. 4 where it is seen that $\bar{\mathrm{Fr}}_{H,FL}^{(N)}$ is relatively insensitive to changes in $\bar{\mathrm{Gr}}$ in the range $2.99(10^7) \le \bar{\mathrm{Gr}} \le 2.91(10^8)$. (As will be explained below, observed variations in $\bar{\mathrm{Fr}}_{H,FL}^{(N)}$ in this range are primarily a result of its dependence on ϵ.) However, there is a significant increase in $\bar{\mathrm{Fr}}_{H,FL}^{(N)}$, over the larger-$\bar{\mathrm{Gr}}$ values, for $\bar{\mathrm{Gr}} \le 1.42(10^7)$, i.e., for the data of Tan and Jaluria (1991). Using flooding data for square, rectangular, and circular vents, acquired over a large range of $\bar{\mathrm{Gr}}$, Fig. 10 of Heskestad and Spaulding (1989) indicates a similar insensitivity in the dependence of $\bar{\mathrm{Fr}}_{H,FL}^{(N)}$ on $\bar{\mathrm{Gr}}$ for $\bar{\mathrm{Gr}} > 2(10^7)$ and a similar, relatively abrupt increase in $\bar{\mathrm{Fr}}_{H,FL}^{(N)}$ as $\bar{\mathrm{Gr}}$ drops below approximately $2(10^7)$. [In computing $\bar{\mathrm{Gr}}$ for the square and rectangular-vent

Table 2 Small-L/D data on flooding conditions from Epstein and Kenton (1989), Tan and Jaluria (1991), and Heskestad and Spaulding (1989)

Reference	ϵ	Configuration Number	$\mathrm{Fr}_{H,FL}^{(1)}$	$\bar{\mathrm{Gr}}$	$C_{D,FL}^{(1)}$	$\Pi_{FL}^{(1)}$
Heskestad and Spaulding (1989)	0.521	1	0.216	$2.99(10^7)$	0.156	0.601
"	0.559	1	0.243	$3.49(10^7)$	0.188	0.532
"	0.282	1	0.186	$4.64(10^7)$	0.146	0.467
"	0.373	1	0.227	$4.74(10^7)$	0.198	0.392
"	0.474	1	0.238	$4.06(10^7)$	0.196	0.456
"	0.260	1	0.248	$4.66(10^7)$	0.214	0.382
Epstein and Kenton (1989)	0.1426	1	0.1917	$5.31(10^7)$	{1}	{1}
"	0.1410	1	0.1755	$5.25(10^7)$	{1}	{1}
"	0.1378	2	0.1632	$5.13(10^7)$	{1}	{1}
"	0.1487	1	0.2057	$5.54(10^7)$	{1}	{1}
"	0.1339	2	0.1783	$4.98(10^7)$	{1}	{1}
"	0.1456	1	0.1826	$2.91(10^8)$	{1}	{1}
"	0.1329	1	0.1709	$2.66(10^8)$	{1}	{1}
"	0.1417	1	0.1618	$2.84(10^8)$	{1}	{1}
Tan and Jaluria (1991)	0.0469	2	0.2534	$4.28(10^6)$	0.0956	1.638
"	0.0656	2	0.4383	$6.00(10^6)$	0.194	1.191
"	0.0898	2	0.3463	$8.20(10^6)$	0.168	0.970
"	0.1208	2	0.4132	$1.10(10^7)$	0.218	0.793
"	0.1550	2	0.3877	$1.41(10^7)$	0.220	0.659

{1} This value is not available since Δp was not measured

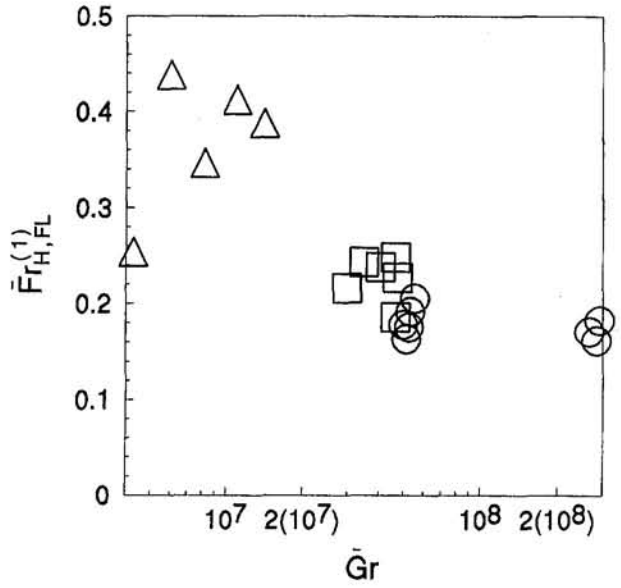

Fig. 4 Plot of $\bar{Fr}^{(1)}_{H,FL}$ as a function of $\bar{Gr}$ for all small-L/D data of Table 2 (○—Epstein and Kenton, 1989; △—Tan and Jaluria, 1991; □—Heskestad and Spaulding, 1989)

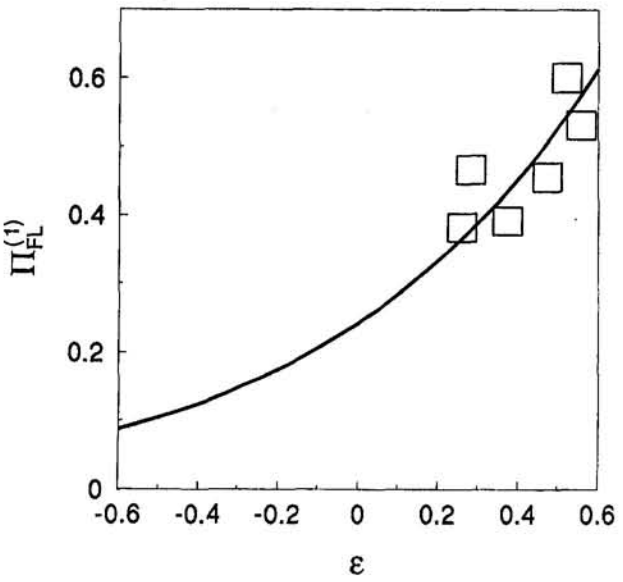

Fig. 6 Plot of the $\Pi^{(1)}_{FL}(\epsilon)$: data of Table 2; ——, least-squares curve fit of Eq. (24)

data of Heskestad and Spaulding (1989), Eq. (15) was used, where D is replaced by the width of the vent. Of these data, the one with the largest $\bar{Gr} = 1.54(10^{10})$, is for flooding flow through a rectangular vent of dimension 2.03 m × 0.91 m.]

Consistent with the above, it is assumed that $\bar{Gr} > 2(10^7)$ defines a range of turbulent buoyancy-driven flows where the $\bar{Gr}$ dependence of the governing boundary value problem is negligible.

This discussion ignores the $\bar{Pr}$ dependence of $\bar{Fr}^{(N)}_{H,FL}$. Here it is reasonable to assume that in the large-$\bar{Gr}$ range of practical interest, molecular diffusion effects of $\bar{Pr}$ variations are negligible, at least for the approximate range, say, $0.7 \le \bar{Pr} \le 7$. Then, for large enough $\bar{Gr}$ and for at least the latter $\bar{Pr}$ range, it is assumed from functional relationships of Eqs. (18)–(20) that $\bar{Fr}^{(N)}_{H}$, $\bar{Fr}^{(N)}_{L}$, and $C^{(N)}_{D}$ are functions only of Π and ϵ, and that $\bar{Fr}^{(N)}_{H,FL}$, $C^{(N)}_{D,FL}$, and $\Pi^{(N)}_{FL}$ are functions only of ϵ, i.e.,

$$\text{For } \bar{Gr} > 2(10^7): \quad \bar{Fr}^{(N)}_{H,FL}(\epsilon, \bar{Gr}, \bar{Pr}) = \bar{Fr}^{(N)}_{H,FL}(\epsilon);$$
$$\bar{Fr}^{(N)}_{H}(\Pi, \epsilon, \bar{Gr}, \bar{Pr}) = \bar{Fr}^{(N)}_{H}(\Pi, \epsilon); \quad \text{etc.} \qquad (21)$$

The Eq. (21) assumption will also be adopted below in the mixed flow regime. In contrast to this, it is assumed that $\bar{Gr} < 2(10^7)$ defines transition and laminar flow regimes of the problem, where $\bar{Gr}$ and possible $\bar{Pr}$ dependence is important.

Practical vent flow problems of the type of interest here, e.g., problems related to fire safety and building ventilation, are typically confined to the large-$\bar{Gr}$ range, $\bar{Gr} > 2(10^7)$. *The remainder of this work focuses only on large-$\bar{Gr}$ problems, and, unless noted otherwise, $\bar{Gr}$ and $\bar{Pr}$ independence of all the flow phenomena is always assumed.*

The Functions $\bar{Fr}^{(N)}_{H,FL}(\epsilon)$, $\Pi^{(N)}_{FL}(\epsilon)$, and $C^{(N)}_{D,FL}(\epsilon)$. The $\bar{Fr}^{(1)}_{H,FL}(\epsilon)$, $\Pi^{(1)}_{FL}(\epsilon)$, and $C^{(1)}_{D,FL}(\epsilon)$ data of Table 2, obtained from results of Epstein and Kenton (1989) and Heskestad and Spaulding (1989), are plotted in Figs. 5, 6, and 7, respectively.

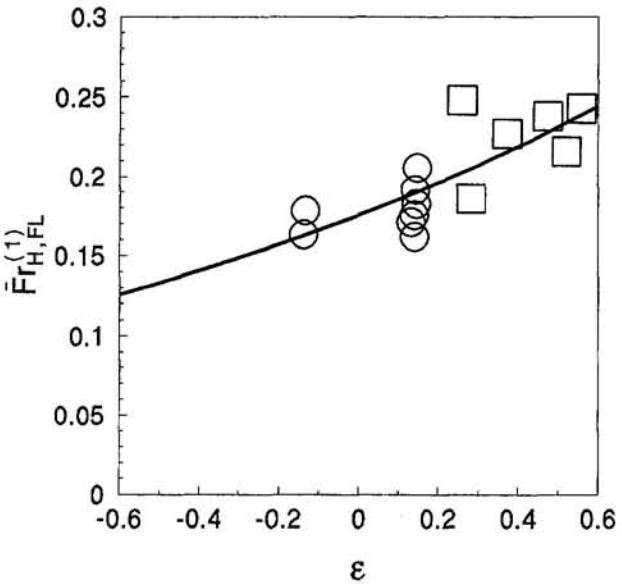

Fig. 5 Plot of $\bar{Fr}^{(1)}_{H,FL}(\epsilon)$: data of Table 2 (○—Epstein and Kenton, 1989, □—Heskestad and Spaulding, 1989); ——, least-squares curve fit of Eq. (22)

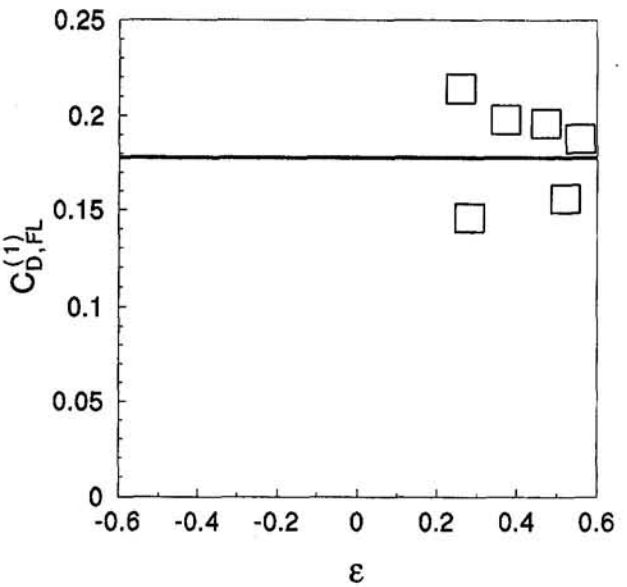

Fig. 7 Plot of $C^{(1)}_{D,FL}(\epsilon)$: □, data of Table 2; ——, curve fit of Eq. (23)

[Tan and Jaluria's (1991) data do not satisfy the large-$\bar{\bar{G}}r$ criterion of Eq. (21).] Equation (17)-type reflection relationships, applicable to each of the plotted functions, are implemented. Thus, the data and solution are plotted in terms of the Configuration-1 problem, with Configuration-2 results presented with $\epsilon < 0$. Also plotted in Fig. 5 is the following least-squares fit of the $\bar{\mathrm{Fr}}^{(1)}_{H,FL}(\epsilon)$ data:

$$\bar{\mathrm{Fr}}^{(1)}_{H,FL}(\epsilon) = 0.1754 \exp(0.5536\epsilon) \tag{22}$$

As seen in Fig. 7, $C^{(1)}_{D,FL}$ data are very sparse, with no entries for small $|\epsilon|$ or $\epsilon < 0$. Also, the data scatter does not provide qualitative insight on the "shape" of the $C^{(1)}_{D,FL}$ function. Until more data become available, it is therefore reasonable to approximate $C^{(1)}_{D,FL}(\epsilon)$ as a constant. A possible choice is the average value, 0.1830. However, since C_D is defined from Eq. (4), and since $C^{(1)}_{D,FL}$ entries of Table 2 are derived from the $\bar{\mathrm{Fr}}^{(1)}_{H,FL}(\epsilon)$ and $\Pi^{(1)}_{FL}(\epsilon)$ data according to Eq. (19), a more appropriate, constant, representive value for $C^{(1)}_{D,FL}$ is the one that provides a least-squares fit of the $\Pi^{(1)}_{FL}(\epsilon)$ data, namely

$$C^{(1)}_{D,FL}(\epsilon) = 0.1780 \tag{23}$$

$$\Pi^{(1)}_{FL}(\epsilon) = \Delta p^{(1)}_{FL}/(4g\Delta\rho D) = 0.2427(1 + \epsilon/2)\exp(1.1072\epsilon) \tag{24}$$

Equation (24) is plotted in Fig. 6 and Eq. (23) is plotted in Fig. 7.

In Fig. 6, the sparseness of the available $\Pi^{(1)}_{FL}(\epsilon)$ data, especially with the absence of entries for small $|\epsilon|$ or $\epsilon < 0$, and the predicted significant $\Pi^{(1)}_{FL}(\epsilon)$ variation of Eq. (24) in the ϵ range of interest, is problematic. Nevertheless, the results of Eqs. (22)–(24) are plausible, and they fill a gap where alternative choices are not available. These results will be used throughout the remainder of this work.

An Estimate for C_D. It is convenient to normalize Eq. (19) as follows:

$$C^{(1)}_D(\Pi, \epsilon)/C_{D,\infty} = [C^{(1)}_{D,FL}(\epsilon)/C_{D,\infty}] \times [\bar{\mathrm{Fr}}^{(1)}_H(\Pi, \epsilon)/\bar{\mathrm{Fr}}^{(1)}_{H,FL}(\epsilon)]/[\Pi/\Pi^{(1)}_{FL}(\epsilon)]^{1/2} \tag{25}$$

where, at the two limits of the unidirectional flow regime,

$$\lim_{\Pi/\Pi^{(1)}_{FL}(\epsilon)\to 1} C^{(1)}_D(\Pi, \epsilon)/C_{D,\infty} = [C^{(1)}_{D,FL}(\epsilon)/C_{D,\infty}] \equiv 1/\sigma_1(\epsilon);$$

$$\lim_{\Pi/\Pi^{(1)}_{FL}(\epsilon)\to\infty} C^{(1)}_D(\Pi, \epsilon)/C_{D,\infty} = 1 \tag{26}$$

To obtain vent flow rate as a function of Δp, it is convenient to choose the functional form

$$\bar{\mathrm{Fr}}^{(1)}_H/\bar{\mathrm{Fr}}^{(1)}_{H,FL} = \dot{V}^{(1)}_H/\dot{V}^{(1)}_{H,FL} = f(\Pi/\Pi^{(1)}_{FL}; \epsilon) = f(\Delta p/\Delta p^{(1)}_{FL}; \epsilon) \tag{27}$$

and to approximate $C^{(1)}_D(\Pi, \epsilon)/C_{D,\infty}$ as

$$C^{(1)}_D(\Pi, \epsilon)/C_{D,\infty} = (\bar{\mathrm{Fr}}^{(1)}_H/\bar{\mathrm{Fr}}^{(1)}_{H,FL})/\{[\bar{\mathrm{Fr}}^{(1)}_H/\bar{\mathrm{Fr}}^{(1)}_{H,FL}) - 1 + \sigma_2^2]^2 + \sigma_1^2 - \sigma_2^4\}^{1/2} \tag{28}$$

where Eq. (28) satisfies Eqs. (26) and $\sigma_2 = \sigma_2(\epsilon)$ would be determined from a fit of $C^{(1)}_D(\Pi, \epsilon)/C_{D,\infty}$ data.

$C^{(1)}_D/C_{D,\infty}$ data for nonflooding conditions include five data points for $\epsilon = 0.521$ and only single data points for each of two other ϵ, $\epsilon = 0.282$ and 0.559. Until further data are available, it is therefore reasonable to approximate $\sigma_2(\epsilon)$ as a constant. Using Eqs. (23) and (26), and choosing σ_2 as the value providing a least-squares fit to Eq. (28) of all available $\bar{\mathrm{Fr}}^{(1)}_H/\bar{\mathrm{Fr}}^{(1)}_{H,FL}$ data, leads to

$$\sigma_1(\epsilon) \approx \text{const} = 0.60/0.1780 = 3.370;$$

$$\sigma_2(\epsilon) \approx \text{const} = 1.045 \tag{29}$$

Using Eq. (29), Eq. (28) is plotted in Fig. 8 along with $C^{(1)}_D(\Pi, \epsilon)/C_{D,\infty}$ versus $\bar{\mathrm{Fr}}^{(1)}_H/\bar{\mathrm{Fr}}^{(1)}_{H,FL}$ data of Table 1.

The Model for the Vent Flow in the Unidirectional Flow Regime. Equations (25) and (28) lead to the solution for $\bar{\mathrm{Fr}}^{(1)}_H$ or $\dot{V}^{(1)}_H$ for the unidirectional flow regime:

$$\text{For } \Delta p/\Delta p^{(1)}_{FL} = \Pi/\Pi^{(1)}_{FL} \geq 1: \tag{30}$$

$$\dot{V}^{(1)}_H/\dot{V}^{(1)}_{H,FL} = \bar{\mathrm{Fr}}^{(1)}_H/\bar{\mathrm{Fr}}^{(1)}_{H,FL} = 1 - \sigma_2^2 + [\sigma_2^4 + \sigma_1^2(\Delta p/\Delta p^{(1)}_{FL} - 1)]^{1/2};$$

$$\dot{V}^{(1)}_L/\dot{V}^{(1)}_{H,FL} = \bar{\mathrm{Fr}}^{(1)}_L/\bar{\mathrm{Fr}}^{(1)}_{H,FL} = 0$$

where σ_1 and σ_2 are given in Eq. (29), $\Delta p^{(1)}_{FL}$ in Eq. (24), and $\dot{V}^{(1)}_{H,FL}$, from Eqs. (18) and (22), is

$$\dot{V}^{(1)}_{H,FL} = 0.1754(2gD|\epsilon|)^{1/2}A_V \exp(0.5536\epsilon) \tag{31}$$

As required, Eq. (30) guarantees that $\dot{V}^{(1)}_H/\dot{V}^{(1)}_{H,FL}$ is a monotonically increasing function of $\Delta p/\Delta p^{(1)}_{FL}$ for $\Delta p/\Delta p^{(1)}_{FL} \geq 1$. [This is a consequence of the chosen form of Eq. (28).] Also, recalling Eq. (26), Eq. (30) is seen to satisfy the large-Δp limit, which is equivalent to the standard Bernoulli orifice flow condition, i.e.,

$$\lim_{\Delta p/\Delta p^{(1)}_{FL}\to\infty} \dot{V}^{(1)}_H/\dot{V}^{(1)}_{H,FL} = (C_{D,\infty}/C^{(1)}_{D,FL})(\Delta p/\Delta p^{(1)}_{FL})^{1/2} \tag{32}$$

Equation (30) is the model equation result for the unidirectional flow regime. From this, a plot of $\dot{V}^{(1)}_H/\dot{V}^{(1)}_{H,FL}$ versus $\Delta p/\Delta p^{(1)}_{FL}$ is presented in Fig. 9 together with plots of the Table 1 data and the Bernoulli-flow limit of Eq. (32). From the figure it can be seen that at the flooding condition the standard Bernoulli-flow equation overestimates the expected flow rate by a factor in excess of 3, and that only after $\Delta p/\Delta p^{(1)}_{FL}$ exceeds 3 or 4 does the standard model provide flow-rate estimates correct to within a few tens of a percent.

The Mixed Flow Regime

Boundary Conditions for the Flow Components. The following representations for $\dot{V}^{(1)}_N/\dot{V}^{(1)}_{H,FL}$, $\dot{V}^{(1)}_L/\dot{V}^{(1)}_{H,FL}$, and

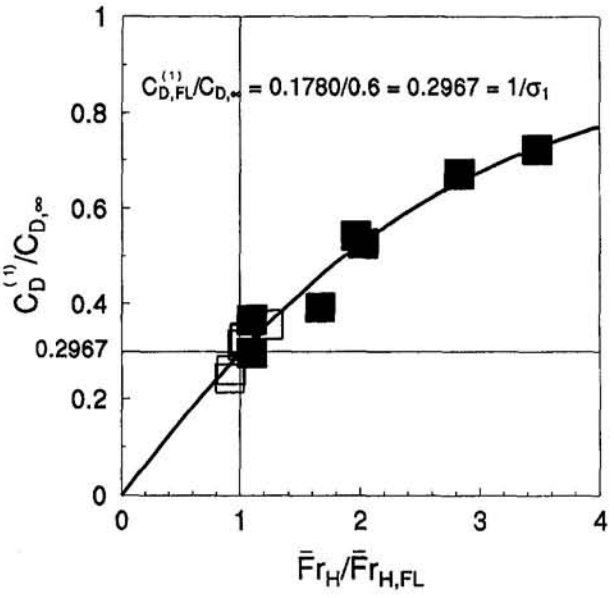

Fig. 8 Plot of $C^{(1)}_D/C_{D,\infty}$ versus $\bar{\mathrm{Fr}}^{(1)}_H/\bar{\mathrm{Fr}}^{(1)}_{H,FL}$: ——, Eqs. (28) and (29); ■, nonflooding data of Table 1; □, flooding data of Table 1

$\dot{V}_H^{(1)}/\dot{V}_{H,FL}^{(1)}$ as functions of $\Delta p/\Delta p_{FL}^{(1)}$ are adopted for the mixed-flow regime. They satisfy Eqs. (5)–(7), and, at the flooding limit boundary, $\Delta p/\Delta p_{FL}^{(1)} = 1$, they join with continuous slope to the unidirectional flow solutions of Eq. (30).

$$\dot{V}_N^{(1)}/\dot{V}_{H,FL}^{(1)} = \{M - [1 + (M^2 - 1) \times (1 - \Delta p/\Delta p_{FL}^{(1)})]^{1/2}\}/(M - 1) \quad (33)$$

$$\dot{V}_L^{(1)}/\dot{V}_{EX,MX} = [(1 + m_1/2)(1 - \Delta p/\Delta p_{FL}^{(1)})^2 - (2 + m_1/2)(1 - \Delta p/\Delta p_{FL}^{(1)})]^2 \quad (34)$$

$$\dot{V}_H^{(1)}/\dot{V}_{H,FL}^{(1)} = \dot{V}_L^{(1)}/\dot{V}_{H,FL}^{(1)} + \dot{V}_N^{(1)}/\dot{V}_{H,FL}^{(1)} \quad (35)$$

$$M = (\sigma_1/\sigma_2)^2 - 1 = 9.400 \quad (36)$$

where $\dot{V}_{EX,MX}$ for shallow circular vents is obtained from Epstein (1988)

$$\dot{V}_{EX,MX} = 0.055(4/\pi)A_V(gD|\epsilon|)^{1/2} \quad (37)$$

and the yet-undetermined value for m_1 is defined in terms of the slope of the $\dot{V}_L^{(1)}/\dot{V}_{H,FL}^{(1)}$ plot of Fig. 2

$$m_1(\epsilon) = (\dot{V}_{H,FL}^{(1)}/\dot{V}_{EX,MX})d(\dot{V}_L^{(1)}/\dot{V}_{H,FL}^{(1)})/d(\Delta p/\Delta p_{FL}^{(1)})|_{\Delta p/\Delta p_{FL}^{(1)}=0} \quad (38)$$

Epstein and Kenton (1989) acquired flow data for circular vents ($L/D = 0.0190$ and 0.113) and tubes ($0.39 \le L/D \le 5.0$) in a limited portion of the mixed flow regime. These are reported to have "experimental uncertainty . . . between 10 and 30 percent." Difficulty in acquiring accurate data close to the unidirectional flow regime ($\dot{V}_N^{(1)}/\dot{V}_{H,FL}^{(1)} > 0.6$, $0 \le \dot{V}_L^{(1)}/\dot{V}_{EX,MX} < 0.1$) apparently precluded measurements in this range.

The ϵ range of the Epstein and Kenton (1989) data is so narrow ($0.12 \le \epsilon \le 0.16$) that they cannot be used to determine ϵ dependence of m_1 that may exist. Accordingly, m_1 is approximated as a constant.

Equations (33) and (34) lead to $\dot{V}_L^{(1)}/\dot{V}_{EX,MX}$ as a function of $\dot{V}_N^{(1)}/\dot{V}_{H,FL}^{(1)}$. The m_1 value providing a least-squares fit of this function to small-L/D data (Epstein and Kenton, 1989) was found to be

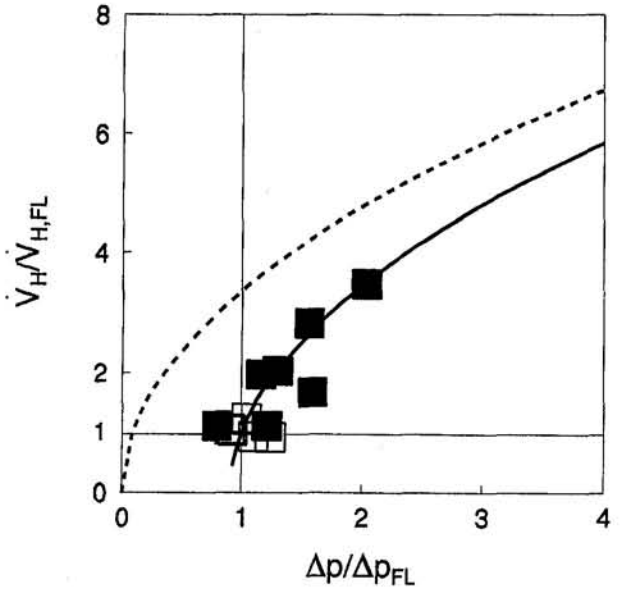

Fig. 9 Plot of $\dot{V}_H^{(1)}/\dot{V}_{H,FL}^{(1)} = \bar{Fr}_H^{(1)}/\bar{Fr}_{H,FL}^{(1)}$ versus $\Delta p/\Delta p_{FL}^{(1)} = \Pi/\Pi_{FL}^{(1)}$: ——, model equation for the unidirectional flow regime, Eqs. (29) and (30); - - -, Bernoulli flow limit of Eq. (32); ■, nonflooding data of Table 1; □, flooding data of Table 1

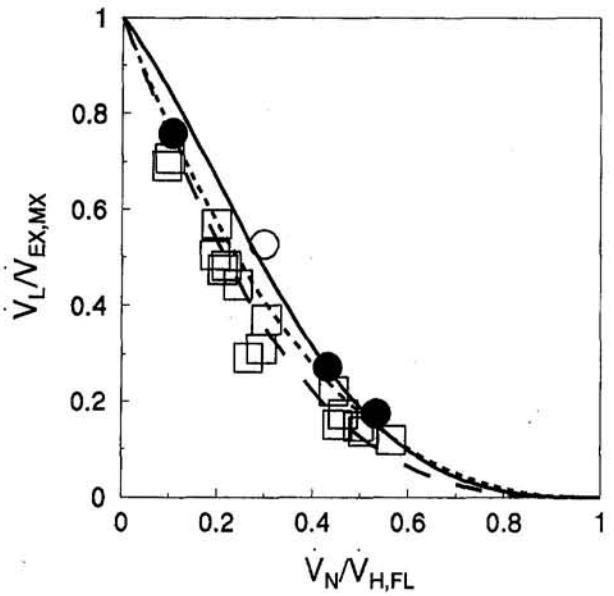

Fig. 10 Plot of $\dot{V}_L^{(1)}/\dot{V}_{EX,MX}$ versus $\dot{V}_N^{(1)}/\dot{V}_{H,FL}^{(1)}$ from Eqs. (24), (31), (33)–(37), and (39), ——; Eqs. (24), (31), (33)–(37), and (40), - - -; and Eq. (42), ···. Plot of data of Epstein and Kenton (1989) ($L/D = 0.0190$ vent, ●; $L/D = 0.113$ vent, ○; and tubes with $0.39 \le L/D \le 5.0$, □).

$$m_1 = -0.7070 \quad \text{(best fit for } L/D = 0.0190 \text{ and } 0.112 \text{ data of Epstein and Kenton, 1989)} \quad (39)$$

Equations (24), (31), (33)–(37), and (39) are the model equations for the mixed flow regime.

Additional Comments Regarding Mixed Flow Data. $\dot{V}_L^{(1)}/\dot{V}_{EX,MX}$ versus $\dot{V}_N^{(1)}/\dot{V}_{H,FL}^{(1)}$ is plotted in Fig. 10 with all Epstein and Kenton (1989) data. Note that these data, the bulk of which involve flow through tubelike vents (i.e., moderate-to-large L/D) rather than shallow vents, are well correlated by the m_1 of Eq. (39), established from the few, available, shallow-vent data. Also determined was the m_1 value providing the least-squares fit of all Epstein and Kenton (1989) data

$$m_1 = -1.8077 \quad \text{(best fit for all data of Epstein and Kenton, 1989, } 0.0190 \le L/D \le 5.0) \quad (40)$$

and $\dot{V}_L^{(1)}/\dot{V}_{EX,MX}$ versus $\dot{V}_N^{(1)}/\dot{V}_{H,FL}^{(1)}$, computed with Eq. (40) instead of Eq. (39), is also plotted in Fig. 10.

It is of interest to compute m_2, the slope of the Fig. 10 plots at $\dot{V}_N^{(1)} = 0$:

$$m_2 = d(\dot{V}_L^{(1)}/\dot{V}_{EX,MX})/d(\dot{V}_N^{(1)}/\dot{V}_{H,FL}^{(1)})|_{\dot{V}_N^{(1)}/\dot{V}_{H,FL}^{(1)}=0}$$
$$= [2m_1M/(M + 1)]$$
$$= -1.2781 \quad [m_1 \text{ from Eq. (39)}];$$
$$= -2.625 \quad [m_1 \text{ from Eq. (40)}] \quad (41)$$

These can be compared to $m_2 = -2.5$, associated with Eq. (22) of Epstein and Kenton (1989), viz.[2]

$$\dot{V}_L^{(1)}/\dot{V}_{EX,MX} = (1 - \dot{V}_N^{(1)}/\dot{V}_{H,FL}^{(1)})^{2.5} \quad (42)$$

A plot of Eq. (42) is included in Fig. 10.

[2] The 2.5 exponent in Eq. (42) is different from that of Eq. (23) of Epstein and Kenton (1989), which seems to be printed incorrectly. Equation (42) corresponds to the correlating function plotted in Fig. 5 of Epstein and Kenton (1989).

VENTCL2—An Algorithm for Combined Buoyancy and Pressure-Driven Flow Through Horizontal Vents; Summary and Conclusions

Analysis of relevant boundary value problems and of previously published data from experiments in salt-water/freshwater and cold-air/hot-air flow configurations has resulted in the following vent flow model, called VENTCL2. This is an algorithm to calculate the flow, for unstable cross-vent density configurations (high density over low density), through shallow (small-L/D), horizontal, circular vents, and under arbitrary cross-vent pressure difference (see Fig. 1):

1 Verify that $\rho_T > \rho_B$, i.e., that the configuration is unstable, and calculate $\Delta\rho$ from Eq. (3); determine $\bar{T}$ from Eq. (10), $\epsilon > 0$ and $\bar{p}$ from Eq. (15), and $\mu(\bar{T})$ from note {6} of Table 1; determine Gr from Eq. (15) and verify that Gr satisfies the large-Gr criterion, $\mathrm{Gr} \geq 2(10^7)$.
2 Determine p_H and p_L, Δp, and $\bar{p}$ from Eqs. (1) and (2); according to Fig. 1 designate the problem type as either Problem 1 or 2, involving Configuration 1 or 2, respectively; if it is Configuration 2, then replace ϵ by $-\epsilon < 0$.
3 Calculate $\bar{\mathrm{Fr}}^{(1)}_{H,FL}$ and then $\dot{V}^{(1)}_{H,FL}$ from Eqs. (22) and (31), $\Delta p^{(1)}_{FL}$ from Eq. (24), and $\Delta p/\Delta p^{(1)}_{FL}$.
4 If $\Delta p/\Delta p^{(1)}_{FL} \geq 1$, expect unidirectional flow. Estimate $\dot{V}_L = \dot{V}^{(1)}_L = 0$ and $\dot{V}_H = \dot{V}^{(1)}_H$ from Eqs. (29) and (30).
5 If $\Delta p/\Delta p_{FL} < 1$, expect mixed flow. Estimate: $\dot{V}_N = \dot{V}^{(1)}_N$ from Eqs. (33) and (36); $\dot{V}_{EX,MX}$ and then $\dot{V}_L = \dot{V}^{(1)}_L$ from Eqs. (37), (34), and (39); and $\dot{V}_H = \dot{V}^{(1)}_H$ from Eq. (35).

As indicated, the applicability of VENTCL2 is limited to large-$\bar{\mathrm{Gr}}$ flow scenarios, $\bar{\mathrm{Gr}} \geq 2(10^7)$, involving shallow, circular vents. The theoretical ideas developed here could be used to remove the these limitations, but additional model development would require experimental data that are not now available. Indeed, even within present limitations, additional data are required to verify the accuracy of VENTCL2. In this regard, the unidirectional flow regime, where high and low-pressure sides of the vent are in the lower and upper space, respectively, is particularly problematic since there are no available data at all in this regime, and none were used in the development of VENTCL2.

A major application of the new flow model would be in problems related to simulating smoke/air movement during fires in buildings and other enclosed facilities. For this, VENTCL2 is in a form that is particularly suitable for use in zone-type compartment fire models.

Acknowledgments

Much of the work presented here was done while the author was a guest of the Fire Research Institute of Japan. The author gratefully acknowledges the gracious hospitality and very useful discussions with the staff of that institution during that visit, and especially with Dr. Tokiyoshi Yamada.

References

Brown, W. G., 1962, "Natural Convection Through Rectangular Openings in Partitions—2. Horizontal Partitions," *International Journal of Heat and Mass Transfer*, Vol. 5, pp. 869–878.

Cooper, L. Y., 1989, "A Note on Calculating Flows Through Vertical Vents in Zone Fire Models Under Conditions of Arbitrary Cross-Vent Pressure Difference," *Combustion Science and Technology*, Vol. 63, Nos. 1–3, pp. 43–50.

Cooper, L. Y., 1990, "Estimating the Environment and the Response of Sprinkler Links in Compartment Fires With Draft Curtains and Fusible Link-Actuated Ceiling Vents—Theory," *Fire Safety Journal*, Vol. 16, pp. 137–163.

Cooper, L. Y., and Forney, G. P., 1990, "The Consolidated Compartment Fire Model Computer Code Application CCFM.VENTS, Parts I, II, III, and IV," NISTIR 4342, 4343, 4344, and 4345, respectively, U.S. National Institute of Standards and Technology, Gaithersburg, MD.

Cooper, L. Y., 1993, "Combined Buoyancy- and Pressure-Driven Flow Through a Horizontal Vent: Theoretical Considerations," NISTIR 5252, U.S. National Institute of Standards and Technology, Gaithersburg, MD.

Cooper, L. Y., 1994, "Combined Buoyancy- and Pressure-Driven Flow Through a Horizontal Vent," NISTIR 5384, U.S. National Institute of Standards and Technology, Gaithersburg, MD.

Emmons, H. W., 1988, "Vent Flows," Section 1, Chap. 8, *SFPE Handbook of Fire Protection Engineering*, P. J. DiNenno et al., eds., SFPE, Boston, MA, pp. 130–138.

Epstein, M., 1988, "Buoyancy-Driven Exchange Flow Through Small Openings in Horizontal Partitions," ASME JOURNAL OF HEAT TRANSFER, Vol. 110, pp. 885–893.

Epstein, M., and Kenton, M. A., 1989, "Combined Natural Convection and Forced Flow Through Small Openings in a Horizontal Partition With Special Reference to Flows in Multicompartment Enclosures," ASME JOURNAL OF HEAT TRANSFER, Vol. 111, pp. 980–987.

Heskestad, G., and Spaulding, R. D., 1989, "Inflow of Air Required at Wall and Ceiling Apertures to Prevent Escape of Fire Smoke," FMRC J.I. OQ4E4.RU, Factory Mutual Research Corporation, Norwood MA; also 1991 (without tables), *Proceedings of the 3rd International Symposium on Fire Safety Science*, Elsevier, New York, pp. 919–928.

Hilsenrath, J., et al., 1955, *Tables of Thermal Properties of Gases*, NBS circular 564, U.S. National Bureau of Standards (presently U.S. National Institute of Standards and Technology), Gaithersburg, MD.

Mitler, H. E., and Emmons, H. W., 1981, "Documentation for CFC V, the Fifth Harvard Computer Fire Code," NBS-GCR-81-344, Harvard University Report to U.S. National Bureau of Standards (presently U.S. National Institute of Standards and Technology), Gaithersburg, MD.

Perry, J. A., 1949, "Critical Flow Through Sharp-Edged Orifices," *Transactions of ASME*, Vol. 71, pp. 757–764.

Tan, Q., and Jaluria, J., 1991, "Flow Through Horizontal Vents as Related to Compartment Fire Environments," NIST-GCR-92-607, Rutgers University Report to NIST, U.S. National Institute of Standards and Technology, Gaithersburg, MD.

Tanaka, T., 1983, "A Model of Multiroom Fire Spread," NBSIR 83-2718, U.S. National Bureau of Standards (presently U.S. National Institute of Standards and Technology), Gaithersburg, MD.

Taylor, G. I., 1950, "The Instability of Liquid Surfaces When Accelerated in a Direction Perpendicular to Their Planes," *Proceedings of the Royal Society A*, Vol. 201, pp. 192–196.

Natural Convection Heat Transfer in a Rectangular Enclosure With a Transverse Magnetic Field

S. Alchaar

P. Vasseur

E. Bilgen

Ecole Polytechnique,
University of Montreal,
C.P. 6079, Succ. "A",
Montreal, P.Q., H3C 3A7, Canada

In this paper the effect of a transverse magnetic field on buoyancy-driven convection in a shallow rectangular cavity is numerically investigated (horizontal Bridgman configuration). The enclosure is insulated on the top and bottom walls while it is heated from one side and cooled from the other. Both cases of a cavity with all rigid boundaries and a cavity with a free upper surface are considered. The study covers the range of the Rayleigh number, Ra, from 10^2 to 10^5, the Hartmann number, Ha, from 0 to 10^2, the Prandtl number, Pr, from 0.005 to 1 and aspect ratio of the cavity, A, from 1 to 6. Comparison is made with an existing analytical solution (Garandet et al., 1992), based on a parallel flow approximation, and its range of validity is delineated. Results are presented for the velocity and temperature profiles and heat transfer in terms of Ha number. At high Hartmann numbers, both analytical and numerical analyses reveal that the velocity gradient in the core is constant outside the two Hartmann layers at the vicinity of the walls normal to the magnetic field.

Introduction

Several aspects of steady free convection of an electrically conducting fluid in a magnetic field have been discussed in recent years by several authors. The interest in such problems lies in the numerous industrial processes in which they are involved (Moreau, 1990). For instance, it is well known that unavoidable convection movements during the manufacturing of crystals can be damped with the help of a magnetic field (Utech and Flemmings, 1966; Vives and Perry, 1987).

The natural convection boundary-layer flow around a semi-infinite vertical plate under a strong cross magnetic field has been studied analytically by Wilks (1976). Using asymptotic expansions, details of heat transfer coefficients were obtained by this author for the Prandtl number of order unity. This solution was extended to the low Prandtl range by Hunt and Wilks (1981). It was found that the rate of heat transfer near the leading edge of the plate increased as the Prandtl number decreased.

The two-dimensional natural convection of a fluid under a magnetic field has been studied numerically by Ozoe and Maruo (1987). Computations were carried out for the case of a square cavity for $10^4 \leq \mathrm{Ra} \leq 10^6$, $1 \leq \mathrm{Ha} \leq 10^3$ and $\mathrm{Pr} = 0.054$. The Nusselt numbers obtained were correlated to give an empirical equation for the rate of heat transfer. Ozoe and Okada (1989) studied the effect of an external magnetic field on the three-dimensional natural convection in a cubical enclosure. The external magnetic field perpendicular to the vertical boundary layer type flow was most effective in suppressing the convection. However, a field horizontal but parallel to the heated surface was observed to be least effective in suppressing the circulation flow. The stationary convection instability in rectangular boxes of finite extent, under the action of an external magnetic field, has been considered by Tabeling (1982) within the framework of linearized theory. The relationship between the direction of the magnetic field and the flow patterns of the Bénard cells was discussed. Calculations performed for various situations show transitions from transverse to longitudinal rolls and suppression of dislocations when the horizontal magnetic field is increased. The mixed convection of liquid metal in a static cylindrical enclosure with a rotating crystal rod was numerically computed by Toh and Ozoe (1992) for a lateral external magnetic field. This configuration was studied as a model for the mixed convection of molten metals in a crucible for the crystallization of semiconducting material by the Czochralski method. It was found that without a lateral magnetic field, the solution gave, as expected, a perfect axisymmetric solution. However, with a lateral magnetic field, the velocity and the average Nusselt number decreased and the profiles were no longer axisymmetric. Magnetohydrodynamic free convection of an electrically conducting fluid, in a rectangular enclosure ($A = 1$ and 2) with two side walls maintained at uniform heat flux condition, has been studied by Venkatachalappa and Subbaraya (1993). Numerical results show that with the application of an external magnetic field, aligned with gravity, the temperature and velocity of fluids are significantly modified. For sufficiently large magnetic field strength the convection was found to be suppressed for all values of the Grashof number. The effect of a transverse magnetic field on buoyancy-driven convection in an inclined two-dimensional cavity heated by a constant heat flux has been studied analytically and numerically by Vasseur et al. (1995). Solutions for the flow fields, temperature distributions, and Nusselt numbers were obtained explicitly in terms of the Rayleigh and Hartmann numbers and the angle of inclination of the cavity. In the case of a horizontal layer heated from below the critical Rayleigh number for the onset of convection was predicted in terms of the Hartmann number.

Recently, an analytical solution to the equations of magnetohydrodynamic has been proposed by Garandet et al. (1992) in order to study the effect of a transverse magnetic field on buoyancy-driven convection in a shallow two-dimensional cavity heated isothermally from the sides. Based on the parallel flow approximation, the velocity and temperature profiles in the core of the cavity were predicted in terms of the governing parameters of the problem. The recirculating part of the flow, near the vertical walls of the cavity, was studied by means of a series expansion that allows for the computation of the stream function. The solution proposed by these authors can be used to model the horizontal Bridgman method and in particular to study solute repartition in a typical horizontal Bridgman growth experiment.

Contributed by the Heat Transfer Division for publication in the JOURNAL OF HEAT TRANSFER. Manuscript received by the Heat Transfer Division September 1993; revision received May 1994. Keywords: Enclosure Flows, Materials Processing and Manufacturing Processes, Natural Convection. Associate Technical Editor: J. R. Lloyd.

The objective of this study is to investigate numerically the problem considered by Garandet et al. (1992) over a large range of the governing parameters and hence gain a better understanding of the effect of a magnetic field on natural convection within cavities. The range of validity of the approximate solution obtained by these authors is discussed. Also, their solution is extended in order to consider the case of a cavity with an upper free surface.

Formulation and Numerical Method

The study domain is a two-dimensional cavity of dimensions $L' \times H'$, and infinite extend in the z' direction, as shown in Fig. 1. The vertical walls are held at constant temperatures T'_H and T'_C ($T'_H > T'_C$) while the horizontal walls are adiabatic. A magnetic field $\vec{B}'$ is applied parallel to gravity. The thermophysical properties of the fluid at a reference temperature T'_0 are assumed to be constant, except for the density in the buoyancy term in the momentum equation (the Boussinesq approximation).

Neglecting the effect of Joule heating and viscous dissipation on heat transfer and also assuming that the induced magnetic field is very small compared to $\vec{B}'$, the governing equations for continuity, momentum transfer, energy, and electric transfers are:

$$\nabla \cdot \vec{V}' = 0 \tag{1}$$

$$\frac{\partial \vec{V}'}{\partial t'} + (\vec{V}' \cdot \nabla)\vec{V}' = -\frac{1}{\rho_0}\nabla p' + \frac{\vec{J}'}{\rho_0} \times \vec{B}' + \nu \nabla^2 \vec{V}' - \beta(T' - T'_0)\vec{g} \tag{2}$$

$$\frac{\partial T'}{\partial t'} + (\vec{V}' \cdot \nabla)T' = \alpha \nabla^2 T' \tag{3}$$

$$\nabla \cdot \vec{J}' = 0 \quad J' = \sigma'(-\nabla\phi' + \vec{V}' \times \vec{B}') \tag{4}$$

In these equations, σ' stands for the electrical conductivity, ϕ' for the electric potential, and $-\nabla\phi'$ for the associated electric field. As discussed by Garandet et al. (1992), for a two-dimensional situation, Eq. (4) for the electric potential reduces to $\nabla^2\phi' = 0$. The unique solution is $\nabla\phi' = 0$ since there is always an electrically insulating boundary around the enclosure. It follows that the electric field vanishes everywhere.

Eliminating the pressure terms appearing in Eq. (2) in the usual way, the governing Eqs. (1) to (3) reduce to

$$\frac{\partial \omega}{\partial t} + u\frac{\partial \omega}{\partial x} + v\frac{\partial \omega}{\partial y} = -\mathrm{Ra}\,\mathrm{Pr}\frac{\partial T}{\partial x} - \mathrm{Pr}\,\mathrm{Ha}^2\frac{\partial u}{\partial y} + \mathrm{Pr}\,\nabla^2\omega \tag{5}$$

$$\frac{\partial T}{\partial t} + u\frac{\partial T}{\partial x} + v\frac{\partial T}{\partial y} = \nabla^2 T \tag{6}$$

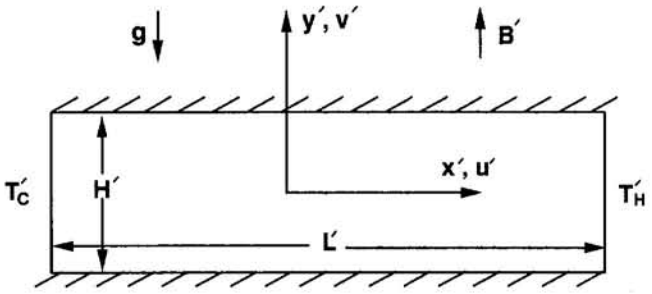

Fig. 1 Schematic of the problem

$$\nabla^2\Psi = -\omega \tag{7}$$

$$u = \frac{\partial \Psi}{\partial y} \quad v = -\frac{\partial \Psi}{\partial x} \tag{8}$$

These equations have been reduced to dimensionless forms by using the following scales: length: H', velocity: α/H', time: H'^2/α, and temperature: $\Delta T' = T'_H - T'_C$.

The associated dimensionless boundary conditions are given by

$$\textit{on all solid boundaries: } \Psi = 0, \quad u = v = 0 \tag{9}$$

$$y = 0, 1: \frac{\partial T}{\partial y} = 0 \tag{10}$$

$$x = A/2: T = 1 \tag{11}$$

$$x = -A/2: T = 0 \tag{12}$$

where $A = L'/H'$ is the enclosure aspect ratio.

Equations (5)–(8) with boundary conditions (9)–(12) complete the formulation of the problem. The governing parameters are the Rayleigh number, $\mathrm{Ra} = g\beta\Delta T' H'^3/\alpha\nu$, the Hartmann number, $\mathrm{Ha} = B'H'(\sigma'/\rho_0\nu)^{1/2}$, the Prandtl number, $\mathrm{Pr} = \nu/\alpha$, and the aspect ratio, A.

Numerical Solution

The governing Eqs. (5)–(8), with boundary conditions (9)–(12), were solved using a finite difference procedure. In the present scheme all spatial derivatives in the governing equations are approximated by their central differences. The vorticity transport Eq. (5) and the energy Eq. (6) are parabolic in time and elliptic in space; they can be solved by the alternating-direction-implicit (ADI) method developed by the Peaceman and Rachford (1955). The stream function Eq. (7) is an elliptic Poisson equation, which can be solved by the successive-over-relaxation

Nomenclature

A = aspect ratio = L'/H'
$\vec{B}'$ = applied magnetic field
g = intensity of gravity
H' = cavity height
Ha = Hartmann number = $B'H'(\sigma'/\rho_0\nu)^{1/2}$
$\vec{J}'$ = electric current
k = thermal conductivity of the fluid
L' = cavity length
Nu = Nusselt number, Eq. (15)
p' = pressure
Pr = Prandtl number = ν/α
Ra = Rayleigh number = $(g\beta\Delta T' H'^3)/(\alpha\nu)$
T = dimensionless temperature = $(T' - T'_C)/\Delta T'$
$\Delta T'$ = temperature difference = $T'_H - T'_C$
$\vec{V}'$ = velocity vector
u, v = dimensionless velocities in x and y directions = $(u', v')H'/\alpha$
x, y = dimensionless Cartesian coordinates = $(x', y')/H'$
α = thermal diffusivity of fluid medium
β = coefficient of thermal expansion of fluid
θ = dimensionless temperature
ν = kinematic viscosity
ρ = density
ϕ' = electric potential
Ψ = dimensionless stream function
ω = vorticity

Superscript

' = dimensional variables

Subscripts

C = cold wall, or evaluated at the center of cavity, or critical
H = hot wall
M = maximum value
0 = reference state

method (SOR) at each time step. The finite-difference form of the equations was written in conservative form for the advective terms in order to preserve the conservative property (Roache, 1985).

The rectangular domain was divided into a uniform mesh, with the end mesh coinciding with the enclosure boundary. Numerical tests, using various mesh sizes, were done for the same conditions in order to determine the best compromise between accuracy of the results and computer time. Based on those results a mesh size of 40×60 was adopted for most of the cases considered in this study ($A = 4$). For a cavity with an aspect ratio of $A = 6$, a mesh size of 40×80 was required. Further increase of the mesh size (50×90) did not cause any significant change in the final results. Computations were performed on an IBM RISC-6000 workstation.

The accuracy of the code was tested by comparing the results with the benchmark solution of De Vahl Davis and Jones (1983) for natural convection of air within a square cavity. Differences on all test parameters were within 3 percent of the benchmark values for $Ra \leq 10^6$. For instance when $Ra = 10^5$ an overall Nusselt number of 4.538 was obtained in the present study, while that reported by De Vahl Davis Jones was 4.519. A second set of tests concerned the shallow cavity which has been investigated by Cormack et al. (1974b) and Shiralkar and Tien (1981). The agreement for this case was very satisfactory with less than 2 percent deviations in all cases.

Results and Discussion

Convective motions in a Boussinesq fluid have been considered in a shallow cavity that is subjected to a constant transverse magnetic field. The parameters that govern the flow in this problem are the Rayleigh, Hartmann, and Prandtl numbers and the aspect ratio of the cavity. The Prandtl number of the electroconducting fluid is generally small and consequently inertia effects are expected to be significant even with a small difference of temperature. In this section, some representative results are presented to illustrate the effects of the various controlling parameters.

Figures $2(a-d)$ illustrate typical contour maps of the stream function and temperature obtained numerically for $A = 4$, $Pr = 0.01$ and various values of Ra and Ha. In all these graphs the increments between adjacent streamlines and isotherms are $\delta\Psi = \Psi_{max}/8$ and $\delta T = 1/8$, where Ψ_{max} is the maximum value of the stream function. It is noted that when the flow in the core of the cavity is parallel, Ψ_C, the value of the stream function at the center of the cavity, is equal to Ψ_{max}.

In the absence of a magnetic field ($Ha = 0$) Fig. $2(a)$ shows the flow pattern obtained when $Ra = 2 \times 10^2$, i.e., when the Rayleigh number is relatively low. It is seen that the flow inside the cavity may be decomposed into three parts: a core region in the center of the fluid layer where essentially the flow is parallel ($v = 0$) and two end regions where the flow turns through 180 deg. Due to the low Prandtl number considered here the convection is relatively large, despite low Ra, as indicated by the value of the stream function $\Psi_C = 0.134$. However, due to weak coupling between the momentum and the energy equations resulting from small Pr, the heat transfer through the cavity is almost by pure conduction, as depicted by the isotherm pattern. In fact, this type of flow configuration can be sustained only when the convection within the fluid layer is sufficiently weak. Thus, for $Ra = 8 \times 10^2$ and $Ha = 0$, Fig. 2 (b) shows that the parallelism of the flow in the core region has been destroyed and the flow pattern consists now of a strong vortex near the center of the cavity ($\Psi_C = 0.575$) and weak circulations near the end regions. As Ra increases further, oscillatory modes (the Hopf bifurcation) are observed to occur at a critical Rayleigh number, which depends upon both Pr and A (see, for instance, Roux et al., 1989). However, the present study is restricted to steady-state situations only.

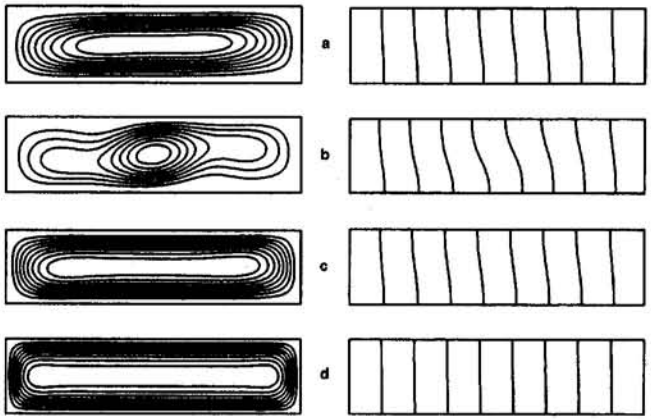

Fig. 2 Computed contour maps of the stream function (left) and isothermal lines (right) for a cavity with all rigid boundaries for $A = 4$, $Pr = 0.01$ and: (a) $Ha = 0$, $Ra = 2 \times 10^2$, $\Psi_C = 0.134$; (b) $Ha = 0$, $Ra = 8 \times 10^2$, $\Psi_C = 0.575$; (c) $Ha = 10$, $Ra = 8 \times 10^2$, $\Psi_C = 0.151$; (d) $Ha = 30$, $Ra = 8 \times 10^2$, $\Psi_C = 0.024$

The retarding effects of magnetic drag on the flow pattern of Fig. $2(b)$, i.e., for $Ra = 8 \times 10^2$, are demonstrated in Figs. $2(c)$ and $2(d)$ for $Ha = 10$ and 30, respectively. It is seen that for a given Ra, as the Hartmann number is increased, the convective circulation within the cavity is progressively inhibited. Thus, for $Ha = 10$, Fig. $2(c)$ shows that the overall strength of the circulation is considerably reduced ($\Psi_C = 0.151$), as compared to that of Fig. $2(b)$, and the resulting flow pattern is now parallel again. For $Ha = 30$, Fig. $2(d)$ indicates that the convective motion within the cavity is almost completely damped ($\Psi_C = 0.024$) by the drag induced by the magnetic field.

As mentioned earlier, the effect of a transverse magnetic field on buoyancy-driven convection in a two-dimensional cavity has been studied recently by Garandet et al. (1992). Based on the parallel flow approximation, it was demonstrated by these authors that the velocity and temperature profiles, in the core region of the cavity, are given respectively, in the present notation, by

$$u = \frac{Ra}{Ha^2}\left[F \sinh (Ha\, y) - y\right] \tag{13}$$

and

$$T = \frac{1}{A}\left\{x + \frac{Ra}{Ha^2}\left[\frac{F}{Ha^2}\sinh (Ha\, y) - \frac{y^3}{6} + \left(\frac{1}{8} - \frac{F}{Ha}\cosh (Ha\, y)\right)y\right]\right\} \tag{14}$$

where $F = 1/[2 \sinh (Ha/2)]$.

These results are strictly valid in the limit of a shallow cavity ($A \to \infty$) for which the core temperature decreases linearly between the extreme ends of the cavity. The range of validity of the above-mentioned equations will be now discussed.

In Figs. $3(a)$ and $3(b)$, the calculated and analytically predicted temperature and velocity distributions, at midlength of the cavity ($x = 0$), are compared for $A = 4$, $Ra = 8 \times 10^2$, $Pr = 0.03$, and various values of Ha. The analytical results, Eqs. (13) and (14) are continuous lines; numerical results shown as solid circles are seen to agree well. For convenience, the profiles have been normalized by u_M and T_M, the maximum velocity and temperature obtained by taking the extremum of the derivatives of Eqs. (13) and (14), respectively. In general, Fig. $3(a)$ indicates that the velocity increases from zero at the wall to a peak in a region called viscous sublayer and then drops back to zero at the center of the cavity ($y = 0$). In the absence of a magnetic field ($Ha = 0$) the profile is cubic, as it has been predicted in the past by Birikh (1966) and Hart (1972). As the value of Ha is increased the velocity gradient tends to be constant almost every-

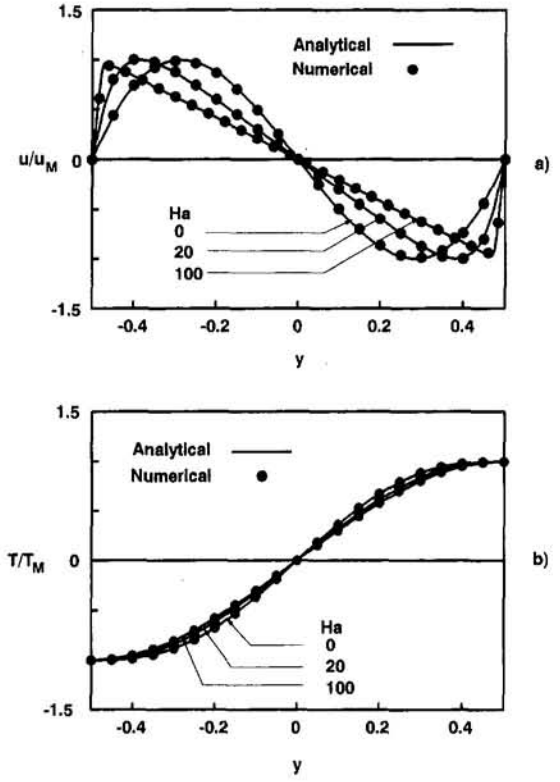

Fig. 3 Velocity and temperature profiles at midlength of a cavity with all rigid boundaries as a function of Ha for $A = 4$, $Ra = 8 \times 10^2$, and $Pr = 0.03$: (*a*) velocity; (*b*) temperature

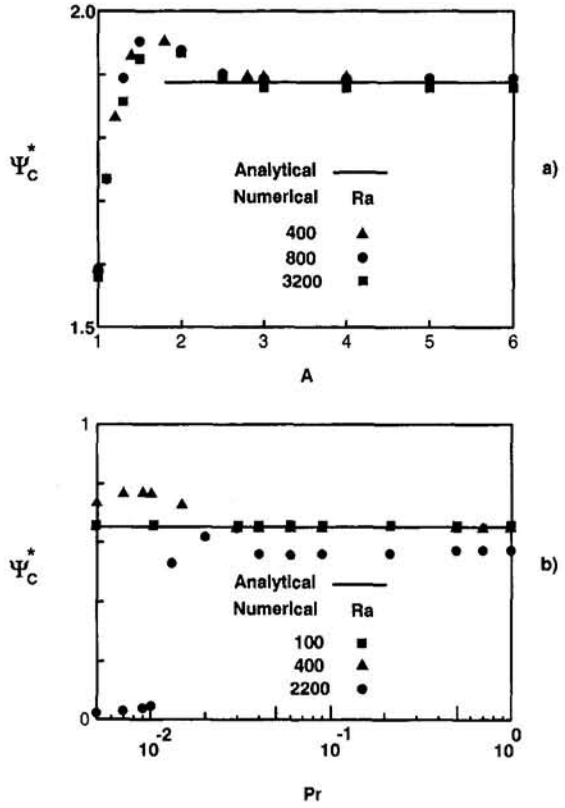

Fig. 4 (*a*) Effect of the aspect ratio A on Ψ_C^* for $Pr = 0.03$, $Ha = 10$, and various values of Ra: (*b*) effect of the Prandtl number Pr on Ψ_C^* for $A = 4$, $Ha = 0$, and various values of Ra

where in the cavity, except in the two thin Hartmann layers near the walls, where the effect of viscosity cannot be neglected. The effect of Ha on the normalized temperature profiles is depicted in Fig. 3(*b*). It is seen that, when Ha increases, there is no significant difference in the shapes of the curves.

The excellent agreement between the analytical and the numerical results of Fig. 3 is essentially due to the fact that the flow in the core of the cavity is parallel. However, such an agreement is not expected to hold true for any combination of the governing parameters. For instance, Fig. 4(*a*) shows the influence of the aspect ratio of the cavity A on Ψ_C^* ($= 1000\ \Psi_C/\mathrm{Ra}$), the normalized value of the stream function at the center of the cavity, for $Ha = 10$, $Pr = 0.03$, and various values of Ra. When A is sufficiently large, namely $A \geq 3$, the analytical solution, derived under the assumption of the shallow enclosure limit ($A \to \infty$), is in good agreement with the numerical simulations. However, for smaller values of A, the parallelism of the flow is progressively destroyed and large discrepancies between the analytical and the numerical results are observed. Thus, when $A = 1$ the analytical solution overpredicts the value of Ψ_C^* by approximately 14 percent. The effect of the Prandtl number, Pr, on Ψ_C^* is illustrated in Fig. 4(*b*) for $A = 4$, $Ha = 0$, and various values of Ra. When $Ra = 10^2$, i.e., when the convection is relatively weak, the analytical solution compares favorably with the numerical results since the condition of parallel flow can be sustained for all the range of Pr considered. As the Rayleigh number is increased to $Ra = 4 \times 10^2$, the agreement between the analytical and the numerical results is observed to be good in the high Pr range but poor when $Pr \leq 0.03$. This is because the inertia effects increase with decreasing Pr and, as a result, the parallelism of the flow is progressively destroyed (see for instance the flow pattern of Fig. 5(*a*) for $Pr = 0.005$). Naturally, this low Pr number effect is enhanced as Ra is made larger as depicted in Fig. 4(*a*) for $Ra = 2.2 \times 10^3$. Thus, for $Pr \leq 0.01$ the value of Ψ_C^* is very small and the flow pattern, as illustrated in Fig. 5(*b*) for $Pr = 0.005$, consists now of two concentrated vortex rotating in the same direction. As the Prandtl number increases the disagreement between the analytical and numerical results is reduced. However, for $Pr \geq 0.04$, discrepancies as high as about 12 percent are nevertheless observed. This behavior can be understood from the examination of the computed contour maps of the stream function and isothermal lines presented in Fig. 5(*c*) for $Pr = 1$. The flow pattern is seen to be parallel in the core of the cavity but the distortion of the isotherms indicates a strong convective motion within the cavity. For this situation, heat transfer by convection is relatively more important than that by conduction resulting in a large axial temperature gradient in the core of the cavity. Thus we cannot expect agreement between the numerical results and the analytical solution, which is valid only in the conduction regime.

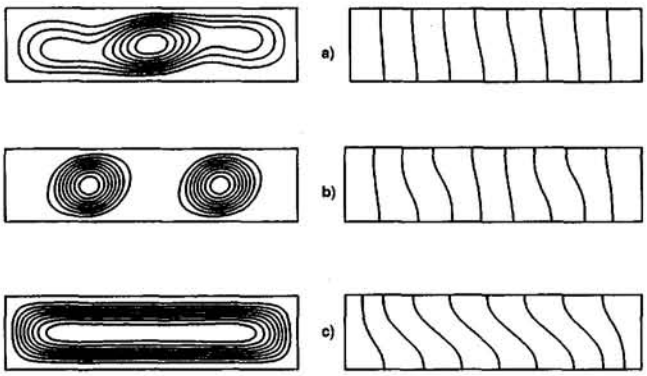

Fig. 5 Computed contour maps of the stream function (left) and isothermal lines (right) for a cavity with all rigid boundaries for $A = 4$, $Ha = 0$, and: (*a*) $Ra = 4 \times 10^2$, $Pr = 0.005$, $\Psi_C = 0.293$; (*b*) $Ra = 2.2 \times 10^3$, $Pr = 0.005$, $\Psi_C = 0.048$; (*c*) $Ra = 2.2 \times 10^3$, $Pr = 1$, $\Psi_C = 1.260$

The influence of Ra on Ψ_C, the value of the stream function at the center of the cavity, is presented in Fig. 6 for $A = 4$, Pr = 0.03, and various values of Ha. This graph illustrates clearly the retarding effect of the magnetic field on the strength of the flow circulation. It is seen that for a given Ra, Ψ_C is a decreasing function of Ha. For instance, for Ra = 3.2×10^3, $\Psi_C = 1.845$ when Ha = 0 but $\Psi_C = 0.0375$ when Ha = 50. This observation is similar to that made earlier regarding the effect of Ha in Fig. 2. In Fig. 6, for each value of Ha, the numerical results are presented up to a critical Ra above which, as already mentioned, the flow bifurcates toward a sustained oscillatory mode. Due to the retarding effect of the magnetic field the range of Ra, for steady flow regimes, is progressively extended as Ha is made larger. In the absence of a magnetic drag (Ha = 0), it is observed that both the analytical and numerical results are in good agreement with each other. However, for a given Ha, the agreement is good only when Ra, i.e., the strength of convection, is weak. As the value of Ra is progressively increased large discrepancies are observed. Naturally the range of validity of the analytical solution is extended as the value of Ha is made larger.

The numerical results for the heat transfer are presented in Fig. 7 as a function of Ra for $A = 4$, Pr = 0.03 and various values of Ha. The heat transfer is determined in terms of the average Nusselt number Nu, defined as

$$\mathrm{Nu} = -A \int_{-1/2}^{1/2} \left.\frac{\partial T}{\partial x}\right|_{x=-A/2} dy \tag{15}$$

As expected, for a given value of Ra it is seen that Nu is a decreasing function of Ha. This is due to the fact that with increasing Ha the convection is progressively reduced by the magnetic drag (see Fig. 6), resulting in a lower heat transfer. Figure 7 also indicates that, for a given Ha, the curve of Nusselt number versus Rayleigh number is similar to that which has been reported in the past in the absence of a magnetic field (Ha = 0). Thus, when Ra → 0, i.e., in the conduction regime, the Nusselt number is unity. As Ra is made larger, the stratification in the core of the cavity is enhanced, and the contribution of heat transfer by convection near the wall increases (asymptotic regime). Finally, a sufficiently large temperature difference across the cavity causes a boundary layer flow in which the dominant mode of heat transfer is convection. The start of these flow regimes is strongly dependent on the Hartmann number. For instance, for Ha = 0, the conduction regime ends at Ra ≃ 8×10^2, whereas for Ha = 50 it continues up to Ra ≃ 8×10^4. Similarly, the ranges of the Rayleigh number for asymptotic and boundary layer flows are also extended. Finally, it must be mentioned that the analytical model proposed by Garandet et al. (1992) is valid only in a pure conduction regime, i.e., when Nu → 1. This is because they have

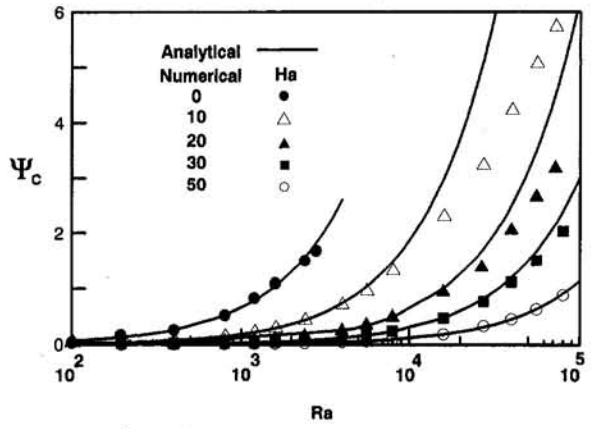

Fig. 6 Effect of Rayleigh and Hartmann numbers on the stream function Ψ_C, at the center of a cavity with all rigid boundaries, for $A = 4$ and Pr = 0.03

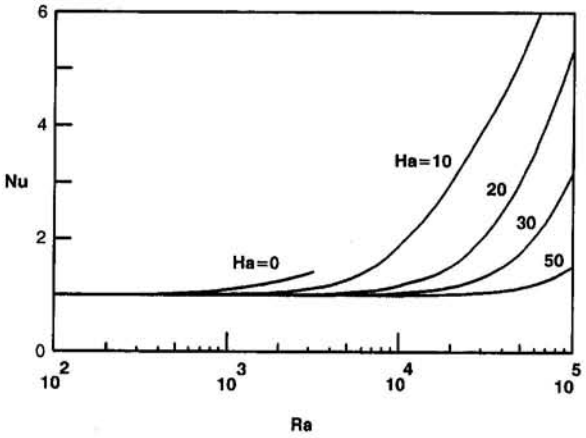

Fig. 7 Heat transfer Nu as a function of Ra and Ha for $A = 4$ and Pr = 0.03

assumed in their analytical model that the core temperature decreases linearly between the two isothermally heated walls of the cavity. In general, the analytical prediction of Nu, when the longitudinal temperature drop across the core region is less than the overall end-to-end temperature difference, is a complex problem that necessitates a detailed analysis of the flow and temperature patterns in the end regions (see, for instance, Cormack et al., 1974a).

The case of a cavity with an upper free surface will be now discussed. We assume that the surface tension is negligible and the free surface remains horizontal everywhere. Since there is no shear stress at the free surface ($y = 1/2$), $\tilde{\Psi}$ and its second normal derivative are both zero. Applying the parallel flow approximation described by Garandet et al. (1992) and making use of the zero shear stress boundary condition at the top of the cavity, it can be shown that the velocity and temperature fields are now given respectively by

$$u = \frac{\mathrm{Ra}}{\mathrm{Ha}^2}\left[Ee^{\mathrm{Hay}} + Fe^{-\mathrm{Hay}} + y + G\right] \tag{16}$$

$$T = \frac{1}{A}\left\{x + \frac{\mathrm{Ra}}{\mathrm{Ha}^2}\left[\left(\frac{E}{\mathrm{Ha}^2}e^{\mathrm{Hay}} + \frac{F}{\mathrm{Ha}^2}e^{-\mathrm{Hay}}\right) + \frac{1}{6}y^3 + \frac{G}{2}y^2 - Hy - L\right]\right\} \tag{17}$$

where

$$\left.\begin{aligned} E &= \frac{\left[(\mathrm{Ha}-1)e^{\mathrm{Ha}/2} + \left(1 - \frac{\mathrm{Ha}^2}{2}\right)e^{-\mathrm{Ha}/2}\right]}{\mathrm{Ha}\,C} \\ F &= \frac{\left[-(\mathrm{Ha}+1)e^{-\mathrm{Ha}/2} + \left(1 - \frac{\mathrm{Ha}^2}{2}\right)e^{\mathrm{Ha}/2}\right]}{\mathrm{Ha}\,C} \\ G &= \frac{[2 - 2\cosh(\mathrm{Ha}) + \mathrm{Ha}\sinh(\mathrm{Ha})]}{\mathrm{Ha}\,C} \\ H &= \left[\frac{(Ee^{\mathrm{Ha}/2} - Fe^{-\mathrm{Ha}/2})}{\mathrm{Ha}} + \frac{G}{2} + \frac{1}{8}\right] \\ C &= 2[\sinh(\mathrm{Ha}) - \mathrm{Ha}\cosh(\mathrm{Ha})] \\ L &= \left[\frac{Ee^{-\mathrm{Ha}/2} + Fe^{\mathrm{Ha}/2}}{\mathrm{Ha}^2} + \frac{G}{8} - \frac{H}{2} - \frac{1}{48}\right] \end{aligned}\right\} \tag{18}$$

Typical velocity and temperature profiles for a cavity with an upper free surface are presented in Figs. 8(*a*) and 8(*b*), respec-

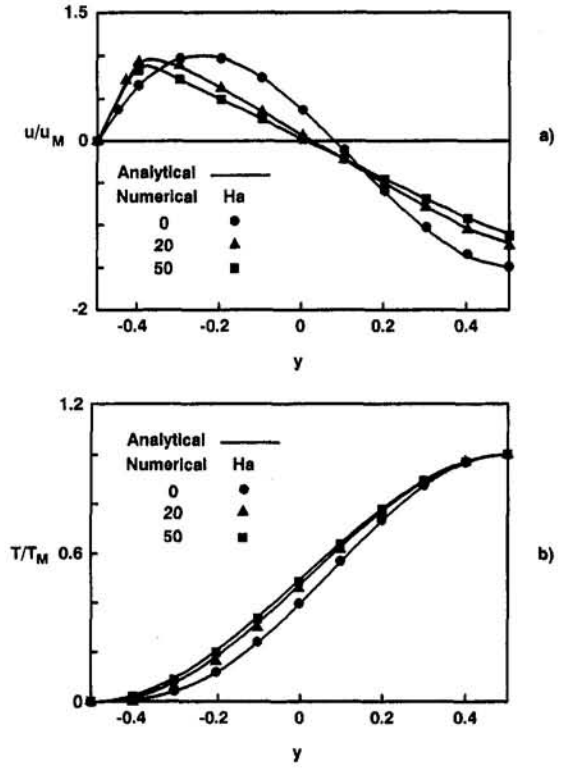

Fig. 8 The velocity and temperature profiles at midlength of a cavity with an upper free surface as a function of Ha for $A = 4$, $Ra = 10^2$, and $Pr = 0.03$: (a) velocity; (b) temperature

tively, for $A = 4$, $Ra = 10^2$, $Pr = 0.03$, and various values of Ha. The good agreement between the analytical and the numerical results is a consequence of the existence, for these particular governing parameters, of a parallel flow in the core of the cavity. The absence of shear at the free surface of the cavity results in larger horizontal velocities at the top rather than at the bottom of the fluid layer. In fact, it was observed from the numerically predicted streamline patterns (not presented here) that the center of the eddy was displaced upward. Figure 8(b) indicates that the antisymmetry of the dimensionless temperature profiles, as observed in Fig. 3 for a rigid-rigid cavity, is now destroyed due to higher velocities at the free surface. For convenience, the temperature distributions in Fig. 8(b) have been set to zero at the bottom of the cavity for both the analytical and the numerical solutions.

Conclusions

The present work is a numerical investigation of the effect of a transverse magnetic field on buoyancy-driven convection in a two-dimensional shallow enclosure. The right and left sides of the cavity are respectively heated and cooled isothermally, and the top and bottom sides are insulated. Both cases of a cavity with all rigid boundaries and with a free upper surface have been considered. Numerical results were obtained for a wide range of the Rayleigh number ($10^2 \leq Ra \leq 10^5$), the Hartmann number ($0 \leq Ha \leq 10^2$), the Prandtl number ($0.005 \leq Pr \leq 1$), and the aspect ratio ($1 \leq A \leq 6$).

The numerical results have been compared with a closed-form solution (Garandet et al., 1992) based on the assumption that, in the limit of a shallow system ($A \gg 1$) the flow remains parallel in the core of the cavity. The theory of Garandet et al. was also extended in order to predict the influence of a free upper surface on the present problem. A good agreement between the numerical and the analytical results was observed provided that (i) the aspect ratio of the cavity is equal to or greater than approximately three and (ii) the effect of convective heat transfer is negligible as it has been assumed in the analytical model. This latest assumption can only be fulfilled for a given range of the governing parameters (Ra, Ha, Pr) that is discussed in the present study in order to provide a basis for the validity of the approximate analytical solution.

Acknowledgments

This work was supported in part by the Natural Sciences and Engineering Research Council of Canada and jointly by the FCAR Government of Quebec.

References

Birikh, R. V., 1966, "Thermocapillary Convection in a Horizontal Layer of Liquid," *J. Appl. Mech. Tech. Phys.*, Vol. 3, pp. 69–72.

Chandrasekhar, S., 1961, *Hydrodynamic and Hydromagnetic Stability*, Oxford University Press, United Kingdom.

Cormack, D. E., Leal, L. G., and Imberger, J., 1974a, "Natural Convection in a Shallow Cavity With Differentially Heated End Walls. Part I, Asymptotic Theory," *J. Fluid Mech.*, Vol. 65, pp. 209–229.

Cormark, D. E., Leal, L. G., and Seinfeld, J. H., 1974b, "Natural Convection in a Shallow Cavity With Differentially Heated End Walls. Part II: Numerical Solutions," *J. Fluid Mech.*, Vol. 65, pp. 231–246.

De Vahl Davis, G., and Jones, I. P., 1983, "Natural Convection in a Square Cavity: A Comparison Exercise," *Int. J. Numerical Methods in Fluids*, Vol. 3, pp. 227–248.

Garandet, J. P., Alboussiere, T., and Moreau, R., 1992, "Buoyancy Driven Convection in a Rectangular Enclosure With a Transverse Magnetic Field," *Int. J. Heat Mass Transfer*, Vol. 35, pp. 741–748.

Hart, J. E., 1972, "Stability of Thin Non-rotating Hadley Circulations," *J. Atmospheric Sci.*, Vol. 29, pp. 687–697.

Hunt, R., and Wilks, G., 1981, "Low Prandtl Number Magnetohydrodynamic Natural Convection in a Strong Cross Field," *Numerical Heat Transfer*, Vol. 4, pp. 303–316.

Moreau, R., 1990, *Magnetohydrodynamics*, Kluwer Academic Publishers, The Netherlands.

Ozoe, H., and Maruo, E., 1987, "Magnetic and Gravitational Natural Convection of Melted Silicon—Two-Dimensional Numerical Computations for the Rate of Heat Transfer," *J.S.M.E.* Vol. 30, pp. 774–784.

Ozoe, H., and Okada, K., 1989, "The Effect of the Direction of the External Magnetic Field on the Three-Dimensional Natural Convection in a Cubical Enclosure," *Int. J. Heat Mass Transfer*, Vol. 32, pp. 1939–1954.

Peaceman, D. W., and Rachford, H. H., 1955, "The Numerical Solution of Parabolic and Elliptic Differential Equations," *J. Soc. Indust. Appl. Mathematics*, Vol. 3, pp. 28–41.

Roache, P. J., 1985, *Computational Fluid Mechanics*, Hermosa, Alberquerque, NM.

Roux, B., Ben Hadid, H., and Laure, P., 1989, "Hydrodynamical Regimes in Metallic Melts Subject to a Horizontal Temperature Gradient," *Eur. J. Mech.*, Vol. 5, pp. 375–396.

Shiralkar, G. S., and Tien, C. L., 1981, "A Numerical Study of Laminar Natural Convection in Shallow Cavities," ASME JOURNAL OF HEAT TRANSFER, Vol. 103, pp. 226–231.

Tabeling, P., 1982, "Convection Flow Patterns in Rectangular Boxes of Finite Extent Under an External Magnetic Field," *J. de Physique*, Vol. 43, pp. 1295–1303.

Toh, K., and Ozoe, H., 1992, "Three-Dimensional Czochralski Flow of Liquid Metal in a Lateral Magnetic Field," *Proc. of the First Intern. Conf. on Transport Phenomena in Processing*, S. I. Guceri, ed., pp. 14–24.

Utech, H. P., and Flemmings, M. C., 1966, "Elimination of Solute Banding in Indium Atimonide Crystals by Growth in a Magnetic Field," *J. Appl. Phys.*, Vol. 37, pp. 2021–2024.

Vasseur, P., Hasnaoui, M., Bilgen, E., and Robillard, L., 1995, "Natural Convection in an Inclined Fluid Layer With a Transverse Magnetic Field: Analogy With a Porous Medium," ASME JOURNAL OF HEAT TRANSFER, Vol. 117, pp. 121–129.

Venkatachalappa, M., and Subbaraya, C. K., 1993, "Natural Convection in a Rectangular Enclosure in the Presence of a Magnetic Field With Uniform Heat Flux From the Side Walls," *Acta Mechanica*, Vol. 96, pp. 13–26.

Vives, C., and Perry, C., 1987, "Effects of Magnetically Damped Convection During the Controlled Solidification of Metals and Alloys," *Int. J. Heat Mass Transfer*, Vol. 30, pp. 479–496.

Wilks, G., 1976, "Magnetohydrodynamic Free Convection About a Semi-infinite Vertical Plate in a Strong Cross Field," *J. Appl. Math. Phys.*, Vol. 27, pp. 621–631.

Thermal Analysis of In-Situ Curing for Thermoset, Hoop-Wound Structures Using Infrared Heating: Part I—Predictions Assuming Independent Scattering

B.-C. Chern
Everest Industrial Co., Inc.,
No. 669 Keng Tze Kou, Feng Keng Tsun,
Hsin Feng Hsiang Hsinchu, Taiwan

T. J. Moon

J. R. Howell

Department of Mechanical Engineering,
University of Texas at Austin,
Austin, TX 78712

A curing process for unidirectional thermoset prepreg wound composite structures using infrared (IR) in-situ heating is investigated. In this method, the infrared energy is from all incident angles onto the composite structure to initiate the curing during processing. Due to the parallel geometry of filaments in wound composite structures, the radiative scattering coefficient and phase function within the structure depend strongly on both the wavelength and the angle of incidence of the IR incident radiation onto the fibers. A two-dimensional thermochemical and radiative heat transfer model for in-situ curing of thermoset, hoop-wound structures using IR heating is presented. The thermal transport properties that depend on the process state are also incorporated in the analysis. A nongray, anisotropic absorbing, emitting, and scattering unidirectional fibrous medium within a matrix of nonunity refractive index is considered. The temperatures and degrees of cure within the composite during processing are demonstrated numerically as a function of the configuration of IR heat source, nondimensional power input, mandrel winding speed, and size of wound composite. Comparison between the numerical result and experimental data is presented.

Introduction

Large thermoset filament-wound or fiber-tape-wound composite structures are widely used to form rigid, lightweight aerospace components, underground pressure vessels, and tubing. In manufacturing such structures, the gathered strands of continuous fibers are wetted with resinous material and wound onto a rotating mandrel by computer-controlled apparatus (wet winding). After winding is finished, the system is subjected to a constant "soak" temperature to release the entrapped gases. Consolidation of the composite is usually required in order to purge entrapped gases from within the material system. Usually, helically winding a permeable cloth around the entire structure provides a radial compaction to partially remove the entrapped gases. Upon completing these procedures, the components are often batch-cured in an oven or autoclave (Stango et al., 1991). During the curing, the resin network grows into longer chains with branches and cross-linking occurring.

The drawbacks of batch autoclave curing are the following: (1) long curing times are involved; (2) component size is limited due to the oven space; (3) nonuniform and incomplete cure of the matrix may occur due to the poor transverse thermal conductivity of the composite. This nonuniformity is blamed for residual stress development in the cured structures. (4) batch curing using large flow rates of heated air is thermally inefficient and results in the emission of large volumes of low-concentration, hydrocarbon–air mixtures and costly emission control equipment is needed for removing these pollutants.

Contributed by the Heat Transfer Division for publication in the JOURNAL OF HEAT TRANSFER. Manuscript received by the Heat Transfer Division March 1994; revision received January 1995. Keywords: Materials Processing and Manufacturing Processes, Radiation, Radiation Interactions. Associate Technical Editor: M. F. Modest.

In the in-situ curing method, an infrared heat source is directly incident on the local area of the wound structures to initiate resin curing during the winding process (Chern et al., 1994b, c). This method offers the possibility of a more uniform degree of cure and hence less severe residual stress distribution in the finished structure. Since only small amounts of air flow are needed to remove the toxic gas evolved during curing, less expensive pollution control can be used. Moreover, this process is expected to have a greater energy efficiency, have higher productivity, be less size restricted, and use less floor space compared with the standard batch-oven curing. Studies related to this thermoset in-situ curing are limited. A thermochemical model was developed by Korotkov et al. (1993) for this process. Axisymmetric and surface radiative conditions were assumed in their analysis. However, if the applied boundary heat flux is limited to some portions of cylindrical wound structures (which is closer to realistic process conditions) and the composite material is semitransparent to the incident radiation, these assumptions will break down.

In our earlier studies (Chern et al., 1992, 1994a), the IR energy is assumed to be normally incident on the fibrous medium, which is assumed to absorb the radiation energy. No radiative emission or scattering within the composite is considered. However, in order to consider the more realistic manufacturing situation, oblique incidence of the light upon the absorbing, emitting, and scattering fibrous medium should be included (Chern et al., 1994b, c). Unlike spherical particles whose radiative properties are not dependent on incident angle, radiative properties of the aligned fibrous medium, such as the absorption and scattering coefficients and the scattering phase function, depend on the angle of incidence of the light. The spectral, anisotropic characteristics of the radiative transport in the absorbing, emitting, and scattering fibrous-matrix medium

are complicated and studies related to these topics are very limited (Howell, 1988). Yuen et al. (1992) took into account the wavelength and incident angle dependence of the extinction and scattering coefficient (but assume isotropic scattering) to calculate the apparent emissivity of an insulation layer by using the Monte Carlo/zonal method. Considering the angle of incidence effect on a planar fibrous medium, Kurosaki et al. (1991) and Lee (1989) solved a pure radiative transfer problem with a planar fibrous medium by using the discrete ordinate method. The results for a single wavelength and assuming no emission from the fibrous medium were presented in their analysis. These studies are each one dimensional.

The two-dimensional thermochemical and radiative heat transfer models for the in-situ curing of thermoset composites using IR heating are presented in this paper. The radiative transport of IR energy through a nongray, anisotropic absorbing, emitting, and scattering fiber-reinforced composite is considered. Temperature and degree of cure profiles within the composite during process are predicted numerically. Comparison between numerical and experimental result is demonstrated.

Analysis

In the analysis, a rectangular, transversely isotropic tape of width w_{ply} and thickness t_{ply} is considered and shown in Fig. 1. The tape is wound circumferentially at a constant 90 deg winding angle (hoop winding) at a feed rate of V onto a cylindrical mandrel of diameter D rotating with angular velocity $2V/D$. Due to the accretion of ply layers during the winding, this condition is not strictly satisfied for long times; however, for a practical winding situation, it is satisfied provided $2H/D \ll 1$. A cylindrical-coordinate system $(R, \bar{\theta}, z)$ having its z axis coincident with the mandrel's axis is used to describe the mandrel and composite geometry. For typical plies used in tape winding, $t_{ply}/w_{ply} \ll 1$ so that variations in the axial (z) direction are negligible; the problem is thereby reduced to two dimensions: R and $\bar{\theta}$. The IR energy is assumed to be diffusely incident upon a given arc length of the cylinder's periphery. All the radiant energy deposition and primary heat transfer are assumed to occur in a thin surface layer of radial thickness H ($\ll D/2$) comprised of the n_{tot} outermost plies. It is further assumed that $2H/D \ll 1$ so that the curvature of the surface layer can be

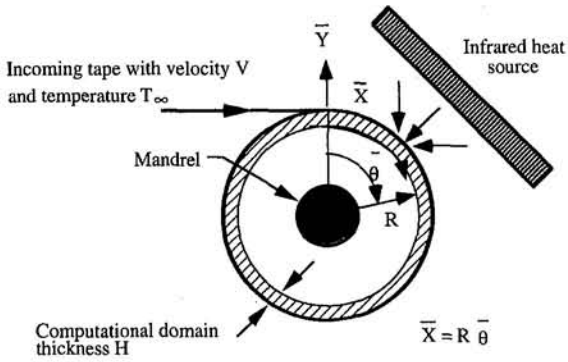

Fig. 1 Physical geometry

Nomenclature

C = specific heat
$\bar{C}$ = nondimensional specific heat $= C(T, a_d)/C_{ref}$
D = diameter of outermost ply
$d\bar{Q}_{ch}/dt$ = nondimensional exothermic heat $= \rho_e(1-f)Q_{tot}V(\pi D)(d\alpha_d/d\bar{X})/(T_{ref}\cdot\kappa_{c,l,ref})$
$F_{d\bar{x}-lamp}$ = view factor from $d\bar{x}$ to IR lamp
g = gravitational constant
H = computational domain thickness $= n_{tot}\cdot t_{ply}$
h = convective heat transfer coefficient
i = radiation intensity
$\bar{i}$ = nondimensional radiation intensity $= i/(q''_{lamp}h_e/p)$
l = directional cosine
$\tilde{m}$ = refractive index
N_{cr} = ratio of conduction to radiation $= \kappa_{c,l,ref}T_{ref}/((q''_{lamp}/\pi)\cdot\eta_e\cdot(\pi D)^2\sigma_{ex_{no}\lambda_{ref}})$
N_{gr} = Grashof number $= g(T_{sur}-T_\infty)D^3/(\nu^2 T_f)$
N_{pr} = Prandtl number $= \nu/\alpha_T$
N_{rot} = rotating Reynolds number $= VD/\nu$
n = index
n_{tot} = total number of plies in the computational domain
$\mathbf{P}$ = phase function
Pe = Peclet number $= \rho_c c_{c,ref}V(\pi D)/\kappa_{c,l,ref}$
Q_{ch} = exothermic heat released up to some time t
Q_r = radiative heat flux
Q_{tot} = enthalpy of reaction
q = rate of energy
$\mathbf{S}$ = source function
S = path length
T = temperature
$\bar{T}$ = nondimensional temperature $= T/T_{ref}$
T_f = film temperature $= (T_{sur}+T_\infty)/2$
t = time
t_{ply} = ply thickness (in y direction)
V = tape feed rate
w_{ply} = ply width (in z direction)
$\bar{X}$ = nondimensional length in the fiber direction $= x/(\pi D)$
$\bar{Y}$ = nondimensional length in the transverse fiber direction $= y/n_{tot}\cdot t_{ply}$
x = length in the fiber direction $= D\bar{\theta}/2$
y = length in the transverse-fiber direction
z = length in axial direction, as shown in Fig. 1
α_d = degree of cure of the resin $= Q_{ch}/Q_{tot}$
α_T = thermal diffusivity
γ = reflectivity
η_e = lamp bank efficiency
$\bar{\theta}$ = angle of mandrel rotation, as shown in Fig. 1
κ = thermal conductivity
$\kappa_{c,tl}$ = anisotropic thermal conductivity number $= \kappa_{c,t,ref}(\pi D)^2/\kappa_{c,l,ref}n_{tot}^2 t_{ply}^2$
$\bar{\kappa}$ = nondimensional thermal conductivity $= \kappa(T)/\kappa_{ref}$
λ = wavelength
ν = kinematic viscosity of the air
ρ = mass density
σ = dimensional radiative property
$\bar{\sigma}$ = nondimensional radiative property $= \sigma/\sigma_{ex_{no}}$
Ω, Ω' = outgoing and incoming direction, respectively

Superscripts

d = diffuse
$''$ = per unit area

Subscripts

a = absorption
b = blackbody
c = composite
ex = extinction
l = along fiber axis direction
lamp = IR lamp
no = normal incidence
r = radiative
ref = reference; $T_{ref} = 298$ K, $\alpha_{d,ref} = 0$, $\lambda_{ref} = 2$ μm
sur = surface of the outermost ply
t = transverse to the fiber direction
tot = total
υ = vacuum
λ = wavelength
∞ = ambient condition
$\cap$ = upper hemisphere
$\cup$ = lower hemisphere
1, 2 = index

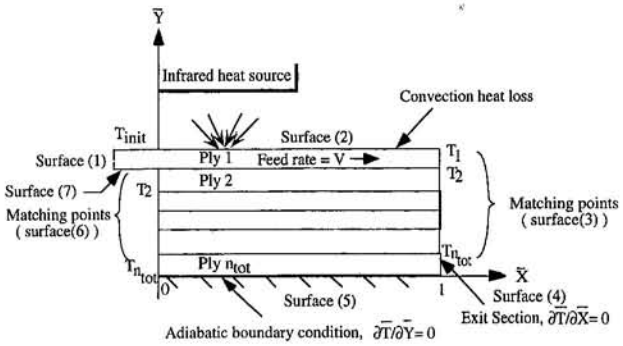

Fig. 2 Computation domain

neglected and the annular physical domain can be mapped into the rectangular computational domain ($\bar{X}$, $\bar{Y}$) with appropriate matching conditions at $\bar{X} = 0$ and $\bar{X} = 1$, which represents the continuity of plies in subsequent layers (see Fig. 2). Although the thin regions of outer layers will actually displace outward along the R direction as the prepreg is being wound, the field quantities are assumed to be steady in this thin computation domain.

Energy Equation. An Eulerian computation domain, shown in Fig. 2, is fixed with respect to the IR lamp bank. Thus the steady-state, nondimensional, energy equation for nonconstant thermal properties is

$$\mathrm{Pe}\ \bar{C}_c \frac{\partial \bar{T}}{\partial \bar{X}} = \frac{\partial}{\partial \bar{X}}\left(\bar{\kappa}_{c,l} \frac{\partial \bar{T}}{\partial \bar{X}}\right) + \kappa_{c,tl} \frac{\partial}{\partial \bar{Y}}\left(\bar{\kappa}_{c,t} \frac{\partial \bar{T}}{\partial \bar{Y}}\right) + \frac{\overline{dQ_{ch}}}{dt} - \frac{1}{N_{cr}} \overline{\nabla \cdot q_r} \quad (1)$$

Here, the temperatures are simply normalized to $\bar{T} = T/T_{\mathrm{ref}}$ where $T_{\mathrm{ref}} = 298$ K. No convenient normalization is available to place the range of dimensionless temperatures between zero and unity, because the chemical energy release term due to epoxy curing causes the temperatures to reach maximum values that cannot be predicted a priori. The $\bar{\kappa}$ and $\bar{C}$ are nondimensional thermal conductivity and specific heat of the composite, respectively. The left-hand side of Eq. (1) is the energy transport by advection due to ply motion; the Peclet number, Pe, is the ratio of energy transport by advection to energy transferred by diffusion along the fiber or $\bar{X}$ direction. The first two terms on the right-hand side of Eq. (1) are energy transport by thermal diffusion along the fiber ($\bar{X}$) and transverse fiber ($\bar{Y}$) directions, respectively. The ratio of the thermal conductance of the latter to the thermal conductance of the former energy transport is defined to be the anisotropic conductivity parameter $\kappa_{c,tl}$; it depends upon the composite's diameter and the ply's thermal conductivities. Due to the steady-state heat transfer assumption in the analysis, the third term on the right-hand side of Eq. (1), which is the rate of chemical energy released, is transformed to the variation of exothermic energy with respect to the distance $\bar{X}$. In the last term of Eq. (1), N_{cr} is the ratio of energy transferred by thermal conduction in the fiber direction to the radiation. Finally, $\overline{\nabla \cdot q_r}$ is the nondimensional divergence of the radiative heat flux.

In our Eulerian control volume, each location within the material has an initial temperature T_∞ and linear velocity V, is assumed to enter the composite at $\bar{X} = -|\bar{x}_{\mathrm{int}}|$ in ply 1 and cascades through the ply stack until it exits at $\bar{X} = 1$ from ply n_{tot}. Here, n_{tot} is estimated by the radiation penetration distance where incident radiation attenuates to less than 0.5 percent. Once the curing is complete, the temperature of the n_{tot}–th ply is expected to be uniform, so that an adiabatic boundary condition is assumed at $\bar{Y} = 0$ and at the exit section $\bar{X} = 1$ of the ply n_{tot}. Along the top surface at $\bar{Y} = 1$, convective heat loss is assumed to occur.

The boundary conditions for Eq. (1) are:

Surface (1): $\bar{T} = \bar{T}_{\mathrm{int}}$ (2)

Surface (2): $\dfrac{\partial \bar{T}}{\partial \bar{Y}} = \dfrac{-hH}{\kappa_{c,t}}(\bar{T} - \bar{T}_\infty)$ (3)

Surfaces (3), (6): At the matching point,

$$\bar{T}_n = \bar{T}_{n+1} \quad (4)$$

Surface (4): $\dfrac{\partial \bar{T}}{\partial \bar{X}} = 0$ (5)

Surface (5): $\dfrac{\partial \bar{T}}{\partial \bar{Y}} = 0$ (6)

Surface (7): $\dfrac{\partial \bar{T}}{\partial \bar{Y}} = \dfrac{-hH}{\kappa_{c,t}}(\bar{T} - \bar{T}_\infty)$ (7)

Note that, because radiation is treated as a volumetric effect, the radiative flux at the boundary appears implicitly within the radiative transfer equation.

An estimate of the local heat transfer coefficient h in the inlet region $\bar{X} \le 0$ due to the motion of the inlet ply (forced convection) and natural convection is obtained from a correlation for air flowing parallel to a semi-infinite isothermal flat plate (Wickern, 1991).

The local convective heat transfer coefficient h in the region $0 \le \bar{X} \le 1$ due to forced and natural convection is obtained from correlation for an isothermal, rotating cylinder. Within various ranges of rotating Reynolds number, N_{rot}, different correlations of heat transfer coefficient are applied in the model (Chern, 1994b). Although the relations for heat transfer coefficient were found experimentally for cylinders with very large length-to-radius ratios, they are adopted for use here. The temperature dependence of h is also considered by including the local properties in the Prandtl number N_{pr} and Grashof number N_{gr} in the correlations. These correlations for h were used for all predictions by the numerical model presented in this paper.

Cure Kinetics Equations. Due to its wide use in industry and the availability of a cure kinetics model (Lee et al., 1982), the Hercules 3501-6 resin system is used in the present study. Lee's model is used to estimate the nondimensional heat release $d\bar{Q}_{ch}/dt$ as a function of degree of cure α_d and temperature T. In this model, α_d is defined to be the ratio of the exothermic heat released Q_{ch} until some intermediate time t to the total exothermic heat released Q_{tot} when all cross-linking reactions are complete. The incoming tape is assumed to be totally uncured: $\alpha_d = 0$.

Radiative Transfer Equation. The radiative transfer through a unidirectional fibrous medium (as shown in Fig. 2) is considered, where the incident radiative energy flux from the infrared lamp bank is q''_{lamp}. For monochromatic incident radiation, the radiative transfer equation, which describes the change in intensity along the light path s in the solid angle $d\Omega$ about the Ω direction, is written as follows (Siegel and Howell, 1992):

$$\frac{di_{\lambda_c}(S, \Omega)}{dS} = \underbrace{-\sigma_{ex_{\lambda_c}}(\Omega) i_{\lambda_c}(S, \Omega)}_{\text{Loss by absorption and outgoing scattering}} + \underbrace{S_{\lambda_c}(S, \Omega)}_{\text{Source function}} \quad (8)$$

$$S_{\lambda_c}(S, \Omega) \equiv \underbrace{\sigma_{a_{\lambda_c}}(\Omega) i^b_{\lambda_c}(S)}_{\text{Gain by emission}} + \underbrace{\frac{1}{4\pi}\int_{4\pi} \sigma_{sc_{\lambda_c}}(\Omega')P_{\lambda_c}(\Omega', \Omega) i_{\lambda_c}(S, \Omega')d\Omega'}_{\text{Gain by incoming scattering}} \quad (9)$$

where $P_{\lambda_c}(\Omega', \Omega)$ is the phase function of the energy transfer from the incoming direction Ω' to the direction of interest Ω and λ_c is the wavelength of light in the composite. Due to the anisotropic characteristics of the unidirectional fibrous medium, the radiative properties $\sigma_{ex}, \sigma_a, \sigma_{sc}$ as well as the phase function, are dependent on the incident angle of the light. It is assumed that axial (z) variations are negligible.

A summary of the boundary conditions for Eqs. (8), (9) is:

Surface (1): $i_{\lambda_c} = i^b_{\lambda_c}$ (10)

Surface (2):

$$i_{\lambda_{c,U}} = \frac{q''_{\text{lamp}\lambda_e}}{\pi}\eta_e F_{d\bar{x}-\text{lamp}}(1 - \gamma^d_{\text{air},\lambda_c}) + \frac{\gamma^d_{\lambda_c}}{\pi}\int_{\cap} i_{\lambda_c}(\Omega')l_y d\Omega' \quad (11)$$

Surfaces (3), (6):

$$\text{from continuity, } i_{\lambda_c}(\Omega)_n = i_{\lambda_c}(\Omega)_{n+1} \quad (12)$$

Surface (4): $i_{\lambda_c} = i^b_{\lambda_c}$ (13)

Surface (5): $i_{\lambda_c} = i^b_{\lambda_c}$ (14)

Surface (7): $i_{\lambda_{c,\Gamma}} = \frac{\gamma^d_{\lambda_c}}{\pi}\int_{\cup} i_{\lambda_c}(\Omega')l_y d\Omega'$ (15)

The incoming tape is assumed to have uniform temperature T_∞. An isothermal region at constant temperature that is optically thick will emit blackbody radiation at the body temperature. Therefore, the blackbody intensity distribution corresponding to the incoming prepreg temperature T_∞ is imposed as the boundary condition at surface (1). (This condition is not strictly true, because the incoming tape is not a semi-infinite region at $\bar{X} < 0$. A more exact condition does not appear justified.) The external diffuse incident radiation from the IR lamp bank is considered in the first term of the right-hand side of Eq. (11). Blackbody spectral emission from the IR lamp bank is assumed in the analysis. However, due to the conduction and convection heat loss from the lamp, the overall lamp bank efficiency η_e is also included in the analysis. By assuming diffuse surfaces (2, 7), the intensity reflection from the interior region is also considered and written in Eqs. (11), (15). Here, γ^d is the boundary diffuse reflectivity. At the internal surface, the diffuse reflectivity was found by averaging the specular reflectivity from the Fresnel relations over all incident angles, accounting for the region of total internal reflection. At the bottom region of the computation domain, the temperature is expected to be uniform and approach radiative equilibrium due to the adiabatic boundary condition at surfaces (4, 5). The blackbody intensity distributions corresponding to the temperatures at surfaces (4, 5) are applied as boundary conditions at these two surfaces, using the same rational as for surface 1.

By neglecting the interaction effects of the radiative transfer through each fiber (Lee, 1989; Houston and Korpela, 1981), the scattering and absorption coefficients of the global material (i.e., the composite) are taken to be the sum of those of the total fibers and the phase function of the composite is equal to that of a single fiber. This is tantamount to assuming independent scattering from each of the embedded fibers. From the refractive index of fiber and matrix, fiber volume fraction, incident angle, and relative fiber size to the incident wavelength of the light, the radiative properties and phase function for the single fiber scattering can be obtained by solving the Maxwell equations (or Helmholtz wave equation) (Kerker, 1969). No specific scattering pattern is assumed.

Because the radiative properties for a single scattering "event" (Kerker, 1969) are expressed in terms of the local fiber coordinate system, the transformations from the local fiber to the global coordinate system for the radiative properties are needed (Chern et al., 1994b, c).

The potential effect of dependent scattering in the studied composites is investigated in Chern (1994b). In the study, it is found the independent scattering theory can be applied to the carbon composite without significant error, because radiation attenuation is so strong that radiation is effectively a surface phenomenon. For the glass composite, the independent scattering theory tends to overestimate the extinction coefficient of the material.

The nondimensionalized divergence of the radiative flux in Eq. (1) is (Siegel and Howell, 1992)

$$\overline{(\nabla \cdot q_r)} = \int_0^\infty \int_{\Omega=4\pi} \frac{\sigma_{ex_{no}\lambda_c}}{\sigma_{ex_{no}\lambda_{\text{ref}}}} \bar{\sigma}_{a\lambda}(\bar{i}^b_{\lambda_c}(T) - \bar{i}_{\lambda_c}(\Omega))d\Omega d\lambda_c \quad (16)$$

Numerical Method of the Model

The control volume formulation is employed to solve the energy equation. Detailed derivation of the two-dimensional discretization equation is given by Patankar (1980). The "SIMPLE" code (Patankar, 1980) is modified to solve for the temperature fields in the computation domain. The power-law scheme is employed in the numerical calculations. In addition, the interface thermal conductivity of the control volume is taken to be the harmonic mean of those of two adjacent grid points.

After obtaining the new temperature fields, the degree of cure of the composite is determined by solving the cure kinetics equations using the fourth-order Runge–Kutta method. For the radiative transfer computation, the radiative properties from independent scattering theory must be calculated. The new temperature fields and the obtained radiative properties are substituted into the radiative transfer equation for obtaining the intensity distributions. The modified discrete ordinate and picket fence methods (Chern et al., 1994b, c) are applied to determine the intensity distributions in discrete ordinate direction and spectral wave band at each position. The divergence of radiative flux is then updated by taking the sum of emission and absorption for each spectral wave band.

The convergence criterion for the divergence of radiative flux is a relative error of less than 10^{-3}. The new source terms (chemical reaction and divergence of radiative flux) in the energy equation are re-applied to evaluate the new temperature profiles. This process is repeated with new temperatures until the relative error for all temperatures from successive iterations does not exceed 2.5×10^{-4}. Since the radiative intensity decays exponentially from the top boundary surface through the computational domain, nonuniform grids along the $\bar{Y}$ direction are employed in the numerical calculations. Numerical results of processing temperature profiles within composite are compared using the S10, S8, and S6 radiative transfer models (Chern,

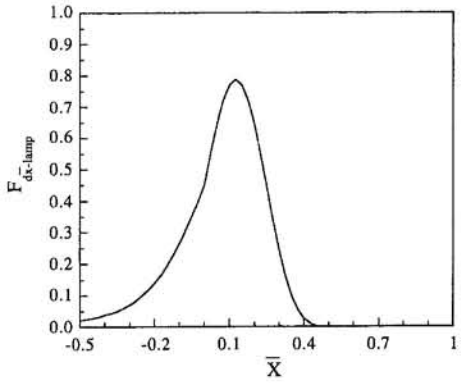

Fig. 3 Viewfactor from infrared lampbank to surface 2 of the computational domain

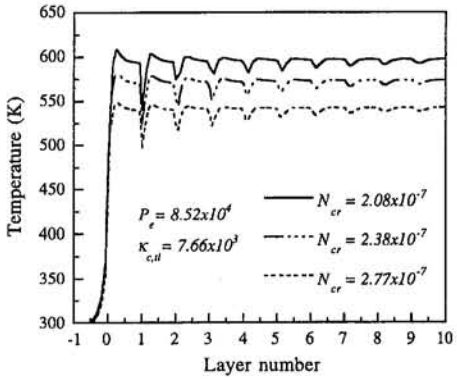

Fig. 4 Temperature versus layer number at various energy levels for AS4/3501-6

1994b). Results from the S8 model, which computes 40 fluxes over the hemisphere, are found to be quite accurate for oblique incident radiation through the composite, and are used for all of the cases considered. In addition, a grid of 122 (in the $\bar{X}$ direction) × 95 (in the $\bar{Y}$ direction) was found to provide sufficiently converged solutions.

Input Data

For model simulation, the lamp bank temperature and configuration, mandrel dimension, thermal properties and radiative properties of the composite are needed.

Typical IR lamp bank size and configuration for our experimental program are given in Chern et al. (1994b, d). The viewfactor associated with the experimental configuration is computed by using the three-dimensional unit-sphere method (Alciatore et al., 1989). The resulting viewfactor is shown in Fig. 3, and it is seen that radiation is incident on the prepreg fiber tape upstream of $\bar{X} = 0$. The viewfactor is set to zero in Eq. (11) outside the range of $\bar{X}$ shown in Fig. 3.

Hercules AS4/3501-6 (carbon fibers) and S-glass/3501-6 (glass fibers) are considered in the present analysis. The fiber diameter and volume fraction for these two commercial products are 7 μm and 62 percent, respectively. The prepreg tape (single ply) thickness is about 1.3×10^{-4} m.

The temperature and degree of cure dependency of specific heat, longitudinal and transverse thermal conductivity of the AS4/3501-6 and S-glass/3501-6 are documented in Chern et al. (1993, 1994b). In addition, to evaluate the radiative properties and phase function in Kerker (1969), the complex refractive index of the matrix and fiber must be known. The simple refractive index of the 3501-6 epoxy is found to approximate a constant value of 1.5. Epoxy resin has strong absorption bands as well in some portions of the spectrum; however, because the fibers embedded in the epoxy (glass and graphite) are very strong absorbers (graphite at all wavelengths and glass over much of the infrared spectrum), we have ignored epoxy absorption in this paper. For carbon fiber, the refractive index approximates a constant value of $1.75 - 0.552i$ for all wavelengths. For *S*-glass fiber, a three spectral wave band approximation is used: wavelength in vacuum, 0–2.5 μm ($\tilde{m}_f = 1.497 - 0.589 \times 10^{-5}\, i$), 2.5–5.0 μm ($\tilde{m}_f = 1.497 - 0.1687 \times 10^{-3}\, i$) and 5.0–100 μm ($\tilde{m}_f = 1.23 - 0.03i$) (Chern, 1994b).

Numerical Results

The most primitive results of the analysis are the layer-by-layer temperature profiles that occur during winding and the corresponding degree of cure in each layer. In Figs. 4–8, the horizontal axis shows the progress of a point from initial contact of the incoming prepreg tape with the cylinder at $\bar{X} = 0$ as the point traverses layer-by-layer through the computational

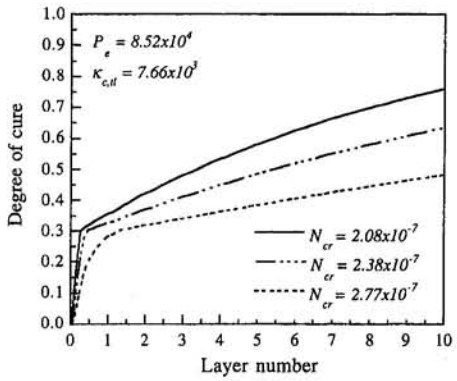

Fig. 5 Degree of cure versus layer number at various energy levels for AS4/3501-6

domain. Each layer of the computational domain is taken to be of thickness $\Delta\bar{Y} = 1.32 \times 10^{-4}$ m, which corresponds to a typical prepreg tape thickness. The computational domain is composed of 30 and 40 ply layers for carbon and glass composites, respectively. Typical temperature profiles for each of the outer 10 layers of AS4/3501-6 composite are shown in Figs. 4 and 5. Figures 4 and 5 show the effect of varying the conduction/radiation parameter N_{cr} on the temperature and the degree of cure profiles when Pe and $\kappa_{c,tl}$ are held constant. The particular Pe and $\kappa_{c,tl}$ used correspond to a composite diameter of 0.2 m and a mandrel winding speed of 0.2 m/s. The different values of N_{cr} correspond to a lamp bank output 10 kW (the lamp bank temperature is 1290 K) and lamp bank efficiencies of 0.8, 0.7, and 0.6. Smaller values of N_{cr}, for a given resin system and winding size, imply increasing IR energy into the matrix.

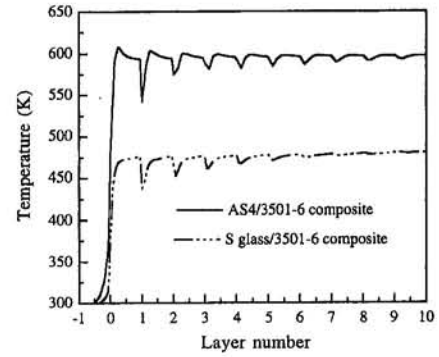

Fig. 6 Temperature versus layer number for carbon and S-glass composites at conditions D = 0.2 m and V = 0.2 m/s

The predicted temperature profiles in Fig. 4 have a sawtooth shape, in which each "tooth" corresponds to one cycle or revolution of the mandrel. The steep ramp-up on the left-hand side of each tooth is primarily due to the IR energy deposited by the lamp bank. The abrupt drop in the temperature on the right-hand side of each tooth is due to the matching conditions forced between the adjacent layers. The inlet tape enters the computational domain with a relatively low temperature. After IR heating, the next layer presents a high-temperature region. When the "cold" and "hot" ply meet at the matching point, large conduction heat transfer occurs in the positive $\bar{Y}$ direction. This causes an abrupt drop in the temperature in the neighborhood of the matching points. The relative "sharpness" of the drop is also attributed to the high Peclet number present in practical situations, which makes the downstream temperature in a given layer insensitive to the upstream heat transfer.

Due to the two-step reactions, the degree of cure profiles in Fig. 5 present a sharp decrease in the rate of degree of cure at about 30 percent. It is important to predict the peak temperature reached during the process, so that resin degradation temperatures are not reached. The reported value for this degradation temperature is about 600 K (Lubin, 1982). It is also equally important to know the degree of cure at some reasonable depth into the composite winding. Moreover, the degree of cure at the end of layer one should not approach 100 percent; otherwise, complete cross-linking will not occur at the knit point between the fresh tow and the fully cured layer.

Although the equations are nondimensionalized, the values of dimensional parameters input for the case studies provide valuable insight into the process. For the two composites considered, the radiative properties are quite different. The carbon fibers are highly absorbing material, while glass fibers are more transparent in the first and second band and will absorb more IR energy in the third spectral band. The same emissive power output (10 kW, $\eta_e = 0.8$) of the IR lamp and winding speed (0.2 m/s) are considered for these two composite systems. The calculated temperature and degree of cure fields for these two materials are shown in Figs. 6 and 7.

Calculation of the divergence of radiative flux shows that the penetration distance of the AS4/3501-6 is less than one layer thickness of composite. However, for S-glass composite, the IR radiation continues to propagate further into deeper regions of the composite. This is a strongly wavelength-dependent effect. Detailed profiles of divergence of radiative flux are given in Chern (1994b), where it is shown that up to 16 percent of the incident radiation may penetrate the computational domain for the S-glass composite.

As noted in the Analysis section, radiative emission within the AS4/3501-6 composite is included in the results of this paper. The maximum processing temperature is limited to 600 K due to potential degradation of the epoxy. In some previous work (Chern et al., 1992, 1994a) emission was neglected, and temperatures were overestimated by about 50 K. This overestimated temperature will also overestimate the degree of cure by up to 20 percent at the tenth layer. Thus, radiative emission plays an important role.

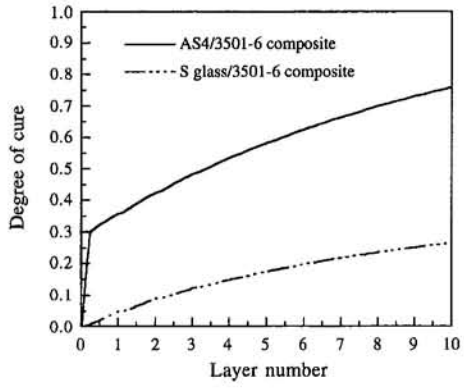

Fig. 7 Degree of cure versus layer number for carbon and S-glass composites at condition $D = 0.2$ m and $V = 0.2$ m/s

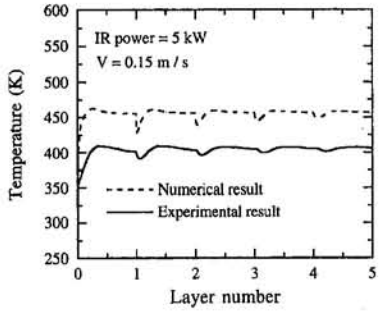

Fig. 8 Comparison of predicted and experimental temperature histories for AS4/3501-6 carbon fiber-epoxy composite between at IR input 5 kW and winding speed 0.15 m/s

Experimental Results

Typical comparison of temperature distribution for numerical prediction and experiment is shown in Fig. 8. The experimental method and additional comparative curves are given in Chern et al. (1994d). In Fig. 8, the input IR power and winding speed are 5 kW and 0.15 m/s, respectively. The estimated overall IR lamp bank efficiency is 63 percent (includes the effect of lamp efficiency, reflector efficiency, and blockage). The qualitative comparison of predicted temperatures with the experiment is good. However, the model tends to overpredict the temperature by about 50 K. This difference is probably due to the model input data for convective heat transfer coefficient and IR lamp bank efficiency. It is, of course, possible to obtain more exact agreement between experiment and prediction by adjusting the modeled values of the lamp bank efficiency, the heat transfer coefficient, or both. However, if we had done so, it was not clear that forcing agreement with the small available experimental data set would make the predictions more accurate for other parametric values. More detailed discussion about the error introduced in the experiment is given by Chern et al. (1994d).

Conclusion

A two-dimensional thermochemical and radiative transfer model for the in-situ IR curing process is established. Typical numerical results for temperatures and degrees of cure of composite during processing are presented. Good qualitative comparison between the numerical and experimental data is also demonstrated.

Since the model can predict the important processing information such as temperature and degree of cure within the composite, the method developed can provide a design tool for the IR in-situ curing of composite. The thermal process windows for potential industrial application for various composite size, IR configuration, input IR energy levels, and winding speeds can be generated through model predictions. These results are demonstrated in Chern et al. (1994d).

Acknowledgments

The authors gratefully acknowledge the support of this research by the NSF Division of Design, Manufacture and Industrial Innovation through grants No. DMI-9109592 and DMI-9258413 and the State of Texas' Higher Education Coordinating Board's Advanced Technology Program under grant 003658-359. They also acknowledge instrumental startup support from The University of Texas at Austin's University Research Insti-

tute, Bureau of Engineering Research and Center for Energy Studies. Use of programs for solving the independent radiative properties from Professor T. W. Tong, Arizona State University, is also gratefully acknowledged.

References

Alciatore, D., Lipp, S., and Janna, W. S., 1989, "Closed Form Solution of the General Three-Dimensional Radiation Configuration Factor Problem With Microcomputer Solution," *National Heat Transfer Conference,* ASME HTD-Vol. 106, pp. 165–169.

Chern, B.-C., Moon, T. J., and Howell, J. R., 1992, "Assessment of Using In-Situ IR-Heat to Cure Thermoset, Filament-Wound Structures," *Proceedings of the First International Conference on Transport Phenomena in Processing,* Honolulu, HI, Mar. 22–26, pp. 1303–1313.

Chern, B.-C., Moon, T. J., and Howell, J. R., 1993, "Measurement of the Temperature- and Cure-Dependence of the Thermal Conductivity of Epoxy Resin," *Experimental Heat Transfer,* Vol. 6, pp. 157–174.

Chern, B.-C., Moon, T. J., and Howell, J. R., 1994a, "Modeling of Radiation-Initiated Cure-on-the-Fly of Epoxy-Matrix Composite Cylinders," *Journal of Materials Processing & Manufacturing Science,* Vol. 2, No. 4, pp. 373–390.

Chern, B.-C., 1994b, "Heat Transfer Analysis of In-Situ Curing for Thermoset Pre-impregnated Tape-Hoop-Wound Structures Using Infrared Heating," Ph.D dissertation, The University of Texas at Austin.

Chern, B.-C., Moon, T. J., and Howell, J. R., 1994c, "Angle of Incidence Dependent Scattering Effects in Arrays of Parallel Cylinders Typical of Filament-Wound Composites," *Proceedings of the 6th AIAA/ASME Thermophysics and Heat Transfer Conference,* Colorado Springs, CO, June 20–22, ASME HTD-Vol. 276, *Radiative Heat Transfer: Current Research,* pp. 79–90.

Chern, B.-C., Moon, T. J., and Howell, J. R., 1994d, "Experimental Validation and Thermal Process Window Development for In-Situ Curing of Thermoset, Hoop-Wound Structures Using Infrared Heating," *Journal of Composite Materials,* in review.

Fiveland, W. A., and Jamaluddin, A. S., 1991, "Three-Dimensional Spectral Radiative Heat Transfer Solutions by the Discrete-Ordinates Method," *Journal of Thermophysics and Heat Transfer,* Vol. 5, No. 3, pp. 335–339.

Houston, R. L., and Korpela, S. A., 1981, "Heat Transfer Through Fiberglass Insulation," *Proceedings of 7th International Heat Transfer Conference,* Vol. 2, pp. 499–504.

Howell, J. R., 1988, "Thermal Radiation in Participating Media; The Past, the Present, and Some Possible Futures," ASME JOURNAL OF HEAT TRANSFER, Vol. 110, pp. 1220–1229.

Kerker, M., 1969, *The Scattering of Light,* Academic Press, New York.

Korotkov, V. N., Chekanov, Y. A., and Rozenberg, B. A., 1993, "The Simultaneous Process of Filament Winding and Curing for Polymer Composites," *Composite Science and Technology,* Vol. 47, pp. 383–388.

Kurosaki, Y., Yamada, J., and Take-Uchi, M., 1991, "Estimation of the Radiative Properties of Fibrous Media Taking Account of Fiber Orientation," *ASME/JSME Thermal Engineering Proceedings,* Vol. 4, pp. 11–18.

Lee, W. I., Loos, A. C., and Springer, G. S., 1982, "Heat of Reaction, Degree of Cure, and Viscosity of Hercules 3506-1 Resin," *Journal of Composite Materials,* Vol. 16, No. 11, pp. 510–520.

Lee, S. C., 1989, "Effect of Fiber Orientation on Thermal Radiation in Fibrous Media," *International Journal of Heat and Mass Transfer,* Vol. 32, No. 2, pp. 311–319.

Lubin, G., 1982, *Handbook of Composites,* Van Nostrand Reinhold Co., New York.

Patankar, S. V., 1980, *Numerical Heat Transfer and Fluid Flow,* Hemisphere Publishing Corporation, New York.

Siegel, R., and Howell, J. R., 1992, *Thermal Radiation Heat Transfer,* 3rd ed., Hemisphere Publishing Corp., Washington, DC.

Stango, R. J., Matar, J. E., and Cariapa, V., 1991, "Effect of Fabrication Parameters on Void Content for Filament-Wound Composite," *ASME Processing and Manufacturing of Composite Materials,* Vol. 27, pp. 277–290.

Wickern, G., 1991, "Mixed Convection From an Arbitrarily Inclined Semi-infinite Flat Plate—I. The Influence of the Inclination Angle," *International Journal of Heat and Mass Transfer,* Vol. 34, No. 8, pp. 1935–1945.

Yuen, W. W., Takara, E. E., and Lee, S. C., 1992, "Evaluation of Effective Radiative Properties of Fibrous Composite Materials," AIAA Paper No. 92-2893.

Thermal Analysis of In-Situ Curing for Thermoset, Hoop-Wound Structures Using Infrared Heating: Part II—Dependent Scattering Effect

B.-C. Chern
Everest Industrial Co., Inc.,
No. 669 Keng Tze Kou, Feng Keng Tsun,
Hsin Feng Hsiang Hsinchu, Taiwan

T. J. Moon

J. R. Howell

Department of Mechanical Engineering,
University of Texas at Austin,
Austin, TX 78712

The volume fraction of the fibers present in commercial filament wound structures, formed from either epoxy-impregnated tapes ("prepreg") or fiber strands pulled through an epoxy bath, approaches 60 percent. Such close-packed structures are near the region that may cause dependent scattering effects to be important; that is, the scattering characteristics of one fiber may be affected by the presence of nearby fibers. This dependent scattering may change the single-fiber extinction coefficient and phase function, and thus may change the radiative transfer in such materials. This effect is studied for unidirectional fibers dispersed in a matrix with nonunity refractive index, and with large size parameter (fiber diameter to wavelength ratio) typical of commercial fiber–matrix composites. Only the case of radiation incident normal to the cylinder axes is considered, as this maximizes the dependent effects. The dependent extinction efficiency is found by solving the dispersion relations for the complex effective propagation constant of the composites. An estimation of this dependent scattering effect on the infrared in-situ curing of thermoset-hoop-wound structures is also conducted. It is found that the wave interference effect is significant for S-glass/3501-6 composite, and neglect of this effect tends to overestimate the temperature and cure state within the materials during IR in-situ curing.

Introduction

The scattering and absorption of radiation by particles is assumed in most cases to be independent of the presence of other particles (Lee, 1989; Houston and Korpela, 1981). However, when the volume fraction occupied by the particles becomes large, the electromagnetic field around any given particle is affected by the presence of similar electromagnetic fields around nearby particles, and the independent scattering and absorption approximation breaks down.

Dependent effects on wave attenuation are dominated by far and near-field effects. The far-field effects involve phase addition and cancellation of the scattered waves; they influence the shape and the amount of scattered radiation. For the case of parallel cylinders, or fibers, the near-field effects account for successive scattering of cylindrical waves by an individual fiber due to the presence of adjacent fibers and increase the radiation absorbed and scattered by each fiber due to the enhancement in the internal field of each fiber. White and Kumar (1989) and Kumar and White (1990) considered dependent interference effects on scattering of normally incident radiation in fibrous materials. They assumed that the phase change across each fiber is small—an assumption that is valid for small fibers relative to the wavelength of the radiation. Lee (1990) developed a formulation that accounts for both near and far-field effects for a collection of parallel fibers in a given configuration that is exposed to oblique incident radiation. For large numbers of fibers (greater than a few hundred), however, the formulation becomes cumbersome and the number of fibers that can be handled becomes limited by computer memory.

Varadan and co-workers (1987, 1990) and Zhu et al. (1987) considered the full dependent scattering theory for spherical particles. They found the average attenuation over an ensemble of configurations. They assumed that an average wave travels as a plane wave in the medium with complex propagation constant. The ensemble of configurations consisted of a random distribution of identical pair-correlated scatterers embedded in a matrix. The pair correlations were described by radial distribution functions and a dispersion relation for the propagation constant was derived. Lee (1992a, b) applied a similar approach to a system of cylindrical fibers. An effective propagation constant was derived and this was used to determine the dependent extinction coefficient and the phase velocity of a wave in high-density composites. A closed-form solution is presented for small values of the size parameter ($\alpha_v = 2\pi r/\lambda_v = 0.01$). A constant pair-distribution function was assumed in the analysis.

In the present analysis, we are concerned with a fiber–matrix combination in which the matrix has a nonunity refractive index. Epoxy resin, for example, has a simple refractive index near 1.5 over the spectrum of interest. Epoxy resin has strong absorption bands as well in some portions of the spectrum; however, because the fibers embedded in the epoxy (glass and graphite) are very strong absorbers over broad spectral ranges (graphite at all wavelengths and glass over much of the infrared spectrum), we have ignored epoxy absorption in this paper.

Commercial fibers exposed to visible or near-infrared wavelengths will have size parameters that are large enough that they cannot be assumed to be governed by the limiting small-size-parameter approximations. Furthermore, the pair-distribution function depends on the volume fraction of the embedded fibers. These three factors (nonunity refractive index of the matrix, large size parameter, and variable pair distribution function)

Contributed by the Heat Transfer Division for publication in the JOURNAL OF HEAT TRANSFER. Manuscript received by the Heat Transfer Division March 1994; revision received January 1995. Keywords: Materials Processing and Manufacturing Processes, Radiation, Radiation Interactions. Associate Technical Editor: M. F. Modest.

considerably complicate the evaluation of the extinction coefficient. However, all three factors must be considered if the effect of dependent extinction is to be accurately determined for practical fiber–matrix composites. In this paper, the dependent extinction efficiency at various fiber size parameters for the commercial thermoset composites, Hercules AS4/3501-6 and S-glass/3501-6, are determined for radiation incident normal to the cylinder axis. In addition, inter-fiber–matrix wave interference effects on the infrared in-situ curing process for these two commercial composites are demonstrated.

Governing Equations

The electromagnetic fields associated with the extinction of a dependently absorbed and scattered wave are governed by Maxwell's equations. These vector equations can be reduced to a set of scalar Helmholtz wave equations. The scalar wave potentials Π_{TM} and Π_{TE}, which satisfy the scalar wave equation, are introduced as aids in solving for the electric and magnetic fields (Balanis, 1989). This approach was used by Lee (1990) in developing the fully dependent extinction theory for wave propagation through a matrix containing parallel fibers. We have extended Lee's analysis to account explicitly for the nonunity refractive index of the matrix, and as noted later have also included the effects of accurate pair distribution functions at large fiber volume fractions.

Consider a plane electromagnetic wave normally incident on a collection of parallel infinite cylinders, as shown in Fig. 1. The total wave potential at any point outside a cylinder subject to an incident wave with TM^Z (transverse magnetic mode; the magnetic field along z direction = 0) and TE^Z (transverse electric mode; the electric field along z direction = 0) is given by the sum of the primary incident wave plus the wave scattered by all of the cylinders. In the vicinity of the jth cylinder, the total wave potential in the external field is thus given by

$$\begin{Bmatrix} \Pi_{TM,j}(\bar{R}) \\ \Pi_{TE,j}(\bar{R}) \end{Bmatrix} = \begin{Bmatrix} \Pi^i_{TM,j}(\bar{R}) \\ \Pi^i_{TE,j}(\bar{R}) \end{Bmatrix} + \sum_{k=1}^{N} \begin{Bmatrix} \Pi^s_{TM,k}(\bar{R} - \bar{R}_k) \\ \Pi^s_{TE,k}(\bar{R} - \bar{R}_k) \end{Bmatrix} \quad (1)$$

Here, Π_{TM} and Π_{TE} are the scalar wave potentials corresponding to the TM^Z and TE^Z incident waves, respectively. The superscripts i and s in Eq. (1) denote the incident and scattered waves.

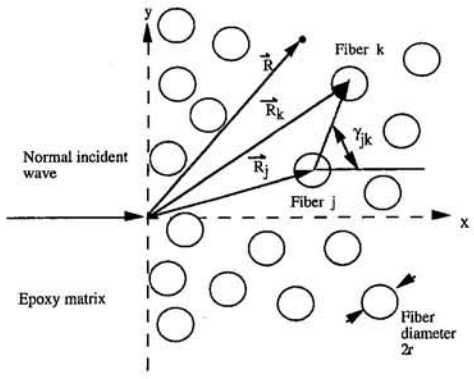

Fig. 1 Physical geometry for normally incident radiation

In order to solve for the external fields for cylinder j, the addition theorem for Hankel functions (Balanis, 1989) is applied to express the scattered fields in terms of the coordinates relative to the jth cylinder. Continuity of the tangential fields across the jth fiber is imposed to solve for the unknown coefficients in the scalar potential. Mathematically, these require the $\tilde{m}\Pi_{TM}$, $\tilde{m}\partial\Pi_{TM}/\partial r^*$, $\tilde{m}^2\Pi_{TE}$ and $\partial\Pi_{TE}/\partial r^*$ to be continuous at $r^* = r$ (Kerker, 1969). Here, $\tilde{m}$ is the refractive index of the epoxy (related to external field) or that of the fiber (related to internal field) and r^* is the radial position expressed in terms of coordinates relative to the jth fiber. The final form of these unknown coefficients for the case of normal incidence is (Lee, 1990):

$$\sum_{k=1}^{N} \sum_{s=-\infty}^{\infty} \left[\delta_{kj}\delta_{ns} - (1 - \delta_{kj}) G^{jn}_{ks} \begin{Bmatrix} {}^{o}b_{jn} \\ {}^{o}a_{jn} \end{Bmatrix} \right] \begin{Bmatrix} b_{ks} \\ a_{ks} \end{Bmatrix} = \epsilon_j \begin{Bmatrix} {}^{o}b_{jn} \\ {}^{o}a_{jn} \end{Bmatrix} \quad (2)$$

$$G^{jn}_{ks} = (-i)^{s-n} H^{(2)}_{s-n}(k_e|\bar{R}_j - \bar{R}_k|) \exp[i(s - n)\gamma_{kj}] \quad (3)$$

where G^{jn}_{ks} describes the influence between a pair of fibers j and k and $\epsilon_j = \exp(-ik_e\bar{R}_j \cdot \bar{e}^{\,o})$. Here, $\bar{e}^{\,o}$ is the unit vector in the propagation direction of the incident wave and k_e is the propagation constant of the matrix. The unknown coefficients a_{jn} (or

Nomenclature

a = scattered wave coefficient, TE mode
b = scattered wave coefficient, TM mode
F_{sn} = $F_{sn,1} + F_{sn,2}$, defined by Eqs. (6) and (7)
f = volume fraction of fibers in matrix
$g(R^*)$ = pair distribution function
$H^{(2)}_n$ = Hankel function of the second kind
J_n = Bessel function of the first kind
k = propagation constant = $k_R - ik_I$
$\tilde{m}$ = refractive index
N = total number of fibers
N_{cr} = ratio of conduction to radiation, as defined by Chern et al. (1995)
n_d = number density of fibers
Pe = Peclet number, as defined by Chern et al. (1995)
Q_{ex} = extinction efficiency of the composite
R^* = nondimensional distance $|\bar{R}|/2r$
$\bar{R}$ = radial position vector
r = radius of fibers
r^* = radial position expressed in terms of the coordinates relative to the jth fiber
x^* = nondimensional distance
α = size parameter of fiber in epoxy = $2\pi r/\lambda$
γ = polar angle, as shown in Fig. 1
δ = Kronecker delta function
ϵ_j = phase shift of the primary incident wave at fiber j
ζ = nondimensional fiber separation distance = $s_l/2r$
$\kappa_{c,il}$ = anisotropic thermal conductivity number, as defined in Chern et al. (1995)
λ = wavelength
Π = scalar wave potential
ψ = dependent scattering function

Superscripts

i = incident wave
o = independent scattering results
s = scattered wave
z = z direction

Subscripts

c = composite
d = density
dep = dependent scattering
e = epoxy matrix
ex = extinction
I = imaginary part
indep = independent scattering
j, k = refers to fibers j, k
n, s = index, $-\infty$ to ∞
v = vacuum
R = real part
TE = transverse electric mode
TM = transverse magnetic mode

a_{ks}) and b_{jn} (or b_{ks}) correspond to the *TE* and *TM* modes of wave propagation, respectively. For normal incidence, depolarization of the incident wave does not occur.

The leading superscript o in Eq. (2) denotes the wave coefficients for the limiting case of independent scattering. Detailed solutions for this case are given by Kerker (1969). These coefficients depend on both the size parameter α_e of the fibers ($\alpha_e = 2\pi r/\lambda_e$, where λ_e is the wavelength in the matrix) and the refractive indices of the matrix and the fiber. In considering the nonunity refractive index of the matrix, the important quantities for computing the independent scattering wave coefficients ${}^oa_{jn}$ and ${}^ob_{jn}$ are the ratio of the refractive index of the fiber relative to that of the matrix, $\tilde{m}_f/\tilde{m}_e$, and the propagation constant of the matrix, k_e.

The dependent scattering wave coefficients in Eq. (2) depend on the number and location of fibers in the system. As the number of fibers increases, the numerical computation of the dependent scattering wave coefficients becomes quite cumbersome. To reduce the computational burden, the discrete fiber–matrix system can be approximated as a continuous medium with an effective propagation constant that relates to the dependent extinction coefficient of the discrete system (Lee, 1992a, b). This approach has been used extensively to study random distributions of spherical particles dispersed in a matrix (Ma et al., 1990; Varadan et al., 1979; Zhu et al., 1987).

In Lee's model, fibers of finite number density are assumed to be dispersed in a semi-infinite region. The effective field approach of Foldy (1945) based on configuration averaging and the quasi-crystalline approximation (QCA) (Lax, 1952) were employed by Lee to construct dispersion relations for the effective propagation constant of the composite with a matrix having a constant refractive index.

For a matrix with a nonunity refractive index and a normal incident wave, the final forms of the dispersion relations are:

$$TM \text{ mode} \quad |\delta_{ns} + n_d {}^ob_n F_{sn}| = 0 \tag{4}$$

$$TE \text{ mode} \quad |\delta_{ns} + n_d {}^oa_n F_{sn}| = 0 \tag{5}$$

The factor $n_d F_{sn}$ consists of two terms, $n_d F_{sn,1}$ and $n_d F_{sn,2}$; these are

$$n_d F_{sn,1} = \frac{2f}{r^2} \frac{1}{(k_e^2 - k_c^2)} \{2k_e r J_{s-n}(2k_c r) H^{(2)\prime}_{s-n}(2k_e r) - 2k_c r H^{(2)}_{s-n}(2k_e r) J'_{s-n}(2k_c r)\} \tag{6}$$

$$n_d F_{sn,2} = 8f \int_1^\infty J_{s-n}(2k_c r R^*) H^{(2)}_{s-n}(2k_e r R^*) [g(R^*) - 1] R^* dR^* \tag{7}$$

where $g(R^*)$ is the pair-correlation function for the fibers. The pair correlation function is defined as the local number density of fibers at a distance R from a fixed particle at the origin divided by the average number density (Chae et al., 1969). The prime superscript in Eq. (6) represents differentiation with respect to the argument. Since nonunity refractive index of matrix is considered, the propagation constant k_v used in Lee's model is replaced by the propagation constant in the matrix, $k_e = \tilde{m}_e k_v$.

Equations (4) and (5) are transcendental with complicated functional dependence and no closed-form solutions are possible for arbitrary fiber size parameter. However, for small size parameter at the Rayleigh limit, Lee (1992a) used the "hole correction" approximation (i.e., $g(R^*) = 1$) to obtain a closed-form solution. This results in

$$\left(\frac{k_c}{k_e}\right)^2 = 1 - i\psi \tag{8}$$

$$\psi_{TM} = \frac{4f}{\pi\alpha_e^2} ({}^ob_o + 2{}^ob_1) \quad (TM \text{ mode}) \tag{9}$$

$$\psi_{TE} = \frac{4f}{\pi\alpha_e^2} ({}^oa_o + 2{}^oa_1) \quad (TE \text{ mode}) \tag{10}$$

Equation (8) provides a good initial guess for numerical calculation using Eqs. (4) and (5) for the case of a random distribution of small fibers at different volume fractions f.

The dependent extinction efficiency Q_{ex} of the medium is related to the imaginary part of the effective propagation constant by (Lee, 1992a)

$$Q_{ex} = \frac{\pi\alpha_e}{f}\left(\frac{k_{c,I}}{k_e}\right) \tag{11}$$

For unpolarized incident radiation, the extinction efficiency is the average of those for the *TM* and *TE* modes.

Pair Correlation Function

For the general case of a random distribution of parallel fibers with a known volume fraction, the pair distribution function $g(R^*)$ must be known as a function of volume fraction f occupied by the fibers. The hole correction approximation $g(R^*) = 1$ is only accurate in the limit of a very small f, i.e., a sparse distribution. For this work, we assume that there is no interpenetration of the rigid fibers so that $g(R^*) = 0$ for $|r_j - r_i| < 2r$ and that for greater radii there is a random distribution of fibers with an average volume fraction.

The pair distribution function for random fiber spacings can be determined by various means. Wood (1968, 1970) used Monte Carlo simulations, which provide accurate results at all volume fractions, but yield tabular results only at the fixed values of f for which simulations were run rather than an analytical dependence on f. Alder and Wainwright (1962) used a molecular dynamics approach. Lado (1968) and Chae et al. (1969) used approximation theory for hard disks. Chae indicates that for $f < 0.36$, approximation theories agrees well with Monte Carlo predictions. For our work, we use tabular Monte Carlo results at $f \geq 0.36$, and below this value we use the approximation theory results from the modified Born-Green-Yvon equation (MBGY) as recommended by Chae et al. (1969):

$$g(R^*) = 1 - \frac{8}{\pi} f g(1) \int_{R^*-1}^{R^*} \cos^{-1}\left(\frac{R^{*2} + x^{*2} - 1}{2R^* x^*}\right) x^* \times [g(x^*) - 1] dx^* + \frac{8}{\pi} f g(1) \int_{R^*}^\infty [(1 - \tfrac{1}{4}x^{*2})^{1/2} - x^* \cos^{-1}(1 - \tfrac{1}{2}x^{*2})][g(x^*) - 1] dx^* \tag{12}$$

Solution Techniques

To obtain the effective propagation constant, the determinants of Eqs. (4) and (5) must be solved for the coefficients. The determinants are of size $2n + 1$ by $2n + 1$, and yield multiple roots for finite number density of fibrous medium. Since many of the roots may meet the physical constraints of being real and having the correct sign, it can be difficult to choose the correct solution. However, for very small size parameter α, Lee (1992a) has shown that a unique propagation constant results. Varadan et al. (1979) applied the closed-form solution for the Rayleigh limit as an initial guess, and then increased the size parameter in small steps to obtain the solutions for large values of the size parameter. We used the solution by Lee (1992a) based on the hole correction approximation for small size parameter (Eq. (8)) as our initial guess, and then marched to increasing size parameter. To determine the root of the dispersion equation, the IMSL library subroutine DZANLY based on Müller's method was used.

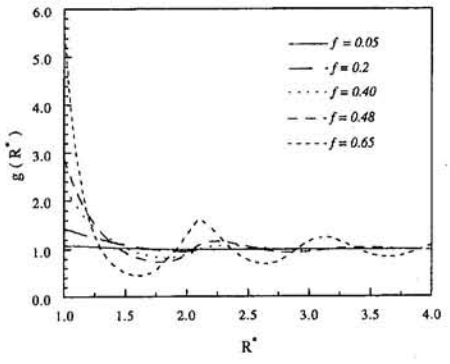

Fig. 2 Pair correlation function of hard disks for various concentration

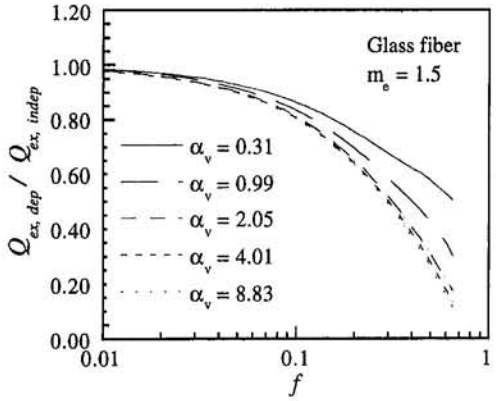

Fig. 4 Variation of the extinction efficiency for normal incidence with fiber size and concentration for S-glass fibers dispersed in epoxy resin

Results and Discussions

For nonunity refractive index of the epoxy matrix, reasonable pair correlation function, and large size parameter of the fibers, the results for coherent wave attenuation through the composites are presented. The pair correlation functions at different fiber concentrations, based on the calculation of Eq. (12) and Wood's (1968, 1970) Monte Carlo simulations, are shown in Fig. 2. Two composite systems, Hercules AS4/3501-6 and S-glass/3501-6, are considered.

Primitive results of the ratio of extinction efficiency for dependent scattering to the independent scattering case for carbon fiber and S-glass fibers (with complex refractive index $1.75 - 0.552i$ and $1.492 - 0.113 \times 10^{-4}\, i$, respectively) dispersed in the 3501-6 epoxy (with constant refractive index 1.5) at various fiber volume fractions and size parameters are shown in Figs. 3 and 4. The dependent scattering effect, which may result in lower or higher extinction efficiency than for the independent case, is evident at high concentrations of fibers. The numerical results for dependent scattering approach the independent scattering results when the fiber concentration is less than 1 percent.

For carbon fibers ($\alpha_v > 4.0$), the maximum deviation of the dependent scattering from the independent scattering results, as shown in Fig. 3, occurs at fiber volume fractions of approximately 45 percent. However, this deviation decreases as the fiber volume fraction increases. Near a fiber concentration of 60 percent, the extinction efficiency for dependent scattering again approaches that of the independent scattering. The same trends are also found in Kamiuto's studies (1990) for dependent scattering of spherical particles. For glass fibers distributed in epoxy, the dependent scattering effect is shown in Fig. 4. The real part of the refractive index ($\mathrm{Re}(\tilde{m}_f) = 1.492$) of the fiber is smaller than for the matrix ($\tilde{m}_e = 1.5$). Due to the refraction effect at the fiber interface, wave interference effects are dominant as the size and the volume fraction of the fibers increase. The dependent scattering effects become more important with size parameter at a given volume fraction for the carbon fibers (Fig. 3) because of the domination of near field effects, while the opposite trend is observed for the glass fibers (Fig. 4), where far-field (interference) effects dominate.

Based on independent scattering theory, the extinction efficiency for commercial AS4/3501-6 composite ($\tilde{m}_e = 1.5$) at various fiber sizes and a fiber volume fraction of 62 percent is shown in Fig. 5. The ratio of extinction efficiency for dependent to independent theory is also shown in this figure. The independent theory is found to underestimate the extinction efficiency in the fiber size range from 0.2 to 12. The maximum effect of dependent scattering is in the range ($0.5 \le 2\pi r/\lambda_v \le 2.5$). For the application of IR curing, the AS4 fiber size parameter is about 11 (this corresponds to a wavelength of 2 μm and a fiber diameter of 7 μm). In this case, it is found that independent scattering theory will underestimate the extinction efficiency by about 7.5 percent.

The radiative properties of the S-glass/3501-6 composite are found to be very wavelength dependent. The three spectral wave band approximation is used for the S-glass composite in the IR in-situ curing analysis (Chern et al., 1995). The spectral bands are 0–2.5 μm ($\tilde{m}_f = 1.497 - 0.589 \times 10^{-5} i$), 2.5–5.0 μm ($\tilde{m}_f = 1.497 - 0.1687 \times 10^{-3} i$) and 5.0–100 μm ($\tilde{m}_f = 1.23 - 0.03i$). The epoxy is assumed to have a constant simple refractive index of 1.50 in each region. The independent extinction efficiency of this composite at various fiber sizes, a fiber volume fraction of 62 percent and within these three spectral wave bands is shown in Fig. 6. The third band is the IR high-absorption region. The result from dependent scattering theory is shown in Fig. 7. Since the S-glass fiber diameter is 7 μm, the corresponding fiber size ($=2\pi r/\lambda_v$) is larger than 8.8 in the first spectral band, 4.4–

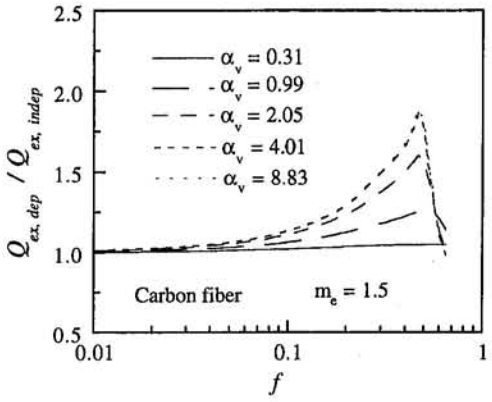

Fig. 3 Variation of the extinction efficiency for normal incidence with fiber size and concentration for carbon fibers dispersed in epoxy resin

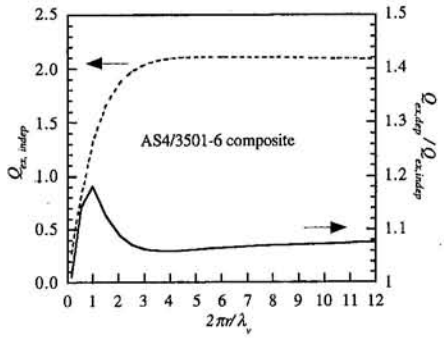

Fig. 5 Variation of independent and dependent extinction efficiency for normal incidence with fiber size for carbon fiber dispersed in epoxy

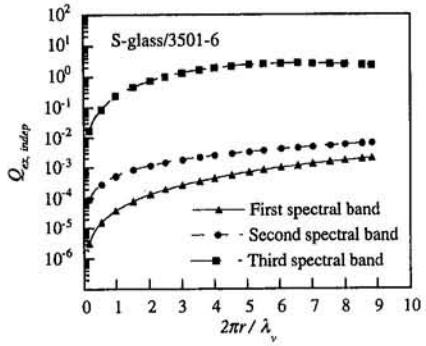

Fig. 6 Variation of the independent extinction efficiency for normal incidence with fiber size for S-glass fiber dispersed in epoxy

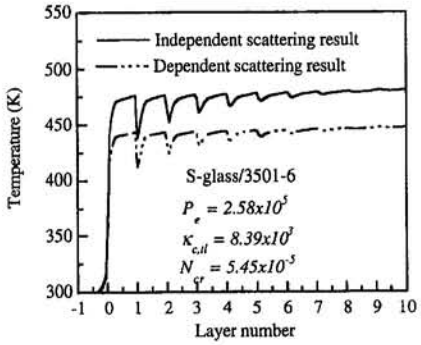

Fig. 8 Temperature versus layer number for S-glass/3501-6 composite

8.8 in the second spectral band and smaller than 4.4 in the third band. Using these fiber size ranges and Fig. 7, the independent theory is found to overestimate the extinction efficiency of the S-glass composite by at least 80 percent in the first spectral band, by about 20 percent in the second spectral band, and by at most 65 percent in the third spectral band. A more complete mapping of the parameters where dependent scattering becomes significant for the parallel fiber systems studied here is given by Chern et al. (1995).

From Lee's (1992a, 1993) numerical results, it is found that the dependent scattering effect is maximum for normal incidence radiation upon a collection of parallel fibers. Therefore, the maximum dependent scattering effect on the IR in-situ curing can be estimated by substituting the dependent extinction efficiency for normal incidence into the radiative transfer equation and by keeping scattering albedo and phase function the same as for the independent scattering case. The numerical method for solving the temperature and degree of cure profiles is the same as discussed by Chern et al. (1995). For more accurate results, the depolarization of the incident wave for dependent scattering should be included in the radiative transfer equation. However, the fundamental theory and the numerical technique for this class of problem are still unavailable. At this stage, calculation using the traditional radiative transfer equation with the dependent extinction efficiency provides an estimate of the dependent scattering effect on the IR curing process.

For AS4/3501-6 composite, it is found that the deviation of temperature and degree of cure using the dependent and independent extinction efficiency are less than 0.3 K and 0.5 percent, respectively. For both the dependent and independent scattering cases, radiation attenuates very quickly and the penetration distance is less than one layer's thickness of prepreg. Under this situation, dependent scattering is not important in that the radiation transport approaches a surface effect. For S-glass/3501-6 composite, the ratio of extinction efficiency for dependent to independent scattering is taken to be 0.2, 0.8, 0.35 in the first, second, and third spectral wave bands, respectively. The numerical results by using this dependent extinction efficiency in the radiative transfer equation are shown in Figs. 8 and 9. It is found that the independent scattering theory will overestimate the temperature and degree of cure profiles about 30 K and 15 percent, respectively.

Conclusion

Dependent scattering effects for normally incident radiation on commercial composites are demonstrated in this paper. The interfiber wave interference effect is dominated by the fiber size, volume fraction, and the relative refractive index of fiber to epoxy matrix. Numerical solutions for dependent scattering studies indicate that the independent scattering theory underestimates the extinction efficiency about 7.5 percent for carbon composite and overestimates the values by at least 80 percent, about 20 percent and at most 65 percent in the first, second, and third spectral bands, respectively, for the S-glass composite. It is found that the dependent scattering effect is insignificant for AS4/3501-6 composite, but neglecting this effect for the S-glass/3501-6 composite tends to overestimate the temperature and cure state within the materials during IR in-situ cure processing.

Acknowledgments

The authors gratefully acknowledge the support of this research by the NSF Division of Design, Manufacture and Industrial Innovation through grants No. DMI-9109592 and DMI-9258413 and the State of Texas' Higher Education Coordinating Board's Advanced Technology Program under grant 003658-359. They also acknowledge instrumental startup support from the The University of Texas at Austin's University Research

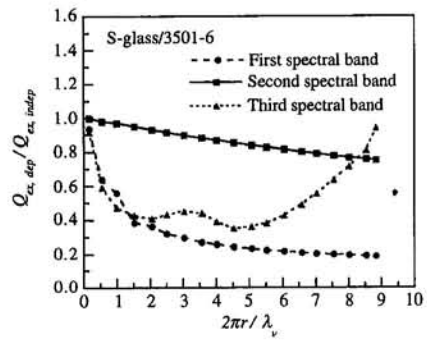

Fig. 7 Variation of the dependent extinction efficiency for normal incidence with fiber size for S-glass fiber dispersed in epoxy

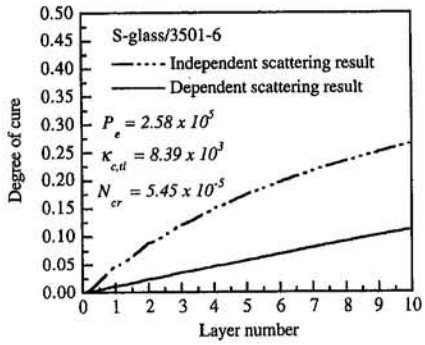

Fig. 9 Degree of cure versus layer number for S-glass/3501-6 composite

Institute, Bureau of Engineering Research and Center for Energy Studies.

References

Alder, B. J., and Wainwright, T. E., 1962, "Phase Transition in Elastic Disks," *Physical Review,* Vol. 127, No. 2, pp. 359–361.

Balanis, C. A., 1989, *Advanced Engineering Electromagnetics,* Wiley, New York.

Chae, D. G., Ree, F. H., and Ree, T., 1969, "Radial Distribution Functions and Equation of State of the Hard-Disk Fluid," *Journal of Chemical Physics,* Vol. 50, No. 4, pp. 1581–1589.

Chern, B.-C., Moon, T. J., and Howell, J. R., 1994, "Dependent Scattering Effects on Wave Propagation Through Filament-Wound Composites," *Radiative Heat Transfer: Current Research* ASME HTD-Vol. 276, pp. 15–20.

Chern, B. C., Moon, T. J., and Howell, J. R., 1995, "Thermal Analysis of In-Situ Curing for Thermoset, Hoop-Wound Structures Using Infrared Heating: Part I—Numerical/Experimental Investigation," ASME JOURNAL OF HEAT TRANSFER, Vol. 117, this issue, pp. 674–680.

Foldy, L. L., 1945, "The Multiple Scattering of Waves. General Theory of Isotropic Scattering by Randomly Distributed Scatterers," *Physical Review,* Vol. 67, No. 3, pp. 107–119.

Houston, R. L., and Korpela, S. A., 1981, "Heat Transfer Through Fiberglass Insulation," *Proceedings of 7th International Heat Transfer Conference,* Vol. 2, pp. 499–504.

Kerker, M., 1969, *The Scattering of Light,* Academic Press, New York.

Kamiuto, K., 1990, "Study of the Scattering Regime Diagrams," *Journal of Thermophysics and Heat Transfer,* Vol. 4, No. 4, pp. 432–435.

Kumar, S., and White, S., 1990, "Scattering Properties of Woven Fibrous Insulations: Effects of Interference for Normal Incidence," AIAA Paper No. 90-1674.

Lado, F., 1968, "Equation of State of the Hard-Disk Fluid From Approximation Integral Equations," *Journal of Chemical Physics,* Vol. 49, No. 7, pp. 3092–3096.

Lax, M., 1952, "Multiple Scattering of Waves. II. The Effective Field in Dense Systems," *Physical Review,* Vol. 85, No. 4, pp. 621–629.

Lee, S. C., 1989, "Effect of Fiber Orientation on Thermal Radiation in Fibrous Media," *International Journal of Heat and Mass Transfer,* Vol. 32, No. 2, pp. 311–319.

Lee, S. C., 1990, "Dependent Scattering of an Oblique Incident Plane Wave by a Collection of Parallel Cylinders," *Journal of Applied Physics,* Vol. 68, No. 10, pp. 4952–4957.

Lee, S. C., 1992a, "Effective Propagation Constant of Fibrous Media Containing Parallel Fibers in the Dependent Scattering Regime," ASME JOURNAL OF HEAT TRANSFER, Vol. 114, pp. 473–478.

Lee, S. C., 1992b, "Extinction and Refraction of Radiation in High-Density Fibrous Composites Containing Nonhomogeneous Fibers," AIAA Paper No. 92-2892.

Ma, Y., Varadan, V. K., and Varadan, V. V., 1990, "Enhanced Absorption Due to Dependent Scattering," ASME JOURNAL OF HEAT TRANSFER, Vol. 112, pp. 402–407.

Varadan, V. K., Bring, V. N., and Varadan, V. V., 1979, "Coherent Electromagnetic Wave Propagation Through Random Distributed Dielectric Scatters," *Physical Review D,* Vol. 19, No. 8, pp. 2480–2489.

Varadan, V. V., Varadan, V. K., and Ma, Y., 1987, "Effects of Nonspherical Statics on EM Wave Propagation in Discrete Random Media," *Radio Science,* Vol. 22, No. 4, pp. 491–498.

White, S., and Kumar, S., 1989, "Interference Effects on Scattering by Parallel Fibers at Normal Incidence," AIAA Paper No. 89-1717.

Wood, W. W., 1968, "Monte Carlo Calculations for Hard Disks in the Isothermal-Isobaric Ensemble," *Journal of Chemical Physics,* Vol. 48, No. 1, pp. 415–434.

Wood, W. W., 1970, "NPT-Ensemble Monte Carlo Calculations for the Hard-Disk Fluid," *Journal of Chemical Physics,* Vol. 52, No. 2, pp. 729–741.

Zhu, P. Y., Fung, A. K., and Wong, K. W., 1987, "Effective Propagation Constants in Dense Random Media Under Effective Medium Approximation," *Radio Science,* Vol. 22, No. 2, pp. 234–250.

S. M. You
Department of Mechanical Engineering,
University of Texas—Arlington,
Arlington, TX 76019

T. W. Simon

A. Bar-Cohen

Department of Mechanical Engineering,
University of Minnesota,
Minneapolis, MN 55455

Y. S. Hong
Department of Mechanical Engineering,
University of Texas—Arlington,
Arlington, TX 76019

Effects of Dissolved Gas Content on Pool Boiling of a Highly Wetting Fluid

Experimental results on pool boiling heat transfer from a horizontal cylinder in an electronic cooling fluid (FC-72) are presented. The effects on the boiling curve of having air dissolved in the fluid are documented, showing that fluid in the vicinity of the heating element is apparently liberated of dissolved gas during boiling. Dissolved gas was found to influence boiling incipience only with high gas concentrations (>0.005 moles/mole). For low-to-moderate concentrations, a larger superheat is required to initiate boiling and a hysteresis is observed between boiling curves taken with increasing and decreasing heat flux steps. Boiling, a very effective mode of heat transfer, is attractive for electronics cooling. The present experiment provides further documentation of the role of dissolved gas on the incipience process and shows similarities with subcooled boiling of a gas-free fluid.

Introduction

The present study was conducted to broaden the knowledge of nucleate boiling heat transfer and critical heat flux (CHF) behavior peculiar to highly wetting dielectric fluids by experimentally investigating the effects of dissolved gas. The fluid used for these tests is FC-72, a fully fluorinated fluid manufactured by the 3M Company. A silicon film (about 0.05 μm thick), sputtered over a platinum-coated quartz cylinder, served as the boiling surface for investigating the incipience and nucleate boiling processes. For the critical heat flux (CHF) investigations, nichrome wires of the same diameter are used.

Although the inherent advantage of liquid cooling has been exploited for nearly 40 years in the general field of thermal control of electronic devices, liquid cooling of microelectronic components is only recently gaining acceptance. Boiling of dielectric fluids is being considered for future electronic cooling applications since three-dimensional packaging of high-gate-count, fast-switching chips is planned for use in high-end computers. Such a packaging scheme may result in a significant increase in power density, yielding heat fluxes approaching 100 W/cm^2 and volumetric heat release rates of 10 W/cm^3 (Bar-Cohen, 1987).

Many of the experimental reports published prior to 1986 on the inception of boiling of dielectric fluids, are reviewed by Bar-Cohen and Simon (1988). Noted are significant variations in the incipience superheat from one report to the next. The authors discussed possible mechanisms for delayed nucleation and presented approximate methods for calculating superheat excursions at incipience. More recently, the nonrepeatable and unsteady behavior of boiling incipience on smooth surfaces was documented for the highly wetting dielectric liquid, R-113 (You et al., 1990).

The theory for computing the wall superheat required to initiate nucleate boiling was described by Griffith and Wallis in 1959. Lorenz et al. (1974) reported that residual bubbles trapped in surface cavities are much smaller for highly wetting liquids than for water and that the bubble configuration at incipience represents the state of minimum radius within the bubble life. Under such conditions, the incipience superheat (the superheat required for bubble growth to begin) is related to the trapped volume. More recently, Tong et al. (1990) reported that the boiling incipience superheat can be dependent upon the bubble dynamics. The movement of the triple (liquid/vapor/solid phase) contact line across a solid surface was known to result in a velocity-dependent contact angle (called dynamic contact angle). This was proposed as a reason for the variability in trapped volume and, hence, measured incipience superheat.

The effect of dissolved air on forced-convection, subcooled nucleate boiling of water was reported by McAdams et al. in 1949. A strong enhancement of the boiling curve at the lower heat fluxes (partially developed nucleate boiling) was observed when air was introduced. However, the dissolved gas effect was weak in single phase and in fully developed nucleate boiling. Similar observations for pool boiling were made by Pike et al. (1955) from experiments with boiling on a nickel wire in water and by Behar et al. (1966) for boiling on a stainless steel tube in metaterphenyl. Torikai et al. (1970) measured incipience wall superheat using platinum wires immersed in water under reduced pressure conditions (0.05–1.0 bar) showing a decrease with increased dissolved air content. In 1972, Murphy and Bergles reported decreased wall superheat at incipience and enhanced heat transfer coefficients during low-heat-flux flow boiling when a stainless steel tube was heated in R-113 saturated with air.

The following presents results of a study on the effects of dissolved noncondensable gas on pool boiling incipience, nucleate boiling, and CHF with highly wetting dielectric fluids.

Experimental Apparatus and Test Procedure

Heating Element and Test Fluid. The present investigation used electrically heated, 0.51-mm-dia, cylindrical heaters within the dielectric cooling fluid, FC-72. This fluid is highly wetting with low surface tension and low viscosity. A relatively large amount of noncondensable gases can be dissolved within FC-72 (48 percent air by volume at 1 atm pressure and 25°C). A thin-film heater, 25.4 mm long and 0.51 mm in diameter, was fabricated by sputtering a film (~0.1 μm) of platinum on a quartz cylinder, then sputtering a film (~0.05 μm) of silicon over the platinum. Data show that the boiling incipience location on the cylinder was not fixed for repeated runs, an indication of uniform heating. The heater displays a linear relationship between temperature and resistance, allowing it to be used as both heater and surface-average wall temperature sensor. The nominal measured resistance was 23.8 Ω and dR/dT was 0.0490

Contributed by the Heat Transfer Division for publication in the JOURNAL OF HEAT TRANSFER. Manuscript received by the Heat Transfer Division March 1994; revision received November 1994. Keywords: Boiling, Electronic Equipment, Phase-Change Phenomena. Associate Technical Editor: R. Viskanta.

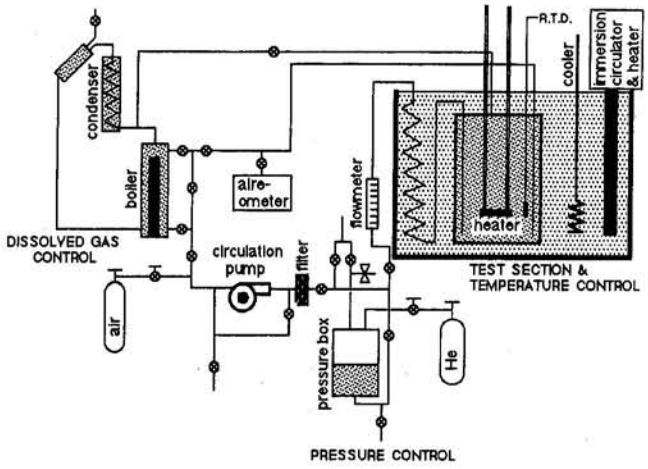

Fig. 1 Pool boiling test facility

Ω/°C, within 3 percent. The thin-film heater was replaced with nichrome wire heaters ($Ni_{80}Cr_{20}$) for the CHF study. The nichrome wire heater was destroyed after each CHF test. The wire heater, 0.51 mm in diameter and 41 mm long, was mounted by soldering it between two prongs constructed of 10-gage copper wire.

Test Loop. The test loop is composed of the test vessel and temperature, gas content, and pressure control subsystems shown in Fig. 1. A magnetically driven pump circulates working fluid through the test loop with flow rates to 550 ml/min. This flow rate was small enough to not disturb even single-phase natural convection (You, 1990). The gas control section contains a degassing system (boiler and condenser), an air supply system, and a dissolved gas measurement device (Seaton-Wilson Aire-Ometer). The pressure of the test section is controlled using pressurized helium gas in an upper volume within a pressure reservoir, separated from the test fluid by a buna-N rubber diaphragm. The lower volume, filled with test fluid, is in communication with the test vessel. A 1 kW immersion circulator/heater and a 300 W cooling unit provide a uniform and constant temperature for the 32 liter glass container in which the test vessel is immersed. The test vessel is a 2 liter glass container in which the test fluid and heating element reside. Once the desired test condition is achieved, the test vessel is isolated and the same amount of noncondensable gas component exists within the vessel. The power to be dissipated from the small heating element is low enough so that only the fluid near the heater surface is degassed. The bulk fluid is confirmed to remain gas-saturated during the gas-saturated cases. The test fluid temperature, measured by copper-constantan thermocouples and by a platinum RTD sensor, remain constant and uniform to within 0.2°C.

Instrumentation and Test Procedures. The facility is monitored and controlled by a laboratory computer. Direct current is supplied by a power supply. A precision resistor is used to determine the current. Separate voltage taps across the heating element and across the precision resistor are used to compute heater resistance and heating element power. The heating element temperature is computed from its resistance via calibration.

Each run is started with incremental increases of heat flux (zero to the maximum value of the test). Heat flux values are next incrementally decreased to zero. Following a 5 minute unpowered waiting period, a new run is begun. Throughout the 10 consecutive runs of each case, the test is completely computer controlled to step through precisely the same conditions. After each power setting change sufficient waiting is allowed so that steady state is reached, and temperature and heat flux are recorded as averages of 20 samples taken over 50 seconds. A standard deviation of less than 1°C in averaged wall temperature (averaged over 5 samples) is taken to indicate that steady state has been reached. Steady state is achieved normally within 1 minute.

The CHF point is determined with tests using the nichrome wire heater. For these, a 0.5 W/cm^2 increment is used. For every measurement, the heater resistance is measured after assuring steady-state operation. The resistance is compared to its previous steady-state value to detect a large resistance jump (>20°C above that of the last reading) corresponding to CHF.

Qualification of the Test Facility. An uncertainty analysis was performed for heat flux and wall superheat values under various modes of operation. The techniques of Kline and McClintock (1953) were used to compute propagation of uncertainties. The computed uncertainty of heat flux was 3 percent and that of the wall superheat was 0.7°C for all but a few points near the boiling incipience (where 1°C was assigned). The increase near incipience was due to the larger unsteadiness at this rather unstable location (You et al., 1990).

When the element, immersed in a pool of quiescent liquid, is electrically heated, the buoyancy-induced motion generates single-phase natural convection flow. The natural convection data agreed to within 5 percent of the value computed from the correlation suggested by Kuehn and Goldstein (1976).

Gas-Saturation and Gassy Subcooling

Figure 2 shows a two-component, two-phase thermodynamic system, which is gas-saturated at the bulk temperature, T_b, under

Nomenclature

C_g = dissolved gas content, moles gas/mole liquid
C_p = specific heat
H = Henry's constant, moles/mole kPa
h = enthalpy
Ja = volumetric Jakob number = $\rho_f C_p \Delta T_{sub}/\rho_g h_{fg}$
P = pressure
P_b = total pressure inside bubble = $P_{vb} + P_{gb}$
P_g = gas pressure in gas-vapor phase above flat interface
P_{gb} = gas pressure inside bubble
P_l = pressure of the liquid
P_t = total pressure in gas-vapor phase above flat interface = $P_v + P_g$
P_v = vapor pressure in gas-vapor phase above flat interface
P_{vb} = vapor pressure inside bubble
q = heat flux
q_{max} = critical heat flux
r_b = embryonic bubble radius inside cavity
T = temperature
T_b = bulk temperature
ΔT_{sub} = subcooling, gassy subcooling
α = ratio of gas partial pressure = P_{gb}/P_g
ρ = density
σ_w = surface tension at the wall temperature

Subscripts

b = inside bubble
fg = liquid/vapor transition
g,sat = gas-saturation
l,f = liquid
sat = saturation
sub = subcooled
v, g = vapor
w = wall

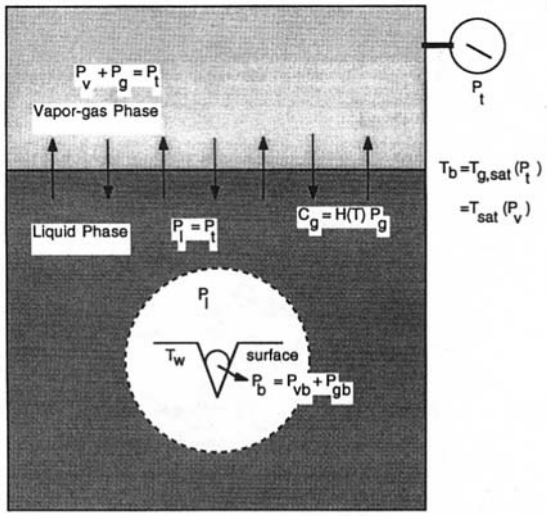

Fig. 2 Local and bulk thermodynamic states for the gas-saturated case

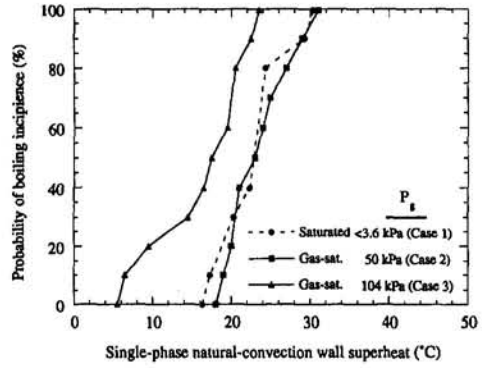

Fig. 3 Probability of boiling incipience; based upon 10 runs for each case

the total pressure, P_t. The following is noted about this system. The total bulk pressure (P_t) is the sum of the vapor pressure (P_v) and the gas pressure (P_g). The bulk temperature (T_b) is equal to the saturation temperature corresponding to P_v. Thermodynamic saturation (saturation of the pure fluid) is a special case of gas-saturation where $P_g = 0$, thus $P_t = P_v$, $T_b = T_{sat}(P_t)$, and $C_g = 0$. In a gas-saturated case, there is a vapor-gas mixture phase with $T_b = T_{sat}(P_v) < T_{sat}(P_t)$. Under these conditions, $T_{sat}(P_t) - T_b$ is called "gassy subcooling." When the bulk fluid is free of dissolved gas and is subcooled, no vapor can exist. And, if T_b is less than $T_{sat}(P_t = P_l)$, the difference, $T_{sat} - T_b$, is the subcooling.

The solubility of gas in highly wetting dielectric fluids is of special concern. These dielectric fluids can contain up to 25 times more dissolved air, by volume, than can water—48 percent air by volume can be dissolved in FC-72 at standard temperature and pressure (Product Manual, 1987). A relationship between the dissolved gas in the liquid phase and the gas partial pressure in the gas-vapor phase is:

$$C_g = \mathrm{H}(T) P_g \tag{1}$$

where $\mathrm{H}(T)$, Henry's constant, is a function of temperature, only. A measured $\mathrm{H}(T)$ value for air in FC-72 is 5.4×10^{-5} moles/mole kPa over $T = 31.5°\mathrm{C}$–$59.5°\mathrm{C}$ (You, 1990). The insensitivity to temperature was also found for R-113 (Murphy and Bergles, 1972). Cases with dissolved gas are established by pressurizing the thermodynamically saturated state (pure fluid) by adding noncondensable gas. The dissolved gas content was calculated using measured P_t and T_b along with Henry's constant. These computed values agreed within 0.2×10^{-3} moles/mole with measured values when the fluid was gas-saturated. For the pure fluid saturation cases, the measured dissolved gas content was less than 0.2×10^{-3} moles/mole. More details about these cases can be found in You (1990).

Effects of Dissolved Gas on Nucleate Boiling

Three gas-saturated cases of different gas contents were run using the thin-film heater. Thermodynamic parameters that describe each test are given in Table 1. The total pressure varied from 148 to 167 kPa. You (1990) reported that the pressure effects on boiling incipience and nucleate boiling regime are negligible for even pressure differences that are four to five times larger.

Boiling Incipience. Initiation of boiling with dielectric fluids requires a heater surface temperature that is well above the saturation temperature. Such incipience superheat can vary widely from run to run. In a previous paper, You et al. (1990), a means of presenting data that display this behavior was proposed. In this method, a series of runs with increasing heat flux was made under ostensibly identical conditions. The "probability of boiling incipience," the fraction of the cases that went into nucleate boiling, was then plotted versus the wall superheat experienced in single-phase operation. For instance, if when the superheat is raised to 24°C, 2 of 10 cases have not boiled, a probability of 80 percent is assigned. This representation is used herein.

The mole fraction of the dissolved air for the three gas-saturated cases ranged from 0.2×10^{-3} to 5.6×10^{-3} moles/mole (Table 1). Case 1 is considered to be for a pure fluid at saturation conditions. The probability curves for boiling incipience for the three cases are compared in Fig. 3. For the case with moderate dissolved gas content (Case 2, $P_g = 50$ kPa), the probability curve matches that of the saturated case. Unlike these two, the probability curve for the case of the highest dissolved gas content (Case 3, $P_g = 104$ kPa) shows much lower incipience superheat values. A larger effect is observed at the lower superheat and lower probability values. The figure shows that boiling incipience occurred with a wall superheat of as low as ~5°C for this gas-saturated case.

Further Discussion on Boiling Incipience. Consider a surface cavity, which has an existing nucleus containing vapor and noncondensable gas. A magnified cavity in which this nucleus resides is drawn in Fig. 2. The effective embryonic bubble size, r_b, under gas-saturated pool boiling can be calculated using a force balance:

$$[P_b - P_l] = [(P_{vb} + P_{gb}) - P_l]$$
$$\cong [(P_{sat}(T_w) + P_{gb}) - P_l] = 2\sigma_w / r_b \tag{2}$$

The vapor partial pressure inside the bubble, P_{vb}, is calculated from $P_{vb} = P_{sat}(T_w)$. For pure saturated liquids ($P_{gb} = 0$), $[P_b - P_l] = P_{sat}(T_w) - P_l = 2\sigma_w / r_b$. Now, P_{gb} is the only unknown

Table 1 Description of the thin-film heater test cases (10 runs each)

CASE	Measured C_g, moles/mole	P_t, kPa	P_g, kPa	$T_{sat}(P_t)$, °C	T_b, °C	r_b, μm
Case 1 (Saturated)	<0.0002	167	<3.6	71.1	70.7	0.046–0.120
Case 2 (Gas-saturated)	~0.0025	165	50	70.8	59.2	0.052–0.120
Case 3 (Gas-saturated)	~0.0056	148	104	67.2	31.5	0.046–0.110

variable that remains if Eq. (2) is to be used to estimate the embryonic bubble size; $P_l (= P_t)$ and T_w are measured values. The evaluation of P_{gb} is complicated if the gas is not uniformly distributed. And, in fact, it would not be uniformly distributed, for the gas would concentrate in the bubbles during earlier boiling events and depart with those bubbles, leaving the fluid near the wall low in gas content. Evaluating P_{gb} therefore involves computing the rate at which the gas returns to the nucleation site in the surface by diffusion. The value of P_{gb} must lie between 0 and the value of P_g, the gas pressure in the gas/vapor mixture above the flat liquid–gas interface shown in Fig. 2.

Experimental results in Fig. 3 indicate that dissolved gas plays an important role at incipience only when a high level is maintained, such as in Case 3, $P_g = 104$ kPa. There, $T_w - T_{sat}$ at incipience is much lower than for Cases 1 and 2. This is apparently due to the higher gas partial pressure (P_{gb}) inside of the embryonic bubble. For a gas-saturated case at $P_g = 50$ kPa, which has a moderate level of dissolved gas, the data would indicate $P_{gb} \approx 0$. Otherwise, a noticeable decrease in superheat would have been observed (as with Case 3). Apparently, liquid adjacent to the site is low in dissolved gas for Case 2, but dissolved gas is available at the nucleation site for Case 3.

To generalize, the following equation set can be applied:

$$r_b = 2\sigma_w/[(P_{vb} + P_{gb}) - P_l]; \quad \sigma_w = \sigma(T_w),$$

$$P_{vb} = P_{sat}(T_w), \quad \text{and} \quad P_{gb} = \alpha P_g, \quad 0 \le \alpha \le 1 \qquad (3)$$

where α allows placing P_{gb} between 0 and P_g. Applying Eq. (3) with $\alpha \approx 0$ for Cases 1 and 2 and $\alpha \approx 1$ for Case 3, the r_b values for various cases in this study are calculated and shown in Table 1. The computed bubble radii for the three cases (10 runs for each case) are comparable to one another (about 0.05–0.1 μm), despite the various bulk-fluid thermodynamic states. In a previous study, You et al. (1990), Scanning Electron Microscope pictures of sputtered boiling surfaces showed feature sizes of ~0.05 μm, consistent with the computed radii. In computing r_b, surface tension value was presumed to be insensitive to dissolved gas content; Tong et al. (1990) estimated a 2 percent reduction in surface tension due to 5×10^{-3} moles/mole of dissolved air.

Experimental Results on Nucleate Boiling With Decreasing Heat Flux. The dissolved gas effect on the nucleate boiling curve under decreasing heat flux conditions is illustrated for the three cases (Table 1) in Fig. 4. As dissolved gas content is increased, nucleate boiling is enhanced. For the low-gas-content case (Case 2), superheat values for fully developed nucleate boiling at higher heat flux levels were nearly the same as those of degassed, saturated fluid base case (Fig. 4). This again indicates that the gas partial pressure within the bubbles at the wall is small for this case. Apparently, the gas is not able to effectively penetrate to the wall. Gas is depleted as it is

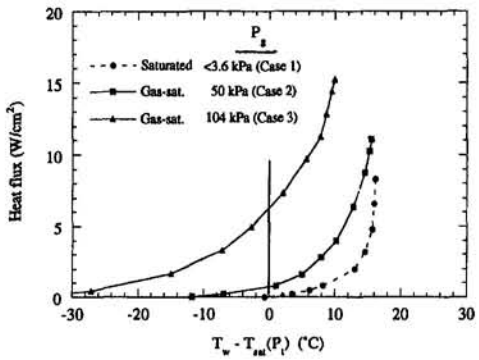

Fig. 4 Boiling curves with decreasing heat flux steps

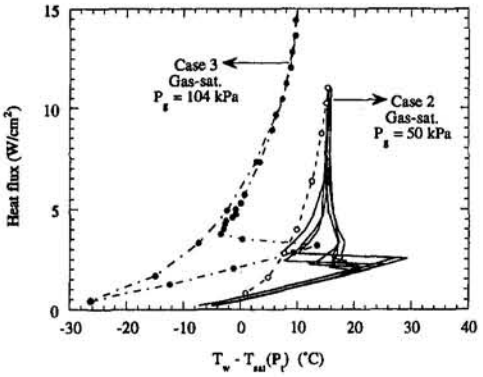

Fig. 5 Boiling curves with increasing heat flux steps

carried away from the wall by the boiling bubbles and the saturation temperature approaches $T_{sat}(P_t)$. As the dissolved gas content is increased further to Case 3, wall superheat values, compared at the same heat fluxes, decrease noticeably. The enhanced heat transfer is considered to be due to dissolved gas, which apparently is carried back to the near-wall region with the approaching liquid flow. The wall superheat ($T_w - T_{sat}(P_t)$) therefore decreases since more gas is available. The increased gas partial pressure within the bubble allows many columns of bubbles even at zero wall superheat.

Experimental Results on Nucleate Boiling With Increasing Heat Flux. For Case 1, boiling curves with increasing or decreasing steps in heat flux were identical and are not shown. By contrast, Cases 2 and 3, increasing and decreasing curves differ from one another, as shown in Fig. 5. Case 2 displayed a "hysteresis" between the two in the nucleate boiling regime, 3 W/cm^2 < q < 10 W/cm^2. This may be caused by the lack of noncondensable gas in the fluid near the heater leaving the near-wall fluid subcooled. Such subcooling may additionally suppress the process by which nucleation at one site induces nucleation at neighboring sites. This is a very tenuous situation and run-to-run variations in incipience superheat are wide (Case 2). In contrast, when heat flux is decreasing, many sites are already active and initiation of new sites is not necessary.

Hysteresis begins to disappear as dissolved gas content is increased, see Case 3 in Fig. 5. In this case, fluid adjacent to the heater is more gassy and nucleation is more effective as with the decreasing-heat-flux portion of the boiling curve.

Effects of Dissolved Gas on CHF

As heat flux is increased in nucleate boiling, CHF, a state characterized by vapor blanketing on the heater surface, eventually occurs. This is the maximum heat flux that can be attained while still within the nucleate boiling regime. With a 0.51-mm-dia, 41-mm-long nichrome wire as the heating element, one saturated and three gas-saturated cases were run. The CHF data with thermodynamically saturated, pure fluid agreed (to within 10 percent) with the CHF correlation proposed for small cylinders by Sun and Lienhard (1970).

In Fig. 6, the data indicate increasing CHF values with increasing dissolved gas content at a constant total pressure. Correlations of Ivy and Morris (1966) and Zuber (1959) are also shown. The Ivey and Morris (1966) correlation captures the effect of subcooling:

$$\frac{q_{max,sub}}{q_{max,sat}} = 1 + 0.1\left(\frac{\rho_g}{\rho_f}\right)^{1/4} \text{Ja}; \quad \text{Ja} = \rho_f C_p \Delta T_{sub}/\rho_g h_{fg}. \qquad (4)$$

In contrast, Zuber's relation captures only the property variation effect due to pressure change:

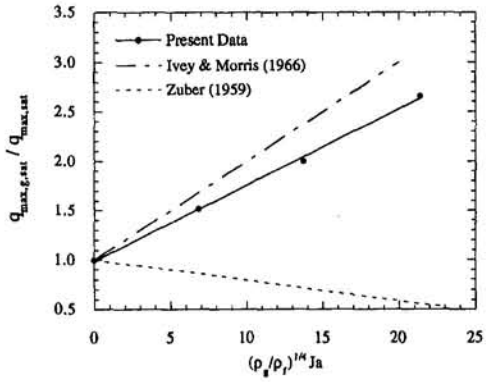

Fig. 6 Effects of gassy subcooling on CHF

$$q_{\max,Z} = \frac{\pi}{24} h_{fg} \rho_g^{0.5} (g\sigma\rho_{fg})^{0.25} \quad (5)$$

If the test fluid is fully gas-saturated, CHF would follow Zuber's correlation, whereas if the fluid were subcooled and without noncondensable gas, CHF should approach the Ivy and Morris correlation. Figure 6 shows that the gas-saturated tests more closely follow Ivy and Morris. This supports the assumption that when the dissolved gas near the test heater is liberated from the fluid, the net effect is to raise the subcooling. The data would also indicate that the near-wall fluid is not entirely degassed, for Ivey and Morris indicate slightly higher CHF than given by the gas-saturated cases. Simply reducing the coefficient from 0.1 in Eq. (4) to 0.077 and expressing the subcooling as $T_{sat}(P_t) - T_b$, allows the CHF behavior for the gas-saturated FC-72 to be captured well:

$$\frac{q_{\max,g,sat}}{q_{\max,sat}} = 1 + 0.077 \left(\frac{\rho_g}{\rho_f}\right)^{1/4} \text{Ja} \quad (6)$$

Videos (Sony Model CCD-V801) taken with 1/10,000 of a second shutter speed (Fig. 7) indicate the nature of the onset of film boiling on the wire. For the gas-saturated cases (Figs. 7*b*, *c* and *d*) the vapor blanket thickness and the sizes of the departing vapor bubbles appear to be smaller than those observed for the saturated, pure-fluid case (Fig. 7*a*). This is attributed to condensation within the locally subcooled fluid near the heater surface, where the gas was depleted during the prior nucleate boiling processes. The pictures show bubble shrinkage within at least a few millimeters above the wire. The Taylor wavelength of departing bubbles for the saturated case is ~4.2 mm, which does not seem to change much for the gas-saturated cases.

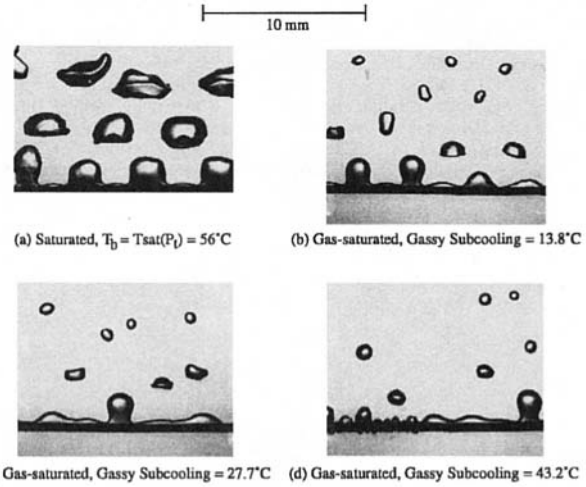

Fig. 7 Photographs of CHF with different values of gassy subcooling

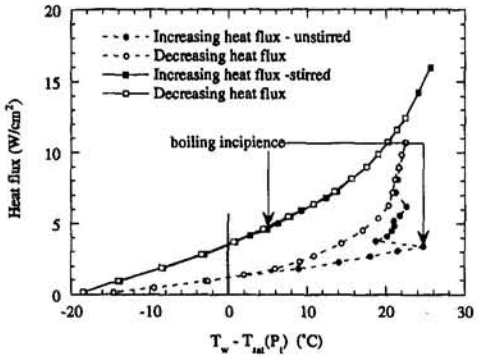

Fig. 8(*a*) Effects of stirring on boiling incipience of gassy FC-72

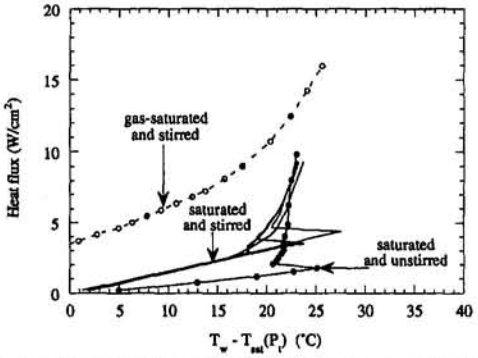

Fig. 8(*b*) Effects of stirring on boiling incipience of saturated FC-72 (increasing heat fluxes); saturated and stirred case shows all 5 runs

Reduced Incipience Superheat

The present observations suggest that the dissolved gas content is not uniform within the liquid. There apparently is degassing very near the wall as a result of boiling. It appears that diffusion of gas back into the near-wall layer that had been degassed by boiling in an earlier run is very slow. To test this idea, a magnetic stirring device was applied to enhance mixing. This should raise the gas partial pressure within the bubbles in the surface cavities. For comparison, a saturated pool and a gas-saturated pool of FC-72 at 1 atm were tested under both quiescent and stirred conditions.

Base Cases. Five ostensibly identical heat-up runs and cool-down runs for each saturated and gas-saturated case were made. Total pressure was maintained constant at ~101 kPa. These cases, performed without stirring, serve as base cases. The gas-saturated case was maintained at a bulk temperature of ~35°C, corresponding to a dissolved gas content of 0.0028 moles/mole. The two cases at $P_t \approx 101$ kPa display negligible differences in the effects of dissolved gas on the entire boiling curve, discussed with Case 1 and 2 ($P_t \approx 165$ kPa) in Table 1.

The Effect of Stirring. A magnetic stirring bar of 2.5 cm length was rotated at ~200 rpm ~7 cm away from the heated surface. The bulk temperature was 35°C and the corresponding dissolved gas content was ~0.0028 moles/mole.

Boiling curves with both increasing and decreasing heat flux values (Fig. 8*a*) show the effect of stirring the gassy fluid. The incipience excursion disappeared for the stirred gassy case. The boiling curves of five repeated runs were identical to one another. The first appearance of boiling was consistently only a few degrees above the saturation temperature, $T_{sat}(P_t)$, compared to 23.9 ~ 26.0°C for the unstirred base case. The nucleate

boiling regime also showed a significant heat transfer enhancement due to stirring; approximately twice the heat flux was achieved at the same wall superheat. Clearly, immersion cooling of electronic devices with boiling heat transfer can best be achieved with mild circulation of gassy fluids. For reference, an effective velocity for the stirring motion of this case is estimated as ~0.5 m/s. This was found by matching the single-phase heat transfer data with a forced-convection correlation.

In contrast, a "pure fluid" saturated case of 5 runs with 200 rpm stirring showed measured incipient superheats ranging over 17.2–27.6°C (Fig. 8*b*). These values are comparable to those of the saturated case without stirring (22.1–25.1°C). Although with pure fluids a decrease in incipience wall superheat with increasing velocity was reported by several in the literature, including Samant and Simon (1989) and Lee and Simon (1989), higher velocities of 4.11 to 8.62 m/s were required before the effect was significant. Thus, the very slight effect of stirring for the pure-fluid saturated case in the present study is consistent with these earlier findings.

The experimental results on nucleation mentioned above can be explained by the following: Stirring of the fluid throughout the test period provides a uniform distribution of dissolved gas. Under stirring, a degassed fluid layer near the wall cannot be sustained; hence, the bubbles in the wall cavities possess a higher gas partial pressure, P_{gb}. This pressure (P_{gb}) may approach the gas partial pressure of the bulk fluid (P_g). As a result, the inception of boiling is at a lower superheat value (only a few degrees above saturation temperature at P_t) in the stirred case and the incipience excursion and hysteresis are significantly reduced.

Conclusions

The effect of dissolved gas content on pool boiling heat transfer with a highly wetting fluid (FC-72) is reported by discussing data taken with 0.51-mm-dia cylindrical heaters. The main observations and conclusions of this study are:

(*i*) The measured dissolved gas effect on boiling incipience is very small for a dissolved gas content values of ~0.0025 moles/mole or less, but dissolved gas results in a distinguishable reduction in wall superheat for a case with a content of 0.0056 moles/mole.

(*ii*) A dissolved gas effect on the nucleate boiling curves emerges as the dissolved gas content becomes high, 0.0056 moles/mole. A hysteresis is observed for a moderate-gas-saturated case of 0.0025 moles/mole. The hysteresis decreases as the dissolved gas content increases.

(*iii*) The CHF data increase with increasing levels of dissolved gas when the total pressure is held constant from case to case. The data apparently show that the gas-saturated behavior is similar in CHF behavior to that of a subcooled case. Photographs are presented to illustrate the subcooled fluid region that apparently is established near the heater surface.

(*iv*) The dissolved gas content of the boiling fluid is apparently not uniform. It appears to be degassed very near the wall by a previous boiling process. The replenishment of that gas is apparently very slow. The gas is presumed to be depleted by being convected away from the heated wall within departing bubbles.

(*v*) With stirring, incipient superheat values were only a few degrees above the saturation temperature and the boiling hysteresis was essentially eliminated. It is recommended that agitation of the fluid be provided in system design where highly wetting fluid is employed for boiling heat transfer.

Acknowledgments

The work performed at the University of Minnesota was supported by a grant from the Commercial Chemicals Division of the 3M Company. Additional support was provided for the work at University of Texas—Arlington by the Texas Higher Education Coordinating Board, Advanced Research/Technology Program Grant No. 003656-101.

References

Bar-Cohen, A., 1987, "Thermal Management of Air- and Liquid-Cooled Multichip Modules," *IEEE CHMT Transactions,* Vol. 10, No. 2, pp. 159–175.

Bar-Cohen, A., and Simon, T. W., 1988, "Wall Superheat Excursions in the Boiling Incipience of Dielectric Fluids," *Heat Transfer Engrg,* Vol. 9, No. 3, pp. 19–31.

Behar, M., Courtaud, M., Ricque, R., and Semeria, R., 1966, "Fundamental Aspects of Subcooled Boiling With and Without Dissolved Gasses," *Proc. 3rd Int. Heat Trans. Conf.,* Vol. IV, pp. 1–11.

Griffith, P., and Wallis, J. D., 1959, "The Role of Surface Conditions in Nucleate Boiling," *Chem. Engrg. Prog. Symp. Series,* Vol. 56, No. 30, pp. 49–63.

Ivey, H. J., and Morris, D. J., 1966, "Critical Heat Flux of Saturation and Subcooled Pool Boiling in Water at Atmospheric Pressure," *Proc. 3rd Int. Heat Trans. Conf.,* Vol. III, pp. 129–142.

Kline, S. J., and McClintock, F. A., 1953, "Describing Uncertainties in Single-Sample Experiments," *Mechanical Engineering,* Vol. 75, Jan., pp. 3–8.

Kuehn, T. H., and Goldstein, R. J., 1976, "Correlating Equations for Natural Convection Heat Transfer Between Horizontal Circular Cylinder," *Int. J. Heat Mass Transfer,* Vol. 19, pp. 1127–1134.

Lee, T. Y., and Simon, T. W., 1989, "High-Heat-Flux Forced Convection Boiling From Small Region," *Heat Transfer in Electronics,* ASME HTD-Vol. 111, pp. 7–16.

Lorenz, J. J., Mikic, B. B., and Rohsenow, W. M., 1974, "The Effect of Surface Condition on Boiling Characteristics," *Proc. 5th Int. Heat Trans. Conf.,* Vol. 4, B2.1, pp. 35–39.

McAdams, W. H., Kennel, W. E., Minden, C. S., Carl, R., Picornell, P. M., and Dew, J. E., 1949, "Heat Transfer at High Rates to Water With Surface Boiling," *Industrial and Engineering Chemistry,* Vol. 41, No. 9.

Murphy, R. W., and Bergles, A. E., 1972, "Subcooled Flow Boiling of Fluorocarbons—Hysteresis and Dissolved Gas Effects on Heat Transfer," *Proceedings of Heat Trans. and Fluid Mech. Inst.,* Stanford Univ. Press, pp. 400–416.

Pike, F. P., Miller, P. D., Jr., and Beatty, K. O., Jr., 1955, "Effect of Gas Evolution on Surface Boiling at Wire Coils," *Chem. Engrg. Prog. Symp. Series,* Vol. 51, No. 17, pp. 13–19.

Product Manual, 1987, Fluorinert Electronic Liquids, Commercial Chemical Products Div., 3M Co., St. Paul, MN.

Samant, K. R., and Simon, T. W., 1989, "Heat Transfer From a Small High-Heat-Flux Patch to a Subcooled Turbulent Flow," ASME JOURNAL OF HEAT TRANSFER, Vol. 111, pp. 1053–1059.

Sun, K. H., and Lienhard, J. H., 1970, "The Peak Boiling Heat Flux on Horizontal Cylinders," *Int. J. Heat Mass Transfer,* Vol. 13, pp. 1425–1439.

Tong, W., Bar-Cohen, A., Simon, T. W., and You, S. M., 1990, "Contact Angle Effects on Boiling Incipience of Highly-Wetting Liquids," *Int. J. Heat Mass Transfer,* Vol. 33, No. 1, pp. 91–103.

Torikai, K., Shimamune, H., and Fujishiro, T., 1970, "The Effects of Dissolved Gas Content Upon Incipient Boiling Superheats," *Proc. 4th Int. Heat Trans. Conf.,* Vol. V, B2.11.

You, S. M., 1990, "Boiling Heat Transfer With Highly-Wetting Dielectric Fluids," Ph.D. Dissertation, University of Minnesota, MN.

You, S. M., Simon, T. W., Bar-Cohen, A., and Tong, W., 1990, "Experimental Investigation of Nucleate Boiling Incipience With a Highly Wetting Dielectric Fluid (R-113)," *Int. J. Heat Mass Transfer,* Vol. 33, No. 1, pp. 105–117.

Zuber, N., 1959, "Hydrodynamic Aspects of Boiling Heat Transfer," Ph.D. Dissertation, UCLA, Los Angeles, CA.

Heat Transfer During Liquid Contact on Superheated Surfaces

J. C. Chen

K. K. Hsu[1]

Institute of Thermo-Fluid Engineering & Science, Lehigh University, Bethlehem, PA 18015

Several boiling regimes are characterized by intermittent contacts of vapor and liquid at the superheated wall surface. A microthermocouple probe was developed capable of detecting transient surface temperatures with a response time better than 1 ms. The transient temperature data were utilized to determine the time-varying heat flux under liquid contacts. The instantaneous surface heat flux was found to vary by orders of magnitude during the milliseconds of liquid residence at the hot surface. The average heat flux during liquid contact was found to range from 10^5 to 10^7 W/m^2 for water at atmospheric pressure, as wall superheat was varied from 50 to 450°C.

Introduction

Transient liquid contacts on superheated surfaces occur in a number of important industrial applications. Examples include spray cooling of hot surfaces, reflood heat transfer in post-dryout situations, and transition boiling under either pool or convective boiling conditions. Transition boiling is of particular concern since it is recognized as the least understood area on the topography of boiling regimes (Auracher, 1990). This arises from two causes: (*a*) the complexity of the heat transfer mechanism involving intermittent contacts of liquid and vapor at the superheated surface, and (*b*) the difficulty of performing experimental measurements in the regime where heat flux decreases with increasing temperature difference (negative slope). Early researchers questioned whether direct contact between the liquid and the heating surface occurs at all in transition boiling (Westwater and Santangelo, 1955). On the other hand, most of the modeling approaches for transition boiling follow the hypothesis of Berenson (1962) that transition boiling is a combination of nucleate boiling during liquid contact and film boiling during vapor contact on the heating surface:

$$\bar{q} = F\bar{q}_l + (1 - F)\bar{q}_v \tag{1}$$

where

$\bar{q}$ = time-averaged heat flux
$\bar{q}_l$ = average heat flux during liquid contact
$\bar{q}_v$ = average heat flux during vapor contact
F = statistical fraction of surface under liquid contact

More recently, a few researchers have succeeded in obtaining direct experimental indications of liquid contact (Ragheb and Cheng, 1979; Yao and Henry, 1978; Dhuga and Winterton, 1985; Lee et al., 1982, 1985). These measurements have provided some indications of the liquid contact fraction F, as summarized by Auracher (1990). In general the contact fraction F decreases rapidly with increasing wall superheat, reaching the order of 10^{-3} when the wall superheat becomes two to three times greater than the superheat at critical heat flux.

To improve our modeling capability, one needs information on both the contact fraction F and the individual heat flux components associated with liquid and vapor ($\bar{q}_l$ and $\bar{q}_v$). Rajabi and Winterton (1988) reported heat flux levels during contact of methanol under steady transition boiling conditions. Marquardt and Auracher (1990) performed an interesting experiment for transition boiling inside an electrically heated tube. From real time measurements of the heat flux at tube wall OD and a temperature in the wall, they estimated the time-varying heat flux and temperature at the tube ID. The authors were able to determine the time-averaged total heat flux ($\bar{q}$) in the transition boiling regime. The objective of the present study was to go beyond this level of information and attempt to obtain direct experimental measurement of the instantaneous local heat flux $q_l(t)$ associated with transient liquid contact.

Experiment

Since liquid contacts in transition boiling are of short duration and occur randomly over the heat transfer surface, several difficult requirements were imposed on the experimental method. The first concern was with the response time required for the measurement. Earlier studies from this research group (Lee et al., 1985) gave indications that the duration of individual liquid contacts in transition boiling was of the order of 10 to 100 ms. To obtain details of the transient heat transfer process, one therefore desired a measurement method with response time of 1 ms or better. After a survey of various possibilities, it was determined that a microthermal probe with detection junction located at the heat transfer surface could best satisfy this requirement. The final test probe, developed after some trials, was found capable of 99 percent response to a step temperature change in 1 ms, and 95 percent response in 0.1 ms. Details of this probe and its mounting are given below.

Since liquid contacts in transition boiling occur randomly over the heat transfer surface, we faced the problem of depending on chance to cause a liquid contact directly at the measurement point of the probe. To avoid this difficulty, it was decided to simulate individual liquid contacts in transition boiling by causing drops of the boiling liquid to fall on a pre-superheated surface, directly at the sensing junction of the microthermal probe. In this way we were able to control the actual location of the liquid contact and the surface superheat at initial moment of contact. The final test system is comprised of a heat transfer plate 3.8 cm in diameter and 3.2 cm thick. The microprobe was mounted with its sensing junction at the center of the circular surface. The plate (Inconel 600 metal) was superheated to the desired temperature by cartridge heaters before each droplet impingement. Auxiliary components provided means to control the temperature of the liquid drops. Details of the experimental apparatus are provided in the following section.

Apparatus. A schematic view of the apparatus is shown in Fig. 1. The droplet generator was a bronze cup, which contained

[1] Current affiliation: Air Products and Chemicals, Inc., 7201 Hamilton Blvd., Allentown, PA 18195.

Contributed by the Heat Transfer Division for publication in the JOURNAL OF HEAT TRANSFER. Manuscript received by the Heat Transfer Division February 1993; revision received August 1994. Keywords: Boiling, Transient and Unsteady Heat Transfer. Associate Technical Editor: V. K. Dhir.

an angle-pattern regulatory valve stretching through the cup with a hypodermic needle attached at the end. The drop rate was so controlled that each droplet was allowed to complete its growth and fall under the influence of gravity alone. The droplet size was determined by the method of gravimetric calibration. An immersion heater was submerged in the dropper to obtain water of different subcoolings.

An aluminum guard tube surrounded by a band heater was placed between the dropper and the target plate. The air temperature inside the tube was monitored near the top and the bottom of the tube and kept as close as possible to the water temperature in the dropper. The target plate contained two cartridge heaters as heat source. Insulation material was placed around the plate to reduce heat loss from the sides of the plate.

The impinging velocity of droplets was varied by adjusting the height of the dropper above the test surface. The apparatus allowed a maximum velocity of 3 m/s. The impact velocity was calculated by assuming free fall of the droplets and neglecting the viscous drag of the air.

Microthermal Probe. As mentioned above, a thermal probe with response time on the order of milliseconds was required in order that the transient thermal exchange between a droplet and the hot surface could be monitored in detail. The final probe utilized thermocouple wires flattened to a thickness of 25 μm and separated by a 5-μm-thick mica sheet. The wire-mica-wire sandwich was electrically insulated by a mica sheet on each side and "clamped" by the two halves of a plug (also Inconel 600). This thermocouple plug was inserted in the center of the target plate and mounted flush with the plate surface, as shown in Fig. 2. A thin layer of nickel was electroplated over the surface to make a thermal junction between the thermocouple wires.

At the end of this research, the test plate was sectioned and the thickness of the nickel layer was measured to be 8 μm under a SEM. Accordingly, the thermal junction where temperatures were measured was at the coating–matrix interface, 8 μm under the actual plate surface.

To estimate the possible error in measured surface temperature, the test plate with the coating was analyzed as a system of composite solids in which one medium (the coating) is of finite thickness and the other (the plate) of infinite thickness. For a unit temperature change at the top surface of the thin layer, transient temperature response at the interface has been given by Carslaw and Jaeger (1959). For the current system of Inconel plate with Ni coating, the calculation indicated that in 1 ms the temperature at the coating–plate interface reaches 99 percent of the temperature change that occurs at the outer surface of the coating. Considering an even shorter time period of 0.1 ms, the response still reflects 95 percent of the outer surface temperature change. Accordingly, it was concluded that the recorded temperature sufficiently represented the droplet–wall heat transfer process occurring at the outermost surface.

Output signals from the thermocouple were first augmented by a differential amplifier and then monitored by a digital oscilloscope. A built-in disk recorder of the oscilloscope was able to store 32K data points along with information indicating the voltage and time setting used in each of the measurement.

The reproducibility of the test surface and the thermocouple tip was checked from time to time by quenching the surface under identical experimental conditions. It was checked seven times during the course of the experimental work and the traces showed very satisfactory reproducibility.

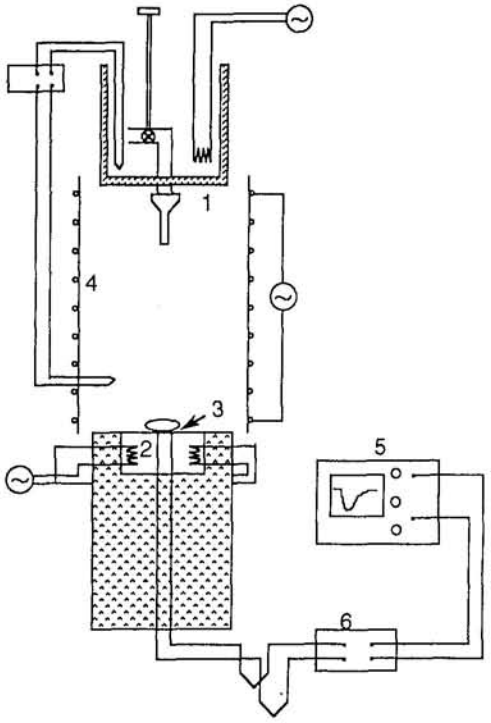

Fig. 1 Experimental apparatus: (1) droplet generator; (2) test plate; (3) microthermal probe; (4) guard tube; (5) digital oscilloscope; (6) differential amplifier

Tests and Results. In each test, the heat transfer surface of the test plate would be cleaned with water and acetone, then preheated to a selected superheat temperature. Distilled water would be preboiled to reduce dissolved gas and then loaded into the droplet generator where it was heated to a selected temperature (saturated or subcooled). Ambient temperature within the guard tube would be adjusted approximately equal to that of the test water, in order to reduce cooling of the droplet during its fall. Upon attaining steady-state temperatures, a droplet of desired size would be allowed to fall from the droplet generator onto the center of the test plate, over the hot junction of the microthermal probe. The transient temperature of the test plate would then be recorded by the differential amplifier and digital oscilloscope at speed of approximately 32,000 to 800,000 measurements per second. In the experiments, drops with diameters varying from 2.8 to 4.8 mm and velocities of 0.5 to 2.0 m/s were attempted.

The hydrodynamics of droplet–surface contact was observed to vary depending on initial surface superheat and droplet subcooling. In general, at low to moderate surface superheat and/or high to moderate droplet subcooling, the impinging drop was observed to spread on the surface upon impact. These drops were observed to undergo boiling/evaporation until eventual dryout.

Nomenclature

D_0 = droplet size
F = statistical fraction of surface under liquid contact
k = thermal conductivity of solid
q = instantaneous heat flux
$\bar{q}$ = time-averaged heat flux
$\bar{q}_l$ = average heat flux during liquid contact
$\bar{q}_v$ = average heat flux during vapor contact
T = temperature
T_0 = initial solid temperature
ΔT = superheat = $T - T_s$
T_m = measured surface temperature
T_s = liquid saturation temperature
t = time
V = droplet impinging velocity
Z = depth into solid
α = thermal diffusivity of solid

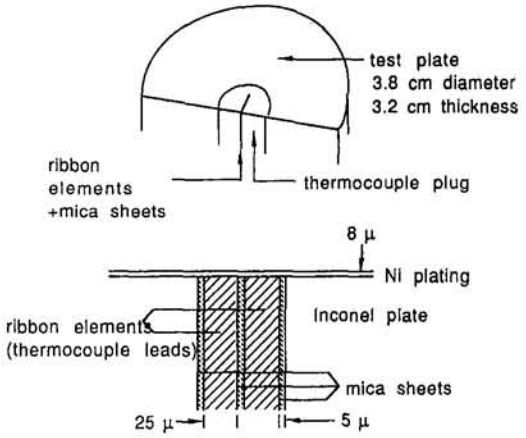

Fig. 2 Test plate and microthermal probe

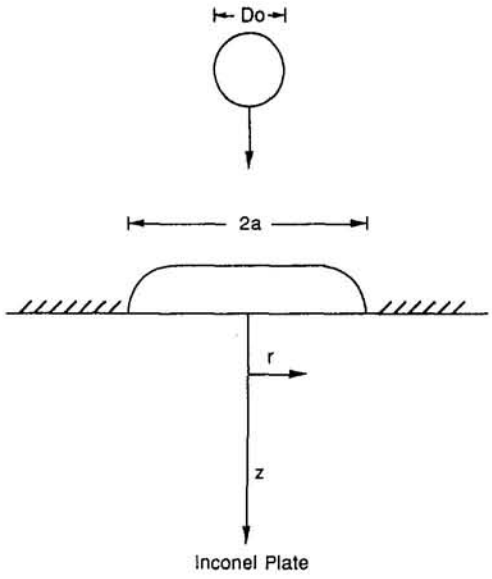

Fig. 3 Geometry for inverse-conduction analysis

At high wall superheats, drops with high subcoolings were observed to disintegrate into several smaller droplets shortly after impact. Saturated drops impinging on highly superheated surfaces tended to be deflected as a single integral drop upon reaching the hot surface.

To determine the instantaneous surface heat flux during droplet residence on the surface (q), the transient temperature recorded by the microthermal probe was utilized in an inverse-conduction analysis. Figure 3 shows the idealized geometry utilized in this analysis. A two-dimensional cylindrical coordinate system was used to describe the temperature field within the test block, with the origin at the center of the liquid disc, coinciding with the sensing tip of the thermal probe. The temperature distribution in the block was assumed to be symmetric about the Z axis. Heat flux outside the liquid disk was taken to be negligible compared to the surface heat flux in the liquid-contact area. Scoping calculations showed that for typical liquid residence durations of (order of 10 to 100 ms) penetration depth of the temperature wave below the surface of the test plate was many orders of magnitude less than the radius of the liquid drop so that one-dimensional analysis would be adequate:

$$\frac{\partial T}{\partial t} = \alpha \frac{\partial^2 T}{\partial Z^2}$$

$$T(t = 0, Z) = T_0$$

$$T(t, z = 0) = T_m(t)$$

$$q(t) = -k \left.\frac{\partial T}{\partial Z}\right|_{Z=0}$$

where T_0 = initial solid temperature; T_m = measured surface temperature. By such a procedure, the instantaneous transient surface heat flux during liquid residence could be determined from the measured transient surface temperatures. Tests were carried out at initial wall superheats of 50°C to 400°C. The liquid (water) temperature was varied from saturation to 80°C subcooling.

Figure 4 shows sample results for the case of 80°C subcooled water contacting a surface with initial superheat of 100°C. These results were measured with a liquid drop of 3.8 mm diameter impacting the test plate at a velocity of 1 m/s. It is seen that the surface temperature of the test plate quickly falls from its initial superheat of 100°C to approximately 30°C, staying at that value for approximately 190 ms before slowly recovering its initial value. The instantaneous heat flux corresponding to this temperature transient is shown in Fig. 4(b). It is seen that the maximum heat flux is attained almost immediately upon initial contact of the liquid, decreasing with time until cessation of liquid contact at approximately 190 ms. The magnitude of the maximum heat flux during this transient was determined to be 3.5×10^6 W/m^2, roughly equal to the critical heat flux that would be expected for this subcooled water.

Figure 5 shows the different thermal response obtained when the initial wall superheat was increased from 100 to 150°C. The first notable difference is that the liquid contact duration was significantly shortened, to the order of 28 ms. In this more rapid time scale, the transient decrease in surface temperature is seen to hesitate momentarily before plunging to a lower plateau of approximately 40°C superheat. The surface temperature was then sustained at this lower value until liquid contact ceased at approximately 28 ms. The corresponding transient heat flux was found to increase to a maximum value of 1.5×10^7 W/m^2 in a period of approximately 2 ms from initial contact. Thereafter the heat flux decreased with increasing time, falling by approxi-

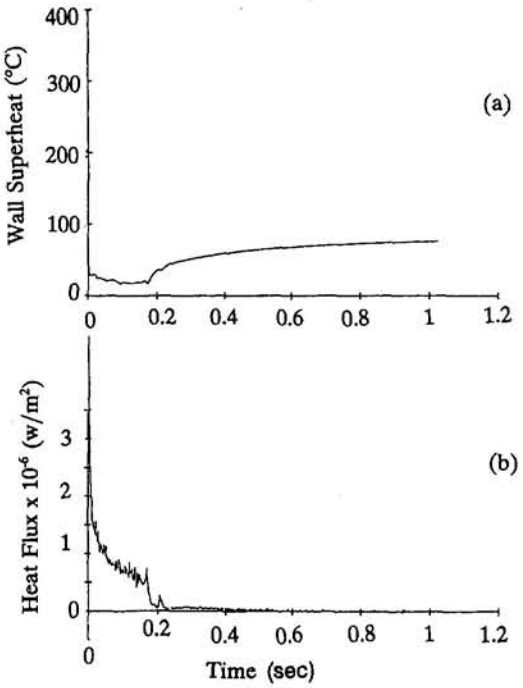

Fig. 4 Transient surface superheat (*a*) and heat flux (*b*) for 80°C subcooled water, with initial wall superheat at 100°C

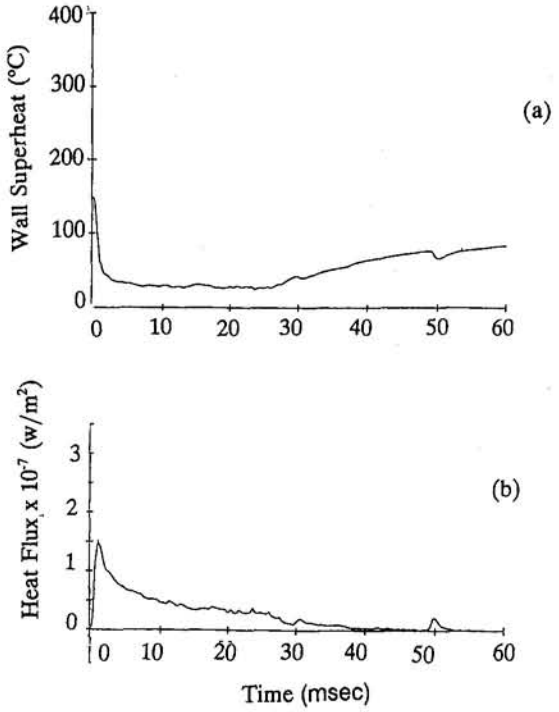

Fig. 5 Transient surface superheat (*a*) and heat flux (*b*) for 80°C subcooled water, with initial wall superheat at 150°C

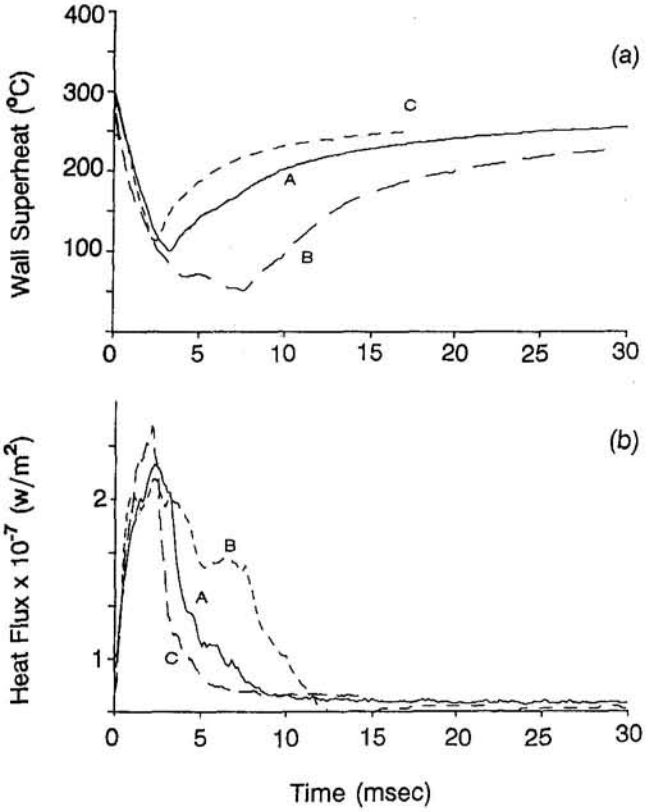

Fig. 7 Effect of drop size and velocity on transient surface superheat (*a*) and heat flux (*b*) for 80°C subcooled drop, with initial wall superheat of 300°C: (A) d_0 = 2.8 mm, V = 1 m/s; (B) d_0 = 3.8 mm, V = 1 m/s; (C) d_0 = 3.8 mm, V = 2 m/s

mately an order of magnitude over the 28 ms duration of liquid contact.

The time duration of the contact transient was further shortened as the initial surface temperature was increased even higher. Figure 6 shows results for an initial wall superheat of 400°C. It is seen that the measured surface superheat dropped rapidly for only 7 ms before start of temperature recovery. This is in contrast to the cases shown in Fig. 4 and 5 where the time of initial temperature recovery was approximately 190 ms and 28 ms, respectively, for initial superheats of 100°C and 150°C. The heat flux transient is also seen to be significantly different. For the case shown in Fig. 6, the instantaneous heat flux reached a value of 2×10^7 W/m^2, and stayed almost constant at that maximum value for a period of approximately 5 ms, before dropping to near zero upon cessation of liquid contact. In contrast, the results in Fig. 5 for the case of 150°C initial superheat showed a smaller maximum heat flux and did not exhibit a period of nearly constant heat flux.

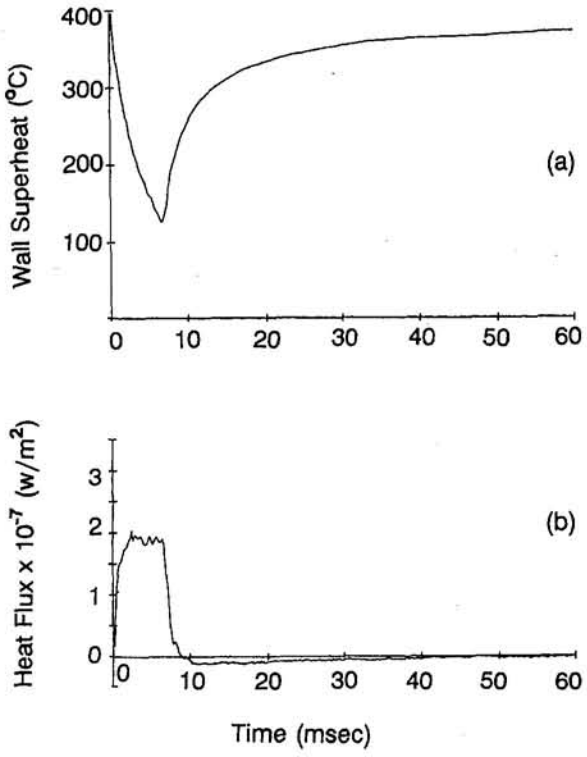

Fig. 6 Transient surface superheat (*a*) and heat flux (*b*) for 80°C subcooled water, with initial wall superheat of 400°C

The parametric effects of initial drop size and impingement velocity are illustrated in Fig. 7. Three cases are presented: cases (*a*) and (*b*) have the same impingement velocity (1 m/s) for two different drop sizes (D_0 of 2.8 and 3.8 mm, respectively), cases (*b*) and (*c*) have the same drop size but two different impingement velocities (1 m/s and 2 m/s, respectively). All three cases had an initial liquid subcooling of 80°C and initial wall superheat of 300°C. Comparing the results for cases (*a*) and (*b*), it is seen that increasing drop size prolonged the temperature transient, causing the instantaneous surface temperature to reach a lower minimum before initiation of recovery. The heat flux transients showed a corresponding longer period of significant heat transfer for the case of the larger drop. Comparing cases (*b*) and (*c*), it is seen that increasing the impingement velocity shortened the contact transient. The time to beginning of temperature recovery diminished from 8 to 3 ms when the impingement velocity was increased from 1 to 2 m/s. It should also be noted that the magnitude of decrease in wall superheat attained during this transient contact was less for the higher velocity droplet with its shorter contact transient. It is also interesting to note that for these three cases, having the same initial surface superheat and liquid subcooling, the peak of maximum instantaneous heat flux increased

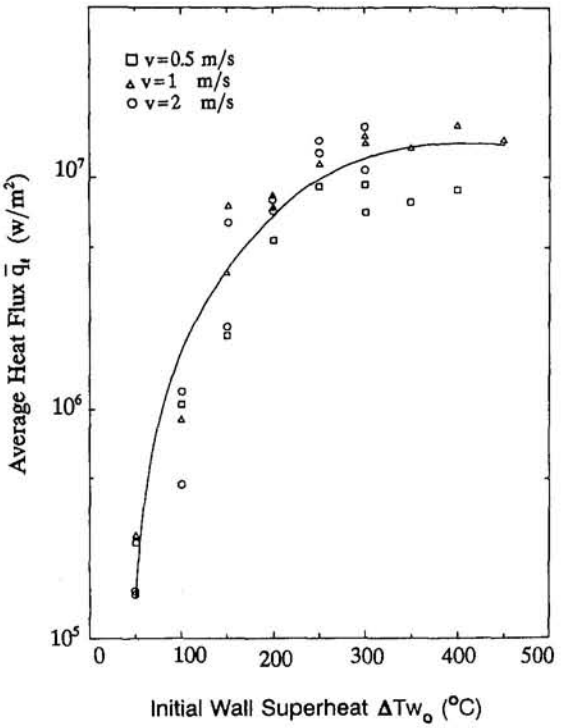

Fig. 8 Average heat flux during droplet impingement

as the contact duration decreased. At this time, there are insufficient data to discern whether this trend is just fortuitous for these cases or is a general behavior to be expected.

The transient heat flux for each test can be integrated over the duration of the liquid contact (e.g., area under the heat flux versus time curves in Figs. 4, 5, and 6) to obtain the total heat transferred during the liquid contact. The duration of the contact was defined as when the total heat transfer reached 95 percent of the asymptotic value at infinite time. With this definition, the end of contact was found to correspond approximately to the time when temperature recovery started. Dividing the total heat transfer by the duration of contact provided a measure of the average heat flux during that liquid contact, $\bar{q}_l$. Results are shown in Fig. 8 for case of 80°C subcooled liquid. The average heat flux ($\bar{q}_l$) is plotted against the initial wall superheat (ΔT_0). The range of initial wall superheat covered in these experiments ranged from 50°C to 450°C. The data shown in this figure encompass droplet impact velocities varying from 0.5 m/s to 2 m/s. It is seen that the droplet impact velocity is only of secondary importance. The primary variable affecting the average heat flux was the initial wall superheat. The data indicate that the average heat flux increased continuously with increasing superheat. Starting with a value of approximately 2×10^5 W/m^2 at a surface superheat of 50°C, the average heat flux increased to over 10^7 W/m^2 as the superheat increased to 450°C.

Conclusions

Results of this investigation indicate that the process of heat transfer during the short duration of direct liquid contacts may be quite complex. Earlier works had shown that the frequency and duration of liquid contacts in transition boiling (F) are functions of the wall superheat and fluid subcooling. This investigation showed that the time-averaged heat flux during liquid contact ($\bar{q}_l$) is also strongly affected by wall superheat. This average heat flux during liquid contact was found to vary from 10^5 to 10^7 W/m^2 for water, as wall superheat was varied from 50 to 450°C. For highly subcooled liquid the average heat flux increased continuously, with indications of approaching an asymptotic value at the maximum superheats reached in these experiments. Clearly the technical community will need to obtain more experimental data and develop some mechanistic model for the transient heat transfer process during liquid contact if the modeling approach suggested by Eq. (1) is to prove useful.

References

Auracher, H., 1990, "Transition Boiling," *Proceedings 9th International Heat Transfer Conference*, Jerusalem, Vol. 1, pp. 59–90.

Berenson, P. J., 1962, "Experiments on Pool-Boiling Heat Transfer," *Int. J. Heat Mass Transfer*, Vol. 5, pp. 985–999.

Carslaw, H. S., and Jaeger, J. C., 1959, *Conduction of Heat in Solids*, 2nd ed., Clarendon, New York.

Dhuga, D. S., and Winterton, R. H. S., 1985, "Measurement of Surface Contact in Transition Boiling," *Int. J. Heat Mass Transfer*, Vol. 28, pp. 1869–1880.

Hsu, K. K., 1986, "Heat Transfer to Droplets Impinging Upon Superheated Surfaces," Ph.D. Thesis, Lehigh University, Bethlehem, PA.

Lee, L. Y. W., Chen, J. C., and Nelson, R. A., 1982, "Surface Probe for Measurement of Liquid Contact in Film and Transition Boiling on High Temperature Surfaces," *Review of Scientific Instruments*, Vol. 53, pp. 1472–1476.

Lee, L. Y. W., Chen, J. C., and Nelson, R. A., 1985, "Liquid–Solid Contact Measurements Using a Surface Thermocouple Temperature Probe in Atmospheric Pool Boiling Water," *Int. J. Heat Mass Transfer*, Vol. 28, pp. 1415–1423.

Marquardt, W., and Auracher, H., 1990, "An Observer-Based Solution of Inverse Heat Conduction Problems," *Int. J. Heat Mass Transfer*, to be published.

Ragheb, H. S., and Cheng, S. C., 1979, "Surface Wetted Area During Transition Boiling in Forced Convective Flow," ASME JOURNAL OF HEAT TRANSFER, Vol. 101, pp. 381–383.

Rajabi, A., and Winterton, R. H. S., 1988, "Liquid–Solid Contact in Steady State Transition Pool Boiling," *Int. J. Heat Fluid Flow*, Vol. 9, pp. 215–219.

Westwater, J. W., and Santangelo, J. G., 1955, "Photographic Study of Boiling," *I & EC Fundamentals*, Vol. 47, pp. 1605–1610.

Yao, S., and Henry, R. E., 1978, "An Investigation of the Minimum Film Boiling Temperature on Horizontal Surfaces," ASME JOURNAL OF HEAT TRANSFER, Vol. 100, pp. 260–267.

A Theoretical Model for Flow Boiling CHF From Short Concave Heaters

J. E. Galloway[1]

I. Mudawar
Professor and Director.

Boiling and Two-Phase Flow Laboratory,
School of Mechanical Engineering,
Purdue University,
West Lafayette, IN 47907

Experiments were performed to enable the development of a new theoretical model for the enhancement in CHF commonly observed with flow boiling on concave heaters as compared to straight heaters. High-speed video imaging and photomicrography were employed to capture the trigger mechanism for CHF for each type of heater. A wavy vapor layer was observed to engulf the heater surface in each case, permitting liquid access to the surface only in regions where depressions (troughs) in the liquid–vapor interface made contact with the surface. CHF in each case occurred when the pressure force exerted upon the wavy vapor–liquid interface in the contact regions could no longer overcome the momentum of the vapor produced in these regions. Shorter interfacial wavelengths with greater curvature were measured on the curved heater than on the straight heater, promoting a greater pressure force on the wavy interface and a corresponding increase in CHF for the curved heater. A theoretical CHF model is developed from these observations, based upon a new theory for hydrodynamic instability along a curved interface. CHF data are predicted with good accuracy for both heaters.

1 Introduction

It is well known that CHF in pool boiling can be ameliorated by increasing the magnitude of body force normal to the heater surface as suggested, for example, by the well-known CHF model of Zuber et al. (1961). Costello and Adams (1963), Marto and Gray (1971), and Usenko and Fainzil'berg (1974) all demonstrated this CHF enhancing effect by rotating the heater and liquid as a solid body. Gambill and Green (1958), Miropol'skiy and Pikus (1969), Hughes and Olson (1975), Iverson and Whitaker (1988), and Gu et al. (1989) proposed more practical means of creating an "effective" body force by supplying subcooled liquid over concave heated surfaces. Today, many heat sinking devices can be found in the aerospace industry that are grooved to accommodate closely spaced serpentine coolant channels in order to increase both CHF and the channel wetted area relative to the device surface area subjected to the heating. It has been postulated by most of the above-cited authors that flow over curved surfaces produces a centrifugal force that facilitates the removal of vapor from the heated surface, thus increasing CHF relative to a straight surface. This effect was accounted for using pool boiling CHF correlations or models that were modified by replacing Earth gravity with centrifugal acceleration.

Curved flow boiling experiments were conducted by the authors of the present study using a stirred cylindrical vessel facility (Galloway and Mudawar, 1989, 1992). Heat sources were flush-mounted to the inner wall of a cylindrical vessel partially filled with liquid. Flow with streamwise curvature was created by rotating a radial-bladed stirrer along the axis of the vessel creating an annular liquid layer as shown in Fig. 1. Photographs were recently taken in a sideview orientation relative to the streamwise direction by a boroscope lens. While accurate measurements of interfacial features were extremely difficult, this new photographic study clearly revealed the formation of a

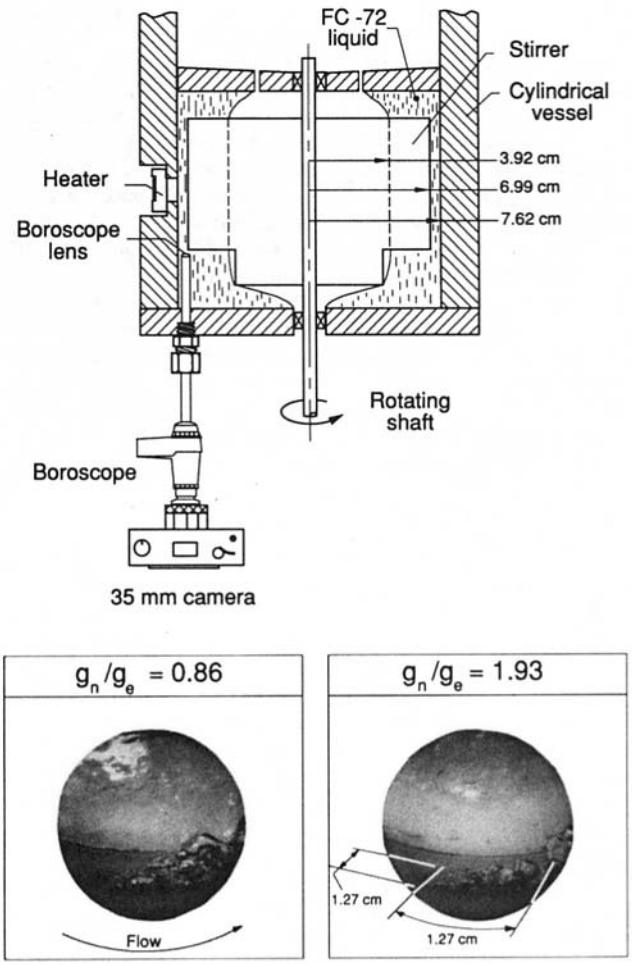

Fig. 1 Stirred vessel boroscope system and photographs of the wavy vapor layer at 99 percent of CHF

[1] Present address: Advanced Manufacturing Technology, Radio Products Group, Motorola, Fort Lauderdale, FL 33322.

Contributed by the Heat Transfer Division for publication in the JOURNAL OF HEAT TRANSFER. Manuscript received by the Heat Transfer Division January 1994; revision received November 1994. Keywords: Augmentation and Enhancement, Boiling, Flow Instability. Associate Technical Editor: V. K. Dhir.

wavy vapor layer at fluxes nearing CHF with nucleate boiling partially persisting beneath the vapor layer. The wavelength of vapor layer decreased with increasing angular velocity.

The objectives of the present study are to explore the mechanisms governing the effects of surface curvature on flow boiling CHF from short heaters, using an apparatus that lends itself better to high-resolution photographic study of interfacial features, and develop a theoretical model for this important flow configuration. These objectives are accomplished by comparing both CHF data and photographic records of vapor production at CHF for a concave heater to that for a straight heater. Relevant mechanisms for CHF on straight heaters will be reviewed first to establish a basis for this comparative study.

2 CHF From Straight Heaters

Interfacial Separation CHF Model. In a recent study, the authors examined near-wall interfacial behavior at CHF from a 12.7 mm long straight heater in vertical upflow using Fluorinert FC-87 (Galloway and Mudawar, 1993a, b). A wavy vapor layer similar to that depicted in Fig. 1 for the stirred vessel was observed over the straight heater as well as illustrated in Fig. 2. At heat fluxes nearing CHF, liquid contact with the heater surface was possible over the most upstream portion of the heater ($0 < z < z^*$) and within *wetting fronts*, corresponding to the wave troughs, while regions between the wetting fronts were dry. Heat could only be transferred within the isolated wetting fronts with a local heat flux many times greater than the average surface heat flux. At CHF, intense vapor production caused separation of the vapor layer interface from the heated surface starting at the location of the most upstream wetting front. This upstream separation increased heat flux in the downstream wetting fronts that lifted off the surface, in succession, until the entire interface separated from the surface, except for the most upstream region of the heater.

Statistical analysis of a large data base of interfacial features revealed the wetting fronts were separated by wavelengths twice the critical Helmholtz wavelength, λ_c, based upon hydrodynamic conditions at z^*. High-speed video imaging showed that only every other wave trough was able to create a wetting front at z^*. Once a wetting front was formed, a thin layer of liquid was splashed upon the surface and the ensuing intense vapor production pushed the next wave trough away from the surface, preventing the formation of a wetting front. Rapid dryout of this liquid cleared the surface for liquid replenishment with the advent of the third wave trough, thus allowing the formation of a new wetting front. This process, therefore, enabled the interfacial waves to produce wave fronts separated by wavelengths equal to $2\lambda_c$.

The data base for the straight heater also revealed that the span (length) of each wetting front was one-fourth the separation distance between wetting fronts. A surface energy balance yielded the following expression for CHF:

$$q_m = \left[1 - \frac{\lambda_c}{16(L - z^*)}\right]\frac{q_l}{4} \tag{1}$$

where the coefficient in the brackets is close to unity (i.e., CHF is about one-fourth the heat flux concentrated in the wetting fronts) for most operating conditions and accounts for continuous wetting in the region $0 < z < z^*$ and any partial wetting fronts in the downstream region, and q_l is the heat flux required to cause lifting of the most upstream wetting front. This lift-off heat flux was assumed to occur when the normal momentum of vapor generated in the wetting front just exceeds the pressure force exerted upon the interface as a result of interfacial curvature.

$$\rho_g\left[\frac{q_l}{\rho_g h_{fg}\left(1 + \frac{c_{p,f}\Delta T_{sub}}{h_{fg}}\right)}\right]^2 = \overline{P_f - P_g}, \tag{2}$$

Nomenclature

a_1, a_2 = coefficients in Eq. (12a)
A_f = coefficient in the liquid mean velocity profile
A_g = coefficient in the vapor mean velocity profile
b_1, b_2 = coefficients in Eq. (12b)
c = wave speed
c_i = imaginary component of wave speed
c_p = specific heat at constant pressure
c_r = real component of wave speed
D_h = hydraulic diameter
f = friction factor
F = amplitude function defined in Eq. (10a)
G = amplitude function defined in Eq. (10b)
g_e = Earth gravity
g_n = component of body force per unit mass normal to liquid–vapor interface
H = channel height = $H_f + H_g$, $R_2 - R_1$
H_f = liquid layer thickness
H_g = vapor layer thickness
h_{fg} = latent heat of vaporization
k = wave number = $2\pi/\lambda$
k_c = critical wave number = $2\pi/\lambda_c$
L = heater length
n = number of wetting fronts
P = pressure
$\overline{P_f - P_g}$ = mean interfacial pressure difference in wetting front $= \frac{1}{0.25\lambda}\left[\int_{3\lambda/8}^{5\lambda/8}(P_f - P_g) \times \frac{2\pi}{\lambda}\, d(\theta R_0 - c_r t)\right]$
ΔP = streamwise pressure drop
q = heat flux (electrical power divided by heater surface area)
q_l = heat flux (at CHF) corresponding to wetting front separation
q_m = critical heat flux (CHF)
r = radial coordinate
R_0 = radius of unperturbed interface
R_1 = inner radius of curved channel
R_2 = outer radius of curved channel
Re = Reynolds number = $\bar{u}_m D_h/\nu$
s = channel thickness normal to viewing axis
t = time
ΔT_{sub} = inlet liquid subcooling
u = phase velocity in the θ direction
u' = fluctuating component of u
$\bar{u}$ = mean component of u
$\bar{u}_i$ = interfacial value of $\bar{u}$
$\bar{u}_m$ = mean of $\bar{u}$ across liquid or vapor layer
U_m = mean liquid velocity upstream of heater
v = phase velocity in the r direction
v' = fluctuating component of v
z = spatial coordinate in the streamwise direction = $R_2\theta$
z^* = distance from leading edge of heater to center of first wetting front = $z_0 + \lambda_c(z^*)$
z_0 = position from leading edge where $\bar{u}_{g,i} - \bar{u}_{f,i} = 0$
δ = mean vapor layer thickness = H_g
η = interfacial displacement
θ = circumferential coordinate
λ = wavelength of interfacial perturbation
λ_c = critical wavelength corresponding to onset of instability
ν = kinematic viscosity
ρ = density
ρ'' = modified density defined in Eq. (3)
ρ''' = modified density defined in Eqs. (18a) and (18b)
σ = surface tension
τ = wetting period
τ_f = wall shear stress in the liquid layer

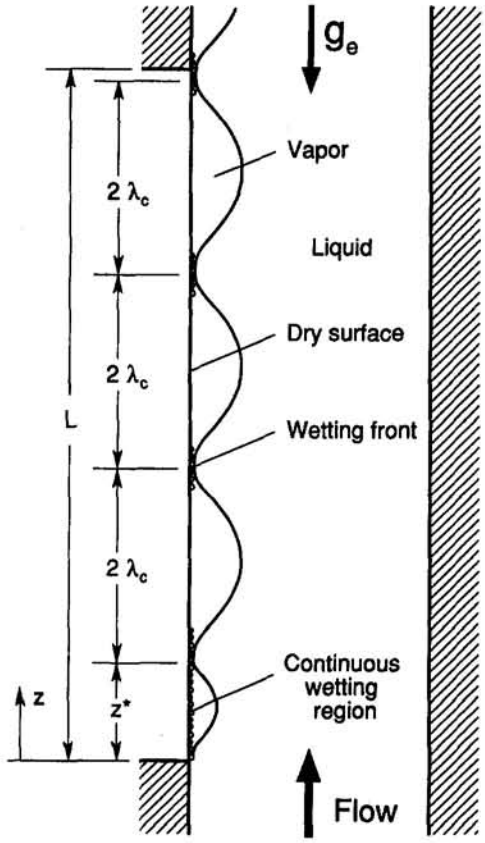

Fig. 2 Wetting front propagation along a straight heater at 99 percent of CHF (adapted from Galloway and Mudawar, 1993b)

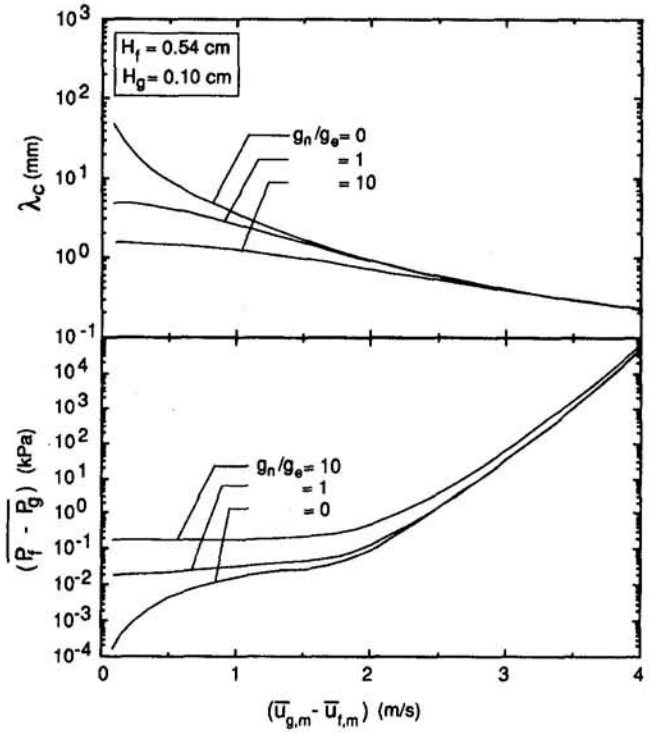

Fig. 3 Predictions of critical wavelength and interfacial pressure difference based on simplified instability theory for different values of velocity difference and body force

where the average pressure difference across the interface, $\overline{P_f - P_g}$, was calculated by integrating the pressure difference over the span of the most upstream wetting front.

Interfacial Instability Over Straight Heaters. The interfacial waviness illustrated in Fig. 2 can be idealized as a hydrodynamic instability of an interface between a vapor layer of mean velocity $\overline{u}_{g,m}$ and height H_g and a liquid layer of mean velocity $\overline{u}_{f,m}$ and height H_f. Using classical instability theory, the interfacial pressure difference resulting from a sinusoidal perturbation η perpendicular to the unperturbed interface can be expressed as (Galloway and Mudawar, 1993b)

$$P_f - P_g = -\eta k[\rho_f''(c - \overline{u}_{f,m})^2 + \rho_g''(\overline{u}_{g,m} - c)^2] - (\rho_f - \rho_g)g_n\eta = -\sigma k^2\eta, \quad (3)$$

where $\rho_f'' = \rho_f \coth(kH_f)$, $\rho_g'' = \rho_g \coth(kH_g)$, and g_n is the body force per unit mass perpendicular to the unperturbed interface ($g_n = 0$ for vertical upflow over a straight heater).

The critical wavelength for a straight channel is given by (Galloway and Mudawar, 1993b)

$$\frac{2\pi}{\lambda_c} = k_c = \frac{\rho_f''\rho_g''(\overline{u}_{g,m} - \overline{u}_{f,m})^2}{2\sigma(\rho_f'' + \rho_g'')} + \sqrt{\left[\frac{\rho_f''\rho_g''(\overline{u}_{g,m} - \overline{u}_{f,m})^2}{2\sigma(\rho_f'' + \rho_g'')}\right]^2 + \frac{g_n(\rho_f - \rho_g)}{\sigma}}. \quad (4)$$

An approximate method to account for the effect of flow curvature on CHF is to define an effective centrifugal force perpendicular to the heater surface based on the mean inlet liquid velocity and the heater radius of curvature, $g_n = U_m^2/R_2$. The effective centrifugal force per unit mass for the conditions of the present study varied from 0.3 to $9.7g_e$ corresponding to flow velocities between 0.35 and 2.0 m/s and a 4.19-cm heater radius of curvature.

Shorter wavelengths increase curvature, allowing the surface tension force to overcome the destabilizing effects of the body force and inertia. However, as the wavelength exceeds λ_c, the surface tension force no longer can maintain stability. Figure 3 shows the destabilizing effects of inertia and body force on the critical wavelength for the operating conditions of the present study as predicted by Eq. (4). The critical wavelength decreases rapidly with increasing velocity difference, $(\overline{u}_{g,m} - \overline{u}_{f,m})$, in the absence of a body force. However, as g_n increases above $10\,g_e$, the critical wavelength becomes relatively insensitive to inertia for velocity differences below 1 m/s. As the velocity difference exceeds 2.0 m/s, the critical wavelength becomes controlled primarily by inertia, insensitive to the magnitude of body force for the range of g_n shown.

Nomenclature (cont.)

τ_g = wall shear stress in the vapor layer
τ_i = interfacial shear stress
ϕ = potential function

Subscripts

f = saturated liquid
g = saturated vapor
i = interface
m = mean
sub = subcooling

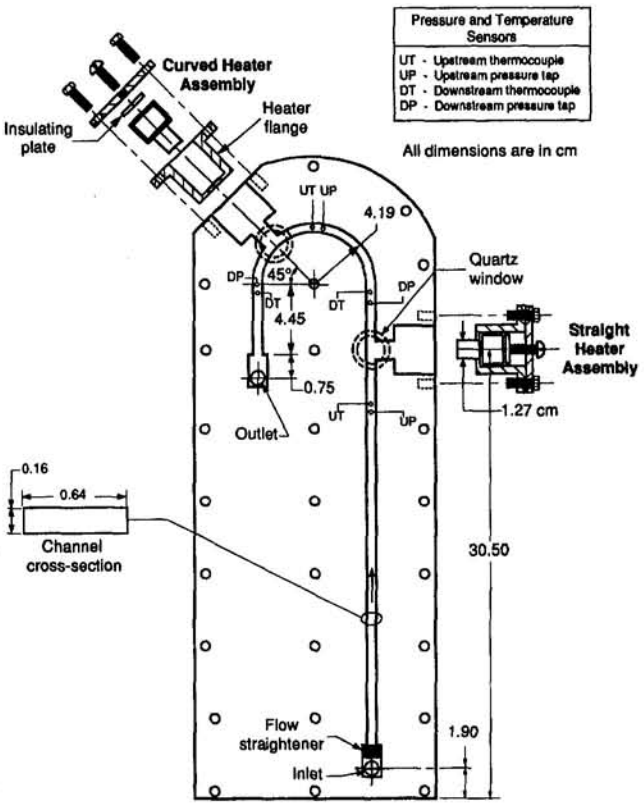

Fig. 4 Planar view of flow channel module

Figure 3 also shows, according to Eq. (3), pressure difference across the liquid–vapor interface, $P_f - P_g$, increases with increasing $(\bar{u}_{g,m} - \bar{u}_{f,m})$. An increase in the body force also produces a greater pressure force against the interface, which enables the interface to sustain a greater vapor momentum, or heat flux, before the interface can be separated from the heater surface. Therefore, increases in body force enhance CHF.

While this analysis clearly suggests that a greater body force would increase CHF, using an effective body force proportional to U_m^2/R_2 is, at best, a rough approximation of the net radial force resulting from the flow curvature. The excess force exerted upon the vapor–liquid interface for a curved heater compared to a straight heater is the result of radial pressure forces, which are dependent upon the channel geometry and the mean thickness and mean velocity of both the vapor and liquid layers. Additionally, the instability relations developed for a straight channel, Eqs. (3) and (4), simply do not apply for curved channels; hence the need for a new instability model applicable to a curved interface. Such a model will be presented later in this paper.

3 Experimental Methods

The curved flow apparatus was carefully designed to maximize photographic access to the heater surface. The apparatus consisted of a curved flow channel having a 4.19-cm outer radius of curvature, which was located downstream from a straight channel. A 1.27-cm-long heater was inserted in each of the straight and curved regions of the channel. As shown in Fig. 4, the flow channel was formed by milling a 0.16 cm × 0.64 cm slot in a Lexan plate. A second Lexan plate was clamped onto the first plate trapping an O-ring seal. Fully developed flow was established upstream of the straight heater by using an entrance length of over 100 times the hydraulic diameter. The centerline of the curved heater was positioned at a 135-deg angle relative to the inlet flow. Each of the straight and curved heaters was constructed from a copper block inserted inside an insulating flange made from G-10 insulating fiberglass. An O-ring was pressed between the base of each heater assembly and the flow channel plate providing a leak proof seal. Maximum errors of 8 percent and ±0.2°C were estimated in the measurement of heat flux and surface temperature, respectively, due to the uncertainty associated with thermocouple placement and calibration. Additional details concerning the flow loop and heater design can be found elsewhere (Galloway and Mudawar, 1993a).

FC-87, a 3M dielectric fluid, was tested at a pressure of 1.37 bars (T_{sat} = 39°C) with 8°C inlet subcooling. The relevant properties of FC-87 at these conditions are: $\rho_f = 1742$ kg/m^3, $\rho_g = 16.8$ kg/m^3, $\nu_f = 2.57 \times 10^{-7}$ m^2/s, $\nu_g = 7.15 \times 10^{-7}$ m^2/s, $c_{p,f} = 1099$ J/kg·K, $h_{fg} = 85{,}500$ J/kg, and $\sigma = 10.9 \times 10^{-3}$ N/m. By tilting the entire flow channel module, all tests were conducted in an upflow configuration with respect to the tested heater; only one heater was operated at a time.

At approximately 85 percent of CHF, a decrease in the slope of the heat flux versus wall superheat curve (detailed boiling curves can be found in Galloway, 1991) signaled the approach of CHF and was used as an indicator to reduce the increments in heater power to values no greater than 0.5 W/cm^2, each time waiting for the surface temperature to assume a new steady-state value before any additional power was supplied. CHF typically commenced from a stable surface temperature of approximately 85°C.

4 Experimental Results

Observations. At a heat flux of about 85 percent of CHF, large coalescent bubbles were observed sliding over the heater surface for both the straight and curved heaters. The length of these coalescent bubbles increased with increasing heat flux until, eventually, a fairly continuous wavy vapor layer was formed over the heater surface at heat fluxes below CHF. Boiling was sustained by liquid entrainment in the heater most upstream region and in the wetting fronts, where the liquid–vapor interface made contact with the heater surface. Experimental evidence supporting this wetting front description is also available from studies by Fiori and Bergles (1970), Hino and Ueda (1985a, b), and Galloway and Mudawar (1992), all of whom measured fluctuations in the heater surface temperature synchronous with the passage of vapor slugs.

The wavy vapor layer is depicted for the curved heater in Fig. 5 corresponding to heat fluxes equal to 99 percent of CHF. Boiling curves over the entire heat flux range leading to CHF proved the conditions depicted in Fig. 5 correspond to the nucleate boiling and not transition or film boiling regimes (Galloway, 1991). Using a magnification better than 50×, no vapor jets could be seen emanating from the heater surface. Rather, a violent surge of small bubbles in the wetting fronts was observed to be feeding the vapor layer. Like the stirred vessel described earlier and the straight heater, the wavelength for the curved heater decreased with increasing velocity. Excluding velocities above 1.25 m/s, the interfacial instability was clearly two dimensional, precluding any significant secondary flow effects. In fact, recent tests with heaters much wider than the one employed in the present study proved this instability is indeed two dimensional, both over straight heaters (Gersey and Mudawar, 1994) and curved heaters (Galloway, 1991).

However, the curved heater exhibited significant differences in the shape of the wavy vapor layer as compared to the straight heater. For equal inlet velocities, the interfacial wavelength was greater for the straight heater than for the curved heater and, occasionally, the curved heater projected vapor away from its surface in the form of vapor slugs, which protruded from the wave peaks at inlet velocities exceeding approximately 1.25 m/s. No such behavior was observed with the straight heater.

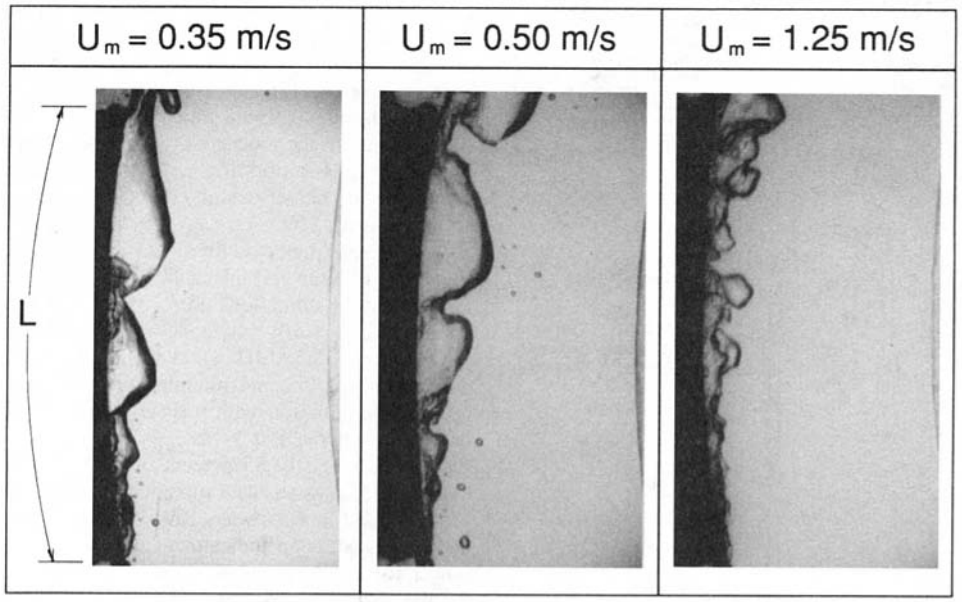

Fig. 5 Curved heater interfacial waves at 99 percent of CHF

Vapor Layer Interfacial Features. Vapor layer mean thickness and wavelength were measured from high-speed video images captured by a 6000 partial frames per second EktaPro 1000 motion analyzer, which were later analyzed on a 55-cm-wide screen. A measurement accuracy of ±0.1 mm was estimated from the combined magnification of the optical hardware and video screen. Thirty measurements were made for each inlet velocity to quantify the randomness of the interfacial features. Figure 6 shows that the wavelength for the straight heater was greater than for the curved heater and the wavelengths for both heaters decreased with increasing inlet velocity. Figure 6 also compares the ratio of wavelength to mean thickness of the vapor layer for both heaters. It should be emphasized that for each value of mean velocity in Fig. 6 a different CHF value was obtained for the curved channel as compared to the straight channel, differences in CHF for each velocity are discussed later (see Fig. 9). Vapor layer thickness was measured as half the normal distance between the surface and vapor layer interface after truncating the vapor projected from the wave peaks. Because vapor slugs perturbed the interface, particularly at velocities above 1.25 m/s, the curved heater thickness measurements tended to underestimate the vapor production for these high velocities. For a sinusoidal wave with wavelength λ and amplitude η_0, curvature at the wave peak is proportional to $(\eta_0/\lambda)^2/\eta_0$. Since the straight and curved heaters produced waves with fairly equal amplitudes, Fig. 6 indicates the waves acquired greater curvature over the curved heater than they did over the straight heater. This increased curvature increases the pressure force exerted upon the interface and, consequently, increases both the lift-off heat flux in the wetting fronts and CHF relative to the straight heater. The curved heater produced an average of 23 percent enhancement in CHF, compared to the straight heater, as shall be seen in the next section.

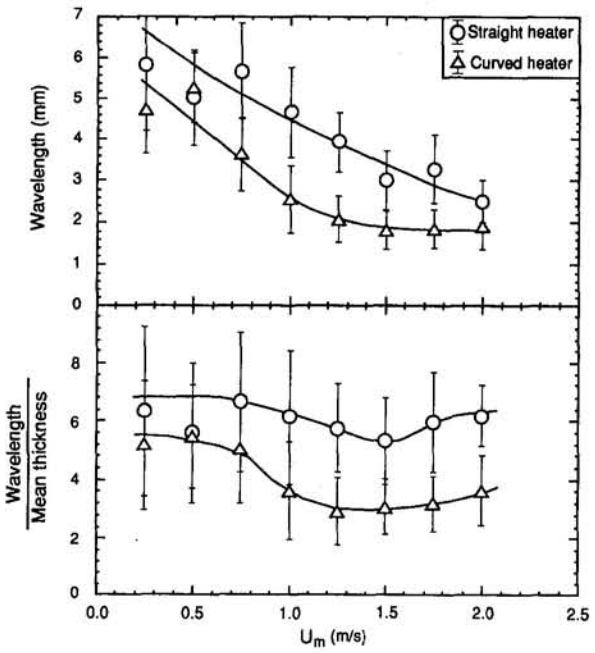

Fig. 6 Vapor layer wavelength and ratio of wavelength to mean thickness at 99 percent of CHF and z/L = 2/3

5 CHF Model

The model presented here is built upon physical observations, which are based on extensive high-speed video imaging studies, as discussed in the previous section, and are illustrated in Fig. 7: (1) at heat fluxes approaching CHF, vapor coalesces to form a fairly continuous wavy vapor layer; (2) liquid is entrained at wetting fronts where the liquid–vapor interface makes contact with the heater surface; (3) vigorous boiling persists near the leading edge of the heater and in the wetting fronts while regions between neighboring wetting fronts dry out; (4) CHF commences when the liquid–vapor interface separates from the heater surface at the location of the most upstream wetting front; and (5) remaining wetting fronts are separated, in succession, after separation of the upstream wetting front.

As shown in Fig. 7, the first wetting front is established at a distance z^* from the leading edge and then propagates along the heater surface at a speed c_r. The vapor layer interfacial wavelength, $2\lambda_c$, was determined from a new hydrodynamic instability model (discussed in the next section) and observations made using the high-speed video imaging. When the liquid–vapor interface is unstable, a disturbance having a wavelength equal to λ_c is assumed to touch the heater surface at $z = z^*$ (z^* is slightly greater than λ_c, the difference being a negligible distance z_0 over which the vapor velocity just exceeds the liquid velocity as

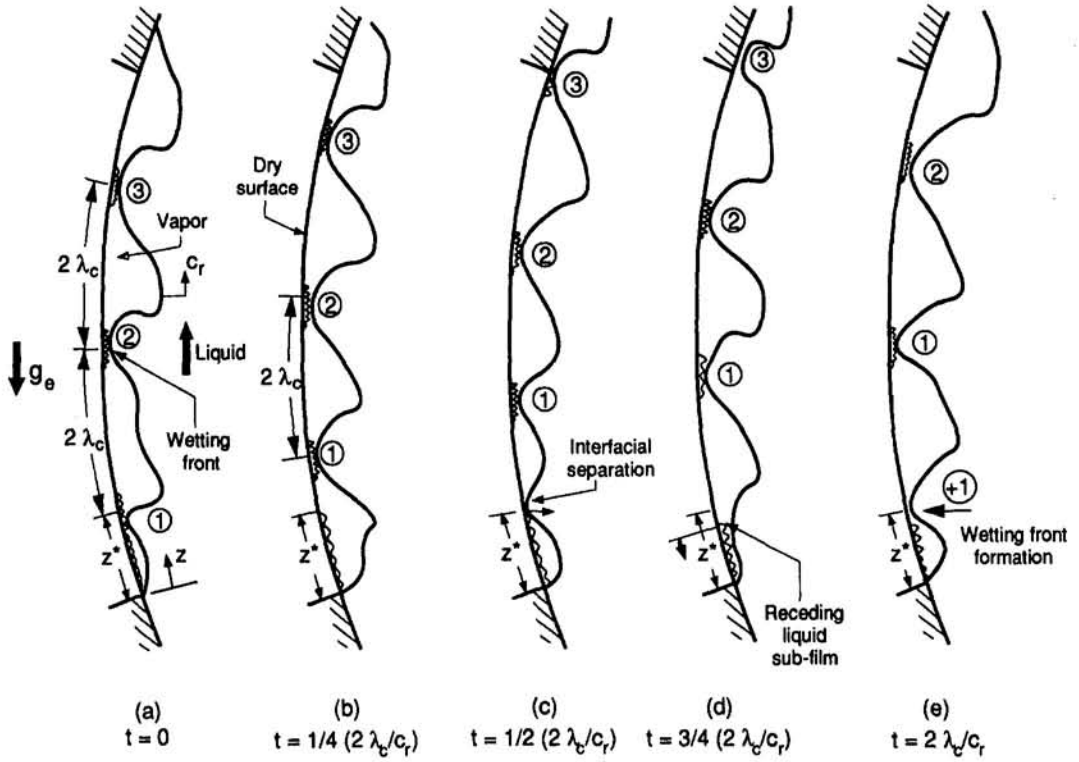

Fig. 7 Wetting front propagation along the heater surface at 99 percent of CHF

discussed by Galloway and Mudawar, 1993b), enabling liquid to contact the heater over a localized region. A short time later, at $t = \lambda_c/c_r$, another disturbance approaching the heater surface will be forced away by the momentum of vapor emanating from residual liquid at $z = z^*$ left after the passage of the previous wetting front. Not until a later time $t = 2\lambda_c/c_r$, after the residual liquid has been consumed at the location of the first wetting front, will a new wetting front be established on the heater surface. Wetting is, therefore, skipped every other cycle and wetting fronts are separated by $2\lambda_c$ wavelengths.

A Lagrangian frame of reference is used to model heat transfer to the moving wetting fronts illustrated in Fig. 7. Equation (5) sums the transient energy removed from the heater by the passage of all wetting fronts in contact with the heater between the time a wetting front first forms on the heater surface and the time the next wetting front is established at the same location. Equation (5) also accounts for the steady heat removal from the continuous wetting zone, $0 < z < z^*$.

$$q_m = \frac{c_r/(2\lambda_c)}{L - z^*}\left[\int_0^\tau\int_{z^*}^L q_{s,1}\,dz\,dt + \int_0^\tau\int_{z^*}^L q_{s,2}\,dz\,dt + \cdots + \int_0^\tau\int_{z^*}^L q_{s,n-1}\,dz\,dt + \int_0^\tau\int_{z^*}^L q_{s,n}\,dz\,dt\right] \quad (5)$$

where $q_{s,1}, q_{s,2}, \ldots, q_{s,n}$ are the local heat fluxes corresponding to wetting fronts 1, 2, ..., n, respectively. Where a wetting front is present, q_s is equal to some localized heat flux value, q_l, otherwise q_s is zero where the heater surface is dry.

The general form of Eq. (5) is identical to that derived by the authors for a short straight heater and, as illustrated in Fig. 7, gives CHF values approximately one-fourth the heat flux in the wetting fronts. Equation (5) can be simplified to the CHF expression given in Eq. (1) (see Galloway and Mudawar, 1993b).

A balance between the net pressure force exerted upon the liquid–vapor interface and the opposing momentum flux of vapor produced in the upstream wetting fronts yields an equation for the curved heater identical to that of the straight heater, Eq. (2), the difference between the two heaters being only the increased lift-off heat flux due to a greater interfacial pressure force for the curved heater as compared to the straight heater.

Combining Eqs. (1) and (2) yields an expression for CHF that is applicable to both straight and curved heaters.

$$q_m = \frac{1}{4}\rho_g h_{fg}\left(1 - \frac{\lambda_c}{16(L - z^*)}\right)\left(1 + \frac{c_{p,f}\Delta T_{sub}}{h_{fg}}\right) \times \left[\frac{\overline{P_f - P_g}}{\rho_g}\right]^{1/2} \quad (6)$$

Equation (6) shows predicting CHF requires estimation of $\overline{P_f - P_g}$. The next section will discuss an instability model, which shall be used to predict this key parameter for curved heaters.

Interfacial Instability of a Curved Vapor–Liquid Interface. The wavy vapor layer depicted in Fig. 5 clearly exhibits behavior characteristic of interfacial instability. A linearized stability analysis is proposed to model the waviness for a curved interface. While existing interfacial instability theories (Lamb, 1945; Milne-Thompson, 1960) are well suited for straight channels, these theories cannot be employed with curved flow since they do not account for the effect of radial pressurization induced by curvature; hence the need for a model specifically tailored to curved flow.

Figure 8 illustrates a wavy interface of the form $\eta = \eta_0 e^{ik(\theta R_0 - ct)}$ separating a liquid layer of thickness H_f from a vapor layer of thickness H_g inside a curved channel, where η represents the displacement of the interface from a mean position $r = R_0$, k is the wave number ($= 2\pi/\lambda$), and c is the wave speed, which can have both real and imaginary components ($c = c_r + ic_i$). Invoking the assumptions of inviscid, incompressible,

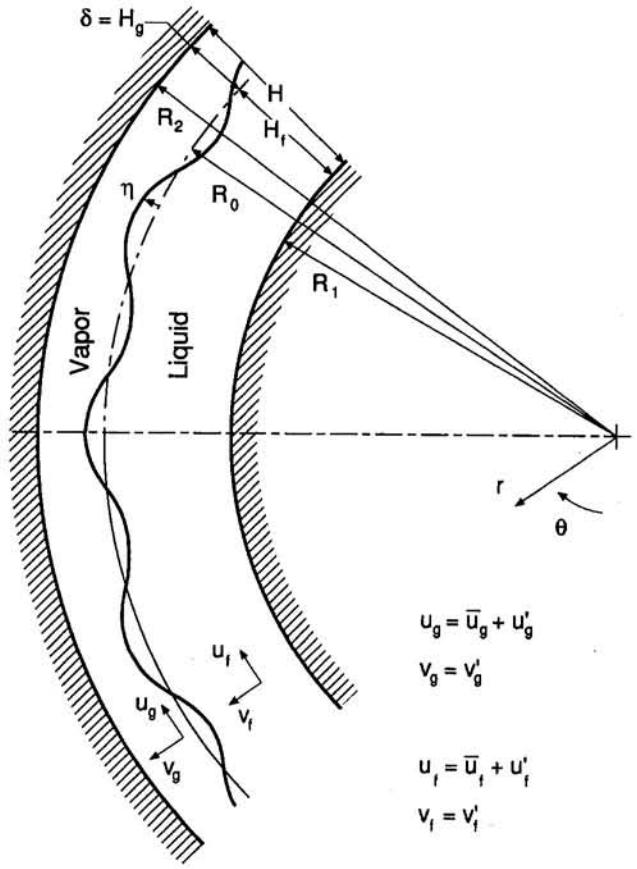

Fig. 8 Definition of hydrodynamic instability configuration and flow parameters

and irrotational flow yields the following potential function relations for liquid and vapor, respectively,

$$\nabla^2\phi_f = \frac{1}{r}\frac{\partial}{\partial r}\left(r\frac{\partial\phi_f}{\partial r}\right) + \frac{1}{r^2}\frac{\partial^2\phi_f}{\partial\theta^2} = 0, \tag{7a}$$

$$\nabla^2\phi_g = \frac{1}{r}\frac{\partial}{\partial r}\left(r\frac{\partial\phi_g}{\partial r}\right) + \frac{1}{r^2}\frac{\partial^2\phi_g}{\partial\theta^2} = 0. \tag{7b}$$

The velocity in each layer can be decomposed into a mean component in the θ direction and fluctuating components in the θ and r directions:

$$\frac{1}{r}\frac{\partial\phi_f}{\partial\theta} = u_f = \bar{u}_f + u'_f, \tag{8a}$$

$$\frac{\partial\phi_f}{\partial r} = v_f = v'_f, \tag{8b}$$

$$\frac{1}{r}\frac{\partial\phi_g}{\partial\theta} = u_g = \bar{u}_g + u'_g, \tag{9a}$$

$$\frac{\partial\phi_g}{\partial r} = v_g = v'_g. \tag{9b}$$

The solutions sought for Eqs. (7a) and (7b) are, respectively,

$$\phi_f = \bar{u}_f r\theta + F(r)e^{ik(\theta R_0 - ct)}, \tag{10a}$$

$$\phi_g = \bar{u}_g r\theta + G(r)e^{ik(\theta R_0 - ct)}, \tag{10b}$$

since, for the irrotational flow illustrated in Fig. 8, the mean tangential velocity is inversely proportional to r, $\bar{u}_f = A_f/r$, and $\bar{u}_g = A_g/r$. Equations (10a) and (10b) can be combined with Eqs. (7a) and (7b), respectively, giving

$$\frac{d^2F}{dr^2} + \frac{1}{r}\frac{dF}{dr} - \frac{(kR_0)^2}{r^2}F = 0, \tag{11a}$$

$$\frac{d^2G}{dr^2} + \frac{1}{r}\frac{dG}{dr} - \frac{(kR_0)^2}{r^2}G = 0. \tag{11b}$$

The general solutions for these equations are, respectively,

$$F(r) = a_1 r^{kR_0} + a_2 r^{-kR_0}, \tag{12a}$$

$$G(r) = b_1 r^{kR_0} + b_2 r^{-kR_0}. \tag{12b}$$

The coefficients a_1, a_2, b_1, and b_2 can be determined by applying the boundary conditions corresponding to the inner and outer solid walls and the kinematic conditions at the interface. The boundary conditions for the solid walls give $v_f]_{r=R_1} = \partial\phi_f/\partial r]_{r=R_1} = 0$ and $v_g]_{r=R_2} = \partial\phi_g/\partial r]_{r=R_2} = 0$ and, assuming particles at the interface move with the interface, these particles must satisfy the kinematic condition

$$\frac{D}{Dt}[(r - R_0) - \eta] = 0. \tag{13}$$

Equation (13) gives the following kinematic relations for the interface ($r = R_0$):

$$\frac{\partial\phi_f}{\partial r} = v_f = \frac{\partial\eta}{\partial t} + \frac{1}{r}\bar{u}_{f,i}\frac{\partial\eta}{\partial\theta}, \tag{14a}$$

$$\frac{\partial\phi_g}{\partial r} = v_g = \frac{\partial\eta}{\partial t} + \frac{1}{r}\bar{u}_{g,i}\frac{\partial\eta}{\partial\theta}. \tag{14b}$$

Combining both the boundary conditions corresponding to the solid walls and the interfacial kinematic conditions with Eqs. (6), (10a), and (12a) for the liquid layer, and Eqs. (6), (10b), and (12b) for the vapor layer gives, respectively,

$$\phi_f = A_f\theta + i(\bar{u}_{f,i} - c)\left[\frac{\left(\frac{r}{R_1}\right)^{kR_0} + \left(\frac{R_1}{r}\right)^{kR_0}}{\left(\frac{R_0}{R_1}\right)^{kR_0} - \left(\frac{R_1}{R_0}\right)^{kR_0}}\right]\eta, \tag{15a}$$

$$\phi_g = A_g\theta - i(\bar{u}_{g,i} - c)\left[\frac{\left(\frac{r}{R_2}\right)^{kR_0} + \left(\frac{R_2}{r}\right)^{kR_0}}{\left(\frac{R_2}{R_0}\right)^{kR_0} - \left(\frac{R_0}{R_2}\right)^{kR_0}}\right]\eta, \tag{15b}$$

Combining the Bernoulli equation for each phase with the mechanical equilibrium condition along the interface yields, for $r = R_0$,

$$P_f - P_g = \left[\frac{1}{2}\rho_g u_g^2 + \rho_g\frac{\partial\phi_g}{\partial t}\right] - \left[\frac{1}{2}\rho_f u_f^2 + \rho_f\frac{\partial\phi_f}{\partial t}\right]$$

$$= -\sigma\frac{\partial^2\eta}{\partial(R_0\theta)^2}. \tag{16}$$

Equation (16) can be reduced to give an expression for the pressure force exerted upon the interface:

$$P_f - P_g = [\rho_f'''(c - \bar{u}_{f,i})^2 + \rho_g'''(\bar{u}_{g,i} - c)^2]k\eta = \sigma k^2\eta, \tag{17}$$

where

$$\rho_f''' \equiv \rho_f \left[\frac{\left(\frac{R_0}{R_1}\right)^{2kR_0} + 1}{\left(\frac{R_0}{R_1}\right)^{2kR_0} - 1} \right], \quad (18a)$$

$$\rho_g''' \equiv \rho_g \left[\frac{\left(\frac{R_0}{R_2}\right)^{2kR_0} + 1}{1 - \left(\frac{R_0}{R_2}\right)^{2kR_0}} \right]. \quad (18b)$$

Solving Eq. (17) yields the following expression for c:

$$c = \frac{\rho_f''' \bar{u}_{f,i} + \rho_g''' \bar{u}_{g,i}}{\rho_f''' + \rho_g'''} \pm \sqrt{\frac{\sigma k}{\rho_f''' + \rho_g'''} - \frac{\rho_f''' \rho_g'''(\bar{u}_{g,i} - \bar{u}_{f,i})^2}{(\rho_f''' + \rho_g''')^2}}. \quad (19)$$

When the argument of the radical in Eq. (19) is negative, c acquires both real and imaginary components. In this case, $\eta = \eta_0 e^{kc_i t} \cos(k(R_0\theta - ct))$, and any interfacial perturbation becomes unstable and grows with time. Neutral stability occurs when $c_i = 0$. Setting the argument of the radical in Eq. (19) equal to zero gives

$$\lambda_c = \frac{2\pi}{k_c} = \frac{2\pi(\rho_f''' + \rho_g''')\sigma}{\rho_f''' \rho_g'''(\bar{u}_{g,i} - \bar{u}_{f,i})^2}. \quad (20)$$

Equations (17), (19), and (20) are presented here in forms that resemble those for a straight channel. The major differences between the two cases are the radial changes in phase velocities and pressure, which are manifested in the velocity terms, $\bar{u}_{f,i}$ and $\bar{u}_{g,i}$, and the new modified density terms, ρ_f''' and ρ_g'''.

CHF Model Predictions. The separated flow model given in the appendix was employed to predict local mean values of vapor layer thickness and velocities of the liquid and vapor layers in terms of inlet velocity, subcooling, and heat flux. These local values are required in order to predict the interfacial wavelength and $\overline{P_f - P_g}$.

CHF was predicted by following an iterative numerical procedure starting with a guessed value for q_m. First, this value is used in the separated flow model to determine the key parameters for the instability analysis. By discretizing z into 0.1 mm steps, an initial value for the vapor layer thickness, δ, is assumed and the interfacial vapor velocity, $\bar{u}_{g,i}$, is determined using Eq. (A.7) (since $\bar{u}_{g,i} = \bar{u}_{g,m}$), while the interfacial liquid velocity, $\bar{u}_{f,i}$, is calculated by combining Eqs. (A.5) and (A.8). The value of δ is then adjusted until the pressure calculated from the vapor layer momentum balance, Eq. (A.1), equals the interfacial liquid pressure, Eq. (A.3). The corresponding convergent values of δ, $\bar{u}_{g,i}$, and $\bar{u}_{f,i}$ are then used to calculate the critical wavelength, λ_c, using Eq. (20). The interfacial pressure difference, Eq. (17), is then averaged over the length of the most upstream wetting front, $0.25\lambda_c$, centered about the location $z = z^*$. Next, a new value for q_m is calculated using Eq. (6). In the second iteration, this newly obtained CHF value is applied through the same numerical procedure. Typically, the solution converged in less than five iterations.

Figure 9 shows that the CHF model predicts the experimental data for the straight heater (using the instability and separated flow models for a straight channel) and the curved heater with mean absolute errors of 7 and 14 percent, respectively. Some departure of the model predictions from the curved heater data at the higher end of the tested velocity range can be attributed to vapor slug detachment from wave peaks as depicted in Fig. 5, which is not accounted for in the present model. The accuracy of the model predictions is proof of the validity of both the new curved heater instability model and the assumptions used in constructing the surface energy balance and lift-off criterion. The CHF enhancement obtained with the curved heater over the straight heater is, therefore, a direct consequence of the increased curvature of the individual interfacial waves causing an increase in the net pressure force exerted upon the interface in the wetting fronts.

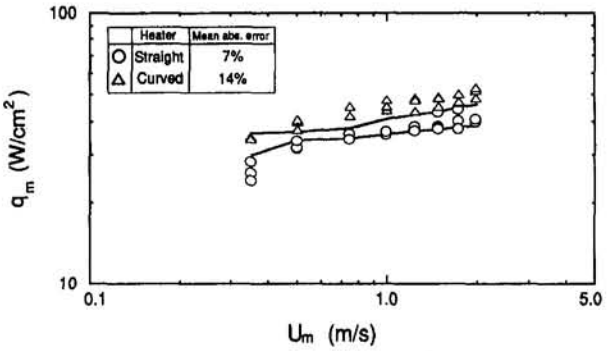

Fig. 9 Comparison of the model predictions and CHF data for the straight and curved heaters

As for the limitations of the present model, several conditions exist for which the assumptions of the model may not be valid. They include (*a*) near-critical pressure, (*b*) highly subcooled flow, where the vapor layer development may be strongly influenced by condensation along the vapor–liquid interface, (*c*) high inlet velocities corresponding to $g_n = U_m^2/R_2 > 10\ g_e$, where vapor slugs begin to detach from peaks in the wavy vapor–liquid interface, and (*d*) long heaters. A recent study by one of the authors (Gersey and Mudawar, 1995) explored the streamwise changes in the interfacial features at CHF over long heaters. The vapor waves between wetting fronts maintained equal wavelength over an axial distance close to the length of the heater used in the present study, but were found to grow downstream due to merging of adjacent waves. This behavior increased the distance between wetting fronts, resulting in smaller CHF for long heaters as compared with heaters close in size to the one used in the present study. These findings, while determined from straight heater experiments, clearly indicate the present model should not be applied to long straight or curved heaters.

6 Summary

Experiments were performed with both straight and curved heaters to ascertain the effect of streamwise curvature on CHF. Key conclusions from the study are as follows:

1 A fairly continuous wavy vapor layer was observed to engulf the heater surface at heat fluxes smaller than CHF with both the straight and curved heaters. Boiling was still active in wetting fronts where the interface of the vapor layer made contact with the heater surface. CHF was triggered when the normal momentum of the vapor produced in the wetting front exceeded the pressure force exerted upon the interface due to interfacial curvature.

2 At high velocities, the curvature caused vapor slugs to detach from peaks in the wavy vapor–liquid interface normal to, and away from the surface. No such behavior was observed with the straight heater.

3 Higher CHF was both measured and predicted for the curved heater, using a new instability model for curved flow, than for the straight heater due to the increased pressure resistance to interfacial separation in the case of the curved heater.

CHF data were predicted for the straight and curved heaters with mean absolute errors of 7 and 14 percent, respectively.

Acknowledgments

The authors are grateful for the support of the Office of Basic Energy Sciences of the U.S. Department of Energy (Grant No. DE-FE02-93ER14394). The authors also thank the Industrial Chemical Products Division of 3M Company for donating samples of Fluorinert FC-87 for the present study.

References

Costello, C. P., and Adams, J. M., 1963, "Burnout Heat Fluxes in Pool Boiling at High Accelerations," *Proc. 2nd Int. Heat Transfer Conf.,* Boulder, CO, pp. 255–261.

Fiori, M. P., and Bergles, A. E., 1970, "Model of Critical Heat Flux in Subcooled Flow Boiling," *Proc. 4th Int. Heat Transfer Conference,* Vol. 6, Versailles, France, pp. 354–355.

Galloway, J. E., and Mudawar, I., 1989, "Boiling Heat Transfer From a Simulated Microelectronic Heat Source to a Dielectric Liquid Film Driven by a Rotating Stirrer," *Heat Transfer in Electronics,* ASME HTD-Vol. 111, pp. 66–77.

Galloway, J. E., 1991, "Critical Heat Flux Enhancement in the Presence of Stream-wise Curvature," Ph.D. Thesis, School of Mechanical Engineering, Purdue University, West Lafayette, IN.

Galloway, J. E., and Mudawar, I., 1992, "Critical Heat Flux Enhancement by Means of Liquid Subcooling and Centrifugal Force Induced by Flow Curvature," *Int. J. Heat Mass Transfer,* Vol. 35, pp. 1247–1260.

Galloway, J. E., and Mudawar, I., 1993a, "CHF Mechanism in Flow Boiling From a Short Heated Wall—Part 1. Examination of Near-Wall Conditions With the aid of Photomicrography and High-Speed Video Imaging," *Int. J. Heat Mass Transfer,* Vol. 36, pp. 2511–2526.

Galloway, J. E., and Mudawar, I., 1993b, "CHF Mechanism in Flow Boiling From a Short Heated Wall—Part 2. Theoretical CHF Model," *Int. J. Heat Mass Transfer,* Vol. 36, pp. 2529–2540.

Gambill, W. R., and Green, N. D., 1958, "Boiling Burnout With Water in Vortex Flow," *Chem. Eng. Prog.,* Vol. 54, pp. 93–102.

Gersey, C. O., 1993, "Effects of Orientation and Heater Length on Critical Heat Flux From Discrete and Continuous Heaters," Ph.D. Thesis, School of Mechanical Engineering, Purdue University, West Lafayette, IN.

Gersey, C. O., and Mudawar, I., 1995, "Effects of Heater Length and Orientation on the Trigger Mechanism for Near-Saturated Boiling CHF—Part 1. Photographic and Statistical Characterization of the Near-Wall Interfacial Features," *Int. J. Heat Mass Transfer,* Vol. 38, pp. 625–642.

Gu, C. B., Chow, L. C., and Beam, J. E., 1989, "Flow Boiling in a Curved Channel," in: *Heat Transfer in High Energy/High Heat Flux Applications,* R. J. Goldstein, L. C. Chow, and E. E. Anderson, eds., ASME HTD-Vol. 119, pp. 25–32.

Hino, R., and Ueda, T., 1985a, "Studies on Heat Transfer and Flow Characteristics in Subcooled Flow Boiling—Part 1. Boiling Characteristics," *Int. J. Multiphase Flow,* Vol. 11, pp. 269–281.

Hino, R., and Ueda, T., 1985b, "Studies on Heat Transfer and Flow Characteristics in Subcooled Flow Boiling—Part 2. Flow Characteristics," *Int. J. Multiphase Flow,* Vol. 11, pp. 283–297.

Hughes, T. G., and Olson, D. R., 1975, "Critical Heat Fluxes for Curved Surface During Subcooled Flow Boiling," *Trans. Canadian Soc. Mech. Eng.,* Vol. 3, pp. 122–130.

Iverson, A. H., and Whitaker, S., 1988, "Progress in the Development of a New High Heat Load X-Ray Tube," *Proc. Society of Photo-Optical Instrumentation Engineers,* Vol. 914, *Medical Imaging II,* pp. 219–230.

Lamb, H., 1945, *Hydrodynamics,* 6th ed., Dover Publications, New York, p. 371.

Marto, P. J., and Gray, V. H., 1971, "Effects of High Acceleration and Heat Fluxes on Nucleate Boiling of Water in an Axisymmetric Rotating Boiler," NASA TN D-6307.

Milne-Thompson, L. M., 1960, *Theoretical Hydrodynamics,* 4th ed., Macmillan, New York, p. 409.

Miropol'skiy, Z. L., and Pikus, V. Y., 1969, "Critical Boiling Heat Fluxes in Curved Channels," *Heat Transfer—Soviet Research,* Vol. 1, pp. 74–79.

Mishra, P., and Gupta, S. N., 1979, "Momentum Transfer in Curved Pipes, 1. Newtonian Fluids," *Ind. Eng. Chem. Process Des. Dev.,* Vol. 18, pp. 130–137.

Mudawar, I., 1986, "Interfacial Instabilities of Air-Driven Liquid Films," *Int. Comm. Heat Mass Transfer,* Vol. 13, pp. 535–543.

Usenko, V. I., and Fainzil'berg, S. N., 1974, "Effects of Acceleration on the Critical Heat Load With the Boiling of Freons on Elements Having Small Transverse Dimensions," *High Temperature,* Vol. 12, pp. 490–495.

Zuber, N., Tribus, M., and Westwater, J. M., 1961, "The Hydrodynamic Crisis in Pool Boiling of Saturated and Subcooled Liquid," *Int. Dev. in Heat Transfer,* ASME, pp. 230–236.

APPENDIX

Separated Flow Model

Variations of the local mean vapor layer thickness and mean liquid and vapor velocities with angular position θ were predicted from a separated two-phase slip flow model. This model employs different velocities for the liquid and vapor phases and, since it does not match these velocities at the interface, an appropriate friction factor is used to match the interfacial shear stresses. The wavy vapor layer depicted in Fig. 5 was approximated as a smooth vapor layer, which increases in thickness in the flow direction due to vapor production in the upstream continuous wetting zone and in the wetting fronts. The radial pressure gradient is proportional to the density of the respective medium. Since the density of vapor is much smaller than that of liquid, the radial changes across the vapor layer are negligible compared to those across the liquid layer. Therefore, both the pressure and mean tangential velocity across the vapor layer can be assumed uniform in the radial direction.

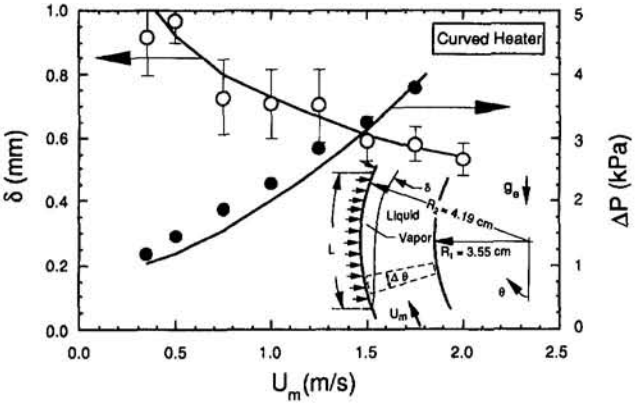

Fig. A.1 Comparison of separated flow model predictions and measurements of mean vapor layer thickness at z/L = 2/3 and pressure drop

Writing a momentum balance across the vapor portion of the differential control volume shown in Fig. A.1, neglecting radial changes in both vapor velocity and vapor pressure, gives

$$\rho_g \frac{d}{dz}(\bar{u}_{g,m}\delta) = \delta \frac{dP_i}{dz} - \tau_g\left(1 + \frac{2\delta}{s}\right) - \tau_i - \rho_g g_e \delta \sin(\theta), \quad \text{(A.1)}$$

where τ_g and τ_i are the wall and interfacial shear stresses, respectively, and $z = R_2\theta$.

The liquid layer thickness and liquid density are much greater than those of the vapor layer; hence, radial changes in velocity and pressure across the liquid layer cannot be ignored. Assuming the liquid flow is irrotational gives $\bar{u}_f = A_f/r$, where A_f is a function of θ only, which can be expressed in terms of the mean velocity across the liquid layer, $\bar{u}_{f,m}$, by integrating $\bar{u}_f$ from $r = R_1$ to $R_2 - \delta$:

$$A_f = \frac{\rho_f \bar{u}_{f,m}[(R_2 - \delta) - R_1]}{\int_{R_1}^{R_2-\delta} \rho_f \frac{1}{r}\, dr} = \left[\frac{(R_2 - \delta) - R_1}{\ln\left(\frac{R_2 - \delta}{R_1}\right)}\right] \bar{u}_{f,m}. \quad \text{(A.2)}$$

Integrating Euler's equation for the liquid, $dP_f/dr = \rho_f \bar{u}_f^2/r$, between any arbitrary radius r and the vapor–liquid

interface, $R_2 - \delta$, gives

$$P_f = P_i - \frac{1}{2}\rho_f \left[\frac{(R_2 - \delta) - R_1}{\ln\left(\frac{R_2 - \delta}{R_1}\right)}\right]^2 \left[\frac{1}{r^2} - \frac{1}{(R_2 - \delta)^2}\right] \bar{u}_{f,m}^2. \quad (A.3)$$

A momentum balance (per unit channel width) for the control volume shown in Fig. A.1 gives

$$\frac{d}{d\theta}(\rho_g \bar{u}_{g,m}^2 \delta) + \frac{d}{d\theta}\left[\int_{R_1}^{R_2-\delta} \rho_f \bar{u}_f^2 dr\right] = -\frac{d(P_i\delta)}{d\theta} - \frac{d}{d\theta}\left[\int_{R_1}^{R_2-\delta} P_f dr\right] - \tau_g\left[R_2 + \frac{2R_2\delta}{s}\right] - \tau_f\left[R_1 + \frac{1}{s}((R_2 - \delta)^2 - R_1^2)\right] - \rho_g R_2 \delta g_e \sin(\theta) - \rho_f\left[\frac{(R_2 - \delta)^2 - R_1^2}{2}\right] g_e \sin(\theta). \quad (A.4)$$

The shear stresses in Eqs. (A.1) and (A.4) are defined, respectively, as $\tau_g = 0.5 f_g \rho_g \bar{u}_{g,m}^2$, $\tau_f = 0.5 f_f \rho_f \bar{u}_{f,m}^2$, and $\tau_i = 0.5 f_i \rho_g (\bar{u}_{g,m}^2 - \bar{u}_{f,i}^2)^2$, where, from Eq. (A.2),

$$\bar{u}_{f,i} = \left[\frac{(R_2 - \delta) - R_1}{\ln\left(\frac{R_2 - \delta}{R_1}\right)}\right] \frac{\bar{u}_{f,m}}{R_2 - \delta}. \quad (A.5)$$

The wall friction factors f_f and f_g were determined from the following curved channel flow correlation (Mishra and Gupta, 1979):

$$f = \frac{0.079}{\mathrm{Re}^{0.25}} + 0.0075\left(\frac{D_h}{2R_2}\right)^{0.5}, \quad (A.6)$$

where Re was based on the hydraulic diameter, D_h, for the liquid or vapor layer cross section and respective mean velocity. For infinite values of R_2 (straight heater), Eq. (A.6) reduces to the Blasius equation for turbulent channel flow.

An approximate range for the interfacial friction factor, f_i, was determined from a study of air flow over solid waves (Mudawar, 1986) having features resembling those observed in the present study. A constant value of 0.5 provided the best agreement between measured and predicted pressure drop and mean vapor layer thickness in the study of CHF over a straight heater (Galloway and Mudawar, 1993b). Gersey (1993) validated the accuracy of setting $f_i = 0.5$ by examining numerous correlations in the two-phase literature for wavy vapor–liquid interfaces. The same value was used in the present study for predicting the curved channel flow parameters.

The momentum Eqs. (A.1) and (A.4) yield two differential equations relating P_i, δ, $\bar{u}_{g,m}$, and $\bar{u}_{f,m}$. Two additional differential equations can be written using mass conservation for the vapor and liquid layers, respectively:

$$\bar{u}_{g,m} = \frac{q_m z}{\rho_g \delta (c_{p,f}\Delta T_{\mathrm{sub}} + h_{fg})}. \quad (A.7)$$

$$\bar{u}_{f,m} = \frac{U_m(R_2 - R_1)}{(R_2 - \delta) - R_1} - \frac{q_m z}{\rho_f((R_2 - \delta) - R_1)(c_{p,f}\Delta T_{\mathrm{sub}} + h_{fg})}. \quad (A.8)$$

Figure A.1 shows that the separated flow model gives excellent predictions of both pressure drop and mean vapor layer thickness at heat fluxes approaching CHF. These results validate the accuracy of the separated flow model independent from the other submodels presented in this paper for predicting CHF. The pressure drop data were measured with an uncertainty of 0.1 kPa.

The key parameters required in the curved heater instability model are δ, $\bar{u}_{f,i}$, and $\bar{u}_{g,i}$. Knowing $\bar{u}_{f,m}$, Eq. (A.5) can be used to determine $\bar{u}_{f,i}$, and, because of the small density of vapor, $\bar{u}_{g,i} = \bar{u}_{g,m}$.

X. Xu[1]

C. P. Grigoropoulos

Department of Mechanical Engineering,
University of California,
Berkeley, CA 94720

R. E. Russo

Energy and Environmental Division,
Lawrence Berkeley Laboratory,
Berkeley, CA 94720

Heat Transfer in Excimer Laser Melting of Thin Polysilicon Layers

A pulsed KrF excimer laser with nanosecond pulse duration is used for surface melting of thin polycrystalline silicon films. The velocity of the moving phase boundary during melting and solidification, the maximum melting depth, as well as the melting duration are experimentally determined by combined optical and electrical methods. A melting interface tracking model is used to calculate the melt front propagation and the transient temperature field in the semiconductor. A phase-change model, which allows the occurrence of melting and solidification at temperatures other than the equilibrium melting temperature, is employed in the numerical calculation. The effect of interfacial superheating/undercooling is discussed.

I Introduction

Interactions of pulsed laser irradiation with matter may lead to controlled phase transformations and material structure modifications. In semiconductor systems pulsed laser irradiation is used to anneal ion-implantation surface damage, recrystallize amorphous and polycrystalline films, and enhance dopant diffusion. Both experimental and computational investigations of pulsed laser interactions with semiconductor materials have been performed. Transient electrical conductance measurements (Thompson and Galvin, 1985; Tsao et al., 1986), nanosecond resolved x-ray diffraction measurements (Larson et al., 1983), and transient reflectivity measurements (Jellison et al., 1986) have been applied to obtain quantities such as melt penetration, melt duration, and melt-front velocities. Numerical heat transfer computations were used indirectly to obtain the transient temperature field (Sasik and Cerny, 1991; Wood and Geist, 1986a). The experimental results were interpreted by numerical simulations to show that the pulsed laser melting of semiconductors in the nanosecond time regime is a thermal phenomenon.

Melt/solid interface velocities in pulsed laser melting and recrystallization of silicon can exceed 15 m/s (Jellison et al., 1986). At such high velocities, the phase change is no longer expected to be an equilibrium process, and the assumption of a constant, thermodynamic equilibrium phase-change temperature is no longer valid (Jackson, 1975). The complex melting and solidification behavior with interface superheating/undercooling has been studied numerically by Wood and Geist (1986b). These investigators extended an enthalpy-based approach to allow simulation of strong undercooling and superheating, and provide a description of nucleation effects. Sasik and Cerny (1991) presented an interface tracking finite element approach to model the phase boundary propagation, including allowance for nonisothermal interface conditions.

The present work examines the transient heating and melting of thin polysilicon (p-Si) layers irradiated by pulsed excimer laser. Experiments are performed under well-controlled conditions, so that experimental results can be compared with numerical simulations. The transient heating process is probed by reflectivity and transmissivity measurements. Transient electrical conductivity measurements are applied to provide the motion of the melt/solid interface. The transient temperature field is calculated via a conductive heat transfer model, which includes the analysis of melting and resolidification by applying an interface tracking finite difference algorithm. This scheme is extended to analyze superheating/undercooling effects that accompany phase change by considering kinetic transition rates. Thin film optics (Born and Wolf, 1980) is used to obtain the optical response based on the calculated temperature field. The effects of superheating and undercooling are studied.

II Experimental Procedure

A schematic drawing of the experimental setup is shown in Fig. 1. A pulsed KrF excimer laser is used to heat the sample. The pulse duration of the excimer laser beam is measured using a fast silicon PIN photo diode with a rise/fall time less than 1 ns and a digitizing oscilloscope with 1 GHz sampling speed (1 ns time resolution). The laser pulse energy is monitored by an energy meter, which receives the laser light reflected from a beamsplitter. The fractional uncertainty in the laser pulse fluence measurement, $\delta F/F$, is 10 percent. The spatial uniformity of laser light is crucial for a planar melt interface propagation. However, the light emitted from the aperture of the excimer laser has a large spatial intensity variation. A tunnel-type beam homogenizer is used to improve the uniformity of the laser light. The output light from the homogenizer has a spatial intensity variation less than 5 percent, over the central 95 percent portion of the laser beam spot. A series of lenses is used to focus the excimer laser light onto the sample surface at normal incidence. The area of the excimer laser beam spot at the sample surface is approximately 0.15 cm^2.

A 0.1 mW continuous wave (CW) unpolarized HeNe laser is used as the probing light source for the reflectivity and transmissivity measurements. The HeNe laser beam is focused at the center of the excimer laser irradiated area by a spherical lens, at the angle of incidence, $\theta_{probe} = 16°$. The diameter of the HeNe laser beam on the sample is measured to be 50 μm. The reflection and transmission of HeNe laser light are focused onto fast silicon PIN photo diodes. The fast digitizing oscilloscope used for data acquisition is triggered by a detector, which senses scattered excimer laser light from a mirror. The accuracies in the absolute reflectivity and transmissivity measurement are estimated to be $\delta R = 0.01$, and $\delta\tau = 0.01$. The room temperature normal incidence reflectivity ($R = 0.36$) and transmissivity ($\tau = 0.44$) are measured to determine the complex refractive index of polysilicon at the $\lambda = 633$ nm wavelength using thin film optics. All connecting cables, detectors, and electronic components are properly shielded to avoid the strong RF interference from the excimer laser.

[1] Present address: School of Mechanical Engineering, Purdue University, West Lafayette, IN 47907.

Contributed by the Heat Transfer Division and presented at the 6th AIAA/ASME Thermophysics and Heat Transfer Conference, Colorado Springs, Colorado, June 19–23, 1994. Manuscript received by the Heat Transfer Division October 1993; revision received May 1994. Keywords: Laser Processing, Materials Processing and Manufacturing Processes, Radiation. Associate Technical Editor: M. F. Modest.

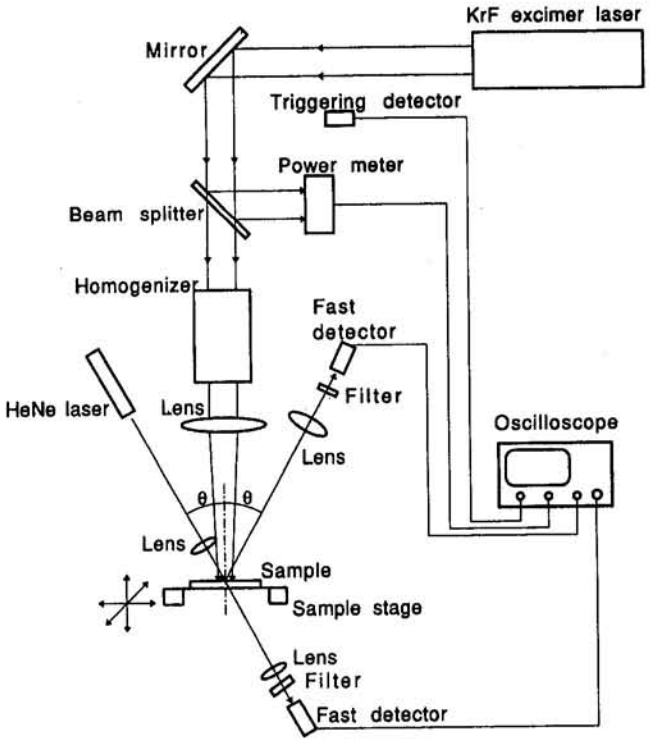

Fig. 1 Experimental setup for optical reflectivity, transmissivity, and electrical conductance measurement during excimer laser melting of polysilicon films

The structure of the sample is shown in Fig. 2. Polycrystalline silicon film 0.20 μm thick is deposited on fused-quartz substrate by LPCVD (Low Pressure Chemical Vapor Deposition) at a temperature of 605°C, and a pressure of 550 mtorr. The microstructure of the polysilicon film was studied by cross section TEM (Transmission Electron Microscopy). It is found that the grain sizes of the polysilicon film vary from 200 Å to 700 Å, and are randomly distributed across the thin film. The thickness of the sample is measured by an α-step profilometer, with an accuracy of 10 nm. Silicon film patterns are made by photolithography, which ensures an accuracy of 2 μm in the lateral dimensions. Aluminum contacts with thickness of 0.2 μm are made by sputtering, which is followed by a lift-off procedure. The aluminum-silicon contact is sintered in dry nitrogen at a temperature of 400°C for 20 minutes.

Transient electrical resistance across the p-Si strip is measured to obtain the melting front position. The electrical resistivity of liquid silicon is lower than that of solid silicon by five orders of magnitude ($\sigma_s = 0.3\ \Omega^{-1}\ \mathrm{cm}^{-1}$, $\sigma_l = 12860 - 8.6 \times (T\,(\mathrm{K}) - 1732)\ \Omega^{-1}\ \mathrm{cm}^{-1}$, Glazov et al., 1969). When the surface of the silicon film is melted, the total resistance of silicon is reduced drastically. The measured transient voltage signal across the p-Si sample yields the depth of the molten layer with nanometer resolution. Such a measurement accuracy can only be achieved for the materials with a large resistance change upon melting. The sensitivity of the measurement also depends on the sample geometry, i.e., the length-to-width ratio, l/w (Fig. 2). In general, a larger length-to-width ratio gives higher sensitivity for measuring a thicker molten layer; a small length-to-width ratio gives higher sensitivity to measure a thinner molten layer. Once the p-Si film starts to melt, the total resistance of the film in principle should be calculated by considering the resistance of a liquid film in parallel to the resistance of a solid film. Since liquid silicon has a much lower resistivity than solid silicon, the resistance of the solid silicon layer can be neglected. Referring to Fig. 2, the resistance of the film, R_{si}, and the melt depth, d_{melt}, can be calculated as:

$$R_{si}(t) = \frac{R_0 V_{si}(t)}{V_0 - V_{si}(t)}, \quad d_{melt}(t) = \frac{l}{w\sigma R_{si}(t)} \tag{1}$$

where l and w are the length and width of the silicon strip. In this experiment, the length l varies from 3.6 mm to 6 mm and the width w is 1 mm. The electrical circuit is biased by a voltage V_0, and includes a resistor, $R_0 = 100\ \Omega$.

Nomenclature

$[A]$ = tridiagonal matrix (Eq. (14*a*))
$\mathbf{b}$ = known right-hand-side vector (Eq. (14*a*))
C_p = specific heat
C_0, C_1 = constants in phase-change kinetic relation
d_p = optical absorption depth
d_{melt} = molten silicon thickness
F = laser fluence
i = imaginary unit
I = laser intensity
IF = number of discretization intervals in the silicon film
IM = number of discretization intervals in the melted portion of the silicon film
IT = total number of discretization intervals
k = thermal conductivity
k_B = Boltzmann constant
k_{ext} = extinction coefficient of silicon
l = length of the polysilicon sample
L = latent heat of fusion
n = real part of the complex refractive index
$\hat{n}$ = complex refractive index
Q = activation energy
Q_{ab} = power absorbed by the thin silicon layer
R = reflectivity
R_0 = resistance
R_M = rate of melting
R_M^0 = rate of melting at equilibrium
R_F = rate of solidification
R_F^0 = rate of solidification at equilibrium
t = time
t_p = pulse duration of excimer laser
T = temperature
T_{eq} = equilibrium melting temperature
T_{int} = temperature of solid/liquid interface
$\mathbf{u}^{p+1}$ = unknown variable vector (Eq. (14*a*, *b*))
V_{int} = interfacial velocity
V_0 = bias voltage
V_{si} = voltage across polysilicon sample
w = width of the polysilicon sample
x = coordinate in the normal to the sample surface direction
X_{int} = interface measured from the location of the surface of the solid layer
γ = absorption coefficient
δ = uncertainties in measurement
ΔT = interfacial undercooling = $T_{eq} - T_{int}$
ζ = dimensionless melt front position = X_{int}
θ = dimensionless temperature
θ_{probe} = incident angle of probing HeNe laser
λ = laser light wavelength
ρ = density
σ = electric conductivity
τ = transmissivity

Subscripts

exc = excimer laser
i = nodal point
l = liquid silicon
probe = probing HeNe laser
s = solid silicon

Superscripts

p = time step

The resistance of the sample drops when the sample surface melts. Another effect that reduces the sample resistance is "photoconductivity." The photoconductivity signal, caused by laser excited free carriers in semiconductors, could last for microseconds in pure, undoped polysilicon. To reduce the excited free carrier life time, so as to reduce the photoconductivity signal, gold is evaporated onto the polysilicon film surface and diffused into the polysilicon film by convective heating. Gold is selected because it is a deep level impurity, which can reduce the free carrier life time in the indirect band gap semiconductors, and because it diffuses rapidly in silicon. Using a diffusion equation (Ghandhi, 1983), it is found that the Au dopant concentration reaches the room temperature solubility ($10^{13}/cm^3$) throughout the film. As will be seen in Section IV, the photoconductance signal in this gold diffused sample is completely separated from the conductance signal caused by phase change. Gold evaporation and diffusion are performed at temperatures below the Si/Au eutectic temperature (370°C), so that Si/Au alloy is not formed, and the microstructure of the film is not expected to be changed.

III Numerical Modeling

III.1 One-Dimensional Conductive Heat Transfer Model. The dimensions of the laser beam spot on the sample surface are of several millimeters, while the penetration depth of the temperature profile is on the order of 10 μm. Therefore, it may be assumed that the heat transfer at the center of the laser beam is essentially one dimensional. The conductive heat transfer, both in the solid and in the liquid silicon, is given by:

$$(\rho C_p)(T)\frac{\partial T}{\partial t} = \frac{\partial}{\partial x}\left(k(T)\frac{\partial T}{\partial x}\right) + Q_{ab}(x, t) \tag{2}$$

The boundary conditions at the solid/liquid phase change interface are:

$$T_s(X_{\text{int}}) = T_l(X_{\text{int}}) = T_{\text{int}} \tag{3a}$$

$$k_s \left.\frac{\partial T_s}{\partial x}\right|_{x=X_{\text{int}}} - k_l \left.\frac{\partial T_l}{\partial x}\right|_{x=X_{\text{int}}} = \rho_s L V_{\text{int}} \tag{3b}$$

The energy absorption, $Q_{ab}(x, t)$, follows an exponential decay in the material:

$$Q_{ab}(x, t) = (1 - R_{\text{exc}})I(t)\gamma e^{-\gamma x} \tag{4}$$

The normal reflectivity of the silicon surface and the absorption coefficient, γ, are given by:

$$R_{\text{exc}} = \frac{(n_{\text{exc}} - 1)^2 + k_{\text{exc}}^2}{(n_{\text{exc}} + 1)^2 + k_{\text{exc}}^2} \tag{5}$$

$$\gamma = \frac{4\pi k_{\text{exc}}}{\lambda_{\text{exc}}} \tag{6}$$

The reflectance R_{exc} is measured at room temperature by a spectrophotometer, $R_{\text{exc}} = 0.24$. Using a spectroscopic ellipsometer, the complex refractive index at the $\lambda_{\text{exc}} = 248$ nm wavelength is determined to be $\hat{n}_{\text{exc}} = 1.45 + i1.29$, which also yields a normal reflectivity of 0.24 using Eq. (5). The complex refractive index data for crystalline silicon (c-Si) at elevated temperatures (Jellison and Modine, 1982) show a weak dependence on temperature in the ultraviolet (UV) range. To the authors' knowledge, no such data for polysilicon have been reported in the literature. It is assumed that the polysilicon complex refractive index at the excimer laser wavelength of 248 nm is not temperature dependent. However, the complex refractive index of polysilicon does show temperature dependence at the probing beam wavelength, $\lambda_{\text{probe}} = 633$ nm, forming the basis of the reflectivity and transmissivity measurement (Xu et al., 1993a, 1995). The refractive index of liquid silicon is given by Shvarev et al. (1975).

The incident laser intensity considered in this problem is so high (of the order of 10^{12} W/m^2) that convection and radiation losses from the top of the surface are negligible. For the time scales considered in this work, the temperature penetration depth into the substrate is small (about 10 μm), so that the bottom substrate surface remains at the ambient temperature. Initially the structure is at the ambient temperature. Thermal properties of bulk materials are used in the calculations. Due to the microstructure of thin film materials, thermal properties of thin film materials can be different from those of bulk materials. The effects of possible deviations of the thermal properties of thin film materials are discussed elsewhere (Xu et al., 1995).

III.2 Superheating/Undercooling Effects. When the melt/solid interface moves with a finite velocity, the temperature at the interface is expected to deviate from the equilibrium melting temperature. The relation between the interfacial undercooling, $\Delta T = T_{eq} - T_{\text{int}}$, and the interface velocity is given by the kinetic theory of crystal growth from the melt (Jackson, 1975). According to the quasi-chemical formulation of this theory, the rate at which atoms join the crystal is:

$$R_F = R_F^0 \exp\left[-\frac{Q}{k_B T_{\text{int}}}\right] \tag{7}$$

where k_B is the Boltzmann constant, T_{int} is the interface temperature, and Q is the activation energy for viscous or diffusive motion in the liquid. Similarly, the rate at which atoms leave the crystal is:

$$R_M = R_M^0 \exp\left[-\frac{Q + L}{k_B T_{\text{int}}}\right] \tag{8}$$

where L is the latent heat of fusion of the phase transformation, and $Q + L$ is the activation energy for melting. At equilibrium, the rates for solidification and melting are equal, $R_F = R_M$, and the interface temperature equals the equilibrium melting temperature, $T_{\text{int}} = T_{eq}$. Combining Eqs. (7) and (8), the following relation is obtained at the solid/liquid interface at equilibrium:

$$\frac{R_M^0}{R_F^0} = \exp\left[-\frac{L}{k_B T_{eq}}\right] \tag{9}$$

The velocity of the moving melt/solid interface as the material solidifies ($V_{\text{int}}(T_{\text{int}}) > 0$), or melts ($V_{\text{int}}(T_{\text{int}}) < 0$) is given by:

$$V_{\text{int}}(T_{\text{int}}) = R_F - R_M \tag{10}$$

Utilizing Eqs. (8) and (9), the velocity of the moving front can be expressed as:

$$V_{\text{int}}(T_{\text{int}}) = C_0 \exp\left[-\frac{Q}{k_B T_{\text{int}}}\right]\left\{1 - \exp\left[-\frac{L\Delta T}{k_B T_{\text{int}} T_{eq}}\right]\right\} \tag{11}$$

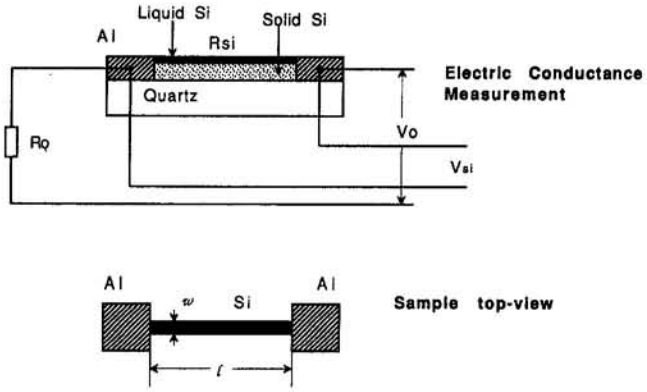

Fig. 2 Sketch of sample and conductance measurement circuit

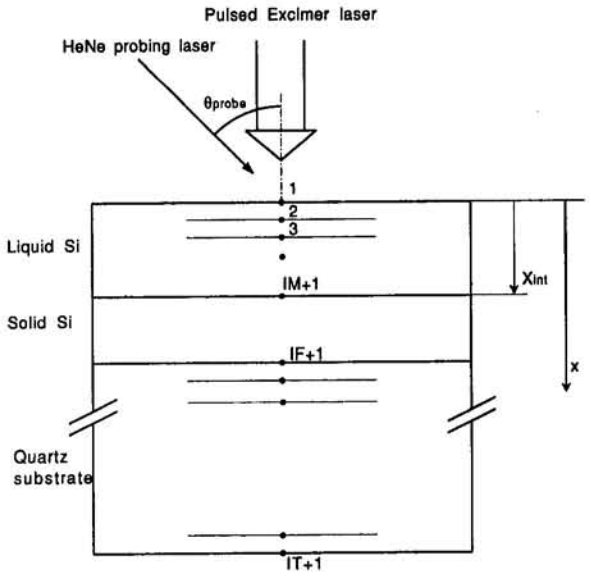

Fig. 3 Schematic of the multilayer, stratified structure

where

$$C_0 = R_M^0 \exp\left[-\frac{L}{k_B T_{eq}}\right]; \quad \Delta T = T_{eq} - T_{\text{int}}.$$

Equation (11) can be approximated by a linear relation between the interface velocity, V_{int}, and the superheating temperature ΔT at the interface:

$$\Delta T = C_1 V_{\text{int}}(T_{\text{int}}) \tag{12}$$

The material constant C_1, which quantifies the effect of the interface velocity on the superheating temperature ΔT, represents the degree of interface superheating. It was determined to be 9.8 K/(m/s) by fitting Eq. (12) to direct molecular dynamics predictions of the interfacial velocity as a function of the superheating temperature for epitaxial silicon crystal growth from the liquid phase (Kluge and Ray, 1989). The constant C_1 is taken as 10 K/(m/s) in the calculation.

III.3 Interface Tracking Algorithm. To solve the heat transfer equation with phase change, a system of coordinates is attached to the moving interface. The heat conduction equation is written in this system of coordinates as:

$$(\rho C_p)(T)\left[\frac{DT}{Dt} - \frac{\partial T}{\partial x}\frac{dx}{dt}\right] = \frac{\partial}{\partial x}\left(k(T)\frac{\partial T}{\partial x}\right) + Q_{ab}(x,t) \tag{13}$$

In this equation DT/Dt is the substantial total time derivative, and dx/dt is the material velocity. Equation (13), with the interface condition, Eq. (3), the kinetic relation, Eq. (12) and the boundary and initial conditions, are solved numerically to yield the transient temperature field and the position of the moving interface. The computational domain in the x direction is discretized into a constant number of intervals (Fig. 3). The node $i = 1$ is located at the silicon layer surface, the node $i = IM + 1$ is fixed at the solid/liquid phase boundary, and the node $i = IF + 1$ is placed on the silicon/substrate interface. The total number of nodes used for the entire structure is $IT + 1$. A Crank–Nicolson numerical scheme is used to discretize the heat conduction equation for the $i = 2, \ldots IM$, $i = IM + 2, \ldots IT$, and the boundary conditions applied on the nodes $i = 1$, and $i = IT + 1$. The number of nodes used in the computation for liquid silicon, solid silicon, and substrate are 20, 100, and 20, respectively. First-order accurate forward finite difference expressions are used for the time derivatives, whereas second-order accurate, central difference approximations are used for the spatial derivatives. The discretized governing Eq. (13) and the interface Eq. (3b) are cast in a dimensionless form:

$$[A]\cdot \mathbf{u}^{p+1} = \mathbf{b}^p \tag{14a}$$

$$\mathbf{u}^{p+1} = (\theta_1^{p+1}, \theta_2^{p+1}, \ldots, \theta_{\text{IM1}}^{p+1}, \theta_{\text{IM}}^{p+1}, \zeta_{\text{IM+1}}^{p+1}, \theta_{\text{IM+2}}^{p+1}, \theta_{\text{IM+3}}^{p+1}, \ldots, \theta_{\text{IT+1}}^{p+1}) \tag{14b}$$

where θ and ζ are dimensionless variables of temperature and melt front position, respectively, [A] is a $IT + 1 \times IT + 1$ square matrix containing material property, grid spacing, and time interval data. In addition, the vector $\mathbf{b}$ of length $IT + 1$ contains temperature and interfacial position data at the old time step.

Other formulations of moving boundary problems require a separate iterative calculation in the solid phase, the liquid phase, and the interface condition to solve the new temperature field and transient interface position (Griffith and Nassersharif, 1990). In contrast, the linear system developed in Eq. (14) can be solved directly by the Thomas algorithm. Computationally, Eq. (14) and the associated kinetic relation, Eq. (12), are implemented by the following procedure: (*i*) initially the interface temperature is assumed equal to the equilibrium melting temperature, T_{eq}. (*ii*) The system of Eq. (14) is solved, and consequently the interface velocity V_{int} is obtained. (*iii*) A new estimate of the interface temperature, T_{int}, is derived using Eq. (12). (*iv*) Steps (*ii*) and (*iii*) are repeated until convergence is achieved. When the temperature field is obtained, the transmissivity of the sample at the $\lambda_{\text{probe}} = 633$ nm wavelength is calculated using thin film optics theory (Born and Wolf, 1980; Xu et al., 1993b).

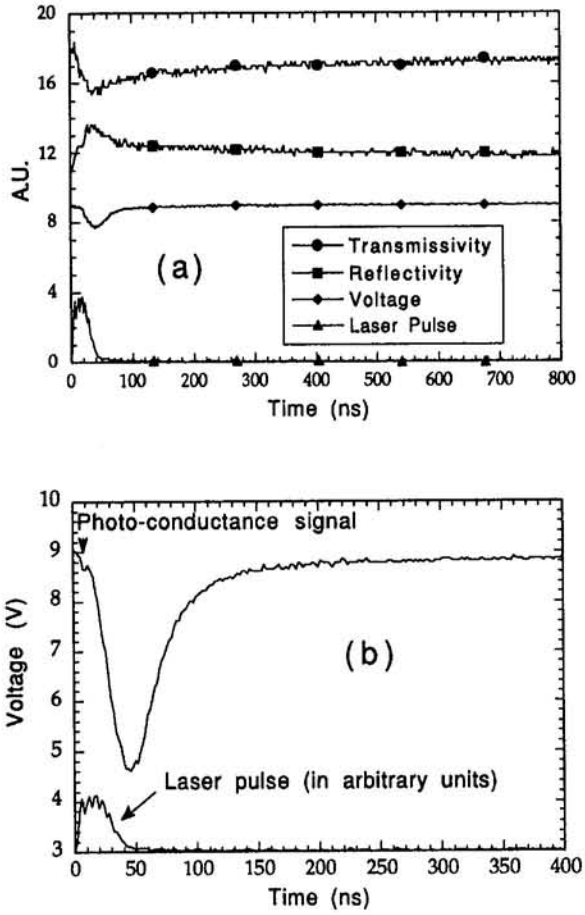

Fig. 4 (*a*) Reflectivity, transmissivity and electric conductance signals at the laser fluence slightly above the melting threshold; (*b*) electric conductance signal at the laser fluence $F = 0.32$ J/cm^2

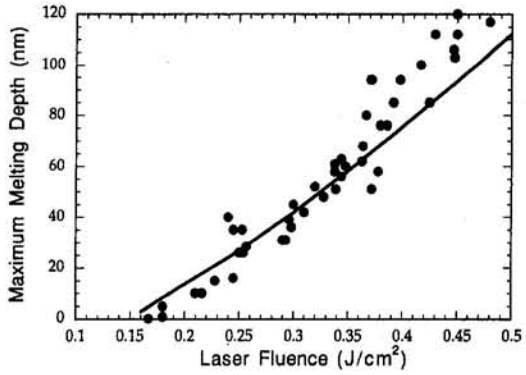

Fig. 5 Comparison between measured (dots) and calculated (solid line) maximum melting depth at different laser fluences

IV Results and Discussion

Typical transient reflectivity, transmissivity, and conductivity signals are shown in Fig. 4. In Fig. 4(a), the laser fluence is just above the melting threshold. Due to the temperature dependence of the complex refractive index of silicon at the $\lambda_{probe} = 633$ nm wavelength, the reflectivity of solid silicon increases with temperature. The reflectivity reaches 0.73 at about $t = 30$ ns, at which time the p-Si is melted. The transmission signal decreases when temperature increases, and drops to zero when the sample is melted to a depth of a few nanometers. In Fig. 4(a), the reflectivity and transmissivity signals do not recover their original values at the time of 800 ns. The electrical voltage signal drop at about 30 ns is due to the melting of the sample surface. In Fig. 4(b), the laser fluence, $F = 0.32$ J/cm^2, is substantially higher. The initial voltage drop (marked by the arrow in Fig. 4b) is caused by photoconductance. The second voltage drop is due to the resistance drop of the silicon layer that accompanies melting. The magnitude of the electrical signal drop due to phase change is much larger than the initial voltage drop caused by photoconductance. It is clear that the photoconductance signal is completely separated from the electrical signal caused by phase change.

Figure 5 shows the calculated and measured maximum melting depths as a function of the excimer laser beam fluences. The solid line shows the calculation results, and the dots are experimental values. The melting threshold fluence, determined by both the experiment and the calculation, is 0.14 J/cm^2. This value is significantly smaller than the melting threshold fluence for undoped silicon. This is because the reflectance of the Au-doped sample at the $\lambda_{exc} = 248$ nm wavelength, which is measured to be 0.24, is much lower than that of the crystalline silicon ($R_{exc} = 0.66$).[2] The measured maximum melting depths agree with the calculated melting depths. Figure 6(a) shows the melting duration determined by the conductance measurements and the by the numerical simulation. At high fluences ($F > 0.4$ J/cm^2) the measured melting duration is longer than the calculated results. Melting duration is also determined from transmissivity measurement (Fig. 6b). The melting duration is taken as the time period over which the transmissivity stays at zero. This assumption gives a lower value for the melting duration because the penetration depth, d_p, in the liquid silicon at the HeNe laser wavelength is about 10 nm. Toward the end of liquid solidification, the liquid layer thickness becomes less than d_p, and the transmissivity starts to rise. The error in determining melting duration from transmissivity measurement is estimated to be 10 percent. A comparison

[2] The *major* reason for this drastic difference in reflectivity is due to the doping of Au, rather than to the difference in microstructure between the thin film material and the bulk, since the reflectivities of undoped polysilicon films are measured to be between 0.6 and 0.7.

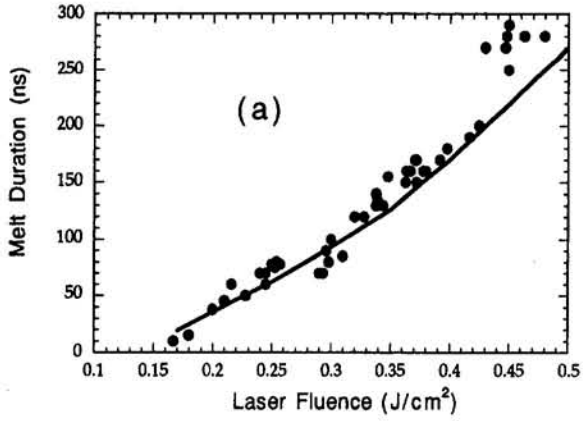

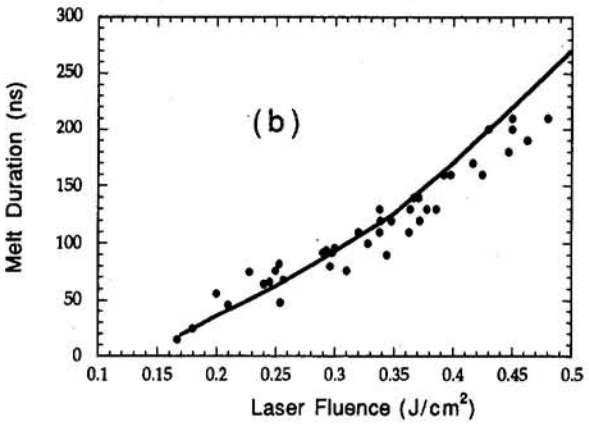

Fig. 6 Comparison between measured (dots) and calculated (solid line) melting duration at different laser fluences: (*a*) the measured results were determined from electric conductance experiment; (*b*) the measured results were determined from optical transmissivity experiment

between the measured and calculated transmissivity is shown in Fig. 7, at a fluence $F = 0.32$ J/cm^2.

Figures 8(a–c) compare the measured transient melting depths with the numerical results for three laser fluences. The maximum melting depth and melt duration (also illustrated in Figs. 5 and 6) agree well with the numerical results. The long-lasting "tail" in the transient voltage signal of melting could be ascribed to liquid undercooling, as suggested by Palmer and Marinero (1987). The melting and resolidification velocity can be determined from the slope of the melting front, and is shown in Figs. 9(a–c). It is noted that the time differentiation of discrete experimental data amplifies the digitization error and produces

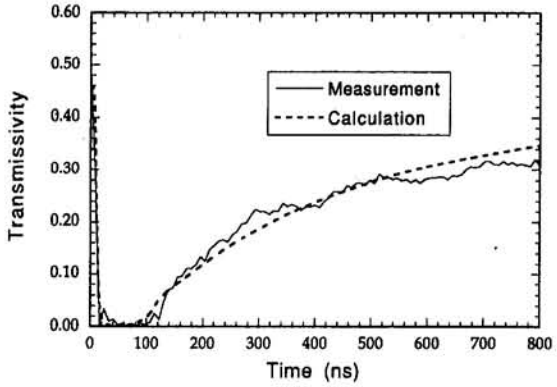

Fig. 7 Comparison between measured and calculated transmissivity: F = 0.32 J/cm^2

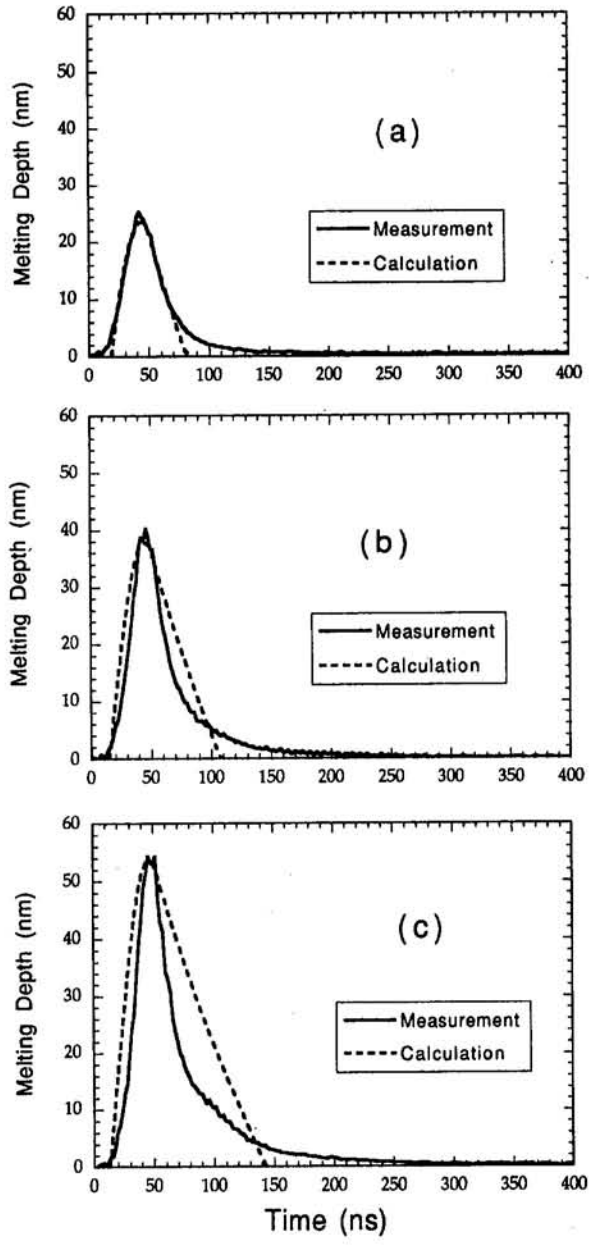

Fig. 8 Comparison between measured and calculated melting depth: (a) $F = 0.25$ J/cm^2, (b) $F = 0.30$ J/cm^2, (c) $F = 0.35$ J/cm^2

curves that appear rather noisy. The experimental maximum resolidification speed determined from Figs. 8(a–c) is higher than the numerical results. The resolidification speed gradually slows to zero, resulting in a longer and slower resolidification process before the molten layer completely solidifies. In contrast, the calculated solidification speed is almost constant during the entire solidification process.

The transient temperature field is obtained from numerical calculation. Figure 10 shows computed surface temperature for several laser fluences. The maximum surface temperatures differ by less than 50 K for all the cases since most of the laser energy is consumed by the latent heat of phase change. The plateau in temperature following shortly after the laser pulse is due to the slower solidification process. The maximum temperature reached in the experiment does not exceed the boiling point (2628 K) of liquid silicon. It is thus assumed that no silicon is evaporated. Figure 11 shows the temperature profile within the silicon film, for a laser fluence of 0.35 J/cm^2, at different time steps. The temperature gradient in the silicon film, which is within the depth of 0 to about 0.2 μm, is the highest at the initiation of melting (t = 15 ns), and the temperature field quickly becomes uniform throughout the silicon layer. On the other hand, numerical calculation shows that the nonuniformity of the laser beam profile (about 5 percent in this experiment) could cause 20 percent underestimation of the melt depth.

Experimental errors in the resistance measurement of melt depth could arise from the Si/Al contact resistance and the spatial nonuniformity of the laser power. The contact resistance is estimated to be around 2 Ω, which is smaller than the liquid silicon resistance (>20 Ω) at the largest melting depth achieved in the experiment (about 100 nm). When the melt depth is small, the liquid silicon resistance is much larger than the contact resistance, so that the contact resistance can be neglected. On the other hand, numerical calculation shows that the nonuniformity of the laser beam profile (about 5 percent in this experiment) could cause 20 percent underestimation of the melt depth. But laser beam nonuniformity has a negligible effect for deeper melting.

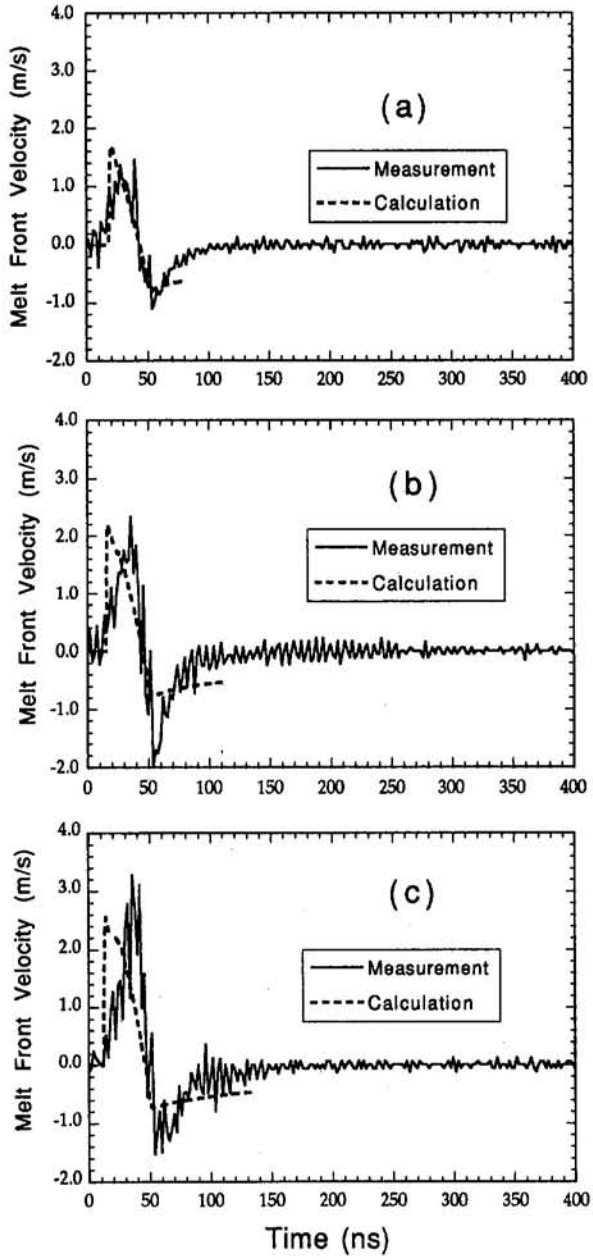

Fig. 9 Comparison between measured and calculated melting front velocity: (a) $F = 0.25$ J/cm^2, (b) $F = 0.30$ J/cm^2, (c) $F = 0.35$ J/cm^2

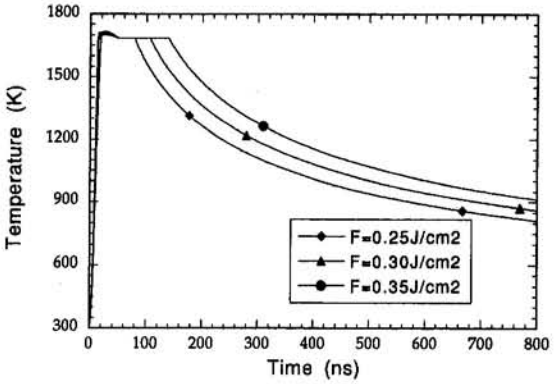

Fig. 10 Calculated transient surface temperature

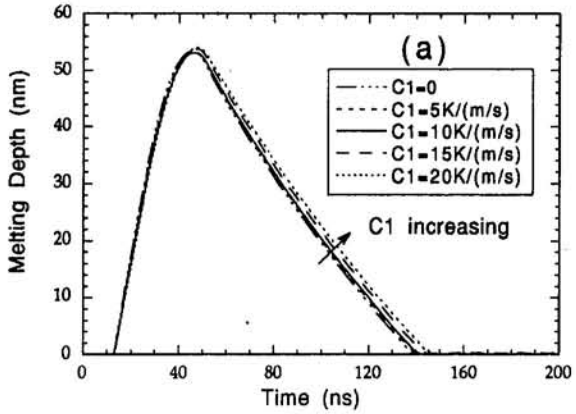

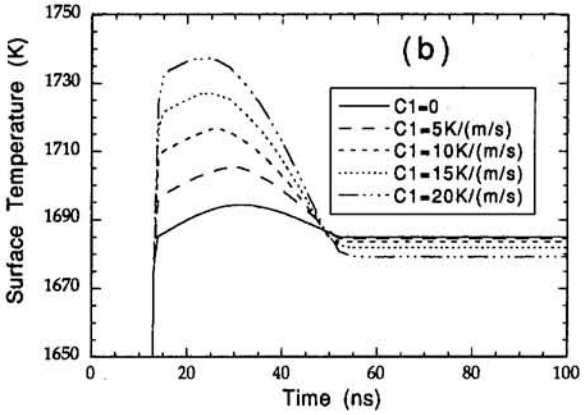

Fig. 12 (a) Calculated melting depth at different superheating levels: F = 0.35 J/cm²; (b) calculated surface temperature at different superheating levels: F = 0.35 J/cm²

The numerical simulation is subjected to an error since bulk materials properties are used, and the thermal properties of thin films are expected to deviate from the bulk properties. The thermal properties of thin film material are currently under investigation. A possible boundary resistance between liquid and solid is also neglected in the calculation. The use of bulk properties and neglect of boundary resistance could cause an underestimation of the melt depth, especially at high laser fluences as shown in Fig. 5, and can be another reason for the long-lasting resolidification process.

As stated earlier, the constant C_1, which indicates the interfacial superheating/undercooling level, is taken as 10 K/(m/s) based on the molecular simulation of crystalline silicon melting. The value of this constant for polycrystalline films can be different due to the different microstructure of the material. The effects of superheating levels on the melting depth, the melting duration, and the surface temperature are examined numerically. The transient melting front position resulting from different degrees of superheating are shown in Fig. 12(a). The coefficient C_1 is varied from 0 (no superheating) to 20 K/(m/s). The calculated melting front histories show no significant dependence on superheating. The melting durations differ only by about 20 ns from the high superheating to no superheating. However, the experimental uncertainty in determining the melting duration is larger than 20 ns (Fig. 6a, 6b). On the other hand, the maximum surface temperature rise is higher when there is stronger superheating (Fig. 12b). To determine the constant C_1 experimentally, a direct surface temperature measurement would be required.

V Conclusion

In this work, the transient surface melting of thin polysilicon layers by excimer laser heating on nanosecond time scales is examined. Melting threshold, melting front velocity, melting duration and maximum melting depth are obtained using electrical conductance and optical transmissivity measurements. The transient temperature field is calculated with a conductive heat transfer model, which is extended to include phase-change simulations. The experimental results agree with the heat transfer analysis. Effects of superheating/undercooling are analyzed numerically, based on the kinetic theory of crystal growth from the melt. It is concluded that superheating has no significant effect on the phase boundary propagation for the range of laser fluences examined.

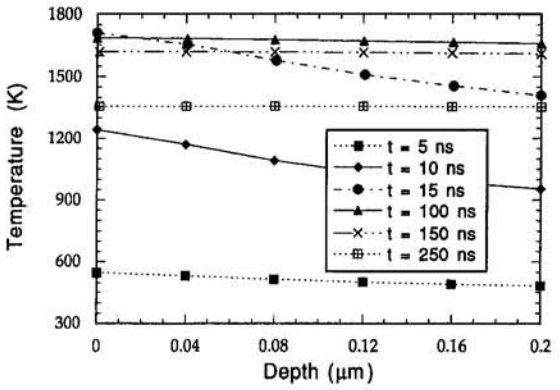

Fig. 11 Calculated temperature profiles in the silicon film at different time steps: F = 0.35 J/cm²

Acknowledgments

Support for this work by the National Science Foundation, under Grant No. CTS-9210333, is gratefully acknowledged. R. Russo acknowledges the support by the U.S. Department of Energy, Office of Basic Energy Sciences, Division of Chemical Sciences, under contract #DE-AC03-76SF00098. The help of Ted Bennett, Hee K. Park, Xiang Zhang, Michael Rubin, and Mark A. Shannon is appreciated.

References

Born, M., and Wolf, E., 1980, *Principles of Optics*, 6th ed., Pergamon, Exeter, United Kingdom, pp. 51–70, 611–633.

Ghandhi, S. K., 1983, *VLSI Fabrication Principles*, Wiley, New York, pp. 133–143.

Glazov, V. M., Chizhevskaya, S. N., and Glagoleva, N. N., 1969, in: *Liquid Semiconductors*, Plenum Press, New York.

Griffith, R., and Nassersharif, B., 1990, "Comparison of One-Dimensional Interface-Following and Enthalpy Methods for the Numerical Solution of Phase Change," *Numerical Heat Transfer*, Part B, Vol. 18, pp. 169–187.

Jackson, K. A., 1975, "Theory of Melt Growth," *Crystal Growth and Characterization*, R. Ueda and J. B. Mullin, eds., North-Holland, Amsterdam.

Jellison, G. E., Jr., and Modine, F. A., 1982, "Optical Absorption of Silicon Between 1.6 and 4.7 eV at Elevated Temperatures," *Applied Physics Letters*, Vol. 41, pp. 180–182.

Jellison, G. E., Jr., Lowndes, D. H., Mashburn, D. N., and Wood, R. F., 1986, "Time-Resolved Reflectivity Measurements on Silicon and Germanium Using a Pulsed Excimer KrF Laser Heating Beam," *Physical Review B*, Vol. 34, No. 4, pp. 2407–2415.

Kluge, M. D., and Ray, J. R., 1989, "Velocity Versus Temperature Relation for Solidification and Melting of Silicon," *Physical Review B*, Vol. 39, No. 3, pp. 1738–1746.

Larson, B. C., White, C. W., Noggle, T. S., Barhorst, J. F., and Mills, D. M., 1983, "Time-Resolved Study of Silicon During Pulsed-Laser Annealing," *Proceedings of Materials Research Society*, J. Narayan et al., eds., Vol. 13, North-Holland, New York, pp. 43–50.

Lowndes, D. H., Penycook, S. J., Jellison, G. E., Jr., Withrow, S. P., and Mashburn, D. N., 1987, "Solidification of Highly Undercooled Liquid Silicon Produced by Pulsed Laser Melting of Ion-implanted Amorphous Silicon: Time-Resolved and Microstructural Studies," *Journal of Materials Research*, Vol. 2, No. 5, pp. 648–680.

Lukes, I., Sasik, R., and Cerny, R., 1992, "Study of Excimer Laser Induced Melting and Solidification of Si by Time-Resolved Reflectivity Measurements," *Applied Physics A*, Vol. 54, pp. 327–333.

Palmer, W., and Marinero, E. E., 1987, "Transient Conductivity Studies in Tellurium Thin Films," *Journal of Applied Physics*, Vol. 61, No. 6, pp. 2294–2300.

Sasik, R., and Cerny, R., 1991, "Numerical Solution of the Non-isothermal Moving Boundary Problem in Heat Conduction," *Computational Physics Communication*, Vol. 64, pp. 241–251.

Shvarev, K. M., Baum, B. A., and Gel'd, P. V., 1975, "Optical Properties of Liquid Silicon," *Soviet Physics of Solid State*, Vol. 16, No. 11, pp. 2111–2112.

Thompson, M. O., and Galvin, G. J., 1985, "Time Resolved Measurements of Interface Dynamics During Pulsed Laser Melting Observed by Transient Conductance," *Proceedings of Materials Research Society*, J. Narayan et al., eds., North-Holland, New York, Vol. 13, pp. 57–67.

Touloukian, Y. S., 1970, *Thermophysical Properties of Matter, Thermal Conductivity*, IFI/Plenum, New York.

Tsao, J. Y., Picraux, S. T., Peercy, P. S., and Thompson, M. O., 1986, "Direct Measurements of Liquid/Solid Interface Kinetics During Pulsed-Laser-Induced Melting of Aluminum," *Applied Physics Letters*, Vol. 48, No. 4, pp. 278–280.

Wood, R. F., and Geist, G. A., 1986a, "Theoretical Analysis of Explosively Propagating Molten Layers in Pulsed Laser-Irradiated a-Si," *Physical Review Letters*, Vol. 57, No. 7, pp. 873–876.

Wood, R. F., and Geist, G. A., 1986b, "Modeling of Nonequilibrium Melting and Solidification in Laser-Irradiated Materials," *Physics Review B*, Vol. 34, No. 4, pp. 2606–2620.

Wood, R. F., White, C. W., and Young, R. T., 1984, eds., "Pulsed Laser Processing of Semiconductors," *Semiconductors and Semimetals*, Vol. 23.

Xu, X., and Grigoropoulos, C. P., 1993a, "High Temperature Radiative Properties of Thin Polysilicon Films," *International Journal of Heat and Mass Transfer*, Vol. 36, No. 17, pp. 4163–4172.

Xu, X., Taylor, S. L., Park, H. K., and Grigoropoulos, C. P., 1993b, "Transient Heating and Melting Transformations in Argon-Ion Laser Irradiation of Polysilicon Films," *Journal of Applied Physics*, Vol. 73, No. 12, pp. 8088–8096.

Xu, X., Grigoropoulos, C. P., and Russo, R. E., 1995, "Transient Temperature Measurement During Pulsed Excimer Laser Heating of Thin Semiconductor Films," ASME JOURNAL OF HEAT TRANSFER, Vol. 117, pp. 17–24.

The Effect of Turbulence on Solidification of a Binary Metal Alloy With Electromagnetic Stirring

P. J. Prescott
Department of Mechanical Engineering,
The Pennsylvania State University,
University Park, PA 16802

F. P. Incropera
Heat Transfer Laboratory,
School of Mechanical Engineering,
Purdue University,
West Lafayette, IN 47907

Electromagnetic induction is considered as a means of altering convection during the solidification of a Pb–19 wt pct Sn alloy. Application of a time-varying magnetic field induces Lorentz forces, which augment thermal buoyancy forces in the melt and oppose solutal buoyancy forces in the mushy zone. A continuum model for binary solid–liquid phase change is extended to account for turbulence, and laminar and turbulent flow predictions are contrasted. Results indicate that turbulence decreases the propensity for channel development and macrosegregation by enhancing mixing and reducing the effective Lewis number from 8600 to near unity.

1 Introduction

During the solidification of a molten alloy, thermosolutal convection may occur in both the melt and a two-phase mushy zone, which separates the melt from the fully solidified material. Temperature gradients, induced by cooling, are accompanied by liquid solute concentration gradients, which arise from thermodynamic equilibrium requirements in binary, solid–liquid systems. Thermal and solutal buoyancy effects can either augment or oppose one another, depending on the constituents and nominal composition of the alloy. Natural convection is known to cause unwanted macrosegregation patterns in castings and to influence properties such as the size, orientation, and distribution of grain structures, all of which affect the degree of variability in mechanical properties. Without a means to control the effects of natural convection, constraints must be placed on the size and/or production rates of castings in order to maintain acceptable limits on property variation.

Means of altering or controlling the flow of molten metal alloys by direct mechanical contact are usually precluded by either the high melt temperatures or concerns over introducing inclusions or other impurities in the material. However, due to their large electrical conductivities, flows in molten metals can be influenced indirectly (without contamination) by imposing a magnetic field. In contrast to the passive (dissipative) influence exerted by a steady (d.c.) magnetic field on a convecting liquid metal (Prescott and Incropera, 1993), a time-harmonic (a.c.) magnetic field has an active influence, which involves stirring of the molten material. The electric field induced by a time-varying magnetic field drives eddy currents, which in turn react with the magnetic field to induce so-called Lorentz forces. Since the current through an external induction coil can be controlled, electromagnetic induction represents a means to control convection phenomena during solidification processes. However, in order to more effectively utilize electromagnetic stirring (EMS) in casting processes, the combined effects of electromagnetically and buoyancy-induced forces in solid–liquid phase change systems must be more fully understood.

Contributed by the Heat Transfer Division and presented at the AIAA/ASME Thermophysics and Heat Transfer Conference, Colorado Springs, Colorado, June 19–23, 1994. Manuscript received by the Heat Transfer Division July 1994; revision received December 1994. Keywords: Liquid Metals, Materials Processing and Manufacturing Processes, Phase-Change Phenomena. Associate Technical Editor: A. Faghri.

In this study, an axisymmetric linear motor is used to induce a magnetic field within a Pb–19 wt pct Sn alloy during its solidification in a vertical annular mold. The magnetic field is characterized by its angular frequency ω and axial phase variation (i.e., wave number) k_ϕ and is, in effect, a *traveling* magnetic field with phase velocity $V_\phi = \omega/k_\phi$. The magnetic field may travel upward or downward, depending on whether its phase $(\omega t - k_\phi z)$ decreases $(k_\phi > 0)$ or increases $(k_\phi < 0)$ with the axial coordinate. Lorentz forces induced in the fluid act primarily in the direction of the phase velocity and decrease with decreasing radius. Thus, an upward traveling magnetic field induces recirculation with the fluid ascending near the outer radius of the cavity and descending near the inner radius. The direction of recirculation would be reversed for a downward traveling magnetic field.

It is instructive to examine the relative influences of Lorentz and buoyancy forces through dimensionless groupings. The Lorentz force is proportional to the electrical conductivity of the fluid, the square of the magnitude of the applied magnetic induction field, and the phase velocity:

$$F_L \sim \tfrac{1}{2}\sigma_{e,l} B^2_{r,\max} V_\phi = \sigma_{e,l} B^2_{r,\mathrm{rms}} \omega/k_\phi \tag{1}$$

Thermal buoyancy forces are approximated as

$$F_B \sim \rho g \beta_T \Delta T \tag{2}$$

and the cumulative effect of thermal and solutal buoyancy forces can be expressed as

$$F_B \sim \rho g \beta_T \Delta T (1 + N) \tag{3}$$

where N is a buoyancy parameter representing the relative influences of solutal and thermal buoyancy within the mushy zone. Thus, the dimensionless grouping

$$G_1 = \frac{\sigma_{e,l} B^2_{r,\mathrm{rms}} \omega/k_\phi}{\rho g \beta_T \Delta T} \tag{4}$$

represents the relative influences of Lorentz and thermal buoyancy forces, while a second grouping

$$G_2 = \frac{\sigma_{e,l} B^2_{r,\mathrm{rms}} \omega/k_\phi}{\rho g \beta_T \Delta T (1 + N)} = \frac{G_1}{(1 + N)} \tag{5}$$

accounts for both thermal and solutal effects.

Cooling curves taken from experiments performed with $G_1 = 3.2$ and $G_2 = -0.25$ (Prescott and Incropera, 1994a) reveal

that EMS increases the magnitude of temperature oscillations in the melt prior to solidification and decreases the time span over which recalescence occurs during early stages of solidification. Both effects indicate enhanced mixing with EMS. The increased temperature oscillations are indicative of increased convection, which increases heat transfer between the bulk melt and the cooled mold wall, thereby delaying the onset of solidification. Furthermore, the decreased time span over which recalescence occurs indicates enhanced mass transfer between the bulk liquid and entrained solid grains.

Although the experimental ingots were solidified in an annular mold, cooled axisymmetrically, chemical analyses and metallographic examinations revealed three-dimensional macrosegregation patterns, which are attributed to the formation of discrete channels in the mushy zone during solidification, both with and without EMS (Prescott, 1992). However, it was also found that the degree of circumferential variation in macrosegregation decreased with a modest increase in electromagnetic stirring forces, suggesting that EMS reduces the propensity for channels to form. The objective of this paper is to assess the effects of turbulence on solidification of a binary metal alloy (Pb–19 wt pct Sn) with electromagnetic stirring by comparing predictions based on a low-Reynolds-number $k-\epsilon$ turbulence model with those obtained for laminar, but otherwise identical, conditions.

Without EMS, a comparison between laminar model predictions and experimental data (Prescott et al., 1994) revealed two noticeable areas of disagreement. First, while axial symmetry was assumed in predictions, the measured macrosegregation pattern was three dimensional, due to discrete, rather than axisymmetric, channel formation in the mushy zone. However, this result does not render axisymmetric calculations meaningless (Neilson and Incropera, 1993), and in view of the computational resources required to perform a transient, three-dimensional simulation, this study uses axisymmetric calculations. The other area of disagreement between predicted and experimental results related to undercooling and recalescence observed in experimental cooling curves, but not predicted by the original continuum model, which assumed local thermodynamic equilibrium. In this study, a (nonequilibrium) supersaturation model (Prescott et al., 1992) is applied, and with proper prescription of model parameters, it predicts recalescence patterns similar to those obtained experimentally (Prescott, 1992; Prescott and Incropera, 1994a).

2 Numerical Model

A continuum model for transport phenomena in binary solid–liquid phase change systems (Bennon and Incropera, 1987; Prescott et al., 1991) is used, and under the assumption of axisymmetric conditions, the model transport equations for conservation of total mass, axial and radial momentum, energy, and species are, respectively,

$$\frac{\partial \rho}{\partial t} + \nabla\cdot(\rho \mathbf{V}) = 0 \tag{6}$$

$$\frac{\partial}{\partial t}(\rho u) + \nabla\cdot(\rho \mathbf{V} u) = \nabla\cdot\left[(\mu_l + \mu_t)\frac{\rho}{\rho_l}\nabla u\right] - \frac{\mu_l}{K}\frac{\rho}{\rho_l}(u - u_s) + \rho_l g\left[\left(\frac{\rho_{\text{ref}}}{\rho_l} - 1\right) + \beta_T(T - T_{\text{ref}})\right] - \frac{\partial P}{\partial z} + F_{L,z} \tag{7}$$

Nomenclature

B = magnetic induction, T
C_1 = turbulence model constant
C_2 = turbulence model parameter
C_μ = turbulence model parameter
c_s^* = specific heat of solid at an arbitrary reference state, J/kg·K
D = binary mass diffusion coefficient, m^2/s
F_L = Lorentz force, N/m^3
f = mass fraction
G = turbulence production by shear, W/m^3
G_1 = dimensionless parameter defined by Eq. (4)
G_2 = dimensionless parameter defined by Eq. (5)
g = gravitational acceleration, m/s^2
H = height of mold cavity, m
h = enthalpy, J/kg
h_s^* = $c_s^* T$, J/kg
j = $\sqrt{-1}$
K = permeability, m^2
k = thermal conductivity, W/m·K
k_e = turbulence kinetic energy, J/kg
k_ϕ = wave number, rad/m
M_{rms} = average macrosegregation = $[(1/V)\int_v (f^{\text{Sn}} - 0.19)^2 dV]^{1/2}$
m = slope of liquidus line on the equilibrium phase diagram, K
N = buoyancy parameter = $\beta_S/m\beta_T$
P = pressure, N/m^2
Pr = Prandtl number
$\text{Pr}_{t,e}$, $\text{Pr}_{t,s}$ $\text{Pr}_{t,k}$, $\text{Pr}_{t,\epsilon}$ = turbulent Prandtl numbers for energy, species, turbulence kinetic energy, and turbulence dissipation rate, respectively
q'' = heat flux, W/m^2
Re = Reynolds number
r = radius, m
r^* = dimensionless radial coordinate = $(r - r_i)/(r_o - r_i)$
Sc = Schmidt number
T = temperature, °C or K
t = time, s; thickness, m
U = overall heat transfer coefficient, $W/m^2\cdot K$
u, v = axial and radial velocity components, m/s
$\mathbf{V}$ = velocity, m/s
V = volume, m^3
V_ϕ = phase velocity, m/s
z = axial coordinate, m
z^* = dimensionless axial coordinate = z/H
α = thermal diffusivity, m^2/s
β_S = solutal expansion coefficient
β_T = thermal expansion coefficient, K^{-1}
ϵ = turbulence dissipation rate, W/kg
λ = dimensionless complex coefficient defined by Eq. (12)
μ = viscosity, $N\cdot s/m^2$
μ_0 = magnetic permeability of free space = $4\pi \times 10^{-7}$ T·m/A
ν = kinematic viscosity, m^2/s
ρ = density, kg/m^3
σ_e = electrical conductivity, A/V·m
τ = time constant, s
Ψ = streamfunction, kg/s·rad
ω = frequency, rad/s
Ω = supersaturation

Subscripts

B = buoyancy
c = coolant
eff = effective
i = initial or inner
l = liquid phase
max = maximum
min = minimum
o = outer
r = radial component
rms = root mean square
s = solid phase; solutal
t = turbulent
z = axial component

Superscripts

Sn = tin
α = constituent α

$$\frac{\partial}{\partial t}(\rho v) + \nabla\cdot(\rho \mathbf{V} v) = \nabla\cdot\left[(\mu_l + \mu_t)\frac{\rho}{\rho_l}\nabla v\right] - (\mu_l + \mu_t)\frac{\rho}{\rho_l}\frac{(v - f_s v_s)}{r^2} - \frac{\mu_l}{K}\frac{\rho}{\rho_l}(v - v_s) - \frac{\partial P}{\partial r} \quad (8)$$

$$\frac{\partial}{\partial t}(\rho h) + \nabla\cdot(\rho \mathbf{V} h) = \nabla\cdot\left[\left(\frac{k}{c_s^*} + \frac{g_l \mu_t c_l}{\mathrm{Pr}_{t,e} c_s^*}\right)\nabla h\right] + \nabla\cdot\left[\left(\frac{\mathrm{k}}{\mathrm{c}_s^*} + \frac{\mathrm{g}_l \mu_t c_l}{\mathrm{Pr}_{t,e} c_s^*}\right)\nabla(h_s^* - h)\right] - \nabla\cdot[f_s \rho(\mathbf{V} - \mathbf{V}_s)(h_l - h_s)] \quad (9)$$

and

$$\frac{\partial}{\partial t}(\rho f^\alpha) + \nabla\cdot(\rho \mathbf{V} f^\alpha) = \nabla\cdot\left[\left(\rho D + \frac{f_l \mu_t}{\mathrm{Pr}_{t,s}}\right)\nabla f^\alpha\right] + \nabla\cdot\left[\left(\rho \mathrm{D} + \frac{\mathrm{f}_l \mu_t}{\mathrm{Pr}_{t,s}}\right)\nabla(f_l^\alpha - f^\alpha)\right] - \nabla\cdot[f_s \rho(\mathbf{V} - \mathbf{V}_s)(f_l^\alpha - f_s^\alpha)] \quad (10)$$

where the dependent field variables are understood to be time-averaged (*mean*) values. Since these equations are extensions of those used in previous studies (Prescott and Incropera, 1991, 1993, 1994b), only the new features are discussed here. The last term on the right-hand side of Eq. (7) represents the axial Lorentz force. Neglecting end effects, it depends only on r, and is accommodated numerically as a volumetric source term. As shown by Prescott (1992), the functional form of the Lorentz force field may be expressed as

$$F_{l,z}(r) = \sigma_{e,l}\frac{\omega}{k_\phi}\left[B_{r,\mathrm{rms}}(r_o)\left|\frac{J_1(r/r_o\sqrt{\lambda})}{J_1(\sqrt{\lambda})}\right|\right]^2 \quad (11)$$

where J_1 is a Bessel function of the first kind and order 1, and

$$\lambda = -[(k_\phi r_o)^2 + j(\sigma_{e,l}\mu_0 r_o^2 \omega)] \quad (12)$$

Radial Lorentz (pinching) forces are implicitly included in Eq. (8) through the pressure gradient term $\partial P/\partial r$, and further treatment of $F_{L,r}$ is unnecessary since it is independent of z. Since the applied pinching forces are small, the top, free surface of the melt is assumed to remain flat. Moreover, since Joulean dissipation is negligible for the conditions of this study, is has been omitted from Eq. (9).

Turbulence effects are considered in Eqs. (7)–(10) through the eddy viscosity μ_t, which is identically zero in the laminar simulation. Assuming the turbulence to be isotropic, a low-Reynolds-number $k-\epsilon$ model (Jones and Launder, 1973; Launder and Spalding, 1974) was used to evaluate the eddy viscosity:

$$\mu_t = C_\mu \rho_l \frac{k_e^2}{\epsilon} \quad (13)$$

where k_e and ϵ are the turbulence kinetic energy and dissipation rate, respectively, and C_μ is a model parameter. Although anisotropy may exist in the actual turbulence and would be influenced by gravitational and electromagnetic fields, it is not considered because of the added complexity of using higher-order models (with additional empirical constants). The transport equations for k_e and ϵ in single-phase systems are, respectively,

$$\frac{\partial}{\partial t}(\rho k_e) + \nabla\cdot(\rho \mathbf{V} k_e) = \nabla\cdot[(\mu_l + \mu_t/\mathrm{Pr}_{t,k})\nabla k_e] + G - \rho\epsilon \quad (14)$$

and

$$\frac{\partial}{\partial t}(\rho \epsilon) + \nabla\cdot(\rho \mathbf{V} \epsilon) = \nabla\cdot[(\mu_l + \mu_t/\mathrm{Pr}_{t,\epsilon})\nabla \epsilon] + C_1 G\frac{\epsilon}{k_e} - C_2 \rho\frac{\epsilon^2}{k_e} \quad (15)$$

where G is the shear production of turbulence kinetic energy, which in an axisymmetric system is

$$G = \mu_t\left\{2\left[\left(\frac{\partial u}{\partial z}\right)^2 + \left(\frac{\partial v}{\partial r}\right)^2 + \left(\frac{v}{r}\right)^2\right] + \left(\frac{\partial u}{\partial r} + \frac{\partial v}{\partial z}\right)^2\right\} \quad (16)$$

The original low-Reynolds-number $k-\epsilon$ model (Jones and Launder, 1973) included an extra term on the right-hand side of the turbulence kinetic energy equation, which permitted the convenient prescription of $\epsilon = 0$ along the wall boundary, while accounting for nonzero turbulence dissipation near the wall. In this study, zero-flux boundary conditions (Patel et al., 1985) are prescribed for the turbulence dissipation rate equation, and the additional term in the turbulence kinetic energy equation is omitted. A similar approach is used to modify the turbulence kinetic energy equation for use in a domain that may include a mushy zone. It is assumed that within a coherent mushy zone, turbulence is dampened by shear having a characteristic length on the order of dendrite arm spacings (i.e., by Darcy damping). Thus, the turbulence kinetic energy equation used in this study is

$$\frac{\partial}{\partial t}(\rho k_e) + \nabla\cdot(\rho \mathbf{V} k_e) = \nabla\cdot[(\mu_l + \mu_t/\mathrm{Pr}_{t,k})\nabla k_e] + G - \rho\epsilon - \frac{\mu_l}{K}k_e \quad (17)$$

Equation (17) reduces to Eq. (14) in the all-liquid region where $K = \infty$, and within most of the mushy zone, the last term on the right-hand side of Eq. (17) drives the turbulence to negligible values.

The $k-\epsilon$ model requires specification of the parameters C_μ, C_1, and C_2, for which several models have been reviewed (Patel et al., 1985). In this study, the following models are used:

$$C_\mu = 0.09\exp\left[\frac{-2.5}{(1 + \mathrm{Re}_t/50)}\right] \quad (18)$$

$$C_1 = 1.44 \quad (19)$$

$$C_2 = 1.92[1 - 0.3\exp(-\mathrm{Re}_t^2)] \quad (20)$$

where the turbulence Reynolds number is

$$\mathrm{Re}_t = \frac{\rho_l k_e^2}{\mu_l \epsilon} \quad (21)$$

Also, $\mathrm{Pr}_{t,e} = 1.2$, $\mathrm{Pr}_{t,s} = 1.0$, $\mathrm{Pr}_{t,k} = 1.0$, and $\mathrm{Pr}_{t,\epsilon} = 1.3$. Although the value of $\mathrm{Pr}_{t,e}$ has been thought to be much larger than unity for liquid metals (Benocci, 1983), recent evidence suggests that a value near unity is appropriate (Bremhorst and Krebs, 1992; Mohamad, 1992).

The experimental conditions of Prescott (1992) are modeled numerically, as illustrated in Fig. 1. The height H of the mold cavity is 150 mm, and the inner and outer radii are $r_i = 15.9$ mm and $r_o = 63.5$ mm, respectively. Initially, both the melt and the mold are isothermal at 305°C, which is 20°C above the nominal liquidus temperature. Also, at $t = 0$ s, the melt is chemically homogeneous and quiescent. Cooling occurs

through the outer vertical surface of the mold, where the heat flux is known to obey the following relation (Prescott, 1992):

$$q'' = U[T(r_o + t_o, z, t) - T_c] \quad (22)$$

with the overall heat transfer coefficient $U = 35$ W/m^2·K and the chill temperature $T_c = 13$°C. The overall heat transfer coefficient was measured to be 35.5 W/m^2·K (±7 percent) during an experiment in which pure tin was solidified (Prescott, 1992). The top, bottom, and inner boundaries are assumed to be adiabatic and the contact resistance between the mold and alloy is assumed to be negligible. The interface between the mold and the melt is modeled to be slip-free and impermeable to both Pb and Sn. It is assumed that the meniscus is shear free and that no mass transfer occurs through the free surface.

The prescribed Lorentz force field is based on the electrical conductivity of the molten alloy $\sigma_{e,l} = 1.5 \times 10^6$ A/V·m and an applied magnetic field with $\omega = 377$ rad/s, $k_\phi = -29$ rad/m, and $B_r(r_o) = 2.9$ mT (rms). With $\rho = 9560$ kg/m^3, $\beta_T = 1.09 \times 10^{-4}$ K^{-1}, ΔT estimated to be 5 K, and $N = -14$, $G_1 = 3.2$, and $G_2 = -0.25$. Thus, thermal convection, which occurs before the onset of solidification, is augmented significantly by the Lorentz forces, while the combined influence of thermal and solutal buoyancy forces within the mushy zone is attenuated slightly (25 percent) by the Lorentz forces.

Turbulence kinetic energy is set to zero at the mold walls, while $\partial k_e/\partial z = 0$ is used along the top free surface. Conditions of $\partial \epsilon/\partial r = 0$ and $\partial \epsilon/\partial z = 0$, respectively, are used for Eq. (15) along the vertical and horizontal boundaries of the mold cavity (Patel et al., 1985). Both k_e and ϵ were initially set to zero. Turbulence is generated through the source term G on the right-hand side of Eq. (17), which is identically zero when $k_e = 0$. Hence, since the model would be unable to predict turbulence without an artificial source, the following model for G was used during the first 60 seconds of the simulation:

$$G = (\mu_t = 0.01\mu_l)\left\{2\left[\left(\frac{\partial u}{\partial z}\right)^2 + \left(\frac{\partial v}{\partial r}\right)^2 + \left(\frac{v}{r}\right)^2\right] + \left(\frac{\partial u}{\partial r} + \frac{\partial v}{\partial z}\right)^2\right\} \quad (23)$$

Although the artificial factor of $0.01\mu_l$ in Eq. (23) would be insignificant in a turbulent flow, it provides a source by which turbulence can develop when an initially quiescent fluid is being strained. Subsequent calculations (see Section 3) reveal that this source acts only as an initial disturbance (required for turbulence to develop) well before the onset of solidification.

A supersaturation model, capable of predicting recalescence, was used to relate local temperatures, species concentrations, and phase fractions. Supersaturation can be approximated to decay exponentially following nucleation (Prescott et al., 1992):

$$\Omega = \Omega_n \exp\left[\frac{-(t - t_n)}{\tau}\right] \quad (24)$$

where Ω_n is the supersaturation at the time of nucleation t_n and the time constant τ is related to the mass transfer coefficient at the microscopic solid–liquid interface and to the volumetric interfacial area. In this study, Ω_n is determined from a maximum undercooling of 3°C, and based on measured recalescence patterns (Prescott, 1992), the time constant τ is approximated as 15 s. Means by which supplemental thermodynamic relationships are implemented and material properties for the Pb–Sn system are provided elsewhere (Prescott and Incropera, 1991, 1993).

It was determined in a previous study (Prescott and Incropera, 1991) that a 50 × 50 mesh of the mold cavity is suitable for resolving important physical features of the problem. Additional nodes were added to accommodate the inner and outer vertical mold walls and the mold bottom, bringing the mesh size to 54

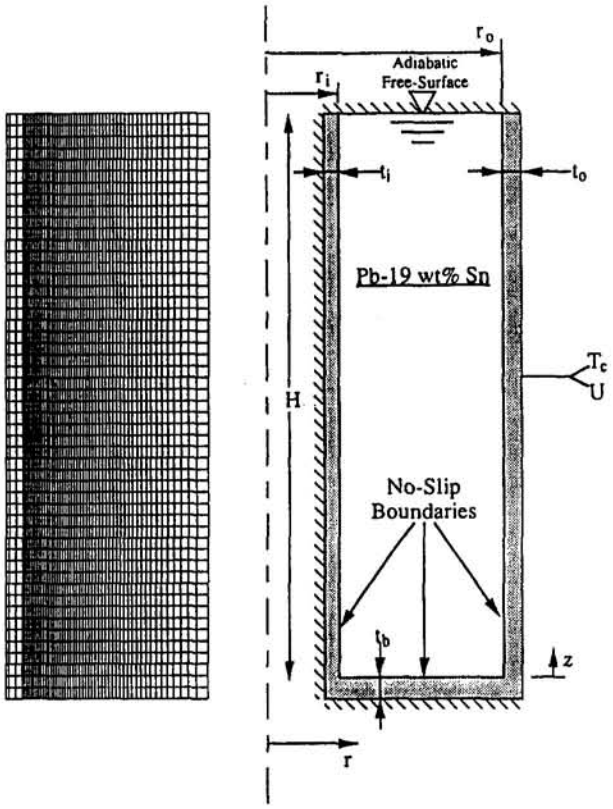

Fig. 1 Simulation system

radial nodes by 53 vertical nodes. Within the mold cavity, the grid was biased in the radial direction such that the total volume was equally distributed among all control volumes. While the mold walls do not significantly increase resistance to heat transfer, they represent approximately 20 percent of the heat capacity of the system and are hence included in the simulations. Time steps of 0.25 s were used to resolve the system transients in a control-volume-based finite-difference method (Patankar, 1980), with a fully implicit time marching scheme.

Figure 2 contrasts cooling curves measured at two radial locations during an experiment with EMS and those predicted by the turbulence model. Figure 2 shows that predicted and measured cooling curves are in reasonable agreement, although some important differences exist. The predicted cooling rate is generally larger than the measured cooling rate, and the difference may be due to uncertainties in prescribed thermodynamic properties, which affect the thermal capacitance of the system, and/or to uncertainties in the heat transfer coefficient on the outer mold wall, which governs the rate of heat transfer from the system (Prescott et al., 1992). Another important difference relates to recalescence. Although it is predicted by the model, it not as pronounced nor as long in duration as the actual recalescence. Differences may be due to uncertainties in prescribed supersaturation parameters and/or to the model assumption of negligible solid particle transport. In addition, the model was unable to predict temperature oscillations before solidification, which suggests that it was unable to predict finer details of the actual flow. Prediction of such details would necessitate waiving the assumption of axial symmetry and performing a transient, fully three-dimensional simulation of the solidification process. Furthermore, second-order finite-difference schemes and/or a very fine grid may be necessary to achieve improved resolution of flow details.

3 Comparison of Simulations for Laminar and Turbulent Flow

Laminar and turbulent flow simulations were performed and results are presented as field plots of velocity vectors, stream-

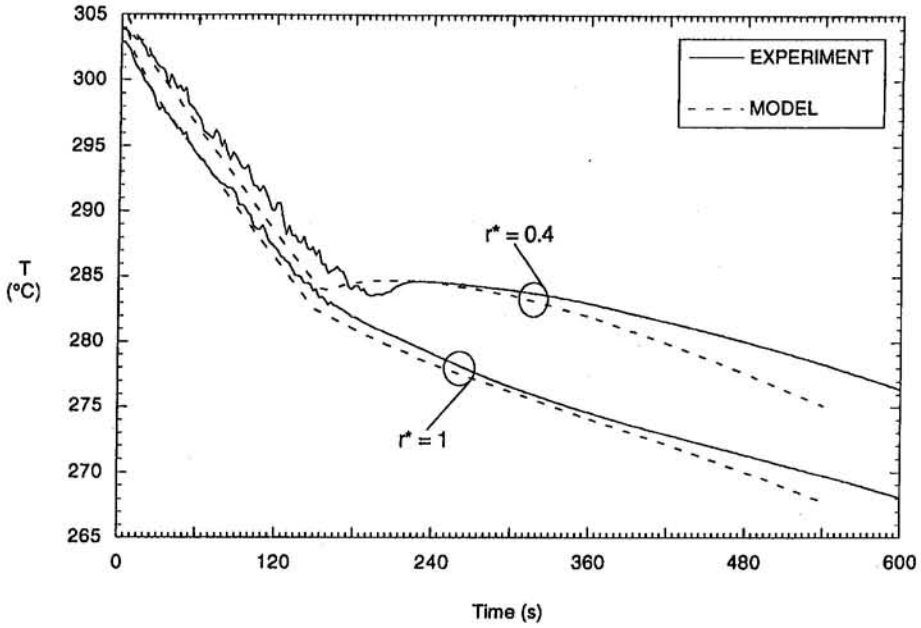

Fig. 2 Comparison between cooling curves measured during solidification with EMS and predicted by the turbulence model at $z^* = 0.083$

lines, isotherms, liquid isocomposition lines (liquid isocomps), and, for the turbulent simulation, dimensionless effective viscosity μ^* (defined by Eq. (25)). These plots are drawn on an $r-z$ plane, with the outer and inner radii shown, respectively, as left and right boundaries. The liquidus interface, which represents the boundary between the melt and mushy zones, is indicated by a thick line on each plot. Fully solidified regions and a solidus interface do not develop until well after convection ceases and hence do not appear at times associated with the figures. Velocity vectors are scaled according to the current maximum velocity, which is indicated at the top of each velocity vector plot. These velocities represent mixture velocities ($\mathbf{V}$), and since $\mathbf{V}_s = 0$, $\mathbf{V} = f_l \mathbf{V}_l$. Streamlines associated with clockwise recirculation have negative values and are plotted in ten equal increments between Ψ_{min} and 0, while counterclockwise recirculation cells have positive values, which are plotted in ten equal increments between 0 and Ψ_{max}. Isotherms are plotted in twenty equal increments between the minimum and maximum temperatures, and liquid isocomps are plotted in twenty equal increments between the minimum and maximum values of the liquid composition (expressed as mass fraction Sn). In general, the minimum temperature and maximum liquid composition are found near the outer (left) boundary of the mold cavity. In addition, macrosegregation plots, which indicate mixture (solid + liquid) composition, are presented with legends provided to facilitate interpretation.

Laminar Flow. Upon initiation of cooling and application of electromagnetic stirring forces, a vigorous convection cell develops in the mold cavity, with predicted velocities greater than 60 mm/s. Hence, convective heat transfer between the melt and the cooled mold wall is increased, delaying the onset of solidification by approximately 10 seconds relative to conditions without EMS (Prescott et al., 1992). During the initial stages of solidification ($t \lesssim 170$ s), the complex temperature field associated with thermally and electromagnetically driven convection yields a mushy zone of highly nonuniform thickness along the cooled mold wall (Prescott and Incropera, 1994a). Due to undercooling and a relatively small time constant τ associated with supersaturation, the mushy zone grows very quickly. Without EMS, τ is approximated to be 45 s (Prescott et al., 1992), and with the smaller time constant for EMS ($\tau = 15$ s), supersaturation decreases more quickly, thereby effecting a larger solidification rate at early times. A smaller time constant corresponds to a larger mass transfer rate between growing crystals and the supersaturated liquid. As Pb-rich material precipitates on a crystal, a layer of Sn-rich liquid is left near the microscopic liquid–solid interface and inhibits further precipitation. By increasing the rate at which Sn is transferred from the interface, the solidification rate is increased and the supersaturated condition of the liquid is relieved more quickly.

At $t = 180$ s, Fig. 3, the mold cavity is occupied almost entirely by a mushy zone. Because of thermal capacitance effects in the mold walls, the lower inside region of the mold cavity is relatively warm and fully melted, Fig. 3(*c*), while the rest of the cavity contains a mushy zone. Velocities through much of the mushy zone are large, Fig. 3(*a*), as the solid volume fraction is very small (less than approximately 1 percent), and although solid dendrites are assumed to remain stationary, conditions are extremely conducive to formation of a

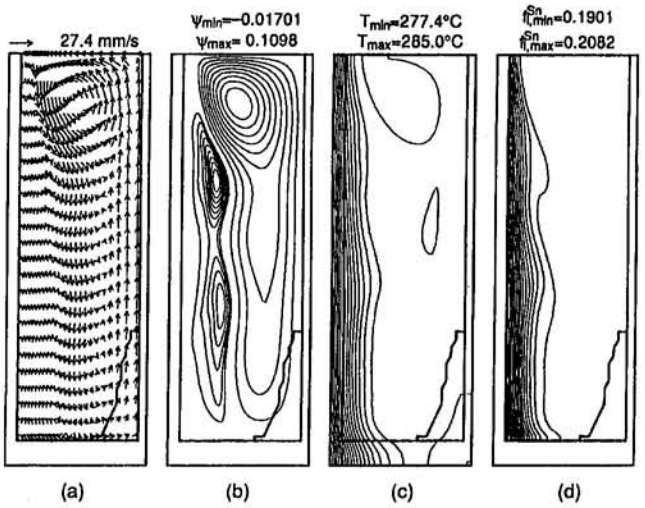

Fig. 3 Laminar convection conditions after 180 seconds of cooling with EMS: (*a*) velocity vectors, (*b*) streamlines, (*c*) isotherms, and (*d*) liquid isocomps

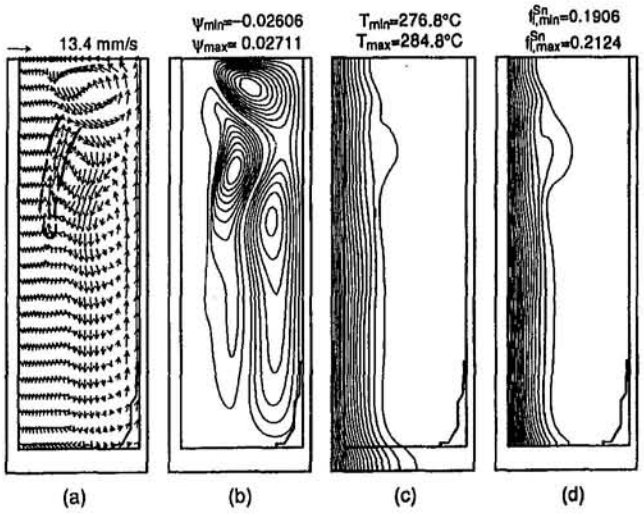

Fig. 4 Laminar convection conditions after 195 seconds of cooling with EMS: (*a*) velocity vectors, (*b*) streamlines, (*c*) isotherms, and (*d*) liquid isocomps

slurry. However, because gradients in temperature, Sn concentration, and solid fraction are very small in the cavity interior, the effects of such a slurry on transport would be small. The radial gradient in liquid Sn concentration, Fig. 3(*d*), drives a clockwise convection cell, Fig. 3(*b*), which interacts near the top of the cavity with the counterclockwise cell driven primarily by Lorentz forces. The interaction yields significant distortions in the temperature and liquid concentration fields, Figs. 3(*c*) and 3(*d*). These conditions strongly favor local remelting and the development of a channel in the mushy zone.

A partially melted channel forms by $t = 195$ s and is outlined with a thick dashed line in Fig. 4(*a*). The solidification rate is no longer enhanced by local nonequilibrium effects, as more than 95 percent of the supersaturation has decayed by 195 seconds. The radial component of the liquid Sn concentration gradient has increased, Fig. 4(*d*), and is responsible for growth of the solutal convection cell, Fig. 4(*b*). However, growth of this cell is slowed by opposing Lorentz forces, which remain constant during the process.

As solidification continues past 195 seconds, the solutal convection cell grows, and the interaction between counterrotating convection cells continues to promote channel development by advecting warm fluid from the interior of the cavity toward the channel site. As this fluid approaches the channel, it cools and precipitates Pb-rich material on dendrites adjacent to the channel, while Sn-enriched liquid is fed into the channel and is transported to the top of the cavity. As the mushy zone and liquid Sn concentration gradients grow, flow conditions become dominated by solutal buoyancy, and the electromagnetically driven cell decays and eventually ($t \approx 240$ s) disappears.

The final macrosegregation pattern is determined by 600 s and is shown in Fig. 5(*a*). The channel that developed in the mushy zone is manifested as a severely segregated region. With electromagnetic stirring, the predicted macrosegregation is significantly larger than that predicted without magnetic field effects (Prescott and Incropera, 1994b). The average macrosegregation M_{rms} increased from 1.34 percent without EMS to 1.61 percent with EMS under the assumption of laminar flow. This increase is attributed to the prominent channel that formed in the electromagnetic stirring simulation, and the result contradicts experimental findings (Prescott, 1992). The discrepancy is believed to be largely due to the assumption of laminar flow, and the following section will assess the effect of turbulence on model predictions.

Turbulent Flow. Flow velocities as high as 60 mm/s were predicted in the laminar simulation, and with the hydraulic diameter of the mold cavity used as the length scale, a Reynolds number greater than 2.5×10^4 is estimated, rendering the assumption of laminar flow suspect. In this section, the influence of turbulence on the solidification of a binary metal alloy is assessed.

It is useful to consider possible ramifications of turbulence before reviewing predicted results. Turbulence has the effect of increasing the effective viscosity, $\mu_{eff} = \mu_l + \mu_t$, and a dimensionless viscosity is defined as

$$\mu^* = (\mu_l + \mu_t)/\mu_l = \mu_{eff}/\mu_l \tag{25}$$

Effective Prandtl and Schmidt numbers are defined, respectively, as

$$\mathrm{Pr}_{eff} = \frac{\nu_{eff}}{\alpha_{eff}} = \frac{\mu_{eff}/\rho}{\alpha + \mu_t/(\rho\ \mathrm{Pr}_{t,e})} = \frac{\mathrm{Pr}\,\mu^*}{1 + \mathrm{Pr}(\mu^* - 1)/\mathrm{Pr}_{t,e}} \tag{26}$$

and

$$\mathrm{Sc}_{eff} = \frac{\nu_{eff}}{D_{eff}} = \frac{\mu_{eff}/\rho}{D + \mu_t/(\rho\ \mathrm{Pr}_{t,s})} = \frac{\mathrm{Sc}\ \mu^*}{1 + \mathrm{Sc}(\mu^* - 1)/\mathrm{Pr}_{t,s}} \tag{27}$$

For the Pb–Sn system, Pr = 0.02 and Sc = 172 (Le = Sc/Pr = 8600). Hence, for $\mu^* = 100$, $\mathrm{Pr}_{t,e} = 1.2$, and $\mathrm{Pr}_{t,s} = 1.0$, $\mathrm{Pr}_{eff} = 0.75$ and $\mathrm{Sc}_{eff} = 1$. Therefore, the effective Lewis number is 1.33, and although the respective molecular diffusion rates of momentum, energy, and species are highly disparate, turbulence has the effect of approximately equalizing these diffusion rates. Furthermore, by increasing the effective diffusion coefficients for all field variables, turbulence reduces the relative influence of advection (transport by the *mean* flow), rendering transport rates less sensitive to velocity *vectors* and more sensitive to *gradients* in the field variables.

With cooling and application of electromagnetic stirring forces, a convection cell develops in the mold cavity and is initially similar to that predicted for laminar flow. However, within approximately 30 seconds, μ^* increases to greater than 200 and flow velocities begin decreasing. The artificial term in Eq. (23) was significant only for a brief period near the beginning of the simulation. Within 90 seconds, the electromagnetically driven flow is essentially steady, with a maximum velocity

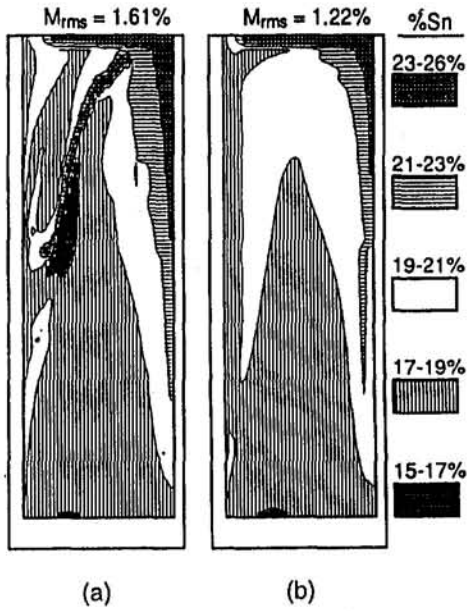

Fig. 5 Macrosegregation patterns at t = 600 s predicted by (*a*) the laminar EMS simulation and (*b*) the turbulent EMS simulation

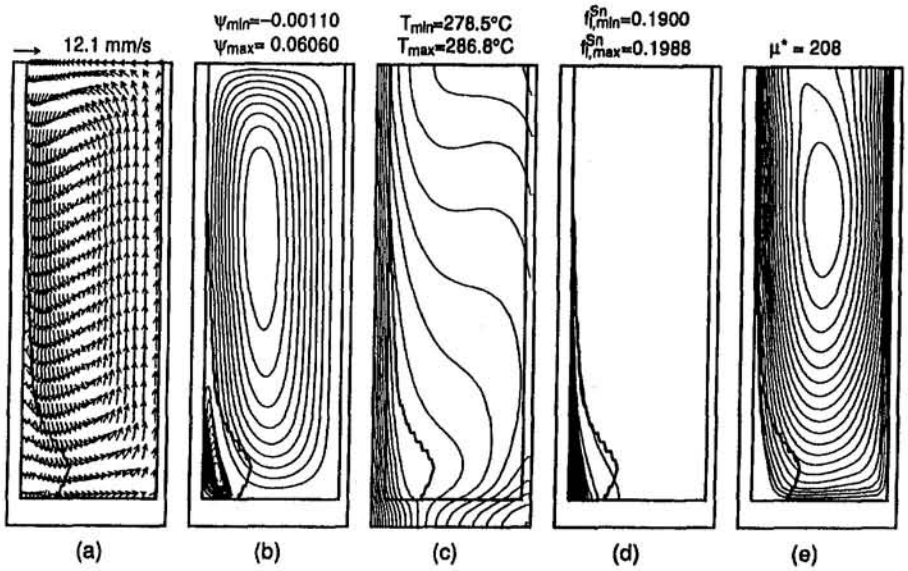

Fig. 6 Turbulent convection conditions after 160 seconds of cooling with EMS: (*a*) velocity vectors, (*b*) streamlines, (*c*) isotherms, (*d*) liquid isocomps, and (*e*) effective viscosity (turbulence)

of 15 mm/s and $\mu^*_{max} = 220$, and the cavity is occupied by a single convection cell. The interior of the melt is thermally stratified, with a temperature difference of approximately 4°C between the top and bottom of the cavity.

Solidification begins at $t \approx 150$ s, which is consistent with the laminar simulation, and convection conditions at $t = 160$ s are shown in Fig. 6. A mushy zone of highly nonuniform thickness covers approximately 60 percent of the cooled mold wall. The shape of the mushy zone is largely determined by the shape of the isotherms, Fig. 6(*c*), which are influenced significantly by the convection cell. The main convection cell in Fig. 6(*b*) is driven by Lorentz forces and is partially deflected by the mushy zone, which is responsible for reducing the peak velocity from approximately 15.0 mm/s to 12.1 mm/s, Fig. 6(*a*). A solutally driven convection cell is developing near the bottom, but is confined within the mushy zone, Fig. 6(*b*). Figure 6(*e*) shows contours of constant μ^*. Along the mold walls, $\mu^* = 1$, but large levels of turbulence exist throughout the melt. Due to the combined effects of turbulence generation by straining, Fig. 6(*a*), and being well removed from the walls, at which $k_e = 0$, the maximum effective viscosity μ^*_{max} occurs at $r^* \approx 0.5$ and $z^* \approx 0.7$, Fig. 6(*e*). Turbulence is dampened in the mushy zone, although some turbulent mixing still occurs near the liquidus interface and is responsible for reducing gradients in liquid Sn concentration, Figs. 6(*d*) and 6(*e*). Turbulence can only survive in regions of the mush with a very small solid volume fraction ($\lesssim$1 percent), where slurry conditions are likely to occur in the actual flow.

Due to undercooling and the relatively small time constant for supersaturation, the mushy zone grows quickly and fluid velocities decrease rapidly. At $t = 180$ s, Fig. 7, a mushy zone occupies almost the entire mold cavity. Although the turbulence intensity has decreased significantly, Fig. 7(*e*), it still enhances mixing in the interior of the cavity, thereby maintaining nearly uniform temperatures and concentrations in much of the mushy zone, Figs. 7(*c*) and 7(*d*), with nearly vertical isotherms and liquid isocomps existing closer to the cooled mold wall. In this region, the temperature and liquid composition fields are nearly diffusion dominated, and with the absence of perturbations in these fields, channel formation is inhibited. Because Darcy damping is relatively small due to small solid volume fractions, and because the boundary condition of $\partial k_e/\partial z = 0$ was applied along the top surface, the turbulence intensity is a maximum along the top surface at $r^* \approx 0.5$, Fig. 7(*e*). Since $|G_2| < 1$, the solutal convection cell is growing and will eventually dominate flow conditions in the cavity. However, because Lorentz forces oppose solutal buoyancy forces, the clockwise convection cell in Fig. 7(*b*) grows less rapidly than it would without electromagnetic stirring.

At 195 seconds, Fig. 8, most of the turbulence has been dissipated by Darcy damping, and its influence is confined to relatively small interior regions near the top and bottom of the cavity, Fig. 8(*e*), where solid volume fractions and Darcy damping are small. However, convection is still influenced by prior turbulent mixing. Uniform temperatures and liquid compositions persist in much of the mushy region, Figs. 8(*c*) and 8(*d*), and except at the top and bottom of the cavity, isotherms and liquid isocomps are nearly vertical in a region adjoining the outer mold wall. The interface between the counterrotating convection cells is smooth and nearly vertical, Fig. 8(*b*), and since radial advective transport occurs primarily at the top and bottom of the cavity, the propensity for a channel to develop is not enhanced by interaction of the two cells. Hence, in contrast to conditions predicted for laminar flow, a channel has not developed and flow velocities are relatively small.

The solutal convection cell continues to grow with time, while the electromagnetically driven cell gradually decays. By $t = 210$ s, turbulence is very weak and solutal buoyancy dominates convection, with layers of Sn-rich liquid causing dendrites to remelt at the top of the cavity. The convection pattern during intermediate stages of solidification supplies cool, Sn-rich liquid to the top interior region of the cavity, thereby establishing vertical gradients of temperature and liquid Sn concentration (Prescott and Incropera, 1994a). However, in the outer periphery of the mold cavity, gradients in temperature and liquid concentration remain primarily radial and nearly uniform in the vertical direction.

The final macrosegregation pattern predicted by the turbulent simulation is shown in Fig. 5(*b*). Although the solutal convection pattern during intermediate stages of solidification caused the formation of a cone of positive segregation at the top of the ingot, Fig. 5(*b*), macrosegregation in the outer periphery of the ingot is small. The average macrosegregation M_{rms} shown in Fig. 5(*b*) is 1.22 percent, which is less than that predicted without electromagnetic stirring (1.34 percent) (Prescott and Incropera, 1994b) and much less than that predicted by the laminar simulation (1.61 percent), Fig. 5(*a*).

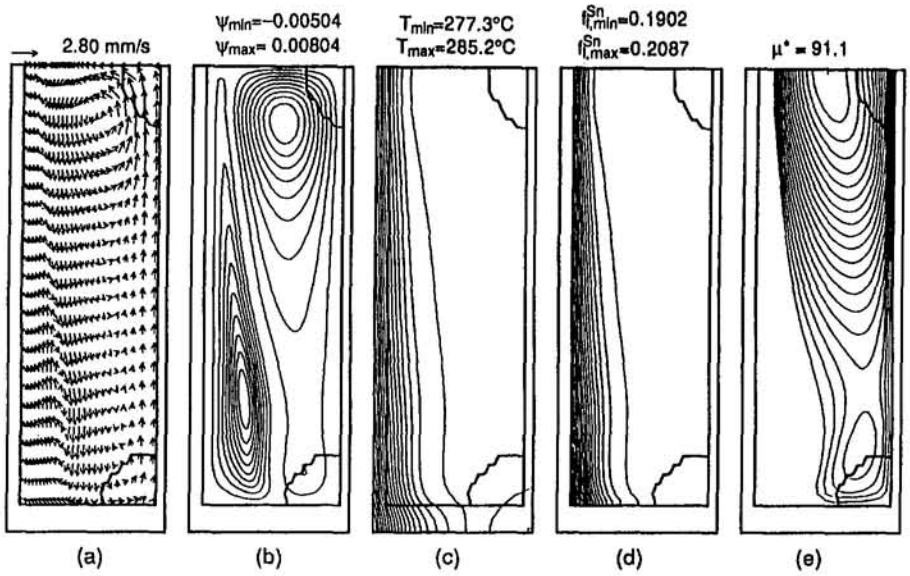

Fig. 7 Turbulent convection conditions after 180 seconds of cooling with EMS: (*a*) velocity vectors, (*b*) streamlines, (*c*) isotherms, (*d*) liquid isocomps, and (*e*) effective viscosity (turbulence)

4 Conclusions

Numerical simulations based on a continuum model of transport phenomena in binary solid–liquid phase-change systems have been performed to investigate the effects of turbulence induced by electromagnetic stirring (EMS). The assessment was made by comparing predictions for a laminar flow model with those obtained using a low-Reynolds-number $k-\epsilon$ model of turbulence. Turbulence was found to have a significant effect on convection conditions that lead to the formation of channels in the mushy zone and, therefore, on macrosegregation. In particular, turbulence reduced perturbations in the temperature and liquid concentration fields, thereby inhibiting the formation of channels in the mushy zone. With increased turbulent mixing, effective diffusion coefficients for momentum, energy, and species transfer were essentially equalized, decreasing the relative effect of advection, and causing gradients in temperature and liquid Sn concentration to remain primarily radial and nearly uniform in the vertical direction. With turbulence, counterrotating convection cells driven by solutal buoyancy and Lorentz forces, occupied the outer and inner portions of the cavity, respectively, during the early stages of solidification. Moreover, mutual interactions between these cells were minimal, in contrast to the stronger and more complex interactions predicted for laminar flow with electromagnetic stirring. Consequently, severely segregated regions associated with channels were not predicted to occur in the turbulent case.

Although the numerical simulations assumed axial symmetry, they can be used to partly explain certain three-dimensional effects observed in experimental ingots (Prescott, 1992; Prescott et al., 1994). Three-dimensional macrosegregation patterns have been attributed primarily to discrete, rather than axisymmetric, channels in the mushy zone during solidification. Since turbulence enhances mixing and reduces the propensity for channels to develop, it follows that the

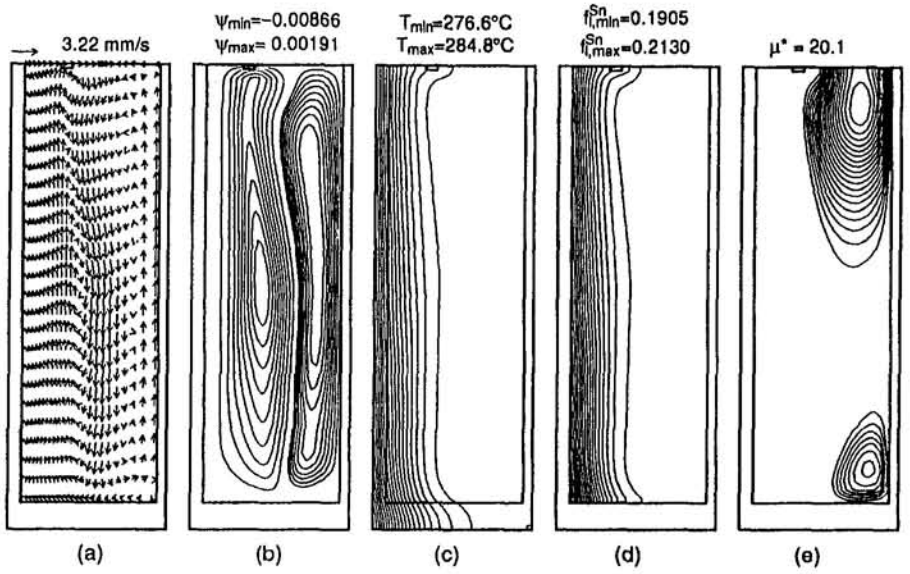

Fig. 8 Turbulent convection conditions after 195 seconds of cooling with EMS: (*a*) velocity vectors, (*b*) streamlines, (*c*) isotherms, (*d*) liquid isocomps, and (*e*) effective viscosity (turbulence)

corresponding macrosegregation in axisymmetrically cooled ingots would be reduced when turbulence is present. Hence, it is concluded that, because electromagnetic stirring tends to promote turbulence, it will decrease channel formation and associated segregation patterns.

Acknowledgments

The authors are grateful to the U.S. Department of Energy for providing financial support of this work through Award Number DE-FG02-87ER 13759.

References

Bennon, W. D., and Incropera, F. P., 1987, "A Continuum Model for Momentum, Heat and Species Transport in Binary Solid-Liquid Phase Change Systems—I. Model Formulation," *Int. J. Heat Mass Transfer,* Vol. 30, pp. 2161–2170.

Benocci, C., 1983, "Turbulence Modeling in Liquid Metal Free Convection," *The von Karman Institute for Fluid Dynamics Lecture Series,* Vol. 1, May 30–June 3, Rhode Saint Genèse, Belgium.

Bremhorst, K., and Krebs, L., 1992, "Experimentally Determined Turbulent Prandtl Numbers in Liquid Sodium at Low Reynolds Numbers," *Int. J. Heat Mass Transfer,* Vol. 35, pp. 351–359.

Jones, W. P., and Launder, B. E., 1973, "The Calculation of Low-Reynolds-Number Phenomena With a Two-Equation Model of Turbulence," *Int. J. Heat Mass Transfer,* Vol. 16, pp. 1119–1130.

Launder, B. E., and Spalding, D. B., 1974, "The Numerical Computation of Turbulent Flows," *Computer Methods in Applied Mechanics and Engineering,* Vol. 3, pp. 269–289.

Mohamad, A. A., 1992, "Mixed Convection in Lid-Driven Shallow Cavities," Ph.D. Thesis, Purdue University, West Lafayette, IN.

Neilson, D. G., and Incropera, F. P., 1993, "Three-Dimensional Considerations of Unidirectional Solidification in a Binary Liquid," *Numerical Heat Transfer Part A,* Vol. 23, pp. 1–20.

Patankar, S. V., 1980, *Numerical Heat Transfer and Fluid Flow,* McGraw-Hill, New York.

Patel, V. C., Rodi, W., and Scheuerer, G., 1985, "Turbulence Models for Near-Wall and Low-Reynolds-Number Flows: A Review," *AIAA Journal,* Vol. 23, pp. 1308–1319.

Prescott, P. J., and Incropera, F. P., 1991, "Numerical Simulation of a Solidifying Pb–Sn Alloy: The Effects of Cooling Rate on Thermosolutal Convection and Macrosegregation," *Metall. Trans. B,* Vol. 22B, pp. 529–540.

Prescott, P. J., Incropera, F. P., and Bennon, W. D., 1991, "Modeling of Dendritic Solidification Systems: Reassessment of the Continuum Momentum Equation," *Int. J. Heat Mass Transfer,* Vol. 34, pp. 2351–2359.

Prescott, P. J., 1992, "Convection Transport Phenomena During Solidification of Binary Metal Alloys and the Effects of Magnetic Fields," Ph.D. Thesis, Purdue University, West Lafayette, IN.

Prescott, P. J., Incropera, F. P., and Gaskell, D. R., 1992, "The Effects of Undercooling, Recalescence and Solid Transport on the Solidification of Binary Metal Alloys," in: *Transport Phenomena in Materials Processing and Manufacturing,* Charmchi et al., eds., ASME HTD-Vol. 196, pp. 31–39.

Prescott, P. J., and Incropera, F. P., 1993, "Magnetically Damped Convection During Solidification of a Binary Metal Alloy," ASME JOURNAL OF HEAT TRANSFER, Vol. 115, pp. 302–310.

Prescott, P. J., and Incropera, F. P., 1994a, "The Effect of Turbulence on Solidification of a Binary Metal Alloy With Electromagnetic Stirring," in: *Transport Phenomena in Materials Processing and Manufacturing 1994,* Alam et al., eds., ASME HTD-Vol. 280, pp. 59–69.

Prescott, P. J., and Incropera, F. P., 1994b, "Convective Transport Phenomena and Macrosegregation During Solidification of a Binary Metal Alloy—I. Numerical Predictions," ASME JOURNAL OF HEAT TRANSFER, Vol. 116, pp. 735–741.

Prescott, P. J., Incropera, F. P., and Gaskell, D. R., 1994, "Convective Transport Phenomena and Macrosegregation During Solidification of a Binary Metal Alloy—II. Experiments and Comparisons With Numerical Predictions," ASME JOURNAL OF HEAT TRANSFER, Vol. 116, pp. 742–749.

Investigation of Non-Darcian Forced Convection in an Asymmetrically Heated Sintered Porous Channel

G. J. Hwang

C. C. Wu

C. H. Chao[1]

Department of Power Mechanical Engineering,
National Tsing Hua University,
Hsinchu 30043, Taiwan

A study of non-Darcian forced convection in an asymmetric heating sintered porous channel is carried out to investigate the feasibility of using this channel as a heat sink for high-performance forced air cooling in microelectronics. A volume-averaging technique is applied to obtain the macroscopic equations with the non-Darcian effects of no-slip boundary, flow inertia, and thermal dispersion. Local non-thermal-equilibrium is assumed between the solid and the fluid phases. The analysis reveals that the particle Reynolds number significantly affects the solid-to-fluid heat transfer coefficients. A wall function is introduced to model the transverse thermal dispersion process for the wall effect on the lateral mixing of fluid. The local heat transfer coefficient at the inlet is modeled by a modified impinging jet result, and the noninsulated thermal condition is considered at exit. The numerical results are found to be in good agreement with the experimental results in the ranges of $32 \leq Re_d \leq 428$ *and* $q = 0.8 \sim 3.2$ *W/cm*^{2} *for* $Pr = 0.71$.

Introduction

This paper investigates the feasibility of using porous channels as heat sinks for high-performance forced air cooling in microelectronics. The demand for high execution speed and memory capacity for modern computers results in an increasing circuit density per unit chip and high power dissipation per unit volume. The heat flux of the chip may be raised to a certain high level, e.g., typical average power densities at the chip level for plastic DIPs and PGA ceramic package are about 10 and 25 W/cm^2, respectively (Mahalingam and Berg, 1984; Mahalingam, 1985). For reliable operation, the temperature of an electronic package must be maintained at a tolerable level, e.g., below 130°C. Generally, natural and forced convection remove only a small amount of heat around 0.001 W/cm^2°C by natural convection, 0.01 W/cm^2°C in forced air, and 0.1 W/cm^2°C in forced liquid (Simons, 1983). Compared to the heat flux level at the chip, heat removal from the package surface by those common heat transfer techniques is quite low. Therefore, efficient cooling schemes must be developed to remove the heat to the environment.

While heat flow inside the package is primarily by thermal conduction and heat removal from the package surface is by convection, the thermal resistance between the coolant and the package surface should be considered a key factor. Therefore, a large heat transfer coefficient and/or large contact surface for heat disposal is pursued for package cooling. Tuckerman and Pease (1981, 1982) pointed out that for laminar flow in confined channels, the heat transfer coefficient is inversely proportional to the width of the channel since the limiting Nusselt number is constant. A water-cooled integral heat sink with microscopic flow channels, typically 50 μm wide and 300 μm deep, was built to demonstrate that extremely high power density circuits could be cooled with a surface flux of 790 W/cm^2 or more. Mahalingam (1985) confirmed the superiority of microchannel cooling on a silicon substrate of 5 × 5 cm by using water and air as coolants. This corresponds to a heat removal of 3.6 W/cm^2°C for water and 0.1 W/cm^2°C for air at the silicon substrate level. It is interesting to note that for the thermal entrance region problem (Graetz problem), the local Nusselt number attains an asymptotic value (a constant minimum value) for fully developed flow. This fact in forced convection was recognized in 1883 and was not utilized for about a hundred years until Tuckerman and Pease (1981, 1982) developed forced convection cooling during the 1980s.

Another cooling technique is heat transfer augmentation using a porous medium. Kuo and Tien (1988) and Hunt and Tien (1988) utilized a foam material to enhance liquid forced convection cooling as a potential application for electronic cooling. The results show that an increase of about two to four times in heat transfer is achievable as compared with that of laminar slug-flow in a clear duct. Thermal dispersion caused by the presence of the solid matrix plays a key role in their heat transfer augmentation. Koh and Colony (1974) and Koh and Stevens (1975) studied the problem of forced convection in a porous channel by using a Darcy flow model and found that under the boundary condition of a constant heat flux, the wall temperature and the temperature difference between wall and coolant can be drastically decreased by insertion of a high-conductivity porous material in the channel.

A porous medium will provide a solid–air contact area many times greater than the duct surface area. The total heat transfer rate will be increased by several orders of magnitude regardless of its lower heat transfer coefficient on the solid–air contact surface. By adopting this idea, the experimental and theoretical investigations are conducted to examine the feasibility of using a high-conductivity porous channel as a heat sink for high-performance forced air cooling in microelectronics. The porous channel 5 × 5 × 1 cm was made of sintered bronze beads with two different mean diameters, d_p equals 0.72 mm and 1.59 mm. Since microelectronic device may be damaged by a local excess high temperature of the heat sink instead of the average one, the local wall temperature distribution and heat transfer coefficient are measured. The results show that the high-conductivity

[1] Current address: Energy & Resources Laboratories, ITRI, Chutung 310, Taiwan.

Contributed by the Heat Transfer Division and presented at the ASME Winter Annual Meeting, New Orleans, Louisiana, November 28-December 3, 1993. Manuscript received by the Heat Transfer Division October 1993; revision received November 1994. Keywords: Electronic Equipment, Forced Convection, Porous Media. Associate Technical Editor: C. E. Hickox, Jr.

porous channel enhances the heat transfer, and the maximum wall temperature could be reduced drastically. The theoretical results are also found to be in good agreement with the experimental results in the present study.

Experimental Apparatus and Procedure

An experimental setup for heat transfer measurement of a sintered copper bead porous channel was established previously (Hwang and Chao, 1994). It was composed of four major parts: (*a*) coolant air supply, (*b*) test section, (*c*) porous medium, and (*d*) data acquisition system. The details of the apparatus will not be described in this paper. The measurements of porosity, bead size distribution, permeability and inertia constant, and the effective thermal conductivity can be also found in the previous work. It is noted that the values of K and F are 2.9×10^{-10} m^2 and 0.242 for $d_p = 0.72$ mm and 10^{-9} m^2 and 0.118 for $d_p = 1.59$ mm.

The test was conducted by increasing the power input to the test section while maintaining a constant flow rate and a constant inlet temperature. The flow rate, inlet and outlet fluid temperatures, the local wall temperatures, and electrical power input were recorded. Preliminary tests were performed for data calibration and error estimation. The errors in the temperature measurement were due to the inaccuracies in the initial calibration of the thermocouples, and the reading of the recorder. The maximum error was within ±0.1°C for the temperature measurement.

The local wall temperatures were read from the outputs of the 36 thermocouples on the copper plates. By using the three-point Gauss integral rule, the regional average wall temperature T_{wi} was calculated by using the three measured data at each axial location i:

$$T_{wi} = (5T_i^{j=1} + 8T_i^{j=2} + 5T_i^{j=3})/18 \quad (1)$$

The local bulk air temperature, T_{bx}, at each section was calculated by assuming a linear air temperature variation along the flow channel. The net heat input to the test section Q_a was computed as the difference between the electric power input Q_e and the heat loss Q_{loss} through the insulation. By performing tests at different electrical power settings, heat loss for the test section was determined. This will be discussed in Fig. 1. The effect of axial wall temperature variation on the local film heater resistance was relatively small. The maximum errors both in the flow rate and pressure drop across the test section were less than 5 percent.

The local heat transfer coefficient, h_x, and Nusselt number, Nu_{fx}, at a specific axial location were calculated as

$$h_x = \frac{q}{T_w - T_{fb}} \quad (2)$$

$$\text{Nu}_{fx} = \frac{h_x H}{k_f} \quad (3)$$

where $q = Q_a/A_{\text{heated}} = (Q_e - Q_{\text{loss}})/A_{\text{heated}}$, is the net heat input per unit area, and k_f is the thermal conductivity of fluid evaluated at local film temperature, $T_{\text{film}} = (T_b + T_w)/2$.

An analysis of the general validity of experimental measurements was performed by using an uncertainty analysis (Kline and McClintock, 1953). The uncertainty of thermocouple temperature reading is within ±0.1°C, thus the uncertainty of $(T_w - T_b)$ is within ±0.2°C. In the present experiment, the values of $(T_w - T_b)$ are about 2°C near inlet region and 50°C near outlet region, therefore the percentage uncertainty of $(T_w - T_b)$ is about ±10 percent and ±0.4 percent near the inlet and outlet regions, respectively. The maximum errors in determining the net heat flux, q, channel height, H, and fluid conductivity, k_f, are estimated within 2, 1, and 1 percent, respectively. Therefore, the uncertainties of the values of h_x and Nu_{fx} by using the root-sum-square method are within 11 percent, in the present experimental study.

Nomenclature

a = specific surface area per unit volume, m^{-1}
Bi = modified Biot number = $h_{\text{loc}}aH^2/k_s^*$
C = dimensionless pressure drop = $-(dP/dx)K/\mu_f U_m$
c_f = isobaric specific heat, J/kgK
Da = Darcy number = $K/\epsilon H^2$
D_t = thermal dispersion constant
d_i = diameter of the beads in a particular size range
d_p = average bead diameter, m
d_v = average void diameter = $4\epsilon/a$, m
F = inertia coefficient constant or variables
Fs = Forchheimer number = $\dot{m}F\sqrt{K}/\mu_f$
H = channel height, m
h_x = local heat transfer coefficient = $q/(T_w - T_{fb})$, W/cm^{2}K
h_{0X} = local heat transfer coefficient = $q/(T_w - T_{in})$, W/cm^{2}K
h_{loc} = internal heat transfer coefficient, W/m^{2}K
K = permeability, m^2
k = thermal conductivity
k_e = effective thermal conductivity of porous media, W/mK
k_r = solid conductivity to fluid conductivity ratio = k_s^*/k_f^*
L = heater length, m
l = wall function defined in Eq. (8)
M = grid number along x direction
$\dot{m}$ = mass flow rate of fluid per unit sectional area, kg/m^{2}s
N = grid number along y direction
Nu_{fx} = local Nusselt number for the rectangular channel = $h_x H/k_f$
P = pressure, N/m^2 or nodal point
Pe_d = particle Peclet number = $c_f\dot{m}d_p/k_f^*$
Pr = fluid Prandtl number = $c_f\mu_f/k_f$
Q, q = power input, W, and wall heat flux per unit area, W/cm^2
R_h = channel height to average particle diameter ratio = H/d_p
Re_d = particle Reynolds number = $\dot{m}d_p/\mu_f$
Re_v = modified Reynolds number = $\dot{m}d_v/\mu_f$
T = temperature, K
U, u = volume average velocity, m/s, and dimensionless volume average velocity
$\dot{V}$ = volume flow rate of fluid, m^3/s
v = volume, m^3
W = heater width, m
w_i = weight fraction
x, y = dimensionless coordinate
X, Y = Cartesian coordinates
ϵ = void fraction or porosity
θ = dimensionless temperature difference = $(T - T_{in})/(qH/k_s^*)$
μ = viscosity, kg/ms
ρ = density, kg/m^3
ω = empirical constant

Superscripts

− = average value
* = equivalent value
k = number of iteration
n = empirical constant

Subscripts

a = energy difference between power input to film heater and heat loss
b = bulk quantity
d = quantity based on Darcy's law
e = power generated by film heater
f = quantity based on fluid
i, j = position of thermocouple
in = inlet value
m = average value
out = exit value
s = quantity based on solid
t = total or quantity based on thermal dispersion
w = quantity based on the wall

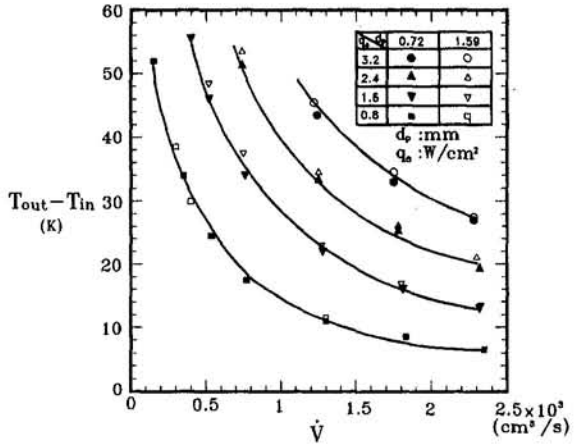

Fig. 1 Effect of input heat flux and $\dot{V}$ on $T_{out} - T_{in}$

Theoretical Analysis

Heat transfer in a porous channel involves a complex thermal transport mechanism between the coolant and sintered metal beads. It is difficult to have exact solutions for the local velocity and temperature fields. The physical configuration considered is two horizontal parallel plates filled with packed spheres. A constant heat flux source of finite length is located on the lower plate ($Y = 0$), and the upper plate ($Y = H$) is insulated. A uniform flow in the X direction with velocity U_{in} and constant temperature T_{in} passes through and cools the channel. To establish a mathematical model for analyzing this problem, the following assumptions and simplifications are employed:

1 The width of the porous channel is much larger than the height; therefore, this is essentially a two-dimensional problem.
2 The porous medium has uniform porosity and is isotropic. The thermophysical properties of the fluid are constant.
3 The fluid flow is steady, incompressible, and one dimensional with the normal velocity zero. The pressure distributions across the porous channel are constant.
4 There is no local thermal equilibrium between the solid and fluid phases.
5 Non-Darcian effects of no-slip boundary, flow inertia, and thermal dispersion are considered.

The governing equations are developed by application of the local volume-averaging technique and coincide with the results obtained using the continuum model, based on the representative elementary volume concept (Nield and Bejan, 1992). This averaging process may obscure local pore phenomena that contribute to the global transport; therefore it requires empirical relations for closure. The volume-averaged governing equations for forced convection in porous media can be written as follows:

$$0 = -\frac{dP}{dX} - \frac{\mu_f}{K}U - \frac{\rho_f F}{\sqrt{K}}U^2 + \frac{\mu_f}{\epsilon}\frac{d^2U}{dY^2} \tag{4}$$

$$0 = h_{loc}a(T_f - T_s) + k_s^*\left(\frac{\partial^2 T_s}{\partial X^2} + \frac{\partial^2 T_s}{\partial Y^2}\right) \tag{5}$$

$$(\rho c)_f U\frac{\partial T_f}{\partial X} = h_{loc}a(T_s - T_f) + (k_f^* + k_t^*)\left(\frac{\partial^2 T_f}{\partial X^2} + \frac{\partial^2 T_f}{\partial Y^2}\right) \tag{6}$$

where Eq. (4) is for x momentum, Eq. (5) is the energy equation for the solid, and Eq. (6) is the energy equation for the fluid. The momentum Eq. (4) neglects the inertia terms. Since an entrance section using the same porous material was employed, the velocity is assumed fully developed. At low velocities, Forchheimer's effect becomes insignificant and Darcy's law is resumed. In the transitional and turbulent flow regions, inertia effect, which is proportional to the square of the velocity, becomes important. The equivalent conductivity of the solid k_s^* in Eq. (5) is a function of the geometry and the solid conductivity k_s. Similarly, the equivalent conductivity of fluid k_f^* in Eq. (6) is simply ϵk_f. k_t^* is the transverse thermal dispersion conductivity. Thermal dispersion results from the existence of the solid matrix, which forces the flow to undergo a tortuous path around the solid particles. The value of the thermal dispersion conductivity is proposed to be proportional to a product of the local velocity and mixing length, which is given as

$$k_t^* = D_t(\rho c)_f d_p U l \tag{7}$$

where D_t is an empirical constant, and l is the wall function for transverse thermal dispersion introduced by Chen and Hsu (1986). To account for the wall effect on reduction of lateral mixing of the fluid, the Van Driest type of wall function l is introduced by Cheng and his co-workers (1986, 1988).

$$l = 1 - \exp[-Y/(\omega d_p)] \quad 0 \le Y \le H/2$$
$$= 1 - \exp[-(H - Y)/\omega d_p] \quad H/2 \le Y \le H \tag{8}$$

where ω is an empirical constant. Note that the empirical constants $D_t = 0.375$ and $\omega = 1.5$ (Hwang and Chao, 1994) are used throughout the present study. Due to the high solid-to-fluid conductivity ratio, the temperature difference between the solid and the fluid should not be negligible. Therefore, the energy conservation equations must be set up for solid and fluid separately, as shown in Eqs. (5) and (6). An empirical correlation form of the particle-to-fluid heat transfer coefficient h_{loc} is chosen from the existing experimental results. Considering the range of the particle Reynolds number Re_d, the empirical correlations of h_{loc} established by Kar and Dybbs (1982) for $Re_d \le 75$ and Gamson et al. (1943) for $Re_d \ge 350$ are used. The heat transfer coefficient between the solid and fluid phases can be expressed in the following form after some manipulation:

$$h_{loc} = 0.004\left(\frac{d_v}{d_p}\right)^{0.35}\left(\frac{k_f}{d_p}\right)Pr^{0.33}\,Re_d^{1.35} \quad Re_d \le 75 \tag{9}$$

(Kar and Dybbs 1982)

$$h_{loc} = 1.064\left(\frac{k_f}{d_p}\right)Pr^{0.33}\,Re_d^{0.59} \quad Re_d \ge 350 \tag{10}$$

(Gamson et al., 1943)

where Pr is the Prandtl number of the fluid, d_p is the average bead diameter, d_v is the average void diameter, and the particle Reynolds number Re_d is based on the particle diameter. The coefficient h_{loc} between $Re_d = 75 \sim 350$ could be obtained from the interpolation of the results of Eqs. (9) and (10). In Eqs. (5) and (6), a stands for the surface area per unit bulk volume of the packed bed:

$$a = 20.346(1 - \epsilon)\epsilon^2/d_p \tag{11}$$

The appropriate boundary conditions are

$$T_f = T_{in} \quad \text{and}$$

$$k_s^*\frac{\partial T_s}{\partial X} = 1.29\left(\frac{d_v}{d_p}\right)^{0.5} Re_d^{0.5}\,Pr^{0.4}\,(k_f^* + k_t^*)(T_s - T_{in})/d_v \quad \text{at } X = 0 \tag{12}$$

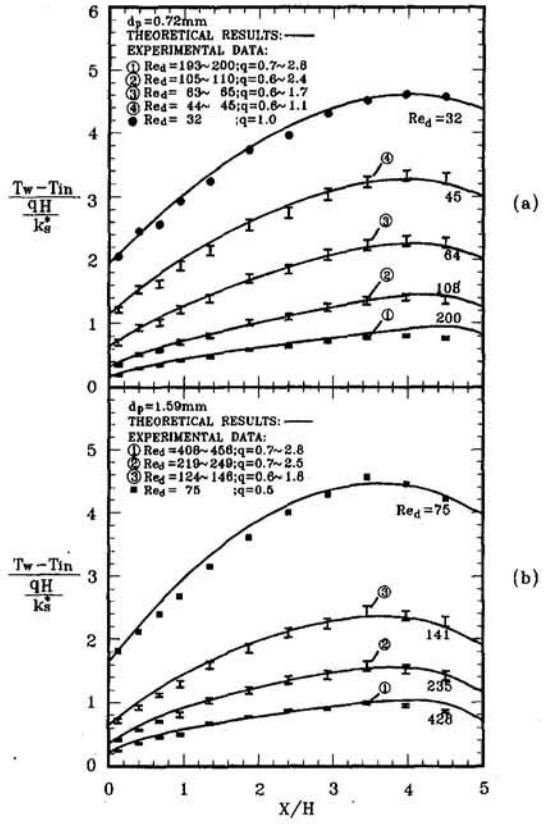

Fig. 2 Dimensionless wall temperature distributions for two porous channels: (*a*) d_p = 0.72 mm, (*b*) d_p = 1.59 mm

$$\frac{\partial T_f}{\partial X} = 0 \quad \text{and}$$

$$k_s^* \frac{\partial T_s}{\partial X} = -0.2776\ \mathrm{Re}_d^{0.5}\ \mathrm{Pr}^{0.4}\ (k_f^* + k_t^*)(T_s - T_f)/d_p \quad \text{at } X = 5H \quad (13)$$

$$U = 0, \quad -\left(k_f^* \frac{\partial T_f}{\partial Y} + k_s^* \frac{\partial T_s}{\partial Y}\right) = q \quad \text{at } Y = 0 \quad (14)$$

$$U = 0, \quad \frac{\partial T_s}{\partial Y} = \frac{\partial T_f}{\partial Y} = 0 \quad \text{at } Y = H \quad (15)$$

In the experiments, to avoid the inlet heat loss by axial conduction, the entrance and test sections were separated by a gap of 1 mm. Fluid leaving the pore area of the porous medium in the upstream entrance section and passing through the gap can be regarded as impinging jet flow. The local heat transfer rate at the inlet surface of the test section is modeled by a modified impinging jet results of Ma and Bergles (1988) as shown in Eq. (12). The exit surface of the test section is cooling convectively, and as depicted by Eq. (13) is modeled by using the local heat transfer coefficients for spheres of Cary (1953). The governing equations can be nondimensionalized by introducing the following variables:

$$x = X/H,\ y = Y/H,\ u = U/U_m,\quad \theta = (T - T_{in})/(qH/k_s^*)$$

$$R_h = H/d_p,\quad k_r = k_s^*/k_f^*,\quad \dot{m} = \rho U_m,\quad D_a = K/(\epsilon H^2),$$

$$\mathrm{Fs} = \dot{m}F\sqrt{K}/\mu_f,$$

$$\mathrm{Re}_d = \dot{m}d_p/\mu_f,\quad \mathrm{Bi} = (h_{\mathrm{loc}}aH^2)/k_s^*,\quad \mathrm{Pe}_d = \dot{m}c_f d_p/k_f^*,$$

$$C = -(dP/dx)K/(\mu_f U_m)$$

where Da is the Darcy number, Fs is the Forchheimer number, Bi is the modified Biot number, Pe_d is the particle Peclet number, k_r is the conductivity ratio of solid to fluid, R_h is the ratio of channel height to average particle diameter, and U_m is the average velocity in the channel. The nondimensionalized equations and boundary conditions are then expressed as follows:

$$\mathrm{Da}\frac{d^2u}{dy^2} - (1 + \mathrm{Fs}u)u + C = 0 \quad (16)$$

$$0 = \mathrm{Bi}(\theta_f - \theta_s) + \frac{\partial^2\theta_s}{\partial x^2} + \frac{\partial^2\theta_s}{\partial y^2} \quad (17)$$

$$\frac{\mathrm{Pe}_d R_h}{k_r} u \frac{\partial\theta_f}{\partial x} = \mathrm{Bi}(\theta_s - \theta_f) + \frac{1 + \mathrm{Pe}_d D_t u l}{k_r}\left(\frac{\partial^2\theta_f}{\partial x^2} + \frac{\partial^2\theta_f}{\partial y^2}\right) \quad (18)$$

$$\theta_f = 0,\ \frac{\partial\theta_s}{\partial x} = 1.29 l D_t \left(\frac{d_v}{d_p}\right)^{0.5}\left(\frac{k_f}{k_s^*}\right)\left(\frac{H}{d_v}\right)\mathrm{Pr}^{1.4}\mathrm{Re}_d^{1.5}\ u\theta_s \quad \text{at } x = 0 \quad (19)$$

$$\frac{\partial\theta_f}{\partial x} = 0,\ \frac{\partial\theta_s}{\partial x} = -0.2776 l D_t \left(\frac{k_f}{k_s^*}\right)\left(\frac{H}{d_p}\right)\mathrm{Pr}^{1.4}\ \mathrm{Re}_d^{1.5} u(\theta_s - \theta_f) \quad \text{at } x = 5 \quad (20)$$

$$u = 0,\ \theta_s = \theta_f,\ \frac{\partial\theta_s}{\partial y} + \frac{1}{k_r}\frac{\partial\theta_f}{\partial y} = -1 \quad \text{at } y = 0 \quad (21)$$

$$u = \frac{\partial\theta_s}{\partial y} = \frac{\partial\theta_f}{\partial y} = 0 \quad \text{at } y = 1 \quad (22)$$

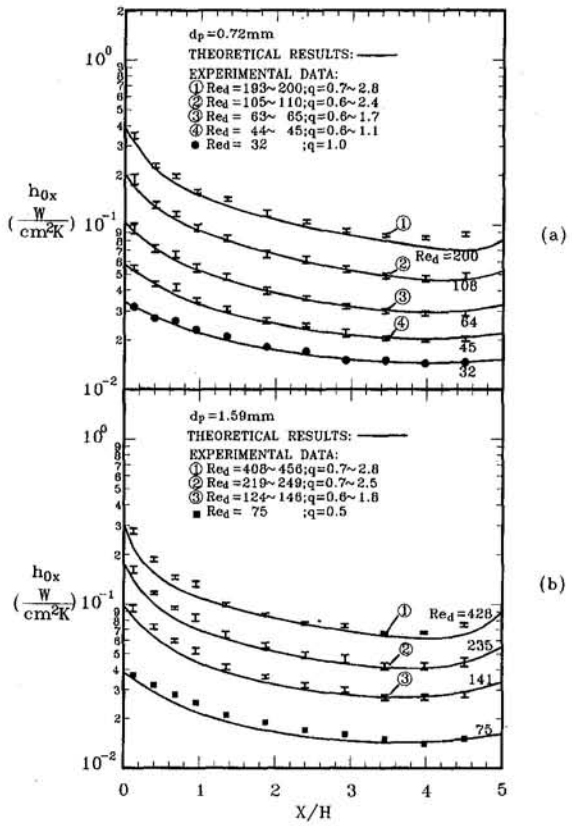

Fig. 3 h_{0x} versus X/H with the effect of particle Reynolds number for (*a*) d_p = 0.72 mm and (*b*) d_p = 1.59 mm

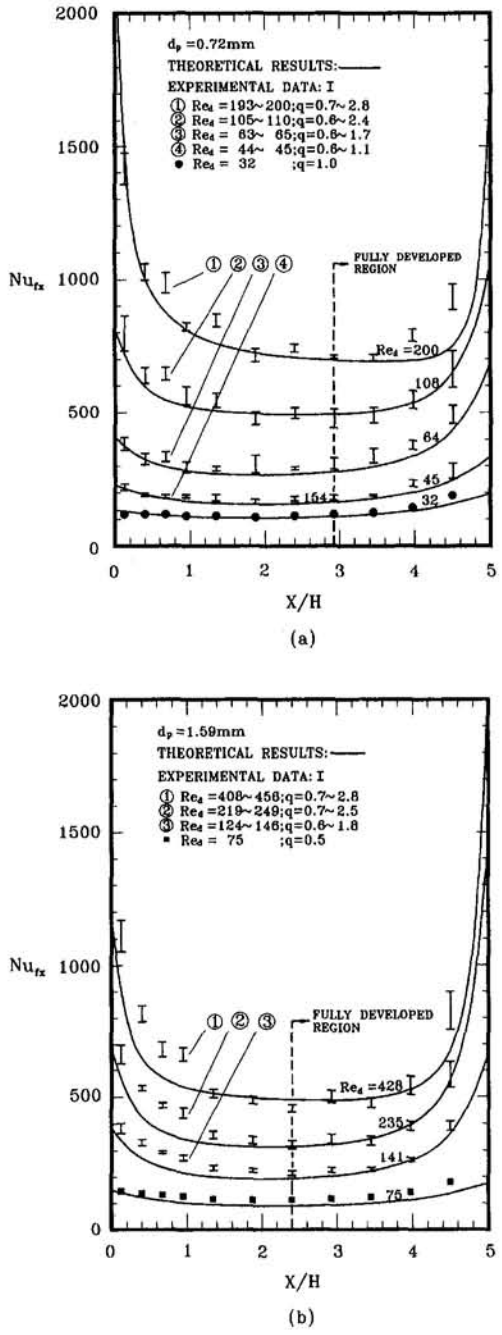

Fig. 4 Nu_{fx} versus X/H with the effect of particle Reynolds number for (a) d_p = 0.72 mm and (b) d_p = 1.59 mm

Note that the assumption of $k_f^* \ll k_i^*$ and Eq. (7) are used in Eqs. (12) and (13) to derive Eqs. (19) and (20).

Numerical Procedure

As it is difficult to derive the analytical solution of the coupled governing equations of the problem under consideration, a finite difference method is utilized. Using the prescribed values of Da, Fs, Bi, Pe_d, D_t, R_k, k_r, and ω, Eqs. (16)–(18) can be used to compute the local volume-averaging velocity, solid, and fluid temperature profiles. In order to predict the flow and temperature fields accurately, particularly for low Darcy number flow, a high density node is required near the walls. Hence, a coordinate stretching transformation is introduced to distribute a reasonable number of grid points near the wall. The y coordinate is transformed by using a simple algebraic relationship

$$\overline{P_1P_J} = \overline{P_1P_N}\left(\frac{J-1}{N-1}\right)^n$$

$$1 \le J \le N \quad \text{and} \quad 1 \le n \le 2 \quad (23)$$

where N is the number of grid points along the y direction, P_1 and P_N are the positions of the end points, and P_J is the position of an intermediate point. A uniform grid was adopted along the x direction. Momentum Eq. (16) was solved by using a three-point finite difference scheme in the y direction. The dimensionless pressure drop C was guessed initially and adjusted by considering the relation

$$C_{new} = C_{old} \Big/ \left(\int u dy\right) \quad (24)$$

It is noted that the value of C will remain constant if the global

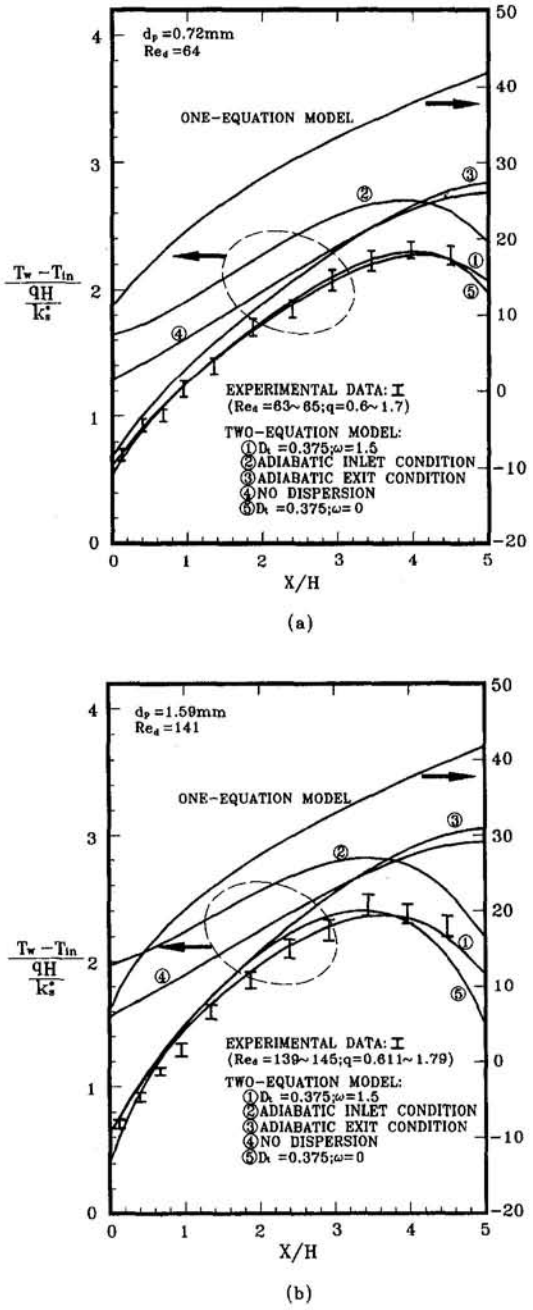

Fig. 5 Comparison of various theoretical models: (a) d_p = 0.72 mm and Re_d = 64, (b) d_p = 1.59 mm and Re_d = 141

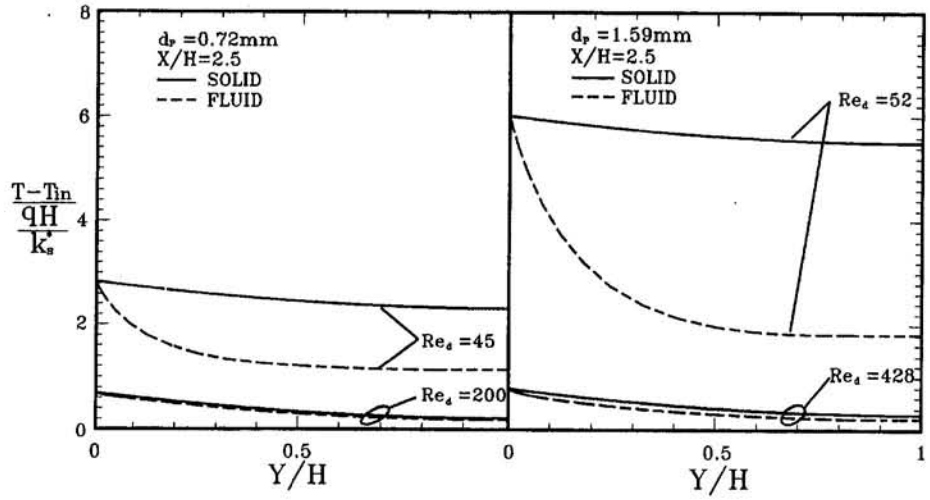

Fig. 6 Effect of Re_d and d_p on transverse temperature distributions

continuity equation $\int u dy = 1$. With the converged velocity distribution, the energy equations of solid and fluid phases together with wall function (8) and boundary conditions (19)–(22) were solved simultaneously. The numerical scheme applied to Eqs. (17) and (18) was a five-point central difference in the x direction for both the first and second-order derivatives and a three-point central difference in the y direction. The algorithm was solved by using a line iterative S.O.R. The convergent criterion was:

$$\max|F_i^{k+1} - F_i^k| / \max|F_i^{k+1}| \leq 10^{-5} \qquad (25)$$

where F denotes the variables of u, θ_f, and θ_s. The stability of the numerical scheme was ensured by choosing a proper combination of Δx and Δy. The numerical experiment for grid size is carried out for the case $d_p = 0.72$ mm, $q = 0.8$ W/cm^2, $D_i = 0.375$, $\omega = 1.5$, and $\mathrm{Re}_d = 200$. The values of $(T_{fb})_{\text{out}} - (T_{fb})_{in}$ are 7.022, 7.036, 7.046, 7.041, and 7.043 for $M \times N = 41 \times 41$, 61×41, 81×41, 61×61, and 61×81, respectively. It was found that the results obtained by using the 61×81 mesh change only less than 0.03 percent from the results obtained by using the 61×41 mesh. Finally, 61×41 mesh was used throughout the computation. The computational results also compared with the results of the sixth-order approximation by using the Richardson extrapolation and the percentage error was within 0.2.

Results and Discussion

Theoretical calculations were carried out for the various experimental measurement conditions in order to confirm the validity of the model and the assumptions. Figure 1 shows the measured results of the bulk mean temperature difference between inlet and outlet with a given volume flow rate from 150 to 2400 cm^3/s for $d_p = 0.72$ mm and 1.59 mm. The net heat flux, q, can be calculated by using the concept of energy conservation as

$$qLW = (\rho c)_f \dot{V}(T_{\text{out}} - T_{in}) \times 10^{-4} \qquad (26)$$

where L and W are the heater length and width, respectively. The product of $(T_{\text{out}} - T_{in})$ and $(\rho c)_f \dot{V}$ is the heat transferred from the bottom plate that equals the electric power input (Q_e) minus the heat loss (Q_{loss}) by conduction. Therefore, the heat loss by conduction at various temperature difference can be estimated from this figure.

In microelectronics, almost all of the electrical energy consumed by microelectronics devices manifests itself as thermal energy and elevates the temperature of the device. The device can be damaged by excess local high temperature instead of the average one, therefore the temperature distribution along the flow direction of the test section is of practical interest in design. Figure 2 presents the local dimensionless wall temperature distribution along the flow direction with the effects of particle Reynolds number for $d_p = 0.72$ mm and 1.59 mm. It is seen that the local dimensionless wall temperatures increase as the axial distance increase for a given particle Reynolds number. As expected, with increasing particle Reynolds number, the local dimensionless wall temperature distributions are decreased. The theoretical results are generally in good agreement with the experimental measurements for $32 \leq \mathrm{Re}_d \leq 428$. The experimental results are tabulated in Table 1. The sharp gradient of temperature distribution near $X = 0$ is well simulated by the thermal boundary conditions of the modified impinging jet model. The temperature gradient is getting smaller with the increase in X. Near the exit, the decrease of the dimensionless wall temperature is due to the discontinuity of wall heat flux at exit. It is noted that the calculated results will deviate significantly from the measured data if the inlet and/or outlet thermal boundary conditions, Eqs. (19) and (20), were not considered. This will be explained in Fig. 5.

A local heat transfer coefficient is defined in terms of the temperature difference between the heated wall and the inlet (or ambient) temperatures when the power dissipation is known. Therefore, the local heat transfer coefficient, h_{0x}, can be calculated as

$$h_{0x} = \frac{q}{T_w - T_{in}} \qquad (27)$$

where q is the wall heat flux from Eq. (26) and T_{in} is the inlet fluid temperature. The distributions of h_{0x} for various particle Reynolds numbers are depicted in Fig. 3. The values of h_{0x} drop rapidly for small X. As shown in this figure, the h_{0x} increases with the decrease in the particle diameter and increases with the particle Reynolds number. The effects of particle size can be explained by the fact that as the particle diameter decreases, the specific surface area a of the porous channel increases. This corollary is different from the one found using the local thermal equilibrium assumption. For this model, a large particle size causes a larger permeability, which in turn leads to a larger velocity. Therefore, smaller size particles cause a thicker thermal boundary layer, leading to smaller heat transfer coefficients (Vafai, 1984).

Figure 4 presents Nu_{fx} versus X/H for $d_p = 0.72$ mm and 1.59 mm, respectively. It is interesting to note that for the thermal entrance region problem (Graetz problem), the local Nusselt number attains an asymptotic value (a constant minimum

value) for fully developed flow. A similar trend is also observed here. For a given particle Reynolds number, the local Nusselt number decreases along the flow direction and then reaches its fully developed value, but increases abruptly at the exit of the test section. This phenomenon can be explained by the fact that the temperature difference $(T_w - T_{fb})$ as shown in Eqs. (2) and (3) decreases near the exit. This is due to the thermal boundary condition at the exit of the test section. In the exit region of a short channel, the thermal energy is conducted in an opposite direction to the exit section. Therefore a declining temperature distribution is obtained.

Heat transfer between the solid and the fluid phases, h_{loc}, is modeled via Eqs. (9) and (10). It can be seen that the difference in the h_{loc} calculated from the two equations is large for the particle Reynolds number between 75 and 350. Equation (9) can be safely used for particle Reynolds number up to 75, while Eq. (10) can be used for particle Reynolds number greater than 350. The values of h_{loc} can be appropriately interpolated from the empirical chart for intermediate values of the particle Reynolds number in a manner suggested by Gamson et al. (1943). This can be explained by the fact that in the intermediate range from 75 to 350 the flow may be transitional.

In order to verify the validity of the present model, comparisons of various test models for $d_p = 0.72$ mm and $d_p = 1.59$ mm are shown in Figs. 5(*a*) and 5(*b*), respectively. In one equation model, local thermal equilibrium is assumed. The extra heat transfer through the high thermal conductivity solid phase is neglected, and therefore the wall temperature distribution is much higher than that of the experimental results. The present model considers the inlet and outlet thermal boundary conditions, thermal dispersion, and wall function. Good agreement between the results of the model and the experimental data is observed. If an inlet adiabatic condition is used, higher wall temperature is found over the whole region, as shown by curve 2. If the exit plane is adiabatic, the wall temperature grows continuously near the outlet region, as shown by curve 3. If thermal dispersion is not considered, the wall temperature is also higher than that of experimental data as shown by curve 4. Finally, curve 5 in Figs. 5(*a*) and 5(*b*) shows the temperature distributions without the wall effect ($\omega = 0$). The wall temperature difference between curve 5 ($\omega = 0$) and curve 1 for large particles is more significant than that for small particles for a fixed channel width. The present results show that the wall function must be introduced to account for the reduction of lateral mixed fluid for large d_p/H. This observation is consistent with that in the fully developed region shown in Fig. 6 of Hwang and Chao (1994).

Although the transverse temperature distribution cannot be measured experimentally, Fig. 6 shows the computed transverse temperature distribution for various Re_d. It is clear that the difference between the temperature of the solid and fluid phases decreases with an increase in particle Reynolds number. Hence the heat exchanges between the solid and fluid phases become more efficient. Therefore the local thermal equilibrium assumption would be more justified at larger particle Reynolds number. This observation agrees with the results of Hwang and Chao (1994) in the thermally fully developed flow.

Table 1 Measured temperature difference $T_w - T_{in}$ for (*a*) $d_p = 0.72$ mm and (*b*) $d_p = 1.59$ mm

Re_d	q_e*	q**	x = 0.13	0.40	0.68	0.95	1.35	1.88	2.40	2.93	3.45	3.98	4.50	5.00
193	3.2	2.8	8.4	12.6	14.5	18.0	19.9	24.8	27.2	30.9	33.2	34.4	32.8	26.9†
197	2.4	2.0	6.0	9.1	10.7	13.2	14.7	18.3	20.0	22.6	24.4	25.4	24.2	19.6
208	1.6	1.4	4.0	6.1	7.1	8.8	9.8	12.2	13.4	15.1	16.3	17.0	16.0	12.9
200	0.8	0.7	1.9	3.0	3.6	4.3	4.9	6.1	6.6	7.4	8.1	8.43	7.73	6.3
105	3.2	2.4	14.0	19.6	21.8	27.2	31.0	38.6	42.3	48.3	52.0	53.9	52.5	45.9
106	2.4	1.9	10.1	14.4	16.1	19.9	22.7	28.3	31.0	35.4	38.2	39.7	38.7	32.6
109	1.6	1.3	6.6	9.4	10.6	13.2	15.0	18.6	20.5	23.3	25.3	26.4	25.8	21.3
110	0.8	0.6	3.2	4.8	5.4	6.5	7.5	9.4	10.2	11.6	12.6	13.2	12.7	10.9
63	2.4	1.7	19.4	25.4	27.4	33.2	37.7	46.0	49.8	56.0	59.8	61.7	60.8	50.1
65	1.6	1.2	12.2	16.3	17.6	21.4	24.5	29.9	32.5	36.6	39.3	40.6	40.0	32.6
65	0.8	0.6	6.0	8.1	8.8	10.6	12.2	15.0	16.3	18.3	19.7	20.6	20.2	17.2
44	1.6	1.1	20.6	25.9	27.3	32.2	36.2	43.0	46.1	51.0	54.0	55.5	54.9	44.9
45	0.8	0.6	10.3	13.0	13.8	16.2	18.3	21.8	23.5	26.1	27.8	28.7	28.3	24.2
32	1.6	1.0	31.0	37.1	38.7	44.3	48.9	56.4	59.7	65.1	68.1	69.6	69.0	54.4

(b)

Re_d	q_e	q	x = 0.13	0.40	0.68	0.95	1.35	1.88	2.40	2.93	3.45	3.98	4.50	5.00
408	3.2	2.8	10.5	15.8	19.4	22.2	29.3	33.4	38.0	39.2	43.3	43.1	39.1	29.4
423	2.4	2.2	7.6	11.6	14.7	16.4	21.7	24.9	28.2	28.9	32.0	32.0	29.0	22.2
441	1.6	1.4	5.2	7.9	10.1	11.0	14.5	16.4	18.6	19.1	21.1	21.1	19.0	13.4
456	0.8	0.7	2.6	3.6	4.7	5.0	6.8	7.9	9.0	9.2	10.2	10.3	9.0	6.5
219	3.2	2.5	16.0	22.1	27.1	31.7	40.5	47.0	53.7	57.0	62.6	63.1	59.5	47.3
222	2.4	2.0	11.9	16.5	20.7	23.6	30.2	35.0	40.0	42.2	46.4	46.8	44.0	35.4
235	1.6	1.3	7.8	11.1	14.0	15.8	20.3	23.4	26.6	28.0	30.8	31.1	29.1	23.0
249	0.8	0.7	4.4	5.8	7.0	7.8	10.0	11.6	13.2	13.9	15.3	15.5	14.3	11.6
124	2.4	1.8	20.0	25.7	30.9	36.1	44.5	51.6	58.5	62.6	67.9	68.7	66.1	53.4
134	1.6	1.3	12.9	16.9	20.9	23.8	29.5	34.2	38.8	41.5	45.2	45.9	43.9	35.6
146	0.8	0.6	6.7	8.5	10.1	11.4	14.3	16.7	18.8	20.1	22.0	22.5	21.4	17.4
75	0.8	0.5	14.8	17.3	19.6	21.9	25.8	29.5	32.7	35.0	37.3	38.0	36.0	29.8

*: Input heat flux by film heater, these values are used in Hwang and Chao, 1994.
**: Net heat flux, these values are used in the present study.
†: These values are exit air temperature difference, T_{out}-T_{in}.

Conclusions

1 A theoretical model is developed with the considerations of boundary, inertia, and transverse thermal dispersion effects to study the non-Darcian forced convection in the high-conductivity porous channels. The theoretical results coincide with the experimental measurement results by using the non-thermal-equilibrium energy equations with proper thermal boundary conditions and selecting an appropriate empirical correlation of solid-to-fluid heat transfer coefficient, h_{loc}.

2 As d_p increases, the specific surface area of the particle decreases. This causes lower heat transfer rate between the solid and the fluid phases, while Re_d was kept constant. For a fixed d_p, higher Re_d indicates higher mass flow rate applied across the porous channel. This will cause an increase in the efficiency of the heat exchange between the solid and the fluid phases. It becomes evident that for low Re_d or large d_p, the temperature difference between the solid and fluid phases will increase, thus the local thermal equilibrium assumption is invalid.

3 A high-conductivity porous channel could meet the requirements of small volume and large heat transfer coefficient in package cooling. For example, the forced air heat transfer coefficient can be increased from 0.01 to a local value of around 0.5 W/cm^2°C by using the porous heat sink of $d_p = 0.72$ mm.

Acknowledgments

The authors would like to thank the National Science Council, ROC for the financial support through Grant No. NSC-80-0404-E007-01.

References

Cary, J. R., 1953, "The Determination of Local Forced-Convection Coefficients for Spheres," *Trans. ASME,* Vol. 75, pp. 483–487.

Cheng, P., and Hsu, C. T., 1986, "Applications of Van Driest's Mixing Length Theory to Transverse Thermal Dispersion in Forced Convective Flow Through a Packed Bed," *Int. Comm. Heat Mass Transfer,* Vol. 13, pp. 613–625.

Cheng, P., Hsu, C. T., and Chowdhury, A., 1988, "Forced Convection in the Entrance Region of a Packed Channel With Asymmetric Heating," ASME JOURNAL OF HEAT TRANSFER, Vol. 110, pp. 946–954.

Gamson, B. W., Thodos, G., and Hougen, O. A., 1943, "Heat, Mass and Momentum Transfer in Flow of Gases," *Trans. AIChE,* Vol. 39, pp. 1–35.

Hunt, M. L., and Tien, C. L., 1988, "Effects of Thermal Dispersion on Forced Convection in Fibrous Media," *Int. J. Heat Mass Transfer,* Vol. 31, pp. 301–309.

Hwang, G. J., and Chao, C. H., 1994, "Heat Transfer Measurement and Analysis for Sintered Porous Channels," ASME JOURNAL OF HEAT TRANSFER, Vol. 116, pp. 456–464.

Kar, K. K., and Dybbs, A., 1982, "Internal Heat Transfer Coefficients of Porous Metals," *Proc. 1982 Winter Annual Meeting of ASME,* Phoenix, AZ, pp. 81–91.

Kline, S. J., and McClintock, F. A., 1953, "Describing Uncertainties in Single-Sample Experiments," *Mech. Eng.,* Jan., pp. 3–8.

Koh, J. C. Y., and Colony, R., 1974, "Analysis of Cooling Effectiveness for Porous Material in Coolant Passages," ASME JOURNAL OF HEAT TRANSFER, Vol. 96, pp. 324–330.

Koh, J. C. Y., and Stevens, R. L., 1975, "Enhancement of Cooling Effectiveness for Porous Material in Coolant Passages," ASME JOURNAL OF HEAT TRANSFER, Vol. 96, pp. 324–330.

Kuo, S. M., and Tien, C. L., 1988, "Heat Transfer Augmentation in a Foam-Material Filled Duct With Discrete Heat Sources," *Proceedings of IEEE Thermal Phenomena in Electronic Components Conference,* Los Angeles, CA, pp. 87–91.

Ma, C. F., and Bergles, A. E., 1988, "Convective Heat Transfer on a Small Vertical Heated Surface in an Impinging Circular Liquid Jet," *Heat Transfer Science and Technology,* Hemisphere Publishing Corp., pp. 193–200.

Mahalingam, M., and Berg, H. M., 1984, "Thermal Trend in Component Level Packaging," *Int. J. Hybrid Microelectron,* Vol. 7, pp. 1–9.

Mahalingam, M., 1985, "Thermal Management in Semiconductor Device Packaging," *Proc. IEEE,* Vol. 73, pp. 1396–1404.

Nield, D. A., and Bejan, A., 1992, *Convection in Porous Media,* Springer-Verlag, New York.

Simons, R. E., 1983, "Thermal Management of Electronic Packages," *Solid State Tech.,* Vol. 26, pp. 131–137.

Tuckerman, D. B., and Pease, R. F., 1981, "High-Performance Heat Sinking for VLSI," *Electron Device Lett.,* Vol. 2, pp. 126–129.

Tuckerman, D. B., and Pease, R. F., 1982, "Ultra High Thermal Conductance Microstructures for Cooling Integrated Circuits," IEEE CH781-4, pp. 145–149.

Vafai, K., 1984, "Convective Flow and Heat Transfer in Variable-Porosity Media," *J. Fluid Mech.,* Vol. 147, pp. 233–259.

Early Initiation of Natural Convection in an Open Porous Layer Due to the Presence of Solid Conductive Inclusions

A. Delmas
Oak Ridge National Laboratory,
Oak Ridge, TN

E. Arquis
Laboratoire MASTER/ENSCPB,
Université de Bordeaux I,
33405 Talence, France

The effects of solid conductive blocks on the initiation of convection in a porous medium are reported in this paper. A two-dimensional convective code was used to determine the temperature field, the structure of the motion, and the global heat transfer through a composite medium consisting of permeable and impermeable areas. Influence of the size of impermeable regions on convection as well as the effect of the distance between these solid blocks was studied in terms of Nusselt number and maximum of the stream function. The predicted heat transfer in this type of composite medium, obtained with the code, was compared with experimental results where the porous medium is a low-density insulating material in which some wood joists are included. This configuration corresponds to the layer of insulation on the floor of a residential attic.

1 Introduction

Natural convection within fiberglass has generally been considered negligible and can be considered so in building applications when two faces of the insulating product are impermeable. However, previous experimental studies have shown that in material such as some low-density loose-fill fiberglass insulation, convection can be a significant heat transfer mechanism (Fournier and Klarsfeld, 1971; Bankvall, 1975; Wilkes and Rucker, 1983) and more recently (Langlais et al., 1990; Silberstein et al., 1990).

In 1990–1992, a series of tests was performed in an attic test module with several types of insulation. One of the objectives was to measure the thermal resistance of the insulation under winter-type conditions in an attic configuration. The test module was used in the Large-Scale Climate Simulator at the Roof Research Center at Oak Ridge National Laboratory. Testing with one type of loose-fill fiberglass insulation clearly showed that, under realistic cold winter conditions, thermal performance of the insulation was reduced considerably.

Many experimental and theoretical studies have been performed on the subject of natural convection in porous media (Nield, 1968; Arquis and Caltagirone, 1987; Wilkes and Childs, 1992), leading to predictions of conditions under which convection occurs within a porous medium. The criteria for the onset of convection, however, depend on particular geometric and dynamic conditions.

Previous studies have shown that the real problem of thermal insulation in buildings is more complex and cannot always be studied under these simplifying assumptions (Delmas and Wilkes, 1992a, b). In particular, routine tests of fiberglass insulation with small-scale heat flow meter apparatuses operated in normal mode have not shown any evidence of convective motion. Although this system is currently used as a standard method to test insulation, it appears not to be sensitive to natural convection. Several reasons have been hypothesized for differing results between the heat meter data and results obtained in the attic test module. First, the mechanical and thermal boundary conditions are different. In the heat meter apparatus, the insulation is sandwiched between two isothermal impermeable plates, while in the attic, the bottom boundary is an impermeable gypsum board and the top boundary is open to the attic air space, with neither boundary being constrained to be isothermal. Secondly, the specimen for the heat meter apparatus consists only of insulation, while the specimen in the attic consists of a combination of insulation, wood joists, and gypsum board. The wood joists may contribute to the early initiation of convection.

The research reported here is a numerical approach describing flow in the system presented above. A two-dimensional code is used to solve the equations of convection in a porous medium representing the insulation; solid blocks are included in the porous bed to model the presence of ceiling joists. Specific thermal and dynamic conditions are applied on the top of the porous layer to characterize the coupling mechanisms between heat transfer inside the insulation and those in the surrounding air.

The effects of the solid conductive inclusions on the early onset of natural convection are studied for several aspect ratios in order to determine how this phenomenon is related to the porous layer thickness.

For existing measured values of the air permeability of the insulation, the variation of the thermal resistance of the insulation over a range of temperature differences across the layer of insulation is derived from the variation of the global Nusselt number with the Rayleigh number.

A comparison between this predicted thermal resistance and data from the attic test module is established. Good agreement is found between experimental results and calculations. The presence of the joists appears to have a significant effect only for initiation of early convection and when the aspect ratio is below a certain value.

2 Problem Formulation

2.1 The Configuration Under Study. We consider a horizontal porous layer bounded by an impermeable bottom surface while the top surface is open to the surrounding air. The configuration under study is depicted in Fig. 1. Because of the symmetry of the configuration, the planes bounding the element

[1] Current position: CETHIL/GMC, INSA de Lyon, 69621 Villeurbanne, France.

Contributed by the Heat Transfer Division for publication in the JOURNAL OF HEAT TRANSFER. Manuscript received by the Heat Transfer Division June 1993; revision received July 1994. Keywords: Modeling and Scaling, Natural Convection, Porous Media. Associate Technical Editor: R. Viskanta.

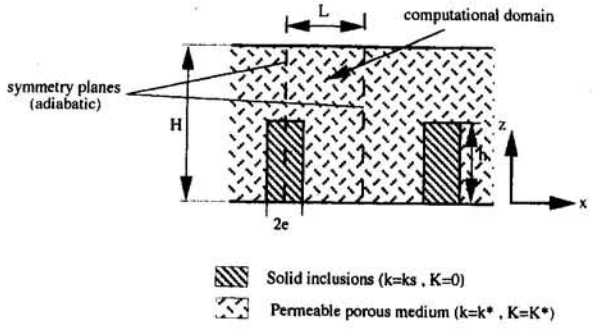

Fig. 1 Configuration under study

to be modeled are assumed adiabatic. The bottom temperature T_1 is uniform and the top surface temperature T_2 is assumed to be either constant or nonuniform ($T_2(x)$). The layer is heated from below ($T_1 > T_2$).

The variable top cold temperature should model the presence of convective cells inside the medium. This distribution was selected as a result of observations of the top surface of the insulation with an infrared camera, during an experiment performed on one type of loose-fill fiberglass, while convection was present within the insulating material (Wilkes et al., 1991a, b).

Although experiment shows evidence of three-dimensional convective structure, our approach to the problem is two dimensional. However, experimental observation helps define the symmetry of the domain under study.

2.2 Nondimensional Equations and Parameters. Because of experimental observations of the convective cells, and considering symmetric conditions respectively on the solid inclusion and between the solid inclusions, allow calculations to be performed in half the domain as presented in Fig. 1. The solid inclusions are assumed to be a part of the domain under study and are treated as porous media with a very low permeability in relation to the permeability K, of the surrounding real porous material. Under Boussinesq's approximation and assuming that the fluid is incompressible, the nondimensional set of equations (in a steady form) for the whole domain is:

$$\nabla \cdot \underline{V} = 0 \tag{2.1}$$

$$\nabla \cdot (k'(x, z) \nabla T) - \underline{V} \cdot \nabla T = 0 \tag{2.2}$$

$$0 = -\nabla P + \mathrm{Ra}^* T \underline{e}_z - \frac{\underline{V}}{K'(x, z)} \tag{2.3}$$

where:

$$k' = k(x, z)/k^*, \quad K' = K(x, z)/K^*$$

The main dimensionless parameters for the problem are: the *porous* Rayleigh number, Ra*, the conductivity ratio, $R_k = k^s/k^*$, and the aspect ratios, $A = L/H$, $B = h/H$, $C = e/L$.

The boundary conditions are:

- At the vertical planes $x = 0$ and $x = A$, the symmetry conditions can be written as follows: $\partial T/\partial x = 0 : \partial P/\partial x = 0$ (equivalent to impermeability condition: $V_x = 0$).
- On the upper permeable horizontal surface ($z = 1$), the temperature distribution is assumed: $P = 0$ (equivalent to $\partial V_z/\partial z = 0$), and $T = T_2(x)$
- The lower horizontal surface ($z = 0$), is assumed to be impermeable and isothermal: $V_z = 0$ (equivalent to $\partial P/\partial z = \mathrm{Ra}T$), and $T = T_1$ = constant

The motion in the air space above the porous medium induces a pressure distribution on the top of the porous layer. However, no pressure measurements were performed on our experiment. We study here heat transfer in the porous layer only; then as a first approximation we do not consider a dynamic coupling between the porous layer and the air space above, when assuming a constant pressure on the top.

Since the solid inclusions are treated as a porous medium, no explicit boundary conditions need to be specified at the porous–solid interface (the low value of the permeability ensures an impermeable condition and the spatially varying conductivity ensures the continuity of temperature and heat fluxes at the solid–porous interface).

The heat transfer through the porous layer is characterized by the Nusselt number Nu* with the common definition:

$$\mathrm{Nu}^* = \frac{1}{A} \int_0^A \left(-k(x, z) \frac{\partial T}{\partial z} - VT \right) dx \tag{2.4}$$

As heat transfer through the domain is due both to the conduction in the solid parts and convection, another Nusselt number noted Nu′ is introduced to characterize the real effect of convection only; this number is defined as follows:

$$\mathrm{Nu}' = \frac{\mathrm{Nu}^*}{\mathrm{Nu}_0^*} \tag{2.5}$$

where Nu_0^* is the specific value of Nu* as Ra* approaches zero.

2.3 Numerical Methodology. Usually the equations of motion in homogeneous porous media are solved using a stream-function formulation: Applying the curl operator to the Darcy's equation, the pressure vanishes and a Poisson equation for the stream function ψ (defined from the velocity component as $V_x = -\partial\psi/\partial z$ and $V_z = -\partial\psi/\partial x$) is obtained. This formulation is not satisfactory when applied to a system where the

Nomenclature

a = amplitude of perturbation in the top temperature distribution
e = thickness of joists
g = gravitational constant
h = height of joists
H = thickness of the porous layer
HSL = number of cells
k^* = thermal conductivity of the porous medium
k^s = thermal conductivity of the solid blocks
K = air permeability
L = length of the medium
LM = number of nodes for the whole domain in the x direction
LG = number of nodes in the solid in the x direction
P = pressure
R = thermal resistance
T = temperature
T_0 = temperature of reference
T_1 = bottom temperature
T_2 = top temperature
T_m = mean temperature
V_x = horizontal component of velocity
V_z = vertical component of velocity
α = coefficient in thermal conductivity
ν = kinematic viscosity
ρ = density
ψ = stream function

Nondimensional parameters

A = aspect ratio = L/H
B = aspect ratio = h/H
C = aspect ratio = e/L
R_k = thermal conductivity ratio = k^s/k^*
$\mathrm{Ra}^* = g\beta(\rho C)_f K^* H \Delta T/\nu k^*$

Table 1 Effect of grid size (Ra* = 50; A = 1.25; B = 0.364; C = 0.0625; R_k = 100)

LM (LG)	NM (NG)	Nu^*	Nu_0^*	Nu′	ψ_{max}	t_{CPU}
16 (2)	16 (5)	2.409	1.125	2.137	4.490	27
32 (4)	32 (10)	2.421	1.127	2.148	4.560	100
48 (6)	48 (15)	2.425	1.128	2.150	4.574	310
64 (8)	64 (20)	2.427	1.128	2.151	4.580	661

Table 1 Effect of the grid size

permeabilities of the porous media vary over a large range, as it does here. In fact we consider that the permeability of the solid areas is five times lower than that of the surrounding porous medium.

In a domain composed of both solid and porous materials, the best way to model the motion is to express Darcy's equation in terms of pressure.

This equation can be obtained by using Eq. (2.1), and by applying the divergence operator to Darcy's Eq. (2.3). The final form is then:

$$\nabla\cdot(K'\nabla P) = \mathrm{Ra}^*\nabla\cdot(K'T\underline{e}_z) \tag{2.6}$$

As mentioned previously, the boundary conditions for this equation are either Dirichlet conditions for permeable surfaces (constant pressure) or Neumann conditions for impermeable surfaces or at planes of symmetry.

The two Eqs. (2.2) and (2.6) are discretized using a usual finite-volume approach (first-order derivatives for the convective terms in the energy equation) and are then solved iteratively in a pseudo-unsteady form by a classical process (conjugate gradient solver). Notice that resolution of the energy equation requires knowledge of the velocity field; the two velocity components are explicitly derived from the Darcy equation, the pressure field having been previously solved for velocity, pressure, and temperature are calculated on staggered grids, so that the numerical scheme is fully conservative. The permeability as well as the conductivity at the faces of the control volume are estimated from their values at the central node centers by the following geometric averaging:

$$K_{i+1/2} = \frac{2k_ik_{i+1}}{k_i + k_{i+1}} \tag{2.7}$$

As a consequence, the interface between the solid and the porous medium is located on the face of the control volume, while the boundaries of the domain correspond to node lines. A nonuniform mesh is built to satisfy this requirement.

The computations were performed on an IBM/RS6000-320. The influence of the mesh on computational time and on the accuracy was tested on a particular case corresponding to Ra* = 50. The computation is assumed to converge, when the following criteria are simultaneously fulfilled (the superscript "n" represents the nth iteration):

$$(\mathrm{Nu}^n - \mathrm{Nu}^{n-1}) < 10^{-5}, \quad \nabla\cdot V^n < 10^{-10},$$
$$(P^n - P^{n-1}) < 10^{-8}$$

In Table 1 are presented the Nusselt number, Nu′, the maximum of the stream function, ψ_{max}, and the corresponding CPU times for four different grid sizes, for Ra* = 50.

According to these tests, a 32 × 32 grid approaches the asymptotic solution at 2 percent for Nu′ and 4 percent for ψ_{max}, in the investigated range, and with a minimum of four points in the solid block in the x direction. This array is adopted for all calculations, with the exception of tests on the influence of the aspect ration A, where the number of nodes in the x direction is increased when large aspect ratios are considered ($A > 2$).

2.4 Results and Discussion

2.4.1 Effects of the Thermal Conductivity of the Inclusions. The objective is to determine the importance of the conductivity of the solid inclusions on the initiation of natural convection within the porous medium. The calculations are performed with the boundary conditions introduced previously, and with T_2 = const. The specific values selected for the aspect ratios A, B, and C, correspond to the particular geometry of the experiment that is described later.

Figure 2 presents the Nusselt number Nu′ versus Ra* for two values of the conductivity ration R_k. In the same figure a curve corresponding to the case of a porous medium without inclusions is presented. For this specific configuration, we can verify that the value of Ra* for the start of convection, obtained with our code, is close to the critical value of 27.1 given by the literature. The values of R_k selected to illustrate the influence of the thermal conductivity go from one extreme to the other in order to compare the behavior of very conductive inclusions (R_k = 100) with the effects caused by solid blocks with a thermal conductivity of the same order of magnitude as the surrounding porous medium (R_k = 2).

Note that the curve corresponding to that last configuration (R_k = 2) and the curve obtained for a homogeneous medium intersect each other when Ra* is approximately 35. This is due to the fact that when convection becomes very active the solid inclusions behave as an obstacle to the motion. This phenomenon can be verified by looking at the value of ψ_{max} over the same range of Rayleigh number, for the same conductivity ratios; results are also shown in Fig. 2. For large Rayleigh numbers the two curves tend to be superimposed on one another.

In order to cover a larger range of configurations, with cases where inclusions are less conductive than the surrounding medium, calculations were performed for values of R_k lying between 0.1 and 100, for Ra* = 25. Results are presented in terms of Nusselt number and maximum of the stream function on the same graph in Fig. 3. One can observe that in the case of a more conductive surrounding medium (i.e., R_k = 1) motion also occurs in the porous medium.

2.4.2 Variable Aspect Ratios. The purpose here is to determine the effect of the aspect ratio of the domain on the heat transfer and the dynamics. For fixed values of Ra*, B, and C, variations of Nusselt and ψ_{max} with the aspect ratio A are presented on the same graph in Fig. 4. The calculations are performed for R_k = 2. To vary A, the total height of the domain H is fixed and the length L varies. Note that the maximum for Nu′ corresponds to A = 1.06, and for ψ_{max} it is located at A = 1.3. A physical explanation of what causes the stream function maximization for A = 1.3, is the following one: As shown by Nield (1968), in an infinitely wide open porous layer with a top uniform temperature, the first convective structure appears for a wave number a_s equal to 2.33; according to the definition of the wave number: $a_s = \pi/A$. This explains that the first

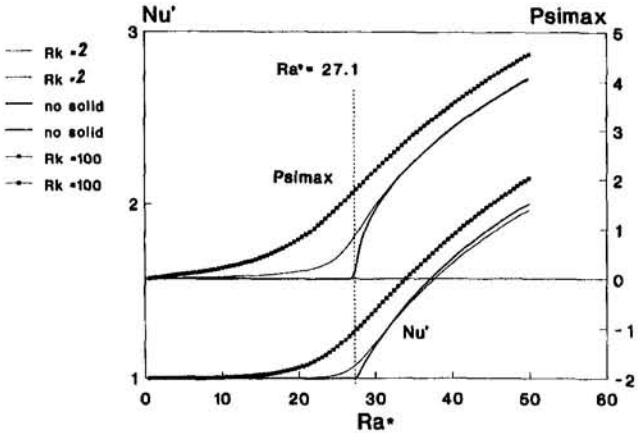

Fig. 2 Nu′ versus Ra*, ψ_{max} versus Ra*, for R_k = 1, 2, 100: A = 1.25; B = 0.3646; C = 0.0625

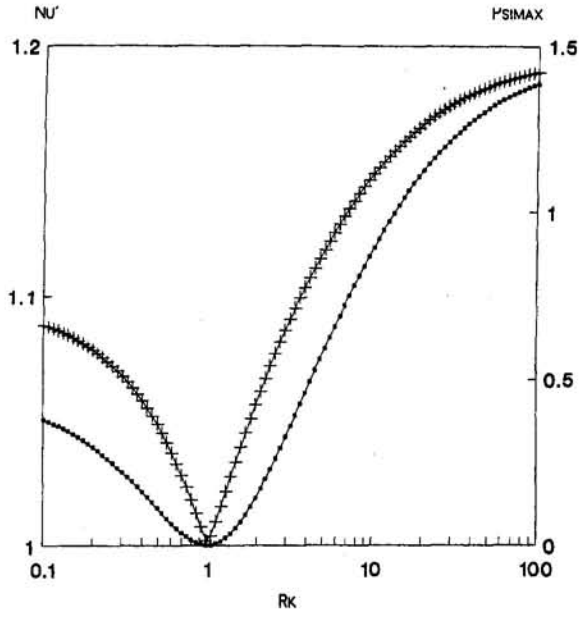

Fig. 3 Nu′ versus R_k, ψ_{max} versus R_k, for Ra* = 25: A = 1.25; B = 0.3646; C = 0.0625

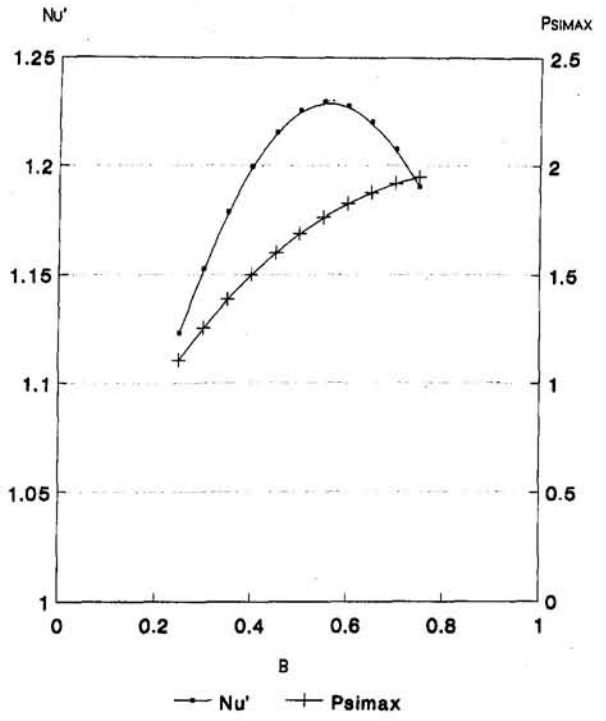

Fig. 5 Nu′ versus b, ψ_{max} versus B, for Ra* = 25: A = 1.25; C = 0.0625

maximum for the stream function is observed for $A = \pi/2.33 = 1.35$; the following maxima correspond to multiples of 1.35.

The influence of the height of the solid inclusions on the total heat transfer and the convective velocities is shown in Fig. 5 in terms of Nu and maximum of the stream function, for values of B lying between 0.2 and 0.8. Here one can again observe a specific value of B for which the heat transfer in the system is maximum; this maximum is obtained when the height of the inclusion is half the thickness of the porous layer (i.e., $B = 0.5$).

When the height of the blocks is greater than half the thickness of the surrounding medium, they tend to slow down convection. They behave like an obstruction to air motion.

To illustrate the temperature, pressure, and stream function fields, isolevel lines are presented in Fig. 6 for one particular configuration. These results correspond to a subcritical value of the Rayleigh number (Ra* = 20) with inclusions characterized by a high thermal conductivity compared to the surrounding medium ($R_k = 100$).

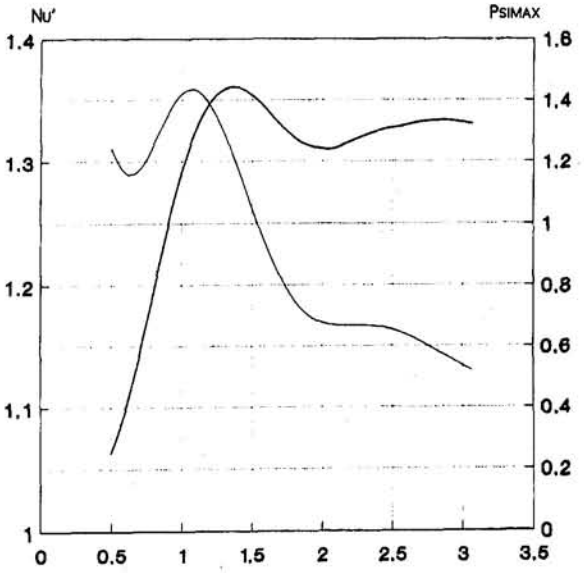

Fig. 4 Nu′ versus A, ψ_{max} versus A, for Ra* = 25: B = 0.3646; C = 0.0625

3 Modeling and Experiment

3.1 Facilities and Experimental Setups. The objective is to apply the previous calculations to the real configuration of an attic insulation. For this purpose, a thermal resistance is evaluated from the value of Nusselt number and the value of the thermal resistance of the material with no convection. From Ra*, derivation of the temperature difference across the layer of insulation requires knowledge of the thermal conductivity k and the air permeability K of the material tested in the Attic Test Module.

Figure 7 shows the Attic Test Module (ATM) inside the Large-Scale Climate Simulator (LSCS) at the Oak Ridge Roof Research Center. The ATM is intended to replicate the typical configuration of the attic insulation in residential buildings. This module is made with wood rafters and joists. Gypsum board is attached to the bottom of the joists, and 1.3-cm-thick plywood is attached to the tops of the rafters. The plywood roof sheathing is covered with roofing paper and medium gray asphalt shingles. The gables are constructed with plywood of the same thickness.

The upper portion of the LSCS constitutes the environmental chamber (climate chamber), which can be operated over an ambient temperature range of −40°C to 65.5°C. An array of infrared heating lamps is mounted on the ceiling of the Climate Chamber to simulate solar radiation.

This study deals only with winter conditions under which the inside of the house loses heat to the attic air space (heat flow upward). In several previous papers, work on other types of insulating material is reported (Wilkes and Childs, 1992; Wilkes and Graves, 1993).

The metering chamber is a guarded hot box maintained at 21°C for all outside temperatures.

3.2 Thermal Properties of Fiberglass Insulation. Analyzing heat transfer through the insulation requires knowledge of the characteristics of the tested material. This study does not treat the coupling of radiation–convection mecha-

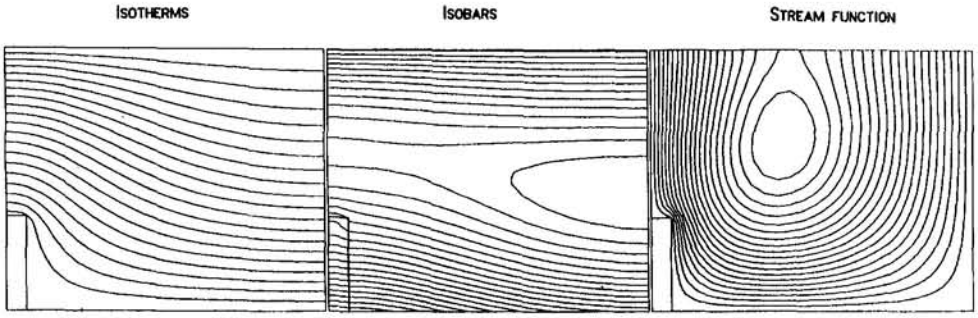

Fig. 6 Isotherms, isobars, stream function, for Ra* = 20: A = 1.25; B = 0.3646; C = 0.0625, R_k = 100

nisms. Consequently, an apparent thermal conductivity k is introduced that accounts for heat transfer by both conduction and radiation.

The thermal conductivity of fiberglass insulation used here includes radiation. The value of k is calculated using a semi-empirical expression. Some experiments performed on one type of loose-fill insulation (Wilkes and Rucker, 1983) showed that the apparent conductivity for a temperature difference lower than 44°C follows the equation:

$$k(T_m) = k_0 \exp[\alpha(T_m - T_0)] \tag{3.1}$$

k_0 is deduced from the attic R values at low ΔT.

The thermal performances of various insulating materials are usually compared in terms of thermal resistance. In the absence of convection, the thermal resistance is evaluated as the ratio of the thickness of insulation H to the thermal conductivity k given by Eq. (3.1). This resistance noted $R_0(T_m)$ has the following expression:

$$R_0(T_m) = \frac{H}{k(T_m)} \tag{3.2}$$

When convection is present, the thermal resistance denoted $R'(T)$ is calculated as follows:

$$R'(T_m) = \frac{R_0'(T_m)}{\mathrm{Nu}'} \tag{3.4}$$

where Nu′ is the Nusselt number defined previously in presence of solid inclusions; $R_0'(T_m)$ is the thermal resistance with inclusions in absence of convection.

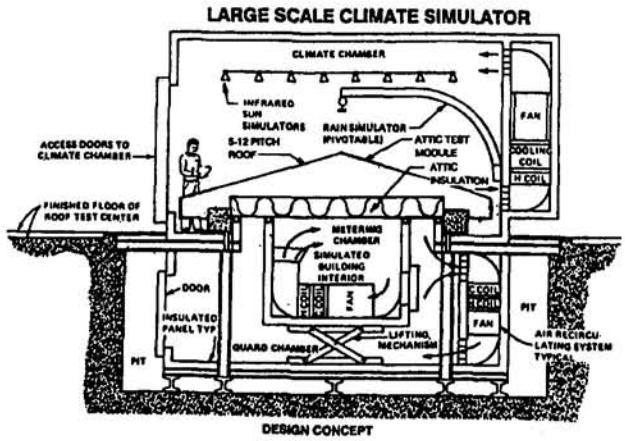

Fig. 7 The Attic Test Module (ATM) inside the Large-Scale Climate Simulator (LSCS)

3.3 Thermal Resistance Versus Temperature Difference. From the definition of Ra*, and using the properties of the material previously introduced, calculation of the temperature difference ΔT across the layer of insulation is possible. Using calculations performed for the same configurations (Nu′ versus Ra* for a specific aspect ratio), one can eventually obtain the variation of the thermal resistance with ΔT.

In the following section, results are presented in terms of variation of thermal resistance with temperature difference across the layer of insulation. The predicted thermal resistance obtained by this method is compared to measurements performed in the Test Module.

3.4 Results and Discussion. Calculations were conducted to simulate several tests performed in the Oak Ridge Roof Research Center facilities, on one type of loose-fill insulation. Three configurations are presented here.

In Table 2 we report the characteristic parameters of the experiment.

To model the coupling mechanism between convection in the attic air space and to represent convective cells within the insulation, the top temperature of the layer of insulation was assumed to be nonuniform and to follow the distribution:

$$T_2(x) = \overline{T_2} + a \cos\left(\pi x \frac{HSL}{A}\right) \tag{3.5}$$

In this distribution, HSL characterizes the number of cells, and corresponds to a half of the temperature amplitude between cold spots in the center and the warmer areas on edges; all tests are run with HSL = 1. $T_2(x)$ refers to IR observations of the top surface of insulation.

Figure 8 shows results in terms of thermal resistance versus temperature difference across the material for two samples of material (loose-fill 1, loose-fill 2); Fig. 9 presents the same type of results for the composite configuration (loose-fill 1 + blanket) presented in the previous table. Results are also presented in terms of Nusselt number versus Rayleigh number in Fig. 10.

The variation of the calculated thermal resistance for these configurations appears to be in good agreement with the experimental values.

Table 2 Characteristic parameters for the experiment (A = 1.25; B = −.364; C = 0.0625; R_k = 2; (a) Beckwith, 1991; (b) Yarbrough, 1991

Configuration	Thickness (mm)	Density (kg/m³)	k_0^* (mW/m K)	K (m²)	Aspect Ratio
Loose-fill 1	240	6.4	80.4	9.3 10^{-8} (a)	1.25
Loose-fill 2	240	7.2	72.1	9.3 10^{-8} (a)	1.25
Loose-fill 1	216	-	65.2	6.1 10^{-8} (b)	1.25
+ Blanket	25.	16.0	41.	6.1 10^{-9} (b)	

Table 2:

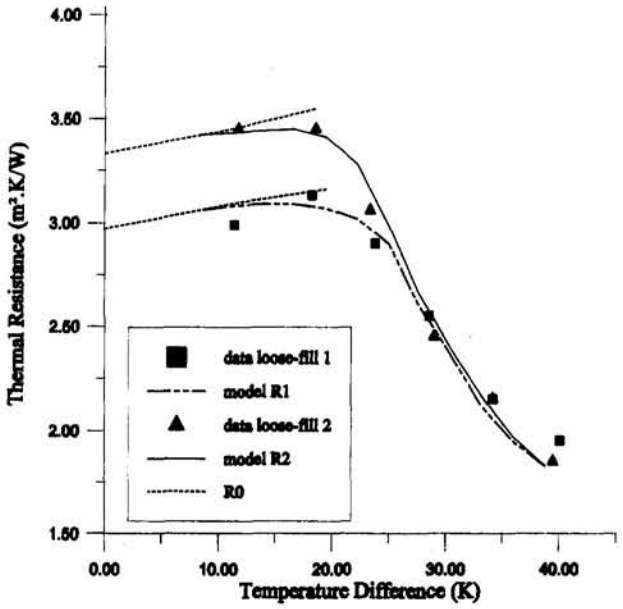

Fig. 8 Thermal resistance versus temperature difference; experimental results and modeling for loose-fill 1 and loose-fill 2

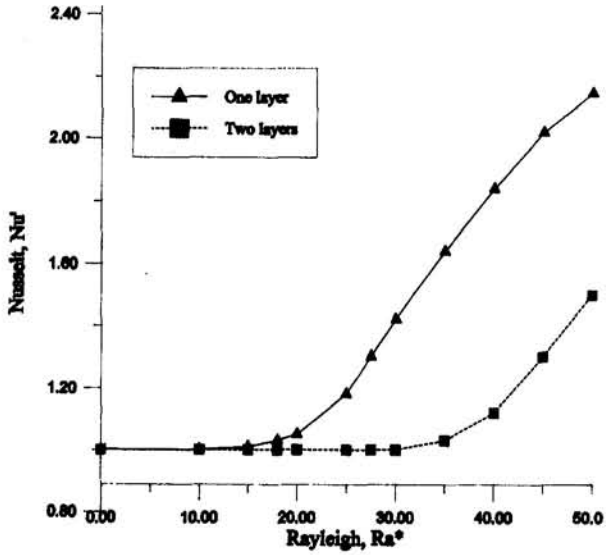

Fig. 10 Nu′ versus Ra* for loose-fill 1 and loose-fill 1 + blanket

4 Conclusions

One of the first conclusions of this work is to show evidence of the early start of convection in a porous medium when solid conductive inclusions are present within the medium. This effect becomes more noticeable as the conductivity ratio R_k increases. Because the air motion near the solid conductive blocks is subjected to a horizontal temperature gradient, it moves along the joists from the bottom to the top. Then air motion can be observed for Ra* lower than the critical value of 27.1. This phenomenon becomes significant when increasing R_k. Motion is observed (i.e., Nu′ > 1) for $R_k = 2$ when Ra* = 20, and for $R_k = 100$ when Ra* = 10; as a consequence, the respective values of Nu′ for $R_k = 2$ and for $R_k = 100$ at Ra* = 27.1 are 1.1 and 1.3. At large Rayleigh numbers (Ra* > 35), joists have a small impact on Nu′ no matter the R_k value; they may even become an obstacle to motion.

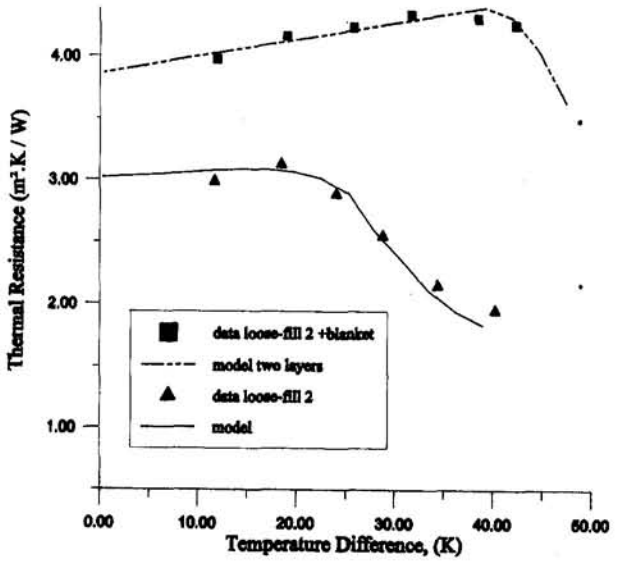

Fig. 9 Thermal resistance versus temperature difference; experimental results and modeling for loose-fill 1 and loose-fill 1 + blanket

The calculations also show the effect of the size of the inclusions in relation to the domain aspect ratio; in particular the choice of the aspect ratio A (half of the distance between inclusions over the porous layer thickness) appears to be a significant parameter. To predict the R value with the model, calculations were performed for $A = 1.25$, which is the real aspect ratio in the attic where experiments were conducted. This value happens to be really close to the value of 1.3 for which the stream function shows the first maximum. Note that in the U.S. there are two standard dimensions between joists: $2L = 30.5$ cm or 20.3 cm; for a porous layer thickness of $H = 24$ cm the aspect ratio is either $A = 1.25$ or 0.83. Figure 2 shows that in both cases the value of Nu′ is close to its maximum.

Calculations confirm the phenomenon of early initiation of convection observed experimentally. Good agreement between predicted heat transfer in the presence of solid conductive blocks and results of thermal resistance measured in the experimental setup is found. The model predicts a shape of the variation of R value versus the temperature difference across the insulation that is the same as the one observed on experimental R-value variations. The model can also predict the temperature difference ΔT at which convection inside the insulation becomes significant for the total heat transfer.

Through these calculations we show that in some particular configurations solid conductive blocks within a porous medium can have a significant effect on the start of convection, leading to an increase on the total heat transfer.

References

Arquis, E., and Caltagirone, J. P., 1987, "Interacting Convection Between Fluid and Open Porous Layer," presented at the ASME Winter Annual Meeting, Boston, MA, Dec. 13–18.

Bankvall, C. G., 1975, "Mechanism of Heat Transfer in Permeable Insulation and Their Investigation in Special Guarded Hot Plate," *Heat Transmission Measurements in Thermal Insulation,* ASTM STP 554, American Society for Testing and Material, Philadelphia, PA, pp. 34–38.

Beckwith, J., 1991, "Air Permeability," Internal report, Certain Teed Corporation.

Delmas, A., and Wilkes, K. E., 1992a, "Numerical Analysis of Heat Transfer by Conduction and Natural Convection in Loose Fill Fiberglass Insulation—Effects of Convection on Thermal Performance," ORNL/CON-338, Oak Ridge National Laboratory, Oak Ridge, TN.

Delmas, A., and Wilkes, K. E., 1992b, "Calculation of Thermal Resistance of Some Loose Fill Insulation When Natural Convection Occurs Within the Insulating Material—Comparison With Experimental Data," ORNL/CON-348, Oak Ridge National Laboratory, Oak Ridge, TN.

Fournier, D., and Klarsfeld, S., 1971, "Utilisation d'un Appareil Orientable à Plaque chaude Gardée pour la Mise en Evidence du Transfert de Chaleur par Convection Naturelle en Milieu Poreux dans des Conditions Simulées," *Proceed-*

ings, 13th International Congress of Refrigeration, W. T. Pentzer et al., eds., Washington, Vol. 2, pp. 53–61.

Langlais, C., Arquis, E., and McCaa, D. J., 1990, "A Theoretical and Experimental Study of Convective Effects in Loose Fill Thermal Insulation," *Insulation Material Testing and Applications,* ASTM STP 1030, American Society for Testing and Material, Philadelphia, PA, pp. 290–310.

Nield, D. A., 1968, "Onset of Thermohaline Convection in Porous Medium," *Water Resour. Res.,* Vol. 4, pp. 553–560.

Silberstein, A., Langlais, C., and Arquis, E., 1990, "Natural Convection in Light Fibrous Insulating Materials With Permeable Interface: Onset Criteria and Its Effects on the Thermal Performances of the Product," *J. Therm. Insul.,* Vol. 14, pp. 22–42.

Wilkes, K. E., and Rucker, J. L., 1983, "Thermal Performance of Residential Attic Insulation," *Energy and Buildings,* Vol. 5, pp. 263–277.

Wilkes, K. E., Wendt, R. L., Delmas, A., and Childs, P. W., 1991a, "Attic Testing at the Roof Research Center—Initial Results," *Proceedings, The International Symposium on Roofing Technology,* National Roofing Contractors Association, Rosemont, IL.

Wilkes, K. E., Wendt, R. L., Delmas, A., and Childs, P. W., 1991b, "Thermal Performance of One Loose-Fill Fiberglass Attic Insulation," *Insulation Materials: Testing and Applications,* ASTM STP 1116, R. S. Graves and D. C. Wysocki, eds., American Society for Testing and Materials, Philadelphia, PA, Vol. 2, pp. 275–291.

Wilkes, K. E., and Childs, P. W., 1992, "Thermal Performance of Fiberglass and Cellulose Attic Insulations," *Thermal Performance of the Exterior Envelopes of Buildings V, Proceedings of the ASHRAE/DOE/BTECC Conference,* American Society of Heating and Air-Conditioning Engineers, Clearwater, FL.

Wilkes, K. E., and Graves, R. S., 1993, "Air-Flow Permeability of Attic Insulation Materials," ORNL/M. 2646, Oak Ridge National Laboratory, Oak Ridge, TN.

Yarbrough, D., 1991, "Reduction in the Thermal Resistance (R-Value) of Loose-Fill Insulation and Fiberglass Batts Due to Compression," ORNL/Sub-7715/2, Oak Ridge, TN.

Heat Transfer During Evaporation on Capillary-Grooved Structures of Heat Pipes

D. Khrustalev

A. Faghri

Department of Mechanical Engineering,
University of Connecticut,
Storrs, CT 06269

A detailed mathematical model is developed that describes heat transfer through thin liquid films in the evaporator of heat pipes with capillary grooves. The model accounts for the effects of interfacial thermal resistance, disjoining pressure, and surface roughness for a given meniscus contact angle. The free surface temperature of the liquid film is determined using the extended Kelvin equation and the expression for interfacial resistance given by the kinetic theory. The numerical results obtained are compared to existing experimental data. The importance of the surface roughness and interfacial thermal resistance in predicting the heat transfer coefficient in the grooved evaporator is demonstrated.

Introduction

Heat pipes with grooved evaporators are of great practical interest. The value of the evaporative heat transfer coefficient is related to the maximum heat flux on the wall by the superheat of the evaporating liquid film, which is critical for the onset of nucleate boiling. Therefore, a detailed mathematical model is developed that includes both the heat transfer through the thin liquid films and heat conduction in the fin between grooves and in the meniscus region film. The present analysis has the following comparatively new features:

- The heat transfer through the liquid films in the evaporator is described with respect to the disjoining pressure, interfacial thermal resistance, and surface roughness or curvature (Fig. 1).
- The free surface temperature of the liquid film is determined using the extended Kelvin equation and the expression for interfacial resistance given by the kinetic theory.
- Heat conduction in the fin between grooves and the liquid meniscus is considered using a one-dimensional approximation.

Emphasis has been placed on the formation of the thin liquid films affected by the operational conditions. During evaporation, liquid in the superheated thin film flows from the meniscus region into the thin-film region, as presented in Fig. 1. The numerical results were obtained using an iterative mathematical procedure, which involved the problems described in detail in the following sections.

Formation of and Heat Transfer in Thin Liquid Films

The thermal resistance of a low-temperature grooved evaporator depends mostly on the thickness of the thin liquid evaporating films. In this section a thin evaporating film on a heat-loaded surface with curvature K_w is considered, as shown in Fig. 1. The local heat flux through the film due to heat conduction is

$$q = k_l \frac{T_w - T_\delta}{\delta} \tag{1}$$

where the local thickness of the liquid layer δ and the temperature of the free liquid film surface T_δ are functions of the s coordinate. For small Reynolds numbers (less than unity), an assumption of a fully developed laminar liquid flow velocity profile is valid:

$$u_l = -\frac{1}{2\mu_l}\frac{dp_l}{ds}(2\eta\delta - \eta^2) \tag{2}$$

where η is the coordinate normal to the solid–liquid interface. The vapor pressure is assumed to be constant along the s coordinate, and the liquid flow is driven mainly by the surface tension and the adhesion forces:

$$\frac{dp_l}{ds} = -\sigma\frac{dK}{ds} + \frac{dp_d}{ds} - K\frac{d\sigma}{dT_\delta}\frac{dT_\delta}{ds} + \frac{d}{ds}(\rho_v^2 v_{v,\delta}^2)\left(\frac{1}{\rho_v} - \frac{1}{\rho_l}\right) \tag{3}$$

K is the local interface curvature, p_d is the disjoining pressure (Derjaguin, 1955) and the last term is the kinetic reaction of the evaporating fluid pressure. The impact of the last two terms on the results was found to be negligible in the present analysis; therefore they are omitted in following equations.

The continuity equation for the evaporating liquid layer is

$$\frac{d}{ds}\int_0^\delta u_l d\eta = \frac{q}{h_{fg}\rho_l} \tag{4}$$

Substituting Eqs. (1)–(3) into Eq. (4) gives the following relation for the thickness of the evaporating film, $\delta(s)$:

$$\frac{1}{3\mu_l}\frac{d}{ds}\left[\delta^3\frac{d}{ds}(p_d - \sigma K)\right] = \frac{k_l(T_w - T_\delta)}{h_{fg}\rho_l\delta} \tag{5}$$

The film surface curvature K is expressed in terms of the solid surface curvature K_w and film thickness as

$$K = K_w + \frac{d^2\delta}{ds^2}\left[1 + \left(\frac{d\delta}{ds}\right)^2\right]^{-3/2} \tag{6}$$

Equations (5) and (6) describe formation of the liquid films during evaporation and condensation as considered by Khrusta-

Contributed by the Heat Transfer Division and presented at the ASME International Mechanical Engineering Congress and Exhibition, Chicago, Illinois, November 6–11, 1994. Manuscript received by the Heat Transfer Division May 1994; revision received January 1995. Keywords: Evaporation, Heat Pipes and Thermosyphons, Thermocapillary Flows. Associate Technical Editor: R. Viskanta.

lev and Faghri (1994). Following Potash and Wayner (1972), a power-law dependence of p_d on δ is given for nonpolar liquids:

$$p_d = -A'\delta^{-B} \tag{7}$$

For water, however, the logarithmic dependence is preferable (Holm and Goplen, 1979).

It is assumed that the absolute value of the vapor core pressure at any z location along the groove is related to vapor temperature by the saturation conditions

$$p_v = p_{sat}(T_v) \tag{8}$$

and therefore can be defined for a given T_v using the saturation tables.

The temperature of the interface T_δ is affected by the disjoining and capillary pressures, and also depends on the value of the interfacial resistance, which is defined for the case of a comparatively small heat flux by the following relation for the heat flux at the interface (Carey, 1992):

$$q = -\left(\frac{2\alpha}{2-\alpha}\right)\frac{h_{fg}}{\sqrt{2\pi R_g}}\left[\frac{p_v}{\sqrt{T_v}} - \frac{(p_{sat})_\delta}{\sqrt{T_\delta}}\right] \tag{9}$$

p_v and $(p_{sat})_\delta$ are the saturation pressures corresponding to T_v in the bulk vapor and at the thin liquid film interface, respectively.

While Eq. (9) is used in the present analysis, it seems useful to mention that for the case of extremely high heat fluxes during intensive evaporation in thin films, Solov'ev and Kovalev (1984) have approximated the interfacial heat flux by the following expression:

$$q = 3.2\sqrt{R_g T_v}[(p_{sat})_\delta - p_v] \tag{10}$$

Equation (10) was derived with the assumption that the accommodation coefficient $\alpha = 1$ from the expressions given by Labuntsov and Krukov (1977).

The relation between the vapor pressure over the thin evaporating film, $(p_{sat})_\delta$, affected by the disjoining pressure, and the saturation pressure corresponding to T_δ, $p_{sat}(T_\delta)$, is given by the extended Kelvin equation (Carey, 1992; Faghri, 1995):

$$(p_{sat})_\delta = p_{sat}(T_\delta)\exp\left[\frac{(p_{sat})_\delta - p_{sat}(T_\delta) + p_d - \sigma K}{\rho_l R_g T_\delta}\right] \tag{11}$$

Equation (11) reflects the fact that under the influence of the disjoining and capillary pressures, the liquid free surface saturation pressure $(p_{sat})_\delta$ is different from the normal saturation pressure $p_{sat}(T_\delta)$ and varies along the thin film (or s coordinate), while p_v and T_v are the same for any value of s at a given z location. This is also due to the fact that T_δ changes along s. For a thinner evaporating film, the difference between $(p_{sat})_\delta$ given by Eq. (11) and that for a given T_δ using the saturation curve table is larger. This difference is the reason for the existence of the thin nonevaporating superheated film, which is in the equilibrium state in spite of the fact that $T_\delta > T_v$.

Under steady-state conditions the right-hand sides of Eqs. (1) and (9) can be equated:

$$T_\delta = T_w + \frac{\delta}{k_l}\left(\frac{2\alpha}{2-\alpha}\right)\frac{h_{fg}}{\sqrt{2\pi R_g}}\left[\frac{p_v}{\sqrt{T_v}} - \frac{(p_{sat})_\delta}{\sqrt{T_\delta}}\right] \tag{12}$$

Equations (11) and (12) determine the interfacial temperature, T_δ, and pressure, $(p_{sat})_\delta$. T_w has to be provided as an input to the solution procedure, resulting from the solution of the heat conduction problem in the fin between the grooves. The four boundary conditions for Eqs. (5) and (6) must be developed, taking the physical situation into account, as shown in the following section.

As the liquid film thins, the disjoining pressure, p_d, and the interfacial temperature, T_δ, increase. Under specific conditions, a nonevaporating film thickness is present that gives the equality of the liquid–vapor interface and the solid surface temperatures, $T_\delta = T_w$. This is the thickness of the equilibrium nonevaporating film δ_0. For a nonevaporating equilibrium film ($q = 0$), it follows from Eqs. (7), (9), and (11) that

Nomenclature

A' = dispersion constant, J
a, b, B = const
h_{fg} = latent heat of vaporization, J/kg
h = heat transfer coefficient, W/(m^2-K)
K = curvature, 1/m
k = thermal conductivity, W/(m-K)
L = length, m
L_1 = half-width of the top of the fin, m
N = number of grooves
p = pressure, Pa
p_d = disjoining pressure, Pa
Q = axial heat flow through the heat pipe cross section, W
Q_a = total heat input, W
Q' = heat flow rate per unit length, W/m
q = heat flux, W/m^2
R_g = individual gas constant, J/(kg-K)
R_m = radius of curvature of the meniscus, m
R_o = outer pipe radius, m
R_r = characteristic roughness size, m
R_v = vapor space radius, m
s = coordinate, m
T = temperature, K
T_w = temperature of the solid–liquid thin film interface, K
t_g = groove depth, m
t_w = thickness of the wall, m
u = velocity of microfilm flow along the s coordinate, m/s
v = vapor velocity along the η coordinate, m/s
W = half-width of a groove, m
x = coordinate, m
z = coordinate along the groove axis, m
α = accommodation coefficient
γ = half-angle of a groove
δ = film thickness, m
Δ_a = absolute error
Δ_r = relative error
$\Delta T = |T_w - T_v|$ = temperature drop, K
η = coordinate normal to the solid–liquid interface, m
θ = contact angle
θ_f = contact angle obtained from the smooth-surface model
μ = dynamic viscosity, Pa-s
ν = kinematic viscosity, m^2/s
ρ = density, kg/m^3
σ = surface tension, N/m
$\chi = \pi/N$ = angle (for circular geometry)
ω_1 = interface between the liquid and the side of the groove
ω_2 = liquid–vapor interface
ω_3 = interface between the liquid and the bottom of the groove

Subscripts

a = adiabatic
bot = bottom of a groove
cap = capillary
e = evaporator
f = thin film
fin = fin
l = liquid
men = meniscus
max = maximum
mic = microfilm region
o = outer
sat = saturation
tot = total
tr = transition region
v = vapor
w = wall
δ = liquid film free surface

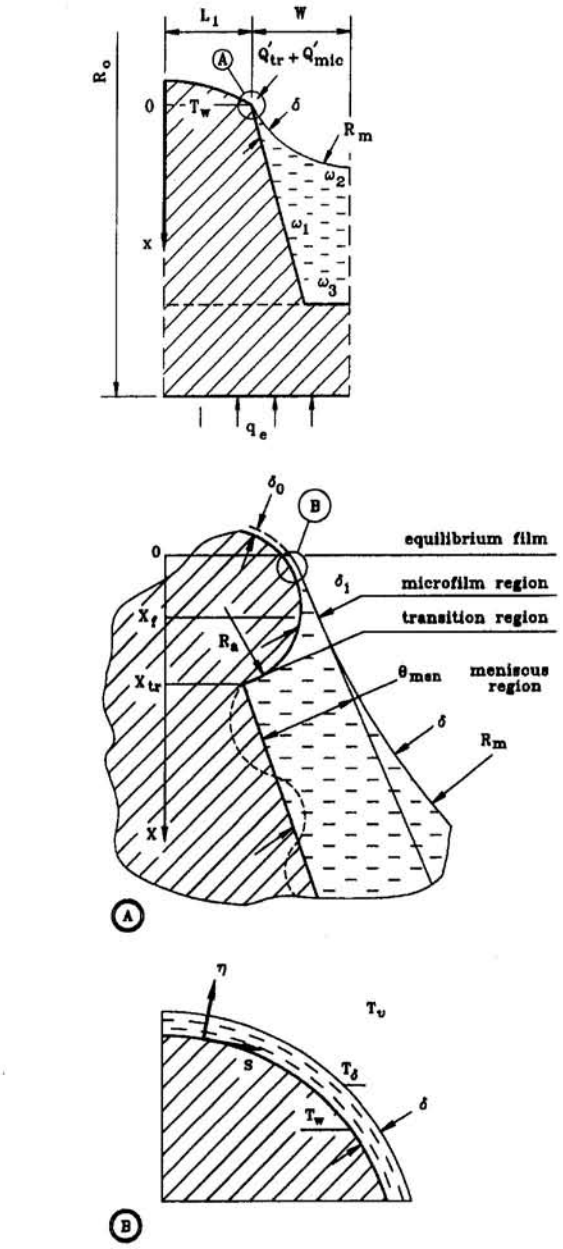

Fig. 1 Cross sections of the characteristic element of an axially grooved evaporator

$$\delta_0 = \left\{ \frac{1}{A'} \left[p_v \sqrt{\frac{T_w}{T_v}} - p_{\text{sat}}(T_w) - \rho_l R_g T_w \ln \left(\frac{p_v}{p_{\text{sat}}(T_w)} \sqrt{\frac{T_w}{T_v}} \right) - \sigma K \right] \right\}^{-1/B} \quad (13)$$

For water the following equation for the disjoining pressure was used (Holm and Goplen, 1979) instead of Eq. (7):

$$p_d = \rho_l R_g T_\delta \ln \left[a \left(\frac{\delta}{3.3} \right)^b \right] \quad (14)$$

where $a = 1.5336$ and $b = 0.0243$.

Heat Transfer in the Thin-Film Region of the Evaporator

This problem has been treated numerically and experimentally by different authors, whose results are mentioned here to understand the basis of the present model. Kamotani (1978), Holm and Goplen (1979), and Stephan and Busse (1992) modeled an evaporating extended meniscus in a capillary groove. In all of the above-mentioned papers, it is emphasized that most of the heat is transfered through the region where the thickness of the liquid layer is extremely small. The significance of the temperature difference between the saturated vapor core and the interface has been stressed by Solov'ev and Kovalev (1984) and Stephan and Busse (1992). In the mathematical models of these authors, the solid surface was assumed to be smooth. Kamotani (1978) noted that this assumption could lead to an overestimation of the total heat transfer coefficient. The same concern has been expressed by Vasiliev et al. (1981).

In light of these findings, in the present analysis the difference between the saturated vapor temperature and that of the free liquid surface was considered, and the existence of the surface roughness and its influence on evaporative heat transfer was taken into consideration. In general, manufacturing processes always leave some degree of roughness on the metallic surface. Alloys of copper, brass, steel, and aluminum invariably have some distinct grain structure, resulting from processing the materials. In addition, corrosion and deposition of some substances on the surface can influence its microrelief. This means the solid surface is totally covered with microroughnesses, where the characteristic size may vary from, for example, $R_r = 10^{-8}$ to 10^{-6} m. Apparently, the thin liquid film formation can be affected by some of these microroughnesses. It can be assumed that at least some part of a single roughness fragment, on which the thin film formation takes place, has a circular cross section and is extended in the z direction due to manufacturing the axial grooves (Fig. 1).

In the present analysis the free liquid surface is divided into four regions (Fig. 1). The first region is the equilibrium nonevaporating film. The second (microfilm) region ranges in the interval $0 \le s \le s_1$ ($\delta_0 \le \delta \le \delta_1$), where the increase of the liquid film thickness up to the value δ_1 is described by Eqs. (5) and (6). In this region, the generalized capillary pressure $p_{\text{cap}} \equiv \sigma K - p_d$ (here p_{cap} was defined so that its value is positive) is changing drastically along the s coordinate from the initial value up to an almost constant value at point s_1, where the film thickness, δ_1, is large enough to neglect the capillary pressure gradient. It is useful to mention that some investigators have denoted this microfilm region as the "interline region." The third (transition) region, where the liquid–vapor interface curvature is constant, is bounded by $\delta_1 < \delta \le R_r + \delta_0$, and the local film thickness is determined by the geometry of the solid surface relief and the value of the meniscus radius R_m. In the fourth (meniscus) region, where by definition $\delta > R_r + \delta_0$, the local film thickness can be considered independent of the solid surface microrelief. In the third and fourth regions, the heat transfer is determined by heat conduction in the meniscus liquid film and the metallic fin between the grooves. However, in the second region, the temperature gradient in the solid body can be neglected in comparison to that in liquid due to the extremely small size of this region.

The total heat flow rate per unit groove length in the microfilm region is defined as

$$Q'_{\text{mic}}(s_1) = \int_0^{s_1} \frac{T_w - T_\delta}{\delta / k_l} \, ds \equiv \int_0^{s_1} q \, ds \quad (15)$$

Differential Eqs. (5) and (6) must be solved for four variables: δ, δ', p_{cap}, and $Q'_{\text{mic}}(s)$ in the interval from $s = 0$ to the point $s = s_1$, where p_{cap} can be considered to be constant, with their respective boundary conditions (Khrustalev and Faghri, 1994):

$$\delta|_{s=0} = \delta_0 \quad (16)$$

$$\delta'|_{s=0} = 0 \quad (17)$$

$$p_{\text{cap}}|_{s=0} = -\frac{\sigma}{R_r + \delta_0} + A' \delta_0^{-B} \quad (18)$$

$$Q'_{\text{mic}}|_{s=0} = 0 \tag{19}$$

The value of δ_0 is found from Eq. (13), where $K = -1/R_r$.

Although the initial-value problem, Eqs. (5), (6), and (16)–(19), is completely determined, its solution must satisfy one more condition:

$$p_{\text{cap}}|_{s=s_1} = \frac{\sigma}{R_m} \tag{20}$$

Since the only parameter not fixed in this problem is connected with the surface roughness characteristics, the boundary condition (20) can be satisfied by the choice of R_r. Physically, it means that the beginning of the evaporating film is shifted along the rough surface depending on the situation so as to satisfy the conservation laws. However, in a smooth surface model ($R_r \to \infty$) the solution will probably not satisfy Eq. (20). As a result of this problem, the values of δ_1 and $Q'_{\text{mic}}(s_1)$ can be determined and the transition region can be considered, provided that $\delta_1 < R_r$, where the free liquid surface curvature is constant and its radius R_m is many times larger than R_r. Based on the geometry shown in Fig. 1, the following approximation for the liquid film thickness in the transition region $x_f \le x \le x_{tr}$ is given:

$$\delta = \delta_0 + R_r - \sqrt{R_r^2 - x^2} - R_m + (R_m^2 + x^2 + 2R_m x \sin\theta_f)^{1/2} \tag{21}$$

Equation (21) is valid for the rough surface model (θ_f can be set equal to zero for very small R_r) and also the smooth surface model in the meniscus region ($R_r \to \infty$ and θ_f is given as a result of the microfilm problem solution). For the smooth surface model, θ_f is the angle between the solid–liquid and liquid–vapor interfaces at the point s_1, where the capillary pressure becomes constant. The heat flow rate per unit groove length in the transition region is

$$Q'_{tr} = \int_{x_f}^{x_{tr}} \frac{T_w - T_\delta}{\delta/k_l}\, dx \tag{22}$$

where x_f and x_{tr} are obtained from Eq. (21) provided $\delta = \delta_1$ and $\delta = R_r + \delta_0$, respectively.

Now the connecting point between the transition and meniscus regions must be considered. At this point, the film thickness, the free surface curvature, and the liquid surface slope angle must coincide from both sides. In the rough surface model, the last condition is always satisfied because the length of the microfilm region is smaller than R_r, and the rough fragment with the film can be "turned" around its center in the needed direction (see Fig. 1). In other words, because of the circular geometry of the rough fragment and the constant temperature of the solid surface in the microfilm region, the slope of the film free surface is not fixed in the mathematical model. On the contrary, in the smooth surface model the numerical results give θ_f, which is generally not equal to θ_{men} determined by the fluid flow along the groove. Here θ_{men} is the macroscopic contact angle between the lines representing the solid surface and the liquid–vapor interface at the end of the transition region shown in Fig. 1. Stephan (1992) seems to have answered this contradiction using a rounded fin corner; however, this explanation is not completely satisfactory. Note that in the situation when $\theta_f \neq \theta_{\text{men}}$, the smooth surface model can be used along with the rounded fin corner, where the radius is R_{fin}. In this case Eq. (21) can also be used provided R_r is changed to R_{fin}.

It is useful to mention here that the values of R_m and θ_{men} are connected by the geometric relation $\theta_{\text{men}} = \arccos(W/R_m) - \gamma$ and should be given as a result of the solution of the problem for the fluid transport along the groove. The fin top temperature T_w should be defined from the consideration of the heat conduction problem in the fin between grooves and in the meniscus liquid film discussed below.

Simplified Model of Heat Transfer in the Evaporating Thin Film. The free liquid surface curvature K in the microfilm region varies from the initial value to that in the meniscus region. Its variation is described by Eqs. (5), (6), and (16)–(20) with respect to the p_{cap} and p_d definitions. In spite of a sharp maximum of the K function in the microfilm region, its variation affects the total heat transfer coefficient only slightly. To check this hypothesis numerically, a simplified version of the heat transfer model of the microfilm region was developed, where it was assumed that the microfilm free surface curvature is equal to that in the meniscus region. Therefore, instead of solving Eqs. (5), (6), and (16)–(20), the microfilm thickness in this region (and also in the transition region) can be given by Eq. (21) for the interval $0 \le x \le x_{tr}$. In this case, the heat flow rate per unit groove length in both the microfilm and transition regions is

$$Q'_{\text{mic}} + Q'_{tr} = \int_0^{x_{tr}} \frac{T_w - T_\delta}{\delta/k_l}\, dx \tag{23}$$

Now, the consideration of the meniscus region gives the opportunity to obtain the heat transfer coefficient.

Heat Conduction in the Metallic Fin and Meniscus Region Film

For low-temperature heat pipes, the thermal conductivity of the metallic casing is several hundred times higher than that of the liquid working fluid. Nearly all of the heat is transferred from the metallic fin between grooves to the saturated vapor through a thin liquid film in the vicinity of the fin top. The temperature drop in the metallic fin is many times smaller than in the liquid film (Stephan and Busse, 1992). Therefore, in the present analysis the temperature gradient in the metallic fin in the direction transverse to the x coordinate is neglected (Fig. 1). The heat conduction in the metallic fin and meniscus liquid film is described by the following equation, which was obtained as a result of an energy balance over a differential element (Vasiliev et al., 1981):

$$\frac{d^2T}{dx^2} + \frac{dT}{dx}\frac{\tan(\gamma + \chi)}{L_{\text{fin}}(x)} + (T_\delta - T)\frac{k_l}{k_w \delta(x) L_{\text{fin}}(x)} = 0 \tag{24}$$

The fin thickness variation is due to the wall inclination angle and the circular tube geometry

$$L_{\text{fin}}(x) = L_1 + x\tan(\gamma + \chi) \tag{25}$$

and the liquid film thickness is

$$\delta = \delta_2 - R_m + \left[R_m^2 + \frac{x^2}{\cos^2(\gamma + \chi)} + \frac{2R_m x}{\cos(\gamma + \chi)}\sin\theta_{\text{men}}\right]^{1/2} \tag{26}$$

where δ is measured perpendicularly from the liquid–vapor interface, and the value of δ_2 should be chosen as follows:

$\delta_2 = R_r + \delta_0$ in the rough surface evaporation model,

$\delta_2 = \delta_1$ in the smooth surface evaporation model.

The boundary conditions for Eq. (24) are

$$\left.\frac{dT}{dx}\right|_{x=0} = \frac{Q'_{\text{mic}} + Q'_{tr}}{k_w L_1} \tag{27}$$

$$\left.\frac{dT}{dx}\right|_{x=l_g} = \frac{q_e \pi R_o}{k_w N[L_1 + t_g \tan(\gamma + \chi)]} \tag{28}$$

where boundary condition (27) is written with the assumption that $x_{tr} \ll t_g$. For the simplified model, Eq. (24) was solved also in the microfilm and transition regions, where δ was given by Eq. (21) and the right-hand side of Eq. (27) was set equal to zero. While the values of Q'_{mic} and Q'_{tr} depend on $T_w \equiv T|_{x=0}$, which is obtained from the solution of Eqs. (24)–(28), this problem is to be solved in conjunction with those concerning heat transfer in the thin film regions.

The local heat transfer coefficient (for a given z) in the evaporator from the bottom of the groove surface to the vapor is

$$\bar{h}_{e,\text{bot}} = \frac{q_e}{[T|_{x=t_g} - T_v]} \frac{R_o}{R_v + t_g} \tag{29}$$

The local heat transfer coefficient from the external surface of the evaporator to the vapor is

$$\bar{h}_e = \left[\frac{R_o}{k_w} \ln \frac{R_o}{R_v + t_g} + \frac{1}{\bar{h}_{e,\text{bot}}} \frac{R_o}{R_v + t_g} \right]^{-1} \tag{30}$$

where the thermal resistance of the circular tube wall is taken into account.

Numerical Treatment

Equations (11) and (12) were simultaneously solved for T_δ (absolute error $\Delta_a = 0.0001$ K) and $(p_{\text{sat}})_\delta$ ($\Delta_a = 1$ Pa) for every point on s by means of Wegstein's iteration method. The system of the two second-order ordinary differential equations with four initial conditions and one constitutive condition describing the evaporating microfilm region, Eqs. (5), (6), and (16)–(20), were solved using the fourth-order Runge–Kutta procedure and the shooting method (on parameter R_r). The controlled relative error was less than 0.001 percent for each of the variables. The results obtained for comparatively small temperature drops through the thin film were compared with those from the simplified model. Since the agreement was good, the simplified model was used further in the prediction of the evaporator characteristics. The heat conduction problem, Eqs. (24)–(28), was also solved by the standard Runge–Kutta method ($\Delta_a = 0.0001$ K and $\Delta_r = 0.001$ percent for the functions T and dT/dx, respectively) within the iterative procedure to find T_w ($\Delta_a = 0.0001$ K).

Results and Discussion

To verify the numerical results obtained, the experimental data provided by Schlitt et al. (1974) were used. Therefore, the results presented mostly refer to the AGHP with the following geometry: $L_{\text{tot}} = 0.914$ m, $L_c = 0.152$ m, $0.15 \le L_e \le 0.343$ m, $W = 0.305$ mm, $t_g = 1.02$ mm, $L_1 = 0.215$ mm, $R_v = 4.43$ mm, $R_o = 7.95$ mm, $\gamma = 0$, $N = 27$. The working fluids were ammonia and ethane, the casing material thermal conductivity was assumed to be $k_w = 170$ W/(m-K), $\alpha = 1$ (if another value is not indicated in the text), dispersion constant $A' = 10^{-21}$ J and $B = 3$.

The data in Figs. 2–4 were obtained for ammonia with a vapor temperature in the evaporator of $T_v = 250$ K and $\alpha = 1$. The solid surface superheat is $\Delta T = |T_w - T_v|$, and the results obtained using the simplified model for evaporating film are denoted as SIMPL. Figure 2(*a*) shows the variations of the free liquid surface temperature along the evaporating film for $\Delta T = 0.047$ K, 0.070 K, and 0.120 K, which are from the solutions of Eqs. (5)–(7), (11)–(12), and (16)–(20) in the microfilm region. These results are compared to those obtained by the simplified model, where Eqs. (7), (11), and (12) were solved along with Eqs. (21), (24), and (25) with the boundary conditions

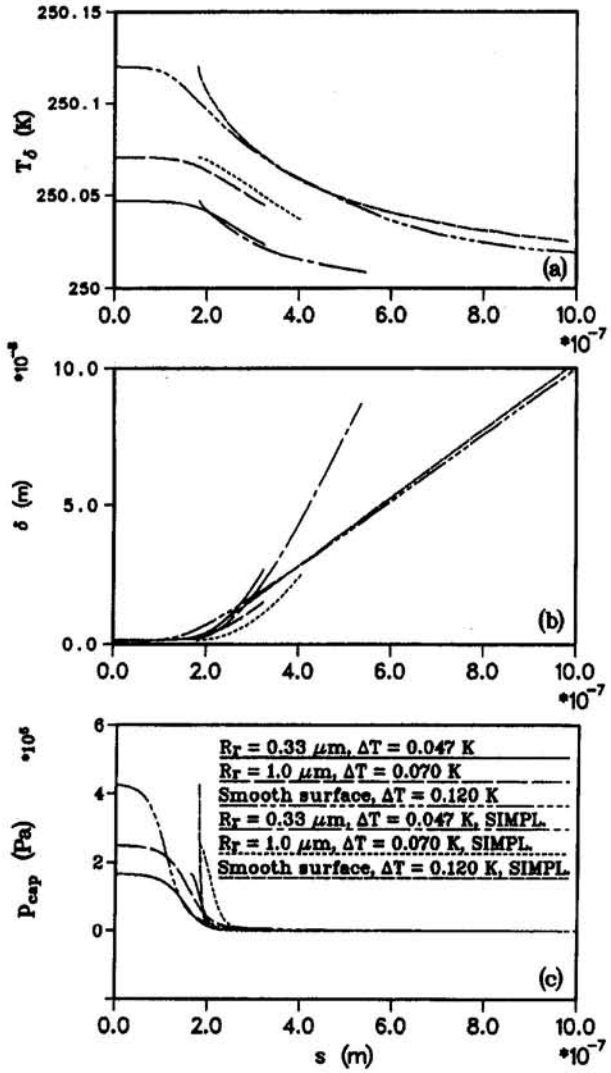

Fig. 2 Characteristics of the evaporating film along the solid–liquid interface (ammonia, $T_v = 250$ K): (*a*) free liquid surface temperature; (*b*) thickness of the film; (*c*) generalized capillary pressure.

$$T|_{x=0} = T_w, \quad \left.\frac{dT}{dx}\right|_{x=0} = 0$$

in the microfilm and transition regions for the same values of the roughness characteristic sizes ($R_r = 0.33$ μm, 1.0 μm, and $R_r \to \infty$). It should be noted that the temperature drop in the solid body in these regions was negligible in the results of the simplified model in comparison to ΔT, and the equilibrium film thickness was defined within the assumption that its free surface curvature was equal to $1/R_m$. In the simplified model for the case of a smooth surface, the value of the contact angle in the microfilm region was $\theta_f = 7$ deg, which was given by the numerical solution of Eqs. (5), (6), and (16)–(20).

The corresponding variations of the film thickness δ and generalized capillary pressure p_{cap} are shown in Figs. 2(*b*) and 2(*c*). The results obtained by the simplified model have been artificially shifted along the s coordinate in these figures (and also in Fig. 3(*a*)) to make the comparison more understandable. Also, it should be noted that there is some difference between the s coordinate and the x coordinate used in the simplified model. The following relation has been used in the present paper: $s = R_r \arcsin(x/R_r)$.

In Fig. 2(*a*), the interval of T_δ variation along the evaporating film from the value of T_w to approximately T_v was more pro-

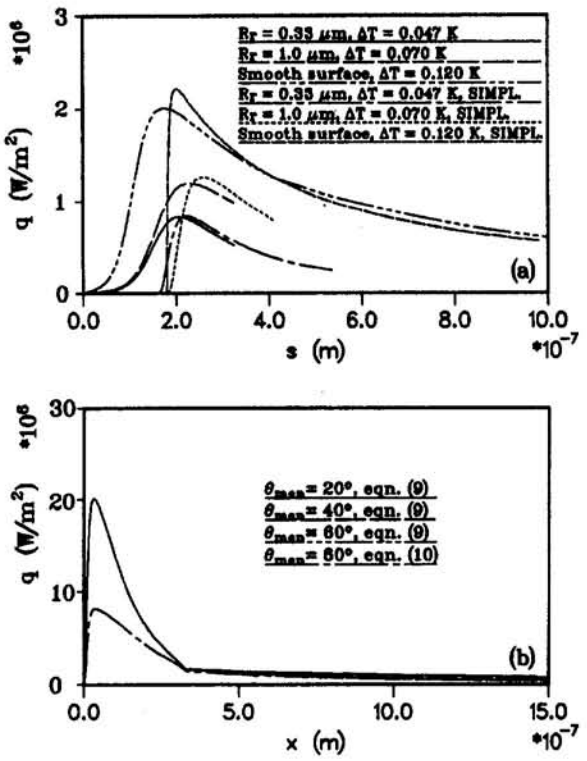

Fig. 3 Heat flux through the evaporating film (ammonia, T_v = 250 K, α = 1): (*a*) along the solid–liquid interface (microfilm region); (*b*) along the fin axis (R_r = 0.33 μm, ΔT = 1 K)

longed in comparison to the results by Stephan and Busse (1992), and the interfacial thermal resistance was still significant even when the film thickness was larger than 0.1 μm. For a smaller characteristic size R_r, the film thickness increased more sharply along the solid surface (Fig. 2(*b*)), which is in agreement with Eq. (21). It should be mentioned that for the problem, Eqs. (5), (6), and (16)–(20) (unlike for the simplified model), R_r is not a parameter but the result of the numerical solution. The values of the maximum heat flux in the microfilm region were extremely high in comparison to those in the meniscus region (Fig. 3). For $\Delta T = 0.120$ K, the generalized capillary pressure p_{cap} decreased from the initial value to the almost constant by approximately 5000 times (Fig. 2(*c*)). For a larger ΔT, this sharp decrease can cause some difficulties in the numerical treatment while solving Eqs. (5), (6), and (16)–(20); that is why the simplified model is useful. The simplified model has given the variation of p_{cap} along the film, which is even more drastic because the surface tension term is absent in the capillary pressure gradient (Fig. 2(*c*)). However, the decrease of the total heat flow rate in the microfilm region caused by this assumption was comparatively small, which is illustrated by Fig. 3(*a*). The distributions of the heat flux in the microfilm, transition, and beginning of meniscus regions for different meniscus contact angles θ_{men} as predicted by the simplified model are presented in Fig. 3(*b*). The total heat flow through the meniscus region was significantly larger in comparison to that through the microfilm region. This means that while estimating the heat transfer coefficient for an evaporator element, shown in Fig. 1, the simplified model should provide the accuracy needed. To verify this, the numerical results for the local heat transfer coefficient $\bar{h}_e$ in Fig. 4(*a*) have been obtained. The simplified model underestimated $\bar{h}_e$ by only 5 percent, which enables its use when it is necessary to avoid the numerical difficulties mentioned above. The local evaporative heat transfer coefficient $\bar{h}_e$ depends upon the meniscus contact angle θ_{men}, especially for small θ_{men}, and is practically independent of the heat flux on the external wall surface of the evaporator and also of ΔT, as shown in Fig. 4(*b*). The characteristic roughness size affected the value of $\bar{h}_e$, decreasing it up to 30 percent for α = 1 in comparison to the value obtained for the smooth solid surface. For large meniscus contact angle the influence of the roughness size on the heat transfer coefficient is at the maximum when R_r is close to the length of the microfilm region. For small values of the accommodation coefficient (for example for α = 0.05) the effect of the surface roughness on the heat transfer is insignificant because the heat flux in the microfilm region in this case is comparatively small (Fig. 5).

The results of the present model were compared with the experimental data by Schlitt et al. (1974) and Ivanovskii et al. (1984) for the case of a small heat load applied to the AGHP (or evaporator). For a small heat load ($Q_a \ll Q_{max}$) the values of the meniscus angle in the evaporator of the AGHP under consideration are comparatively large: $\theta_{men} \geq 60$ deg. This is valid because in the case without a heat load the grooves of an AGHP in the horizontal position are completely filled with liquid (i.e., the meniscus angle is close to 90 deg). For $\theta_{men} \geq 60$ deg the local evaporative heat transfer coefficients are practically independent on θ_{men}, as shown in Fig. 5. The values of the evaporative heat transfer coefficients (based on the outer tube diameter) obtained experimentally by Schlitt et al. (1974) and those reported by Ivanovskii et al. (1984) were also found to be independent of heat load, which resulted in a valid comparison, as given in Table 1. The agreement of the results for ammonia, ethane, and water is good for $\alpha \ll 1$ since it was mentioned by Carey (1992) that, for some substances (ethanol, methanol, water, etc.), the accommodation coefficient had been found to have very small values (0.02 to 0.04) in the experiments by Paul (1962). The physical reason for low α values in the microfilm region of the evaporator can be the concentration of the contaminants that usually exist in a heat pipe in this region. For the case of α = 1, the prediction gave significant (up to 100 percent) overestimations of $\bar{h}_e$ even for a rough

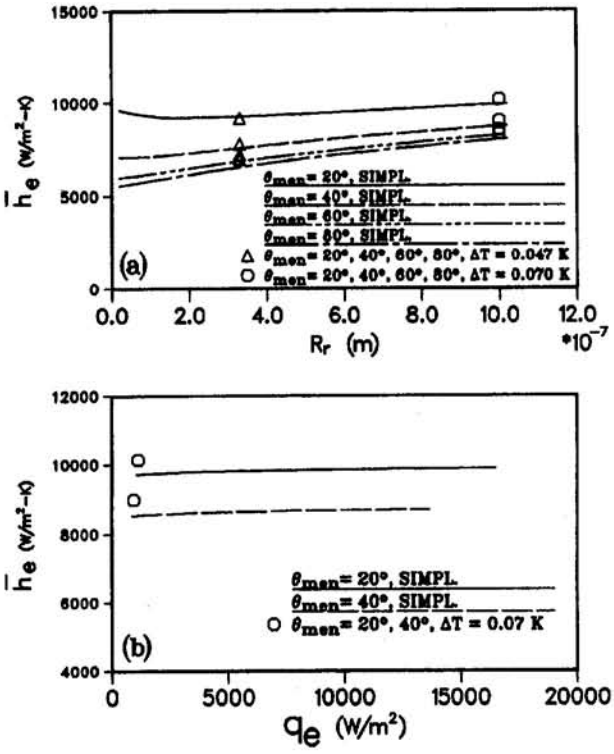

Fig. 4 Local heat transfer coefficient in the evaporator of the ammonia–Al heat pipe (T_v = 250 K): (*a*) versus roughness size; (*b*) versus heat flux (R_r = 1 μm)

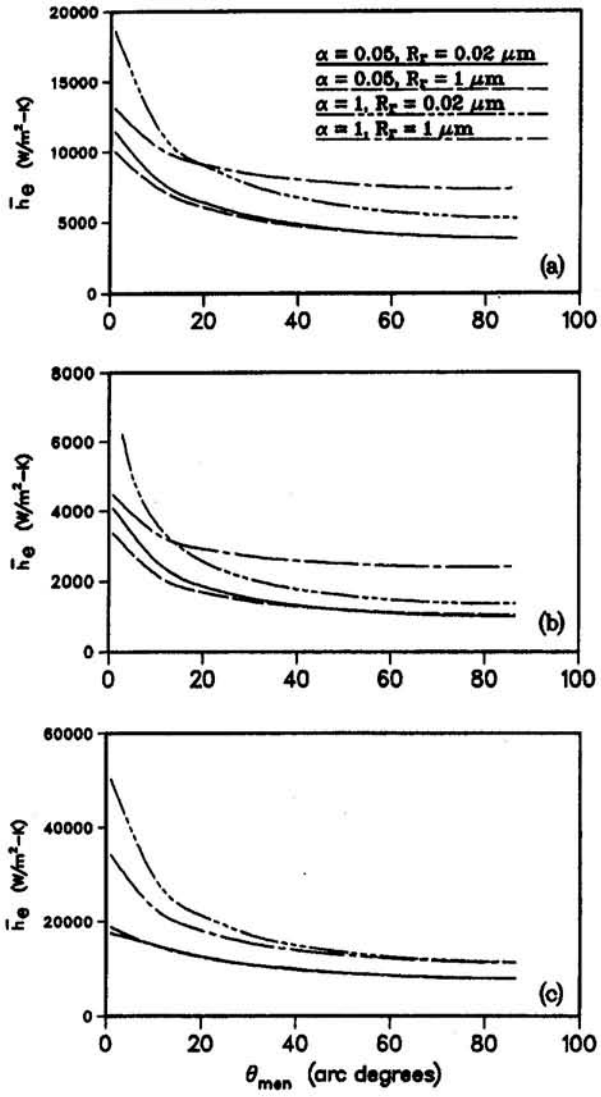

Fig. 5 Effect of the meniscus contact angle on the local evaporative heat transfer coefficients ($\Delta T = 1$ K): (*a*) ammonia–Al heat pipe (Schlitt et al., 1974) ($T_v = 250$ K); (*b*) ethane–Al heat pipe (Schlitt et al., 1974) ($T_v = 200$ K); (*c*) water–copper evaporator (Ivanovskii et al., 1984) ($T_v = 300$ K)

surface, as can be seen from Fig. 5. The experimental data by Ivanovskii et al. (1984) correspond to the case of evaporation of water from a copper plate with rectangular grooves for heat fluxes on the wall up to 20 W/cm^2 ($W = 0.17$ mm, $t_g = 0.8$ mm, $L_1 = 0.25$ mm, $L_e = 100$ mm, $T_v = 300$ K).

A comparison with the numerical data reported by Stephan and Busse (1992) has also been made for ammonia with: $T_v = 300$ K, $k_w = 221$ W/(m^2-K), $A' = 2 \times 10^{-21}$ J, $\alpha = 1$, $L_1 = 0.5 \times 10^{-5}$ m, $W = 0.5 \times 10^{-3}$ m, $\gamma = 45$ deg, $t_g = 0.5 \times 10^{-3}$ m, $R_v = 1$ m, $R_o = 1.0015$ m, $\theta_f = \theta_{men} = 19.7$ deg, $\Delta T = 1.31$ K. The results of the comparison are listed in Table 2, which was prepared by Stephan and Busse (1992), except for the data of the present analysis. $T_{\delta v}$ is the temperature of the vapor side of the interface and Q'_{mic} is the heat flow rate per unit groove length in the region $0 \le x \le 1$ μm. The value of the heat transfer coefficient found by Stephan and Busse (1992) was 23,000 W/(m^2-K), while the result of the present numerical analysis is 17,385 W/(m^2-K) for a rough surface (for $R_r = 0.02$ μm) and 23,900 W/(m^2-K) for a smooth surface, which proves the validity of the present analysis.

Table 1 Comparison of the predicted $\bar{h}_e$ with existing experimental data

Investigators	Schlitt et al. (1974)	Schlitt et al. (1974)	Ivanovskii et al. (1984)
Working fluid	Ammonia	Ethane	Water
T_v (K)	250	200	300
Casing material	Aluminum	Aluminum	Copper
Experimental value of $\bar{h}_e$ (W/m^2-K)	3920	770	9500
Present prediction, $\bar{h}_e$ (W/m^2-K), $\theta = 60°$, $\alpha = 0.05$	4140	1180	8620

Table 2 Comparison of the results with simplified models

Investigators	Present		Stephan and Busse (1992)		Schneider (1976)	Shekriladze (1987)
Assumption: Surface:	$T_\delta > T_v$ rough	$T_\delta > T_v$ smooth	$T_{\delta v} > T_v$ smooth	$T_{\delta v} = T_v$ smooth	$T_\delta = T_v$ smooth	$T_\delta = T_v$ smooth
$T_w - T_v$ (K)	1.31	1.31	1.31	1.31	-	-
$\bar{h}_e$ (W/cm^2-K)	1.74	2.39	2.3	7.9	6.9	3.9
q_e (W/cm^2)	2.56	3.69	3.0	10.4	-	-
Q'_{mic}/Q'_{tot} (%)	37	38	45	94	-	-

Conclusions

The results of the numerical simulation of heat transfer during evaporation on the grooved surfaces of heat pipes are summarized as follows:

1 The validity of the present mathematical model for grooved evaporators has been confirmed, in general, by the comparisons with experimental data of Schlitt et al. (1974) and Ivanovskii et al. (1984), and the numerical results of Stephan and Busse (1992). However, more detailed information concerning the values of the accommodation coefficients and dispersion constants is needed.

2 Accounting for the roughness of the solid surface in the thin evaporating film region resulted in a decrease of the heat transfer coefficient by up to about 30 percent in comparison to that obtained for a smooth surface for the case when the accommodation coefficient was set equal to unity. For $\alpha \ll 1$ the influence of the surface roughness on the evaporative heat transfer coefficient was insignificant.

3 The simplified model of evaporative heat transfer, where it was assumed that the free film surface curvature in the microfilm region was equal to that in the meniscus region, predicted values of the heat transfer coefficient only up to 5 percent smaller in comparison to the case where the curvature variation along the film was taken into account (for $\alpha = 1$).

4 The value of the local evaporative heat transfer coefficient (for a fixed θ_{men}) was practically independent of the heat flux on the evaporator external wall.

5 The interfacial resistance significantly influenced the value of the evaporative heat transfer coefficient. Therefore, the more advanced expressions for this resistance during high intensive evaporation are needed.

6 Due to the fact that the greatest part of the heat flow through the liquid is transferred in the meniscus region where the liquid film is comparatively small, grooved evaporators are capable of withstanding comparatively high heat fluxes. While the model gives the values of the temperature drop in the liquid during evaporation, it provides an opportunity to predict the onset of the nucleate boiling in grooved evaporators.

In order to make the comparisons with experimental data more profound, the longitudinal variation of the meniscus angle should be taken into account. That means that the fluid circula-

tion in an AGHP should be considered in conjunction with the present analysis.

Acknowledgments

Funding for this work was provided by the National Science Foundation, Grant No. CTS-941458, and Thermal Energy Group of the Aero Propulsion Directorate of the U.S. Air Force under contract No. F33615-92-C-2276.

References

Carey, V. P., 1992, *Liquid-Vapor Phase-Change Phenomena: An Introduction to the Thermophysics of Vaporization and Condensation Processes in Heat Transfer Equipment,* Hemisphere, New York.

Derjaguin, B. V., 1955, "Definition of the Concept of and Magnitude of the Disjoining Pressure and Its Role in the Statics and Kinetics of Thin Layers of Liquid," *Kolloidny Zhurnal,* Vol. 17, pp. 191–197 [in Russian].

Faghri, A., 1995, *Heat Pipe Science and Technology,* Taylor & Francis, New York.

Holm, F. W., and Goplen, S. P., 1979, "Heat Transfer in the Meniscus Thin-Film Transition Region," ASME JOURNAL OF HEAT TRANSFER, Vol. 101, pp. 543–547.

Ivanovskii, M. N., Privezentsev, V. V., Il'in, Yu.A., and Sidorenko, E. M., 1984, "Experimental Investigation of Heat Transfer With Evaporation of the Agent From a Corrugated Capillary Structure," *J. Engineering Physics and Thermophysics,* Vol. 46, No. 4, 377–381.

Kamotani, Y., 1978, "Evaporator Film Coefficients of Grooved Heat Pipes," *Proc. 3rd Int. Heat Pipe Conf.,* Palo Alto, CA. pp. 128–130.

Khrustalev, D., and Faghri, A., 1994, "Heat Transfer During Evaporation and Condensation on Capillary-Grooved Structures of Heat Pipes," *Proc. 1994 ASME Winter Annual Meeting,* Chicago, Nov., ASME HTD-Vol. 287, pp. 47–59.

Labuntsov, D. A., and Krukov, A. P., 1977, "Intensive Evaporation Processes," *Thermoenergetics,* No. 4, pp. 8–11.

Paul, B., 1962, "Compilation of Evaporation Coefficients," *ARS J.,* Vol. 32, pp. 1321–1328.

Potash, M., Jr., and Wayner, P. C., Jr., 1972, "Evaporation From a Two-Dimensional Extended Meniscus," *Int. J. Heat Mass Transfer,* Vol. 15, pp. 1851–1863.

Schlitt, K. R., Kirkpatrick, J. P., and Brennan, P. J., 1974, "Parametric Performance of Extruded Axial Grooved Heat Pipes From 100 K to 300 K," *Proc. AIAA/ASME Thermophysics and Heat Transfer Conf.,* AIAA Paper No. 74-724.

Schneider, G. E., Yovanovich, M. M., and Wehrle, V. A., 1976, "Thermal Analysis of Trapezoidal Grooved Heat Pipe Evaporator Walls," AIAA Paper No. 76-481.

Shekriladze, I. G., and Rusishvili, D. G., 1987, "Evaporation and Condensation on Grooved Capillary Surfaces," *Proc. 6th Int. Heat Pipe Conf.,* Grenoble, pp. 173–176.

Solov'ev, S. L., and Kovalev, S. A., 1984, "Mechanism of Evaporation of a Liquid From a Porous Surface," *Proc. 5th Int. Heat Pipe Conf.,* Tsukuba, Japan, Preprints Vol. II, pp. 77–82.

Stephan, P., 1992, *Wärmedurchgang bei Verdampfung aus Kapillarrillen in Wärmerohren,* Fortschr.-Ber. VDI, Vol. 19, No. 59, VDI-Verlag, Düsseldorf, Germany.

Stephan, P. C., and Busse, C. A., 1992, "Analysis of the Heat Transfer Coefficient of Grooved Heat Pipe Evaporator Walls," *Int. J. Heat Mass Transfer,* Vol. 35, No. 2, pp. 383–391.

Vasiliev, L. L., Grakovich, L. P., and Khrustalev, D. K., 1981, "Low-Temperature Axially Grooved Heat Pipes," *Proc. 4th Int. Heat Pipe Conf.,* London, United Kingdom, pp. 337–348.

Journal of Heat Transfer

Technical Notes

This section contains shorter technical papers. These shorter papers will be subjected to the same review process as that for full papers.

Transient Thermal Constriction Resistance in a Finite Heat Flux Tube

H. R. B. Orlande[1,2] and M. N. Özişik[2]

Introduction

The transient constriction resistance has been studied under idealized conditions in a semi-infinite medium with isothermal contact (Sadhal, 1980; Barber, 1989; Greenwood, 1991) and in a semi-infinite cylinder with uniform heat flux over the contact (Beck and Lloyd, 1988). Although the transient constriction resistance in finite length cylinders has several practical applications (Fisher and Yovanovich, 1989), such a problem has not been analyzed, mainly due to mathematical difficulties involved in the solution for the case of isothermal contact.

In this work we use a finite difference scheme with numerical grid generation technique to study the transient constriction resistance in a cylindrical heat flux tube of finite length with a circular contact surface. Two boundary conditions considered for the contact surface included the cases of uniform temperature and uniform heat flux.

Mathematical Formulation and Method of Solution

Consider the transient heat conduction in a cylinder of length L^* and radius b^*, as illustrated in Fig. 1(a). The boundaries at $r^* = b^*$ and at $z^* = 0$, $a^* \le r^* \le b^*$, are considered to be insulated. The boundary at $z^* = L^*$ is maintained at a fixed temperature T_0^*, which is also the initial temperature for the region. Two boundary conditions are considered for the contact surface at $z^* = 0$, $0 \le r^* \le a^*$: (i) a uniform temperature T_c^*; and (ii) a uniform heat flux q_c^*, where the superscript "*" indicates dimensional variables.

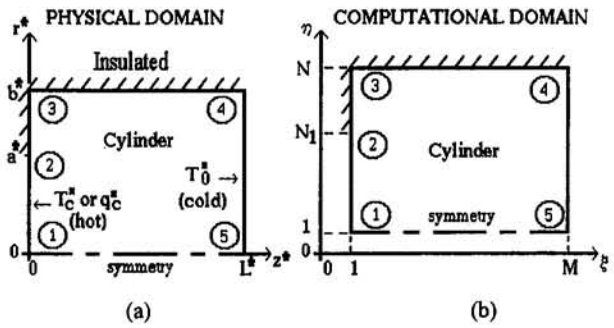

Fig. 1 (a) Geometry and coordinates in the physical domain; (b) computational domain

A numerical difficulty was experienced in finite difference computations with regular grid, because the isothermal boundary condition for the contact surface gave rise to very steep temperature gradients in the region around $r^* = a^*$. To overcome such a difficulty, an elliptic scheme of numerical grid generation (Thomsom et al., 1985) was used in order to concentrate grid points in the regions of very high temperature gradients. Figures 1(a, b) show the mapping of the physical domain (z, r, t) into the computational domain (ξ, η, t).

The heat conduction equation in the computational domain (ξ, η, t) and in dimensionless form is given by:

$$\frac{\partial T}{\partial t} = \left(a_{zz} + a_{rr} + \frac{1}{r}a_r\right)T_\xi + \left(b_{zz} + b_{rr} + \frac{1}{r}b_r\right)T_\eta + \frac{\alpha}{J^2}T_{\xi\xi} + \frac{\gamma}{J^2}T_{\eta\eta} - 2\frac{\beta}{J^2}T_{\xi\eta} \quad \text{in} \quad 1 \le \xi \le M, \quad 1 \le \eta \le N; \quad t > 0 \quad (1.a)$$

and the initial and boundary conditions are taken as:

$$T = 0 \quad \text{for } t = 0; \quad \text{in } 1 \le \xi \le M, \quad 1 \le \eta \le N \quad (1.b)$$

$$-\beta T_\xi + \gamma T_\eta = 0 \quad \text{at } \eta = N, \quad 1 < \xi < M; \quad t > 0 \quad (1.c)$$

$$T = 0 \quad \text{at } \xi = M, \quad 1 < \eta < N; \quad t > 0 \quad (1.d)$$

$$-\alpha T_\xi + \beta T_\eta = 0 \quad \text{at } \xi = 1, \quad N_1 < \eta < M; \quad t > 0 \quad (1.e)$$

$$T = 1 \text{ or } \frac{-\alpha T_\xi + \beta T_\eta}{J\sqrt{\alpha}} = 1 \quad \text{at } \xi = 1, \quad 1 < \eta < N_1; \quad t > 0 \quad (1.f, f')$$

where the subscripts "ξ" and "η" indicate the partial deriva-

[1] Permanent address: Department of Mechanical Engineering, PEM/COPPE/UFRJ, Caixa Postal 68503, Cidade Universitaria, Rio de Janeiro, RJ 21945-970, Brazil.

[2] Department of Mechanical & Aerospace Engineering, North Carolina State University, P.O. Box 7910, Raleigh, NC 27695-7910.

Contributed by the Heat Transfer Division of THE AMERICAN SOCIETY OF MECHANICAL ENGINEERS. Manuscript received by the Heat Transfer Division October 1993; revision received October 1994. Keywords: Conduction, Numerical Methods, Transient and Unsteady Heat Transfer. Associate Technical Editor: L. S. Fletcher.

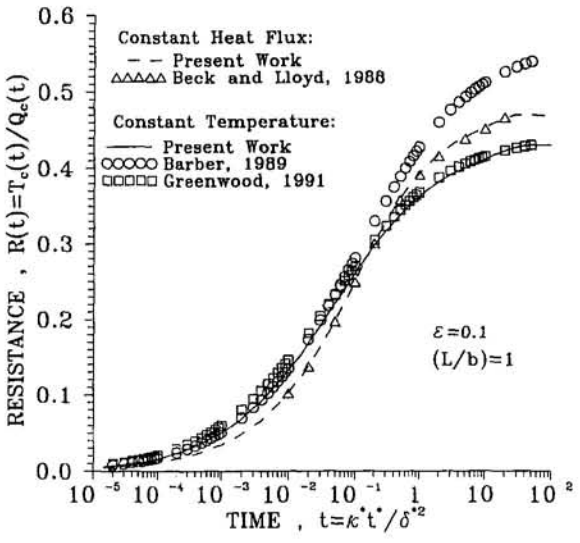

Fig. 2(*a*) Transient constriction resistance: comparison with the results of Beck and Lloyd (1988), Barber (1989), and Greenwood (1991) for ϵ = 0.1 and (L/b) = 1

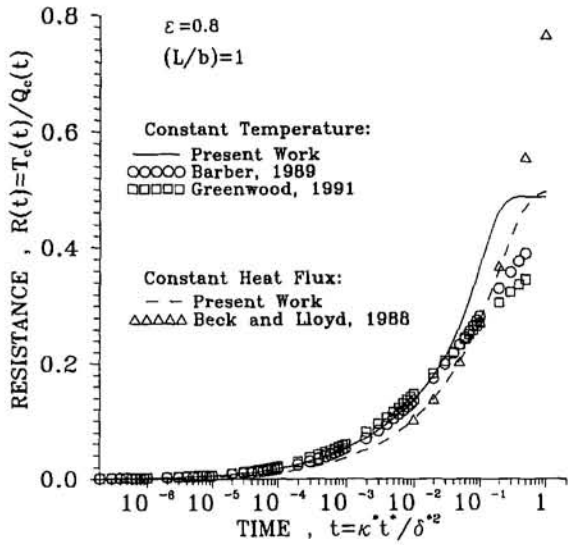

Fig. 2(*b*) Transient constriction resistance: comparison with the results of Beck and Lloyd (1988), Barber (1989), and Greenwood (1991) for ϵ = 0.8 and (L/b) = 1

tives with respect to ξ and η, respectively. The geometric coefficients are given by:

$$a_{zz} = \frac{1}{J^2}\left[r_\eta r_{\xi\eta} - r_\xi r_{\eta\eta} - \frac{r_\eta}{J}(r_\eta J_\xi - r_\xi J_\eta)\right];$$

$$b_{zz} = \frac{1}{J^2}\left[r_\xi r_{\xi\eta} - r_\eta r_{\xi\xi} + \frac{r_\xi}{J}(r_\eta J_\xi - r_\xi J_\eta)\right] \quad (2.a, b)$$

$$a_r = -\frac{z_\eta}{J}; \quad b_r = \frac{z_\xi}{J}; \quad \alpha = z_\eta^2 + r_\eta^2 \quad (2.c-h)$$

$$\beta = z_\xi z_\eta + r_\xi r_\eta; \quad \gamma = z_\xi^2 + r_\xi^2; \quad J = z_\xi r_\eta - r_\xi z_\eta$$

where the coefficients a_{rr} and b_{rr} are obtained from Eqs. (2.*a*, *b*) by replacing r by z.

The following dimensionless quantities were defined based on the characteristic length δ^*, which was taken as the square root of the contact area (Beck and Lloyd, 1988; Negus et al., 1989):

$$z \equiv \frac{z^*}{\delta^*}; \quad L \equiv \frac{L^*}{\delta^*}; \quad r \equiv \frac{r^*}{\delta^*}; \quad a \equiv \frac{a^*}{\delta^*}; \quad b \equiv \frac{b^*}{\delta^*};$$

$$t \equiv \frac{K^* t^*}{\delta^{*2}}; \quad \epsilon \equiv \frac{a^*}{b^*} \quad (3.a-g)$$

The dimensionless temperature, heat flux, and total heat flow rate were, respectively, defined as

$$T \equiv \frac{T^* - T_0^*}{T_c^* - T_0^*}; \quad q \equiv \frac{\delta^* q^*}{k^*(T_c^* - T_0^*)};$$

$$Q \equiv \frac{Q^*}{k^*\delta^*(T_c^* - T_0^*)} \quad (3.h, i, j)$$

for the case of uniform temperature boundary condition, $T^* = T_c^*$, over the contact surface; and as

$$T \equiv \frac{T^* - T_0^*}{q_c^*\delta^*/k^*}; \quad q \equiv \frac{q^*}{q_c^*}; \quad Q \equiv \frac{Q^*}{\delta^{*2} q_c^*} \quad (3.h', i', j')$$

for the case of uniform heat flux boundary condition, $q^* = q_c^*$, over the contact surface.

Equations (1) were discretized with finite differences and the alternating-direction implicit method (Özişik, 1993) was used to march the solution in time. Once the temperature field was found for each time step, the dimensionless constriction resistance was computed from its definition:

$$R(t) = \frac{T_c(t)}{Q_c(t)} \quad (4)$$

where $T_c(t)$ is the dimensionless average temperature and $Q_c(t)$ is the dimensionless total heat flow rate over the contact surface, at time t.

Results and Discussion

We have computed the transient constriction resistance $R(t)$ for values of ϵ ranging from 0.1 to 0.9 and for (L/b) = 0.2, 0.5, and 1.

In order to examine the accuracy of the numerical method considered here, as well as to optimize the number and distribution of grid points, the steady-state constriction parameter Ψ reported by Negus and Yovanovich (1984a, b) was reproduced by using the finite difference scheme with numerical grid generation described above, for both cases of uniform temperature

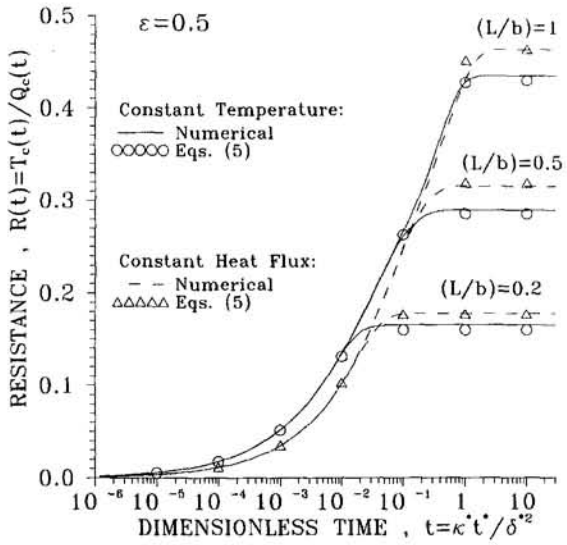

Fig. 3 Transient constriction resistance for ϵ = 0.5

and uniform heat flux over the contact surface. Generally, the errors are less than 0.5 percent, except for $\epsilon = 0.1$ and 0.9 for the uniform temperature boundary condition, when the errors are 1.4 and 2.2 percent, respectively. The error greater than 1 percent for $\epsilon = 0.1$ is probably due to the fact that fewer points are used to compute numerically the integrals to obtain Ψ, and also due to the very large temperature gradients at the edge of the contact, for such small contact area. Although for $\epsilon = 0.9$ the relative error is more than 2 percent, the value of Ψ computed numerically in this work agree with that of Negus and Yovanovich (1984a) up to 3 decimal places.

Figures 2(a, b) give a comparison of our numerical results for $(L/b) = 1$, with the analytical solution of Beck and Lloyd (1988) for a semi-infinite cylinder with uniform heat flux over the contact; and with the asymptotic solutions of Greenwood (1991) and Barber (1989) for a semi-infinite medium with isothermal contact. The approximate solutions of Greenwood (1991) and Barber (1989) are for the long-time and short-time transients, respectively.

Figure 2(a) shows that for $\epsilon = 0.1$, the numerical results for constant heat flux are in good agreement with those from Beck and Lloyd (1988). The numerical results for a constant temperature are also in very good agreement with those from the short-time solution of Barber (1989) up to $t \approx 10^{-2}$. For times greater than 10^{-2}, the numerical solution follows the same trend as Greenwood's (1991) long-time solution. For the case of $\epsilon = 0.1$ and $(L/b) = 1$, it appears that the boundary conditions at $r = b$ and $z = L$ have very little effect on the solution, since the results for a semi-infinite cylinder and for a semi-infinite medium (in the respective validity range) are in good agreement with those for the finite cylinder considered here. However, such is not the case for larger values of ϵ. Figure 2(b) shows that for $\epsilon = 0.8$ Greenwood's (1991) long-time solution does not follow the trend of the numerical solution for the isothermal contact, which is due to the effect of the boundary at $r = b$. The numerical results are in very good agreement with the solution from Beck and Lloyd (1988) for the constant heat flux, up to $t = 0.2$. The discrepancy observed for larger times is due to the effect of the boundary at $z = L$.

Figure 3 presents the transient constriction resistance for $\epsilon = 0.5$ and for $(L/b) = 0.2$, 0.5, and 1. This figure shows that for the two boundary conditions considered for the contact, steady state is approached earlier and the steady-state resistance is smaller for shorter cylinders. On the other hand, cylinders of different length behave identically for small times, since the boundary condition at $z = L$ has very little influence on the solution.

We were able to correlate the transient constriction resistance for both cases of uniform temperature and uniform heat flux boundary conditions, for the range $0.2 \leq \epsilon \leq 0.7$. The correlation is given by Eqs. (5), where the coefficients β_1 to β_6 are given by Eqs. (6) for the isothermal contact and by Eqs. (7) for the uniform heat flux boundary condition.

$$R(t) = \begin{cases} \dfrac{\beta_1}{\left(\dfrac{\beta_2}{\sqrt{t}} + \beta_3\right)} & \text{for } 10^{-3}\,\theta < t < \theta \qquad (5.a) \\ \beta_4 \tanh(\beta_5 t) + \beta_6 & \text{for } t > 20\left(\dfrac{L}{b}\right)^{1.8}\theta \qquad (5.b) \end{cases}$$

where

$$\theta = \begin{cases} 0.002\epsilon^{-2.07} & \text{for } T \text{ uniform over the contact} \qquad (5.c) \\ 0.005\epsilon^{-1.84} & \text{for } q \text{ uniform over the contact} \qquad (5.d) \end{cases}$$

The coefficients β are given by

$$\beta_1 = 1.24 \qquad (6.a)$$

$$\beta_2 = 0.69 \qquad (6.b)$$

$$\beta_3 = 3.2 - 8.65\epsilon + 40.46\epsilon^2 - 93.61\epsilon^3 + 102.58\epsilon^4 - 42.58\epsilon^5 \qquad (6.c)$$

$$\beta_4 = \begin{cases} 0.05 + 0.41\epsilon & \text{for } L/b = 1 \\ 0.03 + 0.76\epsilon - 1.47\epsilon^2 + 0.95\epsilon^3 & \text{for } L/b = 0.5 \\ 0.03 + 0.62\epsilon - 2.15\epsilon^2 + 3.05\epsilon^3 - 1.62\epsilon^4 & \text{for } L/b = 0.2 \end{cases} \qquad (6.d)$$

$$\beta_5 = \begin{cases} -1.09 + 11.09\epsilon - 20.91\epsilon^2 + 27.44\epsilon^3 & \text{for } L/b = 1 \\ -5.2 + 42.81\epsilon - 38.58\epsilon^2 + 50.79\epsilon^3 & \text{for } L/b = 0.5 \\ -31.3 + 356.44\epsilon - 1199.46\epsilon^2 + 2635.5\epsilon^3 - 1590.89\epsilon^4 & \text{for } L/b = 0.2 \end{cases} \qquad (6.e)$$

$$\beta_6 = \begin{cases} 0.38 - 0.52\epsilon + 0.22\epsilon^2 & \text{for } L/b = 1 \\ 0.33 - 0.48\epsilon - 0.43\epsilon^2 + 1.71\epsilon^3 - 1.15\epsilon^4 & \text{for } L/b = 0.5 \\ 0.42 - 1.83\epsilon + 4.17\epsilon^2 - 4.95\epsilon^3 + 2.38\epsilon^4 & \text{for } L/b = 0.2 \end{cases} \qquad (6.f)$$

for the isothermal contact surface, and by

$$\beta_1 = 1.06 \tag{7.a}$$

$$\beta_2 = 0.92 \tag{7.b}$$

$$\beta_3 = 2.11 - 7.08\epsilon + 23.16\epsilon^2 - 41.92\epsilon^3 + 40.02\epsilon^4 - 15.51\epsilon^5 \tag{7.c}$$

$$\beta_4 = \begin{cases} 0.04 + 0.81\epsilon - 0.93\epsilon^2 + 0.55\epsilon^3 & \text{for } L/b = 1 \\ 0.01 + 1.41\epsilon - 3.96\epsilon^2 + 5.3\epsilon^3 - 3.63\epsilon^4 + 1.09\epsilon^5 & \text{for } L/b = 0.5 \\ 0.01 + 1.5\epsilon - 6.3\epsilon^2 + 11.45\epsilon^3 - 9.93\epsilon^4 + 3.35\epsilon^5 & \text{for } L/b = 0.2 \end{cases} \tag{7.d}$$

$$\beta_5 = \begin{cases} 0.43 - 5.18\epsilon + 48.68\epsilon^2 - 119.1\epsilon^3 + 135.87\epsilon^4 - 55.51\epsilon^5 & \text{for } L/b = 1 \\ -1.6 + 32.64\epsilon - 144.03\epsilon^2 + 451.5\epsilon^3 - 552.03\epsilon^4 + 237.25\epsilon^5 & \text{for } L/b = 0.5 \\ -1.21 + 23.3\epsilon + 60.6\epsilon^2 + 87.71\epsilon^3 - 57.32\epsilon^4 & \text{for } L/b = 0.2 \end{cases} \tag{7.e}$$

$$\beta_6 = \begin{cases} 0.42 - 0.60\epsilon - 0.88\epsilon^2 + 4.71\epsilon^3 - 6.27\epsilon^4 + 2.76\epsilon^5 & \text{for } L/b = 1 \\ 0.48 - 1.96\epsilon + 5.04\epsilon^2 - 7.79\epsilon^3 + 6.54\epsilon^4 - 2.25\epsilon^5 & \text{for } L/b = 0.5 \\ 0.48 - 2.69\epsilon + 7.89\epsilon^2 - 12.42\epsilon^3 + 9.94\epsilon^4 - 3.17\epsilon^5 & \text{for } L/b = 0.2 \end{cases} \tag{7.f}$$

for the uniform heat flux boundary condition for the contact surface.

A comparison of the results obtained from Eqs. (5) with those computed with the finite difference scheme described above reveals that the errors are less than 5 percent, which is fairly satisfactory for engineering applications. Figure 3 shows a comparison of the constriction resistance computed from Eqs. (5) with those values computed numerically, for $\epsilon = 0.5$. The agreement is good.

References

Barber, J. R., 1989, "An Asymptotic Solution for Short-Time Transient Heat Conduction Between Two Similar Contacting Bodies," *Int. J. Heat Mass Transfer,* Vol. 32, pp. 943–949.

Beck, J. V., and Lloyd, J. R., 1988, "Transient Surface Temperatures in Solids Due to Small Heat Sources," *Cooling Technology for Electronic Equipment,* Win Aung, ed., Hemisphere, Washington, DC.

Fisher, N. J., and Yovanovich, M. M., 1989, "Thermal Constriction Resistance of Sphere/Layered Flat Contacts: Theory and Experiment," ASME JOURNAL OF HEAT TRANSFER, Vol. 111, pp. 249–256.

Greenwood, J. A., 1991, "Transient Thermal Contact Resistance," *Int. J. Heat Mass Transfer,* Vol. 34, pp. 2287–2290.

Negus, K. J., and Yovanovich, M. M., 1984a, "Constriction Resistance of Circular Flux Tubes With Mixed Boundary Conditions by Linear Superposition of Neumann Solutions," ASME Paper No. 84-HT-84.

Negus, K. J., and Yovanovich, M. M., 1984b, "Application of the Method of Optimized Images to Steady Three-Dimensional Conduction Problems," ASME Paper No. 84-WA/HT-110.

Negus, K. J., Yovanovich, M. M., and Beck, J. V., 1989, "On the Nondimensionalization of Constriction Resistance for Semi-infinite Heat Flux Tubes," ASME JOURNAL OF HEAT TRANSFER, Vol. 111, pp. 804–806.

Özişik, M. N., 1993, *Heat Conduction,* 2nd ed. Wiley, New York.

Sadhal, S. S., 1980, "Transient Thermal Response of Two Solids in Contact Over a Circular Disk," *Int. J. Heat Mass Transfer,* Vol. 23, pp. 731–733.

Thomsom, J. F., Warsi, Z., and Mastin, C., 1985, *Numerical Grid Generation: Foundations and Applications,* North Holland, New York.

Derivation of the Casimir Limit Phonon Distribution Using the Boltzmann Transport Equation

Y. Polsky[1] and Y. Bayazitoglu[2]

Nomenclature

C_v = specific heat per unit volume, $Jm^{-3}K^{-1}$
C_{il} = elastic stiffness constant, Jm^{-3}
e_{il} = elastic strain component
E = energy, J
f = phonon distribution
f^0 = phonon equilibrium distribution
F = force, N; free energy, J
$\hbar$ = Planck constant divided by 2π, Js
k_b = Boltzmann constant, JK^{-1}
K = phonon wave vector, m^{-1}
l = phonon mean free path, m
L = length of the crystal, m
N = number of atoms along length of the crystal
p = carrier momentum, $kgms^{-1}$
P = pressure, Nm^{-2}
$P(x)$ = probability function
q = heat flux, Wm^{-2}
R = the displacement of a deformation, m
s = specific entropy, $Jm^{-3}K^{-1}$
T = temperature, K
u = specific internal energy, Jm^{-3}
u', v', w' = displacements from the equilibrium position of an atom, m
U = elastic energy of a solid, J
v = phonon wave velocity, ms^{-1}
V = crystal volume element, m^3
Z = partition function, JK^{-1}

[1] Graduate Student, Mechanical Engineering and Material Science Department, Rice University, Houston, TX 77005.

[2] Professor, Mechanical Engineering and Material Science Department, Rice University, Houston, TX 77005.

Contributed by the Heat Transfer Division of THE AMERICAN SOCIETY OF MECHANICAL ENGINEERS. Manuscript received by the Heat Transfer Division May 1994; revision received August 1994. Keywords: Conduction. Associate Technical Editor: R. Viskanta.

for the isothermal contact surface, and by

$$\beta_1 = 1.06 \tag{7.a}$$

$$\beta_2 = 0.92 \tag{7.b}$$

$$\beta_3 = 2.11 - 7.08\epsilon + 23.16\epsilon^2 - 41.92\epsilon^3 + 40.02\epsilon^4 - 15.51\epsilon^5 \tag{7.c}$$

$$\beta_4 = \begin{cases} 0.04 + 0.81\epsilon - 0.93\epsilon^2 + 0.55\epsilon^3 & \text{for } L/b = 1 \\ 0.01 + 1.41\epsilon - 3.96\epsilon^2 + 5.3\epsilon^3 - 3.63\epsilon^4 + 1.09\epsilon^5 & \text{for } L/b = 0.5 \\ 0.01 + 1.5\epsilon - 6.3\epsilon^2 + 11.45\epsilon^3 - 9.93\epsilon^4 + 3.35\epsilon^5 & \text{for } L/b = 0.2 \end{cases} \tag{7.d}$$

$$\beta_5 = \begin{cases} 0.43 - 5.18\epsilon + 48.68\epsilon^2 - 119.1\epsilon^3 + 135.87\epsilon^4 - 55.51\epsilon^5 & \text{for } L/b = 1 \\ -1.6 + 32.64\epsilon - 144.03\epsilon^2 + 451.5\epsilon^3 - 552.03\epsilon^4 + 237.25\epsilon^5 & \text{for } L/b = 0.5 \\ -1.21 + 23.3\epsilon + 60.6\epsilon^2 + 87.71\epsilon^3 - 57.32\epsilon^4 & \text{for } L/b = 0.2 \end{cases} \tag{7.e}$$

$$\beta_6 = \begin{cases} 0.42 - 0.60\epsilon - 0.88\epsilon^2 + 4.71\epsilon^3 - 6.27\epsilon^4 + 2.76\epsilon^5 & \text{for } L/b = 1 \\ 0.48 - 1.96\epsilon + 5.04\epsilon^2 - 7.79\epsilon^3 + 6.54\epsilon^4 - 2.25\epsilon^5 & \text{for } L/b = 0.5 \\ 0.48 - 2.69\epsilon + 7.89\epsilon^2 - 12.42\epsilon^3 + 9.94\epsilon^4 - 3.17\epsilon^5 & \text{for } L/b = 0.2 \end{cases} \tag{7.f}$$

for the uniform heat flux boundary condition for the contact surface.

A comparison of the results obtained from Eqs. (5) with those computed with the finite difference scheme described above reveals that the errors are less than 5 percent, which is fairly satisfactory for engineering applications. Figure 3 shows a comparison of the constriction resistance computed from Eqs. (5) with those values computed numerically, for $\epsilon = 0.5$. The agreement is good.

References

Barber, J. R., 1989, "An Asymptotic Solution for Short-Time Transient Heat Conduction Between Two Similar Contacting Bodies," *Int. J. Heat Mass Transfer,* Vol. 32, pp. 943–949.

Beck, J. V., and Lloyd, J. R., 1988, "Transient Surface Temperatures in Solids Due to Small Heat Sources," *Cooling Technology for Electronic Equipment,* Win Aung, ed., Hemisphere, Washington, DC.

Fisher, N. J., and Yovanovich, M. M., 1989, "Thermal Constriction Resistance of Sphere/Layered Flat Contacts: Theory and Experiment," ASME JOURNAL OF HEAT TRANSFER, Vol. 111, pp. 249–256.

Greenwood, J. A., 1991, "Transient Thermal Contact Resistance," *Int. J. Heat Mass Transfer,* Vol. 34, pp. 2287–2290.

Negus, K. J., and Yovanovich, M. M., 1984a, "Constriction Resistance of Circular Flux Tubes With Mixed Boundary Conditions by Linear Superposition of Neumann Solutions," ASME Paper No. 84-HT-84.

Negus, K. J., and Yovanovich, M. M., 1984b, "Application of the Method of Optimized Images to Steady Three-Dimensional Conduction Problems," ASME Paper No. 84-WA/HT-110.

Negus, K. J., Yovanovich, M. M., and Beck, J. V., 1989, "On the Nondimensionalization of Constriction Resistance for Semi-infinite Heat Flux Tubes," ASME JOURNAL OF HEAT TRANSFER, Vol. 111, pp. 804–806.

Özişik, M. N., 1993, *Heat Conduction,* 2nd ed. Wiley, New York.

Sadhal, S. S., 1980, "Transient Thermal Response of Two Solids in Contact Over a Circular Disk," *Int. J. Heat Mass Transfer,* Vol. 23, pp. 731–733.

Thomsom, J. F., Warsi, Z., and Mastin, C., 1985, *Numerical Grid Generation: Foundations and Applications,* North Holland, New York.

Derivation of the Casimir Limit Phonon Distribution Using the Boltzmann Transport Equation

Y. Polsky[1] and Y. Bayazitoglu[2]

Nomenclature

C_v = specific heat per unit volume, $Jm^{-3}K^{-1}$
C_{il} = elastic stiffness constant, Jm^{-3}
e_{il} = elastic strain component
E = energy, J
f = phonon distribution
f^0 = phonon equilibrium distribution
F = force, N; free energy, J
$\hbar$ = Planck constant divided by 2π, Js
k_b = Boltzmann constant, JK^{-1}
K = phonon wave vector, m^{-1}
l = phonon mean free path, m
L = length of the crystal, m
N = number of atoms along length of the crystal
p = carrier momentum, $kgms^{-1}$
P = pressure, Nm^{-2}
$P(x)$ = probability function
q = heat flux, Wm^{-2}
R = the displacement of a deformation, m
s = specific entropy, $Jm^{-3}K^{-1}$
T = temperature, K
u = specific internal energy, Jm^{-3}
u', v', w' = displacements from the equilibrium position of an atom, m
U = elastic energy of a solid, J
v = phonon wave velocity, ms^{-1}
V = crystal volume element, m^3
Z = partition function, JK^{-1}

[1] Graduate Student, Mechanical Engineering and Material Science Department, Rice University, Houston, TX 77005.

[2] Professor, Mechanical Engineering and Material Science Department, Rice University, Houston, TX 77005.

Contributed by the Heat Transfer Division of THE AMERICAN SOCIETY OF MECHANICAL ENGINEERS. Manuscript received by the Heat Transfer Division May 1994; revision received August 1994. Keywords: Conduction. Associate Technical Editor: R. Viskanta.

λ = thermal conductivity, $Wm^{-1}K^{-1}$
ρ = density, kgm^{-3}
σ = Stefan–Boltzmann constant for phonons, $Wm^{-2}K^{-4}$
τ = relaxation time, s
ω = angular frequency, rad s^{-1}

Subscripts and Superscripts

i = tensor subscript
j = tensor subscript
x = component
0 = equilibrium

1 Introduction

The modes of energy transfer in solid thin films of electrically insulating material are lattice vibrations, which take the form of elastic waves. These energy waves are quantized and referred to as phonons. Phonon theory combines mechanics, statistics, thermodynamics, and quantum theory to provide an approximation for the energy transferred through a lattice due to disturbances in the equilibrium distances between atoms.

On the macroscale, the heat transfer can be modeled by Fourier's equation as

$$\bar{q} = -\lambda \nabla T, \tag{1}$$

where ∇T is the local temperature gradient. This model yields accurate results when the mean free path of the phonons is much smaller than the thickness of the film. This form of transport is referred to as conductive transport and is based on an approximation of scattering events and phonon–phonon interference occurring within the solid.

For nano/microscale thin films, there is an alternative model for the heat flux. It is commonly known as the Casimir limit and is based on an analogy of Planck's blackbody radiation theory. In this case the solid is considered to be an empty volume with radiating surfaces from which phonons propagate at a constant velocity equal to the velocity of sound in the material. The heat flux between the two ends of the material is given as

$$\bar{q} = \sigma(T_1^4 - T_2^4), \tag{2}$$

where T_1 and T_2 are the temperatures at the ends. This type of phonon transport is hereafter referred to as ballistic transport and is distinguished from conductive transport by the absence of phonon–phonon interference and scattering.

As the thickness of a film increases from the Casimir limit, we find that sources of thermal resistance such as scattering alter the rate of energy transfer. The heat flux in the x direction is given as (Ziman, 1960)

$$q_x = \int v_x f_\omega(x, t) \hbar\omega D(\omega) d\omega, \tag{3}$$

where $f_\omega(x, t)$ is the distribution of the excitation states of phonon modes, $D(\omega)d\omega$ is the density of states per unit frequency range, and $\hbar\omega$ is the quantal energy associated with a phonon. The scattering model differs from the no-scattering model (the Casimir limit) in its evaluation of the heat flux by the distribution function used to describe the phonon excitation level.

In the Casimir limit, f_ω is assumed to be the equilibrium distribution, which follows the Bose–Einstein statistics (Ziman, 1960):

$$f_\omega^0 = \frac{1}{e^{\hbar\omega/k_b T} - 1}. \tag{4}$$

This distribution is used to determine the energy density of the elastic energy waves that propagate between surfaces in the phonon radiation analogy, which is used to determine heat flux given by Eq. (2) (Kittel, 1968, Casimir, 1938).

In the derivation of Fourier's equation, the phonon distribution function is determined via the Boltzmann transport equation, which is given as (Prigogine, 1958)

$$\frac{\partial f_\omega}{\partial t} = \left.\frac{\partial f_\omega}{\partial t}\right|_{\text{gradients \& fields}} + \left.\frac{\partial f_\omega}{\partial t}\right|_{\text{scattering}}. \tag{5}$$

For transport in the x direction the gradient and field terms of the equation can be given by

$$\left.\frac{\partial f_\omega}{\partial t}\right|_{\text{gradients}} = \vec{v}\cdot\nabla f_\omega = v_x \frac{\partial f_\omega}{\partial x}, \tag{6a}$$

$$\left.\frac{\partial f_\omega}{\partial t}\right|_{\text{fields}} = \vec{F}\cdot\nabla_p f_\omega = F_x \frac{\partial f_\omega}{\partial p_x}. \tag{6b}$$

The second term on the right-hand side of Eq. (5), the scattering term, is given by the relaxation-time approximation as

$$\left.\frac{\partial f_\omega}{\partial t}\right|_{\text{scattering}} = \frac{f_\omega - f_\omega^0}{\tau}. \tag{6c}$$

Thus the Boltzmann transport equation in the x direction can be expressed in the form

$$\frac{\partial f_\omega}{\partial t} + v_x \frac{\partial f_\omega}{\partial x} + F_x \frac{\partial f_\omega}{\partial p_x} = \frac{f_\omega^0 - f_\omega}{\tau}. \tag{7}$$

At steady state, the Boltzmann transport equation becomes

$$v_x \frac{\partial f_\omega}{\partial x} + F_x \frac{\partial f_\omega}{\partial p_x} = \frac{f_\omega^0 - f_\omega}{\tau}. \tag{8}$$

The solution of this equation for the phonon distribution function can be substituted into Eq. (3). Integrating Eq. (3) and using the definition of thermal conductivity, $\lambda = \frac{1}{3} C_v v l$, yields Fourier's equation as given by Eq. (1).

Recent works in microscale heat transfer analysis focus on a variety of different features of the Boltzmann transport equation to modify nano/microscale discrepancies in the heat flux. Some of the earlier attempts at finding the phonon distribution incorporated basic elements of scattering due to point impurities, normal processes, umklapp processes, and boundary scattering to obtain a scattering term (Callaway, 1959). A mathematical analogy has been made between photon energy transfer, as described by the equation of radiative transfer, and phonon energy transfer to obtain a phonon distribution function, which gives the correct thick and thin limits of heat transfer when integrated using Eq. (3) (Majumdar, 1993). Some criteria for determining when Fourier's equation or when the Casimir limit applies have been laid down for use in nano/microscale analysis (Flik et al., 1992).

It will be shown that the Casimir limit phonon distribution can be derived by using the Boltzmann transport equation. This will require describing the energy transfer process within the solid in terms of both phonons and elastic waves. If the scattering term of Eq. (8) is neglected and the field term included, a description of phonons in terms of the elastic properties of the solid facilitates a derivation of the Casimir limit phonon distribution from the Boltzmann transport equation. The derivation presented in this paper helps to understand more clearly where Fourier's equation fails.

2 Analysis

Let us now focus attention on the use of the Boltzmann transport equation to derive the phonon distribution. In the absence of scattering and phonon–phonon interference, the distribution of phonons cannot be accurately obtained as the phonons do not follow the statistical behavior expected in the conduction

regime of the Boltzmann transport equation. When there is very little or no scattering, the time expected between collisions is practically infinite, and the phonon distribution is close to its equilibrium distribution.

For such a case, the gradient term of the Boltzmann transport equation should then equal zero. This implies that the phonon distribution as a function of position within the solid is constant and the heat flux is zero. In the case of ballistic transport, there is no scattering term and yet a heat flux does exist within the solid.

The subsequent derivation of the Casimir limit phonon distribution function by using the Boltzmann transport equation will provide a framework for determining why the distribution obtained in the derivation of Fourier's equation does not accurately model that which is expected for film thicknesses within the Casimir limit.

Using a continuum approximation for the lattice, where the wavelength is much greater than the lattice constant, it is possible to relate elastic properties of the lattice to heat transport phenomena. The utilization of this analysis will be confined to temperatures below the Debye temperature. In this description of the solid, the following assumptions are made: There is no thermal expansion, the adiabatic and isothermal elastic constants are equal, the elastic constants are independent of pressure and temperature, the heat capacity becomes constant at high temperatures, and a single waveform does not decay or change with time (Kittel, 1968). Such a crystal, which contains N atoms interacting according to Hooke's law, is equivalent to a system of 3N independent harmonic oscillators (Seitz, 1940). The interatomic forces between atoms in the crystal can then be viewed as springs that have Hookian properties. This study will limit itself to the elastic region where Hooke's law holds for the elastic constants of the material.

We can view a crystal as an array of atoms connected by springs. If we assume that the atoms are vibrating there will be changes in the spring forces exerted on the atoms. The variations of these forces can be described as induced strains in the solid. The displacement of deformation in a solid can be written as (Stevenson, 1966)

$$R = u'\hat{x} + v'\hat{y} + w'\hat{z}. \tag{9}$$

For a uniform strain these components of R can be specified by

$$u' = e_{xx}x + \tfrac{1}{2}e_{xy}y + \tfrac{1}{2}e_{zx}z, \quad v' = e_{yy}y + \tfrac{1}{2}e_{xy}x + \tfrac{1}{2}e_{yz}z,$$
$$w' = e_{zz}z + \tfrac{1}{2}e_{yz}y + \tfrac{1}{2}e_{zx}z. \tag{10}$$

To obtain the strains explicitly, the partial derivatives of Eq. (10) are taken to yield

$$e_{xx} = \frac{\partial u'}{\partial x}; \quad e_{yy} = \frac{\partial v'}{\partial y}; \quad e_{zz} = \frac{\partial w'}{\partial z}$$

$$e_{xy} = \frac{\partial v'}{\partial x} + \frac{\partial u'}{\partial y}; \; e_{yz} = \frac{\partial w'}{\partial y} + \frac{\partial v'}{\partial z}; \; e_{zx} = \frac{\partial u'}{\partial z} + \frac{\partial w'}{\partial x}. \tag{11}$$

The stress components describing these forces are defined as

$$X_x = C_{11}e_{xx} + C_{12}e_{yy} + C_{13}e_{zz} + C_{14}e_{yz} + C_{15}e_{zx} + C_{16}e_{xy},$$
$$Y_y = C_{21}e_{xx} + C_{22}e_{yy} + C_{23}e_{zz} + C_{24}e_{yz} + C_{25}e_{zx} + C_{26}e_{xy},$$
$$Z_z = C_{31}e_{xx} + C_{32}e_{yy} + C_{33}e_{zz} + C_{34}e_{yz} + C_{35}e_{zx} + C_{36}e_{xy},$$
$$Y_z = C_{41}e_{xx} + C_{42}e_{yy} + C_{43}e_{zz} + C_{44}e_{yz} + C_{45}e_{zx} + C_{46}e_{xy},$$
$$Z_x = C_{51}e_{xx} + C_{52}e_{yy} + C_{53}e_{zz} + C_{54}e_{yz} + C_{55}e_{zx} + C_{56}e_{xy},$$
$$X_y = C_{61}e_{xx} + C_{62}e_{yy} + C_{63}e_{zz} + C_{64}e_{yz} + C_{65}e_{zx} + C_{66}e_{xy}. \tag{12}$$

Therefore Newton's second law for a cubic element of volume in a crystal in the x direction is (Stevenson, 1966)

$$\rho \frac{\partial^2 u'}{\partial t^2} = \frac{\partial X_x}{\partial x} + \frac{\partial X_y}{\partial y} + \frac{\partial X_z}{\partial z}. \tag{13}$$

Using symmetry relations for the elastic stiffness constants this can be rewritten as

$$\rho \frac{\partial^2 u'}{\partial t^2} = C_{11}\frac{\partial e_{xx}}{\partial x} + C_{12}\left(\frac{\partial e_{yy}}{\partial x} + \frac{\partial e_{zz}}{\partial x}\right) + C_{44}\left(\frac{\partial e_{xy}}{\partial y} + \frac{\partial e_{xz}}{\partial z}\right), \tag{14}$$

where the x, y, and z directions are chosen to be parallel to the cube edges.

For a longitudinal wave propagating in the x direction with no shear components, the equation further reduces to

$$\rho \frac{\partial^2 u'}{\partial t^2} = C_{11}\frac{\partial e_{xx}}{\partial x}, \tag{15}$$

thus making the force on a volume element in the crystal

$$F_x = C_{11}\frac{\partial e_{xx}}{\partial x}V. \tag{16}$$

This force expression will be used in the field term of the Boltzmann transport equation to describe the force affecting the excitation state of a phonon in the mechanical description of a crystal's energy properties. The field term in the Boltzmann transport equation represents the influence of a force on the momentum and position of a group of particles. In its conventional usage, such as when an electron moving in a straight path passes through an electric field, it is easy to envision the effect of the field on the particle as the electron path bends. But phonons are not physical particles like electrons, and influences on their behavior are slightly more difficult to see. They can be analyzed with transport theory because the interactions of vibrating atoms can exhibit a net behavior, which can be statistically described in a manner similar to the behavior of a particle. As such, the presence of a temperature gradient acts like a force by changing interatomic potentials and causing the transfer of phonons.

Thus elastic deformations, which represent the influence of temperature on the vibrational energy of a solid, are the source of the elastic energy waves in a mechanically described solid and the excitations in the harmonic oscillator representation of phonons. It is important to note that in this description the interaction of elastic waves is not accounted for. Thus the heat flux process resembles that which is expected in ballistic transport.

It is necessary to look at the energy density of a solid in order to develop a relation between its elastic energy and the energy of a harmonic oscillator. When a solid undergoes a deformation in the x direction, the property relation of the first law of thermodynamics reduces to (Gurevich, 1986)

$$du = Tds + X_i de_{ij}, \quad i, j = x, y, z. \tag{17a}$$

In the case where there are no shear forces, with the use of Eq. (12) for an isentropic deformation process we have

$$du = C_{11}e_{xx}de_{xx}. \tag{17b}$$

Integrating this relation and multiplying by the energy of a solid volume V gives the elastic energy as

$$U = \tfrac{1}{2}C_{11}e_{xx}^2V. \tag{17c}$$

Equating this energy with the energy of the corresponding har-

monic oscillator (given as $E = f_\omega \hbar\omega$), yields an expression for the local distribution function, f_ω, given by

$$f_\omega = \frac{C_{11} e_{xx}^2 V}{2\hbar\omega}. \tag{18}$$

Equation (18), in conjunction with the force expression of Eq. (16), can be used to evaluate the field term of the Boltzmann transport equation given by Eq. (6*b*) as

$$F_x \frac{\partial f_\omega}{\partial p_x} = C_{11} \frac{\partial e_{xx}}{\partial x} V \frac{\partial}{\partial p_x} \left(\frac{C_{11} e_{xx}^2 V}{2\hbar\omega} \right)$$

$$= \frac{C_{11}^2 V^2}{2\hbar^2 v_x} \frac{\partial e_{xx}}{\partial x} \left(\frac{2 e_{xx}}{K_x} \frac{\partial e_{xx}}{\partial K_x} - \frac{e_{xx}^2}{K_x^2} \right), \tag{19}$$

following the substitutions $p_x = \hbar K_x$ and $\omega = v_x K_x$. Using Eq. (10) we see that for the case of a longitudinal wave with no shear forces $u' = e_{xx} x$. Taking the derivative of e_{xx} with respect to K_x and knowing that the solution to Eq. (15) is $u' = u_0' e^{i(K_x x - \omega t)}$ we obtain

$$\frac{\partial e_{xx}}{\partial K_x} = i u' = \frac{e_{xx}}{K_x}, \tag{20}$$

where $e_{xx} = \partial u'/\partial x = i K_x u'$.

Upon substitution of this expression for the rate of change of strain with respect to wavenumber in Eq. (19), the expression for the field term is given by

$$F_x \frac{\partial f_\omega}{\partial p_x} = \frac{C_{11}^2 e_{xx}^2 V^2}{2\hbar^2 \omega K_x} \frac{\partial e_{xx}}{\partial x} \tag{21}$$

Using the Boltzmann transport equation, the distribution function for nonconductive transport can now be found by relating the mechanical and phonon descriptions of the elastic energy waves propagating through a solid as expressed in the previous section. For the condition of no scattering and phonon–phonon interference the $\partial f/\partial t|_{\text{scattering}}$ term equals zero. Therefore the Boltzmann transport equation given by Eq. (8) in conjunction with Eq. (21) becomes

$$v_x \frac{\partial f_\omega}{\partial x} + \frac{C_{11}^2 e_{xx}^2 V^2}{2\hbar^2 \omega K_x} \frac{\partial e_{xx}}{\partial x} = 0. \tag{22}$$

Changing variables in the gradient term and canceling the $\partial e_{xx}/\partial x$ terms enables us to rewrite the expression as

$$v_x \frac{\partial f_\omega}{\partial e_{xx}} + \frac{C_{11}^2 e_{xx}^2 V^2}{2\hbar^2 \omega K_x} = 0. \tag{23}$$

Differentiating Eq. (18), the phonon distribution, with respect to the strain gives

$$\frac{\partial f_\omega}{\partial e_{xx}} = \frac{C_{11} e_{xx} V}{\hbar\omega}. \tag{24}$$

The Boltzmann transport equation given by Eq. (23) can then be reduced by using Eq. (24) to

$$v_x \frac{C_{11} e_{xx} V}{\hbar\omega} + \frac{C_{11}^2 e_{xx}^2 V^2}{2\hbar^2 \omega K_x} = 0. \tag{25}$$

Eliminating terms in the equation, using $\omega = v_x K_x$ and a substitution for f_ω obtainable from Eq. (18) reduces Eq. (25) to

$$f_\omega = -e_{xx}. \tag{26}$$

A thermodynamic expression for the strain can be found by treating the lattice as an empty volume filled with a phonon gas. By relating the first law of thermodynamics to thermodynamic pressure relations it is possible to relate the elastic strain of a solid to its temperature. We begin with the establishment of the partition function for a harmonic oscillator. We know that the energy of an oscillator is given as $E = f_\omega \hbar\omega$. For this study $f = 0$ will be used as the zero point energy. The partition function for the system is given as

$$Z = \sum_j e^{-E_j/k_b T}, \tag{27a}$$

where j values represent the energy states for which the number of particles in the system is constant. It can be simplified to (Kittel, 1969)

$$Z = \frac{1}{(1 - e^{-\hbar\omega/k_b T})}. \tag{27b}$$

Knowing the partition function, we can determine the free energy F of a system by the relation $F = -k_b T \ln Z$ (Kittel, 1969). The pressure P can then be determined from

$$P = -\left(\frac{\partial F}{\partial V} \right)_T = -\hbar \frac{d\omega/dV}{e^{\hbar\omega/k_b T} - 1}. \tag{28}$$

We know that for a crystal with a constant velocity of sound, the values of K_x that are allowed by the Born–Von Karman boundary condition are $K_x = \pm N\pi/L$ (Kittel, 1968). The angular frequency can then be given as

$$\omega = v_x K_x = \pm \frac{v_x N\pi}{L}. \tag{29}$$

For a longitudinal wave in the x direction, the frequency change with volume, $V = L^3$ is

$$\frac{\partial \omega}{\partial V} = \frac{v_x N\pi}{3V^{4/3}} = \frac{\omega}{3V}. \tag{30}$$

Substitution of Eq. (30) into Eq. (28) gives the pressure of the phonon gas as

$$P = -\frac{\hbar\omega}{3V} \frac{1}{(e^{\hbar\omega/k_b T} - 1)}. \tag{31}$$

Assuming that the stress experienced by the lattice is equivalent to the pressure exerted by a phonon gas, it is possible to obtain an expression for the strain via the equation $P = X_x = C_{11} e_{xx}$. The resultant expression for strain is

$$e_{xx} = -\frac{\hbar\omega}{3C_{11}V} \frac{1}{(e^{\hbar\omega/k_b T} - 1)}. \tag{32}$$

Using the dispersion relation for phonon wave number, the elastic stiffness constant is found to be $C_{11} = \rho v_x^2 = \rho v^2/3$ (Stevenson, 1966), assuming that the velocity of the wave is independent of the direction of propagation. The momentum of a phonon is given by $\hbar K_x$. Equating this momentum with that associated with the movement of a lattice or unit cell in a crystal yields the relation $\hbar K = \rho V v$. The substitution of this relation with Eq. (32) finally reduces the Boltzmann transport equation given by Eq. (26) to

$$f_\omega = \frac{1}{e^{\hbar\omega/k_b T} - 1}. \tag{33}$$

This is the Bose–Einstein distribution and shows that the Casimir limit phonon distribution can be derived using the Boltzmann transport equation.

3 Conclusion

The analysis of this paper shows that by relating the mechanically described elastic energy density of a solid to its phonon description, it is possible to obtain the phonon equilibrium distribution function. The elastic representation of a solid provides a perspective for describing how the phonon distribution function is affected by temperature and indicates why the linearized

Boltzmann transport equation used to derive Fourier's equation fails for nano/microscale heat transport phenomena. An incorporation of the field term into the Boltzmann transport equation with scattering term would be the next logical step for future study of nano/microscale analysis. Additionally, for materials whose structure is not as orderly as a crystal, such as amorphous semiconductors, perhaps the elastic description can be used to solve the phonon-based equations used to approximate quantities such as the heat flux.

Acknowledgments

This material is based in part upon work supported by the Texas Advanced Technology Program under Grants No. 003604-027 and 003604-041.

References

Callaway, J., 1959, "Model of Lattice Thermal Conductivity at Low Temperatures," *Physical Review,* Vol. 113, pp. 1046–1051.

Casimir, H. B. G., 1938, "Note on the Conduction of Heat in Crystals," *Physica,* Vol. 5, No. 6, pp. 495–500.

Flik, M. I., Choi, B. I., and Goodson, K. E., 1992, "Heat Transfer Regimes in Microstructures," ASME JOURNAL OF HEAT TRANSFER, Vol. 114, pp. 666–674.

Gurevich, V. L., 1986, *Transport in Phonon Systems,* Elsevier Science Publishers, Amsterdam, Chap. 1.

Kittel, C., 1968, *Introduction to Solid State Physics,* Wiley, New York, Chaps. 4 and 5.

Kittel, C., 1969, *Thermal Physics,* Wiley, New York, pp. 90–100, 298–300.

Klitsner, T., Van Cleve, J. E., Fischer, H. E., and Pohl, R. O., 1988, "Phonon Radiative Heat Transfer and Surface Scattering," *Physical Review B,* Vol. 38, pp. 7576–7594.

Majumdar, A., 1993, "Microscale Heat Conduction in Dielectric Thin Films," ASME JOURNAL OF HEAT TRANSFER, Vol. 115, No. 7, pp. 7–16.

Prigogine, I., 1958, *Proceedings on the International Symposium on Transport Processes in Statistical Mechanics,* Interscience Publishers, Inc., New York, pp. 1–7, 138, 194.

Seitz, F., 1940, *Modern Theory of Solids,* McGraw-Hill, New York, Chap. 3.

Stevenson, R. W. H., 1966, *Phonons in Perfect Lattices and in Lattices With Point Imperfections,* Plenum Press, New York, Chaps. 1 and 2.

Ziman, J. M., 1960, *Electrons and Phonons,* Clarendon Press, Oxford, United Kingdom, Chaps. 1 and 11.

Heat Conduction Through a Barrier Made of a Suspension of Disklike Particles

P. Furmanski[1] and J. M. Floryan[2]

1 Introduction

In the previous paper (Furmanski and Floryan, 1994) we considered a thermal barrier of a finite thickness made of rodlike particles randomly distributed in a suitable carrier fluid. The variations in the range of heat flux control as a function of the orientation of the particles, their aspect ratio, volume fraction, and size, and on the combination of thermal conductivities of the particles and the carrier fluid, were investigated. It was shown that increases in the heat transfer by up to several hundred times (as compared to the case of pure fluid) were possible. The decreases of the heat flux were very small and of no practical importance. The barrier may be considered as representing a "smart" material for the purposes of heat transfer control.

The main purpose of the present analysis is to investigate how the range of heat flux control can be changed by selecting particles of other geometric forms. Disklike particles that can be idealized as oblate spheroids were selected for this purpose. Milton (1981) and Bergman (1982) used particles of such a shape in determining bounds on conductivities of anisotropic, two-component composites. Hatta and Taya (1986a,b) utilized similar particles in calculating thermal conductivity of three-component composites reinforced either with aluminum flakes or with coated disks. Lu and Kim (1990) considered interactions between pairs of oblate spheroidal inclusions. Last, Smereka and Milton (1991) assumed disklike shape of bubbles in their study of nonviscous bubbly flows. In all these cases the medium was considered to be unbounded.

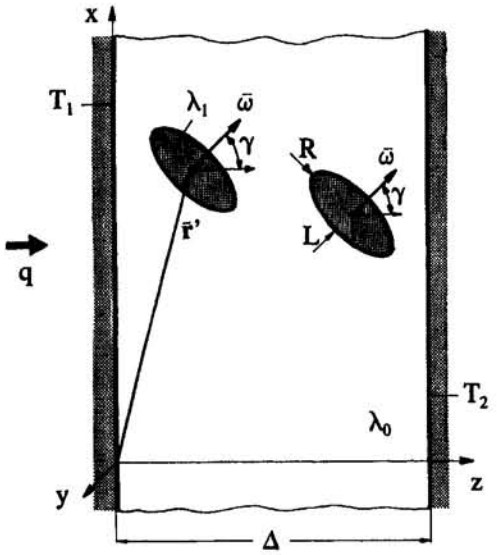

Fig. 1 Schematic diagram of the thermal barrier

2 Mathematical Model of a Thermal Barrier

Let us consider a barrier made of a layer of suspension of thickness Δ (in the z direction) and extending to infinity in the remaining two directions (Fig. 1). The suspension consists of a small volume fraction of particles of the oblate spheroidal shape randomly distributed in a carrier fluid. The size and the shape of the particles are characterized by their length L and radius R so that the particle aspect ratio $\epsilon = L/(2R)$ is smaller than unity. All particles have the same orientation $\bar{\omega}$ defined by angle γ. The angle γ is formed between the particle axis of symmetry and the positive direction of the coordinate axis z perpendicular to the walls. Every particle has thermal conductivity λ_1, while the fluid has thermal conductivity λ_0. Both conductivities are assumed to be independent of temperature. Constant temperatures ($T_1 > T_2$) are applied to the opposite walls of the barrier, resulting in a steady heat flux. Heat conduction in such a barrier can be described using effective medium theory formulated by Furmanski and Floryan (1994). Adaptation of this theory to the oblate spheroidal particles of interest here is described by Furmanski and Floryan (1993).

3 Distribution of the Volume Fraction of the Particles

The local volume fraction $v(z)$ of the particles changes across the barrier. These changes result from geometric constraints

[1] Visiting Professor, Department of Mechanical Engineering, The University of Western Ontario, London, Ontario, Canada N6A 5B9; permanent address: Institute of Heat Engineering, Warsaw University of Technology, ul. Nowowiejska 25, 00-665, Warsaw, Poland.

[2] Professor, Department of Mechanical Engineering, The University of Western Ontario, London, Ontario, Canada N6A 5B9.

Contributed by the Heat Transfer Division of THE AMERICAN SOCIETY OF MECHANICAL ENGINEERS. Manuscript received by the Heat Transfer Division January 1994; revision received September 1994. Keywords: Conduction, Microgravity Heat Transfer. Associate Technical Editor: L. S. Fletcher.

Boltzmann transport equation used to derive Fourier's equation fails for nano/microscale heat transport phenomena. An incorporation of the field term into the Boltzmann transport equation with scattering term would be the next logical step for future study of nano/microscale analysis. Additionally, for materials whose structure is not as orderly as a crystal, such as amorphous semiconductors, perhaps the elastic description can be used to solve the phonon-based equations used to approximate quantities such as the heat flux.

Acknowledgments

This material is based in part upon work supported by the Texas Advanced Technology Program under Grants No. 003604-027 and 003604-041.

References

Callaway, J., 1959, "Model of Lattice Thermal Conductivity at Low Temperatures," *Physical Review,* Vol. 113, pp. 1046–1051.

Casimir, H. B. G., 1938, "Note on the Conduction of Heat in Crystals," *Physica,* Vol. 5, No. 6, pp. 495–500.

Flik, M. I., Choi, B. I., and Goodson, K. E., 1992, "Heat Transfer Regimes in Microstructures," ASME JOURNAL OF HEAT TRANSFER, Vol. 114, pp. 666–674.

Gurevich, V. L., 1986, *Transport in Phonon Systems,* Elsevier Science Publishers, Amsterdam, Chap. 1.

Kittel, C., 1968, *Introduction to Solid State Physics,* Wiley, New York, Chaps. 4 and 5.

Kittel, C., 1969, *Thermal Physics,* Wiley, New York, pp. 90–100, 298–300.

Klitsner, T., Van Cleve, J. E., Fischer, H. E., and Pohl, R. O., 1988, "Phonon Radiative Heat Transfer and Surface Scattering," *Physical Review B,* Vol. 38, pp. 7576–7594.

Majumdar, A., 1993, "Microscale Heat Conduction in Dielectric Thin Films," ASME JOURNAL OF HEAT TRANSFER, Vol. 115, No. 7, pp. 7–16.

Prigogine, I., 1958, *Proceedings on the International Symposium on Transport Processes in Statistical Mechanics,* Interscience Publishers, Inc., New York, pp. 1–7, 138, 194.

Seitz, F., 1940, *Modern Theory of Solids,* McGraw-Hill, New York, Chap. 3.

Stevenson, R. W. H., 1966, *Phonons in Perfect Lattices and in Lattices With Point Imperfections,* Plenum Press, New York, Chaps. 1 and 2.

Ziman, J. M., 1960, *Electrons and Phonons,* Clarendon Press, Oxford, United Kingdom, Chaps. 1 and 11.

Heat Conduction Through a Barrier Made of a Suspension of Disklike Particles

P. Furmanski[1] and J. M. Floryan[2]

1 Introduction

In the previous paper (Furmanski and Floryan, 1994) we considered a thermal barrier of a finite thickness made of rodlike particles randomly distributed in a suitable carrier fluid. The variations in the range of heat flux control as a function of the orientation of the particles, their aspect ratio, volume fraction, and size, and on the combination of thermal conductivities of the particles and the carrier fluid, were investigated. It was shown that increases in the heat transfer by up to several hundred times (as compared to the case of pure fluid) were possible. The decreases of the heat flux were very small and of no practical importance. The barrier may be considered as representing a "smart" material for the purposes of heat transfer control.

The main purpose of the present analysis is to investigate how the range of heat flux control can be changed by selecting particles of other geometric forms. Disklike particles that can be idealized as oblate spheroids were selected for this purpose. Milton (1981) and Bergman (1982) used particles of such a shape in determining bounds on conductivities of anisotropic, two-component composites. Hatta and Taya (1986a,b) utilized similar particles in calculating thermal conductivity of three-component composites reinforced either with aluminum flakes or with coated disks. Lu and Kim (1990) considered interactions between pairs of oblate spheroidal inclusions. Last, Smereka and Milton (1991) assumed disklike shape of bubbles in their study of nonviscous bubbly flows. In all these cases the medium was considered to be unbounded.

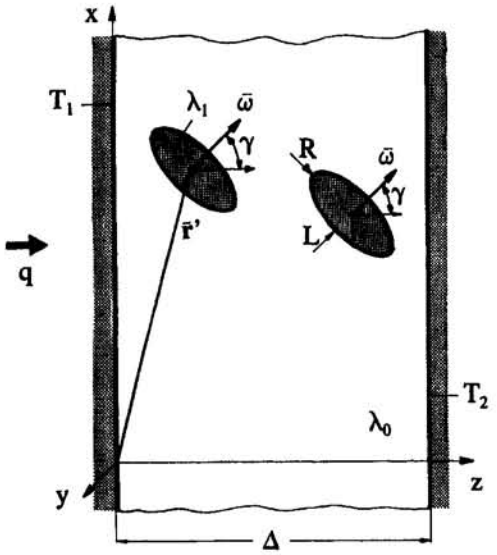

Fig. 1 Schematic diagram of the thermal barrier

2 Mathematical Model of a Thermal Barrier

Let us consider a barrier made of a layer of suspension of thickness Δ (in the z direction) and extending to infinity in the remaining two directions (Fig. 1). The suspension consists of a small volume fraction of particles of the oblate spheroidal shape randomly distributed in a carrier fluid. The size and the shape of the particles are characterized by their length L and radius R so that the particle aspect ratio $\epsilon = L/(2R)$ is smaller than unity. All particles have the same orientation $\bar{\omega}$ defined by angle γ. The angle γ is formed between the particle axis of symmetry and the positive direction of the coordinate axis z perpendicular to the walls. Every particle has thermal conductivity λ_1, while the fluid has thermal conductivity λ_0. Both conductivities are assumed to be independent of temperature. Constant temperatures ($T_1 > T_2$) are applied to the opposite walls of the barrier, resulting in a steady heat flux. Heat conduction in such a barrier can be described using effective medium theory formulated by Furmanski and Floryan (1994). Adaptation of this theory to the oblate spheroidal particles of interest here is described by Furmanski and Floryan (1993).

3 Distribution of the Volume Fraction of the Particles

The local volume fraction $v(z)$ of the particles changes across the barrier. These changes result from geometric constraints

[1] Visiting Professor, Department of Mechanical Engineering, The University of Western Ontario, London, Ontario, Canada N6A 5B9; permanent address: Institute of Heat Engineering, Warsaw University of Technology, ul. Nowowiejska 25, 00-665, Warsaw, Poland.

[2] Professor, Department of Mechanical Engineering, The University of Western Ontario, London, Ontario, Canada N6A 5B9.

Contributed by the Heat Transfer Division of THE AMERICAN SOCIETY OF MECHANICAL ENGINEERS. Manuscript received by the Heat Transfer Division January 1994; revision received September 1994. Keywords: Conduction, Microgravity Heat Transfer. Associate Technical Editor: L. S. Fletcher.

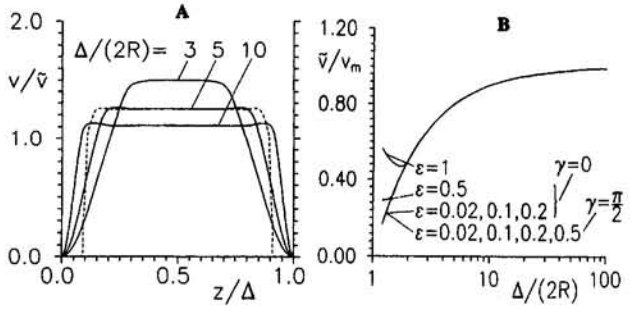

Fig. 2 Local volume fraction $v(z)$ of the particles: (*A*) distribution of $v(z)$ across the barrier for different orientation γ of the particles: —— $\gamma = \pi/2$, --- — $\gamma = 0$; (*B*) relation between the maximum v_m and the average $\tilde{v}$ volume fractions

imposed by the walls on the possible locations of the particles, and from the assumption of a constant average volume fraction $\tilde{v}$ of the particles in the barrier. A typical form of $v(z)$ is plotted in Fig. 2(*a*) as a function of the ratio of the barrier thickness Δ to the particle diameter $2R$ for two extreme particle orientations ($\gamma = 0$ and $\gamma = \pi/2$). This distribution consists of two "wall layers" and a core zone. In the core zone $v(z)$ is constant and greater than $\tilde{v}$, while in the "wall layers" $v(z)$ rapidly decreases and reaches zero at the wall. When $\Delta/(2R)$ increases, the "wall layer" becomes narrower (it is roughly equal to the particle diameter) while the maximum value of the volume fraction v_m in the core zone decreases. When the particles are oriented in such a way that their axes of symmetry are perpendicular to the walls, a layer of pure fluid separates them from the walls and the volume fraction $v(z)$ falls to zero before reaching the wall.

The maximum value of the volume fraction of the particles in the middle of the barrier cannot exceed certain limits. First, it cannot violate the assumption of small volume fraction of the particles that has been made in the analysis and, second, it cannot exceed the maximum packing limit for unidirectionally aligned equal-sized spheroids whose centers are located at the grid points of a periodic array made of the face-centered cubic cells. Due to the assumed distribution of the centers of the particles, there exists a strict relation between the maximum volume fraction v_m and the average volume fraction $\tilde{v}$. This relation is plotted in Fig. 2(*b*) as a function of the ratio $\Delta/(2R)$. If the maximum acceptable value v_m of the volume fraction is known, this diagram permits estimation of the greatest average volume fraction $\tilde{v}$ that can be used in the calculations for a given value of $\Delta/(2R)$. Conversely, if the average volume fraction of the particles $\tilde{v}$ is known, then the diagram permits determination of the lowest acceptable ratio of the barrier thickness to the particle diameter.

4 Distribution of the Effective Thermal Conductivity

Distribution of the effective thermal conductivity $\lambda_{ef}^{\perp}$ across the barrier is determined by the character of the particle distribution in the carrier fluid. Typical distributions shown in Fig. 3 consist of two wall layers and a core zone. In the core zone the effective thermal conductivity is constant and its value is higher (lower) than the value at the walls when $\lambda_1/\lambda_0 > 1$ ($\lambda_1/\lambda_0 < 1$). The width of the core zone increases when the particle diameter decreases ($\Delta/(2R)$ increases). The width of the wall layer is of the order of particle diameter. When the particle axis of symmetry is perpendicular to the wall ($\gamma = 0$), a layer of pure fluid separates particles from the wall, resulting in the effective thermal conductivity reaching the value of λ_0 already at a certain distance away from the wall (Fig. 3*c*). The thickness of the layer of pure fluid is equal to $(R - L/2)$.

5 Temperature Distribution

The form of the temperature distribution across the barrier can be easily calculated for the known variations of the effective thermal conductivity $\lambda_{ef}^{\perp}$ (Furmanski and Floryan, 1994). Here the temperature is understood to be the ensemble average $\{T(z)\}$ taken over all acceptable configurations of the particles. The temperature profile has a complicated form due to variations of $\lambda_{ef}^{\perp}$. In the core zone, where $\lambda_{ef}^{\perp}$ is constant, temperature varies linearly, while in the wall layers it changes very rapidly due to variations of $\lambda_{ef}^{\perp}$ (see Figs. 3*b*,*d*). A decrease of the diameter of the particles (increase of $\Delta/(2R)$) results in an increase of the size of the core zone and more rapid temperature variations in the wall layers. For high, though not extreme, values of $\Delta/(2R)$ the linear temperature profile inside the barrier is usually extrapolated to the wall resulting in an apparent "temperature slip" (Melanson and Dixon, 1985).

6 Discussion of Results

The heat flow through the barrier is strongly influenced by both the structure and the thermal properties of the components, as has already been shown in the case of rodlike particles (Furmanski and Floryan, 1994). The main factor from the point of view of controlling the heat flow is the orientation of the particles. The maximum change occurs by rotating the particles by 90° from their axis of symmetry being perpendicular to the walls, $\gamma = 0$, to being parallel to the walls, $\gamma = \pi/2$. This leads to an increase of the heat flux by about 30 times in the representative case of particles of aspect ratio $\epsilon = 0.02$ (Fig. 4*a*). The heat flow variation is fairly uniformly distributed over the whole interval $0 \le \gamma \le \pi/2$ (Fig. 4*a*) and thus, a small misalignment of the particles around both extreme positions does not appreciably affect the available heat flux control range.

The range of heat flux control depends on the particle aspect ratio ϵ. When the disklike particles become flatter (ϵ decreases),

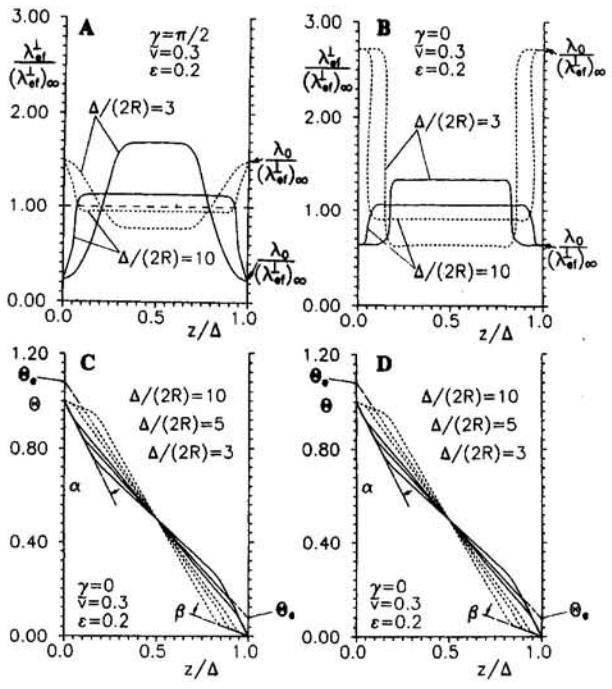

Fig. 3 Distribution of (*A*, *B*) the effective thermal conductivity $\lambda_{ef}^{\perp}/(\lambda_{ef}^{\perp})_{\infty}$ and (*C*, *D*) the temperature $\theta = (\{T\} - T_2)/(T_1 - T_2)$ for the particles axes of symmetry being parallel to the walls ($\gamma = \pi/2$) and perpendicular to the walls ($\gamma = 0$), respectively. $\lambda_{ef}^{\perp}$ = local effective thermal conductivity, $(\lambda_{ef}^{\perp})_{\infty}$ = effective thermal conductivity for infinite medium, α = ctg $[(\lambda_{ef}^{\perp})_{\infty}/\lambda_0]$, β = , $[(\lambda_{ef}^{\perp})_{\infty}/\lambda_0]$, θ_e = temperature at the wall extrapolated from linear temperature distribution inside the barrier, —— $\lambda_1/\lambda_0 \to \infty$, --- — $\lambda_1/\lambda_0 = 0$.

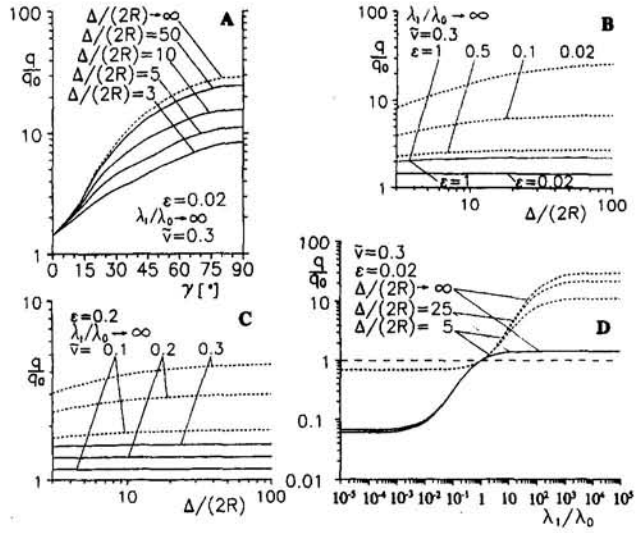

Fig. 4 Variation of the heat flux q/q_0 (*A*) as a function of the particle orientation angle γ, as a function of $\Delta/(2R)$ for (*B*) various particle aspect ratios ϵ and (*C*) various particle average volume fractions $\tilde{v}$ (—— $\gamma = 0$, --- $\gamma = \pi/2$, ··· $\epsilon = 1$; note that q/q_0 for $\epsilon = 1$ is the same for both $\gamma = 0$ and $\gamma = \pi/2$), and (*D*) as a function of the particle relative conductivity λ_1/λ_0 (—— $\gamma = 0$, --- $\gamma = \pi/2$). Particle axes are assumed to be parallel to each other.

the heat flow increases for the particles whose axes of symmetry are perpendicular to the walls, $\gamma = \pi/2$, and decreases for the axis parallel to the walls, $\gamma = 0$ (Fig. 4*b*). This happens regardless of whether the thermal conductivity of the particles is larger or smaller than the thermal conductivity of the carrier fluid. The magnitude of the increase for $\gamma = \pi/2$ is bigger than the magnitude of the decrease for $\gamma = 0$.

The average volume fraction of the particles $\tilde{v}$ also significantly influences the heat flow through the barrier (Fig. 4*b*). As expected, an increase of $\tilde{v}$ leads to a growth of the heat flow for the thermal conductivity of the particles higher than the thermal conductivity of the fluid ($\lambda_1/\lambda_0 > 1$) and leads to a decrease for $\lambda_1/\lambda_0 < 1$.

The thickness of the barrier as compared to the particle diameter $\Delta/(2R)$ plays an important role in controlling the heat flux only when the particles have their axes of symmetry parallel to the walls (Fig. 4*a*) and when thermal conductivity of the particles is greater than the conductivity of the carrier fluid (Figs. 4*b–d*). In all other cases the wall effects can be considered negligible (Fig. 4*d*).

Figure 4(*d*) shows how the ratio of thermal conductivities of the suspension components affects the heat flow. Both, an increase ($\lambda_1/\lambda_0 > 1$) and a decrease ($\lambda_1/\lambda_0 < 1$) of the thermal conductivity of the particles relative to the conductivity of the carrier fluid offer equal opportunity for the control of the heat flux. The heat flow in the case of particles with axes of symmetry perpendicular to the wall ($\gamma = 0$) is always smaller than in the case of the axes being parallel to the wall ($\gamma = \pi/2$).

Comparison of the results presented in this paper for the disklike particles with our previous results for the rodlike particles (Furmanski and Floryan, 1994) permits assessment of the effects of change of the class of shapes of the particles on the heat flow across the barrier. For the rodlike particles the change in the heat flux due to rotation of the particles was practically negligible when the conductivity of the particles was smaller than the conductivity of the carrier fluid. For particle conductivity higher than that of the carrier fluid, heat flux could be changed by up to several hundred times (depending on the particle aspect ratio ϵ). Only an increase of the heat flux as compared to the case of pure fluid was possible. For the case of disklike particles both an increase (for $\lambda_1/\lambda_0 > 1$) and a decrease (for $\lambda_1/\lambda_0 < 1$) of the heat flow as compared to the case of pure fluid are possible. The heat flux can be changed through rotation of the particles by only a factor of up to 30 (compare with several hundred times for the rodlike particles with a corresponding aspect ratio).

One may conclude that classes of shapes of the particles have a very strong effect on the magnitude of the heat flux. This magnitude can be either increased or decreased by a judicious selection of a particular class of geometries. Results for the particle shapes studied so far suggest that it is much easier to increase the heat flux significantly as compared to the case of pure fluid rather than reduce it.

7 Summary

A thermal barrier made of disklike particles suspended in a carrier fluid has been considered. The heat flux control is achieved by changing orientation of the particles. The maximum change in the heat flux is obtained by rotating the particles by 90° from their axes of symmetry being perpendicular to the walls to being parallel to the walls. This results in a heat flux increase by up to 30 times for the particle aspect ratio of practical interest. The increase is not too sensitive to small misalignments of the particles around both extreme positions. An increase in the range of heat flux control is achieved by increasing the average volume fraction of the particles, their aspect ratio (flatter particles), and by using carrier fluid and particles of widely different thermal conductivities. The range of heat flux control using disklike particles is smaller by an order of magnitude than the one obtained with the corresponding rodlike particles studied previously (Furmanski and Floryan, 1994). However, unlike the rodlike particles, the disklike particles offer a possibility for both an increase and a decrease of the heat flux as compared to the case of pure fluid.

Acknowledgments

The authors would like to acknowledge support for this work received form the NSERC of Canada and the KBN of Poland (Grant No 3-1003-91-01).

References

Bergman, D. J., 1982, "Rigorous Bounds for the Complex Dielectric Constant of a Two-Component Composite," *Annalen der Physik,* Vol. 138, p. 78.

Furmanski, P., and Floryan, J. M., 1993, "Heat Conduction Through a Suspension of Disk-Like Particles," Report ESFD-8/93, Department of Mechanical Engineering, The University of Western Ontario, London, Ontario, Canada, N6A 5B9.

Furmanski, P., and Floryan, J. M. 1994, "A Thermal Barrier With Adaptive Heat Transfer Characteristics," ASME JOURNAL OF HEAT TRANSFER, Vol. 116, pp. 302–310.

Hatta, H., and Taya, M., 1986a, "Equivalent Inclusion Method for Steady State Heat Conduction in Composites," *International Journal of Engineering Science,* Vol. 24, pp. 1159–1172.

Hatta, H., and Taya, M., 1986b, "Thermal Conductivity of Coated Filler Composites," *Journal of Applied Physics,* Vol. 59, pp. 1851–1860.

Melanson, M. M., and Dixon, A. G., 1985, "Solid Conduction in Low d_t/d_p Beds of Spheres, Pellets and Rings," *Int. J. Heat Mass Transfer,* Vol. 28, pp. 383–394.

Milton, G., 1981, "Bounds on the Complex Permittivity of a Two Component Composite Material," *Journal of Applied Physics,* Vol. 52, pp. 52–86.

Lu, S.-Y., and Kim, S., 1990, "Effective Thermal Conductivity of Composites Containing Spheroidal Inclusions," *AIChE Journal,* Vol. 36, pp. 927–938.

Smereka, P., and Milton, G. W., 1991, "Bubbly Flow and its Relation to Conduction in Composites," *Journal of Fluid Mechanics,* Vol. 233, pp. 65–81.

Mean Free Path and Apparent Thermal Conductivity of a Gas in a Porous Medium

S. Q. Zeng,[1,2] A. Hunt,[1] and R. Greif[2]

Introduction

Consider a system consisting of two parallel plates at different temperatures (Fig. 1*a*). To reduce the heat transfer, one can place a solid network; e.g., a matrix or lattice, in the system (Fig. 1*b*). The matrix partitions the space into very fine open pores. As a result, the motion of the gas molecules is restricted and the heat transfer is reduced. Silica aerogel is a porous medium, which has pore sizes of about 10 nm (Zeng et al., 1994), which is smaller than the mean free path of gas molecules at atmospheric pressure (about 80 nm) in a free space. Hence, even at atmospheric pressure the matrix restricts the motion of the gas molecules; the effect is more pronounced at lower pressures.

A formula for the apparent thermal conductivity of a gas in two parallel plates was given by Kaganer (1969); namely

$$\lambda_{g_0} = \lambda_g^0 \Big/ \left(1 + 2\,\frac{2\gamma}{\gamma+1}\,\frac{1}{\mathrm{Pr}}\,\frac{2-\alpha}{\alpha}\,\frac{l_{ch}}{l_m}\right) \tag{1}$$

where α is the accommodation coefficient, Pr is the Prandtl number, $\gamma = c_p/c_v$, l_{ch} is the distance between heat exchanging surfaces, l_m is the mean free path of gas molecules, λ_g^0 can be expressed as (Loeb, 1934)

$$\lambda_g^0 = (2.25\gamma - 1.25)0.461(p/k_BT)(8k_BT/\pi m_g)^{1/2} l_m (C_v/N_A) \tag{2}$$

where p is the gas pressure (atm), T is the temperature (K), m_g and d_g are the mass (kg) and the diameter (m) of the gas molecules, respectively.

The mean free path of gas molecules in free space is

$$l_{m_0} = k_BT/\sqrt{2}\pi d_g^2 p, \tag{3}$$

The mean free path of gas molecules in a porous medium (Fig. 1*b*) has not been formulated.

In this study, we derive an equation for the mean free path and an equation for the apparent thermal conductivity of a gas in a porous medium. These equations are used to calculate the apparent thermal conductivity of a gas in aerogel and comparison is made with experimental results.

Mean Free Path and Specific Surface Area

The mean free path is defined as the mean distance traveled by molecules between successive collisions with each other or with a matrix. Let f be the frequency of collisions experienced by a molecule; $1/f$ is the average time between collisions. If the mean speed is u, the mean free path is $l_m = u/f$. The molecules move with a mean speed u in a random manner, as often in one direction as in another. When a molecule collides with the matrix, its center is a distance $d_g/2$ away from the surface of the matrix. When two molecules collide, the minimum distance between the centers of the two molecules is d_g. If attention is fixed on the center of a molecule (say center A), center A cannot occupy a distance $d_g/2$ from the surface of the matrix and also cannot occupy a distance d_g from the centers of other molecules. The region that cannot be occupied by the center A is defined as the volume of exclusion, V_{ex}, which is expressed as

$$V_{ex} = V(1-\Pi)(1 + d_g/\bar{d}_s)^3 + n_g\pi d_g^3/6 \tag{4}$$

where n_g is the number of gas molecules and $\bar{d}_s$ is the average diameter of the solid particles that are assumed to constitute the matrix. The subscripts s and g stand for the solid matrix and gas, respectively. We define a surface of exclusion, S_{ex}, which is the surface of the volume of exclusion and consists of the surface that is $d_g/2$ away from the matrix and each molecule:

$$S_{ex} = S_s m_s (1 + d_g/\bar{d}_s)^2 + n_g 4\pi d_g^2. \tag{5}$$

Here S_s, the specific surface area (m^2/g), is defined as the surface area per unit mass of the solid matrix, which can be determined from the gas adsorption–desorption method (Gregg and Sing, 1982), m_s is the mass of the solid matrix. Usually, $d_g \ll \bar{d}_s$, so that Eqs. (4) and (5) become

$$V_{ex} = V(1-\Pi) + \pi d_g^3 n_g/6 \tag{6a}$$

$$S_{ex} = S_s m_s + n_g 4\pi d_g^2 \tag{6b}$$

The surface of exclusion S_{ex} bounds the regions where the centers of molecules can be present; the collisions of gas molecules can be studied by considering the collisions with the sur-

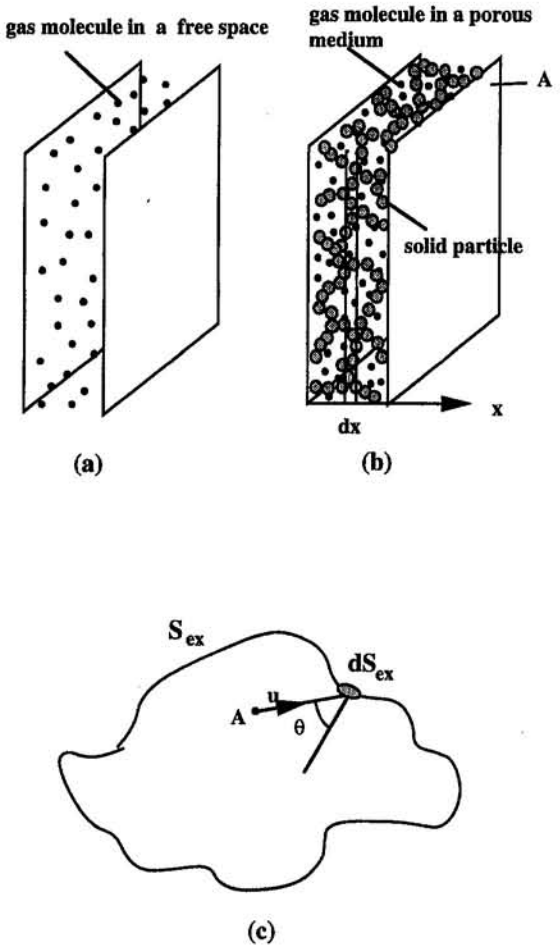

Fig. 1 (*a*) System consisting of two parallel plates; (*b*) system consisting of two parallel plates with a porous medium; (*c*) surface of exclusion

[1] Lawrence Berkeley Laboratory, University of California, Berkeley, CA 94720.
[2] Department of Mechanical Engineering, University of California, Berkeley, CA 94720.

Contributed by the Heat Transfer Division of THE AMERICAN SOCIETY OF MECHANICAL ENGINEERS. Manuscript received by the Heat Transfer Division June 1994; revision received November 1994. Keywords: Modeling and Scaling, Porous Media, Thermophysical Properties. Associate Technical Editor: K. Vafai.

face of exclusion S_{ex}. A molecule might, with equal likelihood, occupy any part of the region bounded by the surface S_{ex}. The volume available to the centers of the molecules is given by

$$V_{av} = V - V_{ex} = V\Pi - n_g\pi d_g^3/6. \quad (7)$$

A schematic drawing of the surface of exclusion is shown in Fig. 1(*c*). Consider an element dS_{ex} (of the surface S_{ex}) toward which a molecule is moving at an angle θ with respect to the normal to the surface. The probability of a collision with dS_{ex} in the direction θ in time dt may be written as

$$P_{\theta\cdot dt\cdot dS_{ex}} = u\cdot\cos\,\theta\cdot dt\cdot dS_{ex}\cdot V_{av}^{-1} \quad (8a)$$

The probability that a molecule is moving toward dS_{ex} in the direction θ is equal to the solid angle ($2\pi\,\sin\,\theta d\theta$) about dS_{ex} divided by the total solid angle (4π). A collision of the molecule with dS_{ex} is possible only when $\theta < \pi/2$. The probability of collision of a molecule with dS_{ex} in the time dt is obtained by averaging over all of the equally probable directions of approach; namely,

$$P_{dt\cdot dS_{ex}} = \int_0^{\pi/2} P_{\theta\cdot dt\cdot dS_{ex}} \frac{2\pi\,\sin\,\theta d\theta}{4\pi} = 0.25u\cdot dt\cdot dS_{ex}\cdot V_{av}^{-1} \quad (8b)$$

The probability that a molecule will collide with any part of the surface S_{ex} over the finite time Δt is

$$P_{\Delta t\cdot S_{ex}} = 0.25u\cdot S_{ex}\cdot\Delta t\cdot V_{av}^{-1} \quad (8c)$$

Choose Δt so that the probability $P_{\Delta t\cdot S_{ex}}$ is equal to unity, which corresponds to the certainty of a collision. From Eq. (8*c*) $\Delta t = 4V_{av}/uS_{ex}$ and the frequency is

$$f = 1/\Delta t = 0.25u\cdot S_{ex}\cdot V_{av}^{-1} \quad (9a)$$

Substituting Eqs. (6*b*) and (7) into Eq. (9*a*) yields

$$f = (uS_sm_s + un_g4\pi d_g^2)/[4(V\Pi - \pi d_g^3n_g/6)] \quad (9b)$$

One assumption that has been implicitly made is that the surface of exclusion S_{ex} is stationary; this is true for the surface related to the matrix ($S_s\cdot m_s$) but is not true for the surface related to the gas molecules ($n_g4\pi d_g^2$). For the latter we should use the mean velocity of the gas molecules relative to each other. Loeb (1934) showed that the relative velocity of the gas molecules is $\sqrt{2}$ times the average velocity of the molecules. Equation (9*b*) then becomes:

$$f = (uS_sm_s + \sqrt{2}un_g4\pi d_g^2)/[4(V\Pi - \pi d_g^3n_g/6)] \quad (9c)$$

and the mean free path is then

$$l_m = u/f = 4(V\Pi - \pi d_g^3n_g/6)/(S_sm_s + \sqrt{2}n_g4\pi d_g^2) \quad (10a)$$

Neglecting the volume occupied by the gas molecules, $\pi d_g^3n_g/6$, yields

$$l_m = 1/(0.25S_s\rho_{por}\Pi^{-1} + \sqrt{2}N_{g_0}\pi d_g^2) \quad (10b)$$

where the density of the porous medium, $\rho_{por} = m_s/V$, N_{g_0} is the number density of the gas molecules, which is defined as the number of the gas molecules divided by the available volume $V\cdot\Pi$,

$$N_{g_0} = n_g/V\Pi = p/k_BT \quad (11)$$

Mean Free Path and Particle Size Distribution

Assume that the matrix of the porous medium is uniformly distributed and is made up of spherical particles. The gas molecules will collide with each other and with the matrix. Each gas molecule presents a target of effective diameter $2d_g$, while the matrix results in a target of effective diameter $(d_s + d_g)$.

The volume available for the gas molecules is obtained by subtracting the volume of the matrix from the total volume. In the differential volume dV ($=A\cdot dx$) (Fig. 1*b*) gas molecules occupy the volume dV_g:

$$dV_g = dV\left[1 - \int_0^\infty \frac{4}{3}\pi r_s^3N_s(r_s)dr_s\right] \quad (12)$$

where $N_s(r_s)dr_s$ is the number density of the solid particles of radius between r_s and $r_s + dr_s$. The volume available to the gas molecules is given by

$$dV_g = \Pi\cdot dV = \Pi\cdot A\cdot dx = A_{eff}dx \quad (13)$$

where A is the total cross-sectional area and $A_{eff} = \Pi A = \Pi\cdot dV/dx$ is the available (effective) cross-sectional area for the gas molecules. The target numbers of solid particles and gas molecules in dV are $\int_0^\infty N_s(r_s)dr_sdV$, and $N_{g_0}dV_g$, respectively. Neglecting overlap, the total target area, S_t, of the solid particles and gas molecules is

$$S_t = \pi\left[N_{g_0}dV_gd_g^2 + \int_0^\infty dV(r_s + r_g)^2N_s(r_s)dr_s\right] \quad (14)$$

The probability that a molecule entering dV will suffer a collision is

$$P = S_t/A = \pi\left[N_{g_0}\Pi d_g^2 + \int_0^\infty (r_s + r_g)^2N_s(r_s)dr_s\right]dx \quad (15)$$

Consider $n(x)$ gas molecules per unit area entering dV at the location x. At the location $x + dx$, $n(x + dx)$ molecules leave dV having not suffered a collision. The number of molecules per unit total cross-sectional area that undergo a collision between x and $x + dx$ is

$$n(x) - n(x + dx) = [n(x)/\Pi]\cdot P \quad (16)$$

where $n(x)/\Pi$ is the number of gas molecules per unit effective area. Substituting Eq. (15) into Eq. (16) yields

$$dn/dx = \frac{n\pi}{\Pi}\left[N_{g_0}\Pi d_g^2 + \int_0^\infty (r_s + r_g)^2N_s(r_s)dr_s\right] \quad (17)$$

Integrating Eq. (17) yields

$$n(x) = n_0\,\exp\left\{-\frac{\pi}{\Pi}\left[N_{g_0}\Pi d_g^2 + \int_0^\infty (r_s + r_g)^2N_s(r_s)dr_s\right]x\right\} \quad (18)$$

where n_0 is the number of the gas molecules per unit area at $x = 0$.

The mean free path of the gas molecules is defined as

$$l_m = -\frac{1}{n_0}\int_0^{n_0} xdn = -\frac{1}{n_0}\int_0^\infty x(dn/dx)dx \quad (19)$$

Substituting Eqs. (17) and (18) into Eq. (19) and integrating yields

$$l_m = 1\Big/\left[N_{g_0}\pi d_g^2 + \frac{1}{\Pi}\int_0^\infty \pi(r_s + r_g)^2N_s(r_s)dr_s\right] \quad (20)$$

The velocities of the gas molecules have been assumed to be the same. For a Maxwellian distribution of velocities, a factor

$\sqrt{2}$ multiplies the first term of the denominator of Eq. (20). Then for $r_g \ll r_s$, Eq. (20) reduces to

$$l_m = 1 \Big/ \left[\sqrt{2} N_{g_0} \pi d_g^2 + \frac{1}{\Pi} \int_0^\infty \pi r_s^2 N_s(r_s) dr_s \right] \quad (21)$$

For spherical particles one has

$$\int_0^\infty 4\pi r_s^2 N_s(r_s) dr_s = \text{surface area/volume} = S_s \cdot \rho_{\text{por}}. \quad (22)$$

Substituting Eq. (22) into Eq. (21) yields Eq. (10*b*).

Transport Properties

From kinetic theory, the viscosity is given by (Loeb, 1934)

$$\eta = 0.461 N_{g_0} m_g (8 k_B T / \pi m_g)^{1/2} l_m \quad (23)$$

The viscosity is related to the thermal conductivity by

$$\lambda_g^0 = (2.25\gamma - 1.25)\eta c_v = (2.25\gamma - 1.25) 0.461 N_{g_0} m_g (8 k_B T / \pi m_g)^{1/2} l_m C_v / (N_A m_g) \quad (24)$$

In the free space, using Eq. (3) for l_m in Eqs. (23) and (24) yields

$$\eta = 0.461 N_{g_0} m_g (8 k_B T / \pi m_g)^{1/2} / \sqrt{2} N_{g_0} \pi d_g^2 \quad (25)$$

$$\lambda_g^0 = \frac{(2.25\gamma - 1.25) 0.461 (p/k_B T)(8 k_B T / \pi m_g)^{1/2}}{\sqrt{2}(p/k_B T)\pi d_g^2} \frac{C_v}{N_A} \quad (26)$$

In a porous medium, using Eq. (10*b*) in Eqs. (23) and (24) yields

$$\eta = 0.461 N_{g_0} m_g (8 k_B T / \pi m_g)^{1/2} / (S_s \rho_{\text{por}} / 4\Pi + \sqrt{2} N_{g_0} \pi d_g^2) \quad (27)$$

$$\lambda_g^0 = \frac{(2.25\gamma - 1.25) 0.461 (p/k_B T)(8 k_B T / \pi m_g)^{1/2}}{0.25 S_s \rho_{\text{por}} \Pi^{-1} + \sqrt{2}(p/k_B T)\pi d_g^2} \frac{C_v}{N_A} \quad (28)$$

Application to a Porous Medium—Silica Aerogel

Aerogel is an open-cell, transparent superinsulator. A mixture containing water, TEOS (tetraethyl orthosilicate), alcohol (ethanol), and catalysts is mixed and poured into a mold where liquids react to form a fine silica particle suspension called an alcosol. The particles grow and interconnect to form alcogel, which is a semisolid gel containing alcohol. Alcohol is removed from the alcogel using a supercritical drying procedure, leaving aerogel. Silica aerogel is a network of short bonded chains of silica particles, which are fused together. Particles of diameters 2–5 nm and pores of diameters of 10–100 nm produce a solid–gas matrix in which the volume fraction of the solid can be less than 5 percent. The small pore size limits the motion of gas molecules and greatly reduces the apparent gas conductivity (Zeng et al., 1994).

Specific Surface Area Measurement. The specific surface area, S_s, of the aerogel can be determined from nitrogen adsorption–desorption measurements (Gregg and Sing, 1982). At a fixed temperature, the adsorption of nitrogen by an aerogel sample is determined by the relative pressure of nitrogen vapor according to the "BET" equation:

$$\frac{1}{z(p_0/p - 1)} = \frac{1}{z_m c} + \frac{c - 1}{z_m c} \frac{p}{p_0} \quad (29)$$

where p is the partial pressure, p_0 is the saturation pressure of the nitrogen vapor, z is the mass of adsorbate (nitrogen) adsorbed on the adsorbent (aerogel sample), and z_m is the monolayer capacity, defined as the quantity of the adsorbate that can be accommodated in a completely filled, single layer of molecules (a "monolayer") on the surface of the absorbent. Plotting $[z(p_0/p - 1)]^{-1}$ against p/p_0 gives a line with slope $s = (c - 1)/(z_m c)$ and intercept $i = 1/(z_m c)$; i.e., $z_m = 1/(s + i)$. The specific surface area S_s is related to the monolayer capacity by $S_s = z_m N_A A_m / MW$. Here M is the molecular weight of the adsorbate, W is the sample weight, and A_m is the molecular

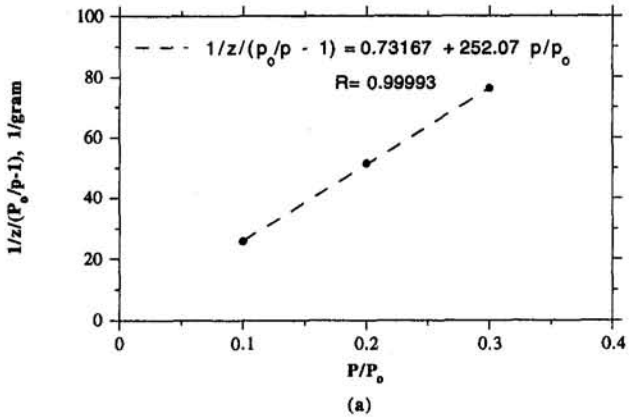

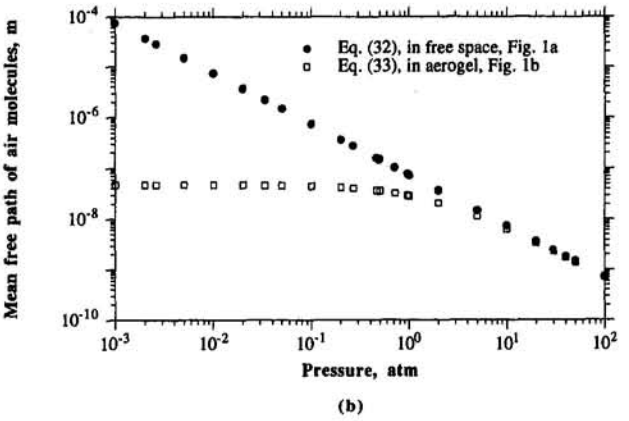

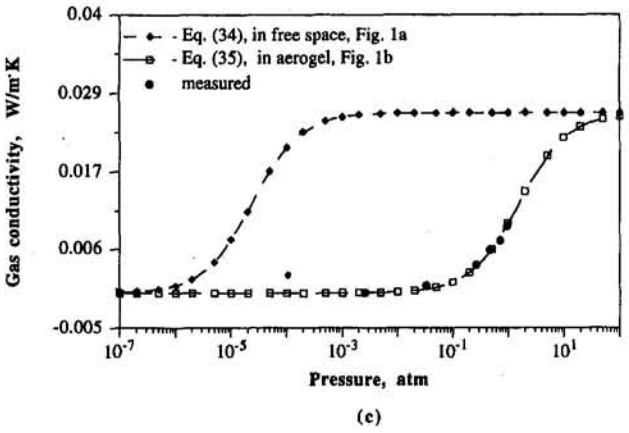

Fig. 2 Results from experiments and calculations: (*a*) "BET" plot; (*b*) pressure dependence of the mean free path of gas molecules; (*c*) pressure dependence of gas thermal conductivity

cross-sectional area of the adsorbate. For a nitrogen adsorbate, $N_A A_m/M = 3484.7$ (m^2/g), which yields

$$S_s\ (m^2/g) = 3484.7\ (m^2/g)\ z_m\ (g)/W\ (g). \quad (30)$$

Measurements were made in a Quantasorb sorption system. An aerogel sample was opacified with carbon particles with porosity of 94 percent and density 1.1×10^5 g/m^3. The mass z of adsorbate (nitrogen) adsorbed on the 0.0173 g aerogel sample was measured at relative pressures p/p_0 of 0.1, 0.2, and 0.3. From Fig. 2(a), $i = 0.732$ and $s = 252.07$. One then obtains

$$z_m = 3.96 \times 10^{-3}\ g \quad \text{and} \quad S_s = 797.6\ m^2/g. \quad (31)$$

The error in the specified relative pressure p/p_0 is negligible. From Eq. (29) it is seen that the error of the mass z of adsorbate is the same as that of the monolayer capacity z_m. The precision limit of S_s is

$$\frac{P_{S_s}}{S_s} = \left[\left(\frac{P_{z_m}}{z_m}\right)^2 + \left(\frac{P_W}{W}\right)^2\right]^{1/2}$$

$$= \left[\left(\frac{8.0 \times 10^{-5}\ g}{4.0 \times 10^{-3}\ g}\right)^2 + \left(\frac{0.0006\ g}{0.0170\ g}\right)^2\right]^{1/2} = 4.1 \text{ percent}$$

The bias limit of S_p is

$$\frac{B_{S_s}}{S_s} = \left[\left(\frac{B_{z_m}}{z_m}\right)^2 + \left(\frac{B_W}{W}\right)^2\right]^{1/2}$$

$$= \left[\left(\frac{0.0002\ g}{0.0040\ g}\right)^2 + \left(\frac{0.0002\ g}{0.0170\ g}\right)^2\right]^{1/2} = 1.3 \text{ percent}$$

The overall uncertainty in the determination of S_s is

$$U_{S_s}/S_s = [0.0406^2 + 0.0128^2]^{1/2} = 4.3 \text{ percent}$$

Thermal Conductivity Measurement. The hot-wire technique (Morrow, 1979) was used to measure the thermal conductivity of the aerogel opacified with carbon particles (see Zeng et al., 1994). An electrical current is passed through a wire imbedded in the test sample. The temperature increase of the wire depends on the thermal conductivity of the sample and is the basis for the experimental technique. The result for the thermal conductivity is (Morrow, 1979) $\lambda = (Q/4\pi)d\ \log\ (t)/dT$ where Q is the power input. The overall uncertainty in the determination of λ, U_λ/λ, is 4.0 percent (Zeng et al., 1994).

The hot-wire technique yields the total conductivity, which includes contributions from the gas and the solid matrix and includes radiative transfer. When the gas pressure is lower than 10^{-3} atm, the apparent gas conductivity is very small, and the total conductivity essentially results from the solid matrix and radiation contributions, which are independent of the pressure. The apparent gas conductivity is then obtained by subtracting the solid and radiative conductivity, i.e., the measured value at low pressure, from the total conductivity.

Calculations and Discussion. An air molecule has a diameter 3.53×10^{-10} m and a mass 4.648×10^{-26} kg (Loeb, 1934), which yields from Eqs. (3), (10b)

$$l_{m_0} = 1/(4.01 \times 10^9 pT^{-1}) \quad (32)$$

$$l_m = 1/(0.25 S_s \cdot \rho_{por} \Pi^{-1} + 4.01 \times 10^9 pT^{-1}) \quad (33)$$

and yields from Eqs. (1), (26), and (28) with $\alpha = 1$

$$\lambda_{g_0} = \frac{1}{1 + 0.808 \times 10^{-9} Tp^{-1} l_{ch}^{-1}} \frac{60.22 \times 10^5 pT^{-0.5}}{4.01 \times 10^9 pT^{-1}} \quad (34)$$

$$\lambda_{g_0} = \frac{1}{1 + 0.808 \times 10^{-9} Tp^{-1} l_{ch}^{-1}} \times \frac{60.22 \times 10^5 pT^{-0.5}}{0.25 S_s \cdot \rho_{por} \Pi^{-1} + 4.01 \times 10^9 pT^{-1}} \quad (35)$$

For a carbon-opacified aerogel having a density 0.11 g/cm^3, porosity 94 percent, and specific surface area S_s 797.6 m^2/g (Eq. (31)), the mean free path of the gas molecules at a temperature 296 K is calculated from Eq. (33) and the mean free path in free space is calculated from Eq. (32). The results are presented in Fig. 2(b). For $p \geq 50$ atm, the mean free path of the gas molecules in the aerogel is the same as in free space. When the pressure is reduced, the mean free path in the aerogel deviates from that in free space and as the pressure approaches zero the mean free path reaches a constant finite value instead of going to infinity in a free space. The results for the thermal conductivity of the gas calculated from Eqs. (34) and (35) (for $l_{ch} = 1$ cm) as well as the experimental results are shown in Fig. 2(c). It is seen that: (1) When the pressure is reduced to 0.1 atm, the thermal conductivity of the gas in the aerogel decreases to almost zero while the thermal conductivity of a gas in free space is not affected by this decrease in pressure. Thus, the small heat transfer resulting from very high vacuum in a free space, e.g., 10^{-7} atm, can be achieved by using aerogel at only a moderate vacuum, e.g., 10^{-2} atm; (2) the calculated apparent thermal conductivity of a gas from Eq. (35) is in good agreement with the experimental results.

Summary

The apparent thermal conductivity of a gas in a porous medium is small because the solid network partitions the space into fine pores, which restrict the motion of the gas molecules. Thus, at low pressures the mean free path is greatly reduced. A relation is obtained for the mean free path of gas molecules in a porous medium in terms of the pore size distribution and the specific surface area, which can be obtained from nitrogen adsorption–desorption measurements. The gas thermal conductivity, which can be determined from the hot-wire technique, is related to the mean free path of the gas. The calculations show that at a pressure of about 0.01 atm, the apparent thermal conductivity of a gas in aerogel is very small and approximately equal to the thermal conductivity of a gas in free space at about 10^{-7} atm. The apparent thermal conductivity of a gas in aerogel predicted by using the equation for the mean free path developed in this study is in good agreement with the experimental results.

Acknowledgments

This work was supported by the Assistant Secretary for Conservation and Renewable Energy, Advanced Industrial concepts (AIC) Materials Program of the Advanced Industrial Concepts Division, Office of Industrial Technologies of the U.S. Department of Energy under Contract No. DE-AC03-76F00098.

References

Gregg, S. I., and Sing, K. S. W., 1982, *Adsorption, Surface Area and Porosity*, 2nd ed., Academic Press, London, United Kingdom.

Kaganer, M. G., 1969, "Thermal Insulation in Cryogenic Engineering," Israel Program of Scientific Translation, Jerusalem, Israel.

Loeb, L. B., 1934, *The Kinetic Theory of Gases*, McGraw-Hill, New York, pp. 214, 245.

Morrow, G. D., 1979, "Improved Hot Wire Thermal Conductivity Technique," *Ceramic Bulletin*, Vol. 58, No. 7, pp. 687–690.

Zeng, S. Q., Hunt, A. J., Cao, W., and Greif, R., 1994, "Pore Size Distribution and Apparent Gas Thermal Conductivity of Silica Aerogel," ASME JOURNAL OF HEAT TRANSFER, Vol. 116, pp. 756–759.

Analytical Solution for Transient Laminar Fully Developed Free Convection in Open-Ended Vertical Concentric Porous Annuli

M. A. Al-Nimr[1] **and T. T. Darabseh**[1]

Nomenclature

b = annular gap width = $r_2 - r_1$
Da = Darcy number = $K/\epsilon r_2^2$
D = equivalent (hydraulic) diameter of annulus = $2b$
Gr = Grashof number, $\mp g\beta(T_w - T_0)D^3/\gamma^2$ in the case of an isothermal boundary or $\mp g\beta qD^4/2k_e\gamma^2$ in the case of uniform heat flux (UHF) heat transfer boundary; the plus and minus signs apply to upward (heating) and downward (cooling) flows, respectively
Gr* = modified Grashof number = $D\text{Gr}/l$
k_e = effective thermal conductivity of porous medium = $\epsilon k_f + (1 - \epsilon)k_s$
k_f, k_s = thermal conductivity of the fluid and solid matrix
K = permeability of the porous medium
l = height of annulus
L = dimensionless height of annulus = $1/\text{Gr}^*$
N = annulus radius ratio = r_1/r_2
p = pressure of fluid inside the channel at any cross section
p' = pressure defect at any point = $p - p_s$
p_s = hydrostatic pressure = $\rho_0 gz$
P = dimensionless pressure defect at any point = $p'r_2^4/\rho_0 l^2\gamma^2\text{Gr}^{*2}$
Pr_e = effective Prandtl number = γ/α_e
q = heat flux at the heat transfer surface = $q = \mp k_e(\partial T/\partial r)_w$ where the minus and plus signs are, respectively, for heating and cooling in case I; these signs should be reversed in case O
r = radial coordinate
r_1, r_2 = inner and outer radii of annulus
R = dimensionless radial coordinate = r/r_2
t = time
T = temperature at any point
T_0 = temperature at the annulus entrance
T_w = temperature of heat transfer boundary
u = volume-averaged axial velocity
U = dimensionless volume averaged axial velocity = $ur_2^2/(l\gamma\text{Gr}^*)$
z = axial coordinate
Z = dimensionless axial coordinate = $z/(l\text{Gr}^*)$
α_e = effective thermal diffusivity = $k_e/\rho_f c_f$
β = volumetric coefficient of thermal expansion
γ = kinematic viscosity of fluid, μ/ρ_0
ϵ = porosity of the medium
θ = dimensionless temperature = $(T - T_0)/(T_w - T_0)$ in the case of an isothermal heat transfer boundary and $(T - T_0)/(qD/2k_e)$ for UHF boundary
ρ = fluid density at temperature T, $\rho_0(1 - \beta(T - T_0))$
σ = ratio of heat capacity of the saturated porous medium to that of the fluid = $(\epsilon\rho_f c_f + (1 - \epsilon)\rho_s c_s)/\rho_f c_f$
τ = dimensionless time = $tk_e/\rho_f c_f r_2^2$

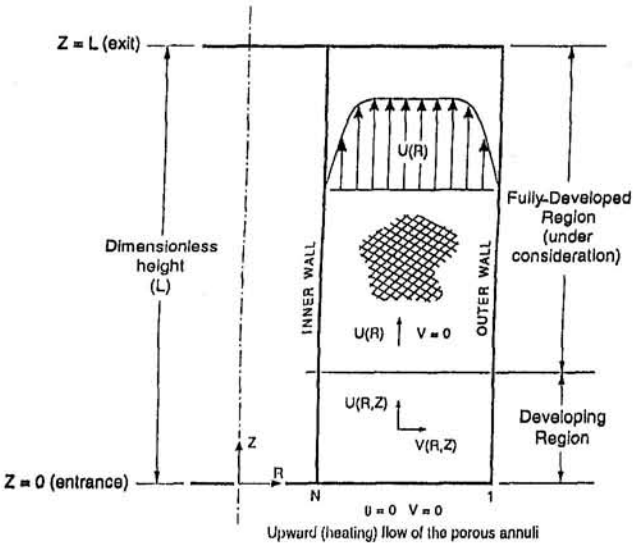

Fig. 1 Schematic diagram

1 Introduction

Free and mixed convection problems in a vertical porous annulus have been extensively studied by Prasad et al. (1985) and Muralidhar (1989). These studies use numerical or experimental techniques to investigate the thermal behavior of the porous annulus. Parang and Keyhani (1987) have obtained closed-form solutions for the special case where the inner and outer walls are heated by uniform but unequal heat fluxes.

The lack of analytical solutions for transient fully developed laminar natural convection in vertical concentric porous annuli, with different fundamental combinations of isothermal and isoflux thermal boundary conditions, motivated the present work. The purpose of this paper is to present, in closed forms, transient fully developed free convection solutions, corresponding to four fundamental thermal boundary conditions in vertical concentric annuli. The solutions obtained, which take both Darcian and Brinkman effects into consideration, may be used as a preliminary check for numerical solutions of more practical situations.

2 Governing Equations and Boundary Conditions

The equations of motion and energy are the following two simultaneous nondimensional equations:

$$\frac{1}{\text{Pr}_e}\frac{\partial U}{\partial \tau} = -\frac{\partial P}{\partial Z} + \frac{1}{R}\frac{\partial}{\partial R}\left[R\frac{\partial U}{\partial R}\right] - \frac{U}{\text{Da}} + \frac{\theta}{16(1-N)^4} \quad (1)$$

$$\sigma\frac{\partial \theta}{\partial \tau} + \text{Pr}_e U\frac{\partial \theta}{\partial Z} = \frac{1}{R}\frac{\partial}{\partial R}\left[R\frac{\partial \theta}{\partial R}\right] \quad (2)$$

Two initial conditions and four boundary conditions are therefore needed to obtain a solution for the above two equations. The two initial conditions are

$$U(0, R, Z) = \theta(0, R, Z) = 0 \quad (3)$$

The two boundary conditions related to U are

$$U(\tau, 1, Z) = U(\tau, N, Z) = 0 \quad (4)$$

On the other hand, there are many possible thermal boundary

[1] Mechanical Engineering Department, Jordan University of Science and Technology, Irbid, Jordan.

Contributed by the Heat Transfer Division of THE AMERICAN SOCIETY OF MECHANICAL ENGINEERS. Manuscript received by the Heat Transfer Division March 1994; revision received November 1994. Keywords: Natural Convection, Porous Media, Transient and Unsteady Heat Transfer. Associate Technical Editor: K. Vafai.

conditions applicable to the annular configuration. These fundamental solutions are summarized by Al-Nimr (1993) and they will be given later.

3 General Analysis

As shown by Al-Nimr (1993), equations similar to Eq. (1) have solutions in the form $U = U(\tau, R)$ only if

$$\frac{\partial^2 P}{\partial Z^2} = \alpha \tag{5}$$

where α is constant. Applying the conditions, for an open-ended channel, that $P = 0$ at both inlet and exit (i.e., at $Z = 0$ and L), gives

$$P = 0.5\alpha Z(Z - L) \tag{6}$$

From Eq. (1) we have

$$\frac{\partial \theta}{\partial Z} = 16\alpha(1 - N)^4 \tag{7}$$

The governing Eqs. (1)–(2) can be simplified if one of the two annulus boundaries is kept isothermal. In order to satisfy this boundary condition, θ must, in this particular case, be independent of Z. Thus, it is concluded that α must, in such a case, equal zero.

4 Fundamental Solutions

If at least one of the two annulus boundaries is kept isothermal, Eqs. (1) and (2) are reduced to

$$\frac{1}{\mathrm{Pr}_e}\frac{\partial U}{\partial r} = \frac{1}{R}\frac{\partial}{\partial R}\left[R\frac{\partial U}{\partial R}\right] - \frac{U}{\mathrm{Da}} + \frac{\theta}{16(1 - N)^4} \tag{8}$$

$$\sigma\frac{\partial \theta}{\partial \tau} = \frac{1}{R}\frac{\partial}{\partial R}\left[R\frac{\partial \theta}{\partial R}\right] \tag{9}$$

Equation (9) assumes a solution in the form

$$\theta(\tau, R) = \theta_1(\tau, R) + \theta_2(R) \tag{10}$$

where $\theta_2(R)$ accounts for the nonhomogeneity in the boundary conditions. The solution of the homogeneous part obtained by the separation of variables as

$$\theta_1(\tau, R) = \sum_{n=1}^{\infty} A_n e^{-(\lambda_n^2/\sigma)\tau}[Y_o(\lambda_n R) - C_n J_0(\lambda_n R)] \tag{11}$$

and

$$A_n = -\frac{\int_N^1 \theta_2(R)R[Y_0(\lambda_n R) - C_n J_0(\lambda_n R)]dR}{\int_N^1 R[Y_0(\lambda_n R) - C_n J_0(\lambda_n R)]^2 dR} \tag{12}$$

where $\theta_2(R)$, C_n and λ_n depend on the kind of fundamental case we have.

The solution of Eq. (8) is obtained by the application of Green's function approach. Let $U(\tau, R)$ be related to $U'(\tau, R)$ by

$$U(\tau, R) = U'(\tau, R)\exp\left[-\frac{\mathrm{Pr}_e}{\mathrm{Da}}\tau\right] \tag{13}$$

Substituting Eq. (13) into Eq. (8), we obtain

$$\frac{1}{\mathrm{Pr}_e}\frac{\partial U'}{\partial \tau} = \frac{1}{R}\frac{\partial}{\partial R}\left(R\frac{\partial U'}{\partial R}\right) + \frac{\theta}{16(1 - N)^4}\exp\left[\frac{\mathrm{Pr}_e}{\mathrm{Da}}\tau\right] \tag{14}$$

5 Fundamental Solutions of the First Kind

In this case, the following thermal boundary conditions can be applied:

Case (I): $\theta(\tau, 1) = 0$, $\theta(\tau, N) = 1$, $\tau > 0$.
Case (O): $\theta(\tau, N) = 0$, $\theta(\tau, 1) = 1$, $\tau > 0$.

The evaluation of the required parameters is as follows:

Case (I): the eigenvalues λ_n, θ_2 and other parameters are given as

$$Y_0(\lambda_n N) - \frac{Y_o(\lambda_n)J_0(\lambda_n N)}{J_o(\lambda_n)} = 0 \tag{15}$$

$$\theta_2(R) = \frac{\ln R}{\ln N} \tag{16}$$

$$A_n = \frac{N}{\lambda_n \mathrm{M}}[Y_1(\lambda_n N) - C_n J_1(\lambda_n N)] \tag{17}$$

$$M = \frac{1}{2}[Y_1(\lambda_n) - C_n J_1(\lambda_n)]^2 - \frac{N^2}{2}[Y_1(\lambda_n N) - C_n J_1(\lambda_n N)]^2 \tag{18}$$

In terms of the appropriate Green's function, the velocity profile is given as:

$$U(\tau, R) = \frac{1}{16(1 - N)^4}\{\sum_{m=1}^{\infty} B_m[1 - e^{-\mathrm{Pr}_e[\beta_m^2 + 1/\mathrm{Da}]\tau}]\phi_m(R) + \sum_{m=1}^{\infty}\sum_{n=1}^{\infty} B_{mn}[e^{-(\lambda_n^2/\sigma)\tau} - e^{-\mathrm{Pr}_e[\beta_m^2 + 1/\mathrm{Da}]\tau}]\phi_m(R)\} \tag{19}$$

$$B_m = -\frac{N[Y_1(\beta_m N) - b_m J_1(\beta_m N)]}{H\left(\beta_m^3 + \dfrac{\beta_m}{\mathrm{Da}}\right)} \tag{20}$$

$$B_{mn} = \begin{cases} 0 & \text{if } \beta_m \neq \lambda_n (m \neq n) \\ \dfrac{A_n}{\beta_m^2 + \dfrac{1}{\mathrm{Da}} - \dfrac{\lambda_n^2}{\sigma \mathrm{Pr}_e}} & \text{if } \beta_m = \lambda_n (m = n) \end{cases} \tag{21}$$

$$H = \frac{1}{2}[Y_1(\beta_m) - b_m J_1(\beta_m)]^2 - \frac{N^2}{2}[Y_1(\beta_m N) - b_m J_1(\beta_m N)]^2 \tag{22}$$

Case (O): Here, different parameters are given as

$$\theta_2(R) = 1 - \frac{\ln R}{\ln N'},\quad A_n = -\frac{1}{\lambda_n M}[Y_1(\lambda_n) - C_n J_1(\lambda_n)] \tag{23}$$

where the eigenvalues λ_n are still given by Eq. (15) and M is given by Eq. (18).

Also, the velocity profile is given as in Eq. (19) with

$$B_m = \frac{Y_1(\beta_m) - b_m J_1(\beta_m)}{H\left(\beta_m^3 + \dfrac{\beta_m}{\mathrm{Da}}\right)} \tag{24}$$

where B_{mn} and H are given as in Eqs. (21) and (22), respectively.

We are unable to get a closed-form solution for fundamental solutions of second kind.

6 Fundamental Solutions of the Third Kind

In this case, since one of the boundaries is isothermal, Eqs. (8) and (9) are the governing equations subject to the following boundary conditions:

Case (I): $\partial\theta/\partial R(\tau, 1) = 0$, $\theta(\tau, N) = 1$, $\tau > 0$.
Case (O): $\partial\theta/\partial R(\tau, N) = 0$, $\theta(\tau, 1) = 1$, $\tau > 0$.

The solutions obtained are as follows:

Case (I): the eigenvalues λ_n, θ_2 and other parameters are given as

$$Y_1(\lambda_n) - \frac{Y_o(\lambda_n N)J_1(\lambda_n)}{J_o(\lambda_n N)} = 0 \tag{25}$$

$$\theta_2(R) = 1, \quad A_n = \frac{N}{\lambda_n M}\left[Y_1(\lambda_n N) - C_n J_1(\lambda_n N)\right] \tag{26}$$

where

$$M = \frac{1}{2}\left[Y_0(\lambda_n) - C_n J_0(\lambda_n)\right]^2 - \frac{N^2}{2}\left[Y_1(\lambda_n N) - C_n J_1(\lambda_n N)\right]^2 \tag{27}$$

Also, the velocity profile is given as in Eq. (19) but with

$$B_m = \frac{\left[Y_1(\beta_m) - b_m J_1(\beta_m)\right] - N\left[Y_1(\beta_m N) - b_m J_1(\beta_m N)\right]}{H\left[\beta_m^3 + \dfrac{\beta_m}{\mathrm{Da}}\right]} \tag{28}$$

$$B_{mn} = A_n\left[\frac{-\beta_m}{\beta_m^2 - \lambda_n^2}\right]\left[Y_0(\lambda_n) - C_n J_0(\lambda_n)\right]\left[Y_1(\beta_m) - b_m J_1(\beta_m)\right] \Big/ H\left[\beta_m^2 + \frac{1}{\mathrm{Da}} - \frac{\lambda_n^2}{\sigma\,\mathrm{Pr}_e}\right] \tag{29}$$

where H is given as in Eq. (22).

Case (O): the eigenvalues λ_n, θ_2 and other parameters are given as

$$Y_1(\lambda_n N) - \frac{Y_o(\lambda_n)J_1(\lambda_n N)}{J_o(\lambda_n)} = 0 \tag{30}$$

$$\theta_2(R) = 1, \quad A_n = \frac{1}{\lambda_n M}\left[C_n J_1(\lambda_n) - Y_1(\lambda_n)\right] \tag{31}$$

$$M = \frac{1}{2}\left[Y_1(\lambda_n) - C_n J_1(\lambda_n)\right]^2 - \frac{N^2}{2}\left[Y_0(\lambda_n N) - C_n J_0(\lambda_n N)\right]^2 \tag{32}$$

$U(\tau, R)$ is the same as case (I), but with

$$B_{mn} = \left\{A_n\left[\frac{\beta_m N}{\beta_m^2 - \lambda_n^2}\right]\left[Y_0(\lambda_n N) - C_n J_0(\lambda_n N)\right] \times \left[Y_1(\beta_m N) - b_m J_1(\beta_m N)\right]\right\} \Big/ H\left[\beta_m^2 + \frac{1}{\mathrm{Da}} - \frac{\lambda_n^2}{\sigma\,\mathrm{Pr}_e}\right] \tag{33}$$

7 Fundamental Solutions of the Fourth Kind

In this case, since one of the boundaries is isothermal, Eqs. (8) and (9) are the governing equations subject to the following boundary conditions:

Case (I): $\partial\theta/\partial R(\tau, N) = -(1/1 - N)$, $\theta(\tau, 1) = 0$, $\tau > 0$.
Case (O): $\partial\theta/\partial R(\tau, 1) = (1/1 - N)$, $\theta(\tau, N) = 0$, $\tau > 0$.

The solutions for both cases are given as:

Case (I): the eigenvalues λ_n, θ_2 and other parameters are given as

$$Y_1(\lambda_n N) - \frac{Y_o(\lambda_n)J_1(\lambda_n N)}{J_o(\lambda_n)} = 0 \tag{34}$$

$$\theta_2(R) = -\frac{N \ln R}{1 - N},$$

$$A_n = \frac{N}{\lambda_n^2 M(N-1)}\left[Y_0(\lambda_n N) - C_n J_0(\lambda_n N)\right] \tag{35}$$

where M is given as in Eq. (32). Also, the velocity profile is given as in Eq. (19) but with

$$B_m = \frac{N^2 \ln N\left[Y_1(\beta_m N) - b_m J_1(\beta_m N)\right]}{(1 - N)H\left[\beta_m^3 + \dfrac{\beta_m}{\mathrm{Da}}\right]} \tag{36}$$

where H and B_{mn} are still given as in Eqs. (22) and (33), respectively.

Case (O): the eigenvalues λ_n, θ_2 and other parameters are given as

$$Y_1(\lambda_n) - \frac{Y_o(\lambda_n N)J_1(\lambda_n)}{J_o(\lambda_n N)} = 0 \tag{37}$$

$$\theta_2(R) = \frac{\ln \dfrac{R}{N}}{1 - N}, \quad A_n = \frac{Y_o(\lambda_n) - C_n J_0(\lambda_n)}{\lambda_n^2 (N-1) M} \tag{38}$$

where M is given as in Eq. (27). Also, the velocity profile is given as in Eq. (19) but with

$$B_m = -\frac{\ln N\left[Y_1(\beta_m) - b_m J_1(\beta_m)\right]}{(1 - N)H\left[\beta_m^3 + \dfrac{\beta_m}{\mathrm{Da}}\right]} \tag{39}$$

where H and B_{mn} are given as in Eqs. (22) and (29), respectively.

References

Al-Nimr, M. A., 1993, "Analytical Solution for Transient Laminar Fully Developed Free Convection in Vertical Concentric Annuli," *Int. J. Heat Mass Transfer*, Vol. 36, pp. 2385–2395.

Muralidhar, M., 1989, "Mixed Convection Flow in a Saturated Porous Annulus," *Int. J. Heat Mass Transfer*, Vol. 32, pp. 881–888.

Parang, M., and Keyhani, M., 1987, "Boundary Effects in Laminar Mixed Convection Flow Through an Annular Porous Medium," ASME JOURNAL OF HEAT TRANSFER, Vol. 109, pp. 1039–1041.

Prasad, V., Kulacki, F. A., and Keyhani, M., 1985, "Natural Convection in Porous Media," *J. Fluid Mech.*, Vol. 150, pp. 89–119.

An Equation for Laminar Flow Heat Transfer for Constant Heat Flux Boundary Condition in Ducts of Arbitrary Cross-Sectional Area

T. Yilmaz[1] and E. Cihan[1]

Introduction

We can calculate the heat transfer in ducts of arbitrary cross section with the definition of the equivalent diameter only in turbulent flow. In laminar flow, it is not sufficient to define an equivalent diameter, because the boundary layer of each wall is influenced by another wall. Therefore, one needs additional quantities to describe the heat transfer and pressure drop. This is shown for pressure drop calculations by Yilmaz (1990) and heat transfer for constant wall temperature by Yilmaz and Cihan (1993). In these works, by using other quantities, it was possible to obtain general equations for pressure drop and heat transfer for constant wall temperature. In the present work, an equation for heat transfer for the boundary condition of constant heat flux at the wall for laminar developed flow in ducts of arbitrary cross-sectional area is given.

Nusselt Number for Thermally Developing Flow

Nusselt number Nu is constant for hydrodynamically and thermally developed flow (HTDF). For thermally developing flow (TDF), Nu can be calculated using the Lévêque-type (1928) solution method. A formula for concentric tubes using this method is given by Shah and London (1978). Yilmaz and Cihan (1994) have given a more general Lévêque-type solution for ducts of arbitrary shape:

$$z^* \to 0; \quad \mathrm{Nu} = \frac{1.303\Phi}{(z^*/\Psi)^{1/3}} \tag{1}$$

where Ψ is the shape factor, which is equal to 1 for a circular cross-sectional duct. To calculate the frictional factor of a duct of arbitrary shape, one has to multiply the value of the circular cross-sectional duct with the shape factor. Yilmaz (1990) has given the following equation for the shape factor:

$$\Psi = 1 + \frac{(3/8)d^{*2}(3 - d^*) - 1}{1 + 0.33d^{*2.25}/(n - 1)} \tag{2}$$

The shape factor Φ for heat transfer is determined using the method described by Yilmaz and Cihan (1994) as

$$\Phi = 1 + \frac{[3(d^*/2)^{2/3}/(1 + d^*)] - 1}{1 + 0.4/(n - 1)} \tag{3}$$

Nusselt number Nu must be at least dependent on z^*, d^*, and n (Yilmaz, 1990). Here, n is the ratio of actual periphery (or cross-sectional area) to the periphery (or cross-sectional area) of the circle with the equivalent diameter. The dimensionless diameter d^* is the ratio of the equivalent diameter to the diameter of the inscribed circle of the actual cross-sectional area. The circular cross-sectional duct is described with $d^* = 1$ and $n = 1$. If one dimension of the cross section is very large compared with the other (similar to a parallel plate duct), one has the case where $n \to \infty$. The dimensionless axial coordinate of the duct is denoted as z^*.

Table 1 Comparison of Eq. (5) with the theoretical data

Duct	Ref.	d^*	n	ϕ Ref. value	ϕ Equation(5)	ϵ (%)
Triangular	Shah (1975 a)	1.000	7.955	0.517	0.513	0.80
		1.000	5.770	0.538	0.530	1.34
		1.000	4.333	0.560	0.552	1.45
		1.000	3.267	0.623	0.618	0.88
		1.000	2.017	0.666	0.667	-0.13
		1.000	1.838	0.686	0.692	-0.75
		1.000	1.783	0.694	0.700	-0.96
		1.000	1.653	0.712	0.724	-1.63
Rectangular	Shah and London (1971)	1.000	1.273	0.826	0.834	-0.96
		1.090	1.283	0.835	0.863	-3.34
		1.166	1.309	0.855	0.887	-3.68
		1.333	1.432	0.944	0.960	-1.66
		1.500	1.697	1.098	1.096	0.20
		1.600	1.989	1.221	1.221	0.0
		1.800	3.536	1.524	1.564	-2.67
		1.904	7.018	1.707	1.758	-3.02
		1.960	16.556	1.811	1.844	-1.81
Parallel Plate	Shah and London (1971)	2	∞	1.8870	1.8870	0
Circular	Iqbal et al. (1975)	1.000	1.000	1.000	1.000	0
Elliptical	Iqbal et al. (1975)	1.051	1.004	1.001	0.996	0.43
		1.167	1.048	1.013	0.975	3.74
		1.230	1.100	1.025	0.964	5.94
		1.365	1.341	1.069	0.983	7.98
		1.432	1.624	1.100	1.033	6.13
		1.495	2.236	1.137	1.115	1.90
		1.535	3.394	1.165	1.192	-2.34
		1.546	4.182	1.174	1.219	-5.99
		1.563	8.177	1.189	1.268	-6.68

Nusselt Number for Hydrodynamically and Thermally Developed Flow

For hydrodynamically and thermally developed flow we define

$$\phi = \mathrm{Nu}_\infty/4.364 \tag{4}$$

where Nu_∞ is the Nusselt number for HTDF. It is seen that ϕ is the ratio of Nu_∞ of a duct to the Nu_∞ (=4.364) of the circular duct. For $n \to \infty$, ϕ is denoted by ϕ_∞. With the formula given by Maclaine-Cross (1969) and the method described by Yilmaz and Cihan (1993) we obtain the following equation:

$$\phi = 1 + \frac{(\phi_\infty - 1)}{1 + 0.6/(n - 1)} \tag{5}$$

where ϕ_∞ is to be determined according to the relation

$$\phi_\infty = 1.4153\,\frac{(7/3 - d^*)}{(3/d^* - 1)^2} \tag{6}$$

In Table 1, ϕ values calculated by Eq. (5) are compared with the theoretically obtained values given in the literature. The maximum and minimum deviations between these values are less than +8.0 and −7.0 percent, respectively.

Equation (5) is only valid for ducts that have no turning points on their periphery. It is not valid for annular ducts. Despite this fact, Nusselt number calculated by Eq. (5) is compared in Table 2 with the theoretically obtained values for annular ducts (inner and outer walls heated). It is seen that the minimum and maximum deviations are −16 and +28 percent, respectively, for all annular ducts.

General Equation for Nusselt Number

To obtain general equations for Nu, we define new dimensionless quantities:

[1] Department of Mechanical Engineering, Çukurova University, 01330-Adana, Turkey.

Contributed by the Heat Transfer Division of THE AMERICAN SOCIETY OF MECHANICAL ENGINEERS. Manuscript received by the Heat Transfer Division April 1994; revision received December 1994. Keywords: Forced Convection. Associate Technical Editor: B. W. Webb.

Table 2 Comparison of Eq. (5) with the theoretical data obtained for annular ducts

Ducts	Ref.	ε(%)
Polygonal ducts with central circular cores	Shah and London (1978)	-1/21
Concentric annular ducts		0/28
Eccentric Annular ducts		-16/28

$$Y = \mathrm{Nu}/\mathrm{Nu}_\infty \tag{7}$$

$$X = z^*\mathrm{Nu}_\infty^3/(\Psi\Phi^3) \tag{8}$$

With this coordinate transformation we obtain only one curve for $z^* \to 0$ and $z^* \to \infty$. The Nusselt number values obtained numerically and those given in the literature for parallel plates, circular, triangular, rectangular, and elliptical ducts are shown in Fig. 1. Using these values and the method described by Yilmaz (1979), we obtain the following equation:

$$Y = \left(1 - \frac{0.76}{X^{2/3}} + \frac{2.212}{X}\right)^{1/3} \tag{9}$$

This equation is compared with the theoretically obtained values for ducts with circular, parallel plates, elliptical, and rectangular cross-sectional areas in Tables 3 and 4. The maximum and minimum deviation are ±6.5 percent, respectively.

Conclusions

For the calculation of heat transfer for constant heat flux boundary condition in ducts of arbitrary cross-sectional area for laminar developed flow, Eq. (9) has been obtained. It is shown that the equation derived compares well with the theoretically obtained values for circular, parallel plates, rectangular, isosceles triangular, right triangular, and elliptical ducts. Minimum and maximum deviations are ±6.5 percent, respectively.

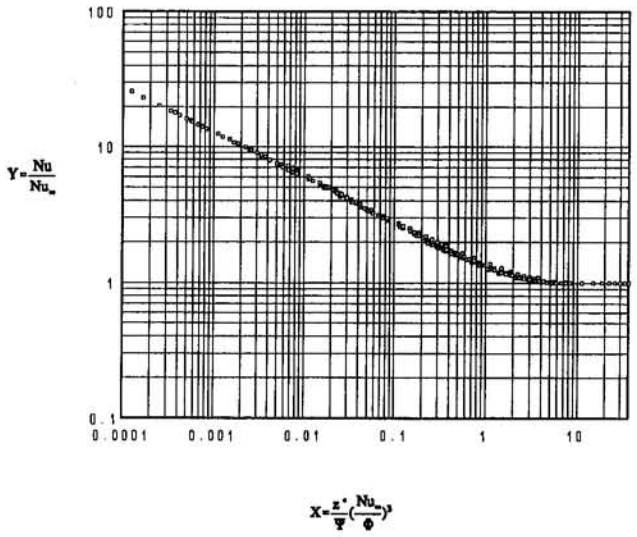

Fig. 1 Graphic representation of numerical results according to definition in Eqs. (7) and (8)

Table 3 Comparison of Eq. (9) with the numerical data given in the literature

Duct	Ref.	d*	n	ε (%) Equation (9)
Circular	Shah (1975 b)	1	1	-2.3/-1.2
Equilateral triangular	Wibulswas (1966)	1	1.654	-0.3/2.6
Square	Chandrupatla (1977)	1	1.273	-0.2/-1.9
Right triangular	Wibulswas (1966)	1	1.855	-6.1/0
Parallel plate	Shah (1975 b)	2	∞	-0.4/-6.4
Semi circular	Hong and Bergles (1974)	1.222	1.339	1.5/-5.4
Rectangular	Wibulswas (1966)	1 1.333 1.5 1.6	1.273 1.432 1.697 1.989	-0.8/-3.9 -5.4/0 0.6/-3.9 1.7/-6.1

Table 4 Comparison of Eq. (9) with the present numerical results

Duct	d*	n	ε (%) Equation (9)
Circular	1	1	-1.3/-2.3
Elliptical	1.051 1.1076	1.004 1.018	-4.7/-1.2 -5.8/-0.8
Rectangular	1 1.333 1.6 1.818	1.273 1.432 1.989 3.851	-3.0/-5.6 -4.9/-2 -0.1/-2.2 -2.7/-5.3
Right triangular	1 1 1	1.855 2.181 3.311	-2.4/-2.9 -3.8/-3.4 -4.92/-1.5
Isosceles triangular	1 1 1	1.666 1.855 2.489	-2.7/-0.1 -2.0/-3.2 -4.6/-3.8

References

Chandrupatla, A. R., and Sastri, V. M. K., 1977, "Laminar Forced Convection Heat Transfer of a Non-Newtonian Fluid in a Square Duct," *Int. J. Heat Mass Transfer,* Vol. 20, pp. 1315–1324.

Hong, S. W., and Bergles, A. E., 1974, "Augmentation of Laminar Flow Heat Transfer in Tubes by Means of Twisted Tape Inserts," Tec. Rep. HTL-5, ISU-ERI-Ames-75011. Eng. Res. Inst., Iowa State University, Ames, IA.

Iqbal, M., Khatry, A. K., and Aggarwala, B. D., 1972, "On the Second Fundamental Problem of Combined Free and Forced Convection Through Vertical Non-circular Ducts," *Appl. Phys.,* Vol. 26, pp. 183–208.

Lévêque, M. A., 1928, "Les Lois de la Transmission de Chaleur par Convection," *Ann. Mines, Mem.,* Ser. 12, Vol. 13, pp. 201–415.

Maclaine-Cross, I. L., 1969, "An Approximate Method for Calculating Heat Transfer and Pressure Drop in Ducts With Laminar Flow," ASME JOURNAL OF HEAT TRANSFER, Vol. 91, pp. 171–173.

Shah, R. K., and London, A. L., 1971, "Laminar Flow Forced Convection Heat Transfer and Flow Friction in Straight and Curved Ducts—A Summary of Analytical Solution," TR No. 75, Dept. Mech. Eng., Stanford University, Stanford, CA.

Shah, R. K., 1975a, "Laminar Flow Friction and Forced Convection Heat Transfer in Ducts of Arbitrary Geometry," *Int. J. Heat Mass Transfer,* Vol. 18, pp. 849–862.

Shah, R. K., 1975b, "Thermal Entry Length Solutions for the Circular Tube and Parallel Plates," *Proc. 3. Heat Mass Transfer Conf.,* Indian Inst. Technol., Bombay, Vol. I, Paper No. HMT-11-75.

Shah, R. K., and London, A. L., 1978, "Laminar Flow Forced Convection in Ducts," in: *Advanced Heat Transfer,* Academic Press, New York.

Wibulswas, P., 1966, "Laminar-Flow Heat Transfer in Non-circular Ducts," Ph.D. Thesis. London University, London, United Kingdom.

Yilmaz, T., 1979, "General Principles for Obtaining of Equations for Theoretically and Experimentally Obtained Results of Transfer Processes," *J. Thermal Sci. Tech.,* Vol. 2/3, pp. 41–46 [in Turkish].

Yilmaz, T., 1990, "General Equation for Pressure Drop for Laminar Flow in Ducts of Arbitrary Cross-Sections," ASME *J. Energy Res. Tech.,* Vol. 112, pp. 220–223.

Yilmaz, T., and Cihan, E., 1993, "General Equation for Heat Transfer for Laminar Flow in Ducts of Arbitrary Cross-Sections," *Int. J. Heat Mass Transfer,* Vol. 36, pp. 3265–3270.

Yilmaz, T., and Cihan, E., 1994, "Lévêque Solution for Heat Transfer in Ducts of Arbitrary Cross-Sections," *J. Thermal Sci. Tech.,* Vol. 17/2, pp. 18–23.

The Optimal Spacing for Cylinders in Crossflow Forced Convection

A. Bejan[1]

Nomenclature

$C_{1,2}$ = functions of $\tilde{S}$
C_D = drag coefficient
D = cylinder diameter
f = friction factor
F_1 = drag force per cylinder
h = average heat transfer coefficient
H = bundle flow length
$\tilde{H}$ = dimensionless length = H/D
k = coolant thermal conductivity
L = cylinder length
$\dot{m}$ = total mass flow rate
n = total number of cylinders
n_l = number of rows in the longitudinal direction
n_t = number of rows in the transversal direction
Nu = average Nusselt number = hD/k
$\tilde{P}$ = pressure drop number = $\Delta P \cdot D^2/(\mu\nu)$
q = total heat transfer rate
q_1 = heat transfer rate per cylinder
Re, Re_{in}, $\mathrm{Re}_{\max}$ = Reynolds numbers = $U_\infty D/\nu$, $U_{in}D/\nu$, $V_{\max}D/\nu$
S = cylinder-to-cylinder spacing
$\tilde{S}$ = dimensionless spacing = S/D
$\bar{S}$ = average spacing
$\tilde{T}$ = dimensionless maximum temperature difference
T_{out} = coolant outlet temperature
T_w = cylinder temperature scale
T_∞ = coolant inlet temperature
U = mean velocity
U_{in} = inlet free-stream velocity
U_∞ = free-stream velocity around one cylinder
$V_{\max}$ = maximum average velocity
W = bundle width
α = coolant thermal diffusivity
ΔP = pressure difference
μ = viscosity
ν = kinematic viscosity
Π = pressure drop number = $\Delta P \cdot D^2/(\mu\alpha)$
ρ = coolant density
χ = correction factor

1 Introduction

In this note I draw attention to a new fundamental aspect of the heat transfer performance of a bundle of parallel cylinders with crossflow forced convection, namely, the maximization of the thermal contact between the bundle and the fluid, when the volume occupied by the bundle is fixed. In the experiments described by Jubran et al. (1993) we have seen empirical evidence that the total heat transfer rate is maximum when the cylinder-to-cylinder spacing S has a certain value. This finding is important because it has been overlooked for decades, while forced convection from cylinders in crossflow grew into one of the most researched topics in heat transfer.

Jubran et al. (1993) did not offer any theoretical explanation or way of predicting the optimal spacing. My objectives in this note are two:

(a) I will show that the optimal S/D ratio can be predicted based on a simple theory (Bejan and Sciubba, 1992; Bejan, 1993), and that contrary to the conclusion of Jubran et al. the S_{opt}/D ratio is not a constant.

(b) I will also show that, if the theory (a) is known, all the empirical information necessary for predicting S_{opt}/D *accurately* is already available in the large volume of heat and fluid flow data published for cylinders in crossflow.

2 The Method of Intersecting the Asymptotes

It is useful to begin with the simplest analysis that (i) proves the existence of an optimal spacing, and (ii) reveals the proper trends and dimensionless groups. Consider the bundle shown in Fig. 1. The cylinders occupy the fixed volume $H \times L \times W$, where H is aligned with the flow direction. The cylinder diameter D, the pressure drop across the bundle ΔP, and the upstream temperature T_∞ are also fixed. The cylinder temperature is of order T_w; this order of magnitude characterizes all the cylinders in the bundle. We are interested in maximizing the total heat transfer q between the bundle and the surrounding fluid, by selecting the cylinder-to-cylinder spacing S, or the number of cylinders in the bundle.

Consider first the limit where the spacing S is sufficiently large that each cylinder acts as if it is alone in its own crossflow of free-stream velocity U_∞. The total heat transfer rate experienced by the bundle is $q = nq_1$, where q_1 is the heat transfer associated with a single cylinder,

$$q_1 = \frac{k}{D}\,\mathrm{Nu}\pi DL(T_w - T_\infty) \tag{1}$$

and n is the total number of cylinders,

$$n = \frac{HW}{(S + D)^2 \cos 30^\circ} \tag{2}$$

We are assuming that W is considerably greater than $(S + D)$. In the range $0.7 < \mathrm{Pr} < 500$ and $40 < U_\infty D/\nu < 1000$, the

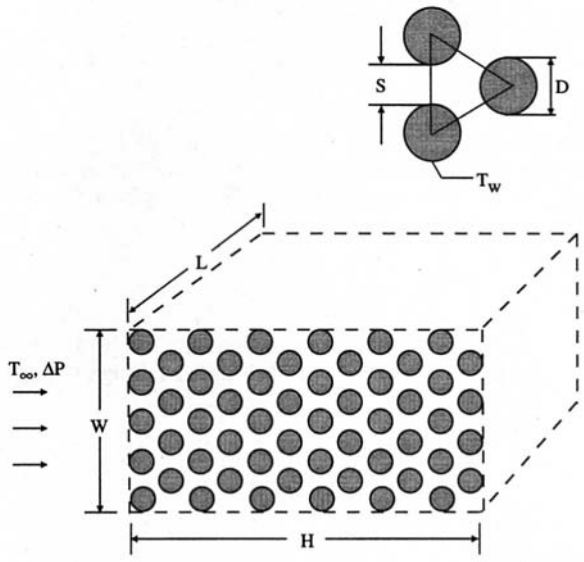

Fig. 1 Fixed volume $H \times L \times W$ containing a bundle of parallel cylinders perpendicular to a free stream

[1] J.A. Jones Professor of Mechanical Engineering, Department of Mechanical Engineering and Materials Science, Duke University, Durham, NC 27708-0300; Fellow ASME.

Contributed by the Heat Transfer Division of THE AMERICAN SOCIETY OF MECHANICAL ENGINEERS. Manuscript received by the Heat Transfer Division January 1994; revision received October 1994. Keywords: Augmentation and Enhancement, Electronic Equipment, Heat Exchangers.

average Nusselt number is given by the correlation (Zukauskas, 1987)

$$\mathrm{Nu} = 0.52\ \mathrm{Pr}^{0.37}\ \mathrm{Re}^{1/2} \tag{3}$$

The free-stream velocity U_∞ is not given. It is determined by the force balance on the entire bundle, $\Delta P{\cdot}WL = nF_1$, where F_1 is the drag force experienced by one cylinder, $F_1 = C_D DL(\rho U_\infty^2/2)$. The drag coefficient varies from 2 to 1 in the Re range 40–1000, therefore in this order-of-magnitude analysis it is sufficient to use $C_D \sim 1.5$. The force balance yields U_∞, or Re,

$$\mathrm{Re} \cong 1.1(\tilde{S}+1)\left(\frac{\tilde{P}}{\tilde{H}}\right)^{1/2}, \quad \text{with} \quad \tilde{S} = \frac{S}{D}, \quad \tilde{H} = \frac{H}{D} \tag{4}$$

where $\tilde{P}$ is the dimensionless pressure group identified by Bhattacharjee and Grosshandler (1988)

$$\tilde{P} = \frac{\Delta P{\cdot}D^2}{\mu\nu} \tag{5}$$

Combining Eqs. (1)–(6) we find that the total heat transfer rate behaves as

$$q_{\text{large } S} \cong 2kL\,\frac{W}{D}\,(T_w - T_\infty)\,\frac{\tilde{H}^{3/4}\tilde{P}^{1/4}\,\mathrm{Pr}^{0.37}}{(\tilde{S}+1)^{3/2}} \tag{6}$$

Consider now the opposite extreme when the cylinders almost touch, and the flow is almost cut off. In this limit the temperature of the coolant that exits slowly through the right end of the bundle (the plane $L \times W$) is essentially the same as the cylinder temperature T_w. The heat transfer from the bundle to the coolant is equal to the enthalpy gained by the coolant, $q = \dot{m}c_P(T_w - T_\infty)$, where $\dot{m}$ is the mass flow rate through the $L \times W$ plane.

To obtain an order-of-magnitude estimate for the flow rate, we note that $\dot{m}$ is composed of several streams [total number $n_t \cong W/(S+D)$], each with a cross-sectional area $S \times L$ in the plane of one row of cylinder axes. The thickness of the channel traveled by each stream varies between a minimum value (S) at the row level, and a maximum value at a certain level between two rows. The volume-averaged thickness of one channel of this kind is

$$\bar{S} = S + D - 0.907\,\frac{D^2}{S+D} \tag{7}$$

however, we may adjust this estimate by using 1 in place of the factor 0.907 to account for the fact that the flow *must* cease when the cylinders touch ($S = 0$):

$$\bar{S} = S\,\frac{S+2D}{S+D} \tag{8}$$

The mean velocity U through a channel of length H and cross-sectional area $\bar{S}L$ can be estimated using the solution for Hagen–Poiseuille flow through a parallel plate channel of spacing $\bar{S}$ and length H,

$$U \cong \frac{\bar{S}^2\Delta P}{12\mu H} \tag{9}$$

The mass flow rate through one channel is $\dot{m}_1 = \rho U\bar{S}L$. There are n_t channels, therefore the mass flow rate through the entire bundle is $\dot{m} = \dot{m}_1 W/(S+D)$, and q becomes

$$q_{\text{small } S} \cong \frac{1}{12}\,kL\,\frac{W}{D}\,(T_w - T_\infty)\,\frac{\tilde{P}\,\mathrm{Pr}\,\tilde{S}^3(\tilde{S}+2)^3}{\tilde{H}(\tilde{S}+1)^4} \tag{10}$$

The two asymptotic trends are sketched in Fig. 2. The actual (unknown) curve $q(S)$, which is indicated by the solid line in the figure, has a maximum where the spacing S is approximately the same as the S value obtained by intersecting the two asymptotes (Bejan and Sciubba, 1992). The S_{opt} value obtained by eliminating q between Eqs. (6) and (10) is given implicitly by

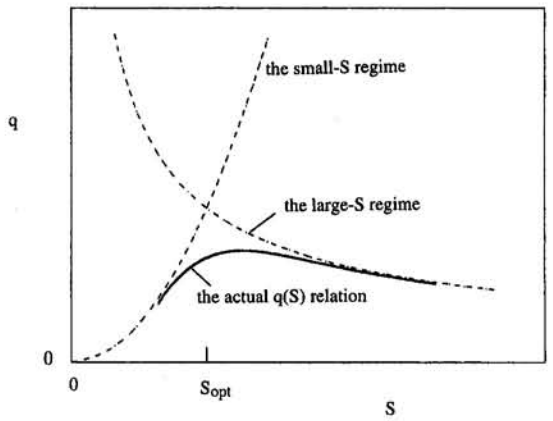

Fig. 2 The optimal cylinder-to-cylinder spacing as the intersection of the large-S and small-S asymptotes

$$\tilde{S}_{\text{opt}}\,\frac{(2+\tilde{S}_{\text{opt}}^{-1})^{6/7}}{(1+\tilde{S}_{\text{opt}}^{-1})^{5/7}} \cong 2.5\,\frac{\tilde{H}^{1/2}}{\tilde{P}^{3/14}\,\mathrm{Pr}^{0.18}} \tag{11}$$

The optimal spacing increases with the length of the bundle, and decreases with the applied pressure difference and the Prandtl number. It is also interesting that in Eq. (11) the exponents of $\tilde{P}$ and Pr are almost the same (note that $\frac{3}{14} = 0.21$). This means that instead of the product $\tilde{P}^{3/14}\,\mathrm{Pr}^{0.18}$ we may use approximately $\Pi^{3/14}$, Fig. 3,

$$\tilde{S}_{\text{opt}}\,\frac{(2+\tilde{S}_{\text{opt}}^{-1})^{6/7}}{(1+\tilde{S}_{\text{opt}}^{-1})^{5/7}} \cong 2.5\,\frac{\tilde{H}^{1/2}}{\Pi^{3/14}} \tag{12}$$

where the Π group is defined as $\Pi = \Delta P{\cdot}D^2/(\mu\alpha) = \tilde{P}\,\mathrm{Pr}$ (Bejan, 1993; see also Petrescu, 1994). The intersection of the large-S and small-S regimes provides also an estimate for the scale of the maximum thermal conductance between bundle and coolant, $q/(T_w - T_\infty)$. Figure 2 shows that the result of this operation will always overestimate the peak value of the actual $q/(T_w - T_\infty)$ curve:

$$\left[\frac{kLW}{qD}\,(T_w - T_\infty)\right]_{\min} \geq \frac{1.85}{\tilde{P}^{4/7}\,\mathrm{Pr}^{3/7}} \tag{13}$$

3 Estimates Based on Experimental Correlations for Crossflow

Now that we have theoretical reasons to expect an optimal spacing and a scaling of type (13), we turn our attention to a more precise analysis that is based on published experimental data. A very large effort has been devoted to documenting the pressure drop and heat transfer coefficient for bundles of parallel cylinders in crossflow (e.g., Zukauskas, 1987). These results are expressed in terms of the Reynolds number based on the maximum average velocity between adjacent cylinders, $\mathrm{Re}_{\max} = V_{\max}D/\nu$. To determine the relation between the applied pressure difference and $\mathrm{Re}_{\max}$ we use

$$\Delta P = n_l f \chi\,\tfrac{1}{2}\,\rho V_{\max}^2 \tag{14}$$

with $\chi = 1$ for the equilateral triangle array, and n_l for the number of rows in the flow direction, $n_l = 1 + (\tilde{H}-1)/0.866(\tilde{S}+1)$. Equation (14) becomes

$$\tilde{P} = \tfrac{1}{2}\,n_l f\,\mathrm{Re}_{\max}^2 \tag{15}$$

The friction factor f is available in graphic form (see Fig. 6.20 in Zukauskas, 1987) as a function of $\mathrm{Re}_{\max}$ and cylinder-to-

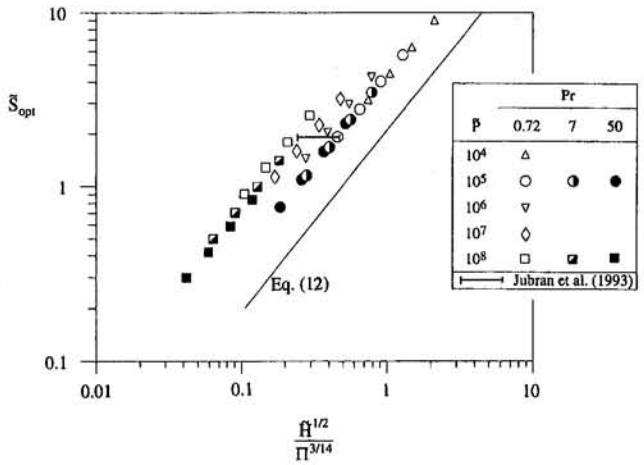

Fig. 3 The optimal cylinder-to-cylinder spacing as a function of the bundle flow length, applied pressure difference, and Prandtl number

cylinder spacing. In the range $10 < \mathrm{Re}_{max} < 10^4$ and $0.25 \le \tilde{S} \le 1.5$, the f curves are approximated within 10 percent by $f = (C_1/\mathrm{Re}_{max}) + C_2$, where $C_1 = 68\tilde{S}^{-0.76}$ and $C_2 = 0.37\tilde{S}^{-0.31}$. Equation (15) provides the function $\mathrm{Re}_{max}(\tilde{P}, \tilde{S})$ that accounts for the flow part of the problem.

When the total heat transfer q is divided equally among the cylinders, the peak temperature (T_{max}) belongs to the cylinders positioned in the last row. The maximum temperature difference ($T_{max} - T_\infty$) can be calculated in two steps (Knight et al., 1991),

$$T_{max} - T_{out} = \frac{(q/n)D}{\pi DLk\mathrm{Nu}} \quad \text{and} \quad T_{out} - T_\infty = \frac{q}{\dot{m}c_P} \tag{16}$$

where T_{out} is the bulk temperature of the fluid leaving the bundle, $\dot{m} = \rho V_{max} SLn_l$ is the total mass flow rate, and $n_l = W/(S + D)$. Eliminating T_{out}, we obtain

$$\tilde{T} = \frac{kLW}{qD}(T_{max} - T_\infty) = \frac{\tilde{S} + 1}{\pi n_l \,\mathrm{Nu}} + \frac{\tilde{S} + 1}{\tilde{S}\,\mathrm{Pr}\,\mathrm{Re}_{max}} \tag{17}$$

where $\tilde{T}$ is the dimensionless maximum temperature difference. Finally, we assume that there are many cylinders in the longitudinal flow direction ($n_l > 16$), such that the Nusselt number for the last row is the same as the value averaged over the entire bundle. The numerical results reported below were developed using Table 6.3 of Zukauskas (1987).

In conclusion, the result of combining Eqs. (15) and (17) is a maximum temperature difference function $\tilde{T}$ that depends on $\tilde{P}$, $\tilde{H}$, Pr, and $\tilde{S}$. The $\tilde{T}$ function can be minimized numerically with respect to the spacing $\tilde{S}$, to obtain the optimal spacing $\tilde{S}_{opt}(\tilde{P}, \tilde{H}, \mathrm{Pr})$. Figure 3 shows the $\tilde{S}_{opt}$ results obtained for a total of 36 $\tilde{P}$, $\tilde{H}$, and Pr combinations in the range $10^4 \le \tilde{P} \le 10^8$, $25 \le \tilde{H} \le 200$, and $0.72 \le \mathrm{Pr} \le 50$. In conclusion, the estimate obtained in the preceding section is adequate as intended (i.e., in an order of magnitude sense), and the predicted trends are also correct.

The scatter of the points plotted in Fig. 3 suggests that the use of the combined group $\tilde{H}^{1/2}/\Pi^{3/14}$ on the abscissa may not be the best way to correlate the empirical data. After examining individually the effects of $\tilde{H}$, $\tilde{P}$, and Pr on $\tilde{S}_{opt}$, I found that the following correlation approximates the data with a standard deviation of 5.6 percent:

$$\tilde{S}_{opt} = 1.59\frac{\tilde{H}^{0.52}}{\tilde{P}^{0.13}\,\mathrm{Pr}^{0.24}} \tag{18}$$

The minimum last-row (i.e., peak) temperature occurs when the spacing is optimal, $\tilde{T}_{min} = \tilde{T}(\tilde{S}_{opt})$. The $\tilde{T}_{min}$ values for the 36 cases documented in Fig. 3 are correlated with a standard deviation of 16 percent by the expression

$$\tilde{T}_{min} = \frac{3.33}{\tilde{P}^{0.45}\,\mathrm{Pr}^{0.64}} \tag{19}$$

In both Eqs. (13) and (19), the denominator on the right-hand side is approximated well by $\Pi^{1/2}$. This allows us to rewrite Eq. (19) as the maximum power density installed in the fixed volume HLW,

$$\frac{q}{HLW} \sim 0.3\Pi^{1/2}\frac{k(T_{max} - T_\infty)}{HD} \tag{20}$$

We note that Π is proportional to D^2, therefore the maximum power density does not depend on the cylinder diameter! It is important to set the spacing S *in proportion to* D, cf. Eq. (18).

4 Concluding Remarks

It is instructive to compare the optimal spacing reported by Jubran et al. (1993) with the data plotted in Fig. 3. In the present notation, the conclusion of Jubran et al. reads $\tilde{S}_{opt} = 1.89$, and was reached during experiments with air flow through arrays of parallel pin fins ($D = 6.35$ mm, $L = 60$ mm) attached to a base plate ($H = 300$ mm, $W = 175$ mm). A direct comparison with the present results is not possible because in the experiments of Jubran et al. S was varied at constant air mass flow rate (or constant upstream velocity, U_{in}), instead of constant ΔP. The experiments covered the U_{in} range 2.2–10 m/s.

An order of magnitude comparison can be made, however, by noting that when $\tilde{S} \sim 2$ the array is dense and long enough such that the overall ΔP scale is $\Delta P \sim \frac{1}{2}\rho U_{in}^2$. The array appears "dense" from the point of view of the approaching stream, to which the array looks opaque (without clear openings). The stream has two choices, to penetrate the array, or to flow around it (Morega et al., 1995). It does both, with less penetration as $\tilde{S}$ decreases.

If we use this approximation we find that the experiments of Jubran et al. cover a range characterized by $4.2 \times 10^5 < \tilde{P} < 9 \times 10^6$, $\tilde{H} = 47.3$, and Pr = 0.72. Their conclusion that $\tilde{S}_{opt} = 1.89$ is shown as a horizontal bar in Fig. 3, and agrees very well with the $\tilde{S}_{opt}$ values determined by minimizing the $\tilde{T}$ expression of Eq. (17). This agreement is remarkable especially in view of the fact that in the experiments of Jubran et al. the cylinders were pin fins attached to a base surface, i.e., the cylinders were not long relative to their diameter, their temperature varied along their length, and the time-averaged flow was not two dimensional.

The same ΔP approximation can be used to convert the empirical correlations (18) and (19) into order-of-magnitude formulas for bundles exposed to a free stream of velocity U_{in},

$$\tilde{S}_{opt} \sim 1.7\frac{\tilde{H}^{0.52}}{\mathrm{Re}_{in}^{0.26}\,\mathrm{Pr}^{0.24}}, \quad \tilde{T}_{min} \sim \frac{4.5}{\mathrm{Re}_{in}^{0.9}\,\mathrm{Pr}^{0.64}} \tag{21}$$

where $\mathrm{Re}_{in} = U_{in}D/\nu$, which is the same as $\mathrm{Re}_{in} \sim (2\tilde{P})^{1/2}$. Correlations (21) cover the range $140 < \mathrm{Re}_{in} < 14{,}000$, $25 < \tilde{H} < 200$, and $0.72 < \mathrm{Pr} < 50$.

The relative progress made in this note is illustrated in Fig. 3. Known until now was the single point reported by Jubran et al. (1993); the point (horizontal bar) shown in Fig. 3, however, is more general because the Cartesian coordinates are dimensionless. These theoretical coordinates are the product of this note. The other product is the complete curve, Eq. (18), which is based on experimental heat and fluid flow data, and covers all the possible flow conditions.

Acknowledgments

This work was supported by the Air Force Office of Scientific Research under the guidance of Major Dan Fant. The assistance received from Dr. A. J. Fowler is appreciated.

References

Bejan, A., and Sciubba, E., 1992, "The Optimal Spacing of Parallel Plates Cooled by Forced Convection," *Int. J. Heat Mass Transfer*, Vol. 35, pp. 3259–3264.

Bejan, A., 1993, *Heat Transfer*, Wiley, New York, p. 328.

Bhattacharjee, S., and Grosshandler, W. L., 1988, "The Formation of a Wall Jet Near a High Temperature Wall Under Microgravity Environment," ASME HTD-Vol. 96, pp. 711–716.

Jubran, B. A., Hamdan, M. A., and Abdualh, R. M., 1993, "Enhanced Heat Transfer, Missing Pin, and Optimization of Cylindrical Pin Fin Arrays," ASME JOURNAL OF HEAT TRANSFER, Vol. 115, pp. 576–583.

Knight, R. W., Goodling, J. S., and Hall, D. J., 1991, "Optimal Thermal Design of Forced Convection Heat Sinks—Analytical," ASME *Journal of Electronic Packaging*, Vol. 113, pp. 313–321.

Morega, Al. M., Bejan, A., and Lee, S. W., 1995, "Free Stream Cooling of a Stack of Parallel Plates," *Int. J. Heat Mass Transfer*, Vol. 38, pp. 519–531.

Petrescu, S., 1994, "Comments on the Optimal Spacing of Parallel Plates Cooled by Forced Convection," *Int. J. Heat Mass Transfer*, Vol. 37, p. 1283.

Zukauskas, A., 1987, "Convective Heat Transfer in Cross Flow," in: S. Kakac, R. K. Shah, and W. Aung, *Handbook of Single-Phase Convective Heat Transfer*, Wiley, New York, Chap. 6.

Exact Solution of Nonsteady Thermal Boundary Layer Equation

A. S. Dorfman[1]

Introduction

There are only a few exact solutions of the thermal boundary layer equation. Most of them are derived for a specific surface temperature distribution. The first exact solution of the steady-state boundary layer equation was given for a plate with constant surface temperature and free-stream velocity (Pohlhausen, 1921). The same problem for a plate with polynomial surface temperature distribution was solved by Chapmen and Rubesin (1949). Levy (1952) gave the exact solution for the case of a power law distribution of both surface temperature and free-stream velocity. The exact solution of the steady-state boundary layer equation for an arbitrary surface temperature and a power law free-stream velocity distribution was given by the author in two forms: of series (1971) and of the integral with an influence function of unheated zone (1973). A similar solution of the nonsteady thermal boundary layer equation for an arbitrary surface temperature and a power law free-stream velocity distribution is presented here. In this case, the coefficients of series depend on time, and in the limit $t \to \infty$ they become the constant coefficients of a similar solution published before (Sparrow, 1958). This solution, unlike the one presented here, does not satisfy the initial conditions at $t = 0$, and, hence, can be used only in time after the beginning of the process. The solution in the form of a series becomes a closed-form exact solution for polynomial surface temperature and a power law free-stream velocity distribution.

Statement and Solution of the Problem

An incompressible fluid with constant properties flows past a body. The laminar flow is steady state; a free-stream velocity $U(x)$ and a temperature T_∞ are known. The surface temperature T_w is constant and also known. At the moment considered as $t = 0$, the surface temperature start to change according to a function $T_w(t, x)$. The problem is to determine the temperature field and the surface heat flux distribution.

The thermal boundary layer equation and the initial and boundary conditions for the case considered are

$$\partial T/\partial t + u(\partial T/\partial x) + v(\partial T/\partial y) - \alpha(\partial^2 T/\partial y^2) = 0$$

$$t < 0 \quad T = T_w = \text{const}; \quad t > 0 \quad y = 0 \quad T = T_w(t, x); \quad y \to \infty \quad T \to T_\infty \quad (1)$$

α is the thermal diffusivity; u, v are velocity components; the subscript w refers to wall.

Using dimensionless variables, one obtains instead of Eq. (1)

$$\{(2\phi\nu/Ux)[(U/u) - z] + 2(\phi\nu/U^2)(dU/dx)z\}(\partial\theta/\partial z) + 2\phi(\partial\theta/\partial\phi) - \varphi(\partial\theta/\partial\varphi) - (1/\mathrm{Pr})\partial[(u/U)(\partial\theta/\partial\varphi)]/\partial\varphi = 0 \quad (2)$$

$$\theta = T - T_\infty \quad \phi = (1/\nu)\int_0^x U(\xi)d\xi$$

$$\varphi = \psi/\nu(2\phi)^{1/2} \quad z = tU/x$$

Here ψ is the stream function; ν is the kinematic viscosity; Pr is the Prandtl number. In the case of a power law free-stream velocity $U \sim x^m$ the terms $2\phi\nu/Ux$ and $2\phi\nu/U^2(dU/dx)$ depend only on exponent m, while $\phi(\partial\theta/\partial\phi) = x(\partial\theta/\partial x)/(m+1)$. Equation (2) becomes

$$[2/(m+1)][(U/u) + (m-1)z](\partial\theta/\partial z) + [2/(m+1)]x(\partial\theta/\partial x) - \varphi(\partial\theta/\partial\varphi) - (1/\mathrm{Pr})\partial[(u/U)(\partial\theta/\partial\varphi)]/\partial\varphi = 0 \quad (3)$$

$$z < 0 \quad \theta = \theta_w = \text{const}; \quad z > 0 \quad \varphi = 0 \quad \theta = \theta_w(z, x); \quad \varphi \to \infty \quad \theta \to 0 \quad (4)$$

The solution of this equation can be presented in series:

$$\theta = \sum_{k=0}^{\infty}\sum_{i=0}^{\infty} G_{ki}(z, \varphi)(x^{k+i}/U^i)(\partial^{k+i}\theta/\partial x^k \partial t^i) = G_{00}\theta_w + G_{10}x(\partial\theta_w/\partial x) + G_{01}(x/U)(\partial\theta_w/\partial t) + G_{20}x^2(\partial^2\theta_w/\partial x^2) + G_{02}(x/U)^2(\partial^2\theta_w/\partial t^2) + G_{11}(x^2/U)(\partial^2\theta_w/\partial x\partial t) + \ldots \quad (5)$$

By substituting this series in Eqs. (3) and (4) one obtains differential equations and initial and boundary conditions that determine the coefficients of the series (5)

$$[2/(m+1)][(U/u) + (m-1)z][\partial G_{ki}/\partial z + G_{k(i-1)}] + [2/(m+1)][(k+i)G_{ki} + G_{(k-1)i}] - \varphi(\partial G_{ki}/\partial\varphi) - (1/\mathrm{Pr})\partial[(u/U)(\partial G_{ki}/\partial\varphi)]/\partial\varphi \quad (6)$$

$$z \le 0 \quad \varphi = 0 \quad G_{00} = 1 \quad G_{ki} = 0\ (k > 0, i > 0); \quad \varphi \to \infty \quad G_{ki} \to 0 \quad (7)$$

For a power law free-stream velocity, the ratio u/U does not depend on variable x. Hence, the coefficients G_{ki} also do not depend on x and are a function only of variables z and φ and parameters m and Pr. The surface heat flux is defined as

$$q_w = -K(\partial T/\partial y)_{y=0} = \sum_{k=0}^{\infty}\sum_{i=0}^{\infty} g_{ki}(z)(x^{k+i}/U^i)(\partial^{k+i}\theta_w/\partial x^k\partial t^i) = h_*[\theta_w + g_{10}x(\partial\theta_w/\partial x) + g_{01}(x/U)(\partial\theta_w/\partial t) + g_{20}x^2(\partial^2\theta_w/\partial x^2) + g_{02}(x/U)^2(\partial^2\theta_w/\partial t^2) + g_{11}(x^2/U)(\partial^2\theta_w/\partial x\partial t) + \ldots] \quad (8)$$

[1] Stamford, CT.

Contributed by the Heat Transfer Division of THE AMERICAN SOCIETY OF MECHANICAL ENGINEERS. Manuscript received by the Heat Transfer Division March 1994; revision received October 1994. Keywords: Forced Convection, Numerical Methods, Transient and Unsteady Heat Transfer. Associate Technical Editor: Y. Jaluria.

References

Bejan, A., and Sciubba, E., 1992, "The Optimal Spacing of Parallel Plates Cooled by Forced Convection," *Int. J. Heat Mass Transfer*, Vol. 35, pp. 3259–3264.

Bejan, A., 1993, *Heat Transfer*, Wiley, New York, p. 328.

Bhattacharjee, S., and Grosshandler, W. L., 1988, "The Formation of a Wall Jet Near a High Temperature Wall Under Microgravity Environment," ASME HTD-Vol. 96, pp. 711–716.

Jubran, B. A., Hamdan, M. A., and Abdualh, R. M., 1993, "Enhanced Heat Transfer, Missing Pin, and Optimization of Cylindrical Pin Fin Arrays," ASME JOURNAL OF HEAT TRANSFER, Vol. 115, pp. 576–583.

Knight, R. W., Goodling, J. S., and Hall, D. J., 1991, "Optimal Thermal Design of Forced Convection Heat Sinks—Analytical," ASME *Journal of Electronic Packaging*, Vol. 113, pp. 313–321.

Morega, Al. M., Bejan, A., and Lee, S. W., 1995, "Free Stream Cooling of a Stack of Parallel Plates," *Int. J. Heat Mass Transfer*, Vol. 38, pp. 519–531.

Petrescu, S., 1994, "Comments on the Optimal Spacing of Parallel Plates Cooled by Forced Convection," *Int. J. Heat Mass Transfer*, Vol. 37, p. 1283.

Zukauskas, A., 1987, "Convective Heat Transfer in Cross Flow," in: S. Kakac, R. K. Shah, and W. Aung, *Handbook of Single-Phase Convective Heat Transfer*, Wiley, New York, Chap. 6.

Exact Solution of Nonsteady Thermal Boundary Layer Equation

A. S. Dorfman[1]

Introduction

There are only a few exact solutions of the thermal boundary layer equation. Most of them are derived for a specific surface temperature distribution. The first exact solution of the steady-state boundary layer equation was given for a plate with constant surface temperature and free-stream velocity (Pohlhausen, 1921). The same problem for a plate with polynomial surface temperature distribution was solved by Chapmen and Rubesin (1949). Levy (1952) gave the exact solution for the case of a power law distribution of both surface temperature and free-stream velocity. The exact solution of the steady-state boundary layer equation for an arbitrary surface temperature and a power law free-stream velocity distribution was given by the author in two forms: of series (1971) and of the integral with an influence function of unheated zone (1973). A similar solution of the nonsteady thermal boundary layer equation for an arbitrary surface temperature and a power law free-stream velocity distribution is presented here. In this case, the coefficients of series depend on time, and in the limit $t \to \infty$ they become the constant coefficients of a similar solution published before (Sparrow, 1958). This solution, unlike the one presented here, does not satisfy the initial conditions at $t = 0$, and, hence, can be used only in time after the beginning of the process. The solution in the form of a series becomes a closed-form exact solution for polynomial surface temperature and a power law free-stream velocity distribution.

Statement and Solution of the Problem

An incompressible fluid with constant properties flows past a body. The laminar flow is steady state; a free-stream velocity $U(x)$ and a temperature T_∞ are known. The surface temperature T_w is constant and also known. At the moment considered as $t = 0$, the surface temperature start to change according to a function $T_w(t, x)$. The problem is to determine the temperature field and the surface heat flux distribution.

The thermal boundary layer equation and the initial and boundary conditions for the case considered are

$$\partial T/\partial t + u(\partial T/\partial x) + v(\partial T/\partial y) - \alpha(\partial^2 T/\partial y^2) = 0$$

$$t < 0 \quad T = T_w = \text{const}; \quad t > 0 \quad y = 0 \quad T = T_w(t, x); \quad y \to \infty \quad T \to T_\infty \quad (1)$$

α is the thermal diffusivity; u, v are velocity components; the subscript w refers to wall.

Using dimensionless variables, one obtains instead of Eq. (1)

$$\{(2\phi\nu/Ux)[(U/u) - z] + 2(\phi\nu/U^2)(dU/dx)z\}(\partial\theta/\partial z) + 2\phi(\partial\theta/\partial\phi) - \varphi(\partial\theta/\partial\varphi) - (1/\mathrm{Pr})\partial[(u/U)(\partial\theta/\partial\varphi)]/\partial\varphi = 0 \quad (2)$$

$$\theta = T - T_\infty \quad \phi = (1/\nu)\int_0^x U(\xi)d\xi$$

$$\varphi = \psi/\nu(2\phi)^{1/2} \quad z = tU/x$$

Here ψ is the stream function; ν is the kinematic viscosity; Pr is the Prandtl number. In the case of a power law free-stream velocity $U \sim x^m$ the terms $2\phi\nu/Ux$ and $2\phi\nu/U^2(dU/dx)$ depend only on exponent m, while $\phi(\partial\theta/\partial\phi) = x(\partial\theta/\partial x)/(m+1)$. Equation (2) becomes

$$[2/(m+1)][(U/u) + (m-1)z](\partial\theta/\partial z) + [2/(m+1)]x(\partial\theta/\partial x) - \varphi(\partial\theta/\partial\varphi) - (1/\mathrm{Pr})\partial[(u/U)(\partial\theta/\partial\varphi)]/\partial\varphi = 0 \quad (3)$$

$$z < 0 \quad \theta = \theta_w = \text{const}; \quad z > 0 \quad \varphi = 0 \quad \theta = \theta_w(z, x); \quad \varphi \to \infty \quad \theta \to 0 \quad (4)$$

The solution of this equation can be presented in series:

$$\theta = \sum_{k=0}^{\infty}\sum_{i=0}^{\infty} G_{ki}(z, \varphi)(x^{k+i}/U^i)(\partial^{k+i}\theta/\partial x^k \partial t^i) = G_{00}\theta_w + G_{10}x(\partial\theta_w/\partial x) + G_{01}(x/U)(\partial\theta_w/\partial t) + G_{20}x^2(\partial^2\theta_w/\partial x^2) + G_{02}(x/U)^2(\partial^2\theta_w/\partial t^2) + G_{11}(x^2/U)(\partial^2\theta_w/\partial x\partial t) + \ldots \quad (5)$$

By substituting this series in Eqs. (3) and (4) one obtains differential equations and initial and boundary conditions that determine the coefficients of the series (5)

$$[2/(m+1)][(U/u) + (m-1)z][\partial G_{ki}/\partial z + G_{k(i-1)}] + [2/(m+1)][(k+i)G_{ki} + G_{(k-1)i}] - \varphi(\partial G_{ki}/\partial\varphi) - (1/\mathrm{Pr})\partial[(u/U)(\partial G_{ki}/\partial\varphi)]/\partial\varphi \quad (6)$$

$$z \le 0 \quad \varphi = 0 \quad G_{00} = 1 \quad G_{ki} = 0\ (k > 0, i > 0); \quad \varphi \to \infty \quad G_{ki} \to 0 \quad (7)$$

For a power law free-stream velocity, the ratio u/U does not depend on variable x. Hence, the coefficients G_{ki} also do not depend on x and are a function only of variables z and φ and parameters m and Pr. The surface heat flux is defined as

$$q_w = -K(\partial T/\partial y)_{y=0} = \sum_{k=0}^{\infty}\sum_{i=0}^{\infty} g_{ki}(z)(x^{k+i}/U^i)(\partial^{k+i}\theta_w/\partial x^k\partial t^i) = h_*[\theta_w + g_{10}x(\partial\theta_w/\partial x) + g_{01}(x/U)(\partial\theta_w/\partial t) + g_{20}x^2(\partial^2\theta_w/\partial x^2) + g_{02}(x/U)^2(\partial^2\theta_w/\partial t^2) + g_{11}(x^2/U)(\partial^2\theta_w/\partial x\partial t) + \ldots] \quad (8)$$

[1] Stamford, CT.

Contributed by the Heat Transfer Division of THE AMERICAN SOCIETY OF MECHANICAL ENGINEERS. Manuscript received by the Heat Transfer Division March 1994; revision received October 1994. Keywords: Forced Convection, Numerical Methods, Transient and Unsteady Heat Transfer. Associate Technical Editor: Y. Jaluria.

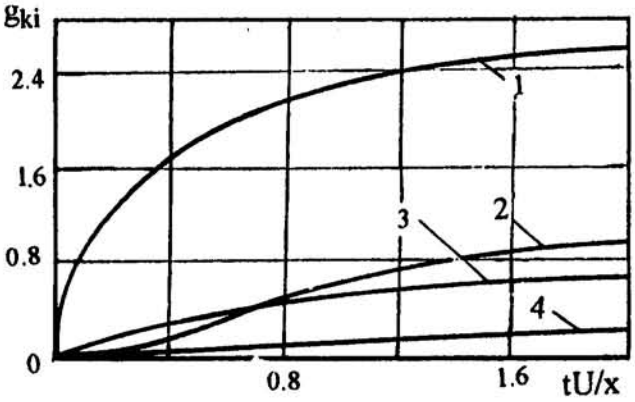

Fig. 1 Coefficients of series (8); $z = tU/x$ = dimensionless time; (1) g_{01}; (2) g_{02}; (3) g_{11}; (4) g_{21}

$$g_{ki} = [(\partial G_{ki}/\partial\varphi)/\partial G_{00}/\partial\varphi)]_{\varphi=0}$$

$$h_* = q_{w*}/\theta_w = -[K(u)_{\varphi=0}/\nu(2\phi)^{1/2}][\partial G_{00}/\partial\varphi]_{\varphi=0}$$

h is the heat transfer coefficient; * refers to isothermal surface; K is thermal conductivity.

Equation (6) under conditions (7) was solved numerically by using the finite difference method. For the flat plate (U = const) and Pr = 1, some coefficients are given in Fig. 1. In time, after the beginning of the process they attain the values of $(g_{ki})_{z\to\infty}$ that coincide with those obtained by Sparrow (1958) without the initial conditions. The ratio $g_{ki}(z)/(g_{ki})_{z\to\infty}$ is about 0.99 when $z = tU/x = 2.4$. Thus, for $z > 2.4$ the coefficients g_{ki} dose not depend on time practically. To obtain satisfactory results, one can apply only several terms of series because the coefficients $g_{ki}(z)$ decrease rapidly with the value (ki). If the surface temperature depends on the coordinate only, one assigns $i = 0$. Then, the expressions (5) and (8) become a proper form of the steady-state case solution for which the coefficients are: $g_{10} = 0.623$; $g_{20} = -0.135$; $g_{30} = 0.030$; $g_{40} = -0.006$.

In some cases the use of solution in the form of series presents difficulties because they contains the sequence of derivatives: in particular, when the function $\theta_w(t, x)$ is given in graphic or numerical form. The solution (8) can be presented in the integral form

$$q_w = h_*\Big[\theta_w(t, 0) + \int_0^x f(\xi/x, 0, z)(\partial\theta_w/\partial\xi)d\xi + \int_0^t f(0, \eta/t, z)(\partial\theta_w/\partial\eta)d\eta + \int_0^t d\eta\int_0^x f(\xi/x, \eta/t, z)(\partial^2\theta_w/\partial\xi\partial\eta)d\xi \quad (9)$$

Here $f(\xi/x, \eta/t, z)$ is an influence function of unheated zone for nonsteady heat transfer that depends on the integration variables ξ/x and η/t and dimensionless time $z = tU/x$. It can be shown by repeated integration by parts that expression (9) is identical with series (8). The procedure of the proof of that is like the one applied for the case of steady-state heat transfer (Dorfman, 1973). The relationship between the function of unheated zone and coefficients of series (8) is given by

$$g_{ki}(z) = [(-1)^{k+i+1}/(k-1)!(i-1)!]\int_0^z (z-\sigma)^{i-1} \times \int_0^1 (1-\zeta)^{k-1} f(\zeta, \sigma/z, z)d\zeta d\sigma;\ (\zeta = \xi/x;\ \sigma = \eta/t)$$

Effect of the Variable Surface Temperature

It is easy to obtain from Eq. (8)

$$h/h_* = 1 + g_{10}(x/\theta_w)(\partial\theta_w/\partial x) + g_{01}(xU/\theta_w)(\partial\theta_w/\partial t) + g_{20}(x^2/\theta_w)(\partial^2\theta_w/\partial x^2) + g_{02}(x^2/U^2\theta_w)(\partial^2\theta_w/\partial t^2) + g_{11}(x^2/U\theta_w)(\partial^2\theta/\partial x\partial t) + \ldots \quad (10)$$

The effect of variable temperature $T_w(x)$ along the surface has been studied by using this series before (Dorfman, 1971). The effect of nonsteady surface temperature $T_w(t)$ is similar. The first coefficients g_{10} and g_{01} are positive. Thus, increasing the temperature difference $\theta_w = T_w - T_\infty$ along the surface or with time ($\partial\theta_w/\partial x > 0$ or $\partial\theta_w/\partial t > 0$) leads to an increase of the heat transfer coefficient h in comparison with h_* for the isothermal surface ($\partial\theta_w/\partial x = \partial\theta_w/\partial t = 0$). Correspondingly, decreasing that difference ($\partial\theta_w/\partial x < 0$ or $\partial\theta_w/\partial t < 0$) leads to a decrease of the heat transfer coefficient. The effect of the second derivatives $\partial^2\theta_w/\partial x^2$ and $\partial^2\theta_w/\partial t^2$ is contrary because the coefficients g_{20} and g_{02} are negative. The other coefficients g_{k0} and g_{0i} are positive for odd and negative for even values, while g_{ki} are positive if $(k + i)$ is odd and negative if $(k + i)$ is even. According to the sign of the coefficients g_{ki}, the derivatives of higher order influence the intensity of heat transfer like the first or the second derivative. If the order of the derivatives does not increase too quickly, the total result is usually like the effect of the first derivative because the first coefficients g_{10} and g_{01} are significantly higher than the others. If the derivatives with respect to time and coordinate are equal, the effect of nonsteady surface temperature is higher than that of nonuniform surface temperature because coefficients g_{0i} are larger than coefficients g_{k0}. In particular, $g_{01}/g_{10} \approx 4$ when $z > 2.4$.

For the polynomial surface temperature distribution, series (5), (8), and (10) become a closed-form solution because all derivatives of order higher than n equal zero for a polynomial of degree n. In particular, for a linear decrease of the temperature difference with time $\theta_w = a_0 - a_1 t$, all derivatives except the first one equal zero. Equations (8) and (10) give

$$q_w/h_*a_0 = 1 - (a_1/a_0)[t - g_{01}(z)x/U]$$

$$h/h_* = 1 - [g_{01}(z)(a_1/a_0)x]/U[1 - (a_1/a_0)t]$$

Figure 2 presented the data for this case. The surface heat flux depends not only on time but on the coordinate x also, despite the fact that the surface temperature depends only on time. It follows from Eq. (8) that it is always true for nonsteady heat transfer because terms with derivatives respect to time depend on coordinate x. In this case, the inversion of heat flux occurs. The temperature difference is not zero at the points $Z = tU/L = 0.4(x/L = 0.25)$ and $Z = 1.4(x/L = 1)$ (L is the plate length) where the heat flux becomes zero. Hence, the heat transfer coefficient becomes zero. Correspondingly, the heat flux is not zero at the point $Z = 2$ where the temperature difference becomes zero for which the heat transfer coefficient becomes infinite. For $Z > 2$ the heat flux becomes negative. The physics of the inversion is explained by the inertial properties of flow (Eckert and Drake, 1959).

Validity of Quasi-Steady Approximation

Consider the symmetric flow past a flat plate with variable surface temperature $T(t)$. After integration across the plate, the heat conduction equation becomes the form

$$(1/\alpha_w)(\partial T_{avg}/\partial t) - \partial^2 T_{avg}/\partial x^2 + (1/K_w\Delta)q_w = 0$$

where 2Δ is the plate thickness, T_{avg} is the average across the plate temperature. Substituting Eq. (8) for q_w, one obtains

$$(1/\alpha_w)(\partial T_{avg}/\partial t) - \partial^2 T_{avg}/\partial x^2 + (h_*/K_w\Delta)[T_w - T_\infty + g_{01}(x/U)(\partial T_w/\partial t) + \ldots] = 0$$

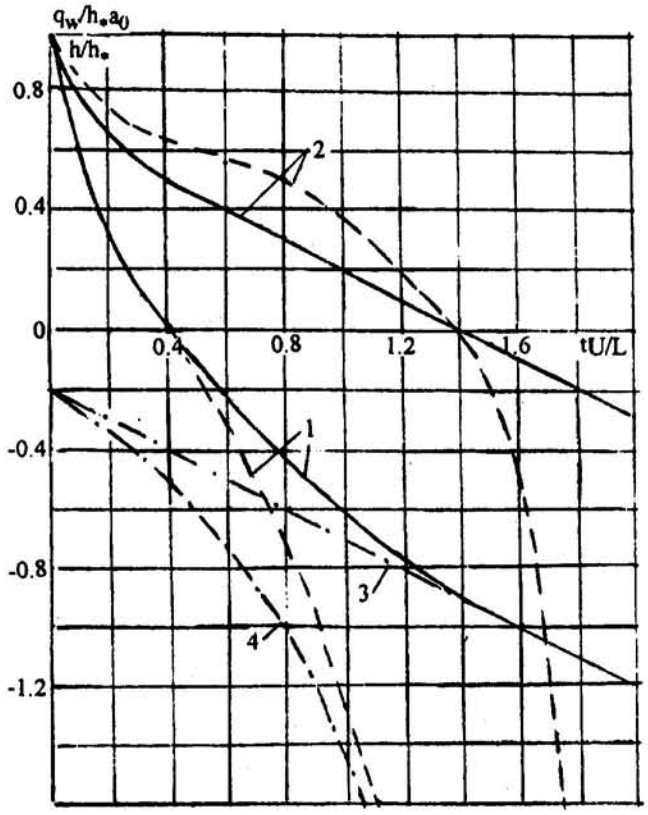

Fig. 2 Variation in surface heat flux and heat transfer coefficient for the case of linear decrease of the surface temperature difference $T_w - T_\infty = a_0 - a_1 t$, exact closed-form solution; $a_1 L/a_0 U = 0.5$; (1) $x/L = 1$; (2) $x/L = 0.25$; $q_w/h_* a_0$—solid curves; h/h_*—dashed curves; (3), (4) solution that does not satisfy the initial conditions (Sparrow, 1958); (3) $q_w/h_* a_0$; (4) h/h_*

The quasi-steady approximation is applicable when the last term in the brackets is small in comparison with the first term of this equation

$$(1/\alpha_w)(\partial T_{avg}/\partial t) \gg g_{01}(h_* x/K_w U\Delta)(\partial T_w/\partial t) \quad (11)$$

If both temperature gradients are close to $\partial T_{avg}/\partial t \approx \partial T_w/\partial t$, the inequality (11) becomes

$$g_{01}(\alpha_w/\alpha) \ll \mathrm{Pe}(\Delta/L)(K_w/h_* x) \quad (12)$$

Here $\mathrm{Pe} = UL/\alpha$ is the Peclet number. At the start the surface temperature of the plate changes faster than the average one, i.e., $\partial T_{avg}/\partial t < \partial T_w/\partial t$. Hence, the inequality (11) is usually not valid. Thus, the quasi-steady approximation cannot be used at the first time after the beginning of the process. As time passes, the plate heats up, and the condition $\partial T_{avg}/\partial t \approx \partial T_w/\partial t$ becomes valid. In that case, to apply the quasi-steady approximation one needs to check only the inequality (12). This inequality is mostly satisfied for the boundary layer problems since the Peclet number is usually high. However, high Peclet number may fail if the ratio Δ/L is small and (or) the Biot number $\sqrt{\mathrm{Bi}} = h_* x/K_w$ is high. It follows from the inequality (12) in the form $g_{01}(\rho c/\rho_w c_w) \ll \mathrm{Pe}(\Delta/L)(K/x h_*)$, where ρ is the density, c is the specific heat.

References

Chapmen, P. R., and Rubesin H. W., 1949, "Temperature and Velocity Profiles in Compressible Laminar Boundary Layer with Arbitrary Distribution of Surface Temperature," *Journal of Aeronautical Science,* Vol. 16, pp. 547–565.

Dorfman, A. Sh., 1971, "Exact Solution of Thermal Boundary Layer Equation for Arbitrary Surface Temperature Distribution," *Teplofizika Vysokikh Temperatur,* Vol. 9, pp. 955–964 (transl., 1971, *High Temperature,* Vol. 9).

Dorfman, A. Sh., 1973, "Influence Function of the Nonheated Zone and the Relation Between the Method of Superposition and of Series Expansion of Solution in Shape Parameters," *Teplofizika Vysokikh Temperatur,* Vol. 11, pp. 99–105 (transl., 1973, *High Temperature,* Vol. 11).

Eckert, E. R. G., and Drake, R. M., 1959, *Heat and Mass Transfer,* McGraw-Hill, New York.

Levy, S., 1952, "Heat Transfer to Constant Property Laminar Boundary Layers Flows With Powerfunction Free-Stream Velocity and Temperature Variation," *Journal of Aeronautical Science,* Vol. 19, pp. 341–348.

Pohlhausen, E., 1921, "Der Warmeaustausch zwischen Festen Korpern und Flussigkeiten mit Kleiner Warmeleitung," *ZAAM,* Vol. 1, p. 115.

Sparrow, E. M., 1958, "Combined Effects of Unsteady Flight Velocity and Surface Temperature on Heat Transfer," *Jet Propulsion,* Vol. 28, pp. 403–405.

Heat Transfer From a Flat Plate to a Fully Developed Axisymmetric Impinging Jet

D. Lee,[1] R. Greif,[2] S. J. Lee,[3] and J. H. Lee[3]

Introduction

Impinging jets have been used in a number of applications to enhance heat and mass transfer; this includes cooling steel plates, the tempering of glass, drying papers and films, cooling turbine blades, cooling electronic components, etc. Studies have included the effects of Reynolds number, nozzle-to-plate distance, nozzle geometry, jet temperature, orientation, multiple jets, crossflow, and impinging surface shape on the resulting flow and heat transfer. Critical reviews of impinging jet heat transfer studies have been published. Martin (1977), Jambunathan et al. (1992), and Viskanta (1993) reviewed the heat transfer data for single jets and for arrays of axisymmetric and planar jets. Heat transfer measurements for various nozzle geometries and flow conditions have been made by Gardon and Akfirat (1965), Chia et al. (1977), Hrycak (1983), Gundappa et al. (1989), and more recently by Lee et al. (1994). Lee et al. (1994) studied the heat transfer characteristics for a turbulent air jet issuing from an elliptical nozzle. Kataoka (1987) studied the surface renewal effect of large scale eddies on the heat transfer augmentation at the stagnation point. Striegl and Diller (1984), Hollworth and Gero (1985), and Baughn et al. (1991) studied the effects of jet entrainment temperature on the heat transfer. Liquid crystals have been used in impinging jet heat transfer studies by Hoogendoorn (1977), Goldstein and Timmer (1982), Goldstein and Franchett (1988), Baughn and Shimizu (1989), Yan et al. (1992), and Lee et al. (1994). Baughn and Shimizu (1989) and Yan et al. (1992) made heat transfer measurements for a fully developed air jet impinging on a flat plate. The results of Yan et al. (1992) that utilized the preheated-wall transient method are in good agreement with those of the steady-state measurements by Baughn and Shimizu (1989). The present experimental conditions are similar to

[1] Department of Mechanical Engineering, Inje University, 607 Obang-Dong, Kimhae, Kyongnam, 621-749, Korea.

[2] Department of Mechanical Engineering, University of California at Berkeley, Berkeley, CA 94720.

[3] Advanced Fluids Engineering Research Center, Department of Mechanical Engineering, Pohang University of Science and Technology, Pohang, Korea.

Contributed by the Heat Transfer Division and presented at the ASME Winter Annual Meeting, New Orleans, Louisiana, November 28–December 3, 1993. Manuscript received by the Heat Transfer Division January 1994; revision received November 1994. Keywords: Augmentation, Forced Convection, Jets. Associate Technical Editor: T. W. Simon.

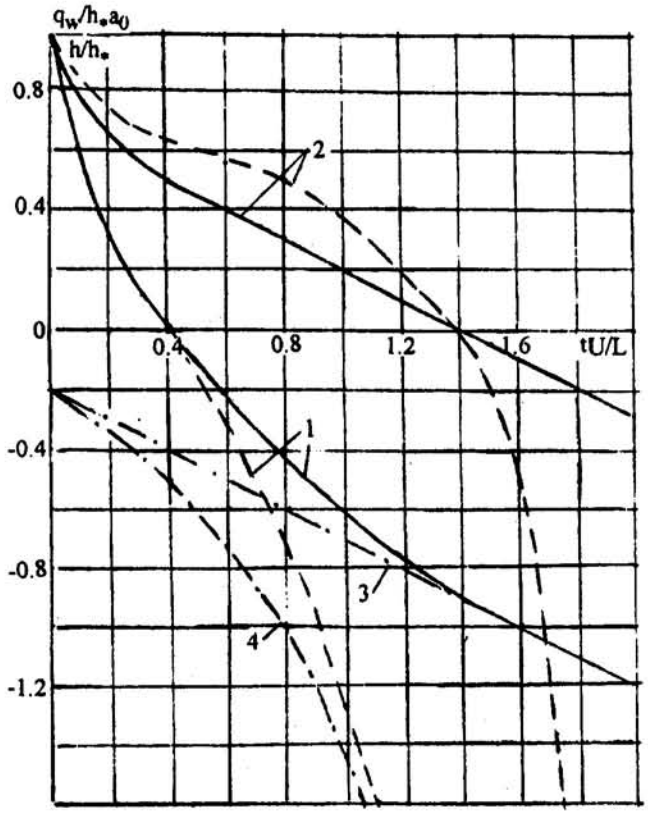

Fig. 2 Variation in surface heat flux and heat transfer coefficient for the case of linear decrease of the surface temperature difference $T_w - T_\infty = a_0 - a_1 t$, exact closed-form solution; $a_1 L/a_0 U = 0.5$; (1) $x/L = 1$; (2) $x/L = 0.25$; $q_w/h_* a_0$—solid curves; h/h_*—dashed curves; (3), (4) solution that does not satisfy the initial conditions (Sparrow, 1958); (3) $q_w/h_* a_0$; (4) h/h_*

The quasi-steady approximation is applicable when the last term in the brackets is small in comparison with the first term of this equation

$$(1/\alpha_w)(\partial T_{avg}/\partial t) \gg g_{01}(h_* x/K_w U\Delta)(\partial T_w/\partial t) \quad (11)$$

If both temperature gradients are close to $\partial T_{avg}/\partial t \approx \partial T_w/\partial t$, the inequality (11) becomes

$$g_{01}(\alpha_w/\alpha) \ll \mathrm{Pe}(\Delta/L)(K_w/h_* x) \quad (12)$$

Here $\mathrm{Pe} = UL/\alpha$ is the Peclet number. At the start the surface temperature of the plate changes faster than the average one, i.e., $\partial T_{avg}/\partial t < \partial T_w/\partial t$. Hence, the inequality (11) is usually not valid. Thus, the quasi-steady approximation cannot be used at the first time after the beginning of the process. As time passes, the plate heats up, and the condition $\partial T_{avg}/\partial t \approx \partial T_w/\partial t$ becomes valid. In that case, to apply the quasi-steady approximation one needs to check only the inequality (12). This inequality is mostly satisfied for the boundary layer problems since the Peclet number is usually high. However, high Peclet number may fail if the ratio Δ/L is small and (or) the Biot number $\sqrt{\mathrm{Bi}} = h_* x/K_w$ is high. It follows from the inequality (12) in the form $g_{01}(\rho c/\rho_w c_w) \ll \mathrm{Pe}(\Delta/L)(K/x h_*)$, where ρ is the density, c is the specific heat.

References

Chapmen, P. R., and Rubesin H. W., 1949, "Temperature and Velocity Profiles in Compressible Laminar Boundary Layer with Arbitrary Distribution of Surface Temperature," *Journal of Aeronautical Science,* Vol. 16, pp. 547–565.

Dorfman, A. Sh., 1971, "Exact Solution of Thermal Boundary Layer Equation for Arbitrary Surface Temperature Distribution," *Teplofizika Vysokikh Temperatur,* Vol. 9, pp. 955–964 (transl., 1971, *High Temperature,* Vol. 9).

Dorfman, A. Sh., 1973, "Influence Function of the Nonheated Zone and the Relation Between the Method of Superposition and of Series Expansion of Solution in Shape Parameters," *Teplofizika Vysokikh Temperatur,* Vol. 11, pp. 99–105 (transl., 1973, *High Temperature,* Vol. 11).

Eckert, E. R. G., and Drake, R. M., 1959, *Heat and Mass Transfer,* McGraw-Hill, New York.

Levy, S., 1952, "Heat Transfer to Constant Property Laminar Boundary Layers Flows With Powerfunction Free-Stream Velocity and Temperature Variation," *Journal of Aeronautical Science,* Vol. 19, pp. 341–348.

Pohlhausen, E., 1921, "Der Warmeaustausch zwischen Festen Korpern und Flussigkeiten mit Kleiner Warmeleitung," *ZAAM,* Vol. 1, p. 115.

Sparrow, E. M., 1958, "Combined Effects of Unsteady Flight Velocity and Surface Temperature on Heat Transfer," *Jet Propulsion,* Vol. 28, pp. 403–405.

Heat Transfer From a Flat Plate to a Fully Developed Axisymmetric Impinging Jet

D. Lee,[1] R. Greif,[2] S. J. Lee,[3] and J. H. Lee[3]

Introduction

Impinging jets have been used in a number of applications to enhance heat and mass transfer; this includes cooling steel plates, the tempering of glass, drying papers and films, cooling turbine blades, cooling electronic components, etc. Studies have included the effects of Reynolds number, nozzle-to-plate distance, nozzle geometry, jet temperature, orientation, multiple jets, crossflow, and impinging surface shape on the resulting flow and heat transfer. Critical reviews of impinging jet heat transfer studies have been published. Martin (1977), Jambunathan et al. (1992), and Viskanta (1993) reviewed the heat transfer data for single jets and for arrays of axisymmetric and planar jets. Heat transfer measurements for various nozzle geometries and flow conditions have been made by Gardon and Akfirat (1965), Chia et al. (1977), Hrycak (1983), Gundappa et al. (1989), and more recently by Lee et al. (1994). Lee et al. (1994) studied the heat transfer characteristics for a turbulent air jet issuing from an elliptical nozzle. Kataoka (1987) studied the surface renewal effect of large scale eddies on the heat transfer augmentation at the stagnation point. Striegl and Diller (1984), Hollworth and Gero (1985), and Baughn et al. (1991) studied the effects of jet entrainment temperature on the heat transfer. Liquid crystals have been used in impinging jet heat transfer studies by Hoogendoorn (1977), Goldstein and Timmer (1982), Goldstein and Franchett (1988), Baughn and Shimizu (1989), Yan et al. (1992), and Lee et al. (1994). Baughn and Shimizu (1989) and Yan et al. (1992) made heat transfer measurements for a fully developed air jet impinging on a flat plate. The results of Yan et al. (1992) that utilized the preheated-wall transient method are in good agreement with those of the steady-state measurements by Baughn and Shimizu (1989). The present experimental conditions are similar to

[1] Department of Mechanical Engineering, Inje University, 607 Obang-Dong, Kimhae, Kyongnam, 621-749, Korea.

[2] Department of Mechanical Engineering, University of California at Berkeley, Berkeley, CA 94720.

[3] Advanced Fluids Engineering Research Center, Department of Mechanical Engineering, Pohang University of Science and Technology, Pohang, Korea.

Contributed by the Heat Transfer Division and presented at the ASME Winter Annual Meeting, New Orleans, Louisiana, November 28–December 3, 1993. Manuscript received by the Heat Transfer Division January 1994; revision received November 1994. Keywords: Augmentation, Forced Convection, Jets. Associate Technical Editor: T. W. Simon.

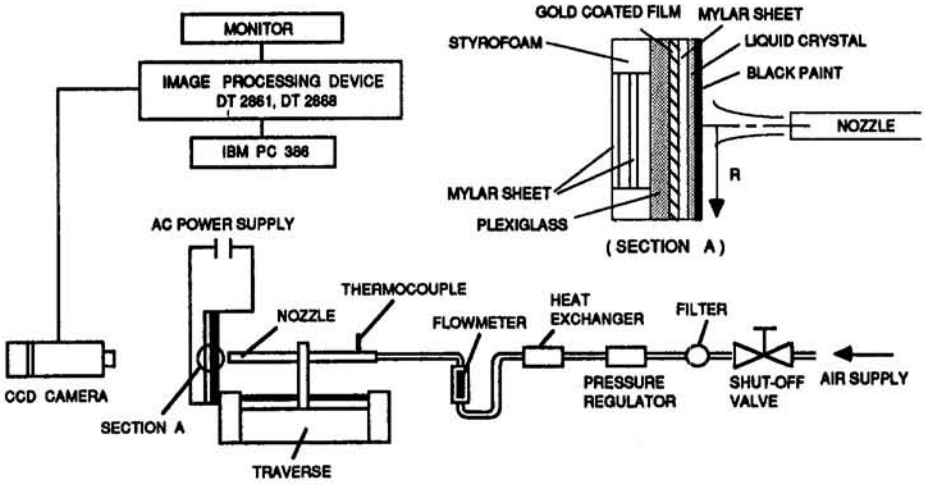

Fig. 1 Schematic diagram of experimental apparatus

those of Yan et al. (1992) except that a steady-state experimental procedure is utilized and the Reynolds number range is from 4000 to 14,400. The present conditions are identical to those of Baughn and Shimizu (1989) except that their experiments were done at a higher Reynolds number (Re = 23,750). Faggiani and Grass (1990) and Huang (1963) carried out experiments over the present Reynolds number range for different boundary conditions. The present work is for an ambient air jet with a fully developed velocity profile and with a uniform wall heat flux thermal boundary.

Apparatus and Measurement Technique

Figure 1 is a schematic diagram of the test apparatus previously utilized by Lee et al. (1993, 1994), which is very similar to the one used by Baughn and Shimizu (1989). The apparatus consists of a compressed air system, a long pipe, and an impinging surface. The development length/diameter ratio of 55 results in a fully developed flow at the nozzle exit. The impinging surface is a clear Plexiglas plate to which a sheet of Intrex (a gold-coated polyester substrate) is glued. An air brush is used to apply first the micro-encapsulated thermochromic liquid crystal and then black backing paint on the Intrex surface. The measurement technique in this study, described by Baughn et al. (1989), Baughn and Shimizu (1989) and Lee et al. (1993, 1994), provides a method for determining surface isotherms using liquid crystals. By electrically heating a very thin gold coating on the Intrex, an essentially uniform wall heat flux condition is established. The heat flux can be adjusted by changing the current through the Intrex, which changes the surface temperature. Under the constant heat flux condition, an isotherm on the Intrex surface corresponds to a contour of a constant heat transfer coefficient. As the heat flux changes, the position of the color isotherm is also moved. The local heat transfer coefficient at the position of the particular color being observed is calculated from

$$h = q_v/(T_w - T_j) \tag{1}$$

where T_w and T_j are the wall and jet temperatures, respectively; q_v is the net heat flux, which is obtained by subtracting the heat losses from the total heat flux through the Intrex; i.e.,

$$q_v = fIV/A - \epsilon\sigma(T_w^4 - T_a^4) - q_c \tag{2}$$

The ratio of the local electrical heating to the average heating, f, is a measure of the uniformity of the gold coating. Baughn et al. (1989) found the uniformity to be as high as 98 percent when the test section of Intrex is small and selected from the middle of a roll where the gold coating is most uniform. This has been the case for the present experiment. Therefore, we assume $f \approx 1$ for the heat flux calculation, but f is maintained in Eq. (2) because it contributes to the overall uncertainty (see Table 1). The conduction loss from the back of the plate, q_c, is small relative to the surface heating and is assumed to be zero. However, it is included in the equation because it also contributes to the overall uncertainty. The variables I, V, A, ϵ, σ, T_a are the current across the Intrex, voltage across the Intrex, surface area of the Intrex, emissivity of black paint on the front

Table 1 Nusselt number uncertainty analysis

x_i	Value	δx_i	$\left(\frac{\delta x_i}{\mathrm{Nu}}\frac{\partial \mathrm{Nu}}{\partial x_i}\right) \times 100$ (%)
T_w	35.2 (°C)	0.15	2.76
f	1.0	0.02	2.03
q_c	0 (W/m^2)	24.8	1.90
T_j	22.16 (°C)	0.10	1.84
A	0.0361 (m^2)	0.000181	1.20
ϵ	0.9	0.1	0.63
D	10.85 (mm)	0.05	0.44
I	1.48 (A)	0.0628	0.43
V	32.16 (V)	0.0965	0.30

Nu uncertainty: δ Nu/Nu = 4.6 percent

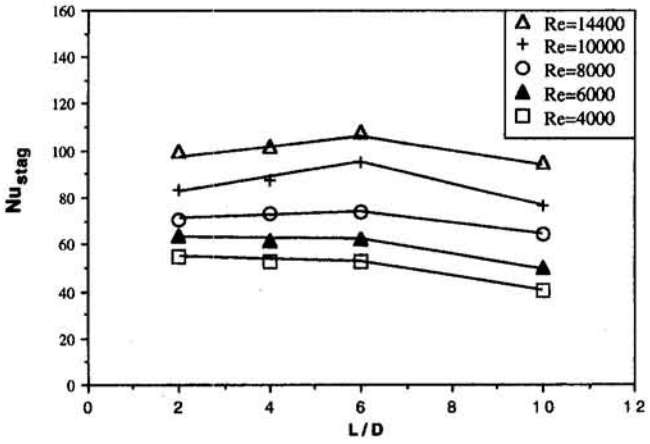

Fig. 2 Effect of the nozzle-to-plate distance on the stagnation point Nusselt number for different jet Reynolds numbers

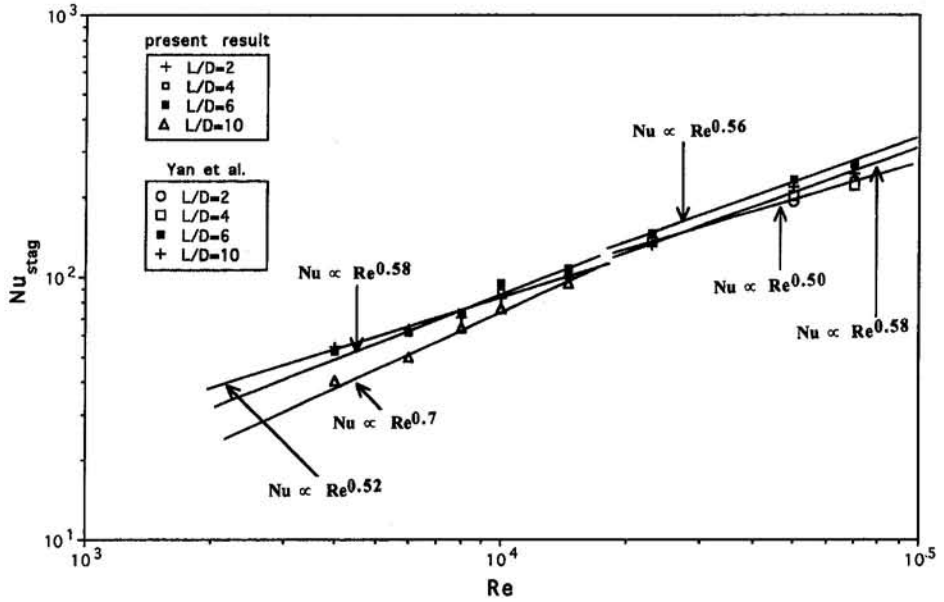

Fig. 3 Variation of the stagnation point Nusselt number with jet Reynolds number for different nozzle-to-plate distances

surface of the plate, Stefan–Boltzmann constant, and ambient temperature, respectively.

The uncertainty analysis has been carried out using the method of Kline and McKlintock (1953). It is shown in Table 1 that the uncertainty in the Nusselt number for $L/D = 4$ and $r/D = 0.88$ at Re = 4000 is 4.6 percent. The uncertainty in the liquid crystal measurement of the wall temperature is the largest contribution to the uncertainty. Another important source of uncertainty is the gold coating uniformity factor, f.

Results and Discussion

Heat Transfer at the Stagnation Point. The variation of the stagnation point Nusselt number, $Nu_{stag} = h_{stag}D/k$, with nozzle-to-plate distance, L/D, is shown in Fig. 2 for different jet Reynolds numbers, $Re = UD/\nu$. There is only a small variation of Nu_{stag} with L/D for $L/D < 6$ and $Re < 8000$. Faggiani and Grassi (1990) investigated the heat transfer for a submerged liquid jet with a uniform velocity profile and also found that Nu_{stag} is nearly independent of L/D for $L/D < 6$ and $Re < 9200$. Huang (1963) reported similar behavior for $1000 \leq Re < 10{,}000$ for an axisymmetric hot air jet with a uniform velocity profile. For $Re \geq 8000$, Nu_{stag} is a maximum at $L/D \cong 6$, which agrees with the results of Yan et al. (1992) for a fully developed impinging air jet for Reynolds numbers over a range from 23,000 to 70,000. Lee et al. (1993) and Kataoka et al. (1987) show that the turbulent intensity reaches a maximum near $L/D = 7$, which corresponds approximately to the location for the maximum value for Nu_{stag}. The variation of Nu_{stag} with Re is shown in Fig. 3 for different nozzle-to-plate distances. The present results are used for low Reynolds numbers ranging from 4000 to 14,000 and the results from Yan et al. (1992) for high Reynolds numbers ranging from 4000 to 14,000 and the results from Yan et al. (1992) for high Reynolds numbers ranging from 23,000 to 70,000. For $L/D = 2$ and 4, the Nusselt numbers at the stagnation point vary according to $Nu_{stag} \propto Re^{0.52}$ and $Nu_{stag} \propto Re^{0.5}$ for the present study and Yan et al., respectively, which agrees closely with the $Re^{0.5}$ laminar boundary flow result. For larger distances the Reynolds number dependence is stronger ($Nu_{stag} \propto Re^{0.58}$ and $Re^{0.7}$ for the present study, and $Nu_{stag} \propto Re^{0.56}$ and $Re^{0.58}$ for Yan et al. for $L/D = 6$ and 10, respectively). Hollworth and Gero (1985) have reported similar results with values of the exponents over the range from 0.65 to 0.80 depending on L/D.

A comparison of the variation of Nu_{stag} with Re between the fully developed velocity profile jet (present results) and the uniform velocity profile jet (Gardon and Akfirat, 1965) is shown in Fig. 4 for $L/D = 2$. The present results are 10–20 percent higher for Nu_{stag}, which is attributed to the higher velocity gradient and turbulent intensity for the fully developed jet. This behavior agrees with the results of Pan et al. (1992) for the variation of Nu_{stag} with respect to Re for four nozzle configurations (sharp-edged orifice without screens, sharp-edged orifice with screens, fully developed pipe nozzle, and contoured orifice) for a nozzle-to-plate distance of $L/D = 1$. They report that the jet issuing from the fully developed pipe nozzle yields values of Nu_{stag} that are approximately 10 percent higher at Re = 16,600 than for the contoured orifice jet.

Local Heat Transfer. The local Nusselt number radial distributions divided by Re^n are presented in Figs. 5–8 for four nozzle-to-plate distances with $n = 0.52$, 0.52, 0.58, and 0.7 for $L/D = 2$, 4, 6, and 10, respectively, and six jet Reynolds numbers from 4000 to 14,400. These results show that in the region near the stagnation point ($r/D < 1.5 - 2$) the Nusselt number distributions reduce to one curve. However, in the wall jet re-

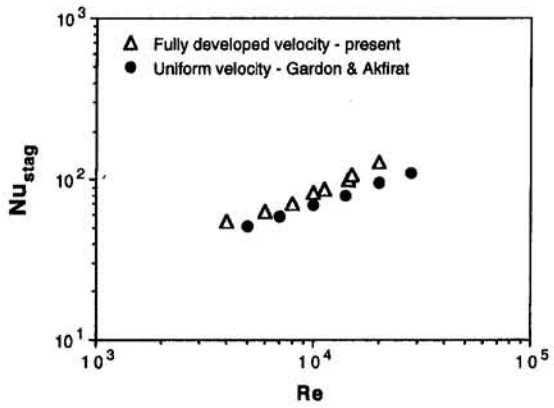

Fig. 4 Comparison of the stagnation point Nusselt number for $L/D = 2$

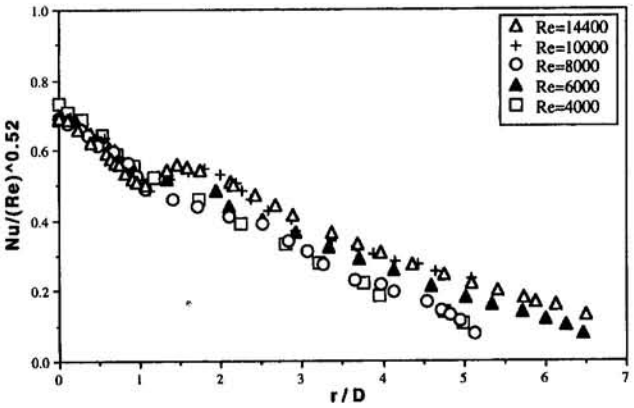

Fig. 5 Radial distributions of the local Nusselt number for $L/D = 2$

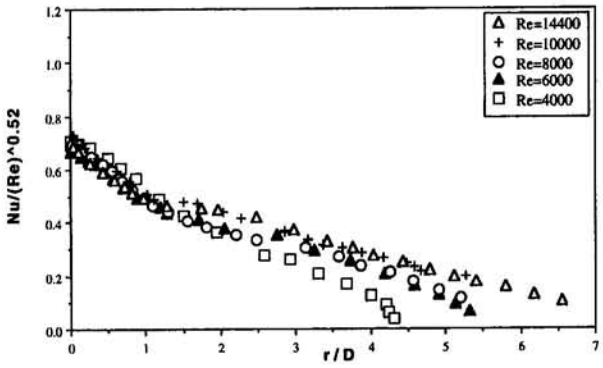

Fig. 6 Radial distributions of the local Nusselt number for $L/D = 4$

gion ($r/D \geq 2$) the local values of Nu/Re^n vary with the Reynolds number; this dependence is attributed to the transition from a laminar to a turbulent boundary layer in the wall jet region. Similar results were reported by Yan et al. (1992) and Hollworth and Gero (1985). Yan et al. (1992) reported $n = 0.5$ for the stagnation region ($r/D < 1.5$) for $L/D = 2$ and 4, and $n = 0.56$ for $L/D = 6$ and $n = 0.58$ for $L/D = 10$ (see Fig. 3); for the wall jet region ($r/D \geq 2$) $n = 0.7$ for all L/D. Hollworth and Gero (1985) studied the heat transfer for the jet issuing from a square-edged orifice for Reynolds numbers from 5000 to 60,000. Their results show $n = 0.65$, 0.76, 0.79, and 0.8 at $r/D = 0$, 3, 6, and 9, respectively, for one nozzle-to-plate distance, $L/D = 5$. They also indicated that similar results were obtained for cases with different L/D. They attribute the larger values of n than are predicted by laminar boundary layer theory to an increase in the turbulence in the approaching jet. This is a result of the stronger exchange of momentum with the surrounding ambient air, which increases the transport in the otherwise laminar boundary layer in the stagnation region.

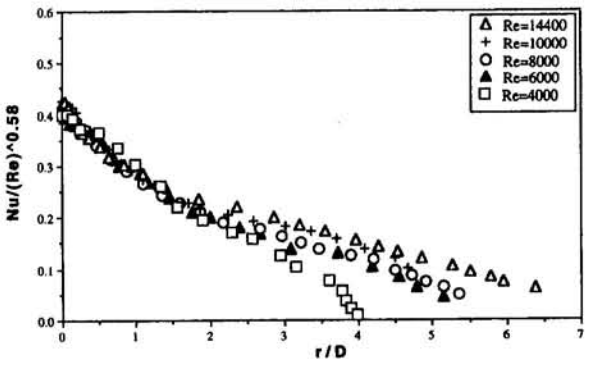

Fig. 7 Radial distributions of the local Nusselt number for $L/D = 6$

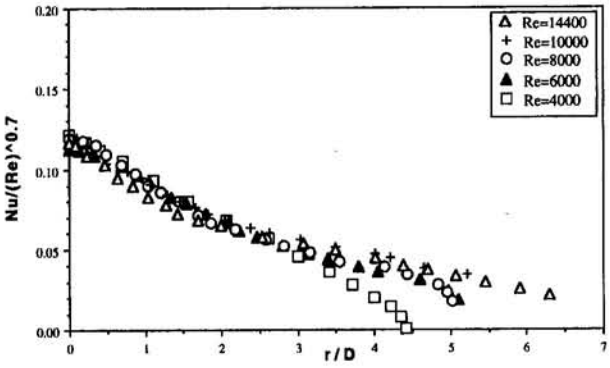

Fig. 8 Radial distributions of the local Nusselt number for $L/D = 10$

Figures 5–8 show that for Reynolds numbers from 4000 to 8000, the local Nusselt number decreases monotonically from its maximum value at the stagnation point. However, for Re = 10,000 and 14,400, and $L/D = 2$, the local Nusselt numbers begin to increase with radial distance near $r/D = 1$, and attain secondary maxima at $r/D \cong 1.5$. Secondary maxima have also been reported by Yan et al. (1992) at $r/D \cong 2$ for $L/D = 2$ and $23{,}000 \leq Re \leq 70{,}000$, and by Martin (1977) at $1.5 \leq r/D \leq 2$ for $L/D = 2.5$ and $2500 \leq Re \leq 375{,}000$. The formation of the secondary maximum is attributed to the increased transport resulting from the transition from a laminar to a turbulent boundary layer. Yan et al. (1992) reported that as the Reynolds number increases from 23,000 to 70,000 the value of the Nusselt number at the secondary maximum approaches that of the Nusselt number at the stagnation point. Martin (1977) reported that for higher Reynolds numbers the secondary maximum exceeds the stagnation point Nusselt number. The heat transfer results for $L/D = 4$, shown in Fig. 6, exhibit changes in slope at $r/D \cong 1.5$ for Re = 10,000 and 14,400 (but secondary maxima do not result as occurs for the $L/D = 2$ case). Chia et al. (1977) reported that for Re = 34,000 the nozzle-to-plate distance threshold for a secondary maximum to occur for the Nusselt number is between $L/D = 5$ and $L/D = 6$.

Acknowledgments

The authors wish to express their appreciation to the Pohang University of Science and Technology, Advanced Fluids Engineering Research Center for the support of this research.

References

Baughn, J. W., Ireland, P. T., Jones, T. V., and Saniei, N., 1989, "A Comparison of the Transient and Heated-Coating Methods for the Measurements of the Local Heat Transfer Coefficients on a Pin Fin," ASME JOURNAL OF HEAT TRANSFER, Vol. 111, pp. 877–881.

Baughn, J. W., and Shimizu, S., 1989, "Heat Transfer Measurement From a Surface With Uniform Heat Flux and an Impinging Jet," ASME JOURNAL OF HEAT TRANSFER, Vol. 111, pp. 1096–1098.

Baughn, J. W., Hechanova, T. E., and Yan, X., 1991, "An Experimental Study on Entrainment Effects on the Heat Transfer From a Flat Surface to a Heated Circular Impinging Jet," ASME JOURNAL OF HEAT TRANSFER, Vol. 113, pp. 1023–1025.

Chia, C., Giralt, F., and Trass, O., 1977, "Mass Transfer in Axisymmetric Turbulent Impinging Jet," *Industrial and Engineering Chemistry Fundamentals*, Vol. 16, pp. 28–35.

Faggiani, S., and Grassi, W., 1990, "Impinging Liquid Jets on Heated Surface," *Proceedings of 9th International Heat Transfer Conference*, Vol. 1, pp. 275–285.

Gardon, R., and Akfirat, J. C., 1965, "The Role of Turbulence in Determining the Heat Transfer Characteristics of Impinging Jets," *International Journal of Heat and Mass Transfer*, Vol. 8, pp. 1261–1272.

Goldstein, R. J., and Timmer, J. F., 1982, "Visualization of Heat Transfer From Arrays of Impinging Jets," *International Journal of Heat and Mass Transfer*, Vol. 125, pp. 1857–1868.

Goldstein, R. J., and Franchett, M. E., 1988, "Heat Transfer From a Flat Surface to an Oblique Impinging Jet," ASME JOURNAL OF HEAT TRANSFER, Vol. 110, pp. 84–90.

Gundappa, M., Hudson, J. F., and Diller, T. E., 1989, "Jet Impingement Heat Transfer From Jet Tubes and Orifices," *National Heat Transfer Conference*, ASME HTD-Vol. 107, pp. 43–50.

Hollworth, B. R., and Gero, L. R., 1985, "Entrainment Effects on Impingement Heat Transfer: Part II—Local Heat Transfer Measurements," ASME JOURNAL OF HEAT TRANSFER, Vol. 107, pp. 910–915.

Hoogendoorn, C. J., 1977, "The Effect of Turbulence on Heat Transfer at Stagnation Point," *International Journal of Heat and Mass Transfer*, Vol. 20, pp. 1333–1338.

Hrycak, P., 1983, "Heat Transfer From Round Impinging Jets to a Flat Plate," *International Journal of Heat and Mass Transfer*, Vol. 26, pp. 1857–1865.

Huang, C. C., 1963, "Investigation of Heat Transfer Coefficients for Air Flow Through Round Jets Impinging Normal to a Heat Transfer Surface," ASME JOURNAL OF HEAT TRANSFER, Vol. 85, pp. 237–245.

Jambunathan, K., Lai, E., Moss, M. A., and Button, B. L., 1992, "A Review of Heat Transfer Data for Single Circular Jet Impingement," *International Journal of Heat and Fluid Flow*, Vol. 13, No. 2, pp. 106–115.

Kataoka, K., Suguro, M., Degawa, K., Maruo, K., and Mihata, I., 1987, "The Effect of Surface Renewal Due to a Large-Scale Eddies on Jet Impingement Heat Transfer," *International Journal of Heat and Mass Transfer*, Vol. 30, pp. 559–567.

Kline, S. J., and McKlintock, F. A., 1953, "Describing Uncertainties in Single Sample Experiments," *Mechanical Engineering*, Vol. 75, Jan., pp. 3–8.

Lee, S. J., Lee, J. H., Lee, D., and Greif, R., 1993, "Heat Transfer From a Surface to a Fully Developed Axisymmetric Impinging Jet," *Enhanced Cooling Techniques for Electronics Applications*, ASME HTD-Vol. 263, pp. 11–18.

Lee, S. J., Lee, J. H., and Lee, D., 1994, "Local Heat Transfer Measurements From an Elliptic Jet Impinging on a Flat Plate Using Liquid Crystal," *International Journal of Heat and Mass Transfer*, Vol. 37, No. 6, pp. 967–976.

Martin, H., 1977, "Heat and Mass Transfer Between Impinging Gas Jets and Solid Surfaces," *Advances in Heat Transfer*, Vol. 13, pp. Academic Press, New York, pp. 1–60.

Pan, Y., Stevens, J., and Webb, B. W., 1992, "Effect of Nozzle Configuration on Transport in the Stagnation Zone of Axisymmetric, Impinging Free Surface Liquid Jets: Part 2—Local Heat Transfer," ASME JOURNAL OF HEAT TRANSFER, Vol. 114, pp. 880–886.

Striegl, S. A., and Diller, T. E., 1984, "An Analysis of the Effect of Entrainment Temperature on Jet Impingement Heat Transfer," ASME JOURNAL OF HEAT TRANSFER, Vol. 106, pp. 804–810.

Viskanta, R., 1993, "Heat Transfer to Impinging Isothermal Gas and Flame Jets," *Experimental Thermal and Fluid Science*, Vol. 6, pp. 111–134.

Yan, X., Baughn, J. W., and Mesbah, M., 1992, "The Effect of Reynolds Number on the Heat Transfer Distribution From a Flat Plate to an Impinging Jet," presented at the ASME Winter Annual Meeting, Anaheim, CA.

Onset of Flow Reversal and Penetration Length of Natural Convective Flow Between Isothermal Vertical Walls

K. D. Kihm,[1,4] J. H. Kim,[2,4] and L. S. Fletcher[3,4]

Nomenclature

b = channel half-spacing
H = channel depth
L = channel height
L_p = penetration length of flow reversal
Nu_b = average Nusselt number based on b
Pr = Prandtl number
R = radius of extended upstream region from the channel entrance
Ra_b = Rayleigh number = $\mathrm{Gr}_b \cdot \mathrm{Pr}$
Ra* = modified Rayleigh number = $\mathrm{Ra}_b \cdot (b/L)$
x, y = coordinate system for physical geometry

Introduction

Thermally driven flows in a vertical heated channel form a basic structure for various heat transfer devices. Typical applications include electronic packaging systems and heat exchangers. Heat transfer characteristics of the flow to and from the channel walls have been studied extensively, with many studies of channel flows available. The onset and penetration lengths of the flow reversals, however, have received only limited attention. The present study of flow reversals occurring in vertical isothermal channels uses a convenient numerical technique with experimental substantiation by means of smoke visualization.

Since the pioneering work of convective heat transfer phenomena in heated vertical channels conducted by Elenbaas (1942), there have been a number of relevant investigations using various analytical, numerical, and experimental techniques. Eckert et al. (1990) presented an extensive review of publications dealing with natural convection in vertical channel flows. Many different aspects of the problem have been identified and investigated, including local and average correlations of heat transfer coefficients, isotherms, and streamlines for narrow or wide channel flows, symmetrically or asymmetrically heated channels, vertical and inclined arrangements and, more recently, parallel and converging channels (Kihm et al., 1993). These aspects have been studied for forced, mixed, and natural convection problems. There are more studies for forced or mixed convection primarily because of their relative simplicity arising from the parabolic nature of the problems. Natural convection problems, however, are generally more cumbersome because of the nontrivial contribution of transverse and axial diffusion effects, i.e., the elliptic nature of the problem.

Sparrow et al. (1984) investigated the flow reversal by visualizing water flows (Pr = 5.0) in a vertical channel heated on one side. They showed that a single dimensionless group, $\mathrm{Ra}_b \cdot (2b/L)$, where $2b$ represents the channel spacing and L is the channel height, correlated their Nusselt number results well. Chang and Lin (1990) presented a numerical simulation of the transient process of flow reversal in a vertical channel with one side heated. They observed that the velocity and temperature wakes above the heated plate were oscillatory when Ra_b was larger than 10^6. Naylor et al. (1991) introduced Jeffrey-Hamel flow for the far-field inlet boundary conditions in their numerical study of flow between isothermal walls. Their elliptic solution identified a flow separation near the channel inlet where the Rayleigh number exceeded a critical value, which resulted in a minimal local Nusselt number. As the study focused on the channel inlet region, the flow reversal occurring near the channel exit was not discussed.

The present paper identifies the occurrence of the onset and penetration lengths of the flow reversal in natural convection flow through vertical isothermal channel walls in terms of the modified Rayleigh number $\mathrm{Ra}^* = \mathrm{Ra}_b \cdot (b/L)$ and the channel aspect ratio L/b (Fig. 1).

Analytical and Numerical Study

The standard elliptic forms of the steady two-dimensional mass, momentum, and energy equations were solved using a finite difference method with a body or boundary-fitted coordinate transformation (BFCT). A comprehensive description of

[1] Associate Professor; Mem. ASME.
[2] Presently at Korea Aerospace Research Institute, Taejon, Korea.
[3] Thomas A. Dietz Professor; Fellow ASME.
[4] Department of Mechanical Engineering, Texas A&M University, College Station, TX 77843-3123.

Contributed by the Heat Transfer Division of THE AMERICAN SOCIETY OF MECHANICAL ENGINEERS. Manuscript received by the Heat Transfer Division October 1994; revision received December 1994. Keywords: Flow Visualization, Natural Convection, Numerical Methods. Associate Technical Editor: R. Viskenta.

Goldstein, R. J., and Timmer, J. F., 1982, "Visualization of Heat Transfer From Arrays of Impinging Jets," *International Journal of Heat and Mass Transfer*, Vol. 125, pp. 1857–1868.

Goldstein, R. J., and Franchett, M. E., 1988, "Heat Transfer From a Flat Surface to an Oblique Impinging Jet," ASME JOURNAL OF HEAT TRANSFER, Vol. 110, pp. 84–90.

Gundappa, M., Hudson, J. F., and Diller, T. E., 1989, "Jet Impingement Heat Transfer From Jet Tubes and Orifices," *National Heat Transfer Conference*, ASME HTD-Vol. 107, pp. 43–50.

Hollworth, B. R., and Gero, L. R., 1985, "Entrainment Effects on Impingement Heat Transfer: Part II—Local Heat Transfer Measurements," ASME JOURNAL OF HEAT TRANSFER, Vol. 107, pp. 910–915.

Hoogendoorn, C. J., 1977, "The Effect of Turbulence on Heat Transfer at Stagnation Point," *International Journal of Heat and Mass Transfer*, Vol. 20, pp. 1333–1338.

Hrycak, P., 1983, "Heat Transfer From Round Impinging Jets to a Flat Plate," *International Journal of Heat and Mass Transfer*, Vol. 26, pp. 1857–1865.

Huang, C. C., 1963, "Investigation of Heat Transfer Coefficients for Air Flow Through Round Jets Impinging Normal to a Heat Transfer Surface," ASME JOURNAL OF HEAT TRANSFER, Vol. 85, pp. 237–245.

Jambunathan, K., Lai, E., Moss, M. A., and Button, B. L., 1992, "A Review of Heat Transfer Data for Single Circular Jet Impingement," *International Journal of Heat and Fluid Flow*, Vol. 13, No. 2, pp. 106–115.

Kataoka, K., Suguro, M., Degawa, K., Maruo, K., and Mihata, I., 1987, "The Effect of Surface Renewal Due to a Large-Scale Eddies on Jet Impingement Heat Transfer," *International Journal of Heat and Mass Transfer*, Vol. 30, pp. 559–567.

Kline, S. J., and McKlintock, F. A., 1953, "Describing Uncertainties in Single Sample Experiments," *Mechanical Engineering*, Vol. 75, Jan., pp. 3–8.

Lee, S. J., Lee, J. H., Lee, D., and Greif, R., 1993, "Heat Transfer From a Surface to a Fully Developed Axisymmetric Impinging Jet," *Enhanced Cooling Techniques for Electronics Applications*, ASME HTD-Vol. 263, pp. 11–18.

Lee, S. J., Lee, J. H., and Lee, D., 1994, "Local Heat Transfer Measurements From an Elliptic Jet Impinging on a Flat Plate Using Liquid Crystal," *International Journal of Heat and Mass Transfer*, Vol. 37, No. 6, pp. 967–976.

Martin, H., 1977, "Heat and Mass Transfer Between Impinging Gas Jets and Solid Surfaces," *Advances in Heat Transfer*, Vol. 13, pp. Academic Press, New York, pp. 1–60.

Pan, Y., Stevens, J., and Webb, B. W., 1992, "Effect of Nozzle Configuration on Transport in the Stagnation Zone of Axisymmetric, Impinging Free Surface Liquid Jets: Part 2—Local Heat Transfer," ASME JOURNAL OF HEAT TRANSFER, Vol. 114, pp. 880–886.

Striegl, S. A., and Diller, T. E., 1984, "An Analysis of the Effect of Entrainment Temperature on Jet Impingement Heat Transfer," ASME JOURNAL OF HEAT TRANSFER, Vol. 106, pp. 804–810.

Viskanta, R., 1993, "Heat Transfer to Impinging Isothermal Gas and Flame Jets," *Experimental Thermal and Fluid Science*, Vol. 6, pp. 111–134.

Yan, X., Baughn, J. W., and Mesbah, M., 1992, "The Effect of Reynolds Number on the Heat Transfer Distribution From a Flat Plate to an Impinging Jet," presented at the ASME Winter Annual Meeting, Anaheim, CA.

Onset of Flow Reversal and Penetration Length of Natural Convective Flow Between Isothermal Vertical Walls

K. D. Kihm,[1,4] J. H. Kim,[2,4] and L. S. Fletcher[3,4]

Nomenclature

b = channel half-spacing
H = channel depth
L = channel height
L_p = penetration length of flow reversal
Nu_b = average Nusselt number based on b
Pr = Prandtl number
R = radius of extended upstream region from the channel entrance
Ra_b = Rayleigh number = $\mathrm{Gr}_b \cdot \mathrm{Pr}$
Ra* = modified Rayleigh number = $\mathrm{Ra}_b \cdot (b/L)$
x, y = coordinate system for physical geometry

Introduction

Thermally driven flows in a vertical heated channel form a basic structure for various heat transfer devices. Typical applications include electronic packaging systems and heat exchangers. Heat transfer characteristics of the flow to and from the channel walls have been studied extensively, with many studies of channel flows available. The onset and penetration lengths of the flow reversals, however, have received only limited attention. The present study of flow reversals occurring in vertical isothermal channels uses a convenient numerical technique with experimental substantiation by means of smoke visualization.

Since the pioneering work of convective heat transfer phenomena in heated vertical channels conducted by Elenbaas (1942), there have been a number of relevant investigations using various analytical, numerical, and experimental techniques. Eckert et al. (1990) presented an extensive review of publications dealing with natural convection in vertical channel flows. Many different aspects of the problem have been identified and investigated, including local and average correlations of heat transfer coefficients, isotherms, and streamlines for narrow or wide channel flows, symmetrically or asymmetrically heated channels, vertical and inclined arrangements and, more recently, parallel and converging channels (Kihm et al., 1993). These aspects have been studied for forced, mixed, and natural convection problems. There are more studies for forced or mixed convection primarily because of their relative simplicity arising from the parabolic nature of the problems. Natural convection problems, however, are generally more cumbersome because of the nontrivial contribution of transverse and axial diffusion effects, i.e., the elliptic nature of the problem.

Sparrow et al. (1984) investigated the flow reversal by visualizing water flows (Pr = 5.0) in a vertical channel heated on one side. They showed that a single dimensionless group, $\mathrm{Ra}_b \cdot (2b/L)$, where $2b$ represents the channel spacing and L is the channel height, correlated their Nusselt number results well. Chang and Lin (1990) presented a numerical simulation of the transient process of flow reversal in a vertical channel with one side heated. They observed that the velocity and temperature wakes above the heated plate were oscillatory when Ra_b was larger than 10^6. Naylor et al. (1991) introduced Jeffrey-Hamel flow for the far-field inlet boundary conditions in their numerical study of flow between isothermal walls. Their elliptic solution identified a flow separation near the channel inlet where the Rayleigh number exceeded a critical value, which resulted in a minimal local Nusselt number. As the study focused on the channel inlet region, the flow reversal occurring near the channel exit was not discussed.

The present paper identifies the occurrence of the onset and penetration lengths of the flow reversal in natural convection flow through vertical isothermal channel walls in terms of the modified Rayleigh number $\mathrm{Ra}^* = \mathrm{Ra}_b \cdot (b/L)$ and the channel aspect ratio L/b (Fig. 1).

Analytical and Numerical Study

The standard elliptic forms of the steady two-dimensional mass, momentum, and energy equations were solved using a finite difference method with a body or boundary-fitted coordinate transformation (BFCT). A comprehensive description of

[1] Associate Professor; Mem. ASME.
[2] Presently at Korea Aerospace Research Institute, Taejon, Korea.
[3] Thomas A. Dietz Professor; Fellow ASME.
[4] Department of Mechanical Engineering, Texas A&M University, College Station, TX 77843-3123.

Contributed by the Heat Transfer Division of THE AMERICAN SOCIETY OF MECHANICAL ENGINEERS. Manuscript received by the Heat Transfer Division October 1994; revision received December 1994. Keywords: Flow Visualization, Natural Convection, Numerical Methods. Associate Technical Editor: R. Viskenta.

general BFCT technique is given by Thompson et al. (1974) and a detailed description of the scheme applied to the present problem is presented by Kim (1993). Laminar flow was assumed with a Boussinesq approximation. The thermal boundary conditions are isothermal at the vertical walls, adiabatic at the ceiling of the extended semicircle, and zero gradient at the extended inlet and channel exit. The boundary conditions imposed for the velocity field are no-slip on all solid surfaces, including the ceiling, with Neumann conditions at the inlet and exit.

The half-domain of symmetry consisted of a total of 4961 graded grids with a 3 percent average expansion or contraction grading. The radius of the extended region, R, was equal to ten times the channel half-spacing, b, as preliminary calculations with a setting $R = 10b$ converged within 2 percent of those with a larger radius of $R = 20b$. The BFCT technique successfully transformed a unique configuration consisting of the channel and the semicircular extended upstream inlet into a rectangular domain on which the numerical analysis was carried out. The dimensionless stream function, vorticity, and temperature were integrated using iterations by successive overrelaxation (SOR) with convergence of 10^{-6} or less until the mass continuity was satisfied.

The onset of flow reversal was the value of Ra* that first resulted in a negative streamline detached from the centerline. Pocketlike streamlines with negative constants represented the formation of a recirculating flow. The recirculating flow penetrates into the channel along the centerline or zero streamline, splits into two separate flows at the stagnation point and then each flow merges into the upcoming flow along the channel wall. The maximum penetration length is the distance from the channel exit to the stagnation point on the centerline.

Calculations were made for air, Pr = 0.7, a modified Rayleigh number range of $0.05 < \text{Ra}^* < 2000$, and channel aspect ratios of L/b = 2, 5, 8, 10, and 24. The calculated heat transfer coefficients showed excellent agreement with previous data (Kim, 1993). The average Nusselt number, Nu_b, correlated well with the modified Rayleigh number $\text{Ra}^* = \text{Ra}_b \cdot (b/L)$.

Flow Visualization Study

An experimental test facility for the flow visualization of recirculating flow behavior in isothermal vertical channels was developed. Each of the vertical isothermal walls was made of 0.826-cm-thick aluminum plate with a vertical length, L, of 12.7 cm and a depth, H, of 20.32 cm. Each plate had a heater pad attached to the backside with a total of nine K-type thermocouples embedded within 1 mm depth from the front surface. When steady-state conditions were reached, the maximum discrepancies between the thermocouple readings were ±0.4°C for the lowest Ra* that required the heated plate temperature only a few degrees higher than the ambient temperature. The channel sides were covered with 3-mm-thick glass plates to reduce the edge effect. To ensure the no-slip condition at the ceiling (y = 0), as specified in the numerical analysis, a Plexiglas panel was placed next to the leading edge of each isothermal plate.

A Rosco Fog machine generated smoke based on the method of nucleus condensation. The smoke passed through several regulation stages to ensure minimal flow momentum near the channel inlet. The chamber contained two guide vanes to reduce and diffuse the smoke flux from the generator and to cool the smoke to the ambient level. 4 × 4 mesh screens (6.35 mm mesh dimension) were installed at both the inlet and exit of the duct to reduce the flow disturbance. A deflector was placed at the duct exit to reduce the directional movement of the smoke flow, which would not be desirable for the flow visualization study. Finally, in order to ensure uniformly distributed smoke flow to the test channel, another fine mesh screen (3.18 mm mesh dimension) was placed at the channel entrance.

The smoke temperature was measured just before the channel entrance and maximum deviations were 1.3°C higher than the ambient temperature. The residual smoke, which was not introduced into the test section, was allowed to diffuse freely into the laboratory. A 35-mm camera, with 1/250 second exposure time, recorded the smoke flow patterns under fluorescent lighting boosted with a strobe flash. A ruler attached to the heated wall measured the penetration lengths.

The length of the recirculating flow was persistent and reasonably stable for the period of observation. The measurement uncertainties associated with the reading errors were estimated to be one medium division of the ruler, i.e., ±2.5 mm, as a very conservative estimation, or less than ±3 percent. The measurement uncertainties of the wall temperature were estimated as a maximum of ±0.3 percent, and the resultant uncertainties in the Rayleigh number were estimated as ±1 percent. Thus, the overall uncertainties involved in measuring the flow reversal lengths were estimated to be less than ±5 percent. An attempt to determine the onset condition experimentally for flow reversal was not successful, since the physical uncertainties of the flow near the onset condition were too high to identify the critical Rayleigh number with acceptable accuracy.

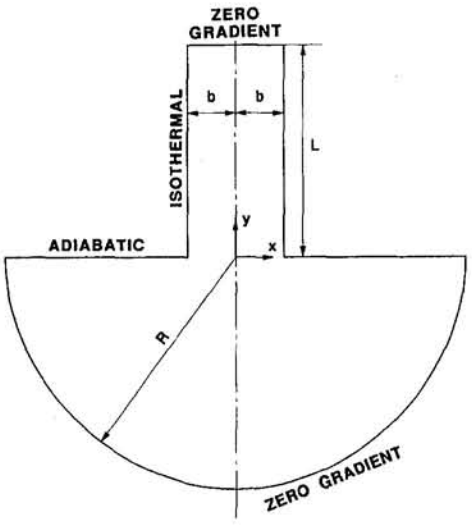

Fig. 1 The computational domain for convective air flow in vertical isothermal channel configuration

Results and Discussion

Figures 2(a, b, c) show the numerically calculated streamlines (left side) and isotherms (right side) for Ra* = 1, 100, and 500 for the case of L/b = 8, respectively. The inset photographs were taken from the smoke visualization experiment of the flow stream at Ra* = 130.2 and 501.8. The extended inlet regions are shown only up to twice the channel half-spacing. The dimensionless isotherms have a value of one at the isothermal wall and zero at free stream and infinity. The dimensionless stream line takes a value of zero at the centerline. For the case of Ra* = 1 (Fig. 2a), the almost uniform intervals between streamlines show that the flow is fully developed. The weak air flow induced by the low thermal driving force allows the isotherms to extend well into the upstream entrance region due to the elliptic nature of the relatively strong conduction effect. As a result, the incoming air is preheated and the temperature at the channel inlet can be as much as 30 percent higher than the ambient or far-field inlet temperature. Thus, a parabolic simplification assuming uniform inlet temperature would cause a significant error for such low Rayleigh number cases.

The flow field at Ra* = 100 (Fig. 2b) deviated from the previous fully developed case and the depleted streamlines near the channel center show separate boundary layer development.

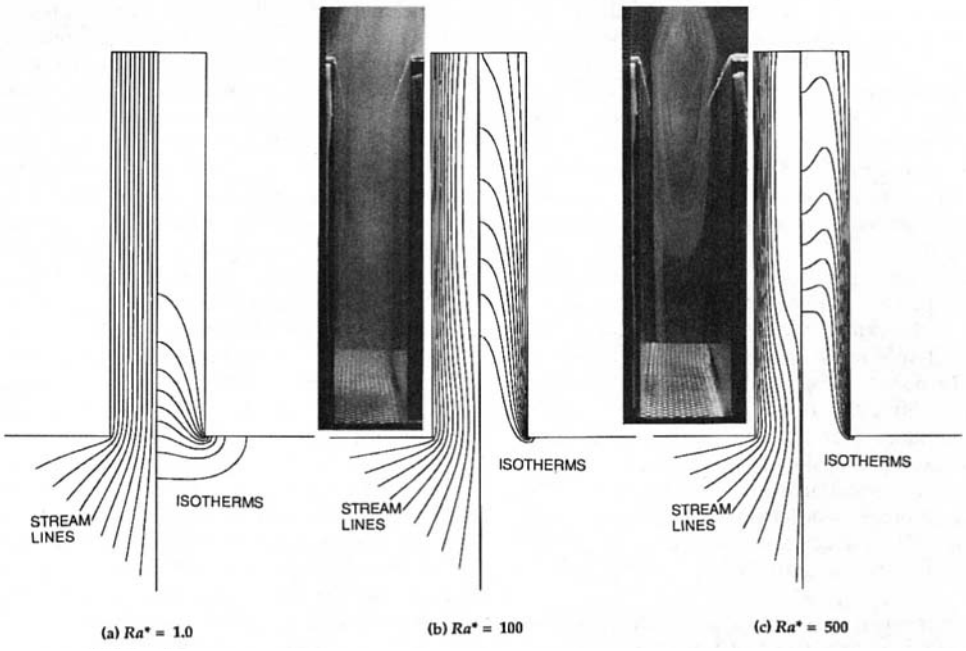

Fig. 2 Calculated flow streamlines and isotherms of convective air (Pr = 0.7) for L/b = 8: (*a*) Ra* = 1.0; (*b*) Ra* = 100; and (*c*) Ra* = 500. The photographs indicate smoke stream visualization at Ra* = 130.2 and 501.8, respectively.

The more concentrated streamlines appearing near the wall suggest increased buoyancy-driven air flow. Also, this increased convection reduces the penetration of the conduction effect at the inlet as seen in the isotherm distributions.

Figure 2(c) shows the streamlines and isotherms when Ra* is increased to 500, which exceeds the critical Rayleigh number (Ra* = 146 as numerically determined). The congested streamlines near the wall indicate that most induced air flow concentrates in the narrower boundary layer next to the wall. The pocketlike streamlines appear with negative constants demonstrating the formation of recirculating flow. Vena-contracta-like streamlines at the entrance appear to reduce the effective opening. This narrower effective opening reduces the incoming air, whereas the increased thermal driving force requires more air flow. When the acceleration of the air flow near the channel wall exceeds a critical point, the incoming air flow through the inlet is insufficient and additional air drawn in through the central portion of the channel exit results in flow reversal. The isotherms show that the temperature in the recirculation region is significantly lower than the air temperature next to the wall at the same y position. This indicates that the convection heat transfer to the recirculating air from the wall is limited and the overall heat transfer is not significantly altered by the presence of the flow reversal. The fact that the conduction preheating of the incoming air, or the elliptic nature of the problem, has noticeably been reduced with the occurrence of flow reversal, implies that the channel flow problem can be approximated with a parabolic simplification when Ra* exceeds the critical value for the flow reversal.

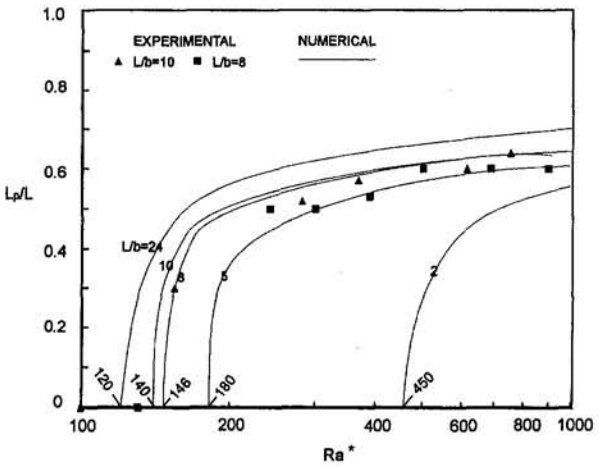

Fig. 3 Experimental and numerical results of the penetration length versus Ra* and numerically predicted onset Rayleigh numbers for flow reversal

Figure 3 shows that the calculated onset Rayleigh numbers that initiate the flow reversals are 120, 140, 146, 180, and 450, respectively, for L/b = 24, 10, 8, 5, and 2. The numerically and experimentally observed penetration lengths of the channel flows are also provided in Fig. 3. Although the present experimental configuration allowed only two channel aspect ratios, 8 and 10, the data favorably supported the numerical results. Ra_b is the flow parameter that determines the level of natural convection strength and L/b is the geometric parameter. It appears that the penetration length increases for increasing channel aspect ratio, L/b, for the same Ra* = $Ra_b \cdot (b/L)$. This is primarily because of higher flow parameter Ra_b required to keep Ra* constant as the channel is longer with smaller b/L. This higher Ra_b also explains the fact that the onset of the flow reversal for longer channel occurs earlier at relatively smaller Ra*. Another thing to note here is that the deviation observed between the data and predictions particularly in lower Ra* range is probably attributed to the simplified free boundary condition imposed at the channel exit. For further investigation of the problem, a downstream extended region with a far-field free boundary condition needs to be considered to incorporate the possible elliptic behavior at the channel exit.

References

Chang, T. S., and Lin, T. F., 1990, "On the Reversed Flow and Oscillating Wake in an Asymmetrically Heated Channel," *International Journal for Numerical Methods in Fluids,* Vol. 10, pp. 443–459.

Eckert, E. R. G., Goldstein, R. J., Irvine, T. F., and Hartnett, J. P., 1990, *Heat Transfer Reviews 1976–1986,* Wiley, New York.

Elenbaas, W., 1942, "Heat Dissipation of Parallel Plates by Free Convection," *Physica*, Vol. 9, pp. 1–28.

Kihm, K. D., Kim, J. H., and Fletcher, L. S., 1993, "Investigation of Natural Convection Heat Transfer in Converging Channel Flows Using a Specklegram Technique," ASME JOURNAL OF HEAT TRANSFER, Vol. 115, No. 1, pp. 140–148.

Kim, J. H., 1993, "Investigation of Heat Transfer Characteristics and Flow Reversal Phenomena in Natural Convecting Parallel/Converging Vertical Channel Flows," Ph.D. Thesis, Department of Mechanical Engineering, Texas A&M University.

Naylor, D., Floryan, J. M., and Tarasuk, J. D., 1991, "A Numerical Study of Developing Free Convection Between Isothermal Vertical Plates," ASME JOURNAL OF HEAT TRANSFER, Vol. 113, pp. 620–626.

Sparrow, E. M., Chrysler, G. M., and Azevedo, L. F., 1984, "Observed Flow Reversals and Measured-Predicted Nusselt Numbers for Natural Convection in a One-Sided Heated Vertical Channel," ASME JOURNAL OF HEAT TRANSFER, Vol. 106, pp. 325–332.

Thompson, J. F., Thames, F. C., and Mastin, C. W., 1974, "Automatic Numerical Generation of Body-Fitted Curvilinear Coordinate System for Field Containing Any Number of Arbitrary Two-Dimensional Bodies," *Journal of Computational Physics*, Vol. 15, pp. 299–319.

An Adsorption Model for the Superheat at the Critical Heat Flux

R. Reyes[1] and P. C. Wayner, Jr.[1]

Nomenclature

A = Hamaker constant
$\bar{A}$ = $A/(6\pi)$
b = defined by Eq. (5)
H = heat of vaporization
M = molecular weight
P = pressure
R = gas constant
T = temperature
x = parallel to flow direction
$\Delta\tau$ = dimensionless temperature difference, Eq. (4)
δ = liquid film thickness
η = dimensionless film thickness, Eq. (5)
ξ = dimensionless position, Eq. (5)
Π = disjoining pressure
σ = surface free energy per unit area
ρ = fluid density
Φ = dimensionless chemical potential difference, Eq. (1)
Ψ = dimensionless curvature, Eq. (3)

Subscripts and Superscripts

c = critical conditions
i = condition i
id = ideal
l = liquid
M = molar
o = characteristic thickness
r = reference
sat = saturation
s = solid
v = vapor

[1] The Isermann Department of Chemical Engineering, Rensselaer Polytechnic Institute, Troy, NY 12180-3590.

Contributed by the Heat Transfer Division of THE AMERICAN SOCIETY OF MECHANICAL ENGINEERS. Manuscript received by the Heat Transfer Division May 1994; revision received September 1994. Keywords: Boiling, Modeling and Scaling, Phase-Change Phenomena. Associate Technical Editor: R. A. Nelson, Jr.

Introduction

The evaluation of the superheat at the critical heat flux (CHF) is a problem of considerable importance to the field of change-of-phase heat transfer. As demonstrated in the recent reviews by Katto (1992) and Bergles (1992) and in a descriptive paper by Unal et al. (1992), there has been extensive prior research on the CHF. In these studies, the following descriptive modeling terms affirm the complex transport processes occurring at CHF: macrolayer, microlayer, apparent contact angle, real contact angle, spreading, dry patch, instability, vapor mushrooms, and interfacial conditions. In order to simplify the analyses of these phenomena, we focus herein on a more tractable model, which emphasizes a characteristic thickness in the contact line region at the vapor–liquid–solid junction, which would be present in the thinnest portion of an evaporating microlayer. A schematic drawing of this region is presented in Fig. 1 for a nonisothermal completely wetting system. This is the region where the substrate dries out in the hot spot hypothesis. The solid substrate is modeled as having an adsorbed ultrathin layer of liquid with a thickness δ, which is a function of the superheat and the interfacial force field. The characteristic thickness, δ_o, can (but does not have to) be of the order of a monolayer or less. Therefore, in the region $x < 0$, the film can be discontinuous and fill in "depressions" on a "rough" surface. Herein, a model of the physically indistinct contact line region, which varies spatially and fluctuates at the molecular level, is used to develop a predictive equation for the average value of the superheat that can be evaluated macroscopically.

In a recent paper, Wayner (1994) discussed a new physical model for the spreading dynamics of fluids on superheated solid surfaces. Using a preliminary algorithm, he demonstrated that this model was also useful in predicting the superheat at the CHF. Below, we re-examine this model by using a different algorithm to predict the change with pressure of the superheat at the CHF. We find that the predictions compare well with the experimental data of Cichelli and Bonilla (1945) on completely wetting systems. These results demonstrate that a simple Kelvin–Clapeyron type of model of adsorption in the contact line region describes this phenomena. In essence, it is a multilayer potential model of physical adsorption in which the van der Waals intermolecular dispersion forces are described using the vapor–liquid–solid Hamaker constant.

Since van der Waals dispersion forces control evaporation and physical adsorption, adsorption models in heat transfer are not new. For example, Segev and Bankoff (1980) used a Langmuir model to determine the minimum film boiling temperature. Using the heat of adsorption, the minimum film boiling temperature (T_{MFB}) was assumed to be the temperature at which 90 percent coverage occurred. An extensive description of the early literature in this field was presented in their paper. Herein, we use a multilayer model and readily available bulk properties to evaluate the superheat at the critical heat flux. We find that this application enhances considerably the understanding of the effect of interfacial forces on CHF. Conceivably, a Langmuir

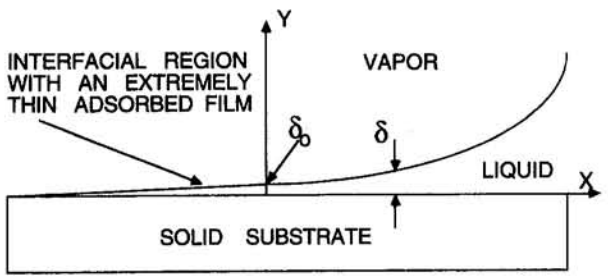

Fig. 1 Conceptual view of the contact line region for a nonisothermal completely wetting system with $\theta \to 0$ and $K = 0$ at $x = 0$ where $\delta = \delta_o$, the characteristic thickness

Elenbaas, W., 1942, "Heat Dissipation of Parallel Plates by Free Convection," *Physica*, Vol. 9, pp. 1–28.

Kihm, K. D., Kim, J. H., and Fletcher, L. S., 1993, "Investigation of Natural Convection Heat Transfer in Converging Channel Flows Using a Specklegram Technique," ASME JOURNAL OF HEAT TRANSFER, Vol. 115, No. 1, pp. 140–148.

Kim, J. H., 1993, "Investigation of Heat Transfer Characteristics and Flow Reversal Phenomena in Natural Convecting Parallel/Converging Vertical Channel Flows," Ph.D. Thesis, Department of Mechanical Engineering, Texas A&M University.

Naylor, D., Floryan, J. M., and Tarasuk, J. D., 1991, "A Numerical Study of Developing Free Convection Between Isothermal Vertical Plates," ASME JOURNAL OF HEAT TRANSFER, Vol. 113, pp. 620–626.

Sparrow, E. M., Chrysler, G. M., and Azevedo, L. F., 1984, "Observed Flow Reversals and Measured-Predicted Nusselt Numbers for Natural Convection in a One-Sided Heated Vertical Channel," ASME JOURNAL OF HEAT TRANSFER, Vol. 106, pp. 325–332.

Thompson, J. F., Thames, F. C., and Mastin, C. W., 1974, "Automatic Numerical Generation of Body-Fitted Curvilinear Coordinate System for Field Containing Any Number of Arbitrary Two-Dimensional Bodies," *Journal of Computational Physics*, Vol. 15, pp. 299–319.

An Adsorption Model for the Superheat at the Critical Heat Flux

R. Reyes[1] and P. C. Wayner, Jr.[1]

Nomenclature

A = Hamaker constant
$\bar{A}$ = $A/(6\pi)$
b = defined by Eq. (5)
H = heat of vaporization
M = molecular weight
P = pressure
R = gas constant
T = temperature
x = parallel to flow direction
$\Delta\tau$ = dimensionless temperature difference, Eq. (4)
δ = liquid film thickness
η = dimensionless film thickness, Eq. (5)
ξ = dimensionless position, Eq. (5)
Π = disjoining pressure
σ = surface free energy per unit area
ρ = fluid density
Φ = dimensionless chemical potential difference, Eq. (1)
Ψ = dimensionless curvature, Eq. (3)

Subscripts and Superscripts

c = critical conditions
i = condition i
id = ideal
l = liquid
M = molar
o = characteristic thickness
r = reference
sat = saturation
s = solid
v = vapor

[1] The Isermann Department of Chemical Engineering, Rensselaer Polytechnic Institute, Troy, NY 12180-3590.

Contributed by the Heat Transfer Division of THE AMERICAN SOCIETY OF MECHANICAL ENGINEERS. Manuscript received by the Heat Transfer Division May 1994; revision received September 1994. Keywords: Boiling, Modeling and Scaling, Phase-Change Phenomena. Associate Technical Editor: R. A. Nelson, Jr.

Introduction

The evaluation of the superheat at the critical heat flux (CHF) is a problem of considerable importance to the field of change-of-phase heat transfer. As demonstrated in the recent reviews by Katto (1992) and Bergles (1992) and in a descriptive paper by Unal et al. (1992), there has been extensive prior research on the CHF. In these studies, the following descriptive modeling terms affirm the complex transport processes occurring at CHF: macrolayer, microlayer, apparent contact angle, real contact angle, spreading, dry patch, instability, vapor mushrooms, and interfacial conditions. In order to simplify the analyses of these phenomena, we focus herein on a more tractable model, which emphasizes a characteristic thickness in the contact line region at the vapor–liquid–solid junction, which would be present in the thinnest portion of an evaporating microlayer. A schematic drawing of this region is presented in Fig. 1 for a nonisothermal completely wetting system. This is the region where the substrate dries out in the hot spot hypothesis. The solid substrate is modeled as having an adsorbed ultrathin layer of liquid with a thickness δ, which is a function of the superheat and the interfacial force field. The characteristic thickness, δ_o, can (but does not have to) be of the order of a monolayer or less. Therefore, in the region $x < 0$, the film can be discontinuous and fill in "depressions" on a "rough" surface. Herein, a model of the physically indistinct contact line region, which varies spatially and fluctuates at the molecular level, is used to develop a predictive equation for the average value of the superheat that can be evaluated macroscopically.

In a recent paper, Wayner (1994) discussed a new physical model for the spreading dynamics of fluids on superheated solid surfaces. Using a preliminary algorithm, he demonstrated that this model was also useful in predicting the superheat at the CHF. Below, we re-examine this model by using a different algorithm to predict the change with pressure of the superheat at the CHF. We find that the predictions compare well with the experimental data of Cichelli and Bonilla (1945) on completely wetting systems. These results demonstrate that a simple Kelvin–Clapeyron type of model of adsorption in the contact line region describes this phenomena. In essence, it is a multilayer potential model of physical adsorption in which the van der Waals intermolecular dispersion forces are described using the vapor–liquid–solid Hamaker constant.

Since van der Waals dispersion forces control evaporation and physical adsorption, adsorption models in heat transfer are not new. For example, Segev and Bankoff (1980) used a Langmuir model to determine the minimum film boiling temperature. Using the heat of adsorption, the minimum film boiling temperature (T_{MFB}) was assumed to be the temperature at which 90 percent coverage occurred. An extensive description of the early literature in this field was presented in their paper. Herein, we use a multilayer model and readily available bulk properties to evaluate the superheat at the critical heat flux. We find that this application enhances considerably the understanding of the effect of interfacial forces on CHF. Conceivably, a Langmuir

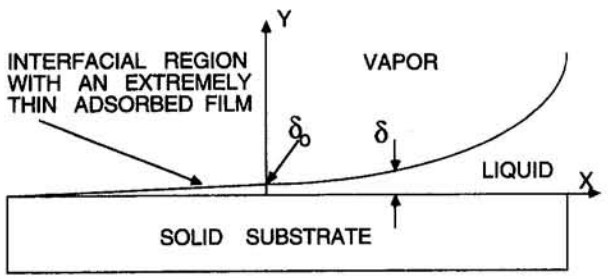

Fig. 1 Conceptual view of the contact line region for a nonisothermal completely wetting system with $\theta \to 0$ and $K = 0$ at $x = 0$ where $\delta = \delta_o$, the characteristic thickness

model describes MFB superheat and a multilayer model describes CHF superheat. The results also demonstrate that, in many cases, the advantages of the availability of bulk properties and the small approximations associated with their use in thin films more than offset the small effect of film thickness on their values in multilayer adsorption. On the other hand, we note that the more complex modified properties for ultrathin films can always be used when the results demonstrate that the bulk approximations do not apply.

Theoretical

First we present a short synopsis of the model developed by Wayner (1994) for the dimensionless chemical potential, Φ, of the extremely thin liquid film presented in Fig. 1:

$$\Phi = (b\eta^3)^{-1} - \Psi + \Delta\tau \tag{1}$$

in which

$$\Phi = \frac{\rho_{lM} R T_{lv} \delta_o}{\sigma_{lv}} \ln \frac{P_{lv}}{P_v} \tag{2}$$

$$\Psi = \left(1 + \left(\frac{d\eta}{d\xi}\right)^2\right)^{-1.5} \frac{d^2\eta}{d\xi^2} \tag{3}$$

$$\Delta\tau = \frac{H_{lv}^{id} \delta_o \rho_{lM}}{\sigma_{lv} T_v} (T_{lv} - T_v) \tag{4}$$

with

$$x = \delta_o \xi, \quad \delta(x) = \delta_o \eta(\xi),$$

$$b = \sigma_{lv} \delta_o^2 / \bar{A}, \quad \bar{A} = \frac{A_{ll} - A_{ls}}{6\pi} \tag{5}$$

and at $\eta = 1$ with $\Psi = 0$ and $\Phi = 0$, Eq. (1) becomes

$$\frac{\bar{A}}{\delta_o^3} = \frac{-\rho_{lM} H_{lv}^{id} (T_{lv} - T_v)_o}{T_v} \tag{6}$$

For the completely wetting case emphasized herein, the thickness at $x = 0$, δ_o, is a characteristic length equal to the average thickness of an adsorbed flat superheated liquid film and A_{ls} and A_{ll} are the Hamaker constants for the liquid–solid and liquid–liquid systems, respectively. For the partially wetting case, $A_{ls} < A_{ll}$. Therefore, the dimensionless chemical potential, Φ, is a function of the film shape (dimensionless thickness, η, and dimensionless curvature, Ψ) and temperature difference. For example, a constant vapor pressure boundary condition would give the local superheat on the liquid side of the liquid–vapor interface, $T_{lv} - T_v$, as a function of film shape for the complete region. For extremely thin films, this is also the approximate superheat at the substrate surface.

Although Eq. (1) has many uses in change-of-phase heat transfer, we will focus herein on a simple application: the prediction of the change of the substrate superheat at CHF, $\Delta T_{CHF} = (T_{lv} - T_v)_{CHF}$, with the saturation bulk vapor pressure. In so doing, we strive to present the simplest view that can be compared with experimental data so that the effects of adsorption and physical properties are obvious. This is accomplished by looking at the dynamic equilibrium (to mass transfer) state, which would occur when the direction of the characteristic thickness motion changes from "rewetting" to "dewetting." If the surface dewets on average because of these motions, the critical heat flux is reached. Admittedly, this instantaneous equilibrium state would be disturbed readily during boiling. At equilibrium for mass transfer, $\Phi = 0$, Eq. (1) leads to the following equation for the effect of superheat on the equilibrium film profile:

$$\Delta\tau = \Psi - (b\eta^3)^{-1} \tag{7}$$

We find that, for a completely wetting fluid, an increase in superheat first gives a decrease in thickness of a flat film and then, when the film thickness is approximately equal to the roughness of the surface (not shown in the figure), both a decrease in film thickness and an increase in interfacial curvature. We note that all surfaces have some "roughness," if only at the molecular scale. These equations can be used to analyze the complete nonisothermal surface temperature field around $x = 0$, which would allow phase change. However, for the following development, we find it sufficient to only analyze the film (line) at $x = 0$ as an adsorbed isothermal flat thin film.

Applying a constant stress model, Wayner (1994) used the following definition of the effective curvature in the region $1 \le \eta \le 3$ to calculate the CHF superheat at atmospheric conditions:

$$\Delta K_{\text{eff}} = \frac{c}{\delta_o} = \frac{\rho_{lM} H_{lv}^{id} (T_{lv} - T_v)_{CHF}}{\sigma_{lv} T_v} \tag{8}$$

The constant stress in a nonuniform film, c, is a function of the film profile:

$$c = \Psi - (b\eta^3)^{-1} \tag{9}$$

Although Eq. (8) gives a descriptive model of the contact line region, additional data on the effect of changing conditions on the effective curvature are needed to determine ΔT_{CHF}. To avoid this unknown, we now present a modification of this equation. Dividing the cube of Eq. (8) by Eq. (6) and taking the square root gives

$$\frac{\rho_{lM} H_{lv}^{id} (T_{lv} - T_v)_{CHF}}{T_v \sigma_{lv}^{1.5}} = \left(\frac{c^3}{-\bar{A}}\right)^{0.5} \tag{10}$$

The advantage of Eq. (10) is that the terms on the left-hand side can be easily obtained experimentally. To obtain more insight, we rewrite the right-hand side in terms of the Hamaker constant. For the assumed flat film (completely wetting case) at $\eta = 1$, $\Psi = 0$, and $c = -b^{-1}$, Eq. (10) becomes

$$\frac{\rho_{lM} H_{lv}^{id} (T_{lv} - T_v)_{CHF}}{T_v \sigma_{lv}^{1.5}} = \left(\frac{(\bar{A}/\delta_o^3)^2}{\sigma_{lv}^3}\right)^{0.5} \tag{11}$$

A portion of the numerator of the right-hand side can also be written in terms of the relevant surface tensions to determine the effect of temperature on the numerator:

$$\frac{\bar{A}}{\delta_o^2} = 2(\sigma_{lv} + \sigma_{ls} - \sigma_{sv}) \tag{12}$$

As the temperature of a system increases, the surface tension and density decrease. We would also expect the adsorbing film thickness to increase as the temperature increases toward the thermodynamic critical temperature. Therefore, since both the numerator and denominator on the right-hand side of Eq. (11) are expected to decrease in value with an increase in thermodynamic pressure, we anticipate and demonstrate below, using experimental data, that (for at least a limited range of pressure)

$$\frac{H_{lv}^{id} \rho_{lM} (T_{lv} - T_v)_{CHF}}{T_v \sigma_{lv}^{1.5}} \cong \text{const} \tag{13}$$

Since the effect of the liquid–solid experimental system on adsorption at the contact line needs to be known in Eq. (11), the experimental intermolecular force for a particular system in pool boiling is characterized using one experimental measurement of the superheat. Using a set of measurements at one pressure to determine the dimensional constant, Eq. (13) is used below to calculate the value of ΔT_{CHF} at other pressures. Based on the results presented by Wayner (1994), we anticipate that

a more fundamental value of this constant will be found in the future.

Prediction of $\Delta T_{CHF}(P_v^{sat})$

Using Eq. (14), which is based on Eq. (13), the superheat at a new bulk saturation condition "i," T_{vi}^{sat} at P_i^{sat}, can be obtained from the measured superheat at a reference saturation condition "r" at P_r^{sat}.

$$\Delta T_{CHF} = T_{si}^{sup} - T_{vi}^{sat} = (T_{sr}^{sup} - T_{vr}^{sat}) \frac{T_{vi}^{sat} \rho_{lr} H_{lvr}}{T_{vr}^{sat} \rho_{li} H_{lvi}} \left(\frac{\sigma_{lvi}}{\sigma_{lvr}} \right)^{1.5} \quad (14)$$

The properties (ρ_l, H_{lv}, σ) of the superheated liquid in Eq. (14) are evaluated at the temperature of the solid, T_s^{sup}. The liquid properties (ρ_l, H_{lv}, σ) with the superscript "sat" in Eq. (15) below are evaluated at the saturation temperature, T_v^{sat}. The temperature effects of superheat on the liquid properties are estimated by:

$$\frac{X_r^{sup}}{X_i^{sup}} = \frac{X_r^{sat}}{X_i^{sat}} \left[\left(\frac{T_c - T_r^{sup}}{T_c - T_i^{sup}} \right) \left(\frac{T_c - T_i^{sat}}{T_c - T_r^{sat}} \right) \right]^p \quad (15)$$

For $X = H_{lv}$, $p = 0.38$ (Watson, 1943). For $X = \rho_l$, $p = 0.25$ for alcohols and water, and $p = 0.31$ for alkanes and benzene (Fishtine, 1963). For $X = \sigma_{lv}$, $p = 1$ for polar substances, and $p = 1.2$ for nonpolar compounds (MacLeod, 1923). T_c is the critical temperature. Combining Eqs. (14)–(15), we obtain

$$T_{si}^{sup} - T_{vi}^{sat} - C_T (T_c - T_{si}^{sup})^n = 0 \quad (16)$$

in which C_T is

$$C_T = (T_{sr}^{sup} - T_{vr}^{sat}) \left(\frac{T_{vi}^{sat} \rho_{lr}^{sat} H_{lvr}^{sat}}{T_{vr}^{sat} \rho_{li}^{sat} H_{lvi}^{sat}} \right) \left(\frac{\sigma_{lvi}^{sat}}{\sigma_{lvr}^{sat}} \right)^{1.5} \times \left(\frac{(T_c - T_{vr}^{sat})}{(T_c - T_{vi}^{sat})(T_c - T_{sr}^{sup})} \right)^n \quad (17)$$

In Eqs. (16) and (17), $n = 0.87$ for alcohol and water, and $n = 1.11$ for the alkanes and benzene. Values of C_T are presented in Table (1) for the data evaluated.

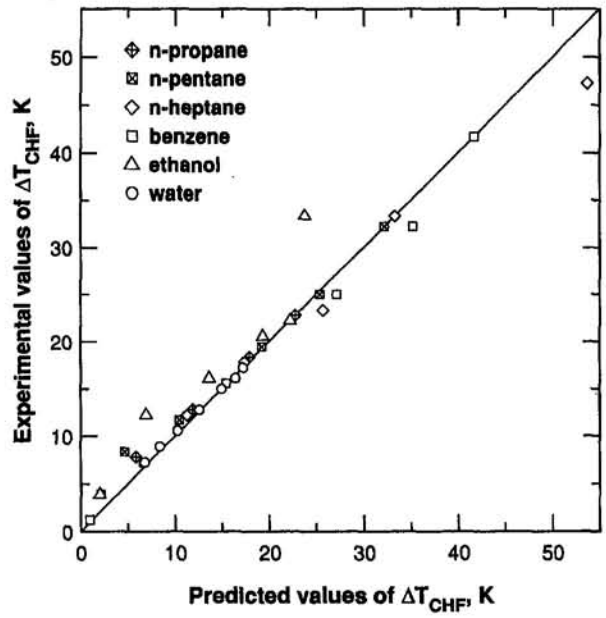

Fig. 2 Comparison of predicted and experimental values of ΔT_{CHF} for polar and nonpolar fluids

Table 1 Experimental conditions, ΔT_{CHF}, and C_T values

pSAT, Pa x 10^{-5}	P/P_{crit}	ΔT_{CHF}, K experimental	ΔT_{CHF}, K predicted	C_T
Propane T_c : 370.000 K	**P_c : 42.538 x 10^5 Pa**			
ref. 16.897	0.397	22.78	ref.	0.7156
i=1 20.345	0.478	18.33	17.92	0.6772
i=2 25.862	0.608	12.78	11.90	0.6855
i=3 32.759	0.770	7.78	5.88	0.6914
n-Pentane T_c : 470.600 K	**P_c : 33.422 x 10^5 Pa**			
ref. 1.517	0.045	32.22	ref.	0.1635
i=1 4.138	0.124	25.00	25.42	0.1772
i=2 7.931	0.237	19.44	19.23	0.1872
i=3 14.828	0.444	11.67	10.44	0.1744
i=4 21.724	0.650	8.33	4.68	0.1387
i=5 28.621	0.856	3.89	2.10	0.1975
n-Heptane T_c : 540.000 K	**P_c : 27.162 x 10^5 Pa**			
ri=0 0.455	0.017	47.22	53.67	0.2180
ref. 1.014	0.037	33.33	ref.	0.1407
i=1 3.448	0.127	23.33	25.74	0.1580
i=2 7.931	0.292	17.78	17.37	0.1709
i=3 14.828	0.546	12.22	11.28	0.2447
Benzene T_c : 561.700 K	**P_c : 48.345 x 10^5 Pa**			
ref. 1.034	0.021	41.67	ref.	0.1429
i=1 3.448	0.071	32.33	35.22	0.1710
i=2 7.931	0.164	25.00	27.17	0.1712
i=3 18.276	0.378	15.56	15.42	0.1694
i=4 32.069	0.663	7.22	6.67	0.1770
i=5 44.483	0.920	1.22	0.97	0.1105
Ethanol T_c : 516.300 K	**P_c : 63.931 x 10^5 Pa**			
i=0 1.034	0.016	33.33	23.83	0.3210
ref. 3.793	0.059	22.22	ref.	0.3851
i=1 7.931	0.124	20.56	19.36	0.4172
i=2 18.276	0.286	16.11	13.60	0.4343
i=3 35.517	0.556	12.22	6.93	0.3994
i=4 52.759	0.825	3.89	2.00	0.2789
Water T_c : 647.110 K	**P_c : 221.379 x 10^5 Pa**			
ref. 1.034	0.005	17.22	ref.	0.1383
i=1 3.448	0.016	16.11	16.39	0.1505
i=2 7.931	0.036	15.00	14.97	0.1554
i=3 18.276	0.083	12.78	12.59	0.1576
i=4 35.517	0.160	10.56	10.23	0.1580
i=5 52.759	0.238	8.89	8.40	0.1545
i=6 70.000	0.316	7.22	6.81	0.1476

Model Evaluation

Predictions of the values of the superheat obtained using Eq. (16) are compared with the experimental data of Cichelli and Bonilla (1945) on completely wetting systems in Fig. 2. The substrate was a thick copper plate with 0.002 in. of polished electroplated chromium. The experimental conditions, the reference value, the measured values of the superheat at CHF (taken to be the maximum value in the heat flux curve), the calculated values of C_T obtained using Eq. (17), and the predicted values of the superheat at CHF are presented in Table 1. Except for a few points, we find that the comparisons between the measured values and the predictions for a very large range in pressures are extremely good. This indicates that a single measurement at atmospheric pressure for a particular system can characterize the experimental surface conditions for a range of pressures. In contrast, the theoretical calculations presented by Wayner (1994) proved to be less accurate because the same value for the unknown constant "c" was assumed for all the systems.

Conclusions

1 A multilayer adsorption model describes the superheat at the critical heat flux.
2 Using bulk properties and the experimental value of the superheat at one pressure, the multilayer adsorption model can predict the values of the superheat at other pressures.

Acknowledgments

This material is based on work partially supported by the National Science Foundation under grant #CTS-9123006 and by Fulbright/CONACYT Grant #15922189. Any opinions,

findings, and conclusions or recommendations expressed in this publication are those of the author and do not necessarily reflect the view of the NSF.

References

Bergles, A. E., 1992, "What is the Real Mechanism of CHF in Pool Boiling?" *Pool and External Flow Boiling,* V. K. Dhir and A. E. Bergles, eds., ASME, New York, pp. 165–170.

Cichelli, M. T., and Bonilla, C. F., 1945, "Heat Transfer to Liquids Boiling Under Pressure," *Trans. Am. Inst. Chem. Engrs.*, Vol. 41, pp. 755–787.

Fishtine, S. H., 1963, "Estimates of Saturated Fluid Densities and Critical Constants," *Ind. Eng. Chem. Fundamentals,* Vol. 2, No. 2, pp. 149–155.

Katto, Y., 1992, "Transition Boiling in Natural Convection Systems," *Pool and External Flow Boiling,* V. K. Dhir and A. E. Bergles, eds., ASME, New York, pp. 151–164.

MacLeod, D. B., 1923, "On a Relation Between Surface Tension and Density," *Trans. Faraday Soc.,* Vol. 19, pp. 38–42.

Segev, A., and Bankoff, S. G., 1980, "The Role of Adsorption in Determining the Minimum Film Boiling Temperature," *Int. J. Heat Mass Transfer,* Vol. 23, pp. 637–642.

Unal, C., Daw, V., and Nelson, R. A., 1992, "Unifying the Controlling Mechanisms for the Critical Heat Flux and Quenching: The Ability of Liquid to Contact the Hot Surface," ASME JOURNAL OF HEAT TRANSFER, Vol. 114, pp. 972–982.

Watson, K. M., 1943, "Thermodynamics of the Liquid State. Generalized Prediction of Properties," *Ind. Eng. Chem.,* Vol. 35(4), pp. 398–406.

Wayner, P. C., Jr., 1994, "Thermal and Mechanical Effects in the Spreading of a Liquid Due to a Change in the Apparent Finite Contact Angel," ASME JOURNAL OF HEAT TRANSFER, in press.

Condensation Heat Transfer on Vertical Axis, Axisymmetric, Rotating Surfaces

L. W. Byrd[1] and M. A. Haney[1]

Nomenclature

Ax = fluid merit number = $(\rho h_{fg} k^3/\nu)^{1/4}$, $Ws^{1/2}/(m^2K^{3/4})$
C_p = liquid specific heat, J/kgK
g = acceleration due to gravity, m/s^2
h_{fg} = modified latent heat of vaporization = latent heat + $0.375C_p\theta_s$, J/kg
h_x, $\bar{h}$, h_∞ = local and average unit convective heat transfer coefficient, h_x evaluated at $x \to \infty$, W/m^2K
h_* = ratio of reported $\bar{h}$ to h_∞ or $\bar{h}$ calculated from present work
k = thermal conductivity of the liquid, W/mK
L = condenser length measured along the x axis, m
$\dot{m}$, $\dot{m}_*$ = dimensional (kg/ms) and dimensionless mass flow rate per unit perimeter
Nu_x, Nu_∞ = Nusselt number $h_x\delta_m/k$, Nu_x evaluated at $x \to \infty$
P, P_* = pressure (pascals) and dimensionless pressure given in Eq. (3)
$\bar{q}$ = average heat flux, W/m^2
r, r_0 = radius and minimum radius of the condenser wall, m
T_{sat}, T_w = saturation and wall temperature, °C
u = local x component of velocity, m/s
u_*, $\bar{u}_*$ = dimensionless local and average x component of velocity
x, x_* = dimensional (m) and dimensionless (x/L) distance along the wall
y, y_* = dimensional (m) and dimensionless (y/δ_m) distance perpendicular to the wall
α = taper angle used by Daniels and Al-Jumaily = $\pi/2 - \phi$
γ = liquid specific weight, N/m^3
δ, δ_*, δ_m = dimensional (m) and dimensionless (δ/δ_m) liquid film thickness, δ evaluated at $x = \infty$
η, η_* = dimensionless driving force per unit weight given in Eq. (3)
θ_s = $T_{sat} - T_w$, °C
ν = liquid kinematic viscosity, m^2/s
ρ = liquid density, kg/m^3
ϕ = taper angle shown in Fig. 1
Ψ, Ψ_* = dimensionless pressure gradient per unit weight given in Eq. (3)
ω, ω_h = angular velocity, angular velocity of horizontal axis heatpipe rad/s
ω_v = angular velocity of vertical axis condenser, which results in the same driving force as a horizontal axis condenser rotating at ω_h rad/s

Introduction

Rotating heatpipes make use of centrifugal effects to return liquid from the condenser to the evaporator without a wick. Daniels and Al-Jumaily (1972), Maezawa et al. (1981), and Marto (1976) used a Nusselt-type analysis for heat pipes rotating about a horizontal axis. Faghri et al. (1993) analyzed the vapor flow in a horizontal rotating heat pipe with a constant radius by numerically solving the momentum and energy equations.

In a related area, condensation on rotating disks and cones has been modeled and similarity solutions found for temperature, tangential velocity, and pressure fields that are independent of the radius (Sparrow and Gregg, 1959, 1960; Sparrow and Hartnett, 1961). Nandapurkar and Beatty (1959) experimentally determined average heat transfer coefficients for condensation on vertical axis rotating disks.

This paper examines an axisymmetric problem with a vertical axis of rotation. Figure 1 presents two possible configurations. The liquid boundary layer equations are written in the form given by Mangler (White, 1974) with gravity included as a body force. The coordinate directions are chosen normal and tangential to the wall. Shear stress at the liquid–vapor interface, surface tension, and disjoining pressure are not included in this model. An ideal mass of liquid was assumed so that any "pooling" effects could be neglected and the base is assumed to be insulated. The equations were first solved analytically in a simplified form. The complete set was also solved numerically but showed little difference from the simplified model if Eq. (5) is satisfied.

Mathematical Formulation

The nondimensional momentum equations for the liquid are given by:

$$0 = -\frac{\partial P_*}{\partial x_*} + \eta_* + \frac{\partial^2 u_*}{\partial y_*^2} \tag{1}$$

$$0 = -\frac{\partial P_*}{\partial y_*} - \psi_* \tag{2}$$

$$y_* = \frac{y}{\delta_m}; \quad x_* = \frac{x}{L}; \quad u_* = \frac{u\delta_m}{\nu};$$

[1] Mechanical Engineer, Wright Laboratory, Wright-Patterson AFB, Dayton, OH 45433.

Contributed by the Heat Transfer Division of THE AMERICAN SOCIETY OF MECHANICAL ENGINEERS. Manuscript received by the Heat Transfer Division June 1994; revision received November 1994. Keywords: Condensation, Heat Pipes and Thermosyphons, Rotating Flows. Associate Technical Editor: R. A. Nelson, Jr.

findings, and conclusions or recommendations expressed in this publication are those of the author and do not necessarily reflect the view of the NSF.

References

Bergles, A. E., 1992, "What is the Real Mechanism of CHF in Pool Boiling?" *Pool and External Flow Boiling*, V. K. Dhir and A. E. Bergles, eds., ASME, New York, pp. 165–170.

Cichelli, M. T., and Bonilla, C. F., 1945, "Heat Transfer to Liquids Boiling Under Pressure," *Trans. Am. Inst. Chem. Engrs.*, Vol. 41, pp. 755–787.

Fishtine, S. H., 1963, "Estimates of Saturated Fluid Densities and Critical Constants," *Ind. Eng. Chem. Fundamentals*, Vol. 2, No. 2, pp. 149–155.

Katto, Y., 1992, "Transition Boiling in Natural Convection Systems," *Pool and External Flow Boiling*, V. K. Dhir and A. E. Bergles, eds., ASME, New York, pp. 151–164.

MacLeod, D. B., 1923, "On a Relation Between Surface Tension and Density," *Trans. Faraday Soc.*, Vol. 19, pp. 38–42.

Segev, A., and Bankoff, S. G., 1980, "The Role of Adsorption in Determining the Minimum Film Boiling Temperature," *Int. J. Heat Mass Transfer*, Vol. 23, pp. 637–642.

Unal, C., Daw, V., and Nelson, R. A., 1992, "Unifying the Controlling Mechanisms for the Critical Heat Flux and Quenching: The Ability of Liquid to Contact the Hot Surface," ASME JOURNAL OF HEAT TRANSFER, Vol. 114, pp. 972–982.

Watson, K. M., 1943, "Thermodynamics of the Liquid State. Generalized Prediction of Properties," *Ind. Eng. Chem.*, Vol. 35(4), pp. 398–406.

Wayner, P. C., Jr., 1994, "Thermal and Mechanical Effects in the Spreading of a Liquid Due to a Change in the Apparent Finite Contact Angel," ASME JOURNAL OF HEAT TRANSFER, in press.

Condensation Heat Transfer on Vertical Axis, Axisymmetric, Rotating Surfaces

L. W. Byrd[1] and M. A. Haney[1]

Nomenclature

Ax = fluid merit number = $(\rho h_{fg} k^3/\nu)^{1/4}$, $Ws^{1/2}/(m^2K^{3/4})$
C_p = liquid specific heat, J/kgK
g = acceleration due to gravity, m/s^2
h_{fg} = modified latent heat of vaporization = latent heat + $0.375C_p\theta_s$, J/kg
h_x, $\bar{h}$, h_∞ = local and average unit convective heat transfer coefficient, h_x evaluated at $x \to \infty$, W/m^2K
h_* = ratio of reported $\bar{h}$ to h_∞ or $\bar{h}$ calculated from present work
k = thermal conductivity of the liquid, W/mK
L = condenser length measured along the x axis, m
$\dot{m}$, $\dot{m}_*$ = dimensional (kg/ms) and dimensionless mass flow rate per unit perimeter
Nu_x, Nu_∞ = Nusselt number $h_x\delta_m/k$, Nu_x evaluated at $x \to \infty$
P, P_* = pressure (pascals) and dimensionless pressure given in Eq. (3)
$\bar{q}$ = average heat flux, W/m^2
r, r_0 = radius and minimum radius of the condenser wall, m
T_{sat}, T_w = saturation and wall temperature, °C
u = local x component of velocity, m/s
u_*, $\bar{u}_*$ = dimensionless local and average x component of velocity
x, x_* = dimensional (m) and dimensionless (x/L) distance along the wall
y, y_* = dimensional (m) and dimensionless (y/δ_m) distance perpendicular to the wall
α = taper angle used by Daniels and Al-Jumaily = $\pi/2 - \phi$
γ = liquid specific weight, N/m^3
δ, δ_*, δ_m = dimensional (m) and dimensionless (δ/δ_m) liquid film thickness, δ evaluated at $x = \infty$
η, η_* = dimensionless driving force per unit weight given in Eq. (3)
θ_s = $T_{sat} - T_w$, °C
ν = liquid kinematic viscosity, m^2/s
ρ = liquid density, kg/m^3
ϕ = taper angle shown in Fig. 1
Ψ, Ψ_* = dimensionless pressure gradient per unit weight given in Eq. (3)
ω, ω_h = angular velocity, angular velocity of horizontal axis heatpipe rad/s
ω_v = angular velocity of vertical axis condenser, which results in the same driving force as a horizontal axis condenser rotating at ω_h rad/s

Introduction

Rotating heatpipes make use of centrifugal effects to return liquid from the condenser to the evaporator without a wick. Daniels and Al-Jumaily (1972), Maezawa et al. (1981), and Marto (1976) used a Nusselt-type analysis for heat pipes rotating about a horizontal axis. Faghri et al. (1993) analyzed the vapor flow in a horizontal rotating heat pipe with a constant radius by numerically solving the momentum and energy equations.

In a related area, condensation on rotating disks and cones has been modeled and similarity solutions found for temperature, tangential velocity, and pressure fields that are independent of the radius (Sparrow and Gregg, 1959, 1960; Sparrow and Hartnett, 1961). Nandapurkar and Beatty (1959) experimentally determined average heat transfer coefficients for condensation on vertical axis rotating disks.

This paper examines an axisymmetric problem with a vertical axis of rotation. Figure 1 presents two possible configurations. The liquid boundary layer equations are written in the form given by Mangler (White, 1974) with gravity included as a body force. The coordinate directions are chosen normal and tangential to the wall. Shear stress at the liquid–vapor interface, surface tension, and disjoining pressure are not included in this model. An ideal mass of liquid was assumed so that any "pooling" effects could be neglected and the base is assumed to be insulated. The equations were first solved analytically in a simplified form. The complete set was also solved numerically but showed little difference from the simplified model if Eq. (5) is satisfied.

Mathematical Formulation

The nondimensional momentum equations for the liquid are given by:

$$0 = -\frac{\partial P_*}{\partial x_*} + \eta_* + \frac{\partial^2 u_*}{\partial y_*^2} \tag{1}$$

$$0 = -\frac{\partial P_*}{\partial y_*} - \psi_* \tag{2}$$

$$y_* = \frac{y}{\delta_m}; \quad x_* = \frac{x}{L}; \quad u_* = \frac{u\delta_m}{\nu};$$

[1] Mechanical Engineer, Wright Laboratory, Wright-Patterson AFB, Dayton, OH 45433.

Contributed by the Heat Transfer Division of THE AMERICAN SOCIETY OF MECHANICAL ENGINEERS. Manuscript received by the Heat Transfer Division June 1994; revision received November 1994. Keywords: Condensation, Heat Pipes and Thermosyphons, Rotating Flows. Associate Technical Editor: R. A. Nelson, Jr.

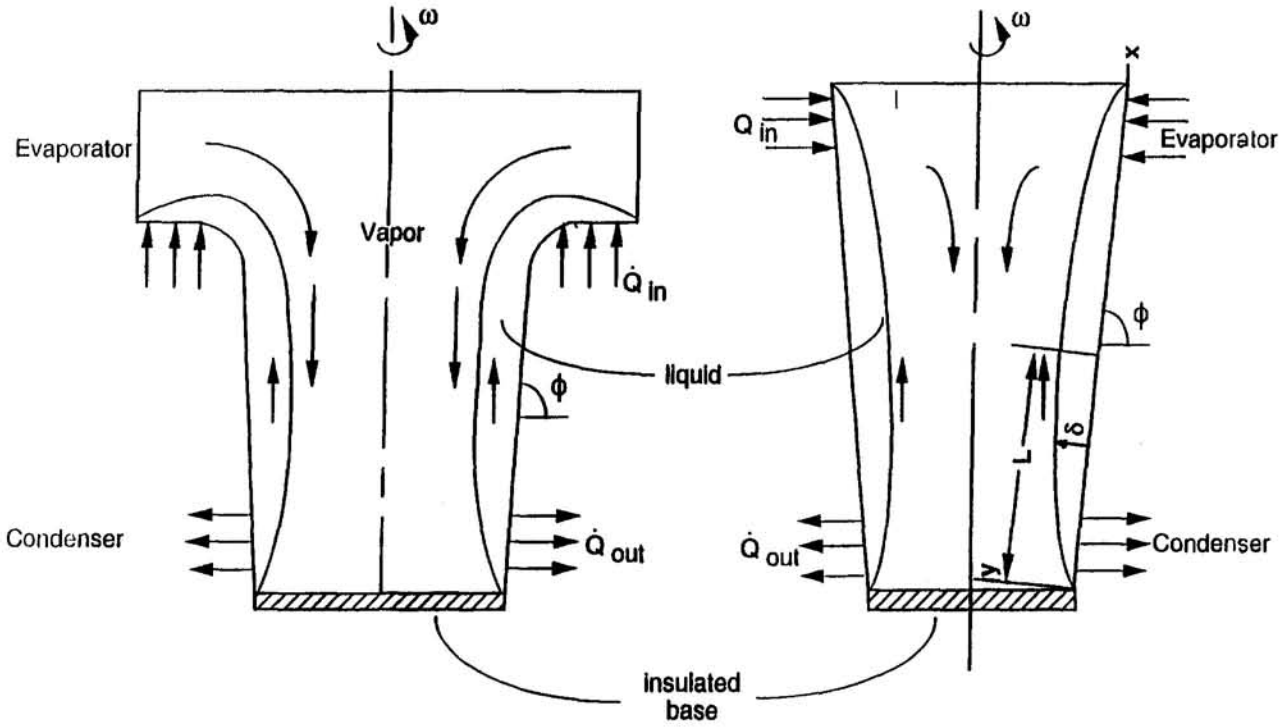

Fig. 1 Vertical axis heat pipe configurations

$$\delta_m = \left(\frac{3\nu k\theta_s}{\rho h_{fg}\omega^2 \cos^2(\phi)}\right)^{1/4};$$

$$\eta = \omega^2 r \cos(\phi)/g - \sin(\phi);$$

$$\psi = \omega^2 r \sin(\phi)/g + \cos(\phi);$$

$$\eta_* = \frac{\eta}{\frac{\nu^2}{g\delta_m^3}};\ \psi_* = \frac{\psi}{\frac{\nu^2 L}{g\delta_m^4}};\ P_* = \frac{P}{\frac{\gamma\nu^2 L}{g\delta_m^3}};\ \theta_s = T_{sat} - T_w \quad (3)$$

δ is the condensate film thickness and $\delta_* = \delta/\delta_m$ is the dimensionless thickness. δ_m is the maximum thickness the layer would achieve provided the condenser was infinitely long. Integrating Eq. (1) and using Eq. (2) while neglecting the vapor pressure gradient gives a differential equation for u_* in terms of δ_*:

$$\frac{\partial^2 u_*}{\partial y_*^2} = \psi_* \frac{d\delta_*}{dx_*} + \frac{d\psi_*}{dx_*}(\delta_* - y_*) - \eta_* \quad (4)$$

The first two terms on the right-hand side of Eq. (4) were neglected for the simplified analysis. An order of magnitude analysis using Eq. (7) for δ_* and its derivatives shows this to be justified provided the inequality in Eq. (5) is satisfied.

$$\frac{\omega^2 r}{g \tan(\phi)} \geq \frac{1}{1 - \sqrt{\frac{20\delta_m}{r_0}\left(1 + \frac{g\cos(\phi)}{\omega^2 r_0}\right)}} \quad (5)$$

As shown in Fig. 3, subsequent numerical solution for δ_* results in a liquid profile practically identical to the analytical result.

The average dimensionless velocity and mass flow rate per unit length given by Eq. (6) has the same form as the classical Nusselt solution except the driving force η_* is a function of x_* (Carey, 1992):

$$\bar{u}_* = \frac{1}{\delta_*}\int_0^{\delta_*} u_* dy_* = \frac{\eta_* \delta_*^2}{3} \Rightarrow$$

$$\dot{m}_* = \frac{\dot{m}}{\rho\nu} = \bar{u}_*\delta_* = \frac{\eta_*\delta_*^3}{3} \quad (6)$$

On substitution of Eq. (6) into an energy balance the differential equation describing the liquid film thickness is obtained. This equation is solved with the resulting dimensionless thickness given by Eq. (7) in terms of $\xi = \eta_0/\eta$:

$$\frac{d\dot{m}}{dx} = \frac{k\theta_s}{h_{fg}\delta} \rightarrow \frac{3\delta_*^3}{(1 - \delta_*^4)}\frac{d\delta_*}{dx_*} = \frac{1}{\eta_*}\frac{d\eta_*}{dx_*} \Rightarrow$$

$$\delta_* = [1 - \xi^{4/3}]^{1/4} \quad (7)$$

The resulting local Nusselt number is given by Eq. (8) and approaches unity as the condenser length goes to infinity:

$$\mathrm{Nu}_x \equiv \frac{h_x\delta_m}{k} = \frac{k}{\delta}\frac{\delta_m}{k} = \frac{1}{\delta_*} \Rightarrow \mathrm{Nu}_\infty = 1 \quad (8)$$

Results and Discussion

The results presented in the following discussion are valid for a condenser with a zero film thickness at $x = 0$. Freon 113 was the working fluid with thermal properties calculated at the average of the wall and vapor temperature. A minimum radius of $r_0 = 0.015$ m and length $L = 0.152$ m were selected to coincide with Daniels and Al-Jumaily (1972). The rpm values ranged from 300 to 2400 with the taper angle being varied from 0 to 88 deg. Figure 2 depicts δ_* as a function of ξ with $\xi \rightarrow 0$ as $L \rightarrow \infty$ and $\xi = 1$ corresponding to $x = 0$. Increasing the rpm enhances heat transfer while increasing ϕ results in a thicker, slower developing condensate layer, which hinders heat transfer.

Figure 3 shows the Nusselt number as a function of x_*. Numerical integration for the average heat transfer coefficient with $\xi_{min} \leq 0.1$ revealed it to be within 10 percent of that for an infinitely long condenser. This gives a simple relation (9), which is useful for design purposes:

$$\bar{q} = \bar{h}\theta_s \approx \frac{k\theta_s}{\delta_m} = Ax\left(\frac{\theta_s^3}{3}\omega^2\cos^2(\phi)\right)^{1/4};$$

$$Ax = \left(\frac{\rho h_{fg} k^3}{\nu}\right)^{1/4} \quad (9)$$

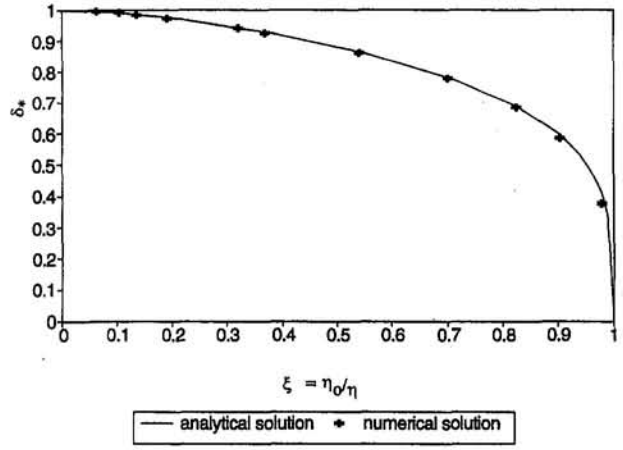

Fig. 2 Dimensionless film thickness as a function of ξ

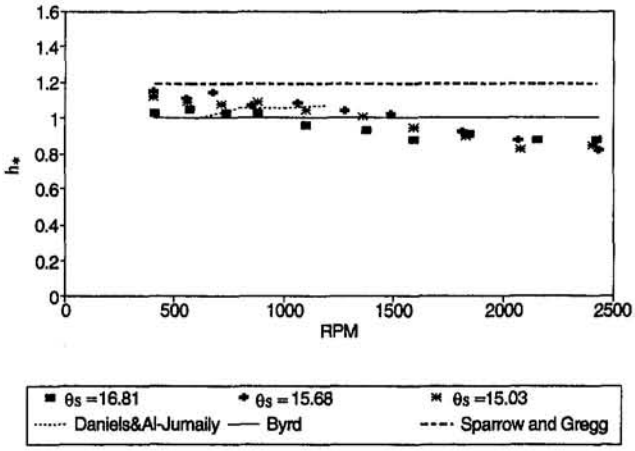

Fig. 4 Comparison with previous work

The fluid property group Ax indicates which fluids yield the highest heat transfer. This is similar to the result presented by Daniels and Al-Jumaily (1972) for horizontal heat pipes. A reasonable value for refrigerant 113 between 250 and 340 K would be 25, while water would have values ranging from 150 to 230 over a temperature range of 290 to 390 K. Other constraints such as material compatibility, cost, and vapor pressure will also influence the choice of working fluid.

The theoretical heat transfer results of Sparrow and Gregg (1959) and the present paper are compared to the experimental results of Nandapurkar and Beatty (1959) for condensation on a rotating flat disk in Fig. 4. Here h_* is the ratio of the reported h and h_∞ from the present work and is plotted against rpm. Each symbol represents an experimental run with an average θ_s given in the legend. As seen, the infinite condenser approximation from the present work gives better agreement with experiment. The experimental data are lower than theory at higher rpm but still within approximately 20 percent over the range studied. This could be due to interfacial shear but surface tension or a systematic experimental error may also contribute.

Also shown is a comparison of the present work with the theoretical values of Daniels and Al-Jumaily for horizontal axis heat pipes. Here h_* is the ratio of the average heat transfer coefficients. $\overline{h}$ from the present work is calculated at an equivalent rpm that gives the same driving force at $x = 0$ as found in the horizontal axis orientation as shown in Eq. (10):

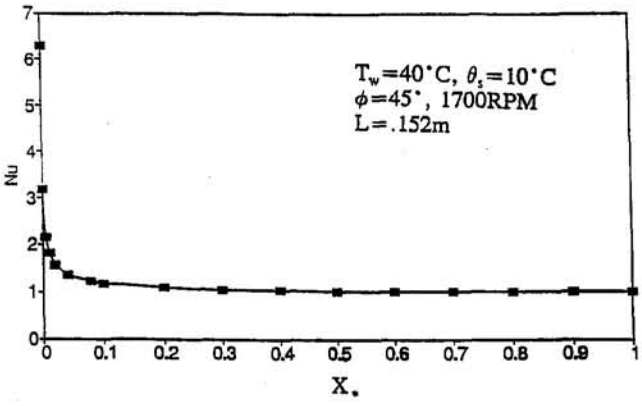

Fig. 3 Nusselt number as a function of x_*

$$\omega_v = \left[\frac{g}{r_0 \cos(\phi)}\left(\left(\frac{\omega_h^2 r_0}{g} - 1\right)\sin(\alpha) + \sin(\phi)\right)\right]^{1/2} \tag{10}$$

Their values are slightly higher, which is unexpected because they include viscous shear at the vapor–liquid interface. This may be because they used slightly different property values. However, it can be seen the results are similar for the same driving force.

Conclusions

The Nusselt analysis of a vertical axis rotating condenser agrees reasonably well with previous experimental and theoretical values. The analysis provides a fluid merit number and a simple form for the Nusselt number, which should prove useful for design purposes.

Acknowledgments

This work was partially supported by the Air Force Office of Scientific Research.

References

Carey, V. P., 1992, *Liquid-Vapor Phase-Change Phenomena,* Hemisphere Publishing Corporation, Philadelphia, PA, p. 353.

Daniels, T. C., and Al-Jumaily, F. K., 1972, "Investigations of the Factors Affecting the Performance of a Rotating Heat Pipe," ASME JOURNAL OF HEAT TRANSFER, Vol. 94, pp. 155–162.

Faghri, A., Gogineni, S., and Thomas, S., 1993, "Vapor Flow Analysis of an Axially Rotating Heat Pipe," *Int. J. Heat Mass Transfer,* Vol. 36, No. 9, pp. 2293–2303.

Maezawa, S., Suzuki, Y., and Tsuchida, A., 1981, "Heat Transfer Characteristics of Disk-Shaped Rotating, Wickless Heat Pipe," *Proc. 4th Int. Heat Pipe Conf.,* London, United Kingdom.

Marto, P. J., 1976, "Performance Characteristics of a Wickless Rotating Heat Pipe," *Proc. 2nd Int. Heat Pipe Conf.,* Bologna, E.S.A.

Nandapurkar, S. S., and Beatty, K. O., Jr., 1959, "Condensation on a Horizontal Rotating Disk," presented at the Third National Heat Transfer Conference, ASME–AIChE, Storrs, CT, Aug.

Sparrow, E. M., and Gregg, J. L., 1959, "A Theory of Rotating Condensation," ASME JOURNAL OF HEAT TRANSFER, Vol. 81, pp. 113–119.

Sparrow, E. M., and Gregg, J. L., 1960, "The Effect of Vapor Drag on Rotating Condensation," ASME JOURNAL OF HEAT TRANSFER, Vol. 82, pp. 71–72.

Sparrow, E. M., and Hartnett, J. P., 1961, "Condensation on a Rotating Cone," ASME JOURNAL OF HEAT TRANSFER, Vol. 83, pp. 101–102.

White, F. M., 1974, *Viscous Fluid Flow,* McGraw-Hill, New York, p. 339.

Pulsed Laser Heating of Highly Absorbing Particles

J. P. Longtin,[1] T. Q. Qiu,[1] and C. L. Tien[1]

Nomenclature

a = particle radius, m
$\mathbf{E}, E$ = electric field vector, magnitude of electric field, V/m
I = laser intensity, W/m^2
i = $(-1)^{1/2}$
K = thermal conductivity, W/m·K
k = imaginary part of complex index of refraction
l = characteristic diffusion distance $\sim(\alpha\tau_p)^{1/2}$, m
N = complex index of refraction = $n + ik$
n = real part of complex index of refraction
r = radial coordinate, m
S = spatial source function = $|\mathbf{E}/E_0|^2$
T = temperature, K
t = time, s
Q = local volumetric heat generation, W/m^3
α = thermal diffusivity, m^2/s
λ = laser wavelength in free space, m
θ = polar angular coordinate, rad
τ_p = laser pulse duration, s

Subscripts

avg = average
m = medium
max = maximum
o = initial
p = particle
∞ = far field; ambient

Superscripts

* = dimensionless quantity

Introduction

The interaction of pulsed laser radiation with small, highly absorbing particles is common to a wide variety of engineering processes. Examples include laser cladding (Komvopoulos and Nagarathnam, 1990), laser surface cleaning (Kelley and Houis, 1993), and laser inclusion damage of high-power optics (Guenther and McIver, 1989). In these applications, detailed knowledge of the radiant energy absorption and heating in the particle and surrounding medium is essential for understanding, controlling, and/or optimizing the process. Often the particles are assumed to absorb the incident radiant energy uniformly throughout their volume, which results in an assumed uniform heating of the particle. The results of this work, however, indicate that the absorption and heating can be highly nonuniform for a wide variety of situations.

The near-field interaction of small particles with laser light has been investigated in the past; however, the work has focused almost exclusively on particles that weakly absorb radiant energy (Prishivalko, 1983; Alexander and Armstrong, 1987; Chitanvis, 1987; Tuntomo et al., 1991). In these cases, there is relatively little attenuation of the incident radiant energy as it propagates through the particle; the nonuniform radiant energy distribution arises predominantly from refraction, diffraction, and interference effects. Tuntomo and Tien (1992) studied the internal absorption and continuous-wave laser heating of weakly absorbing particles in detail. The work, however, did not consider highly absorbing particles, pulsed laser radiation, or heat transfer to a surrounding medium.

This work investigates the nature of the absorption and heating of highly absorbing solid particles embedded in a solid surrounding medium irradiated by pulsed laser light. Since the particles are highly absorbing, the radiant energy distribution mechanism is absorption dominated versus interference and refraction dominated. Additionally, the heating dependence on the pulse duration is considered, and heat transfer to the surrounding medium is included. In the following, the heat transfer in the system is analyzed, followed by a discussion based on sample calculations.

Heat Transfer

The radiant absorption by the particle causes heat generation and heat transfer in the particle–medium system. This radiation heating can be highly nonuniform, and so cannot, in general, be treated as a constant. The distribution of laser radiation absorption in metallic particles was recently investigated by Qiu et al. (1995). They calculated the local volumetric heat generation, Q, in an axisymmetric spherical coordinate system (r, θ) from the relation

$$Q(r, \theta) = \frac{4\pi n k I_0}{\lambda} S(r, \theta). \tag{1}$$

Here n and k are the real and imaginary parts of the particle complex index of refraction, I_0 the incident intensity, λ the wavelength, and $S = |\mathbf{E}/E_0|^2$, called the *spatial source distribution,* is the squared magnitude ratio of the electric field $\mathbf{E}$ to the incident field E_0. The electric field is obtained from Mie's analytic solution to Maxwell's equations. Numerical values are obtained by performing a truncated summation of the infinite series in the analytic solution. The reader is referred to Qiu et al. (1995) for details.

Both the particle–medium system geometry and the radiant absorption in the system are axisymmetric for unpolarized or circularly polarized light. The thermophysical property changes with temperature in this study are assumed to be small, and the optical properties are taken to be constant. The laser pulse is assumed to be temporally uniform, and the maximum temperature is assumed to occur at the end of the laser pulse. The thermal boundary resistance between the particle and medium is taken to be zero, and phase change is not addressed. It is also assumed that classical unsteady Fourier-type conduction occurs in the particle; that is, the pulse duration is always greater than the characteristic particle–medium molecular time scales, i.e., $\tau_p > \sim 10$ ps.

The energy balance equations for the particle and medium, respectively, are

$$\frac{\partial T_p^*}{\partial t^*} = \frac{\alpha_p \tau_p}{a^2}\left[\frac{1}{r^*}\frac{\partial^2(r^* T_p^*)}{\partial r^{*2}} + \frac{1}{r^{*2}\sin\theta}\frac{\partial}{\partial\theta}\left(\sin\theta\frac{\partial T_p^*}{\partial\theta}\right)\right] + \frac{S(r,\theta)}{S_{\max}} \tag{2}$$

$$\frac{\partial T_m^*}{\partial t^*} = \frac{\alpha_m \tau_p}{a^2}\left[\frac{1}{r^*}\frac{\partial^2(r^* T_m^*)}{\partial r^{*2}} + \frac{1}{r^{*2}\sin\theta}\frac{\partial}{\partial\theta}\left(\sin\theta\frac{\partial T_m^*}{\partial\theta}\right)\right] \tag{3}$$

with boundary conditions:

[1] Department of Mechanical Engineering, University of California at Berkeley, Berkeley, CA 94720.

Contributed by the Heat Transfer Division and presented at the 6th AIAA/ASME Thermophysics & Heat Transfer Conference, Colorado Springs, Colorado, June 19–23, 1994. Manuscript received by the Heat Transfer Division February 1994; revision received November 1994. Keywords: Conduction, Modeling and Scaling, Radiation Interactions. Associate Technical Editor: M. F. Modest.

$$T_p^* = T_m^* = 0 \quad \text{at } t^* = 0 \tag{4}$$

$$\frac{\partial T_p^*}{\partial r^*} = 0 \quad \text{at } r^* = 0 \tag{5}$$

$$T_m^* \to 0 \quad \text{as } r^* \to \infty \tag{6}$$

$$T_p^* = T_m^* \quad \text{at } r^* = 1 \tag{7}$$

$$K_p \frac{\partial T_p^*}{\partial r^*} = K_m \frac{\partial T_m^*}{\partial r^*} \quad \text{at } r^* = 1 \tag{8}$$

$$\frac{\partial T_p^*}{\partial \theta} = \frac{\partial T_m^*}{\partial \theta} = 0 \quad \text{at } \theta = 0 \text{ and } \theta = \pi. \tag{9}$$

The nondimensionalizations for r^*, t^*, and T^* are

$$r^* = r/a \tag{10}$$

$$t^* = t/\tau_p \tag{11}$$

$$T^* = \frac{T - T_\infty}{T_c - T_\infty} = \frac{T - T_\infty}{Q_{\max}\alpha_p \tau_p / K_p} \tag{12}$$

where $T_c = Q_{\max}\alpha_p\tau_p/K_p + T_\infty$ and $S_{\max}$ is the maximum value of S in the particle volume.

Equations (2)–(9) are solved numerically for the particle and medium temperatures using the finite difference method. Second-order central differencing on a cell-centered grid is used for the spatial derivatives, and the entire solution is marched forward in time by a first-order explicit scheme. For all calculations the radial grid spacing, $\Delta r/a$, and angular grid spacing, $\Delta\theta$, were less than 1/40. Stability is insured in the explicit scheme by limiting the maximum time step for a given grid spacing; typical time steps, $\Delta t/\tau_p$, were always less than about 10^{-4}.

Results and Discussion

Before discussing numerical solutions to the equations, a scaling analysis is performed to determine the relative importance of the terms in the energy equations, Eqs. (2)–(3). The radial coordinate, r, scales naturally with the particle radius, a, in Eq. (10). Likewise, the laser pulse duration, τ_p, is used to scale the time variable, t, in Eq. (11). There are no imposed temperature differences, hence the temperature in Eq. (12) is scaled with the reference temperature T_c, which represents the temperature an insulated particle with *uniform* volumetric heat generation $Q_{\max} = 4\pi n k I_0 S_{\max}/\lambda$ attains after a time τ_p.

Significant absorption occurs in regions where $S/S_{\max} \sim O(1)$. Then, if the coefficient multiplying the diffusion terms in Eq. (2), $\alpha_p\tau_p/a^2 \ll 1$, diffusion may be neglected. The spatial temperature distribution will then resemble the spatial source distribution. The coefficient $\alpha_p\tau_p/a^2$ is the ratio of the radiation deposition time, τ_p, to the characteristic diffusion time, a^2/α_p, which represents the time for thermal energy to diffuse throughout the particle. Small values of this ratio imply that the laser pulse energy is deposited into the particle much faster than the thermal energy can diffuse away from the deposition site. Likewise, for large values of this ratio, the energy will have ample time to diffuse through the particle and medium, resulting in a nearly uniform temperature distribution. Note also the dependence of this ratio on the inverse square of the particle radius; as the particle size increases, diffusion quickly becomes ineffective in redistributing the absorbed energy. Then, if the initial source distribution is nonuniform, the temperature distribution will be as well.

Similarly, the ratio $\alpha_m\tau_p/a^2$ in Eq. (3) represents the importance of thermal energy conduction in the medium. When this ratio is much less than one, then the thermal energy is unable to travel far away from the particle and the particle is effectively insulated. For very large values, the energy propagates far into the medium, resulting in significant particle cooling.

For the calculations, a platinum particle of radius 10 μm is investigated with the parameters listed in Table 1.

The laser pulse energy is held fixed (shorter pulse durations simply have a higher radiation intensity such that $\tau_p I_0 = \text{const}$) and the particle temperature is computed at the end of the laser pulse, i.e., $t^* = 1$. Since temperature scales linearly with $Q_{\max}$ in Eq. (12), I_0 in Eq. (1) is chosen for simplicity such that $Q_{\max}\alpha_p\tau_p/K_p = 1$ K. Results for the source function and temperature distributions are presented as surface plots for points taken across a midplane of the particle, as shown in the inset in Fig. 1; only half of the particle is shown for clarity. The incident radiation propagates in the $+x$ direction and strikes the front of the particle, where the *front* and *rear* of the particle refer to the illuminated and shadowed halves of the particle, respectively. The radiant energy source distribution inside the particle for these parameters is calculated as described by Qiu et al. (1993), and is shown in Fig. 1.

In Fig. 2, $\tau_p = 20$ μs and $\tau_p\alpha_p/a^2 = 10$, hence the diffusion terms dominate over the source function term in Eq. (2). Consequently, the spatial source nonuniformities are readily smoothed out by diffusion, resulting in nearly uniform heating. Note also that the energy has propagated well into the medium as a result of the relatively long laser pulse duration. In Fig. 3, $\tau_p = 2$ μs, and $\tau_p\alpha_p/a^2 = 1$, thus, the diffusion terms are comparable to the source term. The radial variation of the temperature inside

Table 1 Parameters used in the results presented

Parameter	Value
a	10 μm
$N_m = n_m + ik_m$	1
$N_p = n_p + ik_p$	$10 + i36$
α_p	$5.0 \cdot 10^{-5}$ m²/s
α_m	$5.0 \cdot 10^{-7}$ m²/s
K_p	100 W/m·K
K_m	1 W/m·K
T_∞	300 K

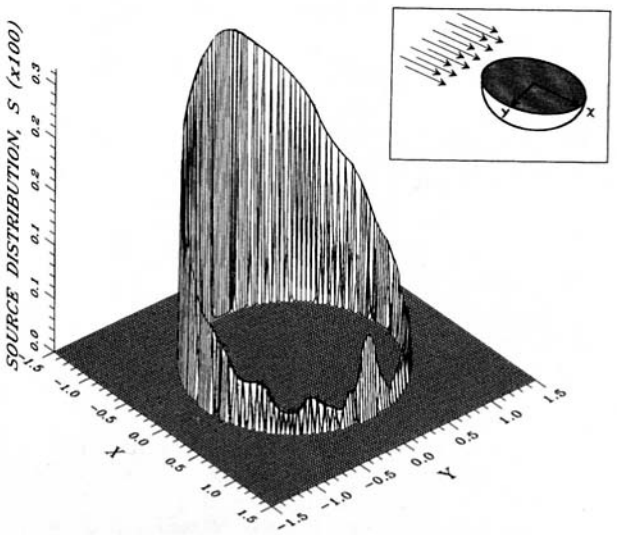

Fig. 1 Source distribution for a = 10 μm (λ = 10 μm)

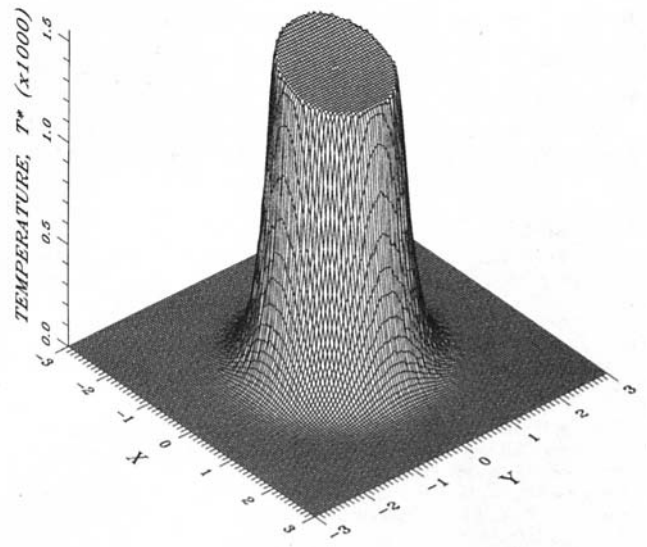

Fig. 2 Temperature distribution for $\tau_p\alpha_p/a^2 = 10$ ($\tau_p = 20$ μs, $a = 10$ μm, $\lambda = 10$ μm)

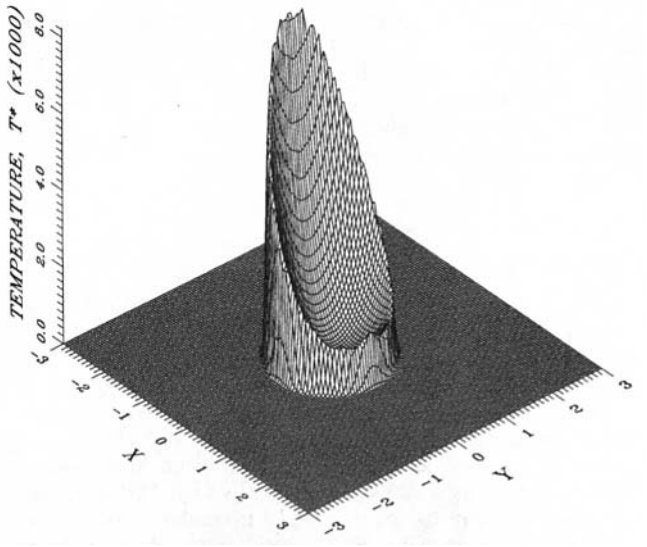

Fig. 4 Temperature distribution for $\tau_p\alpha_p/a^2 = 0.1$ ($\tau_p = 200$ ns, $a = 10$ μm, $\lambda = 10$ μm)

the particle is not very pronounced, which is expected; when $\tau_p\alpha_p/a^2 \sim 1$, the pulse duration is comparable to the time it takes the energy to diffuse one particle diameter. The temperature profile does, however, exhibit a strong angular dependence similar to the source distribution, and the temperature distribution is clearly nonuniform. The temperature at the front of the particle is about twice that near the back. Some thermal energy propagates into the medium, although this effect is much less pronounced than in the prior case, due to the order-of-magnitude reduction in the pulse duration. In Fig. 4, $\tau_p = 200$ ns, and $\tau_p\alpha_p/a^2 = 0.1$. Diffusion becomes markedly ineffective in redistributing the thermal energy, and both the angular and radial characteristics of the temperature distribution resemble those of the source distribution. The temperature distribution is very nonuniform, with a front temperature about seven times as great as that near the back. As a result of the short pulse duration, very little thermal diffusion into the medium occurs. Calculations for shorter pulse durations are not performed as diffusion becomes negligible, and the temperature distribution approaches the spatial source distribution to within a constant of proportionality: $T(r,\theta) = \beta S(r,\theta)$, where $\beta = 4\pi nkI_o\tau_p/\lambda\rho C_p$. It is emphasized that these temperature profiles are for highly absorbing particles. Weakly absorbing particles have a different internal radiation distribution, hence their temperature profiles will, in general, be quite different, although they still can be very nonuniform (Tuntomo and Tien, 1992).

A useful result of this analysis is the minimum pulse duration required for uniform particle heating. Following the analysis of Qiu et al. (1995), it can be shown that particles as small as 10 nm can have nonuniform source distributions. Then, assuming a uniform temperature distribution in the presence of a nonuniform source distribution requires $\tau_p\alpha_p/a^2 \geq 10$, the minimum pulse duration required for uniform heating can be calculated. The results as a function of particle size for the parameters of this study are shown in Table 2.

Another figure of merit is the maximum temperature obtained in the particle compared to the temperature, T_{avg}, the particle would obtain by assuming uniform absorption and heating of the same laser pulse energy. Table 3 lists the ratios of the

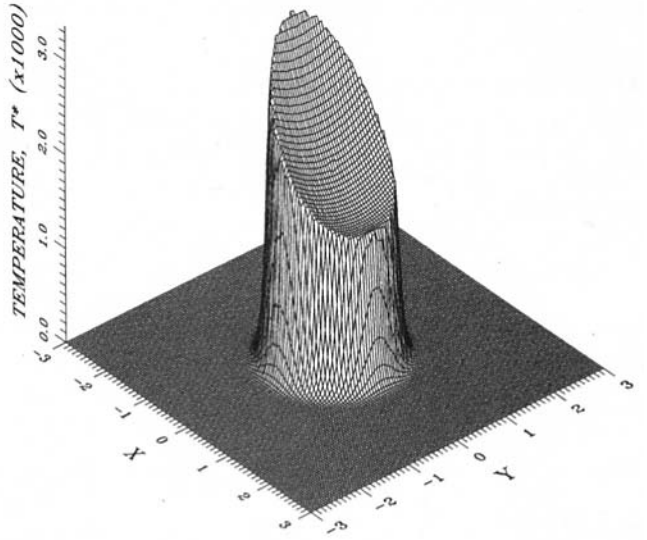

Fig. 3 Temperature distribution for $\tau_p\alpha_p/a^2 = 1$ ($\tau_p = 2$ μs, $a = 10$ μm, $\lambda = 10$ μm)

Table 2 Minimum pulse duration for uniform heating assumption

a	τ_p
10 nm	20 ps
100 nm	2 ns
1 μm	200 ns
10 μm	2 μs

Table 3 Ratio of maximum temperature to uniformly absorbing temperature

	T_{max}/T_{avg}		
a	$\tau_p\alpha_p/a^2 = 0.1$	$\tau_p\alpha_p/a^2 = 1$	$\tau_p\alpha_p/a^2 = 10$
10 nm	3.1	1.7	1.0
100 nm	3.1	1.7	1.0
1 μm	4.9	2.0	1.0
10 μm	6.3	2.4	1.0

maximum particle temperature to those assuming uniform absorption as a function of particle size and the parameters in Table 1. For each particle size, the pulse energy is kept constant as the pulse width is varied. As anticipated, the shorter pulse duration cases have higher peak temperatures. The maximum difference is about a factor of six for the case $a = 10\ \mu m$ and $\tau_p \alpha_p / a^2 = 0.1$.

Concluding Remarks

This work investigates the nature of the internal radiant absorption and heating of highly absorbing spherical particles embedded in a surrounding medium illuminated by pulsed laser light. Mie's analytic solution to Maxwell's equations is used to compute the spatial distribution of the absorbed incident radiation in the particle. The heat transfer in the particle–medium system is modeled as unsteady Fourier conduction, and the resulting equations are solved numerically to yield the temperature distribution in the particle and surrounding medium as a function of position and time. The results show that the absorption and heating can be highly nonuniform for many cases of practical interest. The temperature distribution in the particle depends on the initial radiant energy distribution, laser pulse duration, particle size, and thermophysical properties of the system. Shorter pulse durations result in more nonuniform temperature distributions. Criteria are established by scaling the governing equations to determine when the uniform heating approximation can be made. It is shown that in many cases, this approximation cannot be made, and the maximum temperature obtained in the particle can be several times higher than that predicted for a uniformly heated particle.

Acknowledgments

The authors acknowledge the financial support from the U.S. National Science Foundation and the U.S. Department of Energy.

References

Alexander, D. R., and Armstrong, J. G., 1987, "Explosive Vaporization of Aerosol Drops Under Irradiation by a CO_2 Laser Beam," *Applied Optics,* Vol. 26, pp. 533–538.

Chitanvis, S. M., 1987, "Explosive Vaporization of Small Droplets by a High-Energy Laser Beam," *Journal of Applied Physics,* Vol. 62, pp. 4387–4393.

Guenther, A. H., and McIver, J. K., 1989, "The Pulsed Laser Damage Sensitivity of Optical Thin Films, Thermal Conductivity," *Laser and Particle Beams,* Vol. 7, pp. 433–441.

Kelley, J. D., and Hovis, F. E., 1993, "A Thermal Detachment Mechanism for Particle Removal From Surfaces by Pulsed Laser Irradiation," *Microelectronic Engineering,* Vol. 20, pp. 159–170.

Komvopoulos, K., and Nagarathnam, K., 1990, "Processing and Characterization of Laser-Cladding Coating Materials," ASME *Journal of Engineering Materials and Technology,* Vol. 112, pp. 131–143.

Prishivalko, A. P., 1983, "Heating and Destruction of Water Droplets on Exposure to Radiation With Inhomogeneous Internal Heat Evolution," *Soviet Physics Journal,* Vol. 26, pp. 142–148.

Qiu, T. Q., Longtin, J. P., and Tien, C. L., 1995, "Characteristics of Radiation Absorption in Metallic Particles," ASME JOURNAL OF HEAT TRANSFER, Vol. 117, pp. 340–345.

Tuntomo, A., Park, S. H., and Tien, C. L., 1991, "Internal Distribution of Radiant Absorption in a Spherical Particle," ASME JOURNAL OF HEAT TRANSFER, Vol. 113, pp. 407–412.

Tuntomo, A., and Tien, C. L., 1992, "Transient Heat Transfer in a Conducting Particle With Internal Radiant Absorption," ASME JOURNAL OF HEAT TRANSFER, Vol. 114, pp. 304–309.

The Spectral-Line Weighted-Sum-of-Gray-Gases Model for H_2O/CO_2 Mixtures

M. K. Denison[1] and B. W. Webb[2]

Introduction

The weighted-sum-of-gray-gases model, first introduced by Hottel and Sarofim (1967) for expressing total gas emissivities and in the context of the zone method, has recently been extended to the general form of the radiative transfer equation (RTE) (Modest, 1991; Denison and Webb, 1993a, 1993b, 1995a). The fundamental radiative property of the model is the locally defined absorption coefficient, which permits the use of arbitrary solution methods of the RTE. Denison and Webb (1993a) developed a spectral line-based weighted-sum-of-gray-gases (SLW) model by constructing a histogram representation of the high-resolution spectra of H_2O. Subsequently, a novel absorption-line blackbody distribution function was developed that easily allows the blackbody weights a_j of any desired number of gray gases to be determined by simple differencing rather than accessing detailed spectral line information (Denison and Webb, 1993b, 1995b). The distribution function also provides the means of incorporating a spatial dependence of the gray gas absorption cross sections on temperature, pressure, and species mole in nonisothermal, nonhomogeneous problems (Denison and Webb, 1995a).

The development of the SLW model in these references has only considered individual species (H_2O and CO_2) independent of one another. In most practical gas flames a mixture of gases must be considered. Previous treatment of gas mixtures with the weighted-sum-of-gray-gases models has involved either determining a single set of absorption coefficients and blackbody weights from emissivities of the mixture (Smith et al., 1982; Coppalle and Vervisch, 1983; Taylor and Foster, 1974) or determining the weights of the mixture as a product of the weights of the individual species under the assumption of random positions of absorption lines (Song and Viskanta, 1986). In this paper the SLW model is formulated for H_2O/CO_2 mixtures.

The Double Integration Approach

To calculate total heat transfer rates in a mixture of H_2O and CO_2, the weighted-sum-of-gray-gases RTE is modified by including an additional gray gas index k to account for the second specie:

$$\frac{dI_{j,k}}{ds} = \kappa_{j,k}\left(a_{j,k}\frac{\sigma T^4}{\pi} - I_{j,k}\right) \tag{1}$$

The joint weight $a_{j,k}$ is defined as the fraction of blackbody energy in the overlap of the spectral segments where the effective absorption cross section of H_2O is $C_{w,j}$ and where the effective absorption cross section of CO_2 is $C_{c,k}$. $I_{j,k}$ is the total (spectrally integrated) intensity in these same portions of the spectrum. The indices j and k denote the jth and kth gray gas for H_2O and CO_2, respectively. Including the spectral windows the joint weights sum to unity:

$$\sum_j \sum_k a_{j,k} = 1. \tag{2}$$

[1] Advanced Combustion Engineering Research Center, Brigham Young University, Provo, UT 84602.

[2] Department of Mechanical Engineering, Brigham Young University, Provo, UT 84602.

Contributed by the Heat Transfer Division of THE AMERICAN SOCIETY OF MECHANICAL ENGINEERS. Manuscript received by the Heat Transfer Division July 1994; revision received December 1994. Keywords: Combustion, High-Temperature Phenomena, Radiation. Associate Technical Editor: R. Viskanta.

maximum particle temperature to those assuming uniform absorption as a function of particle size and the parameters in Table 1. For each particle size, the pulse energy is kept constant as the pulse width is varied. As anticipated, the shorter pulse duration cases have higher peak temperatures. The maximum difference is about a factor of six for the case $a = 10\ \mu m$ and $\tau_p \alpha_p / a^2 = 0.1$.

Concluding Remarks

This work investigates the nature of the internal radiant absorption and heating of highly absorbing spherical particles embedded in a surrounding medium illuminated by pulsed laser light. Mie's analytic solution to Maxwell's equations is used to compute the spatial distribution of the absorbed incident radiation in the particle. The heat transfer in the particle–medium system is modeled as unsteady Fourier conduction, and the resulting equations are solved numerically to yield the temperature distribution in the particle and surrounding medium as a function of position and time. The results show that the absorption and heating can be highly nonuniform for many cases of practical interest. The temperature distribution in the particle depends on the initial radiant energy distribution, laser pulse duration, particle size, and thermophysical properties of the system. Shorter pulse durations result in more nonuniform temperature distributions. Criteria are established by scaling the governing equations to determine when the uniform heating approximation can be made. It is shown that in many cases, this approximation cannot be made, and the maximum temperature obtained in the particle can be several times higher than that predicted for a uniformly heated particle.

Acknowledgments

The authors acknowledge the financial support from the U.S. National Science Foundation and the U.S. Department of Energy.

References

Alexander, D. R., and Armstrong, J. G., 1987, "Explosive Vaporization of Aerosol Drops Under Irradiation by a CO_2 Laser Beam," *Applied Optics,* Vol. 26, pp. 533–538.

Chitanvis, S. M., 1987, "Explosive Vaporization of Small Droplets by a High-Energy Laser Beam," *Journal of Applied Physics,* Vol. 62, pp. 4387–4393.

Guenther, A. H., and McIver, J. K., 1989, "The Pulsed Laser Damage Sensitivity of Optical Thin Films, Thermal Conductivity," *Laser and Particle Beams,* Vol. 7, pp. 433–441.

Kelley, J. D., and Hovis, F. E., 1993, "A Thermal Detachment Mechanism for Particle Removal From Surfaces by Pulsed Laser Irradiation," *Microelectronic Engineering,* Vol. 20, pp. 159–170.

Komvopoulos, K., and Nagarathnam, K., 1990, "Processing and Characterization of Laser-Cladding Coating Materials," ASME *Journal of Engineering Materials and Technology,* Vol. 112, pp. 131–143.

Prishivalko, A. P., 1983, "Heating and Destruction of Water Droplets on Exposure to Radiation With Inhomogeneous Internal Heat Evolution," *Soviet Physics Journal,* Vol. 26, pp. 142–148.

Qiu, T. Q., Longtin, J. P., and Tien, C. L., 1995, "Characteristics of Radiation Absorption in Metallic Particles," ASME JOURNAL OF HEAT TRANSFER, Vol. 117, pp. 340–345.

Tuntomo, A., Park, S. H., and Tien, C. L., 1991, "Internal Distribution of Radiant Absorption in a Spherical Particle," ASME JOURNAL OF HEAT TRANSFER, Vol. 113, pp. 407–412.

Tuntomo, A., and Tien, C. L., 1992, "Transient Heat Transfer in a Conducting Particle With Internal Radiant Absorption," ASME JOURNAL OF HEAT TRANSFER, Vol. 114, pp. 304–309.

The Spectral-Line Weighted-Sum-of-Gray-Gases Model for H_2O/CO_2 Mixtures

M. K. Denison[1] and B. W. Webb[2]

Introduction

The weighted-sum-of-gray-gases model, first introduced by Hottel and Sarofim (1967) for expressing total gas emissivities and in the context of the zone method, has recently been extended to the general form of the radiative transfer equation (RTE) (Modest, 1991; Denison and Webb, 1993a, 1993b, 1995a). The fundamental radiative property of the model is the locally defined absorption coefficient, which permits the use of arbitrary solution methods of the RTE. Denison and Webb (1993a) developed a spectral line-based weighted-sum-of-gray-gases (SLW) model by constructing a histogram representation of the high-resolution spectra of H_2O. Subsequently, a novel absorption-line blackbody distribution function was developed that easily allows the blackbody weights a_j of any desired number of gray gases to be determined by simple differencing rather than accessing detailed spectral line information (Denison and Webb, 1993b, 1995b). The distribution function also provides the means of incorporating a spatial dependence of the gray gas absorption cross sections on temperature, pressure, and species mole in nonisothermal, nonhomogeneous problems (Denison and Webb, 1995a).

The development of the SLW model in these references has only considered individual species (H_2O and CO_2) independent of one another. In most practical gas flames a mixture of gases must be considered. Previous treatment of gas mixtures with the weighted-sum-of-gray-gases models has involved either determining a single set of absorption coefficients and blackbody weights from emissivities of the mixture (Smith et al., 1982; Coppalle and Vervisch, 1983; Taylor and Foster, 1974) or determining the weights of the mixture as a product of the weights of the individual species under the assumption of random positions of absorption lines (Song and Viskanta, 1986). In this paper the SLW model is formulated for H_2O/CO_2 mixtures.

The Double Integration Approach

To calculate total heat transfer rates in a mixture of H_2O and CO_2, the weighted-sum-of-gray-gases RTE is modified by including an additional gray gas index k to account for the second specie:

$$\frac{dI_{j,k}}{ds} = \kappa_{j,k}\left(a_{j,k}\frac{\sigma T^4}{\pi} - I_{j,k}\right) \tag{1}$$

The joint weight $a_{j,k}$ is defined as the fraction of blackbody energy in the overlap of the spectral segments where the effective absorption cross section of H_2O is $C_{w,j}$ and where the effective absorption cross section of CO_2 is $C_{c,k}$. $I_{j,k}$ is the total (spectrally integrated) intensity in these same portions of the spectrum. The indices j and k denote the jth and kth gray gas for H_2O and CO_2, respectively. Including the spectral windows the joint weights sum to unity:

$$\sum_j \sum_k a_{j,k} = 1. \tag{2}$$

[1] Advanced Combustion Engineering Research Center, Brigham Young University, Provo, UT 84602.

[2] Department of Mechanical Engineering, Brigham Young University, Provo, UT 84602.

Contributed by the Heat Transfer Division of THE AMERICAN SOCIETY OF MECHANICAL ENGINEERS. Manuscript received by the Heat Transfer Division July 1994; revision received December 1994. Keywords: Combustion, High-Temperature Phenomena, Radiation. Associate Technical Editor: R. Viskanta.

The absorption coefficients $\kappa_{j,k}$ are given as the sum of contributions of the two species:

$$\kappa_{j,k} = N_w C_{w,j} + N_c C_{c,k} \tag{3}$$

where N_w and N_c are the molar densities of H_2O and CO_2, respectively. The total heat transfer rates are then given as the sum of the solutions of Eq. (1) over the two gray gas absorption cross sections:

$$I = \sum_j \sum_k I_{j,k}. \tag{4}$$

A joint absorption-line blackbody distribution function may be defined for a mixture of two gases from which the joint weights $a_{j,k}$ can be determined. The joint distribution function $F_{w,c}$ is defined as that fraction of blackbody energy in the overlapping portions of the spectrum where $C_{w,\eta}$ is less than C_w and where $C_{c,\eta}$ is less than C_c. This is illustrated schematically for a small portion of the high-resolution absorption spectrum in Fig. 1. The overlapping portions of the spectrum over which Planck's function is integrated are denoted with the shaded areas. The joint function is then expressed as

$$F_{w,c}(C_w, C_c, T_b, T_g, P_T, Y_w) = \frac{1}{\sigma T_b^4} \sum_i \int_{\Delta\eta_i(C_w, C_c, T_g, P_T, Y_w)} E_{b\eta}(\eta, T_b) d\eta, \tag{5}$$

where σ is the Stefan–Boltzmann constant and $E_{b\eta}$ is Planck's function evaluated at the wave number η and blackbody (source) temperature T_b. $\Delta\eta_i$ is the ith spectral overlap of the two sets of spectral segments.

The joint absorption-line blackbody distribution function was calculated for an H_2O/CO_2 mixture by determining the spectral locations where a given value of the absorption cross section intersected the high-resolution spectrum as outlined by Denison and Webb (1993b). This was done separately for each species. The overlap of the two sets of spectral segments was then determined over which Planck's function was integrated. The detailed spectral-line data were obtained from the 1991 version of the HITRAN database (Rothman et al., 1992) and from "hot" line estimates (Denison and Webb, 1993b; Denison, 1994).

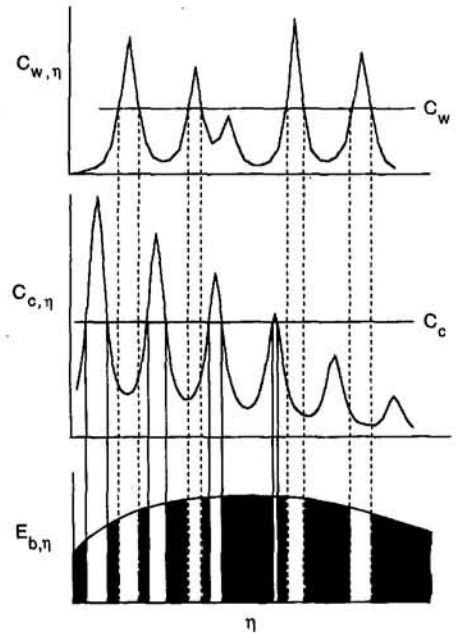

Fig. 1 Portions of the spectrum where the fraction of the blackbody energy is calculated

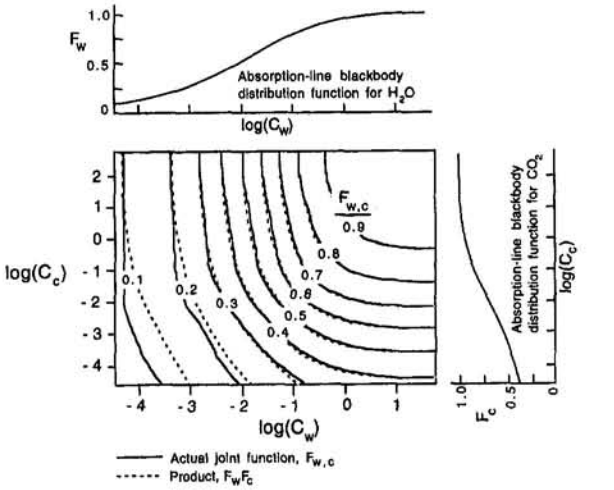

Fig. 2 The joint absorption-line blackbody distribution function for an H_2O/CO_2 mixture calculated from spectral-line data via Eq. (5)

Figure 2 shows the calculated joint distribution function, $F_{w,c}$, at identical gas and source temperatures of 1000 K and in the limit of air broadening at one atmosphere total pressure (solid contour lines). In the limit of large C_c the function is identical to F_w, as illustrated by the line graph above the joint function. Similarly, in the limit of large C_w the function F_c is recovered, illustrated by the graph to the right of the joint function. These limiting absorption-line blackbody distribution functions for the individual species are identical to those presented previously (Denison and Webb, 1993b, 1995b; Denison, 1994). The joint function is monotonic in both C_w and C_c. It has a value of unity at large values of C_w and C_c.

Figure 2 suggests that the joint distribution function may be expressed to a good approximation for H_2O/CO_2 mixtures as the product of the individual functions:

$$F_{w,c}(C_w, C_c) \cong F_w(C_w) F_c(C_c) \tag{6}$$

This approximation is possible due to the statistically uncorrelated spectra. The product of the individual functions, F_wF_c, is shown by dashed contour lines in Fig. 2. The discrepancies between $F_{w,c}$ and F_wF_c are confined to low values of C_w and C_c and may therefore be expected to produce greater error in total radiative transfer predictions for large optical paths. Comparisons between the exact joint function and the product of the separate functions at other temperatures and composition show similar agreement.

The weights $a_{j,k}$ are obtained from the joint absorption-line distribution function through double differencing as:

$$a_{j,k} = F_{w,c}(\tilde{C}_{w,j+1}, \tilde{C}_{c,k+1}) - F_{w,c}(\tilde{C}_{w,j+1}, \tilde{C}_{c,k}) - F_{w,c}(\tilde{C}_{w,j}, \tilde{C}_{c,k+1}) + F_{w,c}(\tilde{C}_{w,j}, \tilde{C}_{c,k}). \tag{7}$$

The tildes are used to distinguish the absorption cross sections used in the double differencing of Eq. (7) from those used in the mixture absorption coefficient of Eq. (3) (i.e., $\tilde{C}_{w,i} < C_{w,i} < \tilde{C}_{w,i+1}$). Note that Eq. (7) applies generally to binary mixtures irrespective of whether Eq. (6) is valid or not. Substituting Eq. (6) into Eq. (7), the joint weight is well approximated by the product of the two individual weights:

$$a_{j,k} \cong [F_w(\tilde{C}_{w,j+1}) - F_w(\tilde{C}_{w,j})][F_c(\tilde{C}_{c,k+1}) - F_c(\tilde{C}_{c,k})] = a_j a_k. \tag{8}$$

Thus under the approximation of Eq. (6) the approach used by Song and Viskanta (1986) has been replicated here, but in terms of the absorption-line blackbody distribution functions. This product approximation is also similar to that used in the k-

distribution method where the product of the quadrature weights are used (Lacis and Oinas, 1991).

The Convolution Approach

The double integration involved in obtaining total heat transfer rates in a binary gas mixture is a significant increase in computational effort over the single integration involved with a single specie (but still an immense decrease over line-by-line calculations). If the ratio of the mole fractions of the two species is spatially constant then it is possible to construct a single absorption cross-section spectrum with lines of both species. An absorption-line distribution function can then be formulated in terms of a single absorption cross section for the gas mixture, C_{mix} in lieu of two absorption cross sections (one for each specie). This permits a single integration instead of a double integration. The development that follows is similar to the convolution theorem found in the literature applicable to the k-distribution method (Goody et al., 1989). The formulation assumes a spatially constant mole fraction ratio. However, it will be shown that in cases where there is moderate spatial variation of the mole fraction ratio, the approach still yields good results using the ratio of the spatially averaged mole fractions.

If the CO_2-to-H_2O molar density ratio is spatially constant, one may define a single absorption cross section C_{mix} by factoring out the combined H_2O/CO_2 molar density from Eq. (3):

$$\kappa = (N_w + N_c)\left(\frac{N_c}{N_w + N_c} C_c + \frac{N_w}{N_w + N_c} C_w\right)$$

$$= (N_w + N_c)[rC_c + (1 - r)C_w] = (N_w + N_c)C_{\text{mix}} \quad (9)$$

The relative CO_2 mole fraction r and mixture absorption cross section C_{mix} are defined, respectively, as $r = N_c/(N_c + N_w)$ and $C_{\text{mix}} = rC_c + (1 - r)C_w$. The subscripts j and k have been deleted from Eq. (9) since ultimately only a single index is required for C_{mix}. This formulation allows treatment of the full range of molar density ratio, including the limiting cases of pure CO_2 or H_2O. For example, if $r = 1$ (pure CO_2) then $(C_{\text{mix}} - rC_c)/(1 - r) \to \infty$, and F_w in this limiting case is unity and the convolution recovers F_c. Similarly, F_w is the result for $r = 0$ (pure H_2O) since $C_{\text{mix}} = C_w$.

Having defined C_{mix} it is possible to define a mixture absorption-line blackbody distribution function F_{mix} as that fraction of blackbody energy in the portions of the absorption spectrum where $(1 - r)C_{w,\eta} + rC_{c,\eta} < C_{\text{mix}}$. If r is spatially constant then C_w can be replaced by $(C_{\text{mix}} - rC_c)/(1 - r)$ and the mixture distribution function can be determined from the joint distribution function as follows. The overlapping portions of the absorption spectrum where $(C_c - dC_c/2) < C_{c,\eta} < (C_c + dC_c/2)$ and where $C_{w,\eta} < (C_{\text{mix}} - rC_c)/(1 - r)$ constitute a differential subset of the portions of the spectrum where $(1 - r)C_{w,\eta} + rC_{c,\eta} < C_{\text{mix}}$. The fraction of blackbody energy in this subset provides a differential contribution to F_{mix}, as:

$$dF_{\text{mix}}(C_{\text{mix}}, C_c) = F_{w,c}\left(\frac{C_{\text{mix}} - rC_c}{1 - r}, C_c + \frac{dC_c}{2}\right) - F_{w,c}\left(\frac{C_{\text{mix}} - rC_c}{1 - r}, C_c - \frac{dC_c}{2}\right) \quad (10)$$

By employing Eq. (6), Eq. (10) becomes:

$$dF_{\text{mix}}(C_{\text{mix}}, C_c) = F_w\left(\frac{C_{\text{mix}} - rC_c}{1 - r}\right) \times \left[F_c\left(C_c + \frac{dC_c}{2}\right) - F_c\left(C_c - \frac{dC_c}{2}\right)\right]$$

$$= F_w\left(\frac{C_{\text{mix}} - rC_c}{1 - r}\right) dF_c(C_c) \quad (11)$$

Equation (11) is integrated over C_c to obtain the mixture distribution function:

$$F_{\text{mix}}(C_{\text{mix}}) = \int_{F_c(C_{c,\min})}^{F_c(C_{c,\max})} F_w\left(\frac{C_{\text{mix}} - rC_c}{1 - r}\right) dF_c(C_c). \quad (12)$$

It must be emphasized that F_{mix} [Eq. (12)] is entirely different from the joint function of Eq. (5); $F_{w,c}$ is a function of two absorption cross sections C_w and C_c, while F_{mix} is a function of a single absorption cross section of the mixture C_{mix}. Note that the form of Eq. (12) is a convolution. The upper limit of integration $C_{c,\max}$ is given as

$$C_{c,\max} = \frac{C_{\text{mix}} - (1 - r)C_{w,\min}}{r}. \quad (13)$$

$C_{c,\min}$ and $C_{w,\min}$ are the minimum CO_2 and H_2O absorption cross sections, respectively, that are used in the calculations. They need not be the absolute minima of the corresponding spectra but must be sufficiently small to cover the longest path lengths relevant to the problem of interest. Here, the minimum absorption cross section is taken as 3×10^{-5} m^2/mole for both CO_2 and H_2O.

Model Validation

The model developed in the foregoing has been evaluated over a wide range of simulation conditions (Denison, 1994). A few one-dimensional problems are presented here illustrating the methods for gas mixtures of H_2O and CO_2 at one atmosphere total pressure between infinite parallel walls. In this work a simple discrete ordinates method, applicable to gray analyses (Carlson and Lathrop, 1968), is used to solve the RTE. The spatial grid in the calculations reported here was systematically refined to assure grid independence of solutions. The model solutions are compared with line-by-line benchmarks. The benchmark predictions for validation of the SLW model approaches presented above were generated by solving for the intensity field line-by-line using detailed spectral line data as described previously (Denison and Webb, 1993a, 1995a, 1995b). These same spectral line data were also used for the generation of the absorption-line blackbody distribution function correlations of the species H_2O and CO_2 given by Denison and Webb (1993b, 1995b). These correlations were used in the model predictions presented. Each of these computer runs involved between 100,000 and 1,000,000 spectral calculations.

The first problem considered consists of spatially constant 40 percent H_2O and 20 percent CO_2 at 1250 K between walls 3 m apart with an emissivity of 0.8. The wall temperatures are 400 K and 1500 K at $x = 0$ and $x = 3.0$ m, respectively. Figure 3(a) shows the predicted local radiative flux divergence and cold wall net flux. The line-by-line benchmark is compared with four model predictions consisting of ten and three gray gases. The ten-gray-gas prediction uses logarithmically spaced absorption cross sections. The three-gray-gas predictions were obtained using absorption cross sections and supplemental absorption cross sections determined from an optimization involving total emissivities (Denison and Webb, 1993a). Predictions were generated using both a double quadrature over absorption cross sections of both species, and a single quadrature over C_{mix} applying the convolution method. All the model predictions agree well with the benchmark and are generally within 5 percent. The good agreement seen here is typical of all isothermal, homogeneous cases.

A nonisothermal, nonhomogeneous mixture of the gases is next considered. The local temperature and H_2O mole fraction profiles are given, respectively, by $T(x) = 700 - 300 \cos(\pi x/L)$ K and $Y(x) = 0.2 - 0.15 \cos(\pi x/L)$. The relative CO_2 mole fraction r is spatially constant at 0.4. This value is roughly representative of conditions for combustion of many gaseous hydrocarbon fuels. The molar density ratio might be assumed

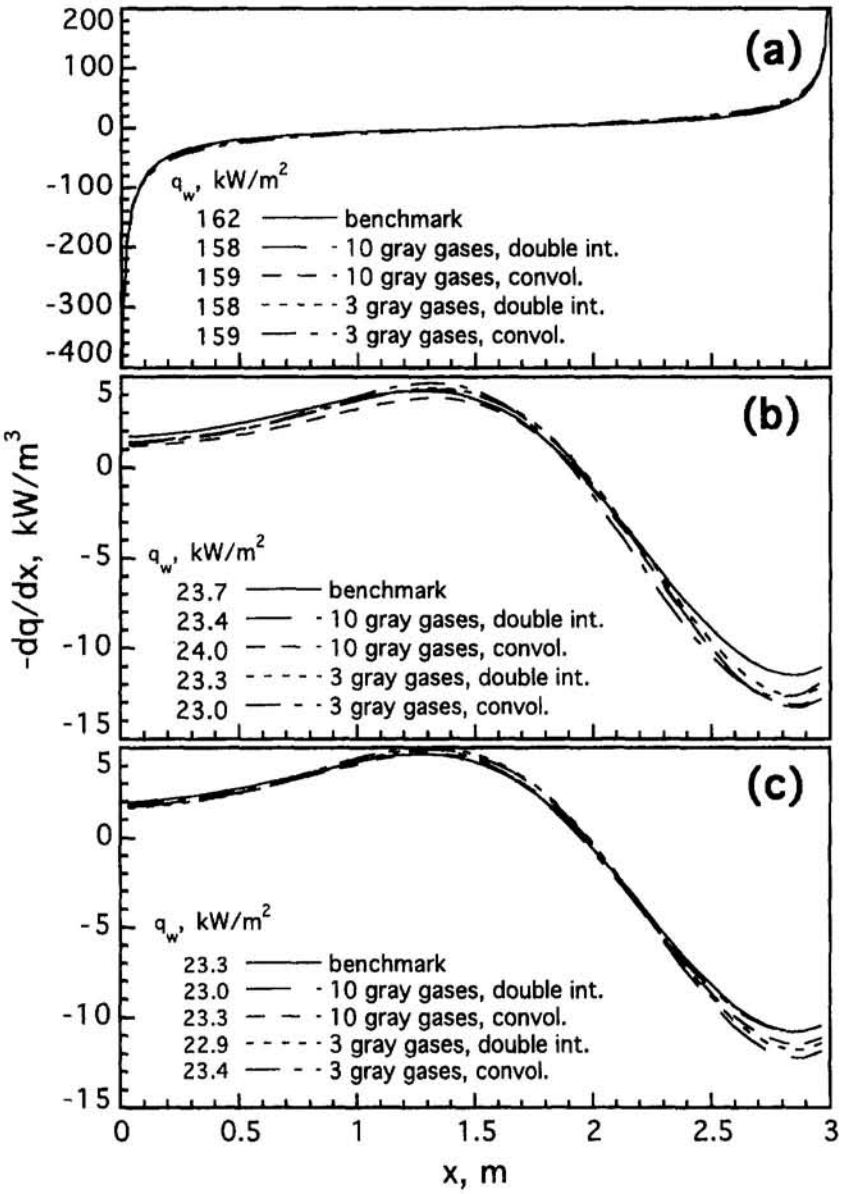

Fig. 3 Radiative source and cold wall net flux for H_2O and CO_2 mixtures between infinite parallel walls: (*a*) isothermal, homogeneous medium, $\epsilon_w = 0.8$; (*b*) & (*c*) cosine temperature and mole fraction profile, $\epsilon_w = 0.75$. (*b*) r is constant at 0.4, (*c*) r is variable between 0.086 and 0.82. The 3 gray gases are optimized and the 10 gray gases are not.

spatially constant in many applications if its variation is small. The walls have an emissivity of 0.75 and are spaced at $L = 3$ m. The predictions are found in Fig. 3(b). Again, the predictions generally agree well with the benchmark. Relative to the full range of the divergence field the predictions of the flux divergence are within 11 percent of those of the benchmark. The errors are somewhat larger in nonisothermal, nonhomogeneous media due to the approximations imposed in the SLW model in such problems (Denison and Webb, 1995a).

The next problem involves a spatially nonconstant molar ratio, $r/(1 - r)$, contrary to the assumption imposed in the development of the convolution approach. Figure 3(c) shows the results of the problem of Fig. 3(b) except that the CO_2 mole fraction profile is given by $Y(x) = 0.133 + 0.1 \cos(\pi x/L)$. In contrast to the H_2O cosine profile where the H_2O mole fraction ranges from 0.05 at the cold wall to 0.35 at the hot wall, the CO_2 profile is a maximum at the cold wall and falls to a minimum at the hot wall. Thus, $r/(1 - r)$ varies from 4.66 to 0.094. The convolution method predictions of Fig. 3(c) were based on the ratio of the spatial average mole fractions (r = 0.4). Although r varies significantly in the problem of Fig. 3(c), the convolution approach still provides results comparable to the double integration for the $Y(x)$ profiles used. Thus, the assumption of constant molar density ratio may be made to achieve considerable computational savings in applications of small to moderate spatial variations in r.

In summary, a SLW model for gas mixtures has been presented with two alternate methods for obtaining total radiative transfer rates: the double integration method and the convolution approach. When the molar ratio is spatially constant or of moderate variation, both methods have been shown to give results that agree well with line-by-line benchmarks. The model may be used in multidimensional geometries with any suitable RTE solver, since κ is specified locally.

Acknowledgments

This work was supported by the Advanced Combustion Engineering Research Center (ACERC) at Brigham Young Univer-

sity. ACERC is sponsored by the National Science Foundation, the State of Utah, the U.S. Department of Energy, and a number of industrial participants. One of the authors (MKD) also wishes to acknowledge the financial support of the NASA Rocky Mountain Grant Consortium.

References

Carlson, B. G., and Lathrop, K. D., 1968, "Transport Theory—The Method of Discrete Ordinates," *Computing Methods in Reactor Physics,* H. Greenspan, C. N. Kelber, and D. Okrent, eds., Gordon and Breach, New York, pp. 171–266.

Coppalle, A., and Vervisch, P., 1983, "The Total Emissivities of High-Temperature Flames," *Comb. Flame,* Vol. 49, pp. 101–108.

Denison, M. K., and Webb, B. W., 1993a, "A Spectral Line-Based Weighted-Sum-of-Gray-Gases Model for Arbitrary RTE Solvers," ASME JOURNAL OF HEAT TRANSFER, Vol. 115, pp. 1004–1012.

Denison, M. K., and Webb, B. W., 1993b, "An Absorption-Line Blackbody Distribution Function for Efficient Calculation of Total Gas Radiative Transfer," *J. Quant. Spectr. Rad. Transfer,* Vol. 50, No. 5, pp. 499–510.

Denison, M. K., 1994, "A Spectral Line-Based Weighted-Sum-of-Gray-Gases Model for Arbitrary RTE Solvers," Ph.D. Dissertation, Mechanical Engineering Department, Brigham Young University, Provo, UT.

Denison, M. K., and Webb, B. W., 1995a, "The Spectral Line-Based Weighted-Sum-of-Gray-Gases Model in Non-isothermal Non-homogeneous Media," ASME JOURNAL OF HEAT TRANSFER, Vol. 117, pp. 359–365.

Denison, M. K., and Webb, B. W., 1995b, "Development and Application of an Absorption-Line Black-body Distribution Function for CO_2," *Int. J. Heat Mass Transfer,* Vol. 38, pp. 1813–1821.

Goody, R. M., West, R., Chen, L., and Chrisp, D., 1989, "The Correlated-k Method for Radiation Calculations in Nonhomogeneous Atmospheres," *J. Quant. Spectr. Rad. Transfer,* Vol. 42, pp. 539–550.

Hottel, H. C., and Sarofim, A. F., 1967, *Radiative Transfer,* McGraw-Hill, New York.

Lacis, A. A., and Oinas, V., 1991, "A Description of the Correlated-k Distribution Method for Modeling Nongray Gaseous Absorption, Thermal Emission, and Multiple Scattering in Vertically Inhomogeneous Atmospheres," *J. Geophys. Res.,* Vol. 96, pp. 9027–9063.

Modest, M. F., 1991, "The Weighted-Sum-of-Gray-Gases Model for Arbitrary Solution Methods in Radiative Transfer," ASME JOURNAL OF HEAT TRANSFER, Vol. 113, pp. 650–656.

Rothman, L. S., Gamache, R. R., Tipping, R. H., Rinsland, C. P., Smith, M. A. H., Chris Benner, D., Malathy Devi, V., Flaud, J. M., Camy-Peyret, C., Perrin, A., Goldman, A., Massie, S. T., and Brown, L. R., 1992, "The HITRAN Molecular Database: Editions of 1991 and 1992," *J. Quant. Spectr. Rad. Transfer,* Vol. 48, No. 5/6, pp. 469–507.

Smith, T. F., Shen, Z. F., and Friedman, J. N., 1982, "Evaluation of Coefficients for the Weighted Sum of Gray Gases Model," ASME JOURNAL OF HEAT TRANSFER, Vol. 104, pp. 602–608.

Song, T. H., and Viskanta, R., 1986, "Development and Application of a Spectral-Group Model to Radiation Heat Transfer," ASME Paper No. 86-WA/HT-36.

Taylor, P. B., and Foster, P. J., 1974, "The Total Emissivities of Luminous and Non-luminous Flames," *Int. J. Heat Mass Transfer,* Vol. 17, pp. 1591–1605.

Monte Carlo Solutions for Radiative Heat Transfer in Irregular Two-Dimensional Geometries

G. Parthasarathy,[1] H. S. Lee,[2] J. C. Chai,[1,3] and S. V. Patankar[1]

Introduction

Several new methods of computing radiation heat transfer have emerged in recent years, and thorough testing is often required to validate these. Monte Carlo methods can provide exact solutions within statistical limits, hence are attractive for validation purposes. Unfortunately, many Monte Carlo solutions currently available in the literature are not useful for testing new solution techniques for complex geometries, because they either treat simple cases or application-specific irregular geometries. The intent of this paper is to provide solutions of general interest for two-dimensional irregular geometries using the Monte Carlo method. The paper presents radiative heat flux solutions for three enclosures with absorbing, emitting, and anisotropically scattering medium.

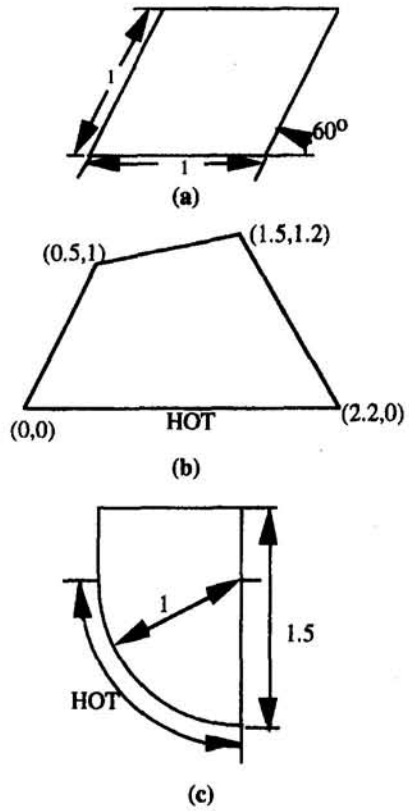

Fig. 1 Irregular geometries

Problem Description

The irregular geometries considered are a rhombus, a quadrilateral, and an enclosure with curved and straight edged boundaries (Figs. 1*a–c*). The enclosure with a curved boundary is a quarter of a circle with a rectangle on top. The distances given in the figures are in units of meters. Two types of problem are considered. In the surface emission problems, the emitting surface is taken as the lower walls of the enclosures; straight horizontal walls for the rhombus and quadrilateral, and the curved surface in Fig. 1(*c*). The emitting surface is maintained at a constant high temperature, and the other walls and the medium are maintained at 0 K. In the volumetric emission problems, the medium is maintained at a constant temperature, whereas all the walls are at 0 K. For all the cases considered, the normalized emissive power of the source or surface is taken as unity. All walls are black and diffuse. The medium is homogeneous and gray with an extinction coefficient of $\beta = 1\ \mathrm{m}^{-1}$. Three Mie-anisotropic phase functions are considered for this work; isotropic, F1, and B1 (Kim and Lee, 1988). F1 is a strongly forward scattering phase function, whereas B1 is a weak back scatterer.

In the Monte Carlo method, histories of a large number of energy bundles are averaged to obtain heat flux rates or tempera-

[1] Department of Mechanical Engineering, University of Minnesota, Minneapolis, MN 55455.

[2] NASA Lewis Research Center, Cleveland, OH 44135.

[3] Current address: Department of Mechanical Engineering, Tennessee Technological University, Cookeville, TN 38505.

Contributed by the Heat Transfer Division of THE AMERICAN SOCIETY OF MECHANICAL ENGINEERS. Manuscript received by the Heat Transfer Division July 1994; revision received December 1994. Keywords: Numerical Methods, Radiation. Associate Technical Editor: M. F. Modest.

sity. ACERC is sponsored by the National Science Foundation, the State of Utah, the U.S. Department of Energy, and a number of industrial participants. One of the authors (MKD) also wishes to acknowledge the financial support of the NASA Rocky Mountain Grant Consortium.

References

Carlson, B. G., and Lathrop, K. D., 1968, "Transport Theory—The Method of Discrete Ordinates," *Computing Methods in Reactor Physics,* H. Greenspan, C. N. Kelber, and D. Okrent, eds., Gordon and Breach, New York, pp. 171–266.

Coppalle, A., and Vervisch, P., 1983, "The Total Emissivities of High-Temperature Flames," *Comb. Flame,* Vol. 49, pp. 101–108.

Denison, M. K., and Webb, B. W., 1993a, "A Spectral Line-Based Weighted-Sum-of-Gray-Gases Model for Arbitrary RTE Solvers," ASME JOURNAL OF HEAT TRANSFER, Vol. 115, pp. 1004–1012.

Denison, M. K., and Webb, B. W., 1993b, "An Absorption-Line Blackbody Distribution Function for Efficient Calculation of Total Gas Radiative Transfer," *J. Quant. Spectr. Rad. Transfer,* Vol. 50, No. 5, pp. 499–510.

Denison, M. K., 1994, "A Spectral Line-Based Weighted-Sum-of-Gray-Gases Model for Arbitrary RTE Solvers," Ph.D. Dissertation, Mechanical Engineering Department, Brigham Young University, Provo, UT.

Denison, M. K., and Webb, B. W., 1995a, "The Spectral Line-Based Weighted-Sum-of-Gray-Gases Model in Non-isothermal Non-homogeneous Media," ASME JOURNAL OF HEAT TRANSFER, Vol. 117, pp. 359–365.

Denison, M. K., and Webb, B. W., 1995b, "Development and Application of an Absorption-Line Black-body Distribution Function for CO_2," *Int. J. Heat Mass Transfer,* Vol. 38, pp. 1813–1821.

Goody, R. M., West, R., Chen, L., and Chrisp, D., 1989, "The Correlated-k Method for Radiation Calculations in Nonhomogeneous Atmospheres," *J. Quant. Spectr. Rad. Transfer,* Vol. 42, pp. 539–550.

Hottel, H. C., and Sarofim, A. F., 1967, *Radiative Transfer,* McGraw-Hill, New York.

Lacis, A. A., and Oinas, V., 1991, "A Description of the Correlated-k Distribution Method for Modeling Nongray Gaseous Absorption, Thermal Emission, and Multiple Scattering in Vertically Inhomogeneous Atmospheres," *J. Geophys. Res.,* Vol. 96, pp. 9027–9063.

Modest, M. F., 1991, "The Weighted-Sum-of-Gray-Gases Model for Arbitrary Solution Methods in Radiative Transfer," ASME JOURNAL OF HEAT TRANSFER, Vol. 113, pp. 650–656.

Rothman, L. S., Gamache, R. R., Tipping, R. H., Rinsland, C. P., Smith, M. A. H., Chris Benner, D., Malathy Devi, V., Flaud, J. M., Camy-Peyret, C., Perrin, A., Goldman, A., Massie, S. T., and Brown, L. R., 1992, "The HITRAN Molecular Database: Editions of 1991 and 1992," *J. Quant. Spectr. Rad. Transfer,* Vol. 48, No. 5/6, pp. 469–507.

Smith, T. F., Shen, Z. F., and Friedman, J. N., 1982, "Evaluation of Coefficients for the Weighted Sum of Gray Gases Model," ASME JOURNAL OF HEAT TRANSFER, Vol. 104, pp. 602–608.

Song, T. H., and Viskanta, R., 1986, "Development and Application of a Spectral-Group Model to Radiation Heat Transfer," ASME Paper No. 86-WA/HT-36.

Taylor, P. B., and Foster, P. J., 1974, "The Total Emissivities of Luminous and Non-luminous Flames," *Int. J. Heat Mass Transfer,* Vol. 17, pp. 1591–1605.

Monte Carlo Solutions for Radiative Heat Transfer in Irregular Two-Dimensional Geometries

G. Parthasarathy,[1] H. S. Lee,[2] J. C. Chai,[1,3] and S. V. Patankar[1]

Introduction

Several new methods of computing radiation heat transfer have emerged in recent years, and thorough testing is often required to validate these. Monte Carlo methods can provide exact solutions within statistical limits, hence are attractive for validation purposes. Unfortunately, many Monte Carlo solutions currently available in the literature are not useful for testing new solution techniques for complex geometries, because they either treat simple cases or application-specific irregular geometries. The intent of this paper is to provide solutions of general interest for two-dimensional irregular geometries using the Monte Carlo method. The paper presents radiative heat flux solutions for three enclosures with absorbing, emitting, and anisotropically scattering medium.

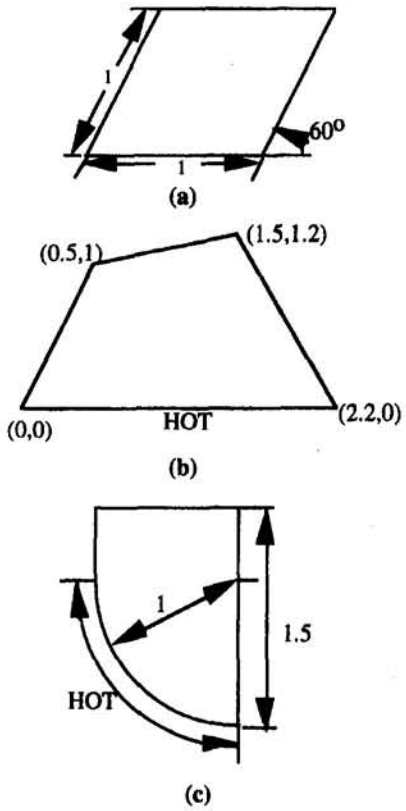

Fig. 1 Irregular geometries

Problem Description

The irregular geometries considered are a rhombus, a quadrilateral, and an enclosure with curved and straight edged boundaries (Figs. 1*a–c*). The enclosure with a curved boundary is a quarter of a circle with a rectangle on top. The distances given in the figures are in units of meters. Two types of problem are considered. In the surface emission problems, the emitting surface is taken as the lower walls of the enclosures; straight horizontal walls for the rhombus and quadrilateral, and the curved surface in Fig. 1(*c*). The emitting surface is maintained at a constant high temperature, and the other walls and the medium are maintained at 0 K. In the volumetric emission problems, the medium is maintained at a constant temperature, whereas all the walls are at 0 K. For all the cases considered, the normalized emissive power of the source or surface is taken as unity. All walls are black and diffuse. The medium is homogeneous and gray with an extinction coefficient of $\beta = 1\ \mathrm{m}^{-1}$. Three Mie-anisotropic phase functions are considered for this work; isotropic, F1, and B1 (Kim and Lee, 1988). F1 is a strongly forward scattering phase function, whereas B1 is a weak back scatterer.

In the Monte Carlo method, histories of a large number of energy bundles are averaged to obtain heat flux rates or tempera-

[1] Department of Mechanical Engineering, University of Minnesota, Minneapolis, MN 55455.

[2] NASA Lewis Research Center, Cleveland, OH 44135.

[3] Current address: Department of Mechanical Engineering, Tennessee Technological University, Cookeville, TN 38505.

Contributed by the Heat Transfer Division of THE AMERICAN SOCIETY OF MECHANICAL ENGINEERS. Manuscript received by the Heat Transfer Division July 1994; revision received December 1994. Keywords: Numerical Methods, Radiation. Associate Technical Editor: M. F. Modest.

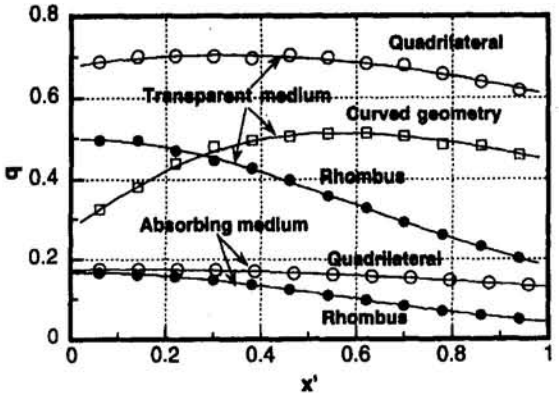

Fig. 2 Comparison of top wall heat fluxes obtained by the Monte Carlo method (symbols) with exact solutions (solid lines)

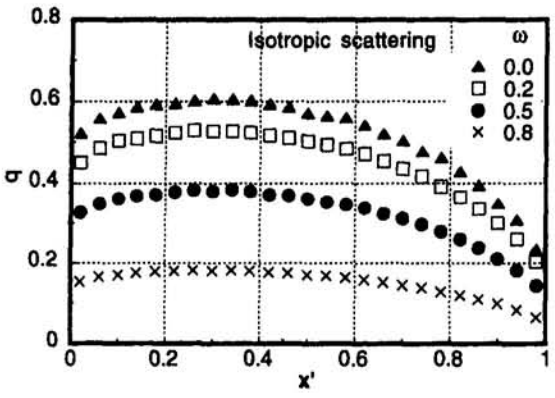

Fig. 4 Heat flux on the top wall of rhombus (isothermal medium emission)

ture distributions. The Monte Carlo technique followed here is described in the excellent reviews of Howell (1968), Haji Sheikh (1988), and Walters and Buckius (1993) and in the work of Howell and Perlmutter (1964). Anisotropic scattering is handled in a manner similar to that described by Stockham and Love (1968).

Results

The Monte Carlo method used was first tested for a two-dimensional square geometry with an absorbing, emitting, and anisotropically scattering medium. The results were found to be in very good agreement with those of Kim and Lee (1988). The method was also checked for correctness in irregular geometries with exact solutions for the case of transparent medium, and with exact solutions obtained by numerical integration, for nonscattering medium. As shown in Fig. 2, the heat flux results are in excellent agreement with exact solutions. The Monte Carlo solutions for scattering cases in irregular geometries were checked with finite volume solutions (Chai et al., 1994) and found to be in very good agreement.

For the three geometries considered, results shown are heat flux distributions along the top or right walls. The effects of scattering albedo and phase function are considered for each geometry. All fluxes are plotted against location x' along the surface, starting from the left-upper corner along the top wall, and from the bottom-right corner up the right wall.

Figure 3 shows the top wall heat flux results for the rhombus surface emission case for different scattering albedos (ω). The three sets of results in the figure correspond to the isotropic, F1, and B1 phase functions. The results are consistent with the physics of the problem. The heat flux is seen to increase with the scattering albedo ω, as the medium absorbs smaller amounts of energy. As the F1 phase function scatters more energy in the forward direction, the top wall heat flux is higher in this case for any given albedo. The reverse is the case for the B1 phase function, but its effect is far less significant because of its weak anisotropy.

Figure 4 shows the heat flux along the top wall of the rhombus for the isothermal medium emission problem. The results are the same for any of the other surfaces; there is no difference in

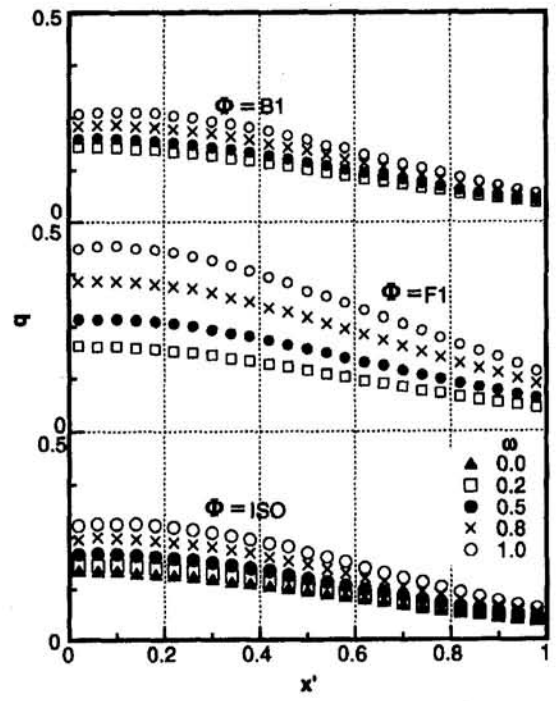

Fig. 3 Heat flux on the top wall of rhombus (surface emission problem)

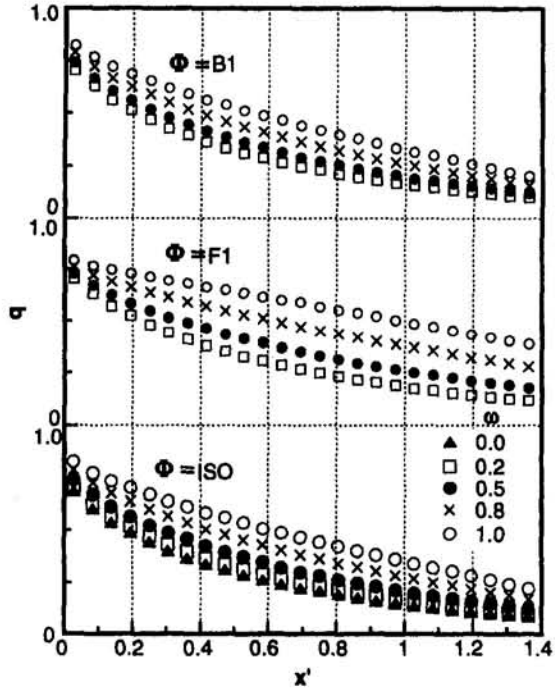

Fig. 5 Heat flux on the right wall of the quadrilateral (surface emission problem)

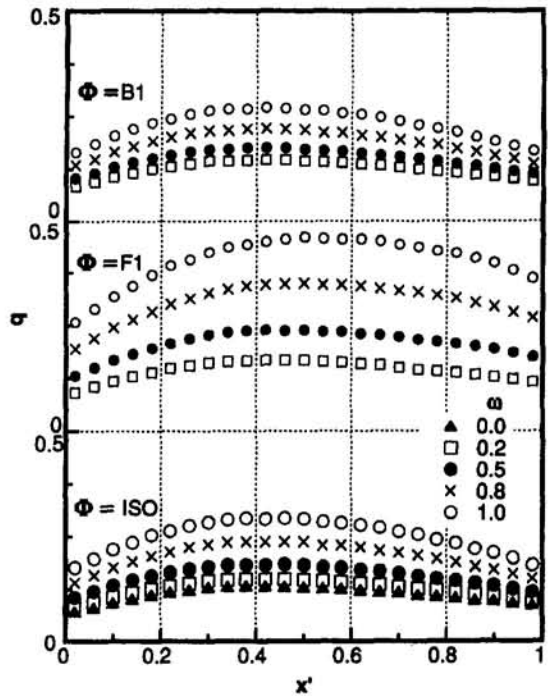

Fig. 6 Heat flux on the top wall of the curved geometry (surface emission problem)

the heat flux profiles because of the symmetry. Anisotropy of the scattering phase functions affects the heat flux distributions only minimally. The only variable of importance for the isothermal emission problem is the scattering albedo. The wall heat fluxes decrease as the scattering albedo is increased to 0.8, since the medium emission decreases with decreasing absorption coefficient.

Figure 5 presents right wall heat flux results for the quadrilateral surface emission problem. The heat flux is again higher for higher scattering albedos. The relative orientation of the right wall to the bottom wall compounds the forward scattering effect of the F1 phase function to produce higher heat fluxes for most of the right wall, whereas it nullifies that of the backward scattering B1 phase function.

Figure 6 presents the solutions for the surface emission case of the curved geometry of Fig. 1(*c*). Again, the physically correct higher top-wall heat fluxes are observed for higher scattering albedos. The forward scattering phase function F1 gives the highest heat flux for a given albedo, since the receiving surface is situated in the forward direction to the emitting curved surface. The results for the isotropic and B1 phase functions are again similar, due to the fact that B1 phase function is not strongly biased.

The numerical values for all the above-mentioned results have been documented by Parthasarathy et al. (1994).

The forms of the emitting and receiving surfaces are described by analytic expressions in this study. Discretization of the geometries may be needed to compute points of emission of energy bundles, and this can induce grid-dependent errors, apart from the statistical errors. However, these errors are quite small. If the actual surface itself is not represented analytically, each discrete element of the surface should be treated as a separate surface for Monte Carlo application. In the results presented here, discrete approximation of geometry has not been used.

Accuracy Considerations

The Monte Carlo simulation requires a large number of energy bundles for sufficiently accurate results. An estimate of the variance, or precision, of the solution can be obtained by performing several runs with different sets of random numbers (Walters and Buckius, 1993). The variance was computed for the surface emission case for the rhombus with $\omega = 0$, with 5 runs, each using 2×10^6 energy bundles. If $\bar{q}$ denotes the mean heat flux of the individual runs, and $e = |q - \bar{q}|$, the error, the precision limits $e/\bar{q}$ for the top wall heat flux, at a confidence level of 99 percent, are given below:

x' (m)	0.02	0.5	0.98
$e/\bar{q}$ (percent)	1.5	1.2	1.2

This means that at $x' = 0.5$, the probability of the error being less than 1.2 percent is 99 percent. For all the results shown in the paper, the number of energy bundles N used was 10^7 or higher.

Conclusion

Solutions for radiative heat transfer in three irregular geometries with absorbing, emitting, and Mie anisotropic scattering media have been obtained using the Monte Carlo method. Results are presented for these geometries for three different scattering phase functions and five scattering albedos from purely absorbing ($\omega = 0.0$) to purely scattering ($\omega = 1.0$). These results will be particularly useful for validation of new solution methods for radiation heat transfer in complex geometries.

Acknowledgments

This work was supported in part by NASA Lewis Research Center under Cooperative Agreement No. NCC3-238. The first author wishes to thank Dr. C. R. Swaminathan for his efforts in initiating this Monte Carlo work. A grant from the Minnesota Supercomputer Institute is also gratefully acknowledged.

References

Chai, J., Parthasarathy, G., Lee, H.-S., and Patankar, S. V., 1994, "A Finite Volume Radiation Heat Transfer Procedure for Irregular Geometries," presented at the AIAA/ASME 6th Joint Thermophysics and Heat Transfer conference, Colorado Springs, CO.

Haji Sheikh, A., 1988, "Monte Carlo Methods," in: *Handbook of Numerical Heat Transfer*, W. J. Minkowycz, E. M. Sparrow, R. H. Pletcher, and G. E. Schneider, eds., Wiley, New York.

Howell, J. R., and Perlmutter, M., 1964, "Monte Carlo Solution of Thermal Transfer Through Radiant Media Between Gray Walls," ASME JOURNAL OF HEAT TRANSFER, Vol. 86, pp. 116–122.

Howell, J. R., 1968, "Application of Monte Carlo Method to Heat Transfer Problems," in: *Advances in Heat Transfer*, J. P. Hartnett and T. F. Irvine, eds., Vol. 5, Academic Press, New York, pp. 1–54.

Kim, T.-K., and Lee, H., 1988, "Effect of Anisotropic Scattering on Radiative Heat Transfer in Two-Dimensional Rectangular Enclosures," *Int. J. Heat Mass Transfer*, Vol. 31, 8, pp. 1711–1721.

Parthasarathy, G., Lee, H.-S., Patankar, S. V., and Chai, J., 1994, "Monte Carlo Solutions for Radiative Heat Transfer in Irregular Two-Dimensional Geometries," University of Minnesota Supercomputer Institute Research Report UMSI 94/107.

Stockham, L. W., and Love, T. J., 1968, "Radiative Heat Transfer From a Cylindrical Cloud of Particles," *AIAA Journal*, Vol. 6, No. 10, pp. 1935–1940.

Walters, D. V., and Buckius, R. O., 1993, "Monte Carlo Methods for Radiative Heat Transfer in Scattering Media," in: *Annual Review of Heat Transfer*, Vol. 5, pp. 131–176.

Radiometric Measurements of Wall Temperatures in the 800 K to 1150 K Range for a Quartz Radiant Heating Tube

L. G. Blevins,[1] Y. R. Sivathanu,[1] J. P. Gore,[1] and M. A. Shahien[2]

Introduction

Many industrial applications require heat transfer to a load in an inert environment, which can be achieved by using gas-fired radiant tubes. A radiant tube consists of a flame confined in a cylindrical metal or ceramic chamber. The flame heats the tube wall, which in turn radiates to the load. One important characteristic of radiant heating tubes is wall temperature uniformity (Harder et al., 1987). Numerical models of radiant tubes have been used to predict wall temperatures, but there is a lack of experimental data for validation (Harder et al., 1987; Ramamurthy, 1993). Recently, Namazian et al. (1992), Singh and Gorski (1990), and Peters et al. (1990) have measured wall temperature profiles of radiant tubes using thermocouples.

Most of these studies were performed with ceramic or metal tubes. To observe the confined flames visually, a quartz tube can be used. Since it is difficult to measure the temperature of a quartz tube using thermocouples, it is desirable to use nonintrusive radiation thermometry (DeWitt and Incropera, 1988). Single wavelength thermometry is currently used in the glass industry, but uncertainty is introduced by the lack of information about high-temperature properties of glass and the difficulty of defining the surface emissivity of a semitransparent material (Barber, 1988).

There are two issues to be addressed in using radiation thermometry for a quartz radiant tube. First, high-temperature spectral absorption coefficients for quartz in the infrared are not available (Rajaram, 1994), and must be obtained in-situ. Second, interference from the emission by the combustion gases, primarily carbon dioxide (CO_2) and water vapor (H_2O), must be avoided by selecting wavelengths away from the discrete wavelength gas radiation bands (Siegel and Howell, 1981). The objective of the present study is to use a multiwavelength radiometric technique to measure the wall temperature of a quartz radiant tube. The technique involves measuring quartz radiant emission intensity at wavelengths away from gas bands and graphically comparing the intensity distributions with solutions of the radiative transfer equation to deduce equivalent wall temperatures. Properties are measured in-situ.

Experimental Procedure

The vertical straight-through radiant tube apparatus is shown in Fig. 1. The present radiant tube is 1.8 m long, 95 mm ID, and 100 mm OD, and is made of fused quartz (General Electric, Type 214). An industrial fuel/air nozzle consisting of a central fuel port with angled fuel injection surrounded by six air swirl vanes is used. Utility natural gas is burned with air. For the current study, the heat release rates (Q_f) of the flames based on the ideal lower heat of combustion were 10, 15, and 20 kW. The equivalence ratio (Φ) for the flames, calculated from the mass flow rates of the fuel and air, was 0.8. Steady-state quartz equivalent wall temperature measurements were obtained at axial locations of 15, 30, and 45 cm from the fuel nozzle.

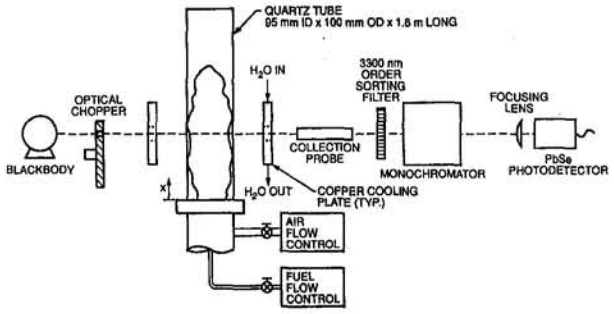

Fig. 1 Schematic of quartz radiant heating tube with optical train used for collecting transmittance data

The optical arrangement used to make quartz surface transmittance measurements is also shown in Fig. 1. During emission measurements, the optical chopper is placed between the collection probe and the filter, and the blackbody is removed. The emission receiving optics consist of a 6-mm-dia, 125-mm-long collection probe, the chopper, an order sorting filter, a monochromator, a calcium fluoride focusing lens, and a lead selenide (PbSe) photodetector. The chopper is necessary because the PbSe detector responds only to a modulated signal. Copper plates with water cooling are used to protect the optical components from the high heat flux of the radiant tube. Measurements of spectral emission intensity are made from 3.52 to 4.64 μm, in increments of 0.16 μm. The spectral width of the monochromator (full width at half maximum, FWHM) is 50 nm. The detector output voltages are converted to radiation intensities using a calibration performed with an Infrared Industries Model 464 blackbody set at 1000 ± 1°C. An uncertainty analysis was performed using the method recommended by Moffat (1988). The uncertainty in the blackbody calibration constant based on the random noise, the data acquisition system least count, the blackbody temperature uncertainty, and monochromator repeatability is typically less than 3 percent, yielding quartz radiant intensities that are accurate to within 5 percent. Details of the experimental apparatus and calibration procedure were presented by Blevins et al. (1994).

The spectral intensity inside the quartz at wavelengths where the flame is transparent is governed by the radiative transfer equation, neglecting scattering:

$$\frac{dI_{\lambda Q}}{ds} = -a_\lambda I_{\lambda Q} + n^2 a_\lambda I_{\lambda b} \qquad (1)$$

Here, $I_{\lambda Q}$ is the radiation intensity inside the quartz ($W \cdot m^{-2} \cdot \mu m^{-1} \cdot sr^{-1}$), $I_{\lambda b}$ is the Planck blackbody intensity ($W \cdot m^{-2} \cdot \mu m^{-1} \cdot sr^{-1}$), a_λ is the absorption coefficient of the quartz (cm^{-1}), s is the distance along the optical path (cm), and n is the quartz refractive index.

Equation (1) is solved for a radiation path consisting of the two sections of the cylindrical quartz wall in a direction aligned with a diameter. The normal radiation path minimizes reflection (Hecht, 1987). Assuming a constant equivalent emission temperature across the quartz, the equation is solved for the case of normally incident blackbody radiation ($I_{\lambda b0}$) on the left boundary of the tube. The blackbody intensity is amplified to $n^2 \cdot I_{\lambda b0}$ inside the quartz tube at the left boundary. The intensity is attenuated by a factor of $1/n^2$ while entering the air from the quartz. Solution of Eq. (1) yields the intensity (I_λ) measured by the detector for wavelengths with no flame gas band interference:

[1] Thermal Sciences and Propulsion Center, Mechanical Engineering, Purdue University, West Lafayette, IN 47907.

[2] Faculty of Engineering and Technology at El-Mataria, Helwan University, Cairo, Egypt.

Contributed by the Heat Transfer Division of THE AMERICAN SOCIETY OF MECHANICAL ENGINEERS. Manuscript received by the Heat Transfer Division April 1994; revision received October 1994. Keywords: Furnaces and Combustors, Measurement Techniques, Thermophysical Properties. Associate Technical Editor: W. L. Grosshandler.

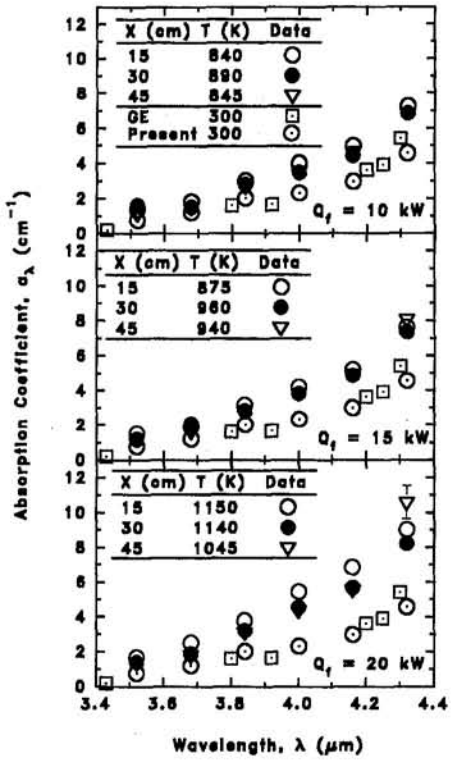

Fig. 2 Absorption coefficient as a function of wavelength for 10, 15, and 20 kW (Φ = 0.8) flames at axial locations of x = 15, 30, and 45 cm

$$I_\lambda = \tau_\lambda^2 I_{\lambda b0} + (1 - \tau_\lambda^2) I_{\lambda b} \tag{2}$$

where

$$\tau_\lambda = \exp(-a_\lambda \Delta s) \tag{3}$$

Here, τ_λ is the spectral transmittance of one section of the cylindrical wall of thickness Δs. Since τ_λ is obtained in-situ as described below, the equivalent temperature is calculated using graphic solution of Eq. (2).

The transmittance is measured using the optical arrangement as depicted in Fig. 1. During the transmittance measurement, a chopper and lock-in amplifier are used to filter out the quartz tube emission from the transmitted blackbody signal. Hence, the measured intensity, $I_{\lambda\tau}$, is:

$$I_{\lambda\tau} = \tau_\lambda^2 I_{\lambda b0} \tag{4}$$

The quantity τ_λ^2 is calculated from measurements of $I_{\lambda\tau}$ and $I_{\lambda b0}$. The calculated values of τ_λ^2 are estimated to be accurate to within 3 percent, based on the least count of the data acquisition system and a random noise estimate. The data are repeatable within these uncertainty limits. Absorption coefficients calculated from room temperature transmittance measurements agree well with those provided by the quartz manufacturer (GE), with the maximum difference between the values of 10 percent.

Once τ_λ^2 is known, the solutions to the radiative transfer equation in the absence of the blackbody for several temperatures are plotted on a graph along with the quartz emission data. The equivalent temperature is deduced graphically as the value corresponding to the closest intensity curve. By combining the uncertainties of the transmittance measurement, the emission measurement, and the ability to read the graph, it is estimated that the graphic solution technique yields equivalent temperatures, which are repeatable to within ±10 K. Based on the Fresnel equations, the measured transmittance is lower than the actual value by up to 8 percent due to reflectance. This causes an error of about 5 K in the measured temperatures.

Results and Discussion

Figure 2 shows absorption coefficient as a function of wavelength for the 10, 15, and 20 kW flames at three axial positions for wavelengths between 3.4 and 4.4 μm. Room temperature data provided by the quartz manufacturer and measured in the present study are also plotted on this figure. The absorption coefficient is lowest for the shorter wavelengths and then steadily increases with λ. The figure shows that although absorption coefficients at elevated temperatures are higher than those at room temperature, there is only a slight increase of a_λ with temperature in the range of 800 K to 1150 K. The trend of increased a_λ with temperature is in agreement with 4.5 μm quartz absorption data between 0 and 300°C presented by Sosman (1927).

Spectral emission intensity of the quartz and flame for the 10 kW flame is shown in Fig. 3 for the three axial positions. Quartz emission increases with wavelength, which is in agreement with similar emission data collected at 800°C and shown by Sosman (1927). Figure 3 shows the existence of some interference from CO_2 at the strong 4.3 μm band in spite of the low transmittance of quartz in this region. Wavelengths away from this band were hence used to deduce the equivalent temperature of the quartz. The expected emission intensities of the quartz calculated using Eq. (2) at different temperatures are plotted as solid curves. The equivalent temperatures deduced are 840 K at x = 15 cm, 890 K at 30 cm, and 845 K at 45 cm, since wavelengths in the range of 3.5 to 4.2 μm are the most suitable ones for determining quartz temperature. Similar results obtained for the 15 and 20 kW flames yielded equivalent temperatures up to 1150 K. These data were presented in more detail by Blevins et al. (1994).

The results of deducing the equivalent wall temperature using Eq. (2) with in-situ transmittance measurements were compared to those obtained using transmittance data provided by the manufacturer for room temperature. In the temperature range of this study, the deduced quartz wall temperatures would have been approximately 50 K–100 K lower if room temperature proper-

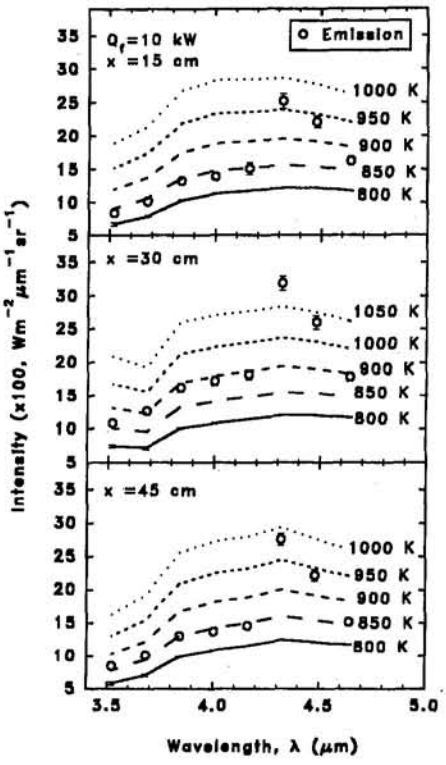

Fig. 3 Quartz emission intensity for the 10 kW flame versus wavelength plotted with solutions to the radiative transfer equation

ties had been used. Thus, in-situ property measurement improves the accuracy of the temperature measurements.

Conclusions

Two conclusions can be drawn from this study. First, a spectral radiometric technique with in-situ radiative property measurements can be used to obtain equivalent wall temperatures of a quartz radiant heating tube. Second, measuring the spectral transmittance of the quartz at elevated temperatures improves the accuracy of the temperature measurements by 50–100 K. To the author's knowledge, the present quartz property measurements are the first high-temperature quartz absorption coefficient measurements in the wavelength range of 3.5 to 4.5 μm.

Acknowledgments

This study is sponsored by the National Science Foundation under grant CTS 9157920, and by the Gas Research Institute under grant No. GRI 5093-260-2666. The burner was donated by Eclipse Inc., Rockford, IL.

References

Barber, R., 1988, "Glass Industry Applications," in: *Theory and Practice of Radiation Thermometry,* D. P. DeWitt and G. Nutter, eds., Wiley, New York.

Blevins, L. G., Sivathanu, Y. R., Gore, J. P., and Shahien, M. A., 1994, "Radiometric Measurements of Wall Temperatures in the 800 K to 1150 K Range for a Quartz Radiant Heating Tube," *Radiative Heat Transfer: Current Research,* Y. Bayazitoglu et al., eds., ASME HTD-Vol. 276, pp. 115–120.

DeWitt, D. P., and Incropera, F. P., 1988, "Physics of Thermal Radiation," in: *Theory and Practice of Radiation Thermometry,* D. P. DeWitt and Gene Nutter, eds., Wiley, New York.

Harder, R. F., Viskanta, R., and Ramadhyani, S., 1987, "Gas-Fired Radiant Tubes: A Review of Literature," Gas Research Institute Report GRI-87/0343.

Hecht, E., 1987, *Optics,* Addison-Wesley Publishing Company, Inc., MA.

Moffat, R. J., 1988, "Describing the Uncertainties in Experimental Results," *Experimental Thermal and Fluid Science,* Vol. 1, pp. 3–17.

Namazian, M., Kelly, J., and Pereira, J., 1992, "Characterization of Nonpremixed Turbulent Bluff-Body Burner Flames," Gas Research Institute Report GRI-92/0120.

Peters, J. E., Brewster, M. Q., and Buckius, R. O., 1990, "Radiative Heat Transfer Augmentation in High Temperature Combustion Systems With Application to Radiant Tube Burners," Gas Research Institute Report GRI-91/0101.

Rajaram, M., 1994, General Electric Co. Quartz Products, personal communication.

Ramamurthy, H., 1993, "Analysis of Energy Transfer in Industrial Gas-Fired Radiant Tube Furnaces," Ph.D. Thesis, Purdue University, West Lafayette, IN.

Siegel, R., and Howell, J. R., 1981, *Thermal Radiation Heat Transfer,* 2nd ed., Hemisphere Publishing, Washington, DC.

Singh, S. N., and Gorski, L. M., 1990, "Ceramic Single Ended Recuperative Radiant Tube (Phase I)," Gas Research Institute Report GRI-90/0327.

Sosman, R. B., 1927, *The Properties of Silica,* American Chemical Society Monograph Series, The Chemical Catalog Company, Inc., New York.

Approximate Formulation for Coupled Conduction and Radiation Through a Medium With Arbitrary Optical Thickness

S. Q. Zeng,[1,2] A. J. Hunt,[1] R. Greif,[2] and W. Cao[1]

[1] Lawrence Berkeley Laboratory, University of California, Berkeley, CA 94720.

[2] Department of Mechanical Engineering, University of California at Berkeley, Berkeley, CA 94720.

Contributed by the Heat Transfer Division of THE AMERICAN SOCIETY OF MECHANICAL ENGINEERS. Manuscript received by the Heat Transfer Division April 1994; revision received October 1994. Keywords: Modeling and Scaling, Porous Media, Radiation. Associate Technical Editor: S. H. Chan.

Introduction

In evaluating the thermal properties of some porous media, such as aerogels, difficulties arise due to the following: (1) The media are transparent in some spectral intervals and opaque over other intervals and cannot therefore be treated as optically thin or as optically thick; (2) the conductive and the radiative heat transfer are coupled. In general, the coupled conduction and radiation transport in a nongray medium with nongray walls is described mathematically by a nonlinear, integrodifferential equation, which is difficult to solve.

The following limiting conditions for the radiative transport are noted: I. optically thin over the entire spectral range ($t_{L_\lambda} < 1, 0 \le \lambda < \infty$), II. optically thick over the entire spectral range ($t_{L_\lambda} > 1, 0 \le \lambda < \infty$), III. optically thin over some spectral intervals ($t_{L_\lambda} < 1$) and optically thick over the other intervals ($t_{L_\lambda} > 1$).

For case I the conductive and radiative transport may be readily determined. For case II with a gray medium and gray wall, Brewster (1992) presents a solution. For case III, Scheuerpflug et al. (1985) developed an approximate relation for the radiative transport starting with the following equation:

$$q_r = \int_0^\infty \frac{e_{b_\lambda}(T_1) - e_{b_\lambda}(T_2)}{\frac{1}{\epsilon_{1\lambda}} + \frac{1}{\epsilon_{2\lambda}} - 1 + \frac{3}{4} t_\lambda} d\lambda \qquad (1)$$

They claimed that the accuracy of Eq. (1) could be improved by introducing the Rosseland function according to

$$q_r = \sigma n^2 (T_1^4 - T_2^4) \int_0^\infty \frac{\partial e_{b_\lambda}(T)/\partial e_b(T)}{\frac{1}{\epsilon_{1\lambda}} + \frac{1}{\epsilon_{2\lambda}} - 1 + \frac{3}{4} t_\lambda} d\lambda \qquad (2)$$

which was called a "modified diffusion method." Note that Eq. (2) can be obtained from a Taylor series expansion for the numerator of the integrand in Eq. (1), where T is a value between T_1 and T_2. Therefore, Eqs. (1) and (2) may be considered to be equivalent. Equation (1) was derived under the assumption of radiative equilibrium ($\nabla \cdot q_r = 0$); in general, Eq. (1) or (2) may not be specified a priori for coupled conduction and radiation.

In this work we develop approximate results for case III, that is, for coupled conduction and radiation in a nongray medium that is both optically thin and thick. The approximate results are compared numerically with exact results (Özişik, 1973).

Approximate Formulation

Consider heat transfer through a slab (thickness L) with a medium that is both optically thin and thick (case III). The energy equation can be written as

$$q_c + q_r(t_{L_\lambda} > 1) = q - q_r(t_{L_\lambda} \le 1) \qquad (3)$$

where t_{L_λ} is equal to $\kappa_\lambda \cdot L$ and κ_λ is the spectral absorption coefficient. In the spectral range where $t_{L_\lambda} \le 1$, the net spectral radiative flux is written as (Brewster, 1992)

$$q_{r_\lambda}(t_{L_\lambda} \le 1) = \frac{e_{b\lambda}(T_1) - e_{b\lambda}(T_2)}{1/\epsilon_{1_\lambda} + 1/\epsilon_{2_\lambda} - 2 + [1/(1 - \bar{\tau}_{m_\lambda}/2)]} \qquad (4)$$

where

$$\bar{\tau}_{m_\lambda} = 1 - 2E_3(t_{L_\lambda}) = 1 - 2\int_0^1 \mu \exp(-t_{L_\lambda}/\mu) d\mu \qquad (5)$$

ties had been used. Thus, in-situ property measurement improves the accuracy of the temperature measurements.

Conclusions

Two conclusions can be drawn from this study. First, a spectral radiometric technique with in-situ radiative property measurements can be used to obtain equivalent wall temperatures of a quartz radiant heating tube. Second, measuring the spectral transmittance of the quartz at elevated temperatures improves the accuracy of the temperature measurements by 50–100 K. To the author's knowledge, the present quartz property measurements are the first high-temperature quartz absorption coefficient measurements in the wavelength range of 3.5 to 4.5 μm.

Acknowledgments

This study is sponsored by the National Science Foundation under grant CTS 9157920, and by the Gas Research Institute under grant No. GRI 5093-260-2666. The burner was donated by Eclipse Inc., Rockford, IL.

References

Barber, R., 1988, "Glass Industry Applications," in: *Theory and Practice of Radiation Thermometry,* D. P. DeWitt and G. Nutter, eds., Wiley, New York.

Blevins, L. G., Sivathanu, Y. R., Gore, J. P., and Shahien, M. A., 1994, "Radiometric Measurements of Wall Temperatures in the 800 K to 1150 K Range for a Quartz Radiant Heating Tube," *Radiative Heat Transfer: Current Research,* Y. Bayazitoglu et al., eds., ASME HTD-Vol. 276, pp. 115–120.

DeWitt, D. P., and Incropera, F. P., 1988, "Physics of Thermal Radiation," in: *Theory and Practice of Radiation Thermometry,* D. P. DeWitt and Gene Nutter, eds., Wiley, New York.

Harder, R. F., Viskanta, R., and Ramadhyani, S., 1987, "Gas-Fired Radiant Tubes: A Review of Literature," Gas Research Institute Report GRI-87/0343.

Hecht, E., 1987, *Optics,* Addison-Wesley Publishing Company, Inc., MA.

Moffat, R. J., 1988, "Describing the Uncertainties in Experimental Results," *Experimental Thermal and Fluid Science,* Vol. 1, pp. 3–17.

Namazian, M., Kelly, J., and Pereira, J., 1992, "Characterization of Nonpremixed Turbulent Bluff-Body Burner Flames," Gas Research Institute Report GRI-92/0120.

Peters, J. E., Brewster, M. Q., and Buckius, R. O., 1990, "Radiative Heat Transfer Augmentation in High Temperature Combustion Systems With Application to Radiant Tube Burners," Gas Research Institute Report GRI-91/0101.

Rajaram, M., 1994, General Electric Co. Quartz Products, personal communication.

Ramamurthy, H., 1993, "Analysis of Energy Transfer in Industrial Gas-Fired Radiant Tube Furnaces," Ph.D. Thesis, Purdue University, West Lafayette, IN.

Siegel, R., and Howell, J. R., 1981, *Thermal Radiation Heat Transfer,* 2nd ed., Hemisphere Publishing, Washington, DC.

Singh, S. N., and Gorski, L. M., 1990, "Ceramic Single Ended Recuperative Radiant Tube (Phase I)," Gas Research Institute Report GRI-90/0327.

Sosman, R. B., 1927, *The Properties of Silica,* American Chemical Society Monograph Series, The Chemical Catalog Company, Inc., New York.

Approximate Formulation for Coupled Conduction and Radiation Through a Medium With Arbitrary Optical Thickness

S. Q. Zeng,[1,2] A. J. Hunt,[1] R. Greif,[2] and W. Cao[1]

[1] Lawrence Berkeley Laboratory, University of California, Berkeley, CA 94720.

[2] Department of Mechanical Engineering, University of California at Berkeley, Berkeley, CA 94720.

Contributed by the Heat Transfer Division of THE AMERICAN SOCIETY OF MECHANICAL ENGINEERS. Manuscript received by the Heat Transfer Division April 1994; revision received October 1994. Keywords: Modeling and Scaling, Porous Media, Radiation. Associate Technical Editor: S. H. Chan.

Introduction

In evaluating the thermal properties of some porous media, such as aerogels, difficulties arise due to the following: (1) The media are transparent in some spectral intervals and opaque over other intervals and cannot therefore be treated as optically thin or as optically thick; (2) the conductive and the radiative heat transfer are coupled. In general, the coupled conduction and radiation transport in a nongray medium with nongray walls is described mathematically by a nonlinear, integrodifferential equation, which is difficult to solve.

The following limiting conditions for the radiative transport are noted: I. optically thin over the entire spectral range ($t_{L_\lambda} < 1, 0 \le \lambda < \infty$), II. optically thick over the entire spectral range ($t_{L_\lambda} > 1, 0 \le \lambda < \infty$), III. optically thin over some spectral intervals ($t_{L_\lambda} < 1$) and optically thick over the other intervals ($t_{L_\lambda} > 1$).

For case I the conductive and radiative transport may be readily determined. For case II with a gray medium and gray wall, Brewster (1992) presents a solution. For case III, Scheuerpflug et al. (1985) developed an approximate relation for the radiative transport starting with the following equation:

$$q_r = \int_0^\infty \frac{e_{b_\lambda}(T_1) - e_{b_\lambda}(T_2)}{\frac{1}{\epsilon_{1\lambda}} + \frac{1}{\epsilon_{2\lambda}} - 1 + \frac{3}{4} t_\lambda} d\lambda \qquad (1)$$

They claimed that the accuracy of Eq. (1) could be improved by introducing the Rosseland function according to

$$q_r = \sigma n^2 (T_1^4 - T_2^4) \int_0^\infty \frac{\partial e_{b_\lambda}(T)/\partial e_b(T)}{\frac{1}{\epsilon_{1\lambda}} + \frac{1}{\epsilon_{2\lambda}} - 1 + \frac{3}{4} t_\lambda} d\lambda \qquad (2)$$

which was called a "modified diffusion method." Note that Eq. (2) can be obtained from a Taylor series expansion for the numerator of the integrand in Eq. (1), where T is a value between T_1 and T_2. Therefore, Eqs. (1) and (2) may be considered to be equivalent. Equation (1) was derived under the assumption of radiative equilibrium ($\nabla \cdot q_r = 0$); in general, Eq. (1) or (2) may not be specified a priori for coupled conduction and radiation.

In this work we develop approximate results for case III, that is, for coupled conduction and radiation in a nongray medium that is both optically thin and thick. The approximate results are compared numerically with exact results (Özişik, 1973).

Approximate Formulation

Consider heat transfer through a slab (thickness L) with a medium that is both optically thin and thick (case III). The energy equation can be written as

$$q_c + q_r(t_{L_\lambda} > 1) = q - q_r(t_{L_\lambda} \le 1) \qquad (3)$$

where t_{L_λ} is equal to $\kappa_\lambda \cdot L$ and κ_λ is the spectral absorption coefficient. In the spectral range where $t_{L_\lambda} \le 1$, the net spectral radiative flux is written as (Brewster, 1992)

$$q_{r_\lambda}(t_{L_\lambda} \le 1) = \frac{e_{b\lambda}(T_1) - e_{b\lambda}(T_2)}{1/\epsilon_{1_\lambda} + 1/\epsilon_{2_\lambda} - 2 + [1/(1 - \bar{\tau}_{m_\lambda}/2)]} \qquad (4)$$

where

$$\bar{\tau}_{m_\lambda} = 1 - 2E_3(t_{L_\lambda}) = 1 - 2\int_0^1 \mu \exp(-t_{L_\lambda}/\mu) d\mu \qquad (5)$$

Integrating gives

$$q_r(t_{L_\lambda} \le 1) = \int_{\lambda, t_{L_\lambda} \le 1} A_\lambda [e_{b_\lambda}(T_1) - e_{b_\lambda}(T_2)] d\lambda;$$

$$A_\lambda = \frac{1}{1/\epsilon_{1_\lambda} + 1/\epsilon_{2_\lambda} - 2 + [1/(1 - \bar{\epsilon}_{m_\lambda}/2)]} \tag{6}$$

For $t_{L_\lambda} > 1$ we have

$$q_r(t_{L_\lambda} > 1) = -k_r \frac{dT}{dx}; \quad k_r = \frac{16\sigma T^3}{3K_{a_R}};$$

$$\frac{1}{K_{a_R}} = \int_{\lambda, t_{L\lambda} > 1} \frac{1}{\kappa_\lambda} \frac{\partial e_{b_\lambda}}{\partial e_b} d\lambda \Big/ \int_{\lambda, t_{L\lambda} \ge 1} \frac{\partial e_{b_\lambda}}{\partial e_b} d\lambda \tag{7}$$

Substituting Eqs. (7) into Eq. (3), using Fourier's law for q_c, and integrating yield

$$k_s(T_2 - T_1) + \frac{4\sigma(T_L^4 - T_0^4)}{3\bar{K}_{a_R}} = -[q - q_r(t_{L_\lambda} \le 1)]L \tag{8}$$

where $\bar{K}_{a_R}$ is the average value for K_{a_R}. The slip boundary conditions are given by Siegel and Howell (1981):

$$\frac{1}{\epsilon_{1_\lambda}} - \frac{1}{2} = \frac{e_{b\lambda 1} - e_{b\lambda}(0)}{q_{r_{\lambda 0}}}; \quad \frac{1}{\epsilon_{2_\lambda}} - \frac{1}{2} = \frac{e_{b\lambda}(L) - e_{b\lambda 2}}{q_{r_{\lambda L}}} \tag{9}$$

Integration of Eq. (9) with respect to wavelength over the ranges $t_{L_\lambda} > 1$ gives

$$q_{r_0} = A_1\sigma(T_1^4 - T_0^4); \quad q_{r_L} = A_2\sigma(T_L^4 - T_2^4) \tag{10}$$

where

$$A_1 = \int_{\lambda, t_{L\lambda} > 1} \frac{[e_{b\lambda}(T_1) - e_{b\lambda}(T_0)]/[e_b(T_1) - e_b(T_0)]}{1/\epsilon_{1_\lambda} - 1/2} d\lambda$$

$$\approx \int_{\lambda, t_{L\lambda} > 1} \frac{\partial e_{b_\lambda}(T_1)/\partial e_b(T_1)}{1/\epsilon_{1_\lambda} - 1/2} d\lambda \tag{11a}$$

$$A_2 = \int_{\lambda, t_{L\lambda} > 1} \frac{[e_{b\lambda}(T_L) - e_{b\lambda}(T_2)]/[e_b(T_L) - e_b(T_2)]}{1/\epsilon_{2_\lambda} - 1/2} d\lambda$$

$$\approx \int_{\lambda, t_{L\lambda} > 1} \frac{\partial e_{b_\lambda}(T_2)/\partial e_b(T_2)}{1/\epsilon_{2_\lambda} - 1/2} d\lambda \tag{11b}$$

From Eqs. (7) and (3), and noting that q = const, one obtains

$$q_{r_0} = \frac{q - q_r(t_{L_\lambda} \le 1)}{1 + k_s/k_r(T_0)}; \quad q_{r_L} = \frac{q - q_r(t_{L_\lambda} \le 1)}{1 + k_s/k_r(T_L)} \tag{12}$$

Combining Eqs. (10) and (12) gives

$$T_0^4 = T_1^4 - \frac{q - q_r(t_{L_\lambda} \le 1)}{[1 + k_s/k_r(T_0)]A_1\sigma};$$

$$T_L^4 = T_2^4 + \frac{q - q_r(t_{L_\lambda} \le 1)}{[1 + k_s/k_r(T_L)]A_2\sigma} \tag{13}$$

Substituting Eq. (13) into Eq. (8) gives

$$q = q_r(t_{L_\lambda} \le 1) + \frac{\sigma(T_1^4 - T_2^4) + k_s(T_1 - T_2)\frac{3}{4}\bar{K}_{a_R}}{\frac{3}{4}\bar{K}_{a_R}L + \frac{1}{A_1[1 + k_s/k_r(T_0)]} + \frac{1}{A_2[1 + k_s/k_r(T_L)]}} \tag{14}$$

Equations (13) and (14) are solved simultaneously to obtain T_0, T_L, and q. Note that Eq. (14) does not readily permit a determination of the separate conductive and radiative fluxes.

When $t_{L_\lambda} \le 1$ over the entire spectral range (optically thick, case II), $q_r(t_{L_\lambda} \le 1) = 0$, Eq. (14) reduces to

$$q = \frac{\sigma(T_1^4 - T_2^4) + k_s(T_1 - T_2)\frac{3}{4}\bar{K}_{a_R}}{\frac{3}{4}\bar{K}_{a_R}L + \frac{1}{A_1[1 + k_s/k_r(T_0)]} + \frac{1}{A_2[1 + k_s/k_r(T_L)]}} \tag{15}$$

where

$$A_1 \approx \int_0^\infty \frac{\partial e_{b_\lambda}(T_1)/\partial e_b(T_1)}{1/\epsilon_{1_\lambda} - 1/2} d\lambda;$$

$$A_2 \approx \int_0^\infty \frac{\partial e_{b_\lambda}(T_2)/\partial e_b(T_1)}{1/\epsilon_{2_\lambda} - 1/2} d\lambda;$$

$$\frac{1}{K_{a_R}} = \int_0^\infty \frac{1}{\kappa_\lambda} \frac{\partial e_{b_\lambda}}{\partial e_b} d\lambda \tag{16}$$

When $t_{L_\lambda} \le 1$ over the entire range (optically thin, case I), $1/K_{a_R} = 0$ and $k_r = 0$ (Eq. (7)); Eq. (14) reduces to

$$q = k_s(T_1 - T_2)/L + \int_0^\infty A_\lambda [e_{b_\lambda}(T_1) - e_{b_\lambda}(T_2)] d\lambda \tag{17}$$

Applications and Discussion

Silica aerogel is a microporous material made by supercritical extraction of the interstitial liquid from the voids of a colloidal gel of silica (Hunt et al., 1991). Bulk fused silica is opaque due to the fundamental Si-O molecular vibrations at about 9 and 21 μm; aerogel, which is composed primarily of silica and air, also absorbs strongly in these spectral regions. In the 3–6 μm range aerogel is almost transparent. Aerogel is highly porous with a porosity exceeding 90 percent. Due to its fine microstructure, which restricts the mean free paths of the gas molecules, and due to its low solid fraction, the thermal conductivity of aerogel is lower than that of still air even at atmospheric pressure (Zeng et al., 1994). As a result of its high void fraction and its inability to absorb photons over certain spectral ranges, the mean free paths of these photons can be large, and radiation can become an important mode of heat transfer relative to conduction even at moderate temperatures.

The approximate formulations developed in the previous section and the exact formulation (Özişik, 1973) may be used to calculate the heat flux through an aerogel slab comprised of both optically thin and thick spectral regions. First, one needs the absorption coefficient of the aerogel. Transmission data measured with a spectrophotometer were used to calculate the spectral absorption coefficient from Beer's law,

$$I_\lambda(x)/I_{0_\lambda} = \exp(-\kappa_\lambda x).$$

Silica aerogel has particles of size about 3–5 nm and pores of size 10–20 nm. These sizes are much smaller than infrared wavelength and therefore scattering in silica aerogel is negligible compared to absorption. The result for κ_λ for silica aerogel is shown in Fig. 1(*a*). It is seen that for a 1-cm-thick plate, aerogel is comprised of both optically thin and thick spectral regions. At a temperature of 725 K, most of the radiative energy ($\lambda_{max} = 4$ μm from Wien's law $\lambda_{max} T = 2898$ μm·K) will be transmitted through the aerogel with little extinction.

The result for the absorption coefficient, κ_λ (Fig. 1*a*), may be used to determine the heat flux, q, from Eq. (14). Calculations were carried out for a range of plate thicknesses for surface temperatures of 320 K and 280 K and surface emissivities of 0.8. The conductivity of aerogel due to conduction is 19.0 mW/m·K and the density is 0.135 g/cm^3 (Hartmann, 1986). The

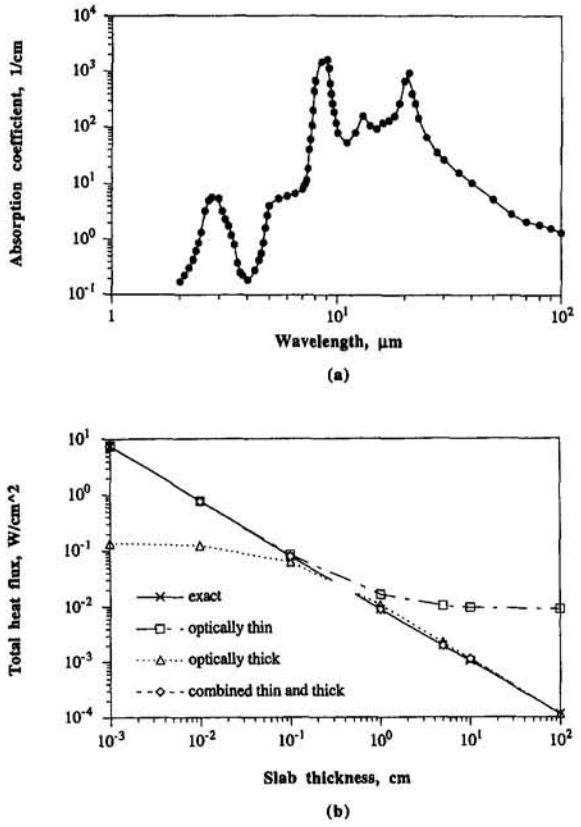

Fig. 1 (*a*) Spectral absorption coefficient of silica aerogel; (*b*) combined conductive and radiative heat flux in an aerogel slab

porosity of the aerogel is 0.94. The exact formulation for coupled conduction and radiation in an absorbing-emitting medium is solved by numerical integration using Simpson's rule, which has an accuracy for the temperature less than 0.1 percent (Lichtenstein, 1931; Crosbie and Viskanta, 1971).

The calculated heat fluxes are shown in Fig. 1(*b*). The combined thin and thick method gives good agreement with the exact results for all thicknesses, while the optically thin approximation is accurate only when the slab thickness is less than about 0.1 cm and the optically thick approximation is accurate only when the slab thickness is greater than about 10 cm. Note that the Rosseland mean absorption coefficient of the aerogel is 8.6 cm^{-1}. Note that for a 1-cm-thick aerogel plate ($t_L = \bar{K}_{a_R} \times L = 8.6$), there is still significant radiative transport through the 3–6 μm region.

Acknowledgments

This work was supported by the Assistant Secretary for Conservation and Renewable Energy, Advanced Industrial concepts (AIC) Materials Program of the Advanced Industrial Concepts Division, Office of Industrial Technologies of the U.S. Department of Energy under Contract No. DE-AC03-76F00098.

References

Brewster, M., 1992, *Thermal Radiative Transfer and Properties,* Wiley, New York, pp. 434–442.

Crosbie, A. L., and Viskanta, R., 1971, "Interaction of Heat Transfer by Conduction and Radiation in a Nongray Planar Medium," *Wärme- und Stoffübertragung,* Vol. 4, pp. 205–212.

Hartmann, J., 1986, "Thermal and Solar Optical Properties of Silica Aerogel," Lawrence Berkeley Laboratory Report LBL-22371.

Hunt, A. J., Jantzen, C. A., and Cao, W., 1991, "Aerogel—A High Performance Insulating Material at 0.1 Bar," *Insulation Materials: Testing and Applications,* Vol. 2, ASTM STP 1116, R. S. Graves and D. C. Wysocki, eds., American Society for Testing and Materials, Philadelphia, PA, pp. 455–463.

Lichtenstein, L., 1931, *Vorlesungen über einige Klassen Nichtlinearean Integralgleichungen und Integro-Differential Gleichungen,* Berlin.

Özişik, M. N., 1973, *Radiative Transfer,* Wiley, New York.

Scheuerpflug, P., Caps, R., Buettner, D., and Fricke, J., 1985, "Apparent Thermal Conductivity of Evacuated SiO_2—Aerogel Tiles Under Variation of Radiative Boundary Conditions," *International Journal of Heat and Mass Transfer,* Vol. 28, pp. 2299–2306.

Siegel, R., and Howell, J. R., 1981, *Thermal Radiation Heat Transfer,* 2nd ed., Hemisphere Publishing Corp., Washington, DC.

Zeng, S. Q., Hunt, A. J., Cao, W., and Greif, R., 1994, "Pore Size Distribution and Apparent Gas Thermal Conductivity of Silica Aerogel," ASME JOURNAL OF HEAT TRANSFER, accepted for publication.

Predictions of Void Fraction in Convective Subcooled Boiling Channels Using a One-Dimensional Two-Fluid Model

Lin-Wen Hu[1] and Chin Pan[1]

Nomenclature

A_{XS} = cross-sectional area, m^2
C_p = specific heat, J kg^{-1} K^{-1}
C_v = virtual mass force coefficient
D_h = channel diameter, m
D_b = bubble diameter, m
$F_{w,l}$ = liquid-wall friction force per unit volume, N m^{-3}
F_s = interfacial drag force, N m^{-3}
G = mass flux, kg m^{-2} s^{-1}
g = gravitational acceleration, m s^{-2}
h = enthalpy, J kg^{-1}
k = thermal conductivity, W m^{-1} K^{-1}
P = pressure, N m^{-2}
P_H = channel perimeter, m
$Q_{w,l}$ = heat transfer rate from wall to liquid per unit volume, J m^{-3} s^{-1}
q'' = heat flux, J m^{-2} s^{-1}
R = ideal gas constant for steam, J kg^{-1} K^{-1}
T = temperature, K
V = velocity, m s^{-1}
v = specific volume, m^3 kg^{-1}
x_t = true quality
Z = axial coordinate, m
α = void fraction
Γ = interfacial mass transfer rate per unit volume, kg m^{-3} s^{-1}
ΔT_{sat} = wall superheat, K
ΔT_{sub} = subcooling, K
λ = arbitrary constant in the virtual mass force
μ = viscosity, kg m^{-1} s^{-1}
ρ = density, kg m^{-3}
σ = surface tension, N m^{-1}
τ = shear stress, N m^{-2}

Subscripts

f = saturated liquid
fg = difference between saturated vapor and liquid

[1] Department of Nuclear Engineering, National Tsing Hua University, 101, Sect. 2, Kuang Fu Road, Hsinchu, Taiwan 30043.

Contributed by the Heat Transfer Division of THE AMERICAN SOCIETY OF MECHANICAL ENGINEERS. Manuscript received by the Heat Transfer Division March 1994; revision received November 1994. Keywords: Boiling, Forced Convection, Multiphase Flows. Associate Technical Editor: R. A. Nelson, Jr.

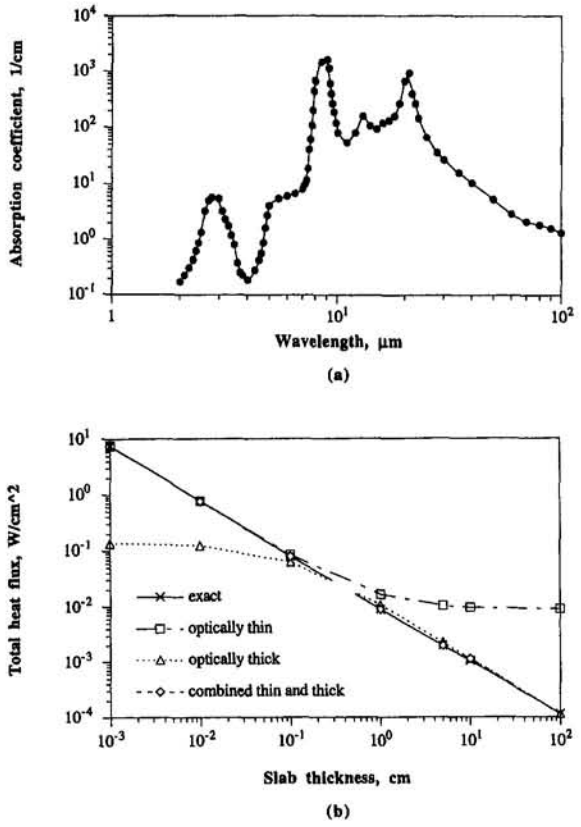

Fig. 1 (*a*) Spectral absorption coefficient of silica aerogel; (*b*) combined conductive and radiative heat flux in an aerogel slab

porosity of the aerogel is 0.94. The exact formulation for coupled conduction and radiation in an absorbing-emitting medium is solved by numerical integration using Simpson's rule, which has an accuracy for the temperature less than 0.1 percent (Lichtenstein, 1931; Crosbie and Viskanta, 1971).

The calculated heat fluxes are shown in Fig. 1(*b*). The combined thin and thick method gives good agreement with the exact results for all thicknesses, while the optically thin approximation is accurate only when the slab thickness is less than about 0.1 cm and the optically thick approximation is accurate only when the slab thickness is greater than about 10 cm. Note that the Rosseland mean absorption coefficient of the aerogel is 8.6 cm^{-1}. Note that for a 1-cm-thick aerogel plate ($t_L = \bar{K}_{a_R} \times L = 8.6$), there is still significant radiative transport through the 3–6 μm region.

Acknowledgments

This work was supported by the Assistant Secretary for Conservation and Renewable Energy, Advanced Industrial concepts (AIC) Materials Program of the Advanced Industrial Concepts Division, Office of Industrial Technologies of the U.S. Department of Energy under Contract No. DE-AC03-76F00098.

References

Brewster, M., 1992, *Thermal Radiative Transfer and Properties,* Wiley, New York, pp. 434–442.

Crosbie, A. L., and Viskanta, R., 1971, "Interaction of Heat Transfer by Conduction and Radiation in a Nongray Planar Medium," *Wärme- und Stoffübertragung,* Vol. 4, pp. 205–212.

Hartmann, J., 1986, "Thermal and Solar Optical Properties of Silica Aerogel," Lawrence Berkeley Laboratory Report LBL-22371.

Hunt, A. J., Jantzen, C. A., and Cao, W., 1991, "Aerogel—A High Performance Insulating Material at 0.1 Bar," *Insulation Materials: Testing and Applications,* Vol. 2, ASTM STP 1116, R. S. Graves and D. C. Wysocki, eds., American Society for Testing and Materials, Philadelphia, PA, pp. 455–463.

Lichtenstein, L., 1931, *Vorlesungen über einige Klassen Nichtlinearean Integralgleichungen und Integro-Differential Gleichungen,* Berlin.

Özişik, M. N., 1973, *Radiative Transfer,* Wiley, New York.

Scheuerpflug, P., Caps, R., Buettner, D., and Fricke, J., 1985, "Apparent Thermal Conductivity of Evacuated SiO_2—Aerogel Tiles Under Variation of Radiative Boundary Conditions," *International Journal of Heat and Mass Transfer,* Vol. 28, pp. 2299–2306.

Siegel, R., and Howell, J. R., 1981, *Thermal Radiation Heat Transfer,* 2nd ed., Hemisphere Publishing Corp., Washington, DC.

Zeng, S. Q., Hunt, A. J., Cao, W., and Greif, R., 1994, "Pore Size Distribution and Apparent Gas Thermal Conductivity of Silica Aerogel," ASME JOURNAL OF HEAT TRANSFER, accepted for publication.

Predictions of Void Fraction in Convective Subcooled Boiling Channels Using a One-Dimensional Two-Fluid Model

Lin-Wen Hu[1] and Chin Pan[1]

Nomenclature

A_{XS} = cross-sectional area, m^2
C_p = specific heat, J kg^{-1} K^{-1}
C_v = virtual mass force coefficient
D_h = channel diameter, m
D_b = bubble diameter, m
$F_{w,l}$ = liquid-wall friction force per unit volume, N m^{-3}
F_s = interfacial drag force, N m^{-3}
G = mass flux, kg m^{-2} s^{-1}
g = gravitational acceleration, m s^{-2}
h = enthalpy, J kg^{-1}
k = thermal conductivity, W m^{-1} K^{-1}
P = pressure, N m^{-2}
P_H = channel perimeter, m
$Q_{w,l}$ = heat transfer rate from wall to liquid per unit volume, J m^{-3} s^{-1}
q'' = heat flux, J m^{-2} s^{-1}
R = ideal gas constant for steam, J kg^{-1} K^{-1}
T = temperature, K
V = velocity, m s^{-1}
v = specific volume, m^3 kg^{-1}
x_t = true quality
Z = axial coordinate, m
α = void fraction
Γ = interfacial mass transfer rate per unit volume, kg m^{-3} s^{-1}
ΔT_{sat} = wall superheat, K
ΔT_{sub} = subcooling, K
λ = arbitrary constant in the virtual mass force
μ = viscosity, kg m^{-1} s^{-1}
ρ = density, kg m^{-3}
σ = surface tension, N m^{-1}
τ = shear stress, N m^{-2}

Subscripts

f = saturated liquid
fg = difference between saturated vapor and liquid

[1] Department of Nuclear Engineering, National Tsing Hua University, 101, Sect. 2, Kuang Fu Road, Hsinchu, Taiwan 30043.

Contributed by the Heat Transfer Division of THE AMERICAN SOCIETY OF MECHANICAL ENGINEERS. Manuscript received by the Heat Transfer Division March 1994; revision received November 1994. Keywords: Boiling, Forced Convection, Multiphase Flows. Associate Technical Editor: R. A. Nelson, Jr.

g = saturated vapor
i = interface
in = channel inlet
l = liquid
ld = net vapor generation point
v = vapor
w = wall

1 Introduction

Subcooled nucleate boiling under forced convective conditions is of considerable interest for many disciplines, such as nuclear reactor technology and other energy conversion systems, due to its high heat transfer capability. For such applications, the liquid entering the heating channel is usually in a subcooled state and nucleate boiling is initiated at some distance from the entrance. Further downstream from the boiling incipient point, the bubbles may depart from the heating wall. The point of first bubble departure is called the net vapor generation (NVG) point, because after this point, significant void is present in the subcooled liquid and the void fraction rises very rapidly even though the bulk liquid may still be in a highly subcooled state. The presence of vapor bubbles, which are at a temperature near the saturation temperature, in a subcooled liquid shows the existence of thermal nonequilibrium, which complicates the analysis of this boiling regime.

With progress in the two-phase flow modeling, it becomes possible to investigate the two-phase flow characteristics in a boiling channel by solving the conservation equations. The present study adopts a one-dimensional two-fluid model and employs a computer subroutine in the literature (Kahaner et al., 1989) to predict the two-phase flow characteristics, especially the void fraction distribution in a boiling channel with subcooled boiling. The predictions of void fraction are compared with two well-known void profile-fit models in the literature, i.e., Levy's (Levy, 1967) and Saha/Zuber's (Saha and Zuber, 1974) models, and a data bank covering a wide range of experimental conditions.

2 Model

The present study treats the fluid flow in front of the point of NVG as single-phase flow and two-phase flow afterward. Thus, the conservation equations are written for each region separately.

2.1 Conservation Equations. For the single-phase region, the standard one-dimensional conservation equations are used. For the two-phase region, the following assumptions are made to simplify the problem:

(a) The vapor temperature is equal to the saturation temperature.
(b) Vapor and liquid densities are functions of system pressure only and are considered as constants at a given system pressure.
(c) All heat input from the heating wall is first transferred to liquid phase only. A fraction of this energy is then transferred from the liquid phase to the vapor phase by interfacial energy transfer.
(d) Consistent with the assumption above, wall friction is exerted on the liquid phase only.

The steady-state, one-dimensional, two-fluid, two-phase flow model is as follows:

Conservation of mass for phase k:

$$\frac{d}{dZ}(\alpha_k \rho_k V_k) = \Gamma_k, \quad k = l \text{ or } v \tag{1}$$

Conservation of momentum: The mixture momentum equation for the two-fluid model can be obtained by summing up the phasic momentum equations as:

$$\alpha\rho_g V_v \frac{dV_v}{dZ} + (1-\alpha)\rho_f V_l \frac{dV_l}{dZ} = \Gamma_v(V_l - V_v) - \frac{dP}{dZ} - [\alpha\rho_g + (1-\alpha)\rho_f]g - F_{w,l} \tag{2}$$

The other momentum equation can be obtained by eliminating dP/dZ from the phasic momentum equations and inserting the expression for the virtual mass force (No and Kazimi, 1985) as:

$$A_v \frac{dV_v}{dZ} + A_l \frac{dV_l}{dZ} = \Gamma_v[V_i - \alpha V_l - (1-\alpha)V_v] - F_s + (1-\alpha)\alpha(\rho_f - \rho_g)g + \alpha F_{w,l} \tag{3}$$

where

$$A_v = [(1-\alpha)\alpha\rho_g + \alpha\rho_f C_v(\lambda - 1)]V_v - \alpha\rho_f C_v(\lambda - 2)V_l \tag{4}$$

$$A_l = -[(1-\alpha)\alpha\rho_f - \alpha\rho_f C_v(\lambda - 1)]V_l - \alpha\rho_f C_v(\lambda - 2)V_v \tag{5}$$

Conservation of liquid energy:

$$\rho_f \frac{d}{dZ}[(1-\alpha)h_l V_l] = \frac{P_H q''}{A_{xs}} - \Gamma_v h_g \tag{6}$$

Here the interfacial energy transfer has been included implicitly in the energy equation.

2.2 Constitutive Equations. Well-known constitutive equations, listed in Table 1, have been selected for the present study. Moreover, the interfacial velocity (Vi) is assumed to be equal to the vapor phase velocity. The inclusion of the virtual mass term is found to have only a minor effect on the result (Hu, 1991); therefore, it is not listed in Table 1. With the assumption of no direct momentum exchange between vapor flow and wall, the liquid–wall friction force, $F_{w,l}$, can be evaluated by the following equation:

$$F_{w,l} = -\left(\frac{dP}{dZ}F\right)_{2\phi} = -\left(\frac{dP}{dZ}F\right)_{fo}\phi_{fo}^2 \tag{7}$$

where ϕ_{fo}^2 is the two-phase frictional multiplier, which is evaluated by using the Chisholm (1973) correlation (see Table 1).

2.3 Boundary Conditions. At the channel inlet, the subcooled liquid is at a given velocity and enthalpy. At the NVG point, which is determined by the model developed by Saha and Zuber (1974, see Table 1), it is assumed that the slip ratio is only 0.1 percent greater than unity. A value of one for the slip ratio will introduce a singularity at this point in evaluating the drag coefficient (see Table 1) and is thus avoided. The void fraction at the point of NVG can be evaluated by the following equation based on the active nucleation site density:

$$\alpha = \frac{N_b(\pi D_h dZ)\frac{4}{3}\pi r_{b,ld}^3}{\frac{1}{4}\pi D_h^2 dZ} = \frac{16}{3}\frac{\pi N_b r_{b,ld}^3}{D_h} \tag{8}$$

where N_b is the population density of active nucleation sites and $r_{b,ld}$ is the bubble radius at the point of NVG. The equation obtained by Kocamustafaogullari and Ishii (1983) is used to evaluate N_b (see Table 1). In the present study, an equation

Table 1 Constitutive equations in the conservation equations and boundary conditions

Constitutive equations	Reference/Comments
• Vapor generation rate $\Gamma_v = \frac{P_h q''}{A_{xs}} \frac{\rho_g(h_l - h_{ld})}{(h_f - h_{ld})[\rho_g h_{fg} + \rho_f(h_f - h_l)]}$ $- \frac{H_o \alpha}{v_{fg} C_{pf}} (h_f - h_l)$	Lahey and Moody (1979) $H_o = 0.075$ (°C sec)$^{-1}$ for void data of interest to BWR technology
• Interfacial drag force $F_s = \frac{1}{8} a_i C_D \rho_f (V_v - V_l) \lvert V_v - V_l \rvert$ for bubbly and slug flow, $a_i = \frac{4.5}{D_h} \frac{\alpha - \alpha_{gs}}{1 - \alpha_{gs}} + \frac{6\alpha_{gs}}{D_b} \frac{1 - \alpha}{1 - \alpha_{gs}}$ $\alpha_{gs} = \min(\alpha, 0.25)$ $C_D = 24(1 + 0.1 Re_m^{0.75})/Re_m$ $Re_m = \rho_f D_h (1 - \alpha)(V_v - V_l)/\mu_f$	Ishii and Mishima (1984) The correlation has been extensively tested against a wide range of data (Ishii and Mishima, 1984) and is better than the existing correlations.
• Bubble diameter $D_b = \frac{D_{b,ld}}{\alpha_{ld}^{0.5}} \alpha^{0.5}$	Roy et al. (1988) $D_{b,ld}$ and α_{ld} refer to the bubble diameter and void fraction at the NVG point.
• Two-phase frictional multiplier $\phi_{fo}^2 = 1 + (I^2 - 1)[Bx^{(2-n)/2}(1 - x_t)^{(2-n)/2} + x_t^{2-n}]$ $I = (\rho_f/\rho_g)^{0.5}(\mu_g/\mu_f)^{n/2}$ I: 9.5 < I < 28, G ≤ 600: B = 520/I G$^{0.5}$; G > 600: B = 21/I I > 28: B = 15000/(I^2 G$^{0.5}$) n=0 is used for the present study. It may limit the present study for rough surfaces. However, it is found that the effect of the exponent, i.e., n=0 or 0.2, in subcooling regime is insignificant.	Chisholm (1973) "The correlation is a compromise between the correlations of Baroczy, Lockhart-Martinelli, and Chisholm such that the greatest estimate of pressure gradient will be obtained." (Chisholm, 1973)
• NVG point $h_{ld} = \begin{cases} 0.0022 \frac{q'' C_{pf} D_h}{k_f}, & Pe < 70000 \\ 154 \frac{q''}{\rho_f V_{in}}, & Pe > 70000 \end{cases}$ $Pe = G D_h C_{pf}/k_f$	Saha and Zuber (1974) The correlation was based on a data bank covering water, Freon-22, Freon-114 systems with pressures from 1.01 to 138 bars.
• Nucleation site density $N_b = D_F^2 R_{ce}^{*-4.4}[2.157 \times 10^{-7}(\rho^*)^{-3.2}(1 + 0.0049\rho^*)^{4.13}]$ $R_{ce}^* = \{2\sigma[1 + (\rho_g/\rho_f)/\rho_f]\}/(D_P/2)$ $/\{\exp[h_{fg}(T_g - T_{sat})/(R\, T_g T_{sat})] - 1\}$ $D_P = 0.0208\, \theta (\sigma/g\Delta\rho)^{1/2}$ $\rho^* = (\rho_f - \rho_g)/\rho_g$ $T_g = T_{sat} + S(T_w - T_{sat})$ and S is from Chen's correlation.	Kocamustafaogullari and Ishii (1983). The correlation was based on a data bank covering water on various heating surfaces with pressures from 1.01 to 107 bars. θ is the contact angle and θ = 60° is used for the present study.
• Wall shear stress in Eq.(10) $\tau_w = fG^2/\rho_f/8$ $f = 0.0055\{1 + [20000(\varepsilon/D_h) + 10^6/(GD_h/\mu_f)]^{1/3}\}$	Levy (1967). The channel relative roughness ε/D_h is taken to be 10^{-4} (same as that used by Levy).

with modified empirical constants from Levy's model, which was obtained on a sound physical basis, is adopted for $r_{b,ld}$:

$$r_{b,ld} = 0.039 \frac{(\sigma D_h \rho_f)^{1/2}}{\mu_f} \left[1 + 0.98 g \frac{(\rho_f - \rho_g) D_h}{\tau_w}\right]^{-1/2} \quad (9)$$

where the wall shear stress, τ_w, is evaluated based on the friction factor equation suggested by Levy (1967) (see Table 1). The new set of empirical constants is obtained by the least-square fitting of Levy's model from the data (of NVG point). Levy's equation with modified empirical constants results in better prediction than the original one (Hu, 1991).

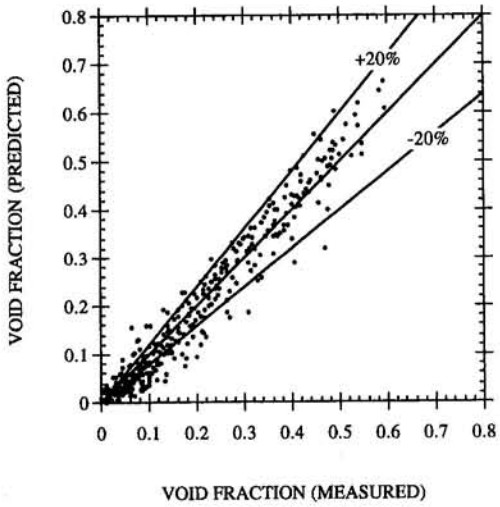

Fig. 1 Overall comparison of present model with experimental data

3 Solving Methodology

The model developed in the previous section constitutes a nonlinear, nonhomogeneous system of ordinary differential equations. To solve the equations, the system is transferred from its original implicit form to its explicit form at first. The system of explicit equations is then solved by using the subroutine SDRIV2 (Kahaner et al., 1989). The integration method adopted by the routine dynamically selects the Adams method when the problem is nonstiff and the Gear method when the problem is stiff. The relative accuracy for the solution requested for this study is 10^{-6}.

4 Results and Discussion

A data bank consisting of the work of Christensen (1961) and Bartolomei et al. (1982) is established for comparison. The data bank covers a wide range of experimental conditions as follows: $2.76 \times 10^6 \le P(\mathrm{N/m^2}) \le 14.99 \times 10^6$; $0.213 \times 10^6 \le q''(\mathrm{J/m^2\ s}) \le 2.21 \times 10^6$; $0.546 \le V_{in}\ (\mathrm{m/s}) \le 3.49$; $8.7 \le \Delta T_{sub,in}\ (\mathrm{K}) \le 137$. The uncertainty in the void fraction data of Bartolomei et al. (1982) is not higher than 0.01. Direct comparisons among predictions of the present model, Levy's model, and Saha/Zuber's model respectively, with each of the 26 sets of data of void fraction distribution are given by Hu (1991).

Overall comparisons of the present model, Levy's model, and Saha/Zuber's model predictions, respectively, with experimental data of void fraction apart from the NVG point are shown in Figs. 1, 2, and 3, respectively. Some of the experimental data, which are in the wall voidage region between the boiling incipience point and the NVG point, are disregarded. The present model treats the fluid in the upstream of the NVG point as the single-phase flow; therefore, such data are considered as being out of the scope of the present and the other two models in the literature. As a result, the present model and Saha/Zuber's model have the same data points for comparison (330 points) because both models use the same bubble departure model, while Levy's model has fewer experimental data points (313 points) for comparison. It can be seen from these figures that the present model significantly prevails over Levy's and Saha/Zuber's model. Predictions of the present model are quite satisfactory. Most of the discrepancies between the present model predictions and data occur at the region of low void

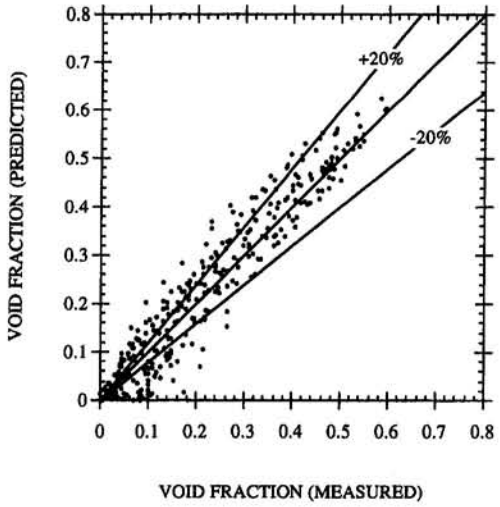

Fig. 2 Overall comparison of Levy's model prediction with experimental data

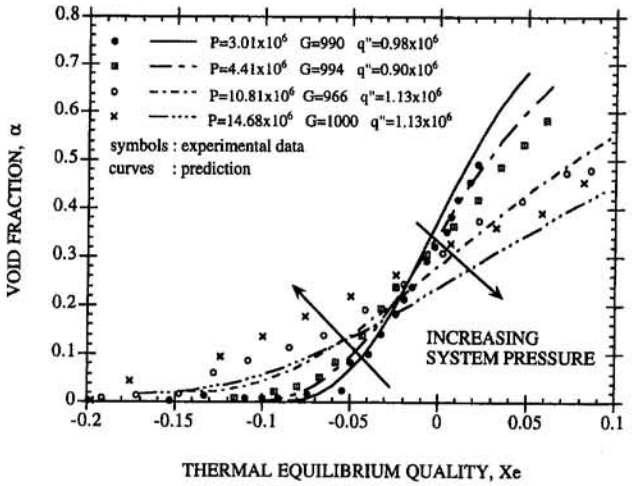

Fig. 4 Effect of system pressure on void fraction distribution

fractions. For the other two models, large discrepancies are also present at low void fractions; moreover, Levy's model shows significant discrepancies at intermediate void fractions too and Saha/Zuber's model tends to overestimate in this region and for even higher void fractions. As had been reported previously by Ahmad (1970), the results predicted by Levy's NVG model were unsatisfactory for low mass flow rates. It is also found in this study that Levy's model deviates significantly from the experimental data at high mass flow rates (Hu, 1991). On the other hand, Saha/Zuber's model shows significant discrepancies under low system pressures, i.e., lower than 5 MPa (Hu, 1991); for these cases the profile fit apparently overestimates the void fraction rise in the axial direction.

4.2 Some Parameter Effects on the Void Fraction Predictions. The present model is able to predict the effects of mass flux and heat flux on the void fraction distribution and show the same trend as experimental data (Hu, 1991), i.e., the void fraction decreases with increasing mass flux or decreasing heat flux at a given thermal equilibrium quality.

The present model is also able to predict the system pressure effect. Figure 4 shows the system pressure effect on void fraction profile. In the predictions of the present model, parameters other than system pressure also varied slightly to comply with the experimental conditions of Bartolomei et al. (1982) as indicated on the figure.

Since the latent heat of evaporation increases with decreasing system pressure, both Saha/Zuber's and Levy's NVG models predict that the NVG point occurs at a greater thermal equilibrium quality for a lower pressure system. The vapor generation rate keeps almost the same profile after the NVG point for each case since the heat flux remains constant. Although the liquid/vapor enthalpy difference (latent heat of evaporation) decreases with increasing system pressure, the change of latent heat of evaporation is negligible comparing to the change of density ratio. A certain vapor generation (mass) rate leads to a different void fraction depending on the corresponding vapor–liquid density ratio, i.e., the system pressure. Thus what results in a rapid increase of void fraction in a low pressure system is that the vapor–liquid density ratio is much higher than that of a high-pressure system. The same trend of the pressure effect on experimental data has also been reported by Zielke et al. (1980).

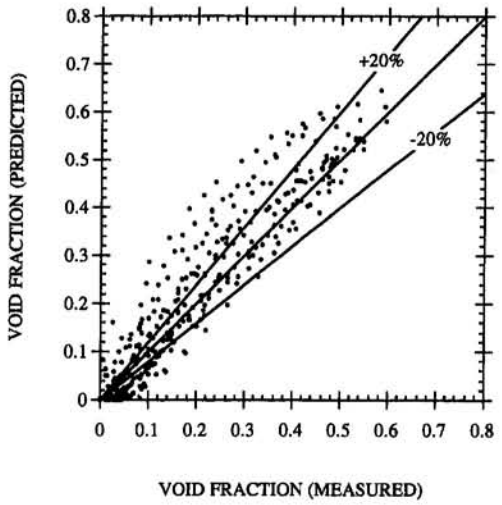

Fig. 3 Overall comparison of Saha/Zuber's model prediction with experimental data

5 Conclusions

The present paper adopts a steady-state, one-dimensional, two-fluid model to investigate the steady two-phase flow characteristics in a subcooled boiling channel. A computer program of general purpose, which is easy to program and to use, is then employed for the solution. Predicted results of void fractions of the present model agree reasonably well with experimental data in a wide range of experimental conditions. The agreement is much better than the semi-empirical correlations in the literature. The effects of mass flux, heat flux, and system pressure on the void fraction profile are also predicted satisfactorily.

Acknowledgments

This study was supported by the Atomic Energy Council of the Republic of China.

References

Ahmad, S. Y., 1970, "Axial Distribution of Bulk Temperature and Void Fraction in a Heated Channel With Inlet Subcooling," ASME JOURNAL OF HEAT TRANSFER, Vol. 92, pp. 595–609.

Bartolomei, G. G., Brantov, V. G., Molochnikov, Yu. S., Kharitonov, Yu. V., Solodkii, V. A., Batashova, G. N., and Mikhalov, V. N., 1982, "An Experimental Investigation of True Volumetric Vapour Content With Subcooled Boiling in Tube," *Thermal Engineering*, Vol. 29, pp. 132–135.

Chisholm, D., 1973, "Pressure Gradients Due to Friction During the Flow of Evaporating Two-Phase Mixtures in Smooth Tubes and Channels," *Int. J. Heat Mass Transfer*, Vol. 16, pp. 347–358.

Christensen, H., 1961, "Power-to-Void Transfer Functions," ANL-6385.

Hu, L.-W., 1991, "Steady Two-Phase Flow Characteristics in a Boiling Channel," M.S. Thesis, Department of Nuclear Engineering, National Tsing Hua University, Taiwan.

Ishii, M., and Mishima, K., 1984, "Two-Fluid Model for Hydrodynamic Constitutive Relations," *Nuclear Engineering and Design,* Vol. 82, pp. 107–126.

Kahaner, D., Molder, C., and Nash, S., 1989, *Numerical Methods and Software,* Prentice-Hall, Englewood Cliffs, NJ.

Kocamustafaogullari, G., and Ishii, M., 1983, "Interfacial Area and Nucleation Site Density in Boiling Systems," *Int. J. Heat Mass Transfer,* Vol. 26, pp. 1377–1387.

Lahey, R. T., Jr., and Moody, F. J., 1979, *The Thermal Hydraulics of a Boiling Water Nuclear Reactor,* American Nuclear Society, La Grange Park, IL.

Levy, S., 1967, "Forced Convective Subcooled Boiling—Prediction of Vapor Volumetric Fraction," *Int. J. Heat Mass Transfer,* Vol. 10, pp. 951–965.

No, H. C., and Kazimi, M. S., 1985, "Effects of Virtual Mass on the Mathematical Characteristics and Numerical Stability of the Two-Fluid Model," *Nuclear Science and Engineering,* Vol. 89, pp. 197–206.

Roy, R. P., Dykhuizen, R. C., Su, M. G., and Jain, P., 1988, "The Stability Analysis Using Two Fluids (SAT™) Code for Boiling Flow Systems," EPRI NP-6103-CCM.

Saha, P., and Zuber, N., 1974, "Point of Net Vapor Generation and Vapor Void Fraction in Subcooled Boiling," *Proc. Fifth Int. Heat Transfer Conf.,* Tokyo, Vol. 4.

Zielke, L. A., Grant, K. W., and Mackinnon, J. G., 1980, "Subchannel Thermal-Hydraulic Experimental Program (STEP)," EPRI NP-1493.

Phase Transformation in Materials With Nonuniform Phase Transition Temperatures

Jen Shin Hong[1,3] **and B. Rubinsky**[2,3]

Nomenclature

- Bi = hD/k_s = Biot number
- D = half slab thickness, m
- h = heat transfer coefficient, W/m^{2}K
- k = thermal conductivity, W/mK
- $\bar{k}$ = k_s/k_l dimensionless thermal conductivity
- L = latent heat of fusion, J/kg
- s = distance of change of phase interface from the center of the slab
- S = s/D dimensionless distance of change of phase interface
- Ste = $c(T_\infty - T_{ph1})/L$ = Stefan number
- t = time, s
- T = temperature, K
- T_{ph1} = phase transition temperature on outer surface, K
- T_{ph2} = phase transition temperature in center of slab, K
- x = rectangular coordinates, m
- α = thermal difussivity, m^2/s
- $\bar{\alpha}$ = α_s/α_l = dimensionless thermal diffusivity
- θ = $(T - T_\infty)/(T_\infty - T_{ph1})$ = dimensionless temperature
- ξ = x/D =dimensionless = dimensionless space variable
- ψ = $(T_{ph1} - T_{ph2})/(T_\infty - T_{ph1})$ = dimensionless melting point difference
- τ = $\alpha_l t/D^2$ = dimensionless time

Subscripts

- l = liquid phase
- ph = phase transition
- s = solid phase
- ∞ = free-stream conditions

Introduction

Every-day experience teaches that when energy is applied to the exterior of a solid, the solid will melt from the exterior inward. The melting of a solid from the exterior inward sometimes has undesirable effects. In energy storage, materials used to store energy must be confined in containers because they loose structural integrity upon melting. The inconvenience of ice cream melting on the way from the supermarket and the health threat of frozen foods partially melting from the exterior during transportation are other examples of undesirable effects. We have found a method through which solids can be made to melt from their interior outward while inhibiting melting from the exterior. This can be achieved using chemical additives that lower colligatively the phase transition temperature in the core of the solid. Here we use a mathematical study to introduce the method.

Analysis

To illustrate the technique by which a solid can be made to melt from its interior outward, we analyze the melting of a material with a slab like geometry. In the analysis it is assumed that solutes have been added to the material in the slab to modify colligatively the local change of phase temperature in such a way that the change of phase temperature in the center of the slab is lower than on the outer surfaces. The change of phase temperature varies linearly from T_{ph1} on the outer surface to T_{ph2} in the center of the slab,

$$T_{ph}(x) = T_{ph2} + (T_{ph1} - T_{ph2})\frac{x}{D} \tag{1}$$

where the coordinates origin is in the center of the slab. There is symmetry along the center of the slab.

The problem is formulated in terms of the following dimensionless variables and parameters:

$$\theta = \frac{T - T_\infty}{T_\infty - T_{ph1}}, \quad \psi = \frac{T_{ph1} - T_{ph2}}{T_\infty - T_{ph1}}, \quad \mathrm{Bi} = \frac{hD}{k_s},$$

$$\mathrm{Ste} = \frac{c(T_\infty - T_{ph1})}{L}, \bar{k} = \frac{k_s}{k_l}, \quad \bar{\alpha} = \frac{\alpha_s}{\alpha_l},$$

$$\tau = \frac{\alpha_l t}{D^2}, \quad \xi = \frac{x}{D}, \tag{2}$$

The analysis assumes that the slab is initially at the phase transition temperature, and is exposed to convection heat transfer on the outer surfaces. The energy equations in the solid and liquid regions are given by,

$$\frac{\partial^2 \theta_i}{\partial \xi^2} = \frac{\alpha_l}{\alpha_i}\frac{\partial \theta_i}{\partial \tau}, \tag{3}$$

where $i = s, l$, for the solid and liquid phases respectively.

The initial condition is

$$\theta(\xi, 0) = \xi\psi - \psi - 1 \tag{4}$$

and the boundary conditions are

$$\frac{\partial \theta_i}{\partial \xi} = \mathrm{Bi}\,\frac{k_s}{k_i}\,\theta_i, \tag{5}$$

[1] Graduate Student.

[2] Professor; Fellow ASME; to whom correspondence should be addressed.

[3] Biomedical Engineering Laboratory, Department of Mechanical Engineering, University of California at Berkeley, Berkeley CA 94720.

Contributed by the Heat Transfer Division of THE AMERICAN SOCIETY OF MECHANICAL ENGINEERS. Manuscript received by the Heat Transfer Division April 1994; revision received October 1994. Keywords: Biotechnology, Phase-Change Phenomena, Thermal Energy Storage. Associate Technical Editor: A. Faghri.

Hu, L.-W., 1991, "Steady Two-Phase Flow Characteristics in a Boiling Channel," M.S. Thesis, Department of Nuclear Engineering, National Tsing Hua University, Taiwan.

Ishii, M., and Mishima, K., 1984, "Two-Fluid Model for Hydrodynamic Constitutive Relations," *Nuclear Engineering and Design,* Vol. 82, pp. 107–126.

Kahaner, D., Molder, C., and Nash, S., 1989, *Numerical Methods and Software,* Prentice-Hall, Englewood Cliffs, NJ.

Kocamustafaogullari, G., and Ishii, M., 1983, "Interfacial Area and Nucleation Site Density in Boiling Systems," *Int. J. Heat Mass Transfer,* Vol. 26, pp. 1377–1387.

Lahey, R. T., Jr., and Moody, F. J., 1979, *The Thermal Hydraulics of a Boiling Water Nuclear Reactor,* American Nuclear Society, La Grange Park, IL.

Levy, S., 1967, "Forced Convective Subcooled Boiling—Prediction of Vapor Volumetric Fraction," *Int. J. Heat Mass Transfer,* Vol. 10, pp. 951–965.

No, H. C., and Kazimi, M. S., 1985, "Effects of Virtual Mass on the Mathematical Characteristics and Numerical Stability of the Two-Fluid Model," *Nuclear Science and Engineering,* Vol. 89, pp. 197–206.

Roy, R. P., Dykhuizen, R. C., Su, M. G., and Jain, P., 1988, "The Stability Analysis Using Two Fluids (SAT™) Code for Boiling Flow Systems," EPRI NP-6103-CCM.

Saha, P., and Zuber, N., 1974, "Point of Net Vapor Generation and Vapor Void Fraction in Subcooled Boiling," *Proc. Fifth Int. Heat Transfer Conf.,* Tokyo, Vol. 4.

Zielke, L. A., Grant, K. W., and Mackinnon, J. G., 1980, "Subchannel Thermal-Hydraulic Experimental Program (STEP)," EPRI NP-1493.

Phase Transformation in Materials With Nonuniform Phase Transition Temperatures

Jen Shin Hong[1,3] **and B. Rubinsky**[2,3]

Nomenclature

Bi = hD/k_s = Biot number
D = half slab thickness, m
h = heat transfer coefficient, W/m^{2}K
k = thermal conductivity, W/mK
$\bar{k}$ = k_s/k_l dimensionless thermal conductivity
L = latent heat of fusion, J/kg
s = distance of change of phase interface from the center of the slab
S = s/D dimensionless distance of change of phase interface
Ste = $c(T_\infty - T_{ph1})/L$ = Stefan number
t = time, s
T = temperature, K
T_{ph1} = phase transition temperature on outer surface, K
T_{ph2} = phase transition temperature in center of slab, K
x = rectangular coordinates, m
α = thermal difussivity, m^2/s
$\bar{\alpha}$ = α_s/α_l = dimensionless thermal diffusivity
θ = $(T - T_\infty)/(T_\infty - T_{ph1})$ = dimensionless temperature
ξ = x/D =dimensionless = dimensionless space variable
ψ = $(T_{ph1} - T_{ph2})/(T_\infty - T_{ph1})$ = dimensionless melting point difference
τ = $\alpha_l t/D^2$ = dimensionless time

Subscripts

l = liquid phase
ph = phase transition
s = solid phase
∞ = free-stream conditions

Introduction

Every-day experience teaches that when energy is applied to the exterior of a solid, the solid will melt from the exterior inward. The melting of a solid from the exterior inward sometimes has undesirable effects. In energy storage, materials used to store energy must be confined in containers because they loose structural integrity upon melting. The inconvenience of ice cream melting on the way from the supermarket and the health threat of frozen foods partially melting from the exterior during transportation are other examples of undesirable effects. We have found a method through which solids can be made to melt from their interior outward while inhibiting melting from the exterior. This can be achieved using chemical additives that lower colligatively the phase transition temperature in the core of the solid. Here we use a mathematical study to introduce the method.

Analysis

To illustrate the technique by which a solid can be made to melt from its interior outward, we analyze the melting of a material with a slab like geometry. In the analysis it is assumed that solutes have been added to the material in the slab to modify colligatively the local change of phase temperature in such a way that the change of phase temperature in the center of the slab is lower than on the outer surfaces. The change of phase temperature varies linearly from T_{ph1} on the outer surface to T_{ph2} in the center of the slab,

$$T_{ph}(x) = T_{ph2} + (T_{ph1} - T_{ph2})\frac{x}{D} \tag{1}$$

where the coordinates origin is in the center of the slab. There is symmetry along the center of the slab.

The problem is formulated in terms of the following dimensionless variables and parameters:

$$\theta = \frac{T - T_\infty}{T_\infty - T_{ph1}}, \quad \psi = \frac{T_{ph1} - T_{ph2}}{T_\infty - T_{ph1}}, \quad \mathrm{Bi} = \frac{hD}{k_s},$$

$$\mathrm{Ste} = \frac{c(T_\infty - T_{ph1})}{L}, \bar{k} = \frac{k_s}{k_l}, \quad \bar{\alpha} = \frac{\alpha_s}{\alpha_l},$$

$$\tau = \frac{\alpha_l t}{D^2}, \quad \xi = \frac{x}{D}, \tag{2}$$

The analysis assumes that the slab is initially at the phase transition temperature, and is exposed to convection heat transfer on the outer surfaces. The energy equations in the solid and liquid regions are given by,

$$\frac{\partial^2 \theta_i}{\partial \xi^2} = \frac{\alpha_l}{\alpha_i}\frac{\partial \theta_i}{\partial \tau}, \tag{3}$$

where $i = s, l$, for the solid and liquid phases respectively.

The initial condition is

$$\theta(\xi, 0) = \xi\psi - \psi - 1 \tag{4}$$

and the boundary conditions are

$$\frac{\partial \theta_i}{\partial \xi} = \mathrm{Bi}\,\frac{k_s}{k_i}\,\theta_i, \tag{5}$$

[1] Graduate Student.
[2] Professor; Fellow ASME; to whom correspondence should be addressed.
[3] Biomedical Engineering Laboratory, Department of Mechanical Engineering, University of California at Berkeley, Berkeley CA 94720.

Contributed by the Heat Transfer Division of THE AMERICAN SOCIETY OF MECHANICAL ENGINEERS. Manuscript received by the Heat Transfer Division April 1994; revision received October 1994. Keywords: Biotechnology, Phase-Change Phenomena, Thermal Energy Storage. Associate Technical Editor: A. Faghri.

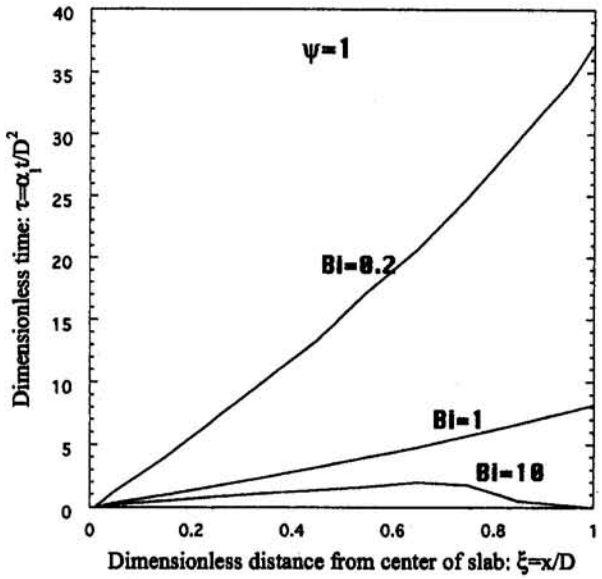

Fig. 1 Curves showing the dimensionless time at which melting occurs in the slab as a function of distance from the center of the slab to the exterior at $\xi = +1$, for various Biot numbers. The slab material has a variable change of phase temperature, $\psi = 1$. The various Biot numbers used in the analysis are indicated in the figure.

on the outer surfaces at $\xi = \pm 1$ and

$$\theta_{ph}(S, \tau) = S\psi - \psi - 1, \tag{6}$$

on the change of phase interface.

The energy balance on the change of phase interface is given by

$$\frac{1}{\text{Ste}} \frac{dS(\xi)}{d\tau} = \bar{k} \frac{\partial \theta_s}{\partial \xi} - \frac{\partial \theta_l}{\partial \xi} \tag{7}$$

The equations listed above can be solved with a standard method of solution using the enthalpy model and an Euler forward integration scheme. The energy equation in terms of enthalpy becomes

$$\frac{\partial^2 \theta_i}{\partial \xi^2} = \frac{\alpha_s}{\alpha_l} \frac{\partial H}{\partial \tau} \tag{8}$$

where

$$H = \frac{(\rho c)_l}{(\rho c)_s} \theta, \quad \theta(\xi) \le \theta_{ph}(\xi) H$$

$$= \frac{1}{\text{Ste}} + \theta, \quad \theta(\xi) \ge \theta_{ph}(\xi)$$

The enthalpy method is fully described in many texts, i.e., Lunardini (1981). The only difference between this paper and earlier studies is that here the change of phase temperature varies as a function of location (Eq. (6)).

The Euler forward integration scheme was implemented on a Spark 10 Sun Workstation and written in FORTRAN. The time stepping in this formulation is explicit and was chosen to satisfy the stability criterion (Lunardini, 1981). To verify the convergence of the results, a halving procedure was used both in time and space until the results ceased to be affected by the spatial and temporal discretization.

Results and Discussion

A numerical analysis was performed to study the effect of a spatially variable change of phase temperature on the melting process in a slab. The Stefan number in this analysis is 0.1.

Figure 1 shows the dimensionless time at which the material melts at different locations in the slab when the material of the slab has a spatially linear varying phase-change temperature with a $\psi = 1$, for various Biot numbers. The propagation of the change of phase interface is entirely different from that observed in conventional problems of heat transfer with phase transformation, which is from the exterior inward. For lower Biot numbers the melting starts first in the center of the slab and propagates toward the exterior. The velocity of the change of phase interface increases with an increase in the Biot numbers. For higher Biot numbers the melting starts in both the exterior and the interior of the slab, and the two change of phase interfaces propagate toward each other. The results demonstrate that in a solid with a locally variable phase-change temperature melting can start from the interior of the object outward or from both the interior and the exterior as a function of the Biot number of the problem.

Figure 2 shows the nondimensional temperature distribution in a slab with a material that has a linear change of phase temperature distribution, $\psi = 0.1$, and in which the melting is from the center of the slab outward. The Biot number is 0.2. The initial temperature is the local phase-change temperature, given by the heavy line in the figure. The melting process shown in Fig. 2 is unusual and starts at the inner core of the slab and propagates outward. (Regions in which the material has melted are those with temperatures higher than the local phase-change temperature, given by the heavy line in the figure.) It is evident that the outer surface of the slab remains frozen and actually drops to a temperature lower than the initial phase-change temperature at that location, while the melting interface propagates from the interior outward. The temperature distribution is unusual. For many instances in time the temperature distribution is made of three different segments. The first segment from the exterior of the slab is below the local change of phase temperature. The second segment coincides with the local change of phase temperature. The third segment, which starts from the location of the change of phase interface inward, is above the local change of phase temperature. This unusual temperature distribution can be used to explain why melting starts from the

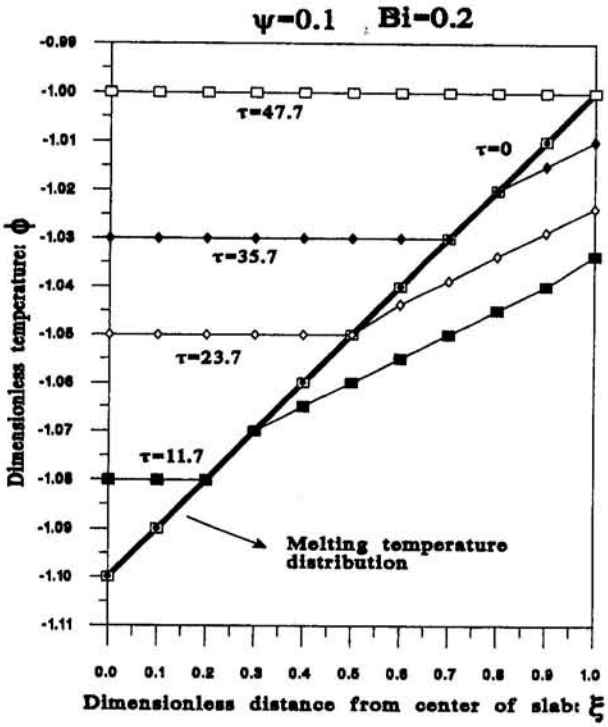

Fig. 2 Temperature distributions during the thawing of a slab that has a nonuniform change of phase temperature, $\psi = 0.1$, and is thawed with a Biot number of 0.2. The dimensionless times at which the different temperature profiles are plotted are given on the figure.

interior. The temperature at any location in the solid region cannot rise above the change of phase temperature unless sufficient energy is supplied for phase transformation and only after the phase transformation has occurred. It has been shown by Rubinsky and Cravalho (1979) that the temperature history during melting occurs in two different time scales. During the short time scale the temperature rapidly approaches the local change of phase temperature, and during the long time scale the temperature stays at the phase-change temperature until melting occurs. Therefore, during any melting process, the temperature at any location will rise first to the local change of phase temperature and stay at that temperature until local melting occurs. However, when the local change of phase temperature is not constant in space, a temperature gradient prescribed by the local change of phase temperature develops in the solid. Whenever a temperature gradient is established, heat moves along this temperature gradient. This temperature gradient enforced by the local change of phase temperature distribution will cause the melting to begin in the core of the slab, independent of the outer surface boundary conditions, whenever the outer surface temperature rises above the change of phase temperature in the core. For the low Biot number in Fig. 2, the energy transported from the interior along the temperature gradient enforced by the local change of phase temperature is greater than the outer surface heat flux and therefore the outer surface cannot melt. Numerical experiments show that melting will always start in the interior of a material with a variable local change of phase temperature of the type analyzed here and will propagate outward.

Figure 3 illustrates the mode of melting, from both the exterior and the interior when the Biot number is larger, 1.0. The heavier line is the original temperature distribution in the slab. Here the temperature profiles have also three segments. The first from the outer surface is above the local change of phase temperature, the second coincides with the local change of phase temperature, and the third is above the local change of phase temperature. The difference between the behavior in Figs. 2 and 3 is the higher Biot number. Melting occurs from the interior outward due to the temperature gradient imposed by the local change of phase temperature distribution (see middle temperature segment). However, in this case the heat flux on the outer surface is high enough to allow both removal of the energy brought from the interior along the local change of phase temperature gradient and melting from the outer surface also.

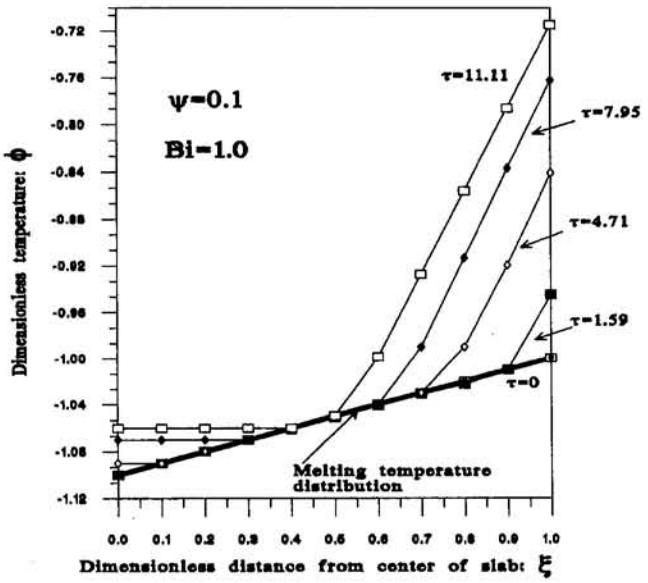

Fig. 3 Temperature distributions during the thawing of a slab that has a nonuniform change of phase temperature, ψ = 0.1, and is thawed with a Biot number of 1. The dimensionless times at which the different temperature profiles are plotted are given on the figure.

Conclusions

The analysis shown here demonstrates that during heat transfer with phase transformation, the process of phase transformation can start from the interior, outward when using materials with nonuniform change of phase temperatures. For higher Biot numbers the melting can also start simultaneously from both the interior and the exterior. This technology could become useful in controlling heat transfer with phase transformation for such applications as energy storage systems and frozen food transportation. For example, addition of sugar to the core of an ice cream block or addition of salt to the core of a block of meat can prevent melting on the outer surface during transportation.

References

Lunardini, V. J., 1981, *Heat Transfer in Cold Climates,* Litton Ed. Pub., Inc., New York.

Rubinsky, B., and Cravalho, E. G., 1979. "Analysis of the Temperature Distribution During the Thawing of a Frozen Biological Organ," *AIChE Symposium Series,* Vol. 75; pp. 81–88.